

Vol. 21, No. 1, March, 2022

ISSN (Print): 0972-6268; ISSN (Online) : 2395-3454

NATURE ENVIRONMENT & POLLUTION TECHNOLOGY

*A Multidisciplinary, International Journal
on Diverse Aspects of Environment*



Technoscience Publications

website: www.neptjournal.com



Technoscience Publications

A-504, Bliss Avenue, Balewadi,
Opp. SKP Campus, Pune-411 045
Maharashtra, India

www.neptjournal.com

Nature Environment and Pollution Technology

(An International Quarterly Scientific Research Journal)

EDITORS

Dr. P. K. Goel (Chief Editor)

Former Head, Deptt. of Pollution Studies
Y. C. College of Science, Vidyanagar
Karad-415 124, Maharashtra, India

Dr. K. P. Sharma

Former Professor, Deptt. of Botany
University of Rajasthan
Jaipur-302 004, India

Managing Editor : Mrs. Apurva Goel Garg, C-102, Building No. 12, Swarna CGHS, Beverly Park, Kanakia, Mira Road (E) (Thane) Mumbai-401107, Maharashtra, India

Published by : Mrs. T. P. Goel, Technoscience Publications, A-504, Bliss Avenue, Balewadi, Pune-411 045, Maharashtra, India

E-mail : contact@neptjournal.com; operations@neptjournal.com

INSTRUCTIONS TO AUTHORS

Scope of the Journal

The Journal publishes original research/review papers covering almost all aspects of environment like monitoring, control and management of air, water, soil and noise pollution; solid waste management; industrial hygiene and occupational health hazards; biomedical aspects of pollution; conservation and management of resources; environmental laws and legal aspects of pollution; toxicology; radiation and recycling etc. Reports of important events, environmental news, environmental highlights and book reviews are also published in the journal.

Format of Manuscript

- The manuscript (*mss*) should be typed in double space leaving wide margins on both the sides.
- First page of *mss* should contain only the title of the paper, name(s) of author(s) and name and address of Organization(s) where the work has been carried out along with the affiliation of the authors.

Continued on back inner cover...

Nature Environment and Pollution Technology

Vol. 21, No. (1), March 2022

CONTENTS

1. **Manli Lin, Hao Yu and Weihua Peng**, Hydrochemical Characteristics and Irrigation Water Evaluation of Suburban River: A Case Study of Suzhou City, Anhui Province, China 1-10
2. **Wenju Zhao, Yali Wang, Zongli Li and Taohong Cao**, Effect on Soil Hydrodynamic Parameters in Fields Mulched with Gravel for Different Periods of Time 11-20
3. **L. Balaji, M. Muthukannan and R. Kanniga Devi**, A GIS-Based Study of Air and Water Quality Trends in Madurai City, India 21-32
4. **Wenfeng Gong, Tiedong Liu, Tao Liu, Xuanyu Duan, Yueyang Liu and Philip Stott**, Land Use/Land Cover Evaluation Using Trajectory Maps Based on Landsat TM/OLI in Southwest China 33-40
5. **Paper retracted** 41-51
6. **O. D. Hajoeningtjas, I. Mansur, N. Ekowati and Tamad**, The Indigenous Arbuscular Mycorrhizal Fungi Consortium in Shallot Cultivation with Lead-Polluted Media 53-59
7. **Hai-Feng Huang and Ni Zhu**, Rural Financial Efficiency, Agricultural Technological Progress and Agricultural Carbon Emissions: Evidence from China 61-69
8. **V. Vinoth Kumar and G. Sasikala**, Internet of Things (IoT) Enabled Air Quality Monitoring System for Conventional and UAV Application 71-81
9. **Xiaojie Sun, Zhihan Tan, Xiaosong He, Hongxia Zhang, Beidou Xi, Hongtao Zhou and Hong Xiang Zhu**, Initial Active Phase of In-Vessel Composting of Sewage Sludge, Leaves and Rice Straw 83-90
10. **A. Kesavan, H. Kaur and S. Chaudhuri**, Unpacking Land Degradation Neutrality (LDN), An Emerging Paradigm to Conserve Land Systems' Sustainability in the 21st Century? Meta-analysis of Challenges and Opportunities 91-100
11. **Malsawmtuanga and Ch. Vabeihmo**, Assessment of Flood Hazard Zonation Using Geographic Information System and Analytical Hierarchy Process: A Case Study of Tlawng River Watershed in Sairang, Mizoram, India 101-109
12. **Frances Roi Seston Tampubolon, Arief Sabdo Yuwono, Armansyah Halomoan Tambunan and Noer Azam Achsani**, Process of Life Cycle Installation of Wastewater Treatment and up to Water Reuse 111-118
13. **Mei Yang, Yaojun Fan, Xiaoxue Zhang and Shoufeng Wu**, Time Series Analysis of Economic Growth, Environmental Conditions and Their Coordination Degree: A Case Study of Provinces in Northeast China 119-126
14. **Nitin Verma and Vivek Kumar**, Influence of Sugars, Sugar Alcohols and Their Combinations on Environmentally Significant Cellulase Production Under Liquid State Fermentation 127-139
15. **Bei Zhu, Shiyan Wang, Chang Liu, Wei Su, Jiapeng Wu, Cunwu Li and Jingshi Shang**, Impacts of Discharged Low-Temperature Water on Water Table and Temperature in the Riparian Zone 141-148
16. **Anu Bela Lakra, Suryapratap Ray and Tejasvi Bhatia**, Impact of Endocrine Disrupting Chemicals on Human Reproductive System: A Toxicological Perspective 149-157
17. **Shuang Li, Xiang Wu, Faming Sun, Jie Yang and Jian Li**, Environmental Geological Problems in Southwest China: A Case Study from the Researches of Regional Landslide Hazards 159-165
18. **Yeshi Choden, M. P. Sharma, Gaurav Pandey, S. K. Gupta and K. D. Dema**, Ecological Health Assessment of Renuka Lake, Himachal Pradesh, India 167-174
19. **S. Tshering and P. Rinzin**, Terrestrial Biomass and Carbon Stock in Broad-leaved Forests of Punakha District, Western Bhutan 175-181
20. **V. Murugesan, D. Joshua Amarnath and P. Shanmugam**, Investigation of Water Hyacinth in Anaerobic Co-Digestion for Biogas Production - A measure to Reduce Kosavampatti and Phoosur Lake Municipal Solid Waste Loading 183-191
21. **Hongbao Dai and Jiying Xu**, Application of UAV Photogrammetry on Ecological Restoration of Abandoned Open-pit mines, Northern Anhui Province, China 193-199
22. **Mohana Yadav, Sushil Manderia, Shweta Singh and Mohd. Adil Deva**, Isolation and Characterization of Polyvinyl Chloride (PVC) Degrading Bacteria from Polluted Sites of Gwalior City, M.P., India 201-207
23. **U. V. Aswathy, S. Abhirami, S. R. Flanet Raj and G. Prasad**, Tissue Repairing Activity of *Glycosmis pentaphylla* Leaf Extract on *Oreochromis mossambicus* Against Arsenic Induced Toxicity 209-215
24. **Megat Ahmad Kamal Megat Hanafiah, Nurul Amira Abu Bakar, Waheeba A. Al-Amrani, Shariff Ibrahim, Nik Ahmad Nizam Nik Malek and Ali H. Jawad**, Preparation, Characterization and Application of Sulphuric Acid-Treated Soursop (*Annona muricata L.*) Seeds Powder in the Adsorption of Cu(II) Ions 217-223
25. **Fenfen Xi, Liping Liang, Weishou Tan, Yanyan Dong, Linshuang Yu, Huiting Ma, Gaosheng Yue and Xu Meng**, Preparation of Copolymer of 2-Methacryloyloxyethyl-dimethyl-3-sulfonic Acid Propylammonium Hydroxide and 3-(Methacryloyloxy) Propyltrimethoxysilane and Its Dye Adsorption Properties 225-230

26. **G. Ayush, A. J. Elizabeth, V. V. Patil and M. Herlekar**, Noise Levels in Urban and Rural Settlements of Bhubaneswar: A Case Study 231-239
27. **M.A. López-Ramírez, C. Argüelles-López, M.R. Aguilar-Rodríguez, J. Barragán-Díaz, O.P. Castellanos-Onorio and F. Lango-Reynoso**The Effect of *Moringa oleifera* as a Primary Treatment in Urban Wastewater in Martínez De La Torre, Veracruz 241-246
28. **M. Jamuna, M. Gandhimathi, J. Abdul Bari and T. Niveditha**, Florida's Aquifer Vulnerability to Nitrate Contamination: A GIS Model 247-253
29. **S. B. Joshi and D. D. Kulkarni**, Use of Remote Sensing and GIS Techniques in Identification of Landslide Vulnerable Zones of Shastri River Basin Along the West Coast of Ratnagiri District, Maharashtra 255-262
30. **Erhui Zhao, Anjie Wang, LuoJia Huang, Chengguang Chen and Muqing Qiu**, Mechanism and Chemical Stability of U(VI) Removal by Magnetic Fe₃O₄@Biochar Composites 263-268
31. **Aping Chang, Hua Qiong and Zheng Binguo**, Analysis of Agricultural Non-point Source Pollution in Henan Province (China) from the Perspective of Time and Space 269-274
32. **Resmi G. and Vinod V.**, Development and Fabrication of A Portable Shredding Machine for Rapid Composting of Organic Waste 275-281
33. **Gnanasekaran Sasikumar, A. Sivasangari and N.Venkatachalam**, Application of Analytical Hierarchy Process (AHP) for Assessment of Collection and Transportation of Solid Waste: An Empirical Study 283-288
34. **R. Abirami and S. P. Sangeetha**, Effect of Surface Modification on the Characteristics of Sisal Fiber Reinforced Concrete Treated with Na₂CO₃ 289-295
35. **Ji He, Xiao-Ling Hou and Wen-chuan Wang**, Study of Water Quality Pollution Index, Land-Use and Socio-Economic Factors in Yingkou Irrigation District of China Based on Redundancy Analysis 297-302
36. **O. M. Abioye, K. A. Adeniran and T. Abadunmi**, Poultry Wastes Effect on Water Quality of Shallow Wells of Farms in Two Locations of Kwara State, Nigeria 303-308
37. **Zizhen Zhou, Yu Xu and Zhen Dai**, Pollution Characteristics of Surface Sediments in Luhun Drinking Water Reservoir in the Middle China 309-313
38. **Huifen Luo and Junlin Wu**, Exploring the Spatial Pattern of Damage Caused by Typhoon Meranti on the Urban Green Space on Xiamen Island 315-319
39. **Sneh Lata and Sukhminderjit Kaur**, Evolution of Technologies for Cadmium Remediation and Detoxification 321-330
40. **M. Sh. Aswood, Sh. F. Alhous and S. A. Abdulridha**, Life Time Cancer Risk Evaluation Due to Inhalation of Radon Gas in Dwellings of Al-Diwaniyah Governorate, Iraq 331-337
41. **R. Purbakawaca, A.S. Yuwono, I.D.M. Subrata and H. Alatas**, Low-Cost Calibration MOS Gas Sensor for Measuring SO₂ Pollutants in Ambient Air 339-347
42. **Y. Wang, F.W. Wang, M.F. Jia, L.N. Huang, Y.Q. He and S.Q. Dong**, Rapid Extraction of Yam Peel Total Flavonoids in A Cholinium-Based Magnetic Ionic Liquid Aqueous Biphasic System 349-354
43. **Mohammed A. Atiya, Ahmed K. Hassan and Imad M. Luaibi**, Green Synthesis Of Bimetallic Iron/Copper Nanoparticles Using Ficus Leaves Extract For Removing Orange G (OG) Dye From Aqueous Medium 355-365
44. **K.Q. Zhang, X.C. Yang, Z. Shen, L.Y. Ma, J. Duan and Y. Li**, Properties and Distribution of Seed Banks in a Black Locust (*Robinia pseudoacacia*) Plantation in Central China 367-376
45. **Yu Li, Yuran Su, Bin Hu and Chuang Ma**, Insight into Effects of Initial Moisture Content on the Heat-Up of Sewage Sludge Composting During Mesophilic Phase 377-383
46. **Silin Yang, Pengrui Du, Yungen Liu, Yan Wang, Rong Ma and Yunhui Gong**, The Effects of Disturbance on the Release of Nitrogen and Phosphorus from Sediment in Rural Ditches 385-391
47. **Wei Liu, Fuji Chen and Yihui Chen**, PM2.5 Concentration Prediction Based on Pollutant Pattern Recognition Using PCA-clustering Method and CS Algorithm Optimized SVR 393-403
48. **Yonghong Zheng, Zhiguo Zhang, Yongchun Chen, Shikai An, Lei Zhang, Fangling Chen, Chengnan Ma and Weiqing Cai**, Influence of Dissolved Organic Carbon on the Adsorption and Desorption of Cadmium in Reclaimed Soil 405-412
49. **Jiyang Cai**, Application of KOH-ethanol Solution in Separation of Waste Photovoltaic Panels 413-420

The Journal
is
Currently
Abstracted
and
Indexed
in:

Scopus CiteScore (2020) = 0.6

Ulrich's (Refereed) database

Zetoc

J-Gate

Centre for Research Libraries

Connect Journals (India)

Research Bible (Japan)

Elektronische
Zeitschriftenbibliothek (EZB)

CNKI Scholar (China National
Knowledge Infrastructure)

AGRIS (UN-FAO)

CNKI Scholar (China National Knowledge Infrastructure)

Scopus CiteScore (2020) 0.60

Scopus®, SJR (0.154) 2020

Chemical Abstracts, U.S.A.

Pollution Abstracts, U.S.A.

Paryavaran Abstract,
New Delhi, India

Electronic Social and Science
Citation Index (ESSCI)

CrossRef (DOI)

Google Scholar

Environment Abstract, U.S.A.

WorldCat (OCLC)

Indian Science

SHERPA/RoMEO

CSA: Environmental Sciences and Pollution Management

Access to Global Online Research in Agriculture (AGORA)

Present in UGC-CARE List (Group II)

Index Copernicus (2020) = 119.70

Indian Science Abstracts,
New Delhi, India

Elsevier Bibliographic
Databases

Zoological Records

Indian Citation Index (ICI)

EBSCO: Environment Index™

DOAJ

ProQuest, U.K.

British Library

JournalSeek

Directory of Science

UDL-EDGE (Malaysia) Products like *i*-Journals, *i*-Focus and *i*-Future

www.neptjournal.com

Nature Environment and Pollution Technology

EDITORS

Dr. P. K. Goel (Chief Editor)

Former Head, Deptt. of Pollution Studies
Yashwantrao Chavan College of Science
Vidyanagar, Karad-415 124
Maharashtra, India

Dr. K. P. Sharma

Former Professor, Ecology Lab, Deptt. of Botany
University of Rajasthan
Jaipur-302 004, India
Rajasthan, India

Managing Editor: Mrs. Apurva Goel Garg, C-102, Building No. 12, Swarna CGHS, Beverly Park, Kanakia, Mira Road (E) (Thane) Mumbai-401107, Maharashtra, India (**E-mail: operations@neptjournal.com**)

Business Manager: Mrs. Tara P. Goel, Technoscience Publications, A-504, Bliss Avenue, Balewadi, Pune-411 045, Maharashtra, India (**E-mail: contact@neptjournal.com**)

EDITORIAL ADVISORY BOARD

1. **Dr. Prof. Malay Chaudhury**, Department of Civil Engineering, Universiti Teknologi PETRONAS, Malaysia
2. **Dr. Saikat Kumar Basu**, University of Lethbridge, Lethbridge AB, Canada
3. **Dr. Sudip Datta Banik**, Department of Human Ecology Cinvestav-IPN Merida, Yucatan, Mexico
4. **Dr. Elsayed Elsayed Hafez**, Deptt. of of Molecular Plant Pathology, Arid Land Institute, Egypt
5. **Dr. Dilip Nandwani**, College of Agriculture, Human & Natural Sciences, Tennessee State Univ., Nashville, TN, USA
6. **Dr. Ibrahim Umaru**, Department of Economics, Nasarawa State University, Keffi, Nigeria
7. **Dr. Tri Nguyen-Quang**, Department of Engineering Agricultural Campus, Dalhousie University, Canada
8. **Dr. Hoang Anh Tuan**, Deptt. of Science and Technology Ho Chi Minh City University of Transport, Vietnam
9. **Mr. Shun-Chung Lee**, Deptt. of Resources Engineering, National Cheng Kung University, Tainan City, Taiwan
10. **Samir Kumar Khanal**, Deptt. of Molecular Biosciences & Bioengineering, University of Hawaii, Honolulu, Hawaii
11. **Dr. Sang-Bing Tsai**, Zhongshan Institute, University of Electronic Science and Technology, China
12. **Dr. Zawawi Bin Daud**, Faculty of Civil and Environmental Engg., Universiti Tun Hussein Onn Malaysia, Johor, Malaysia
13. **Dr. Srijan Aggarwal**, Civil and Environmental Engg. University of Alaska, Fairbanks, USA
14. **Dr. M. I. Zuberi**, Department of Environmental Science, Ambo University, Ambo, Ethiopia
15. **Dr. Prof. A.B. Gupta**, Dept. of Civil Engineering, MREC, Jaipur, India
16. **Dr. B. Akbar John**, Kulliyyah of Science, International Islamic University, Kuantan, Pahang, Malaysia
17. **Dr. Bing Jie Ni**, Advanced Water Management Centre, The University of Queensland, Australia
18. **Dr. Prof. S. Krishnamoorthy**, National Institute of Technology, Tiruchirapally, India
19. **Dr. Prof. (Mrs.) Madhoolika Agarwal**, Dept. of Botany, B.H.U., Varanasi, India
20. **Dr. Anthony Horton**, Envirocarb Pty Ltd., Australia
21. **Dr. C. Stella**, School of Marine Sciences, Alagappa University, Thondi -623409, Tamil Nadu, India
22. **Dr. Ahmed Jalal Khan Chowdhury**, International Islamic University, Kuantan, Pahang Darul Makmur, Malaysia
23. **Dr. Prof. M.P. Sinha**, Dumka University, Dumka, India
24. **Dr. G.R. Pathade**, H.V. Desai College, Pune, India
25. **Dr. Hossam Adel Zaqoot**, Ministry of Environmental Affairs, Ramallah, Palestine
26. **Prof. Riccardo Buccolieri**, Deptt. of Atmospheric Physics, University of Salento-Dipartimento di Scienze e Tecnologie Biologiche ed Ambientali Complesso Ecotekne-Palazzina M S.P. 6 Lecce-Monteroni, Lecce, Italy
27. **Dr. James J. Newton**, Environmental Program Manager 701 S. Walnut St. Milford, DE 19963, USA
28. **Prof. Subhashini Sharma**, Dept. of Zoology, University of Rajasthan, Jaipur, India
29. **Dr. Murat Eyvaz**, Department of Environmental Engg. Gebze Inst. of Technology, Gebze-Kocaeli, Turkey
30. **Dr. Zhihui Liu**, School of Resources and Environment Science, Xinjiang University, Urumqi, China
31. **Claudio M. Amescua García**, Department of Publications Centro de Ciencias de la Atmósfera, Universidad Nacional Autónoma de México
32. **Dr. D. R. Khanna**, Gurukul Kangri Vishwavidyalaya, Haridwar, India
33. **Dr. S. Dawood Sharief**, Dept. of Zoology, The New College, Chennai, T. N., India
34. **Dr. Amit Arora**, Department of Chemical Engineering Shaheed Bhagat Singh State Technical Campus Ferozepur -152004, Punjab, India
35. **Dr. Xianyong Meng**, Xinjiang Inst. of Ecology and Geography, Chinese Academy of Sciences, Urumqi, China
36. **Dr. Sandra Gómez-Arroyo**, Centre of Atmospheric Sciences National Autonomous University, Mexico
37. **Dr. Manish Sharma**, Research and Development Cell, Bahra University, Shimla Hills, Shimla, India
38. **Dr. Wen Zhang**, Deptt. of Civil and Environmental Engineering, New Jersey Institute of Technology, USA



Hydrochemical Characteristics and Irrigation Water Evaluation of Suburban River: A Case Study of Suzhou City, Anhui Province, China

Manli Lin^(**), Hao Yu^{**} and Weihua Peng^(***)†

*School of Resources and Civil Engineering, Suzhou University, Suzhou 234000, PR China

**National Engineering Research Center of Coal Mine Water Hazard Controlling, Suzhou University, Suzhou 234000, PR China

***Key Laboratory of Mine Water Resource Utilization of Anhui Higher Education Institutes, Suzhou University, Suzhou 234000, PR China

†Corresponding author: Weihua Peng; pengweihuapwh@126.com

Nat. Env. & Poll. Tech.
Website: www.neptjournal.com

Received: 20-02-2021
Revised: 25-03-2021
Accepted: 03-04-2021

Key Words:

Hydrochemical characteristics
Principal component analysis
Agricultural non-point source
pollution
Xinbian river

ABSTRACT

To study the evolution of hydrochemical characteristics and the quality of irrigation water from a suburban river, a total of 54 water samples were collected from Xinbian River in Suzhou City (Anhui Province, China) from December 2019 to May 2020. Piper diagrams, Gibbs diagrams, and multivariate statistical analysis were used to analyze the hydrochemical characteristics and main ion sources. Research results showed that the content of main ions increased continuously from December 2019 to May 2020, among which SO_4^{2-} and F^- exceeded China's surface water quality standards in April and May. The main hydrochemical type was Na-SO_4 , accounting for 77.77%, of water samples with the main ion components found to be related to rock weathering. Correlation analysis and principal component analysis showed that agricultural non-point source pollution was the main factor affecting the water quality of the Xinbian River. Overall, the evaluation index of irrigation water shows that Xinbian River was suitable for irrigation utilization, although the effects of magnesium damage should be prevented.

INTRODUCTION

Urban rivers play an important role in urban development, supplying water for cities and maintaining urban ecological balance (Hu et al. 2020). However, with the rapid development of urbanization and industrialization in recent years, the concentration of pollutants in urban watersheds is continually increasing (Valappil et al. 2020, Yu et al. 2020a), especially in urban fringe areas where there is no obvious boundary between urban and rural environments and where different ecosystems merge and compete. For example, a large amount of agricultural land has been converted for use as urban construction land and industrial land (Tang et al. 2020). The disposal of pesticides, chemical fertilizers, wastewater, waste gas, and solid waste produced industrially has a direct effect on the chemical characteristics and water quality of rivers in urban fringe areas (Jiang et al. 2020, Yu et al. 2020a).

The hydrochemical characteristics of surface water are mainly affected by water-rock interactions, evaporation concentration, and human activities (Wang et al. 2019a). Through the analysis of river water chemistry, the geochemical source of river ions can be clarified (Xia et al. 2019). Based on this,

many previous studies have assessed river water chemistry characteristics and evaluated potential applications. Valappil et al. (2020) assessed surface water from the Limbang River Basin in Kalimantan, using Piper diagrams, Gibbs diagrams, and multivariate statistical analysis, showing that atmospheric rainfall and rock weathering were the main factors affecting the chemical characteristics of surface water in the study area. Hu et al. (2020) compared differences in the conventional components and heavy metal content of wetland water under various land-use conditions, finding that Cl^- the content was mainly related to pesticides and chemical fertilizers used in agricultural production, while heavy metal element concentrations were affected by both natural and human sources. Wang et al. (2019b) studied the water chemistry characteristics, control factors, and water quality of the Nu River, finding that rock weathering was the main source of ions and that most Nu River water samples were suitable for irrigation use.

Xinbian River is a large-scale artificial river, which plays an important role in both agricultural development and maintaining the aquatic ecological balance of Suzhou city. The Xinbian River was continuously monitored for six months in this study, according to the features of the local farming cycle.

Samples were taken to examine the evolution of chemical characteristics in Xinbian River water as well as the quality of irrigation water generated, providing a scientific basis for river aquatic environment protection in urban fringe areas.

MATERIALS AND METHODS

Study Area

Suzhou is located in the northernmost part of Anhui Province (Fig. 1a), in the northeast of Huaibei plain, covering a total area of 9787 km² (Li et al. 2020.). The city's permanent resident population is 5.68 million and water resources in the city are relatively scarce, reaching a total volume of about 3.48 billion m³. Xinbian River is located in the northern suburbs of Suzhou City (Fig. 1b), with a total length of 127.2 km and a drainage area of 6562 km². The annual average discharge and annual average water level elevations are 3.52-72.10 m³.s⁻¹ and 14.73-26.56 m, respectively. The climate includes very cold and long-lasting winters, with hot summers and long rainy seasons, during which time the precipitation level is concentrated and high. Since its establishment, the Xinbian River has exhibited multiple benefits such as flood control, drainage, and irrigation, contributing significantly to agricultural production and both urban and rural economic development.

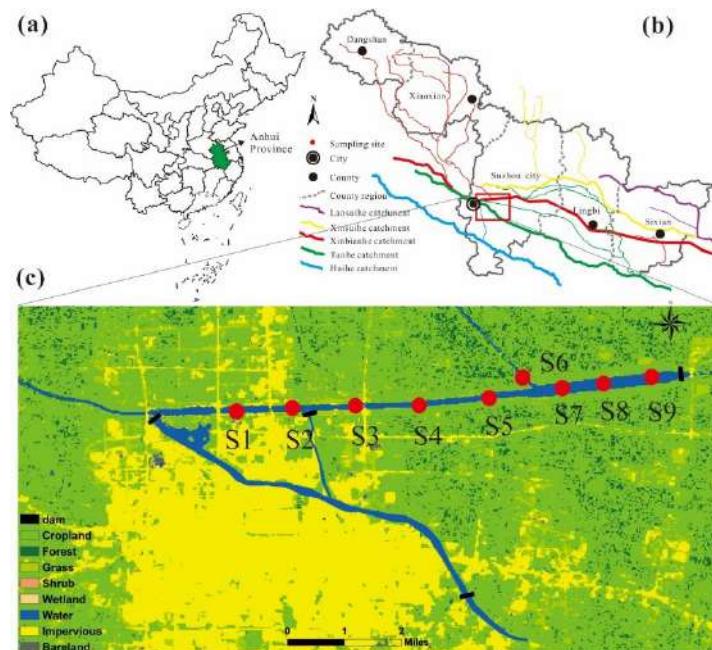
Sampling and Testing

From December 2019 to May 2020, the Suzhou Urban Section of the Xinbian River was monitored in six consecutive monthly sampling campaigns. Nine monitoring points (Fig. 1c) were sampled each month and 54 water samples were collected totally. The sampling specifications were based on the technical specification for surface water and sewage monitoring (HJ/T 91-2002) (SEPA 2002). The water samples were sampled below 0.5 m of the water surface using a self-made surface water sampler. Conductivity (EC), pH, and total dissolved solids (TDS) were measured on-site using portable devices. All samples were sent to the laboratory within 24 h and stored at 4°C.

After water samples were filtered through 0.45 μm filter membranes, the content of Na⁺, K⁺, Ca²⁺, Mg²⁺, Cl⁻, F⁻, and SO₄²⁻ in water was tested by ion chromatography (ICS-600-900, Diane Co., US). The content of CO₃²⁻ and HCO₃⁻ was measured by the acid-base titration method, and the milligram equivalent balance of cations and anions was controlled within 5%.

Data analysis

Xinbian River is mostly within an agricultural irrigation area and therefore, water quality is very important for the growth



(Source: (a) from Chen et al. 2020; (c) from Jiang et al. 2020)

Fig. 1: Study area and sampling locations.

of crops. Excessive sodium levels in the water will result in soil permeability being reduced (Bob et al. 2016), which adversely affects crop quality and yield (Guan et al. 2018). Therefore, the irrigation water quality model was used to evaluate the water quality in the present study. The selected indicators were sodium absorption ratio (SAR), residual sodium carbonate (RSC), sodium percentage (Na%), permeability index (PI), magnesium hazard (MH), and Kelley's ratio (KR). These indicators were calculated according to Eq. (1)-(7) as follows:

$$Na\% = \frac{(Na^+ + K^+) \times 100}{Ca^{2+} + Mg^{2+} + Na^+ + K^+} \quad \dots(1)$$

$$SAR = \frac{Na^+}{\sqrt{(Ca^{2+} + Mg^{2+})/2}} \quad \dots(2)$$

$$RSC = (CO_3^{2-} + HCO_3^-) - (Ca^{2+} + Mg^{2+}) \quad \dots(3)$$

$$MH = \frac{Mg^{2+}}{Ca^{2+} + Mg^{2+}} \times 100 \quad \dots(4)$$

$$PI = \frac{Na^+ + \sqrt{HCO_3^-}}{Ca^{2+} + Mg^{2+} + Na^+ + K^+} \quad \dots(5)$$

$$KR = \frac{Na^+}{Ca^{2+} + Mg^{2+}} \quad \dots(6)$$

$$PS = Cl^- + \frac{1}{2}SO_4^{2-} \quad \dots(7)$$

RESULTS AND DISCUSSION

Ion Content Characteristics

The results of statistical analysis of the water chemical parameters for the Xinbian River from December 2019 to May 2020 are shown in Table 1. The pH value (Fig. 2a) of the Xinbian River ranged from 7.75 to 9.50, with an average of 8.57 which was classified as weakly alkaline water. The TDS value ranged between 445.67 and 732.00 mg.L⁻¹, with an average of 633.49 mg.L⁻¹, while the TDS content exhibited an increasing trend overall (Fig. 2b).

The TDS content of water is related to the total ion content, as shown by the hydrochemical parameters for the Xinbian River in Fig. 2b. Agricultural activities, evaporation, and human activities may increase the TDS content of river water. The Ca²⁺ content ranged from 28.34 mg.L⁻¹ to 69.74 mg.L⁻¹, with an average value of 48.74 mg.L⁻¹ (Fig. 2c). The trend in variation of Ca²⁺ exhibited an initial increase, followed by a decrease. The Mg²⁺ content ranged from 35.24 mg.L⁻¹ to 62.31 mg.L⁻¹, with an average of 48.49 mg.L⁻¹,

exhibiting an overall increasing trend (Fig. 2d). The Na⁺ and K⁺ concentrations ranged from 128 mg.L⁻¹ to 269 mg.L⁻¹ and from 7.34 mg.L⁻¹ to 12.66 mg.L⁻¹, with averages of 157.21 mg.L⁻¹ and 10.11 mg.L⁻¹, respectively (Fig. 2e and Fig. 2f). The HCO₃⁻ concentration ranged between 276.51 mg.L⁻¹ and 138.96 mg.L⁻¹, with an average of 232.86 mg.L⁻¹, exhibiting a gradually decreasing trend overall (Fig. 2g). The SO₄²⁻ content ranged from 178.34 mg.L⁻¹ to 406.03 mg.L⁻¹, with an average value of 270.62 mg.L⁻¹, exhibiting a rapidly increasing trend. From February to May 2020, the content of SO₄²⁻ in water samples regularly exceeded the standard of 250 mg.L⁻¹ (Fig. 2h), as defined by the China surface water quality standard (GB 3838-2002) (except for some samples in March 2020). The change in Cl⁻ concentration was consistent with that of SO₄²⁻ (Fig. 2i), showing an increasing trend. Cl⁻ and SO₄²⁻ are usually associated with strong evaporation, agricultural non-point source pollution, and sewage discharge. F⁻ concentrations increased between December 2019 and May 2020 (Fig. 2j).

Sources of Major Ions and Hydrogeochemical Evolution

Hydrochemical characteristics: Piper three-line diagrams are commonly used to examine the chemical composition features of water and can intuitively reflect the composition and concentration of anions and cations in the water body (Chen et al. 2019, 2020). Fig. 3 shows the hydrochemical characteristics of the Xinbian River from December 2019 to May 2020, exhibiting three types of water chemistry characteristics: Na-HCO₃, Na-Cl, and Na-SO₄, among which the Na-SO₄ type was the dominant type.

From the distribution of cations in the lower-left corner of Fig. 3, it can be seen that the proportion of Na⁺+K⁺ in cations in the Xinbian River was higher than other cations, indicating Xinbian River water was Na type. According to the distribution of anions in the lower right corner of Fig. 3 and the trend of change of anions in Fig. 2, SO₄²⁻ was the dominant anion in water samples except for December 2019 (dominated by HCO₃⁻) and January 2020 (mixed type). It can be concluded that the chemical characteristics type of the Xinbian River gradually changed from Na-HCO₃ to Na-SO₄, which may be related to agricultural activities in the surrounding area. Sulfate is the main component of compound fertilizer, providing SO₄²⁻ for crop growth. Therefore, the high concentration of SO₄²⁻ may be related to the use of chemical fertilizer in agricultural production (Hu et al. 2020).

Mechanistic Analysis of Water-rock Interactions

The Gibbs map was established based on surface waters worldwide. In the Gibbs diagram, rock weathering, evaporative crystallization, and atmospheric precipitation are con-

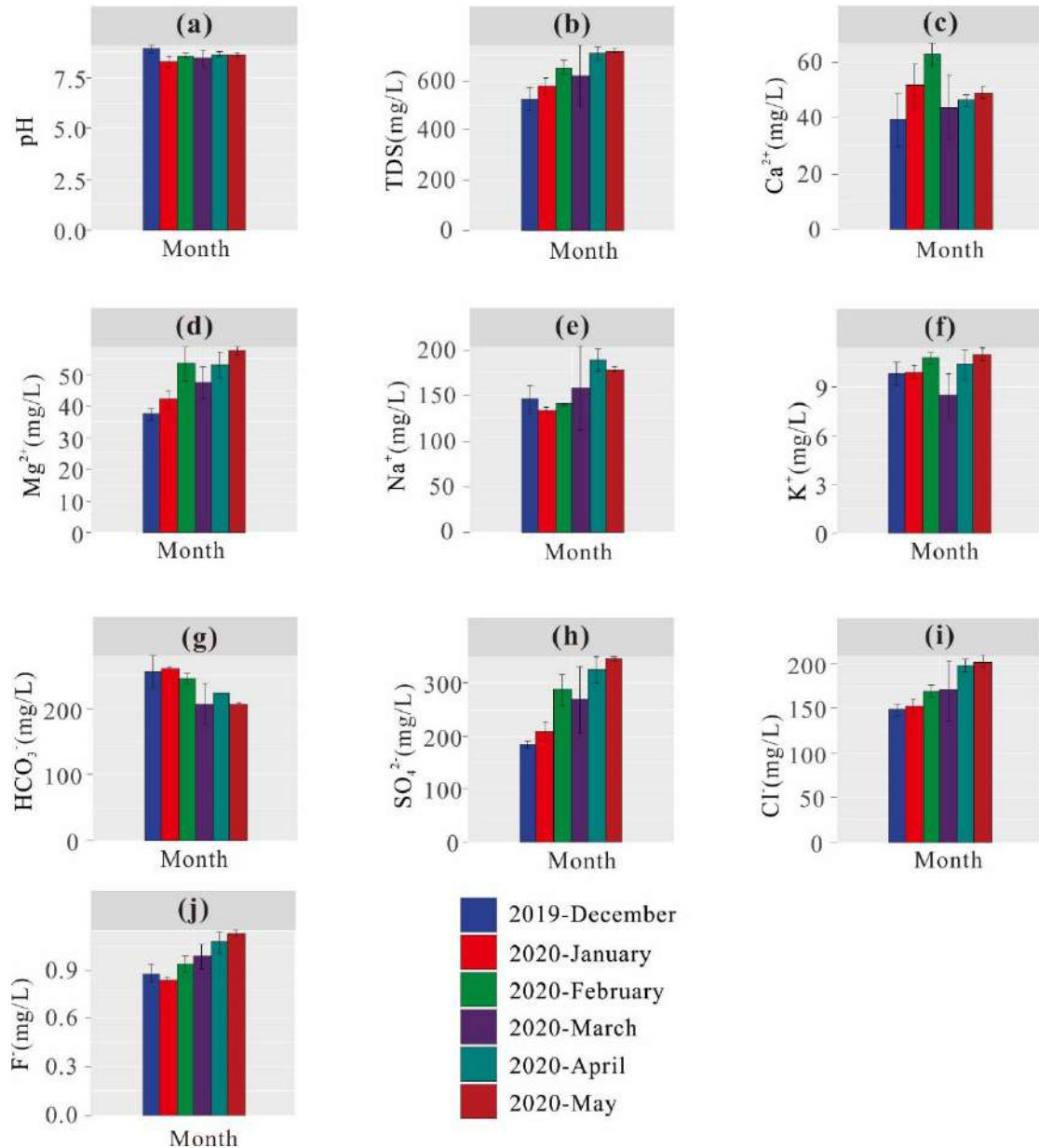


Fig. 2: Variation in average hydrochemical parameters in Xinbian River from December 2019 to May 2020.

sidered to be the three main factors controlling the chemical composition of natural water. Samples dominated by rock weathering are located in the middle left area of the Gibbs diagram, while samples dominated by evaporation crystallization are located in the upper right corner, and samples dominated by atmospheric precipitation are located in the lower right corner. It can be seen from Fig. 4a that water samples from the Xinbian River were mostly located in the rock weathering control region of the Gibbs diagram, indicating

that the ions in the Xinbian River were mainly from rock weathering. In addition, it can be seen from Fig. 4b that some samples were located in the middle left region, indicating that the ions in the Xinbian River not only originated from rock weathering, evaporative crystallization, and atmospheric precipitation, but also human activities, ion exchange, and other factors (Wang et al. 2019a).

Based on the study of solutes in major rivers worldwide, Gaillardet et al. (1999) found that the influence of silicate

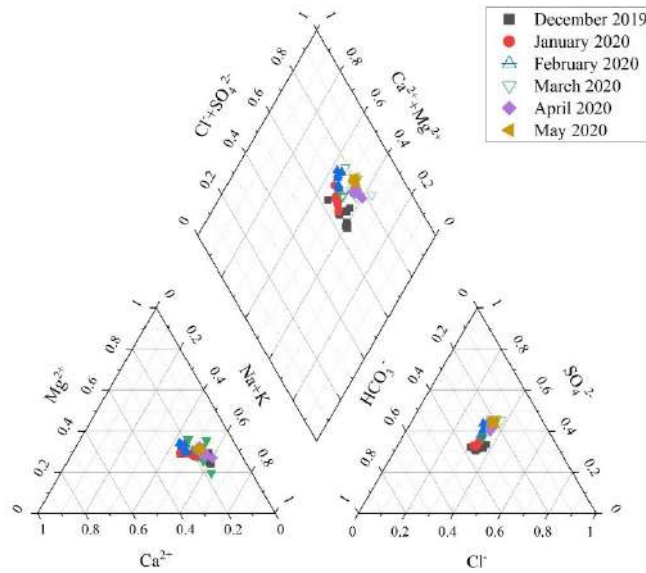


Fig. 3: Piper diagram of the hydrochemical characteristics of the Xinbian River throughout the sampling period from December 2019 to May 2020.

weathering, evaporite, and carbonate dissolution on the water can be determined by the ion molar ratio. As shown in Fig. 5, the Xinbian River water samples were mainly located near the silicate region, while some water samples

were located in the evaporite region, which indicates that the solutes in the Xinbian River were mainly affected by silicate weathering, while the impact of evaporite was relatively small.

Table 1: Descriptive statistics of hydrochemical parameters.

Month	Parameter	pH	TDS	Ca ²⁺	Mg ²⁺	Na ⁺	K ⁺	HCO ₃ ⁻	SO ₄ ²⁻	Cl ⁻	F ⁻
December 2019	Max	9.22	594.67	61.10	40.87	163.85	11.02	276.51	192.24	155.03	0.95
	Min	8.49	445.67	28.34	35.24	119.79	8.71	200.63	178.34	132.90	0.78
	mean	8.90	527.04	39.20	37.37	145.37	9.84	255.53	184.95	148.64	0.88
January 2020	Max	8.68	640.00	69.35	47.94	137.70	11.04	261.93	245.78	166.40	0.88
	Min	7.75	538.33	44.23	38.89	128.71	9.60	257.36	193.52	137.15	0.81
	mean	8.25	577.22	51.57	42.15	133.96	9.96	260.69	210.18	151.89	0.84
February 2020	Max	8.72	704.00	69.74	61.57	140.83	11.47	249.19	332.43	177.27	1.04
	Min	8.30	612.00	58.62	46.82	138.73	10.35	225.40	253.22	160.04	0.87
	mean	8.53	650.96	62.71	53.53	139.63	10.82	245.50	287.66	169.02	0.94
March 2020	Max	9.50	923.00	65.37	60.39	269.99	11.61	228.75	406.03	250.22	1.12
	Min	8.14	540.50	25.08	43.52	132.13	7.34	138.96	215.10	147.18	0.86
	mean	8.45	619.72	43.83	47.19	157.83	8.51	206.90	269.38	169.87	0.98
April 2020	Max	8.76	741.00	48.67	62.31	213.89	12.66	224.79	363.82	212.58	1.21
	Min	8.51	669.00	41.06	49.60	173.35	9.59	221.67	288.05	186.55	1.02
	mean	8.64	709.94	46.27	53.00	187.89	10.41	223.38	325.86	197.59	1.08
May 2020	Max	8.73	732.00	53.61	59.48	182.72	11.56	206.36	356.89	210.47	1.16
	Min	8.50	704.50	47.42	55.56	173.54	10.51	203.92	336.79	193.23	1.09
	mean	8.62	716.06	48.85	57.69	178.58	11.10	205.17	345.70	201.83	1.13

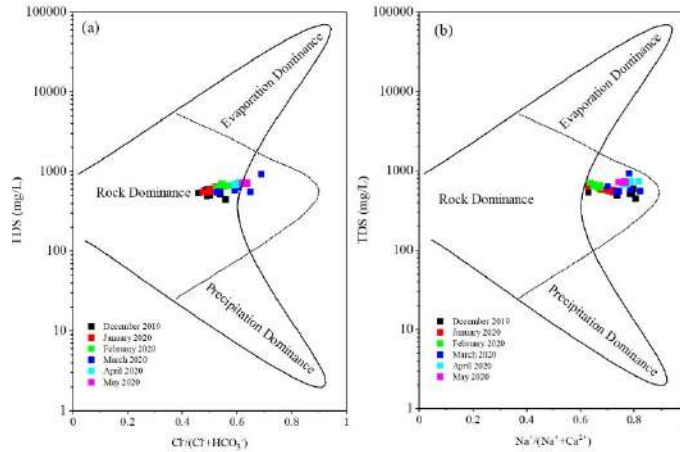


Fig. 4: Gibbs diagrams showing the influence of factors controlling the chemical composition of the Xinbian River throughout the sampling period from December 2019 to May 2020 (a: TDS versus $\text{Na}^+ / (\text{Na}^+ + \text{Ca}^{2+})$; b TDS versus $\text{Cl}^- / (\text{Cl}^- + \text{HCO}_3^-)$).

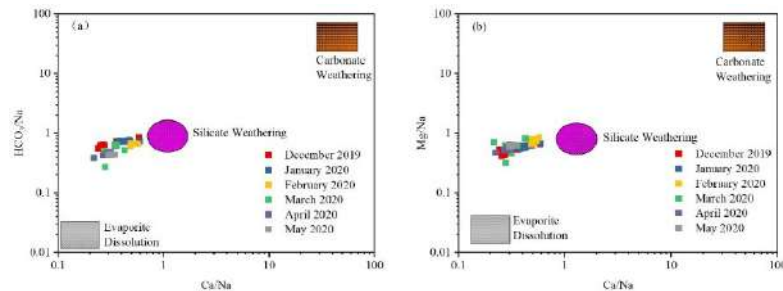


Fig. 5: The normalized diagram a) $\text{Mg}^{2+}/\text{Na}^+$ vs $\text{Ca}^{2+}/\text{Na}^+$; b) $\text{HCO}_3^-/\text{Na}^+$ vs $\text{Ca}^{2+}/\text{Na}^+$ in the Xinbian River throughout the sampling period from December 2019 to May 2020.

Correlation Analysis

Correlation analysis is useful for determining the degree of connection between two or more ions in water and determining statistical significance (Jehan et al. 2019). Therefore, using correlation analysis is helpful to further establish the hydrochemical formation processes and ion sources for the Xinbian River. The correlation analysis results for the main conventional ions in the Xinbian River are shown in Fig. 6. It is generally considered that a correlation coefficient less than 0.5 indicates a weak correlation, while correlation coefficients between 0.5 and 0.75 indicate a moderate correlation, and correlation coefficients greater than 0.75 indicate a strong correlation.

It can be seen from Fig. 6 that EC, TDS, F, Cl, and SO_4^{2-} were strongly correlated with each other, indicating that these water quality parameters may be associated with the same source. Only a weak negative correlation was observed between pH, Ca^{2+} , and HCO_3^- . There was a moderate correlation between EC, TDS, and most of the conventional water ions, indicating that these water ions contributed to both EC

and TDS to some degree. The correlation coefficients of Ca^{2+} with Mg^{2+} and K^+ were 0.43 and 0.56, respectively, which indicates that cation exchange affected the conventional ions in Xinbian River water (Guan et al. 2018). The correlation coefficients for F^- with Cl^- and SO_4^{2-} were 0.86 and 0.88, respectively, with these strong correlations indicating that F^- , Cl^- and SO_4^{2-} may have a common source. Combined with the results shown in Fig. 2, these findings indicate that the content of F^- exhibited an increasing trend, exceeding the standard limit for F^- according to the surface water quality standard ($1 \text{ mg}\cdot\text{L}^{-1}$) in April and May 2020. Generally, there was a good degree of correlation observed between Cl^- and SO_4^{2-} in surface waters and their concentrations were high, indicating that Cl^- and SO_4^{2-} came from human activities such as agricultural non-point source pollution, domestic sewage, and industrial wastewater discharge.

Principal Component Analysis

The principal component analysis is a dimensionality reduction analytic method that divides a large number of variables

into small, identifiable groups, allowing for the use of fewer variables to describe groupings of data (Singh et al. 2014). Therefore, principal component analysis is widely used in geochemical data sets (Li et al. 2018, Yu et al. 2020a). The water quality parameters of 54 water samples collected in the Xinbian River from December 2019 to May 2020 were analyzed by principal component analysis and the results are shown in Fig. 6. The first principal component (PC1) accounted for 60.5% of the total variation, while the second principal component (PC2) accounted for 18.1% of the total variation, resulting in a cumulative contribution of 78.6%. Therefore, the hydrogeochemical information of the Xinbian River can be generally reflected through principal component 1 and principal component 2. It can be seen from Fig. 7 that TDS, F⁻, Cl⁻, SO₄²⁻, Na⁺, K⁺, and Mg²⁺ had relatively high positive loads in PC1; therefore, PC1 can be classified as being related to human activities. In contrast, PC2 was dominated by positive loads of Ca²⁺, K⁺, and HCO₃⁻, with a negative load from pH, indicating that PC2 may be related to rock weathering, e.g. natural activities.

As shown in Fig. 7, the 54 samples from the Xinbian River from December 2019 to May 2020 are scattered across all four quadrants. Among them, the water samples in December 2019 and March 2020 were mainly located in the third quadrant, the water samples in January 2020 and February 2020 were located in the second quadrant and the first quadrant, respectively, and water samples in April and May

2020 were mainly located in the fourth quadrant. The water quality indicators SO₄²⁻, Cl⁻, and F⁻, related to agricultural non-point source pollution, exhibited a higher contribution to the fourth quadrant, which indicates that agricultural non-point source pollution gradually began to adversely affect water quality in April and May 2020.

Irrigation Water Quality Evaluation

Suzhou is located in the Huanghuai plain, which is an important grain-growing region in China. Owing to the developed water system in the study area, river water is mostly used to irrigate crops. An excess of dissolved ions in irrigation water affects the soil structure, reducing the production capacity of the soil and affecting the quality of agricultural products. Therefore, it is necessary to evaluate the quality of irrigation water taken from the Xinbian River. The irrigation water quality of the Xinbian River from December 2019 to May 2020 was calculated using Eq. (1)-(7), with the results given in Table 2.

SAR is an important parameter for the evaluation of irrigation water quality. Incorporating the concentrations of Na⁺, Ca²⁺, and Mg²⁺ with Eq. 2 (Lin et al. 2016), can reflect the degree to which Na⁺ replaces Ca²⁺ and Mg²⁺ in the soil (Jiang et al. 2020). According to the SAR value, irrigation water can be divided into three categories: suitable for irrigation (SAR<18); unsuitable for irrigation (18<SAR<26); unsuitable for irrigation and harmful to

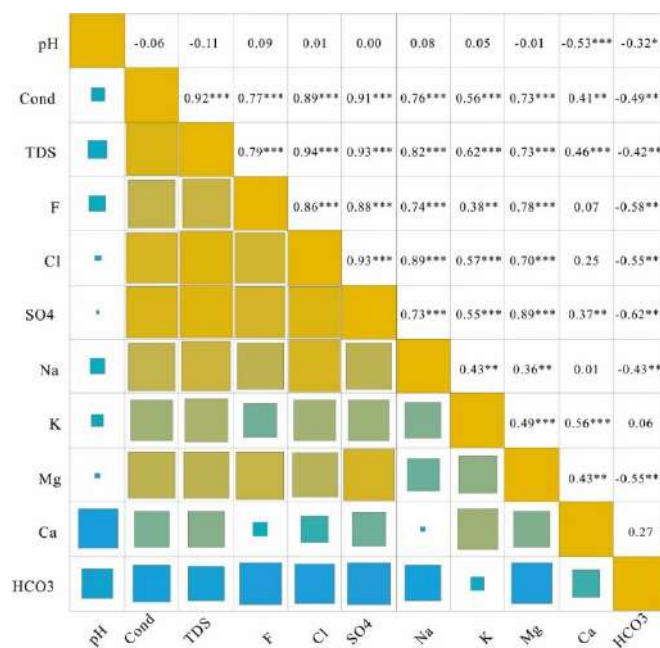


Fig. 6: Correlation analysis of hydrochemical parameters for the Xinbian River from December 2019 to May 2020.

Table 2: Irrigation water quality indices.

Index	Minimum	Maximum	Mean	SD	Permissible limit	Unsuitable samples	Suitable samples [%]
SAR	2.90	6.27	3.82	0.65	≤ 18	0	100
Na%	42.65	63.21	52.22	4.70	≤ 60	3	94.44
RSC	-4.57	-0.21	-2.66	1.17	≤ 2.5	0	100
MH	52.71	76.32	62.46	4.67	≤ 50	54	0
PI	54.14	76.31	64.94	5.09	≥ 25	0	100
KR	0.71	1.68	1.07	0.21	≤ 1.0	39	27.78
PS	5.69	11.28	7.70	1.35	≤ 10	1	98.20

crops ($26 < \text{SAR}$). As shown in Table 2, the SAR values of all water samples in this study were less than 18, indicating that the water Na^+ hazard of Xinbian River water was within the safety limit.

EC is an important indicator of salinity and irrigation water with high EC content can easily lead to soil salinization. According to the EC value, irrigation water can be classified as C1, indicating low salinization ($\text{EC} < 250 \mu\text{S}\cdot\text{cm}^{-1}$); C2, indicating medium salinization ($250\text{--}750 \mu\text{S}\cdot\text{cm}^{-1}$); C3, indicating high salinization ($750\text{--}2250 \mu\text{S}\cdot\text{cm}^{-1}$); or C4, indicating high salinization ($>2250 \mu\text{S}\cdot\text{cm}^{-1}$). The effects of SAR and EC values on soil are integrated into the USSS diagram (Yu et al. 2020b) (Fig. 8a), showing that 52 of the water samples (96.30%) fell in the C3S1 area, indicating high salinity. If the soil leaching conditions are good, water samples in the C3S1 area can be used for irrigation, otherwise, they should only be used for irrigating plants with strong salt tolerance.

Na% is an important indicator of sodium harm, as higher Na% values may affect the structure of the soil, reduce soil permeability, harden soil, and reduce gas exchange between the soil and the atmosphere. In this study, the Na% value of the Xinbian River ranged between 2.90 and 6.27, exhibiting an average of 3.82, with only three water samples exceeding the standard limit.

Wilcox diagram analysis was used to show the effects of Na% and EC on soil and crops. According to the Wilcox diagram (Fig. 8b), 36 water samples (66.67%) were in the good allowable region, while 18 water samples were in the suspicious region.

RSC is an important parameter to evaluate the quality of irrigation water (Ghobadi et al. 2020), comprehensively characterizing the relationship between $\text{HCO}_3^- + \text{CO}_3^{2-}$ and $\text{Ca}^{2+} + \text{Mg}^{2+}$. Large amounts of calcium and magnesium ions can reduce soil permeability, while high RSC values in irrigation water indicate an increase in the content of sodium in the soil. Therefore, if the RSC value is greater than $2.5 \text{ meq}\cdot\text{L}^{-1}$, the water is not suitable for use for irrigation. As shown in

Table 2, the RSC values of all water samples were less than $2.5 \text{ meq}\cdot\text{L}^{-1}$ and therefore, were below the standard limit.

MH is another important index to evaluate irrigation water quality, mainly reflecting the proportional relationship between Mg^{2+} and $\text{Ca}^{2+} + \text{Mg}^{2+}$. When the proportion of Mg^{2+} is large, it will cause the dispersion of soil clay particles, changing the soil structure and reducing crop yields. If the MH value is less than 50, the water is suitable for irrigation. As shown in Table 2, the MH value of Xinbian River water ranged between 52.71–76.32 (average 62.46), indicating that corresponding measures should be taken to reduce the proportion of Mg^{2+} in irrigation water.

In addition, the permeability index (PI) is also a key parameter to evaluate the quality of irrigation water (Sehlaoui et al. 2020) and it can be seen from Table 2 that the PI values of all water samples were within the limit. The KR parameter proposed by Keely can be used to evaluate the quality of irrigation water. As shown in Table 2, the KR value of Xinbian River water ranged between 0.71 and 1.68 (average 1.07), with the KR value of 39 water samples exceeding the limit value (< 1).

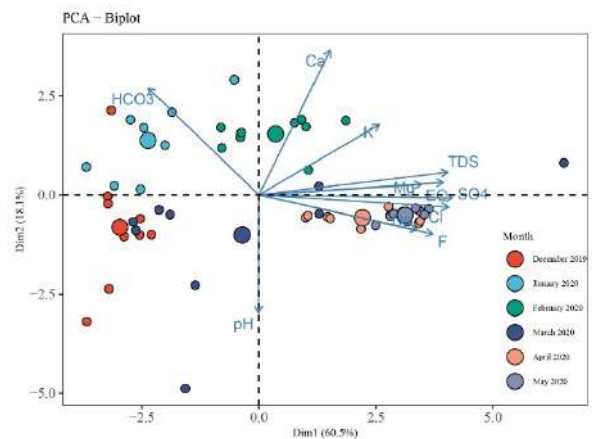


Fig. 7: The Principal component analysis loading plot for hydrochemical parameters in the Xinbian River from December 2019 to May 2020.

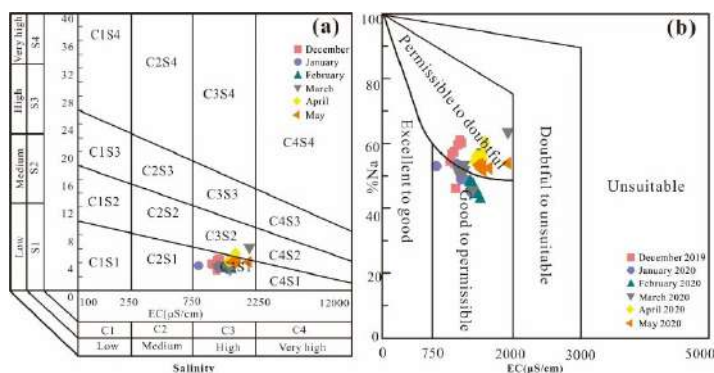


Fig. 8: USSL diagram (a) and Wilcox diagram (b) for the Xinbian River from December 2019 to May 2020.

CONCLUSION

- (1) From December 2019 to May 2020, the concentrations of Cl^- , EC, F^- , Mg^{2+} , Na^+ , SO_4^{2-} , and TDS in the Xinbian River increased, with indicators related to agricultural non-point source pollution (SO_4^{2-} and F^-) exceeding the standard limits in May 2020, according to China's surface water quality standard. There were three hydrochemical characteristic types identified in the Xinbian River: Na-HCO_3^- , Na-Cl , and Na-SO_4 , with Na-SO_4 being the dominant hydrochemical type (77.77%).
- (2) Gibbs diagram analysis showed that from December 2019 to May 2020, Xinbian River water was mainly affected by rock weathering, while a few water samples indicated an effect from rocks, indicating that the ions in Xinbian River water mainly originated from rock weathering, while agricultural non-point source pollution also exerted a certain impact on the ion composition of the Xinbian River.
- (3) The findings of the correlation study for the primary water quality metrics revealed a relationship between EC and TDS and the majority of water quality indicators. Furthermore, SO_4^{2-} , Cl^- , and F^- exhibited a good positive correlation with each other, indicating that SO_4^{2-} , Cl^- , and F^- may originate from the same source. The results of the principal component analysis showed that the intensity of interference from agricultural non-point source pollution on Xinbian River water increased from December 2019 to May 2020.
- (4) The overall water quality of irrigation water from the Xinbian River was good and most of the irrigation water index evaluation results were good. The calculation results for the indices SAR, RSC, and PI show that from December 2019 to May 2020, Xinbian River water was consistently suitable for use as irrigation water.

However, the potential for magnesium damage should be monitored and mitigated by regulating the release of Ca^{2+} .

ACKNOWLEDGMENTS

This research was supported by Anhui Provincial Natural Science Foundation of China (2008085MD122), Zhejiang Provincial Natural Science Foundation of China under Grant No. LQ20D010009, Key Program for Outstanding Young Talents in Higher Education Institutions of Anhui Province (gxyqZD2021134), Research development foundation of Suzhou University (2021fzjj28), Doctoral Scientific Research Foundation of Suzhou University (2019jb15), and Demonstration Teaching Organization of Anhui Education Department (416), and Dual-ability Teaching Team Project of Suzhou University (2020XJSN06).

REFERENCES

- Bob, M., Abd Rahman, N., Elamin, A. and Taher, S. 2016. Assessment of groundwater suitability for irrigation in Madinah City, Saudi Arabia. *Arab. J. Geosci.*, 9: 38.
- Chen, K., Sun, L., Liu, Q., Cao, W. and Tang, J. 2019. Quality evaluation and its controlling factor analyses of shallow groundwater in the urban area of Suzhou, Anhui province, China. *Fresenius Environ. Bull.*, 28(9): 6801-6807.
- Chen, K., Sun, L.L. and Tang, J. 2020. Hydrochemical differences between river water and groundwater in Suzhou, Northern Anhui Province, China. *Open Geosci.*, 12(1): 1421-1429.
- Gaillardet, J., Dupre, B., Louvat, P. and Allegre, J.C. 1999. Global silicate weathering and CO_2 consumption rates are deduced from the chemistry of large rivers. *Chem. Geol.*, 159(1-4): 3-30.
- Ghobadi, A., Cheraghi, M., Sobhanardakani, S., Lorestani, B. and Merrikh-pour, H. 2020. Hydrogeochemical characteristics, temporal, and spatial variations for evaluation of groundwater quality of Hamedan-Bahar Plain as a major agricultural region, West of Iran. *Environ. Earth. Sci.*, 79: 428.
- Guan, L.S., Gui, H.R., Kang, Z.Y., Zhao, H.H and Li, J. 2018. Hydrochemical characteristics and water quality assessment in goaf water of Kouquanguo mining area in Datong, Shanxi, China. *Fresenius Environ. Bull.*, 27(12A): 9315-9324.

- Hu, J., Long, Y., Zhou, W., Zhu, C., Yang, Q., Zhou, S. and Wu, P. 2020. Influence of different land-use types on hydrochemistry and heavy metals in surface water in the lakeshore zone of the Caohai wetland, China. *Environ. Pollut.*, 267: 115454.
- Jiang, Y., Gui, H., Yu, H., Wang, M., Fang, H., Wang, C., Chen, C., Zhang, Y. and Huang, Y. 2020. Hydrochemical characteristics and water quality evaluation of rivers in different regions of cities: A case study of Suzhou City in Northern Anhui Province, China. *Water*, 12(4): 950.
- Jehan, S., Khan, S., Khattak, S.A., Muhammad, S., Rashid, A. and Muhammad, N. 2019. Hydrochemical properties of drinking water and their sources apportionment of pollution in Bajaur agency, Pakistan. *Measurement*, 139: 249-257.
- Li, J., Gui, H., Hu, R., Chen, L., Xia, Y., Fan, H., Yu, H. and Wang, M. 2020. Analysis of heavy metal sources and health risk assessment of typical coal mine collapsed lakes in Huaibei Coalfield, Anhui Province, China. *Pol. J. Environ. Stud.*, 29(5): 3193-3202.
- Li, Z., Li, Z., Song, L., Ma, J. and Song, Y. 2018. Environment significance and hydrochemical characteristics of supra-permafrost water in the source region of the Yangtze River. *Sci. Total Environ.*, 644: 1141-1151.
- Lin, M.L., Peng, W.H. and Gui, H.R. 2016. Hydrochemical characteristics and quality assessment of deep groundwater from the coal-bearing aquifer of the Linhuan coal-mining district, Northern Anhui Province, China. *Environ. Monit. Assess.*, 11: 188: 202.
- Sehlaoui, H., Hassikou, R., Moussadek, R., Zouahri, A., Douaik, A., Iach, H., Ghanimi, A. and Dakak, H. 2020. Evaluation of water quality for agricultural suitability in the Benslimane region, Morocco. *Environ. Monit. Assess.*, 17: 192: 587.
- State Environmental Protection Administration (SEPA). 2002. Technical Specifications Requirements for Monitoring of Surface Water and Waste Water (HJ/T 91-2002). (in Chinese)
- Singh, V.B., Ramanathan, A.L., Pottakkal, J.G. and Kumar, M. 2014. Seasonal variation of the solute and suspended sediment load in Gangotri glacier meltwater, central Himalaya, India. *J. Asian Earth Sci.*, 79: 224-234.
- Tang, J.F., Wang, W.D., Yang, L., Qiu, Q.L.L., Lin, M.X., Cao, C.L. and Li, X.H. 2020. Seasonal variation and ecological risk assessment of dissolved organic matter in a peri-urban critical zone observatory watershed. *Sci. Total Environ.*, 707: 136093.
- Valappil, N.K.M., Viswanathan, P.M. and Hamza, V. 2020. Seasonal hydrochemical dynamics of surface water in the Limbang River, Northern Borneo: Evaluating for spatial and temporal trends. *Arab. J. Geosci.*, 13: 980.
- Wang, M., Gui, H., Hu, R., Zhao, H., Li, J., Yu, H. and Fang, H. 2019a. Hydrogeochemical characteristics and water quality evaluation of carboniferous Taiyuan formation limestone water in Sulin mining area in Northern Anhui, China. *Int. J. Environ. Res. Public Health*, 16: 2512.
- Wang, F., Zhao, Y., Chen, X. and Zhao, H. 2019b. Hydrochemistry and its controlling factors of rivers in the source region of the Nujiang River on the Tibetan Plateau. *Water*, 11: 2166.
- Xia, Y.T., Gui, H.R., Zhao, H.H., Li, J. and Guan, L.S. 2019. Temporal variability of hydro-chemical characteristics and water quality assessment of collapse pond in Zhuxianzhuang coal mining area, China. *Fresenius Environ. Bull.*, 28(1): 402-409.
- Yu, H., Gui, H., Jiang, Y., Li, Z., Wang, M., Fang, H., Wang, C., Chen, C., Qiu, H. and Zhang, Y. 2020a. Characteristics of dissolved organic matter content in urban rivers under different environmental impact zones: A case study of China's Tuo River. *Pol. J. Environ. Stud.*, 29(5): 3891-3900.
- Yu, H., Gui, H., Zhao, H., Wang, M., Li, J., Fang, H., Jiang, Y. and Zhang, Y. 2020b. Hydrochemical characteristics and water quality evaluation of shallow groundwater in Suxian mining area, Huaibei coalfield, China. *Int. J. Coal Sci. Technol.*, 7: 825-835.



Effect on Soil Hydrodynamic Parameters in Fields Mulched with Gravel for Different Periods of Time

Wenju Zhao*†, Yali Wang*, Zongli Li** and Taohong Cao*

*College of Energy and Power Engineering, Lanzhou University of Technology, Lanzhou 730050, China

**General Institute for Water Resources and Hydropower Planning and Design, Ministry of Water Resources, Beijing 100120, China

†Corresponding author: Wenju Zhao; wenjuzhao@126.com

Nat. Env. & Poll. Tech.
Website: www.neptjournal.com

Received: 23-02-2021
Revised: 27-04-2021
Accepted: 01-05-2021

Key Words:

Gravel mulched fields
Soil-water characteristics
Soil hydrodynamics

ABSTRACT

Soil-water characteristic curve (SWCC) and soil hydraulic conductivity are important soil hydrodynamic parameters, which are of great significance in production practice. In 128 soil samples collected from 0-20, 20-40 cm layers at sampling scales of 32×32 m, the authors determined the effect of different periods of time on SWCC and soil hydraulic conductivity in fields mulched gravel. The water holding capacity of soil changes dramatically throughout time, with NEW having the maximum water holding capacity. As the planting time increases, the soil water holding capacity decreases. Both van Genuchten (VG) and Gardner models can fit SWCC in different time periods well, but the fitting accuracy of the VG model is higher. Geostatistics and Kriging interpolation are used to study the spatial variability of the VG model parameters of the SWCCs. The parameters θ_s , α , and n show a strong spatial correlation as a whole and are slightly affected by random factors. The changing trend of soil unsaturated hydraulic conductivity ($K(\theta)$) in gravel-mulched fields is faster than the CHECK, and the NEW has the fastest change trend. The data suggest that fields mulched with gravel retain more water, with the NEW having the most noticeable water retention effect. The study's findings can be used to investigate the regional variations in soil hydrodynamic characteristics in gravel mulched fields in arid locations.

INTRODUCTION

Soil is not only the basis of sustainable agricultural development but also the environmental resources on which mankind depends for survival (Russo et al. 2015, Ren et al. 2018). The soil-water characteristic curve (SWCC) and soil hydraulic conductivity are significant factors for describing soil qualities that are crucial in production (Kishné et al. 2017, Pannecoucke et al. 2019). SWCC is the basic characteristic curve for studying soil water holding capacity, which can provide a scientific basis for studying the mechanism analysis and numerical simulation of water flow in the soil-plant-atmosphere continuum (SPAC system) (Raghuram et al. 2020). Soil hydraulic conductivity is of great significance in farmland irrigation and drainage and soil and water conservation projects (Fang et al. 2016). It has considerable spatial variability, which is mainly related to soil texture, structure, bulk density, nutrients, salinity, and organic matter content, and not simply represents the features of soil infiltration and leakage (She et al. 2014). The importance of studying soil hydrodynamic characteristics for agricultural productivity and soil moisture management cannot be overstated.

Many researchers have looked into the temporal and geographical variability of soil hydraulic parameters and

discovered that they are linked to soil texture and structure. The majority of SWCC research focuses on the model's applicability (Dong et al. 2017, Zhao et al. 2020a) and geographical variability (Xing et al. 2015, Shi et al. 2014). Zhao et al. (2020a) investigated the SWCC model in gravel-covered fields in Northwest China and discovered that the van Genuchten (VG) model fits well and is more accurate in predicting soil moisture. According to Wang et al. (2015b), the SWCC is influenced by elements like soil texture and structure, and due to the heterogeneity of these components, the SWCC undergoes significant changes over time and space (Amanabadi et al. 2018). The saturated permeability of the soil is measured by soil hydraulic conductivity, which is also an important parameter in the hydrological model (Mao et al. 2019). Yu et al. (2018) investigated the spatial distribution characteristics of saturated hydraulic conductivity of different soil layers at the regional scale of the loess area using classical statistics and geostatistics and discovered that soil hydraulic conductivity gradually decreased with increasing soil depth. Li et al. (2019) investigated the regional variability of soil hydraulic parameters in Xinjiang and discovered that soil hydraulic conductivity has a considerable spatial dependence.

For more than 300 years, many lands in Northwest China's arid and semi-arid regions have been covered with

gravel and sand as a “no-tillage protection scheme” (Li 2003, Zhao et al. 2017a). This model can effectively reduce surface runoff, increase water infiltration rate, reduce evaporation, and have a thermal insulation effect (Li 2003, Qiu et al. 2014, Zhao et al. 2020b). Many countries with precipitation < 400 mm have applied various patterns of sandstone coverage (Modaihsh et al. 1985, Kemper et al. 1994). However, due to human or natural reasons, this kind of land will degenerate after several years of planting (Wang et al. 2010), causing the interface between the gravel and the soil layer to become unclear. The influence and interaction of various processes in the soil profile of this soil at different periods can produce variable soils (Harguindeguy et al. 2018).

However, most scholars are concerned about the spatial change of a single soil property. Little attention has been paid to the changing laws of hydraulic parameters of soil mulched with gravel. The objectives of the study are to (1) compare and analyze the change laws of SWCCs in different periods, obtain changing laws of soil water holding capacity of fields mulched with gravel at different planting periods, and use VG and Gardner empirical models to fit the SWCCs and analyze the VG model parameters and determine its spatial statistical characteristics, and (2) analyze the differences of soil hydraulic conductivity at different depths in fields mulched with gravel for different periods of time. By examining changes in soil hydrodynamic characteristics in fields mulched with gravel over different lengths of time in the arid area of Northwest China, it is expected to provide theoretical support for soil moisture management and crop planting benefits of fields mulched with gravel. Our findings have important significance for small-scale hydrological studies in the sand and gravel-covered arid and semi-arid areas.

MATERIALS AND METHODS

Description of the Study Area and Sample Collection

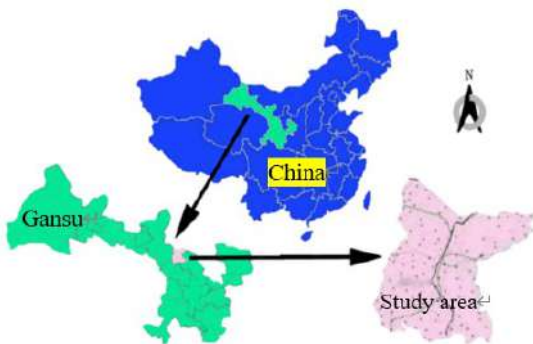


Fig. 1: Study area and the soil sampling locations in the study area situated in Gansu, China.

The study was conducted in Jingtai County near the Lanzhou University of Technology experimental station in the middle of the western portion of China’s Gansu province (on the east side of the Hexi corridor, at the junction of provinces (regions) of Gansu, Ningxia, and Inner Mongolia) (Fig. 1). The planting area of gravel mulched field in the study area occupies an area of approximately 33.3 km². The climate is intermediate between continental monsoon and non-monsoon regions. The temperature fluctuates from -27.3 to 36.6°C from the winter to summer seasons, with a mean annual temperature of 8.2°C. The mean annual precipitation is 185 mm, with a rainy season (accounting for approximately 61.4% of the annual rainfall) from July to September. The mean annual evaporation is 3038 mm, with annual average evaporation to precipitation ratio of 16 (Wu et al. 2019). The predominant soils are sandy loam, and the particles size was classified into three grades: clay (0-0.002 mm), silt (0.002-0.05 mm), and sand (0.05-2 mm), following the USDA Soil Taxonomy (Table 1).

The fields were 32×32 m and consisted of a new field mulched with gravel (NEW) planted for less than 10 years, a moderately aged field mulched with gravel (MOD) planted for 25-30 years, an old field mulched with gravel (OLD) planted for 45-60 years and bare land (no vegetation or gravel) as a control (CHECK). The surface sand was carefully removed, and all samples were then collected using stainless-steel cutting rings (5 cm in height by 5 cm in diameter) from the 0-20 and 20-40 cm layers. The samples were collected from the two layers in 64 evenly distributed 1×1 m quadrats 4 m apart, center to center, for a total of 128 samples (Fig. 2). Saturated hydraulic conductivity was determined by the constant-head method using a constant-head permeation apparatus (TST-70, China). Data for constructing SWCCs were obtained using a Hitachi CR21 high-speed constant-temperature refrigerated centrifuge (Vero et al. 2016).

Analysis Methods

Soil saturated hydraulic conductivity, K_s (mm/min), was calculated by:

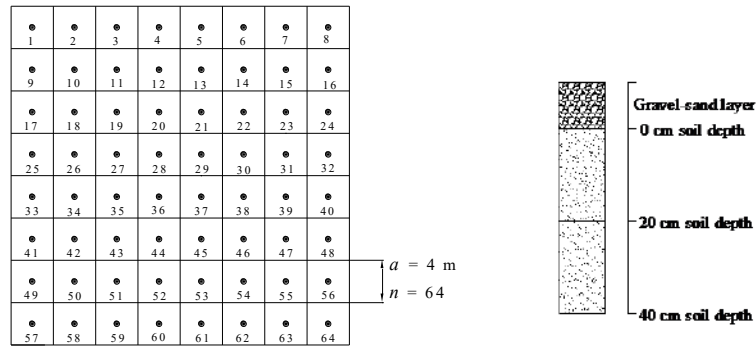
$$K_s = \frac{V_s}{I} \quad \dots(1)$$

where V_s is the infiltration rate and I is the water pressure gradient.

The van Genuchten model is:

$$\alpha(h) = \theta_r + \frac{\theta_s - \theta_r}{(1 + |\alpha h|^n)^m} \quad \dots(2)$$

where θ is volumetric water content (cm³.cm⁻³), θ_s is saturated volumetric water content (cm³/cm³), θ_r is residual



Note: a is the grid-scale and n is the total number of sampling points.

Fig. 2: Distribution map of the sampling points.

volumetric water content ($\text{cm}^3 \cdot \text{cm}^{-3}$), h is the pressure head (m), α is a scaling parameter that is inversely proportional to mean pore diameter, and m and n are shape coefficients, where m and n are related, $m=1-1/n$.

The Gardner model is:

$$\lg h = -A \lg \theta - B \quad \dots(3)$$

where A and B are empirical parameters >0 , with a linear relationship.

$K(\theta)$ is the unsaturated hydraulic conductivity of the soil ($\text{mm} \cdot \text{min}^{-1}$). It is a function of soil water content and soil suction, and increases with SWC and decreases as soil suction increases (Wang et al. 2012). The hydraulic conductivity model for unsaturated soil is (van Genuchten et al. 1980):

$$K(\theta) = K_s \left(\frac{\theta - \theta_r}{\theta_s - \theta_r} \right)^{1/2} \left[1 - \left(1 - \left(\frac{\theta - \theta_r}{\theta_s - \theta_r} \right)^{1/m} \right)^m \right]^2 \quad \dots(4)$$

Based on the regionalized variables theory and intrinsic hypothesis, the semivariogram, $\gamma(h)$, was estimated by:

$$\gamma(h) = \frac{1}{2N(h)} \sum_{i=1}^{N(h)} [Z(x_i + h) - Z(x_i)]^2 \quad \dots(5)$$

where $N(h)$ is the number of pairs of observations ($Z(x_i)$ and $Z(x_i+h)$) separated by a distance h . Only isotropic semivariograms are considered.

The following is the equation of the Kriging interpolation method:

$$Z(x_0) = \sum_{i=1}^n \lambda_i Z(x_i) \quad \dots(6)$$

Where $Z(x_0)$ is the estimated value at point x_0 , n is the number of known points around the point to be estimated, λ_i is the weight of each sample, and $Z(x_i)$ is the sample value at point x_i .

The coefficient of determination (R^2) between measured and predicted values and root mean square error (RMSE) was used to evaluate the performance of the regression models as follows:

Table 1: Basic nature of the various layers of the fields.

Test Soil	Soil Depth [cm]	Clay [%]	Silt [%]	Sand [%]	K_s [mm/min]
		<0.002 mm	0.002-0.05 mm	0.05-2 mm	
NEW	0-20	2.42	55.15	42.44	0.48
	20-40	2.74	55.35	41.92	0.46
MOD	0-20	2.59	53.94	43.48	0.44
	20-40	2.93	53.25	43.83	0.41
OLD	0-20	2.65	60.44	36.92	0.42
	20-40	3.15	65.41	31.45	0.38
CHECK	0-20	2.82	53.67	43.52	0.36
	20-40	3.32	55.93	40.76	0.33

$$R^2 = \left[\frac{\sum_{i=1}^n (O_i - \bar{O})(P_i - \bar{P})}{\left[\sum_{i=1}^n (O_i - \bar{O})^2 \right]^{0.5} \left[\sum_{i=1}^n (P_i - \bar{P})^2 \right]^{0.5}} \right]^2 \quad \dots(7)$$

$$RMSE = \sqrt{\frac{\sum_{i=1}^n (P_i - O_i)^2}{n}} \quad \dots(8)$$

where O_i and P_i are the measured and predicted values, respectively, \bar{O} and \bar{P} are the average measured and predicted values, respectively, and n is the number of observations in the validation data set. Both R^2 and RMSE range from 0 to 1. A high R^2 and a low RMSE indicate high predictive accuracy (Zhang et al. 2012).

RESULTS AND DISCUSSION

Influence of Different Periods of Time on SWCCs

The relationship between soil water content (SWC) and soil suction was established by characterizing dehydration (Fig. 3). The SWCCs of different soil layers at different time periods are consistent. In the low suction phase (<1 bar), the SWC of different soil layers at different time periods decreases rapidly with the increase of suction, while in the intermediate and high suction phases (1-10 bar), the SWC at different periods of time decreases slowly with the increase of suction. The SWC is 20-40 cm > 0-20 cm when the soil suction is the same. The capacity of the soil to hold water differed greatly between times. The NEW had the most capacity for water storage. The soil water holding capacity decreased as the planting time increased, and the CHECK was the lowest. This is because as the number of planting years increases, the amount of sand and gravel particles in the soil increases. Compared with the CHECK, the mixing

coarser particles in the soil reduces the total porosity of the soil, resulting in a gradual decrease in soil water holding capacity (Udawatta et al. 2008).

Fitting of SWCCs for Different Periods of Time

The VG model and Gardner model were used to fit the SWCCs at different periods of time, and the error analysis of the measured and predicted SWC under different suction was performed (Table 2). The fitting results reveal that the predicted value of SWC is similar to the measured value, with an R^2 value of 0.990-0.997 and an RMSE of 0.080-0.086. The VG model is built on *RETC* software to parameterize SWCCs. The Gardner model, which was fitted using Origin 2019b, has a lower R^2 and RMSE than the VG model. The VG model may be used to fit SWCCs in fields mulched with gravel for various periods of time due to its improved accuracy; the results were compatible with Fu et al. (2011).

The tested soil type in this experiment is sandy loam, the θ_r fitted by *RETC* software is very low and almost close to zero, so this paper only discusses the θ_s , α , and n . The effect of different planting years on the SWCCs parameters in fields mulched gravel also has certain differences. θ_s and α are significantly affected, and the influence on n is small. Planting years have a great impact on the physical properties of the soil, which is reflected in the impact of different planting years on the saturated soil moisture content. The θ_s of fields mulched gravel is higher than CHECK, and NEW is the highest. The α is the reciprocal of the air intake value. The air intake value of NEW is the largest, and that of CHECK is the smallest. The results show that the NEW has the best soil structure compared to CHECK, which is conducive to the escape of air inside the structure and increases the saturation of soil moisture to a certain extent. The change of the empirical parameter n in different planting years is relatively

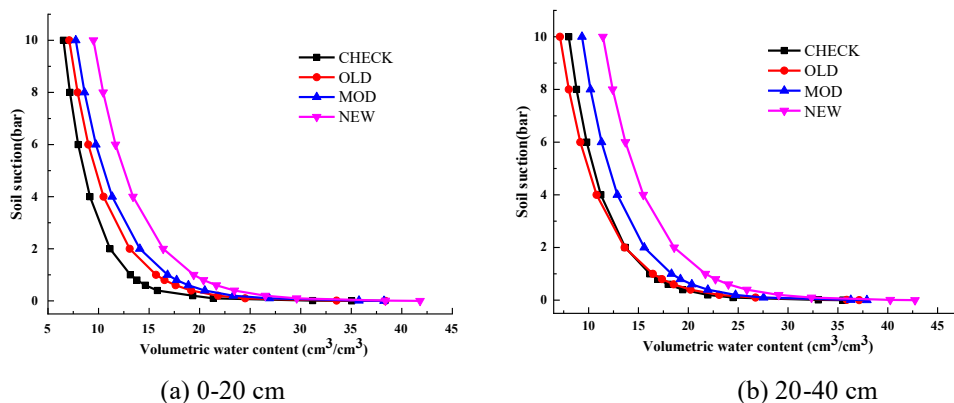


Fig. 3: The SWCCs of fields mulched with gravel for different periods of time.

Table 2: Fitting values and fitting errors of hydraulic parameters with VG and Gardner models.

Test Soil	Soil Depth [cm]	VG Model					Gardner Model			
		θ_s	α	n	R^2	RMSE	A	B	R^2	RMSE
NEW	0-20	0.406	2.447	1.242	0.993	0.085	4.543	2.396	0.942	0.212
	20-40	0.418	1.948	1.229	0.995	0.086	4.989	2.465	0.942	0.213
MOD	0-20	0.376	2.567	1.260	0.995	0.084	4.187	2.399	0.946	0.205
	20-40	0.378	2.476	1.234	0.995	0.081	4.731	2.639	0.951	0.195
OLD	0-20	0.371	3.977	1.247	0.990	0.083	4.144	2.501	0.944	0.208
	20-40	0.369	2.167	1.277	0.995	0.084	3.949	2.265	0.940	0.214
CHECK	0-20	0.346	5.875	1.244	0.997	0.083	4.257	2.851	0.975	0.139
	20-40	0.350	3.100	1.236	0.994	0.080	4.567	2.769	0.952	0.191

Table 3: Theoretical Model and Parameters of Semi-variance Function.

Hydraulic Parameters	Test Soil	Soil Depth [cm]	Theoretical model	C_0 [10^{-3}]	C_0+C [10^{-3}]	A_0	C_0/C_0+C	R^2
θ_s	NEW	0-20	Exponential	0.0049	0.050	7.62	0.098	0.733
		20-40	Gaussian	0.0234	0.248	58.73	0.094	0.918
	MOD	0-20	Exponential	0.1250	0.495	70.00	0.253	0.738
		20-40	Linear	0.6265	0.626	29.20	1.000	0.755
	OLD	0-20	Exponential	0.0023	0.026	5.61	0.089	0.821
		20-40	Spherical	0.0005	0.013	7.02	0.035	0.726
	CHECK	0-20	Spherical	0.0003	0.014	6.86	0.021	0.763
		20-40	Exponential	0.0106	0.033	71.00	0.032	0.708
α	NEW	0-20	Exponential	0.0004	0.005	6.81	0.080	0.757
		20-40	Gaussian	0.0001	0.201	58.90	0.0004	0.955
	MOD	0-20	Gaussian	0.6503	5.77	57.99	0.113	0.956
		20-40	Linear	0.6256	0.626	29.20	1.000	0.830
	OLD	0-20	Linear	0.0190	0.019	29.20	1.000	0.742
		20-40	Exponential	0.0214	0.063	71.00	0.341	0.741
	CHECK	0-20	Exponential	0.0160	0.194	7.08	0.082	0.740
		20-40	Linear	0.0150	0.015	29.20	1.000	0.785
n	NEW	0-20	Gaussian	0.0410	0.360	110.70	0.114	0.943
		20-40	Exponential	0.0208	0.145	4.18	0.143	0.753
	MOD	0-20	Exponential	0.2650	0.765	71.00	0.346	0.806
		20-40	Gaussian	29.3000	139.100	59.92	0.211	0.748
	OLD	0-20	Linear	0.1220	0.122	29.20	1.000	0.774
		20-40	Linear	0.0580	0.058	29.20	1.000	0.781
	CHECK	0-20	Exponential	0.0083	0.082	9.00	0.101	0.821
		20-40	Linear	0.0200	0.020	29.20	1.000	0.958

stable, between 1.229 and 1.277. Except for the OLD, n decreases with the increase of soil depth. This is consistent

with the results of Gao et al. (2014) on the spatial variability of SWCCs under different fertilization.

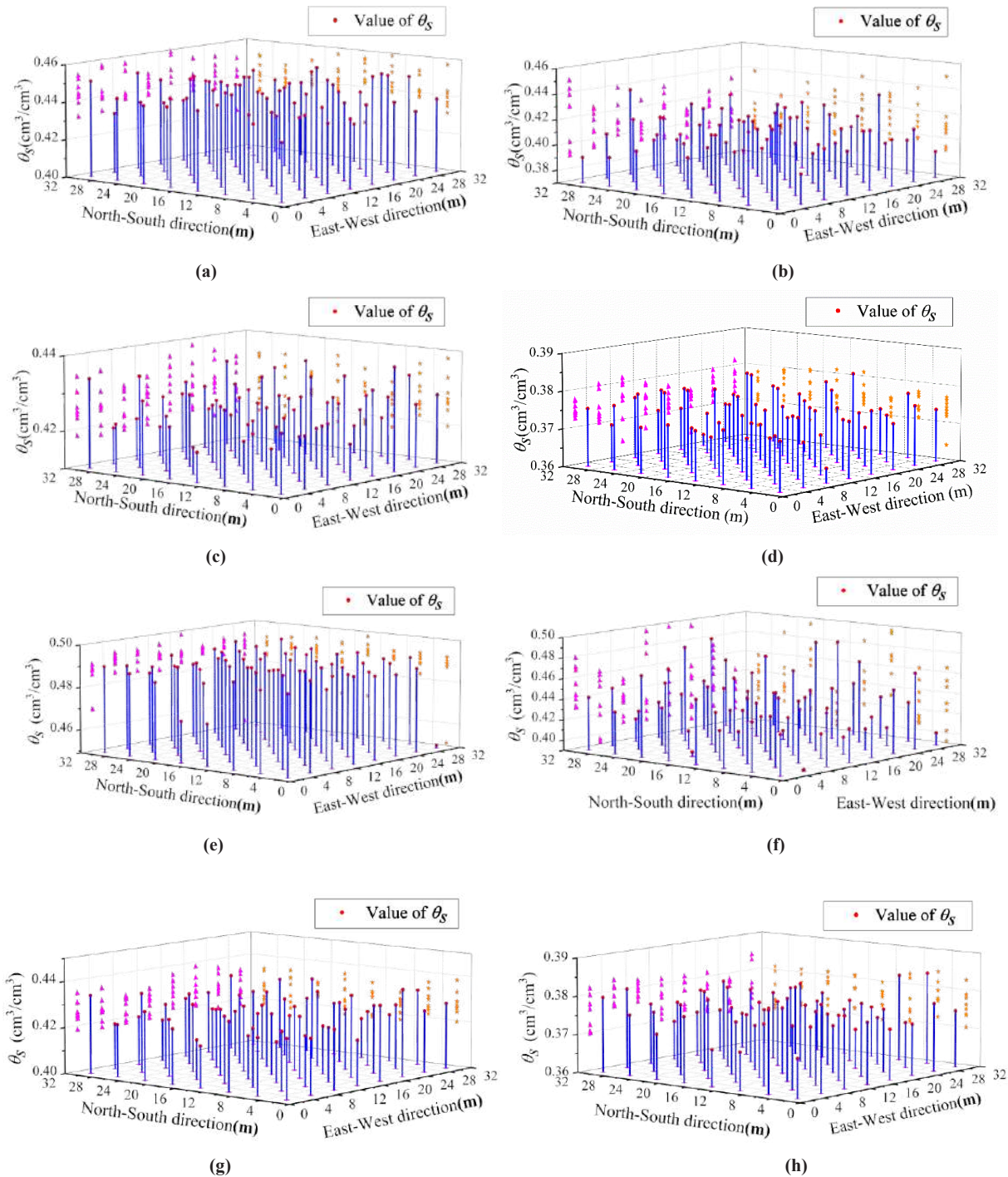


Fig. 4: Trend surface analysis of θ_S : (a) NEW: 0-20cm; (b) MOD: 0-20cm; (c) OLD: 0-20cm; (d) CHECK: 0-20cm; (e) NEW: 20-40cm; (f) MOD: 20-40cm; (g) OLD: 20-40cm; (h) CHECK: 20-40cm.

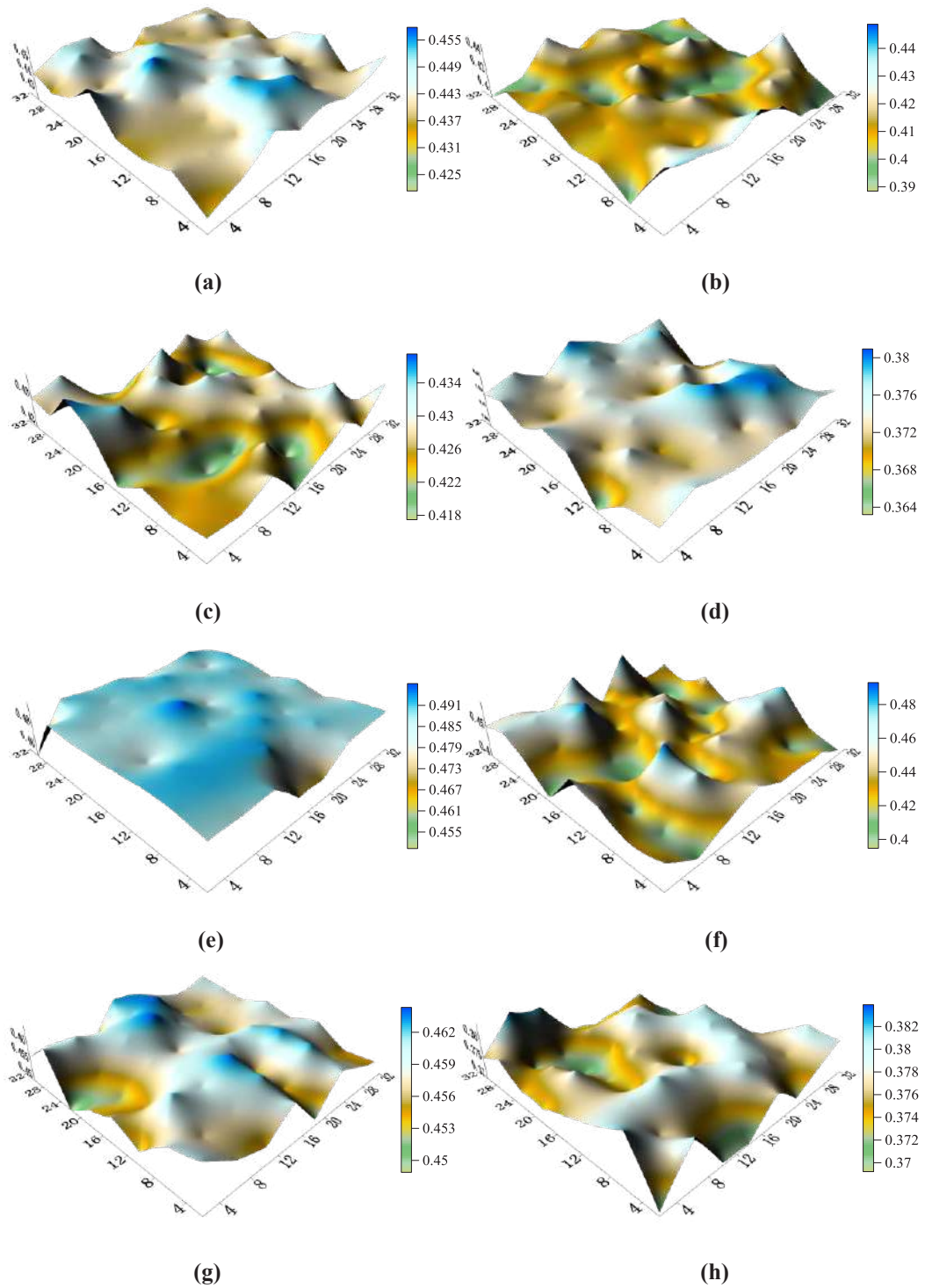


Fig. 5: Distribution maps of θ , predicted by Kriging: (a) NEW: 0-20cm; (b) MOD: 0-20cm; (c) OLD: 0-20cm; (d) CHECK: 0-20cm; (e) NEW: 20-40cm; (f) MOD: 20-40cm; (g) OLD: 20-40cm; (h) CHECK: 20-40cm.

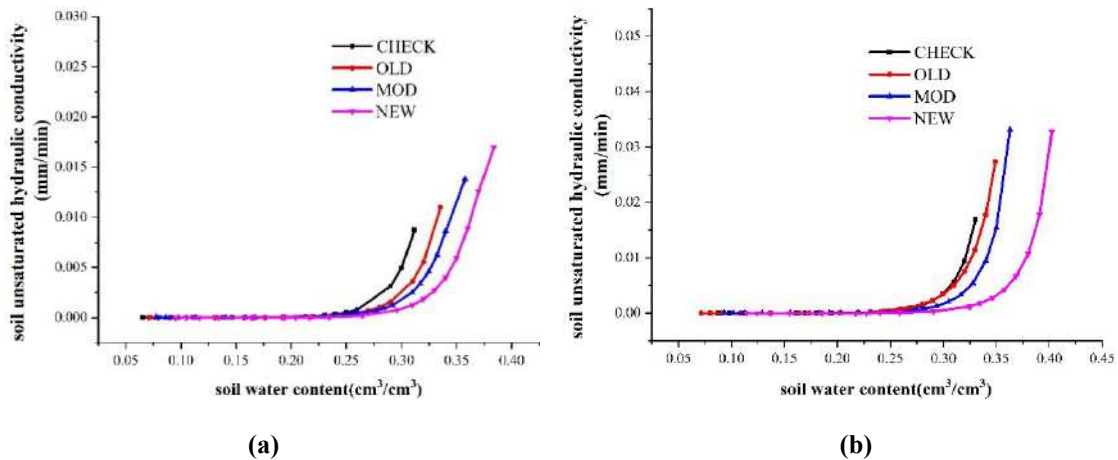


Fig. 6: Curves for soil hydraulic conductivity in (a) 0-20 cm; (b) 20-40 cm layer.

Geostatistical Analysis of VG Model Parameters

To analyze the spatial variability of the VG model parameters of each soil layer for different periods of time, the θ_s , α and n were analyzed by semi-variance using *GS+9.0* software, and the spatial variability function model parameters and regression model test parameters were obtained (Table 3). The results of the spatial variability analysis of the VG model parameters show that the θ_s , α , and n can be fitted with Gaussian, Linear, and Exponential models, and the Gaussian model has higher accuracy. The average values of nugget values (C_0) of θ_s , α , and n are 0.099×10^{-3} , 0.168×10^{-3} , and 3.729×10^{-3} , respectively. Except for the large change of n in MOD, the C_0 of other test soil types are relatively stable and the degree of change is small, indicating that the degree of spatial variation is caused by random factors such as soil characteristics, sampling, or measurement errors is small. The variable range (A_0) is larger than the sampling interval of 4 m, indicating that the selected model is ideal and can reflect the spatial correlation of the parameters of the soil moisture characteristic curve. For θ_s , α , and n , most of the nugget variance values $C_0/(C_0+C)$ are less than 0.25, only a few $C_0/(C_0+C)$ values are between 0.25-1, indicating that the θ_s , α , and n in the 0-40cm soil layer show strong spatial correlation (Cambardella et al.1994), and the overall degree of variation of random factors is small, which means the spatial heterogeneity caused by the spatial variability of soil structure is the dominant factor. This is consistent with the results of studies such as Xing et al. (2014), even if multi-point sampling is used to determine the SWCC on a small scale, it will inevitably exhibit different spatial distribution characteristics. Zhu et al. (2003) showed that the spatial variability of VG model parameters

is related to soil texture, organic matter content, and bulk density.

Spatial Distribution of VG Model Parameters

The combination of trend surface analysis (Fig. 4) and Kriging interpolation (Fig. 5) can more intuitively reflect the spatial distribution characteristics of VG model parameters. In this study, we used distribution characteristics of θ_s as examples. Each blue vertical line in Fig. 4 represents the θ_s value of a sampling point. These points are projected on the orthogonal plane of the East-west direction and North-south direction. The spatial distribution of θ_s in 0-20 cm and 20-40 cm soil layers of different periods of time have obvious patches and stripes. The distribution area of high-value areas in NEW, MOD, and OLD is significantly larger than CHECK. Compared with CHECK, the projection points of the θ_s of the NEW are most concentrated, while the distribution of the θ_s of the MOD and the OLD is relatively scattered, indicating that with the increase of planting years, the fields mulched with gravel will be more affected by random factors.

As shown in Fig. 5, the θ_s of each SWCC present a “bump” and “sag”. The distribution of θ_s in NEW is relatively “flat”, indicating that θ_s in NEW have strong spatial autocorrelation, and the spatial heterogeneity caused by spatial autocorrelation is greater than that caused by random factors. The θ_s of CHECK have obvious “bump and sag”, which indicates that the θ_s of CHECK is greatly affected by random factors, which further proves that the water retention of fields mulched with gravel is better. The number of bumps decreases with increasing depth, which may be related to the irregular surface topography of the

study area, and tends to stabilize with increasing depth (Zhao et al. 2017b).

Comparative Analysis of $K(\theta)$ with Different Periods of Time

Substituting the fitting parameter values of the VG model in Table 3 and the values of K_s from Table 1 in Eq. (4), the $K(\theta)$ formulas of tested soils are obtained. With $K(\theta)$ as the ordinate and the volume SWC as the abscissa, plot the $K(\theta)$ curves of 0-20 cm and 20-40 cm soil layers in different planting years (Fig. 6). When the SWC is close to saturation, the four types of $K(\theta)$ curves all have an inflection point showing a sharp vertical upward trend. Before the inflection point, the $K(\theta)$ curves are almost parallel to the horizontal axis, indicating that the $K(\theta)$ has become stable and close to 0. The abrupt inflection point of the $K(\theta)$ curves are mainly caused by the different soil water suction and the different connectivity of the water in the soil pores (Wang et al. 2015a). When the $K(\theta)$ is the same, the SWC of the fields mulched with gravel is greater than that of the CHECK, indicating that the water-holding capacity of the fields mulched with gravel is better than that of the CHECK.

When the $K(\theta)$ is the same, the changing trend of water content at different depths is NEW > MOD > OLD > CHECK. The large-pore structure of the soil in the mulched fields was destroyed as period of gravel mulching increased. According to She et al. (2014) showed that SWC and friction during the outflow were also large, so $K(\theta)$ curve is highest for OLD.

CONCLUSIONS

The authors of this paper examined SWCCs in fields mulched with gravel for different periods of time and discovered that the soil water retention capacity varies substantially. The NEW has the highest capacity for water holding. The soil water holding capacity decreases as planting time advances, and the CHECK is at its lowest. The results of fitting the SWCCs with the VG model and the Gardner model show that the VG model has a higher fitting accuracy. Geostatistics and Kriging interpolation are used to study the spatial variability of the VG model parameters. The nugget coefficient values $C_0/(C_0+C)$ of the θ_s , α , and n are mostly less than 0.25, showing a strong spatial correlation overall. It can be seen from the spatial distribution map of θ_s in the OLD are "high" and "sag", while the distribution map of the NEW is relatively "flat". The changing trend of $K(\theta)$ of fields mulched gravel is faster than that of CHECK, and the changing trend of NEW is the fastest.

ACKNOWLEDGMENTS

This research was supported by the National Natural Science Foundation of China (51869010), Guidance Program for Industrial Support of Colleges and Universities in Gansu Province (2019C-13), Longyuan Youth Innovation and Entrepreneurship Project, and the Lanzhou University of Technology Hongliu first-class discipline funding.

REFERENCES

- Amanabadi, S., Mohammadi, M.H. and Masihabadi, M.H. 2018. Predicting continuous form of soil-water characteristics curve from limited particle size distribution data. *Water SA*, 44(3): 428-435.
- Cambardella, C.A., Moorman, T.B. and Novak, J.M. 1994. Field-scale variability of soil properties in central Iowa soils. *Soil. Sci. Soc. Am. J.*, 58(5): 1501-1511.
- Dong, Y.Y., Zhao, C.Y. and Yu, Z.T. 2017. Characteristic curves and models analysis of soil water in interdune at the southern edge of Gurbantunggut Desert. *J. Soil. Water. Conserv.*, 31(1): 166-171.
- Fang, K., Li, H. and Wang, Z. 2016. Comparative analysis on spatial variability of soil moisture under different land-use types in the orchard. *Sci. Hortic.*, 207: 65-72.
- Fu, X.L., Shao, M.A. and Lu, D.Q. 2011. Soil water characteristic curve measurement without bulk density changes and its implications in the estimation of soil hydraulic properties. *Geoderma*, 167: 1-8.
- Gao, H.Y., Guo, S.L. and Liu, W.Z. 2014. Spatial variability of soil water retention curve under fertilization practices in arid-highland of the Loess Plateau. *Trans. Chin. Soc. Agric. Mach.*, 45(6): 161-165 and 176.
- Harguindeguy, S., Pierre C. and Martine P.G. 2018. Colloidal mobilization from soil and transport of uranium in (sub)-surface waters. *Environ. Sci. Pollut. Res.*, 26(2): 5294-5304.
- Kemper, W., Nicks, A. and Corey, A.J. 1994. Accumulation of water in soils under gravel and sand mulches. *Soil Sci. Soc. Am. J.*, 58(1): 56-63.
- Kishné, A.S., Yimam, Y.T. and Morgan, C.L.S. 2017. Evaluation and improvement of the default soil hydraulic parameters for the Noah land surface model. *Geoderma*, 285: 247-259.
- Li, X.D., Shao, M.A. and Zhao, C.L. 2019. Spatial variability and simulation of soil hydraulic parameters in arid northwest China. *Arid Zone Res.*, 36(6): 1325-1332.
- Li, X.Y. 2003. Gravel-sand mulch for soil and water conservation in the semiarid loess region of northwest China. *Catena*, 52(2): 105-127.
- Mao, N., Huang, L.M. and Shao, M.G. 2019. Profile distribution of soil saturated hydraulic conductivity and controlling factors under different vegetations on a slope in the loess region. *Soils*, 51(2): 381-389.
- Modaihsh, A.S., Horton, R. and Kirkham, D.J. 1985. Soil water evaporation suppression by sand mulches. *Soil. Sci.*, 139(4): 357-361.
- Pannecoucke, L., Le Coz, M. and Houzé, C. 2019. Impact of spatial variability in hydraulic parameters on plume migration within unsaturated surficial formations. *J. Hydrol.*, 574: 160-168.
- Qiu, Y., Wang, Y. and Xie, Z. 2014. Long-term gravel-sand mulch affects soil physicochemical properties, microbial biomass, and enzyme activities in the semi-arid Loess plateau of north-western China. *Acta Agric. Scand. Sect. B.*, 64(4): 294-303.
- Raghuram, A.S.S., Basha, B.M. and Moghal, A.A.B. 2020. Effect of fines content on the hysteretic behavior of water-retention characteristic curves of reconstituted soils. *J. Mater. Civ. Eng.*, 32(4): 04020057.1-04020057.13.
- Ren, C., Zhang, W. and Zhong, Z. 2018. Differential responses of soil microbial biomass, diversity, and compositions to altitudinal gradients depend on plant and soil characteristics. *Sci. Tot. Environ.*, 610: 750-758.

- Russo, G., Vivaldi, G.A. and De Gennaro B. 2015. Environmental sustainability of different soil management techniques in a high-density olive orchard. *J. Cleaner Prod.*, 107: 498-508.
- She, D.L., Liu, Y.Y. and Yu, S.E. 2014. Comparison of soil hydraulic properties under different land-use patterns. *Trans. Chin. Soc. Agric. Mach.*, 45(9): 175-179 and 186.
- Shi, W.J., Ma, Y., Xu F. 2014. Spatial variability of soil moisture and salt content in a cotton field on microscales under mulch drip irrigation. *Adv. Water Sci.*, 25 4 : 585-593.
- Udawatta, R.P., Kremer, R.J. and Adamson, B.W. 2008. Variations in soil aggregate stability and enzyme activities in temperate agroforestry practice. *Agric. Ecosyst. Environ.*, 39: 153-160.
- Van Genuchten, M T. 1980. A closed-form equation for predicting the hydraulic conductivity of unsaturated soils. *Soil Sci. Soc. Am. J.*, 44(5): 892-898.
- Vero, S.E., Healy, M.G. and Henry, T. 2016. A methodological framework to determine optimum durations for the construction of soil water characteristic curves using centrifugation. *Ir. J. Agric. Food Res.*, 55(2): 91-99.
- Wang, H.L., Tang, X.Y. and Zhang, W. 2015a. Effects of biochar application on tilth soil hydraulic properties of slope cropland of purple soil. *Trans. Chin. Soc. Agric. Eng.*, 4: 107-112.
- Wang, J.N., Xie, Z.K. and Guo, Z.H. 2010. Simulating the effect of gravel-sand mulched field degradation on soil temperature and evaporation. *J. Desert. Res.*, 30(2): 388-393.
- Wang, P., Xie, C.J. and Chen, J. 2012. Degradation of sand fields and water-salt variations with different planting years. *Bull. Soil Water Conserv.*, 32(2): 251-254.
- Wang, Z.C., Li, X.Y. and Shi, H.B. 2015b. Effects of residual plastic film on soil hydrodynamic parameters and soil structure. *Trans. Chin. Soc. Agric. Mach.*, 46(5): 101-106.
- Wu, J., Liv, Y.N. and Li, C.B. 2019. Fine classification of county crops based on multi-temporal images of Sentinel-2A. *Trans. Chin. Soc. Agric. Mach.*, 50(9): 194-200.
- Xing, X.G., Zhao, W.G. and Liu, Y. 2015. Spatial variability of soil moisture in the kiwi field under different sampling density conditions. *Trans. Chin. Soc. Agric. Mach.*, 46(8): 138-145.
- Yu, D.X., Jia, X.X. and Huang, L.M. 2018. Spatial variation and influencing factors of saturated hydraulic conductivity in different soil layers of the loess area. *Chin. J. Soil Sci.*, 49(5): 71-77.
- Zhang, S.W., Huang, Y.F. and Shen, C.Y. 2012. Spatial prediction of soil organic matter using terrain indices and categorical variables as auxiliary information. *Geoderma*, 171(2): 35-43.
- Zhao, W.J., Cao, T.H. and Li, Z.L. 2020a. Spatial variability of the parameters of soil-water characteristic curves in gravel-mulched fields. *Water Sci. Technol.*, 20(1): 231-239.
- Zhao, W.J., Cui, Z. and Zhang, J.Y. 2017a. Temporal stability and variability of soil-water content in a gravel-mulched field in northwestern China. *J. Hydrol.*, 552: 249-257.
- Zhao, W.J., Cui, Z. and Zhou, C.Q. 2020b. Spatiotemporal variability of soil-water content at different depths in fields mulched with gravel for different planting years. *J. Hydrol.*, 590.
- Zhao, W.J., Sheng, J. and Li, Z.L. 2017b. Spatial variability of soil salinity in a gravel-sand mulched jujube orchard at different scales. *J. Irrig. Drain. Eng.*, 143: 0401700911-0401700918.
- Zhu, A.N., Zhang, J.B., Chen X.M. et al. 2003. Study on Pedo-Transfer function in FENGQIU. *Acta Pedol. Sin.*, 1: 53-58.



A GIS-Based Study of Air and Water Quality Trends in Madurai City, India

L. Balaji*, M. Muthukannan**† and R. Kanniga Devi***

*Kalasalingam Academy of Research and Education, Krishnankoil, Tamil Nadu, India

**Department of Civil Engineering, Kalasalingam Academy of Research and Education, Krishnankoil, Tamil Nadu, India

***Department of Computer Science and Engineering, Kalasalingam Academy of Research and Education, Krishnankoil, Tamil Nadu, India

†Corresponding author: M. Muthukannan; m.muthukannan@klu.ac.in, civilkannan@gmail.com

Nat. Env. & Poll. Tech.
Website: www.neptjournal.com

Received: 28-05-2021
Revised: 26-06-2021
Accepted: 04-07-2021

Key Words:

Air pollution
Water pollution
TNPCB standards
GIS
Interpolation
Mitigation

ABSTRACT

The objective of this study is to assess the air quality and water quality at Madurai city using the spatial interpolation technique of the Geographic Information System (GIS). Inverse Distance Weighting (IDW), Kriging, Gaussian- Kriging methods of interpolation are used in the study. The study area is divided into 8 zones and primary data is collected through direct sampling for water. The air pollution concentration data on Suspended Particulate Matter (SPM), Respirable Particulate Matter (RPM), and Lead are collected from an air quality monitoring network system of Tamilnadu Pollution Control Board (TNPCB). The results indicate that the Kriging interpolation method performs well with an error value of 0.02. The data collected from the years 2006 and 2020 are compared using GIS and observed data. The comparison of results indicates that there is a good accord with the predicted value using Inverse Distance Weighting (IDW) and Kriging interpolation with the observed data. The analysis report indicates that the pollution level at all 8 blocks was severely affected in 2020 and it is above the prescribed standard of TNPCB. Particularly, Kalavasal, Arapalyam, and Periyar blocks are severely affected. This work also presents suitable mitigation measures to reduce pollution.

INTRODUCTION

Rapid industrial development, employment opportunities, and urbanization have led to the large-scale migration of people into developed cities (Patel & Burkle 2012, Muthukannan et al. 2019). Migration and industrial development create a negative impact on the environment especially on water, air, and soil (Huff & Angeles 2011, Cassidy et al. 2014). Air and water are the most important for all forms of life on Earth, and polluting either one or both will be a serious problem. The Government is taking all initiatives to monitor and control air and water pollution. Air and water quality monitoring networks have been established to assess the daily pollution level and improve policymaking to monitor pollution. Madurai city is now facing all kinds of water pollution and air pollution and as a consequence, environmental degradation is taking place. Madurai is one of the districts in Tamilnadu, which is known for its cultural heritage and historical importance. Today, the city is facing a lot of problems due to the increase in population, vehicle, and development in all four directions. As a result of urbanization, extensive quarrying, a rise in automobile population, and mining activities, the historical city's air and groundwater have been polluted. (Prince et al. 2020). Hence, there is a pressing need to study the present

and past status of pollution in the city and as well as to develop a database tool for prediction.

Air and water quality monitoring and evaluation have become a critical issue in the past years and every year the severity is increasing steadily (Varol et al. 2012). The recent study shows that for assessing air quality and water quality various techniques have been used by the researchers, Water Quality Identification (WQI) (Xu 2005, Shankar & Sanjeev 2008), Single Factor Pollution Index (SFPI) (Guo 1999), Complex Pollution Indices (CPI) (Meng et al. 2009), fuzzy and Artificial Neural Network (ANN) (Jiang et al. 2006, Liu et al. 2010), Analytic Hierarchy Process (AHP) (Pang et al. 2008). However, all the practicing methods are focused on a single location, are parameter centric and data are spatially discontinuous. As a result of the data discontinuity, it is impossible to identify hazardous and vulnerable locations and implement mitigation measures. (Gerdol et al. 2014). The air quality and water quality involve a large number of variables and the associated factors need to be evaluated individually (Yan et al. 2015). Hence, GIS is the most powerful tool for spatial interpolation of data, which creates surface grid maps and facilitates spatial analysis (Vairavamoorthy et al. 2007).

A Geographical Information System (GIS) is a tool, which is used to store, manage, retrieve and analyze all

types of spatial data, and provides excellent analysis and solutions to spatial problems (Kumar et al. 2015, Facchinelli et al. 2001). GIS and modeling have been used by various researchers for air pollution monitoring (Maantay 2007, Sohrabinia & Khorshiddoust 2007, Dikshit 2020), air pollution and health impact assessment (Lai et al. 2012), water quality and environmental impact (Donohue et al. 2006, Chang 2008, Jiang et al. 2014, Jasmin & Mallikarjuna 2014). Many studies have been conducted using GIS and spatial interpolation. Kim et al. (2014) studied air quality data monitoring using spatial interpolation methods, Ryan & Lemasters (2008) conducted epidemic logical studies. The study conducted by various researchers has used air and water quality models for mapping of air quality (Kumar et al. 2015), however, it is observed that the air and water quality models underestimate the pollution level (Kumar et al. 2015, Rood 2014). In addition, some unidentified ground-level data are also found missing and have uncertainty in prediction due to multiple assumptions. As a result, the observed air and water quality data are used in this study to make accurate inferences about the impact and policymaking. The study also uses the interpolation technique for air and water quality levels in the study area. Finally, the study compares the interpolation

values to the observed data to ensure that the results are reliable.

STUDY AREA

Madurai is the third-largest city in Tamilnadu and twenty fourth in India consisting of 100 wards. The city is located at 9.93°N latitude and 78.12°E longitude. The altitude of the city is 101m above sea level. The temperature during summer is 40°C max and 26.3°C min and during winter 29.6°C max and 18°C min and the average rainfall is 85.76 cm. The city extends to an area of 147.97 km² and the population is 14.62 lakhs as per the 2011 census. The river Vaigai flows across the city from North West to South East. The National Highways NH 7, NH 45B, NH 208, and NH 49 pass through Madurai. The State Highways, SH 32, SH 33, and SH 42 connect various parts of Madurai city. Fig. 1 shows the location map of Madurai city and the roads in the city.

DATA COLLECTION

The water samples were collected from all the eight blocks of Madurai namely, Matuthavani, Arapalayam, Thepaku-lam, Goripalayam, Kalavasal, Periyar, Palanganatham and

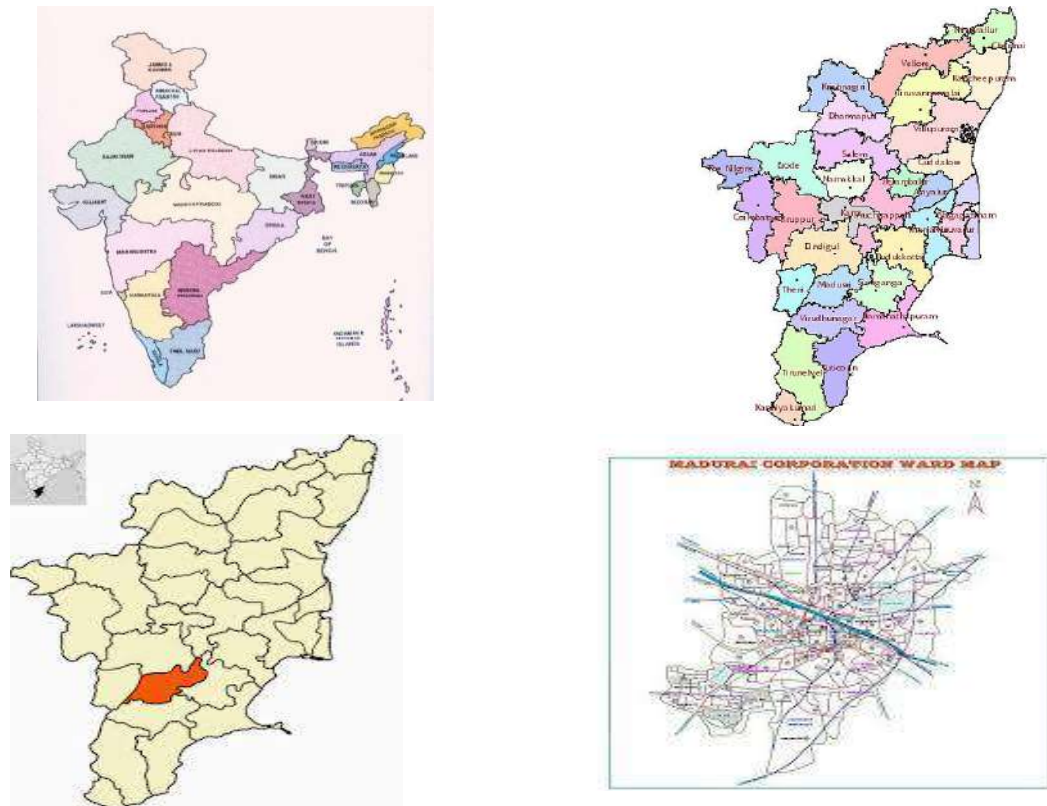


Fig. 1: Location map and road map of Madurai city.

Avaniyapuram. The houses were identified using a random numbering system that took into account the distance between them. The bore water samples were collected, labeled according to the blocks, and stored for analysis. To study the air pollution in all these eight blocks, air samplers were used. Air pollution concentration data on SPM, RPM, and Lead were collected from an air quality monitoring network system. These monitoring stations are operated continuously by Tamilnadu Pollution Control Board (TNPCB). TNPCB monitors air quality data at eight locations. The suspended particulate matter, irrespirable particulate matter, lead and carbon monoxide content was examined in the study area and recorded. Tamilnadu Water Supply and Drainage (TWAD) board kit was used for testing the water samples in the field and laboratory. Fig. 2 shows the TWAD board kit.

MATERIALS AND METHODS

To study the pollution level, it is required to formulate the following objectives (i) To study the past and present status of water and air pollution at Madurai city (ii) To develop GIS structure based on different attributes using Arc View 3.2 software (iii) To compare the air and water quality standards with WHO requirements and study the impact of air and water pollution in the study area (iv) To compare the interpolation values with the observed data to ensure the reliability of the results (v) To suggest possible solution for mitigating air and water pollution.

A shapefile for Madurai city was collected with geo-referencing associated with physical earth space using ArcGIS. Madurai city was divided into eight blocks and a point shapefile for water quality and air quality monitoring stations was created. The water quality and air quality concentrations of alkalinity, hardness, chloride, total dissolved solids, ammonia, fluoride, phosphate, residual chlorine, SPM, RPM and lead were attributed to the concerned point shapefile. The average annual concentrations were obtained



Fig. 2: TWAD Board kit for testing water samples.

from TNPCB and compared with the observed data. Inverse Distance Weighting (IDW), Kriging, and spline are the interpolation technique used in GIS (Colin 2004, Jha et al. 2011). In particular, IDW is used when the points are closely packed. This technique uses the grid values using a linear weighted combination of a dataset and its functions (Gunnink & Burrough 1996). The points with more weights are assigned to the point where SPM is to be interpolated. As per Equation (1) the weightage is an inverse function of distance.

$$Z_j = \frac{\sum_{i=1}^n W_i Z_i}{\sum_{i=1}^n W_i} \text{ and } W_i = \frac{1}{d_{ji}^P} \quad \dots(1)$$

Where,

Z_j = j^{th} Perception Point

W_i = Weight of recorded i^{th} point

d_{ji}^P = i^{th} to j^{th} point distance, P= Power

n = Total number of point in the neighborhood

Kriging's method of interpolation using the Gaussian process is a powerful interpolation technique (Bailey & Gatrell 1995) used for various applications like health science, geochemistry, and modeling (Griffith 1988). This interpolation technique produces better estimates assuming that the distance and direction reflect in spatial correlations. The mathematical interpolation and correlation model Kriging Gaussian is as given in Equation (2)

$$Z^*(u) - m(u) = \sum_{i=1}^n \gamma_i (Z(u_i) - m(u_i)) \quad \dots(2)$$

Where,

u and u_i = Location Vectors indexed by i

n (u) = Number of points

m (u), m (u_i)= Mean value expected of Z_u and Z (u_i)

γ_i = Kriging Weight assigned fo datum Z (u_i) for specific locations u

To evaluate the water quality using the spatial analysis with GIS as a tool, a potentially polluted area was identified using the observed data in the study area. The water quality assessment was made with a single factor pollution index method to identify alkalinity, hardness, chloride, ammonia, fluoride, and phosphate. SPSS was used to perform mathematical and statistical analyses. Ordinary Kriging method of geospatial interpolation was done (Deutsch 1996) and compared with the observed data. The single factor pollution index was formulated as given in Equation (3)

$$P_i = \frac{C_i}{S_i} \quad \dots(3)$$

Where,

P_i = Pollution index of i units

C_i = Concentrations of i units pollutants (mg.L^{-1})

S_i = Standard Water quality level

$P_i \leq 1$ = Better quality of water

The water quality depends on many factors and involves many components and chemicals. Hence, a comprehensive pollution index is essential to reflect all the pollutants. The comprehensive pollutants were assessed using Equation (4). The P-value indicates pollution level: Clean (0.2-0.4), Slight to medium pollutants (0.4-0.7), Medium (0.7-1.0) and Heavy pollution (1-2).

$$P = \frac{1}{n} \sum_{i=1}^n \frac{C_i}{S_i} \quad \dots(4)$$

Where,

P = Comprehensive pollution index

C_i = Pollution concentrations i units

S_i = Water Quality standard

N = Number of selected pollutants

RESULTS AND DISCUSSIONS

Water was collected from various places like Palanganatham, Avaniyapuram, Kalavasal, Arapalayam, Thepakulam, Ma-

tuthavani, Goripalayam and Periyar. The water quality was measured using TWAD BOARD kit to test Alkalinity, Hardness, Chloride, TDS, Ammonia, Fluoride, Phosphate, and Residual chlorine. The air quality parameters SPM, RPM, and Lead were studied and inferred. The collected water quality and air quality parameter dataset were given as input to point shapefiles. The observed value and model value were compared with TNPCB, and CPCB (2009) standards. The standard given by CPCB (2009) for air quality is 500, 150, and $0.5 \mu\text{g.m}^{-3}$ for SPM, RPM, and Lead respectively. The standard for water quality for Alkalinity, Hardness, Chloride, TDS, Ammonia, Fluoride, Phosphate, Residual chlorine is given as 500, 500, 500, 1000, 1, 1.5, 1 mg.L^{-1} respectively. To analyze the changes in the air and water quality the data were collected from TNPCB for the year 2006 and compared with the current observed air and water quality levels. In addition, the efficiency of the developed model Inverse Distance Weighting (IDW), Kriging, and ordinary Kriging were compared with the observed data in the selected locations. Table 1 shows the observed level of concentration of Water and Air pollution and level of concentration in the year 2006.

Table 1: Observed level of concentration of Water and Air pollution in 2020 (level of concentration in the year 2006 is given inside bracket).

Name of the Salt/ Pollutants	Standards in mg/ liter (Water), $\mu\text{g}/$ m^3 for Air	Name of the Block								
		Palanganatham	Avaniyapuram	Kalavasal	Arapalayam	Thepakulam	Matuthavani	Goripalayam	Periyar	
WATER POLLUTION	Alkalinity	500 (495)	620 (410)	645 (575)	725 (510)	695 (390)	550 (475)	625 (440)	630 (485)	685 (360)
	Hardness	500 (520)	700 (425)	655 (565)	745 (535)	685 (430)	630 (395)	560 (475)	680 (475)	545 (360)
	Chloride	500 (420)	595 (420)	680 (375)	715 (580)	715 (510)	580 (420)	590 (465)	535 (390)	690 (450)
	TDS	1000 (1722)	2298 (1722)	2376 (1452)	2622 (2064)	2514 (1866)	2112 (1488)	2130 (1602)	2214 (1566)	2304 (1554)
	Ammonia	1 (0.77)	1.20 (0.77)	0.35 (0.12)	1.20 (1.10)	0.80 (0.65)	0.62 (0.23)	0.20 (0)	0.90 (0.40)	1 (0.68)
	Fluoride	1.5 (1)	1.5 (1)	1.6 (1.2)	1.7 (1.6)	1.7 (1.1)	1.6 (1.2)	1 (0.7)	1.8 (1.5)	1.8 (0.9)
	Phosphate	1 (0.86)	0.9 (0.86)	0.70 (0.34)	1.05 (1.01)	1 (0.88)	0.90 (0.56)	0.59 (0.23)	0.60 (0.42)	0.90 (0.84)
	Residual Chlorine	1 (0.82)	1 (0.82)	0 (0)	1.25 (1.13)	0.95 (0.62)	0.95 (0.65)	0.14 (0)	0.74 (0.49)	0.84 (0.76)
AIR POLLUTION	SPM	$500 \mu\text{g.m}^{-3}$ (469.2)	985.4 (469.2)	985.4 (469.2)	985.4 (469.2)	985.4 (469.2)	985.4 (469.2)	985.4 (469.2)	985.4 (469.2)	985.4 (469.2)
	RPM	$150 \mu\text{g.m}^{-3}$ (129.6)	258.4 (129.6)	258.4 (129.6)	258.4 (129.6)	258.4 (129.6)	258.4 (129.6)	258.4 (129.6)	258.4 (129.6)	258.4 (129.6)
	Lead	$0.5 \mu\text{g.m}^{-3}$ (0.42)	0.48 (0.42)	0.48 (0.42)	0.48 (0.42)	0.48 (0.42)	0.48 (0.42)	0.48 (0.42)	0.48 (0.42)	0.48 (0.42)

Table 1 shows that the salt content and air pollution level in the study area. It is observed that the alkalinity in all the blocks has been increased considerably up to 40 per cent in the study area. This indirectly makes the water very hard. The permissible standard for hardness is 500 mg.L⁻¹. it is observed that the hardness level is increased up to 50 per cent in the Kalavasal region compared to the year 2006. The standard permissible limit for chloride is 500 mg.L⁻¹. It is observed that Avaniyapuram, Kalavasal, Arapalayam, and Periyar blocks are affected by the increase in chloride content.

WHO prescribed the maximum permissible limit for TDS as 1000 mg.L⁻¹ and it is very clear that all the blocks, the TDS level are increased by 100 per cent. The standard for Ammonia is 1 mg.L⁻¹. It is observed that the ammonia level has been increased up to 40 per cent in the study area. The standard permissible limit of fluoride is 1.5 mg.L⁻¹.

The fluoride content has been increased by 50 per cent and above. The permissible limit of phosphate is 1 mg.L⁻¹ and it is evident that the level has faced 10 per cent increases in the study area. The standard level of residual chlorine is 1 mg.L⁻¹ and it is evident that the level has been increased to 40 per cent in the study area. The standard permissible limit is about 500 µg.m⁻³. The suspended particulate matter is increased to 90 per cent in the study area.

The standard limit for residual particulate matter is 150 µg.m⁻³ and it is clear that the RPM level got increased to 80 per cent in the study area. The standard level for lead is 0.5µg.m⁻³ and it is clear that the lead level got maintained below the standard limit. Fig. 3 (a-k) shows the effect of water pollution and air pollution in the study area. Fig. 4 (a-c) shows the effect of water and air pollution at the station Kalavasal with the performance of the IDW and Kriging

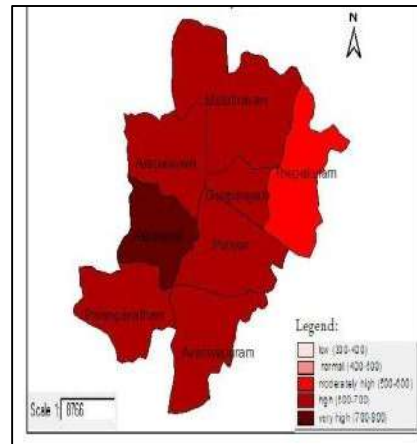
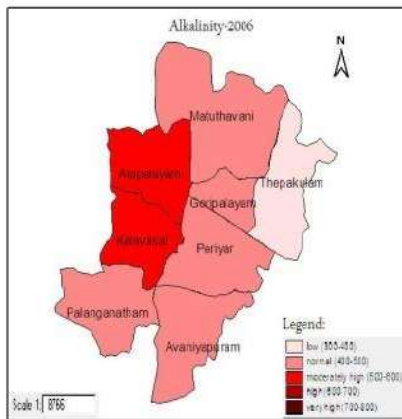


Fig. 3a: The changes in alkalinity level at Madurai City.

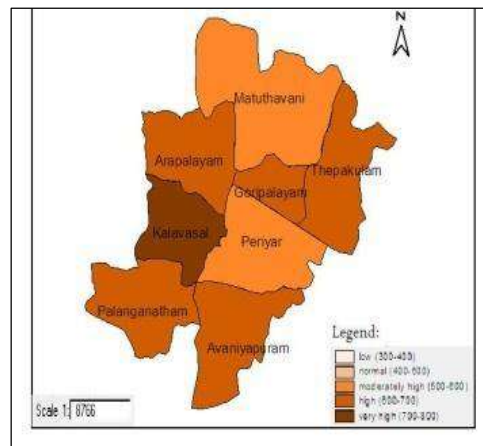


Fig. 3b: The changes in hardness level at Madurai City.

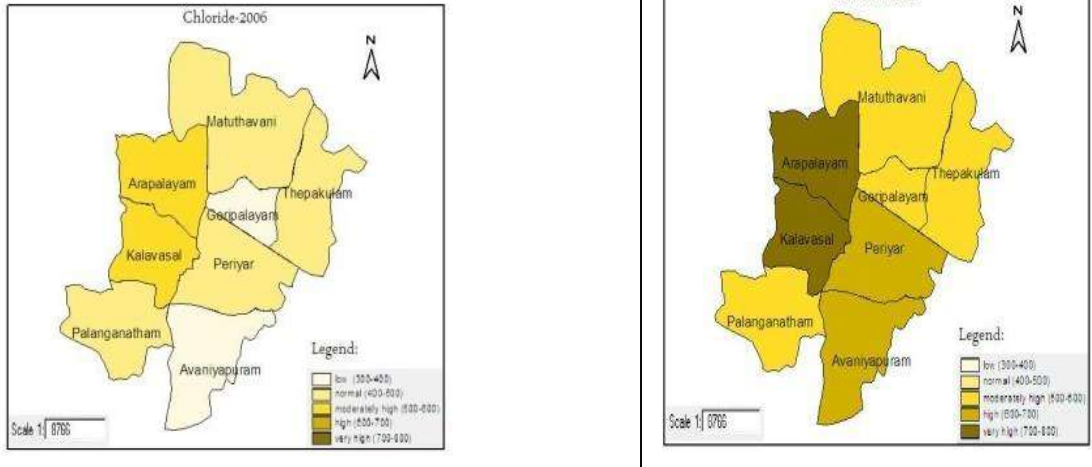


Fig. 3c: The changes in chloride level at Madurai City.

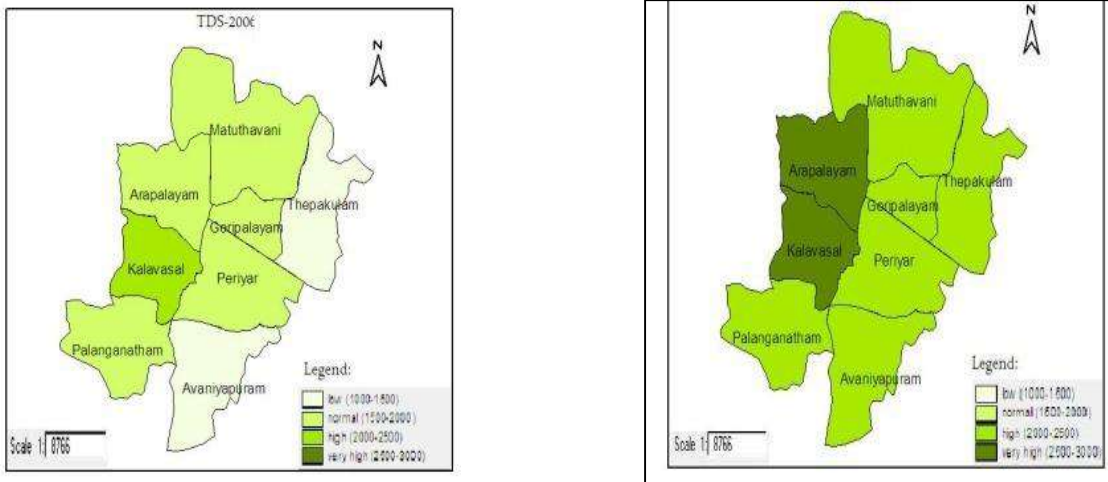


Fig. 3d: The changes in TDS level at Madurai City.

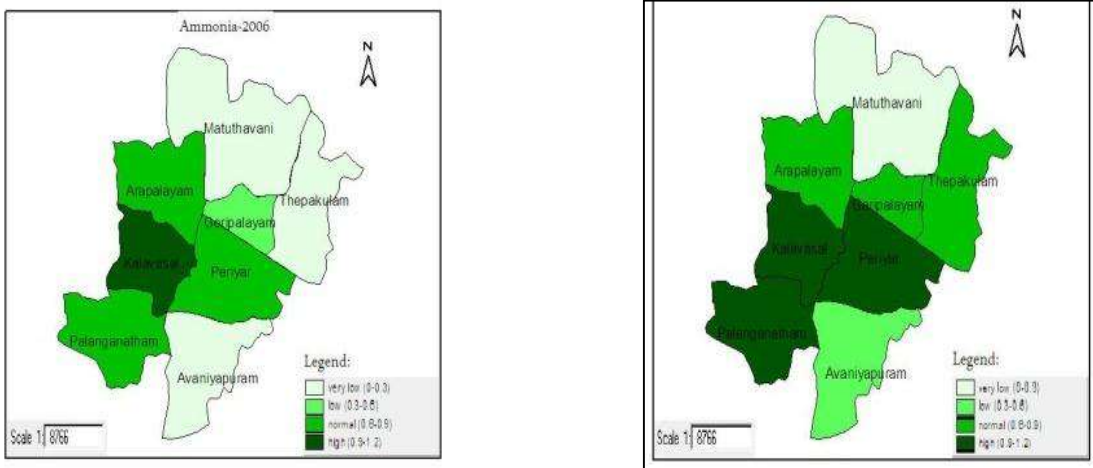


Fig. 3e: The changes in ammonia level at Madurai City.

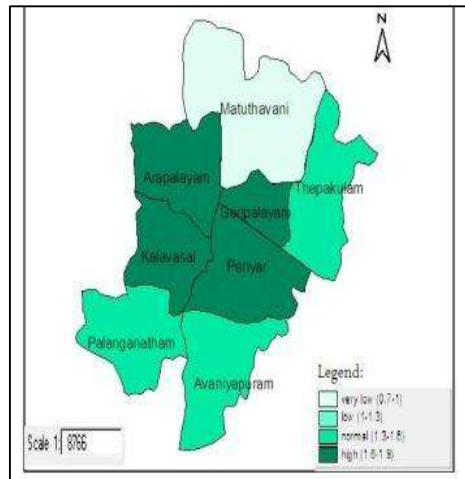
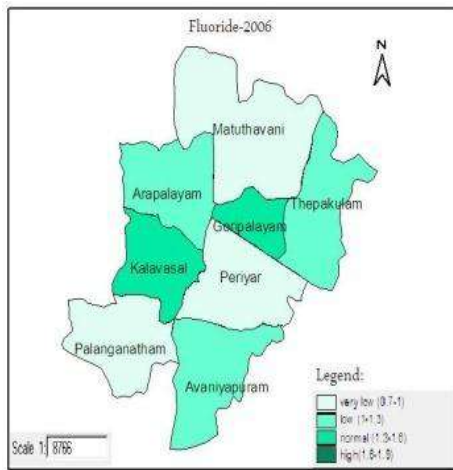


Fig. 3f: The changes in fluoride level at Madurai City.

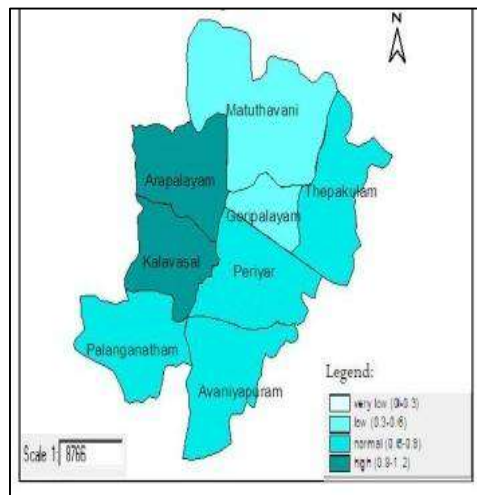
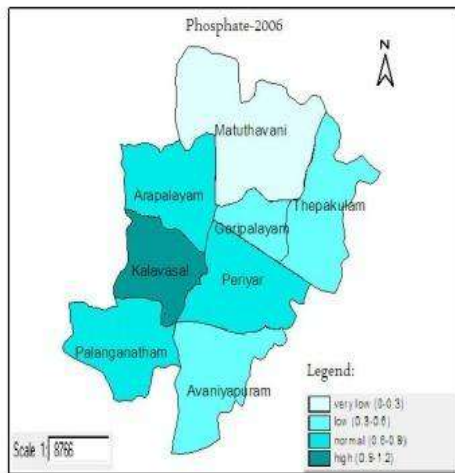


Fig. 3g: The changes in phosphate level at Madurai City.

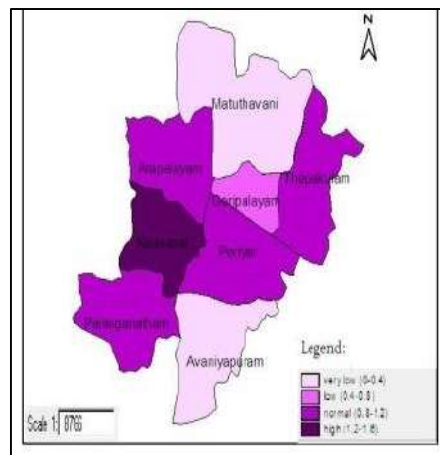


Fig. 3h: The changes in residual chlorine level at Madurai City.

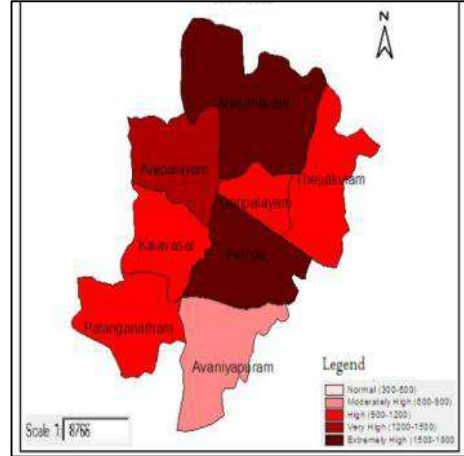
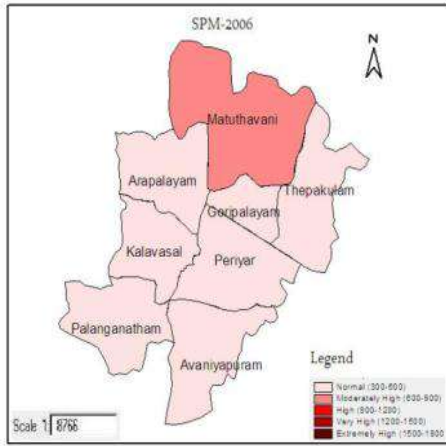


Fig. 3i: The changes in SPM level at Madurai City.

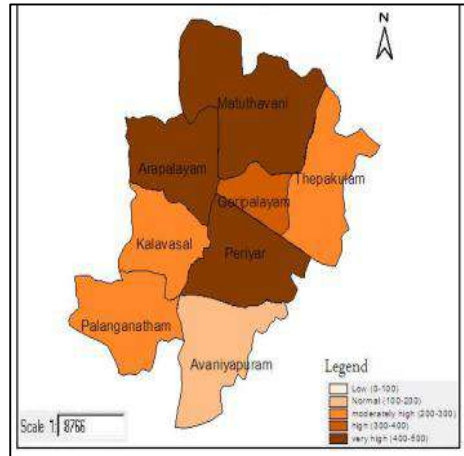
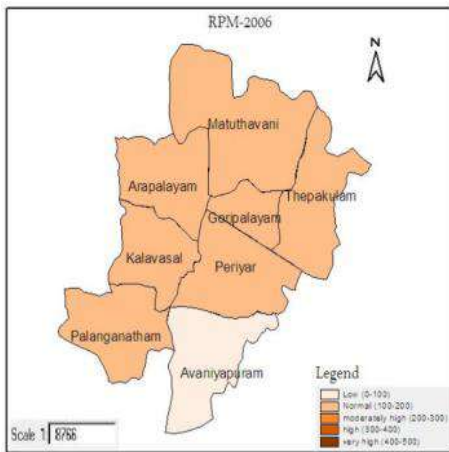


Fig. 3j: The changes in RPM level at Madurai City.

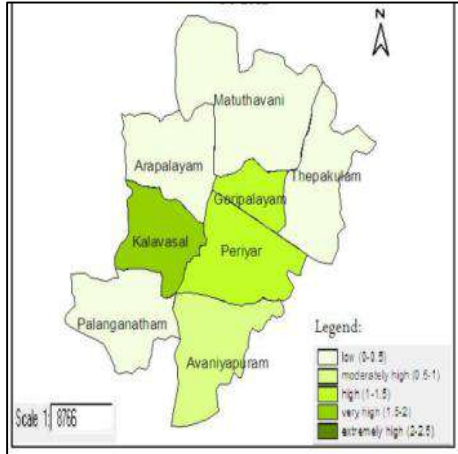
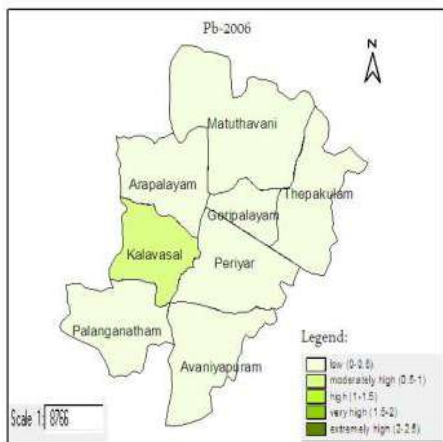


Fig. 3k: The changes in lead level at Madurai City.

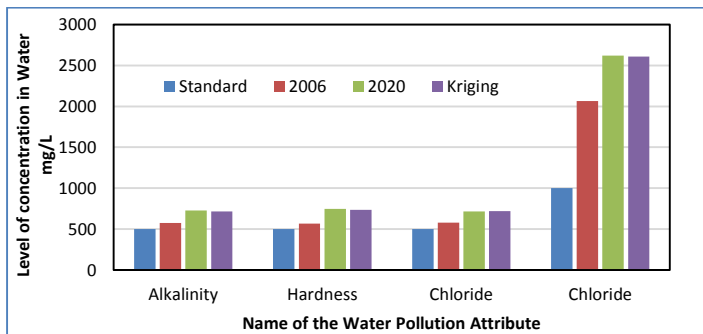


Fig. 4a: Water pollution and level of concentration at Kalavasal.

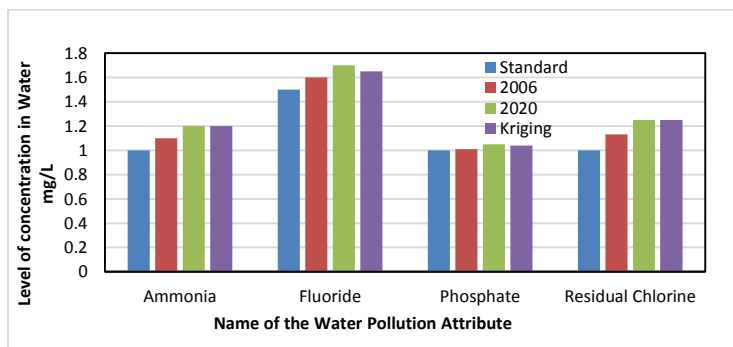


Fig. 4b: Water pollution and level of concentration at Kalavasal.

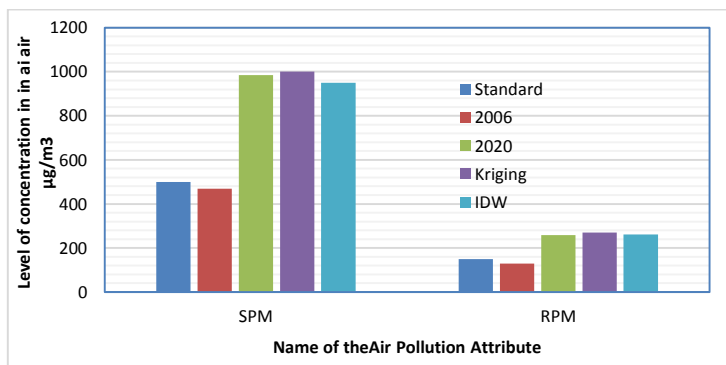


Fig. 4c: Air pollution and level of concentration at Kalavasal.

model. From Fig. 4 (a-c), it is observed that the model and observed value are similar and of error less than 2 percentage. The results of the interpolation models and observed data are shown in Table 2.

DISCUSSION

To study the impact of air and water pollution, data were collected for the years 2006 and 2020. A shapefile for Madurai city was collected with geo-referencing associated

with physical earth space using ArcGIS. Madurai city was divided into eight blocks and a point shapefile for water quality and air quality monitoring stations was created. The water quality and air quality concentrations pertaining to alkalinity, hardness, chloride, tds, ammonia, fluoride, phosphate, residual chlorine, SPM, RPM, and lead were attributed to the concerned point shapefile. The average annual concentrations were obtained from TNPCB and compared with the observed data. The Inverse Distance

Table 2: Performance of Spatial Interpolation Models and observed data for Kalavasal Block.

Attribute	Standard	2006	2020	Kriging (Gaussian)	Kriging	IDW	SD	Trend	Error	RMSE
Alkalinity	500	575	725	715	--	--	3.3	Increase	1.0140	1.0282
Hardness	500	565	745	735	--	--	2.1	Increase	1.0136	1.0274
Chloride	500	580	715	720	--	--	4.4	Increase	0.9931	0.9862
Chloride	1000	2064	2622	2610	--	--	3.3	Increase	1.0046	1.0092
Ammonia	1	1.1	1.2	1.2	--	--	2.8	Increase	1.0000	1.0000
Fluoride	1.5	1.6	1.7	1.65	--	--	2.9	Increase	1.0303	1.0615
Phosphate	1	1.01	1.05	1.04	--	--	2.6	Increase	1.0096	1.0193
Residual Chlorine	1	1.13	1.25	1.25	--	--	1.6	Increase	1.0000	1.0000
SPM	500	469.2	985.4	--	1000	950		Increase	0.9854	0.9710
RPM	150	129.6	258.4	--	270	262		Increase	0.9570	0.9159
Lead	0.5	0.42	0.48	--	0.46	0.42	0.45	Normal	1.0435	1.0888

Weighting (IDW) and Kriging interpolation techniques are used with GIS and compared to the observed data to avoid any missing data and underestimating of pollution levels. The results of the observed and arrived value using interpolation spatial model are given in Fig. 3 (a-k) and Fig. 4 (a-c). Inverse Distance Weighting (IDW), Kriging and Kriging Gaussian interpolation technique predicted the pollution level accurately with an error of less than 2 percentage. Hence, the model provides efficient predictions. Overall, the population and pollution level from 2006 to 2020 has drastically increased due to large-scale urbanization, industrial development, and migration of the people into the city (Balaji & Muthukannan 2020, 2021). In most of the parameters, alkalinity, hardness, chloride, TDS, ammonia, fluoride, phosphate and residual chlorine are found to be above the standard prescribed by the TNPCB and CPCB.

The alkalinity of Madurai city has increased up to 725 mg.L⁻¹, which is above the standard value of 500 mg.L⁻¹. The effect of alkalinity will seriously affect the kidney and other functions of humans. Particularly, Fluoride which is above the limit of 1 mg.L⁻¹ will seriously affect the tooth and make dental-related problems. The increase in water pollution was observed due to continuous pumping of groundwater through bore wells and recharge well that have also not been constructed properly in which, the stations like Periyar, Mattuthavanui, and Kalavasal are found to be the highly polluted area. In 2006, only some places out of 8 zones were affected, but in 2020, all the 8 zones are above the specified limit. Hence, to improve the water quality, (i) Artificial recharge bore wells and percolation pond to be created, (ii) Check dams can be provided in the water flowing streams to retain water to recharge the bore wells, (iii) De-silting the existing water sources dams and ponds will also improve water recharge (iv) To construct in rainwater recharge wells at each house

and make it mandatory (v) Good soil management measures and practice can be adopted improve surface percolation. (vi) Good sanitation facilities to be provided to avoid mixing of sewerage in the surface water bodies.

Air quality is a serious problem in all the cities in the world. The air pollution is not only due to urbanization, industrial development but also due to the increase in the traffic into the city. As Madurai is the center place for all eight districts, all the wholesale and retail markets are available in the city Central Business District (CBD). Hence, naturally, the traffic will be heavy in the CBD of the city. From the analysis, it could be observed that the stations Matthuthavani, and Periyar are the most affected by air quality attributes like SPM and RPM, whereas stations Kalavasal and Periyar are affected by lead. The concentration of lead in these stations is due to more industries. Hence, to avoid and improve the air qualities (i) Divert the traffic through the ring road and thereby avoid air pollution into the city, (ii) To restrict the industrial development inside the city, (iii) Industry that emits pollutants like NO_x and SO_x should be restricted, (iv) To create awareness about air pollution among the community.

CONCLUSIONS

The study was conducted at Madurai City to assess the air and water quality changes from 2006 to 2020. The study area was divided into 8 blocks and the primary data were collected from bore wells to assess the groundwater quality and the air quality data were obtained from network stations of TNPCB. To assess the impact on air and water quality, a GIS tool was used. The study used Inverse Distance Weighting (IDW), Kriging and Kriging Gaussian interpolation technique to predict the pollution level accurately and the results were compared with the observed data and it was found that the

error was less than 2 percentage. Hence, the model provides efficient predictions. Kriging Gaussian interpolation technique performed best among all the interpolation techniques. The results of the air and water pollution assessment indicate that in 2006 only 2 blocks had pollution levels beyond the threshold level of CPCB but, in 2020 all the 8 blocks were found to be polluted and the pollution level was much higher than the standards given by CPCB. The most affected blocks were found to be Kalavasal, Arapalayam, and Periyar. The maximum water pollution and air pollution recorded in Madurai was Alkalinity 725 mg.L^{-1} (Std. 500), Hardness 745 mg.L^{-1} (Std. 500), Chloride 715 mg.L^{-1} (Std. 500), TDS 2622 mg.L^{-1} (Std. 1000), Ammonia 1.1 mg.L^{-1} (std. 1), Fluoride 1.7 mg.L^{-1} (Std. 1), Phosphate 1 mg.L^{-1} (1), Residual chlorine 1.25 mg.L^{-1} (1), SPM $985 \mu\text{g.m}^{-3}$ (Std. 500), RPM $258.4 \mu\text{g.m}^{-3}$ (std. 150), and Lead $0.48 \mu\text{g.m}^{-3}$ (0.5). Hence, immediate mitigation methods should be carried out to stop further development of air and water pollution in Madurai city. The conclusion may be very useful for efficient air and water quality management at Madurai City.

REFERENCES

- Bailey, T.C. and Gatrell, A.C. 1995. *Interactive Spatial Data Analysis*. Longman, London, UK.
- Balaji, L. and Muthukannan, M. 2020. Investigation into the valuation of land using remote sensing and GIS in Madurai, Tamilnadu, India. *Europ. J. Remote Sensing*, 6: 1-9, -https://doi.org/10.1080/22797254.2020.1772118
- Balaji, L. and Muthukannan, M. 2021. Land use Land cover studies and its effects on Valuation using GIS Techniques in Madurai Town Planning Area, Tamilnadu, India. *IOP Conf. Series: Mater. Sci. Eng.*, 983(1), 012012. doi:10.1088/1757-899X/983/1/012012
- Cassidy, T., Inglis, G., Wiysonge, C. and Matzopoulos, R. 2014. A systematic review of the effects of poverty deconcentration and urban upgrading on youth violence. *Health Place* 26: 78-87. doi:10.1016/j.healthplace.2013.12.009
- Chang, H. 2008. Spatial analysis of water quality trends in the Han River basin, South Korea. *Water Res.*, 42: 3285-3304. doi: 10.1016/j.watres.2008.04.006
- Colin, C. 2004. *Interpolating Surfaces in Arcgis Spatial Analyst*. Arcuser, ESRI Education Services. www.esri.com
- CPCB 2009. Status of Water Supply, Wastewater Generation and Treatment in Class I Cities & Class II Towns of India 2009. CPCB, Central Pollution Control Board, Delhi.
- Deutsch, C.V. 1996. Correcting for negative weights in ordinary kriging. *Comp. Geosci.*, 22(7): 765-773.
- Dikshit, V.M. 2020. Groundwater Recharge Potential Sites in Semi-Arid Region of Man River Basin, Maharashtra State, India: A Geoinformatic Approach. *Nat. Environment and Pollution Technology*, 19(4), pp.1367-1378.
- Donohue, I., McGarrigle, M.L. and Mills, P. 2006. Linking catchment characteristics and her chemistry with the ecological status of Irish rivers. *Water Res.*, 40(1): 91-98.
- Facchinelli, A., Sacchi, E. and Mallen, L. 2001. Multivariate statistic a land GIS-based approach to identify heavy metal sources in soils. *Environ. Pollut.*, 114: 313-324.
- Gerdol, R., Marchesini, R., Iacumin, P. and Brancaleoni, L. 2014. Chemosphere monitoring temporal trends of air pollution in an urban area using mosses and lichens as biomonitors. *Chemosphere*, 108: 388-395. doi:10.1016/j.chemosphere.2014.02.035
- Griffith, D.A. 1988. *Advanced Spatial Statistics*. Kluwer Academic, Dordrecht, The Netherlands.
- Gunnink, J.L. and Burrough, P.A. 1996. Interactive spatial analysis of soil attribute patterns using exploratory data analysis (EDA) and GIS. In Masse, I. and Salge, F. (eds), *Spatial Analytical Perspectives on GIS*, Taylor & Francis, New York, pp. 87-99.
- Guo, J.S., Wang, H. and Long, T.R. 1999. Analysis and development of water quality evaluation method. *Chongqing Environ. Sci.*, 21(6): 1-9.
- Huff, G. and Angeles, L. 2011. Globalization, industrialization, and urbanization in pre-World War II Southeast Asia. *Explor. Econ. Hist.*, 48(1): 20-36. doi:10.1016/j.eeh.2010.08.001
- Jasmin, I. and Mallikarjuna, P. 2014. Physicochemical quality evaluation of groundwater and development of drinking water quality index for Araniar River Basin, Tamil Nadu, India. *Environ. Monit. Assess.*, 186(2): 935-948. doi: 10.1007/s10661-013-3425-7 PMID: 24052238
- Jha, D.K., Sabesan, M., Das, A., Vinithkumar, N.V. and Kirubakaran, R. 2011. Evaluation of interpolation technique for air quality parameters in Port Blair, India. *Univ. J. Environ. Res. Technol.*, 1: 301-310.
- Jiang, W.J., Cai, Q., Xu, W., Yang, M., Cai, Y. and Dionysiou, D.D. 2014. Cr(VI) adsorption and reduction by humic acid-coated magnetite. *Environ. Sci. Technol.*, 48(14): 8078-8085. doi: 10.1021/es405804m PMID: 24901955 24.
- Jiang, Y.P., Xu, Z.X. and Yin, H.L. 2006. Study on improved BP artificial neural networks in eutrophication assessment of China eastern lakes. *Journal of Hydrodynamics.*; 18(3): 528-532
- Kim, S., Yi, S., Eum, Y.S., Choi, Shin, H., Ryou, H.G. and Kim, H. 2014. Ordinary Kriging approach to predicting long-term particulate matter concentrations in seven major Korean cities. *Environ. Health Toxicol.*, 29: 1-8. doi:10.5620/eht.e2014012
- Kumar, A., Dikshit, A.K., Fatima, S. and Patil, R.S. 2015. Application of WRF model for vehicular pollution modelling using AERMOD. *Atmos. Clim. Sci.*, 5: 57-62.
- Lai, A.C.K., Thatcher, T.L. and Nazaroff, W.W. 2012. Inhalation transfer factors for air pollution health risk assessment. *J. Air Waste Manage. Assoc.*, 50: 1688-1699. doi:10.1080/10473289.2000.10464196.
- Liu, J.T., Gao, J.F. and Jiang, J.H. 2010. Application of different fuzzy assessment methods of water quality assessment in Dianchi Lake. *Environ. Pollut. Control*, 32(1): 20-25.
- Maantay, J. 2007. Asthma and air pollution in the Bronx: Methodological and data considerations in using GIS for environmental justice and health research. *Health Place*, 13(1): 32-56. doi:10.1016/j.healthplace.2005.09.009
- Meng, W., Zhang, N., Zhang, Y. and Zhang, B.H. 2009. Integrated assessment of river health based on water quality, aquatic life, and physical habitat. *J. Environ. Sci.*, 21: 1017-1027.
- Muthukannan, M. and Aruna, S. and Chithambar, G. 2019. The environmental impact caused by the ceramic industries and assessment methodologies. *Int. J. Quality Res.*, 13(2): 315-334. Doi: 10.24874/IJQR13.02-05
- Pang, Z.L., Chang, H.J., Li, Y.Y., Zhang, N.Q., Du, R.Q. and Hu, L.Q. 2008. Analytical hierarchy process (AHP) evaluation of water quality in Danjiangkou reservoir-source of the middle line project to transfer water from south to north, China. *Acta Ecol. Sin.*, 28(4): 1810-1819.
- Patel, R.B. and Burkle, F.M. 2012. Rapid urbanization and the growing threat of violence and conflict: A 21st century crisis. *Prehosp. Disaster Med.*, 27(2): 194-97. doi:10.1017/S1049023X12000568
- Prince, O.U., Ugochukwu, E. and Chibuzo, V.O. 2020. Environmental pollution: Causes, effects, and the remedies. *Microorg. Sustain. Environ. Health*, 87: 419-429. Doi: 10.1016/B978-0-12-819001-2.00021-8.
- Rood, A.S. 2014. Performance evaluation of AERMOD, CALPUFF, and Legacy Air Dispersion Models using the winter validation tracer study dataset. *Atmos. Environ.*, 89: 707-20. doi:10.1016/j.atmosenv.2014.02.054

- Ryan, P.H. and Lemasters, G.K. 2008. A review of land-use regression models for characterizing intraurban air pollution exposure. *Natl. Inst. Health Public Access*, 19(2): 127-33.
- Shankar, B.S. and Sanjeev, L. 2008. Assessment of water quality index for the groundwaters of an industrial area in Bangalore, India. *Environ. Eng. Sci.*, 25(6): 911-915
- Sohrabinia, M. and Khorshiddoust, A.M. 2007. Application of satellite data and GIS in studying air pollutants in Tehran. *Habitat Int.*, 31(2): 268-75. doi:10.1016/j.habitatint.2007.02.003
- Vairavamorthy, K., Yan, J.M., Galgale, H.M. and Gorantiwar, S.D. 2007. IRA-WDS: A GIS-based risk analysis tool for water distribution systems. *Environ. Model. Software*, 22: 951-965.
- Varol, M., Gökot, B., Bekleyen, A. and Sen B. 2012. Water quality assessment and apportionment of pollution sources of Tigris River (Tukey) using the multivariate statistical techniques-A case study. *River Res. Appl.*, 28(9): 1428-1438.
- Xu, Z.X. 2005. Comprehensive water quality identification index for environmental quality assessment of surface water. *J. Tongji Univ. Nat. Sci.*, 33(4): 482-488.
- Yan, C.A, Zhang, W., Zhang, Z., Liu, Y., Deng, C. and Nie, N. 2015. Assessment of water quality and identification of polluted risky regions based on field observations & GIS in the Honghe River watershed, China. *PLoS ONE* 10(3): e0119130. doi:10.1371/journal.pone.0119130



Land Use/Land Cover Evaluation Using Trajectory Maps Based on Landsat TM/OLI in Southwest China

Wenfeng Gong*, Tiedong Liu*, Tao Liu**†, Xuanyu Duan*, Yueyang Liu** and Philip Stott***

*College of Forestry, Hainan University, Haikou 570228, China

**College of Hydraulic and Electrical Engineering, Heilongjiang University, Harbin 150086, China

***School of Animal and Veterinary Sciences, University of Adelaide, Roseworthy 5371, Australia

†Corresponding author: Tao Liu; daliu_1978@126.com

Nat. Env. & Poll. Tech.
Website: www.neptjournal.com

Received: 19-01-2021

Revised: 24-04-2021

Accepted: 30-04-2021

Key Words:

Change trajectories
Mountainous area
LULCC patterns
Trajectory maps

ABSTRACT

This study mainly aims to detect the county-level spatio-temporal variability of LULCC (Land Use and Land Cover Change) spatial patterns in Southwest China. Multi-temporal Remote Sensing (RS) images (Landsat TM/OLI in 2000, 2005, 2010, and 2015) were applied to extract land use/cover types at each of the four-time nodes using the Support Vector Machine (SVM) method. Then, the trajectory map methodology was adopted to identify the spatio-temporal distribution characteristics of LULCC patterns throughout the given time series. According to the results, the area of unused land decreased continuously, 0.094% total. An evident decline of grassland by 2.17% was documented, and a notable increase was observed in forestland by 63.94 km² during the period from 2000 to 2015. Water bodies, built-up land, and unused land showed no significant change throughout the study period. The conversion from grassland to forestland and vice-versa (code 13 or 31) was prominent due to an adjustment made to local forestry policy during the first two periods (2000-2005 and 2005-2010), accounting for 17.55% and 17.56% of the study region, respectively. The anaphase trajectory transition type occupied the smallest area of all the trajectory maps. By contrast, the repetitive trajectory was the leading land-use transition type and covered the largest area. Trajectory analysis provides an effective approach for detecting the spatio-temporal changes in LULCC patterns.

INTRODUCTION

Human activities contribute to LULCC through their impact on the regional ecological environment, changes in climate, hydrology, vegetation, biogeochemical cycles, and biodiversity across a range of temporal and spatial scales (Collier et al. 2013). LULCC has become the core research focus in global change studies and also a significant facet of sustainable land use around the world. Over the last decade, as local socio-economic development has accelerated, as has regional industrialization and urbanization, a growing number of LULCC scholars have reduced their focus from the macro to the regional and micro scales. Furthermore, for LULC globally, understanding the temporal and spatial evolution process of regional LULCC has become critical, and several methodologies have been used to discover regional LULCC (Hao et al. 2009). These researches try to detect changes in the biological environment that drive human activities (Petrosillo et al. 2013), simulate and investigate the LULCC process (Hao et al. 2009), and anticipate future land use dynamics (Verburg et al. 2004). However, land-use change models have uncertainties due to the use of different sources for initialization, such as land use maps (Zomlot et

al. 2017, Verburg et al. 2013). Moreover, the general approach to analysis with land-use change models cannot fully reveal the complex and dynamic process of local, regional and global land uses. Thus, there is a need to develop a new methodology to better express the complex characteristics of spatial patterns and the various temporal processes in land-use change at various spatial and temporal scales.

Liu and Zhou (2004) provided a supplementary methodology for evaluating the accuracy of land cover change trajectories, in which a set of reasonable principles for evaluating the land cover change can be defined. By generating the 'curves' or 'profiles' of multi-temporal remotely sensed imagery, Zhou et al. (2008a, 2000b) developed and interpreted the spatial pattern metrics of multi-epoch trajectories of land cover change. The main benefit of trajectory analysis over other LULCC research methods is that it has been integrated into LULCC to assure data series continuity by interpolating or extending the temporal scale of the study (prospectively and retrospectively) beyond the period during which data is accessible (Wang et al. 2012, Zhou et al. 2008a, 2000b). The changing trajectory of LULCC has gained growing attention in studies of economically developed regions, basins,

and other areas over the last two decades. Using different temporal and spatial scales of RS image data and GIS, many studies on landscape pattern changes and the spatio-temporal process evolution of LULCC have used trajectory map methodology (Herold et al. 2003, Liu & Zhou 2004, Musa et al. 2020, Narasimhan & Stow 2010, Tang et al. 2005, Zhou et al. 2008a). However, to our knowledge, no studies have carried out the spatio-temporal trajectory analysis of LULCC at the county level for Youyang City in Southwest China.

Youyang, the largest county in Chongqing City, is situated in southwest China. Furthermore, it is not only a National Key Poverty Alleviation County but is also part of the important ecological zones along the Yangtze River Basin and in the Three Gorges Reservoir Area (Hua et al. 2014). It has played a significant role in ecological protection for the upper reaches of the Yangtze River. However, Youyang county is geographically dominated by mountainous areas. Further, the caster landform dominates, with an area of $0.31 \times 10^4 \text{ km}^2$, and accounts for nearly 60% of the total coverage. The usual erosion type is rocky desertification, which is widespread (0.15104 km^2) and poses a threat to both local socio-economic growth and regional ecological security. Furthermore, 40.28% of the municipality's agricultural areas have varying degrees of soil erosion (Yan et al. 2016), and this number is anticipated to rise in the future. The current state of the environment has been a key source of concern for the local administration, particularly when it comes to afforestation and the Green for Grain Project (GGP). The population density is about 170 km^2 , which is about 1.14 times higher than the national average, and 82.8% of the population is farmers. Additionally, the arable land per capita is less than 0.18 ha (Shi et al. 2018). Under the strong support of the central government, the Youyang government has implemented a series of policies and measures to encourage more young agricultural laborers to forgo agricultural activities. Though this increases the household income for residents and accelerates urbanization, this will also lead to a shortage in the traditional farming sector and increase the probability of cropland abandonment (Yan et al. 2016), thus affecting the local land-use change models. Hence, it is essential to gain an in-depth understanding of the status of spatial and temporal LULC dynamics in the study region to provide valuable guidance for future smart land-use management and planning, and to balance out the micro-rationality of farmers in decisions on farming intensity and the macro-rationality for the development of national food security policy (Yan et al. 2016).

In this paper, a study was conducted to 1) develop a methodology combining GIS and RS to identify spatio-temporal LULC change trajectories by overlaying the four stages of

binary images in 2000, 2005, 2010, and 2015) to investigate the spatio-temporal characteristics of LULCC evolution by analyzing the metrics of the spatio-temporal patterns of those change trajectories at 5-year intervals, and 3) to investigate the potential environmental impacts on the metrics for characterizing those.

MATERIALS AND METHODS

Study Area and Data

Located in the southeast part of Chongqing City at $28^{\circ}19'28''$ - $29^{\circ}24'18''$ N and $108^{\circ}18'25''$ - $109^{\circ}19'02''$ E, Youyang County, covers an area of about 5150 km^2 (Fig. 1), with forests accounting for about 52.2% of its territory. It is situated in the Wuling mountain region and dominated by mountains, covering the Yuanjiang River basin and the Wujiang River basin in the upper reaches of the Yangtze River. The local altitude ranges from 263 m to 1895 m. Meanwhile, the region's climate is subtropical humid monsoon, and the annual precipitation varies from 1000 mm to 1500 mm on average. The average annual temperature is 14.4°C (Shi et al. 2018).

Data Processing

Landsat data pre-processing: We downloaded all Landsat TM pictures (2000, 2005, and 2010) and Landsat OLI imagery (2015) from the USGS using a cloud threshold of 10%. At a spatial resolution of 30 m, all the images were geo-referenced to the same Universal Transverse Mercator (UTM, 49 N) map projection using a second-order polynomial transformation using a bilinear interpolation algorithm. The graphics were then created using a red-green-blue (RGB) color scheme using bands 543 (TM) and 654. (OLI). All the images were

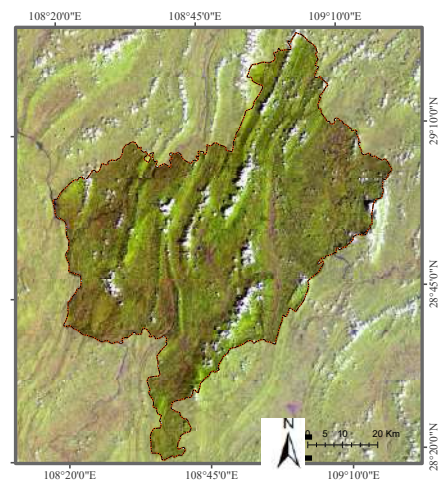


Fig. 1: Geographic location of Youyang County.

converted to surface reflectance using the sensor calibration algorithm, and the atmospheric correction was done with ENVI 5.3 software. Based on the national standard of land use classification system (GB/T 21010-2017), as developed by the Ministry of Land and Resources of China, the status of local land use and the field survey data was collected by a simple GPS instrument. This study involved six land-use types, cropland, forest, grassland, bodies of water, built-up land, and unused land. ENVI 5.3 software was used to classify all images via the SVM method. The overall accuracy of the land use data for the four periods was determined as 85.2%, 85.7%, 86.8%, and 88.9%, respectively, and the Kappa coefficient exceeded 72% for all types of land use. Then, the land cover classes were classified into one of six classes and denoted as 1, 2, 3, 4, 5, or 6 (1-forestland; 2-cropland; 3-grassland; 4-waterbody; 5-built-upland; 6-unused land). Finally, the land-use and land-cover maps for all the study periods were generated in Grid format using ArcGIS10.6 to facilitate further study in the subsequent change trajectory analysis.

Change trajectory analysis: Six land-use types from the four stages were included in the trajectory analysis mapping of the research region to investigate overall gains and losses of area for different temporal slices of land cover type. The land cover codes 1 through 6 were shown first. Second, using the raster calculation module in ArcGIS10.6, as well as the equation below, the trajectory codes for each raster pixel were calculated.

$$Z_{ij} = M_{ij} \times 10 + N_{ij} \quad \dots(1)$$

Where, Z_{ij} represents the trajectory layer with the trajectory code of the pixel at row i and column j , with no mathematical sense, while M_{ij} and N_{ij} refer to the code of LULC types from the beginning to the end of the study period.

In this study, to build a time series trajectory map, the ArcGIS spatial analysis module was used, and trajectory codes were formed using the following method.

$$T_{ij} = (G1)_{ij} \times 10^{n-1} + (G2)_{ij} \times 10^{n-2} + \dots + (Gn)_{ij} \times 10^{n-n} \quad \dots(2)$$

Where, T_{ij} has no mathematical sense and represents the trajectory code of the pixel at row i and column j in the trajectory layer, n refers to the number of time codes, while $(G1)_{ij}$, $(G2)_{ij}$ and $(Gn)_{ij}$ represents the LULC map code values in different periods. A numeric trajectory code in the form of $xxxx$ was treated as stable, $xyyy$ as prophasic, $xxxy$ as an aphasic, $xyxy$ as middle, $xyzx$ as repetitive, and $xyxz$ or others as continual.

Change trajectories and mapping: To gain a deeper understanding of LULCC processes and to depict the spatial pattern of change dynamics, we analyzed the spatio-temporal

dynamics of LULCC during different periods in the GIS environment. To begin, the LULCC transfer matrix model was used to calculate the area of various land-use transitions from 2000 to 2005, 2005 to 2010, and 2010 to 2015. Second, the spatial analysis tool "Overlay" in ArcMap 10.6 was used to determine the spatio-temporal trajectory map of LULCC for each of the three periods. The following is how the transfer matrix was calculated:

$$P_{ij} = \begin{pmatrix} P_{11} & P_{12} & \dots & P_{1m} \\ P_{21} & P_{22} & \dots & P_{2m} \\ \dots & \dots & \dots & \dots \\ P_{m1} & P_{m2} & \dots & P_{mm} \end{pmatrix} \quad \dots(3)$$

Where, P_{ij} , with non-negative value, indicates the land area in transition from type i to j , and $\sum_{i=1}^m P_{ij} = 1, 0 < P_{ij} \leq 1$.

RESULTS AND DISCUSSION

LULC Status and Change

The LULC types extracted from 2000, 2005, 2010, and 2015 images were forestland, grassland, cropland, water bodies, built-up land, and unused land (Fig. 2). Forestland and grassland were the main land use types across the study region, with a combined proportion of 86.79%, 88.54%, 86.13%, and 85.86% of land area in the four years, respectively (Table 1). This is consistent with the characteristics of regional socio-economic development. Forestland accounted for the largest proportion in the study area, comprising 52.95%, 66.64%, 54.27%, and 54.19% of total land cover, respectively. During the study period, the net area of forestland increased by 63.94 km², with an overall annual change ratio of 0.47%, which was largely attributed to the implementation of the GGP which was launched by the government in 1999. The grassland was the second most prominent and comprised 33.84%, 21.83%, 31.86%, and 31.67% of the study region, respectively. Overall, grassland declined, with an overall annual change ratio of -1.28% throughout the study period. This indicates that overgrazing and encroachment are still major stressors on grasslands. Over the past 15 years, the cropland covered an area of 630.64 km², 557.8 km², 660.77 km², and 660.10 km² in the four study periods, respectively, with the net increase area of 12.12 km². Cropland has faced renewed pressure in recent years due to urban expansion of the built-up area. Built-up land was the smallest man-made land use type, accounting for 0.38%, 0.14%, 0.43%, and 0.62% of total land cover, respectively. The smallest proportion of land was covered by unused land, with areas reaching only

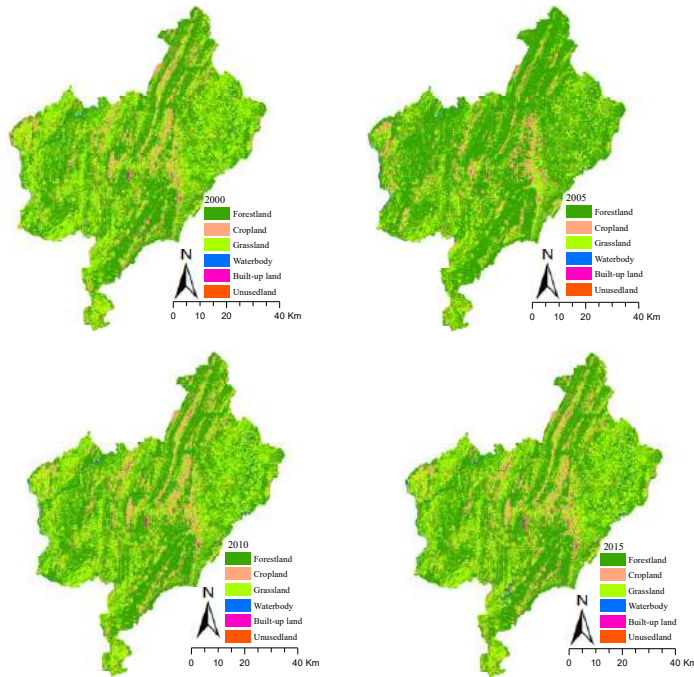


Fig. 2: Land-use maps of the study region in 2000, 2005, 2010 and 2015.

5.26 km², 2.04 km², 0.43 km² and 0.42 km², respectively. It seemed that water bodies, built-up land, and unused land showed no significant change throughout the study period.

Land Trajectory Analysis

The LULCC maps for each of the four years were obtained from RS satellites and analyzed using ArcGIS software to generate the spatio-temporal trajectory map. Here we characterize region-wide spatio-temporal trajectory maps for each of the three-time frames (Table 2).

Land trajectory analysis map for 2000-2005: We identified 34 trajectories of total land cover (Fig. 3-a), with 28 different land-use changes accounting for 35.56% of the total land area. As shown in Table 2, the conversion from grassland

to forestland (code 31) makes up the largest area at 695.21 km². This conversion accounted for 38.09% of the total area of land-use changes and was mainly scattered across the slopes. This highly significant change in the trajectory map is attributed to the implementation of various forestry policies and the adjustment made to agricultural policies during this period, especially regarding the ecological protection of ecological zones. Through these measures, the government encouraged local households to develop local forest industries of characteristic species. The cropland was abandoned and gradually transformed into grassland. However, the proportion of transition (code 13) reached 7.64%, indicating that a large amount of former forestland was occupied by grassland. Cropland→forestland (code 21) comprised

Table 1: Land use changes from 2000 to 2015 in Youyang County.

Land cover class	2000		2005		2010		2015	
	Area in km ²	In %	Area in km ²	In %	Area in km ²	In %	Area in km ²	In %
Forestland	2725.70	52.95	3430.59	66.64	2793.72	54.27	2789.64	54.19
Grassland	1742.22	33.84	1127.13	21.90	1640.07	31.86	1630.36	31.67
Cropland	630.64	12.25	557.81	10.84	660.77	12.84	660.10	12.82
Water body	24.22	0.47	22.87	0.44	30.81	0.60	35.40	0.69
Built-up land	19.71	0.38	7.29	0.14	21.94	0.43	31.83	0.62
Unused land	5.26	0.10	2.04	0.04	0.43	0.01	0.42	0.01
Sum	5147.75	100	5147.75	100	5147.75	100	5147.75	100

the second-largest area on the trajectory maps, covering an area of 343.02 km² and accounting for 18.80% of the total area of land-use changes. This change was also attributable to the implementation of GGP. As a result of GGP, a large amount of cropland was abandoned (or unoccupied) and then converted into forestland. The study region has drawn a lot of attention from the local government as a major forestry county in Chongqing and a candidate county for China's National Afforestation Model City. Forestry has become the region's main industry. Cropland to forest conversion occurred in mountainous areas with steep slopes (>25°) and high elevations (over 800 m). In the flatter mountain region, where a local minority population lives, forestland (123.91 km²) changed to farmland (code 12). In this stage, it appeared that there was a substantial imbalance in the creation and destruction of forestland. Cropland is the most essential natural asset for a household's subsistence in the study region's poor mountainous terrain (Hua et al. 2016). Furthermore, Youyang County's population increased dramatically from 5.94105 in 2000 to 8.56105 in 2019. Mountain dwellers in this area must deal with the problem of more people sharing less land. Forestland was cleared for agricultural expansion by humans to make a living. Local villagers' livelihoods were harmed, and regional soil erosion was increased. A total of 279.73 km² (16.06%) of grassland was converted to cropland (code 32), indicating that grassland was the primary source of new cropland. The lack of high-quality land resources and crops in Youyang county has hampered local economic development to some extent. Grasslands distributed in the central region along the river valley are often converted to

obtain more agricultural products. Comparatively, the conversion from cropland to grassland (code 23) accounts for 137.26 km² (21.76%), indicating that the implementation of forestry ecological policies by the local government has made an impact.

Land trajectory analysis map for 2005-2010: Using the ArcGIS 10.6 spatial analysis module, we obtained the spatio-temporal trajectory map for the period from 2005-2010 (Fig.3-b). Major mutual conversions between forestland and grassland continued to occur, making this stage's most critical trajectory. The conversion of 658.38 km² of forestland to grassland (code 13) accounted for 35.61% of all land-use conversions. In deforested places, this process is linked to forestland degradation and grassland restoration. The shift from grassland to forestland (code 31) covered 245.66 km² (21.84%), owing to natural vegetation succession in the mountainous region and the local Forestry Bureau's implementation of environmental protection policies. "Forestland-cropland" (Code 12) was another important trajectory, accounting for 19.15% of the total area of land-use change. Despite the GGP and the associated subsidy starting in 1999, deforestation still occurred in some areas. To meet the demands of both agriculture production and livestock, a typical farming household, particularly of the Tujia ethnic group, appeared to prefer foraging in forestland near cropland. Smallholders cultivate the majority of forestland plots of high or middling quality with a modest or abrupt slope (Hua et al. 2016). Furthermore, the codes 23 and 21 in the trajectory map, which account for regions of 267.62 km² and 128.79 km², respectively, represent a considerable change.

Table 2: Trajectory map order of LULCC from 2000 to 2015 in study region.

2000-2005			2005-2010			2010-2015		
Code	Area (km ²)	Change ratio / %	Code	Area (km ²)	Change ratio / %	Code	Area (km ²)	Change ratio %
31	695.21	38.09	13	658.38	35.61	35	8.15	54.58
21	343.02	18.80	12	353.99	19.15	14	2.46	16.49
32	279.73	15.33	23	267.62	14.48	15	1.60	10.70
13	208.29	11.41	31	245.66	13.29	34	1.53	10.28
23	137.26	7.52	32	149.31	8.08	25	0.40	2.67
12	123.91	6.79	21	128.79	6.97	54	0.31	2.09
53	10.64	0.58	35	12.33	0.67	45	0.05	0.36
41	6.96	0.38	14	7.39	0.40	12	0.04	0.26
43	4.86	0.27	34	7.03	0.38	32	0.02	0.14
51	3.82	0.21	15	3.97	0.21	31	0.01	0.09
14	3.73	0.20	41	3.90	0.21	65	0.01	0.05
34	3.70	0.20	43	2.48	0.13	-	-	-
63	2.47	0.14	64	1.79	0.10	-	-	-
52	1.40	0.08	54	1.61	0.09	-	-	-

The local government implemented four strategic initiatives in 2009 for Industrial County, Forestry County, Tourism County, and Environmental County, which advanced local urbanization and industrialization while expanding rural people's economic prospects beyond farming. As a result, more workers were migrating into urban areas for non-farm employment opportunities. Further, the remaining farmers were primarily elderly people and women with relatively low labor capacity (Li et al. 2014). These new developments raised the opportunity cost for farming, thus reducing the relative profitability of traditional farming businesses (Yan et al. 2016). Consequently, a lot of cropland was abandoned or converted for other uses (Zhang et al. 2014). This indicates that the extent and dynamics of cropland abandonment may undermine national food security for China in the future.

Land trajectory analysis map for 2010-2015: With 17 different trajectories in this stage, the spatial distribution of trajectories throughout this time differed significantly from prior periods (Fig. 3-c). The most visible path was “grassland built-up land” (Code 35), which covered 8.15 km² and had a 54.58 per cent change ratio. Meanwhile, 2.00 km² of land was transformed from forestland or agriculture to built-up land (Codes 15 and 25), accounting for 13.3% of all converted land-use types. Due to rapid economic development and accelerated industrialization and urbanization, especially for the implementation policies of “one district and four parks”, the expansion of constructed land caused some of the grassland, forestland, and cropland to be permanently converted. Meanwhile, Youyang county is well known for its karst. The lack of optimal land use will exacerbate rocky desertification and regional soil erosion, thus further deteriorating environmental quality and causing more environmental problems. Therefore, it will be important to prioritize reasonable utilization of land in the future. The conversion from forestland to water (code 14) accounted for 2.46 km², while the area of other trajectories was limited.

Land use Pattern for Trajectory Analysis

To determine the full spatio-temporal trajectory map for the study area, the trajectory map method was applied to identify a time series for spatio-temporal trajectory maps of four types in ArcGIS10.6, which are detailed as follows:

Prophase trajectory map analysis: The prophase transition trajectory map accounted for 37.02 km². The trajectory codes 3111 and 3222 were the major prophase transition types, accounting for 25.91 km² and 7.30 km², respectively. This indicates that conversions to forestland and cropland mostly occurred from grassland. The initial transition was influenced by local agricultural policies, whereas the latter transition showed that grassland was converted to cropland

at a consistent rate across the research period. The proportions of trajectory codes 3444 and 6333, which accounted for 1.08 km² and 0.99 km², respectively, were likewise major components of the prophase transition map.

Anaphase trajectory map analysis: The anaphase transition type only occurred during the period from 2010-2015

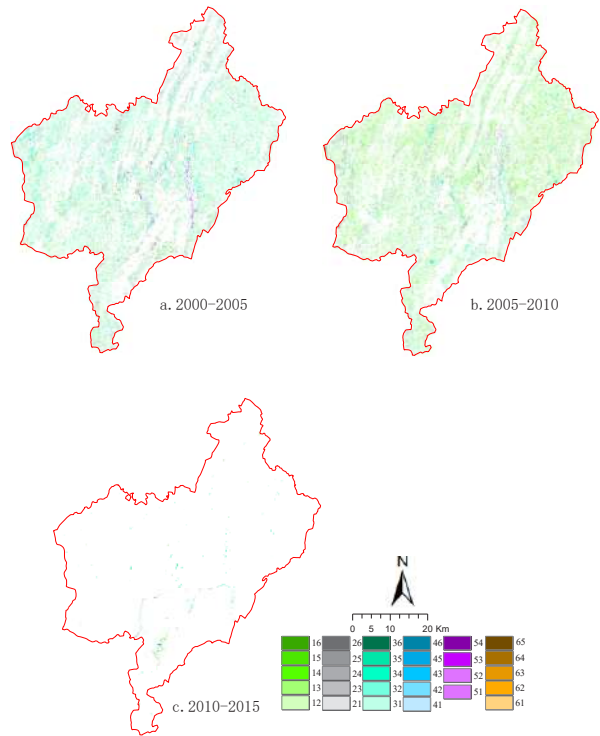


Fig. 3: Distribution map of LULCC trajectories from 2000 to 2015 of the study region.

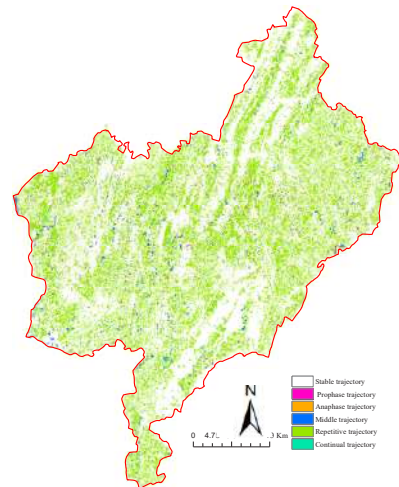


Fig.4: LULCC trajectory map of study region from 2000 to 2015

(Chen et al. 2020). The area was 9.35 km², which was the smallest of all the trajectory maps. Trajectory code 3335 comprised the largest area at 5.50 km². This was followed by trajectory code 1115, which accounted for 17.83% of the total area of the anaphase trajectory map. A major consequence is that this transition reduced ecosystem services that were previously rendered by the forestland and grassland. The other anaphase transition types comprised 2.18 km².

Middle trajectory map analysis: In the middle trajectory map, the land use types only transitioned during the period from 2005-2010 and remained unchanged during the other two periods (Chen et al. 2020). The area of the middle trajectory map was 55.21 km². Trajectory code 3311 covered the largest area at 36.95 km². Next code 3322 covered an area of 11.56 km², and code 2233 only covered 0.23 km². In this stage, it appeared that there was a large imbalance in grassland destruction. During each of these four periods, the phenomena of grassland restoration to agriculture persisted.

Repetitive trajectory map analysis: The repetitive trajectory map was the major land-use transition type, accounting for 34.35% of the total area. This was larger in area than any other trajectory map. Trajectory code 3133 had the largest area, accounting for 656.03 km². Codes 2122 and 3233 followed in prevalence, accounting for 19.37% and 15.06% of the study region, respectively. Due to the prominence of trajectory codes 3133 and 3233, the natural transition between grassland to forestland or cropland was very frequent.

Continual trajectory map analysis: The continual trajectory map comprised 25.60 km². Trajectory codes 3122 and 3211 were the major types of continual transition, accounting for 10.84 km² and 4.84 km², respectively. This indicates that the mutual transition between grassland and forestland to cropland occurred on a frequent basis under the context of human activities and land protection policies. Codes 3135 and 3235 represented the main transition types for the continual trajectory map throughout the study period, accounting for 6.06 km² and 4.02 km², respectively. This means a certain amount of grassland transitioned into built-up land due to the expansion of urbanization across the study region.

CONCLUSIONS

In this study, the LULC types at 2000, 2005, 2010 and 2015 were extracted from Landsat TM/OLI images using the SVM method, and the trajectory analysis method was applied to establish the trajectory maps illustrating three phases, to reveal the spatio-temporal variability of land use patterns and to explore the characteristics exhibited by the trajectories of change in the study region. During the period from 2000-2015, forestland and grassland dominated the study region, covering 86.79%, 88.54%, 86.13%, and 85.86% of the total

land area, respectively. A net increase of 1.24%, 0.57%, 0.22%, and 0.24% was observed in forestland, cropland, water bodies, and built-up land, respectively, while unused land continuously declined (0.094%). Grassland was reduced to 2.73%. The major mutual conversion between grassland and forestland (Codes 13 or 31) occurred during the former two periods (from 2000-2005 and 2005-2010), accounting for 49.36% and 48.90% of the total land-use types converted, respectively. The repetitive trajectory type was the most prominent land-use transition type, covering the largest transition area of the total coverage trajectory map. By contrast, the anaphase transition type contributed to the smallest trajectory during the period from 2000-2015. The findings in this study demonstrate that trajectory analysis can provide an effective approach for detecting characteristics exhibited by the spatio-temporal change in LULCC patterns.

ACKNOWLEDGEMENT

We appreciate the staff of the platform for the Wuzhishan Ecological Station and Science and Technology Project of Haikou City (Grant number 2020-057). This research was supported by the Natural Science Foundation of Hainan University (Grant No. KYQD (ZR) 20058 and 1863), and the National Weather Service Foundation of China (Grant No. HD-KYH-2020162), Natural Scientific Foundation of Hainan Province (Grant No. 621RC507).

REFERENCES

- Chen, W.X., Zhao, H.B., Li, J.F., Zhu, L.J., Wang, Z.Y. and Zeng, J. 2020. Land use transitions and the associated impacts on ecosystem services in the Middle Reaches of the Yangtze River Economic Belt in China based on the geo-informatics Tupu method. *Sci. Tot. Environ.*, 701: 134690.
- Collier, K.J., Clappcott, J.E., Hamer, M.P. and Young, R.G. 2013. Extent estimates and land cover relationships for functional indicators in non-wadeable rivers. *Ecol. Indic.*, 34: 53-59.
- Hao, H.M. and Ren, Z.Y. 2009. Land use/land cover change (LUCC) and Eco-environment response to LUCC in Farming-pastoral zone, China. *Agric. Sci. China*, 8(1): 91-97.
- Herold, M., Goldstein, N.C. and Clarke, K.C. 2003. The spatio-temporal form of urban growth: measurement, analysis, and modeling. *Remote Sens. Environ.*, 86: 286-302.
- Hua, X., Yan, J. and Yuan, X. 2014. The impact of the rise of labor opportunity cost on farmers' land abandonment behavior in hilly areas: A case study of Youyang County in Chongqing. *J. Southwest Univ.*, 36: 111-119.
- Hua, X.B., Yan, J.Z., Li, H.L., He, W.F. and Li, X.B. 2016. Wildlife damage and cultivated land abandonment: Findings from the mountainous areas of Chongqing, China. *Crop Protect.*, 84: 141-149.
- Liu, H. and Zhou, Q. 2004. Accuracy analysis of remote sensing change detection by rule-based rationality evaluation with post-classification comparison. *Int. J. Remote Sens.*, 25(5): 1037-1050.
- Li, Z.H., Yan, J.Z., Hua, X.B., Xin, L.J. and Li, X.B. 2014. Factors influencing the cultivated land abandonment of households of different types: A case study of 12 typical villages in Chongqing Municipality. *Geogr. Res.*, 33(4): 721-734

- Musa, T., Xu, W.B., Hou, W.M., Terence, D.M. and Matthew, B.K. 2020. Land use/land cover change evaluation using land change modeler: A comparative analysis between two main cities in Sierra Leone. *Remote Sens. Appl.: Society Environ.*, 16: 100262.
- Narasimhan, R. and Stow, D. 2010. Daily MODIS products for analyzing early season, vegetation dynamics across the north slope of Alaska. *Remote Sens. Environ.*, 114(6): 1251-1262.
- Petrosillo, I., Semeraro, T., Zaccarelli, N., Aretano, R. and Zurlini, G. 2013. The possible combined effects of land-use changes and climate conditions on the spatial-temporal patterns of primary production in a natural protected area. *Ecol. Indic.*, 29: 367-375.
- Shi, T.C., Li, X.B., Xin, L.J. and Xu, X.H. 2018. The spatial distribution of farmland abandonment and its influential factors at the township level: A case study in the mountainous area of China. *Land Use Policy*, 70: 510-520.
- Tang, Z., Engel, A., Pijanowski, C. and Lim, J. 2005. Forecasting land-use change and its environmental impact at a watershed scale. *J. Environ. Manag.*, 76: 35-45.
- Wang, D.C., Gong, J.H., Chen, L.D., Zhang, H., Song, Y.Q. and Yue, Y.J. 2012. Spatio-temporal pattern analysis of land use/cover change trajectories in Xihe watershed. *Int. J. Appl. Earth Observ. Geoinform.*, 14: 12-21.
- Verburg, P.H., Erb, K.H., Mertz, O. and Espindola, G. 2013. Land system science: between global challenges and local realities. *Current Research in Environmental Sustainability*, 5(5): 433-437. <https://doi.org/10.1016/j.cosust.2013.08.001>
- Verburg, H., Schot, P., Dijst, J. and Veldkamp, A. 2004. Land use change modelling: current practice and research priorities. *Geo. J.*, 61: 309-324.
- Yan, J.Z., Yang, Z.Y., Li Zan, H., Li, X.B., Xin, L.J. and Sun, L.X. 2016. Drivers of cropland abandonment in mountainous areas: A household decision model on the farming scale in Southwest China. *Land Use Policy*, 57: 459-469.
- Zhang, Y., Li, X.B. and Song, W. 2014. Determinants of cropland abandonment at the parcel, household, and village levels in mountain areas of China: a multi-level analysis. *Land Use Policy*, 41: 186-192.
- Zhou, Q., Li, B. and Kurban, A. 2008a. Trajectory analysis of land cover change in the arid environment of China. *Int. J. Remote Sens.*, 29(4): 1093-1107.
- Zhou, Q., Li, B. and Kurban, A. 2008b. Spatial pattern analysis of land cover change trajectories in Tarim Basin, northwest China. *Int. J. Remote Sens.*, 29(19): 5495-5509.
- Zomlot, Z., Verbeiren, B., Huysmans, M. and Batelaan, O. 2017. Trajectory analysis of land use and land cover maps to improve spatial-temporal patterns and impact assessment on groundwater recharge. *J. Hydrol.*, 554: 558-569.

Paper retracted



The Indigenous Arbuscular Mycorrhizal Fungi Consortium in Shallot Cultivation with Lead-Polluted Media

O. D. Hajoeningtjas*†, I. Mansur**, N. Ekowati*** and Tamad****

*Biology Faculty, Jenderal Soedirman University of Purwokerto, Agrotechnology Department, Agriculture Faculty of Muhammadiyah Purwokerto University, Indonesia

**Agroforestry Department of Bogor Agricultural University, Indonesia

***Biology Faculty, Jenderal Soedirman University of Purwokerto, Indonesia

****Agriculture Faculty, Jenderal Soedirman University of Purwokerto, Indonesia

†Corresponding author: O. D. Hajoeningtjas; oetamidwihajoeningtyas@ump.ac.id

Nat. Env. & Poll. Tech.
Website: www.neptjournal.com

Received: 19-02-2021

Revised: 08-04-2021

Accepted: 30-04-2021

Key Words:

Shallots

Arbuscular mycorrhizal fungi

Consortium

Lead

ABSTRACT

This study aims to test a consortium of indigenous Arbuscular Mycorrhizal Fungi (AMF) in shallot cultivation with Pb contaminated media. The experiment was carried out in a greenhouse. A completely randomized design (CRD) was used in this study with one treatment factor. The treatment was the customary consortium of indigenous AMF from 17 locations of shallot land contaminated by Pb. The application of AMF showed no significant effect on fresh bulb fresh weight, leaf fresh weight, plant fresh weight, the total length of leaves, and the number of shallots. The percentage of infection in all treatments, except controls, showed a high percentage of AMF infection. AMF treatment from Slatri Land II showed the highest percentage of infection, that is 93.33%. The consortium of indigenous AMF from Kupu Land II was able to reduce the highest Pb accumulation of tubers compared to the control by up to 83.660%.

INTRODUCTION

One of the issues with shallot production is the use of too many pesticides and fertilizers, which results in pollution, a clogged drainage system, and unresponsive agroecological conditions, especially on sensitive and dry soil (Nendissa 2008). Previous research in the Tegal and Brebes areas has revealed that the heavy metal Pb level in the soil and shallots is relatively high, with the Pb content in the soil ranging from 12.33-19.74 ppm and the range in shallots ranging from 0.41-5.51 ppm (Badrudin & Jazilah 2013).

Heavy metals must be handled properly because they are harmful contaminants for living beings. One of the ways to deal with the toxicity of heavy metals in contaminated land and plants is bioremediation. An effective step to reduce the contamination is by making use of microorganisms to restore the land conditions (Gandjar et al. 2006). Heavy metals are also a pollution problem for the soil, and the use of organisms to overcome them is called bioremediation (Leyval et al. 2002).

Rejuvenation of the polluted land can improve its functions, nourish plants, and will have a positive impact on people's health. Bioremediation using AMF is considered as a solution to this problem. Mycorrhizal potential can increase phytoremediation in a polluted land. The AMF can absorb

heavy metals in it, reducing toxicity and allowing plants to thrive much better (Gaur & Adholeya 2004). Fungi connected with the roots of live plants in the soil are known as AMF. AMF-inoculated roots were found to be effective at absorbing nutrients and water. In a root area in the soil, fungal hyphae threads have a wider range of nutrient use.

Bai et al. (2008) stated that AMF has an effect on metal uptake (movement and collection in plants) and host development. According to Sudová et al. (2007), the occurrence of excessive metal contamination in inoculation corn seedlings is a problem. As a result, plant growth is accelerated, and metals are delivered to the plant's roots and crown.

The issue is how successful the Fungi Mycorrhizal Arbuscula indigenous onion planting soil contaminated with Pb on media contaminated with Pb consortium is. It was also attempted to observe the influence on tuber growth and yield, as well as tuber Pb buildup.

MATERIALS AND METHODS

Materials and Tools

The materials and tools used in this study include the soils-contaminated with heavy metal Pb (24.75 ppm) from Larangan Village, Larangan District, Brebes Regency,

indigenous AMF from 17 locations in Wanasari and Larangan District, the shallot seeds of Tuk Tuk variety, rockwool, UV plastic, fertilizer (SP36, KCL, urea and rice washing water), cheerful, hoes, shovels, drums, gas stoves, plastic trays, sprayers, 11 cm × 12 cm pots, trays, rulers and cameras.

Research Methods

For the treatment of indigenous AMF from 17 shallot areas affected with heavy metals, this study used a completely randomized design (CRD) with one component. They are: L0 = Control (without AMF treatment); L1 = Indigenous AMF, Wanasari Land I; L2 = Indigenous AMF, Wanasari Land II; L3 = Indigenous AMF, Wanasari Land III; L4 = Indigenous AMF, Sigentung Land I; L5 = Indigenous AMF, Sigentung Land II; L7 = Indigenous AMF, Kupu Land I; L8 = Indigenous AMF, Kupu Land II; L9 = Indigenous AMF, Kupu Land III; L10 = Indigenous AMF, Karangbale Land I; L11 = Indigenous AMF, Karangbale Land II; L12 = Indigenous AMF, Karangbale Land III; L13 = Indigenous AMF, Slati Land I; L14 = Indigenous AMF, Slati Land II; L15 = Indigenous AMF, Slati Land III

L16 = Indigenous AMF, Larangan Land I; L17 = Indigenous AMF, Larangan Land II; L6 = Indigenous AMF, Larangan Land III. Each treatment was repeated 3 times, then 54 experimental units were obtained.

Observation Variables

The observation variables in this study are total leaf-length (cm), number of leaves (strands), number of tubers (piece) per plant, fresh tuber weight (gram) per plant, total root length (cm), analysis of Pb content in roots, tubers and leaves of the shallot (ppm) using Atomic Absorption Spectrophotometer (AAS), root infection intensity (%). The root infection intensity was measured by looking at the percentage of roots infected by AMF. It was carried out through staining techniques using the ink-vinegar solution. The formula for calculating the percentage of infected roots is (Nusantara et al. 2012) :

$$\% \text{ Colonized roots} = \frac{\sum \text{mycorrhizal field of view}}{\sum \text{the observed field of view}} \times 100 \%$$

The intensity of infection was classified according to the criteria of O'Connor et al. (2001).

Research Implementation

The steps in implementing this research are as follows:

The planting medium was soil contaminated with heavy metal Pb (24.75 ppm), taken from Larangan District, Brebes Regency. The soil was sterilized using a steam pressurized drum at a temperature of 80°C for 8 h. It was stirred manually

using a hoe. It was then placed in a pot measuring 11 cm × 12 cm with a volume fitting its size. It was coded, based on the respected treatment.

The seeds used are the Tuk-Tuk variety. Prepare a tray filled with soaked rockwool. The shallot seeds are put into the rockwool that has been perforated by two seeds in each hole. Put in a dark place for 2 days and after germination moves them into the sunlight. After 14 days, the seedlings are transferred to polybags with sterilized soil as the planting medium. Seedlings were moved after 40 days and have 3-5 leaves to pots with Pb-contaminated soil as the planting medium.

The AMF application was carried out directly during planting by placing it in a planting hole with 150 g per plant and then covered with thin soil.

Fertilization was done three times, that is before planting, using SP-36, N, and KCl. This initial fertilization dosage is SP-36 (250 kg.ha⁻¹ or the equivalent of 4.80 g.pot⁻¹). It was applied three days before planting by spreading and stirring it evenly with the sterilized planting media. The second fertilization was carried out at 15 DAP; the fertilizers given were KCl and N with a dose of 200 kg.ha⁻¹ or equivalent to 3.84 g.pot⁻¹. The third fertilization uses the same fertilizer, Urea, and KCl at 30 DAP with a dose of 100 kg.ha⁻¹ or the equivalent of 1.92 g.pot⁻¹. Harvesting was done at 60 DAP.

Data Analysis

Hypothesis testing is carried out using the F test. The results of the F test show the real effect of the treatment carried out, so the Least Significant Difference Test (LSD) can be performed with an error rate of 5%. Previously, all observations were collected then organized and prerequisite tests were carried out (normality test and homogeneity test of variance) to fulfill the assumptions in the parametric statistical analysis. Because these two assumptions were not fulfilled, the Kruskal-Wallis non-parametric test was performed.

RESULTS AND DISCUSSION

The AMF Effects on Shallot Plants

The results showed that AMF did not significantly affect the number and total length of plant leaves (Table 2). The number and total length of the leaves are influenced by the availability of N in the planting medium. Based on the analysis of the soil as the planting medium, the total N content was 0.12% and it was in a low category (Table 1). In this study, N fertilization using urea was also carried out according to the dosage required for the shallot cultivation. Nitrogen elements belong to soluble nutrients for plants, so that they can be absorbed directly by their roots. The limited reliance on mycorrhiza

is assumed to be due to the availability of sufficient N in the soil, which is a crucial factor for the formation of leaf organs.

According to Setiadi & Setiawan (2011), not all types of arbuscular mycorrhizae can significantly affect the growth of a plant. This effect can be determined by the effectiveness of the nutrient status of the media, isolates, and the level of dependence of plants on mycorrhizae. Wang et al. (2011) research also shows that co-inoculation with rhizobia and AM fungi significantly increased soybean growth under low P and/or low N conditions as indicated by increased shoot dry weight, along with plant N and P content. There were no significant effects of inoculation under adequate N and P conditions. Likewise, as stated by Saputra et al. (2015), environmental factors such as soil moisture, soil pH, rainfall, C-organic content, and NPK nutrient content affect mycorrhizal activity.

Mycorrhizal fungi are part of obligate fungi that combine to live with plant roots through spores. AMF, among other things, helps to increase the plant's nutrient uptake of P elements, can increase resistance to disease, drought, and other hazardous conditions. Based on the research finding of Moelyohadi et al. (2012), AMF can be used as a technology for fertilizing and plant-nutrients fertilizing and is also able to increase the corn yield.

The AMF treatment had no significant influence on plant root length, according to the results of the variance analysis, possibly due to environmental conditions that promote shallot growth. They include, among other things, sunlight and nutrient-dense foods.

Because it can improve root conditions, AMF treatment

has a considerable impact on the percentage of root infections in shallots in this circumstance. It can also improve the ability to adjust to drought concerns relating to root growth, water absorption, a

This is due to the availability of nutrients and water in the planting medium. The fertilizers given to all shallot plants are SP36, KCL and Urea. According to Bangun et al. (2000), fertilization is a critical component of increasing crop yields. Furthermore, the shallot plants require favorable environmental circumstances to assist the tuber production process, one of which is water.

The results of the variance analysis indicated that mycorrhizal administration has a very significant effect on the intensity of plant root infections. The indigenous AMFs of the shallot land contaminated with Pb from 17 locations are a consortium of the genera of *Glomus*, *Gigaspora*, *Acaulospora*, and *Scutellospora* (Hajoeningtijas et al. 2019). According to Tamin et al. (2012), many factors contribute to the prevalence of mycorrhizal infections. Mycorrhizae of *Gigaspora margarita* type is a type having the ability to adapt to the surrounding habitat. *Gigaspora margarita*, *Acaulospora sp*, and *Glomus etunicatum* have various environmental conditions to survive. These three types of mycorrhizae are a type of *endomycorrhizae*. Many types of *endomycorrhizae* are found in nature. They can be found in most soils and do not have a specific host. The level of population and species composition varies due to plant characteristics and environmental factors such as temperature, soil pH, soil moisture, and phosphorus and nitrogen contents.

Table 1: The analysis results of soil and Pb in Larangan Village. Larangan District. Brebes Regency.

Parameter	Value		Criteria
Total N [%]	0.12	0.1-0.2 R	L
Organis C [%]	0.78	<1 SR	VL
C/N	6.31	5-10	L
Total P ₂ O ₅ [%]	0.05	<15	VL
Total K ₂ O [%]	0.11	<10	VL
pH H ₂ O	6.60	-	-
KTK [me%]	45.45	>40	VH
KB [me%]	78.86	61-80	H
Ca [me%]	23.35	>20	VH
Mg [me%]	6.65	2.1-8.0	H
Na [me%]	5.00	0.4-0.7	M
K [me%]	0.87	0.6-0.10	H
Soil Pb tanah [ppm]	24.75*		
Texture	Clay		

Note : *= threshold value of 12.75 ppm (Balai Penelitian Tanah 2002)

VL = Very Low; L = Low; M = Medium; H = Height; VH = Very High

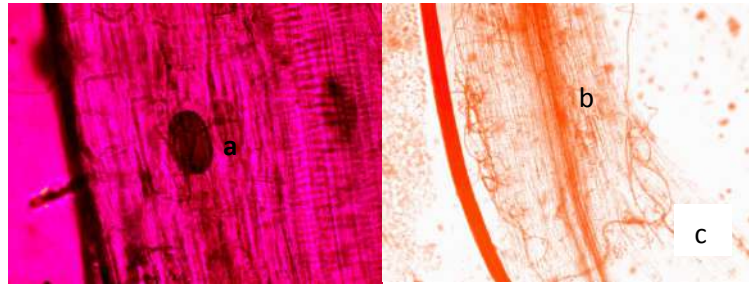


Fig. 1: The shallot roots infected by AMF show the presence of vesicles (a) (40/0.65), internal hyphae (b) and external hyphae (c) (5/0.10).

AMF will infect plant roots, thereby expanding the absorption area for nutrients and water. As stated by Prasasti et al. (2013), the higher the dose of AMF fertilizer, the more roots were infected with mycorrhizae, thus making the roots longer.

The workings of mycorrhizal infections, according to Novriani and Madjid (2009), occur when the infection is in the canal or root tissue, beginning with the spore germination process in the soil. There will be penetration of hyphae development and development in the cortex in the roots. The arbuscules, intracellular vesicles (Fig. 1 (a)), and internal hyphae (Fig. 1 (b)) between the cortical cells are generated at the afflicted section of the root. Hyphae penetration and development are most common in areas that are still going through a differentiation and growth phase. The formation of hyphae causes no harm to the cells.

The Effects of Land Characteristic in Wanasari and Larangan Districts on The Pb Levels of the Shallot

Based on Table 4, it is seen that the shallot tubers planted in contaminated media and given with AMF contain a heavy

Table 2: The result matrix of various effects of amf application on the shallots growth (*Allium ascalonicum* L.) in the Pb-contaminated media.

Observation Variables	Analysis Result of Variety Scan
Fresh Plant Weight	ns
Fresh Leaf Weight	ns
Fresh Tuber Weight	ns
Total Root Length	ns
Number of leaves 15 DAP	ns
Number of leaves 30 DAP	ns
Number of leaves 45 DAP	ns
Number of leaves 60 DAP	ns
Number of leaves 67 DAP	ns
Height of Plant 30 DAP	ns
Height of Plant 45 DAP	ns
Height of Plant 60 DAP	ns
Height of Plant 67 DAP	ns
Percent of Root Infection	*

Note : ns = Not significant; * = Significant

metal of Pb under its safe threshold. The threshold for Pb content in plant tissue, according to the Directorate General of POM, Ministry of Health, is a maximum of 0.2 ppm.

Pb buildup in the tubers is considerable after L0 treatment. The roots were thought to absorb more Pb, which was then dispersed to all parts of the plant, including the tuber. AMF was able to collect and accumulate metals in the vesicles near the root in the AMF treatment plant, thus only a tiny fraction was transferred to other areas. As seen in Table 4., in the L0 treatment, the Pb content is 12.754 ppm and the L8 treatment shows the lowest Pb content, 2.084 ppm, a difference of 83.660% compared to the control. According to Hartini (2011), agricultural products may contain heavy metals, because the nutrients from the soil containing heavy metal Pb will be absorbed by plants in the growing process.

There are 2 types of heavy metals in the soil, free (mobile) and non-free (immobile). The difference between mobile and immobile metals is that free metals are toxic and absorbed by plants, whereas immobile metals are bound to nutrients, organic materials, or inorganic materials. In these circumstances, apart from having an effect on the amount of nutrient content in plants, they can also be contaminated by heavy metals. The heavy metals bound by the soil will combine in the soil, then be absorbed by plant roots, and then they will spread to other parts (Charlena 2004).

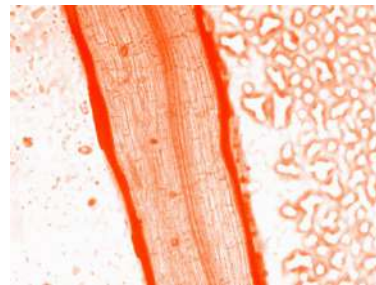


Fig. 2: Shallot roots uninfected by AMF (5/0.10).

The lead from the soil is mostly absorbed by the land plants and they retain the lead in large quantities in the roots. The leaves are also proven to contain lead (it is very likely that this lead is transferred to all other parts). To prevent the absorption of lead by the roots, calcium, and phosphorus can be applied to the soil (Asati et al. 2016). Pb is bound by the ions in the organophosphate in the center of shallot roots. Pb uptake in tubers is very low due to the minimal amount of Pb translocated from the roots to the top of the plant (Nurjaya et al. 2006). The rise in Pb uptake by plant roots rose with AMF infection (the maximum at L9, 52.041 ppm), then collected metal in the roots' vesicles, with only a small percentage being transported to other areas, including tubers, according to this study (6.748 ppm in leaves and 4.840 ppm in the tubers).

Fungi, yeast, bacteria, algae, and cyanobacteria are included in the types of microorganisms that can act as heavy-metal absorbers, as proved in several studies. Protonation, chelation, and chemical transformation are processes of program mobility by micro-organisms in the soil. Metals and phosphates in the soil will be easily dissolved by plant roots due to the excretion of microorganisms in the soil. This will undoubtedly have an impact on crops (Gonzalez-Chavez et al. 2002).

AMF is thought to be able to collect and absorb metals in host plant roots and biomass. Due to the influence of the extent and area of absorption in the soil, both AMF and ectomycorrhizae have the potential for metal absorption in both intracellular and extracellular mycelium (Jones et al. 2004). Cellulose, a cellulose derivative of chitin and melanin of the fungus AMF is a type of metal that binds to the wall components of the cells (Galii et al. 1993). Evidence has shown that AMF activity has a major role in removing metals bound by soil components in recent years (Gohre & Paszkowski 2006).

Other factors that influence metal absorption include (Joner et al. 2000, Leyval & Joner 2001): a.) Metabolite composition, b.) AMF type, c.) Fungal biomass cation exchange capacity, d.) metal pools, e.) Edaphic and environmental conditions, f.) Electrochemical properties of metals, g.) Competition between metals at absorption sites of mycorrhizal surfaces, h.) Natural host plants, i.) Root exudation patterns.

Bai et al. (2008) argued that AMF also affects metal absorption (translocation and accumulation in plant tissue) and the development of host plants. Sudová et al. (2007) discovered that mycorrhizal-inoculated corn absorbs Pb at high

Table 3: Mean matrix of each observation variable of AMF application in Pb-contaminated media in shallots.

Variety component	Total Root length[cm] (67 DAP)	Fresh Plant Weight [g] (67 DAP)	Fresh Tuber Weight [g] (67 DAP)	Fresh Leaf Weight [cm] (67 DAP)	Height of Plant (60 DAP)	Number of Leaves (60 DAP)	Per cent of Infection [%] (67 DAP)	
L0	24.33	4.67	8.33	4.33	10.83	12.33	0.00	a
L1	18.33	9.00	9.00	13.67	10.67	17.33	56.66	bcd
L2	45.33	47.50	34.67	38.33	32.83	29.50	73.33	bcd
L3	35.33	31.00	23.67	20.00	20.33	17.00	70.00	bcd
L4	31.00	30.00	32.33	30.67	30.83	15.67	40.00	b
L5	39.33	31.00	29.67	35.67	34.50	25.67	63.33	bcd
L7	24.00	32.33	34.67	28.33	36.83	34.50	46.66	bc
L8	38.00	34.67	32.33	35.67	34.33	34.83	46.66	bc
L9	7.00	16.50	21.33	25.00	16.50	22.17	63.33	bcd
L10	34.33	31.00	34.00	37.00	26.17	43.67	63.33	bcd
L11	20.00	36.83	33.67	39.33	35.33	40.83	60.00	bcd
L12	35.67	21.00	24.67	19.33	32.00	24.33	83.33	cd
L13	18.33	34.67	26.00	21.33	28.50	35.00	70.00	bcd
L14	20.67	27.00	27.67	31.67	30.83	28.33	93.33	d
L15	26.00	21.53	21.00	28.33	27.33	20.33	73.33	bcd
L16	21.33	23.17	31.00	22.33	22.33	35.33	66.66	bcd
L17	41.00	36.00	33.67	39.67	44.17	31.00	83.33	cd
L6	14.50	25.67	37.33	24.33	20.67	30.50	46.66	bc

Note: The different letters at the same column, of the same variable, represent significant differences

Table 4: Matrix of analysis results of Pb level in the roots, leaves, and shallots with AMF treatment in Pb-contaminated soil.

No.	Code	Pb Content [ppm]			
		Root	Leaf	Tuber	Decrease in the Accumulated Pb of Tubers [%]
1	L0	8.555	4.798	12.754	
2	L1	0.529	2.335	3.209	74.840
3	L2	9.076	3.240	5.546	56.516
4	L3	16.369	2.640	3.289	74.212
5	L4	29.335	4.276	3.331	73.882
6	L6	5.945	11.596	2.368	81.433
7	L7	12.365	3.027	2.654	79.191
8	L8	5.908	2.582	2.084	83.660
9	L9	52.041	6.748	4.840	62.051
10	L10	30.483	2.801	3.025	76.282
11	L11	-	2.755	2.645	79.261
12	L12	6.935	2.842	3.029	76.251
13	L13	22.385	3.445	3.368	73.593
14	L14	3.426	3.148	3.351	73.726
15	L15	46.965	3.452	3.095	75.733
16	L16	23.335	4.102	2.283	82.100
17	L5	4.648	2.195	2.919	77.113
18	L17	10.417	3.265	2.504	80.367

amounts. The plant has the benefit of growing well and accumulating and transporting metals. Increased development of phytochelatins, glutathione-derived peptides, which are only produced by higher plants, is another intriguing way by which mycorrhizal plants absorb heavy metals. Heavy metals and metalloids will thus be chelated by plants (Grill et al. 1987, Garg & Aggarwal 2011, Pollard et al. 2014). Glomalin, an insoluble glycoprotein, is synthesized in excess in AMF hyphae. Glomalin should be explored for biostabilization that leads to improved polluted soil conditions (González-Chávez et al. 2004, 2009).

Although the use of fungi is a suitable method for soil bioremediation, it is not the only method to apply. When it is combined with other bioremediation methods, it can work more effectively (Miransari 2017). Phytoremediation can utilize a modified AMF to support the accumulation of non-toxic heavy metals in plant roots and fungal mycelium (González-Chávez et al. 2002).

CONCLUSION

Based on the results of the analysis, it can be concluded that the application of indigenous AMF consortium from 17 locations with different Pb-contaminated land on the shallot

varieties showed no significant effect on tuber weight, fresh leaf weight, fresh plant weight, total leaf length, and the number of leaves. The different applications of AMF show a good response to the per cent of infections in which the indigenous AMF consortium treatment from Slati Land II shows the highest percentage of infections at 93.33%. The AMF treatment can reduce the Pb content of tubers compared to the control, up to 83.660%. It is necessary to carry out further research with single spores of AMF as a bioremediation agent on land contaminated with heavy metal Pb.

ACKNOWLEDGMENT

The authors acknowledge Muhammadiyah Purwokerto University for funding this research.

REFERENCES

- Asati, A.M. Pichhode, K. and Nikhil 2016. Effect of heavy metals on plants: An overview. *Int. J. Appl. Innov. Eng. Manag.*, 5(3): 56-66
- Badrudin, U. and Jazilah, S. 2013. Analysis of pesticide residue on shallots (*Allium ascalonicum* L.) in Brebes Regency. *Pen J. Sci. Technol.*, 24(1): 75-86.
- Bai, H.J., Zhang, Z.M., Yang, G.E. and Li, B.Z. 2008. Bioremediation of cadmium by rowing *Rhodobacter sphaeroides*: Kinetic characteristic and mechanism studies. *Bioresour. Technol.*, 99: 7716-7722.

- Balai, Penelitian Tanah 2002. Environmental Impact Management and Inventory Research. Final report. Part of the Research and Development Project on Soil Fertility and Climate. Bogor, pp. 1-5.
- Bangun, E., Nur, M., Silalahi, H.I., F.H. and Ali, J. 2000. Assessment of Shallot Fertilization Technology in North Sumatra. Proceedings of the National Seminar on Location-Specific Technologies Towards Decentralized Agricultural Development, 13-14, March 2000. Medan, pp. 338-342.
- Charlena, K. 2004. Lead (Pb) and Cadmium (Cd) Heavy Metal Pollution in Vegetables. http://www.rudyc.com/paps702_ipb/09145/charlena.pdf.
- Galii, U., Meier, M. and Brunold, C. 1993. Effect of cadmium on non-mycorrhizal and mycorrhizal fungus (*Laccasaria laccata* Scop.Ex.Fr) Bk and Br.: Sulphate reduction, thiols, and distribution of the heavy metal. *New Phytol.*, 125: 837-843.
- Gandjar, I., Sjamsuridzal, W. and Ariyanti, O. 2006. Basic and Applied Mycology. Indonesian Torch Foundation, Jakarta.
- Garg, N. and Aggarwal, N. 2011. Effects of interactions between cadmium and lead on growth, nitrogen fixation, phytochelatin, and glutathione production in mycorrhizal *Cajanus cajan* (L.) Millsp. *J. Pl. Growth Regul.*, 30: 286-300.
- Gaur, A. and Adholeya, A. 2004. Prospect of arbuscular mycorrhizal fungi in phytoremediation of heavy metal contaminated soils. *Cur. Sci.*, 86: 528-534.
- Gohre, V. and Paszkowski, U. 2006. Contribution of the arbuscular mycorrhizal symbiosis to heavy metal phytoremediation. *Planta*, 223: 1115-1122.
- Gonzalez-Chavez, M.C., D'Haen, J., Vangronsveld, J.J. and Dodd, J.D. 2002. Copper sorption and accumulation by the extraradical mycelium of different *Glomus* spp. (Arbuscular Mycorrhizal Fungi) isolated from the same polluted soil. *Pl. Soil*, 240(2): 287-297.
- González-Chávez, M.C., Carrillo-González, R., Wright, S.F. and Nichols, K.A. 2004. Role of glomalin, protein produced by hypha of arbuscular mycorrhizal fungi in the sequestration of potentially toxic elements. *Environ. Pollut.*, 130: 317-323.
- González-Chávez, M.C., Carrillo-González, R. and Gutiérrez-Castorena, M.C. 2009. Natural attenuation in a slag heap contaminated with cadmium: The role of plants and arbuscular mycorrhizal fungi. *J. Hazard. Mater.*, 161: 1288-1298.
- Grill, E., Winnacker, E. and Zenk, M. 1987. Phytochelatin, a class of heavy metal-binding peptides from plants are functionally analogous to metallothioneins. *Proc. Nat. Acad. Sci.*, 84: 439-443.
- Hajoeningtjas, O.D., Mansur, I., Ekowati, N. and Tamad, K. 2019. Diversity of mycorrhizal fungi *Arbuscula* indigenous rhizosphere of shallots contaminated with heavy metal Pb. Research Results Report, Unpublished Bachelor Thesis, Universitas Muhammadiyah Purwokerto.
- Hartini, E. 2011. Levels of Plumbum (Pb) in Shallot Bulbs in Kersana District, Brebes Regency. *J. Visikes* 10(1): 56.
- Joner, E.J., Briones, R. and Leyval, C. 2000. The metal-binding capacity of arbuscular-mycorrhizal mycelium. *Pl. Soil*, 226(2): 227-234.
- Jones, R., Sun, W., Tang, C.S. and Robert, F.M. 2004. Phytoremediation of petroleum hydrocarbons in tropical control soils. II: Microbial responses to plant roots and contaminants. *Environ. Sci. Pollut. Res.*, 11: 340-346.
- Leyval, C., Joner, E.J., Val, C. and Haselwandter, K. 2002. Potential of Arbuscular Mycorrhizal Fungi for Bioremediation. In: Gianinazzi, S., Schuepp, H., Barea, J.M. and Haselwandter, K. (eds), *Mycorrhizal Technology in Agriculture*, Burkholder Verlag, Switzerland, pp. 175-186.
- Leyval, C. and Joner, E.J., 2001. Bioavailability of Heavy Metal in the Mycorrhizosphere. In: Gobran, G.R., Menzel, W.W. and Lombi, E. (eds), *Trace Elements in the Rhizosphere*, CRC. Boca Raton, FL, pp. 165-188.
- Miransari, M. 2017. Arbuscular Mycorrhizal Fungi and Heavy Metal Tolerance in Plants. In: Wu, Q.S. (ed.), *Arbuscular Mycorrhizas and Stress Tolerance of Plants*, Springer, New York, pp.147-161. DOI 10.1007/978-981-10-4115-0_7.
- Moelyohadi, Y., Harun, M.U., Munandar, Hayati, R. and Gofar, N. 2012. Utilization of various types of biological fertilizers in nutrient efficient corn (*Zea mays* L.): Cultivation in a marginal dry land. *J. Subopt. Land* 1(1): 31-39.
- Nendissa, J.I. 2008. The influence of organic soil treatment (OST) and time of the landeto solution application on the growth and yield of shallots on Regosol. *J. Budid. Pertan.*, 4: 122-131.
- Nurjaya, K.M., Zihan, E. and Saeni, S. 2006. The effect of amelioration on soil Pb levels, uptake, and yield of shallots on inceptisols. *Indones. J. Agric. Sci.*, 8(2): 110-119.
- Nusantara, A.D., Bertham, Y.H. and Mansur, I. 2012. Working with Arbuscular Mycorrhizal Fungi. IPB Press, Seameo Biotrop.
- Novriani, M. and Madjid, A. 2009. The Role And Prospects of Mycorrhizae. Palembang : Postgraduate, Sriwijaya University.
- O'Connor, P.J., Smith, S.E. and Smith, F.A. 2001. Arbuscular mycorrhizal associations in the southern Simpson Desert. *Aust. J. Bot.*, 49(4): 493. doi:10.1071/bt00014.
- Pollard, A.J., Reeves, R.D. and Baker, A.J.M. 2014. Facultative hyper-accumulation of heavy metals and metalloids. *Plant Sci.*, 217-218: 8-17. doi:10.1016/j.plantsci.2013.11.011.
- Prasasti., O.H., Purwani, K. I. and Nurhatika, S. 2013. Effect of mycorrhiza *glomus fasciculatum* on vegetative growth of peanut plants infected by pathogen *Sclerotium rolfsii*. *J. Sci. Arts*, 2(2): 2337-3520. doi: 10.12962/j23373520.v2i2.3624.
- Saputra, B., Riza, L. and Irwan, L. 2015. Vesicular arbuscular mycorrhizal fungus (MVA) in three types of rhizosphere soil of banana nipah (*Musa paradisiaca* L. var. Nipah): Plant in Pontianak Regency. *Protobiont* 4(1): 160-169.
- Setiadi, Y. and Setiawan, A. 2011. Study on the status of arbuscular mycorrhizal fungi in the post-nickel mining rehabilitation area: A case study of PT INCO Tbk. Sorowako, South Sulawesi.. *J Trop. Silvicult.*, 3(1): 88-95.
- Sudová, R. and Vosátka, M. 2007. Differences in the effects of three arbuscular mycorrhizal fungal on P and Pb accumulation by maize plants. *Plant Soil*, 296: 77-83.
- Tamin, R.P., Nursanti, M. and Albayudi, K. 2012. Identification of types and propagation of local endomycorrhizae in the Jambi University campus forest. *J. Res. Univ. Jambi SAINS Ser.*, 14(1): 23-28.
- Wang, X., Pan, Q., Chen, F., Yan., X. and Liao., H. 2011. Effects of co-inoculation with arbuscular mycorrhizal fungi and rhizobia on soybean growth as related to root architecture and availability of N and P. *Mycorrhiza*, 21: 173-181. <https://doi.org/10.1007/s00572-010-0319-1>



Rural Financial Efficiency, Agricultural Technological Progress and Agricultural Carbon Emissions: Evidence from China

Hai-Feng Huang* and Ni Zhu*†

*School of Economics and Management, Beijing University of Technology, Beijing 100124, China

†Corresponding author: Ni Zhu; 819407202@qq.com

Nat. Env. & Poll. Tech.
Website: www.neptjournal.com

Received: 14-03-2021

Revised: 19-04-2021

Accepted: 05-05-2021

Key Words:

Rural financial efficiency
Agricultural carbon emissions
Mediating effect
Threshold effect

ABSTRACT

Based on the 30-province panel data in China during 2005-2018, this paper uses the DEA-SBM model and DEA-Malmquist model to measure rural financial efficiency and agricultural technological progress respectively and then uses the mediating effect model to analyze the linear influence. The results show that rural financial efficiency and agricultural technological progress both can inhibit agricultural carbon emissions, while agricultural technological progress plays a mediating role when rural financial efficiency influences agricultural carbon emissions. What's more, this paper uses the threshold effect model to analyze the non-linear influence. The findings reveal that when rural financial efficiency improves, the effects of rural financial efficiency and agricultural technology advances on agricultural carbon emissions shift from promoter to inhibitor.

INTRODUCTION

Since the industrial revolution, mankind has over-exploited and over-utilized natural resources, and the global climate has become worse and worse. The greenhouse effect, which is produced by excess carbon dioxide emissions, has become a major source of worry among academics. Global warming might reach 1.5°C between 2030 and 2052 (IPCC 2018). The world is actively taking measures to combat global warming. At the 75th United Nations General Assembly in 2020, China stated that it will strive to peak carbon emissions by 2030 and achieve carbon neutrality by 2060. Various industries in China are actively exploring measures to reduce carbon emissions that are appropriate for them to meet these targets as soon as feasible.

Rapid agricultural development can ensure food security and economic benefits (Maraseni et al. 2020). However, as a largely agricultural country, China's share of global agricultural greenhouse gas emissions is constantly increasing, and in 2016 this share reached 13.07% (FAO 2020). Therefore, the current goal of China's agriculture isn't only to ensure food security, but also to protect the environment (Luo et al. 2014). Exploring the method of reducing agricultural carbon emissions is of great significance.

The Paris Agreement on Climate Change emphasized the important role of funding to address the challenges of climate change. Some academics have researched the

influence of financial development on carbon emissions from a macroeconomic viewpoint in recent years. Shahbaz et al. (2018) stated that financial development can reduce carbon emissions. What's more, scholars have studied various influencing factors of agricultural carbon emissions, such as agricultural production (Owusu & Asumadu-Sarkodie 2016), rural population scale (Chen et al. 2018), agricultural economic development (Zhang & Liu 2018), energy consumption (Zhang et al. 2019), urbanization (Ridzuan et al. 2020), R&D investment (Chen & Li 2020) and industrial structure (Guo et al. 2021). But there is little literature studying the influencing factor - rural finance. Therefore, the purpose of this paper is to investigate how rural financing influences agricultural carbon emissions.

Financial development helps to fund technical advancement, which in turn helps to minimize greenhouse gas emissions (Paroussos et al. 2020). Some researchers have looked at the mechanism of "financial development → technological progress → carbon emissions" from a macroeconomic perspective (Tamazian et al. 2009, Shahbaz et al. 2013, Yan et al. 2016). From the agricultural sector perspective, some scholars have only studied the relationship between the two, such as the impact of financial development on technological progress (Liu et al. 2021), and the impact of technological progress on carbon emissions (Chen & Li 2020). In general, only a few scholars have studied the mechanism of "rural financial development → agricultural technological progress → agricultural carbon emissions".

Based on the above background, this article, by using 30-province panel data in China during 2005-2018, studies the mechanism of “rural financial efficiency → agricultural technological progress → agricultural carbon emissions”, and focuses on the following four analyses: (1) By measuring rural financial efficiency by DEA-SBM model, analyze the efficiency and quality of rural financial development, instead of only focusing on the financial scale and quantity. (2) By measuring agricultural technological progress by DEA-Malmquist model, analyze the dynamic changes of agricultural technological progress. (3) Using the mediating effect model, analyze the influence mechanism of rural financial efficiency on agricultural carbon emissions when agricultural technological progress plays the mediating role. (4) Using the threshold effect model, analyze the non-linear impact of rural financial efficiency and agricultural technological progress on agricultural carbon emissions.

This paper is structured as follows: Section 2 introduces past studies and hypothesis development. Section 3 introduces methodology. Section 4 presents results and discussion. Section 5 concludes.

Past Studies and Hypothesis Development

In the literature on the relationship between financial development and carbon emissions, scholars have different views. Some scholars believe that financial development can reduce carbon emissions. The main mechanisms are as follows: (1) A sound financial system can provide a good environment for carbon trading activities (Claessens & Feijen 2007). (2) Mature financial system can provide sufficient funds and comprehensive financial services for environmentally friendly projects (Tamazian & Rao 2010) and emission reduction projects (Zhou et al. 2019). (3) A sound financial system can provide support for low-carbon development through fiscal policy. For example, financial policy tools optimize the energy consumption structure of enterprises by adjusting energy prices (Zhou et al. 2019). However, some scholars believe that financial development can promote carbon emissions. According to Shen et al. (2021), a well-developed financial system aids corporations in expanding output and consumers in obtaining sufficient consumer credit, making it simpler to acquire high-energy-consuming commodities and thereby boosting carbon emissions.

There is little literature on the impact of rural finance on agricultural carbon emissions. This article will learn from the above mechanism, focus the research perspective on rural areas and the agricultural sector, and propose the following hypothesis:

Hypothesis 1: Rural financial efficiency can inhibit agricultural carbon emissions: In recent years, some

scholars have begun to study the impact mechanism of financial development on carbon emissions. Technological progress has been extensively studied as a mediating role of financial development influencing carbon emissions on the macro-level. The main mechanisms are as follows: (1) An open and free financial policy and a developed financial system can attract more R&D-related foreign direct investment, thereby promoting technological progress and then mitigating the country’s environmental degradation (Tamazian et al. 2009) (2) A mature financial market has a strong and complete information disclosure system, which can reduce adverse selection and moral hazard caused by information asymmetry, and can enable the healthy development of technological innovation projects. Then technological progress will optimize the utilization of energy, thereby reducing carbon emissions (Shahbaz et al. 2013) (3) A well-developed finance market provides investors with a sound risk diversification mechanism. It can share the risk of return among different investors, thereby reducing investors’ worries about investment in technology projects. Therefore, technology projects can proceed smoothly, and low-carbon technology projects will also receive strong support from the financial market to achieve emission reduction targets. (Zhou et al. 2019) (4) Financial development can improve the education system, thereby promoting the accumulation of human capital. Human capital carries out technological innovation, thereby promoting technological progress. Then technological progress will contribute to exploring new clean energy, thereby reducing carbon emissions (Zhou et al. 2019)

Some literature has studied the impact of rural finance on agricultural technology and the impact of agricultural technology on agricultural carbon emissions. Rural finance, according to Liu et al. (2021), may help agricultural technological innovation by easing the financial burden on creative businesses, diversifying investment risks in technology projects, and fostering talent for scientific research organizations. In particular, rural finance can provide financial support for farmers to use new technological tools, which can promote the application of agricultural technological innovation (Makate et al. 2019). Chen & Li (2020) stated that the advancement of agricultural technology will contribute to the low-carbon development of agriculture.

This article will learn from the above mechanism, focus the research perspective on rural areas and the agricultural sector, and establish a research mechanism of “rural financial efficiency → agricultural technological progress → agricultural carbon emissions”. Hypothesis 2 is as follows:

Hypothesis 2: Agricultural technological progress plays a mediating role when rural financial efficiency influences agricultural carbon emissions

MATERIALS AND METHODS

Modeling

To verify hypothesis 1, the econometric equation (1) is set as:

$$ACEI_{it} = \alpha_0 + \alpha_1 fin_{it} + \alpha_2 gov_{it} + \alpha_3 stru_{it} + \alpha_4 env_{it} + \varepsilon_{it} \quad \dots(1)$$

To verify hypothesis 2, referring to the research of mediating effect of Wen and Ye (2014), equations (2) (3) are set as

$$tech_{it} = \beta_0 + \beta_1 fin_{it} + \beta_2 gov_{it} + \beta_3 stru_{it} + \beta_4 env_{it} + \varepsilon_{it} \quad \dots(2)$$

$$ACEI_{it} = \gamma_0 + \gamma_1 fin_{it} + \gamma_2 tech_{it} + \gamma_3 gov_{it} + \gamma_4 stru_{it} + \gamma_5 env_{it} + \varepsilon_{it} \quad \dots(3)$$

To analyze the non-linear impacts on agricultural carbon emissions, referring to the research of threshold effect of Hansen (1999), equations (4) (5) are set as:

$$ACEI_{it} = \theta_0 + \theta_1 fin_{it} \cdot I(fin_{it} \leq \eta_1) + \theta_2 fin_{it} \cdot I(fin_{it} > \eta_1) + \theta X_{it} + \varepsilon_{it} \quad \dots(4)$$

$$ACEI_{it} = \sigma_0 + \sigma_1 tech_{it} \cdot I(fin_{it} \leq \rho_1) + \sigma_2 tech_{it} \cdot I(fin_{it} > \rho_1) + \sigma X_{it} + \varepsilon_{it} \quad \dots(5)$$

Equations (1)-(5), *i* represents the area. *t* represents time. ε_{it} is a random interference term. $\varepsilon_0, \beta_0, \gamma_0, \theta_0$ and σ_0 all represent constant terms. In equations (1)-(3), α_1 and γ_1 represent the linear influence of *fin* on *ACEI*. β_1 represents the linear influence of *fin* on *tech*. The meanings of the rest of the coefficients can be deduced by analogy. In equations (4)-(5), X_{it} represent the control variable. η_1 and ρ_1 are the threshold values. *I*(•) is the index function. When *fin* meets the conditions in (), the value of the index function is 1, otherwise, it's 0. When *fin* is less than or equal to the threshold value, the coefficient is θ_1 or σ_1 . When *fin* is greater than the threshold value, the coefficient is θ_2 or σ_2 . Equations (4) and (5) are situations where there is a single threshold. If there are more thresholds, equations can be extended.

Variables

Dependent variable: Agricultural carbon emission intensity (ACEI): Because agricultural carbon emissions are mostly caused by the use of agricultural resources (Hu et al. 2020), this article focuses on six key carbon sources. Table 1 shows the complete details. And the quantity of agricultural fertilizers, pesticides, agricultural diesel, agricultural plastic

films, total planted area of crops, and effective irrigation area are all measured separately. The calculation formula for total agricultural carbon emissions is as follows:

$$ACE = \sum ACE_i = \sum \omega_i \cdot \mu_i \quad \dots(6)$$

ACE is the total agricultural carbon emissions. *ACE_i* is the carbon emissions of each carbon source. ω_i is the amount of each carbon source. μ_i is the carbon emissions coefficient of each carbon source.

Since agricultural carbon emission intensity (*ACEI*) is of greater practical meaning, this paper uses it to represent agricultural carbon emissions. And it's measured by the ratio of the total agricultural carbon emissions (*ACE*) to the total agricultural output value.

Independent variable and threshold variable: Rural financial efficiency (fin): This paper uses the DEA-SBM model proposed by Tone (2003) to measure China's rural financial efficiency. This model is a non-radial variable returns to scale DEA model that avoids mistakes due to radial direction assumptions while disregarding slack variables. The model is as follows:

$$\left\{ \begin{array}{l} \min \alpha = \frac{1 - \frac{1}{a} \sum_{p=1}^a \frac{S_p^-}{m_{p0}}}{1 + \frac{1}{b} \sum_{q=1}^b \frac{S_q^+}{n_{q0}}} \\ m_0 = Mv + s^- \\ n_0 = Nv - s^+ \\ \sum v = 1 \\ v \geq 0, s^- \geq 0, s^+ \geq 0 \end{array} \right. \quad \dots(7)$$

Table 1: The agricultural carbon source coefficients and references.

Source	Coefficient	Reference
Fertilizers	0.8956kg CE.kg ⁻¹	Oak Ridge National Laboratory
Pesticides	4.9341kg CE.kg ⁻¹	Oak Ridge National Laboratory
Diesel fuel	0.5927kg CE.kg ⁻¹	IPCC
Agricultural film	5.1800kg CE.kg ⁻¹	Institute of Agricultural Resources and Ecological Environment, Nanjing Agricultural University
Plowing	312.6000kg CE.km ²	College of Biology and Technology, China Agricultural University
Irrigation	20.4760kg CE.hm ²	Dubey and Lal (2009)

The number of DMUs is W . The number of input variables is a . The number of output variables is b . v is the weight vector. M represents the input index. N represents the output index. α is the efficiency value of DMU(m_0, n_0). S_p^- is the input slack variable. S_q^- is the output slack variable. $\alpha \in [0, 1]$. If and only if $S^- = S^+ = 0$, $\alpha = 1$ and DMU is valid.

Based on the research of Atici et al. (2018), considering the rationality and availability of data, the following evaluation index system (shown in Table 2) is constructed:

Mediating variable: Agricultural technological progress (tech): In this paper, the DEA-Malmquist model proposed by Fare et al. (1994) is used to measure the agricultural technological progress in China. The advantage of this model is that it can reflect the dynamic changes of agricultural technological progress and the method isn't restricted by the function form or distribution assumptions. The corresponding frontier function can be obtained just by the method of linear programming, and the technological progress index can be calculated.

First, the DEA-BBC model is as follows:

$$\left\{ \begin{array}{l} \min \beta = \theta - \varepsilon \left(\sum_{p=1}^a S_p^- + \sum_{q=1}^b S_q^+ \right) \\ \theta m_0 = Xv + s^- \\ n_0 = Yv - s^+ \\ \sum v = 1 \\ v \geq 0, s^- \geq 0, s^+ \geq 0 \end{array} \right. \dots(8)$$

The number of DMUs is W . The number of input variables is a . The number of output variables is b . θ is the target planning value. v is the planning decision variable. ε is non-Archimedes infinitesimal. X represents the input

Table 2: Evaluation index system of rural financial efficiency.

Evaluation subject	Index type	Index
Rural financial efficiency	Input	Total assets of rural financial institutions
		Number of rural financial institution outlets
		Number of employees in rural financial institutions
	Output	Agricultural loan balance of financial institutions
	Output	Added-value of agriculture

index, and Y represents the output index. β is the efficiency value of DMU (m_0, n_0). S_p^- is the input slack variable, and S_q^- is the output slack variable. If $\theta = 1$, $S^- = S^+ = 0$, DMU is valid. If $\theta < 1$, DMU is invalid. If $\theta = 1$, and $S^- \neq 0$ or $S^+ \neq 0$, DMU is weak valid.

Second, the Malmquist index model is as follows:

$$M(x^{t+1}, y^{t+1}, x^t, y^t) = \left[\frac{D^t(x^{t+1}, y^{t+1})}{D^t(x^t, y^t)} \times \frac{D^{t+1}(x^{t+1}, y^{t+1})}{D^{t+1}(x^t, y^t)} \right]^{\frac{1}{2}} \dots(9)$$

$$Effch = \frac{D^t(x^{t+1}, y^{t+1})}{D^t(x^t, y^t)} \dots(10)$$

$$Tech = \left[\frac{D^t(x^{t+1}, y^{t+1})}{D^{t+1}(x^{t+1}, y^{t+1})} \times \frac{D^t(x^t, y^t)}{D^{t+1}(x^t, y^t)} \right]^{\frac{1}{2}} \dots(11)$$

$$Tfpch = Effch \times Tech = (Pech \times Sech) \times Tech \dots(12)$$

(x^t, y^t) and (x^{t+1}, y^{t+1}) represent the input-output vector in period t and $t+1$ respectively. If index $M > 1$, it means the efficiency increased. If index $M < 1$, it means the efficiency declined.

Based on the research of Wang & Tan (2021), considering the rationality and availability of data, the following evaluation index system (as shown in Table 3) is constructed:

Other Control Variables

Fiscal policy of supporting agriculture (gov): It refers to the fiscal expenditure provided by the government to support local agricultural development. This article uses the ratio of fiscal expenditures of supporting agriculture to the total output value of agriculture to measure gov, which can reflect the extent of government support for local agricultural development.

Farmland planting structure (stru): It can be measured by the proportion of the sown area of food crops to the total sown area of crops. Different planting structures will have different impacts on agricultural carbon emissions. Compared with non-food crops, food crops require less agricultural

Table 3: Evaluation index system of agricultural technological progress.

Evaluation subject	Index type	Index
Agricultural technological progress	Input	Number of employees in agriculture
		Total sown area of crops
		Fixed asset investment in agriculture
	Output	Total power of agricultural machinery
	Output	Gross output value of agriculture

film, fertilizers, pesticides, and other agricultural chemicals. Therefore, the larger the proportion is, the lower agricultural carbon emissions will be.

Deterioration of rural environment (env): It can be measured by the proportion of the affected area of crops to the total sown area of crops. Deterioration of the rural environment will lead to more natural disasters in rural areas. The more severe the damage to crops is, the greater the energy consumption and the increase in agricultural carbon emissions will be.

Data Sources

Because the data of Tibet, Hong Kong, Macao, and Taiwan is incomplete, this paper uses 30-province panel data in China during 2005-2018 to empirically analyze the impact of *fin* and *tech* on *ACEI*. The main sources of the above data are the open data of the National Bureau of Statistics, Wind database, China Regional Financial Operation Report, China Financial Yearbook, China Rural Statistical Yearbook, China Agricultural Machinery Industry Yearbook, and China Statistical Yearbook. Parts of missing values are filled by interpolation. This article adjusts the magnitude of *ACEI* and *gov* so that the value of all variables is between 0-10. The detailed information of variables is shown in Table 4.

RESULTS AND DISCUSSION

Total Effect Analysis

This article uses a 14-year and 30-province short panel, so unit root testing isn't required. The results of the F-test and Hausman-test show that the fixed effects model is better than the OLS model and the random effects model. Table 5 lists the results of the OLS model (model 1), random effects model (model 2), and fixed effects model (model 3).

In model 3, the coefficient of the independent variable - *fin* is -1.0815, which is significant at 1%, indicating that *fin* can inhibit *ACEI*. Therefore, the validity of hypothesis 1 is proved. High-efficiency rural finance supports low-carbon agricultural development by capital turnover, risk-taking, etc. The analysis of the control variables is as follows: the

Table 4: Descriptive statistics of variables.

Variable	Obs	Mean	Std. Dev.	Min	Max
ACEI	420	2.3163	0.8444	0.5451	5.1907
fin	420	0.5234	0.2809	0.0543	1.1232
tech	420	1.5956	0.7537	0.1864	6.2962
gov	420	0.1839	0.2168	0.0194	1.9408
stru	420	0.6624	0.1336	0.3628	0.9687
env	420	0.2111	0.1479	0.0000	0.9357

coefficient of *gov* is significantly negative at 1%, which reflects the great inclination extent of government policy toward green agriculture. The coefficient of *stru* is significantly negative at 1%. This is because food crops have lower demand for agricultural chemicals, resulting in lower carbon emissions. The coefficient of *env* is significantly positive at 1%, indicating that the higher the extent of rural environmental degradation is, the harder the low-carbon production of agriculture is achieved.

Mediating Effect Analysis

Wen & Ye (2014) found that when the test results are significant, the sequential test is better than the Sobel test. And the Bootstrap test is better than the Sobel test. Therefore, the appropriate mediating effect test procedure is shown in Fig. 1. First, the coefficient α_1 of the independent variable - *fin* in model 3 is -1.0815, and it's significant at 1%, so the argument of mediating effect can be grounded. Second, the coefficient β_1 of *fin* in model 4 is 0.7900, which is significant at 1%. And the coefficient γ_2 of the mediating variable - *tech* in model 5 is -0.5978, which is significant at 1%. Therefore, there is a significant indirect effect. Third, the coefficient γ_1 of *fin* in model 5 is -0.6092, which is significant at 1%, so there is also a significant direct effect. Fourth, compare the sign of $\beta_1\gamma_2$ and γ_1 . If their signs are the same, there is a partial mediating effect. The ratio of the mediating effect to the total effect is 43.67% ($\beta_1\gamma_2/\alpha_1$). Therefore, the validity of hypothesis 2 is proved.

Robustness Test

This article uses three methods to test the robustness of the regression results:

- (1) The samples from 2005 and 2018 are excluded. In Table 6, models 6 and 7 illustrate the findings. A mediating impact still exists, accounting for 42.28 percent of the total.
- (2) Replace the mediating variable. Agricultural technological progress is measured by agricultural mechanization (*tech'*) instead, which is the ratio of the total power of agricultural machinery to the total sown area of crops. The results are shown in models 8 and 9 in Table 6. There is still a mediating effect, accounting for 33.65%.
- (3) Insert the dependent variable's one-period lagged term into the model. The two-step SYS-GMM can effectively solve the dynamic panel's endogenous issue. The results are shown in models 10-12 in Table 6. In model 10, *fin* still inhibits *ACEI*. In model 11, *fin* still promotes *tech*. In model 12, *fin* and *tech* both still inhibit *ACEI*. The mediating effect is still significant. Therefore, the regression results are robust.

Table 5: Results of total effect test and mediating effect test.

Variable	Model 1 OLS	Model 2 RE	Model 3 FE	Model 4 FE	Model 5 FE
	ACEI	ACEI	ACEI	tech	ACEI
fin	-0.8280*** (-5.96)	-1.0482*** (-5.50)	-1.0815*** (-4.60)	0.7900*** (3.93)	-0.6092*** (-2.95)
tech					-0.5978*** (-11.67)
gov	-1.5388*** (-8.37)	-1.8929*** (-9.41)	-2.0265*** (-9.58)	0.7513*** (4.15)	-1.5773*** (-8.48)
stru	0.2004 (0.76)	-0.7884* (-1.66)	-3.6829*** (-4.11)	-1.1232 (-1.46)	-4.3544*** (-5.63)
env	2.1204*** (9.06)	2.4680*** (10.50)	2.5915*** (10.82)	-1.4809*** (-7.23)	1.7061*** (7.77)
cons	2.4523*** (10.90)	3.2143*** (8.93)	5.1476*** (8.44)	2.1007*** (4.03)	6.4035*** (11.95)
N	420	420	420	420	420
R ²	0.3275	0.4151	0.4302	0.2182	0.5791
F	52.01***		72.85***	26.94***	105.95***
Wald Chi ²		267.37***			
Hausman		Chi ² = 20.92 P = 0.0003		Mediating Effect/Total Effect = 43.67%	

Note: The t/z statistics are in parentheses, and the 10%, 5%, and 1% significance levels are represented by *, ** and ***, respectively.

Table 6: Robustness test results.

Variable	Model 6 FE	Model 7 FE	Model 8 FE	Model 9 FE	Model 10 SYS-GMM	Model 11 SYS-GMM	Model 12 SYS-GMM
	tech	ACEI	tech'	ACEI	ACEI	tech	ACEI
fin	0.7577*** (3.49)	-0.5029** (-2.30)	0.1225*** (3.34)	-0.7175*** (-3.39)	-0.3990*** (-9.16)	0.3956*** (12.91)	-0.1655*** (-2.63)
tech		-0.6035*** (-11.03)					-0.0450** (-2.28)
tech'				-2.9709*** (-10.25)			
controls	yes	yes	yes	yes	yes	yes	yes
ACEI(-1)					0.8713*** (104.18)		0.8578*** (44.79)
tech(-1)						0.9760*** (97.68)	
cons	2.4114*** (4.05)	5.5679*** (9.23)	0.7572*** (7.97)	7.3973*** (12.66)	0.1095 (0.36)	0.5041 (1.63)	0.0910 (0.17)
N	360	360	420	420	360	360	360
R ²	0.1907	0.5664	0.1791	0.5523			
F	19.20***	84.91***	21.06***	94.98***			
AR(1)-P					0.0002	0.0235	0.0002
AR(2)-P					0.1053	0.7406	0.1261
Sargan-P					0.9737	0.9969	1.0000
	Mediating Effect/Total Effect =42.28%		Mediating Effect/Total Effect =33.65%				

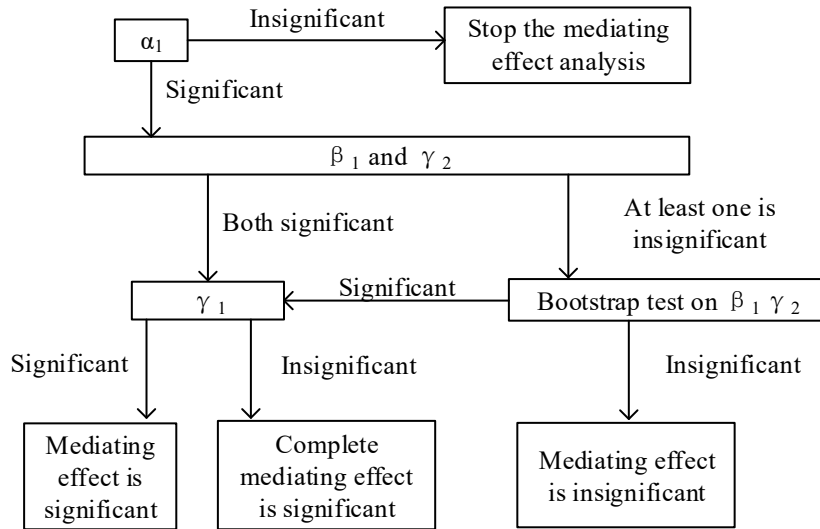


Fig.1: The mediating effect test procedure.

Further Analysis: Threshold Effect Test

This paper selects *fin* as the threshold variable and selects *fin* and *tech* as threshold-dependent variables. To calculate the threshold values more precisely, the self-sampling approach (Bootstrap) is used 300 times. The results of the threshold effect test are shown in Table 7. When the threshold-dependent variable is *fin*, the single threshold test is significant at 1%, and the double threshold and triple threshold tests are not significant, so there is a single threshold with a threshold value of 0.0776, as shown in Fig. 2. When the threshold-dependent variable is *tech*, the double threshold test is significant at 5%, and the single threshold and triple threshold tests are not significant, so there is a double threshold with threshold values of 0.0776 and 0.4480, as shown in Fig. 3.

Then, regression estimation of the threshold effect model is performed, and the results are shown in Table 8. In model

13, when $fin \leq 0.0776$, the coefficient of *fin* is 17.0382, which is significant at 1%, indicating that when *fin* doesn't cross the single threshold, it's at a low level and it promotes *ACEI*. The reason may be that, at this time, its effect on the expansion of the agricultural production scale is greater than its effect on technology improvement. When $fin > 0.0776$, the coefficient of *fin* is -1.1360, which is significant at 1%, indicating that when *fin* crosses the single threshold, it's at a relatively high level and it has an inhibitory effect on *ACEI*. The reason may be that, at this time, its effect on technology improvement is greater than its effect on the expansion of the agricultural production scale. In model 14, when $fin \leq 0.0776$, the coefficient of *tech* is 0.6250, which is significant at 1%, indicating that when *fin* is too low, *tech* has a positive impact on *ACEI*. The reason may be that, at this time, rural finance cannot provide sufficient support for agricultural technological innovation. When $0.0776 < fin \leq 0.4480$, the coefficient of *tech* is -0.3946,

Table 7: Results of the significance test of the threshold effect.

Threshold-dependent variable	Item	F-statistics	P-value	Threshold Estimation value	95% confidence interval	10% Critical value	5% Critical value	1% Critical value
Fin	Th-1	33.39***	0.0033	0.0776	[0.0752 , 0.0851]	18.5435	24.2863	29.0024
	Th-21	14.24	0.3267	0.0776	[0.0752 , 0.0851]	88.2282	100.8478	115.5176
	Th-22			0.5337	[0.5233, 0.5424]			
	Th-3	9.23	0.7300	0.8995	[0.8330 , 0.9439]	55.3573	73.0685	116.7123
tech	Th-1	35.33	0.1033	0.4480	[0.4360 , 0.4587]	35.3562	41.5207	54.1176
	Th-21	42.31**	0.0133	0.4480	[0.4272 , 0.4587]	24.4556	29.4876	43.9099
	Th-22			0.0776	[0.0752 , 0.0851]			
	Th-3	29.40	0.6533	0.1876	[0.1818 , 0.2061]	115.9801	126.1179	146.6378

Table 8: Regression results of the threshold effect.

Variable	Model 13	Model 14
$fin(fin \leq 0.0776)$	17.0382*** (5.28)	
$fin(0.0776 < fin)$	-1.1360*** (-5.01)	
$tech (fin \leq 0.0776)$		0.6250*** (3.53)
$tech(0.0776 < fin \leq 0.4480)$		-0.3946*** (-7.03)
$tech (0.4480 < fin)$		-0.7409*** (-14.35)
controls	yes	yes
cons	4.6868*** (7.91)	5.6276*** (11.23)
N	420	420
R ²	0.4735	0.6416
F	69.24***	114.57***

which is significant at 1%, indicating that when fin crosses the first threshold, $tech$ has an inhibitory effect on $ACEI$. When $fin > 0.4480$, the coefficient of $tech$ is -0.7409 , which is significant at 1%, indicating that the higher rural financial efficiency is, the stronger the support for agricultural technological progress will be, resulting in the stronger inhibition on agricultural carbon emissions.

CONCLUSIONS

This paper uses the DEA-SBM model and DEA-Malmquist model to measure rural financial efficiency and agricultural technological progress respectively from the perspective of

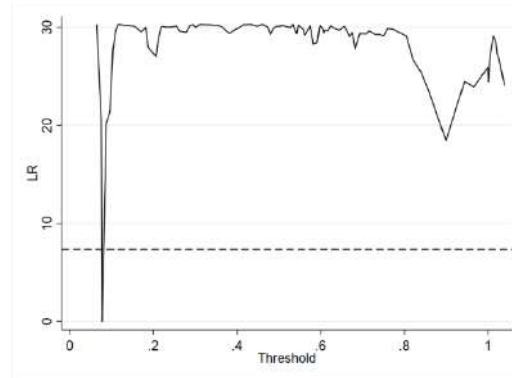
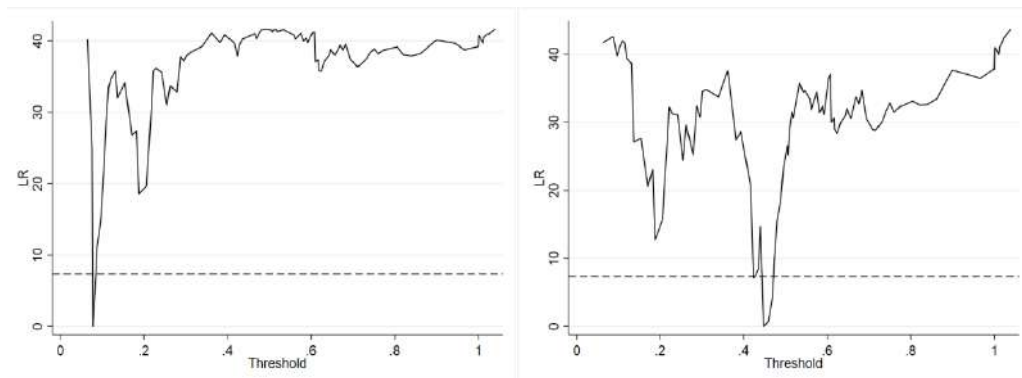


Fig. 2: Threshold estimated value and confidence interval (threshold-dependent variable: fin).

input and output. And it empirically studies the impact of rural financial efficiency and agricultural technological progress on agricultural carbon emissions by using provincial panel data from 2005-2018. The mediating effect model is used to demonstrate the mechanism of “rural financial efficiency-agricultural technological progress-agricultural carbon emissions”. The panel threshold effect model is used to study the non-linear impact of rural financial efficiency and agricultural technological progress on agricultural carbon emissions. The main conclusions are as follows:

- (1) Rural financial efficiency not only has a direct inhibitory effect on agricultural carbon emissions but can also inhibit agricultural carbon emissions by promoting agricultural technological progress.
- (2) When rural financial efficiency is the threshold-dependent variable, it has a single threshold effect on agricultural carbon emissions. When rural financial efficiency



(a)

(b)

Fig. 3: The first (a) and second (b) threshold estimated values and confidence intervals (threshold-dependent variable: $tech$).

does not exceed the threshold, it promotes agricultural carbon emissions. And when rural financial efficiency crosses the threshold, it inhibits agricultural carbon emissions.

- (3) When agricultural technological progress is the threshold-dependent variable, it has a double threshold effect on agricultural carbon emissions. When rural financial efficiency hasn't crossed the first threshold, agricultural technological progress promotes agricultural carbon emissions. When rural financial efficiency crosses the first threshold, agricultural technological progress inhibits agricultural carbon emissions. When rural financial efficiency crosses the second threshold, agricultural technological progress has a stronger inhibitory effect on agricultural carbon emissions.

ACKNOWLEDGEMENT

The study was supported by a grant from the project of Beijing University of Technology (40011212202101).

REFERENCES

- Atici, K.B., Ulucan, A. and Bayar, I.U. 2018. The measurement of agricultural productivity changes in OECD countries with fuzzy data. *RAIRO: Oper. Res.*, 52(3): 1003-1017.
- Claessens, S. and Feijen, E. 2007. Financial Sector Development and the Millennium Development Goals. World Bank Working Paper, 89(2006038987). The World Bank, Washington DC.
- Chen, J., Cheng, S. and Song, M. 2018. Changes in energy-related carbon dioxide emissions of the agricultural sector in China from 2005 to 2013. *Ren. Sust. Energy Rev.*, 94(10): 748-761.
- Chen, Y. and Li, M. 2020. The measurement and influencing factors of agricultural carbon emissions in China's western Taiwan straits economic zone. *Nat. Environ. Pollut. Technol.*, 19(2): 587-601.
- Dubey, A. and Lal, R. 2009. Carbon footprint and sustainability of agricultural production systems in Punjab, India, and Ohio, USA. *J. Crop Improv.*, 6: 17-34.
- Fare, R., Grosskopf, S. and Norris, M. 1994. Productivity growth, technical progress, and efficiency change in industrialized countries. *Am. Econ. Rev.*, 84 (5): 1040-1044.
- Food and Agriculture Organization of the United Nations (FAO). 2020. FAO statistical database. <http://www.fao.org/faostat/zh/#data/GT>.
- Guo, H., Fan, B. and Pan, C. 2021. Study on mechanisms underlying changes in agricultural carbon emissions: A case in Jilin province, China, 1998-2018. *Int. J. Environ. Res. Public Health*, 18: 919.
- Hansen, B. E. 1999. Threshold effects in non-dynamic panels: Estimation, testing, and inference. *J. Econ.*, 93(2): 345-368.
- Hu, W.L., Zhang, J.X. and Wang, H.L. 2020. Characteristics and influencing factors of agricultural carbon emission in China. *Stat. Decis.*, 36(05): 56-62.
- IPCC. 2018. Special report on global warming of 1.5 (SR15). <https://www.ipcc.ch/sr15/>.
- Luo, L., Wang, Y. and Qin, L. 2014. Incentives for promoting agricultural clean production technologies in China. *J. Cleaner Prod.*, 74(1): 54-61.
- Liu, Y., Ji, D., Zhang, L., An, J. and Sun, W. 2021. Rural financial development impacts on agricultural technology innovation: evidence from china. *Int. J. Environ. Res. Pub. Health*, 18(3): 1110.
- Makate, C., Makate, M., Mutenje, M., Mango, N. and Siziba, S. 2019. Synergistic impacts of agricultural credit and extension on the adoption of climate-smart agricultural technologies in southern Africa. *Environ. Develop.*, 32: 100458.
- Maraseni, T., An-Vo, D.A., Mushtaq, S. and Reardon-Smith, K. 2020. Carbon smart agriculture: an integrated regional approach offers significant potential to increase profit and resource use efficiency, and reduce emissions. *J. Cleaner Prod.*, 12(4): 555.
- Owusu, P. A. and Asumadu-Sarkodie, S. 2016. Is there a causal effect between agricultural production and carbon dioxide emissions in Ghana? *Environ. Eng. Res.*, 22(1): 40-54.
- Paroussos, L., Fragkiadakis, K. and Fragkos, P. 2020. Macro-economic analysis of green growth policies: The role of finance and the technical progress in Italian green growth. *Clim. Change*, 160: 591-608.
- Ridzuan, N.H.A.M., Marwan, N.F., Khalid, N., Ali, M.H. and Tseng, M. 2020. Effects of agriculture, renewable energy, and economic growth on carbon dioxide emissions: evidence of the environmental Kuznets curve. *Resour. Conserv. Recycl.*, 160: 104879.
- Shahbaz, M., Solarin, S.A., Mahmood, H. and Arouri, M. 2013. Does financial development reduce CO2 emissions in the Malaysian economy? A time-series analysis. *Econ. Model.*, 35(1):145-152.
- Shahbaz, M., Nasir, M.A. and Roubaud, D. 2018. Environmental degradation in France: The effects of FDI, financial development, and energy innovations. *Energy Econ.*, 74:843-857.
- Shen, Y., Su, Z., Malik, M.Y., Umar, M., Khan, Z. and Khan, M. 2021. Does green investment, financial development and natural resources rent limit carbon emissions? a provincial panel analysis of china. *Sci. Tot. Environ.*, 755: 142538.
- Tone, K. 2003. Dealing with undesirable outputs in DEA: A slacks-based measure (SBM) approach. *GRIPS Res. Rep. Ser.*, 5: 203.
- Tamazian, A., Chousa, P.J. and Vadlamannati, K.C. 2009. Does higher economic and financial development lead to environmental degradation: Evidence from BRIC countries. *Energy Pol.*, 37: 246-253.
- Tamazian, A. and Rao, B.B. 2010. Do economic, financial, and institutional developments matter for environmental degradation? Evidence from transitional economies. *Energy Econ.*, 32 (1): 137-145.
- Wen, Z. and Ye, B. 2014. Analyses of mediating effects: the development of methods and models. *Adv. Psychol. Sci.*, 22(005): 731-745.
- Wang, R. and Tan, J. 2021. Exploring the coupling and forecasting of financial development, technological innovation, and economic growth. *Technol. Forecast. Soc. Change*, 163: 1151-1163.
- Yan, C., Li, T. and Lan, W. 2016. Financial development, innovation, and carbon emission. *J. Fin. Res.*, 1(427): 14-30.
- Zhang, H. and Liu, F. 2018. Spatial and temporal disparities in agricultural carbon emissions in Xinjiang and decomposition of impact factors. *Chem. Eng., Trans.*, 66:553-558.
- Zhou, Y., Fang, Z., Li, N., Wu, X., Du, Y. and Liu, Z. 2019. How does financial development affect reductions in carbon emissions in high-energy industries?-a perspective on technological progress. *Int. J. Environ. Res. Pub. Health.*, 16(30): 18.
- Zhang, L., Pang, J., Chen, X. and Lu, Z. 2019. Carbon emissions, energy consumption, and economic growth: evidence from the agricultural sector of china's main grain-producing areas. *Sci. Total Environ.*, 665(15): 1017-1025.



Internet of Things (IoT) Enabled Air Quality Monitoring System for Conventional and UAV Application

V. Vinoth Kumar[†] and G. Sasikala

Department of Electronics and Communication Engineering, Vel Tech Rangarajan Dr. Sagunthala R&D Institute of Science and Technology, Avadi, Chennai, Tamil Nadu, India

[†]Corresponding author: V. Vinoth Kumar: vinothkumarv@veltech.edu.in

Nat. Env. & Poll. Tech.
Website: www.neptjournal.com

Received: 17-02-2021

Revised: 09-04-2021

Accepted: 30-04-2021

Key Words:

IoT
UAV
Arduino UNO
Node MCU
Air quality monitoring

ABSTRACT

The purpose of this research is to make a system to read the air quality by detecting the various gases existing in the air by using Arduino UNO and node MCU module for conventional as well as UAV applications. The emergence of the Internet of Things (IoT) has made it easier to read the various gases present in the environment using smartphones from the workplace. The use of an Arduino processor with a Node MCU to construct an air quality monitoring system is discussed in this paper. The Node MCU is used to transmit live data for CO, CO₂, and PM_{2.5} concentrations that are sensed by sensors. This data can be monitored continuously by the user via the mobile phone. The calibration of sensors is highly important while reviewing and grasping the large literature on the subject of IoT-based air quality monitoring. The proposed low-cost live air quality monitoring system uses commercially available gas sensors to detect environmental gases such as CO, CO₂ and PM_{2.5} to monitor air quality in an outdoor area. The proposed system is used to correctly evaluate the experimental outcomes. This proposed prototype model incorporates an open-source cloud facility with Arduino for air quality monitoring, confirming low cost, comfort, and convenience for a customizable air quality monitoring system. As a result, the suggested system can simply be converted to use in a UAV for monitoring air quality in the outdoors at various altitudes, and it can be scaled up in the future.

INTRODUCTION

Nowadays, environmental gas monitoring is critical for observing the concentrations of numerous dangerous gases in both indoor and outdoor environments, as well as for studying the state of the environment in today's society. The gases in the environment such as CO, CO₂, PM_{2.5} cause more health-related issues for human beings. The low-cost pollution tracking system needs to be installed in many places to track the level of hazardous gases present in the environment. The aim of tracking the level of hazardous gas around the environment is to give useful information related to the impact of pollution on the people and also it is very much helpful to take remedial action to improve the quality of the environment. There is a plethora of conventional methods used to monitor the quality of environmental conditions (Sirsikar & Karemore 2015). The major goal of environmental parameter monitoring is to continuously observe the concentration of hazardous gases and to analyze the impact of environmental pollution due to the emission of gases from the vehicles and industries and to provide this information to the people to create awareness about global warming and health-related issues caused by the emission of hazardous gases such as CO, CO₂, nitric oxide, PM_{2.5}, PM₁₀ and so on.

The Korea Ministry of Environment (KMOE) prescribed the Indoor Air Quality (IAQ) act to minimize the effect of various gases present in the environment such as PM_{2.5}, particulate matter 10, and carbon monoxide from these listed pollutants. The Indoor Air Quality (IAQ) standard for the PM_{2.5} level is around 150 $\mu\text{g}\cdot\text{m}^{-3}$ (Dinh et al. 2014). The proposed environmental gas sensing system may help to reduce the rate of health-related problems due to the excess amount of hazardous gases present in the environment by identifying the high concentration regions in the environment. The presence of very small particles between 2.5 microns or less causes more health problems in the brain and lungs. In general, the suggested IoT-based real-time environmental gas monitoring system is used to map high concentration zones at a lower cost of installation.

RELATED WORK

With a limited number of air quality monitoring systems, the Internet of Things (IoT) was deployed in a smart environmental pollution monitoring system Shitole & Markande (2016). Okokpujie et al. (2016) presented a request and response protocol with a combination of address and data-centric protocol for air quality monitoring at home. Alvear et al.

(2017) presented a pollution-based UAV control system. The data is collected using an unmanned aerial vehicle equipped with a Pixhawk autopilot and a Raspberry Pi controller board, which is then compared to the simulation findings using OMNeT++. Wei-Ying et al. (2016) proposed a model that displayed the quantity of real-time air pollutants using several air quality sensors. Saha et al. (2017) proposed an IoT-based sensor-based air quality measurement. Short message service is shared with the public whenever the air quality level exceeds the threshold level of the standard air quality index. Sammarco et al. (2017) proposed an ambient real-time air quality monitoring system that consists of several air quality monitoring stations placed in various locations that are connected via wireless protocol using machine-to-machine communication. For air quality monitoring, supervisory control and data acquisition (SCADA) is used, which allows the user to monitor pollution data quickly using smart SCADA (Anil kumar et al. 2017). The Raspberry module is used to measure CO and other gases at normal levels, and the data may be viewed via a web page within the network range. However, using the parameters, accurate long-term prediction of air pollution data is not possible (Nayak et al. 2017). Balasubramanian & Manivannan (2016) proposed an IoT-based air quality monitoring system with alarm indication, in which the data can be accessed from a web server and the alarm will be activated if the air pollution level exceeds the threshold level, otherwise, the air pollution data will be indicated and accessed from the webserver. The MQ 135 sensor is used (Rukmani. et al. 2018) to measure various hazardous chemicals present in the environment, and an Arduino-based controller is used to control the entire process, as well as image processing and deep learning. Vinoth Kumar et al. (2017) proposed IoT based smart irrigation system using an Arduino processor in which various information is transmitted. Xioajun et al. (2015) proposed IoT based air quality monitoring system with a large number of sensors.

MATERIALS AND METHODS

The proposed system is used to assess the air quality in a given location where gas sensors detected air samples. Thus it consists of MG 811 (CO₂), MQ 7 (CO) and PM_{2.5} sensor modules, Arduino UNO, Node MCU, and ground station to obtain live pollution data from the environment. CO₂ sensor MG 811 was calibrated with the known values from the various vehicles. The operating voltage for MG 811 was 6 V and the detection zone is about 0 to 10000 ppm. The MQ 7 sensor was used to monitor CO levels in the external environment, and it was calibrated using known values from various vehicles. The CO sensor's operating voltage is 5V dc, so the CO gas may be felt by the sensor, which has a range of 10 to 1000 ppm. The PM_{2.5} sensor is utilized in

the proposed system to measure the particulate matter in the environment. The PM_{2.5} sensor measures the concentration of small particles with a diameter of less than 2.5 microns. The PM_{2.5} sensor's supply voltage and operating current are around 5 V dc and 20 mA, respectively. The PM_{2.5} sensor has a sensitivity of 0.5 V (0.1 mg.m⁻³), and all of these air quality sensors are sent into the Arduino UNO CPU to provide valuable data to the user. The controller's power source is around 5 volts. Because of its many capabilities and low cost, the Arduino UNO controller is used. The suggested system employs Node MCUs to transport data from one site to the control station. The Node MCU may be coupled with the Blynk app, which is highly beneficial for constructing IoT projects. With the Blynk app, the user can see live data monitoring on their mobile phone. Because a scalable unmanned aerial vehicle platform must be suitable for real-time monitoring of environmental pollution related parameters, the UAV for air quality monitoring plays a critical role in this application, and quad copter UAV is suitable for air quality measurement application due to its hovering capability, greater manoeuvrability, lower cost, ease-of-use, and higher payload capacity. As a result, this suggested air quality monitoring system is more suited for use by UAVs to detect the various gases present in the environment at different altitudes.

PROPOSED SYSTEM

In the proposed system low-cost air quality monitoring system for the outdoor environment is implemented using various air quality sensors, arduino UNO and node MCU module. Fig. 1, shows the proposed air pollution monitoring system.

Arduino UNO was used to convert the sensor signals into the respective gas concentration in ppm as well as in the unit of mg.m⁻³. Because the node MCU module was used for wireless air quality monitoring, the arduino signal was further delivered and received to the user's mobile phone. Environmental parameter measuring and analysis systems that use wired networks have more design complexity and are more expensive than wireless environmental parameter

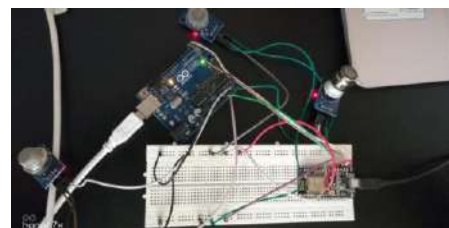


Fig 1: Proposed air pollution monitoring system.

measuring systems. This suggested system uses IoT approaches to monitor environmental indicators, resulting in a system with more functionality and a lower installation cost. Sensors to measure gases such as CO, CO₂, and PM_{2.5} are calibrated and integrated with an Arduino controller, after which the measured values from the sensors are converted to electrical quantities, such as voltage signals, which are then converted to the respective ppm units as mg.m⁻³ units using codes uploaded in the Arduino, and finally transmitted to the user's mobile phone using a node MCU module and Wi-Fi protocol.

The sensor calibration and the sensor measurements are tested by using different gases emitted from various vehicles. Finally, the suggested system for real-time environmental gas measurement in an outdoor location was measured, and real-time live data was transferred and received by the user. For testing, the breadboard was used to connect the sensors like MQ 7, MG 811, PM_{2.5} and other controller modules. Android type mobile phone is used in the proposed system and the live environmental parameter in ppm and mg.m⁻³, as well as the corresponding sensor output in voltage, also can be displayed in the mobile phone which is connected to cloud database so that variations in the graph can be viewed based on various level of pollution concentration. Fig. 2, shows the block diagram for the proposed air quality monitoring system in which the CO sensor, CO₂, and PM_{2.5} sensors were connected to the Arduino controller, and the output of the Arduino connected to the node MCU and from the node MCU, the live pollution data was transmitted.

RESULTS AND DISCUSSION

We focused on measuring gases such as CO, CO₂, and PM_{2.5} that are emitted by automobiles. In the suggested system, measurements of various gases such as CO, CO₂, and PM_{2.5} were made with various condition vehicles. The CO₂ sensor,

CO sensors, and PM_{2.5} sensors were linked to the analog input pins of the controller throughout the experimental inquiry, which involved roughly 12 different motorcycles in various conditions. The vehicles were categorized based on their condition as well as the year of the purchase or the different old vehicles such as 1-year old vehicle category, 3-year old vehicle category, 6-year old vehicle category, and 12-year old vehicle category. From each category, three vehicles were chosen, and emitted gas measurements were taken using the proposed system. CO, CO₂, and PM_{2.5} are some of the gases released by cars. Five pollutants were analyzed, and the results of the research revealed that the amount of pollution varies on the condition and age of the vehicles. The arduino controller was coded to output the calibrated sensor electrical signal voltage as well as the associated value of the pollutants in mg.m⁻³ and ppm, which are also employed in the deep analysis. The system was then used to measure various pollutions present in the environment in real-time, and the measured data was then transmitted to the user mobile using IoT application with all the parameters in different units of measured pollutant gases, and the data collected from the proposed system was very useful to analyze in light of health issues and others. Hence, the system's installation cost is low. To investigate gas emissions from various vehicle conditions, sensors were attached to an Arduino controller that was combined with a node MCU. After processing the data with the Arduino UNO module, the measured pollutant values from the vehicles were transmitted to the user's mobile phone via the cloud, and then interpretations were made using the collected data. Case-1 category vehicles were purchased and used for less than or equal to one year. Vehicles in the case-2 category were purchased and used for about three years, vehicles in the case-3 category were purchased and used for about six years, and vehicles in the case-4 category were purchased and used for about ten years. In each category, three vehicles were used for testing purposes to measure the CO₂, CO, and PM_{2.5} that were emitted from those different cases of a vehicle.

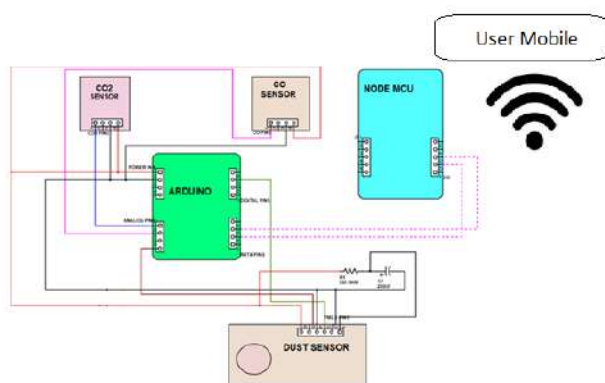


Fig. 2: Block diagram of proposed air quality monitoring system.

MEASUREMENT OF CO₂

The amount of CO₂ emitted from four distinct types of automobiles was measured. Fig. 2 depicts the testing of emitted gas detection for CO₂ gas, with a CO₂ gas sensor MG-811 put at the vehicle's gas emitted place. The sensor's function is to measure the concentration of CO₂ gas emitted from the vehicle; additionally, the sensor was connected to an Arduino UNO board to obtain the corresponding emitted gas concentration values in various units such as ppm, mg.m⁻³, and the corresponding sensor output voltage in mV. Then the device was embedded with Node MCU and after

further configuration, the system was ready to connect with the Smartphone to monitor the live data of the CO₂ gas. Table 1 shows the measured gas concentration values from the various conditions of vehicles to observe the dynamic range of measured values of gas concentrations including ppm, mg/mg³ and mV.

In the first case, three different one-year-old vehicles were chosen for the test, and the emitted gases were measured. The results show that the CO₂ concentration varies in ppm from 744.882 ppm to 749.072 ppm, the CO₂ gas concentration in mg.m⁻³ varies from 853.244 mg.m⁻³ to 858.964 mg.m⁻³, and the corresponding sensor output in mV varies from 436.873 mV to 439.331 mV. From the measurement of CO₂ gas, a small amount variation in emitted gas concentration was observed from the measurement.

In the second case of CO₂ measurement, three different 3-years old vehicles were chosen for the test, from the result the CO₂ gas ppm value varies from 769.570 ppm to 775.892 ppm, the CO₂ gas concentration in mg.m⁻³ varies from 904.319 mg.m⁻³ to 910 mg.m⁻³ and the corresponding sensor output values vary from 463.024 mV to 466.122 mV. It was observed that the variation of CO₂ gas concentration

from case-1 to case-2 was quite large due to the conditions of vehicles.

In the third case, the emitted CO₂ gas was measured from three 6-years old vehicles for testing purposes, from the result, the concentration of CO₂ gas in ppm varies from 789.470 ppm to 794.75 ppm, the emitted CO₂ gas concentration in mg.m⁻³ varies from 904.319 mg.m⁻³ to 910.369 mg.m⁻³ and the corresponding sensor output voltages ranges from 463.024 mV to 466.122 mV, from the observation even though there is a little variation in the vehicles among the case-3 category, There is quite large variations observed from case-2 category vehicles to case-3 categories of vehicles. Three different ten years old vehicles were chosen in the case-4 category for the test to measure the emitted CO₂ concentration for the analysis purpose at last from the result the variation of CO₂ gas in ppm was from 808.382 ppm to 816.339 ppm, the concentration of CO₂ in mg.m⁻³ varies from 925.982 mg.m⁻³ to 935.09 mg.m⁻³, and the corresponding sensor output voltage varies from 474.116 mV to 478.783 mV. The various cases of emitted CO₂ measurement give the observation of variations in the dynamic range of the measured values from the sensors using a controller.

Table 1: Measured CO₂ values from different vehicles.

Vehicle	Vehicle Period	Sensor output (mV)	Concentration of CO ₂ (ppm)	Gas concentration (mg.m ⁻³)
Vehicle-1	1 year old	436.873	744.882	853.244
Vehicle-2		438.266	747.256	855.964
Vehicle-3		439.331	749.072	858.044
Vehicle-4	3 years old	451.353	769.570	881.524
Vehicle-5		452.160	770.946	883.100
Vehicle-6		455.061	775.892	888.766
Vehicle-7	6 years old	463.024	789.470	904.319
Vehicle-8		464.409	791.831	907.023
Vehicle-9		466.122	794.752	910.369
Vehicle-10	10 years old	474.116	808.382	925.982
Vehicle-11		475.901	811.425	929.468
Vehicle-12		478.783	816.339	935.097



Fig. 3: Measurement of CO₂ from different vehicles.

Measurement of CO

Thus the measurement of CO from the various categories of vehicles was observed. The testing of emitted gas detection for CO gas is shown in Fig. 5 and Fig. 6. The figures depict the measured gas concentration values from various vehicle

conditions to demonstrate the dynamic range of recorded gas concentration values, such as ppm, mg.mg⁻³, and mV.

Three different 1-year old used vehicles were chosen for test in case-1 for the measurement of emitted CO from vehicles, and from the result, the CO gas concentration in

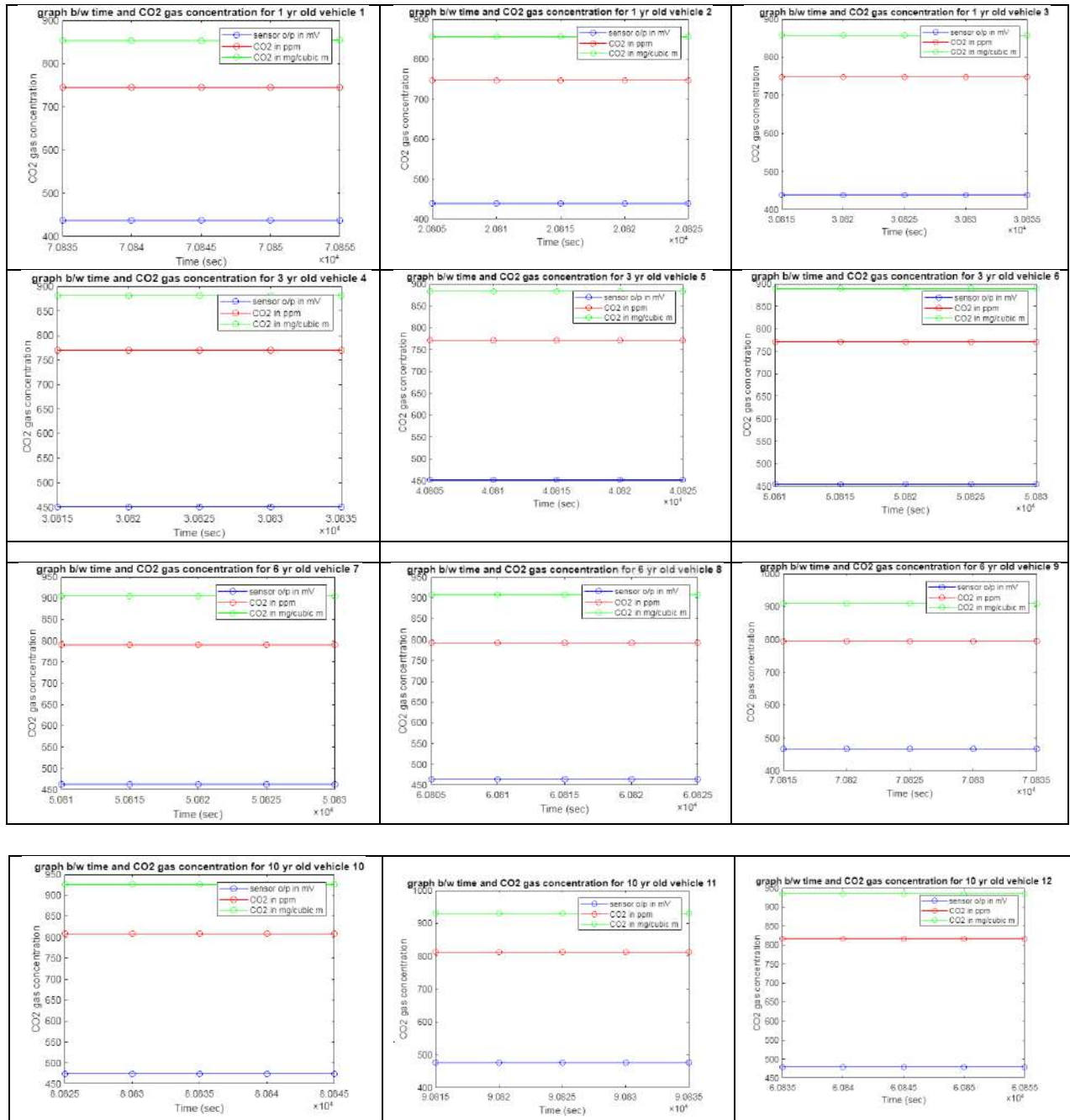


Fig. 4: Arduino UNO controller output for CO₂ from different vehicles.



Fig. 5: Measurement of CO from different vehicles.

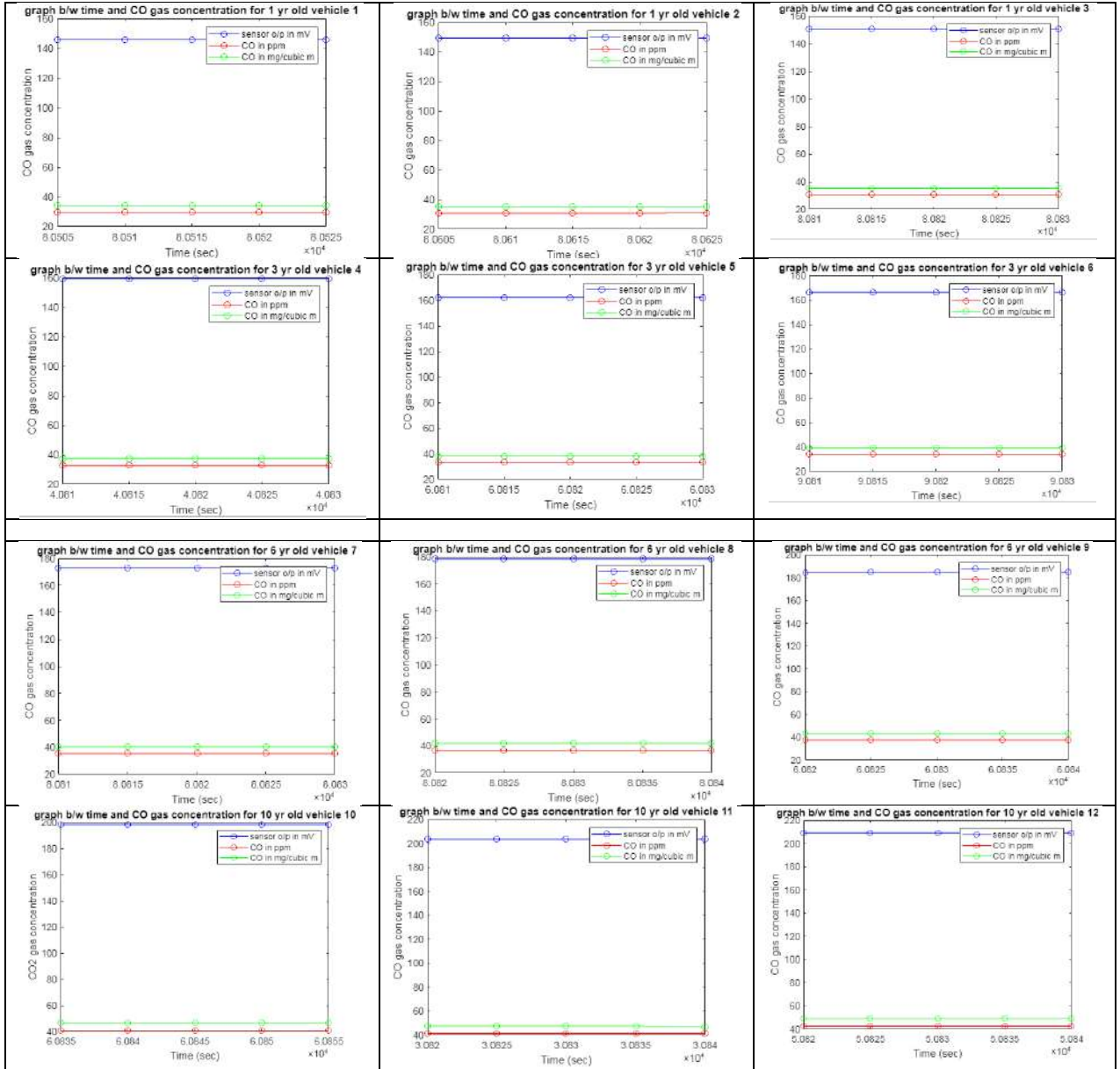


Fig 6: Arduino UNO controller output for CO from different vehicles.

ppm values varies from 29.833 ppm to 30.806 ppm, the CO gas concentration in mg.mg^{-3} varies from 34.173 to 35.288 mg.mg^{-3} and the corresponding sensor output voltage varies from 145.811 mV to 150.566 mV. For the case-1, it was observed that there is a small amount of variation in emitted gas concentration for CO. In the second case of CO measurement, three different three-years-old vehicles were chosen for the test to observe the dynamic range of sensor output, and from the result, the emitted CO gas concentration in ppm varies from 32.621 ppm to 33.996 ppm, the CO gas concentration in mg.mg^{-3} varies from 37.367 mg.mg^{-3} to 38.942 mg.mg^{-3} and the corresponding sensor output voltage variation in mV is from 159.418 mV to 166.131 mV. It was observed that the variation of emitted CO gas concentration from case-1 to case-2 is quite large due to the conditions of vehicles (Table 2).

In the third case of CO measurement, three different 6-years used old vehicles were chosen for the test, and from the result, it was observed that the variation of CO gas in ppm was from 35.380 ppm to 37.754 ppm, the emitted CO gas concentration in mg.mg^{-3} varies from 40.577 mg.mg^{-3} to 43.247 mg.mg^{-3} and the corresponding sensor output variation in mV vary from 172.902 mV to 184.503 mV. In the fourth case of CO measurement, three 10-years old used vehicles were chosen for the test to measure the emitted gas measurement, and from the result, it was observed that the CO gas concentration in ppm varies from 40.579 ppm to 42.792 ppm. The concentration of CO in mg.mg^{-3} varies from 46.483 mg.mg^{-3} to 49.018 mg.mg^{-3} , and the corresponding sensor output in voltage varies from 198.309 mV to 209.124 mV. It was observed that from the first case to the fourth case the output of the sensor varies with the category and condition of vehicles.

Measurement of Fine Particulate Matter $\text{PM}_{2.5}$

In the first case of $\text{PM}_{2.5}$ measurements, three different 1-year old vehicles were chosen for the test, thus the measurement of $\text{PM}_{2.5}$ from the various categories of vehicles was observed. The testing of emitted gas detection for $\text{PM}_{2.5}$ gas is shown in Fig. 7, where the $\text{PM}_{2.5}$ gas sensor was placed in the gas emitted place of the vehicles. The function of the sensor is to measure the concentration $\text{PM}_{2.5}$ gas emitted from the vehicle and after further configuration, the system was ready to connect to the Smartphone to monitor the live data of the $\text{PM}_{2.5}$ gas. Fig. 8, shows the measured gas concentration values from the various conditions of vehicles to observe the dynamic range of measured values of gas concentrations including ppm, mg.mg^{-3} , and mV.

In case-1, the measured value of $\text{PM}_{2.5}$ in ppm varies from 0.0229 to 0.0235 ppm, the $\text{PM}_{2.5}$ concentrations in mg.m^{-3} varies from 0.0262 mg.m^{-3} to 0.0269 mg.m^{-3} and corresponding sensor output voltage varies from 0.367 mV to 0.371 mV. In the second case of $\text{PM}_{2.5}$ measurements, three different 3-years old used vehicles were chosen for the test. Results show that $\text{PM}_{2.5}$ concentrations in ppm varies from 0.0246 ppm to 0.0252 ppm, the $\text{PM}_{2.5}$ concentration in mg.m^{-3} varies from 0.0281 mg.m^{-3} to 0.0288 mg.m^{-3} and the corresponding sensor output voltage varies from 0.394 mV to 0.403 mV. In the third case of $\text{PM}_{2.5}$ measurements, three different 6-years old vehicles were chosen for the test. Results show that the concentration of $\text{PM}_{2.5}$ in ppm varies from 0.0254 ppm to 0.0261 ppm, the $\text{PM}_{2.5}$ concentrations in mg.m^{-3} varies from 0.0292 to 0.0299 mg.m^{-3} and the corresponding sensor output voltage varies from 0.408 mV to 0.418 mV. Due to the similar vehicle conditions, the

Table: 2 Measured CO values from different vehicles.

Vehicle	Vehicle Period	Sensor output (mV)	Concentration of CO (ppm)	Gas concentration.(mg/m^3)
Vehicle-1	1 year old	145.811	29.833	34.173
Vehicle-2		149.217	30.530	34.942
Vehicle-3		150.566	30.806	35.288
Vehicle-4	3 years old	159.418	32.621	37.367
Vehicle-5		162.233	33.197	38.027
Vehicle-6		166.138	33.996	38.942
Vehicle-7	6 years old	172.902	35.380	40.527
Vehicle-8		178.414	36.508	41.820
Vehicle-9		184.503	37.754	43.247
Vehicle-10	10 years old	198.309	40.579	46.483
Vehicle-11		203.338	41.608	47.661
Vehicle-12		209.124	42.792	49.018



Fig. 7: Arduino UNO controller output for PM_{2.5} from different vehicles.

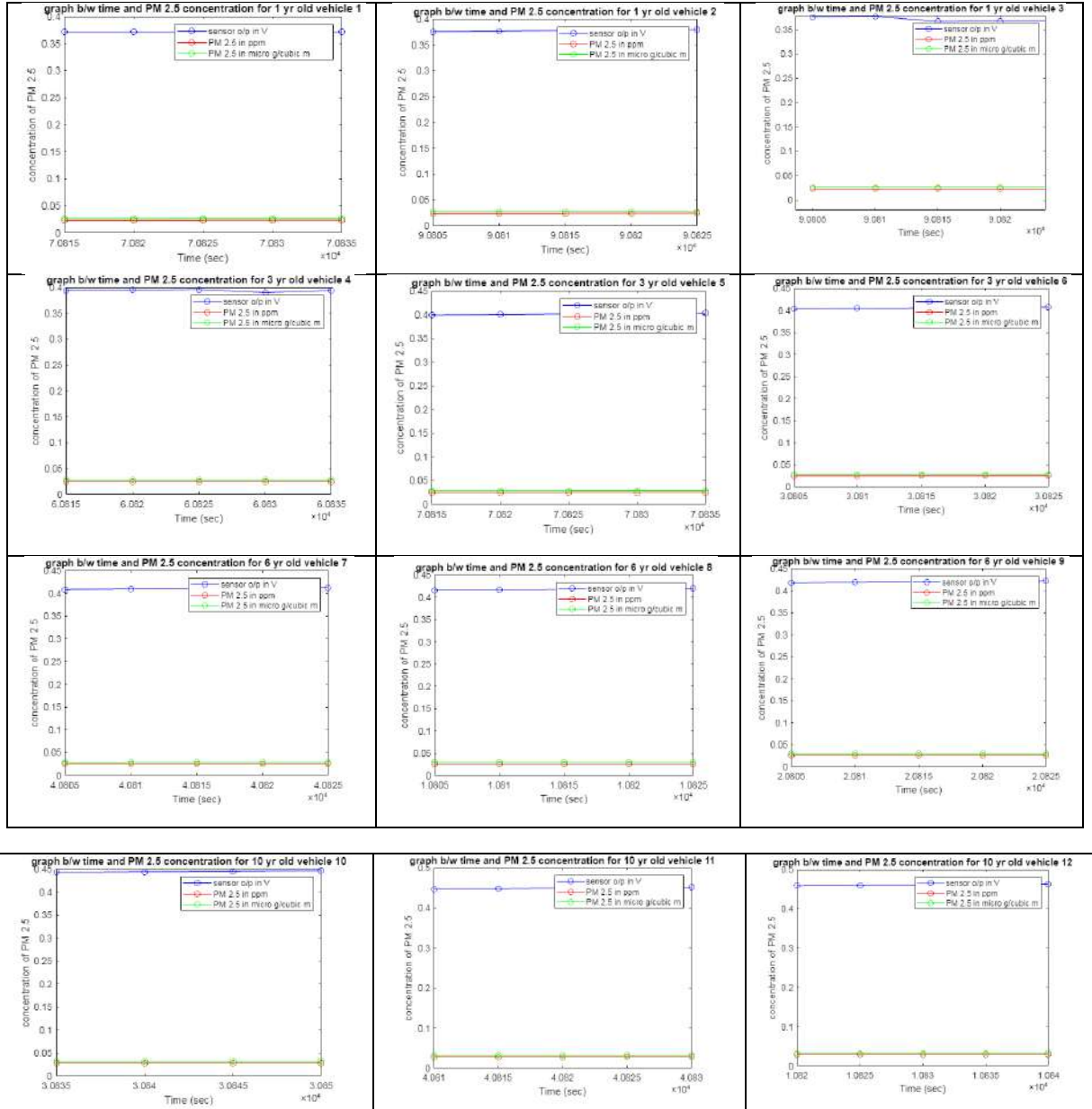


Fig 8: Measurement of PM_{2.5} from different vehicles.

difference between the emitted $PM_{2.5}$ concentration values of this category of chosen vehicles was very small, and a significant difference was observed between the second case category of vehicles and the third case category of vehicles due to the different vehicle conditions between case-2 and case-3. In the fourth case of $PM_{2.5}$ measurements, three different 10-years old vehicles were chosen for the test. The result was observed that the variation in $PM_{2.5}$ in ppm varies from 0.0277 ppm to 0.0287 ppm. The $PM_{2.5}$ concentration in $mg.m^{-3}$ varies from 0.0317 $mg.m^{-3}$ to 0.0328 $mg.m^{-3}$ and the corresponding output voltage varies from 0.443 mV to 0.459 mV. From the measurement, considerable variation exists between those two cases (Table 3).

Environmental Parameter Measurement

In this proposed system, measurement of CO, CO₂, and $PM_{2.5}$ using different gas sensors was done and the sensor outputs were transmitted using node MCU, and the same module was used for live data monitoring. The analog values

received from the sensors were processed by the controller via a Wi-Fi connection to the Internet. Once the values were obtained from the sensors, they were converted to various units of gas concentrations such as ppm, $mg.m^{-3}$, and sensor output in mV, which the user could monitor via their mobile phone. The air quality data such as CO, CO₂, and $PM_{2.5}$ were sensed by the sensors interfaced with the controller board and those were transmitted to the user's mobile phone. The user could monitor the live air quality data from their working place. As a result, the suggested air quality monitoring system's main feature is its low cost. The main goal of IoT was to have the values of real-time data updated to the user at any given time via the cloud.

The proposed system was used for real-time air pollution monitoring after completion of the various emitted gas measurement from the vehicles. Fig. 9, shows the live data for CO, CO₂, and $PM_{2.5}$ in ppm. Fig. 10, shows the live data for CO, CO₂, and $PM_{2.5}$ in $mg.m^{-3}$, and Fig. 11, shows the live data for CO, CO₂, and $PM_{2.5}$ in ppm. These pollutant

Table: 3 measured $PM_{2.5}$ values from different vehicles.

Vehicle	Vehicle Period	Sensor output (mV)	Concentration of $PM_{2.5}$ (ppm)	Gas concentration ($mg.m^{-3}$)
Vehicle-1	1 year old	0.371	0.0232	0.0265
Vehicle-2		0.376	0.0235	0.0269
Vehicle-3		0.367	0.0229	0.0262
Vehicle-4	3 years old	0.394	0.0246	0.0281
Vehicle-5		0.399	0.0249	0.0286
Vehicle-6		0.403	0.0252	0.0288
Vehicle-7	6 years old	0.408	0.0254	0.0292
Vehicle-8		0.415	0.0259	0.0297
Vehicle-9		0.418	0.0261	0.0299
Vehicle-10	10 years old	0.443	0.0277	0.0317
Vehicle-11		0.447	0.0279	0.0320
Vehicle-12		0.459	0.0287	0.0328

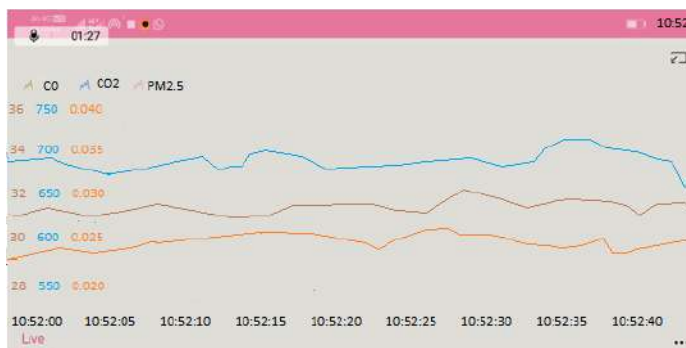


Fig. 9: Live data for CO, CO₂, $PM_{2.5}$ in ppm from node MCU.

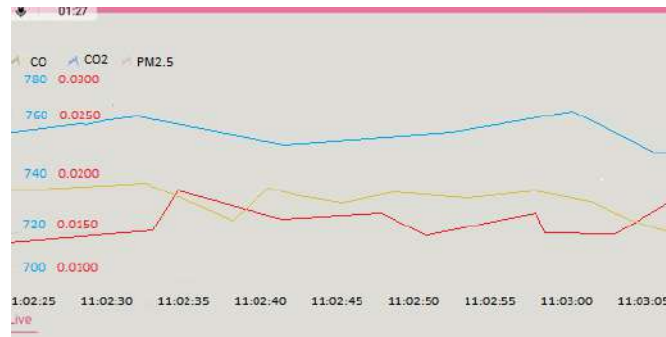


Fig. 10: Live data for CO, CO₂, PM_{2.5} in mg.m⁻³ from node MCU.

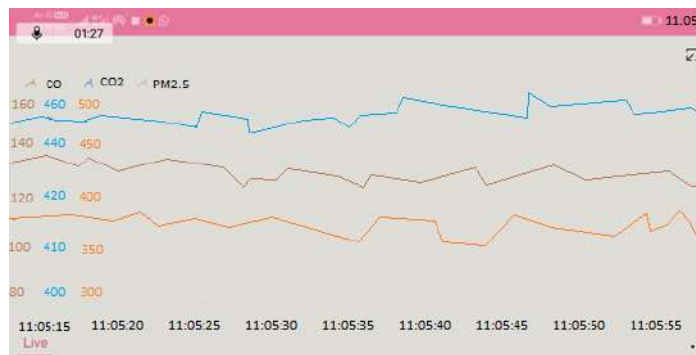


Fig. 11: Live data for CO, CO₂, PM_{2.5} in mV from node MCU.

measurements were obtained from the proposed system and this system was more suitable for an unmanned aerial vehicle (UAV) for the measurement of various hazardous gasses present in the different altitudes of the environment.

CONCLUSION

The proposed system is integrated with various environmental parameter measuring sensors, controller, and node MCU modules for the transmission of data to the user. Further, this system can be utilized for the measurement of hazardous gases present in the various altitude of the environment using unmanned aerial vehicles (UAV). The cost of installing the system is low, and it has a high sensitivity for measuring various ambient gases in both the interior and outdoor environments. An aspect of IoT applications is the ability to monitor environmental pollutants using smartphones. It is very convenient for the user to monitor the pollutant gases present at various altitudes from the control station whenever the system is used with an unmanned aerial vehicle. By deploying our system in various locations, we can quickly obtain measurements of various gases present in the environment, which can then be updated on the cloud. Environmental

parameters were also collected by the system, which was then stored in the cloud and analyzed to determine air quality in both urban and rural areas. This aids in determining and analyzing the principal cause of health-related difficulties caused by various levels of pollutants in the air, so that appropriate precautionary actions can be taken to overcome and reduce air pollution.

REFERENCES

- Alvear, O., Zema, N.R. and Natalizio, E.2017. Using UAV-based systems to monitor air pollution in areas with poor accessibility. *J. Adv. Transp.*, 16: 14.
- Anil Kumar, U., Keerthi, G., Sumalatha, M. and Sushma, R. 2017. Iot based noise and air pollution monitoring system Using Raspberry Pi. *Int. J. Adv. Technol. Eng. Sci.*, 5(3): 183-187.
- Balasubramanian, C. and Manivannan, D. 2016. IoT enabled air quality monitoring system (AQMS) using raspberry Pi. *Indian J. Sci. Technol.*, 9(39): 63-79.
- Dinh, T.V., Son, Y.S., Chung, S.G., Lee, J.H. and Kim, J.C. 2014. Removal of particulate matter emitted from a subway tunnel using magnetic filters. *Environ. Sci. Technol.*, 48(5): 2870-2876.
- Nayak, R., Panigrahy, M.R., Rai, V.K. and Rao, T.A. 2017. IoT based air pollution monitoring system. *Imp. J. Interdiscip. Res.*, 3(4): 111-121.
- Okokpuije, K.O., Orimogunje, A., Noma-Osaghae, E. and Alashiri, O. 2017. An intelligent online diagnostic system with epidemic alert. *Int. J. Innov. Sci. Res. Technol.*, 2: 327-331.

- Rukmani, P., Teja, G.K. and Vinay, M.S. 2018. Industrial monitoring using image processing IoT and analyzing the sensor values using big data *Procedia Comp. Sci.*, 133: 991-997.
- Saha, D., Shinde, M. and Thadeshwar, S. 2017. Iot-based air quality monitoring system using wireless sensors deployed in public bus services. ICC '17: Proceedings of the Second International Conference on Internet of things, Data and Cloud Computing, Cambridge, UK, 22-23 March 2017, Association for Computing Machinery. New York, United States, pp. 1-6
- Sammarco, M., Tse, R., Pau, G. and Marfia, G. 2017. Using geosocial search for urban air pollution monitoring. *Pervasive Mobile Comp.*, 35: 414-426.
- Shitole, P.V. and Markande, S.D. 2016. Review: Air quality monitoring system. *Int. J. Adv. Res. Comp. Commun. Eng.*, 5(6): 56-73.
- Sirsikar, S. and Karemore, P. 2015. Review paper on air pollution monitoring system. *Int. J. Adv. Res. Comp. Commun. Eng.*, 4(1): 218-220
- Vinoth Kumar, V., Ramasamy, R., Janarthanan, S. and VasimBabu, M. 2017. Implementation of IoT in smart irrigation system using Arduino processor. *Int. J. Civil Eng. Tech.*, 61: 1304-1314.
- Wei-Ying, Y., Leung, K.S., Leung, Y., Meng, M.L. and Terrence, M. 2016. The modular sensor system (MSS) for urban air pollution monitoring. *Sensors*, 18(1): 7. DOI:10.3390/s18010007.
- Xiaojun, C., Xianpeng, L. and Peng, X. 2015. IOT-based air pollution monitoring and forecasting system. 2015 International Conference Computer and Computational Sciences (ICCCS) at IEEE, India, 27-29 January, IEEE, Piscataway, NJ, pp. 257-260.



Initial Active Phase of In-Vessel Composting of Sewage Sludge, Leaves and Rice Straw

Xiaojie Sun*(**), Zhihan Tan*(**), Xiaosong He***, Hongxia Zhang*(**), Beidou Xi*(***), Hongtao Zhou* and Hong Xiang Zhu****

*Guangxi Key Laboratory of Environmental Pollution Control Theory and Technology, Guilin University of Technology, Guilin 541004, China

**Guangxi Collaborative Innovation Center for Water Pollution Control and Water Safety in Karst Area, Guilin University of Technology, Guilin 541004, China

***State Key Laboratory of Environmental Criteria and Risk Assessment, Chinese Research Academy of Environmental Sciences, Beijing 100012, China

****College of Light Industry and Food Engineering, Guangxi University, Nanning, 530004, China

†Corresponding authors: Hongxia Zhang: zhx75@glut.edu.cn

Nat. Env. & Poll. Tech.
Website: www.neptjournal.com

Received: 05-03-2021

Revised: 26-05-2021

Accepted: 06-06-2021

Key Words:

Aerobic composting
Leaves
Rice straw
Sewage sludge

ABSTRACT

This work studied the characteristics of leaf, rice straw, and sewage sludge (SS) co-composting with the aim of determining the best composting ratio by monitoring temperature changes, oxygen (O₂) concentration, carbon dioxide (CO₂) concentration, ammonia (NH₃) concentration, hydrogen sulfide (H₂S) concentration, pH, electrical conductivity (EC), heavy metal content, carbon-nitrogen ratio (C/N ratio), germination index (GI), moisture content (MC), and volatile solids (VS) content during the composting process. Three composting piles with the mixture ratios of 4:1:1 (Pile A), 5:1:1 (Pile B), and 6:1:1 (Pile C) (SS: leaf: rice straw) were tested. According to the temperature, C/N ratio, germination index, MC, and VS, the level of compost maturity in Pile B with a 5:1:1 mixing ratio was higher than that in Piles A and C. The contents of heavy metals in the composts were shown to meet the grade A standard in C/J/T 309-2009 (2009), except Cu and Zn, which was within the grade B standard.

INTRODUCTION

With the development of urban landscaping and agriculture, green waste (garden waste and agricultural waste) production has increased in China. The annual amount of garden waste reached approximately 2.0×10^7 tons in China. Generally, green waste is incinerated or deposited in landfills in China (Zhang & Sun 2014). The average annual agricultural residue yield reached 5.2×10^8 tons during 2002-2011, approximately 19% of which was burned openly (Yang et al. 2015). Given the rapid increase of urban populations, SS has also continuously increased in the past twenty years. The annual amount of SS reached approximately 30,000,000 tons (Dai 2012). SS is mainly treated for landfills (30%) and agricultural use (45%) in China (Su et al. 2010). However, these treatments of SS have caused significant environmental perturbations, such as water and air and soil pollution (Dennehy et al. 2017). Therefore, it is critical to develop strategies to effectively recycle the wastes and alleviate environmental pollution meanwhile (Lu et al. 2009)

Green waste products are rich in fiber, protein, fat, and trace elements such as calcium (Ca), iron (Fe), copper (Cu), zinc (Zn), cobalt (Co), phosphorus (P), and manganese (Mn), among others. Previous research has shown that green waste composting can improve soil fertility and soil physical properties, maintain soil moisture levels, and prevent soil erosion (Tong et al. 2018). SS contains many soil nutrients such as organic matter (OM), nitrogen (N), phosphorus (P) and other micronutrients. However, using SS without prior stabilization has potentially negative effects on the remediation of degraded soils because they may contain phytotoxic or pathogenic substances, which have a highly unstable nature. One of the efficient techniques for treating and reusing organic waste is composting (Jayanta et al. 2021). The ratio of materials in the mixture is one of the key factors during composting. However, past research hasn't yielded a clear optimal ratio since the materials and composting circumstances differed. Banegas et al. (2007) recommended a 1:3 ratio (sludge: sawdust), based on the dilution effect caused by anaerobic sludge. Zubillaga & Lavado (2003) reported that the compost was not affected by the sawdust ratio. Lu

et al. (2009) recommended a 3:1:1 (v:v:v) mixture ratio of municipal solid waste: SS: mature compost in an in-vessel composting.

The aim of the present study is to examine the effects of the ratio of feedstock (i.e., leaf, rice straw, and SS) on the characteristics of the co-composting process and to obtain an optimum composting ratio based on the changes in temperature, O₂ concentration, CO₂ concentration, NH₃ concentration, H₂S concentration, pH, EC, heavy metal content, C/N ratio, GI, MC, and VS content during the composting process.

MATERIALS AND METHODS

Composting Materials

The dewatered SS with an MC of approximately 86.3% was obtained from the Qilidian Sewage Treatment Plant in Guilin City. The leaves (approximately 3.8% in MC) were collected from the Yanshan Botanical Garden in Guilin, whereas the rice straw (approximately 0.7% in MC) was collected from a rice farm in the Guilin Suburb. We chose leaves with sizes less than 100 mm and the whole leaves were used without cutting or grinding. A 9CFZ-40 feed grinder was used to cut the rice straw into small pieces of less than 40 mm. Table 1 shows the properties of the composting raw materials.

Experimental Set-up

The control technology for a bio-composting (CTB) system with intelligent real-time monitoring was used in this study. The system included three subsystems: three composting bioreactors, a real-time monitoring system, and the intelligent control system, as shown in Fig. 1. Each reactor was 1.3 m tall with a diameter of 0.8 m, and the effective volume was 250 L. The reactors had a double-cylinder structure and a

polyethylene material was wrapped in an insulating layer. The monitoring system monitored composting parameters in the reactor in real-time and provided automatic feedback for controlling during the composting process. This system had a reaction chamber, a pump, gas flow meters, temperature probes, a CO₂ monitor, an H₂S monitor, an NH₃ monitor, an O₂ monitor and a control cabinet. Two groups of temperature probes were linked to the control cabinet and placed at a distance of 0.0 and 0.2 m from the composting reactor's cylindrical centerline. Each group of temperature probes was mounted 0.15, 0.3, 0.6, and 1.2 m above the bottom of the reactor to monitor the pile body temperatures at 1-min intervals. Each reactor installed four O₂ probes for monitoring the O₂ concentrations, which were mounted 0.2 m away from the cylindrical centerline of the composting reactor and 0.15, 0.3, 0.6, and 1.2 m above the bottom of the reactor. The CO₂, NH₃, and H₂S probes were connected to the exhaust collection tube to determine the CO₂, NH₃, H₂S concentrations. Temperature, as well as O₂, CO₂, NH₃, and H₂S concentrations, were recorded in the three reactors using the CTB automated control system and software (Compsort 2.0; ZKBL Co., Ltd., China). The composting lasted for 300 h in this study.

Composting Methods

In this study, rice straw and leaves were cut into small pieces of less than 100 mm by a 9CFZ-40 feed grinder. The leaves and rice straw were mixed with SS by hand, using three mixing ratios, namely, Pile A, B, and C (4:1:1, 5:1:1, and 6:1:1, respectively; SS: leaf: rice straw, w:w:w). Table 2 shows the designs of the composting experiments and the main characteristics of the composting materials. The aeration rate was designed based on the pile's temperature during different composting stages (Table 3).

Sample Analysis

The solid and gas samples were analyzed during the composting process. The heavy metal content was determined by inductively coupled plasma emission spectrometry (IRIS Intrepid II XSP, Thermo Elemental Corporation, Franklin,

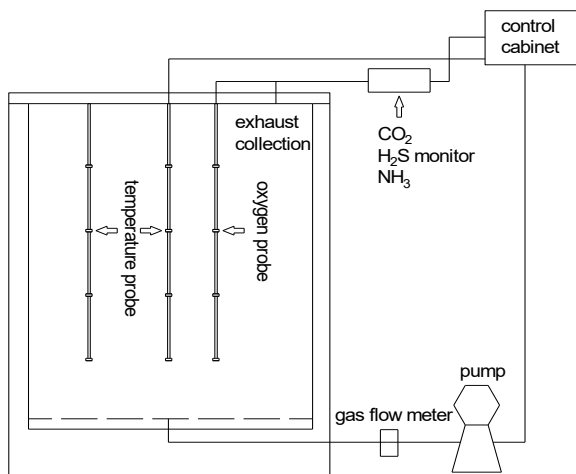


Fig. 1: Schematic of laboratory-scale composting device.

Table 1: The initial properties of raw materials.

Parameter	Sewage sludge	Leaf	Rice straw
Moisture content (%)	86.3 ± 1.7	7.9 ± 0.4	8.1 ± 0.26
Organic carbon (%)	46.56 ± 0.20	39.03 ± 0.38	39.49 ± 0.54
Total nitrogen (%)	4.80 ± 0.02	1.30 ± 0.01	1.06 ± 0.06
C/N Ratio	9.7 ± 0.07	30.1 ± 0.13	37.22 ± 2.3
TP (%)	1.09 ± 0.07	0.094 ± 0.018	0.08 ± 0.01
K (%)	0.61 ± 0.07	2.42 ± 0.66	2.22 ± 0.11
GI (%)	1.6 ± 0.5	60.1 ± 3.2	62.3 ± 4.7

Note: Reported values are mean ± STDEV of the three repeats

MA, USA). The GI was determined by the germination test (Sun et al. 2012a). The MC was analyzed by the weight loss after the sample was oven-dried at 105°C for 24 h. The VS content was determined by the additional weight loss after the sample was dried at 550°C for 4 h in a muffle furnace based on previously oven-dried weight. Other analytical methods involved in the protocol are shown in Table 4. The data was analyzed using SPSS 14.0 software. The differential analysis was used with the paired-sample *t*-test, and the bivariate correlation analysis was performed to analyze the relationship between the indexes.

RESULTS AND DISCUSSION

Changes in Temperature

The temperatures of the three composting piles of leaves, rice straw, and SS are shown in Fig. 2. The time-temperature curves at the central axis and edge of the bottom, lower-middle, middle, and surface layers in each reactor were different. The temperatures at the central axis of the reactor were higher than those at the edge. The temperatures at the lower-middle and bottom layers were higher than those at the middle and surface layers. The peak temperature reached 64.2, 62.2, and 65.9°C after 79, 78, and 46 h at the lower-middle layer in Piles A, B, and C respectively, while the peak temperature reached 59.2, 62.2, and 57.8°C after 71, 77, and 98 h at the bottom layer in Piles A, B, and C, respectively.

To meet the relevant composting requirements, the temperature needs to be maintained at above 55°C for at

least 72 h or above 50-55°C for at least 120-168 h to kill pathogens (Chang et al. 2017, GB7959-2012 2012). Table 5 gives the highest temperature and the length of time each pile was over 50°C in both horizontal and vertical directions. In Pile A, the temperature at the central axis of the lower middle layer met the regulatory requirement for composting temperature, whereas, in Pile B and C, the temperatures at the center axis of the lower middle and bottom layers met the regulatory requirement. For Piles A, B, and C, the total time when the temperature was over 50°C was 240, 421, and 314 h, respectively. The temperature variations during the composting process indicated that the 5:1:1 ratio (SS: leaf: rice straw) gave the best performance in terms of maintaining a high temperature.

Changes in O₂ and CO₂ Concentrations

The changes in the O₂ consumption and CO₂ concentration are shown in Fig. 3. The O₂ consumption and CO₂ concentration increased as the temperature increased and they decreased as the temperature decreased. The lowest O₂ concentration was recorded at 72, 73, and 43 h in Piles A, B, and C, respectively, which was consistent with the appearance of the temperature peak (Fig. 2). The O₂ concentration was significantly different at the surface, middle, lower-middle, and bottom layers of the three piles. For the lower-middle layer, the O₂ concentration was not significantly different in Piles A and B ($P=0.562q$) but was significantly higher than that in Pile C ($P<0.01$). At the middle and surface layers, the O₂ concentration in Pile B was apparently lower than that

Table 2: Designs of the composting experiments.

Piles	Weight ratio	Quality [kg]	Volume [m ³]	MC [%]	VS [%]
Pile A	4:1:1	46.2	0.245	63.7	82.23
Pile B	5:1:1	56.0	0.248	69.5	81.45
Pile C	6:1:1	60.0	0.250	73.0	80.20

Table 3: Designs of the aeration rate.

	The aeration rate [L.min ⁻¹]		
	mesophilic phase	thermophilic phase	cooling phase
Pile A	6	4	6
Pile B	7	5	7
Pile C	8	6	8

Table 4: The main analytical project and methods.

Analysis items	Analytical methods and instruments	Instrument types
O ₂	oxygen on-line monitor	I/-01, Shenzhen, China
NH ₃	ammonia on-line monitor	MR-100/1000, Membrapor, Switzerland SwitzerlandChina
H ₂ S	hydrogen sulfide on-line monitor	M-100/500, Membrapor, Switzerland
CO ₂	carbon dioxide on-line monitor	GM220, VAISALA, Finland
Temperature	temperature probe	PT100, Shenzhen, China
pH	portable pH meter	pH330, WTW, Germany
EC	conductivity meter	M280536, Beijing, China

in Piles A and C ($P < 0.01$). The trend indicates that the O_2 utilization in Pile B was higher than that in other piles. Based on the examination of testing data for each pile, a substantial negative correlation ($r^2 > 0.83$, $P < 0.01$) was discovered between CO_2 and O_2 concentrations.

Changes in NH_3 Concentration

The changes in NH_3 concentration over time are shown in Fig. 4. The NH_3 concentration in Pile C was higher than that in Piles A and B ($P < 0.01$). NH_3 was detected at approximately 90, 40, and 20 h in Piles A, B, and C, respectively. Then the NH_3 concentration increased and reached the peak values of 19, 66, and 84 ppm in Piles A, B, and C at 164, 190, and 186 h, respectively. Therefore, controlling NH_3 emission at 160-190 h was important for odor minimization.

After 190 h, the NH_3 emissions decreased quickly in all the piles and reached almost 0 ppm in Pile A at the end of composting. In Pile B, the NH_3 emissions fluctuated between 20-30 ppm after 220 h until the end of composting. However, the NH_3 concentration in Pile C continued to increase after 225 h and reached 60 ppm at the end of composting. This trend may be due to localized anaerobic conditions caused by the higher SS ratio in Pile C. The anaerobic bacteria might use CO_2 as a carbon source and produce more NH_3 . This hypothesis could be confirmed by the changes in CO_2 concentration (Fig. 3). The CO_2 concentration of the exhaust gas in Pile C was lower than that in Piles A and B. As a result, effective measures to avoid and regulate NH_3 contamination during composting with a high sludge ratio should be adopted. Some additives including exogenous microbes such as

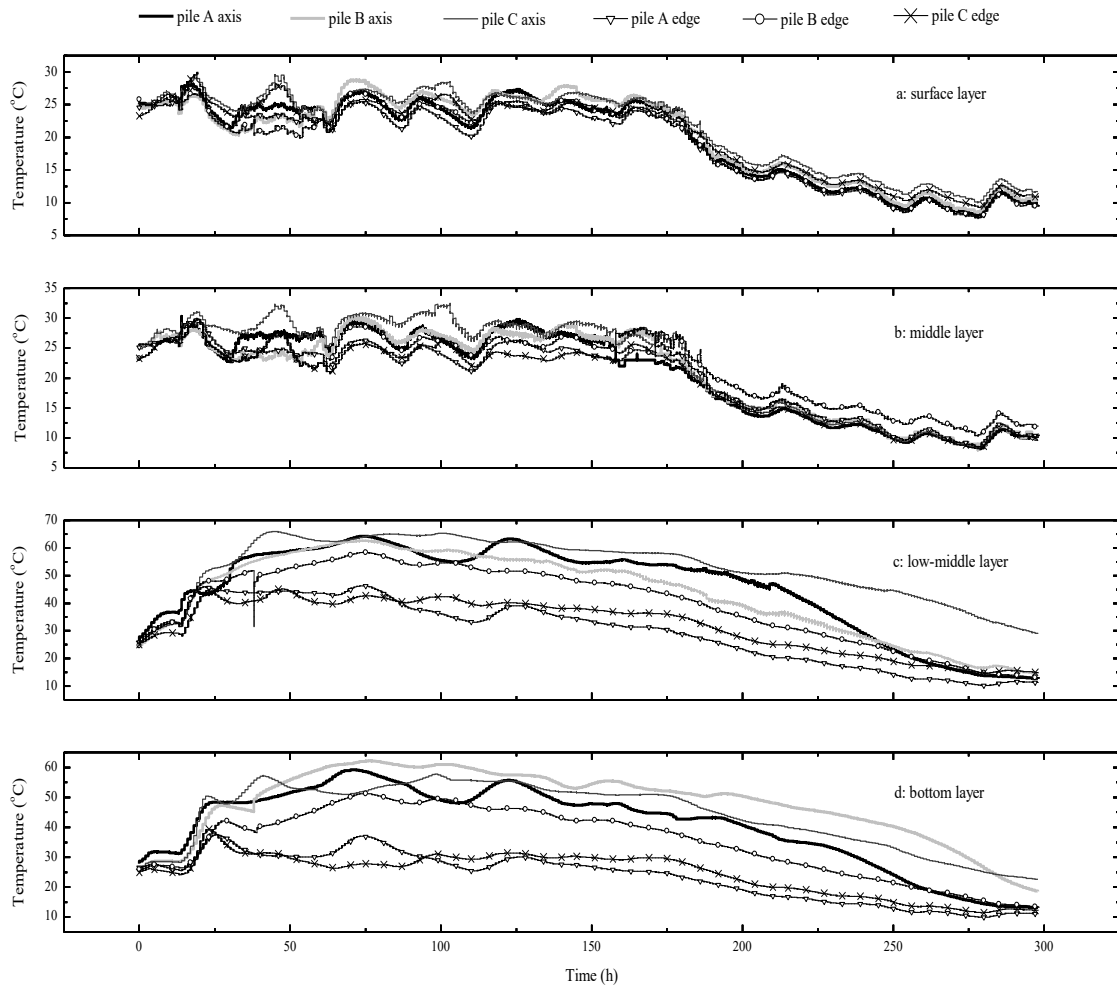


Fig. 2: Changes of temperature in vertical and horizontal gradient in the piles.

Table 5: The highest temperature and the duration of temperature above 50 °C in a horizontal and vertical gradient of each pile.

Horizontal gradient	Vertical gradient	Pile A	Pile B	Pile C
axis	Surface layer	$\frac{0}{28.4}$	$\frac{0}{28.8}$	$\frac{0}{29.6}$
		$\frac{0}{30.3}$	$\frac{0}{30.3}$	$\frac{0}{32.5}$
	Low-middle layer	$\frac{148}{64.2}$	$\frac{138}{62.7}$	$\frac{158}{65.9}$
		Bottom layer	$\frac{92}{59.2}$	$\frac{164}{62.2}$
edge	Surface layer		$\frac{0}{27.7}$	$\frac{0}{26.9}$
		Middle layer	$\frac{0}{29.5}$	$\frac{0}{30}$
	Low-middle layer		$\frac{0}{46.4}$	$\frac{106}{58.3}$
		Bottom layer	$\frac{0}{37.6}$	$\frac{13}{51.3}$

Note: Numerator means the duration of temperature above 50°C (h), denominator means the highest temperature (°C)

cellulose-degrading bacteria, Azotobacter, the absorbent such as clay and zeolite, and metallic salt such as calcium salt and magnesium salts, could be used to reduce nitrogen loss during the composting.

Changes in H₂S Concentration

A similar H₂S emission profile was found in the three piles (Fig. 5). H₂S emissions were first discovered 10 h after the commencement of composting and quickly rose to 45 ppm at 18 h for Pile A, 63 ppm at 15 h for Pile B, and 63ppm at 20 ho for Pile C. The H₂S emission decreased quickly afterward and approached zero after 80h in the three piles. Within this, the H₂S emission in the three piles decreased fast and reached zero after 80 h As a result, H₂S emissions were concentrated between 10 and 20 h following the start of composting, with the highest levels of H₂S emissions occurring between 15 and 20 h. The findings showed that controlling H₂S emissions before 80 h was critical for odor reduction. Li et al. (2008) reported that H₂S maintained a high level in the first 4 days, especially after 1 and 2 days of the experiment.

The results of the H₂S emission showed no significant difference between Piles A and B ($P = 0.402$), and between Piles B and C ($P=0.086$). However, a significant difference was observed between Piles A and C ($P=0.042$). The results also suggest a good correlation between H₂S production and the amount of SS in three piles. The H₂S emissions increased as the sludge content increased in the three piles.

Changes in pH and EC Values

The pH and EC values are presented in Table 6. Overall, the final pH values of compost products of the three piles were higher than the initial pH values, which might be due to the ammonization of organic nitrogen by microbes. The pH values in the surface and middle layers were higher than those in the bottom layer. The difference in pH value in different layers might be caused by the volatilization of ammonium in the nitrification process. The pH values of compost products met the allowed range of 6.5-8.5 for land use (GB8172-87 1987).

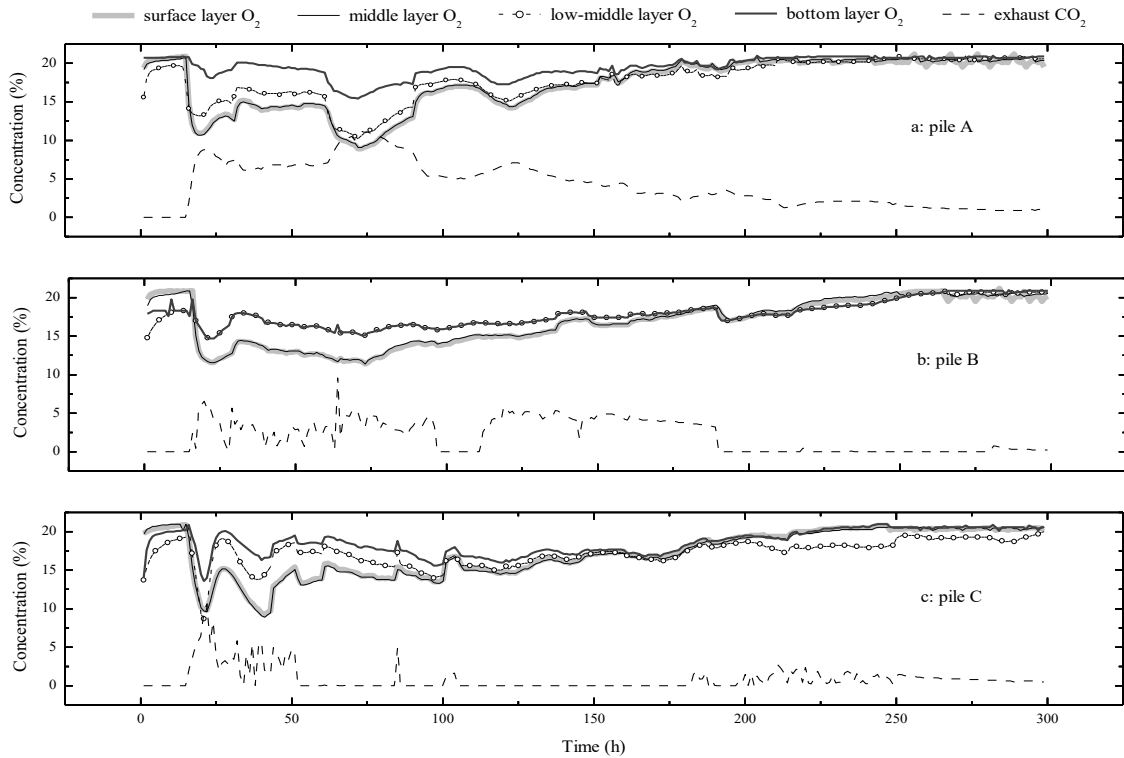


Fig. 3: Changes in oxygen and carbon dioxide concentrations.

The changes in EC values indicated the possible phytotoxicity or phyto-inhibitory effects (Zhang & He 2006). As shown in Table 6, the compost products at the middle and bottom layers recorded higher EC values than other layers. At the middle and bottom layers, microorganisms were more intensely activated so that more biodegradable organics were decomposed into inorganic salt, which might explain the difference in different layers. The EC values of the compost samples in this study were notably within the Greek standard (e.g., the upper limit is $4.0 \text{ mS}\cdot\text{cm}^{-1}$) (Lasaridi et al. 2006). Therefore, the compost products were possibly suitable for land application with proper usage provisions.

Changes in Heavy Metal Concentrations

The heavy metals contents are inclined to increase in the compost product; thus, evaluation of heavy metal content is essential. Table 7 shows the control standards about heavy metals (GB4284-84 1984, CJ/T 309-2009 2009). The contents of heavy metals As, Cd, Cr, Cu, Ni, Pb, and Zn in the end products are listed in Table 8. The heavy metals Zn and Cu exceeded the limits in GB4284-84 (1984), but they were within the B grade standard in CJ/T 309-2009 (2009). Other heavy metal contents in the end products were under the A grade standard in CJ/T 309-2009 (2009). However, metal accumulation should be given sufficient attention

when the compost products are repeatedly applied to the soil (Ko et al. 2008).

Changes in Other Chemical and Maturity Parameters

The chemical and maturity parameters before and after composting are shown in Table 9. The C/N ratio of the composting raw materials was approximately 6-8, which declined to 3-5 in the end products (Table 9). Generally, a final C/N ratio of 20 or below indicates the maturity of the compost with an initial C/N ratio of 25-30. However, the C/N ratio observed in this study did not sufficiently indicate the maturity of the compost because the initial C/N ratio (6 - 8) was not in the range of the initial C/N ratio in the general rule. Another maturity parameter $T = (C/N)_{\text{final}} / (C/N)_{\text{initial}}$ was proposed by Morel et al. (1985), and compost products were considered as mature when the parameter $T \leq 0.6$. Similarly, Sun et al. (2012b) stated that the compost became mature when T was approximately 0.7. In the present study, T was approximately 0.63, 0.51, and 0.57 in Piles A, B, and C, respectively. Therefore, the compost products reached complete maturity. The compost of Pile B was more mature than that of Piles A and C.

The GI can assess the toxicity and maturity level of compost products. A GI of 50% was used to indicate that the

Table 6: Changes of pH and EC during composting.

	pH			EC[mS.cm ⁻¹]		
	Pile A	Pile B	Pile C	Pile A	Pile B	Pile C
Raw material	7.91	7.53	8.21	1.69	1.15	1.71
Product surface layer	8.21	8.44	8.47	1.37	1.34	1.23
Product middle layer	8.3	8.17	8.2	2.44	2.41	2.56
Product bottom layer	8.17	8.23	8.03	2.43	2.46	2.45

Table 7: Control standards for heavy metal content for agricultural use [mg.kg⁻¹].

Control standards		As	Cd	Cr	Cu	Ni	Pb	Zn
GB4284-84	pH<6.5	75	5	600	250	100	300	500
	pH≥6.5	75	20	1000	500	200	1000	1000
CJ/T309-2009	A Grade	30	3	500	500	100	300	1500
	B Grade	75	15	1000	1500	200	1000	3000

compost was phytotoxin-free (Wong et al. 2001). The GI values of end products in three piles increased significantly and reached 47.5%-70.1%. Therefore, the compost in Piles A and B were sufficiently stable at 300 h.

The MC of compost significantly decreased in the three piles. The MC of end products in piles A and B was within the acceptable limit of 20-35% (CJJT52-93 1993). The largest decrease in MC was found in Pile B, which was 36.7%.

The VS decreased during the composting process for all the piles. Similar results were observed in Wong (2001) and Zhou et al. (2014). Among the three piles, Pile B with a 5:1:1 mixture ratio had the highest loss of VS content (14.37%).

CONCLUSION

The co-composting of SS with leaves and rice straw was realized at the mixture ratios of 4:1:1 (Pile A), 5:1:1 (Pile B), and 6:1:1 (Pile C). A ratio of 5:1:1 was found to be the optimum ratio for maintaining the highest temperature. A significant negative correlation was observed between CO₂ and O₂ concentrations. The O₂ utilization in Pile B was higher than that in other piles. The NH₃ and H₂S emissions significantly increased as the ratio of sludge increased. Therefore, special attention should be given to controlling NH₃ pollution caused by composts with a high sludge ratio. Higher EC values were observed in the middle and bottom layers than the top layers in the composting products, but

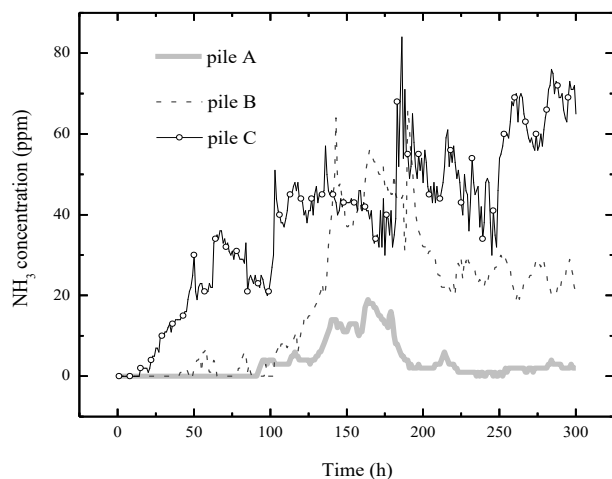


Fig. 4: Changes in ammonia concentrations during the composting.

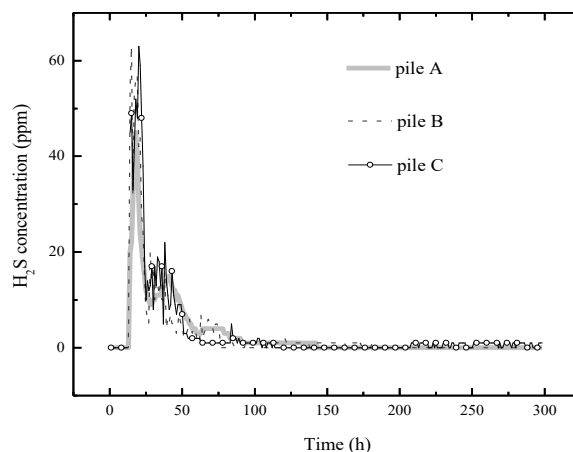


Fig. 5: Changes in hydrogen sulfide concentrations during the composting.

Table 8: Changes in the amount of heavy metals before and after composting [mg.kg⁻¹].

Piles	Time(h)	As	Cd	Cr	Cu	Ni	Pb	Zn
Pile A	0	15.8	0.7	85.8	560.2	45.2	22.5	472.5
	300	15.2	0.9	102.7	653.4	47.5	27.4	523.7
Pile B	0	16.2	0.5	91.0	584.7	43.7	25.6	511.4
	300	18.4	0.8	112.5	705.3	47.8	21.9	463.2
Pile C	0	17.5	0.7	110.4	642.5	55.4	24.3	526.1
	300	20.1	1.1	93.6	589.6	44.6	22.7	447.3

they did not exceed the tolerance level for plants of medium sensitivity according to the Greek standard. The pH values in the surface and middle layer were higher than those in the bottom layer, and the pH of the composting products was within the accepted range of 6.5-8.5 for land use. While the Cu and Zn concentrations were within the grade B standard, other heavy metal contents in all the compost products were shown to meet the grade A standard in CJ/T 309-2009 (2009). According to the C/N ratio, GI, MC, and VS, Pile B with a 5:1:1 mixing ratio were more mature than Piles A and C.

ACKNOWLEDGMENTS

This work was financially supported by the Natural Science Foundation of Guangxi (No. 2018GXNSFGA281001), the Science and Technology Major Project of Guangxi (GuiKeAA18118013), the Guangxi Science and Technology Planning Project (No. GuiKe-AD18126018), and Guangxi 'Bagui Scholar' Construction Project.

REFERENCES

- Banegas, V., Moreno, J.L., Moreno, J.I., García, C., León, G. and Hernández, T. 2007. Composting anaerobic and aerobic sewage sludges using two proportions of sawdust. *Waste Manag.*, 27: 1317-1327.
- Chang, H.Q., Zheng C.J., Zhang, J.Y. and Deng Q. 2017. Effects of different environmental temperatures on dewatered sludge composting. *J. Ecol. Environ.*, 26(10): 1755-1760.
- CJ/T 309-2009. 2009. Disposal of Sludge from Municipal Wastewater Treatment Plant - Control Standards for Agricultural Use. Ministry of Housing and Urban-Rural Development of the People's Republic of China.
- CJJT52-93. 1993. Technical Regulations for the Aerobic Static Composting of Municipal Solid Waste. Industry-Standard of the People's Republic of China.
- Dai X. 2012. Comparison of Sludge disposal techniques at home and abroad. *Water Ind. Mkt.*, 4: 15-17.
- Dennehy, C., Lawlor, P.G., Jiang, Y., Gardiner, G.E., Xie, S., Nghiem, L.D. and Zhan, X. 2017. Greenhouse gas emissions from different pig manure management techniques: A critical analysis. *Front. Environ. Sci. Eng.*, 11: 11-16.
- GB4284-84. 1984. Control Standards for Pollutants in Sludge from Agricultural Use. Ministry Of Urban and Rural Construction and Environmental Protection, Beijing, China.
- GB7959-2012. 2012. Sanitary Standard of No-Hazardous Treatment of Night Soil. Ministry of Health, Beijing, China.

Table 9: The changes of other chemical and maturity parameters before and after composting.

Parameter	Time [h]	Pile A	Pile B	Pile C
C/N	0	7.67	7.31	5.94
	300	4.86	3.73	3.38
GI [%]	0	33.5	30.2	25.4
	300	70.1	70.0	47.5
MC [%]	0	63.8	69.5	73.1
	300	28.7	32.8	41.7
VS [%]	0	82.2	81.17	80.2
	300	70.9	66.8	74.3

- GB8172-87. 1987. Control Standards for Urban Wastes for Agricultural Use. State Bureau of Environmental Protection, The People's Republic of China, Beijing, China.
- Jayanta, A., Shailendra, Y. and Atya, K. 2021. Challenges and control strategies of odor emission from composting operation. *Appl. Biochem. Biotechnol.*, 12: 490-499. <https://doi.org/10.1007/s12010-021-03490-3>.
- Ko, H.J., Kim, K.Y., Kim, H.T., Kim, C.N. and Umeda, M. 2008. Evaluation of maturity parameters and heavy metal contents in composts made from animal manure. *Waste Manag.*, 28: 813-820.
- Lasaridi, K., Protoukaki, I., Kotsou, M., Pilidis, G., Manios, T. and Kyriacou, A. 2006. Quality assessment of composts in the Greek market: the need for standards and quality assurance. *J. Environ. Manag.*, 80: 58-65.
- Li X.J., Zhang R.H. and Pang Y.Z. 2008. Characteristics of dairy manure composting with rice straw. *Bioresour. Technol.*, 99: 359-367.
- Lu, Y., Wu, X. and Guo, J. 2009. Characteristics of municipal solid waste and sewage sludge co-composting. *Waste Manag.*, 29: 1152-1157.
- Morel, J.L., Colin, F., Germon, J.C., Godin, P. and Juste, C. 1985. Methods for the evaluation of the maturity of municipal refuse compost. In: Gasser, J.K.R. (ed.), *Composting of Agricultural and Other Wastes*, Elsevier, London, pp. 56-72.
- Su, C.X., Wang, L.B., Li, L.X. and Cao, J. 2010. Sludge handling and reuse into resources in a sewage treatment plant. *China Resour. Compr. Util.*, 28(5): 50-52.
- Sun, X.J., Wang, D.Q., Lu, W.J. and Wang, H.T. 2012a. Characteristics of night soil and leaf co-composting using an aerobic static method. *Front. Environ. Sci. Eng.*, 6(3): 421-427.
- Sun, X.J., Wang, S.M. and Wang, J.J. 2012b. Composting of night soil and green wastes. *Compost Sci. Util.*, 20: 254-259.
- Tong, J., Sun, X., Li, S., Qu, B. and Wan, L. Reutilization of green waste as compost for soil improvement in the afforested land of the Beijing Plain. *Sustainability*, 10(7): 2376.
- Wong, J.W.C., Mak, K.F., Chan, N.W., Lam, A., Fang, M., Zhou, L.X., Wu, Q.T. and Liao, X.D. 2001. Co-composting of soybean residues and leaves in Hong Kong. *Bioresour. Technol.*, 76: 99-106.
- Yang, X.L., Jiang, Q., Song, H.L., Gu, T.T. and Xia, M.Q. 2015. Selection and application of agricultural wastes as solid carbon sources and biofilm carriers in MBR. *J. Hazard. Mater.*, 283: 186-192.
- Zhang, L. and Sun, X. 2014. Changes in physical, chemical, and microbiological properties during the two-stage co-composting of green waste with spent mushroom compost and biochar. *Bioresour. Technol.*, 171: 274-284.
- Zhang, Y. and He, Y. 2006. Co-composting solid swine manure with pine sawdust as organic substrate. *Bioresour. Technol.*, 97: 2024-2031.
- Zhou, H.B., Chen, T.B., Gao, D., Zheng, G.D., Chen, J., Pan, T.H., Liu, H.T. and Gu, R.Y. 2014. Simulation of water removal process and optimization of aeration strategy in sewage sludge composting. *Bioresour. Technol.*, 171: 452-460.
- Zubillaga, M.S. and Lavado, R.S. 2003. Stability indexes of sewage sludge compost were obtained with different proportions of the bulking agent. *Commun. Soil Sci. Plant Anal.*, 34: 581-591.



Unpacking Land Degradation Neutrality (LDN), An Emerging Paradigm to Conserve Land Systems' Sustainability in the 21st Century? Meta-analysis of Challenges and Opportunities

A. Kesavan*, H. Kaur** and S. Chaudhuri***†

*School of Geographical Sciences, University of Bristol, UK

**Monitoring, Evaluation, Resolution and Learning (MERL) Associate, The Water Project, 17 Depot Street, Concord, NH 03301, USA

***Center for Environment, Sustainability and Human Development, CESH; Jindal School of Liberal Arts and Humanities, O.P. Jindal Global University, Sonipat, Haryana, 131001, India

†Corresponding author: S. Chaudhuri (schaudhuri@jgu.edu.in)

Nat. Env. & Poll. Tech.
Website: www.neptjournal.com

Received: 21-02-2021

Revised: 20-04-2021

Accepted: 30-04-2021

Key Words:

Land degradation neutrality
Causal framework
Logic model
Response hierarchy
Gender responsiveness

ABSTRACT

The UN Sustainable Development Goals specifically note the growing importance of land degradation management and mitigation strategies, advocating for global collaboration and innovative research and policy outlook. In this reflective summary, we synthesize the current worldview (post-2000) on land degradation neutrality (LDN), an emerging concept in the field of environmental sustainability that advocates a dynamic balance between degradation and restoration, to ensure no net loss in productive land resources. We first introduce the LDN Causal Framework (theoretical framework of LDN), followed by the Logic Model – guideline for on-ground LDN method implementation (comprising preparatory activities, followed by Integrated Land Use Planning (ILUP), and LDN Response Hierarchy (Avoid-Reduce-Reverse)). We draw attention to growing concerns about LDN technical problems: restore vs. rehabilitate; selecting indicator variables, and establishing a baseline. In the final section, we reflect on the social-ecological aspect of LDN – harnessing participatory action (multi-stakeholder engagement) and gender mainstreaming. Overall, LDN presents an umbrella vision for environmental regeneration and land capital management, that requires seamless integration of natural with social sciences, the policy with law, and requires strategic community mobilization.

INTRODUCTION

The 1992 Rio+20 Earth Summit identified Land Degradation as an imminent threat to global sustainable development initiatives (Sterk et al. 2016). Land degradation, negatively impacts about 40% of the total global landmass (Veron & Paruelo 2018), compromises livelihood opportunities of about 3.2 billion people, with an estimated annual reduction of about 10% of global gross products in biodiversity and ecosystem services (IPBES 2018). Between 1998 and 2013, nearly 20% of the Earth's vegetated land surface experienced persistent declining trends in productivity - apparent in 20% of global croplands, 16% of forest lands, 19% of grassland, and 27% of rangeland (UNCCD 2017). A prime driver of land degradation is unregulated growth in industrial agriculture (iPES Food 2016) - input-intensive crop monocultures, coupled with industrial-scale feedlots. Such intensive farming operations aggravate soil degradation (a) physically (erosion and compaction), (2) chemically (salinization and acidification), and (c) biologically (destruction of soil organic matter) (Fig. 1) that collectively threatens land systems' sustainability

(long-term delivery of goods and services), and ecosystem functioning (Keestra et al. 2018). Macro-scale outcomes of land degradation include soil productivity loss (Tang et al. 2016), competition for scarce resources (UNCCD 2017), human displacement (Cherlet et al. 2018), and climate change, to name a few (Amiraslani & Caiserman 2018, IPBES 2018). The importance of land degradation is acknowledged by the United Nation's Sustainable Development Goals (SDG Target 15.3). The global cost of land degradation could reach €20 billion annually (UNCCD 2013). Mounting need to protect land-based natural capital has led to the development of innovative ideas, including Land Degradation Neutrality (LDN) – a rapidly emerging concept that vies for a state whereby the quantity and quality of land resources, necessary to support ecosystem functions and services, remain stable (or increase) within specified temporal and spatial scales, without compromising existing food/water/energy security (Akhtar-Shuster et al. 2017; UNCCD 2016a).

However, till date, LDN has been an elusive concept (due yet to lack of adequate and targeted research), and a

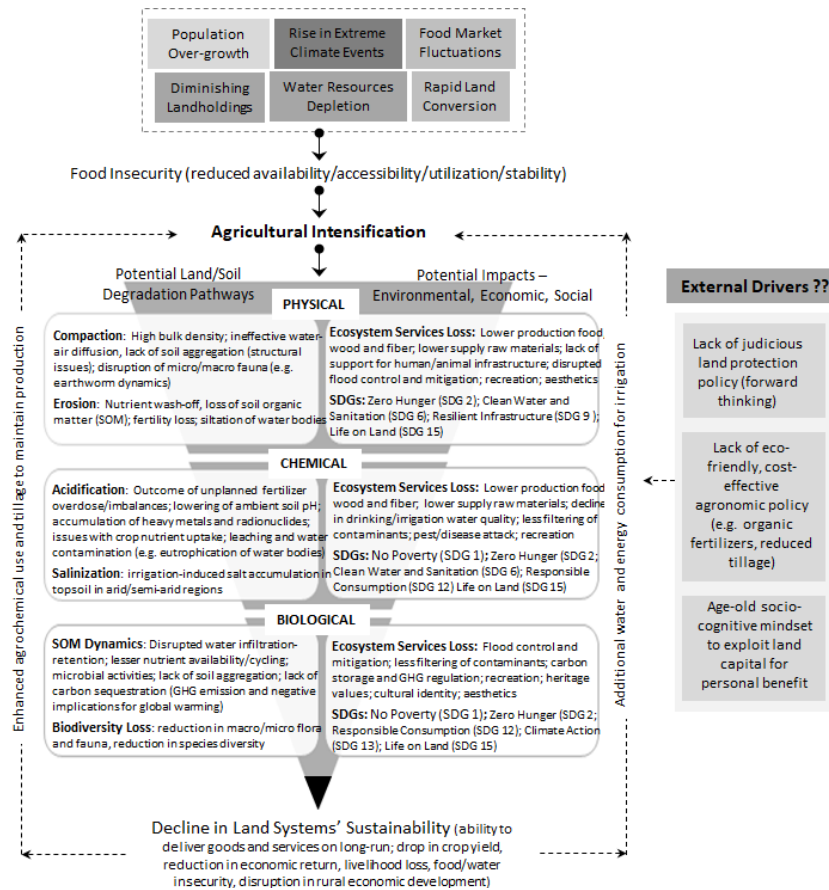


Fig. 1: Simplified depiction of interlinks between food insecurity, agricultural intensification, and major land/soil degradation pathways, with potential eco-environmental and social impacts on ecosystem services and Sustainable Development Goals (SDG). (adopted and modified from Keestra et al. (2018))

challenge to attain as it demands a thoroughly integrative vision, melding multiple development spheres, within a sound institutional structure and right political will (Cowie 2020, UNCCD 2014). In this reflective discourse, we aim to synthesize and present, to the relevant authorities (environmental and land systems' managers), ideas from global literature, to (i) outline core tents of LDN, (ii) emphasize the need to integrate natural with social sciences (stakeholder participation and gender empowerment) to turn theory into practices; and (iii) reflect on challenges vis-a-vis future opportunities to maintain land/ecosystem sustainability (ability to deliver goods and services on long-term). A subsidiary idea is also to showcase the structural, legal, and policy requirements to strive for LDN in future.

MATERIALS AND METHODS

A comprehensive literature search was performed across different databases and search engines including SCOPUS, PubMed, Science Direct, Springer Link, Blackwell, and

Social Citation Index, Web of Science (WoS), EconLit, JSTOR, Google Scholar, etc. using a variety of keywords/search phrases (detail given below). In addition to peer-reviewed journal articles, the search also included working papers, white papers, dissertations, newspaper articles, book chapters, grey literature, and any other technical reports/notes from government/non-government organizations published between January 2000 and July 2020. References cited in the literature were cross-searched and important studies were collected in full text.

A systematic literature search was conducted using the following search phrases:

- Category I : 'industrial agric*'; 'agric* intensi*'; 'agric* diversi*'; 'irrigat* agric*', 'agric* subsid*', 'till*'; and 'fertilizer'
- Category II: 'soil erosion*'; 'soil compact*'; and 'soil salin*'
- Category III: 'restor*', and 'rehabilitat*'

- Category IV: ‘stakeholder participation’; ‘stakeholder dialogue’; ‘multi-stakeholder *’; and ‘participatory *’
- Category V: ‘Gender*’; ‘women’ and
- Category VI: Various combinations of Category I – V.

The ‘*’ includes any extension of a word/phrase that precedes or succeeds to target a wider spectrum of topics and maximize the number of hits.

LDN: Theory and Practice

LDN is often equated with Zero Net Land Degradation (ZNLD), under which the extent of degraded land is expected to decrease or at least, remain stable over a definite time period (Stavi & Lal 2015). To understand the core

tents of the LDN vision, however, the authorities (land and environmental systems’ managers) should be cognizant about the multidimensional linkages between the drivers (natural or anthropogenic) of land degradation and their physical manifestations across a well-defined space-time continuum. In other words, there is a need to locate LDN within a cause-effect web - the LDN Causal Framework. Such introspective appraisals are more critical because of growing climatic anomalies and rapid socio-demographic shifts that endanger land capital in multiple ways.

LDN Causal Framework: Theoretical Underpinnings

The framework links five generic elements: Drivers (D); Pressures (P); State of land degradation (S); Response (R);

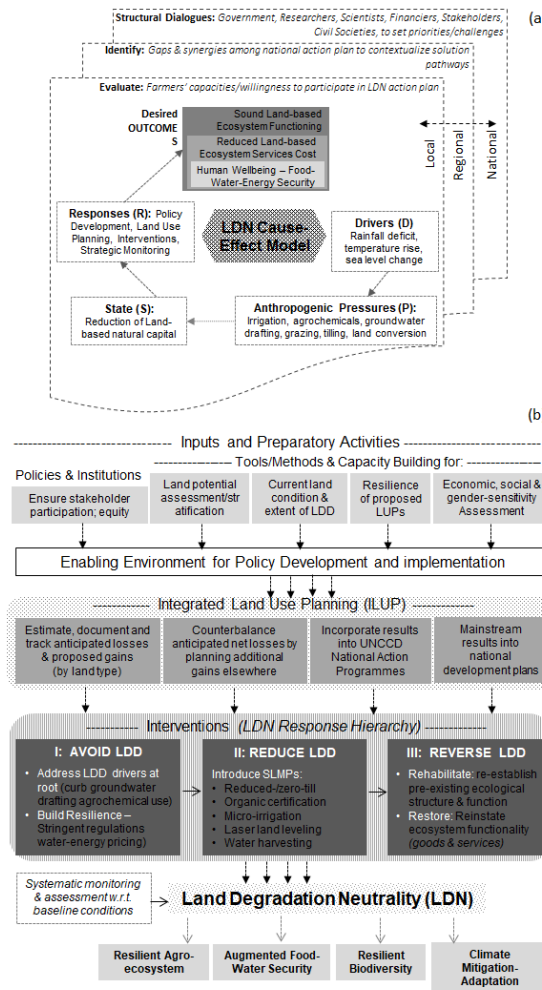


Fig. 2: (a) LDN Causal Framework (adopted from Cowie et al. (2018)) and (b) the generic workflow design involving LDN Logic Model (adopted from Orr et al. (2017)).

and Outcomes (O) over multiple spatial and temporal scales (Fig. 2a) (Cowie 2020). Elements ‘D’ and ‘P’ denote the biophysical and anthropogenic drivers of land degradation, respectively; while the ‘R’ term denotes Sustainable Land Management Practices (SLMPs). LDN causal framework offers a theoretical guide to understand how eco-environmental and human components overlap (Opakara et al. 2018), such as:

- I. Perceptions about broader environmental issues on arable land (e.g. drought, flood, heat waves, sea-level rise etc.)
- II. Contextual knowledge to link specific farming practices (groundwater-sourced irrigation, deep tillage, agro-chemical application) with ecosystem parameters.
- III. Adaptive capacity; ability to plan suitable response actions to adjust to such changes (SLMPs). This is also complemented by the level of governmental support systems.

(I) and (II) embodies the ‘D’ and ‘P’ components in the causal framework, while (III) denotes the ‘R’ (Fig. 2a)’. The ‘O’ term underscores human wellbeing, realized by (i) rejuvenation of ecosystem services (ii) improving natural resources conditions while operating within the biophysical limits of land systems, (iii) reduction in ecosystem services costs (increasing availability/accessibility), and (iv) judicious allocation of land resources for various purposes. The LDN, unlike the traditional view of halting land degradation completely, which seems unrealistic, advocates a dynamic balance between the rate of land degradation and remediation (Orr et al. 2017):

- Maintain and improve sustainable delivery of goods and services in long run
- Increase the resilience of population reliant on land-based natural capital (train/equip them with context-relevant adaptive skills)
- Harness synergies with other social, economic and environmental initiatives
- Institute responsible and inclusive land governance.

LDN Logic Model: Putting Idea into Action

Existing LDN literature advocates a generic workflow structure, comprising of three broad stages of systems’ action: (1) conducting input and LDN preparatory analysis, (2) developing integrated land use plans (ILUP), and (3) understanding choice of interventions (Cowie et al. 2018) (Fig. 2b). The LDN Logic Model begins with input and preparatory analysis (Cowie et al. 2018, Orr et al. 2017):

- Assessment of initial land degradation status
- Evaluation of existing land tenures

- Realistic estimation of land capacities to deliver desired ecosystem services
- Assessment of land stratification (types and extent of vegetative cover)
- Level of maximum resilience potentially achievable.

The next stage is the ILUP design:

- Realistic estimation of potential gains-losses due to proposed land use programs (loss in one location should be counterbalanced by gains in others)
- Strategic integration of the proposed land use programs with other sustainable development paradigms as a complementary action strategy
- Identifying strategic means to integrate it with the national sustainable development agenda

The final stage calls in land-based interventions, centering on the LD Response Hierarchy, founded on three principles:

- AVOID: adopting pre-emptive regulation/planning to keep land degradation processes at bay
- REDUCE: resorting to various SLMPs to curb impacts of different human activities
- REVERSE: develop restoration or rehabilitation projects to assist in the recovery of already degraded land to rejuvenate ecosystem functions.

Avoiding land degradation should be the first priority, followed by reducing degradation, while restore/rehabilitate, to reverse degradation. The latter is more appropriate for land already degraded.

LDN IMPLEMENTATION: TECHNICAL CONCERNS

Rehab or Restore?

Rehabilitation encompasses a set of measures that aim to reinstate ecosystem functionality, focusing on sustainable/equitable provisions of goods and services (McDonald et al. 2016). On the other hand, Restoration seeks to re-establish pre-existing ecological structure and functions, including biotic integrity. The choice of action depends on careful deliberation on (1) types and magnitude of drivers of land degradation; (2) long-term land potentials; (3) land management history; (4) snowballing pressure on land capital (unregulated natural resources extraction); and (5) climatic conditions, to name a few. However, the authorities should bear in mind that neither rehabilitation nor restoration can return degraded ecosystems to the pre-disturbance configuration in the short/medium term (Maron et al. 2015), and thus, pre-emptive action (avoid land degradation) is the most desired strategy. Authorities should also realize that

response to any 'corrective' intervention is a slow process and follows mostly a non-linear trajectory - perceptible changes in ecosystem parameters are only observed after a certain threshold point is reached, over a certain period of time (Bestelmeyer et al. 2015).

Selecting LDN Indicator Variables

There are three prime indicators, to monitor progress towards achieving LDN (Sims et al. 2019, UNCCD 2016b): (i) land cover and changes; (ii) land productivity; and (iii) carbon stocks. These indicators are applied in a 'one out, all out' approach: where any of the indicators show significant negative change, it is considered a loss, and conversely, if at least one indicator shows a positive trend and none shows a negative trend, it is considered a gain (UNCCD 2017). However, for more practical and local applications, there should be more targeted parameters (e.g. groundwater levels, streamflow, precipitation, soil organic matter content, cation exchange capacity etc.) (Tilahun et al. 2018). Indicators should be identified by (i) combining ground-level survey with remotely sensed observation (e.g. satellite imagery), and (ii) active consultation with local communities, rather than solely relying on external specialists who, most times have little familiarity with local conditions, and come with pre-conceived notions (Opakara et al. 2018).

Establishing Baseline

The baseline represents a standardized frame of reference (initial value of each LDN indicator variable) against which neutrality achievements/failures are assessed within a suitable timeframe (Cowie et al. 2018). Broad steps include:

1. Setting LDN target (realistic; based on the current level of land degradation)
2. Identification of indicator variables (stakeholder consultation to include local/traditional knowledge of ecosystem parameters)
3. Systematic monitoring with the help of local communities (inflow and outflow patterns of land-based natural stocks).

The baseline for each indicator variable should be computed over an extended timeframe (averaging values over decadal-scale; statistically accounting for temporal variability), instead of 'conventional' single-point-in-time approach (Orr et al. 2017)

SOCIO-ECOLOGY OF LDN: HUMAN-NATURE INTERACTIONS

Growing advocacy worldwide to implement LDN principles is to adopt a *socio-ecological* lens (Ostrom 2009), consciously apportion environmental systems into two mutually

reinforcing domains of development and action: (1) ecosystem-based and (2) society- and economy-based (Okpara et al. 2018). The latter is founded on two key policy approaches: (i) harnessing participatory engagement – multi-stakeholder dialogue, and (ii) women's strategic, active, and purposeful involvement.

Multi-Stakeholder Dialogue

Strategic implementation of LDN systems' governance calls for structural dialogues between multiple agencies: a platform comprising of actors ranging from local to national levels- with diverse perceptual, educational, and technical backgrounds; diverse expectations and priorities (Amiraslani & Caiserman 2018). Such a carefully designed multi-stakeholder platform increases opportunities for a coordinated action network (harnessing synergies in actions) that acknowledges different claims/demands on land capital while reconciling the needs and consumer demands (UNCCD 2015). Current global literature (Kust et al. 2017), indicates that participatory action helps to:

- Promote awareness about land restoration/rehabilitation
- Inspire sense of shared responsibilities towards land systems protection (viewing land as common-pool resources for mutual benefits)
- Develop means to remove legal, institutional, social barriers/conflicts to work towards a common and mutually re-assuring goal

To develop a participatory action plan, the authorities will need to (i) identify and reach out to all interested parties/stakeholders and indoctrinate them to LDN principles; and (ii) strategically engage them at all stages of decision making (Fig. 3a) (IUCN 2018). The stakeholders must adopt voluntary responsibilities (time-bound targets) to contribute meaningfully to land-based projects, with minimal conflicts. However, it will require an 'enabling' environment for the stakeholders. According to Verburg et al. (2019), the authorities need to deliberate on three ideas: (i) respecting farmers' perceptions, about the mode of LDN systems' operation (are the farmers apprehensive of outcomes?), (ii) systems' inadequacies (is there enough infra, knowledge, finance?), and (iii) expectations of the system (will LDN curtail farmers' incomes?) (Fig. 3b). Along similar lines, Crossland et al. (2018) suggested certain systems' checks: (i) negotiating priorities and incentivizing farmers' actions towards LDN, (ii) devising contextual solutions to problems, and (iii) co-production of knowledge (basing LDN assessment on local farmers' inputs).

Last but not the least, for the developing rural economies, there should be conscious deliberation on behalf of the authorities, to safeguard small/marginal holders' interests - LDN strategy implementation (targets, methods,

timeframe) should not endanger livelihood opportunities of this less-endowed and already vulnerable population, and/or evict them from their lands, in the name of land ‘restoration/rehabilitation’ (IUCN 2018). Additional benefits might be realized by promoting farmers’ social networks to disseminate new paradigms (e.g. optimize deep tillage, controlled/planned agrochemical use, water-efficient crops, irrigation tariffing) (Chaudhuri et al. 2020a).

Harnessing Gender Responsivity

The value (urgency) of gender mainstreaming in LDN strategy implementation is yet fully acknowledged, with inadequate policy attention (Okpara et al. 2019). Lower access to productive resources; lack of information, technology, and extension services; lower awareness levels; patriarchal outlook; and ulterior political dynamics, still keep a vast cross-section of the women workforce from participating in environmental initiatives around the world (Chaudhuri et al. 2021a, 2018, Chaudhuri & Roy 2017). Okpara et al.

(2018) urged for developing targeted and context-relevant socioeconomic interventions for (1) safeguarding women’s land rights (tenure); (2) creating legal provisions to enhance the ability to exercise land rights freely (ability to sell/lease out); (3) ensuring equitable access to all productive resources; and (4) developing targeted financial packages to rightfully compensate women for their contributions. In this regard, Mor (2019) has shortlisted certain socioeconomic indicators that might be used to assess gender inequality (Fig. 4). In rural societies, women are more tied to land-based natural capital (in charge of the collection of water/fuelwood/fodder/herbs/fruits), and thus land degradation affects them disproportionately (UNCCD 2017). Broad measures could include (Global Mechanisms 2019):

- Developing strategic sensitization programs to make women (farmers) aware of new cropping systems (tools, seeds, irrigation, harvesting practices)
- Helping women’s groups get connected through information networks

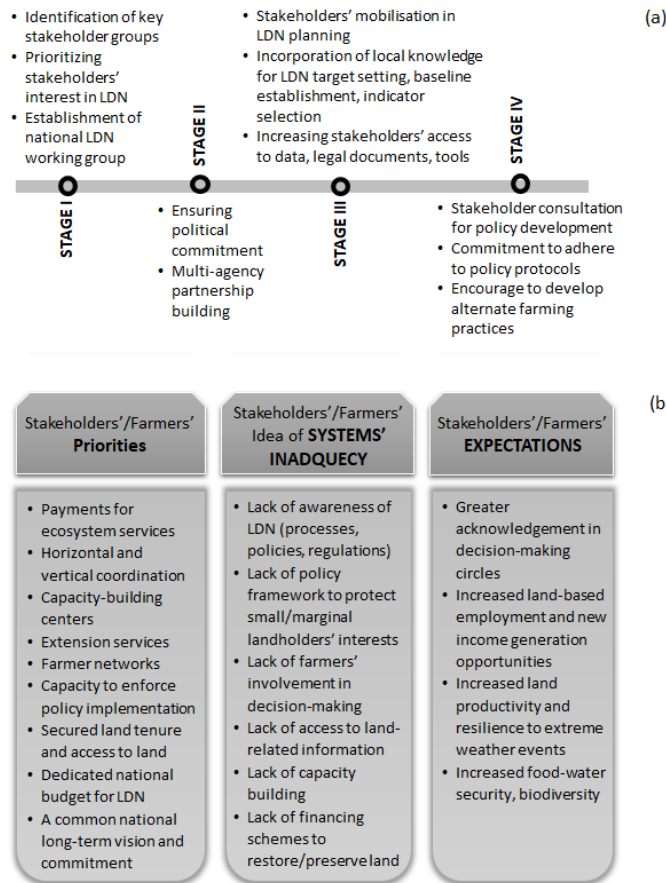


Fig. 3: (a) Main stages of developing a functional participatory action framework that respects stakeholders'/farmers' priorities; and (b) current institutional systems' inadequacies for the same (adopted from Verburg et al. (2019)).

Gender Responsive LDN Theme	Potential Checklist for Authorities
Creating an Enabling Environment for Women in Land-based Projects	<ul style="list-style-type: none"> • Are women actively participating in land-based project development meetings (restoration/rehabilitation)? • Are women holding influential positions in decision-making circles (e.g. manager, lead farmer, entrepreneur)? • Are women part of self-help groups, information networks? • Are there legal provisions to promote and protect women's interests in land-based projects?
Women Equally Reaping of the Benefits of Land-based Projects as Men	<ul style="list-style-type: none"> • Are the women benefitting from organized workshops and skill-development initiatives? • Can women freely access latest tools and resources? • Are women actively participating in main policy discussions? • Are women-headed households land project beneficiaries? • Can women accessing financial schemes (loans, subsidies)?
Women's Ownership Status of Productive Asset base (<i>land, livestock, tools</i>)	<ul style="list-style-type: none"> • Do the women possess legal land documents? • Do they have equal rights as men to sell/mortgage/use land whenever necessary? • Are women aware of land rights/tenure issues (and changes therein) and associated redress mechanisms? • Do women own other productive assets?
Women's Level of Access to Resources and Inputs for Land-based Projects	<ul style="list-style-type: none"> • Do women have access to (i) improved seeds/saplings/fertilizer/fodder; (ii) agricultural extension services; (iii) climate-smart agriculture/technology; (iv) information/data • Is there land earmarked for restoration under LDN to women to use their own discretion to rehabilitate?

Fig. 4: Thematic survey to assess women's empowerment/involvement in land/environmental projects (could be expressed in terms of relative percentages of women, wherever applicable) (adopted from Mor (2019))

- Making legal and institutional provisions for women to participate in, and contribute to, land research and development activities
- Increasing the number of women personnel in the extension services

In this regard, the authorities may also want to consult the guidelines developed by the International Union for Conservation of Nature (Table 1) (IUCN 2018).

CONCLUSION

The LDN approach supports multiple sustainability paradigms, including food/nutritional security (SDG 2: Zero Hunger), livelihood and income (SDG 1: No Poverty), terrestrial biodiversity (SDG 14: Life on Land), and (SDG 5: Gender Inequity), to name a few (Stavi & Lal 2015). Moreover, the LDN falls in line with the Aichi Biodiversity Targets (Target 5: reduce habitat loss/degradation close; Target 7: sustainable management of areas under agriculture and forestry; Target 14 and 15: safeguarding essential ecosystem services and harnessing resilience, increasing carbon stocks, restoring degraded ecosystems) (IUCN 2015). LDN could even become a critical component to the Sendai Framework for Disaster Risk Reduction 2015-2030 (Priorities 2 and 3: strengthening

disaster risk governance) (UN 2015). The incorporation of LDN in national development agendas could also bolster emission reduction efforts (SDG 13: Climate Action). Collectively, the successful implementation of LDN offers a milieu of opportunities to the authorities (environmental and land systems' managers) that could be critical in days ahead to brace up against 'unpredictability' (e.g. climatic anomalies), while bolstering food-water-energy security programs, and diversifying rural livelihood-income opportunities.

On-ground implementation of LDN should be planned within a participatory engagement framework, marked by strategic cross-linking of multiple development domains, agencies and actors (Table 2). It requires a robust institutional structure, stable finance (Public-Private Partnerships), social capital building, and technology support (Fig. 5). A major obstacle, however, will be to ward off political influences, which almost always take the populist path, and argues against any stringent intervention (Chaudhuri and Roy, 2019). Environmental reforms are vehemently repealed, branded as "anti-farmer", "anti-poor by regional/local parties to win electoral battles (Chaudhuri et al. 2021, 2020b).

To that end, we urge the authorities to adopt an integrative vision:

Table 1: Best practices to ensure women’s participation in LDN projects (adopted from IUCN (2018))

Proposed Objective	Potential Method Implementation Action Plan
Women leading initiatives as major stakeholders in the land-based projects	<ul style="list-style-type: none"> Engaging with NGOs and public sector offices with prior experience and equipped with ideas/techniques/manuals Organizing focused group discussions (FGDs) with women to assess their expectations, aspirations, capacities Conducting regular capacity-building workshops (hands-on demonstrations) to train and equip women Mobilizing women’s self-help groups towards LDN projects
Harness women’s financial capacities	<ul style="list-style-type: none"> Enabling women to access credits micro/mesoscale enterprises and formal banking sector Identifying means to directly transfer credits/support to women without intermediary stage (not via husband/male family members) Incentivizing the public and private sectors to source their raw material directly from women Training women for value-added production Developing new/alternate income generation opportunities from various land-based projects
Voluntary Guidelines on the Responsible Governance of Tenure (VGGT)	<ul style="list-style-type: none"> Recognize women’s land tenure right by ensuring a non-discriminatory LDN work plan Safeguard legitimate land tenure rights against all potential threats (maintain equity, justice, human dignity by all means) Prevent disputes, conflicts, and corruption by practicing transparency and accountability in the LDN systems’ approach
Sensitizing success stories	<ul style="list-style-type: none"> Using social/print/electronic media to sensitize success stories women leadership roles in various land/environmental projects
Gender-responsive knowledge products	<ul style="list-style-type: none"> Elaborating studies/research/consultancies to incorporate gender-responsive ideas Engaging reputed gender specialists to provide guidance and directions for LDN design Circulating to national gender/women’s experts/advocacy groups for inclusion of women in land-based projects
Gender message included in training and awareness events/campaigns	<ul style="list-style-type: none"> National gender focal point and gender working group draft standard gender message Include gender analysis as a requirement in the Terms of Reference (TORs) of LDN Fact sheet on gender and restoration

- Identify ongoing environmental initiatives that would directly patronize LDN systems’ thinking and implementation
- Found LDN on principles of equity, inclusivity, fairness and transparency (pro-poor; gender-sensitive)
- Incorporate LDN into mainstream rural economic development agenda
- Identify all potential stakeholders
 - Acknowledge priorities and capacities
 - Identify means to harness synergies (develop grievance redress protocols)

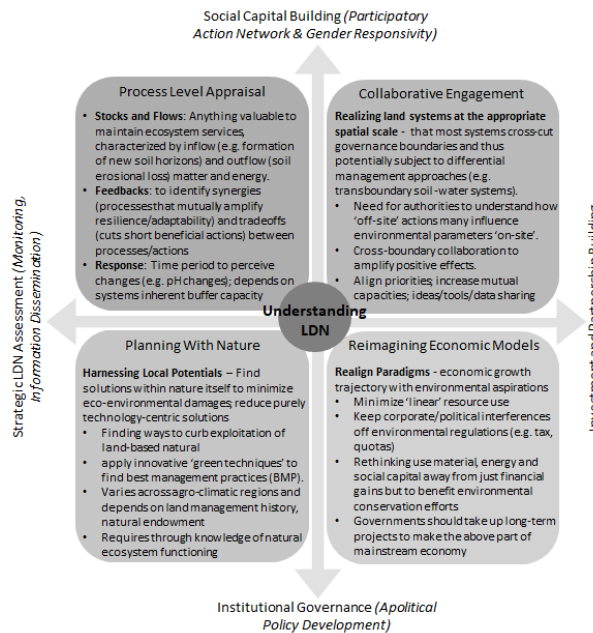


Fig. 5: Conceptual underpinning of LDN strategy development (concepts adopted from Keestra et al. (2018); authors’ own illustration)

Table 2: Key developmental domains to maximize LDN benefits (adopted from IUCN (2015))

Development Domain	Key Areas of Emphasis
Strengthening natural resource governance and land tenure security	<ul style="list-style-type: none"> • Ensuring equitable rights of men and women to access land • Special LDN targets for lands not legally titled and/or land where indigenous peoples or ethnic minorities hold customary rights • Ensuring environmental justice and social protection to curb the risk of out-migration of the native population due to LDN projects • Implementing principle of free, prior, and informed consent when setting LDN targets and strategy implementing methods • Ensuring equity at the lowest practical and accountable level of the institutional governance system • Incorporating traditional/indigenous knowledge at every level of LDN systems' design
Integrating LDN with other Development initiatives	<ul style="list-style-type: none"> • Harnessing synergies between LDN actions/targets and other initiatives (biodiversity, carbon sequestration, climate action) • The full range of sustainable land management and restoration approaches, thereby leveraging other sectors and stakeholders as implementation actors • Evidence-based LDN target-setting using integrative vision (environment, agriculture, water, energy, climate, humans) • Restoration opportunities are decided based on the existing state of the land, the potential for restoration/rehabilitation, the cost-benefit ratio of LDN actions planned, threats to the native population
Collecting more evidence for LDN achievement (Monitoring and reappraisal of LDN targets over time)	<ul style="list-style-type: none"> • Disseminating open-sourced data to research communities on the state of land degradation, restoration, rehabilitation • Strategic monitoring and evaluation for adaptive management • The above includes selection, monitoring, and assessment of appropriate biodiversity indicators and analysis of multiple ecosystem services thereof • Scale-up of best management practices, evidence-based, accounting for cost-benefit of interventions on the full range of ecosystem services

- Conduct strategic sensitization/outreach/promotion programs (assurance about food-water-energy security and dispelling myths about income loss)
- Deploy dedicated extension service agents (preferably by choosing individuals from local population – good communication skill; impartial attitude; aware of local expectations vis-à-vis grievances; demonstrated commitment to environmental causes; well-connected in community and influential)
- Ramp up technology support system (on-ground and remotely sensed)
- Choose local indicator variables using local wisdom/experience
- Design novel monitoring and data reporting systems; train chosen individuals from local communities to assist in the process

REFERENCES

- Akhtar-Schuster M., Stringer, L., Erlewein, A., Metternicht, G., Minelli, S., Safriel, U. and Sommer, S. 2017. Unpacking the concept of land degradation neutrality and addressing its operation through the Rio Conventions. *J. Environ. Manage.*, 195: 4-15.
- Amiraslani, F. and Caiserman, A. 2018. Multi-stakeholder and multi-level interventions to tackle climate change and land degradation: The case of Iran. *Sustainability*, 10(6): 1-17. DOI:10.3390/su10062000.
- Bestelmeyer, B.T., Okin, G.S., Duniway, M.C., Archer, S.R., Sayre, N.F., Williamson, J.C. and Herrick, J.E. 2015. Desertification, land use, and the transformation of global drylands. *Frontiers Ecol. Environ.*, 13(1): 28-36.
- Chaudhuri, S., Roy, M., McDonald, L.M. and Emendak, Y. 2021a. Coping Behaviours and the concept of Time Poverty: a review of perceived social and health outcomes of food insecurity on women and children. *Food Security*. 13: 1049-1068.
- Chaudhuri, S., Parakh, D., Roy, M. and Kaur, H. 2021b. Groundwater-sourced Irrigation and Agro-power Subsidies: Boon or Bane for Small/Marginal Farmers in India? *Groundwater for Sustainable Development*. 15(100690). DOI: 10.1016/j.gsd.2021.100690.
- Chaudhuri, S., Roy, M., McDonald, L.M. and Emendack, E. 2020a. Reflections on farmers' social networks: A means for sustainable agricultural development? *Environ. Dev. Sustain.*, 23(3): 2973-3008. DOI: 10.1007/s10668-020-00762-6
- Chaudhuri, S., M. Roy, L.M. McDonald and Y. Emendack. 2020b. Water for all (Har Ghar Jal): Rural water supply services (RWSS) in India (2013-20180, Challenges and Opportunities. *International Journal of Rural Management*. 16(2): 254-284.
- Chaudhuri, S. and Roy, M. 2019. Irrigation water pricing in India as a means to conserve water resources: Challenges and Potential future directions. *Environ. Conserv.*, 46(1): 99-102.
- Chaudhuri, S., Roy, M. and Jain, A. 2018. Appraisal of WaSH (Water-Sanitation-Hygiene) infrastructure using a composite index, spatial algorithms and sociodemographic correlates in rural India. *J. Environ. Informat.*, 35(1): 1-22.
- Chaudhuri, S. and Roy, M. 2017. Rural-urban spatial inequality in water and sanitation facilities in India: A cross-sectional study from household to national level. *Appl. Geog.*, 85: 27-38.
- Cherlet, M., Hutchinson, C., Reynolds, J., Hill, J., Sommer, S. and von Maltitz, G. (Eds.). 2018. *World Atlas of Desertification*, Publication Office of the European Union, Luxembourg.
- Cowie, A. 2020. Guidelines for Land Degradation Neutrality: A Report Prepared for the Scientific and Technical Advisory Panel of the Global Environment Facility, Washington D.C.
- Cowie, A.L., Orr, B.J., Sanchez, V.M.C., Chasek, P., Crossman, N.D., Erlewin, A., Louwagie, G., Maron, M., Metternicht, G.I., Minelli, S., Tengberg, A.E., Walter, S. and Welton, S. 2018. Land in balance: The scientific conceptual framework for land degradation neutrality. *Environmental Science and Policy*. 79: 25-35.
- Crossland, M., Winowiecki, L.A., Pagella, T. and Hadgu, K. 2018. Implications of variation in the local perception of degradation and restoration

- processes for implementing land degradation neutrality. *Environ. Develop.*, 28: 42-54.
- Global Mechanisms. 2019. Land Degradation Neutrality Transformative Projects and Programmes: Operational Guidance for Country Support. UNCCD, Bonn, Germany.
- IPBES. 2018. Summary for policymakers of the assessment report on land degradation and restoration of the intergovernmental science-policy platform on biodiversity and ecosystem services. In: R. Scholes, L. Montanarella, A. Brainich, N. Barger, B. ten Brink, M. Cantele, B. Erasmus, J. Fisher, T. Gardner, T. G. Holland, F. Kohler, J. S. Kotiaho, G. Von Maltitz, G. Nangendo, R. Pandit, J. Parrotta, M. D. Potts, S. Prince, M. Sankaran and L. Willemen (eds.). IPBES Secretariat, Bonn, Germany, p.44.
- iPES Food. 2016. From uniformity to diversity: a paradigm shift from industrial agriculture to diversified agroecological systems. International Panel of Experts on Sustainable Food Systems. https://www.ipes-food.org/_img/upload/files/UniformityToDiversity_FULLL.pdf
- IUCN. 2018. A review of land degradation neutrality process. International Union for Conservation of the Nation. Gland, Switzerland.
- IUCN. 2015. Land Degradation Neutrality: Implications and Opportunities for Conservation. International Union for Conservation of the nation. Gland, Switzerland.
- Keestra, S., Mol, G., De, Leeuw, J., Okx, J., Molenaar, C., De, Cleen, M. and Visser, S. 2018. Soil-related sustainable development goals: Four concepts to make land degradation neutrality and restoration work. *Land*, 7(4): 133. Doi: 10.3390/land7040133.
- Kust, G., Andreeva, O. and Cowie, A. 2017. Land degradation neutrality: Concept development, practical applications, and assessment. *Environ. Manage.*, 195(1): 16-24.
- Maron, M., Bull, J.W., Evans, M.C. and Gordon, A. 2015. Locking in loss: Baselines of decline in Australian biodiversity offset policies. *Biol. Conserv.*, 192: 504-512.
- McDonald, T., Gann, G.D., Jonson, J. and Dixon, K.W. 2016. International Standards for the Practice of Ecological Restoration-Including Principles and Key Concepts (first edition), Society for Ecological Restoration (SER), Washington, D.C.
- Mor, T. 2019. A Manual for Gender-Responsive Land Degradation Neutrality Transformative Projects and Programs. UN Women, IUCN.
- Okpara, U.T., Stringer, L.C. and Akhtar-Schuster, M. 2019. Gender and land degradation neutrality: A cross-country analysis to support more equitable practices. *Land. Degrad. Develop.*, 30(11): 1368-1378.
- Okpara, U.T., Stringer, L.C., Akhtar-Schuster, M., Metternicht, G.I., Dal-limer, M. and Requier-Desjardins, M. 2018. A socio-ecological systems approach is necessary to achieve land degradation neutrality. *Environ. Sci. Policy*, 89: 59-66.
- Orr, B.J., Cowie, A.L., Sanchez, V.M.C., Chasek, P., Crossman, N.D., Erlewein, A., Louwagie, G., Maron, M., Metternicht, G.I., Minelli, S., Tengberg, A.E., Walter, S. and Welton, S. 2017. Scientific Conceptual Framework for Land Degradation Neutrality. A Report of the Science-Policy Interface. United Nations Convention to Combat Desertification (UNCCD), Bonn, Germany.
- Ostrom, E. 2009. A general framework for analyzing sustainability in social-ecological systems. *Science*, 325: 419-422.
- Sims, N.C., England, J.R., Newnham, G.J., Alexander, S., Green, C. and Held, A. 2019. Developing good practice guidance for estimating land degradation in the context of the United Nations Sustainable Development Goals. *Environ. Sci. and Policy*, 92: 349-355.
- Stavi, I. and Lal, R. 2015. Achieving net-zero land degradation: Challenges and opportunities. *J. Arid Environ.*, 112: 44-51.
- Sterk, G., Boardman, J. and Verdoort, A. 2016. Desertification: History, causes, and options for its control. *Land Degrad. Dev.*, 27: 1783-1787.
- Tang, Z., An, H., Deng, L., Wang, Y., Zhu, G. and Shanguan, Z. 2016. Effect of desertification on productivity in a desert steppe. *Sci. Reports*, 6: 27839. DOI:10.1038/srep27839.
- Tilahun, M., Singh, A., Kumar, P., Apindi, E., Schauer, M., Libera, J. and Lund, H.G. 2018. The Economics of Land Degradation Neutrality in Asia: Empirical Analyses and Policy Implications for the Sustainable Development Goals. https://www.eld-initiative.org/fileadmin/pdf/Asia_Report_EN.pdf
- UNCCD. 2017. Global Land Outlook: First Edition. United Nations Convention to Combat Desertification, Bonn, Germany. http://www2.unccd.int/sites/default/files/documents/2017-09/GLO_Full_Report_low_res.pdf
- UNCCD. 2016. United Nations Convention to Combat Desertification. Report of the Conference of the Parties on its twelfth session, held in Ankara from 12 to 23 October 2015. Part two: Actions. ICCD/COP(12)/20/Add.1. United Nations Convention to Combat Desertification, Bonn.
- UNCCD. 2015. Climate Change and Land Degradation: Bridging Knowledge and Stakeholders. United Nations Convention to Combat Desertification, 3rd Scientific Conference, 9-12 March, Cancun, Mexico
- UNCCD. 2013. United Nations Convention to Combat Desertification. The Economics of Desertification, Land Degradation, and Drought: Methodologies and Analysis for Decision-Making. In Proceedings of the UNCCD 2nd Scientific Conference, Bonn, Germany, 9-12 April 2013.
- Verburg, P.H., Metternicht, G., Allen, C., Debonne, N., Akhtar-Schuster, M., Inácio, da Cunha, M., Karim, Z., Pilon, A., Raja, O., Sánchez Santivañez, M. and Sényaz, A. 2019. Creating an Enabling Environment for Land Degradation Neutrality and its Potential Contribution to Enhancing Well-being, Livelihoods and the Environment. A Report of the Science-Policy Interface. United Nations Convention to Combat Desertification (UNCCD), Bonn, Germany.
- Veron, S.R. and Paruelo, J.M. 2010. Desertification alters the response of vegetation to changes in precipitation. *J. Appl. Ecol.*, 47: 1233-1241.



Assessment of Flood Hazard Zonation Using Geographic Information System and Analytical Hierarchy Process: A Case Study of Tlawng River Watershed in Sairang, Mizoram, India

Malsawmtluanga*† and Ch. Vabeiemo**

Department of Geology, Lunglei Govt College, Mizoram-796 701, India

Department of Geology, NEHU, Shillong-793022, Meghalaya, India

†Corresponding author: Malsawmtluanga; mstmzu.gps@gmail.com

Nat. Env. & Poll. Tech.
Website: www.neptjournal.com

Received: 04-06-2021
Revised: 26-06-2021
Accepted: 13-07-2021

Key Words:

Flood hazard
GIS
AHP
Tlawng river watershed

ABSTRACT

Flood occurs when the water inundates normally dry ground, which could happen in a variety of ways like excessive rainfall, overflowing of embankments, dams, rivers, snowmelt, and other factors. Floods are one form of a natural hazard which are difficult to contain and control. A flood susceptibility mapping using Geographic Information System (GIS) and Analytical Hierarchy Process (AHP) techniques were carried out at Sairang village in Aizawl, Mizoram in Northeast India. The study area Sairang is situated on the banks of the Tlawng river, the longest river in Mizoram. Floods have wreaked havoc in Sairang frequently resulting in huge losses and damage to property with numerous loss of life over the years. The total study area is 131.27 sq km and the resulting flood hazard potential zonation map shows that 1/3 of the watershed area falls in Vey High and High Potential Flood Hazard Zonation areas.

INTRODUCTION

Sairang in Mizoram is a thriving village in the Northwestern part of Aizawl, the capital of Mizoram. The NH306, Mizoram's lifeline which connects to the rest of the country runs through the village which is 20 km from Aizawl. The Tlawng river basin enhances Sairang's local economy as well as supplies a majority of the sand for construction activities in and around Aizawl city. Apart from small-scale and marginal farming, fishing, recreational activities, and other sources of income are practiced along the river, as are a variety of other economic activities. However, in the Tlawng river basin in Sairang, floods have caused disasters frequently in the past decade (Lalhmingliana et al. 2019). The watershed lies between 92° 35'0" E, 23°50'0"N to 92°45'0"E 23°50'0"N and is covered under Toposheet sheet no.84 A/9 by the Survey of India Fig.1.

Flood Hazard maps provide useful and critical information to help people and authorities to understand the risks of natural disasters, to aid in disaster mitigation and its management. And because of these reasons, many workers have been using GIS-AHP methods to successfully delineate flood hazard zonations across the world (Ouma & Tateishi 2014, Gigovic et al. 2017, Khaleghi & Mahmoodi 2017, Das 2018, Hammami et al. 2019, Ghezelsoffoo & Hajibigloo

2020). Also, preparations of flood hazard maps using GIS-AHP have been successfully implemented in many areas in mainland India (Sinha et al. 2008, Ajin et al. 2013,

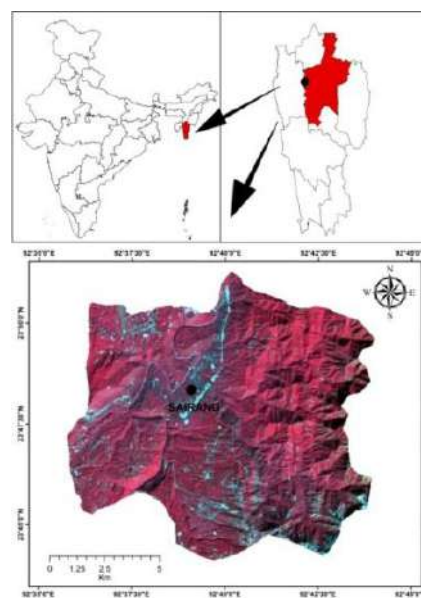


Fig.1: Location map of the study area Sairang, Mizoram in northeast India.

Das et al. 2017, Dash & Sar 2020, Vignesh et al. 2020). In the mountainous regions of Northeast India, flood hazard maps were prepared to tackle flooding in the river basins (Ganguly & De 2015, Hazarika et al. 2016, Laikangbam et al. 2019). Flood hazard mapping along the Tlawng river basin in Sairang in Aizawl will make it possible to quantify what is at risk of flooding, such as the number of households, economic activities, and businesses, etc that are under threat from floods.

MATERIALS AND METHODS

A toposheet map at a scale of 1:50,000 obtained from the Survey of India, as well as satellite photos Landsat-8 and Digital Elevation Model (DEM) of *ALOS PALSAR* (12.3 m resolution), were utilized to create thematic layers in a GIS environment to delineate the flood hazard potential zone of the Sairang watershed. Alaska Satellite Facility provided *ALOS PALSAR* (DEM) with a resolution of 12.3 m, which was processed in *ArcMap 10.2* software to outline the watershed and provide elevation, slope, and curvature maps. The resultant drainage network, drainage density, and flow accumulation were created using *ArcMap 10.2* software. The United States Geological Survey (USGS) Landsat-8 satellite photos of the study area were subsequently processed in *ERDAS IMAGINE 2014* and *ArcMap 10.2* software to create the land use classification and vegetation cover maps. Rainfall data for the last eight years was obtained (Economics and Statistics 2019). The mean rainfall for the eight years was processed in *Microsoft Excel* software, and the data were then spatially interpolated using the Inverse Distance Weighted (IDW) method to produce the rainfall distribution map. The soil map was derived from Maji et al. (2001) and was geo-referenced and digitized before being used to construct theme layer maps. Following the production of the theme layers, all of the layers were converted to raster format and used for the overlay analysis. During weighted overlay analysis, a rank was assigned to each individual parameter of each thematic layer map, and weights were assigned based on the output of the MCDM (AHP) approach, and the resulting output map depicts the flood hazard potential zones of the research area. The schematic graphic depicts the approach used in this investigation (Fig. 2.)

Analytical Hierarchy Process

The AHP assigns a weight to each evaluation criterion based on the decision-pair-wise maker's comparisons of the criteria, as shown in Table 1. The consistency ratio has been tested for accuracy. The following equation would be used to check the table's consistency ratio.

Strength of Significance Explanation

After completion of preparing the data layers, the variables were weighted according to the Analytical Hierarchy Process (AHP) method, which is a multi-criteria decision-making process based on a 9-point scale (Table 1) (Saaty 1980). Following the construction of a decision hierarchy, this method involved a pair-wise evaluation of the relative preferences of a small number of decision criteria for flood risk assessment. Experts assign weights to form the pair-wise comparison matrix (Saaty 2008). These weights were calculated automatically using *Expert Choice* software's Multi-Criteria Decision Analysis (MCDA) tool (Siddayao et al. 2015). The AHP approach used pair-wise comparisons of all the criteria as inputs and the relative weights of the crite-

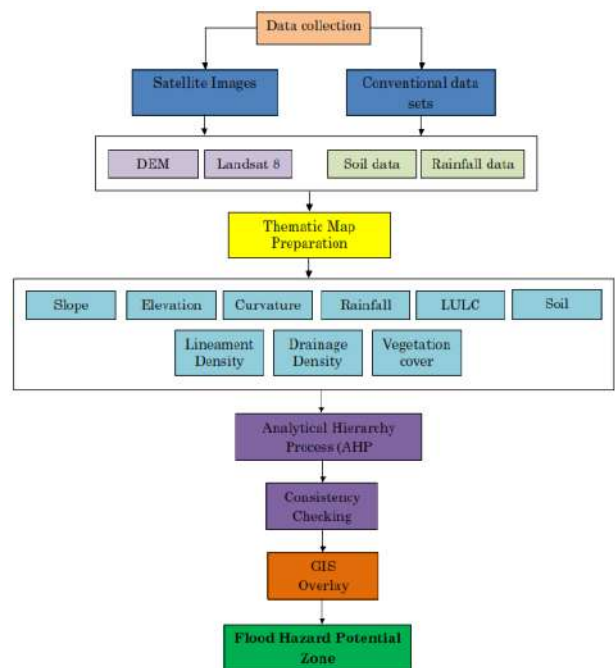


Fig.2: Flow chart of methodologies used in the study.

Table 1: The fundamental scale of absolute numbers (Saaty 1980).

Strength of significance	Explanation
1	Equal significance
3	Medium significance
5	Strong
7	Very strong significance
9	Maximum significance
2,4,6 and 8	Interim number between two adjacent numbers

tion as outputs. Furthermore, because the final weightings for the criteria are the normalized values of the Eigenvectors associated with the highest Eigenvalues of the AHP matrix, its consistency must be checked. The consistency of the comparisons was then examined using the consistency ratio (CR). The consistency ratio (CR) cannot be more than 0.1.

As a result, CR is a numerical index used to assess the consistency of the pairwise comparison matrix, and it is defined as

$$CR = CI/RI$$

Where CI stands for Consistency Index and RI stands for Random Index.

$$CI = \lambda_{max} - n / n - 1$$

Where ‘λ max’ is the main Eigenvalue and ‘n’ is the number of comparisons.

RESULTS AND DISCUSSION

Results

The different elevation values of the areas in Sairang are represented in the Elevation map Fig. 3 and the elevation values are given in Table 2.

The areas near the Tlawng river in Sairang are represented by variable slope angles which are represented in degrees. They range from the lowest slope angle category (Very gentle

slope) to the highest slope angle (Escarpment/cliff) category (Fig.4) and the areas covered in sq km are given in Table 3.

Table 2: Elevation details of the study area.

Height [in m]	Area [Sq km]	Percentage [%]
59 – 266.435	26.77	20.39
266.436 – 439.298	35.26	26.85
439.299 – 594.874	33.45	25.48
549.875 – 776.380	23.04	17.55
776.381 – 1156.678	12.77	9.72

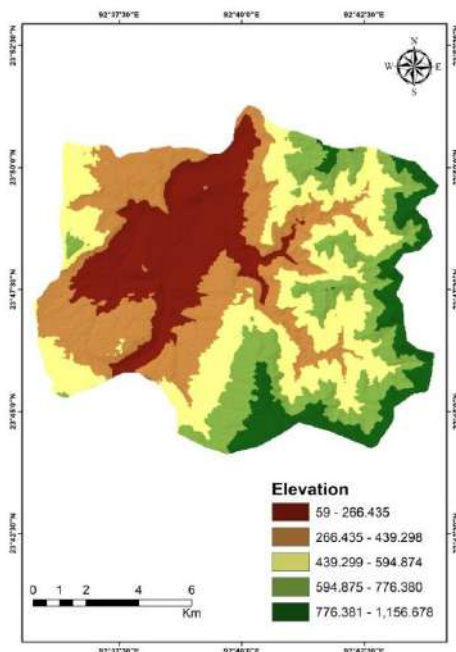


Fig. 3: Elevation map of the study area.

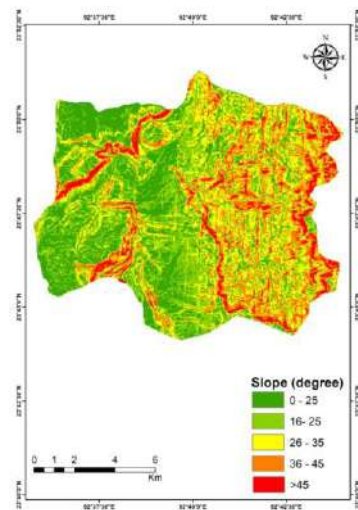


Fig. 4: Variable slope angles of the study area.

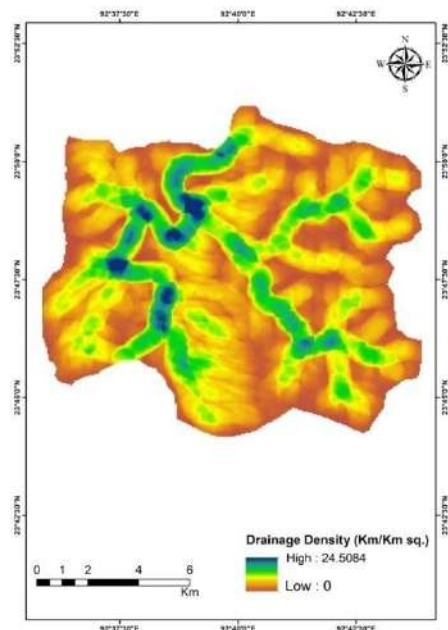


Fig. 5: Drainage density of the different areas in the watershed.

Drainage and drainage density factors are critical for calculating and assessing flood-prone locations along the Tlawng River. The drainage density calculations are given in Table 4 and the drainage density and drainage areas in and around Sairang village are given in Fig. 5 and Fig. 6 respectively.

A relevant part of waterlogging can be described by the flow accumulation which is the water flow below the downslope of the Tlawng river and it represents the ability to drain the excess water in the watershed area. This is represented by the flow accumulation values given in Table 5 and is also represented in Fig. 7.

The occurrence of floods is determined by the slope curvatures. The curvature values are given in Table 6 and are represented in Fig. 8. The areas having curvature values of -0.31-0.49 have the strongest correlation for the occurrence of floods. This covers 40.81% of the watershed area.

The thematic map for Land Use/ Land Cover for Sairang village is represented in Fig. 9 and the LULC values are given in Table 7. The built-up and cropland plantations have higher flood hazard values as compared to the other Land Use/ Land Covers.

The vegetation areas near the Tlawng river with different values are given in Table 8 and the different vegetation

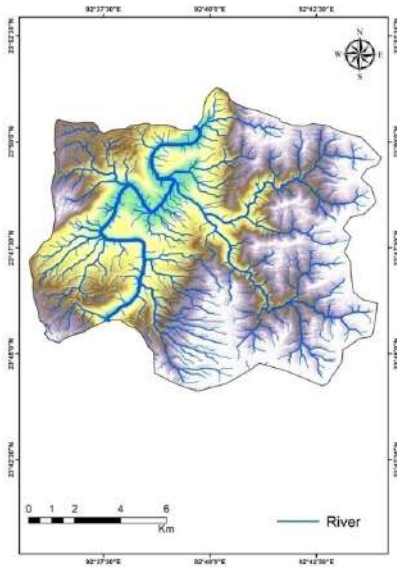


Fig. 6: Drainage of Tlawng river in Sairang.

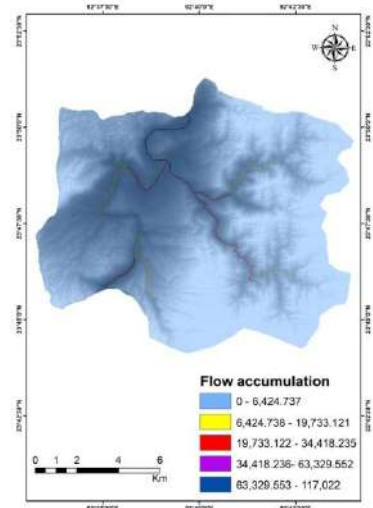


Fig. 7: Flow accumulation of different areas of the watershed.

Table 3: Slope angles of the study area.

Slope Angle	Category	Area [Sq km]	Percentage [%]
<15°	Very gentle slope	30.95	23.57
16°-25°	Gentle slope	37.10	28.26
26°-35°	Moderately slope	31.36	23.89
36°-45°	Steep slope	22.82	17.39
>45°	Escarpment/cliff	9.03	6.88

Table 4: Drainage Density of the study areas.

Category	Area [Sq km]	Percentage [%]
0 – 3.13	41.36	31.39
3.14 – 6.04	36.79	27.92
6.05 – 9.28	31.08	23.59
9.29 – 13.33	16.30	12.37
13.34 – 24.51	6.21	4.71

Table 5: Flow accumulation.

Category	Area [Sq km]	Percentage [%]
0 – 6,424.737	130.43	99.35
6,424.738 – 19,733.121	0.35	0.27
19,733.122 – 34,418.235	0.32	0.24
34,418.236 – 63,329.552	0.05	0.04
63,329.553 – 117,022	0.13	0.10

Table 6: Different areas with different curvature categories.

Category	Area [Sq km]	Percentage [%]
-9.68 – -1.49	5.67	4.32
-1.50 – -0.30	39.82	30.33
-0.31 – 0.49	53.58	40.81
0.50 – 1.57	26.75	20.38
1.58 – 15.39	5.46	4.16

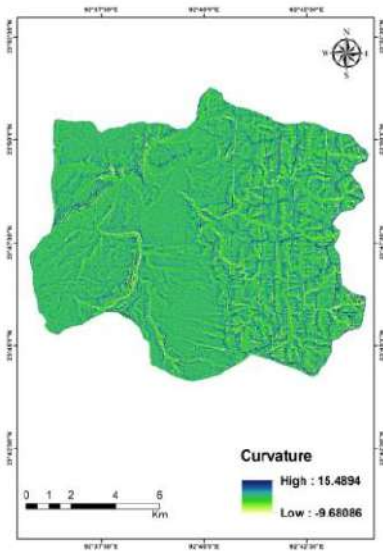


Fig. 8: Areas representing the Low and High Curvatures.

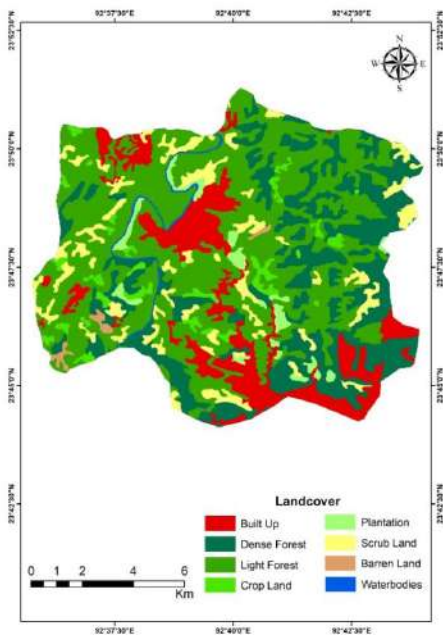


Fig. 9: Land Use classes in and around Sairang village.

Table 7: Different Land Use/ Land Cover classes.

Description	Area [Sq km]	Percentage [%]
Built Up	17.86	13.58
Dense Forest	32.19	24.48
Light Forest	61.53	46.80
Crop Land	4.15	3.15
Plantation	3.31	2.52
Scrub Land	10.72	8.16
Barren Land	0.75	0.57
Water bodies	0.95	0.73

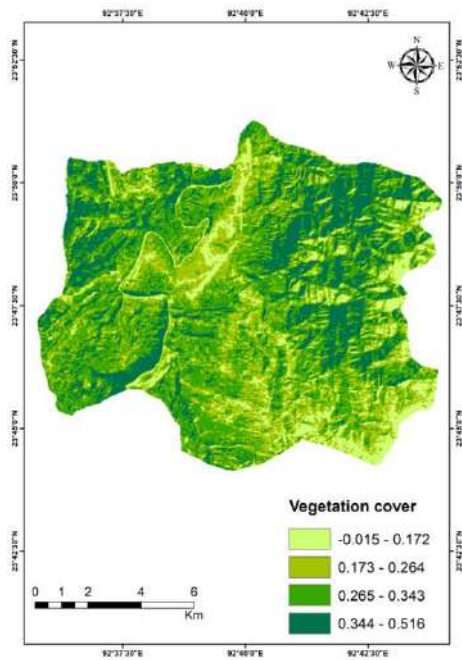


Fig. 10: Different vegetative covers in and around Sairang village.

Table 8: Vegetation cover in Sairang.

Category	Area [sq km]	Percentage [%]
-0.015 – 0.172	14.55	11.05
0.173 – 0.264	35.39	26.89
0.265 – 0.343	50.60	38.45
0.344 – 0.516	31.08	23.61

covers are represented in Fig. 10. The vegetative areas in the Sairang watershed have low flood hazards as there is a negative relationship between floods and vegetative cover density. The volume and pace of stormwater runoff are significantly reduced by vegetation and this prevents soil erosion and lowers flooding. The rainfall map and the soil map are given in Fig. 11 and Fig. 12 respectively.

Consistency Ratio

$$CR = CI/RI$$

$$CI = \lambda \max - n / n - 1$$

$$\lambda \max = 9.73$$

CI = 0.09

RI = 1.45

CR = 0.06 which is <0.1

Hence the consistency ratio is <0.1 and which is significant and the assigned weightage value is acceptable. To obtain the Consistency ratio 'CR', the Ratio Index 'RI'

is given in Table 9 and the pair-wise comparison matrix and normalized weight in Table 10. To obtain the weight

Table 9: Ratio index (RI) table for various n scores.

N	3	4	5	6	7	8	9	10
RI	0.58	0.89	1.12	1.24	1.32	1.41	1.45	1.49

Table 10: Pair wise comparison matrix and normalized weight.

Thematic map	Elevation	Slope	Drainage Density	Rainfall	Flow Accumulation	Landuse	Soil	Vegetation Cover	Curvature	Normalized Weight
Elevation	1.000	2.000	2.000	3.000	4.000	5.000	6.000	6.000	6.000	0.27
Slope	0.500	1.000	1.000	2.000	3.000	5.000	5.000	6.000	6.000	0.18
Drainage Density	0.500	1.000	1.000	2.000	3.000	5.000	6.000	6.000	6.000	0.19
Rainfall	0.333	0.500	0.500	1.000	2.000	3.000	4.000	6.000	6.000	0.12
Flow accumulation	0.250	0.333	0.333	0.500	1.000	2.000	3.000	5.000	6.000	0.09
Landuse	0.200	0.200	0.200	0.333	0.500	1.000	2.000	4.000	6.000	0.06
Soil	0.167	0.200	0.167	0.250	0.333	0.500	1.000	3.000	4.000	0.04
Vegetation cover	0.167	0.167	0.167	0.167	0.200	0.250	0.333	1.000	3.000	0.03
Topographic Curvature	0.167	0.167	0.167	0.167	0.167	0.167	0.250	1.000	1.000	0.02
SUM	3.283	5.567	5.533	9.417	14.200	21.917	27.583	38.000	44.000	1.00

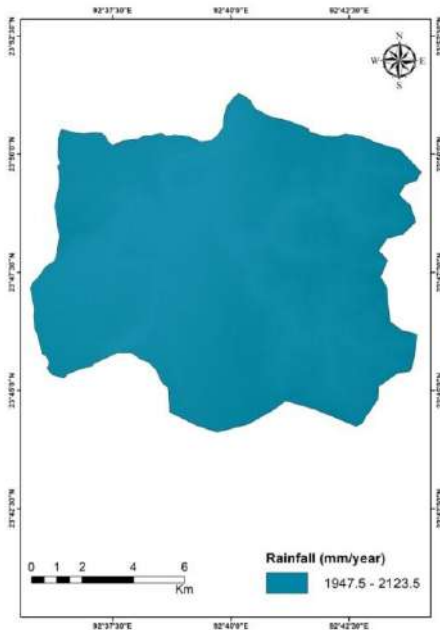


Fig.11: Rainfall map of Sairang watershed area.

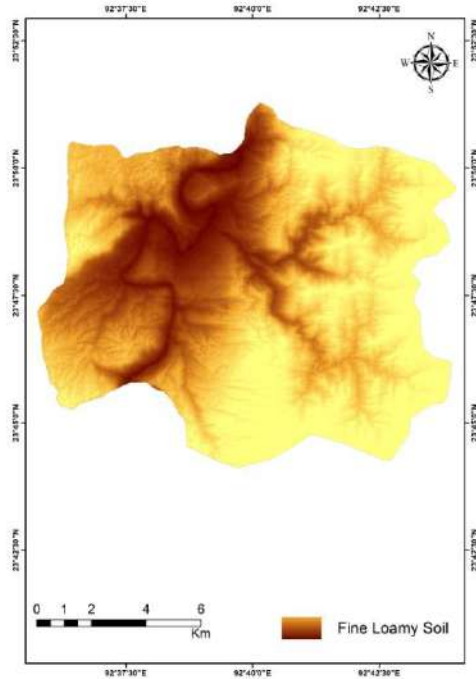


Fig. 12: Soil map of Sairang watershed area.

and ranks for each class, the aggregated weights for each parameter were given in Table 11 and the Assigned, Normalized weight and Ranks for the individual classes in Table 12.

Estimation of the Flood Hazard Potential Index (FHPI)

All of the aforementioned criteria were created as themed layers. It is also weighted and rated based on the nature of

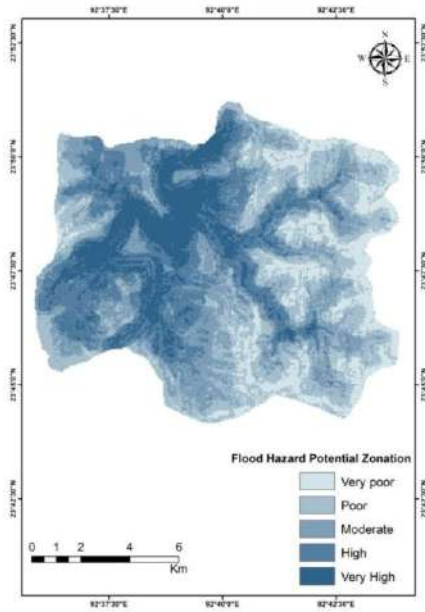


Fig. 13: Flood hazard potential zone map.

Table 11: Aggregated weight for each parameters.

Elevation	0.27
Slope	0.18
Drainage Density	0.19
Rainfall	0.12
Flow accumulation	0.09
Landuse	0.06
Soil	0.04
Vegetation cover	0.03
Topographic Curvature	0.02

layers were integrated into the *ArcGIS 10.2* software’s GIS environment. The table showed the weightage and rank. Flood hazard potential index can be calculated accordingly:

$$FHPI = (Ws*Rs) + (We*Re) + (Wcv*Rcv) + (Wvg*Rvg) + (Wdd*Rdd) + (Wt*Rt) + (Wlu*Rlu) + (Wr*Rr) + (Wfa*Rfa)$$

Where, W – Weightage, R- Rank, s – Slope, e – Elevation, cv – Curvature, vg – Vegetation Cover, dd- Drainage Density, r- Rainfall, t- Soil Texture, lu- Landuse, fa- Flow accumulation

its effects. The AHP technique was used to assign weightage. It is ranked based on its priorities. The weighted and ranked

Table 12: The Assigned, Normalized weight and Ranks for the individual classes.

Parameters	Class	Weight	Assigned Rank	Normalized Rank (NR)
Elevation	59 – 266.435	27	9	0.41
	266.436 – 439.298		7	0.32
	439.299 – 594.874		3	0.14
	549.875 – 776.380		2	0.09
	776.381 – 1156.678		1	0.04
Slope	<15°	18	5	0.33
	16°-25°		4	0.27
	26°-35°		3	0.2
	36°-45°		2	0.13
	>45°		1	0.07
Drainage Density	0 – 3.13	19	1	0.03
	3.14 – 6.04		5	0.17
	6.05 – 9.28		7	0.23
	9.29 – 13.33		8	0.27
	13.34 – 24.51		9	0.30
Rainfall	1947.5 – 2123.5	12	9	1

Table cont....

Parameters	Class	Weight	Assigned Rank	Normalized Rank (NR)
Flow accumulation	0 – 6,424.737	9	3	0.12
	6,424.738 – 19,733.121		4	0.16
	19,733.122 – 34,418.235		5	0.20
	34,418.236 – 63,329.552		6	0.24
	63,329.553 – 117,022		7	0.28
Land Use	Built Up	6	3	0.11
	Dense Forest		1	0.04
	Light Forest		2	0.07
	Crop Land		3	0.11
	Plantation		3	0.11
	Scrub Land		4	0.15
	Barren Land		4	0.15
	Water bodies		7	0.26
Soil	Fine Loamy Soil	4	3	1
Vegetation cover	-0.015 – 0.172	3	4	0.40
	0.173 – 0.264		3	0.30
	0.265 – 0.343		2	0.20
	0.344 – 0.516		1	0.10
Topographic Curvature	-9.68 – -1.49	2	1	0.07
	-1.50 – -0.30		2	0.13
	-0.31 – 0.49		3	0.20
	0.50 – 1.57		4	0.27
	1.58 – 15.39		5	0.33

Table 13: Flood Hazard potential zone of Sairang

Category	Area	Percentage
Very poor	17.05	13.11
Poor	33.85	36.01
Moderate	30.43	23.39
High	29.64	22.78
Very high	19.15	14.72

DISCUSSION

combining GIS and AHP for assessing flood susceptibility mapping in and around Tlawng river in the Sairang watershed area, a flood hazard zonation map was created based on different criteria such as slope, elevation, flow accumulation, drainage density, curvature, drainage (size of the watershed), soil, vegetation cover, LULC, and rainfall. Results for the study show that in this area, the flow accumulation, the elevation of the location of habitat areas, the distance from the Tlawng river drainage network, and the degree of the

slope are crucial for the flood risk in and around the Sairang watershed area. The resultant flood hazard potential zone of Sairang in Aizawl is categorized into five classes: Very Poor, Poor, Moderate, High, and Very High zones Fig.13. The affirmation and verification of this flood hazard map for Sairang are validated by flood events that have occurred in the Very High and High flood hazard areas of Sairang. Areas of the catchment, sub-catchment and the Tlawng river flood plain all have the potential for flooding.

More than 1/3 of the total watershed areas are lying in the Very High and High Hazard zones. 22.78% of the watershed falls in the High hazard zones and 14.72% of the watershed falls in the Very High Hazard zones (Table 13). Farming, fishing, and other activities which are carried out in the catchment area are all prone to flooding. To reduce flood risks along the Tlawng river and for flood hazard mitigation, integrated catchment management along the river should be developed. The local authorities, government officials, and other stakeholders can use this flood hazard potential zonation map to reduce the impact of floods in this hilly catchment area.

ACKNOWLEDGMENT

Malsawmtluanga is thankful to the Ministry of Earth Sciences, Govt of India for the work which is carried out under the project sanction no MoES/PAMC/H&C/ 115/ 2018-PC-II dated 24.01.2020.

REFERENCES

- Ajin, R.S., Krishnamurthy, R.R., Jayaprakash, M. and Vinod, P.G. 2013. Flood hazard assessment of Vamanapuram river basin, Kerala, India: An approach using remote sensing & GIS techniques. *Adv. Appl. Sci. Res.*, 4(3): 263-274.
- Danumah, J. H., Odai, S. N., Saley, B. M., Szarzynski, J., Thiel, M., Kwaku, A., Kouame, F.K. and Akpa, L. Y. 2016. Flood risk assessment and mapping in Abidjan district using multi-criteria analysis (AHP) model and geoinformation techniques, (Cote D'Ivoire). *Geoenvironmental Disasters.*, 3(1): 1-13.
- Das, B., Pal, S.C. and Malik, S. 2017. Assessment of flood hazard in a riverine tract between Damodar and Dwarkeswar river, Hugli district, West Bengal, India. *Spatial Infor. Res.*, 26(1): 91-101.
- Das, S. 2018. Geographic information system and AHP-based flood hazard zonation of Vaitarna basin, Maharashtra, India. *Arab. J. Geosci.*, 11(19): 1-13.
- Dash, P. and Sar, J. 2020. Identification and validation of potential flood hazard areas using GIS-based multi-criteria analysis and satellite data-derived water index. *J. Flood Risk Manag.*, 13(3): 1-14.
- Economics and Statistics. 2019. *Statistical Handbook of Mizoram*. Govt of Mizoram, pp. 78.
- Ganguly, K. and De, S.K. 2015. Spatio-temporal analysis of flood and identification of flood hazard zone of West Tripura district, India using Integrated Geospatial Technique. *Hill Geograp.*, 31(1): 1-22.
- Ghezelsofloo, A.A. and Hajibigloo, M. 2020. Application of flood hazard potential zoning by using AHP Algorithm. *Civil Eng. Res. J.*, 9(5): 150-159.
- Gigovic, L., Pamučar, D., Bajić, Z. and Drobnjak, S. 2017. Application of GIS-interval rough AHP methodology for flood hazard mapping in urban areas. *Water*. 9(6): 360-366.
- Hammami, S., Zouhri, L., Souissi, D., Souei, A., Zghibi, A., Marzougui, A. and Dlala, M. 2019. Application of the GIS-based multi-criteria decision analysis and analytical hierarchy process (AHP) in the flood susceptibility mapping (Tunisia). *Arabian J. Geosciences.*, 12(21): 1-16.
- Hazarika, N., Barman, D., Das, A.K., Sarma, A.K. and Borah, S.B. 2018. Assessing and mapping flood hazard, vulnerability, and risk in the upper Brahmaputra River valley using stakeholders' knowledge and multicriteria evaluation (MCE). *J. Flood Risk Manag.*, 11: 700-716.
- Khaleghi, S. and Mahmoodi, M. 2017. Assessment of flood hazard zonation in a mountainous area based on GIS and analytical hierarchy process. *Carpathian J. Earth Environ. Sci.*, 12(1): 311-322.
- Laikangbam, L., Loukrakpam, C. and Singh, T. S. 2019. Flood hazard zonation of Imphal river, Manipur, India, using AWS data. *Int. J. Eng. Adv. Technol.*, 8(4): 1676-1680.
- Lalhmingliana., R., Ch, U.B. and Saha, G. 2019. Computational water management strategy of Tlawng river basin using geoinformatics. *Environ. Eng. Res.*, 25(5): 693-699.
- Maji, A.K., Dubey, P.N., Sen, T.K., Verma, T.P., Marathe, R.A., Chamuah, G.S. and Gajbhiye, K.S. 2001. Soils of Mizoram: Their kinds, distribution, characterization, and interpretations for optimizing land use. *NBSS Publ.*, 75: 28.
- Ouma, O.Y. and Tateishi, R. 2014. Urban flood vulnerability and risk mapping using integrated multi-parametric AHP and GIS: Methodological overview and case study assessment. *Water*, 6(6): 1515-1545.
- Saaty, T.L. 1980. *The Analytic Hierarchy Process*. McGraw Hill, New York, pp.70.
- Saaty, T.L. 2008. Decision making with the analytic hierarchy process. *Int. J. of Ser. Sci.*, 1(1): 83-98.
- Siddayao, G.P., Valdez, S.E. and Fernandez, P.L. 2015. Modeling flood risk for an urban CBD using AHP and GIS. *Int. J. Inform. Edu. Technol.*, 5(10): 748-753.
- Sinha, R., Bapalu, G.V. Singh., L.K. and Rath, B. 2008. Flood risk analysis in the Kosi river basin, north Bihar using the multi-parametric approach of analytical hierarchy process (AHP). *J. Indian Soc. Remote Sens.*, 36(4): 335-349.
- Vignesh, K.S., Anandakumar, I., Ranjan, R. and Borah, D. 2021. Flood vulnerability assessment using an integrated approach of multi-criteria decision-making model and geospatial techniques. *Model. Earth Sys. Environ.*, 7(2): 767-781.



Process of Life Cycle Installation of Wastewater Treatment and up to Water Reuse

Frances Roi Seston Tampubolon*†, Arief Sabdo Yuwono**, Armansyah Halomoan Tambunan*** and Noer Azam Achsani****

*Natural Resources and Environmental Management, Bogor Agricultural Institute, 16177, Indonesia

**Department of Civil and Environmental Engineering, IPB University, Bogor, 16680, Indonesia

***Department of Mechanical and Biosystems Engineering, IPB University, Bogor, 16680, Indonesia

****School of Business, IPB University, Bogor, 16151, Indonesia

†Corresponding author: Frances Roi Seston Tampubolon; roipb19frances@apps.ipb.ac.id

Nat. Env. & Poll. Tech.
Website: www.neptjournal.com

Received: 07-03-2021

Revised: 15-04-2021

Accepted: 01-05-2021

Key Words:

Wastewater management
Global warming
Holistic
Life Cycle

ABSTRACT

The life cycle assessment (LCA) of the wastewater treatment plant (WWTP) has several categories in the resulting impact analysis. One of them is a wastewater treatment plant on campus or university. Various emissions from WWTP and their impact factors are analyzed using software and utilizing the Eco-inventory database. Recycled water from factories has a positive impact on the categories assessed. System treatment overrides the effects of recycled water in other types such as potential terrestrial eco-toxicity, global warming potential, particulate matter formation, fossil depletion potential, and others. However, untreated sewers' social effects and the environmental impact of compost generated by the system have not been thoroughly analyzed by a more holistic analysis. By using the LCA method, these results can be seen in Enim River's environment expressed in GWP units (global warming potential) and human health expressed in ODP units (Ozone Depletion Potential). Several studies have also been conducted on LCA, which has problems with wastewater. One of the most recent research analyses various wastewater treatment strategies, such as aerobic against anaerobic, chemical versus chemical, and biological combinations. The Enim River is found in the Indonesian province of South Sumatra. The Muara Enim Regency area is where the river flows from upstream to downstream. The Enim River is a child of the Lematang River. The GWP value had a GWP of 16% before being treated in wastewater, and it had a GWP of 41.3% after being treated with sewage. This result means that treating wastewater requires energy to do so. Before treatment, the MDP value was 10.4%, and after treatment was 20.4%. However, further action after the management of wastewater gives significant value to the assessment of GWP, MDP, and ODP. The three results provided a reduction value for the reuse of treated water and reused as water needs.

INTRODUCTION

Water is everyone's survival because it is their primary source of income (Maktabifard et al. 2018). As a result, in some dry places and semi-arid circumstances, it is increasingly vital to pay attention to water scarcity (Reznik et al. 2019, Paskett 1998). Water scarcity will result if rainfall drops (Lotfi et al. 2020), causing more serious difficulties. Water management will be required to meet the increased needs of a rapidly rising population and the complete depletion of water supplies (Glenn et al. 2009). Any new water sources to be regenerated or wastewater treatment techniques must be established and developed to provide an adequate water supply (Lahrich et al. 2021). There will be several essential options given the various treatment techniques that can be created whereby wastewater can be treated and used for other purposes, such as the need for gardening

and bathing (Dingemans et al. 2020, Raschid-sally et al. 2001).

Wastewater treatment facilities are typically built by government departments (Hartley et al. 2019), although major organizations (Juan-García et al. 2017) or businesses can also build their WWTP (Waste Water Treatment Plant) (Raghuvanshi et al. 2017). The WWTP's mission is to purify untreated water from a wide range of sources, including households, offices, laboratories, and sanitation facilities so that it can be reused. There are both primary and secondary process steps at the WWTP (Abdel-Fatah 2018).

The water then flows into the aeration tank in the primary treatment process and then adds chemicals with high nutritional content, such as diammonium phosphate (DAP). For this condition, most of the microbial action is still in the air (Kheiri et al. 2013). Aerobic oxidation in the aeration tank causes organic matter degradation in microorganisms' pres-

ence (Wang et al. 2017). Furthermore, in the clarifier, sludge (Araromi et al. 2018) and water are separated outside. This is also part of the secondary processing process. The sludge is then collected and air-dried before storage and further use.

The semi-treated water then enters the chlorination tank, where disinfection is carried out. The disinfected water then passes through a double filter media to maintain the water condition for further storage (Zhu et al. 2012). Untreated sewers have social and environmental impacts (Dolar et al. 2019) if disposed of without proper treatment (Maktabifard et al. 2018). Wastewater treatment is also not an environmentally friendly process (Salem 2012) and even economically. Such processing will require a lot of energy and several forms of chemicals. An analysis will then be needed for the environmental benefits of water savings and ecological damage done to water treatment (Shakouri & Yazdi 2014, Zarei 2020).

Some wastewater treatment can be done physically, chemically, and biologically. Physical therapy is to remove suspended or levitated material from wastewater through gravity deposition. Meanwhile, chemical processing is by reducing the chemical content in sewage with the addition of chemicals. Deposition or filtering can physically separate the sediment as a result of the process. Finally, biological processing involves eliminating or removing pollutants using biological activity (microorganisms) in aerobic or anaerobic environments. In general, the physical processing units include bar screen, communicator, grit chamber, equalization, sedimentation, centrifugation, flocculation, and membrane filtration.

Whereas the residual pollutant discharge from the infiltration field drainage is subject to wastewater costs, the treated wastewater irrigation in the agricultural sector during the vegetation period is considered agricultural land treatment measures exempted from the cost of wastewater. This practice's cost reduction is estimated by calculating the wastewater's hypothetical cost (Diaz-Elsayed et al. 2019) operator. If the mixed-sludge irrigated wastewater was discharged directly into surface water bodies, the treatment facility would be compensated (Maaß & Grundmann 2016).

Another example of a unit process carried out in the United States, namely, the wastewater pasteurization (WP) process, is a disinfection technology that may have developed rapidly with cost and environmental advantages over traditional wastewater treatment processes (Sanciole et al. 2020). It could exploit waste heat from on-site power plants by using biogas or gas from cities or community supplies to heat wastewater to inactivate associated Pasteurization technology has been widely used in the food industry for many years, but its application on a large scale to treat wastewater has only recently emerged. It has been demonstrated in the city of the Laguna Santa Rosa Wastewater Reclamation

Plant, where validation testing was carried out as part of the California Department of Public Health (CDPH, now called the Drinking Water Division (DDW)) to review new technologies for treating wastewater for reuse and provision conditional consent water (Sanciole et al. 2020).

There are advantages of using pasteurization to disinfect wastewater because it does not contain the harmful effects of unreacted disinfectant chemicals and the formation of hazardous disinfection byproducts known as a disinfectant byproduct (DBP). Chlorination and ozonation are commonly used for the disinfection of wastewater, and their extensive use has resulted in disinfectant byproducts (DBP) which are very dangerous. DBP from chlorination is harmful to humans and the environment (Chon et al. 2012) and causes acute, measurable toxicity effects even from low residual chlorine levels (Hamilton & Miller 2002).

The methodological framework used on the life cycle provided by the international standards organization (ISO) 14040 assesses the environmental impact of the wastewater treatment process on campus or university sites (Vedachalam 2012). The impact assessment carried out with a simple LCA is to visualize and analyze wastewater treatment processes' environmental impact. The Eco-invent data set software was used to model the movement of materials and energy (Raghuvanshi et al. 2017). After entering the input value into the LCA process, the Ecoinvent OpenLCA software can likewise produce good results.

A life cycle assessment (LCA) based on a thorough understanding of the true quantity of data received is used to conduct this analysis. LCA is a compilation and evaluation of the outputs and potential environmental consequences during a product's life cycle. LCA studies aid in determining the best method/technique from an ecological point of view. For LCA, four phases are required for the LCA study, namely definition of objectives and scope, analysis of life cycle inventory (LCI), life cycle impact assessment (LCIA), and interpretation (Raghuvanshi et al. 2017). LCA water treatment systems have found importance in recent literature due to their holistic approach. Several studies have also been conducted on LCA, which has problems with wastewater. One of the most recent studies compares different wastewater treatment techniques such as aerobic to anaerobic, chemical to chemical and biological combinations (Sode et al. 2013). Phosphorus recycling for agricultural land (because of its potential for fertilization) (Shamblen & Binder 1996) is more suitable to control to reduce the impact of depletion of fossil fuels and climate change compared to sludge incineration (Najafzadeh & Zeinolabedini 2018, Mannino et al. 2008).

Another method related to LCA WWTP carried out in China has revealed that the use of renewable energy (wind,

in this case) increasing the quality of waste will reduce environmental impact (Jain et al. 2020). This study highlights the importance of generating electricity from renewable sources to minimize fossil fuel depletion and pollutant emissions. A more refined approach is used to study LCA in WWTP by finding out characterization factors (CFs) for measuring pharmaceutical and personal care products (PPCP) in wastewater. Other studies have reported on a novel strategy for identifying the optimum WWTP process that tries to incorporate environmental concerns with LCA methodology and economic criteria.

MATERIALS AND METHODS

Unit Process Mechanism

The unit process mechanism is used to evaluate the environmental impact of process wastewater treatment at a specific place, such as a riverbank (Kristensen et al. 2018). For the LCA process, it is necessary to set goals or goals to be done. One of them is the boundary, namely gate to gate. What is meant by the gate to gate? Is it from processed wastewater to treated wastewater?

Data collection is carried out during operation over a period repeated. The operational input and quantity of wastewater inflows are measured at different times of the year. Specific processor maintenance-related data were obtained by conducting semi-structured interviews with staff working in the factory. Secondary data for modeling the flow of materials and energy are collected from the internet, datasheets, etc.

Research using tools to test the use of treated wastewater along the Enim River has a relationship with other available water resources taking into account their quantity and quality

(Carey & Migliaccio 2009, Almanaseer et al. 2020), including the agronomic, environmental, and economic components (Rossum 2020). The study area's location is in the overall district of Muara Enim, consisting of 7.483 km², and the number of sections is 22, and the number of villages is 246, as shown in Fig. 1.

In this study's results, the operational input is measured in terms of electricity, and diesel is burned for power generation, urea and chlorine. Chlorine is used through a dosing pump to kill bacteria and other microbes remaining in treated water, but chlorine is a very toxic substance (Shakouri & Yazdi 2014)(Skander et al. 2015). The ReCiPe method (LCA Ecoinvent) provides results in three main endpoint categories: ecosystem quality, human health, and resources (Rathod et al. 2009). Ecosystem quality has nine sub-categories: agricultural land use, climate change, freshwater eco-toxicity, freshwater eutrophication, marine eco-toxicity, transformed natural land, terrestrial acidification, terrestrial eco-toxicity (Godoy et al. 2020), and city land occupation. There are six sub-categories regarding human health, namely climate change (human health) (Dingemans et al. 2020), human toxicity, ionizing radiation, ozone depletion, particulate matter photochemical oxidant formation. In the end, resources have two sub-categories, namely fossil depletion and metal depletion. The results of this study have 18 categories selected to show the environmental impacts of treated wastewater. The nine types determined by their abbreviations are climate change or global warming potential (GWP), freshwater eco-toxicity potential (FETP), freshwater eutrophication potential (FEP), human toxicity potential (HTP), metal depletion potential (MDP), ozone depletion potential (ODP), particulate matter formation (PMF), terrestrial eco-toxicity

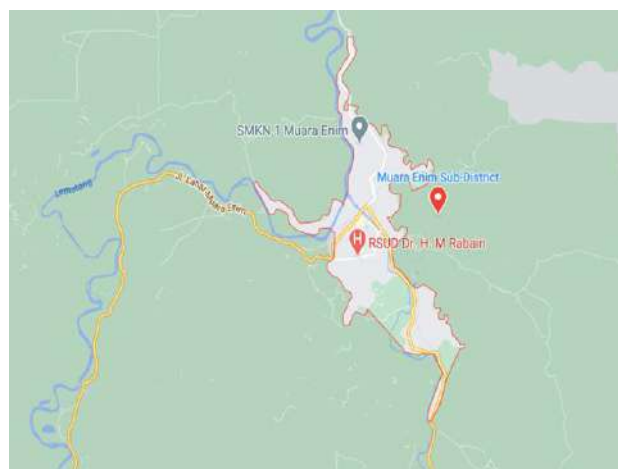


Fig. 1: Location of study area of Enim River in south Sumatra, Indonesia.

potential (TETP), and water depletion potential (WDP) as can be seen at Fig. 2 and Fig. 3.

RESULTS

Water Quality Before Treatment

Electricity and diesel are used to generate electricity, urea, and chlorine. The process of the energy source used affects the resulting emissions. These emissions cause damage to ambient air quality and ultimately to human health. It was found that energy requirements for the aeration tank, distribution treated water, collection tank, and dual media filters significantly affected the environment in the GWP, CC-HH,

PMF, and FDP (Atiqah et al. 2014) categories (Lotfi et al. 2020). The actual yield values from the endpoint assessment of the treatment phase are tabulated in Table 1.

Water Quality after Treatment

The percentage distribution of the midpoint assessment result indicates that the wastewater treatment process stage has a nearly negligible effect on the environment than the other phases. Additionally, all steps show similar patterns of impact across all categories. As in the endpoint assessment, the treatment phases that impact water collection and sludge activation (Owusu-Twum & Sharara 2020, Brockmann et al. 2021) and redistribution are presented in Table 2.

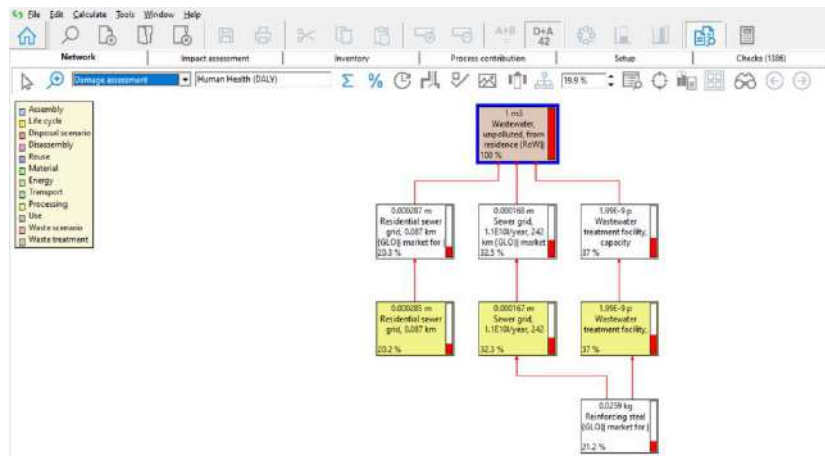


Fig. 2: Networking the normalization of the human health.

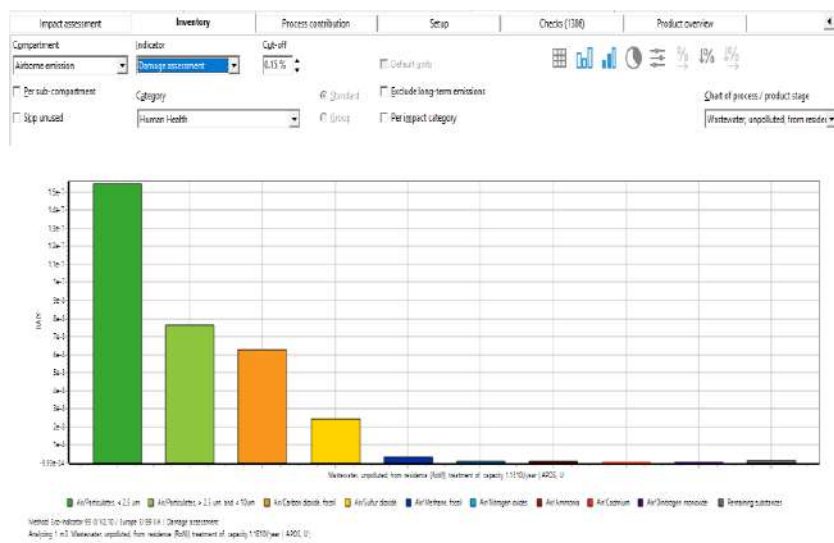


Fig. 3: Inventory airborne emissions damage emissions.

Table 1: The results of the study midpoint assessment.

Item	Ecosystem Quality (GWP)	Human Health (ODP/ Ozone Depletion Potential)	Resources (MDP/Metal Depletion Potential)
Water Collection (%)	16	26.4	10.4
Sludge Activation (%)	31.3	39.6	52
Treatment (%)	0.8	0.9	1
Purification (%)	12.4	9.9	10.4
Redistribution (%)	38.9	23.1	26

Table 2: Results of the study midpoint assessment.

Item	Ecosystem Quality (GWP)	Human Health (ODP/ Ozone Depletion Potential)	Resources (MDP/Metal Depletion Potential)
Water Collection (%)	41.3	35.4	20.4
Sludge Activation (%)	16	30.6	40
Treatment (%)	0.8	0.9	3
Purification (%)	10.4	10.9	11.4
Redistribution (%)	30.9	22.1	25

It was found that the energy requirements for the aeration tank, distribution treated water, collection tank, and dual media filter significantly affected the environment in the GWP, CC-HH, PMF, and FDP categories.

The first condition is if the wastewater is treated and its impact on the environment (Wagner 2005) and further assessed. The second condition is a consequence of wastewater treatment, and the treated water is used for irrigation purposes.

The effect of an equivalent amount of fresh water is then saved. The third condition depicts the consequences of not reusing purified water. This may be seen in the treatment outcomes of irrigation water, which have dramatically reduced environmental consequences across the board (Table 3). Fig. 4 and Fig. 5 below presents an impact assessment covering climate change, ozone layer depletion, acidification, and land use. The unit is stated as DALY (Disability Adjusted Life Year).

DISCUSSION

The results of a review of articles from research conducted by (Raghuvanshi et al. 2017) provide an analysis that when processing industrial wastewater requires electrical energy in its processing. The most significant consideration is the energy source process used, which affects the emissions produced (Ramírez-Melgarejo et al. 2019). These emissions cause damage to ambient air quality and ultimately to human health. The impact of the FDP is due to the significant amount of fossil fuels required for energy. These results can be seen in the environment expressed in GWP units (global warming potential) and human health expressed in units of ODP (Ozone Depletion Potential). Before treatment, the MDP value was 10.4%, and after treatment was 20.4%. This result means that treating wastewater requires energy to do so. This energy in the form of energy requirements for the aeration tank, distribution treated water, collection tank, and dual filter media significantly affects the environment in the GWP, ODP and PMF categories.

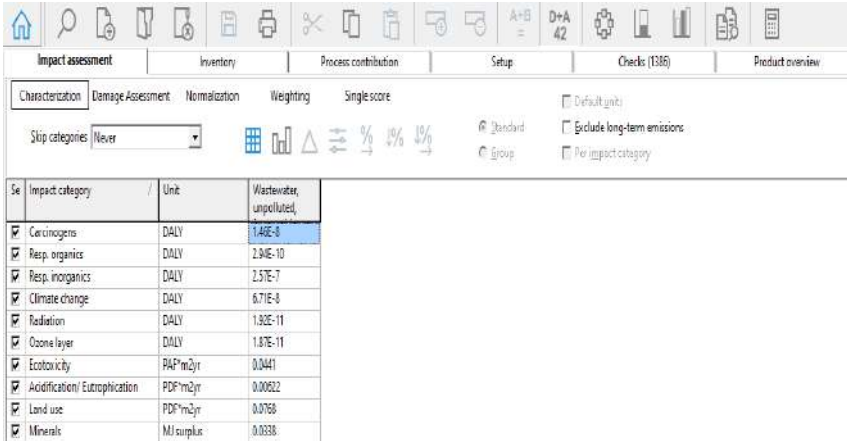
Table 3: Results of impact savings through reuse of treated water.

Item	Ecosystem Quality (GWP)	Human Health (ODP/ Ozone Depletion Potential)	Resources (MDP/Metal Depletion Potential)
Water Collection (%)	11.4	53.1	35.5
Sludge Activation (%)	41.3	29.6	32
Treatment (%)	0.8	0.9	1
Purification (%)	19.4	9.9	10.4
Redistribution (%)	26.9	6.5	21

Likewise, the results on MDP and ODP were given before and after treating the wastewater produced. Before treatment in wastewater, the GWP value gave a GWP of 16%, and after being treated with sewage, it gave a GWP of 41.3%. However, subsequent action following wastewater management adds significant value to the GWP, MDP, and ODP assessments (Enström et al. 2019). The three outcomes showed a reduction in the cost of reusing treated water for other purposes. Functional water, on the other hand, cannot be utilized as drinking water. Watering plants (gardening) or irrigation systems for rice fields are the following applications.

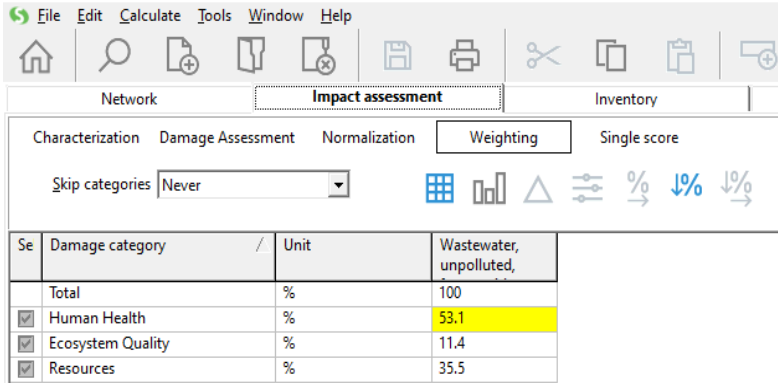
The most important thing from the article review analysis that I have done is on the sludge produced from wastewater. The most important thing is that it has not considered sludge for fields and can be used as a fertilizer substitute. Studies like these can guide authorities and governments to optimize process parameters to reduce environmental impacts.

Although in wastewater management, it is for the reuse of water for the purposes it is intended for, and it is necessary to consider environmental protection. At the time of wastewater management will require electrical energy needs to do it. Electrical power is whether using fossil energy sources or using electrical energy from renewable energy (An et al. 2019). Suppose the use of electricity still uses fossil energy, of course. In that case, it will impact the potential for global warming or the potential for depletion of the ozone layer. Therefore it provides an LCA (life cycle assessment) analysis in the process. This is very important because it has been explained at the beginning of the introduction in this review article that LCA analysis will require a goal or goals to be achieved. When treating wastewater, the limitations will yield the best outcomes. If the limit is to reuse water, it must be verified that it has no substantial environmental impact during the processing process, either through emissions or later environmental improvements.



Se	Impact category	Unit	Wastewater, unpolluted,
<input checked="" type="checkbox"/>	Carcinogens	DALY	1.46E-8
<input checked="" type="checkbox"/>	Resp. organics	DALY	2.94E-10
<input checked="" type="checkbox"/>	Resp. inorganics	DALY	2.57E-7
<input checked="" type="checkbox"/>	Climate change	DALY	6.71E-8
<input checked="" type="checkbox"/>	Radiation	DALY	1.92E-11
<input checked="" type="checkbox"/>	Ozone layer	DALY	1.87E-11
<input checked="" type="checkbox"/>	Ecotoxicity	PAP* m^2 /yr	0.0441
<input checked="" type="checkbox"/>	Acidification/ Eutrophication	PDP* m^2 /yr	0.00922
<input checked="" type="checkbox"/>	Land use	PDP* m^2 /yr	0.0768
<input checked="" type="checkbox"/>	Minerals	MJ surplus	-0.0338

Fig. 4: Impact assessment wastewater unpolluted.



Se	Damage category	Unit	Wastewater, unpolluted,
	Total	%	100
<input checked="" type="checkbox"/>	Human Health	%	53.1
<input checked="" type="checkbox"/>	Ecosystem Quality	%	11.4
<input checked="" type="checkbox"/>	Resources	%	35.5

Fig. 5: Weighting of Impact Assessment

CONCLUSION

This paper presents an assessment of wastewater treatment along a watershed. The results obtained have provided information that the electricity required to carry out the entire treatment process (water collection, sludge activation, treatment, purification, and redistribution) has the highest impact across all category assessments. Moreover, the use of water for irrigation purposes reduces the impact caused by the treatment process to a large extent and ultimately reduces the environmental burden. It should be noted that the global warming potential increases with treatment, but the water depletion potential decreases. The research helps decision-makers to make informed decisions to choose between medicine or no treatment (no reuse) of wastewater. This may be observed in the results of MDP and ODP tests performed before and after the effluent was treated. The GWP value had a GWP of 16 per cent before being treated in wastewater, and it had a GWP of 41.3 per cent after being treated with sewage. The analysis in this work is restricted to the system boundaries (gate to gate) and research considerations.

This study has not considered sludge for fields and can be used as a substitute for fertilizer. Studies such as these can guide authorities and governments to optimize process parameters to reduce environmental impacts. This wastewater treatment model can be continued to assess the ecological impact in larger areas such as large or small cities, where the supply network and redistribution of wastewater also play an essential role in energy consumption. Therefore it will be interesting to look at the negative environmental impacts with the combined treatment and positive effects of reusing treated water and using sludge as compost for gardening or agriculture.

ACKNOWLEDGMENT

This research was funded by the Education Fund Management Agency (LPDP) from the Ministry of Finance of the Republic of Indonesia.

REFERENCES

Abdel-Fatah, M.A. 2018. Nanofiltration systems and applications in wastewater treatment: Review article. *Ain Shams Eng.*, 9(4): 3077-3092. <https://doi.org/10.1016/j.asej.2018.08.001>.

Almanaseer, N., Muna, H. and Raha, A. 2020. Hydrological and environmental impact of wastewater treatment and reuse on Zarqa river basin in Jordan. *Environ. MDPI*, 7(2): 14. <https://doi.org/10.3390/environments7020014>.

An, Y., Zhang, L. and Adom, P.K. 2019. Economics of wastewater management in China's industry. *Environment and Development Economics*, 24 (5): 457-78. <https://doi.org/10.1017/S1355770X19000202>.

Araromi, D.O., Majekodunmi, O.T., Adeniran, J.A. and Salawudeen, T.O. 2018. Modeling of an activated sludge process for effluent prediction-a

comparative study using ANFIS and GLM regression. *Environmental Monitoring and Assessment*, 190(9): 1-17.

Atiqah, N., Abustan, I., Mahyun A.W. and Rose, F.M. 2014. Water quality changes due to effect of Arowana aquaculture activities at Bukit Merah. *Advances in Environmental Biology*, 8(22): 30-34.

Brockmann, D., Yves, G., Chul, P., Kim, M., Arnaud, H. and Jérôme, H. 2021. Wastewater treatment using an anoxygenic photogravure-based process has a lower environmental impact than conventional activated sludge processes. *Bioresour. Technol.*, 9: 319. <https://doi.org/10.1016/j.biortech.2020.124204>.

Carey, R.O. and Migliaccio, K.W. 2009. Contribution of wastewater treatment plant effluents to nutrient dynamics in aquatic systems. *Environ. Manag.*, 44(2): 205-217. <https://doi.org/10.1007/s00267-009-9309-5>.

Chon, H.S., Dieudonné, G.O. and Nikolaos, V. 2012. Assessing the relative contribution of wastewater treatment plants to levels of metals in receiving waters for catchment management. *Water Air Soil Pollut.*, 223(7): 3987-4006. <https://doi.org/10.1007/s11270-012-1166-9>.

Díaz-Elsayed, N., Nader, R., Tianjiao, G., Shima, M. and Qiong, Z. 2019. Wastewater-based resource recovery technologies across scale: A review. *Resour. Conserv. Recycl.*, 145: 94-112. <https://doi.org/10.1016/j.resconrec.2018.12.035>.

Dingemans, M.M., Smeets, P.W., Medema, G., Frijns, J., Raat, K.J., van Wezel, A.P. and Bartholomeus, R.P., 2020. Responsible water reuse needs an interdisciplinary approach to balance risks and benefits. *Water*, 12(5), p.1264. Doi: 10.3390/w12051264.

Dolar, D.M., Racar, S. and Košuti, K. 2019. Municipal wastewater reclamation and water reuse for irrigation by membrane processes. *Chem. Biochem. Eng. Quart.*, 33(3): 417-425. <https://doi.org/10.15255/CABEQ.2018/1571>.

Enström, A., Timo, H., Adrian, S., Michael, G. and Kuan, Y.L. 2019. Introducing a new GHG emission calculation approach for alternative methane reduction measures in the wastewater treatment of a palm oil mill. *Environ. Develop. Sustain.*, 21(6): 3065-3076. <https://doi.org/10.1007/s10668-018-0181-4>.

Glenn, E.P., Casey, M., Vanda, G., Pamela, L.N., Fiona, J. and Janick, A. 2009. Deficit irrigation of a landscape halophyte for reuse of saline wastewater in a desert city. *Landsc. Urban Plan.*, 89(3-4): 57-64. <https://doi.org/10.1016/j.landurbplan.2008.10.008>.

Godoy, L., Gabriel, G., Abrahão, B.R., Mônica, R.G., Silvana, D.D. and Lucas, B.G. 2020. Production of supplementary cementitious material as a sustainable management strategy for water treatment sludge waste. *Case Stud. Constr. Mater.*, 12: 329. <https://doi.org/10.1016/j.cscm.2020.e00329>.

Hamilton, A.P.A. and Miller, T.L. 2002. Lessons from the national water-quality assessment : A decade of intensive water-quality studies indicates that reducing diffuse nonpoint water contamination requires new tools and a holistic management approach. *J. Soil Water Conserv.*, 57(1): 16A-21A

Hartley, K., Cecilia, T. and Asit, K.B. 2019. A formal model concerning policy strategies to build public acceptance of potable water reuse. *J. Environ. Manag.*, 250: 109505. <https://doi.org/10.1016/j.jenvman.2019.109505>.

Jain, R., Harshita, N., Megha, M., Anushree, M. and Upain, K.A. 2020. Towards green thermal power plants with blowdown water reuse and simultaneous biogenic nanostructures recovery from waste. *Resour. Conserv. Recycl.*, 11: 105283. <https://doi.org/10.1016/j.resconrec.2020.105283>.

Juan-García, P., Butler, D., Comas, J., Darch, G., Sweetapple, A. and Corominas, L. 2017. Resilience theory incorporated into urban wastewater systems management. *Water Res.*, 115: 149-61. <https://doi.org/10.1016/j.watres.2017.02.047>.

Kheiri, R., Naser, H. and Mehrouz D. 2013. Efficacy evaluation of four different culture and PCR-based methods of *Escherichia coli* detection in water samples. *Advances in Environmental Biology*, 7(9): 2689-2694.

- Kristensen, E., Mikkel, M., Philippe Massicotte, O., Pedersen, S., Markager, R. and Theis, K. 2018. Catchment tracers reveal discharge, recharge, and sources of groundwater-borne pollutants in a novel lake modeling approach. *Biogeosciences*, 15(4): 1203-1216. <https://doi.org/10.5194/bg-15-1203-2018>.
- Lahrich, S.F., Laghrib, A., Farahi, M., Bakasse, S., Saqrane, K. and M.A. and Mhammed, E. 2021. Review on the contamination of wastewater by COVID-19 virus: Impact and treatment. *Sci. Total Environ.*, 751: 142325. <https://doi.org/10.1016/j.scitotenv.2020.142325>.
- Lotfi, K., Hossein, B., Isa Ebtehaj, R., Ali Akbar, Z. and Bahram, G. 2020. A novel stochastic wastewater quality modeling based on fuzzy techniques. *J. Environ. Health Sci. Eng.*, 20: 530 <https://doi.org/10.1007/s40201-020-00530-8>.
- Maaß, O. and Grundmann, P. 2016. Added-value from linking the value chains of wastewater treatment, crop production, and bioenergy production: A case study on reusing wastewater and sludge in crop production in Braunschweig (Germany). *Resour. Conserv. Recycl.*, 107: 195-211. <https://doi.org/10.1016/j.resconrec.2016.01.002>.
- Maktabifard, M., Ewa, Z. and Jacek, M. 2018. Achieving energy neutrality in wastewater treatment plants through energy savings and enhancing renewable energy production. *Rev. Environ. Sci. Biotechnol.*, 17: 540. <https://doi.org/10.1007/s11157-018-9478-x>.
- Mannino, I., Daniel, F., Enrico, P., Laura, F., Erika, M. and Gabriele, Z. 2008. A cost-effectiveness analysis of seminatural wetlands and activated sludge wastewater treatment systems. *Environ. Manag.*, 41(1): 118-29. <https://doi.org/10.1007/s00267-007-9001-9006>.
- Najafzadeh, M. and Zeinolabedini, M. 2018. Derivation of optimal equations for prediction of sewage sludge quantity using wavelet conjunction models: An environmental assessment. *Environ. Sci. Pollut. Res.*, 25(23): 22931-22943. <https://doi.org/10.1007/s11356-018-1975-5>.
- Owusu-Twum, M.Y. and Sharara, M.A. 2020. Sludge management in anaerobic swine lagoons: A review. *J. Environ. Manag.*, 271: 110949. <https://doi.org/10.1016/j.jenvman.2020.110949>.
- Paskett, C.J. 1998. Refugees and land use: the need for change is a growing problem. *J. Soil Water Conserv.*, 53(1): 57-58.
- Raghuvanshi, S., Vikrant, B., Chelikani, S. and Sangwan, K.S. 2017. Wastewater treatment plant life cycle assessment: Treatment process to reuse of water. *Procedia CIRP*, 61: 761-66. <https://doi.org/10.1016/j.procir.2016.11.170>.
- Ramírez-Melgarejo, M., Santiago, G.D. and Leonor, P. G. 2019. Evaluation of N₂O emissions in wastewater treatment systems: A comparative analysis of emission between case studies of developed and developing countries. *Water Air Soil Pollut.*, 230(2): 4086. <https://doi.org/10.1007/s11270-019-4086-0>.
- Raschid-Sally, L., Wim, V.D. H. and Mala, R. 2001. Wastewater reuse in agriculture in Vietnam : *Water Manag. Environ. Human Health Aspects*, 45: 1106.
- Rathod, P.H., Jyotindra, C., Patel, M.R.S. and Amit J.J. 2009. Recycling gamma-irradiated sewage sludge as fertilizer: A case study using onion (*Alium cepa*). *Appl. Soil Ecol.*, 41(2): 223-33. <https://doi.org/10.1016/j.apsoil.2008.11.001>.
- Reznik, A., Ariel, D. and Francesc, H.S. 2019. Treated wastewater reuse: An efficient and sustainable solution for water resource scarcity. *Environ. Resour. Econ.*, 74: 383. <https://doi.org/10.1007/s10640-019-00383-2>.
- Rossum, T.V. 2020. Water reuse and recycling in Canada: History, current situation, and future perspectives. *Water Cycl.*, 4 : 98-103. <https://doi.org/10.1016/j.watcyc.2020.07.001>.
- Salem, S.S. Al. 2012. Wastewater reuse for agriculture: Regional health perspective . *Eastern Mediterranean Health Journal*, 12(3): 446-458.
- Sanciolo, P., Paul, M., Justin, L., Greg, R., Andrew, S., Nicola, F., Judy, B. and Stephen, G. 2020. Water effectiveness and energy requirements of pasteurization for the treatment of unfiltered secondary effluent from a municipal wastewater treatment plant. *Water*, 12(8): 2100.
- Shakouri, B. and Yazdi, S.K. 2014. Environment and water pollution. *Advances in Environmental Biology*, 8(5): 1328-1332.
- Shamblen, R.G. and Binder, D.M. 1996. The effect of the watershed, reservoir volume, and rainfall on nitrate levels in surface drinking water supplies. *J. Soil Water Conserv.*, 51(6): 457-461.
- Skander, K., Dahel, A., Djebbari, N., Barour, C. and Bensouilah, M.. 2015. Environmental parameters influence on the bacteriological water quality of the Algerian North East Coast. *Advances in Environmental Biology*, 9(18): 180-189.
- Sode, S., Annette Bruhn, T., Balsby, J.S., Martin, M.L., Annemarie, G. and Michael, B.R. 2013. Bioremediation of reject water from anaerobically digested wastewater sludge with Macroalgae (*Ulva Lactuca*, Chlorophyta). *Bioresour. Technol.*, 146: 426-435. <https://doi.org/10.1016/j.biortech.2013.06.062>.
- Vedachalam, S. 2012. Water_resources_and_wastewater reuse: perception of students at the Ohio State University Campus. *Ohio Journal of Science*. (110) 5: 104-113.
- Wagner, Mimi M. 2005. Watershed-scale social assessment. *Journal of Soil and Water Conservation*, 60(4): 177-86.
- Wang, Jing Han, Tian Yuan Zhang, Guo Hua Dao, Xue Qiao Xu, Xiao Xiong Wang, and Hong Ying Hu. 2017. Microalgae-based advanced municipal wastewater treatment for reuse in water bodies. *Applied Microbiology and Biotechnology*, 101 (7): 2659-75. <https://doi.org/10.1007/s00253-017-8184-x>.
- Zarei, M. 2020. Wastewater resources management for energy recovery from a circular economy perspective. *Water-Energy Nex.*, 3: 170-185. <https://doi.org/10.1016/j.wen.2020.11.001>.
- Zhu, H., Huang, G.H. and Guo, P. 2012. SIFNP: Simulation-based interval-fuzzy nonlinear programming for seasonal planning of stream water quality management. *Water Air Soil Pollut.*, 223(5): 2051-2072. <https://doi.org/10.1007/s11270-011-1004-5>.



Time Series Analysis of Economic Growth, Environmental Conditions and Their Coordination Degree: A Case Study of Provinces in Northeast China

Mei Yang*, Yaojun Fan**†, Xiaoxue Zhang*(***) and Shoufeng Wu****

*Institute of Educational Sciences, Comillas Pontifical University, Madrid 28080, Spain

**CHINA-ASEAN International College, Dhurakij Pundit University, Bangkok 10210, Thailand

***Institute of Finance and Economics, Qinghai University, Xining 810000, China

****Guizhou Radio and TV Station, Guiyang 550002, China

†Corresponding author: Yaojun Fan: yaojun.fan@dpu.ac.th

Nat. Env. & Poll. Tech.
Website: www.neptjournal.com

Received: 16-04-2021

Revised: 14-05-2021

Accepted: 07-06-2021

Key Words:

Regional economy
Population
Land use
GDP growth
Environmental investment

ABSTRACT

Northeast China is an old industrial base and agricultural production base with a long history of industrial and agricultural development. Since the beginning of the 21st century, the contradiction between economic and social development and resource depletion and environmental damage has become increasingly acute due to the long-term extensive development model. Based on a long time-series data set, this paper aims to explore the regional economic development model, environmental problems, and coordination degree between them in Northeast China. The results show that the population in Northeast China presents an increasing trend at first and then a decreasing one, and the population distribution shows an agglomeration in the cities of Harbin, Changchun, Shenyang, and Dalian. Urban-related land uses and GDP growth also exhibits agglomerations centered on these large cities. According to the changing trend of regional GDP and environmental investment, the synergistic relationship between the parameters is compared on a temporal scale, and a positive correlation between economic growth and environmental development is observed. We conclude that economic growth is closely correlated with environmental protection. If more attention is likely to be paid to environmental protection, the cities will develop more healthily under the background of urbanization. Based on the current status of the economy and environment, this paper puts forward constructive suggestions on promoting the coordinated development of regional economy and improving the ability of ecological environment governance. Improving the ecological environment's overall improvement capability through approaches such as adjusting the industrial structure, promoting the use of clean energy, strengthening industrial pollution control, controlling pollutant emissions, and promoting the construction of regional environmental infrastructure are all critical issues that must be resolved quickly to achieve coordinated development.

INTRODUCTION

The economy and the environment have a complex relationship, and economic development will inevitably result in ecological and environmental concerns. Globalization, dynamism, and integration are typical characteristics of this type of challenge, and environmental degradation is progressively becoming one of the elements impeding global development and human social progress. Exploring a harmonious relationship between the economy and the ecosystem is critical for developing a long-term economic development model and enhancing regional environmental governance capabilities (Liu et al. 2021, Xu et al. 2019, Zhang et al. 2020, Zhao et al. 2016). During the early stages of economic development, the government and businesses normally focus solely on economic growth. Mining and heavy industry, which are accompanied by excessive natural resource consumption, can

successfully boost economic growth rates and become pillar industries in many local economies. However, the industry has an unnoticed impact on the natural equilibrium, resulting in ecological devastation and pollution, and so creating an imbalance between the environment, resources, and economic progress. Environmental issues will gradually improve as the economic model matures, the industrial structure is upgraded, and production technology advances. The relationship between economic development and the environment has been recorded in previous studies, with the environmental Kuznets curve being a commonly acknowledged economic model that reflects the inverted U-shaped link between environmental pollution and per capita income. According to the Environmental Kuznets Curve, when a country's economic development level is low, environmental pollution is light; as per capita income rises, environmental pollution rises, and the degree of environmental deterioration rises with

economic growth; as economic development reaches a certain level, environmental pollution decreases from high to low, and the degree of environmental deterioration decreases with economic growth; as economic development reaches a certain level, environmental pollution decreases from high to low, and the degree of environmental. The notion of the relationship between environmental quality and income has been regularly studied, enriched, and improved since the introduction of the environmental Kuznets curve. Grossman & Krueger (1995), for example, pointed out that economic growth has three effects on environmental quality: scale effect, technology effect, and structural effect. With the rapid development of the global economy and the deterioration of the environment in recent decades, experts have focused their attention on the relationship between the environment and economic development. In various areas and sectors, EKC curves were used to undertake the empirical study (Cantavella 2020, Chen & Ieee 2008, Gill et al. 2019, Tzeremes 2019, Ying-Chun et al. 2021). The results show that in regions with different industrial structures and economic development patterns, the evolution of environmental pollution and economic growth presents different characteristics.

Since the 1980s, with China's fast industrialization and urbanization, economic expansion and population agglomeration have accelerated the plundering of natural resources, resulting in a slew of issues including pollution, resource depletion, and ecological degradation. These issues have posed significant obstacles to human existence and living situations, as well as stifled the country's and region's economic development, drawing the government's attention (Chen et al. 2010, Wang et al. 2020, Zhou et al. 2016). In recent years, one of China's national strategies has been the development of ecological civilization. Land, mineral, and petroleum resources abound in northeast China. The economy of this region began early, and a complete industrial system was constructed as early as the 1930s, making it Northeast Asia's most advanced industrial base. Northeast China has made significant contributions to China's economic development and government funding for more than half a century as the country's heavy industry base. However, due to the implementation of market-oriented reform in the 1990s, the economy of Northeast China has usually faced many difficulties, including the failure of firms and significant employment conflicts. Because of the advent of new sectors in those developed areas, the economic growth rate of Northeast China, which is dominated by conventional industries, has lagged substantially behind that of China's coastal cities in recent years. Furthermore, the long-term comprehensive development paradigm creates a growing conflict between economic and social development, resource depletion, and environmental degradation. Achieving coordinated develop-

ment of ecological environment and social economy in this region is an important goal of regional development, and it is also the key to regional sustainable development.

The research objects in this study are the Heilongjiang, Jilin, and Liaoning provinces in Northeast China, which are being investigated for their coordinated development level between regional economy and environmental protection, against the backdrop of coupling changes in economy, land, and population. This article analyses the degree of coordinated growth of the economy and environment in Northeast China, and analyses the association between economic development speed and environmental investment, using the variation trend of some economic and environmental indicators during a 12-year period. The findings of this research will be useful in enriching and broadening environmental assessment research methodologies in the context of economic transformation and development, as well as providing a reference for regional industrial adjustment and policymaking.

MATERIALS AND METHODS

Overview of the Study Area

Northeast China is located in a temperate monsoon climate zone with four distinct seasons. The weather is hot and rainy in summer and cold and dry in winter. The landform in this area is mainly plain, with high forest coverage and abundant water and soil resources. Northeast China has a land area of 1.45 million square kilometers and a total population of 120 million. The geographical locations of the provinces of Heilongjiang, Jilin, and Liaoning are shown in Fig. 1. There is vast land suitable for cultivation in Northeast China, and the cultivated land area accounts for 20.6% of the national total. The soil in the northeast plain is fertile, and it is home to one of the world's three famous black land belts, which is ideal for agricultural cultivation and serves as China's main commodity grain source. Mineral resources abound in northeast China as well. Iron, manganese, and copper are the most common metal minerals, while coal, oil, and graphite are non-metal minerals. Northeast China's economy grew swiftly in the early years of the new China, thanks to abundant mineral resources and heavy industry. Northeast China's GDP accounted for more than 80% of the country's total in the 1950s. Although Northeast China is enriched in natural resources, a large number of non-renewable resources are consumed due to the long-term development of heavy industry, so many cities in Northeast China are now facing the problem of resource depletion.

Description of Data Source and Statistical Methods

The economic data and environmental indicators in this study come from the Chinese Urban Statistics Yearbook and the

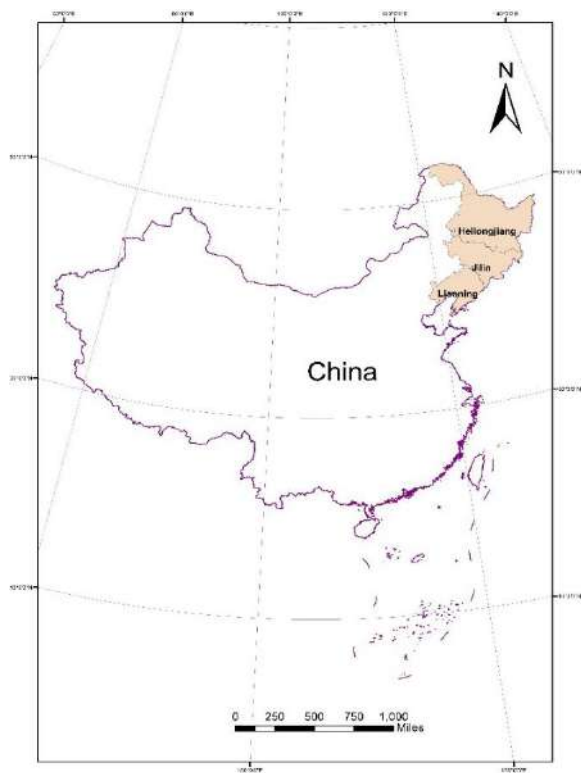


Fig. 1: Geographical location of provinces in Northeastern China: Heilongjiang, Jilin and Liaoning.

The spatial distribution of GDP refers to the km grid data of GDP spatial distribution in the resolution of 1 km grid, which reflects the detailed spatial distribution of GDP data in the whole country (Ling et al. 2006). The distribution data of population is calculated by grid space, which combines the population number in unit weight with the total weight distribution map to spatialize the population. Statistical analyses were performed by IBM’s statistical software Statistical Product and Service Solutions (SPSS 26).

RESULTS AND DISCUSSION

Evolution of the Population and Land Uses of Provinces in Northeast China

The trend of population variation in Liaoning, Jilin, and Heilongjiang from 2004 to 2015 is shown in Fig. 2. Before 2008, the population of the three provinces showed an increasing annual trend, which was relatively stable from 2008 to 2010 and began to decline after 2010. The long-term low fertility level and the increase of net outflow population are the reasons for the population decrease in Northeast China. On the one hand, the population outflow in Northeast China is due to the decline of industrial bases, and the demand for personnel in energy and manufacturing industries, which are the pillars of the local economy, has decreased. On the other hand, the tertiary industry in developed cities in southern China is developing rapidly with large population demands. The salary in these cities is generally higher than that in Northeast China. Convenient high-speed rail transportation saves the transportation time for inter-provincial travel. These factors demonstrate a considerable desire among young people in

Chinese Environmental Statistics Yearbook from 2004 to 2015. The spatial distribution maps of GDP, land use and population come from the Resource and Environment Science and Data Center of the Chinese Academy of Sciences.

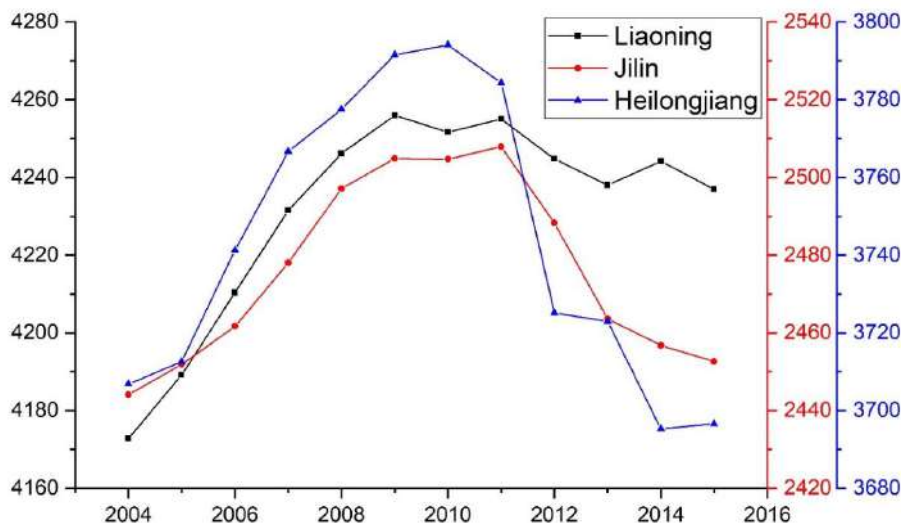


Fig. 2: The variation trend of the total population in Liaoning, Jilin, and Heilongjiang during the period of 2004-2015.

Northeast China to work in the south. Heilongjiang is the province with the most population fluctuations, with a total population of 37.9405 million in 2010, but 36.9664 million in 2015, which is lower than in 2004. Because Heilongjiang is located on the Chinese-Russian border, its population movement may be linked to trade cooperation between the two countries. The population decrease in Liaoning from 2010 to 2015 is the least among the three provinces. Liaoning is located in the south of Northeast China, and it is close to the Beijing-Tianjin-Hebei economy, serving as the gateway to the opening up of Northeast China. In comparison to the other two provinces, Liaoning has substantial geographic and economic advantages, as well as the ability to absorb population inflow. Northeast China has a low population density. Because of the low population density, the scale of population outflow continues to expand, and population growth is modest, posing a greater threat to regional development.

The evolution of population distribution in northeast China during a 10-year period is shown in Fig. 3. Spatially, the overall population distribution characteristics did not change significantly from 2005 to 2015. The densest population appeared in four large cities (Harbin, Changchun, Shenyang, and Dalian) and their surrounding areas, while the population in northern Heilongjiang Province with higher latitude was the rarest. The center of population hot spots shows a trend of gathering from north to south, indicating that the region's population movement is from north to south. Between 2010 and 2015, Liaoning Province saw a variety of population gathering places emerge, with Dalian and Shenyang having the highest population density. In Liaoning, the urban distribution is defined by a double-center structural

pattern. Liaoning is home to two megacities: Shenyang and Dalian. Shenyang is the provincial capital and a famous heavy industry base in China, while Dalian is a famous port city in North China and a window of foreign trade in Northeast China. These two cities have become the main inflow places of population movement in Northeast China and are also the centers of Liaoning's economy, whose regional GDP accounts for over 50% of the province's total. Industrial agglomeration makes these two regions have concentrated jobs and higher income levels, attracting young people to flow in and thus bringing about population agglomeration.

Fig. 4 depicts the spatial characteristics of land use categories in Northeast China in 2005, 2010, and 2015. Land use statistics based on Landsat 8 are separated into agricultural and forestry land, urban and industrial land, and unused land to better comprehend the relationship between potential environmental problems and human activities. The share of urban-related land in Northeast China is progressively increasing, similar to the developing trend of land use in other parts of China. Three urban agglomerations centered on central and southern Liaoning, central Jilin, and central Heilongjiang has gradually formed and expanded in Northeast China. However, the connectivity among the three urban agglomerations is weak. Compared with the urban agglomerations in developed provinces in China (such as Yangtze River Delta, Pearl River Delta, and Chengdu-Chongqing City Circle), there is a huge gap in the scale of urban agglomerations. Large cities are not able to gather resources and drive the development of surrounding cities. Northeast China is also characterized by an imbalanced level of urbanization and industry within the region. Shenyang, Dalian, Chang-

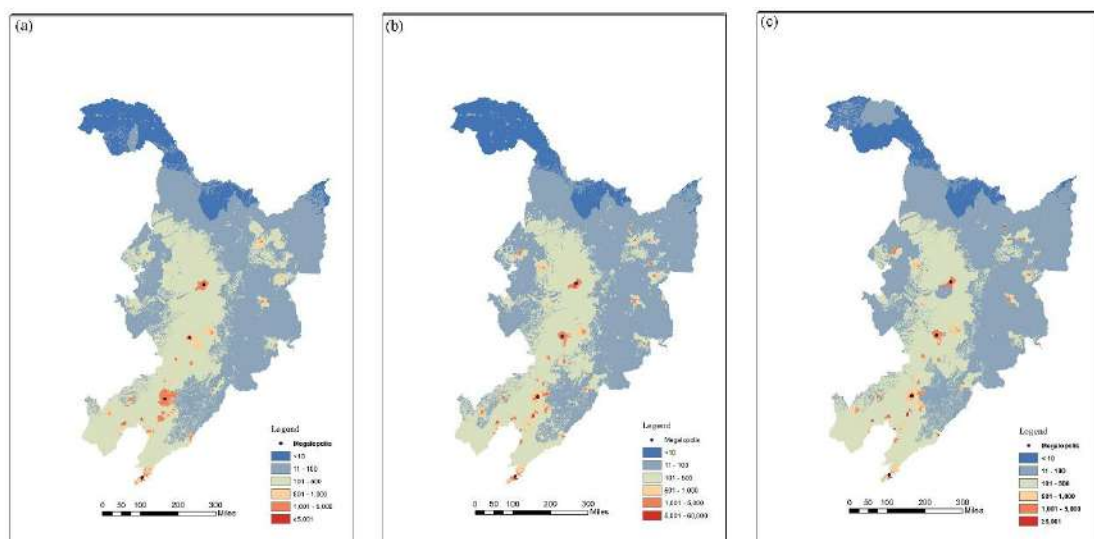


Fig. 3: Evolution of the population density in Northeast China during the ages of (a) 2005, (b) 2010, and (c) 2015.

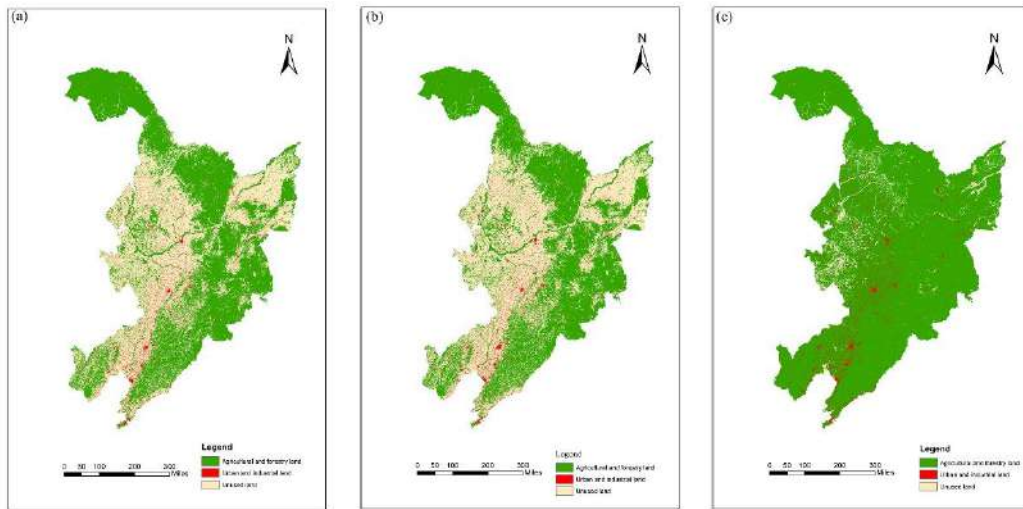


Fig. 4: Spatial variation in land-use types in Northeast China through a time span of 2005 to 2015. The green spots represent the land uses related to agriculture and forestry, the red ones represent those related to urban activities, and the yellow ones represent unused land.

chun, and Harbin, as well as their surrounding districts, saw the largest expansion of urban and industry-related land, which is consistent with the trend of population agglomeration shown in the preceding section. Large cities are faced with the problems of over-concentration of population and industry, while the county economy is backward, the town scale is small, the infrastructure is undeveloped, the industrialization foundation is weak, and urbanization is a typical urban-rural dual structure. This makes the environmental quality of large cities in Northeast China decline, and the ecological destruction is prominent, while the economic

development momentum of small and medium-sized cities is insufficient.

Development of the GDP Growth in Northeast China

By comparing the km grid data sets of GDP spatial distribution in 2005, 2010, and 2015, the spatial pattern and evolution law of economic development in Northeast China are reflected (Fig. 5), and each grid represents the GDP within 1 square kilometer. It can be observed that the economic development of coastal cities in the south of Northeast China is relatively fast, while that of coastal cities in the north is

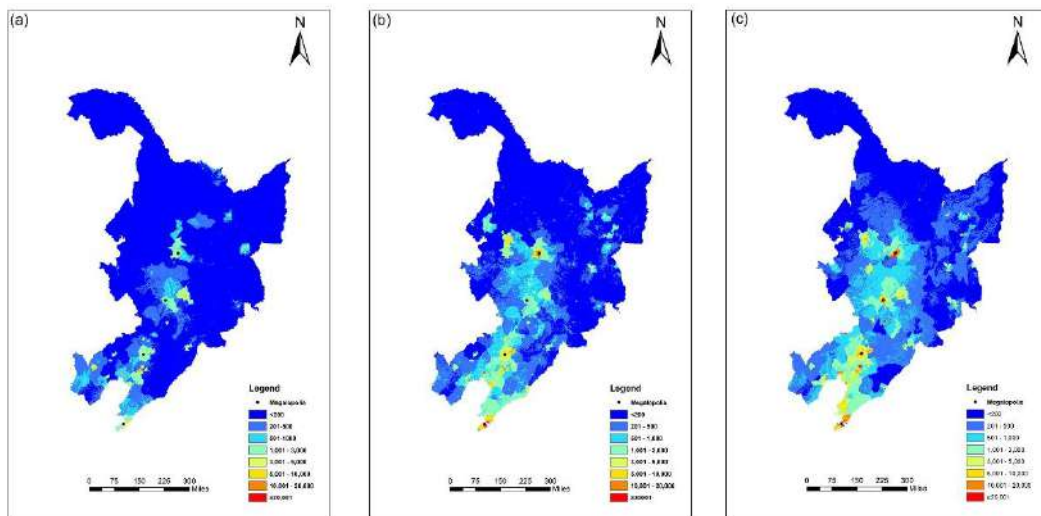


Fig. 5: Distribution of GDP per capita in provinces of Northeast China in the ages of (a) 2005, (b) 2010, and (c) 2015.

much slower. With the improvement of economic level, the agglomeration trend around Dalian, Shenyang, Changchun, and Harbin is further strengthened, and the spatial differences of regional economic development are increasing. The spatial differentiation of economic development level in Northeast China has a great relationship with its natural factors, traffic location, and the dependence and development degree of early mineral resources. The economic growth of resource-based cities and traditional industrial cities (e.g., Hegang, Panjin, Anshan, Baishan, and Daqing) slows down, which is mainly influenced by many factors such as industrial structure, human capital, technological progress, and system improvement. Because mineral resources are unsustainable, cities that rely on mining as a major source of revenue will inevitably undergo a downturn. The output of resources is rapidly reduced in these cities as a result of long-term continuous exploitation, a large number of connected firms are closed and bankrupt, environmental degradation is severe, and the number of unemployed people rises sharply.

Principal Environmental Problems in Northeast China

The environmental problems in Northeast China are outstanding, the environmental quality is gradually deteriorating, and the carrying capacity of resources and environment is facing challenges, which has greatly bound the economic development in Northeast China. The main environmental problems in Northeast China can be divided into the following three types:

(1) Environmental problems caused by industrial development. In recent hundred years, large-scale development has seriously deteriorated the ecological environment in Northeast China, and the problems are increasingly prominent. Before 1949, colonists from Japan and Russia plundered a large amount of iron ore, coal, and other forest resources, which led to great damage to resources and the ecological environment in Northeast China. Since the 1950s, Northeast China, as an old industrial base in China, has carried out large-scale

industrial development to achieve the urgent demand of rapid economic development. In addition, the pollution control level seriously lagged, which caused extremely high resource consumption in Northeast China and make the ecological environment seriously deteriorate. At present, the proportion of heavy industry in the industrial structure of Northeast China is too large, and this feature has not been completely changed, which increases the utilization of natural resources and the pollution of the ecological environment.

- (2) Environmental problems caused by agricultural and forestry activities. As one of the most suitable agricultural areas for cultivation, Northeast China plays an important role in crop production in China all along. The large-scale agricultural land reclamation in Northeast China has changed the grassland landscape, resulting in serious vegetation destruction, land desertification, and salinization. Due to the over-reclamation, more than half of the cultivated land suffered serious soil erosion and fertility decline. The natural wetlands are greatly shrunk and degraded, and their ecological functions are seriously impaired. In addition, Northeast China is the largest timber production base in China. Long-term imbalance of harvesting and compensation and deforestation have reduced the area of natural forests and weakened the ecological functions of forests.
- (3) Pollution of the air and water in huge cities. With the growth of cities and the concentration of population, resource scarcity, pollution, and ecological degradation are frequent elements that stifle urban development. In large cities such as Harbin, Changchun, Shenyang, and Dalian, the exhaust pollution caused by the increase in the number of motor vehicles is increasing, and the air pollution results from the smoke and industrial dust emitted by coal-burning (especially in the winter heating period) is becoming serious. As most polluting industries in Northeast China are located in dense urban areas, concentrated sewage makes rivers polluted.

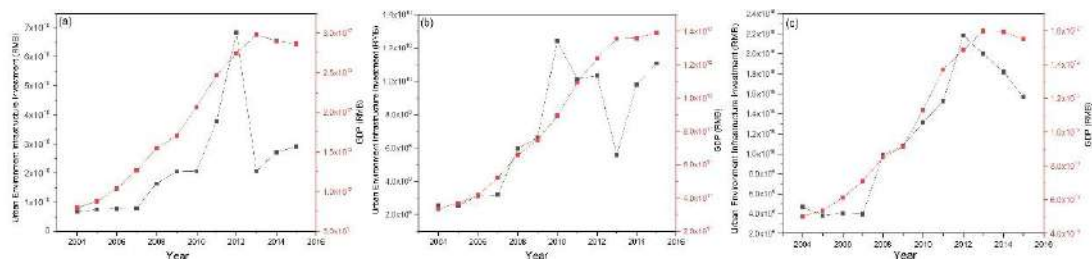


Fig. 6: Variation trend of GDP growth and Investment in Urban Environment Infrastructure during the period of 2004 to 2015 in (a) Liaoning, (b) Jilin and (c) Heilongjiang.

Coordination Degree Between Economic Growth and Environment

Coordinated development of economy and environment is a necessary condition for achieving sustainability, and it is also an important issue in regional development. Coordinated development should aim at reaching the all-around development of human beings, and form a virtuous circle of social development through the cooperation and promotion among the subsystems of population, society, economy, science, and technology, environment, and resources in the region. Investment in Urban Environment Infrastructure (IUEI) is mainly from the local finance and government-induced social capital, aiming to promote the environmental quality in urban regions. The investment is used in areas of gas supply, central heating, sewage projects, gardening & greening, sanitation, and garbage treatment. It demonstrates both the local government's financial capabilities and its commitment to environmental betterment. To evaluate the coordination degree between economy and environment in Northeast China, the changing trend of GDP and IUEI from 2004 to 2015 is shown in Fig. 6. The total GDP and per capita GDP of Liaoning Province are both the highest in Northeast China. From 2004 to 2010, the GDP of Liaoning Province increased rapidly, but the growth rate of IUEI was slow, which may be because local policies attached importance to economic development and ignored environmental protection; from 2010 to 2012, the investment in urban environmental facilities in Liaoning Province increased rapidly; after 2012, the IUEI showed a decreasing trend. In Jilin and Heilongjiang, IUEI was relatively fixed from 2004 to 2007; after the year 2007, IUEI and GDP grew rapidly simultaneously, showing a high degree of coordination, which shows that local governments increased the proportion of environmental protection budget in finance and increased financial support for environmental protection in the process of economic growth with the rapid economic growth and the country's emphasis on environmental protection. However, after the year of 2012, all three provinces experienced stagnation or even negative growth in GDP, and IUEI also experienced a significant decline. In Liaoning province, IUEI dropped sharply from 68.34 billion in 2012 to 20.34 billion in 2013 and then remained stable. In Jilin Province, IUEI experienced a sudden decline in 2012-2013 and then gradually picked up. In Heilongjiang Province, IUEI decreased by 8%-15% yearly after 2012. The presented trends show that there is a significant positive correlation between economic growth and environmental investment. In a period of rapid economic growth, the coordination between economy and environment is high. The stagflation or recession of the economy has a serious negative impact on

environmental protection, but the degree of negative impact is also controlled by the local government's emphasis on environmental governance.

Suggestions for Improving the Coordinated Development of the Economy and Environment

The stagnation and recession of economic development are important factors hindering environmental governance. Currently, the heavy industry still accounts for a large proportion of the regional economy of Northeast China. However, the surplus of energy production leads to the development of resource-concentrated enterprises in trouble in the current development stage of China, and the industrial model dominated by heavy industry has a great hindrance to the development of the ecological economy. Therefore, it is urgent to upgrade the industrial structure, accelerate the industrial transformation, and develop strategic new industries and high-tech industries in Northeast China, to solve the industrial pollution problems in the development of industrial enterprises and promote the coordinated development of the environment and economy. To achieve the virtuous circle of the ecological environment during the process of economic growth and promote sustainable development, it is important to improve the comprehensive improvement ability of the ecological environment by approaches of adjusting the industrial structure, promoting the use of clean energy, strengthening industrial pollution control, controlling pollutant emissions and promoting the construction of regional environmental infrastructure.

On the other hand, the higher urbanization development stage will be accompanied by the population explosion in large cities, and the ecological carrying capacity will be under great pressure. It is a strategy for alleviating population, resource, and environmental pressures on large cities by encouraging the development of nearby villages and towns and promoting the integration of urban and rural areas. Therefore, accelerating the construction of transportation and township infrastructure, forming a fast railway, highway, waterway, and air transportation network, and thus accelerating the radiation of the center to the surrounding small and medium-sized cities and towns will be effective means to alleviate the environmental pollution of urban agglomerations.

CONCLUSION

Based on a 12-year long time-series data set, this paper introduces the economic development and environmental characteristics of Liaoning, Jilin, and Heilongjiang provinces in Northeast China, and analyzes the coordination degree of

economy and environment in this region through the temporal variation trends of GDP and IUEI. The trends of population agglomeration and urban expansion in Northeast China are centered on four large cities of Harbin, Changchun, Shenyang, and Dalian, and spreads to surrounding areas, which is consistent with the spatial pattern and evolution trend of regional economic growth. The main environmental problems in North China include long-term resource exploitation and industrial production, excessive agricultural reclamation and deforestation, and concentrated pollutant emission in urban areas. During the study period, the economy in Northeast China transitioned from the rapid growth stage to the stagflation recession stage due to the recession of industry and mining and the prominent problem of overcapacity. There is a positive feedback relationship between economic growth and the government's environmental investment, and the sluggish or declining economic situation will inevitably lead to the shortage of environmental governance funds. The most essential means of solving environmental problems in the process of urban expansion and promoting the coordinated development of the environment and economy is to follow a sustainable economic development pattern. On the one hand, provinces in Northeast China should urgently speed up the optimization and upgrading of industrial structure, reduce the proportion of high-pollution heavy industrial enterprises in the regional economy, attach importance to the development of emerging industries, and control the generation and emission of environmental pollutants from the source; On the other hand, urban agglomerations centered on four large cities should be taken as the main body to promote regional urbanization and thus ease the ecological environment pressure faced by large cities.

REFERENCES

- Cantavella, M. 2020. The role of services in the environmental Kuznets curve for Spain. *Econ. Bus. Lett.*, 9(4): 326-333.
- Chen, M., Lu, D. and Zha, L. 2010. The comprehensive evaluation of China's urbanization and effects on resources and the environment. *J. Geogr. Sci.*, 20(1): 17-30.
- Chen, W. and Ieee, M. 2008. An empirical test on the environmental Kuznets Curve hypothesis in China. *China Econ. Rev.*, 19(3): 381-392.
- Gill, A.R., Hassan, S. and Viswanathan, K.K. 2019. Is democracy enough to get the early turn of the environmental Kuznets curve in ASEAN countries? *Energy Environ.*, 30(8): 1491-1505.
- Grossman, G.M. and Krueger, A.B. 1995. Economic growth and the environment. *Q. J. Econ.*, 110(2): 353-377.
- Ling, Y.I., Xiong, L.Y. and Yang, X.H. 2006. Method of pixelizing GDP data based on the GIS. *J. Gansu Sci.*, 6: 71-89.
- Liu, K., Qiao, Y., Shi, T. and Zhou, Q. 2021. Study on coupling coordination and spatiotemporal heterogeneity between economic development and ecological environment of cities along the Yellow River Basin. *Environ. Sci. Pollut. Res.*, 28(6): 6898-6912.
- Tzeremes, P. 2019. Does the environmental Kuznets Curve exist in the Chinese region? *Glob. Econ. Rev.*, 48(4): 363-377.
- Wang, Y., Geng, Q., Si, X. and Kan, L. 2020. Coupling and coordination analysis of urbanization, economy, and environment of Shandong Province, China. *Environ. Develop. Sustain.*, 31(11): 234-249
- Xu, M., Chen, C. and Deng, X. 2019. Systematic analysis of the coordination degree of China's economy-ecological environment system and its influencing factor. *Environ. Sci. Pollut. Res.*, 26(29): 29722-29735.
- Ying-Chun, L., Yuan-Ying, C., Xiao-Ru, N., Xiang-Dong, L. and Rui, P. 2021. Kuznets Curve based analysis on the relationship between economic growth and environmental quality in Beijing. *IOP Conference Series: Materials Science and Engineering*, 1043: 022009
- Zhang, W., Zhang, X., Zhang, M. and Li, W. 2020. How to coordinate economic, logistics and ecological environment? Evidence from 30 provinces and cities in China. *Sustainability*, 12(3): 14-27.
- Zhao, F., Zhang, W. and Zhang, C. 2016. quantifying the coordination of energy development and environmental protection: A case study of China. *Energy Proc.*, 104: 520-525.
- Zhou, M., Zhao, X.L. and Huang, L. 2016. The Effects of Urbanization on the Environment Pollution in China. *Int. Conf. Elect. Inform. Computer Eng.*, 44: 2047-2051.



Influence of Sugars, Sugar Alcohols and Their Combinations on Environmentally Significant Cellulase Production Under Liquid State Fermentation

Nitin Verma*(***)† and Vivek Kumar**(***)

*Department of Biotechnology, Meerut Institute of Engineering & Technology MIET, Meerut-250 005, U.P., India

**Biotechnology Division, CRDT, Indian Institute of Technology, Hauz Khas New Delhi-110 016, India

***Department of Paper Technology, Indian Institute of Technology, Roorkee Saharanpur Campus, Saharanpur-247001, U.P., India

†Corresponding author: Nitin Verma: nitin.verma@miet.ac.in; nitiniit2008@gmail.com

Nat. Env. & Poll. Tech.

Website: www.neptjournal.com

Received: 16-01-2021

Revised: 15-04-2021

Accepted: 30-04-2021

Key Words:

Cellulase

Sugar

Sugar alcohol

Inducer

Liquid state fermentation

ABSTRACT

To expand the range of soluble carbon sources for enzyme production by the microbial system, we investigated the ability of different sugars in cellulase production. Carbon sources play a vital role in cell metabolism and the synthesis of cellulase. Although the insoluble cellulosic materials are considered the most effective natural inducers for cellulase production by microorganisms in terms of both enzyme yield and productivity, their insolubility causes many problems and presents a major drawback that is partly responsible for the high cost of cellulase production. Mostly, the insolubility of sugar polymer leads to difficult and complex fermentation operations, including sterilization, cell biomass measurement, mixing and aeration of the fermentation broth, continuous feeding/sampling, and subsequent enzyme purification. Second, cellulase gets absorbed into the solid cellulose surface, leading to enzyme loss. The present paper gives a comparative view on the utility of pure sugars (lactose, CMC, sucrose, maltose, cellobiose, xylose, trehalose, arabinose) and sugar alcohols (sorbitol, mannitol) on cellulase production by various fungal strains. It also describes the blending effect of sugars as well as sugar alcohols on cellulase production by fungal strains.

INTRODUCTION

Cellulase is an enzyme that is capable of hydrolyzing the complex organic form of cellulose into simple sugar (glucose). Sugars play a significant role in cellulase biosynthesis and act as an inducer (Lin et al. 2017). Cotoras & Agosin (1992) found that brown rot fungus *Gloeophyllum trabeum* produced endoglucanases in the presence of monosaccharides such as glucose or mannose as the sole carbon source, but the expression of these enzymes was 4-5 times higher in the presence of cellulose or cellobiose. They concluded that endoglucanase production by brown rot fungi is inducible by cellulose and not subject to catabolite repression. Cellobiose is the most effective inducer of the system. Morikova et al. (1995) suggested lactose as an inducer for cellulase formation in *Trichoderma reesei* PC-3-7. Schaffner & Toledo (1991) reported that cellulase activity was increased in conditions containing xylose supplemented with sorbose compared to xylose alone as a carbon source by *T. reesei*. Janas et al. (2002) reported that enzymatic activities of cellulases obtained by *T. reesei* M-7 in presence of lactobionic acid and lactose were about 20% higher than in the presence of only lactose. Thirumale et al. (2001)

were the first to report trehalose as a cellulase biosynthesis inducer. Trehalose is the most effective inducer when compared to lactose and cellobiose. Lactose was also suggested by Sehnem et al. (2006) as an inducer in *Penicillium echinulatum* 9A0251 cellulase production. Cultures grown in lactose produced low FPA activity ($0.1 \text{ FPU} \cdot \text{mL}^{-1}$), whereas cultures grown on lactose with cellulose-containing media produced high enzyme activity ($1.5 \text{ FPU} \cdot \text{mL}^{-1}$), implying that increasing the lactose/cellulose ratio results in a proportional rise in enzymatic activity. Morrison et al. (1987) discovered that *Taloromyces emersonioi* CBS 814.70 could grow on lactose-containing media when lactose was used as an inducer. Kamagata et al. (1991) reported cellulase production by *Penicillium purpogenum* strain P-26, which was strongly induced by cellobiose octaacetate (COA) in the presence of microcrystalline cellulose as a cosubstrate. A fraction of cello-oligosaccharides with a high degree of polymerization (GX) was found to be a potent cellulase inducer in *Trichoderma koningii* G-39 (Wang et al. 1988). *T. reesei* uses sophorose metabolism to induce cellulase production (Loewenberg & Chapman 1997). Cellobiono1-5 lactone or oxidized cellulose, a cellulose degradation product, has also been shown to increase the synthesis of cellulase in

T. reesei. (Cotoras & Agosin 1992). Any soluble substrate with a -1-4 glucan linkage, such as carboxymethyl cellulose and cellobiose, produced induction, however, these are weaker inducers than cellulose itself. Cellulase biosynthesis has been observed to be induced by cellobiose, the smallest cellooligosaccharides with a -1-4 linkage. Surprisingly, sophorose, a glucose disaccharide with a -1-2 bond, can generate 2500 times more cellulase in *T. reesei* than cellobiose. Gentiobiose, a glucose disaccharide having a -1-6 bond, was discovered to produce 50 times more cellulase in *Penicillium* (Suto & Tomita 2001). Cellulase produced on lactose was more than the cellobiose. Cellobiose is an excellent growth substrate for these fungi and is rapidly consumed, whereas lactose which differs from the cellobiose only in configuration around the number four carbon in the glucoside ring is a poor growth substrate for fungi and is poorly consumed. For most of the cellulase producers, the inducing rate of the inducers for cellulase production is as follows - Cellulose > cellobiose > octa acetate > lactose > cellobiose. Binder & Ghosh (1978) claim that the actual contact between hyphae and cellulose is essential for cellulase induction. Sophorose is produced by the acid hydrolysis of starch, it is a potent inducer of cellulase in *T. reesei*. Both cellobiose and lactose are inducers, although cellobiose is more effective due to its high initial concentration. Glucosyl transfer products are present in the medium during cellobiose growth and are said to be greater inducers than cellobiose. *Trichoderma viride* and *Neurospora crassa* have different cellulase production systems. Sophorose and cellulose are the only two substances that have a substantial effect. The activity of the CMCase enzyme: CMCase is not induced by CMC, cellobiose, or lactulose; instead, it is induced by -glucosidase. Although lactose metabolism is slower than cellulose, lactose is an important carbon source for the fungus *T. reesei*, which produces cellulolytic enzymes (Wang & Reesei 1994). In a continuous culture of *T. reesei*, Ju & Afolabi (1999) tested the potential of waste paper hydrolysate to induce cellulase and employed it as a soluble substrate for cellulase synthesis. Wyman & Chen (1992) looked at soluble inducers obtained from whole wheat flour for *T. reesei* cellulase synthesis. Wyman & Chen (1991) have described cellulase production using a carbon source sourced from discarded office paper, which serves as both raw material and an inducing agent. Lactose is a low commercial cost disaccharide and also acts as the source of carbon and inducer for cellulase production by fermentation (Sehnm et al. 2006). Soluble carbon sources such as lactose, cellobiose give significantly lower cellulase activity compared to pure insoluble cellulosic substances such as cotton, avicel, solka floc at the same concentration (Morikova et al. 1995, Bhatt 2000). Niranjane et al. (2007) investigated the influence of different carbohydrates such as glucose, xylose,

carboxymethyl cellulose (CMC), microcrystalline cellulose (avicel), and cellobiose as carbon sources for the production of cellulase by *Phlebia gigantea* fungus. Carboxymethyl cellulose gave the highest yield, followed by cellobiose and avicel. Glucose and xylose did not produce any detectable cellulases which suggest the repression of cellulase in the presence of these simple carbohydrates by *P. gigantea*. Several substrates have been used for the fermentative production of cellulase. Although the insoluble cellulosic materials are considered the most effective natural inducers for cellulase production by microorganisms in terms of both enzyme yield and productivity, their insolubility causes many problems and presents a major drawback that is partly responsible for the high cost of cellulase production. Mostly, the insolubility of sugar polymer leads to complex fermentation operations such as sterilization, cell biomass measurement, mixing/aeration of the fermentation broth, continuous feeding/sampling, and subsequent enzyme purification. It also creates the adsorption of cellulase onto the solid cellulose surface, leading to enzyme loss. The use of soluble sugars and sugar alcohols to handle such fermentation activities based on limits would be useful. The present paper emphasized the utility of various sugars (lactose, CMC, cellobiose, sucrose, maltose, xylose, arabinose, trehalose) and sugar alcohols (sorbitol, mannitol) in cellulase production by fungal strains under liquid state fermentation. It also portrays the effect of mixed pure sugars as well as sugar alcohols on cellulase production by various fungal strains.

MATERIALS AND METHODS

Materials

Chemicals: Chemicals used in the experimental studies were AR grade and of Himedia, Merck and Sigma Aldrich make.

Microorganisms: Five standard fungal strains, *Trichoderma reesei* NCIM 1186, *Trichoderma viride* NCIM 1195, *Aspergillus niger* NCIM 777, *Aspergillus fumigatus* NCIM 902, and *Neurospora crassa* NCIM 1021 were procured from National Chemical Laboratory (NCL), Pune, India.

Media for Culture Development: Potato dextrose agar (PDA) medium was used for culture development and maintenance of *Trichoderma* and *Aspergillus* strains, whereas *Neurospora* strain was developed and maintained on M₂ agar medium as recommended by National Chemical Laboratory, Pune. PDA medium contains (g.L⁻¹) Peeled potato, 200; Dextrose, 20; Yeast extract, 0.1; Agar 15 at pH 5.6. M₂ agar medium contains (g.L⁻¹) Glucose, 10; Glycerine, 10; Yeast extract, 5; KH₂PO₄, 0.3; MgSO₄.7H₂O, 0.1; Agar, 20 at pH 6.8.

Production of Media for Submerged Fermentation:

In (g.L^{-1}); Urea, 0.3; $(\text{NH}_4)_2\text{SO}_4$, 1.4; KH_2PO_4 , 2.0; $\text{MgSO}_4 \cdot 7\text{H}_2\text{O}$, 0.3; Peptone, 1.0; Tween80, 0.2; $\text{FeSO}_4 \cdot 7\text{H}_2\text{O}$, 0.005; $\text{MnSO}_4 \cdot 7\text{H}_2\text{O}$, 0.0016; $\text{ZnSO}_4 \cdot 7\text{H}_2\text{O}$, 0.0014; $\text{CaCl}_2 \cdot 2\text{H}_2\text{O}$; $\text{CoCl}_2 \cdot 6\text{H}_2\text{O}$, 0.02 and pure sugar 10.0., pH 5.0.

Methods

Maintenance of Stock Culture

The stock culture of *Trichoderma*, *Aspergillus*, and *Neurospora* strains were maintained on potato dextrose agar slants and M₂ agar slant respectively. The same media was also used for subculturing of the respective fungal strains. The procured fungal stock was kept at 40°C in 20% (v/v) glycerol.

Inoculum Development

Inoculum development experiments were performed in 250 mL Erlenmeyer flasks containing 100 mL of Potato Dextrose Broth (PDB) medium (in g.L^{-1}) Peeled Potato - 200; Dextrose - 20; and Yeast extract - 0.1) and M₂ broth medium in which 5 loopful cultures of fungal spores or mycelial conidia were added and shaken at 180 rpm at 30°C in an incubator shaker for 3-4 days (Domingues et al. 2004). A definite volume of prepared cultures in PDB or M₂ broth suspension (having 0.56 g.L^{-1} cell dry weight) was used as inoculum for further production studies.

Submerged Fermentation

Separate set of batch experiments were carried out in 250 mL Erlenmeyer flasks containing 100 mL of production media having components (in g.L^{-1}) Urea - 0.3; $(\text{NH}_4)_2\text{SO}_4$ - 1.4; KH_2PO_4 - 2.0; $\text{MgSO}_4 \cdot 7\text{H}_2\text{O}$ - 0.3; Peptone - 1.0; Tween80 - 0.2; $\text{FeSO}_4 \cdot 7\text{H}_2\text{O}$ - 0.005; $\text{MnSO}_4 \cdot 7\text{H}_2\text{O}$ - 0.0016; $\text{ZnSO}_4 \cdot 7\text{H}_2\text{O}$ - 0.0014; $\text{CaCl}_2 \cdot 2\text{H}_2\text{O}$, $\text{CoCl}_2 \cdot 6\text{H}_2\text{O}$ - 0.02; Pure sugars or sugar alcohols or mixtures - 10.

Flasks containing production media with different pure sugars, sugar alcohols, or their mixtures are used separately for cellulase production by various fungal strains under liquid state fermentation. Each production media contacting flasks were autoclaved, cooled, and then inoculated with a specific volume having (0.56 g.L^{-1} cell dry weight) of PD and M₂ broth culture solution of respective strains. The autoclaved and inoculated flasks were placed in an incubator shaker at 30°C at 180 rpm for 5 days.

Cellulase Activity

Filter paper activity (FPA) and carboxymethyl cellulase (CMCase) were determined by the method recommended by Ghose (1987).

RESULTS AND DISCUSSION

Sugar plays a vital and critical role in cellulase biosynthesis as it acts as an inducer. Soluble carbon sources such as lactose, cellobiose give significantly lower cellulase activity compared to pure insoluble cellulosic substances such as cotton, avicel, solka floc at the same concentration. Many substrates have been utilized for the fermentative production of cellulase. Various purified cellulose such as avicel, solka floc, and cotton have been used as a carbon source for cellulase production (Allan & Roche 1989, Schaffner & Toledo 1991). For large-scale production of the enzyme, pure cellulose would be too costly and expensive to be applied in large-scale processes.

Effect of Lactose on Cellulase Production under Submerged Cultivation

Separate sets of batch experiments have been performed to study the effect of pure sugar such as lactose (10 g.L^{-1}) as a carbon source on cellulase production by various fungal strains under submerged cultivation. It was observed from Figs. 1 (a) and 1(b) that fungal strains produced significantly good cellulase activities under a lactose-based fermentation medium. When cellulase activity was measured using a lactose-based medium, it was discovered that fungal strains produced much reduced cellulase activity. This could be related to lactose disaccharide's soluble nature, as literature has shown that soluble carbon sources have much lower cellulase activity than pure insoluble cellulosic compounds at the same pH concentrations (Morikova et al. 1995, Bhatt 2000).

The maximum cellulase activities (IU.mL^{-1}) in terms of FPA and CMCase achieved by *T. reesei*, *T. viride*, *N. crassa*, *A. niger* and *A. fumigatus* were 2.31, 1.63; 1.26, 2.55; 1.06, 2.13; 0.433, 1.96; 0.556, 1.98 at 120, 96; 144, 144; 144, 120; 96, 72; 96, 72 h respectively under lactose-based fermentation medium. It has been observed from Fig 1(a) that *T. reesei* produced higher FPA activity under lactose-based fermentation medium as compared to the other fungal strains, which states that lactose acts as a better inducer for cellulase production by *T. reesei*. Li et al. (2017) reported cellulase hyperproduction by *T. reesei* mutant SEU-7 on lactose. A sharp increment in FPA activities was observed after 48, 72, and 96 h by *T. reesei*, *T. viride*, and *N. crassa* strains. Ivanova et al. (2013) suggested that lactose permease is the main component essential for cellulase induction. On the other hand, higher CMCases were achieved by *T. viride* followed by *N. crassa* and *A. niger* fungal strains. A sharp increment has been observed in CMCase activity till 72 h by *A. niger* while a steep increment has been observed in CMCase after 72 h, as viewed from Fig. 1(b).

Effect of CMC as a Carbon Source on Cellulase Production under Submerged Cultivation

Individual sets of batch experiments have been performed to study the effect of carboxy methyl cellulose (10 g.L^{-1}) as a carbon source on cellulase production by various fungal strains under submerged cultivation. It was observed from Figs. 2(a) and 2(b) that various fungal strains produce significantly better cellulase activities under carboxymethylcellulose-based fermentation medium. Maximum cellulase activities (IU.mL^{-1}) in terms of FPA and CMCase attained by *T. reesei*, *T. viride*, *N. crassa*, *A. niger* and *A. fumigatus* were 2.46, 1.83; 1.31, 3.08; 0.986, 1.89; 0.523, 2.41; 0.603, 2.23 at 120, 96; 120, 144; 144, 120; 120, 120; 96, 120 h respectively under carboxymethylcellulose-based fermentation medium. It has been observed from Fig. 2(a) that *T. reesei* and *T. viride* produce higher FPA under CMC-

based fermentation medium as compared to the other fungal strains. Waghmare et al. (2018) used CMC as a substrate for cellulase production by cellulolytic isolate *Enterobactor* sp. SUK-Bio. A steep increment in FPA was observed after 72 h by *T. reesei* which suggests that up to 72 h, *T. reesei* used energy for their growth, and after this period microbes used all the energy for enzyme production and reached their maximum at 120 h of the fermentation period. Niranjane et al. (2007) reported that carboxymethyl cellulose gave the highest yield, followed by cellobiose and avicel. On the other hand, higher CMCases were achieved by *T. viride* followed by *Aspergillus* strains. A steep increment in the CMCase has been observed until 72 h by *T. viride* and *Aspergillus* strains as viewed from Fig. 2(b).

Effect of Cellobiose on Cellulase Production under Submerged Cultivation

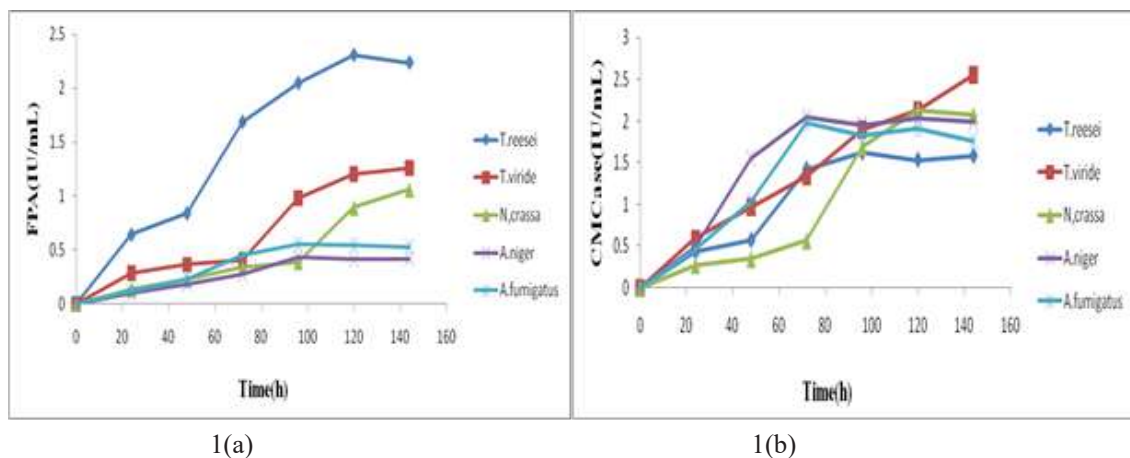


Fig. 1: Comparative FPA and CMCase achieved by various fungal strains under lactose-based production medium at 30°C and pH 5.0.

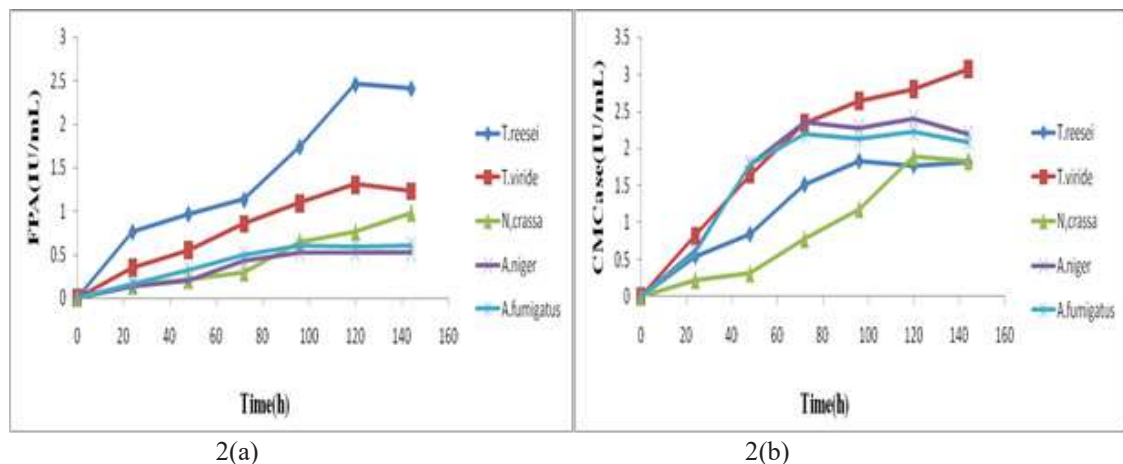


Fig. 2: Comparative FPA and CMCase achieved by various fungal strains under CMC-based production medium at 30°C and pH 5.0.

Individual sets of batch experiments have been performed to study the effect of cellobiose (10 g.L^{-1}) as a carbon source on cellulase production by various fungal strains under submerged cultivation. It was observed from Figs. 3(a) and 3(b) that various fungal strains produce a significant amount of cellulase activities under a cellobiose-based fermentation medium. Maximum cellulase activities (IU.mL^{-1}) in terms of FPA and CMCase attained by *T.reesei*, *T.viride*, *N.crassa*, *A.niger* and *A.fumigatus* were 2.02, 1.75; 1.08, 2.81; 0.955, 1.92; 0.795, 3.72; 0.885, 3.19 at 120, 96; 120, 144; 144, 120; 96, 72; 120; 96, 120 h respectively under cellobiose-based fermentation medium. It has been observed from Fig. 3(a) that *T.reesei* produces higher FPA activity under cellobiose-based fermentation medium as compared to the other fungal strains but when compared the cellulases produced by *T.reesei* under cellulose, lactose, and CMC, somewhat lower activity was observed under cellobiose-based fermentation medium as compared to other sugar-based media. FPA produced by *Aspergillus* strains were higher under cellobiose-based medium as compared to other sugars while the performance of *N.crassa* strain was found lower in cellobiose-based fermentation medium as compared to other sugar-based media as observed from Fig. 3(b).

Effect of Sucrose on Cellulase Production Under Submerged Cultivation

Separate sets of batch experiments have been performed to study the effect of sucrose (10 g.L^{-1}) as a carbon source on cellulase production by various fungal strains under submerged cultivation. It was observed from Figs. 4(a) and 4(b) that various fungal strains produce significant cellulase

activities under the sucrose-based fermentation medium. Ike & Tokuyasu (2018) investigated cellulase production of *T.reesei* using sucrose as a primary carbon source.

Maximum cellulase activities (IU.mL^{-1}) in terms of FPA and CMCase attained by *T.reesei*, *T.viride*, *N.crassa*, *A.niger* and *A.fumigatus* were 1.93, 1.71; 1.01, 2.46; 1.18, 2.36; 0.401, 1.97; 0.483, 1.81 at 120, 96; 120, 144; 144, 120; 96, 72; 96, 72 h respectively under sucrose-based fermentation medium. It has been observed from Fig. 4(a) that *T.reesei*, *T.viride*, and *N.crassa* yield higher FPA activity under a sucrose-based fermentation medium as compared to *Aspergillus* strains. On the other hand, higher, CMCases were achieved by *T.viride* and *N.crassa* strains under sucrose-based fermentation medium as viewed from Fig. 4(b). Overall we can infer that *Trichoderma*, as well as *Neurospora* strains, performed better under sucrose-based fermentation medium in terms of cellulase production as compared to *Aspergillus* strains.

Effect of Maltose Sugar on Cellulase Production Under Submerged Cultivation

Separate sets of batch experiments have been performed to study the effect of maltose (10 g.L^{-1}) as a carbon source on cellulase production by various fungal strains under submerged cultivation. It was observed from Figs. 5(a) and 5(b) that various fungal strains produce significantly better cellulase activities except for *Trichoderma* under maltose-based fermentation medium. Maximum cellulase activities (IU.mL^{-1}) in terms of FPA and CMCase attained by *T.reesei*, *T.viride*, *N.crassa*, *A.niger* and *A.fumigatus* were 1.13, 1.21; 0.698, 1.91; 1.43, 2.78; 0.571, 2.81; 0.685, 2.51 at 120, 96;

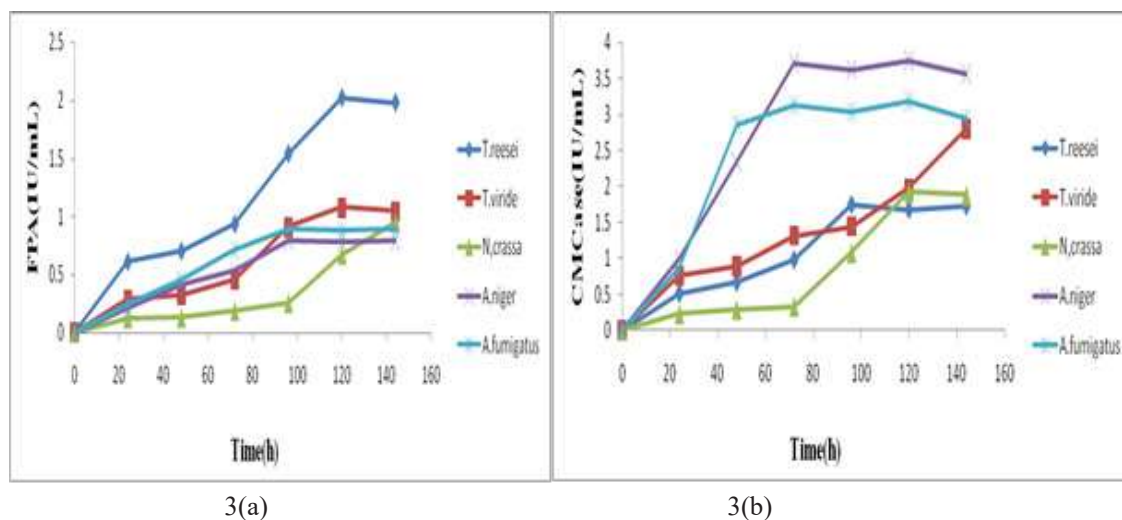


Fig. 3: Comparative FPA and CMCase achieved by various fungal strains under cellobiose based production medium at 30°C and pH 5.0.

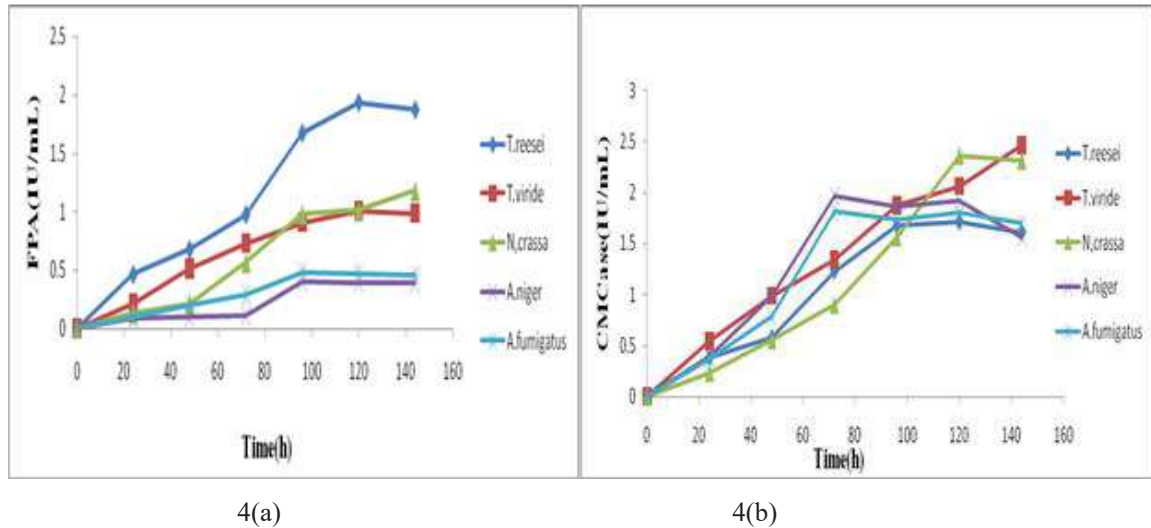


Fig. 4: Comparative FPA and CMCase achieved by various fungal strains under sucrose based production medium at 30°C and pH 5.0

120, 144; 144, 120; 96, 72; 96, 72 h respectively under maltose-based fermentation medium. It has been observed from Fig. 5(a) that *N. crassa* produces higher FPA activity under a maltose-based fermentation medium as compared to the other fungal strains. Good improvement in FPAs activity of *Aspergillus* strains was observed in the maltose-based medium as compared to the sucrose-based fermentation medium. On the other hand, higher CMCases were achieved by *Aspergillus* as well as *Neurospora* strains. A steep increment in the CMCase has been observed until 48 h by *Aspergillus* strains as viewed from Fig. 5(b).

The effect of carbon sources such as glucose, sucrose, cellulose, carboxymethyl cellulose, and maltose on the pro-

duction of enzymes by *A. niger* and *Trichoderma* sp. was investigated by Gautam et al. (2011). Significant cellulase activity was reported under cellulose, CMC, sucrose, and maltose-based fermentation.

Effect of Xylose as Carbon Source on Cellulase Production Under Submerged Cultivation

Individual sets of batch experiments have been performed to study the effect of xylose (10 g.L^{-1}) as a carbon source on cellulase production by various fungal strains under submerged cultivation. Schuerg et al. (2017) reported that Xylose induces both cellulase and xylanase production in *T. aurantiacus*. It was observed from Figs. 6(a) and 6(b) that various fungal

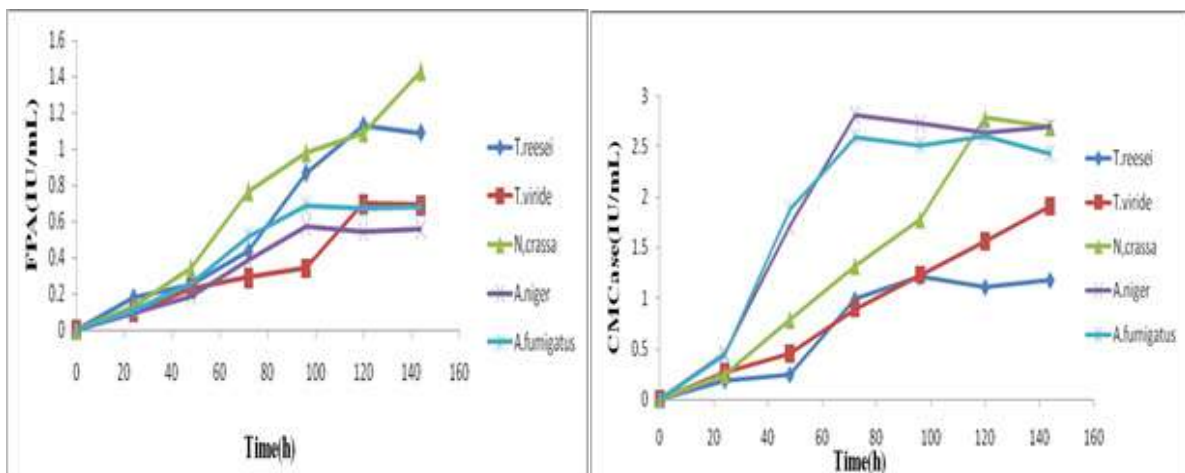


Fig. 5: Comparative FPA and CMCase achieved by various fungal strains under maltose based production medium at 30°C and pH 5.0.

strains produce significantly lesser cellulase activities except for *Trichoderma* strains. Maximum cellulase activities (IU. mL⁻¹) in terms of FPA and CMCase attained by *T. reesei*, *T. viride*, *N. crassa*, *A. niger* and *A. fumigatus* were 1.53, 1.15; 0.780, 1.54; 0.639, 1.30; 0.239, 1.21; 0.341, 1.29 at 120, 96; 96, 120; 144, 144; 96, 72; 96, 72 h respectively under xylose based fermentation medium. It has been observed from Fig. 6(a) that higher FPA activity was produced by *T. reesei* under a xylose-based fermentation medium as compared to the other fungal strains. A steep increment in FPA was observed after 96 h by *T. reesei* which suggests that up to 96 h *T. reesei* used energy for their growth and after this period microbes used all the energy for enzyme production and reached their maximum at 120 h of the fermentation period. On the other hand, higher CMCases were achieved by *T. viride*. A steady increment in the CMCase has been

observed until 120 h by *T. viride* strain as viewed from Fig. 6(b). Maibam & Maity (2019) developed a strategy for simultaneous xylose utilization and enhancement in cellulase enzyme production by *T. reesei*.

Effect of Arabinose as Carbon Source on Cellulase Production Under Submerged Cultivation

Separate sets of batch experiments have been performed to study the effect of arabinose pure sugar (10 g.L⁻¹) as a carbon source on cellulase production by various fungal strains under submerged cultivation. It was observed from Figs. 7(a) and 7(b) that various fungal strains produce significantly reduced cellulase activities under arabinose-based fermentation medium. Maximum cellulase activities (IU.mL⁻¹) in terms of FPA and CMCase attained by *T. reesei*, *T. viride*, *N. crassa*, *A. niger* and *A. fumigatus* were 0.693, 0.490; 0.402,

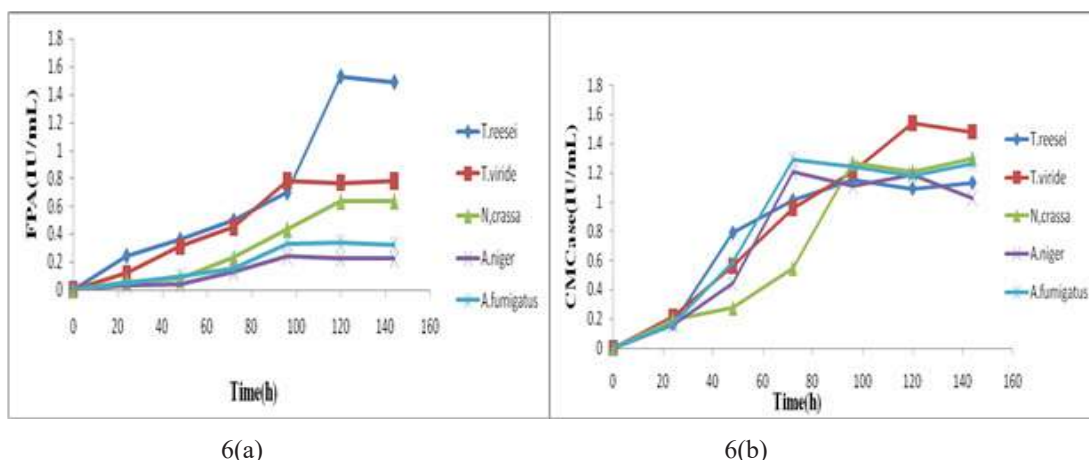


Fig. 6: Comparative FPA and CMCase achieved by various fungal strains under xylose based production medium at 30°C and pH 5.0.

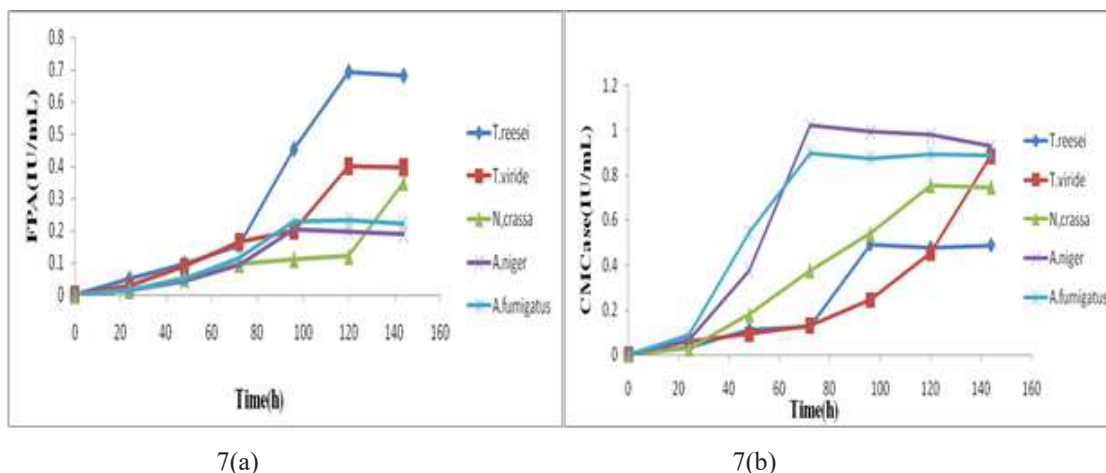


Fig. 7: Comparative FPA and CMCase achieved by various fungal strains under arabinose based production medium at 30°C and pH 5.0.

0.886; 0.351, 0.755; 0.203, 1.02; 0.231, 0.896 at 120, 96; 120, 144; 144, 120; 120, 96; 120, 72 h respectively under arabinose based fermentation medium. It has been observed from Fig. 7(a) that higher FPA activity was produced by *T. reesei* under an arabinose-based fermentation medium as compared to the other fungal strains. A steep increment in FPA was observed after 72 h by *T. reesei*. On the other hand, higher CMCase were achieved by *Aspergillus* strains followed by *T. viride* and *N. crassa*. A sharp increment in the CMCase has been observed till 72 h by *Aspergillus* strains while CMCase produced by *T. viride* at a steady rate till 120 h after that period a sharp increment has been observed as viewed from Fig. 7(b).

Effect of Trehalose as Carbon Source on Cellulase Production Under Submerged Cultivation

Separate sets of batch experiments have been performed to study the effect of trehalose sugar (10 g.L^{-1}) as a carbon source on cellulase production by various fungal strains under submerged cultivation. Thirumale et al. (2001) reported cellulase formation by trehalose in *clostridium papyrosolvans* CFR-703. It was observed from Figs. 8(a) and 8(b) that various fungal strains produce significantly lower cellulase activities under the trehalose sugar-based fermentation medium. Maximum cellulase activities (IU. mL^{-1}) in terms of FPA and CMCase attained by *T. reesei*, *T. viride*, *N. crassa*, *A. niger* and *A. fumigatus* were 0.831, 0.589; 0.482, 1.07; 0.158, 0.302; 0.434, 2.18; 0.439, 1.19 at 120, 96; 120, 144; 144, 120; 96, 120; 96, 120, 72 h respectively. Higher FPA activity was observed by *T. reesei* followed by *T. viride* and *Aspergillus* strains under a trehalose-based fermentation medium. A steep increment in FPA activity was observed after 72 h by *T. reesei* and *A. fumigatus* strain as observed from Fig. 8(a).

On the other hand, higher CMCases were achieved by *A. niger* followed by *A. fumigatus* strain while *N. crassa*

sa showed lower CMCase activity under trehalose-based fermentation medium. A steep increment in the CMCase has been observed after 24 h by *Aspergillus* strains as viewed from Fig. 8(b).

Effect of Sorbitol on Cellulase Production Under Submerged Cultivation

Individual sets of batch experiments have been performed to study the effect of sugar alcohol such as sorbitol (10 g.L^{-1}) as a carbon source on cellulase production by various fungal strains under submerged cultivation. It was observed from Figs. 9(a) and 9(b) that various fungal strains produce significantly reduced cellulase activities under sorbitol-based fermentation medium. Maximum cellulase activities (IU. mL^{-1}) in terms of FPA and CMCase attained by *T. reesei*, *T. viride*, *N. crassa*, *A. niger* and *A. fumigatus* were 0.709, 0.506; 0.312, 0.786; 0.423, 0.795; 0.278, 1.18; 0.239, 0.911 at 120, 96; 120, 144; 144, 120; 96, 120; 96, 120 h respectively. Higher FPA was observed by *T. reesei* followed by *N. crassa* and *T. viride* strains under sorbitol-based fermentation medium. A steep increment in FPA activities was observed after 48 h by *T. reesei* as observed from Fig. 9(a), while smooth increments were observed after 96 and 120 h by *T. viride* and *N. crassa* strains respectively. On the other hand, higher CMCases were achieved by *Aspergillus* strains followed by *T. viride* and *N. crassa* strains under sorbitol-based fermentation medium as viewed from Fig. 9(b).

Effect of Mannitol as a Carbon Source on Cellulase Production Under Submerged Cultivation

Separate sets of batch experiments have been performed to study the effect of sugar alcohol such as mannitol (10 g.L^{-1}) as a carbon source on cellulase production by various fungal strains under submerged cultivation. It was observed from Figs. 10(a) and 10(b) that various fungal strains produce the least cellulase activities under mannitol-based fermentation

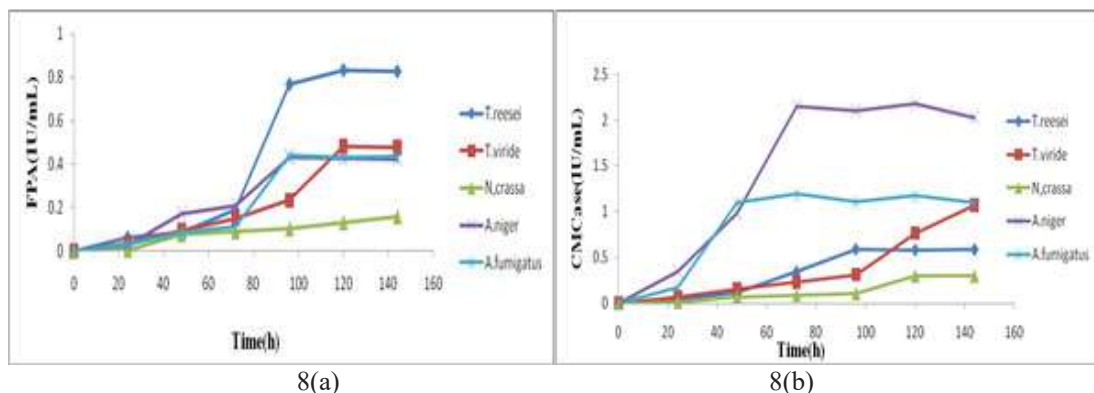


Fig. 8: Comparative FPA and CMCase achieved by various fungal strains under trehalose based production medium at 30°C and pH 5.0.

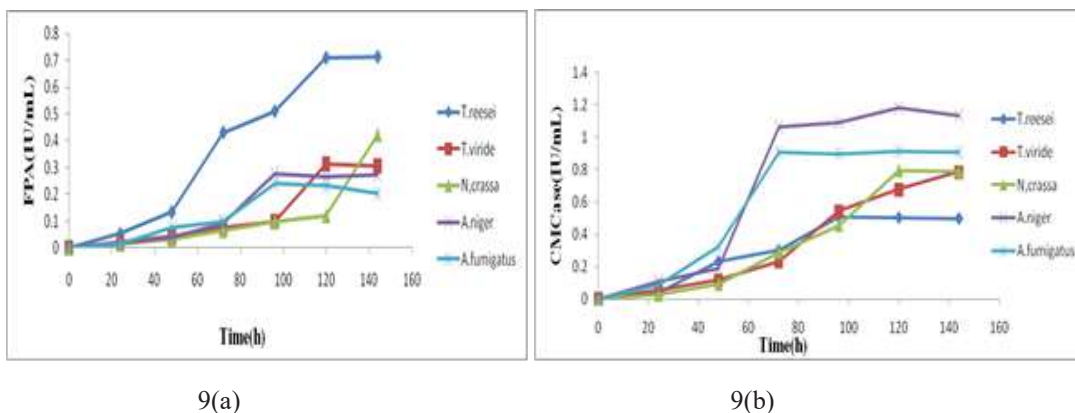


Fig. 9: Comparative FPA and CMCase achieved by various fungal strains under sorbitol based production medium at 30°C and pH 5.0.

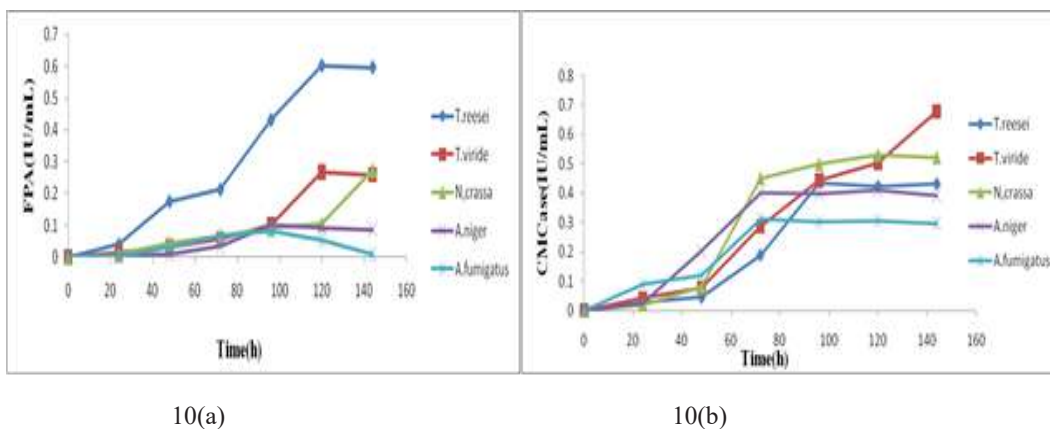


Fig. 10: Comparative FPA and CMCase achieved by various fungal strains under mannitol based production medium at 30°C and pH 5.0.

medium. Maximum cellulase activities (IU.mL⁻¹) in terms of FPA and CMCase attained by *T. reesei*, *T. viride*, *N. crassa*, *A. niger* and *A. fumigatus* were 0.602, 0.435; 0.267, 0.678; 0.274, 0.530; 0.102, 0.411; 0.083, 0.311 at 120, 96; 120, 144; 144, 120; 96, 120; 96, 72 h respectively. It has been observed from Fig. 10(a) that *T. reesei* produces higher FPA activity under mannitol-based fermentation medium as compared to the other used fungal strains. On the other hand, significantly good CMCases were observed by all the used fungal strains except *A. fumigatus* strain as viewed from Fig. 10(b). When the cellulase activities of various fungal strains under sorbitol and mannitol-based mediums are examined, it can be concluded that sorbitol-based mediums are considerably more suited for cellulase production than mannitol-based mediums.

Effect of Mixed Pure Sugars as Carbon Source on Cellulase Production Under Submerged Cultivation

Individual sets of batch experiments have been performed to

study the effect of mixed pure sugars (total 10 g.L⁻¹) such as cellulose + lactose (5+5), cellulose + xylose (5+5), cellulose + sorbitol (5+5), cellulose+ lactose + xylose (4+3+3), cellulose+ lactose + sorbitol (4+3+3), cellulose +lactose+xylose +sorbitol (2.5+2.5+2.5+2.5) in g.L⁻¹ as mixed carbon source on cellulase production by various fungal strains under submerged cultivation. It was observed from Figs. 11(a) (b), 12(a) (b), 13(a) (b),14(a) (b), 15(a) (b), 16(a) (b) that various fungal strains produce significantly better cellulase activities under carbon sources used as mixed condition than taken singly as lactose, sorbitol and xylose sugars. Ritter et al. (2013) investigated cellulase and xylanase production by *P. echinulatum* in submerged media containing cellulose amended with sorbitol. Maximum cellulase activities (IU. mL⁻¹) in terms of FPA and CMCase attained by *T. reesei*, *T. viride*, *N. crassa*, *A. niger* and *A. fumigatus* were 2.93, 2.59; 1.43, 3.17; 1.39, 2.75; 0.670, 4.03; 0.833, 3.46 : 2.29, 2.19; 1.26, 2.96; 1.08, 2.45; 0.593, 3.75; 0.711, 3.11 : 1.91, 1.78; 1.01, 2.41; 0.987, 2.19; 0.523, 3.64; 0.634, 3.01 : 2.47, 2.11;

1.51, 3.02; 1.29, 2.41; 0.541, 3.87; 0.765, 3.32; 2.20, 1.96; 1.31, 2.67; 1.13, 2.34; 0.592, 3.70; 0.751, 3.08 : 2.04, 1.61; 1.09, 2.28; 0.968, 1.96; 0.469, 2.78; 0.557, 2.49 under mixed sugars condition such as (L + C), (X + C), (S + C), (L + X + C), (L + S + C), (L + X + S + C) respectively.

(C+L: cellulose + lactose; C+X: cellulose + xylose; C+S: cellulose + sorbitol; C+L+X: cellulose+ lactose+ xylose; C+L+S: cellulose + lactose+ sorbitol; C+L+X+S: cellulose + lactose+ xylose+sorbitol).

Whereas cellulase activities (IU.mL⁻¹) in terms of FPA and CMCase attained by *T. reesei*, *T. viride*, *N. crassa*, *A. niger* and *A. fumigatus* were 2.31, 1.63; 1.26, 2.55; 1.06, 2.13; 0.433, 1.96; 0.556, 1.98 : 1.53, 1.15; 0.780, 1.54; 0.639, 1.30; 0.239, 1.21; 0.341, 1.29 : 0.709, 0.506; 0.312, 0.786; 0.423, 0.795; 0.278, 1.18; 0.239, 0.911 under single sugars

containing fermentation medium such as lactose, xylose and sorbitol respectively.

It has been observed from Figs. 11(a) (b), 12(a) (b), 13(a) (b), 14(a) (b) that cellulases activity is achieved by using fungal strains under mixed sugars (lactose + cellulose), (lactose + xylose + cellulose); (xylose + cellulose); (sorbitol + cellulose) were somewhat higher than lactose, xylose, and sorbitol-based medium taken singly and separately, which suggests that under mixed sugars condition microbes can take both types of sugars either required for growth or for cellulase induction rather than sugars taken singly in fermentation medium having higher growth-promoting with lesser enzyme induction capability. Pure soluble sugars play a significant role in the production process to overcome critical fermentation circumstances (mixing, aeration), and partially adding

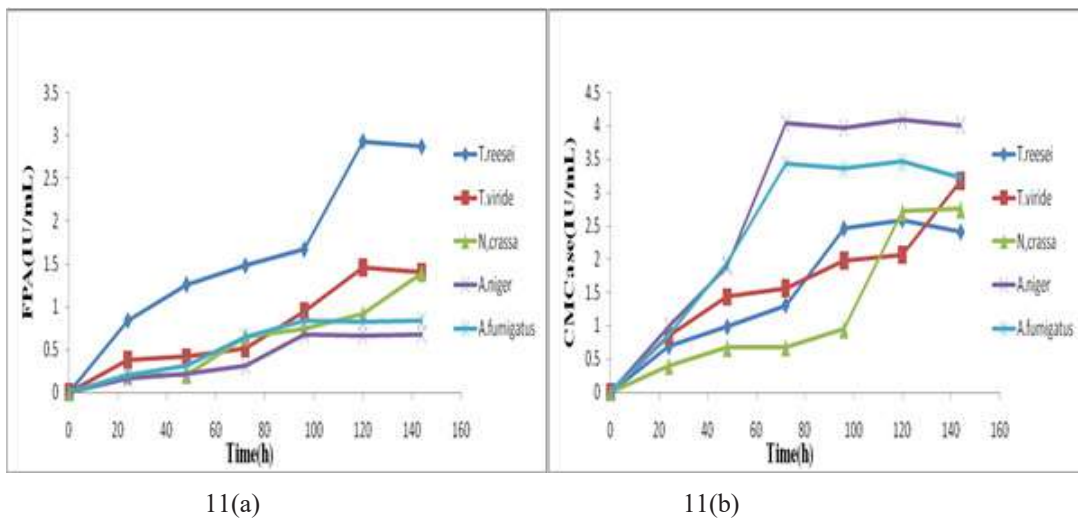


Fig. 11: Comparative FPA and CMCase achieved by various fungal strains under cellulose + lactose based production medium at 30°C and pH 5.0.

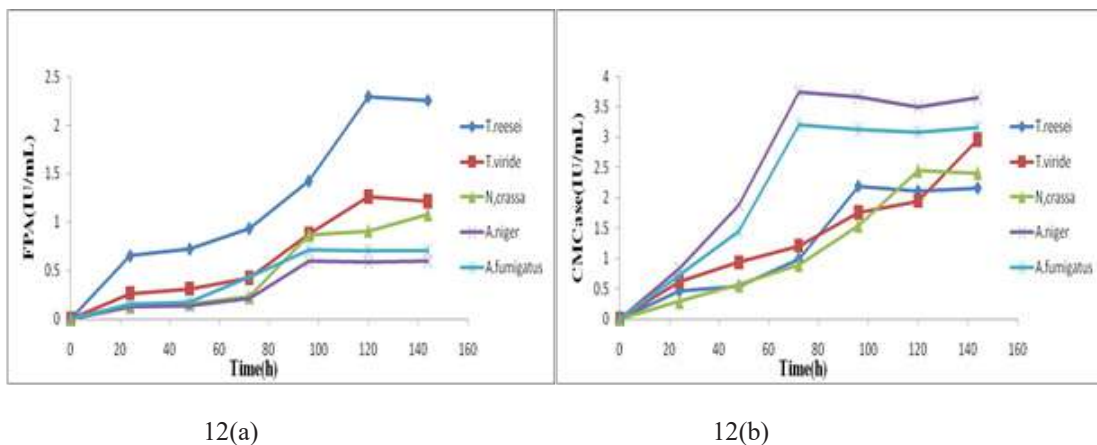


Fig. 12: Comparative FPA and CMCase achieved by various fungal strains under cellulose + xylose based production medium at 30°C and pH 5.0.

insoluble cellulose to soluble sugar-based media may boost cellulase induction capability while maintaining a smooth fermentation condition.

CONCLUSION

The induction of cellulase production by insoluble carbon source cellulose was a common and efficient strategy, but has some drawbacks, such as difficult fermentation operation, substantial cellulase loss, long fermentation time, and high energy consumption, resulting in the high cost of cellulase production in the industry. These drawbacks can be overcome if soluble carbon sources are used as the inducers for cellulase production. When the cellulase activity produced by fungal strains under pure sugars based liquid-state fermentation

was compared, it was discovered that *Trichoderma* strains produce higher activity under lactose, CMC and sucrose, xylose, trehalose, and sorbitol based medium, whereas *Aspergillus* strains produce higher activity under maltose and cellobiose, xylose, trehalose based medium. On the other hand, *Neurospora* showed higher activity under sucrose and maltose and arabinose-based medium while the least activity was observed with lactose-based media. Arabinose sugar was found least effective for cellulase production with *Trichoderma* and *Aspergillus* strains. In sugar alcohols, sorbitol was found quite effective for cellulase production as compared to mannitol. Cellulases activity achieved by fungal strains under mixed sugars condition (lactose + cellulose) (lactose + xylose + cellulose) (xylose + cellulose) (sorbitol +

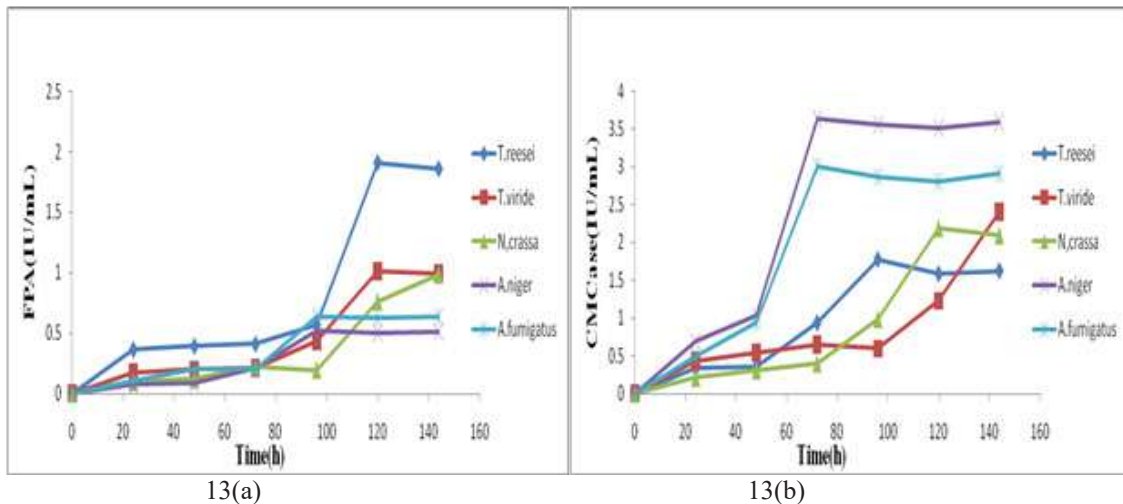


Fig. 13: Comparative FPA and CMCCase achieved by various fungal strains under cellulose + sorbitol based production medium at 30°C and pH 5.0.

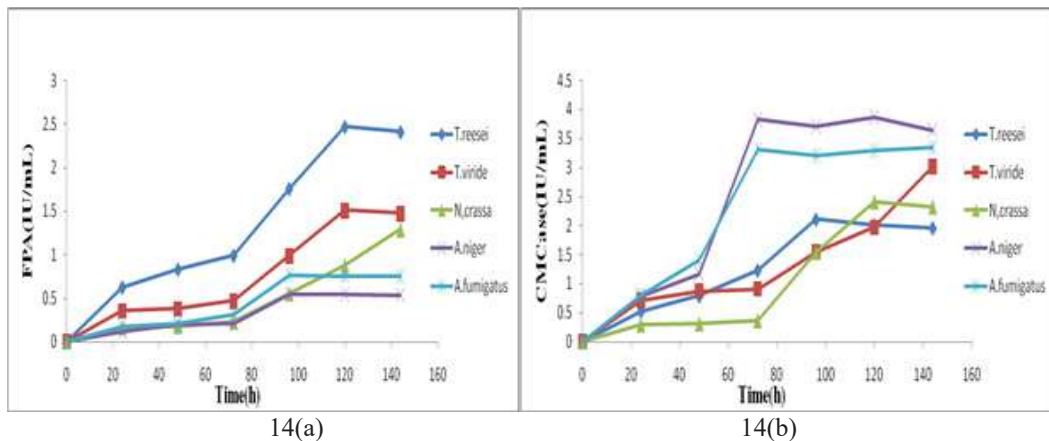


Fig. 14: Comparative FPA and CMCCase achieved by various fungal strains under cellulose + lactose + xylose based production medium at 30°C and pH 5.0.

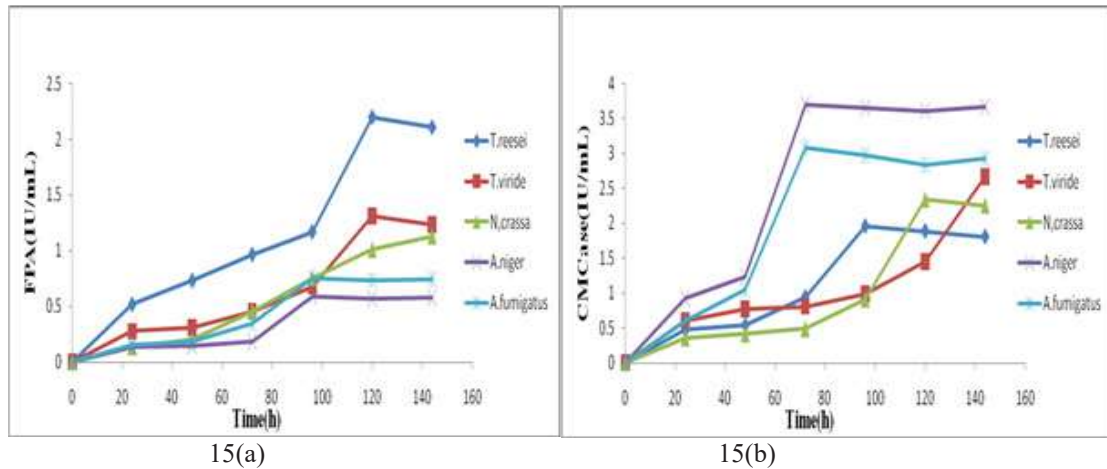


Fig. 15: Comparative FPA and CMC_{case} achieved by various fungal strains under cellulose + lactose + sorbitol based production medium at 30°C and pH 5.0.

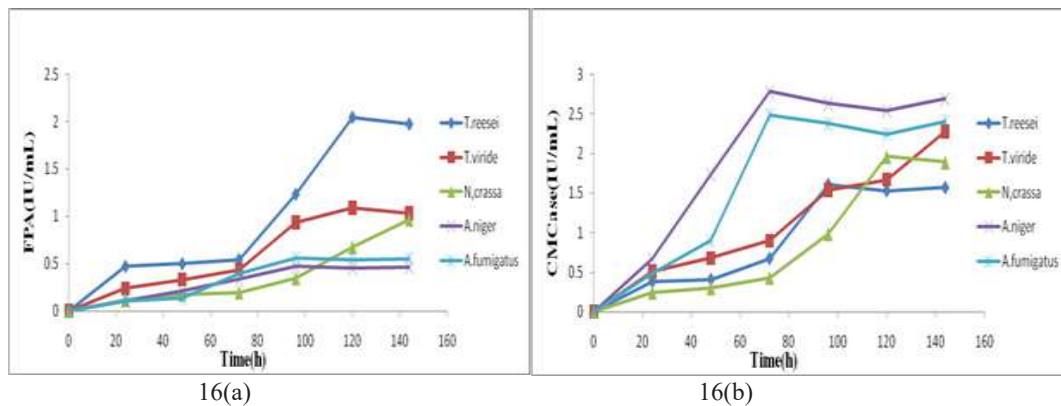


Fig. 16: Comparative FPA and CMC_{case} achieved by various fungal strains under cellulose + lactose + sorbitol + xylose based production medium at 30°C and pH 5.0.

cellulose) were somewhat higher than only lactose or xylose or sorbitol-based medium. It has also been concluded that different fungal strains used pure sugars and sugar alcohols differently for cellulase induction and production.

ACKNOWLEDGMENTS

The authors gratefully acknowledged the ministry of human resource and development, India for providing fellowship to carry out present research work.

REFERENCES

- Allan, A.L. and Roche, C.D. 1989. Effects of strain and fermentation conditions on the production of cellulases by *T. reesei*. *Biotechnol. Bioeng.*, 33: 650-656.
- Bhatt, M.K. 2000. Cellulases and related enzymes in biotechnology. *Biotechnol. Adv.*, 18: 355-383.
- Binder, A.T.K. and Ghose. C. 1978. Adsorption of cellulose by *Trichoderma viride*. *Biotechnol. Bioeng.*, 20: 1187-1199.
- Cotoras, M. and Agosin, E. 1992. Regulatory aspects of endoglucanase production by the brown rot fungus *Gleophyllum trabeum*. *Exper. Microbiol.*, 16: 253-260.
- Domingues, F.C., Queinoz, J.A., Cabral, J.M.S. and Fonseca, L.P. 2004. The influence of culture conditions on the mycelial structure and cellulase production by *Trichoderma reesei* RUT C 30. *Enzyme Microbial Technol.*, 5: 26-34.
- Gautam, S.P., Bundela, P.S., Pandey, A.K., Khan, J., Awasthi, M.K. and Sarsaiya, S. 2011. Optimization for the production of cellulase enzyme from the municipal solid waste residue by two novel cellulolytic fungi. *Biotechnol. Res. J.*, 11: 8-17.
- Ghose, T.K. 1987. Measurement of cellulase activities. *Pure Appl. Chem.*, 59(2): 257-268.
- Ike M. and Tokuyasu, K. 2018. Cellulase production of *Trichoderma reesei* (*Hypocrea jecorina*) by continuously fed cultivation using sucrose as primary carbon source. *J. Appl. Glycosci.*, 65(4): 51-56.
- Ivanova, C., Baath, J.A., Seiboth, B. and Kubicek, C.P. 2013. Systems analysis of lactose metabolism in *Trichoderma reesei* identifies a lactose

- permease that is essential for cellulase induction. PLoS ONE, 8(5): 463.
- Janas, P., Targonski, Z. and Mleko, S. 2002. New inducers for cellulase production by *Trichoderma reesei* -7. Polish Agri. Uni. Food Technol. Series. 5: 14-27
- Ju, L.K. and Afolabi, O.A. 1999. Waste paper hydrolysate as a soluble inducing substrate for cellulase production in continuous culture of *Trichoderma reesei*., Biotechnol Prog., 5: 91-97.
- Kamagata, Y., Yachi, M., Kurasawa, T., Suto, M., Sasaki, H., Takao, S. and Tomito, F. 1991. Cellulase induction by cellobiose octaacetate in *Penicillium purpogenum*. J. Fermentation Bioengg., 72: 217-220.
- Li, C., Lin, F., Zhou, L., Qin, L., Li B., Zhou Z., Jin, M. and Chen Z. 2017. Cellulase hyper-production by *Trichoderma reesei* mutant SEU-7 on lactose., Biotechnol Biofuels. 10: 228.
- Lin, J., Zhang, X., Song, B., Xue, W., Su, X., Chen, X. and Dong, Z. 2017. Improving cellulase production in submerged fermentation by the expression of a Vitreoscilla hemoglobin in *Trichoderma reesei*. AMB Express, 7: 203.
- Loewenberg, J.R. and Chapman, C.M. 1997. Sophrose metabolism and cellulase induction in *Trichoderma*. Archives Microbiol., 113: 61-64.
- Maibam, P.D. and Maiti, S.K. 2019. A strategy for simultaneous xylose utilization and enhancement of cellulase enzyme production by *Trichoderma reesei* cultivated on liquid hydrolysate followed by induction with the feeding of solid sugarcane bagasse. Waste and Biomass Valoriz., 2019: 1-10
- Morikova, Y., Ohashi, T., Mantani, O. and Okada, H. 1995. Cellulase induction by lactose in *Trichoderma reesei* PC3-7. Appl. Microbiol. Technol., 44: 106-111.
- Morrison, J., McCarthy, U. and Michal, A.P. 1987. Cellulase production by *Taloromyces emersonii* CBS 814.70 and a mutant UV7 during growth on cellulose, lactose, and glucose-containing media. Enzyme Microbial Technol., 9: 422-425.
- Niranjane, A.P., Madhou, P. and Stevenson, T.W. 2007. The effect of carbohydrate carbon sources on the production of cellulase by *Phlebia gigantean*. Enzyme and Microbial Technol., 40(6): 1464-1468.
- Ritter, C.E.T., Camassola, M., Zampieri D., Silveira, M.M. and Dillon A.J.P. 2013. Cellulase and xylanase production by *Penicillium echinulatum* in submerged media containing cellulose amended with sorbitol. Enzyme Res., 2013: 9.
- Schaffner, O.W. and Toledo, R.T. 1991. Cellulase production by *Trichoderma reesei* when culture on xylose-based media supplemented with sorbose. Biotechnol. Bioengg., 7: 12-16.
- Schuerg, T., Prah, J.P., Gabriel, R., Harth, S., Tachea, F., Chen, C.S., Miller M., Masson F., He Q., Brown, S., Mirshahi, M., Liang, L., Tom, L.M., Tanjore, D., Sun N., Pray T.R. and Singer S.W. 2017. Xylose induces cellulase production in *Thermoascus aurantiacus*. Biotechnol. Biofuels, 10: 271.
- Sehnm, N.T., Bitteencourt, L.R.D., Camassola, M. and Dillon, A.J.P. 2006. Cellulase production by *Penicillium echinulatum* on lactose. Appl. Microbial. Biotechnol., 72: 1 63-167.
- Suto, M. and Tomita, F. 2001, Induction and catabolite repression mechanisms of cellulase in fungi. J. Biosci. Bioengg., 92: 305-311.
- Thirumale, S., Rani, D.S. and Nand, K. 2001. Control of cellulase formation by trehalose in *Clostridium papyrosolvans* CFR-703. Process Biochem., 37(3): 241-245.
- Waghmare, P.K.R., Patil, S.M., Jadhav, S.L., Jeon, B.H. and Govindwar, S.P. 2018. Utilization of agricultural waste biomass by cellulolytic isolate *Enterobacter* sp. SUK-Bio. Agric. Natural Resour., 52(5): 399-406.
- Wang, C.H., Hseu, T.H. and Huang, C.M. 1988. Induction of cellulases by cellooligosaccharides in *Trichoderma koningii* G-39. J. Biotechnol., 9: 47-60.
- Wang, C.H. and Reesei, E.T. 1994. Lactose utilization by fungal system an approach. Enzyme Microbial Technol., 66(3): 506-577.
- Wyman, M. and Chen, S. 1992. Cellulase production by *Trichoderma reesei* using whole wheat flour as a carbon source. Enzyme Microbial Technol., 14: 825-831.
- Wyman, M. and Chen, S. 1991. Cellulase production is induced by carbon sources derived from the waste newspaper. Process Biochem., 26: 93-100.



Impacts of Discharged Low-Temperature Water on Water Table and Temperature in the Riparian Zone

Bei Zhu^{*(**)}†, Shiyan Wang^{*(**)}, Chang Liu^{**}, Wei Su^{**(***)}, Jiapeng Wu^{**}, Cunwu Li^{****} and Jingshi Shang^{**}

*State Key Laboratory of Simulation and Regulation of Water Cycle in River Basin, Beijing 100038, China

**China Institute of Water Resources and Hydropower Research, Beijing 100038, China

***College of Science and Technology, Hebei Agricultural University, Huanghua 061100, China

****Guangxi Institute of Water Resources and Hydropower Research, Nanning 530023, China

†Corresponding author: Bei Zhu; zhubei_hhu@163.com

ABSTRACT

Nat. Env. & Poll. Tech.

Website: www.neptjournal.com

Received: 16-04-2021

Revised: 14-05-2021

Accepted: 07-06-2021

Key Words:

Lateral hyporheic exchange

Discharged low-temperature water

Water fluctuations

Temperature distribution

We observed the water level and temperature in the lower stretch of the Hsin-an river in China for different times to show the characteristics of the water table and temperature in the riparian zone under the influence of discharged low-temperature water. The water table in the riparian zone showed a typical daily cycle change with a fluctuation range of 239.42-275.99 cm, according to the findings. With increasing distance from the river, the amplitudes of the water table fluctuation were reduced, and the phases were lagged. In the high-temperature period, riparian temperatures range from 20.4°C to 26.0°C, whereas in the low-temperature phase, temperatures range from 12.9°C to 19.2°C. The temperature distribution in the riparian zone was described in the vertical direction as "warmer on the surface and cooler at the bottom" during high-temperature periods and "cooler on the surface and warmer at the bottom" during low-temperature periods, with the temperature gradient gradually decreasing with depth. There was clear temperature zonation in the horizontal direction during the high-temperature phase but none during the low-temperature period. The study will serve as a benchmark for future hyporheic zone ecological impact assessments.

INTRODUCTION

The hyporheic zone is a band of permeable, saturated sediment surrounding a river where surface water and ground-water mix, and includes riverbeds (shallow hyporheic zone), riverbanks, saturated sediments under dry bars (parafluvial hyporheic zone), and riparian and floodplain areas (floodplain hyporheic zone) (Jones et al. 2000, Tonina & Buffington 2007, Zhou et al. 2014). The material and energy transfer between the riparian zone and the river is driven by the lateral hyporheic exchange, which plays a key role in the regulation of river ecosystem health (Casas et al. 2015).

The power station's diversion port is located in the reservoir's low-temperature layer (Harleman 1982), where the temperature is lower than that of natural water for the majority of the year. Low-temperature water flows downstream, changing the distribution of flow field and temperature field in the riparian zone through the lateral hyporheic exchange (Boutt & Fleming 2009), having a significant impact on aquatic organisms, benthic organisms, and microbial communities, as well as the river ecosystem (Greenwood et al. 2007). The average water temperature of the Luotong Port, downstream of the Hsin-an river reservoir, was 19°C

before the reservoir was built, and decreased by 5.5°C after the reservoir was built (Weiwu 2001). Casado et al. (2013) studied the water temperature of the Sauce Grande river in Argentina and revealed that water temperatures immediately below the dam were notably reduced, and diurnal cycles were reduced and delayed in magnitude. Several scholars have studied the impact of discharged low-temperature water on temperature distribution in the hyporheic zone. Gerech et al. (2011) carried out a study at Hornsby Bend in the lower Colorado river of Texas using hydraulic and thermal measurements to identify the hyporheic zone's depth and determine its variation, both spatially and temporally. Molina et al. (2011) analyzed the temperature time series of the river course and riverbank of the Tuer river and found that the fluctuating river water temperature decays exponentially along the lateral riverbank, and the rate of decay is related to the groundwater velocity, thermal diffusion coefficient, and frequency of the temperature time series. Vogt et al. (2012) applied distributed temperature sensing (DTS) along optical fibers wrapped around tubes to measure high-resolution vertical temperature profiles of the unsaturated zone and shallow riparian groundwater. They found that the observed riparian groundwater temperature distribution could not be described

by uniform flow, but by horizontal groundwater flow velocities with varying depth. Hucks et al. (2009) found that the temperature in the near-bank is significantly associated with the river temperature with a certain lag, while it is steadily away from the bank.

The fluctuating stage has a significant effect on the interaction between river water and groundwater downstream of the dam (Hancock 2002, Nilsson & Berggren 2000, Hamilton 2005). Hanrahan (2008) monitored and analyzed the water pressure and temperature in the riverbed downstream of the dam and showed that the operation of a dam power station can reverse the direction and intensity of vertical hyporheic exchange. Arntzen et al. (2006) monitored the water pressure, temperature, and hydrochemical index in the hyporheic zone of a regulated, large cobble bed river in Columbia and reported that the vertical hydraulic gradient, water temperature, and hydrochemical reaction in the riverbed all responded to the fluctuating river flow. Based on this study, Fritz & Arntzen (2007) further estimated the relationship between vertical exchange rate and river stage. Kiel & Cardenas (2014) calculated the extent and duration of lateral hyporheic exchange throughout the Mississippi River network using a physics-based numerical model that considered the distribution of groundwater baseflow, river discharge, alluvium permeability, and river morphology.

Some scholars have studied the effect of reservoir operation on vertical or lateral hyporheic exchange at different scales. However, the in-depth quantitative characterization of

the dynamic processes of exchange intensity and direction in response to river stage fluctuations has been minimal. This study carried out a hyporheic exchange test in the riparian zone downstream of the Hsin-an River dam, monitored the water level and temperature of the river and riparian zone, characterized the dynamic processes of lateral hyporheic exchange intensity and direction in response to river stage fluctuations, and assessed the dam operations on fluid exchange and temperature conditions in the riparian zone.

MATERIALS AND METHODS

The study area is located in the riparian zone ($29^{\circ}24' N$, $119^{\circ}2' E$) of the Hsin-an river in Jiande City, Zhejiang Province, China, approximately 20 km downstream of the dam. The annual range of river temperature at the study site affected by dam operation is $13.5\text{--}17.5^{\circ}\text{C}$, and the fluctuation range of the river water level is as high as 1 m, with a daily cycle. It is typical low-temperature water discharged from a reservoir. Seven observation wells G1, G2, G3, G4, G5, G6, and G7 were arranged in the riparian zone (Fig. 1). G1, G2, G3, G4, and G5 were in a transect perpendicular to the river, being 3.00 m, 5.79 m, 8.46 m, 10.81 m, 13.59 m offshore, respectively. G5, G6, and G7 were parallel to the river. The observation wells were made of plastic blind pipes. Each pipe was 4 m long with an outer diameter of 100 mm and an inner diameter of 80 mm and covered with a layer of extremely permeable non-woven geotextile. HM21 input liquid level transmitters (measuring accuracy: 0.1 cm) were

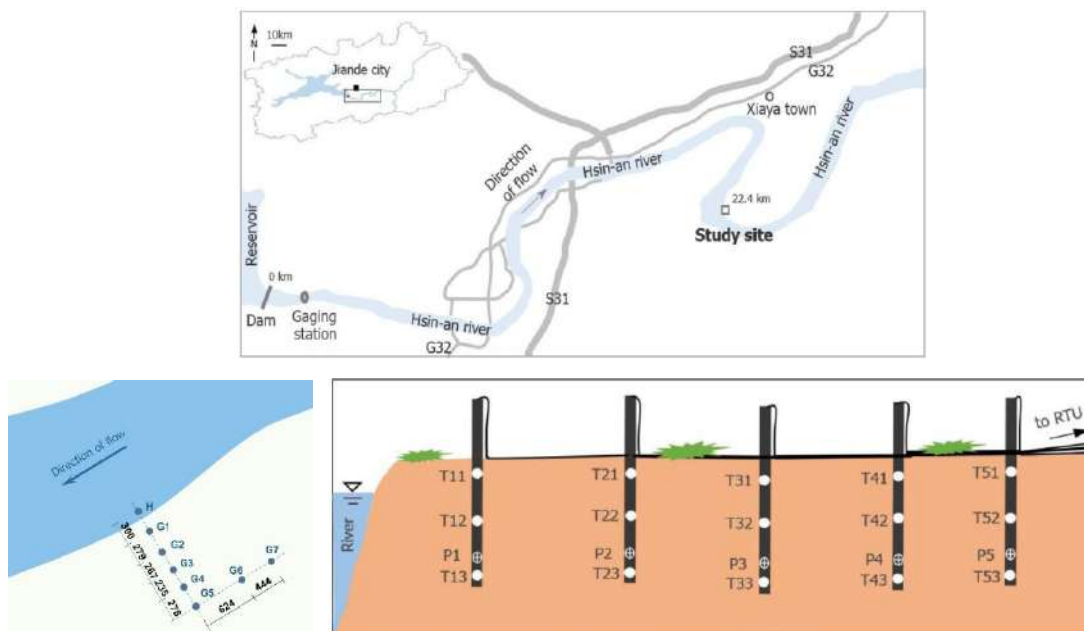


Fig. 1: Layout diagram of the study site and cross-sectional views of G1, G2, G3, G4, and G5 (T: a temperature sensor; P: pressure sensor).

used for sensing pressure, and PT100 thermal resistance temperature sensors (measuring accuracy: 0.1°C) were used for sensing temperature. To monitor the river's water level and temperature, a pressure sensor, and two temperature sensors were placed near the shoreline at H. Temperature sensors were placed in the air and in the soil layer at the same time to monitor the air and ground temperatures. Using a temperature-water level analog signal automatic acquisition system, the temperature and pressure sensed by the sensors were automatically recorded and stored every 5 min.

RESULTS AND DISCUSSION

The water table in the riparian zone simultaneously varied at different times of the day and different distances from

the river. The interaction between the surface water and groundwater varied in different seasons. Overall, the water table fluctuated from 239.42 ~ 275.99 cm with an amplitude of 36.57 cm on September 4, 2014 (Fig. 2). At 22:00, the water table was the highest, the river stage was higher than the water table, and the river recharged the groundwater. At 14:00, the water table was the lowest, the river stage was lower than the water table, and the groundwater recharged the river. On December 3, 2014, the groundwater level fluctuated from 266.96-281.39 cm with an amplitude of 14.43 cm. At 10:00, the water table was the highest, the river stage was lower than the water table, and the groundwater recharged the river. At 2:00, the water table was the lowest, the river stage was higher than the water table, and the river recharged the groundwater. The amplitude of the water table in Sep-

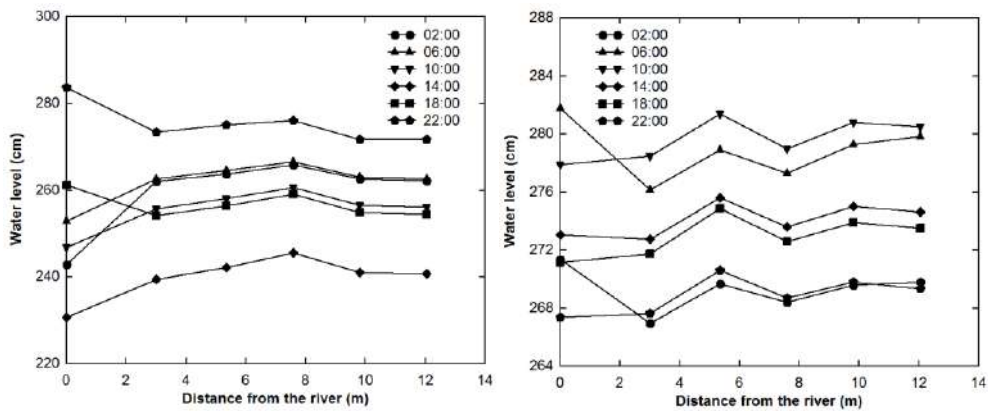


Fig. 2: Temporal and spatial distribution of the water table in the riparian zone (Left: September 4, 2014; Right: December 3, 2014).

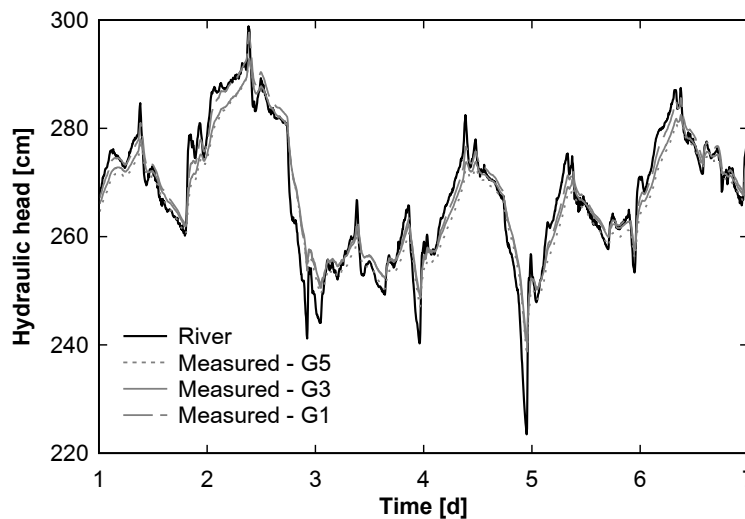


Fig. 3: Water table elevation time series at the study site river, G5, G3, and G1 denotes the water level of the river and each observation well, respectively. The lines G1, G3, and G5 are perpendicular to the river. The distances of wells G5, G3, and G1 from the river were 13.59, 8.46, and 3 m, respectively. Water table fluctuations were relatively attenuated and lagged relative to the river stage fluctuations.

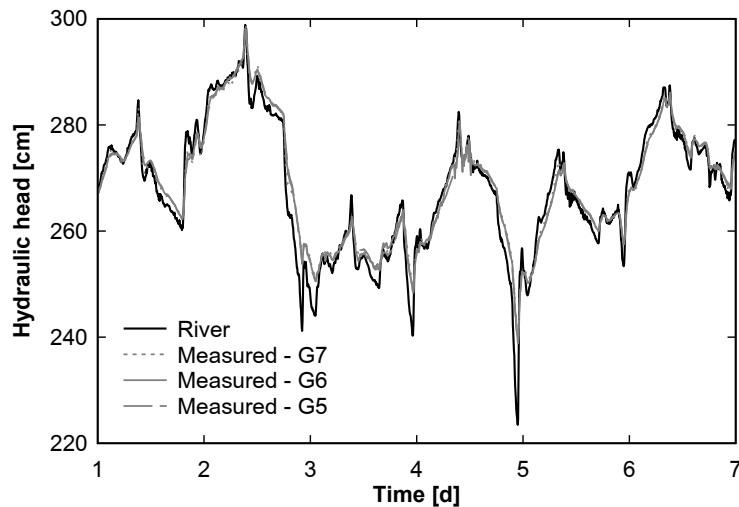


Fig. 4: Water table elevation time series at the study site river, G7, G6, and G5 denote the water level of the river and each observation well, respectively. The lines of G7, G6, and G5 are parallel to the river. The water table fluctuations of G7, G6, and G5 were almost the same.

tember was higher than that in December, which indicated that the operation of the upstream reservoir was stronger in September than in December.

To study the response of the water table in the riparian zone to the fluctuating river stage, measured data of G1, G3, G5, G6, and G7 from November 28–December 3, 2014 were taken as an example for analysis. The lines G1, G3, and G5 are perpendicular to the river, and the lines G5, G6, and G7 are parallel to the river. During this period, the river stage fluctuated significantly, and the temperature remained in the range of 15.3–16.9°C. The fluctuation of the river water level was approximately a sinusoidal curve, showing a typical

diurnal variation (Fig. 3). The river stage fluctuated widely, ranging from 223 ~ 299 cm. The highest value of the river stage appeared at 10:00 am and the lowest value at night. The response time and amplitude of different observation wells to the fluctuation of river stage were different, showing that water table fluctuations were damped and lagged away from the river. The amplitudes of the water table fluctuations of G1, G3, and G5 were 61%, 54%, and 49% of the river stage, respectively, and the phase lags were approximately 6, 11, and 15 mins, respectively. G5, G6, and G7 were equidistant from the river, and the fluctuations of the water table in the three wells were almost the same, exhibiting amplitude

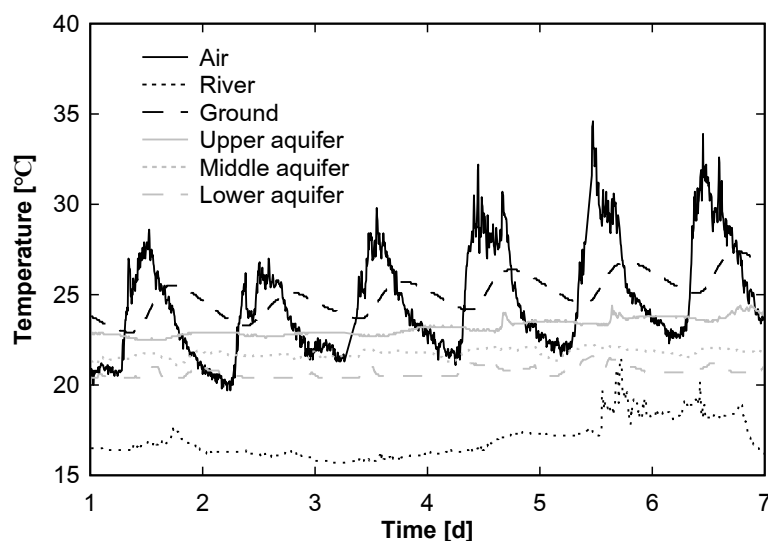


Fig. 5: Temperature distribution of air, river, ground, and groundwater in the riparian zone (high-temperature period).

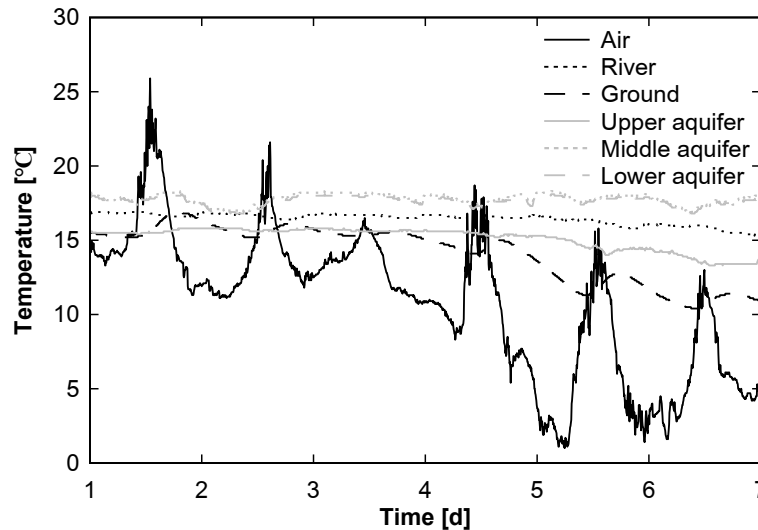


Fig. 6: Temperature distribution of air, river, ground, and groundwater in the riparian zone (low-temperature period).

attenuation when compared with the fluctuation of the river stage (Fig. 4). In other words, the riparian zone's fluctuating water table's amplitude attenuation was proportional to its distance from the river, and the oscillations in the water table were nearly identical at the same distance.

Temperature Response

During the monitoring period, the daily temperature showed a typical cyclic fluctuation (Fig. 5 and Fig. 6), with the highest, lowest, and average temperatures of 34.6, 19.7 and 24.7°C in the high-temperature period, and 25.9, 1.0 and 10.74°C in the low-temperature period, respectively. The ground temperature variation was similar to that of air temperature, but its amplitude was approximately one-third of the air temperature, and its phase lagged behind air temperature, indicating that a certain duration was necessary for the ground to be heated by the sun. The river water temperature was affected by the low-temperature water discharged from the upstream reservoir. The daily temperature fluctuation of the river was approximately 0.5°C. The river temperature was about 16.97°C in the high-temperature period and 16.45°C in the low-temperature period. The highest and lowest temperatures were recorded in the evening and morning of each day, respectively, as is typical of the river's daily temperature range. The temperature change in the downstream river caused by the operation of the upstream reservoir was smaller than in the natural river.

The dam-induced low-temperature water discharged into the downstream river, and the interaction between the river and riparian aquifer caused a change in the heat transfer and exchange in the riparian zone, which led to a change in

the temperature distribution in the riparian zone. Under the bidirectional radiation of the lower low-temperature water layer and the higher natural temperature surface layer, the infiltration of low-temperature water will result in a non-isothermal soil environment, resulting in the redistribution of the temperature field. To further clarify the temporal and spatial distribution of temperature in the riparian zone and the dynamic characteristics of diurnal cycle changes, contour maps of profiles in the riparian zone were drawn at different times of the day for the high-temperature and low-temperature periods (Fig. 7 and Fig. 8). The temperature contours of the sections G1, G2, G3, G4, G5, and the river sensor were plotted at a 4-hour interval from 2:00~22:00 on September 4, 2014, and December 3, 2014. The boundary between the river and bank was located at $x=0$. The riparian surface was $y=0$, and $y < 0$ was below the surface.

As shown in Fig.7 and Fig.8, the spatial distribution of temperature in the riparian aquifer was uneven and changed over time. During the monitoring period, the temperature of the riparian aquifer varied between 20.4 ~ 26.0°C in the high-temperature period and between 12.9-19.2°C in the low-temperature period. The aquifer of the riparian zone had obvious temperature stratification in the vertical direction, characterized as "warmer on the surface and cooler at the bottom" in the high-temperature period and "cooler on the surface and warmer at the bottom" in the low-temperature period. Moreover, the temperature gradient gradually decreased with depth. In the horizontal direction, it could be divided into low-temperature, medium-temperature, and high-temperature zones from near shore to far shore. The temperature zone area changes with time, showing that cold

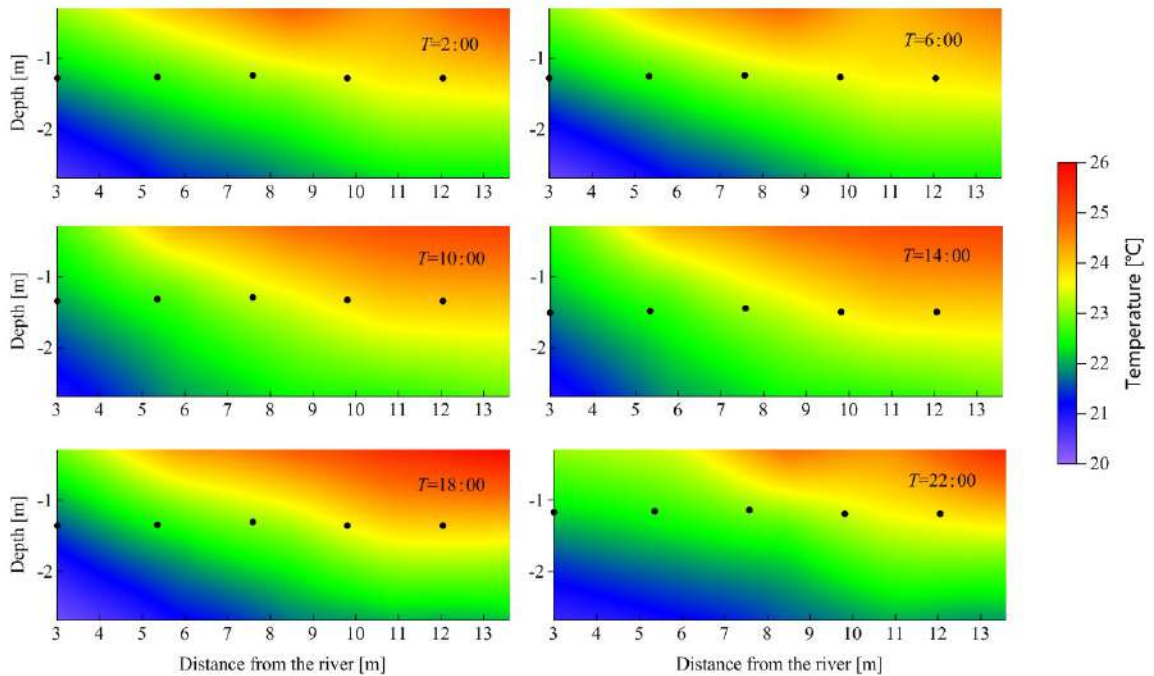


Fig. 7: Temperature distribution in the riparian zone at different times on September 4, 2014 (high-temperature period). The black spots represent the water levels in each of the monitoring wells

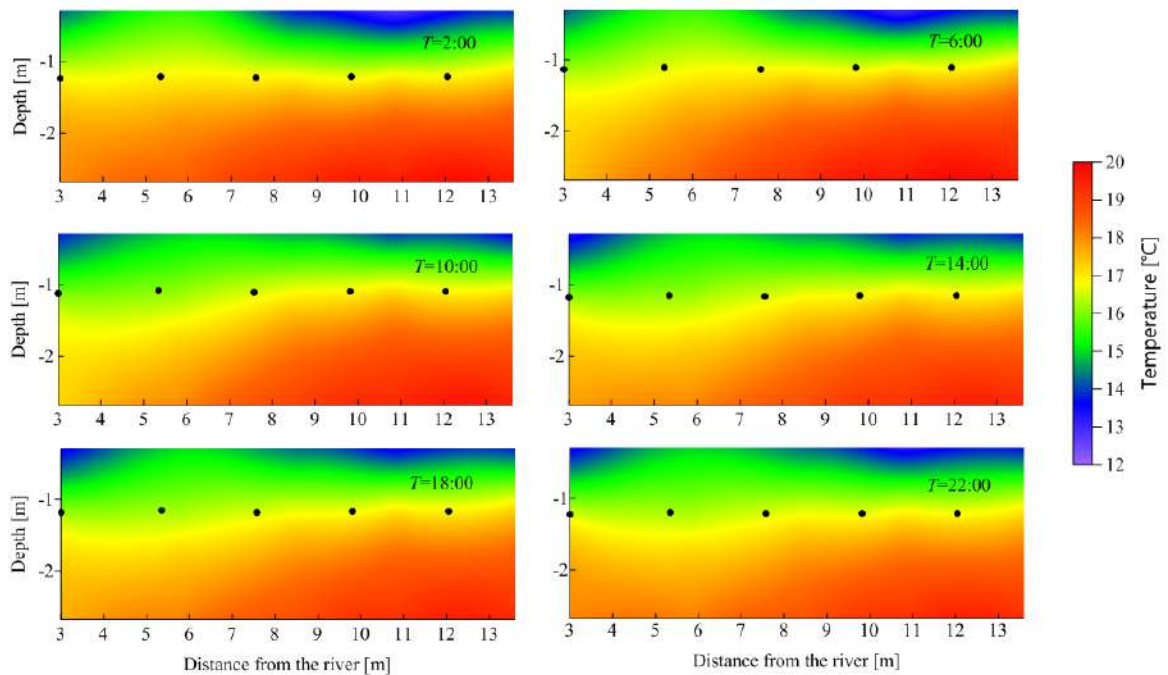


Fig. 8: Temperature distribution in the riparian zone at different times on December 3, 2014 (low-temperature period). The black spots represent the water levels in each of the monitoring wells.

water diffuses at a distance and the temperature gradient gradually decreases in the high-temperature period, while there is no obvious zonation in the low-temperature period, and the temperature fluctuation amplitude in the high-temperature period is higher than that in the low-temperature period. This was because the magnitude and range of lateral hyporheic exchange in the riparian zone were much higher than those in the vertical direction, and the hyporheic exchange intensity was stronger in the high-temperature period, which promoted the lateral propagation and diffusion of temperature. Under the influence of solar radiation, the temperature in the shallow riparian aquifer obviously changed with time. Taking the high-temperature period as an example, the shallow layer temperature reached the maximum value at 14:00, and the area of the high-temperature region was the largest. When T=22:00, the area of the high-temperature region reached the minimum, and the area of the low-temperature region reached the maximum. This was because the temperature of the unsaturated soil and shallow aquifer increased with the increase in illumination intensity. With heat conduction, the temperature of the unsaturated soil and shallow aquifer increased and peaked at 14:00. The influence of air temperature on the temperature of the riparian zone got weaker as the illumination intensity reduced, the low-temperature zone began to expand, and the high-temperature zone gradually shrank.

CONCLUSION

This study investigated the dynamic processes of hyporheic exchange and temperature distribution in the riparian zone in response to dam-induced low-temperature water fluctuations downstream of the Hsin-an river dam by monitoring the temperature and water level of the river and riparian zone. The conclusions are as follows:

- (1) The water table in the riparian aquifer showed a significant fluctuation between 223 ~ 298 cm, a typical daily cycle variation. The fluctuations of the water table in the hyporheic zone were affected by fluctuations in the river stage: the farther it was from the river, the smaller the fluctuation amplitude was and the slower was its phase lag, that is, the slower was the response of lateral exchange intensity to river stage fluctuations.
- (2) The temperature distribution in the riparian aquifer was affected by low-temperature water infiltration, which was shown as “upper warm and lower cool” in the high-temperature period and “upper cool and lower warm” in a low-temperature period in the vertical direction. Moreover, the temperature gradient decreased gradually with depth. The temperature distribution could also be divided into low-temperature, medium-tempera-

ture, and high-temperature zones from near shore to far shore in the high-temperature period in the horizontal direction, and a gradually decreasing gradient was observed. However, there is no obvious division of temperature in the low-temperature period.

The hydrological variation in rivers caused by low-temperature water discharged from large reservoirs has a significant impact on the habitat structure and flow-temperature environment in the riparian zone. The mechanism of water exchange and temperature transfer in riparian zones can be used to quantitatively assess the effects of low-temperature discharged water on flow, temperature, and the ecological environment in riparian zones, as well as to improve overall river ecological health evaluation and coordination. The temperature in the riparian zone is affected by unsaturated layer temperature, river water temperature, and exchange rates between river and groundwater, while the temperature in the unsaturated layer is affected by light intensity and air temperature (Jie et al. 2014). The response mechanism of temperature in the hyporheic zone needs to be further studied quantitatively. Meanwhile, research on the response mechanism of the riparian hyporheic zone to biochemistry (such as redox reactions) and ecological changes (such as biocenosis) caused by dam operation at the basin scale still needs to be strengthened.

ACKNOWLEDGEMENT

This research was funded by the Major Science and Technology Program for Water Pollution Control and Treatment (2018ZX07111003), National Natural Science Foundation of China (Grant No.91647212); IWHR Research & Development Support Program (WE0163A052018, WE0163A042018, WE0145B422019, HTWE0202A242016), Program for Innovative Research Team of IWHR (WE0145B592017).

REFERENCES

- Arntzen, E.V., Geist, D.R. and Dresel, P.E. 2006. Effects of fluctuating river flow on groundwater/surface water mixing in the hyporheic zone of a regulated, large cobble bed river. *River Res. Appl.*, 22(8): 937-946.
- Boutt, D.F. and Fleming, B.J. 2009. Implications of anthropogenic river stage fluctuations on mass transport in a valley fill aquifer. *Water Resour. Res.*, 45(4): 546-550.
- Casado, A., Hannah, D.M., Peiry, J.L. and Campo, A.M. 2013. Influence of dam-induced hydrological regulation on summer water temperature: Sauce Grande River, Argentina. *Ecology*, 6(4): 523-535.
- Casas, R., Saltveit, S.J. and Alfredsen, K. 2015. The survival of Atlantic salmon (*Salmo salar*) eggs during dewatering in a river subjected to hydropeaking. *River Res. Appl.*, 31(4): 433-446.
- Fritz, B.G. and Arntzen, E.V. 2007. Effect of rapidly changing river stage on uranium flux through the hyporheic zone. *Groundwater*, 45(6): 753-760.
- Gerecht, K.E., Cardenas, M.B., Guswa, A.J., Sawyer, A.H., Nowinski, J.D. and Swanson, T.E. 2011. Dynamics of hyporheic flow and heat

- transport across a bed-to-bank continuum in a large regulated river. *Water Resour. Res.*, 47(3): 104-121.
- Greenwood, M.H., Sims, R.C., McLean, J.E. and Doucette, W.J. 2007. Temperature effect on tert-butyl alcohol (TBA) biodegradation kinetics in hyporheic zone soils. *Biomed. Eng. Online*, 6(1):34-41.
- Hamilton, P. 2005. Groundwater and surface water: a single resource. *Water Environ. Technol.*, 17(5): 37-41.
- Hancock, P.J. 2002. Human impacts on the stream-groundwater exchange zone. *Environ Manag.*, 29(6): 763-781.
- Hanrahan, T.P. 2008. Effects of river discharge on hyporheic exchange flow in salmon spawning areas of a large gravel-bed river. *Hydrol. Proc. Int. J.*, 22(1): 127-141.
- Harleman, D.R. 1982. Hydrothermal analysis of lakes and reservoirs. *J. Hydraul Eng. Division*, 108(3): 301-325.
- Hucks, A., Bayani, M., Bomar, A. and Mackey, M. 2009. Impact of dam operations on hyporheic exchange in the riparian zone of a regulated river. *Hydrol. Proc. Int. J.*, 23(15): 2129-2137.
- Jones, J., Biology, I. and Fairbanks, U.O. 2000. Streams and groundwaters. *J. N. Am. n Benthol. Soc.*, 19(4): 760-761.
- Kiel, B.A. and Cardenas, M.B. 2014. Lateral hyporheic exchange throughout the Mississippi River network. *Nat. Geosci.*, 7(6): 413-417.
- Molina, N., Bayer, P., Blum, P. and Cirpka, O.A. 2011. Propagation of seasonal temperature signals into an aquifer upon bank infiltration. *Groundwater*, 49(4): 491-502.
- Nilsson, C. and Berggren, K. 2000. Alterations of riparian ecosystems caused by river regulation: Dam operations have caused global-scale ecological changes in riparian ecosystems. How to protect river environments and the human needs of rivers remains one of the most important questions of our time. *BioScience*, 50(9): 783-792.
- Tonina, D. and Buffington, J.M. 2007. Hyporheic exchange in gravel-bed rivers with pool-riffle morphology: Laboratory experiments and three-dimensional modeling. *Water Resour. Res.*, 43(1): 1421-1435.
- Vogt, T., Schirmer, M. and Cirpka, O. 2012. Investigating riparian groundwater flow close to a losing river using diurnal temperature oscillations at high vertical resolution. *Hydrol. Earth Sys. Sci.*, 16(2): 473-487.
- Weiwei, C. 2001. Research on the water temperature analysis of reservoir and river downstream. *Adv. Sci. Technol. Water Resour.*, 5(1): 20-23.
- Zhou, S., Yuan, X., Peng, S., Yue, J., Wang, X., Liu, H. and Williams, D.D. 2014. Groundwater-surface water interactions in the hyporheic zone under climate change scenarios. *Environ. Sci. Pollut. Res.*, 21(24): 13943-13955.



Impact of Endocrine Disrupting Chemicals on Human Reproductive System: A Toxicological Perspective

Anu Bela Lakra, Suryapratap Ray and Tejasvi Bhatia[†]

Department of Forensic Science, Lovely Professional University, Jalandhar-144 411, Punjab, India

[†]Corresponding author: Tejasvi Bhatia; tejasvi.25999@lpu.co.in

ABSTRACT

Recent clinical or epidemiological studies are reporting alarming results on the effects of certain groups of chemicals on the female reproductive system. These endocrine disrupting chemicals (EDCs) influence the normal activities of hormones secreted from the female hypothalamus, ovary, pituitary & uterus. The female reproductive disorders are mainly observed at embryonic or during fetal development and subsequently get matured during puberty. Various toxic chemicals and other pollutants interact with the chemical structure of the hormones and hence prolonged effects are seen at the cellular and molecular level of hormones resulting in disruption of secretion and function. Due to poor coordination of hormones and other reproductive organs of the body vital functions are compromised. Hence it's highly significant to study and explore the toxicity of chemicals that play a key role in the malfunctioning of the female reproductive system. In this review, we are concerned about the influence of EDCs and their significance in public health. Furthermore, we illustrated the discussion on the increasing effects of EDCs in various parts such as clinical, animal models, or epidemiological studies to develop awareness among the people.

Nat. Env. & Poll. Tech.

Website: www.neptjournal.com

Received: 11-03-2021

Revised: 23-04-2021

Accepted: 02-05-2021

Key Words:

Endocrine disrupting chemicals
Reproductive health
Pralidoxime
Pesticide toxicity

INTRODUCTION

The endocrine system is a part of the organ system that involves chemical messenger as a group of complex networks of the internal gland. It produces, stores, and releases various types of hormones passing through the circulatory system and regulates the target organ and tissue in the body. They perform various functions on the body such as respiration, metabolism, reproduction, sensory perception, movement, sexual development, and growth. Hypothalamus, pituitary, adrenal, penial, ovaries and testes are major hormone producing organs. The chemical structure of hormones can be mainly categorized as proteins & steroids which have functional moiety that interact with various toxic chemicals. These toxic chemicals which are released in the environment may be natural, synthetic, industrial discharge or pesticides. Hence, they can alter the normal hormone function and may cause prolonged effects on living organisms and human health. Such a highly profound class of compounds is known as endocrine disruptor chemicals. An endocrine disrupting chemical (EDC) was defined by the U.S Environment Protection Agency (EPA) as an exogenous agent or mixture that prevent the action of synthesis, secretion, transport, metabolism, binding, action, or elimination of natural Hormone which are responsible for homeostasis, reproduction, and development (Palioura & Diamanti-Kandarakis 2015).

The activity of Endocrine disruptors can be classified as deleterious, pathologic and endocrine mediated disruptions. Since the mid-20th century, numerous studies have reported that Diethylstilbestrol (DES), ethinyl estradiol and synthetic estrogens bind the estrogen receptor and stimulate transcription of estrogen-response genes, which may cause long term effects such as endometriosis, reproductive dysfunction or dysplastic change in humans (Karoutsou et al. 2017). Bisphenol A (BPA) and estrogen receptor (ER) are two contemporary examples of chemicals that have been widely used and have been found in human exposure. Figs. 1, 2 and 3 suggest the chemical structures of some of the PCB and PBBs. Detectable Dioxins, polychlorinated biphenyl (PCBs), polybrominated biphenyl (PBB), polybrominated phenyl ether (PBDE), and insecticides containing halogen groups, among others, imitate natural steroids and serve as antagonists on steroid hormone receptors (Palioura & Diamanti-Kandarakis 2015). Progesterone receptors (PR) are potential targets for many chlorinated EDC such as alkyl-phenols, dichloro- diphenyl- trichloroethane (DDT), and its derivatives (Scippo et al. 2004). Dicarboximide fungicides are major androgen receptors. The important sources of the exposure of EDCs are the food chain, environment, and consumer products. Mostly in human beings and animals, 90% of exposure to EDCs is through contaminants in water, breathing, pollutants in the air, ingesting food, or contam-

inated soil. These environmental toxicants affect human health by absorption, metabolism, accumulation, and interfering through normal functioning and stability. The effect of various toxic chemicals on human health depends on the mechanism of action, solubility in water, the dose-response, and the stability time (Johansson et al. 2021). The steroids and certain groups of pesticides have a large lifetime and hence remain in the environment for a long time.

MECHANISM OF ACTION

Endocrine disruptors affect the endocrine system of humans and animals by mimicking, obstructing, or interfering with the usual plan of action, in which the natural direction of hormones to cells is altered. When EDCs bind to hormone receptors, the transcription of Messenger RNA is altered. This is followed by changes in gene expression, which appears to be one of the most common ways for EDCs to impact endocrine function. The Main nuclear receptors involved in EDCs are ER alpha and beta, AR, thyroid receptors, AhR glucocorticoid receptors (GR) (Bodwell et al. 2004). The progesterone receptor (PR) has recently been highlighted as being more sensitive than the ER-alpha receptor, which has been the target of numerous persistent organic pollutants (POPs) (Villa et al. 2004). Consider the binding/transactivation of Nuclear Receptors in vivo or in vitro models have proved extremely applicable for screening of probable EDCs. Many EDCs do not interact with Nuclear Receptors in any way. Other applicable mechanisms are inhibition of hormone synthesis, transport or metabolism, and activation of Receptors through Receptors phosphorylation or cellular release for hormone action and changes in the hypothalamic-pituitary-gonadal axis. The EDCs mechanisms are depended on Dose-response.

The most disputed issue regarding EDCs is to balance the relationship between dose-response and their mechanism. Because the mimicking or antagonizing activities in normal hormones occur at physiological functional concentrations, the dose-response deliberation for EDCs and other substances working through various routes is less complicated. The estrogenic chemicals produce an inverted U dose-response curve, which can lead to low-dose response activation. Low-dose estrogenic chemicals, such as Bisphenol A and octal phenols, cause deleterious effects. The present criterion Models for assessing modest doses of chemicals that show the form of the dose-response curve are used to undervalue the danger and should be given more consideration (Weltje et al. 2005). Chemicals with distinct mechanisms of action, such as estrogenic, antiandrogenic, growth factor modulation, cytokine and thyroid modulation, and hormone metabolism modulation, have different dose-response curves. Complex mixtures of chemicals have complicated exposure mechanisms; they can affect, but they may not be assigned cautions when compared to single chemicals. EDCs cumulatively, low dose exposure is more potent than high dose exposure, and this shift challenges the traditional toxicological concept. Individual drugs will be studied for probable interactions in the setting of receptor dosage (Koppe et al. 2006). The combined effect of each chemical present at low concentrations was studied (Rasmussen et al. 2003).

When endocrine-disrupting Chemical binds to the specific receptors they inhibit or block or interfere with the mode of action in the endocrine gland. As a result of the buildup of EDCs in the body, gene expression is altered, receptor phosphorylation is altered, and cellular release in the body is altered. The main role of AhR, which are ligand triggered transcription factors, is to regulate the cellular response to-

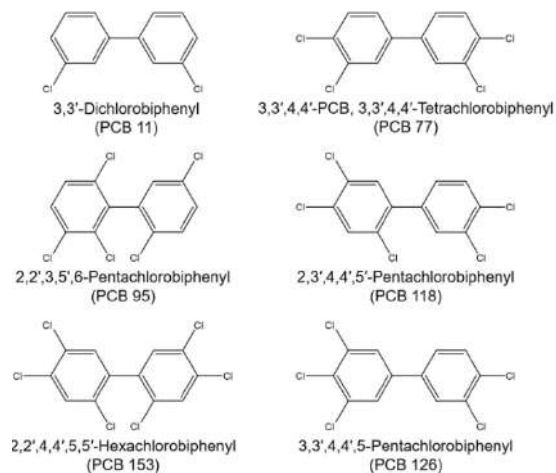


Fig. 1: Chemical Structure of some commonly encountered PCBs.

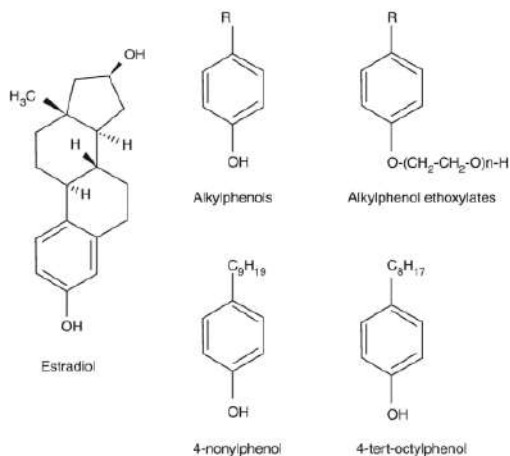


Fig. 2: Structure of some other endocrine disrupting chemicals.

nobiotic exposure. Nuclear receptors are the most commonly targeted receptors by EDCs. These transcription factors are hormone-dependent and may affect the target cells. Many endocrine disrupting drugs (EDCs) have structures that are comparable to NR ligands and can bind to NRs directly. These can either act as agonists and increase gene expression, or they can function as antagonists and block receptor action. EDCs can impact receptor function by promoting receptor degradation, activating the AhR signaling pathway, which will direct the appropriate or common co-activators to the AhR, and interconnect the AhR to bind inhibitory XREs (Swedenborg et al. 2009). Hormone availability is dependent on hormone biosynthesis, transport of the hormone to the target tissue, levels of hormone-binding proteins, and hormone catabolism. EDCs have been described to interfere with all of these processes (Baker et al. 1998; You et al. 2001; Boas et al. 2009). EDCs have a particularly negative impact on steroid hormone catabolism, and many xenobiotic-metabolizing enzymes are implicated in both of these processes. The hydroxylation of 17-estradiol is carried out by the P450 enzymes CYP1A2, CYP3A4, CYP1A1, and CYP1B1, which are all key AhR target genes (Tsuchiya et al. 2005). Upon enzyme activation, xenobiotic exposure causes enhanced hormone catabolism, which compromises hormone signaling. According to a recent experiment, CYP19B (aromatase) is an AhR direct gene that transforms testosterone into estradiol. EDEs prevent AhR activation and increased steroid hormone breakdown, as well as higher estradiol synthesis (Ptak & Gregoraszczyk 2012). Endogenous hormone receptor interferes with endocrine homeostasis. BPA binds with the leptin receptor and it can express itself as ovarian cancer cells and cause ovarian cancer (Ptak & Gregoraszczyk 2012). BPA binds with estrogen and androgen receptors in hypothalamic cells and may cause breast or prostate cancer (Rebuli et al. 2014). Polybrominated diphenyl ethers operate on a hepatic enzyme involved in the glucuronidation pathway, potentially increasing T4 elimination and lowering hormone levels in the blood (Boas et al. 2009). 17 beta-hydroxysteroid hydrogenation binds to parabens. It prevents estrogen dehydration and may even raise hormone levels in the blood (Engeli et al. 2017).

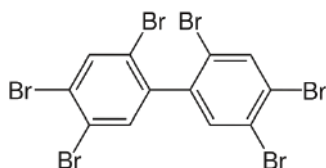


Fig. 3: Structure of polybrominated biphenyl (hexabromobiphenyl).

EDCS RISK ASSESSMENT

Epidemiological studies will discuss the interaction between nutrient toxicants and the new approach will be used in Molecular and epidemiology toxicology, which has been targeted the valuable information about experimental protocol and the mechanistic detection of specific low dose exposure to potential EDCs and has been improved the risk assessment of the adverse health effects of EDCs.

The above-discussed areas such as sources of toxicity, classification, pathways of exposure and mechanism of action have been summarized in Table 1.

EDCS ON FEMALE REPRODUCTIVE HEALTH

Female reproduction and function rely on the coordination of biological processes, which can be disrupted by endogenous or external variables during the developmental stage of life, resulting in negative consequences on female health and reproductive function. The fertility of a woman depends on her reproductive health. Exposure to EDCs, cigarette smoke, and alcohol may exacerbate a woman's fertility problems. Because of lifestyle choices, environmental influences, and older ovulation planning, the female fertility rate has fallen and ovarian disorders such as polycystic ovary syndrome (PCOS), premature ovarian failure (PCF), and primary ovarian insufficiency (POI) have become more common. Bisphenol A (BPA), perfluorooctanoic acid, and perfluorooctane sulfonate are the main causes of these ovarian disorders, according to an epidemiological study. These may disrupt the menstrual cycle's regularities, affecting the quantity and quality of available oocytes, gestational age, weight gain throughout pregnancy, miscarriage risk, and duration of pregnancy in women. This stage begins during embryonic and fetal development and continues through puberty. The interference of EDCs on hormones causes feminine problems in maturity.

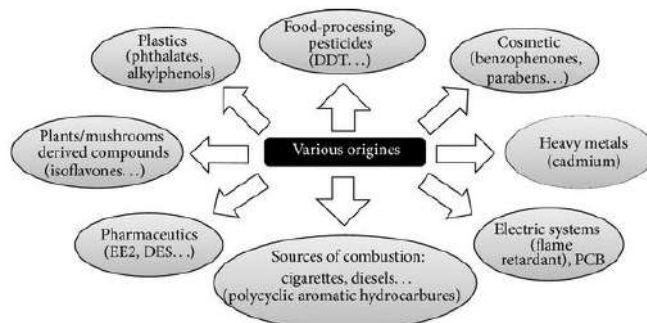


Fig. 4: Sources of EDCs (Kerdivel et al. 2013).

Table 1: Sources of different chemicals, categories, pathways of exposure and mechanism of action.

Chemical(s)	Source	Category	Pathway of exposure	Mechanism of action	Reference
PCBs	Incineration/Landfill	Polychlorinated compounds	Food-chain/living organism	Alteration in steroid hormone/thyroxine transport	(Mantovani et al. 1998, Mantovani 2002)
DDT/DDE/dieldrin	Agriculture run off/atmospheric transport	Organochlorine pesticide	Food-chain/living organisms	Estrogenic activity	(Mantovani et al. 1998, Mantovani 2002)
Triazoles/imidazole			Food-chain/living organism/industrial workplace	Inhibition of steroid hormone biosynthesis	(Mantovani et al. 1998, Mantovani 2002)
Bisphenol A	Consumer products		Food-chain Cosmetics/personal/care/Cleaners/plastics	estrogen agonist-ER alpha (increased ER alpha expression in hypothalamus)	(Scippo et al. 2004)
Parabens	Consumer products		Cosmetics/personal/care/Cleaners/plastics	estrogen agonist-ER alpha and beta	(Oishi et al. 2002, Kunz & Fent 2009)

Fertility and Fecundity

Occupational exposure to insecticides, pesticides, and herbicides plays a significant impact on female fertility and has also been linked to early pregnancy termination and delivery of an immature infant. Direct exposure to these chemicals, primarily through agriculture, has been found in rural women who have worked in the field. In this area, 281 women have been diagnosed with infertility, compared to 216 women who have worked in the agriculture industry. According to this study, women who have been exposed to pesticides for a long time would have an elevated risk of fertility and fecundity (Fuortes et al. 1997) Some males were also exposed to these chemicals, which had negative impacts on their reproductive

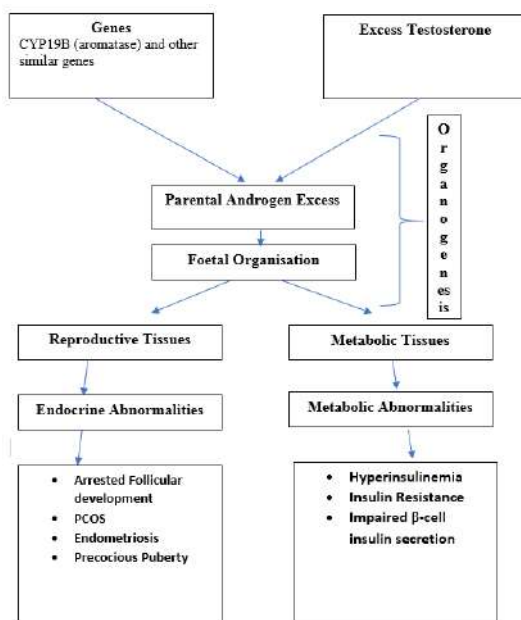


Fig. 5: Diagram illustrating EDCs mechanism of action.

systems. Pesticides such as EDCs, thiocarbamates, atrazine, and phenoxy are to blame, and additional people were exposed through the food chain (Savitz et al. 1997). The chemicals were impurities in water that entered our bodies and disrupted hormone function, resulting in decreased fertility and fecundity in humans and animals.

PCOS (Polycystic Ovarian Syndrome)

PCOS is a heterogeneous syndrome marked by anovulation, oligomenorrhea, and hyperandrogenism in the absence of thyroid, pituitary, or adrenal illness. Insulin resistance is present in PCOS, and the body is unable to utilize insulin effectively as a result of excessive insulin levels in the bloodstream, known as hyperinsulinemia. Increased testosterone levels, as well as obesity and type 2 diabetes, were linked to hyperinsulinemia. Obesity causes a worsening of PCOS by raising insulin levels, which affects the endocrine system and causes problems in the female reproductive system. Obesity and insulin resistance affect roughly half of all women with PCOS, while obese women account for 12% of all PCOS cases (Yildiz et al. 2008). PCOS is a severe illness that affects roughly 6.6 per cent of women in their reproductive years.

Endometriosis

Endometriosis is an estrogen-dependent disease that af-

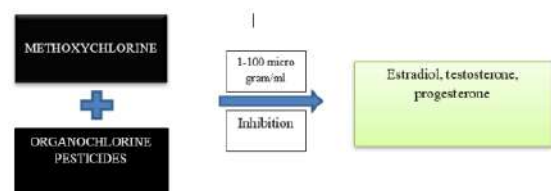


Fig. 6: Inhibition of sex hormones by different pesticides at certain dosages.

fects the endometrial gland and stroma, which are located outside the uterine cavity. It is a prevalent disorder that causes female infertility (Chedid et al. 1995). This condition afflicts approximately 14% of women (Vercillini et al. 1995). While plausible mechanistic hypothesis, the main cause of this condition is influenced by EDCs chemical in estrogen hormone and malfunction the normal function of endometriosis. Endometriosis is caused by chemicals such as polychlorinated biphenyls (PCBs) and TCDD (2, 3,7,8-tetrachlorodibenzo-P-dioxin) (Rier & Foster 2003). These toxic substances alter the menstrual cycle and gonadal steroids and cause female fertility (Yang et al. 2000).

Precocious Puberty

Precocious puberty refers to when a child's puberty begins before the actual age of puberty. It has now become a severe issue in youngsters. The youngsters are affected by pollution and harmful chemicals, which disrupt the hormone function of puberty females and result in negative consequences such as premature breast development or puberty before the age of puberty. Premature breast development in girls and gynecomastia in boys were seen in Puerto Rico in the 1980s. The serum sample was collected from 41 girls. After investigation, it was discovered that 68 per cent of the girls (mean 28 girls) had quantifiable levels of Phthalates (dimethyl, diethyl, dibutyl, and di-(2-ethyl hexyl) in their serum. This toxin is caused by pesticide exposure (root) and induces premature breast development (Colon et al. 2000). The effects of uterine exposure to polybrominated biphenyls (PBS) on sexual maturity were seen in Michigan females whose mothers inadvertently ingested flame retardants as a result of their diet (Blanck et al. 2000).

Uterine Leiomyomas

Smoothing muscle turns into myometrium in the uterus, causing morbidity in women such as menorrhagia, abdominal pain, pelvic prolapse, infertility, and miscarriage. Organochlorine and DES chemicals generated uterine Leiomyomas by causing germ-line mutation. (Buttram et al. 1981).

Breast and Endometrial Cancer

Menarche, first pregnancy, menopause, lactation, and parity are all risk factors for breast cancer. All of these parameters are linked to ovarian hormone exposure throughout time.

Breast cancer

Breast cancer risk is influenced by dietary variables. Dietary substances that are phytoestrogens (soy products) have been linked to a decrease in steroid hormone levels due to the direct regulation of 17 beta - E2 biosynthesis and metabolism (Lim-

er & Speirs 2004). DDT metabolism has been discovered in human serum, adipose tissue, and breast milk. There is an increased risk of estrogen-dependent malignancies like breast cancer as a result of occupational exposure through food. The link between polychlorinated biphenyl (PCB) exposure and breast cancer is occupational, although there is no evidence of a positive effect. According to recent research, underarm cosmetics may contribute to the development and progression of breast cancer. A range of endocrine active substances (e.g., parabens) is used in cosmetics and are typically used in the area directly adjacent to the breast (Darbre 2006).

Endometrial Cancer

After 5 years of treatment with 50 mg of soy isoflavones, a study of 298 postmenopausal women found an elevated risk of endometrial hypoplasia (Unfer et al. 2004). Phytoestrogen is being re-evaluated as a high-risk factor for endometrial cancer in women. Diethylstilbestrol (DES) exposure increased the incidence of a host, altered the ovary and reproductive tract, and caused the ovarian effect, reproductive abnormalities in women, such as vaginal adenosis, cervical and vaginal hypoplasia, uterine and tubal abnormalities, infertility, early menopause, and breast cancer. The spectrum of possibilities is demonstrated by changes in the developing ovary with or without changes in hormonal signaling.

EDCS ON MALE REPRODUCTIVE HEALTH

The endocrine system's function was affected by environmental pollutants. Epidemiological research is being used to better understand the impact of EDCs on human reproductive development and function. This research examined the failure of normal hormone activity and how it affected male reproductive health, among other things. Changed fetal development, manifested as urogenital tract anomalies, and disrupted reproduction function, manifested as lower semen quality and sterility (Hypospadias, Cryptorchidism) Germ cell cancer of the testes (TGCC).

Hypospadias

The effect of hypospadias was increased by 0.4 per cent when the meatus was on the central side of the penis at the time of birth (Nassar et al. 2007). VCZ (vinclozolin) and phthalates are two factors that contribute to EDCs (Schneider et al. 2011, Mylchurst et al. 2000).

Cryptorchidism

Failure of one or both testicles, resulting in abnormalities in the scrotal sac, is a 2-4 per cent common congenital condition affecting male children (Boisen et al. 2004). Adulthood is an

Table 2 : Targeted organs and resulting diseases by different groups of pesticides.

Pesticides Category	Targeted organ(s)/function	Diseases
Organochlorine DDT/DDE Aldrin and Dieldrin	Acetylcholinesterase inhibitors / Liver	Metabolic syndrome (diabetes and obesity), precocious puberty, breast cancer, reduced semen quality disrupted mensuration, lactation problem
Organophosphate Malathion and parathion Chlorpyrifos	Acetylcholinesterase inhibitors /cardiovascular system, nervous system, respiratory	Breast cancer Developmental delays, attention problems, ADHD in children
Methyl parathion, Ronnel, Dione fox		Endometriosis, prostate cancer
Carbamates Carbofuran	Acetylcholinesterase inhibitors/central nervous system, nicotinic receptor in skeletal muscle tissue	Autoimmune disease
Pyrethroids Deltamethrin	Act on the neural dopamine transport/alter the function of the central nervous system	Parkinson disease Sleep disorder, impaired memory

unfavorable risk factor for infertility and testicular cancer (Foresta et al. 2007). Leydig cells exposed to ED (Endocrine disruptors) at both stages were lowering insulin-like 3 factors (Emmen et al. 2000) and impairing steroidogenesis (related to testosterone deficiency), PBDE exposure through nursing has been linked to cryptorchidism in newborns (Main et al. 2007).

Testicular Dysgenesis Syndrome

A Unifying Theorem: - The Hypothesis will reduce TGCC and male urogenital tract abnormalities, which are two typical pathways for sperm quality. EDCs, environmental chemicals, and genetic variables all interact through a similar pathway to produce anomalies in fetal testis development, resulting in Testicular Dysgenesis (Skakkebaek et al. 2001). All of these disorders show a higher incidence of urogenital anomalies in newborn males, as well as impaired semen quality and TGCC in young men. TDS (Testicular Dysgenesis Syndrome) is caused by a combination of parental Leydig cell failure and sertoli cell dysfunction, as well as secondary androgen and poor germ cell development. (Słowikowska-Hilczer et al. 2001). Semen quality, TGCC, and urogenital abnormalities are caused by chemicals such as PCBs, pesticides (persistent or non-persistent), and phthalates. There was no link between TCDD and sperm quality in men aged 18 to 26. Men who were exposed between the ages of 1 and 9 and between the ages of 10 and 17 had lower estradiol and higher FSH concentration than men who were not exposed (Evanthia et al. 2009). These findings show that the timing of exposure,

or life stage, may play a role in determining the impact of environmental exposure (Roberts et al. 2005).

Pesticides are a large group of heterogeneous chemicals that may cover various products such as insecticide, herbicides fungicides, and rodenticide. Acetylcholinesterase inhibitors include organochlorine, organophosphate, and carbamates. In cases of accidental or deliberate drunkenness, this is a common occurrence. Carbamates and organochlorine insecticides cause fatal poisoning, but herbicides, chlorophenoxyacetic acid, and some pyrethroids cause less poisoning (Goel & Aggarwal 2007, Singh & Sharma 2000). Different classes of pesticides act on different sites and may cause various diseases. Table 2 below illustrates the summary of such activities. The first symptoms in the muscarinic and central nervous systems develop within 1-2 hours of organophosphate exposure. Salvation, lacrimation, urine, feces, gastrointestinal cramps, and emesis are all symptoms of muscarinic toxicity. SLUDED was used to represent all of these qualities, and DUMBLES was used for other acronyms (diarrhea, urination, miosis, bronchorrhoea, emesis, and sweating) (Sivagnanam 2002, Karatas et al. 2006). Headache, tremors, restlessness, ataxia, weakness, emotional lability, disorientation, slurring, coma, and seizure are all neurological clinical characteristics. The first signs of organochlorine poisoning are nausea, vomiting, dizziness, convulsions, confusion, or coma, which appear within 30 minutes of exposure (Karatas et al. 2006). The impact on the presynaptic and postsynaptic junction is the acute poisoning syndrome of organophosphate related to toxic-induced my-

opathy (Singh & Sharma 2000). After 1-4 days of exposure to OP, neuropathic targets are inhibited, and the respiratory system fails or weakens (Singh & Sharma 2000). After 10-20 days, the delayed effect caused a neuropathy known as ginger paralysis syndrome (Ladell 1961). Table 2 represents the classification of pesticides while suggesting the targeted organs and the resulting diseases (Balali-Mood & Shariat 1998, Ladell 1961).

The activity of Butyrylcholinesterase, plasma cholinesterase, and red cell cholinesterase can be used to make a diagnosis. The typical exposure of red cell cholinesterase is roughly 30-50 per cent; this will be lowered to 20%. Pseudocholinesterase activity can be used to identify intoxicating drugs at low concentrations (morphine or codeine), which can induce chronic liver disease, pregnancy, neoplasm, infection, and malnutrition, but it is also unreliable due to these circumstances. Diazinon has a greater effect on plasma cholinesterase than on red cell acetylcholinesterase (Eddleston et al. 2002).

For monitoring the seizure, we use the ABC (absorption, breathing, and circulation) method to avoid toxin absorption, and then we use various medications such as Epinephrine and cholestyramine for further therapy. Patients' heart rates can be controlled using dopamine. In some cases, cholestyramine resin is utilized for fecal excretion in Organochlorine compounds at a dose of 4 g four times a day. In the event of myocardial infarction, epinephrine should be avoided (Cohn et al. 1978). When first exposed to OP, we shall use the ABC approach, i.e. (Airways, Breathing, Circulation, Distribution). For toxic patients, early oxygen treatment is critical. During oxygen treatment, the patient's head is normally put on the lower side and the abdomen region is placed on the left side. Atropine and pralidoxime (PAM/2-pyridine aldoxime Methyl chloride) are two medications that are used for therapy (Sivakumar et al. 2006). Atropine medications, which are used to treat hypothermic patients but are preferable to Diazepam, will be avoided in Haloperidol for sedation since they are pro-convulsant and will disrupt the central thermoregulation of the QT interval. (Balali & Shariat 1998, Roberts & Buckley 2005). PAM can be used in various anticholinesterase functions (Eddleston et al. 2002). PAM will be avoided in case of carbamate poisoning because of the short period of action of carbamates (Goel et al. 2007).

Pralidoxime and Carbamate Toxicity

Pralidoxime or (2- PAM) at carbamates toxicity cannot be engaged due to the following reason. Carbamate reversibly binds to Acetylcholinesterase (Eddleston et al. 2002). Carbamate such as carbaryl has shown poor outcomes when treated with pralidoxime. They activate the cholinesterase

inhibitor (such as neostigmine and pyridostigmine) at the absorption or redistribution process (Ekins & Geller 1994). Carbamate is avoided at "aging" because they occur during the phosphorylation of organophosphate to acetylcholinesterase. Carbamate-cholinesterase bond does not hydrolyze at aging because this does not have phosphate groups. 2-PAM mostly affects nicotinic receptors as well as Muscarinic receptors because 2-PAM is a quaternary nitrogen compound and cannot cross the blood-brain barriers (BBB). When 2-Pam will be administrated that will be disbalancing the CNS system and the patient can be in a coma (Kurtz 1990).

CONCLUSION

It is clear from the above discussion that the extensive bioavailability of EDCs in the environment causes various health issues in humans. For such toxic elements, various animals including other ecosystems are getting affected as well. The disturbances in the food chain due to the fluctuation in ecosystem health are a threat to earth. Awareness among people can reduce toxicity which can help recreate a healthy atmosphere. However, different toxicities are already mentioned in the above discussion. The toxicological assessment was done including the diagnosis, treatment, etc. Pralidoxime is not being used in carbamate intoxication treatment. Atropine and the PAM can be used in other pesticide intoxication treatments though. The reduction in the use of various synthetic chemicals for various purposes must be done earlier to reform our ecosystems, which can ultimately provide improved public health.

REFERENCES

- Arbuckle, T. E., Savitz, D. A., Mery, L. S. and Curtis, K. M. 1999. Exposure to phenoxy herbicides and the risk of spontaneous abortion. *Epidemiology* (Cambridge, Mass.), 10(6): 752-760. doi:10.1097/00001648-199911000-00017
- Baker, M. E., Medlock, K. L. and Sheehan, D. M. 1998. Flavonoids inhibit estrogen binding to rat alpha-fetoprotein. *Proceedings of the Society for Experimental Biology and Medicine. Society for Experimental Biology and Medicine* (New York, N.Y.), 217(3): 317-321. doi:10.3181/00379727-217-44238
- Balali-Mood, M. and Shariat, M. 1998. Treatment of organophosphate poisoning. Experience of nerve agents and acute pesticide poisoning on the effects of oximes. *J. Physiol.*, 92(5-6): 375-378.
- Blanck, H.M., Marcus, M., Tolbert, B.E., Rubin, C., Henderson, A.K., Vs, H. and Cameron, L. 2000. Age at menarche and tanner stage in girls exposed in utero and postnatally to polybrominated biphenyl. *Epidemiology*, 11: 641-647.
- Boas, M., Main, K. M. and Feldt-Rasmussen, U. 2009. Environmental chemicals and thyroid function: an update. *Current Opinion in Endocrinology, Diabetes, and Obesity*, 16(5): 385-391. doi:10.1097/MED.0b013e3283305af7
- Bodwell, J.E., La, K. and Hamilton, J.W. 2004. Arsenic at very low concentration alters glucocorticoid receptor (GR) – Mediated gene activation but not GR- mediated gene repression: Complex dose-response effects

- are closely correlated with the level of activated GR and required a functional GR DNA binding domain. *Chem. Res. Toxicol.*, 17: 1064-1076.
- Boisen, K.A., Kaleva, M., Main, K.M., Virtanen, H.E., Haavisto, A.M., Schmidt, I. M. and Reunanen, M. 2004. The difference in the prevalence of congenital cryptorchidism in infants between two Nordic countries. *Lancet*, 363: 1264-1269.
- Buttram, V. C., Jr. and Reiter, R. C. 1981. Uterine leiomyomata: Etiology, symptomatology, and management. *Fertility and Sterility*, 36(4): 433-445. doi:10.1016/s0015-0282(16)45789-4
- Chedd, S., Camus, M., Smitz, J., Van Steirteghem, A. C. and Devroey, P. 1995. Comparison among different ovarian stimulation regimens for assisted procreation procedures in patients with endometriosis. *Human Reproduction (Oxford, England)*, 10(9): 2406-2411. doi:10.1093/oxfordjournals.humrep.a136308.
- Cohn, W. J., Boylan, J. J., Blanke, R. V., Fariss, M. W., Howell, G. and P S. 1978. Treatment of chlordecone (Kepone) toxicity with cholestyramine: Results of a controlled clinical trial. *N. Engl. J. Med.*, 298: 243-8.
- Colon, I., Caro, D., Bourdony, C.J. and Rosario, O. 2000. Identification of phthalate esters in the serum of young Puerto Rican girls with premature breast development. *Environ. Health Persp.*, 108(9): 895-900.
- Darbre, P.D. 2006. Environmental estrogens, cosmetics, and breast cancer: Best practice & research. *Clinical Endocrinol. Metabol.*, 20(1): 121-143.
- Eddleston, M., Szinicz, L., Eyer, P. and Buckley, N. 2002. Oximes in acute organophosphorus pesticide poisoning: A systematic review of clinical trials. *QJM*, 95(275-83): 24.
- Ekins, B.R. and Geller, R.J. 1994. Methomyl-induced carbamate poisoning treated with pralidoxime chloride. *Western J. Med.*, 161(1): 68-70.
- Emmen, J.M., McLuskey, A., Adham, I.M., Engel, W., Verhoef-Post, M., Themmen, A.P. and Brinkmann, A.O. 2000. Involvement of insulin-like factor 3 (InsI3) in diethylstilbestrol-induced cryptorchidism. *Endocrinology*, 141: 846-849.
- Engeli, R.T., Rohrer, S.R., Vuorinen, A., Herdinger, S., Kaserer, T., Leugger, S., Schuster, D. and Odermatt, A. 2017. Interference of paraben compounds with estrogen metabolism by inhibition of 17 -hydroxysteroid dehydrogenases. *International journal of molecular sciences*, 18(9): 2007.
- Foresta, C., Zuccarello, D., Garolla, A. and Ferlin, A. 2008. Role of hormones, genes, and environment in human cryptorchidism. *Endoc. Rev.*, 29(5): 560-580.
- Fuortes, L., Clark, M. K., Kirchner, H. L. and Smith, E. M. 1997. Association between female infertility and agricultural work history. *American Journal of Industrial Medicine*, 31(4): 445-451.
- Goel, A., Aggarwal, P., Bhoi, S. and Gupta, V. 2007. High-dose pralidoxime for organophosphorus poisoning. *Lancet*, 369(9571): 1425. doi:10.1016/s0140-6736(07)60657-6
- Johansson, H. K. L., Christiansen, S., Draskau, M. K., Svingen, T. and Boberg, J. 2021. Classical toxicity endpoints in female rats are insensitive to the human endocrine disruptors diethylstilbestrol and ketoconazole. *Reproductive Toxicology (Elmsford, N.Y.)*, 101: 9-17. doi:10.1016/j.reprotox.2021.01.003
- Karatas, A.D., Aygun, D. and Baydin, A. 2006. Characteristics of endosulfan poisoning: A study of 23 cases. *Sing. Med. J.*, 47(12): 1030-1032.
- Karoutsou, E., Karoutsos, P. and Karoutsos, D. 2017. Endocrine disruptors and carcinogenesis. *Archives in Cancer Research*, 05(01) doi:10.21767/2254-6081.1000131
- Kerdivel, G., Habauzit, D. and Pakdel, F. 2013. Assessment and molecular actions of endocrine-disrupting chemicals that interfere with estrogen receptor pathways. *International Journal of Endocrinology*. doi:10.1155/2013/501851
- Koppe, J.G., Bartonova, A., Bolte, G., Bistrup, M.L., Busby, C., Butter, M. and Zuurbier, M. 2006. Exposure to multiple environmental agents and their effect. *Acta Paed.*, 95(453): 106-113.
- Kunz, P.Y. and Fent, K. 2009. Estrogenic activity of ternary UV filter mixtures in fish (*Pimephales promelas*): An analysis with nonlinear isobolograms. *Toxicol. Appl. Pharmacol.*, 234(1): 77-88.
- Kurtz, P.H. 1990. Pralidoxime in the treatment of carbamate intoxication. *The Amer. J. Emergency Med.*, 8(1): 68-70.
- Ladell, W.S. 1961. Physiological and clinical effects of organophosphorus compounds. *J. R. Soc. Med.*, 54(5): 405-406.
- Limer, J.L. and Speirs, V. 2004. Phyto-oestrogens and breast cancer chemoprevention. *Breast Cancer Res.*, 6: 119-127.
- Main, K.M., Kiviranta, H., Virtanen, H.E., Sundqvist, E., Tuomisto, J.T., Tuomisto, J. and Toppari, J. 2007. Flame retardants in the placenta and breast milk and cryptorchidism in newborn boys. *Environ. Health Persp.*, 115(10): 1519-1526.
- Mantovani, A. 2002. Hazard identification and risk assessment of endocrine-disrupting chemicals with regard to developmental effects. *Toxicology*, 181-182, 367-370.
- Mantovani, A., Stazi, A.V., Macrì, C., Maranghi, F. and Ricciardi, C. 1998. Problems in testing and risk assessment of endocrine-disrupting chemicals with regard to developmental toxicology. *Chemosphere*, 39(8): 1293-1300.
- Mylchrest, E., Wallace, D.G., Cattley, R.C. and Foster, P.M. 2000. Dose-dependent alterations in androgen-regulated male reproductive development in rats exposed to di(n-butyl) phthalate during late gestation. *Toxicol. Sci.*, 55: 143-151.
- Nassar, N., Bower, C. and Barker, A. 2007. Increasing Prevalence of Hyposadias in Western Australia, 1980-2000.
- Palioura, E. and Diamanti-Kandarakis, E. 2015. Polycystic ovary syndrome (PCOS) and endocrine disrupting chemicals (EDCs). *Reviews in Endocrine & Metabolic Disorders*, 16(4): 365-371. doi:10.1007/s11154-016-9326-7
- Ptak, A. and Gregoraszczuk, E.L. 2012. Bisphenol A induces leptin receptor expression, creating more binding sites for leptin, and activates the JAK/Stat, MAPK/ERK and PI3K/Akt signalling pathways in human ovarian cancer cell. *Toxicology Letters*, 210(3): 332-337.
- Rasmussen, T.H., Nielsen, F., Andersen, H.R., Nielsen, J.B., Weihe, P. and Grandjean, P. 2003. Assessment of xenoestrogenic exposure by a biomarker approach: application of the E-Screen bioassay to determine the estrogenic response of serum extracts. *Environ. Health - Global Access Sci. Source*, 2(1): 12.
- Rebuli, M.E., Cao, J., Sluzas, E., Delclos, K.B., Camacho, L., Lewis, S.M., Vanlandingham, M.M. and Patisaul, H.B. 2014. Investigation of the effects of subchronic low dose oral exposure to bisphenol A (BPA) and ethinyl estradiol (EE) on estrogen receptor expression in the juvenile and adult female rat hypothalamus. *Toxicological Sciences*, 140(1): 190-203.
- Rier, S. and Foster, W.G. 2003. Environmental dioxins and endometriosis. *Seminars in Reprod. Med.*, 21(2): 145-154.
- Roberts, D. and Buckley, N.A. 2005. Alkalinisation for organophosphorus pesticide poisoning. *Cochrane Database System. Rev.*, (1): CD004897.
- Roberts, D. M., Fraser, J. F., Buckley, N. A. and Venkatesh, B. 2005. Experiences of anticholinesterase pesticide poisonings in an Australian tertiary hospital. *Anaesthesia and Intensive Care*, 33(4): 469-476. doi:10.1177/0310057X0503300408.
- Savitz, D.A., Arbuckle, T., Kaczor, D. and Curtis, K.M. 1997. Male pesticide exposure and pregnancy outcome. *Amer. J. Epidemiol.*, 146(12): 1025-1036.
- Schneider, S., Kaufmann, W., Strauss, V. and Ravenzwaay, B. 2011. Vinclozolin: a feasibility and sensitivity study of the ILSI-HESI F1-extended one-generation rat reproduction protocol. *Regul. Toxicol. Pharmacol.*, 59: 91-100.
- Scippo, M.L., Argiris, C., Van De Weerd, C., Muller, M., Willemsen, P., Martial, J. and Maghuin-Rogister, G. 2004. Recombinant human estrogen, androgen, and progesterone receptors for detection of potential endocrine disruptors. *Anal. Bioanal. Chem.*, 378(3): 664-669.

- Sivakumar, S., Raghavan, K., Ishaq, R. M. and Geetha, S. 2006. Organophosphorus poisoning: A study on the effectiveness of therapy with oximes. *J. Assoc. Physicians*, 54(250): 1.
- Singh, S. and Sharma, N. 2000. Neurological syndromes following organophosphate poisoning. *Neurol. India*, 48(4): 308-313.
- Sivagnanam, S. 2002. Potential therapeutic agents in the management of organophosphorus poisoning. *Critical Care*, 6(3): 260-261.
- Skakkebaek, N.-E., Meyts, E. R. and Main, K. M. 2001. Testicular dysgenesis syndrome: an increasingly common developmental disorder with environmental aspects. *APMIS: Acta Pathologica, Microbiologica, et Immunologica Scandinavica*, 109(S103): S22-S30. doi:10.1111/j.1600-0463.2001.tb05770.x
- Slowikowska-Hilczer, J., Szarras-Czapnik, M. and Kula, K. 2001. Testicular Pathology in 46, XY genetic male pseudohermaphroditism: an approach to the pathogenesis of testis cancer. *J. Androl.*, 22: 781-792.
- Swedenborg, E., Rüegg, J., Mäkelä, S. and Pongratz, I. 2009. Endocrine disruptive chemicals: mechanisms of action and involvement in metabolic disorders. *Journal of Molecular Endocrinology*, 43(1): 1-10. doi:10.1677/JME-08-0132.
- Tsuchiya, Y., Nakajima, M. and Yokoi, T. 2005. Cytochrome P450-mediated metabolism of estrogens and its regulation in humans. *Cancer Letters*, 227(2): 115-124. doi:10.1016/j.canlet.2004.10.007
- Unfer, V., Casini, M. L., Costabile, L., Mignosa, M., Gerli, S. and Di Renzo, G. C. 2004. Endometrial effects of long-term treatment with phytoestrogens: a randomized, double-blind, placebo-controlled study. *Fertility and Sterility*, 82(1): 145-148. doi:10.1016/j.fertnstert.2003.11.041
- Vercillini, P., Oldani, S., De Giorgi, O., Coutinho, C. P. G., Em, S. and P, de Moura. (1995). *Endometriosis: An Overview of Descriptive and Analytic Epidemiological Studies, Progress in the Management Of Endometriosis*. New York Parthenon Publishing Group.
- Villa, R., Bonetti, E., Penza, M.L., Lacobello, C., Bugari, G., Bailo, M. and Ciana, P. 2004. Target-specific action of an organochlorine compound in reproduction and non-reproduction tissue of estrogen-reporter male mice. *Toxicol. Appl. Pharmacol.*, 201: 137-148.
- Weltje, L., Vom Saal, F.S. and Oehlmann, J. 2005. Reproductive stimulation by the low dose of xenoestrogens contrasts with the view of hormesis as an adaptative response. *Hum. Exp. Toxicol.*, 24: 431-437.
- Yang, J.Z., Agarwal, S.K. and Foster, W.G. 2000. Subchronic exposure to 2,3,7,8-tetrachlorodibenzo-p-dioxin modulates the pathophysiology of endometriosis in the cynomolgus monkey. *Toxicol. Sci.: J. Society Toxicol.*, 56(2): 374-381.
- Yildiz, B. O., Knochenhauer, E. S. and Azziz, R. 2008. Impact of obesity on the risk for polycystic ovary syndrome. *The Journal of Clinical Endocrinology and Metabolism*, 93(1): 162-168. doi:10.1210/jc.2007-1834
- You, L., Sar, M., Bartolucci, E., Ploch, S. and Whitt, M. 2001. Induction of hepatic aromatase by p,p'-DDE in adult male rats. *Molecular and Cellular Endocrinology*, 178(1-2): 207-214. doi:10.1016/s0303-7207(01)00445-2



Environmental Geological Problems in Southwest China: A Case Study from the Researches of Regional Landslide Hazards

Shuang Li*, Xiang Wu**, Faming Sun***†, Jie Yang*** and Jian Li***

*College of Civil Engineering, Fuzhou University, Fuzhou 350108, China

**School of Public Administration, Zhongnan University of Economics and Law, Wuhan 430073, China

***No. 205 Geological Team, Chongqing Bureau of Geology and Minerals Exploration, Chongqing 402160, China

†Corresponding author: Faming Sun; 33317801@qq.com

Nat. Env. & Poll. Tech.
Website: www.neptjournal.com

Received: 19-04-2021

Revised: 05-05-2021

Accepted: 08-06-2021

Key Words:

Environmental geology
Southwest China
Landslide mechanism
Monitoring and prediction

ABSTRACT

Humans have paid a lot of attention to environmental geological challenges in recent years. Landslides, being one of the most prevalent geological disasters, are characterized by their suddenness and destructiveness. Southwest China is prone to landslides and debris flows due to its unique geological structure. This paper uses landslides in southwest China as an example, focusing on research on landslide initiation mechanisms and outlining modern landslide monitoring devices and prediction models. Landslides are caused by external variables such as persistent precipitation, groundwater movement, and significant seismic activity, as well as interior reasons such as fine particle rearrangement and the action of positive pore water. The reduction of the friction coefficient of the shear surface, which is induced by the increase of the shear rate, the supercritical carbon dioxide and superheated steam of the shear zone, and the mineral recrystallization process on the shear surface, all have an important impact on reducing the friction coefficient of the shear surface, is a key factor in the occurrence of high-speed remote landslides. Real-time landslide monitoring using space-air-ground and acoustic emission technology, as well as the creation of machine learning-based forecast models, have aided in the research of landslide development and early warning.

INTRODUCTION

Southwest China is located on the east side of the Qinghai-Tibet Plateau. Various geological factors have influenced the formation of a complex geological environment and valley dynamic conditions over time, including high ground stress, strong fault structure-activity, frequent strong earthquakes, the dynamic characteristics of a strong river in a deep-cut canyon, the complex rock-soil environment, and hydrogeological conditions, and the deep overburden of the river bed, among others. After the Wenchuan earthquake in 2008, the frequency of these geological disasters has increased significantly, which provided a lot of data for the study of debris flow (Li et al. 2021a, 2021b, 2021c, Peng et al. 2021, Hu et al. 2014, 2016, 2018a, 2018b, 2018c, 2018d, Liao et al. 2020, 2021, Liu et al. 2020, 2021, Chang et al. 2021).

The international definition of a landslide isn't agreed upon. Simply put, a landslide is a natural geological phenomenon in which the rock and soil mass on a slope slide downward along a weak surface or zone under the action of gravity (Nemok et al. 1972, Varnes 1978), and its action process is one of the manifestations of the geomorphology evolution process (Glade & Crozier 2005, Irasema 2002).

The landslide's massive volume is usually large, which is owing not only to the rock and soil being transported by themselves but also to the entrainment effect of the landslide movement process, which causes the ultimate landslide body volume to be much larger than the initial volume (Gao et al. 2020). Because the dangers of landslides are self-evident, an in-depth study of existing landslides can guide future landslide prevention and management, and it is also a manifestation of humans learning from and modifying nature. Shao et al. (2020) studied the identification, classification, and characteristics of landslides in Baoshan City, Yunnan Province, China, and established a detailed landslide list, which provided the necessary basis for further study of landslide development and spatial distribution, landslide prediction, and geological disaster evaluation in Southwest China. According to satellite images, there was an ancient landslide in this area before 2008. Wasowski et al. (2021) studied the Yangjiagou landslide formed after Wenchuan Earthquake and combined it with the existing landslide research. Finally, the seismic activity pattern in the surrounding area of the Longmenshan fault was inferred, and other works of literature also reported it (Ouimet 2010; Tang et al. 2011, 2012; Fan et al. 2018, 2020). Wang et al. (2021a, 2021b)

conducted a field investigation and experimental research on the occurrence mechanism of the Donghekou landslide, and the results obtained were used to guide landslide research in Japan. iRALL also organized a thematic meeting on the issue of landslides after the 2008 Wenchuan earthquake (Huang et al. 2018).

In this paper, the current developments in the study of landslide occurrence mechanisms are strongly introduced, and finally, numerous approaches and models for landslide monitoring and prediction are summarized, with a focus on typical landslides in Southwest China. We know the landslide-prone locations, the landslide occurrence mechanism, expand the depth and breadth of the study mechanism and compare the accuracy of monitoring means and forecasting models from a macro perspective. It helps us to have an overall understanding of the existing prevention and control methods, to guide the prevention and control of landslide disasters.

Landslide Mechanisms

Influencing factor: The occurrence of landslide needs to meet specific mechanical conditions, that is, when the sliding resistance of the weak surface of landslide is less than the sliding force, a certain volume of rock and soil will move along the sliding surface. The mechanism of landslides is closely related to the inducing factors. Table 1 depicts the conditions that may cause a landslide from four perspectives.

Mechanisms of the Soil landslides: When the landslide material is made up of a loose accumulation of dirt, it would start up and move like water under the impact of an earthquake or a high-intensity continuous rain. To study its

mechanism, Hu et al. (2017a, 2017b, 2018a, 2018b, 2019) experimented with artificial imitation particle slope in the laboratory and revealed the instability and failure mechanism of this system. Hu et al. (2016, 2019, 2020) also believed that under gravity, a precise combination of normal stress and shear strain rate would cause dry particle flow to move, and that particle breaking would considerably lower following shear resistance due to particle thixotropy.

In addition to the influence of soil particle size, the excessive positive pore water pressure in a landslide is also considered as one of the important factors triggering landslide (Wang et al. 2020), so the monitoring of on-site pore water pressure can be used as a reliable indicator for landslide early warning (Hu et al. 2017a). Hu et al. (2017b) studied the influence of particle size and pore water on the start of landslides. As mentioned earlier, precipitation often plays a key role in the occurrence of landslides, and its time evolution has a positive correlation with the landslide process (Wang et al. 2019, Yang et al. 2019, Gao et al. 2020, Li et al. 2020). Besides precipitation, terrain factors also have a significant influence on the occurrence of landslides (Fan et al. 2020). For reservoir landslide, Wang et al. (2021a, 2021b) and Li et al. (2021a, 2021b, 2021c) have reached similar conclusions, namely, the dominant failure mechanism of landslide changes with the change of reservoir water level and slope saturation. The periodic fluctuation of reservoir water level, according to Liao et al. (2021), has a significant impact on the mechanical characteristics of the sliding zone soil in the water-fluctuating zone, and the area of the water-fluctuating zone regulates landslide stability. Xia et al. (2021) introduced a two-dimensional Discontinuous Deformation Analysis

Table 1: The factors affecting the occurrence of landslides (Cruden & Varnes 1996).

Geological factor	Geomorphological factors	Natural factors	Human factors
soft rock-soil	Structure or volcanic uplift	Rainstorm	Excavation of slope and slope foot
weathered rock	Ice cover spring back	Quick snowmelt	Loading weight on slope or slope top
shear band cutting rock mass	River erosion slope toe or its side edge	continuous rainfall	reservoir construction
Rock mass with developed joint fissures	Wind erosion slope toe	Flood or tidal impact	disafforestation
Reverse discontinuity surface (fault, unconformity surface, fracture, etc.)	Ice erosion slope toe	Earthquake	irrigation
Significant difference in permeability of rock-soil	Underground erosion (dissolution and sub-erosion)	volcanic eruption	Mining, quarrying
Significant difference in the strength of rock-soil	Vegetation destruction	melting ice	artificial vibration
	Slope or slope top stacking interaction	Freezing and dissolved	conduit leakage
		shrinkage and swelling	

(DDA) that may be used to mimic the fracture tensile behavior of rock in a rock avalanche generated by seismic force.

Mechanisms of the rock landslides: Rock landslides are also common in the Sichuan Basin and the Three Gorges area of China. The typical feature of this kind of landslides is the alternating layers of mudstone and sandstone in a bedding-control cataclastic slope. Hu et al. (2019, 2014, 2016) studied the starting mechanism of the Daguangbao landslide formed after the Wenchuan earthquake, it was found that the high temperature of 800°C was generated during the sliding process of the basement, which made dolomite thermally decompose to form lime (CaO) and magnesia (MgO) (Fig. 1), and some minerals in the shear zone were heated to form a dynamic recrystallization layer about 0.1 mm thick (Fig. 2).

In addition, hot supercritical carbon dioxide and superheated steam with a pressure of > 10MPa could produce high pore-fluid pressure, and the dynamic recrystallization of minerals and supercritical gas together constituted the drag reduction mechanism of landslide movement, which was consistent with Habib (1975) and Goguel (1978). As a result, quick long-run-out landslides are easy to form. Hu & McSaveney (2018) and Hu et al. (2018b) then conducted extensive investigations into two rock failures in Jiweishan and came to the same result. This is because as soil saturation and shear rate increase, the residual friction coefficient of the soil decreases significantly, and the critical stress triggering large displacement is related to the residual shear strength related to soil rate (Hu et al. 2018a, Scaringi et al. 2018), while another paper (Xu et al. 2021) shows that under the action of larger normal stress (> 100kPa), the soil in the slip

zone is more likely to fail than the soil-bedrock interlayer.

Landslide Monitoring and Prediction

Landslide activity can be observed in all weathers using monitoring equipment based on the integration of space, air, and ground. Landslide prediction models have been swiftly constructed using a combination of statistics and computer science, and their accuracy and scope of application have been greatly upgraded and enlarged, as described in this study.

Monitoring technology: Interferometry Synthetic Aperture Radar (InSAR) is a real-time landslide monitoring system that has been successfully utilized for landslide monitoring in Southwest China (Zhang et al. 2021, Woods et al. 2021). Hu et al. (2018a) discovered a creep-like link between acoustic emission technology and density and cumulated acoustic energy of slope material by capturing and analyzing the high-frequency atomic spectrum generated by particle rearrangement in landslides. The literature also mentions sonic emission technology as an early warning approach for landslide monitoring (Xiaoan et al. 2020). The dam height of the dammed lake generated by the second landslide is larger when more than two landslides occur in the same location on both bank slopes of the river, but its stability is lower (Liao et al. 2020). As a result, it is vital to estimate the landslide risk in the area, predict the likely dammed lake shape, and execute control measures ahead of time to minimize damage. As demonstrated in Tables 2, 3, and 4, it separates the monitoring technical principles, benefits, and drawbacks of space-air-ground monitoring.

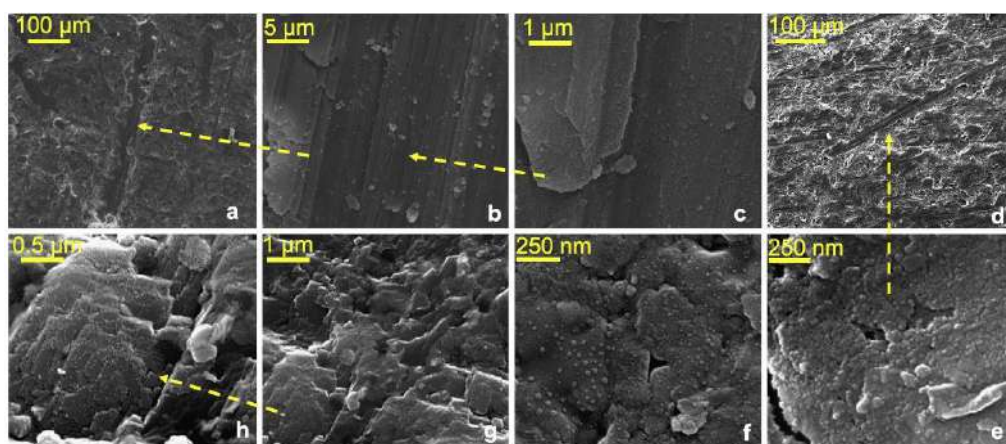


Fig. 1: Electronic image of sliding surface and internal structure in cataclastic dolomite near the sliding surface of Daguangbao landslide. a. Two sets of micro-scratches, vertical scratches indicate the direction of landslide movement; another group of scratches may be the direction of past tectonic movement. b. and c. Nano-sphere structure is a typical feature of dolomite decarbonization into lime (CaO) and magnesia (MgO). d. and e. The micro-scratch on the surface of another sample, which has a similar structure to b. and c. f. The nano-sphere structure found about 3mm below the sliding surface indicates the source of recrystallized materials in b. c. and e. g. and h. The remains of formerly decomposed dolomite grains (now reconstituted) (Hu et al. 2019).

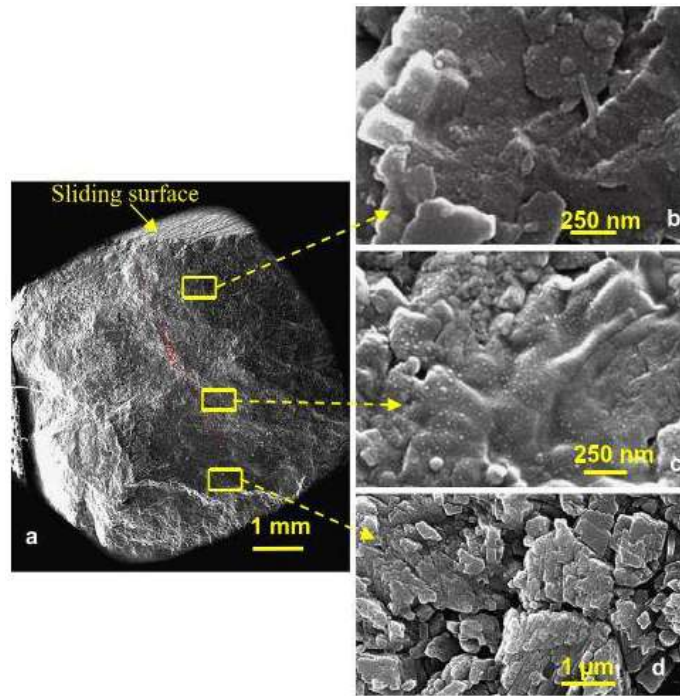


Fig. 2: Electronic images of internal structures at different depths under the sliding surface in cataclastic dolomite of Daguangbao Mountain. a. Dolomite fragments under the sliding surface. b. and c. Skeletal remains of extensively decomposed dolomite. d. Partially decomposed dolomite fragments covered with tiny spheres (nano- sphere) typical of thermal decarbonization of dolomite to lime (CaO) and magnesia (MgO) (but now carbonated in the nine years' exposure) (Hu et al. 2019).

Prediction models: It is far from sufficient to rely exclusively on monitoring technology to avoid and control landslides. Because precipitation has such a large impact on the commencement of a landslide, some researchers (Yang et al. 2019, Yu et al. 2020) suggested a precipitation threshold prediction model and verified its validity with existing data, resulting in an excellent prediction result. Liu & Wang (2021) simulated the whole process of a landslide caused by rainfall, which provided a new perspective for the quantitative risk assessment (QRA) study of landslide-induced landslides. In recent years, machine learning has played an increasingly

important role in fuzzy reasoning and data statistics. For instance, the neural network model (Abbaszadeh et al. 2020, Liu et al. 2021), neuro-fuzzy reasoning, and ant colony algorithm (Razavi-Termeh et al. 2021) have great advantages in evaluating landslide susceptibility. Zhou et al. (2018) combined the support vector machine (SVM) and artificial neural network (ANN) with multivariate statistical model logistic regression (LR) to propose the landslide susceptibility modeling (LSM). Goetz et al. (2015) and Chen et al. (2018) respectively selected six and four landslide sensitivity evaluation models based on machine learning. Sun et al.

Table 2: Monitoring methods on space.

Monitoring methods	Principle	Advantages	Disadvantages
Global Navigation Satellite System, GNSS	The position of the monitoring point is acquired by satellite in real-time	24h-monitoring; all-weather	The number of monitoring stations is limited and the data processing process is complex
Interferometry Synthetic aperture radar, InSAR	The image of the landslide is obtained by SAR satellite, and then the three-dimensional terrain information of the landslide is obtained by processing the photo	24h-monitoring; all-weather; high precision	It is difficult to select monitoring points, which is affected by spatial loss correlation and atmospheric delay
Unmanned Aerial Vehicle, UAV	The UAV is equipped with a camera, flies along the design route and takes pictures, and then obtains a three-dimensional slope model through the image data processing	High precision, automation, intelligence, not affected by clouds	It cannot be monitored all-weather due to the weather

(2021) established two optimized landslide susceptibility mapping models (LSM): logistic regression (LR) and random forest (RF) based on Bayesian algorithm hyper parameter optimization. In terms of landslide distance prediction, Zhou et al. (2020) proposed an optimized neural network model whose advantages are significantly greater than the multiple regression model. Li et al. (2021a, 2021b) used PFC software to predict the runout behavior of landslides and provided a new method for landslide hazard risk assessment.

CONCLUSION

In this paper, the present situation of landslide research in Southwest China is summarized, with emphasis on the landslide starting mechanism, and a brief overview of landslide monitoring technology and prediction model.

1. There are many factors contributing to the initiation of landslide, among which precipitation and earthquake are two major inducing factors. For soil landslide, precipitation leading to seepage in the landslide and fine particles recombined by water migration induces deformation of landslide to a certain extent. On the one hand, the stability of a landslide

could be broken by an earthquake. On the other hand, the positive pore water pressure in a landslide may rise due to vibration, which will also trigger a landslide. Rock landslide has the characteristics of fast speed, long-distance, and large volume because high temperatures are generated in the shear zone of a landslide during movement, the minerals at a certain thickness of interface dynamically recrystallize, and high temperatures also produce supercritical carbon dioxide and superheated steam, lowering friction coefficient and friction resistance. The friction coefficient of the shear surface will also decrease with the increase of normal stress and shear rate during the movement of soil landslide.

2. It's a quick rundown of landslide monitoring and forecasting technology. Landslide monitoring technology evolves in tandem with scientific and technological advancements. Real-time landslide monitoring and accurate forecasting will advance to a new level if the integrated monitoring technology in the space-air-ground can be fully employed. The landslide prediction model is mainly based on statistical analysis and machine learning to make a landslide susceptibility model (LSM), combine the model with existing landslide data, and constantly adjust parameters to achieve

Table 3: Monitoring methods on air.

Monitoring methods	Principle	Advantages	Disadvantages
Robot monitoring	The total station automatically monitors the prism on the landslide in 24 hours	Automation, 24-hour monitoring, high precision	The monitoring range of a single robot is small, but the cost of arranging multiple robots is high
3-D laser scanning	By measuring the time difference between transmitting and receiving laser and the horizontal angle and zenith distance of each pulse laser, the three-dimensional coordinates of the measured object are obtained	24-hour dynamic monitoring; high precision	The data processing is complex and the measurement accuracy is affected by surface objects
GB-InSAR	The LIDAR sensor emits and receives microwave signals, and the image is synthesized by SAR technology.	High precision; 24h monitoring; all-weather; not affected by the weather	Lack of data processing; monitoring environment has an impact on the results

Table 4: Monitoring methods on ground.

Monitoring methods	Principle	Advantages	Disadvantages
Time Domain Radiation, TDA	The deformation position and displacement can be determined by processing the echo signal.	Short monitoring time, low cost, and accurate positioning of sliding surface	Unable to determine the position of the sliding surface, low sensitivity to uniform deformation, point style monitoring
Borehole inclinometer	There is a certain angle between the inclinometer probe and the deformation of rock and soil, and the horizontal displacement of the inclinometer probe can be calculated by using the angle.	Accurately monitor the direction of sliding surface	Point monitoring, orientation is susceptible to interference
Distributed fiber optic sensing	Through the reception and analysis of scattered light, the changes of strain and temperature in optical fiber are obtained	High precision, distributed monitoring, high survival rate, anti-corrosion and anti-interference	Unable to determine the direction of sliding surface

the expected accuracy. However, due to the limitations of the existing technology, no model can accurately predict all types of landslide characteristics.

AUTHOR CONTRIBUTION STATEMENT

The authors confirm contribution to the paper as follows: Shuang Li: Conceptualization, Formal Analysis, Writing - Original Draft; Xiang Wu: Investigation, Data Curation, Writing - Original Draft; Faming Sun: Conceptualization, Supervision, Writing - Review & Editing; Jie Yang: Investigation, Writing - Original Draft; Jian Li: Resources, Supervision.

REFERENCES

- Abbaszadeh, S., Abbas, M. and Fardad, M.M. 2020. Landslide susceptibility mapping using hybridized block modular intelligence model. *Bull. Eng. Geol. Environ.*, 80: 267-284.
- Chang, M., Xiangyang, D., Tristram, C.H. and Bin, Y. 2021. Patterns of rainfall-threshold for debris-flow occurrence in the Wenchuan seismic region, Southwest China. *Bull. Eng. Geol. Environ.*, 80: 2117-2130.
- Chen, W., Peng, J., Hong, H., Shahabi, H., Pradhan, J., Liu, A., Zhu, X., Pei, C.X. and Duan, Z. 2018. Landslide susceptibility modeling using GIS-based machine learning techniques for Chongren County, Jiangxi Province, China. *Sci. Total Environ.*, 626: 1121-1135.
- Cruden, D.M. and Varnes, D.J. 1996. *Landslide Types and Processes*. Special Report - National Research Council, Transportation Research Board, 247: 36-75.
- Fan, X., Junjie, T., Shujun, T. and Yuanjun, J. 2020. Rainfall-induced is rapid and long-runout catastrophic landslide on July 23, 2019, in Shuicheng, Guizhou, China. *Landslides*, 17: 2161-2171.
- Fan, X., Hsein Juang, C., Wasowski, J., Huang, R., Xu, Q., Scaringi, G., Cees, J. and Hans-Balder, H. 2018. What we have learned from the 2008 Wenchuan Earthquake and its aftermath: A decade of research and challenges. *Eng. Geol.*, 241 6: 25-32.
- Gao, Y., Bin, L., Haoyuan, G., Lichuan, C. and Yongfu, W. 2020. Dynamic characteristics of high-elevation and long-runout landslides in the Emeishan basalt area: a case study of the Shuicheng "7.23" landslide in Guizhou, China. *Landslides*, 17: 1663-1677.
- Glade, T. and Crozier, M.J. 2005. The nature of landslide hazard impact. *Landslide Hazard Risk*, 5: 43-74.
- Goetz, J.N., Brenning, A., Petschko, H. and Leopold, P. 2015. Evaluating machine learning and statistical prediction techniques for landslide susceptibility modeling. *Comp. Geosci.*, 81: 1-11.
- Goguel, J. 1978. Scale-dependent rockslide mechanisms, with emphasis on the role of pore fluid vaporization. *Develop. Geotech. Eng.*, 53: 985-1011.
- Habib, P. 1975. Production of gaseous pore pressure during rock slides. *Rock Mech.*, 7: 193-197.
- Hu, W., Xu, Q., Wang, G.H., Van Asch, T.W.J. and Hicher, P.Y. 2016. Initiation processes for run-off generated debris flows in the Wenchuan earthquake area of China. *Geomorphology*, 253: 468-477.
- Hu, W. and McSaveney, M.J. 2018. A polished and striated pavement formed by a rock avalanche in under 90 s mimics a glacially striated pavement. *Geomorphology*, 320: 154-161.
- Hu, W., Xu, Q., Wang, G.H., Van Asch, T.W.J. and Hicher, P.Y. 2014. Sensitivity of the initiation of debris flow to initial soil moisture. *Landslides*, 12: 1139-1145.
- Hu, W., Xu, Q., Wang, G.H., Van Asch, T.W.J. and Hicher, P.Y. 2020. Weakening rheology of dry granular flows with extensive brittle grain damage in high speed rotary shear experiments. *Geophys. Res. Lett.*, 6: 47.
- Hu, W., Runqiu, H., Mauri, M., Lu, Y., Qiang, X., Mingshi, F. and Xianghui, Z. 2019. Superheated steam, hot CO₂, and dynamic recrystallization from frictional heat jointly lubricated a giant landslide: Field and experimental evidence. *Earth Planet. Sci. Lett.*, 510: 85-93.
- Hu, W., Runqiu, H., Mauri, M., Lu, Y., Qiang, X., Mingshi, F. and Xianghui, Z. 2018a. Mineral changes quantify frictional heating during a large low-friction landslide. *Geology*, 46: 223-226.
- Hu, W., Runqiu, H., Mauri, M., Lu, Y., Qiang, X., Mingshi, F. and Xianghui, Z. 2018b. Acoustic emissions and microseismicity in granular slopes prior to failure and flow like motion: The potential for early warning. *Geophys. Res. Lett.*, 45: 10406-10415.
- Hu, W., Runqiu, H., Mauri, M., Lu, Y., Qiang, X., Mingshi, F. and Xianghui, Z. 2018c. Internal erosion controls failure and runout of loose granular deposits: Evidence from flume tests and implications for postseismic slope healing. *Geophys. Res. Lett.*, 45: 5518-5527.
- Hu, W., Runqiu, H., Mauri, M., Lu, Y., Qiang, X., Mingshi, F. and Xianghui, Z. 2018d. Suction and rate-dependent behavior of a shear-zone soil from a landslide in a gently-inclined mudstone-sandstone sequence in the Sichuan basin, China. *Eng. Geol.*, 237: 1-11.
- Hu, W., Xu, Q., Wang, G.H., Van Asch, T.W.J. and Hicher, P.Y. 2017a. Sensitivity of the initiation and runout of flow slides in loose granular deposits to the content of small particles: An insight from flume tests. *Eng. Geol.*, 231: 34-44.
- Hu, W., Qiang, X., Gonghui, W., Gianvito, S., Mauri, M. and Hicher, P.Y. 2017b. Shear resistance variations in experimentally sheared mudstone granules: A possible shear-thinning and thixotropic mechanism. *Geophys. Res. Lett.*, 11: 44.
- Huang, R., Xuanmei, F., Qiang, X., Gianvito, S., Wei, H., Niek, R. and Gonghui, W. 2018. The iRALL Doctoral School 2018: Advanced studies on large landslides on the 10th anniversary of the Wenchuan earthquake. *Landslides*, 15: 1901-1903.
- Irasema, A. 2002. Geomorphology, natural hazards, vulnerability, and prevention of natural disasters in developing countries. *Geomorphology*, 47: 107-124.
- Li, B., Wenping, G., Huiming, T., Zongxing, Z., Victor, M.B. and Hsein Juang, C. 2021a. Probabilistic analysis of a discrete element modeling of the runout behavior of the Jiweishan landslide. *Int. J. Num. Anal. Methods Geomech.*, 32(7): 661-673.
- Li, S., Guoping, L., Xiaofang, W., Chao, L., Haizhi, L. and Gang, Li. 2020. Precipitation characteristics of an abrupt heavy rainfall event over the complex terrain of southwest China were observed by the FY-4A satellite and doppler weather radar. *Water*, 12: 513.
- Li, Y., Wei, H., Janusz, W., Yangshuai, Z. and Mauri, M. 2021b. Rapid episodic erosion of a cohesionless landslide dam: Insights from loss to scour of Yangjia Gully check dams and from flume experiments. *Engineering Geol.*, 91: 180-187.
- Li, Y., Stefano, U., David, M., Lixia, C. and Kunlong, Y. 2021c. Chasing a complete understanding of the failure mechanisms and potential hazards of the slow-moving Liangshuijing landslide. *Eng. Geol.*, 5: 281-296.
- Liao, H., Xing-Guo, Y., Hai-bo, L., Bin-Rui, G. and Jia-wen, Z. 2020. Increase in hazard from successive landslide-dammed lakes along the Jinsha River, Southwest China. *Geom. Nat. Hazards Risk*, 11: 1115-1128.
- Liao, K., Yiping Wu, Fasheng Miao, Linwei Li, and Yang, X. 2021. Effect of weakening of sliding zone soils in hydro-fluctuation belt on the long-term reliability of reservoir landslides. *Bull. Eng. Geol. Environ.*, 80: 3801-3815.
- Liu, M., Yong, Z., Shu-Feng, T., Ning-Sheng, C., Rahman, M. and Iqbal, J. 2020. Effects of loose deposits on debris flow processes in the Aizi Valley, southwest China. *J. Mount. Sci.*, 17: 156-172.
- Liu, Q., Guangyin, L. and Jie, D. 2021. Prediction of landslide displacement with step-like curve using variational mode decomposition and periodic neural network. *Bull. Eng. Geol. Environ.*, 80: 3783-3799.
- Liu, X. and Wang, Y. 2021. Probabilistic simulation of the entire process of

- rainfall-induced landslides using random finite element and material point methods with hydro-mechanical coupling. *Comp. Geotech.*, 9: 132.
- Nemok, A., Paek, J. and Rybá, J. 1972. Classification of landslides and other mass movements. *Rock Mech.*, 4: 71-78.
- Ouimet, W.B. 2010. Landslides associated with the May 12, 2008, Wenchuan earthquake: Implications for the erosion and tectonic evolution of the Longmen Shan. *Tectonophysics*, 491(6): 244-252.
- Peng, T., Chen, N.S., Hu, G., Tian, S. and Liu, E. 2021. New insights into the delayed initiation of a debris flow in southwest China. *Nat. Hazards*, 17: 227-236.
- Razavi-Termeh, S.V., Kourosh, S. and Mehrdad, P. 2021. Mapping of landslide susceptibility using the combination of neuro-fuzzy inference system (ANFIS), ant colony (ANFIS-ACOR), and differential evolution (ANFIS-DE) models', *Bull. Eng. Geol. Environ.*, 80: 2045-2067.
- Scaringi, G., Wei Hu, Q.X. and Runqiu, H. 2018. Shear rate dependent behavior of clayey bimaterial interfaces at landslide stress levels. *Geophys. Res. Lett.*, 45: 766-77.
- Shao, X., Siyuan, M., Chong, X., Lingling, S. and Yongkun, L. 2020. Inventory, distribution, and geometric characteristics of landslides in Baoshan City, Yunnan Province, China. *Sustainability*, 12: 45-66.
- Sun, D., Jiahui, X., Haijia, W. and Danzhou, W. 2021. Assessment of landslide susceptibility mapping based on Bayesian hyperparameter optimization: A comparison between logistic regression and random forest. *Eng. Geol.*, 17: 281.
- Tang, C., Van Asch, T.W.J., Chang, M., Chen, G.Q., Zhao, X.H. and Huang, X.C. 2012. Catastrophic debris flows on 13 August 2010 in the Qingping area, southwestern China: The combined effects of a strong earthquake and subsequent rainstorms. *Geomorphology*, 6: 559-576
- Tang, C., Jing Zhu, X.Q. and Jun, D. 2011. Landslides induced by the Wenchuan earthquake and the subsequent strong rainfall event: A case study in the Beichuan area of China. *Eng. Geol.*, 122(6): 22-33.
- Varnes, D.J. 1978. Slope movement and types and processes. *Landslides Anal. Cont.*, 16: 711-728.
- Wang, D., Mengliang, L., Xing, Z., Hongsheng, M., Qiang, Cheng, M., Zhu, Z.C. and Chaojun, O. 2019. Failure mechanisms and deformation processes of a high-locality landslide at Tonghua Town, Li County, China, 2017. *Landslides*, 17: 165-177.
- Wang, D., Mengliang, L., Xing, Z., Hongsheng, M., Qiang, Cheng, M., Zhu, Z.C. and Chaojun, O. 2021a. The debris avalanche in Donghekou area triggered by the 2008 Wenchuan (M8.0) earthquake: Features and possible transportation mechanisms. *Eng. Geol.*, 14: 280.
- Wang, L., Wenhua, L., Wei Hu, W. and De'an, S. 2020. Effects of seismic force and pore water pressure on the stability of 3D unsaturated hillslopes. *Nat. Hazards*, 105: 2093-2116.
- Wang, S., Yuchen Pan, L., Wang, F.G., Yushan, C. and Wenduo, S. 2021b. Deformation characteristics, mechanisms, and influencing factors of hydrodynamic pressure landslides in the Three Gorges Reservoir: a case study and model test study', *Bulletin of Engineering Geology and the Environment*, 80: 3513-33.
- Wasowski, J., McSaveney, M.J., Pisano, L., Del Gaudio, V., Li, Y. and Hu, W. 2021. Recurrent rock avalanches progressively dismantle a mountain ridge in Beichuan County, Sichuan, most recently in the 2008 Wenchuan earthquake. *Geomorphology*, 41: 374.
- Woods, A., Macciotta, M.T., Hendry, T., Stewart, M. and Marsh, J. 2021. Updated understanding of the deformation characteristics of the Checkerboard Creek rock slope through GB-InSAR monitoring. *Eng. Geol.*, 281(6): 105974.
- Xia, M., Guangqi, C., Pengcheng, Y., Xinyan, P. and Jinfeng, Z. 2021. Improvement of DDA with a new unified tensile fracture model for rock fragmentation and its application on dynamic seismic landslides. *Rock Mech. Rock Eng.*, 54: 1055-1075.
- Xiaoyan, Z., Hu, W., Zheng, Y., Gou, H. and Gao, X. 2020. Effects of relative density in progressive sliding of tailings deposits: insights from flume tests. *Eng. Geol.*, 6: 279.
- Xu, Q., Weizao, W., Litao, L. and Yingdong, C. 2021. The failure mechanism of gently inclined shallow landslides along with the soil-bedrock interface on ring shear tests. *Bull. Eng. Geol. Environ.*, 80: 3733-3746.
- Yang, H., Fangqiang, W. and Shaojie, Z. 2019. Rainfall threshold for landslide activity in Dazhou, southwest China. *Landslides*, 17: 61-77.
- Yu, B., Erlong, M., Jiajun, C. and Guang, Z. 2020. A prediction model for rock planar slides with large displacement triggered by heavy rainfall in the Red bed area, Southwest, China. *Landslides*, 18: 773-783.
- Zhang, T., Shuai, X., Jinghui, F., Bo, H., Qun, W., Weilin, Y., Hongli, Z., Jianping, C., Hongzhou, L. and Liqiang, T. 2021. Detection of active landslides in Southwest China using Sentinel-1 and ALOS-2 Data. *Proc. Comp. Sci.*, 181: 1138-1145.
- Zhou, C., Kunlong, Y., Ying, C., Bayes, A., Yuanyao, L., Filippo, C. and Hamid, R.P. 2018. Landslide susceptibility modeling applying machine learning methods: A case study from Longju in the Three Gorges Reservoir area, China. *Comp. Geosci.*, 112: 23-37.
- Zhou, H., Yong, C. and Ruoying, T. 2020. Distance prediction of slope-foot landslide in the southwest of China based on GA-BP neural network. *IOP Conf. Ser. Mater. Sci. Eng.*, 11: 730.



Ecological Health Assessment of Renuka Lake, Himachal Pradesh, India

Yeshi Choden*†, M. P. Sharma**, Gaurav Pandey**, S. K. Gupta** and K. D. Dema***

*Department of Civil Engineering, College of Science and Technology, Royal University of Bhutan, 21101, Bhutan

**Department of Hydro and Renewable Energy, Indian Institute of Technology, Roorkee-247667, Uttarakhand, India

***Department of Information and Technology, College of Science and Technology, Royal University of Bhutan, 21101, Bhutan

†Corresponding author: Yeshi Choden; yeshichoden.cst@rub.edu.bt

Nat. Env. & Poll. Tech.

Website: www.neptjournal.com

Received: 02-06-2021

Revised: 23-06-2021

Accepted: 13-07-2021

Key Words:

NFSWQI

Water quality index (WQI)

Ecological health index

Diversity index

ABSTRACT

Researchers, policymakers, and governments are increasingly interested in assessing the ecological health (EH) of lakes and streams. The EH of a lake can be expressed in terms of water quality, trophic state and biodiversity of riparian vegetation, macroinvertebrates and fishes. The ecological health index (EHI) of Renuka lake, Himachal Pradesh of India, was analyzed based on National Sanitation Foundation Water Quality Index (NSFWQI), Carlson's Trophic State Index (TSI), Simpson Diversity Index (SDI), and Shannon-Weiner index (SWI). The results of NSFWQI and CTSI are found in the range of 40-59 and 49.9-58.9 respectively indicating that the water quality was poor to medium and not suitable for drinking purposes but can be used for secondary purposes such as agriculture, industry, and recreation etc. The trophic state of the lake is similarly in the eutrophic range, with an overall EHI of 1.81-2.47, indicating poor to medium trophic status. Apart from analyzed results, the EH category from mesotrophic to a eutrophic state of the lake is caused due to the cultural siltation/nutrient loading, religious practices, land tenurial issues, and uncontrolled tourist pressure followed by recreational activities on water bodies and lake vicinity. Accordingly, suitable restoration methods such as source control, desilting/dredging, and lake aquatic plantation are suggested to recover the ecological health of the lake back to a mesotrophic or oligotrophic state.

INTRODUCTION

The water resources, mainly, rivers, lakes, glaciers, rainwater, groundwater, etc., meet the need for water for drinking, agriculture, livestock production, forestry, industrial activities, hydropower generation, fisheries, and other creative activities. The quality of both surface and groundwater is deteriorating rapidly due to the increasing population, industrialization, urbanization, etc (Tyagi et al. 2020). These sectors directly dispose huge quantities of untreated urban and industrial effluents to nearby drains/water bodies, thus building up high concentrations of toxic pollutants and contaminating the resources (Choden et al. 2020). Out of various water bodies, lakes, a large area of variable sizes filled with water and surrounded by land, constitute an important part of the landscape, having no direct exchange of water with the ocean but provide extremely valuable ecosystems and goods and services to humankind (Cantonati et al. 2020). The EH assessment of such water bodies is based on their ecosystem health, which encompasses not only the water quality but also the diversity of plants and organisms that populate there. A lake or any water body has both, natural and social attributes each contributing to its overall health. Ecosystem or Ecological Health (EH)

is defined by the interaction between lake biota and their hydrodynamical and geochemical environment. Therefore, it depends on the diversity of habitats of plants and animal species and also on the effectiveness of the linkages and maintenance of ecological processes including its water quality. In recent years, there has been a lot of research on this topic. For example, (Kumar et al. 2015) analyzed the EH of Baiyangdian lake in China using the ecological health index and classified the EH as a medium: 40-60. (Yadav et al. 2015) determined the EH of the Chambal River using EQI and RPI methods based on WQ parameters and found that water parameters are the most important tool for assessing overall river health, and the EH of the river was found satisfactory in the range of 1-2, indicating that the water is not suitable for drinking but is suitable for irrigation, bathing, and aquaculture. (Sharma et al. 2010) used WQ and the Trophic State Index (TSI) to assess the EH of Mansi Ganga Lake in Vrindavan, Uttar Pradesh, India. They found that the lake was oligotrophic in 2006 but became mesotrophic later and that in 2008, there was a significant increase in pollution due to massive algae growth. The treatment of algae with copper sulphate was proposed and used, followed by the draining of all toxic water and the refilling of the lake with canal water. This had made a huge

difference in the lake's health. Further, the water quality assessment of Nanital lake of Uttarakhand, India was carried out by (Sharma 2014) using physio-chemical parameters and found the lake was highly polluted due to receiving illegal disposal of construction wastes and discharge of domestic and industrial wastewater including agriculture runoffs from the catchment. The lake restoration was carried out by using 35 discs embedded at the lake bottom for the purpose of oxygenation of the lake, stratification breakage, and catchment area remediation. This has restored the lake to an oligotrophic state, making it a role model for lake management. It has also reclaimed its natural beauty, as seen by the influx of large numbers of tourists desiring navigation and natural beauty. The Surha Lake, located in district Ballia of Uttar Pradesh, India, is the main source of livelihood for the local population which has been badly affected by a huge growth of algae due to receiving huge agricultural runoffs and wastewater from the surrounding population. The EH of this lake was conducted during the wet and dry season from 2014 to 2015 using EHI based on NSFQI, CTSI, and SDI. The results indicated that the lake was in a eutrophic state both during the wet and dry seasons with an average CTSI of 76.30 and 79.49 respectively, thereby, indicating the poor quality of water as unsuitable for human use. The SDI was found as 0.67 and 0.65 in wet and dry seasons i.e., poor diversity (Mishra et al. 2016). (Sunil et al. 2016) studied the structure and diversity of riparian forests across forest and agro-ecosystem landscapes along the river Cauvery of southern India using the Shannon-Wiener Index (SWI) method. The results showed that the expansion of agricultural activities and other biotic pressures might have led to the variation in species composition between the forest and agro-ecosystem, declining some evergreen species, subsequently affecting the connected biodiversity of the river in the agro-ecosystem.

According to the above literature, EH assessments of various Himalayan and mountain lakes are lacking and no work on Renuka Lake, a Ramsar site, in terms of ecological and biodiversity health is available. Renuka Lake is a sacred lake in Himachal Pradesh, India, that has been designated as a Ramsar site. Because of the importance of Renuka Lake and the benefits it provides to the local community, the current study was done to assess the lake's ecological health. The findings are likely to be valuable to policymakers and stakeholders in the future to restore it.

MATERIALS AND METHODS

About the Study Area

A religious Renuka lake lies in the Sirmour district of Hi-

machal Pradesh and its location map and lake catchment are shown in Fig. 1. This natural Ramsar lake has a wildlife sanctuary covering one-third of its circumference in its catchment making it a center of attraction. Renuka Lake has a small outlet that drains its water to Parshhuram Tal, a manmade pool, and then to River Giri, a tributary of the Yamuna River. Its maximum depth is approximately 13 m and minimum about 0.5 m. Its maximum length is 1706.7 m and its width is in the range of 132.5 -246.8 m. Its shoreline length is 3214 m, surface area and catchment areas are 0.18 km² and 2.5 km² respectively (Singh 2012) and (Diwate et al. 2020).

Renuka lake is a perennial water body fed by 21 seasonal streams which remain vigorously full of water, particularly, during the monsoon season. The internal springs of the lake are the perennial source of water. The underground network of channels in the Limestone and Dolomite formations of the area are possible conduits to get the groundwater to the lake. Given its rich biodiversity and uniqueness of the area, the Renuka lake was declared as a Ramsar site in the year 2005. The climate of the area is of sub-tropical monsoonal type. Renuka Lake receives 150-199.9 cm of precipitation each year, with an average maximum temperature of 32°C. Low-lying locations experience warm winters, whereas high mountain ranges experience snowfall. Springtime is warm and sunny. The rainy seasons are the wettest parts of the year, with high levels of humidity. During the monsoon season,

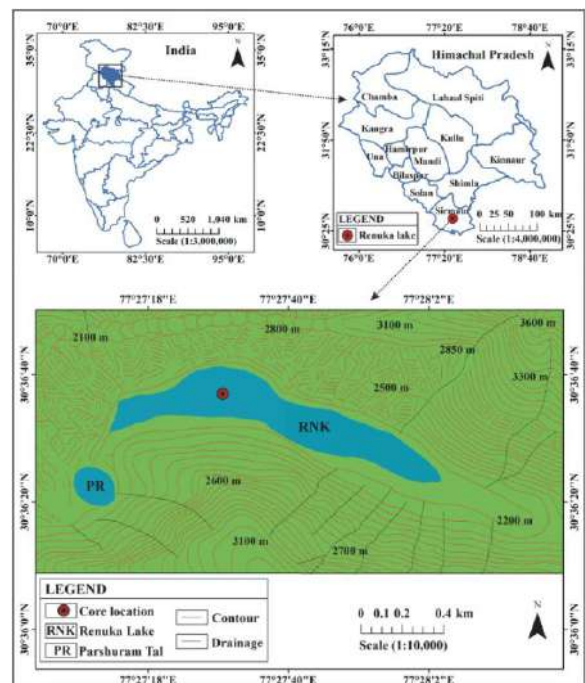


Fig. 1: Renuka lake.

the summers are scorching hot (Himachal Pradesh Council for Science, Technology & Environment 2017).

Sample Collection for WQI Assessment

A total of 15 samples were collected from 5 locations during pre and post-moon 2018-2019 as shown in Fig. 2 and data analysis is presented in Table 3 which gives the details of sampling locations. All the WQ parameters are the average values of all the 3 samples from each site. Fig. 3 gives a spatial representation of each water quality parameter. The samples were analyzed for temperature, pH, total solids, total suspended solids, and total dissolved solids, turbidity, transparency, specific conductivity, dissolved oxygen, alkalinity, total hardness, calcium, and magnesium hardness, nitrates, phosphates, sodium, COD, BOD, *E. coli*, and pH as per the standard procedures (APHA 2018).

The parameters like temperature, pH, turbidity, fecal coliforms, dissolved oxygen (DO), BOD, total phosphates (TP), COD and total solids (TS) were converted to NFSWQI (Tyagi et al. 2020). The mathematical expression of this index is given by Eq. 1:

$$WQI = \sum_{i=1}^n QiWi \quad \dots (1)$$

Where Qi= sub-index for ith water quality parameter;
 Wi= weight associated with ith water quality parameter;
 n= number of water quality parameters.

Arc-GIS Interpolation and Spatial Representation

To predict water quality status at various locations of the lake, the water quality parameters of 15 samples as reported in Table 3, were interpolated using arc-GIS and spatially represented using inverse distance weighted technique (IDW) (Childs 2004, Ozturk & Kilic 2016). Fig. 3 gives spatial reference as to how each parameter is concentrated

throughout the lake and how critical the level of pollution is based on each quality parameter.

Trophic State Index (TSI)

The trophic status refers to the level of productivity in a lake as measured by Total phosphorous (TP), algal abundance in terms of Chlorophyll (Chlor), and Secchi depth (SD) for the extent of light penetration. TSI rates individual lakes, ponds, and reservoirs based on the amount of biological productivity occurring in the water body. Using TSI, one can get a quick idea about the extent of productivity and hence the health of a lake (Hillsborough 2008). The well-known Carlson TSI can be used to rank lakes based on pollution and biomass productivity both within and between regions. This ranking allows water managers to focus on lakes that may require restoration or conservation efforts in the future. An increase in the trend of TSI over a period of several years may indicate the level of degradation of the health of the lake. The CTSI is briefly discussed below:

Carlson's Trophic Status Index: Carlson (Carlson 1977) developed CTSI in the year 1977 based on WQ parameters like Total P, Chlorophyll, and Secchi depth.

The following equations are used to compute CTSI of a lake:

$$TSI - P = 14.42 * Ln [TP] + 4.15 \text{ (in } \mu\text{g.L}^{-1}\text{)}$$

$$TSI - C = 30.6 + 9.81 Ln [\text{Chlor-a}] \text{ (in } \mu\text{g.L}^{-1}\text{)}$$

$$TSI - S = 60 - 14.41 * Ln [SD] \text{ (in meters)}$$

$$\text{Average TSI} = [TSI (P) + TSI (\text{Chlor 'a'}) + TSI (SD)]/3$$

Where TP is total phosphorus, chlor-a is chlorophyll 'a', SD is the Secchi depth. Table 1 gives the range of index values showing the trophic status of the lake.

Diversity Index (DI) of Riparian Vegetation

DI depends on the patterns of species distribution and abundance and gives a fair idea about lake health. For Riparian vegetation, the entire length of Renuka Lake was divided into 10 plots (five on each side of the length of the lake), each plot had a dimension of 1m*1m. The plant or vegetation species were counted and their abundance ratio was calculated as presented in Table 5, which is further used as a parameter to determine DI. DI is a mathematical tool to express the number of species in a biological community used to understand the community structure. It provides information about community composition and species richness by taking the relative abundances of different species available. The riparian zone consists of stream banks and floodplain vegetation (Mendes et al). The following DIs were calculated based on the ecological indicator handbook (Jorgenus et al. 2016).



Fig. 2: Sample collection points.

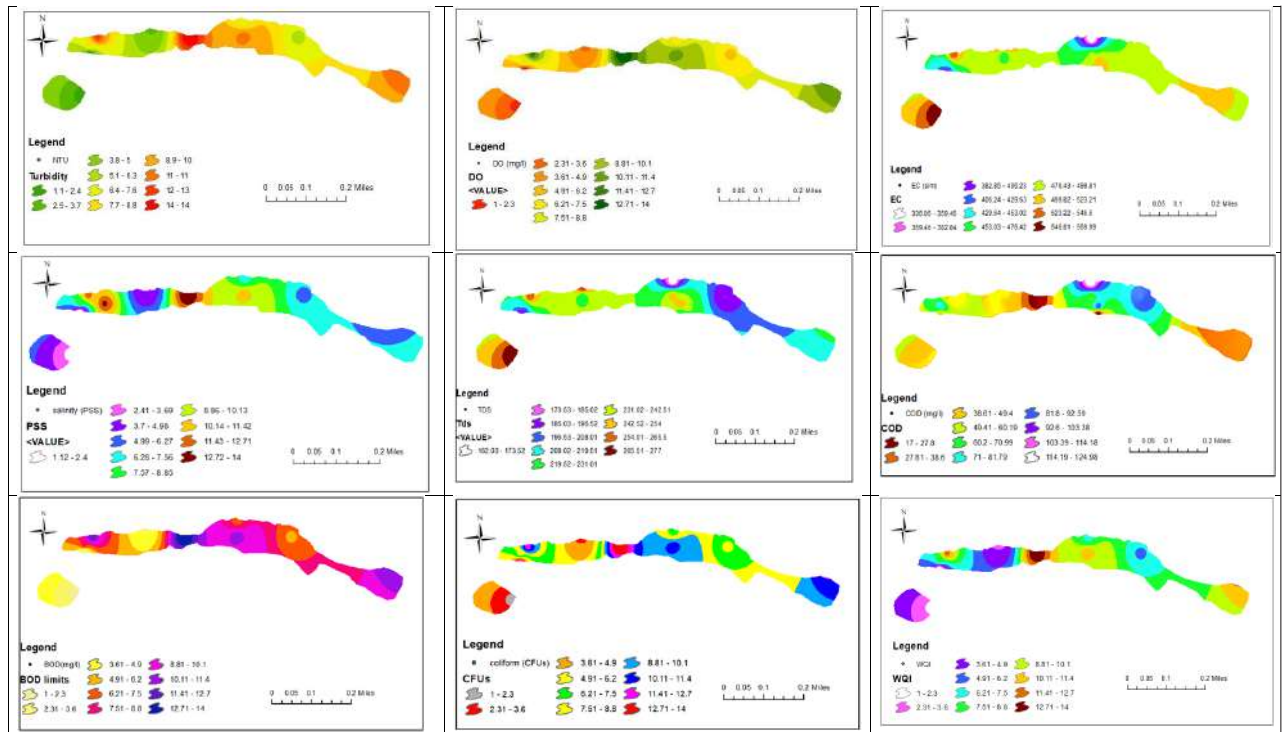


Fig. 3: Interpolated spatial representation of water quality parameters throughout the lake.

Table 1: Range of index values showing the trophic class (Pavluk & Vaate 2018).

TSI	Chl.	P	SD	Trophic status
<30-40	0-2.6	0-12	>8-4	Oligotrophic: Clearwater, oxygen throughout the year in the entire hypolimnion.
40-50	2.6-20	12-24	4-2	Mesotrophic: water moderately clear; increasing probability of hypolimnetic anoxia during summer
50-70	20-56	24-96	2-0.5	Eutrophic: anoxic hypolimnia, macrophyte problem possible
70-100 ⁺	56-155 ⁺	96-384 ⁺	0.5-<0.25	Hypereutrophic: dense algae and macrophytes, algal blooms possible throughout summer.

Shannon-Wiener Index: This is based on the information theory and assumes that individuals are sampled at random out of an “indefinitely large” community and that all the species are represented in the sample. The index is represented by Eq. 2:

$$H' = - \sum p_i \log p_i \quad \dots(2)$$

Where p_i is the proportion of individuals found in the species i .

The index ranges between 0 and 5. Higher value implies higher diversity

Simpson Index: It is based on the probability that two individuals randomly extracted from an infinitely large community belong to the same species: It is expressed by Eq. 3 as:

$$D = \sum \left[\frac{ni(ni-1)}{N(N-1)} \right] \quad \dots(3)$$

Where ni is the number of individuals in the species i and N is the total number of individuals.

It ranges from 0 to 1 where a higher value implies a low diversity and vice-versa.

Ecological Health Index (EHI)

EHI was proposed by Joshi (2013) to assess the EH of a water body based on NSFQI and CTSI. Further, the EHI equation was modified by adding SDI to WQI and CTSI as reported by (Yadav et al. 2015). The final equation to calculate the overall EHI of the lake is represented by Eq. 4. Table 2 reports the results of WQI, CTSI and DI converted into EHI scores.

The resulting scores (EHI of NSFQI and CTSI) and SDI were used to evaluate EHI mathematically as shown by Eq. 4:

$$EHI = \frac{[EHI(CTSI)+EHI(WQI)+(\frac{1}{SDI})]}{3} \dots(4)$$

Where EHI (CTSI) is the score for CTSI; EHI (WQI) is the score for WQI. The EHI range from 0-5 and classifies the ecological health of a water body as: excellent (0-1); good (1-2); average (2-3); poor (3-4); and very poor (4-5).

RESULTS AND DISCUSSION

All the WQ parameters of 15 samples (3 samples at each site) were interpolated using arc-GIS to predict the concentration level of each parameter throughout the lake indicating the pollution level. Locations 2 and 3 (bathing and recreational area) had higher TDS, Turbidity, COD, BOD, Salinity, and total Coliform limits, as shown in the color-coded legend in Fig. 3, indicating water pollution. Similarly, the NSFQI data in Table 3 shows that overall lake water quality ranged from poor to medium, with locations 2 and 3 being the most polluted, with NSFQI values in the 40-45 range.

Furthermore, the CTSI indicates that the lake is eutrophic both before and after the monsoon. The bathing ghat and recreational area at locations 2&3 had a higher level of eutrophication (Table 4), which could be owing to the nearby location having the popular Himachal Pradesh temple, Renukaji temple, which is situated on the lake’s bank and attracts a large number of pilgrims/tourists (Pillai 2003). Weathering rocks/catchment, which regulates the principal

Table 2: EHI based on WQI & CTSI (Joshi 2013).

NSFWQI	Carlson’s TSI	EHI	EHI Range	Status
90-100	10-30	1	0-1	Excellent
70-90	30-50	2	1-2	Good
50-70	50-70	3	2-3	Medium
25-50	70-90	4	3-4	Poor
0-25	90-100	5	4-5	Very poor

ions chemistry of lake water, could also be a cause of high nutrient content (Das & Kaur 2001). The mesotrophic state of its site confirmed that the unusual part of the lake had minimal pollution.

For DI, plant species of 15 different plants were identified. Their abundance ratios were further used to calculate Shannon-Wiener index and Simpson index giving average DI of 2.4 as given in Table 5. Based on the two indices, uniform distribution of the biodiversity was observed with the SWI of 4.784 which is considered higher biodiversity (Jorgenus et al. 2016), whereas SI: 0.002, ranges from 0 to 1 where a lower value implies a higher status of biodiversity.

The overall EHI (Table 6) shows the lake is of medium quality at all the locations except location no.5, which is the rear end of the lake in the range of 1.81 - 2.47.

Apart from the findings of this study, the greatest ecological stress on Renuka Lake is cultural siltation/nutrient loading in the form of idol immersion during specific festivals, owing to its holistic relevance, i.e. religious practices/land tenurial activities. As a high-altitude lake, uncontrolled tourist pressure, followed by increased recreational activities in and around the lake, has been identified as the greatest disturbance/reduction in plant and fauna biodiversity. All these have led to the eutrophic state of the lake and may likely affect the fisheries seriously if periodic timely restoration is not initiated.

Restoration Recommendation

Pre restoration: source control

Following are the options that could control the quality of the lake biodiversity index at the source level.

1. To prevent pollution from human wastes, community toilet facilities must be provided around the periphery of the lake.
2. Solid waste management measures could be introduced.
3. Demarcation of lake boundaries could be done with fencing around the lake periphery.
4. Ecotourism should be developed to have better control and management of the lake.
5. Restrictions and guidelines could be developed on the idol/devotee’s immersions.

Post Restoration:

1) Desilting/ Dredging

Well-organized local and periodic desilting/dredging be undertaken to improve like Truxor amphibious vehicle, dredge pump, floating dredgers, excavators, etc., may be employed to remove silt using a dredge pump.

2) Bank protection and Plantation

Non-hazardous dredged sediments may be reused to build up the bank areas that can be planted with a diverse range of native plants, grasses, and wildflowers including *Pontederia cordata*, sweet flag, flag iris, water mint, gypsywort, *Lobelia cardinalis* and Native sedges which have lots of benefiting properties thus improving the quality of water. The new riprap plantation is expected to diffuse the energy of spring water entering Renuka Lake, oxygenate it, and help invertebrates and fish. In addition, a new reedbed will be naturally produced to supply food for a variety of birds, including reed warblers, reed bunting, bats, damselflies, dragonflies, and butterflies.

CONCLUSION

The ecological health of Renuka lake has been assessed based on NSFQI, CTSI, and Biodiversity index (SWI & SDI). The results from the analysis and final EHI of Renuka lake reveal that the ecological health of the lake lies in the medium category (Table 6) indicating that lake health in

terms of water quality is degrading and it could result in a hyper-eutrophic state if suitable restoration is not timely undertaken by the concern authorities. Also, because Renukaji is a significant temple, worshippers and locals may be able to drink and bathe in the water if the lake changes from eutrophic to oligotrophic. The water, however, is not suitable for drinking due to the presence of *E. coli*. The Diversity Index showed uniform biodiversity meaning better ecosystem but overall ecological health of Renuka lake in medium quality range. The proper mitigation and timely assessment of the lake are essential for the restoration and revival of the lake. Some other measures are also suggested in addition to the above.

1. Treatment of catchment area through afforestation and use of organic farming.
2. Control of excessive and illegal encroachments of lake catchment.
3. Treatment of human and other wastes through proper treatment and discharge of treated wastewater to the lake through treatment and monitoring WQ of lake

Table 3: Water Quality data and its conversion to NSFQI.

Location No.	Coordinates		Name of location	Average value WQ parameters									NSF-QI VALUE	Water quality status
	Latitude	Longitude		EC [μ s]	Salinity [PSU]	NTU	BOD [mg.L ⁻¹]	COD	DO [mg.L ⁻¹]	TDS [mg.L ⁻¹]	pH	Temp °C		
1	30°36'29"	77°26'59"	Outlet to Parshuramtal	394 ±40	0.2 ±0.13	12 ±5	10 ± 10	45 ±20	5 ±2.3	189 ±33	7.5 ±0.61	21.7 ±0.76	53	Medium
2	30°36'37"	77°27'07"	Bathing Ghat	570 ±40	0.5 ±0.13	23 ±5	40 ± 10	125 ±20	2.58 ±2.3	277 ±33	7.4 ±0.61	20.3 ±0.76	40	Poor
3	30°36'35"	77°27'00"	Recreational area	559 ±40	0.2 ±0.13	17 ±5	35 ± 10	90 ±20	3.25 ±2.3	266 ±33	7.5 ±0.61	22.2 ±0.76	45	Poor
4	30°36'37"	77°27'07"	Dudhdara	455 ±40	0.45 ±0.13	10 ±5	10 ± 10	48 ±20	6.5 ±2.3	220 ±33	7.9 ±0.61	21.9 ±0.76	54	Medium
5	30°36'34"	77°27'37"	Rare end area of the lake	531 ±40	0.30 ±0.13	3 ±5	25 ± 10	30 ±20	5.5 ±2.3	190 ±33	7.8 ±0.61	20 ±0.76	59	Medium

Table 4: Analysis of water sample of Renuka lake and its TSI (average of pre- and post-monsoon).

S.No.	Sampling points	Secchi Disc Transparency (m)		Total Phosphorous (mg.L ⁻¹)		Chlorophyll a (μ g.L ⁻¹)		Average	
		SD	TSI	TP	TSI	Chl 'a'	TSI		
1	Outlet to Parshuramtal	1.52	53.97	35	55.42	11.5	54.56	54.7	Eutrophic
2	Bathing Ghat	1.10	58.63	50	60.56	15.49	57.48	58.9	Eutrophic
3	Recreational area	1.15	57.98	45	59.04	14.8	57	58.0	Eutrophic
4	Dudhdara	1.86	51.06	30	53.19	7.9	50.98	51.7	Eutrophic
5	Rare end area of lake	2.05	49.60	25	50.56	6.8	49.4	49.9	Mesotrophic

Carlson's TSI average = 55 (Eutrophic)

Table 5: Diversity Index of riparian vegetation around Renuka lake.

Species type	The scientific name of species/ plant	Abundance ratio	Shannon–Wiener Index $H_i = \sum p_i \log p_i$	Simpson Index $D = \sum [n_i(n_i - 1) / N(N-1)]$
1	Saxifragaceae	0.128	2.962 ± 0.816	0.014 ± 0.003
2	<i>Terminalia chebula</i>	0.024	5.361 ± 0.816	0.001 ± 0.003
3	<i>Solanum verbascifolium</i>	0.038	4.733 ± 0.816	0.001 ± 0.003
4	<i>Vitex nagundo</i>	0.033	4.913 ± 0.816	0.001 ± 0.003
5	<i>Woodfordia floribunda</i>	0.024	5.361 ± 0.816	0.001 ± 0.003
6	<i>Ziziphus jujube</i>	0.031	5.013 ± 0.816	0.001 ± 0.003
7	<i>Salix alba</i>	0.055	4.176 ± 0.816	0.003 ± 0.003
8	<i>Albizia lebbek</i>	0.022	5.498 ± 0.816	0.000 ± 0.003
9	<i>Bauhinia variegata</i>	0.060	4.065 ± 0.816	0.003 ± 0.003
10	<i>Ficus palmate</i>	0.053	4.235 ± 0.816	0.002 ± 0.003
11	<i>Adhatoda vasica</i>	0.007	7.235 ± 0.816	0.000 ± 0.003
12	<i>Ageve americana</i>	0.033	4.913 ± 0.816	0.001 ± 0.003
13	<i>Anemone obtusiloba</i>	0.024	5.361 ± 0.816	0.001 ± 0.003
14	<i>Berberis aristata</i>	0.027	5.235 ± 0.816	0.001 ± 0.003
15	<i>Euphorbia royleana</i>	0.046	4.428 ± 0.816	0.002 ± 0.003
16	<i>Dodonaeaviscosa</i>	0.027	5.235 ± 0.816	0.001 ± 0.003
17	<i>Glycosmis pentaphylla</i>	0.024	5.361 ± 0.816	0.001 ± 0.003
18	<i>Indigofera hirsuta</i>	0.051	4.297 ± 0.816	0.002 ± 0.003
19	<i>Murraya koenigii</i>	0.080	3.650 ± 0.816	0.005 ± 0.003
20	<i>Punica granatum</i>	0.100	3.328 ± 0.816	0.009 ± 0.003
21	<i>Berberis chitria</i>	0.027	4.768 ± 0.816	0.001 ± 0.003
22	<i>Carissa opaca</i>	0.022	4.858 ± 0.816	0.000 ± 0.003
23	<i>Jasminum humile</i>	0.024	4.833 ± 0.816	0.001 ± 0.003
24	<i>Lantana camara</i>	0.069	4.838 ± 0.816	0.004 ± 0.003
25	<i>Dhatura suaveolens</i>	0.049	4.835 ± 0.816	0.002 ± 0.003
	Average Index		4.780	0.002
Average index= 2.4				

Table 6: Ecological health Index of Renuka lake.

Sl.no	Name	NSFWQI		C-STI		SDI	Overall EHI	
1	Out let to Parshuram tal	53	Medium	54.7	Eutrophic	2.4	2.14	medium
2	Bathing Ghat	40	Poor	58.9	Eutrophic	2.4	2.47	Medium
3	Recreational area	45	Poor	58.0	Eutrophic	2.4	2.47	medium
4	Dudhdara	54	Medium	51.7	Eutrophic	2.4	2.14	medium
5	Rare end area of lake	59	Medium	49.9	Mesotrophic	2.4	1.81	good

4. Public awareness about the benefits of good health of lake through posters, videos, and other mediums

REFERENCES

- APHA 2002. Standard Methods for the Examination of Water and Wastewater. American Public Health Association; American Water Works Association; Water Environment Federation, pp. 1-541.
- Cantonati, M., Poikane, S., Pringle, C. M., Stevens, L. E., Turak, E., Heino, J. and Znachor, P. 2020. Natural and artificial freshwater environments : consequences for biodiversity conservation. *Water*, 12(1): 260.
- Carlson, R.E. 1977. A trophic state index for lakes. *Limnol. Oceanogr.*, 22(2): 361-369.
- Childs, C. 2004. Interpolating Surfaces in ArcGIS Spatial Analysts. *ArcUser*, pp. 32-35.
- Choden, Y., Badewa, G.K., Cheki, T. and Yangzom, K. 2020. Groundwater quality index of Saharanpur city, India and its spatial representation using geographical information systems. *Int. J. Emerg. Technol.*, 11(4): 157-162.
- Das, B.K. and Kaur, P. 2001. Major ion chemistry of Renuka Lake and weathering processes, Sirmaur District, Himachal Pradesh, India. *Environ. Geol.*, 40(7): 908-917.
- Diwate, P., Meena, N.K., Bhushan, R., Pandita, S., Chandana, K.R. and Kumar, P. 2020. Sedimentation rate (210Pb and 137Cs), grain size, organic matter, and bathymetric studies in Renuka lake, Himachal Pradesh, India. *Himalayan Geol.*, 41(1): 51-62.
- Hillsborough, M. 2008. Trophic State Index (TSI), in Hillsborough Community Atlas, City of Tampa, Florida: Hillsborough County; URL: www.hillsborough.community.atlas.usf.edu.
- Himachal Pradesh Council For Science, Technology & Environment 2017. Major Wetlands of Himachal Pradesh. Himachal Pradesh State Wetland Authority, pp. 1-22.
- Jorgenus, S.E., Costanza, R. and Fu liu, X. 2016. Handbook of Ecological Indicators for Assessment of Ecosystem Health. Taylor Francis, London, UK.
- Joshi. 2013. SERI News. Retrieved from <http://seriecotech.com/blog/?p=377>. Accessed 7, 2013
- Kumar, A., Mishra, S. and Sharma, M.P. 2015. Assessment of ecological health of Baiyangdian lake in China using ecological health index. *J. Appl. Natural Sci.*, 7(2): 955-959.
- Mendes, R. S., Evangelista, L. R., Thomaz, S. M., Agostinho, A. A. and Gomes, L. C. 2008. A unified index to measure ecological diversity and species rarity. *Ecography*, 31(4): 450-456.
- Mishra, S., Sharma, M.P. and Kumar, A. 2016. Ecological health assessment of Surha Lake, India. *J. Mater. Environ. Sci.*, 7(5): 1708-1715.
- Ozturk, D. and Kilic, F. 2016. Geostatistical approach for spatial interpolation of meteorological data. *An. Acad. Bras. Cienc.*, 88(4): 2121-2136.
- Pavluk, T. and Abraham, B.D.V. 2018. Trophic index and efficiency. In Fath, B. (ed.), Reference Module in Earth Systems and Environmental Sciences: Encyclopaedia of Ecology, 2nd edition, Elsevier, The Netherlands, pp. 495-502
- Pillai, S. 2003. Information Sheet on Ramsar Wetlands - Solent. Ramsar, 1-8.
- Sharma, M. 2014. Water quality assessment of the Central Himalayan Lake, Nainital. *Advances in Environmental Chemistry*, Hindawi Publishing Corporation, pp. 1-5.
- Sharma, M. P., Kumar, A. and Rajvanshi, S. 2010. Assessment of trophic state of lakes: a case of Mansi Ganga Lake in India. *Hydro Nepal: Journal of Water, Energy and Environment*, 6(6): 65-72.
- Singh, O.K and Sharma M. K. 2012. Water quality and eutrophication of Renuka lake, Sirmaur district (H.P.). *J. Indian Water Resour.Soc.*, 32: 3-4.
- Sunil, C., Somashekar, R.K. and Nagaraja, B.C. 2016. Diversity and composition of riparian vegetation across forest and agroecosystem landscapes of river Cauvery, southern India. *Trop. Ecol.*, 57(2): 343-354.
- Tyagi, S., Sharma, B., Singh, P. and Dobhal, R. 2020. Water quality assessment in terms of water quality index. *Am. J. Water Resour.*, 1(3): 34-38.
- Yadav, N.S., Sharma, M.P. and Kumar, A. 2015. Assessment of ecological health of Chambal River using plant species diversity. *J. Mater. Environ. Sci.*, 6(9): 2624-2630.



Terrestrial Biomass and Carbon Stock in Broad-leaved Forests of Punakha District, Western Bhutan

S. Tshering*† and P. Rinzin**

*Department of Environment and Climate Studies, College of Natural Resources, Royal University of Bhutan, Punakha, Bhutan

**Department of Sustainable Development, College of Natural Resources, Royal University of Bhutan, Punakha, Bhutan

†Corresponding author: S. Tshering; desangma06@gmail.com

Nat. Env. & Poll. Tech.
Website: www.neptjournal.com

Received: 16-04-2021

Revised: 27-05-2021

Accepted: 06-06-2021

Key Words:

Carbon stock
Terrestrial biomass
Broad-leaved forest
Volumetric equation

ABSTRACT

The present study assessed the terrestrial biomass of broad-leaved forests to determine the carbon storage potential of each tree species in Punakha. The assessment was based on a woody stem having a minimum of 10 cm diameter at breast height (DBH) and tree height. Biomass was estimated using volumetric equations and carbon stock by multiplying the constant factor 0.5 to biomass. The study covered 41 sampling plots of 31.62 m × 31.62 m and recorded a total of 24 tree species. Total biomass was 274.68 Mg.ha⁻¹ with AGTB 196.36 Mg.ha⁻¹, BGTB 51.07 Mg.ha⁻¹ and DOM 27.22 Mg.ha⁻¹. The total carbon stock estimated was 137.34 MgC.ha⁻¹. The present study used a non-destructive approach to assess the carbon storage potential of each broad-leaved tree species and concludes that Punakha broad-leaved forest has the potential to accumulate more biomass and carbon stock, as DBH class-wise biomass and carbon distribution showed right-skewed trend indicating young forest stands.

INTRODUCTION

Bhutan today has a total forest coverage of 2,730,889 ha which constitutes 71% of the total geographical area of the country (Amatya et al. 2018, Forest Resources Management Division [FRMD] 2016a). The present study area alone contributes 79,316 ha (72%) of forest cover of the total area of 109,878 ha of the Punakha District (FRMD 2016a). The total biomass of Bhutan's forests was estimated to be about 1109 million tonnes and forest carbon stock 709 million tonnes including 188 million tonnes of soil organic carbon (Forest Resources Management Division [FRMD] 2016b). Bhutan's rich forest cover and its high Green House Gas (GHG) sequestration potential were reinforced by a constitutional mandate that a minimum of 60% of the country's total land be maintained under forest cover for all times (Ministry of Agriculture 2009).

The importance of forests have attracted considerable attention in the recent past especially after the inception of the Kyoto Protocol as it provides ecosystem services as significant terrestrial carbon (C) sink (FRMD 2016b, Rabha 2014, Wellbrock et al. 2017). Forests are one of the vital components in the socio-economic system especially for forest-dependent households (Sahu et al. 2015, Salunkhe et al. 2018). Furthermore, forests have led to estimate global

carbon budget and the estimation of carbon (C) stocks to better understand their function in the global carbon cycle as a mitigation measure or a source of carbon in response to climate change (Malhi et al. 1998, Murthy et al. 2015, Nakai et al. 2009).

Aboveground tree biomass (AGTB), belowground tree biomass (BGTB), deadwood, litter, and soil organic matter (SOM) are five carbon pools in the forest ecosystem (FRMD 2016b). Biomass can be measured either in terms of fresh weight or dry weight and it can be both dead and living components. The amount of C sequestered by broad-leaved forests can be inferred from total biomass accumulated as approximately 50% of forest dry biomass is C (Beets et al. 2012, Cairns et al. 2003, Justine et al. 2015, Vashum & Jayakumar 2012, Wolf et al. 2011). Forest ecosystem which covers about 4.1 billion ha globally store about 80% of aboveground terrestrial C and 40% of belowground C to mitigate global climate change (Ahmad et al. 2015, Lal 2005, Sahu et al. 2015, Wellbrock et al. 2017).

To understand the carbon storage potential of Punakha broad-leaved forests (PBFR), volumetric equations and specific wood density with variables DBH and tree height were used to calculate biomass accumulation and C stock following a non-destructive approach. The present study

found out that PBFr plays a vital role as C sinks. Carbon storage potential in different tree species differ depending upon management practices, disturbances, and age of the trees (Mendoza-Ponce & Galicia 2010).

MATERIALS AND METHODS

Study Area

The study was carried out in Punakha District (Fig. 1) approximately located between latitude 27°39'59.99" N and longitude 89°49'59.99" E with elevation ranging from 1200 to above 4500 meters above sea level. It is bordered by Thimphu, Gasa, and Wangdue Phodrang Districts. Temperature varies approximately from minus 4°C to 35°C. The District consists of 79,316 ha (72%) of forest cover of a total area of 109,878 ha (FRMD 2016a). Natural mixed forests of broad-leaved evergreen and coniferous trees covered the study area. Dominant tree species recorded were *Quercus lanata*, *Castanopsis tribuloides* and *Rhododendron arboretum*.

Forests are under threat as a result of increased developmental activities, limiting carbon sequestration capability. Furthermore, only a few studies carried out concentrating on the value of individual broad-leaved tree species' carbon stock potential. In this study, floristic composition and importance level of specific broad-leaved tree species in connection

to their carbon storage potential were investigated using a total of 41 sampling sites.

Tree Height and DBH Measurement

The Forest Survey of India (FSI) (2015) and Tshering (2019) methodologies were used to lay a quadrat measuring 31.62 m × 31.62 m and recorded a total of 24 tree species. For the enumeration, trees were defined as circumferences with a minimum diameter of 10 cm at breast height (DBH), i.e. 1.37 m above the ground (Borah et al. 2013, FRMD 2016a, FRMD 2016b, Mani & Parthasarathy 2009, Rabha 2014, Salunkhe et al. 2016, Shahid & Joshi 2015). The height and DBH of the trees were measured using a non-destructive approach (Pragasam 2015, Tshering 2019). Clinometer and diameter tape were used to measure the tree height and DBH, respectively. Non-broad-leaved tree species such as conifer species sampled in the same quadrats were excluded as it was not the focus of the current study.

Terrestrial Tree Biomass Estimation

Non-destructive estimation of biomass was carried out using a volumetric equation (Forest Survey of India [FSI] 1996). The following procedures were considered for the current study. (1) Bole biomass was calculated using the formula $V \times WD$ (where, V =volume of trees [$v: m^3 \cdot tree^{-1}$], WD =wood specific density [$Mg \cdot m^{-3}$]) (Ahmad et al. 2014, Mandal & Joshi 2015). (2) Aboveground tree biomass (AGTB) was derived by using the formula $BB \times BEF$ (where, BB =bole biomass [$Mg \cdot ha^{-1}$], BEF =biomass extension factor 1.59) (Khan et al. 2015, Mandal & Joshi 2015). (3) Belowground tree biomass (BGTB) was calculated by $AGB \times 0.26$ (where, 0.26=constant root-shoot ratio) (Joshi et al. 2020, Shahid & Joshi 2015, Srinivas & Sundarapandian 2019, Subashree & Sundarapandian 2017, Mandal & Joshi 2015, Sahu et al. 2015). (4) The dead woods and leaf litter in the form of dead organic matter (DOM) were calculated, $(AGTB + BGTB) \times 0.11$ (where 0.11 = default factor) (Joshi et al. 2020, Sahu et al. 2015). The total biomass ($Mg \cdot ha^{-1}$) was obtained by adding aboveground and belowground tree biomass including dead woods and leaf litter biomass (DOM).

Total Carbon Stock

Carbon values for each forest carbon pool were summed to estimate total forest carbon stock (Joshi et al. 2020). Total carbon stock ($MgC \cdot ha^{-1}$) of the broad-leaved forests of Punakha District was then converted into tonnes of CO_2 equivalent by multiplying with constant conversion factor 0.5 following the methods of Borah et al. (2013), Chaudhury & Upadhaya (2016), Shahid & Joshi (2015), Sun et al. (2016), Terakunpisut et al. (2007) and Tshering (2019).

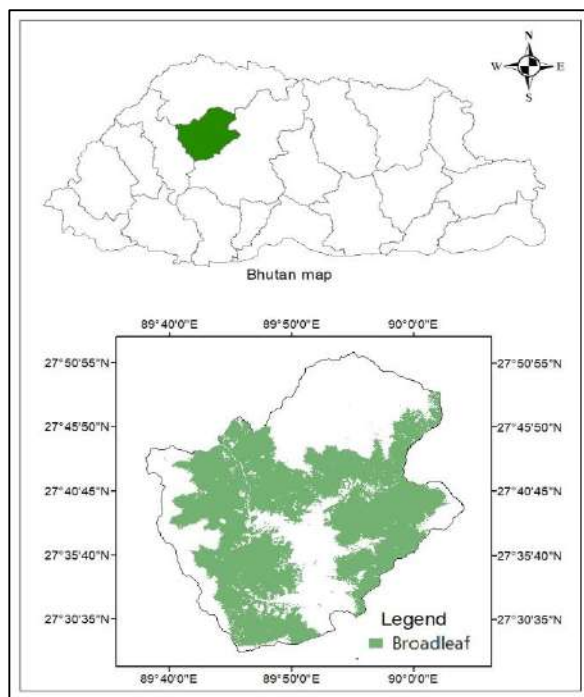


Fig. 1: Map of Bhutan showing the study area.

The following equation was used to calculate the total forest carbon stock:

$$TC = C (AGTB) + C (BGTB) + C (DOM)$$

Where, TC=Total carbon stock (CMg.ha⁻¹), C (AGTB)=Carbon stock in aboveground tree biomass, C (BGTB)=Carbon stock in belowground tree biomass, and C (DOM)=Carbon stock in dead woods and leaf litter in the form of dead organic matter.

RESULTS AND DISCUSSION

Biomass and Carbon

Total biomass and C stock accumulations were 274.68 Mg.ha⁻¹ and 137.33 MgC.ha⁻¹ respectively (Table 1) and it

is within the range of the standing biomass of different forest types of Western Himalaya ranging from 123.89±26.33 to 537.77±56.34 Mg.ha⁻¹ (Singh & Verma 2018). Values reported in the present results were lower than the values of tropical evergreen and deciduous forests of Uttara Kannada District with 344-417 MgC.ha⁻¹ (Murthy et al. 2015). Further, total biomass (54±19 million tonnes) and C stock (25±9 million tonnes) reported for the whole Punakha District by FRMD (2016b) was much higher than the values reported in the present results. This was owing to the fact that the previous study included total biomass estimates of trees (all forest types), saplings, shrubs, and herbs, as well as soil carbon, but the current study only included biomass and C estimates of trees (of the broad-leaved forest). However, the C stock of the study area was found comparable to tropical rain

Table 1: Species-wise tree density (count.ha⁻¹), biomass (Mg.ha⁻¹), and carbon (MgC.ha⁻¹).

Sl. No.	Species	Tree density	Biomass			Total biomass	Total carbon
			AGTB	BGTB	DOM		
1	<i>Quercus lamellosa</i>	43.44	0.2	0.05	0.03	0.28	0.14
2	<i>Michelia doltsopa</i>	19.59	1.85	0.48	0.26	2.59	1.30
3	<i>Myrsine semiserrata</i>	14.48	2.11	0.55	0.29	2.95	1.48
4	<i>Lindera pulcherrima</i>	15.33	1.15	0.3	0.16	1.61	0.81
5	<i>Quercus Glauca</i>	27.26	8.34	2.17	1.16	11.67	5.84
6	<i>Quercus oxyodon</i>	29.81	16.33	4.25	2.26	22.84	11.42
7	<i>Symplocos glomerata</i>	19.59	6.83	1.78	0.95	9.56	4.78
8	<i>Symplocos ramosissima</i>	30.66	3.91	1.02	0.54	5.47	2.74
9	<i>Rhododendron arboreum</i>	115.84	6.65	1.73	0.92	9.30	4.65
10	<i>Quercus semecarpifolia</i>	11.93	6.97	1.81	0.97	9.75	4.88
11	<i>Lyonia ovalifolia</i>	102.21	0.29	0.07	0.04	0.40	0.20
12	<i>Castanopsis tribuloides</i>	118.40	76.86	19.98	10.65	107.49	53.75
13	<i>Quercus griffithii</i>	58.77	10.29	2.68	1.43	14.40	7.20
14	<i>Quercus lanata</i>	120.95	11.98	3.12	1.66	16.76	8.38
15	<i>Schima wallichii</i>	34.07	5.16	1.34	0.71	7.21	3.61
16	<i>Michelia champaca</i>	12.78	8.08	2.1	1.12	11.30	5.65
17	<i>Daphniphyllum chartaceum</i>	52.81	4.8	1.25	0.66	6.71	3.36
18	<i>Myrica esculenta</i>	14.48	0.99	0.26	0.14	1.39	0.70
19	<i>Toona ciliata</i>	20.44	0.06	0.02	0.01	0.09	0.05
20	<i>Ilex dipyrena</i>	31.52	18.14	4.72	2.51	25.37	12.69
21	<i>Albizia lebbeck</i>	28.11	5.27	1.37	0.73	7.37	3.69
22	<i>Eurya acuminata</i>	15.33	0.05	0.01	0.01	0.07	0.04
23	<i>Cinnamomum glauduliferum</i>	13.63	0.04	0.01	0.01	0.06	0.03
24	<i>Juglans regia</i>	48.55	0.014	0.004	0.002	0.02	0.01
	Poll biomass	–	196.36	51.07	27.22	–	–
	Pool carbon	–	98.18	25.54	13.61	–	–
	Total	999.98	196.36	51.07	27.22	274.68	137.33
	Mean	41.67	8.18	2.13	1.13	11.44	5.72

forest (Ton Mai Yak station) (137.73 ± 48.07 tonne.C.ha⁻¹), dry evergreen forest (KP 27 station) (70.29 ± 7.38 tonneC.ha⁻¹), and mixed deciduous forest (Pong Phu Ron station) 48.14 ± 16.72 tonneC.ha⁻¹ of Thong Pha Phum National Forest (Terakunpisut et al. 2007).

The AGTB score of the present study (196.36 Mg.ha⁻¹) was found lower than the tropical forest of Nagathol forest (261.64 Mg.ha⁻¹) and higher than that of Monbel forest (166.94 Mg.ha⁻¹), Rose Kandy (144.01 Mg.ha⁻¹), Bhuban hill (116.8 Mg.ha⁻¹) and Dolu forest (99.10 Mg.ha⁻¹) (Borah et al. 2013). However, the present AGTB score falls within the biomass range of temperate forests of Kashmir Himaraya (Dar & Sundarapandian 2015) and tropical dry forest of East Godavari region, Andhra Pradesh (58.04 to 368.39 Mg.ha⁻¹) (Srinivas & Sundarapandian 2019). The variation in the distribution of biomass and C stocks in forest ecosystems could be due to geographical regions and their locality factors (Joshi et al. 2020), forest types, species composition, vegetation management pattern, and stand age (Chaudhury & Upadhaya 2016, Singh & Verma 2018).

Biomass accumulation and C stock potential varied among the tree species of Punakha Broad-leaved Forests

(PBFr). The *Castanopsis tribuloides* had the highest biomass accumulation and C stock (107.49 Mg.ha⁻¹ and 53.75 MgC.ha⁻¹ respectively) whereas the lowest value was recorded in *Juglans regia* (0.02 Mg.ha⁻¹ and 0.01 MgC.ha⁻¹ respectively) among 24 tree species studied (Table 1). The *Castanopsis* sp was also reported by FRMD (2016b) as one of the 28 major trees to be an important source of biomass in Bhutan. Punakha broadleaf forest was dominated by *Quercus lanata*, *Castanopsis tribuloides*, and *Rhododendron arboreum* with a tree density of 120.95 count.ha⁻¹, 118.40 count.ha⁻¹, 115.84 count.ha⁻¹ respectively and the least in *Quercus semecarpifolia* with 11.93 count.ha⁻¹ of the total 999.98 count.ha⁻¹. The considerable variation in tree density could be due to variation in species richness, DBH size, different anthropogenic activities, and environmental factors affecting plant growth (Chaudhury & Upadhaya 2016, Rabha 2014, Tshering, 2019).

Biomass and Carbon Estimates by DBH Class

The distribution of biomass and carbon stock in different DBH classes is shown in Fig. 2. The maximum biomass accumulation and carbon stock were observed in 10-19.9

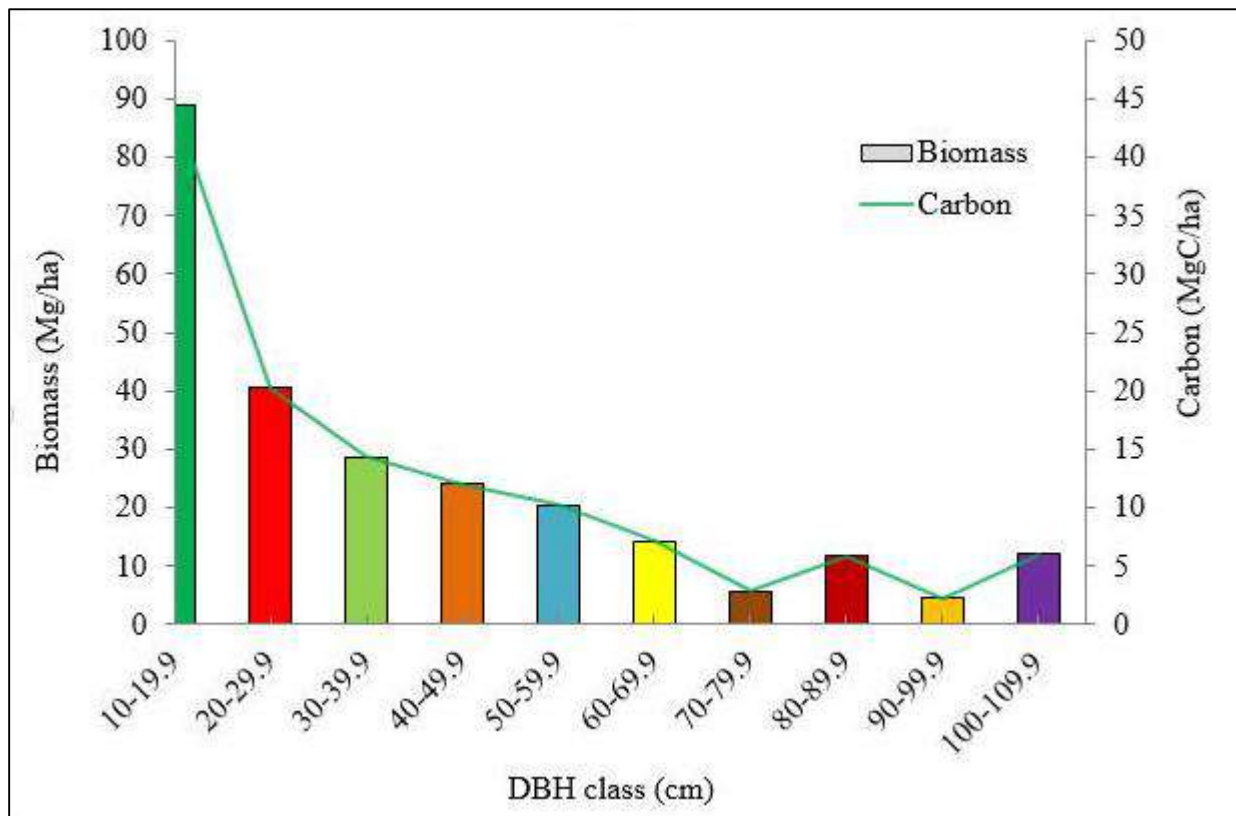


Fig. 2: Biomass and carbon storage in different DBH classes.

Table 2: Biomass (Mg.ha⁻¹) and carbon stock (MgC.ha⁻¹) in different tree families.

Sl.No.	Family	BB	AGTB	BGTB	DOM	TB	TC
1	Fagaceae	77.62	123.42	32.09	17.11	172.62	86.31
2	Magnoliaceae	5.95	9.46	2.46	11.92	23.85	11.92
3	Myrsinaceae	1.33	2.11	0.55	0.29	2.96	1.48
4	Lauraceae	1.98	3.15	0.82	0.44	4.40	2.20
5	Symplocaceae	5.15	8.18	2.13	1.13	11.45	5.72
6	Ericaceae	4.36	6.94	1.80	0.96	9.70	4.85
7	Juglandaceae	2.71	4.31	1.12	0.60	6.03	3.01
8	Theaceae	2.60	4.13	1.07	0.57	5.78	2.89
9	Daphniphyllaceae	3.02	4.80	1.25	0.66	6.71	3.35
10	Myricaceae	0.62	0.99	0.26	0.14	1.39	0.69
11	Meliaceae	1.99	3.16	0.82	0.44	4.43	2.21
12	Aquifoliaceae	11.41	18.14	4.72	2.51	25.37	12.69
	Total	118.74	188.79	49.09	36.76	274.68	137.33
	Mean	9.90	15.73	4.09	3.06	22.89	11.44

cm (88.94 Mg.ha⁻¹ and 44.47 MgC.ha⁻¹ respectively) followed by 20-29.9 cm (40.54 Mg.ha⁻¹ and 20.27 MgC.ha⁻¹ respectively) contrasting the findings of FRMD (2016b), where total aboveground biomass and carbon increased with increasing diameter class peaking at DBH class of 60-70 cm with 59±3 and 28±2 million tonnes, though the gradual decrease of biomass accumulation and carbon stock were observed in higher DBH class after picking at mid. However, current findings are similar to the dominant size class at 4.5-20 cm where it potentially provided greater carbon sequestration in the tropical rain forest and dry evergreen forest (Terakunpisut et al. 2007). The least was in 90-99.9 cm with total biomass 4.49 Mg.ha⁻¹ and carbon 2.24 MgC.ha⁻¹, contradicting the findings of Singh and Verma (2018), where individuals lying in DBH class >150 cm contributed significantly to carbon stocks.

Variation of different biomass accumulation and carbon stock potential at different DBH classes could be due to the greater number of individuals recorded at lower diameter class (≥10-19.9 and 20-29.9 cm DBH) showing a right-skewed trend indicating young forest stands (Fig. 2). Maximum tree count in the DBH class of 10-20 cm and minimum in 90-100 cm DBH were also reported during the National Forest Inventory of Bhutan by Amatya et al. (2018). Additionally, similar findings were reported by Srinivas and Sundarapandian (2019) in the tropical dry forest of the East Godavari region and by Dar and Sundarapandian (2015) in temperate forests of Kashmir Himalaya.

Tree Family-wise Carbon Stock and Biomass Accumulation

Fagaceae had a maximum biomass accumulation of 172.62 Mg.ha⁻¹ sequestering carbon 86.31 MgC.ha⁻¹ followed by Aquifoliaceae with biomass 25.37 Mg.ha⁻¹ and carbon 12.69 MgC.ha⁻¹. The reason for the highest value of biomass and carbon stock in Fagaceae and Aquifoliaceae could be due to higher number of individuals unlike the lowest value estimated in Myricaceae with biomass 1.39 Mg.ha⁻¹ and carbon 0.69 MgC.ha⁻¹. Singh and Verma (2018) found that a larger number of people has a similar effect on biomass and carbon density in diverse forest types in the Western Himalaya. Other reasons for biomass and carbon distribution variation in different tree families could be higher DBH size, age, and environmental factors (Chaudhury & Upadhaya 2016, Rabha 2014, Tshering 2019, Zhang et al. 2019). Biomass accumulation and carbon sequestration potential variation of different tree families were shown in Table 2.

The *Castanopsis tribuloides* and *Quercus lamellose* under family Fagaceae, and *Lyonia ovalifolia* and *Rhododendron arboretum* belonging to Ericaceae were found with greater biomass storage and carbon sequestration potential. Species that have high carbon sequestration potential should be planted that might be capable of reducing the carbon emitted due to deforestation and other anthropogenic activities. If the carbon problem is to be managed through forest management, trees with low biomass and carbon sequestration capacity must be eliminated or replaced with other tree species that store more carbon.

CONCLUSIONS

The study pertaining to estimation of carbon stock in broad-leaved forests of Punakha District covered 41 sampling plots of 31.62 m x 31.62 m and recorded a total of 24 tree species. Total biomass and carbon stock estimated were 274.68 Mg.ha⁻¹ and 137.33 MgC.ha⁻¹ respectively. Biomass accumulation and carbon stock distribution in different DBH classes showed a right-skewed trend indicating young forests for huge carbon sequestration potential in the future if it's conserved sustainably. The present study covered only broad-leaved forests, so we recommend future researchers to carry out similar studies on conifer tree species.

ACKNOWLEDGEMENT

We are thankful to the College of Natural Resources (CNR) for providing financial support. We are grateful to Mr. Karma Sherub from the Department of Forest Science in College of Natural Resources and Mr. Chetenla from Thimphu Forest Division under Department of Forests and Park Services for their support during fieldwork and analysis.

REFERENCES

- Ahmad, A., Mirza, S.N. and Nizami, S.M. 2014. Assessment of biomass and carbon stocks in the coniferous forest of Dir Kohistan, Kpk. Pak. J. Agric. Sci., 51(2): 345-350.
- Ahmad, A., Nizami, S.M., Marwat, K.B. and Muhammad, J. 2015. Annual accumulation of carbon in the coniferous forest of Dir Kohistan: an inventory-based estimate. Pak. J. Bot., 47: 115-118.
- Amatya, S., Yangden, K., Wangdi, D., Phuntsho, Y. and Dorji, L. 2018. National forest inventory of Bhutan: Shift in role from traditional forestry to diverse contemporary global requirements. Journal of Forest and Livelihood, 17(1): 127-138.
- Beets, P.N., Kimberley, M.O., Oliver, G.R., Pearce, S.H., Graham, J.D. and Brandon, A. 2012. Allometric equations for estimating carbon stocks in natural forests in New Zealand. Forests, 3: 818-839.
- Borah, N., Nath, A.J. and Das, A. K. 2013. Aboveground biomass and carbon stocks of tree species in tropical forests of Cachar District, Assam, Northeast India. Int. J. Econ. Environ. Stud., 39(2): 97-106.
- Chaudhury, G. and Upadhaya, K. 2016. Biomass and carbon stock in subtropical broad-leaved forest ecosystem of Meghalaya, Northeast India. Int. J. Econ. Environ. Stud., 42(2): 125-133.
- Cairns, M.A., Olmsted, I., Granados, J. and Argaez, J. 2003. Composition and aboveground tree biomass of a dry semi-evergreen forest on Mexico's Yucatan Peninsula. Forest Ecol. Mang., 186(1): 125-132.
- Dar, J. A. and Sundarapandian, S. 2015. Variation of biomass and carbon pools with forest type in temperate forests of Kashmir Himalaya, India. Environ. Monit. Assess., 5(3): 81-96.
- Forest Resources Management Division (FRMD) 2016a. National Forest Inventory Report: Stocktaking Nation's Forest Resources Volume I. Thimphu: Department of Forests & Park Services, Ministry of Agriculture & Forests, Royal Government of Bhutan.
- Forest Resources Management Division (FRMD) 2016b. National Forest Inventory Report: Stocktaking Nation's Forest Resources Volume II. Thimphu: Department of Forests & Park Services, Ministry of Agriculture & Forests, Royal Government of Bhutan.
- Forest Survey of India (FSI) 1996. Volume Equations for Forests of India, Nepal, and Bhutan. Forest Survey of India, Ministry of Environment, Forest and Climate Change, Kaulagarh, Dehradun, Uttarakhand, India, pp. 249.
- Forest Survey of India (FSI) 2015. India State of Forest Report. Forest Survey of India, Ministry of Environment, Forest and Climate Change, Kaulagarh, Dehradun, Uttarakhand, India.
- Joshi, R., Singh, H., Chhetri, R. and Yadav, K. 2020. Assessment of carbon sequestration potential in degraded and non-degraded community forests in the Terai region of Nepal. Journal of Forest and Environmental Science, 36(2):113-121.
- Justine, M.F., Wanqin, Y., Wu, F., Tan, B., Khan, M.N. and Zhao, Y. 2015. Biomass stock and carbon sequestration in a chronosequence of pinus massoniana plantations in the upper reaches of the Yangtze River. Forests, 6: 3665-3682.
- Khan, A., Ahmad, A., Rahman, Z., Siraj-ud-Din., Qureshi, R. and Muhammad, J. 2015. The assessment of carbon stocks in the oak scrub forest of Sheringal valley Dir Kohistan. Open Journal of Forestry, 5: 510-517.
- Lal, R. 2005. Forest soils and carbon sequestration. Forest Ecol. Manag., 220:242-258.
- Malhi, Y., Nobre, A.D., Grace, J., Kruijt, B., Pereira, M.G.P., Culf, A. and Scott, S. 1998. Carbon dioxide is transferred over a central Amazonian rain forest. J. Geophys. Res., 103: 31,593-31,612.
- Mandal, G. and Joshi, S. 2015. Biomass accumulation and carbon sequestration potential of dry deciduous forests. International Journal of Ecology and Development, 30(1).
- Mani, S. and Parthasarathy, N. 2009. Tree population and above-ground biomass changes in two disturbed tropical dry evergreen forests of peninsular India. Tropical Ecology, 50(2): 249-258.
- Murthy, I.K., Bhat, S., Sathyanarayan, V., Patgar, S., Beerappa, M., Bhat, P.R. and Bhat, D.M., Ravindranath, N.H., Khalid, M.A., Prashant, M., Iyer, S., Bebbler, D.M. and Saxena, R. 2015. Biomass and carbon stock dynamics in tropical evergreen and deciduous forests of Uttara Kannada District, Western Ghats, India. Glob. J. Sci. Frontier Res., 15(5): 54-69.
- Mendoza-Ponce, M. and Galicia, L. 2010. Above-ground and below-ground biomass and carbon pools in a highland temperate forest landscape in central Mexico. Int. J. Forest. Res., 83(5): 497-506.
- Nakai, Y., Hosoi, F. and Omasa, K. 2009. Estimating carbon stocks of coniferous woody canopy trees using airborne lidar and passive optical sensor.
- Pragasam, L. A. 2015. Assessment of aboveground biomass stock in the Pachaimalai forest of the Eastern Ghats in India. Applied Ecology and Environmental Research, 13(1): 133-145.
- Rabha, D. 2014. Aboveground biomass and carbon stocks of an undisturbed regenerating sal (*Shorea robusta* Gaertn. f.) forest of Goalpara District, Assam, Northeast India. Int. J. Environ., 3(4): 121.
- Ministry of Agriculture. 2009. National Forest Policy of Bhutan. Ministry of Agriculture, Thimphu, Bhutan, pp. 16.
- Sahu, S.C., Sharma, J. and Ravindranath, N.H. 2015. Carbon stocks and fluxes for forests in Odisha (India). Trop. Ecol., 56(1): 77-85.
- Salunkhe, O., Khare, P.K., Kumari, R. and Khan, M.L. 2018. A systematic review on the aboveground biomass and carbon stocks of Indian forest ecosystems. Ecol. Processes.
- Salunkhe, O., Khare, P.K., Sahu, T.R. and Singh, S. 2016. Estimation of tree biomass reserves in tropical deciduous forests of central India by non-destructive approach. Trop.Ecol., 57(2): 153-161.
- Shahid, M. and Joshi, S.P. 2015. Biomass and carbon stock assessment in moist deciduous forests of Doon Valley, Western Himalaya, India. Taiwania, 60(2): 71-76. <https://doi.org/10.6165/tai.2015.60.71>.
- Singh, S. and Verma, A. K. 2018. Biomass and carbon stocks in different forest types of western Himalaya. Tropical Ecology, 59(4): 647-658.
- Srinivas, K. and Sundarapandian, S. 2019. Biomass and carbon stocks of trees in the tropical dry forest of east Godavari region, Andhra Pradesh, India. Geology, Ecology, and Landscapes, 3(2):114-122.

- Subashree, K. and Sundarapandian, S. 2017. Biomass and carbon stock assessment in two savannahs of Western Ghats, India. *Taiwania*, 62(3):272-282.
- Sun, X., Wang, G., Huang, M., Chang, R. and Ran, F. 2016. Forest biomass carbon stocks and variation in Tibet's carbon-dense forests from 2001 to 2050. *Scientific Reports*, 6(1).
- Terakunpisut, J., Gajaseni, N. and Ruankawe, N. 2007. Carbon sequestration potential in aboveground biomass of Thong Pha Phum National Forest, Thailand. *Appl. Ecol. Environ. Res.*, 5(2): 93-102.
- Tshering, S. 2019. Importance value index and assessment of carbon stocks in western Bhutan Himalaya (Thimphu). *Curr. J. Appl. Sci. Technol.*, 32(2):1-8.
- Vashum, K.T. and Jayakumar, S. 2012. Methods to estimate above-ground biomass and carbon stock in natural forests-a review. *J. Ecosys. Ecogr.*, 2(4): 45.
- Wellbrock, N., Grüneberg, E., Riedel, T. and Polley, H. 2017. Carbon stocks in tree biomass and soils of German forests. *Cent. Eur. For. J.*, 63: 105-112.
- Wolf, S., Eugster, W., Potvin, C., Turner, B.L. and Buchmann, N. 2011. Carbon sequestration potential of tropical pasture compared with afforestation in Panama. *Glob. Change Biol.*, 17: 2763-2780.
- Zhang, X., Zhang, X., Han, H., Shi, Z. and Yang, Z. 2019. Biomass accumulation and carbon sequestration in an age-sequence of Mongolian pine plantations in Horqin sandy land, China. *Forests*, 10: 96.



Investigation on Water Hyacinth in Anaerobic Co-Digestion for Biogas Production: A measure to Reduce Kosavampatti and Phoosur Lake Municipal Solid Waste Loading

V. Murugesan*, D. Joshua Amarnath**† and P. Shanmugam***

* Department of Civil Engineering, Sathyabama Institute of Science and Technology, Chennai, India

**Department of Chemical Engineering, Sathyabama Institute of Science and Technology, Chennai, India

***Environmental Science Laboratory, CSIR-Central Leather Research Institute, Adyar, Chennai-600 02, India

†Corresponding author: D. Joshua Amarnath; drjoshua.chem@sathyabama.ac.in

Nat. Env. & Poll. Tech.

Website: www.neptjournal.com

Received: 05-03-2021

Revised: 20-04-2021

Accepted: 02-05-2021

Key Words:

Cow dung

Water hyacinth

Poultry litter

Mesophilic anaerobic bacteria

Co-digestion

ABSTRACT

The main aim of this study was to evaluate the lab scale, microbe-enhanced biogas production from water hyacinth blended with poultry waste and cow dung. A mesophilic anaerobic two-stage continuous reactor was set up to study the co-digestion for enhanced biogas production. The optimized mixing ratio of cow dung, water hyacinth, and poultry litter (2:1:1; 4:3:1 and 5:2:1) was used along with the effective microbial solution in a two-stage continuous reactor. The biogas yield was maximum in the 2:1:1 blend than the blends with a mixing ratio of 4:3:1 and 5:2:1. The reactor-loading rate was 4 and 5 g.L⁻¹.day⁻¹ with a retention time of 30 and 60 days respectively. The two-stage anaerobic digestion helps in controlling toxicity by acidogenesis and enhances energy production, thereby proving to be a technology that prevents environmental deterioration and enhances energy recovery, both of which are twin issues that need scientific attention. Maximum specific biogas of 0.128 Nm.L.g⁻¹ of Volatile solid reduction (VSR) in hydrolyzer and 0.205 Nm.L.g⁻¹ of VSR in methanizer was obtained at an optimized Carbon/Nitrogen (C/N) ratio of 20.8. The co-digestion of protein-rich waste with a carbon-rich source offers a reduced acclimatization period in the hydrolyzer with an increased C/N ratio, thereby increasing the biogas yield as observed in the methanizer. Several other parameters including Ammonia level, Volatile Fatty Acids influenced by the reactor alkalinity also determine the biogas yield. With increased alkalinity, free ammonia increases and may be inhibitory for anaerobic fermentation and may be toxic for methanogenic bacteria, thereby contributing to the reduction in biogas yield. The present investigation has led to a novel biogas and power-producing clean development mechanism (CDM) for the first time from a heterogeneous mixture of animal excreta and plant waste (livestock droppings, cow dung, and water hyacinths). The waste samples have been collected from sewage and sullage polluted Kosavampatti Lake and Phoosur lake in Namakkal district of Tamilnadu, India therein ending up in a high quantity of CO₂ mitigation.

INTRODUCTION

Tropical and subtropical regions are encountering increasing abundances of invasive floating species (Gopal 1987, Arya et al. 2016, Portielje & Roijackers 1995). Moreover, aquatic species perform important ecosystem functions, particularly in shallow ecosystems, where they may act as engineer species, changing the structure of the ecosystems that they colonize (Bartoli et al. 2010). Most of India's water bodies are small (<1 km²) water-harvesting ponds and lakes that are often characterized by high nutrient inputs and substantial floating species coverage (Murthy et al. 2012). A common floating species in India is the invasive water hyacinth present since 1890 (*Eichhornia crassipes*), which is native to the lowlands of South America (Barrett & Forno 1982). Because of its rapid growth rate, which can double

the biomass within five days, and its ability to successfully compete with other aquatic plants, water hyacinths now cover more than 2,000 km² of the freshwater bodies in India, which corresponds to 10% - 15% of the total area covered by aquatic vegetation (Venugopal 2002, Attermeyer et al. 2016). Reports are evident that the invasive weed is a very good source of renewable energy for the biosynthesis of biofuel (Antai et al. 2014) and hence, biogas production by anaerobic digestion would provide a means for their disposal as well as an added benefit of energy production.

Anaerobic digestion is one such energy-efficient technology in which microorganisms utilize carbon as a sole energy source which subsequently gets converted by oxidation and reduction to its oxidized state (CO₂) and reduced state (CH₄) (Ahring et al. 2003, Ahring & Angelidaki 1993). The merits

of this anaerobic digestion process from agricultural biomass are of growing importance as it offers considerable monetary and environmental benefits (Chen et al., 1980, Chynoweth 2004) and becomes an additional source of income to farmers. Anaerobic digestion of lignocellulosic substrates is a much more complex process, requiring the syntrophic and cooperative interaction between several types of microorganisms. It is a multi-stage, complex, natural process in which a consortium of microbes degrades organic molecules into methane and carbon dioxide via a variety of intermediates (Gujer & Zehnder 1983, Gyllenberg et al. 2002, Healy 1979 Tadrup 1994, 1995). It's a four-step process with various trophic groups participating at each stage. In the first (hydrolysis) stage, organic macromolecules are broken down into monomers like sugars, fatty acids, and amino acids. In the second, the acidogenesis stage, these components are further broken down into VFAs (volatile fatty acids: short-chained fatty acids like acetate, butyrate, or propionate), organic acids, and alcohols, along with small amounts of hydrogen. The largest fraction of H_2 and acetate comes from the third step, the acetogenesis stage, in which bigger VFAs and other organic acids from the previous stage are converted into the two substances. After the final methanogenesis stage, methane and carbon dioxide are formed as the final products (Miyamoto 1997, Murugesan et al. 2020).

Among the different substrates exposed to anaerobic processing (Gyllenberg et al. 2002) for biogas production, better yields of biogas are achieved utilizing a combination of animal waste and lignocellulosic waste. Animal waste especially cow dung has a huge syntrophic system upgrading microbes preferring biogas production. Since the plant has plentiful nitrogen content, it tends to be utilized as a substrate for biogas production. For enhancing the C/N proportion of agricultural waste, co-digestion with sewage slime, animal excrement, or poultry litter is suggested. Then again, the high nitrogenous mixes in the livestock and cattle manure upgrade the ammonia toxicity in the anaerobic digestion and thereby hinder the methane formation (Heinrichs et al. 1990, Addink et al. 1988). However, these nitrogenous compounds were decreased by the co-digestion with different carbonaceous wastewater which could reduce the toxic effect for methane formation (Tadrup 1995, Catharina et al. 2015). Various examinations exhibit the process stability, control, smaller reactor volumes, and high tolerance to toxicity effect and shock loads, as an advantage of anaerobic digester over regular anaerobic digester (Borja et al. 2009a, Chen et al. 2010, Borja et al. 2009b, Koutrouli et al. 2009, Chen & Demirel 2004, Demirel & Yilmaz 2008, Demirel & Othman 2008).

Generally, animal manures contain high protein which on degradation releases ammonia which is a potent inhibitor of methanogenesis (Heinrichs et al. 1990). To meet the

problem, co-digestion technology has been followed to provide nutrient balance (Lebiocka et al. 2008), relatively high methane yield, dilution of a toxic substance (Borja et al. 2009), thereby providing better digester performance and maximum biogas production. In rural and semi-urban areas, handling and utilization of agricultural waste and livestock droppings is a major problem. Many existing solid waste management methods such as landfilling, incineration, composting, and pyrolysis always trigger primary, secondary, and tertiary environmental impacts such as odor problems, Green House Gases (GHG) emissions, and groundwater contamination, etc Abbasi et al. 2005. Alternately, the waste to energy technology through biomass has attracted the solid waste managers for the production of biogas and power coupled with a high quantity of CO_2 mitigation as an initiative to clean development mechanism (CDM). In this study, a solution to the water hyacinth menace in the water bodies that are ultimately dumped into the landfills has been attempted. A dual-stage biogas production technology was developed using livestock droppings, cow dung, and water hyacinths as raw materials collected from sewage and sullage polluted Kosavampatti Lake and Phoosur lake in Namakkal district of Tamilnadu, India.

MATERIALS AND METHODS

Sample Collection and Feed Stock Preparation

Water hyacinth used for the study was obtained from Kosavampatti lake and Phoosur lake; Fresh poultry litter was collected from Municipality and cow dung was obtained from the livestock farm all located in Namakkal District, Tamilnadu, India. The inoculum was prepared using 150 grams crushed jaggery, 100 grams curd, and 1 L pure water. It was kept for 6 days under anaerobic conditions to ferment. After the fermentation period, three different substrates viz., cow dung, water hyacinth, and poultry waste were mixed in three different ratios (2:1:1, 4:3:1, and 5:2:1) for processing.

Characterization of Feedstock and Digester Material

The samples prepared in three different ratios were analyzed for total solids (TS), volatile solids (VS), volatile fatty acids (VFA), pH, and Alkalinity using a standard protocol (APHA 1998). The moisture content (MC) in the test samples was determined according to ASTM- D 3173-87 (ASTM 2002). The pH was recorded daily using a digital pH meter Eco-Scan (Eu-tech instrument Singapore) and adjusted to neutral by the addition of either 6 N NaOH or 1 N HCl.

Batch and Dual-Stage Continuous Reactor Operation

The study was carried in two different reactor arrangements i) anaerobic Biochemical Methane Potential (BMP)

batch reactor and ii) mixed continuous dual-stage anaerobic reactor to evaluate the maximum stable biogas yield.

Biogas Generation in BMP Reactor

The serum bottles of capacity 500 mL considered equivalent to batch BMP reactors were used. The mixing ratios of the three proposed waste were decided based on the Mariotee principle (Tadруп 1995). The study was carried to evaluate the gas yield potential of co-digested slurry containing cow dung, water hyacinth, and poultry waste in three different mixing ratios 2:1:1, 4:3:1, and 5:2:1 in three different anaerobic BMR. The pH was checked daily and adjusted by the addition of either 6 N NaOH or 1 N H₂SO₄. The Biogas generation was measured; the biogas yield and the effect of substrate mixing ratios on it is shown in Fig. 3a.

Biogas Generation in a Two-stage (Hydolyzer and Methanizer) Anaerobic Reactor

The waste mixed in optimal proportions was subsequently fed into the dual-stage anaerobic reactor (hydrolyzer and methanizer) shown in Fig. 1, the configuration of which is given in Table 1. Both the digesters were initially fed with inoculum which was collected from Common Effluent Treatment Plant (CETP), Pallavaram, and mixed with substrates cow dung, poultry waste, and water hyacinth for the acclimatization of the anaerobic organism for a period of one month. The prepared feedstock of 50% TS was used as an influent for the first stage hydrolyzer reactor after being purged with nitrogen gas for 10 min to achieve strict anaerobic conditions. The effluent of the hydrolytic reactor was used as an influent for the second stage methanogenic reactor after adjusting the pH to 7 with 5N NaOH. The volume of biogas production was measured by a water displacement system at STP (Standard Temperature and Pressure).



Fig. 1: Schematic representation of two-stage continuous anaerobic digester.

RESULTS AND DISCUSSION

Characterization of Waste and Composition

Primarily, physico-chemical properties of cow dung, water hyacinth, and poultry waste were determined, and the results are given in Fig. 2(a) and Table 2. It is evident from Fig. 2(a), TS and Moisture of both cow dung and water hyacinth are in proximity while in the poultry waste the TS is predominantly higher than the Moisture. The predominance of Carbon in the slurry makes them suitable for Biogas production (McCarty & McKinney 1961). The elemental analysis of the cow dung, water hyacinth, and poultry waste is taken in the slurry in different proportions is given in Fig. 2(b). A higher percentage of Oxygen, zero % Sulphur, lower ash content makes water hyacinth a suitable waste material that can be potentially blended with the cow dung used in biogas production (EI-Mashad & Zhang 2007).

Effect of Mixing Ratio on Biogas Yield in BMR

The study was carried to evaluate the gas yield potential of co-digested slurry containing cow dung, water hyacinth, and poultry waste in three different mixing ratios 2:1:1, 4:3:1, and 5:2:1 in three different anaerobic BMR. From Fig. 3(a) it is evident that biogas production in all three digesters with respective mixed substrates starts without any lag. Surprisingly, the 2:1:1 substrate ratio produces the most biogas and is stable for longer periods. On the contrary biogas generation potential and its stabilization while compared to other co digested slurry (4:3:1 and 5:2:1) shows slight variation because of ammonia release and VFA which is toxic to methanogenesis. The maximum biogas yield was obtained in a blend ratio of 2:1:1 (cow dung, water hyacinth, and poultry waste) in the pH of 6.5 in which the cumulative biogas yield was observed as 895 Nm.mL⁻¹ whereas, in the

Table 1: Configurations and operations of anaerobic lab-scale continuous reactors.

Sl. No.	Description	Dimension [cm]	Volume [mL]
1	Total height of Cylinder 1	10	
2	Inner diameter of cylinder 1	11.5	1038
3	Effective Liquid Volume	7.4	778
4	Effective liquid volume of cylinder 2	14.2	2255
5	Inner diameter of Cylinder 2	14.2	3007
6	Total height of Cylinder 2	18	
7	Sample Draining 1	½ inch pipe connected to similar valve (1/2 inch)	

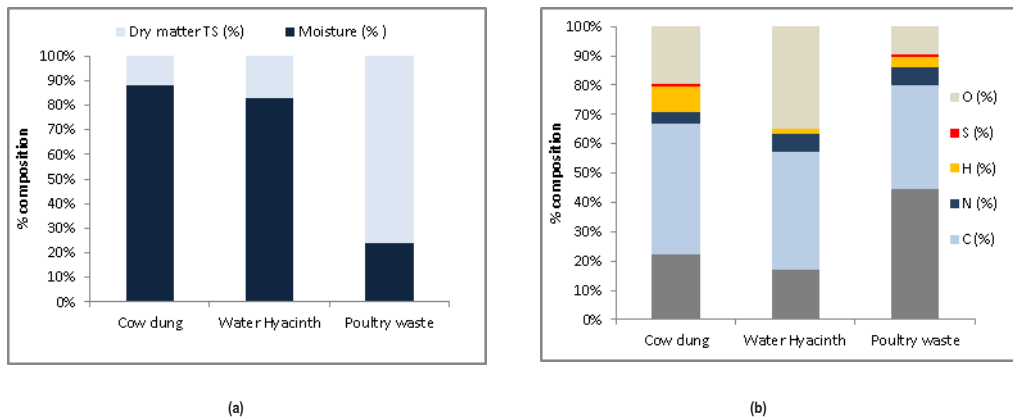


Fig. 2: Characterization of waste and composition. (a) composition analysis; (b) elemental analysis

ratio of 4:3:1, the same was reduced to 694 Nm.mL^{-1} . Dichtl et al. (2007) stated that ammonia levels exceeding 100 mM could inhibit methanogenesis (Manoharan et al. 2014, Samuel & Ukwuaba 2018).

Biogas Yield in the Dual-Stage Anaerobic Reactor

In the case of two-stage continuous reactors (Fig. 3b), the biogas yield was high when compared to the batch reactor. Cooney (2007) also reported that a dual-stage continuous reactor will provide a considerably better yield compared to the batch reactor. In hydrolyzer, the biogas yield was about 3605 mL and 5221 mL in methanizer (Fig. 3b). Since the hydrolyzing reaction is carried out separately, it produces a considerable yield of biogas.

Table 3 shows the specific biogas yield in a dual-stage continuous reactor with a shorter period of HRT i.e. during

maximum gas production. In this study, the co-digestion of cow dung, water hyacinth, and poultry litter produced enhanced biogas with optimized conditions. The specific gas yield in the hydrolyzer was $0.128 \text{ L.g}^{-1} \text{ VSR}$ whereas in the methanizer was $0.205 \text{ L.g}^{-1} \text{ VSR}$. Several previous studies on the anaerobic co-digestion of water hyacinth with other organic waste like cattle dung were reported to increase biogas yield and COD removal (Tadруп 1995, El-Mashad & Zhang 2007, Koutrouli et al. (2009)). Table 3 shows the process performance of a dual-stage anaerobic digester with 30.4 per cent of volatile solids removal in the hydrolyzer and 26.6 per cent in the methanizer (Fig. 4a and 4b). Patil et al. 2014 reported a biogas yield of $0.36 \text{ L.g}^{-1} \text{ VS}$ for an HRT of 60 days in a batch reactor of co-digestion of water hyacinth with sheep waste. Comparing the results obtained with reported literature provides a clear idea that the

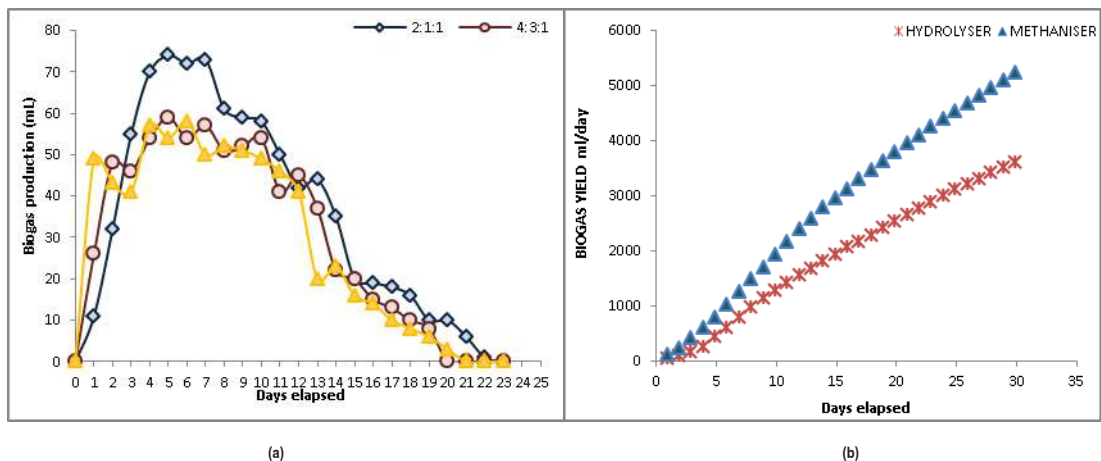


Fig. 3: Cumulative biogas yield for three different substrate ratios. (a) Biogas yield in BMR; (b) Biogas yield in two-stage continuous reactors

Table 2: Characteristics of the feedstock.

Parameters	Cow dung	Water Hyacinth	Poultry waste
Moisture (%)	88±2.3	83.1	26
Dry matter TS (%)	12±2.3	16.9	74
Organic matter VS (%)	77.9±4.5	82.8	72.3
Inorganic matter (% of TS)	22.1±2.5	17.2	27.7
C (% wt /wt)	44.7	40.2	33.3
N (% wt /wt)	4.1	1.8	3.2
P (% wt /wt)01	2.5	1.0	2.99
K (% wt /wt)	3.4	2.9	2.35

Table 3: Specific biogas per gm fed and VS removed in Hydrolyser and Methanizer.

Digester sample	OLR [g.L ⁻¹ .d ⁻¹]	HRT [days]	TS _{in} [%]	VS _{in} [%]	TS _{out} [%]	VS _{out} [%]	VS _r [%]	SPG [L.g ⁻¹ VS _r]
Hydrolyser	4	17	23.01	68.31	16.06	44.7	30.4	0.128
Methanizer	5	11	12.01	44.7	10.3	32.21	26.6	0.205

*SPG- Specific Gas yield, HRT- Hydraulic retention time, TS –Total Solids, VS- Volatile solids

dual-stage is more effective and provides better biogas yield when compared to the batch reactor within a shorter span of HRT.

Effect of Ammonia and Alkalinity on Biogas Yield

The minimum and maximum level (Table 4) of NH₃ in the batch was observed as 1500 mg.L⁻¹ and 5500 mg.L⁻¹. The average NH₃ level in the whole of the batch experiment was 4500 mg.L⁻¹. The observed minima and maxima NH₃ level was correlated with an alkalinity level of 6500 mg.L⁻¹ on the same day, which confirms that the formation of high NH₃ was

triggered by the digester alkalinity conditions. Similar results were also observed by Sung & Liu et al. (2003) which caused the methane production rate to drop approximately 39% and 64%. It was clear that the initial ammonia concentration was high in the three mesophilic batch reactors due to the protein substance present in animal manure.

The initial concentration of NH₃-N in reactor 1 containing the 2:1:1 of Cow dung: poultry waste: water hyacinth slurry is 2732 mg.L⁻¹. Despite this, researchers have shown that as ammonia is introduced to the digester, the pH rises until it reaches equilibrium, after which it drops, resulting in VFA

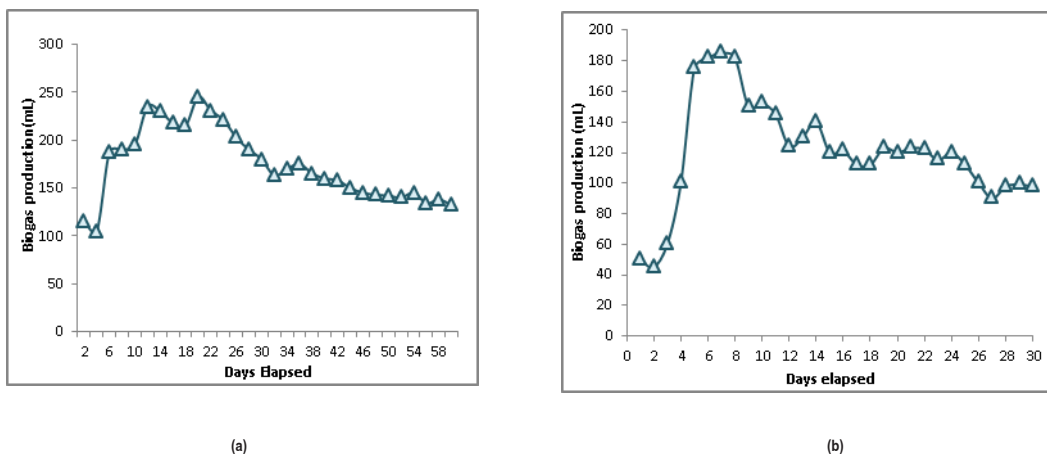


Fig. 4: Biogas production in two-stage continuous reactor (a) Hydrolyser (b) Methanizer

Table 4: Process performance evaluation for three different mixing ratios.

Parameters	2:1:1		4:3:1		5:2:1	
	[Max]	[Min]	[Max]	[Min]	[Max]	[Min]
TS (%)	11	5	16.5	3	21	7
VS (%)	89	40	52.7	50	42.8	35.7
pH	7.2	6.2	7.5	5	7.1	8.3
VFA (mg. L ⁻¹)	1200	5600	1500	7600	800	5950
Alkalinity (mg. L ⁻¹)	2500	3200	3200	2100	1500	5500
NH ₃ -N (mg. L ⁻¹)	2530	2100	3210	1820	2520	4500
C/N	20.8		23.3		24.4	

formation as a result of the pH drop (Engler et al. 2001). In contrast, the waste (cow dung) containing the methanogenic bacteria are used in mixing ratio 5:2:1 the unionized ammonia on the 10th day was too high (5200 mg.L⁻¹) would be attributed to the drop in biogas production. For instance, free ammonia may be inhibitory for anaerobic fermentation and may be toxic for methanogenic bacteria (Gyllenberg et al. 2002, EI-Mashad & Zhang 2007, Demirer & Yilmaz 2008).

Effect of VFA and alkalinity on Biogas Yield

Cessation of biogas production could be attributed to the accumulation of volatile fatty acids, whereas high protein substrate leads to a high ammonia concentration. Process instability due to ammonia often results in volatile fatty acids (VFAs) accumulation, which again leads to a decrease in pH and thereby a declining concentration of ammonia. Before digestion, the pH of the reactor is 7 and after 20 days

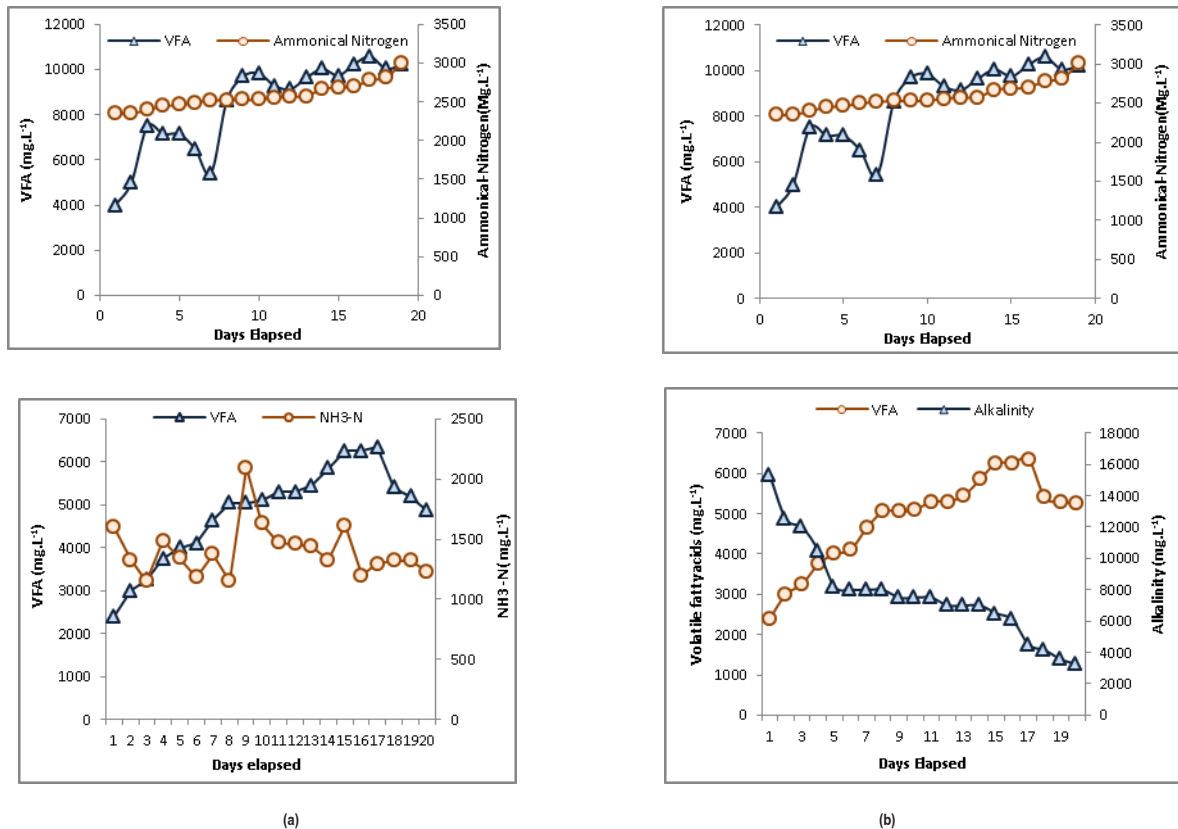


Fig. 5: Relationship between VFA, Alkalinity and Ammonical nitrogen in (a) Hydrolyzer (b) methanizer.

Table 5: Performance indicators of Hydrolyser and Methanizer.

Parameter/mixing ratio	Hydrolyser		Methanizer	
	Maximum	Minimum	Maximum	Minimum
TS [%]	23.1	16.01	12	8.2
VS [%]	68.3	81.5	40.3	45.23
pH	8.3	5.2	6.5	7.1
VFA [mg. L ⁻¹]	10050	4000	5450	3250
Alkalinity [mg. L ⁻¹]	6500	6000	5000	10500
NH ₃ -N [mg. L ⁻¹]	2400	2576	1600	1296
ORP	-250	-256	-270	-280

it dropped to acidic condition, where the process is made stable by adding NaOH at regular intervals 0, 5, 10, 15, and 20th day. It has been reported that a concentration of volatile fatty acids (VFA) of more than 2000 ppm inhibits methane formation in an anaerobic digester (Tadup 1995). Initially, the VFA and alkalinity of reactor 1 containing the 2:1:1 blend had 1500 mg.L⁻¹ and 2000 mg.L⁻¹. As the days progressed, the CO₂ evolution increased which showed a drop in biogas after the 9th day. A detailed picture is shown in Table 4.

Process Performance in a Two-Stage Continuous Reactor

The initial pH of the inoculum used for the seed microflora was 8.3 (Table 5). Once the feeding process started, the pH steadily decreased to 5.2 due to high acidification in the hydrolyzer. However, this sudden decrement due to acidification was balanced and maintained at the pH of 6 with the alkaline solution. Further, no corrections were undertaken until the next feeding process in the hydrolyzer. The alkaline solution was sufficiently concentrated to ensure that the volume added was insignificant relative to the amount of substrate fed into the system. The oxidation-reduction potential (ORP) of hydrolyzer and methanizer was -250 mV and -280 mV (Table 5) respectively, which showed the high reduction potential in methanizer due to the high biological conversion of organic matter into bio-energy. This was attributed to the high biogas yield (245 mL) on the methanizer.

Further, the high reduction potential by high activity of anaerobic bacteria was confirmed by the reduced pH of 5.2 in the hydrolyzer which evidenced the high acidification due to high VFA production of 10500 mg.L⁻¹. The gas production in the hydrolyzer started on 1st day and the maximum (185 mL) was observed on the 6th day and this was consistent with the average VFA of 5400 mg.L⁻¹ on the 6th day. After the systems started up, gas production reached maximum value over the first 5 days and then the production of biogas was slightly stable after the 10th day and continued until biogas

production ceases. After the 27th day the peak was observed to be stable and may be attributed to the acclimation of acidogens in the hydrolyzer.

Contemporarily, the increased total ammonical nitrogen with increased VFA was observed in the hydrolyzer (Fig. 5a and Fig. 5b). This may be because of increased total ammonical nitrogen due to the hydrolyzation of protein compounds in the hydrolyzer. However, the decreased alkalinity due to increased VFA (Fig. 6a and Fig. 6b) in the hydrolyzer confirms that there is no negative impact. On the other hand, the lower total ammonia in the methanizer indicates that the reactor is in good health, which is further supported by the lower alkalinity in the methanizer due to the high VFA.

CONCLUSION

The mesophilic anaerobic two-stage continuous reactor was designed to study the optimized mixing ratio of cow dung, water hyacinth and poultry litter of 2:1:1, 4:3:1 and 5:2:1 for the co-digestion for enhanced biogas production using the effective microbial solution. The reactor-loading rate was 4 and 5 g.L⁻¹.day⁻¹ with a retention time of 30 and 60 days. Maximum specific biogas of 0.128 Nm.L.g⁻¹ of Volatile solid reduction (VSR) in hydrolyzer and 0.205 Nm.L.g⁻¹ of VSR in methanizer was obtained at an optimized Carbon/Nitrogen (C/N) ratio of 20.8. In addition, it is observed that dual-stage anaerobic digestion helps in controlling toxicity by acidogenesis. Thus, the implementation of this technology would benefit the environment and play a major role in energy production.

REFERENCES

- Abbasi, S.A., Gajalakshmi, S., Ramasamy, E.V. and Sankar Ganesh, P. 2005. Extraction of volatile fatty acids (VFAs) from water hyacinth using inexpensive contraptions, and the use of the VFAs as a feed supplement in conventional biogas digesters with the concomitant final disposal of water hyacinth as vermicompost. *Biochem. Eng. J.*, 27: 17-23. doi:10.1016/j.bej.2005.06.010

- Addink, A.D.F., Smit, H., Van Waversveld, J. and Van Den Thillart, G. 1988. Anaerobic heat production measurements: A new perspective. *J. Exp. Biol.*, 138: 529-533.
- Ahring, B. K. and Angelidaki, I. 1993. Thermophilic anaerobic digestion of livestock waste: the effect of ammonia. *Appl. Microbiol. Biotechnol.*, 38, 560-564.
- Ahring, B.K., Angelidaki, I. and Ellegaard, L. 2003. Application of anaerobic digestion process. *Adv. Biochem. Eng. Biotechnol.*, 82: 1-33.
- Antai, E.E., Asikong, B.E., Eja, E.M., Epoke, J. and Udensi, O.U. 2014. Microbial analysis and biogas yield of water hyacinth, cow dung, and poultry dropping fed anaerobic digesters. *Br. J. Appl. Sci. Technol.*, 4(4): 650-661.
- APHA 1998. Standard Methods for the Examination of Water and Wastewater. 20th Edition, American Public Health Association, American Water Works Association and Water Environmental Federation, Washington DC.
- Arya, V., Fiener, S., Flury, S., Jayakumar, R., Premke, K., Steger, K., Van Geldern, R. and Wilken, F. 2016. Invasive floating macrophytes reduce greenhouse gas emissions from a small tropical lake. *Sci. Rep.*, 10: 38. DOI: 10.1038/srep20424
- ASTM 2002. Water and Environmental Technology. Annual Book of American Society for Testing and Materials Standards, West Conshohocken.
- Attermeyer, K., Flury, S., Jayakumar, R., Fiener, P., Steger, K., Arya, V., Wilken, F., Van Geldern, R. and Premke, K. 2016. Invasive floating macrophytes reduce greenhouse gas emissions from a small tropical lake. *Scientific Reports*, 6(1): 1-10.
- Barrett, S. and Forno, I. 1982. Style morph distribution in new world populations of *Eichhornia crassipes* (Mart.) Solms-Laubach (water hyacinth). *Aquat. Bot.*, 13: 299-306.
- Bartoli, M., Bolpagni, R., Pierobon, E. and Viaroli, P. 2010. Net primary production and seasonal CO₂ and CH₄ fluxes in a *Trapa natans* L. meadow. *J. Limnol.*, 69: 225-234. DOI:10.4081/jlimnol.2010.225
- Borja, R., De La Rubia, M.A., Raposo, F. and Rincon, B. 2009a. Evaluation of the hydrolytic-acidogenic step of a two-stage mesophilic anaerobic digestion process of sunflower oil cake. *Bioresour. Technol.*, 100: 4133-4138. doi: 10.1016/j.biortech.2009.04.001
- Borja, R., Martin, M. A., Martin, A. and Rincon, B. 2009b. Evaluation of the methanogenic step of a two-stage anaerobic digestion process of acidified olive mill solid residue from a previous hydrolytic-acidogenic step. *Waste Manag.*, 29: 2566-2573. DOI: 10.1016/j.wasman.2009.04.009
- Catharina, V., Marcus, C., Mathew, S., Keith, L., Jurgen, H., Michael, K. and Adam, M. 2015. Decreasing methane yield with increasing food intake keeps daily methane emissions constant in two foregut fermenting marsupials, the western grey kangaroo and red kangaroo. *J. Exp. Biol.*, 218: 3425-3434.
- Chen, S. and Demirel, G.N. 2004. Effect of retention time and organic loading rate on anaerobic acidification and bio-gasification of dairy manure. *J. Chem. Technol. Biotechnol.*, 79(12): 1381-7. <https://doi.org/10.1002/jctb.1138>
- Chen, S., Hashimoto, A.G., Varel, V.H. and Len, Y. 1980. Enhancement of biogas different substrates. *Indian Eng. Chem. Prod. Resour. Devel.*, 19: 471.
- Chen, S., Li, R. and Li, X. 2010. Biogas production from anaerobic co-digestion of food waste with dairy manure in a two-phase digestion system. *Appl. Biochem. Biotechnol.*, 160: 643-654. doi: 10.1007/s12010-009-8533-z
- Chynoweth, D.P. 2004. Biomethane from energy crops and organic wastes. In: International Water Association (Eds.), *Anaerobic Digestion 2004. Anaerobic Bioconversion. Answer for Sustainability, Proceedings 10th World Congress*, vol. 1, Montreal, Canada, pp. 525-530.
- Cooney, Rosie 2007. Sustainable use: concepts, ambiguities, challenges. Sustainable Use Specialist Group Strategic Planning Meeting, 10-13 July.
- Demirel, G.N. and Yilmaz, V. 2008. Improved anaerobic acidification of unscreened dairy manure. *Environ. Eng. Sci.*, 25: 309-318. DOI: 10.1089/ees.2006.0222
- Demirel, G.N. and Othman, M. 2008. Two-phase thermophilic acidification and mesophilic methanogenesis anaerobic digestion of waste-activated sludge. *Environ. Eng. Sci.*, 25(9): 1291-300.
- Dichtl, N., Fricke, K., Huttner, A., Santen, H. and Wallmann, R. 2007. Operating problems in anaerobic digestion plants resulting from nitrogen in MSW. *Waste Manag.*, 27: 30-43. DOI: 10.1016/j.wasman.2006.03.003.
- El-Mashad, H.M. and Zhang, R. 2007. Co-digestion of food waste and dairy manure for biogas production. *Transactions of the ASABE*, 50(5): 1815-1821. doi: 10.13031/2013.23945
- Engler, C.R., Lacey, R.E., Ricke, S.C. and Sterling, M.C. 2001. Effect of ammonia nitrogen on H₂ and CH₄ production during anaerobic digestion of dairy cattle manure. *Bioresour. Technol.*, 77: 9-1. DOI: 10.1016/S0960-8524(00)0138-3
- Gavala, H. N., C., Kalfas, H., Lyberatos, G., Skiadas, V. and Stamatelatu, K. 2009. Hydrogen and methane production through two-stage mesophilic anaerobic digestion of olive pulp. *Bioresour. Technol.*, 100: 3718-23. doi: 10.1016/j.biortech.2009.01.037 .
- Gopal, B. 1987. *Water Hyacinth (Aquatic Plant Studies)*. Elsevier Science Publisher, Amsterdam, pp. 471- 477.
- Gujer, W. and Zehnder, A.J.B. 1983. Conversion processes in anaerobic digestion. *Water Sci. Technol.*, 15: 127-167.
- Gyllenberg, M., Noykova, N., Thorsten, G.M. and Timmer, J. 2002. Quantitative analyses of anaerobic wastewater treatment process identifiability and parameter estimation. *Biotechnol. Bioeng.*, 78: 89-103. <https://doi.org/10.1002/bit.10179>
- Healy, J.B., Owen, W.F., Stuckev, D.C., Young Jr., L.Y. and McCagrv, P.L. 1979. Bioassay for monitoring biochemical methane potential and anaerobic toxicity. *Water Res.*, 13: 485-492.
- Heinrichs, D. M., Olieskewicz, J.A. and Poggi-Valardo, H.M. 1990. Effects of ammonia on anaerobic digestion of simple organic substrates. *J. Environ. Eng.*, 116: 698-710. [https://doi.org/10.1061/\(ASCE\)0733-9372\(1990\)116:4\(698\)](https://doi.org/10.1061/(ASCE)0733-9372(1990)116:4(698))
- Patil, J.H., AntonyRaj, M.A.L., Shankar, B.B., Shetty, M.K. and Kumar, B.P. 2014. Anaerobic co-digestion of water hyacinth and sheep waste. *Energy Procedia*, 52: 572-578.
- Koutrouli, E.C., Kalfas, H., Gavala, H.N., Skiadas, I.V., Stamatelatu, K. and Lyberatos, G. 2009. Hydrogen and methane production through two-stage mesophilic anaerobic digestion of olive pulp. *Bioresource Technology*, 100(15): 3718-3723.
- Lebioccka, M., Montusiewicz, A. and Pawłowska, M. 2008. Characterization of the biomethanization process in selected waste mixtures. *Arch. Environ. Protect.*, 34(3): 49-61.
- Manoharan, D., Priya, E., Seshadri, S. and Sugumaran, P. 2014. Biogas production from water hyacinth blended with cow dung. *Indian J. Energ.*, 3(1): 134-139.
- McCarty, P.L. and McKinney, R.E. 1961. Salt toxicity in anaerobic digestion. *J. Water Pollut. Control Fed.*, 33: 23.
- Miyamoto, K. 1997. Renewable biological systems for alternative sustainable energy production. *FAO Agric. Services Bull.*, 128: 405
- Murthy, T., Panigrahy, S., Patel, J. and Singh, T. 2012. Wetlands of India: inventory and assessment at 1:50,000 scale using geospatial techniques. *Curr. Sci.*, 102: 852-856.
- Murugesan, V. and Joshua, A.D. 2020. Bio-process performance, evaluation of enzyme and non-enzyme mediated composting of vegetable market complex waste. *Nature Sci. Rep.*, 6: 66-73. 10.1038/s41598-020-75766-3
- Portielje, R. and Roijackers, R.M.M. 1995. Primary succession of aquatic macrophytes in experimental ditches in relation to nutrient input. *Aquat. Bot.*, 50: 127-140. [https://doi.org/10.1016/0304-3770\(94\)00439-S](https://doi.org/10.1016/0304-3770(94)00439-S)
- Samuel, I. and Ukwuaba, R. 2018. Performance evaluation of biogas yields potential from co-digestion of water hyacinth and kitchen waste. *Eur.*

- J. Eng. Res. Sci., 3(4): 36-39. <https://www.ejers.org/index.php/ejers/article/view/684/277>
- Sung, S. and Liu, T. 2003. Ammonia inhibition on thermophilic anaerobic digestion. *Chemosphere*, 53(1): 43- 52.
- Tadруп, S. 1994. Centralized biogas plants, combined agriculture, and environmental benefits with energy production. *Water Sci. Technol.*, 30(12): 133-141. <https://doi.org/10.2166/wst.1994.0597>
- Tadруп, S. 1995. Viable energy production and waste recycling from anaerobic digestion of manure and other biomass materials. *Biomass Bioenerg.*, 9 (1-5): 303-315.
- Venugopal, G. 2002. Monitoring the effects of biological control of water hyacinths using remotely sensed data: A case study of Bangalore, India. *Singap. J. Trop. Geogr.*, 19: 91-105. <https://doi.org/10.1111/1467-9493.00027>



Application of UAV Photogrammetry on Ecological Restoration of Abandoned Open-pit mines, Northern Anhui Province, China

Hongbao Dai* and Jiying Xu**(***)[†]

*School of Environment and Surveying Engineering, Suzhou University, Suzhou, 234000, Anhui, China

**School of Resources and Civil Engineering, Suzhou University, Suzhou, 234000, Anhui, China

***National Engineering Research Center of Coal Mine Water Hazard Controlling (Suzhou University), Suzhou, 234000, Anhui, China

[†]Corresponding author: Jiying Xu; jiyingxu1986@163.com

Nat. Env. & Poll. Tech.
Website: www.neptjournal.com

Received: 16-04-2021

Revised: 23-05-2021

Accepted: 07-06-2021

Key Words:

UAV

Abandoned mines

Ecological restoration

Earthwork calculation

Photogrammetry technology

ABSTRACT

Mine survey is an important part of the ecological restoration design of an abandoned open-pit mine because it gives precise survey data for mine management. Unmanned aerial vehicle (UAV) photogrammetry technology is applied to mine 3D modeling and earthwork calculation to tackle the problems of high cost, low efficiency, and high labor intensity in traditional manual field mine surveys. Using the abandoned quarries in Baitu, Suzhou City, as the study area, 82 ground control points were set up, and massive elevation data of the ground was obtained using a Dajiang spirit 4 RTK UAV for aerial photography and extracted from a 3D model created with Context Capture software, while a digital orthophoto image of the study area was created. The earthwork volume is calculated using the square grid method. UAV photogrammetry has a considerably higher efficiency than typical manual field measurement results, and it meets the precision criteria of mine geological environment assessment. According to the findings, UAV photogrammetry technology has a promising future in mine geological environment monitoring and ecological environment repair.

INTRODUCTION

Mineral resources are the material basis of human economic and social development, and the “food” and main power source of industry, agriculture, national defense, and other social industries (Zhai & Hu 2021). Large scale and excessive exploitation of mineral resources will bring about environmental problems such as vegetation destruction, soil erosion, ecological environment deterioration, and so on (Hu et al. 2015, Mohammad et al. 2016)(Hu, Fu et al. 2015, Mohammad, Wahsha et al. 2016). Various mines have not returned to their former ecological state after shutting, and there are some issues that need to be addressed, such as land idleness, tailings buildup, ground accretion, and mineral pollution (Sivarajah et al. 2019). The foundation of abandoned mine restoration, land reclamation, and mine green sustainable development is mine ecological environment repair. The mining survey is the key step that can give an accurate measuring basis for the design of ecological restoration during the restoration project (Isiaka et al. 2019).

The traditional manual field mine survey approach, which employs a total station and GPS technology, has drawbacks such as expensive costs, long lead times, and vulnerability to the field environment, among others (Jie et al. 2018). The 3D

laser scanning technology has been used in mine geological monitoring because of its advantages of telemetry, speed, and efficiency, but it also has the disadvantages of high labor intensity and inability to acquire reliable information in the blind area (Thurley et al. 2015). The key difficulty in the field of mine survey is how to lower costs while maintaining high quality and efficient access to geometric information and physical properties of mining areas. In recent years, (unmanned aerial vehicle) UAV technology has become widely used in a variety of fields, particularly in engineering geology research, including basic theory research (Xing et al. 2011, Shan et al. 2013), rock discontinuity investigation (Salvini et al. 2020), underground tunnel mapping (Wirachman et al. 2010), slope stability analysis (Wang et al. 2019), and landslide deformation monitoring. However, there are few studies on ecological restoration of abandoned open-pit mines using UAV photogrammetry.

The study’s goal was to see if UAV photogrammetry might be used to help with open-pit mine ecological restoration. The Dajiang spirit 4 RTK UAV was employed for aerial photography in this paper, with the abandoned quarries in Baitu town of Suzhou City as the study region. Massive elevation data was retrieved from a 3D model created with the Context Capture software. The earthwork

volume is calculated using the square grid method, and the measurement accuracy is compared to traditional manual field measurement findings. The findings will be used to establish sustainable development plans, as well as to better understand the management and development of abandoned mining resources.

MATERIALS AND METHODS

Study Area

The abandoned quarries are located 55 km north of Suzhou city in Anhui province, China. Its geographical coordinates are 117°2'1"–117°7'22" north and 34°9'26"–34°4'32" east, as shown in Fig. 1. The climate of the study area belongs to the warm temperate zone and semi-humid monsoon section, characterized by a mild climate and four distinct seasons, with an average annual temperature of 14.5°C and an average annual rainfall of around 774 mm. Geologically, the quarries area is located between Su Bei Fault and the Feng Pei fault.

The abandoned quarries are limestone mines for building stone, which consist of four mines and cover a damaged area of 322450.8 m² and an undamaged area of the original mountain 68226.5 m² respectively (Fig. 1). In the study region, there are several dangerous rocks, and the rock at the top of the cliff face is relatively shattered. There is a risk of geological disasters such as collapse and landslides as a result of local slope mining along the rock layers.

Principle of Photogrammetry

UAV photogrammetry uses theories and algorithms such as computer technology, digital picture feature extraction, and image matching to create a three-dimensional model

and extract relevant geometric and physical information, all based on the basic principle of photogrammetry (Lin et al. 2018, Wang et al. 2020). The image-object relationship model is constructed based on the collinear relationship of the image point, photogrammetry center, and object point (Qiang & Tian 2019).

$$x - x_0 = -f \frac{a_1(X - X_S) + b_1(Y - Y_S) + c_1(Z - Z_S)}{a_3(X - X_S) + b_3(Y - Y_S) + c_3(Z - Z_S)}$$

$$y - y_0 = -f \frac{a_2(X - X_S) + b_2(Y - Y_S) + c_2(Z - Z_S)}{a_3(X - X_S) + b_3(Y - Y_S) + c_3(Z - Z_S)}$$

... (1)

The photographing scale is determined by the focal length f and the height h of the camera (Meng et al. 2020). According to the photographing scale and the pixel size a of the camera, the ground resolution G can be determined by the formula (2).

$$\frac{1}{m} = \frac{F}{H} = \frac{a}{G}$$

... (2)

In the formula (2): $1/m$ represents photographing scale.

Principle of Square Grid Method

The square grid method is common and effective in earthwork calculation (Zhang et al. 2015, Guo et al. 2016). The calculation steps are as follows: (1) the study area is divided into several squares. (2) For each grid, the product of the grid area and difference value (between design elevation and measured elevation) is regarded as the engineering quantity of a single grid. (3) The calculation results of each grid are accumulated to obtain the total quantities of the study area.

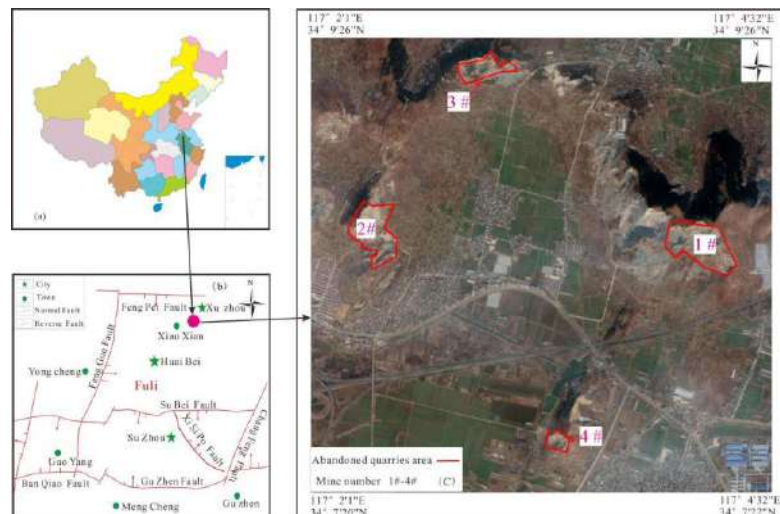


Fig. 1: Geographical location map of the study area.

The calculation formula is shown in (3) (4).

$$H_{ij} = \frac{1}{k} \sum_{j=1}^k (H_j - H_D) \quad \dots(3)$$

$$V = \sum_{i=1}^n H_{ij} \cdot ab \quad \dots(4)$$

In the formula (3): H_{ij} is the elevation of i row and j column grid; K represents the number of points in the grid; H_j is the actual elevation of points in the grid; H_D is the design elevation. In the formula (4): V represents the total amount of work; n is the number of squares in the survey area; a and b are the side length of the grid respectively.

Backfill in earthwork should be taken during ecological restoration if the design elevation is higher than the observed elevation. On the other hand, if the design elevation is lower than the observed elevation, excavation measures should be taken. Furthermore, a significant number of elevation data are generated in a single grid due to the dense matching program of UAV photogrammetry, and the measured height can use the average value of all elevation data in the grid to ensure accuracy.

Three-Dimensional (3D) Modeling

Control surveying and UAV route planning were used in the project to gather images of abandoned quarries (He et al. 2020). Using context capture software, a 3D model was created, and the geometric information for the earthwork computation was extracted from the model.

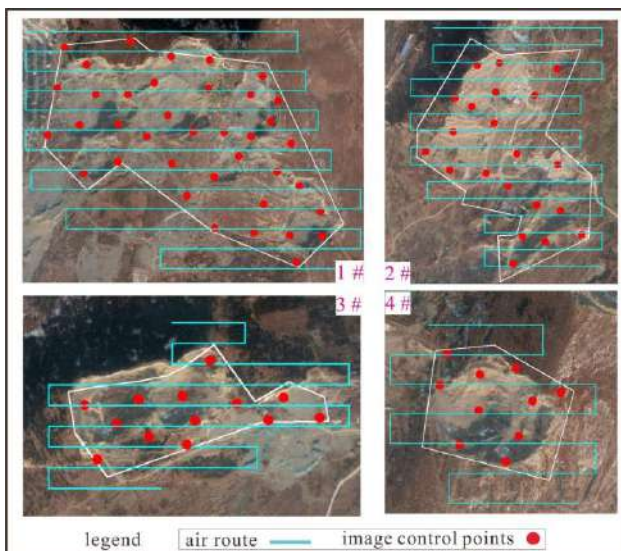


Fig. 2: Layout of image control points and routes in the study area.

Control Surveying

The photo control points are primarily used for photogrammetric picture recognition, which is often based on the principle of “more around, less in the middle,” and is in accordance with the coordinate system developed afterwards (Sun et al. 2018). To make the control network more stable and match the accuracy requirements, 82 image control points (Fig. 2) are set up in the study region due to the substantial topography fluctuation of the open-pit quarry.

UAV Image Acquisition

There are several high and steep slopes in the research region, with a maximum slope of 80° and a difference between the platform surface and the top of the hill in the treatment area ranging from 90 to 140 m, due to the influence of mining technologies and natural conditions. As a result, the study area’s layers and blocks follow the design path (Xu et al. 2016). The center of each block area is chosen as the flight site to assure the quality of the images. The relative elevation of the study area is higher during the field survey, the wind speed is strong and changes often, and the field aerial survey difficulty coefficient is higher than that of residential aerial survey.

The UAV of Dajiang spirit 4 RTK was used to obtain the image. To meet the accuracy requirements of earthwork

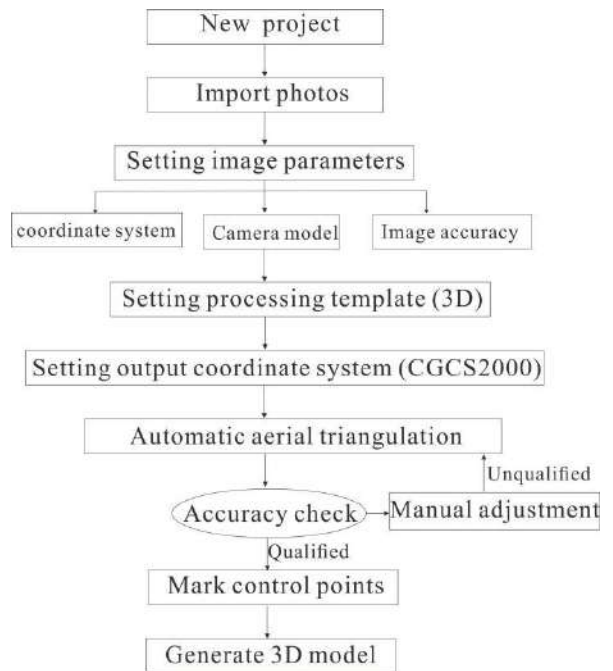


Fig. 3: Flow chart of 3D modeling.

calculation, the mapping scale of 1:1000 and the photography scale of 1:5000 are selected. The designed altitude is set at 90 m, and the overlap of heading and side direction is 80%. A total of 12 routes (Fig. 2) are arranged, flying in three voyages, and the horizontal flight speed is $6\text{m}\cdot\text{s}^{-1}$. A total of 805 images were obtained from the front, back, left and right orthophoto 5 cameras, the image size is $5472\text{ pixels} \times 3678\text{ pixels}$, and the average ground resolution of tilt image is 2.08 cm.

3D Modeling

According to the results of the control survey and the images obtained by UAV, the 3D model of the abandoned outcrop mine is established by using context capture software and the process shown in Fig. 3 (Jing et al. 2015). The model post-processing is carried out by using the software of EPT and EPS (encapsulated postscript). The 3D modelings of abandoned mines are shown in Fig.4.

Model Accuracy Evaluation

Mean square error is often used to evaluate the accuracy of mapping, including M_S (plane) and M_H (elevation) (Puliti et al. 2018). The calculation formula is as follows (5), (6), and (7).

$$M_S = \sqrt{\frac{\sum(\Delta S)^2}{n}} \quad \dots(5)$$

$$M_H = \sqrt{\frac{\sum(\Delta H)^2}{n}} \quad \dots(6)$$

$$\Delta S = \sqrt{(\Delta X)^2 + (\Delta Y)^2} \quad \dots(7)$$

In the above formulas, the Δs represents the plane distance error, Δx , Δy , and Δh represent the absolute error of three-dimensional coordinates respectively, and n is the number of measuring points. Based on the manual measurement data (measured by total station) and 3D model measurement data (extracted from UAV), M_S and M_H are calculated.

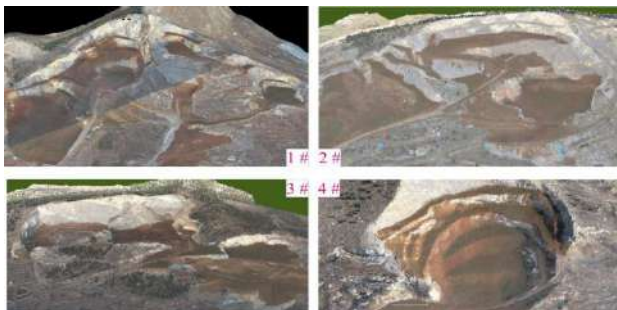


Fig. 4: 3D model of the abandoned quarries.

RESULTS AND DISCUSSION

First, 50 checking points were evenly selected in the survey area, and the total station was used to obtain the three-dimensional coordinates (X, Y, H); second, the total station measurement results are subtracted from the corresponding 3D model measurement data, and the absolute errors of the Δx , Δy , Δh , and Δs are calculated; finally, M_S and M_H are used to calculated by the formulas (5), (6) and (7). The accuracy evaluation results of the 3D model in the study area are shown in Table 1.

According to “Specification for aerial photogrammetry of 1 : 500 1 : 1000 1 : 2000 topographic map” (China National Standardization Committee 2008), M_S and M_H of 1 : 1000 topographic map in mountainous and hilly areas should be less than 0.4m and 0.35 m respectively. The calculated results of M_S and M_H for the study area are 0.083 m and 0.069 m respectively, indicating 3D modeling meets the accuracy requirements, which can be used for earthwork calculation.

Earthwork Calculation of Abandoned Mines

Based on the manual measurement data (total station) and 3D model measurement data (extracted from UAV), the volume of earthwork was calculated by the square grid method (Liu et al. 2020). To create the original topographic map and the construction topographic map, the original elevation points and construction elevation points obtained by two types of survey methods are first loaded into Cass 9.1 software. Second, the boundary between filling and excavation is delineated by superimposing and comparing the elevation data of the two maps, and the region is divided into blocks and serially numbered, generating a block map. Finally, the original map and construction map for a single block is superimposed on the block map, and the block's volume V_1 and V_2 are calculated using 0 elevations as the datum plane and 5 meters as the grid length. The value of V_1 minus V_2 is the block's excavation or filling volume. Finally, the regional blocks are added together to determine the mine's earthwork volume. Table 2, Fig. 5, and Fig. 6 present the results of four abandoned quarries' calculations.

Hence, the excavation difference between the two methods is 4577.36m^3 , and the difference rate is between 0.019-0.035, with an average of 0.023. Meanwhile, the filling difference between the two methods is 1669.41m^3 , and the difference rate is between 0.018-0.014, with an average of 0.020. The engineering earthwork calculation is a complex problem involving multiple influencing factors, which cannot be accurately calculated in advance, and the current specifications do not specify the error of earthwork measurement. Generally, the error of earthwork measurement from relatively flat to uneven is controlled within 5% (Li

Table 1: The calculation results of accuracy evaluation.

point	$\Delta X(m)$	$\Delta Y(m)$	$\Delta H (m)$	$\Delta S (m)$	point	$\Delta X (m)$	$\Delta Y(m)$	$\Delta H(m)$	$\Delta S(m)$
1	-0.018	0.043	0.056	0.047	26	0.061	0.029	0.042	0.068
2	0.053	0.021	0.034	0.057	27	0.025	-0.082	-0.069	0.086
3	0.017	-0.090	-0.077	0.092	28	-0.013	0.048	0.061	0.050
4	-0.021	0.040	0.053	0.045	29	0.057	0.077	0.090	0.096
5	0.049	0.089	0.102	0.102	30	0.026	0.058	0.071	0.064
6	0.018	0.070	0.083	0.072	31	-0.085	0.022	0.135	0.088
7	-0.093	0.134	0.087	0.163	32	0.045	-0.016	-0.003	0.048
8	0.037	-0.004	0.009	0.037	33	0.074	0.054	0.067	0.092
9	0.086	0.066	0.079	0.108	34	0.055	0.023	0.036	0.060
10	0.067	0.035	0.048	0.076	35	0.019	-0.088	-0.075	0.090
11	0.031	-0.076	-0.063	0.082	36	-0.019	0.042	0.055	0.046
12	-0.007	0.054	0.067	0.054	37	0.051	0.091	0.104	0.104
13	0.063	0.069	0.082	0.093	38	0.020	0.072	0.085	0.075
14	0.032	0.050	0.063	0.059	39	-0.091	0.136	0.149	0.164
15	-0.079	0.014	0.027	0.080	40	0.039	-0.002	0.011	0.039
16	0.051	-0.024	-0.011	0.056	41	0.088	0.068	0.081	0.111
17	0.066	0.046	0.059	0.080	42	0.069	0.037	0.050	0.078
18	0.047	0.015	0.028	0.049	43	0.033	-0.074	-0.061	0.081
19	-0.089	-0.096	-0.083	0.131	44	-0.005	0.056	0.069	0.056
20	-0.027	0.034	0.047	0.043	45	0.065	0.071	0.084	0.096
21	0.043	0.083	0.096	0.093	46	0.034	0.052	0.065	0.062
22	0.012	0.064	0.077	0.065	47	-0.077	0.054	0.067	0.094
23	-0.099	0.039	0.031	0.106	48	0.053	0.023	0.036	0.058
24	0.031	-0.010	0.003	0.033	49	0.068	-0.058	-0.075	0.089
25	0.080	0.060	0.073	0.100	50	0.049	0.042	0.055	0.065

& Yang 2020, Contreras & Chung 2012). As a result, the process of determining the earthwork volume of an open pit mine using a UAV aerial survey may fully meet engineering precision criteria.

The workload of manual measurement and UAV is shown in Table 3. Table 3 shows that UAV photogrammetry requires two surveyors and two days for outdoor work, and two surveyors and 2.5 days for indoor work. Manual measurement, on the other hand, necessitates 4 surveyors and 4.75 days for fieldwork, and 1 surveyor and 2.5 days for indoor work. The conclusion can be made that UAV photogrammetry

has a substantially higher work efficiency than traditional manual measuring.

CONCLUSION

- (1) Using context capture software, a 3D model of an abandoned mine was created based on the ground control survey and images obtained by the Dajiang spirit 4 RTK UAV. The horizontal and elevation mean square errors are 0.083 m and 0.069 m, respectively, which meet the accuracy standards.

Table 2: Comparison of earthwork calculation results between manual measurement and UAV.

No.	Area [m ²]	Excavation			backfill		
		UAV [m ³]	Manual measurement [m ³]	Difference rate	UAV [m ³]	Manual measurement [m ³]	Difference rate
1#	166821.1	195680.31	192840.65	0.015	36182.96	36845.52	0.018
2#	137486.9	58959.95	56974.14	0.035	29147.04	29642.73	0.017
3#	59779.6	59080.51	60222.98	0.019	12520.85	12342.92	0.014
4#	26589.7	42243.72	41349.36	0.022	22226.26	22915.35	0.030

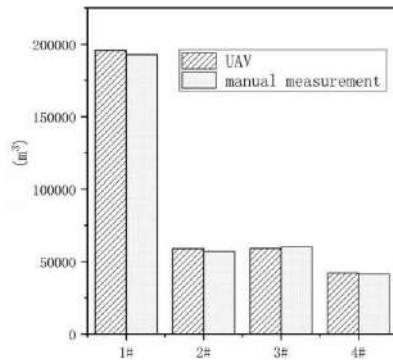


Fig. 5: Comparison chart of earthwork calculation results between manual measurement and UAV.

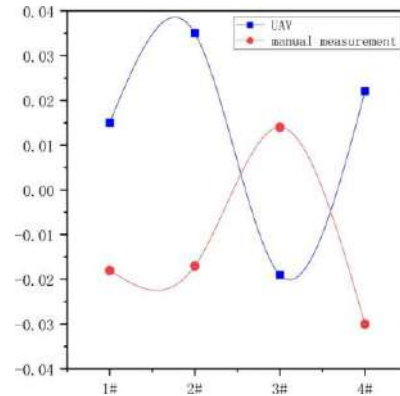


Fig. 6: Difference rate of earthwork calculation results.

Table 3: Workload table of manual measurement and UAV.

No.	UAV				Manual measurement			
	Field survey		indoor work		Field survey		Indoor work	
	Surveyors	Days	Days	Days	Surveyors	Days	Days	
1	2	1	1	1	4	2	2	1
2	2	0.5	1	0.5	4	1	2	0.5
3	2	0.5	1	0.5	4	1	2	0.5
4	2	0.5	1	0.5	4	0.75	2	0.5
Total	2	2.5	1	2.5	4	4.75	2	2.5

(2) The earthwork volume was calculated using the square grid method, which was based on data from UAV photogrammetry and a classical total station survey. The average difference rate is 0.022, which satisfies the earthwork measuring standards. In comparison to traditional field surveys, UAV photogrammetry provides the advantages of a shorter field time and automatic data processing, which considerably enhances labor productivity and is unaffected by external topographical impediments, particularly in large-area surveys.

The 3D mine model has a good overall situation, and it is also an image model that can measure and extract information, which provides significant basic data for mine ecological restoration design, and it has a promising future use in mine ecological restoration.

ACKNOWLEDGEMENT

This research was funded by the Key natural science research projects of Suzhou University (2020ydz03, 2020ydz07, 2019ydz01), National Natural Science Foundation of China (41773100), and Funding projects for research activities of academic and technological leaders of Anhui Province (2020D239).

REFERENCES

- China National Standardization Committee. 2008. Specification for aerial photogrammetry of 1 : 500 1 : 1000 1 : 2000 topographic map, 3. Southwest Jiaotong University, GIS Engineering Center, Chengdu, China.
- Contreras, A. and Chung, X. 2012. Improving accuracy in earthwork volume estimation for proposed forest roads using a high-resolution digital elevation model. *Croatian J. Forest Eng.*, 33(1): 456-463.
- Guo, J., Mingxing, Y.I. and Xue, M.C.C. 2016. Engineering application study of earthwork calculation with square grid method by southern CASS. *Min. Eng.*, 54: 616-636.
- He, X., Yang, X., Luo, Z. and Guan, T. 2020. Application of unmanned aerial vehicle (UAV) thermal infrared remote sensing to identify coal fires in the Huojitu coal mine in Shenmu City, China. *Sci. Rep.*, 10(1): 56-71.
- Hu, Z.Q., Fu, Y.H., Xiao W. and Wei, T.T. 2015. Ecological restoration plan for an abandoned underground coal mine site in Eastern China. *Int. J. Min. Reclam. Environ.*, 29(4): 316-330.
- Isiaka, A.I., Durrheim, R.J. and Manzi, M.S.D. 2019. High-resolution seismic reflection investigation of subsidence and sinkholes at an abandoned coal mine site in South Africa. *Pure Appl. Geophys.*, 176(4): 1531-1548.
- Jie, X., Chen, J., Sofia, G., Yi, T. and Tarolli, P.J.E.E.S. 2018. Open-pit mine geomorphic changes analysis using multi-temporal UAV survey. *Springer Berlin Heidelberg*, 77(6): 1-18.
- Jing, Q.Q., Zhi, X.D., Wang, J., Wang, X.H., Amp, A.G. and Center, R.S. 2015. Remote sensing survey of iron mine exploitation using UAV technology in Yuanjiang, Shanxi. *Miner. Explor.*, 2: 79.
- Li, W.J. and Yang, J. 2020. The application of UAV Photogrammetry in the Calculation of the amount of Earth and Stone excavation. *Beij. Survey. Map.*, 34(10): 106-109.

- Lin, Z., Xie, F. and Guozhong, S.U. 2018. Accuracy analysis of low altitude photogrammetry with a wide-angle camera. *J.Survey. Map.*, 11(1): 30-38.
- Liu, X.Y., Li, Y.P. and Wu, J.C. 2020. Earthwork measurement based on UAV tilt Photogrammetry. *Survey. Map. Technol. Equip.*, 22(01): 53-56.
- Meng, Q., Li, W., Raspini, F., Xu, Q. and Casagli, N.J.L. 2020. Time-series analysis of the evolution of large-scale loess landslides using InSAR and UAV photogrammetry techniques: a case study in Hongheyan, Gansu Province, Northwest China. *Landslides*, 2: 54.
- Mohammad, W., Mandana, N. and Claudio, B.J.J.O. 2016. Land contamination by toxic elements in abandoned mine areas in Italy. *Soils Sediments*, 16(4): 1300-1305.
- Puliti, T., Astrup, M. and Forests, R.J. 2018. Tree-stump detection, segmentation, classification, and measurement using unmanned aerial vehicle (UAV) Imagery. *Forests*, 9(3): 102.
- Qiang, L.I. and Tian, L.I. 2019. Application of UAV photogrammetry in reserves calculation in the coal yard. *Beij. Survey. Map.*, 5: 11-29.
- Salvini, R., Vanneschi, C., Coggan, J.S. and Mastrococco, G. 2020. Evaluation of the use of UAV photogrammetry for rock discontinuity roughness characterization. *Rock Mech. Rock Eng.*, 53(8): 3699-3720.
- Shan, B.J., LuoXu, Y.Y. and Liang, L.X. 2013. Application of UAV in open-pit mine disaster monitoring. *Opencast Min. Technol.*, 8: 63-78.
- Sivarajah, B.J.B., Korosi, J.M., Blais, R.M. and Smol, J.P. 2019. Multiple environmental variables influence diatom assemblages across an arsenic gradient in 33 subarctic lakes near abandoned gold mines. *Hydrobiologia*, 841(1): 133-151.
- Sun, K., Zhao, K. and Liu, Y. 2018. Research on the influence of photo-control-points layout on aero-triangulation accuracy by UAV aerial in zonal terrain. *Western Devel.*, 16(9): 111-123.
- Thurley, M.J., Onederra, I., Catalan, M. and Metallurgy, S. A. 2015. Measuring blast fragmentation at Esperanza mine using high-resolution 3D laser scanning. *Min. Technol.*, 11: 54-63.
- Wang, F.Y., Zhao, M.Y., Wang, M.C., Zhang, J.Q. and Zhou, K. 2020. Application of UAV Photogrammetry in mine geological environment survey. *J. Jilin Univ.*, 50(03): 194-202.
- Wang, S., Ahmed, Z., Hashmi, M.Z. and Wang, P.G.F. 2019. Cliff faces rock slope stability analysis based on unmanned aerial vehicle (UAV) photogrammetry. *Geo-Energy Geo-Resour.*, 46: 537-553.
- Wirachman, W., Wahyu, K., Nasir, R.M. and Aman, M.R. 2010. Aerodynamics prediction of Blended Wing Body (BWB) Unmanned Aerial Vehicle (UAV) using wind tunnel experimental approach. *Development and Commercialization*, Universiti Teknologi MARA, Malaysia.
- Xing, X.J., Yan, J.G. and Yuan, D.L. 2011. Augmented-stability controller design and its simulation for a UAV based on LQR theory. *Flight Dyn.*, 11: 98-121.
- Xu, Z.H., Wu, L.X., Chen, S.J. and Wang, Z. 2016. Method of engineering volume monitoring and calculation for open-pit mine from UAV images. *J. Northeastern Univ. Nat. Sci.*, 15: 413-429.
- Zhai, M.G. and Hu, B. 2021. Thinking to state security, international competition, and national strategy of mineral resources. *J.Earth Sci. Environ.*, 43(1): 1-11.
- Zhang, S.Y., Wang, R.H. and Dong-Mei, L.I. 2015. Earthwork calculation by CASS2008 square grid method. *Jilin Geol.*, 5(9): 35-47.



Isolation and Characterization of Polyvinyl Chloride (PVC) Degrading Bacteria from Polluted Sites of Gwalior City, M.P., India

Mohana Yadav*†, Sushil Manderia**, Shweta Singh* and Mohd. Adil Deva**

*School of Studies in Microbiology, Jiwaji University, Gwalior, M.P., India

**School of Studies in Botany, Jiwaji University, Gwalior, M.P., India

†Corresponding author: Mohana Yadav: yadavmohna29nov@gmail.com

Nat. Env. & Poll. Tech.

Website: www.neptjournal.com

Received: 11-03-2021

Revised: 27-04-2021

Accepted: 02-05-2021

Key Words:

Polyvinyl chloride
Degradation

Bacillus species

Micrococcus species

Enrichment culture

ABSTRACT

Plastic is harmful to nature and this issue could be solved by its degradation. Biodegradation of plastic waste utilizing bacterial strain is an eco-friendly approach. In this study, top bacterial strains that degrade the polymeric ingredient of the polymer polyvinyl chloride (PVC) were isolated and identified using a development culture procedure. For this investigation, soil from various contaminated areas was collected, which had abundant plastic waste. The biodegradation of polyvinylchloride films was studied using a liquid culture approach for six months. A couple of bacterial organism packs were then limited to emulsifying the commonly used PVC polymer in agar media. The PVC strain showed particular degradation and was chosen for further testing because the species *Bacillus* and *Micrococcus* were considered more credible. *Bacillus* and *Micrococcus* species have both proven the biodegradability of PVC based on the mean weight decrease, which was 0.873 for *Bacillus* species and 0.916 for *Micrococcus* species after a period of around six months. The FTIR study confirmed the breaking down by demonstrating the proximity of porosity and sensitivity of bacteria-infested polythene surfaces. *Bacillus* has a higher degradation potential than *Micrococcus* in our research.

INTRODUCTION

Plastic is artificially synthesized material particularly synthesized from oil-based materials called pitches (e.g., polythene and polypropylene). Currently, the use of plastic materials across the globe has increased particularly for food packing, dress, lodging, transport, building, clinical, and meat businesses. Plastics are preferred by people since they are light in weight, strong, and almost impenetrable. Plastic usage has risen steadily over the last three decades, with an average annual growth rate of 10% (Shristi Kumar et al. 2007). Plastics thrown in landfills remain there indefinitely because it contains compounds that are non-biodegradable and unsafe. At least 14 million tons of plastic end up in the ocean every year. Plastic debris is currently the most abundant type of litter in the ocean, making up 80% of all marine debris found from surface waters to deep-sea sediments (Spear et al. 1995).

Landfilling, incineration, and mechanical and chemical recycling are the most common methods for removing plastic waste nowadays (Peng et al. 2018). Landfilling is the primary method for removing plastic waste in many countries, particularly in developing countries, due to its ease of usage and low cost. By the way, the accumulated plastic garbage has poisoned a large area of land. Although

the recycling of plastic waste will reduce landfill demand and recover heat, we must also reduce the normal impacts of alternative incineration spreads, like dioxin models, carbon mono-oxide, nitrogen oxides, and other pollutants. Although mechanical recycling has become an excellent method for recycling and is used for thermoplastic waste recycling, the properties of most reused materials are completely disturbed after several cycles, and so market gauges are limited. Incineration, on the other hand, can reclaim monomers and various synthetic substances from plastic waste, but its success relies on the affordability of processes and the efficiency of catalysts (Rahimi & Garca 2017). Currently, between 9% and 12% of global plastic waste is recycled and burned, while the remaining 79% is discarded in landfills or the ecosystem. It is proposed that new ways for recycling plastic waste should be investigated (Geyer et al. 2017, Garcia & Robertson 2017). Despite the fact that various reviews and points of view on plastic biodegradation have been conveyed, they have largely focused on the biodegradation of a single plastic microbial variety PS (Ho et al. 2018), PE (Restrepo-Flórez et al. 2014), PUR (Cregut et al. 2013, Peng et al. 2018, Magnin et al. 2019), PP (Arutchelvi et al. 2008), and PET (Wei & Zimmermann 2017a, Kawai et al. 2019) Thorough examination concerning the biodegradation of all plastic materials are required (Wei & Zimmermann 2017b).

Advancement culture procedure is utilized to isolate the ideal objective species from different kinds of creatures that have existed together in nature and are normally expected to expand the overall quantities of a particular living being by advancing development, endurance (i.e., physiological rivalry) or spatial partition from other populace individuals (Tomita et al. 2004).

The goal of this study was to isolate and depict extreme polyvinyl chloride (PVC) degrading bacteria from polluted plastic waste far away from the study sites using a technique for improving the quality of collected samples and separating them from the strong mineral agar media converged with emulsified polyvinyl chloride from that point. Similarly, the study combined the initial characterization and assessment of the certain degradation perimeter of the selected bacterial strain using several experiment methods.

MATERIALS AND METHODS

Soil Sample Collection

Soil samples with plastic waste were gathered from different waste dumping sites around Gwalior city. Samples were collected in a sterile polythene pack and used to isolate bacteria that debase PVC.

Polymer Sample

The PVC film was obtained from the Gwalior plastic industry and Polyvinyl chloride resin (powder) was obtained from Supreme Pvt. Ltd. Malanpur, Industrial area, Gwalior (M.P.).

Isolation of Polyvinyl Chloride (PVC) Degrading Bacterial Strains through Enrichment Methods

Natural samples from different waste-rich plastic sites were gathered, comparably as washings of soil-made sure about plastic strips were utilized as inoculants. Every 1 to 2 g soil sample and 1 mL liquid sample was debilitated to 10 mL and 9 mL utilizing standard saline and utilized as inoculum in the 1 to 100 mL proportion of the MSV. The mineral salt improvement (MSV) was comparative with the late utilized by, yet sustained by a slight change in the enhancement biotin (20 mg) and B12 (10 mg). NH_4NO_3 , 1 g; KH_2PO_4 , 0.7 g; K_2HPO_4 , 0.7 g; NaCl, 0.005 g; $\text{FeSO}_4 \cdot \text{H}_2\text{O}$, 0.002 g; $\text{ZnSO}_4 \cdot 7\text{H}_2\text{O}$, 0.002 g; $\text{MnSO}_4 \cdot 4\text{H}_2\text{O}$, 0.001 g; Biotin, 20 mg; PVC, 1 g; PH-7. By then the flask was anguished at any rate for 14 days in the shaker brooding focus (Neolab, India). Following fourteen days 1 mL of supernatant was moved into the comparable new medium. Reiterated on various occasions over a comparative methodology. In each repeated upgrade culture, the centralization of PVC in the medium ceaselessly expanded from 0.1 to 0.5 per cent. Visual

assessment watched the advancement as an expansion in the turbidity of the lifestyle stock

Screening of Polyvinyl Chloride Degrading Bacteria Strain

A part of advancement culture was weakened satisfactorily with clean saline and spread on the supplement agar plates. Emerging was done at 30°C for 48 h. Singular colonies shaped on supplement agar were picked and tried for their capacity to develop on a strong MSV medium containing emulsified PVC, where the medium was braced with supplement and with no enhancement, for example, 0.1% yeast extricate and 0.1% glucose. The strong MSV medium containing emulsified PVC was set up by altering the system recently utilized by Ishigaki et al. (2000). The agar plates were set up by dissolving 0.1 g of polyvinyl chloride in 25 mL of tetrahydrofuran. The arrangement was then added to liquid MSV agar medium at 50°C to 60°C with delicate shaking and plates were poured right away. The covers of the plate were kept part of the way opened for at any rate 30 min to permit total dissipation of dissolvable. The tops of the plates were then supplanted. Unadulterated societies of the PVC debasing microscopic organisms were gotten by rehashed sub-refined of the segregated provinces on a similar medium. The chosen detaches were allotted with codes, for instance, DS-A, DS-B etc., for additional examination.

The chosen segregates were portrayed utilizing Bergey's manual of determinative bacteriology. A part of advancement culture was weakened satisfactorily with clean saline and spread on the supplement agar plates. Hatching was done at 30°C for 48 h. Singular provinces shaped on supplement agar were picked and tried for their capacity to develop on a strong MSV medium containing emulsified PVC, where the medium was braced with supplement and with no enhancement, for example, 0.1% yeast extricate and 0.1% glucose. The strong MSV medium containing emulsified PVC was set up by altering the system recently utilized by Ishigaki et al. (2000). The agar plates were set up by dissolving 0.1 g of polyvinyl chloride in 25 mL of tetrahydrofuran. The arrangement was then added to liquid MSV agar medium at 50°C to 60°C with delicate shaking and plates were poured right away. The covers of the plate were kept part of the way opened for at any rate 30 min to permit total dissipation of dissolvable. The tops of the plates were then supplanted. Unadulterated societies of the PVC debasing microscopic organisms were gotten by rehashed sub-refined of the segregated provinces on a similar medium. The selected isolates were allotted with codes, for instance, DS A, DS B, etc., for additional examination. The chosen segregates were portrayed utilizing Bergey's manual of determinative bacteriology.

RESULTS AND DISCUSSION

Identification, Isolation and Capability of Plastic Microorganisms Degrading from Soil

This investigation manages the isolation, distinguishing proof, and capacity of plastic microorganisms degrading from the soil. Identification of isolated bacterial strains was done by Bergey's manual followed by plate morphology,

physiological test and biochemical test (Table 1). During the biochemical examination, different sorts of changes are delivered by the microorganism. Through perceptible and minuscule investigations these bacterial strains were confined and portrayed. Polymer biodegradation was estimated in polymer and FTIR spectroscopy utilizing weight reduction. In this manner, microbial colonization term is a significant factor that impacts the period.

Table 1: Bacterial strain morphology by serial dilution method.

Characteristics of the colony and morphological tests								
Test	Isolate 1			Isolate 2				
Margin	Entire			Rhizoid				
Configuration	Circular			Circular				
Surface	Smooth			Granular Shiny				
Elevation	Convex			Slightly raised				
Opacity	Opaque			Opaque				
Pigment	Creamish yellow			White/Pale				
Cell shape	Rods			Rods				
Grams reaction	-			+				
Arrangement	Scattered			Short chains				
Size (µm)	3 – 4 µm			0.8 – 1.0µm				
Motility	+			+				
Spore(s)	-			+				
B. Physiological test								
Growth at pH			Growth at temperature			Growth on NaCl [%]		
pH	Isolate 1	Isolate 2	temperature	Isolate 1	Isolate 2	NaCl	Isolate 1	Isolate 2
pH 5	-	-	4°C	-	-	2.0	+	+
pH 6	+	+	10°C	-	-	4.0	+	+
pH 7	+	+	25°C	+	+	6.0	-	+
pH 8	+	+	30°C	+	+	8.0	-	+
pH 9	+	+	37°C	+	+	10.0	-	+
			42°C	+	+	13.0	-	+
			55°C	-	+			
C. Biochemical tests						D. Sugar fermentation		
Tests	Isolate 1	Isolate 2				Tests	Isolate 1	Isolate 2
Voges Proskauer test	-	-				Trehalose		
Indole test	-	-				Xylose		
Methyl red test	-	+				Mannose		
H ₂ S production	-	-				Sorbitol		
Citrate utilization	-	-				Lactose		
Gelatin hydrolysis	+	+				Galactose		
Production of Gas from glucose	-	-						
Oxidase test	+	+						
Catalase test	+	+						
E. Probable identification of isolates								
Isolates	Identified isolate							
Isolate 1	<i>Bacillus</i> sp.							
Isolate 2	<i>Micrococcus</i> sp.							

For the isolation of polyvinyl chloride degrading bacteria, soil samples taken from several contaminated sites were used as a microbial source. PVC's potential Degrading microbial strains from enriched sources were first grown on nutrient agar, resulting in high cell density and big, cultivable colonies (Fig. 1), then the obtained culture named DS A and DS B were transferred into minimal agar medium plates enriched with PVC resin for the carbon source and incubate for 15 days at 30°C temperature (Fig. 2).

PVC Film Degradation

After 1.5 long stretches of brooding, the plaques were watched. During the trial, following fourteen days of hatching, microbial settlement began showing up from the film's edges and secured the whole film inside the 6th seven-day stretch of brooding. Anyway, it was impractical to do the test after that because of the parchedness of the way of life media. After the sixth seven-day stretch of hatching the photos of the biofilms were taken. (Fig. 3 &4). Individual colonies were then examined to see whether they could grow on polyvinyl chloride (PVC) film in mineral salt agar media with and without replenishment (Fig. 5).

Result of Plastic Samples Being Degraded by Bacteria

The bacterial strains are disengaged and performed based on plainly visible and tiny assessment and biochemical tests with the capacity to debase. Bacterial secludes were visibly recognized by looking at state attributes, color, size shape,

edge, and minuscule assessment including recoloring grams to examine the recoloring conduct, shape, and cell plan and granulation, just as spore recoloring, biochemical testing of motility. There was an aggregate of 2 cutoff points disengaged from the dirt dumped from the Gwalior City dumping zone. Recommendations 2 separate were cleaned to tilt to the going with test and screened for plastic contamination by anguishing under 37°C temperature conditions in a 130 rpm alarming incubation center shaker for half year. The bacteria explicitly got from the above biochemical tests are the PIBWIN (Probabilistic Bacterial Identification) software *Bacillus* and *Micrococcus*. Sullied Polyethylene Plastic Waste (Kathiresan 2003). Gage polyethylene plastic (beginning weight), wash with refined sterile water by then and sprinkle with 70 per cent liquor. Plastic is embedded aseptically into the 100 mL Erlenmeyer that contains as much as 50 mL of both NB and TSB media. The media had immunized as much as 2 circles for isolated bacteria. By at that point, struggled at room temperature in a hatching community shaker, with a perturbation of 130 rpm for every month. Polyethylene plastic, conveyed for a colossal piece of a year, washed with refined sterile water and then washed with dried alcohol, evaluated by then (last weight). Picking the corruption level of polyethylene plastic by bacteria utilizing condition:

$$\% \text{ Degradation} = \frac{\text{Initial weight} - \text{Final weight}}{\text{Initial weight}} \times 100\%$$

To examine this, pre-assessed 1 cm wide circles arranged from polythene sacks were moved aseptically to a fixed carafe containing 50 mL of medium culture stock, self-rulingly immunized with different bacterial species. Control was kept up in a free creature medium, with plastic sheets. Two



Fig. 1: Isolated culture colonies on the nutrient agar plate.



Fig. 2: Isolated colonies of strain DS A and DS B on MSM PVC agar plate (After 15 days of incubation).



Fig. 3: Biofilm formed on PVC strip by strain A.



Fig. 4: Biofilm formed on PVC strip by strain B.

carafes had been held up for every treatment and left in a shaker. Following a half year of shaking, the plastic circles were assembled, washed totally utilizing refined water, dried in shade and then weighed for conclusive weight. The weight reduction for the polythene pack was settled from the data accumulated. The attempted species incorporated the *Bacillus* and the *Micrococcus*. *Bacillus* and *Micrococcus* were found in the half-year time period as being typically unique in degrading 12.7% of the bacteria and 8.4% liberated from PVC (Table 2) and graphical representation of % degradation of PVC film by *Bacillus* and *Micrococcus* sp. (Fig. 6).

FTIR Spectra of BOPP Film in Compost and Media, Before and After Degradation

Fourier Transform Infrared Spectroscopy test was utilized to see the movement of new handy parties or changes in the

Table 2: Consequence of plastic samples being corrupted by bacteria.

Isolates no.	Bacteria name	Initial wt [g]	Final wt [g]	Weight Loss in percentage after 6 month
1	<i>Bacillus</i>	1.0	0.873	12.7
2	<i>Micrococcus</i>	1.0	0.916	8.4
	Control	1.0	0.00	00



Fig. 5: Growth of strain B on polyvinyl chloride film placed on mineral salt media.

current utilitarian ties (Milstein et al. 1994); FTIR Spectra Plastic Material (Figs. 7, 8, and 9) show contamination of the plastic material FTIR spectra in the wake of being segregated from bacterial strain. The covering spectra inside the expanded structure, which clearly shows the movements watched, are likewise open to a relationship.

Figs. 7 and 9 show plastic corruption in made media, utilizing bacteria. Gathered and included soil-hawked plastic strips to the organized medium containing bacterial species *Bacillus* and *Micrococcus* which are viewed as less plastic degrading as an extra decomposer. In the medium, weight mishaps of polymer strips could be seen as a marker of biodegradation in landfills, or standard living space. Microorganisms have attacked the Polymer strips in the soil.

DISCUSSION

The present study deals with the Isolation and characterization of Polyvinyl chloride degrading bacteria from polluted sites. Different types of changes are observed by the isolates during morphological and chemical analysis. Another area examined has been the biodegradation of plastic by the liquid culture method. It is clear that the polymers to some extent can be degraded in the appropriate environment in the right concentration. Here, it was concluded that *Bacillus* show a

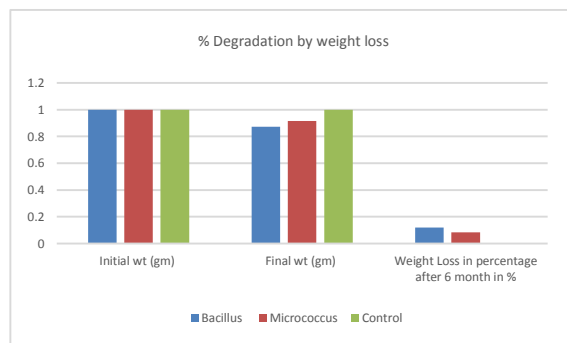


Fig. 6: Graph of PVC degradation after six months.

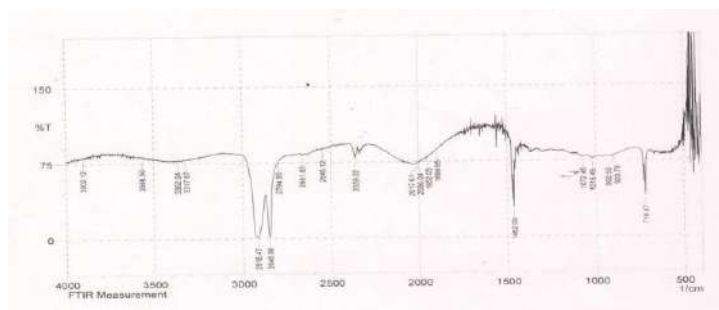


Fig. 7: FTIR plastic spectra before decay.

- Garcia, J.M. and Robertson, M.L. 2017. The future of plastics recycling. *Science*, 358: 870-872.
- Geyer, R., Jambeck, J. and Law, K.L. 2017. Production, use, and the fate of all plastics ever made. *Sci. Adv.*, 3: e1700782. doi: 10.1126/sciadv.1700782
- Ho, B.T., Roberts, T.K. and Lucas, S. 2018. An overview on biodegradation of polystyrene and modified polystyrene: The microbial approach. *Crit. Rev. Biotechnol.*, 38: 308-320. doi: 10.1080/07388551.2017.1355293
- Ishigaki, T., Kawagoshi Y., Ike, M. and Fujita, M. 2000. Abundance of polymer degrading microorganisms in sea-based soil waste landfill sites. *Joun. Basic. Microbiol.*, 90: 400-405
- Kathiresan, K. 2003. Polythene and plastic-degrading microbes in an Indian mangrove soil. *Rev. Biologica. Tropica*. 51: 629-633
- Kawai, F., Kawabata, T. and Oda, M. 2019. Current knowledge on enzymatic PET degradation and its possible application to waste stream management and other fields. *Appl. Microbiol. Biotechnol.*, 103: 4253-4268. doi: 10.1007/s00253-019-09717-y
- Magnin, A., Hoornaert, L., Pollet, E., Laurichesse, S., Phalip, V. and Avérous, L. 2019. Isolation and characterization of different promising fungi for biological waste management of polyurethanes. *Microb. Biotechnol.*, 12: 544-555. doi: 10.1111/1751-7915.13346
- Milstein O., Gersonde R., Huttermann A., Frund R., Feine H.J., Ludermann. D.H., Chen. J.M. and Meister J. J. 1994. Infrared and nuclear magnetic Resonance evidence of degradation in thermoplastic based on forest products. *Joun. of Environ. Polymer Degradat.*, 2: 137-15.
- Patil R. and Bagde S.U. 2012. Isolation of Polyvinyl chloride degrading bacterial strains from environmental samples using enrichment culture technique. *African Joun. of Biotechnol.*, 11(13): 7947-7956
- Peng, R.T., Xia, M.L., Ru, J.K., Huo, Y.X. and Yang, Y. 2018. Microbial degradation of polyurethane plastics. *Chin. J. Biotechnol.*, 34: 1398-1409.
- Rahimi, A. and García, J.M. 2017. Chemical recycling of waste plastics for new materials production. *Nat. Rev. Chem.*, 1: 0046.
- Restrepo-Flórez, J., Bassi, A. and Thompson, M.R. 2014. Microbial degradation and deterioration of polyethylene: A review. *Int. Biodeter. Biodegr.*, 88, 83-90. doi: 10.1016/j.ibiod.2013.12.014
- Sharma, J., Gurung, T., Upadhyay, A., Nandy, K., Agnihotri, P. and Mitra, A. K. 2015. Isolation and characterization of plastic degrading bacteria from soil collected from the dumping grounds of an industrial area. *Int. J. Adv. Innov. Res.*, 3: 2278-7844.
- Shristi Kumar, K., Hatha, A.A.M. and Christi, K.S. 2007. Diversity and effectiveness of tropical mangrove soil microflora on the degradation of polythene carry bags. *Int. J. Trop. Biol.*, 55: 777-786.
- Spear, L.B., Ainley, D.G. and Ribic, C.A. 1995. Incidence of plastic in seabirds from the tropical Pacific 1984-91: Relation with the distribution of species, sex, age, season, year, and body weight. *Mar. Environ. Res.*, 40: 123-141.
- Tomita, K., Nakajima, T., Kikuchi, Y. and Miwa, N. 2004. Degradation of poly (L-lactic acid) by a newly isolated thermophile. *Polym. Degrad. Stab.*, 84: 433-438.
- Wei, R. and Zimmermann, W. 2017a. Biocatalysis as a green route for recycling the recalcitrant plastic polyethylene terephthalate. *Microb. Biotechnol.*, 10: 1302-1307. doi: 10.1111/1751-7915.12714
- Wei, R. and Zimmermann, W. 2017b. Microbial enzymes for the recycling of recalcitrant petroleum-based plastics: How far are we? *Microb. Biotechnol.*, 10: 1308-1322. doi: 10.1111/1751-7915.12710



Tissue Repairing Activity of *Glycosmis pentaphylla* Leaf Extract on *Oreochromis mossambicus* Against Arsenic Induced Toxicity

U. V. Aswathy*, S. Abhirami**, S. R. Flanet Raj* and G. Prasad**†

*Department of Zoology, Nesamony Memorial Christian College, Marthandam, Tamil Nadu, India

**Department of Zoology, University of Kerala, Kariavattom, Thiruvananthapuram, Kerala, India

†Corresponding author: G. Prasad; probios1@gmail.com

Nat. Env. & Poll. Tech.

Website: www.neptjournal.com

Received: 16-04-2021

Revised: 03-05-2021

Accepted: 25-05-2021

Key Words:

Oreochromis mossambicus

Glycosmis pentaphylla

Karyolysis

Histopathology

ABSTRACT

Acute toxicity of arsenic to Tilapia (*Oreochromis mossambicus*) and tissue repairing activity of *Glycosmis pentaphylla* leaf extract and its histological impacts on gill, liver, and kidney tissues were evaluated. Fish were divided into six groups viz. control, group 1, group 2, group 3, group 4, and group 5. 4.87 ppm of NaAsO₂ was administered in group 1, group 3, and group 5. In group 3, after arsenic exposure, 2.5 g of leaf extract of *Glycosmis pentaphylla* per kg of fish food was added. In group 5, 5g of *G. pentaphylla* leaf extract per kg of fish food was added. In group 2, 2.5 g of leaf extract per kg of fish food was added and in group 4, 5g leaf extract per kg of fish food was added. The control group showed normal histology of the gill, liver, and kidney. The histological observations revealed the tissue repairing activities in group 2 fish's gill, liver, and kidney. These results revealed the protective and tissue repairing potential of *G. pentaphylla* as a feed supplement against NaAsO₂ induced toxicity.

INTRODUCTION

Arsenic (As) is a moderately toxic, naturally abundant element with no known nutritional or metabolic roles. The chemical form of arsenic in the surface water is dependent on redox potential, pH, and biological processes; however, the thermodynamically stable arsenate predominates in both freshwater and saltwater. Arsenic concentrations are much more variable in freshwater than in estuaries and oceans. Natural and anthropogenic sources can cause a high concentration of arsenic in freshwater without apparent effects on fish. Approximately 90% of As in fish is organic As, with arsenobetaine being the dominant species in marine fish; speciation in freshwater fish is much more variable. Except in the case of unusually high inorganic waterborne and food exposure, few environmental situations caused fish to lose their homeostatic regulatory mechanisms (McIntyre & Linton 2012). Bioaccumulation occurs when freshwater creatures, such as fish, are continuously exposed to low levels of As, particularly in the liver and kidney. As a result, As causes hyperglycemia, enzymatic activity depletion, acute and chronic toxicity, as well as immune system malfunction (BibhaKumari et al. 2016).

Arsenic exists in the environment as pentavalent (As⁵⁺, arsenate) and trivalent (As³⁺, arsenite) forms and arsenite has been considered to be more toxic when compared with

arsenate (Domingo 1995). On absorption, arsenic is stored in the liver, kidney, heart, and lungs. A lower amount of arsenic is observed in muscles and neuronal tissues (Klaassen 1996). The accumulation of arsenic in these tissues is associated with many disorders including cancer, diabetes, hepatotoxicity, neurotoxicity, and cardiac dysfunction. Acute arsenic poisoning is associated with nausea, vomiting, abdominal pain, and severe diarrhea (Ratnaik 2003).

Nature has provided a source of medicinal agents for thousands of years and an impressive number of modern drugs have been isolated from natural sources, many based on their use in traditional medicine (Cragg & Newman 2002). *Calotropis gigantea* is used in some parts of India for wound healing in combination with other plants (Ahmed et al. 2005, Chitme et al. 2004, Argal & Pathak 2005).

Stems and fruits of *Glycosmis pentaphylla* are used by medicinal practitioners in Bangladesh for the treatment of rheumatoid arthritis (Mohammed et al. 2010). Roots were used in India against facial inflammation, rheumatism, jaundice, and anemia (Oudhia et al. 2007). Leaf juice along with gingili oil is used internally as a vermifuge (Sivarajan & Balachandran 1994).

The aim of the present study was to examine the efficacy of tissue repairing activity of *G. pentaphylla* leaf extract on *Oreochromis mossambicus* against arsenic-induced toxicity.

MATERIALS AND METHODS

Experimental Design

The experimental fish *O. mossambicus* was identified from the Department of Zoology, University of Kerala. Fishes with an average body weight of 75.67 ± 5 g and an average length of 13 ± 1.65 cm were used for the experiment. The fishes were raised in aerated glass aquaria of about 50 L capacity and acclimatized for two weeks before the experiment. In this study, fishes were exposed to 4.87 ppm of waterborne NaAsO₂ which correspond to 10% of the 96 h LC50. The stock solution of 1000 ppm NaAsO₂ was prepared with deionized water and further diluted to the required concentrations. After the acclimation period, the fish were randomly divided into 6 groups containing 6 fishes in each group.

Collection of Plant Material

The fresh leaves of *G. pentaphylla* were collected from the University of Kerala campus, Kariavattom.

Preparation of Plant Extract

The collected plant leaves were washed, cut into small pieces, and air-dried in shade for 2 weeks. They are crushed into a fine powder using a grinder, which was used for the preparation of aqueous leaf extract using the Soxhlet apparatus.

Determination of the 96-h LC50 of Sodium Arsenite on *O. mossambicus*

An acute toxicity experiment was conducted to determine the 96-hour LC50 value for *O. mossambicus* exposed to sodium arsenite. Design and calculation for the acute toxicity experiment were done based on the procedure of Finney (1952). The LC50 values are derived from the curve drawn using working probits and log doses. Antilog of the dose corresponds to respective probit value (Finney 1952).

Experimental Diet Formulation

A Basal diet that included 43% crude protein was formulated by an Excel-based feed formulating software. One control and two experimental feeds were compounded by adding 0, 2.5, and 5 g.kg⁻¹ of leaf extract to the basal diet. Dry fishes were purchased from the local market, washed and dried in a hot air oven at 60°C to constant weight, and then powdered. All the other feed components were cleaned, powdered. The feed components were thoroughly mixed and made into a hard dough by adding a sufficient quantity of water. The dough was pressure cooked at 15 lb.sq inch⁻¹ for 15 minutes. Vit/min mix, leaf extract and cod liver oil were added to the dough and extruded in the form of noodles using an extruder having 1 mm diameter perforations. The pellets were dried

at room temperature and then dried in a hot air oven at 60°C for 6 hours and stored in airtight containers.

Histological Analysis

Fishes were slit open ventrally from head to the anus to expose the organs. The organs which include the gill, liver, kidney were removed and fixed in Bouin's solution. The specimens were processed as usual in the recognized method of dehydration, cleared in xylene, and processed for paraffin embedment. Thin sections of tissues were cut using a rotary microtome. They were stained with hematoxylin and eosin (H&E) stain. Finally, the slides were observed under a Labomed microscope at 100x and 400x magnification and photomicrographs were taken using MICAPS micro view software 3.7 version.

RESULTS AND DISCUSSION

In the present study, the 96-hour LC50 of *O. mossambicus* against NaAsO₂ was determined as 4.8790 ppm with 95% confidence intervals. The proximate analysis of the experimental feed revealed that the prepared feed consists of 43.57% of crude protein, 3.62% of crude fiber, 7.77% ether extract, 9.32% of total ash, 11.27% of moisture content, and 4319 kcal/kg of gross energy. No mortality was observed in any of the aquaria during the 30 days experimental period. Increased irritability, mucus secretion, color changes, swimming in the surface water were important notable alterations evidenced in the fish groups exposed to sodium arsenite.

H and E Staining

In the present study, the histological studies were carried out for the control, Arsenic and *G. pentaphylla* treated fish gill, liver and kidney.

Plate 1A-1C: Gill, Liver, Trunk kidney (X100). PL: Primary Lamellae; SL: Secondary Lamellae; D: Basal cells; H: Hepatocytes; S: Sinusoid; A; Pigment; P: Pancreas; BV: Blood Vessel; GL: Glomerulus; BS: Bowman's Space; CT:

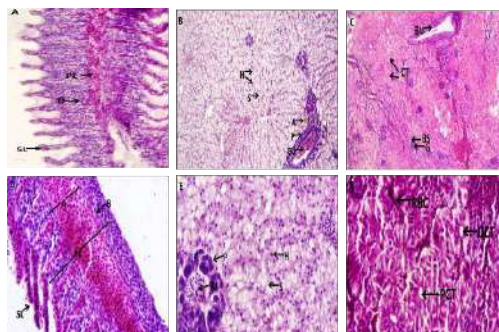


Fig 1: Plate 1: Control group: Fed with normal fish food.

Collecting Tubule; BV: Hepatic Portal Vein.

Plate 1D-1F: Gill, Liver, Trunk kidney (X400). PL: Primary Lamellae; SL: Secondary Lamellae; B: Basal cells; A: Central Venous Sinus; P: Pancreas; H: Hepatocytes; S: Sinusoid; BV: Blood Vessel; RBC: Red Blood Cells; DCT: Distal Convoluted Tubule.

Plate 2A-2C: Gill, Liver, Trunk kidney (X100). H: Hemorrhage; A: Curling; HY: Hyperplasia; N: Necrosis; LV: Lipid Vacuoles; A: Apoptosis; P: Pigment; CV: Central Vein; LI: Lymphocytic Infiltration; D, N: Degeneration and Necrosis.

Plate 2D-2F: Gill, Liver, Trunk kidney (X400). H: Hemorrhage; D, N: Desquamation and Necrosis; C: Curling; A: Aneurysm; D: Degeneration; HY: Hyperplasia; PN: Pyknotic nuclei; LV: Lipid Vacuoles; LI: Lymphocytic Infiltration; MC: Mild Congestion; K: Kupffer Cells; DH: Degenerated Hepatocytes; EL: Epithelial Lifting; V: Vacuole Formation.

Plate 3A-3C: Gill, Liver, Trunk kidney (X100). PL: Primary Lamellae; SL: Secondary Lamellae; H: Hepatocyte; S: Sinusoid; A: Pigment; P: Pancreas; G: Glomerulus; CT: Convoluted Tubules.

Plate 3D-3F: Gill, Liver, Trunk kidney (X400). EC: Epithelial Cell; M: Mucous Cell; SL: Secondary Lamellae; K: Kupffer Cells; P: Pancreas; S: Sinusoid; CT: Convoluted Tubule; GB: Glomerular Blood; CE: Capsular Endothelium; BC: Bowman's capsule.

Plate 4A-4C: Gill, Liver, Trunk kidney (X100). N: Necrosis; HP: Hyperplasia; C: Congestion; H: Hepatocyte; S: Sinusoid; CV: Central Vein; PA: Portal Area; V: Vacuole Formation; G: Glomerulus; M: Melanomacrophages.

Plate 4D-4F: Gill, Liver, Trunk kidney (X400). MC: Mucous Cell; RBM: Rupture Basement Membrane; HY: Hyperplasia; LV: Lipid Vacuoles; H: Hepatocyte; MC: Leucocyte Infiltration; CV: Cytoplasmic Vacuolation; V: Vacuole Formation; MC: Mild Congestion; K: Karyorrhexis.

Plate 5A-5C: Gill, Liver, Trunk kidney (X100). N: Necrosis; HP: Hyperplasia; C: Curling; S: Shortening of Secondary lamellae; SL: Malformed Secondary lamellae; H: Hepatocyte; S: Sinusoid; P: Pancreas; N: Mild Necrosis; K: Karyolysis; H: Severe Hemorrhage; N: Necrosis; V: Vacuole Formation; NR: Necrosis of renal cells.

Plate 5D-5F: Gill, Liver, Trunk kidney (X400). HP, HT: Hypertrophy, Hyperplasia; SL: Secondary Lamellae; H: Hemorrhage; NP: Necrotic Pancreas; AB: Apoptotic Body; N: Necrosis; LV: Lipid Vacuoles; LC: Multinucleated Large Cell; K: Karyorrhexis; KL: Karyolysis; V: Vein; N: Tubular Necrosis; C: Congestion.

Plate 6A-6C: Gill, Liver, Trunk kidney (X100). RBM: Rupture Basement Membrane; HP, HT: Hypertrophy, Hyper-

plasia; C: Congestion; LF: Lamellar Fusion; H: Hepatocyte with enlarged nuclei; BD: Bile Duct; LV: Lipid Vacuoles; H: Hemorrhage; N: Necrosis; TN: Tubular Necrosis; V: Vacuole Formation; IH: Intertubular Hemorrhages; D: Degeneration of cells. **Plate 6D - 6F: Gill, Liver, Trunk kidney (X400).** RBM: Rupture Basement Membrane; HP, HT: Hypertrophy, Hyperplasia; LF: Lamellar Fusion; H: Hepatocyte with ballooning degeneration; PD: Patchy degeneration; PN: Necrotic Pancreas; K: Kupffer cell.

Gill

The gill is the organ for respiration in fish. They are directly exposed to the external environment. So minute changes in the environment can directly affect the gills. The H and E stained gill sections of the control group showed normal histology. In group 1 (Fig. 2), the gills exposed to NaAsO₂ showed hemorrhage, curling of secondary lamellae, desquamation, necrosis, and hyperplasia of epithelial cells. Group 2 (Fig. 3) the fish fed with 2.5 g of leaf extract /kg of fish food showed normal primary lamellae, secondary lamellae, mucous cells, and epithelial cells. Group 3 (Fig. 4) fish exposed to 4.87 ppm of NaAsO₂ and fed with fish food mixed

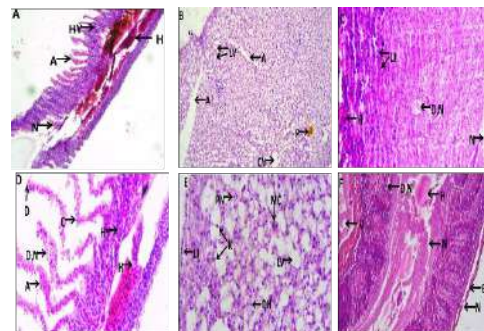


Fig. 2: Plate 2 Group 1: Treated with 4.87 ppm of NaAsO₂ and fed with normal fish food.

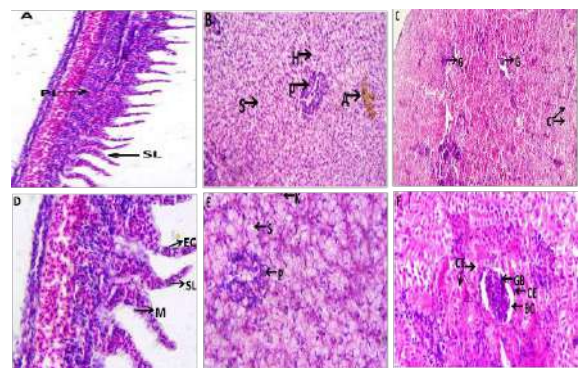


Fig. 3: Plate 3 Group 2: Fed with fish food mixed with 2.5 g of leaf extract /kg of fish food.

with 2.5 g of leaf extract showed tissue repairing activity such as decreased necrosis, hemorrhage, curling, and neofomed secondary lamellae. In group 4 (Fig. 5), the fishes were fed 5g of leaf extract per kg of fish meal, which resulted in secondary lamellae curling and shortening, necrosis, hyperplasia, and hypertrophy of epithelial cells, deformed secondary lamellae, and bleeding. Ruptured basement membrane, hypertrophy, hyperplasia, lamellar fusion, and congestion were seen in group 5 (Fig. 6) treated with NaAsO₂ and fed fish food with 5 g of leaf extract/kg of fish food.

Liver

The liver is the large vital organ in fish for detoxification, protein synthesis, and production of biochemicals necessary for digestion. Histological studies of the control fish liver fed with normal fish food showed normal pancreas, blood vessels, hepatocytes, sinusoids, and pigment. The NaAsO₂ exposed group 1 (Fig. 2) showed fatty infiltration, apoptosis, pigment, central vein, pyknotic nuclei, mild congestion, an abundance of kupffer cell, leucocyte infiltration, and degenerated hepatocytes. Group 2 (Fig. 3) fish fed with fish food mixed with 2.5 g of leaf extract/kg of fish food showed normal hepatocyte, sinusoids, kupffer cells, pancreas, and pigment. Group 3 (Fig. 4) fish treated with 4.87 ppm of NaAsO₂ and fed with fish food mixed with 2.5 g of leaf extract/kg of fish food showed a reduction in fatty infiltration, vacuoles, and decreased necrosis. Group 4 (Fig. 5) fish fed with fish food mixed with 5g of leaf extract showed mild necrosis, karyolysis, hepatocytes, sinusoids, apoptotic body, necrotic pancreas, and lipid vacuoles. Group 5 (Fig. 6) fish treated with 4.87 ppm of NaAsO₂ and fed with fish food mixed with 5 g of leaf extract showed hepatocytes with enlarged nuclei, necrotic bile duct and pancreas, pyknotic nuclei, patchy degeneration, and hepatic cells with ballooning degeneration.

Kidney

The kidney is responsible for excretion, removal of toxins and waste products from the body, and water balance maintenance. The control group (Fig. 1) fed with normal fish food showed normal glomerulus, bowman's space, collecting tubule, distal convoluted tubule, proximal convoluted tubule, and RBC. The NaAsO₂ exposed group 1 (Fig. 1) fish's kidney showed epithelial lifting, necrosis, vacuole formation, degeneration and necrosis of cells, hemorrhage, and lymphocytic infiltration. In group 2 (Fig. 3), the fish fed with 2.5 g of leaf extract/kg of fish food showed capsular endothelium, glomerular blood, bowman's capsule, and convoluted tubules. In group 3 (Fig. 4), fish treated with NaAsO₂ and fed with fish food mixed with 2.5 g of leaf extract showed distinct glomerulus, bowman's space, and convoluted tubules. Group 4 (Fig. 5) fed with fish food mixed with 5g of leaf extract

showed karyolysis, karyorrhexis, necrosis, large cells with multi nuclei, mild glomerular congestion, hemorrhage, vacuole formation, and necrosis of renal vein. In group 5 (Fig. 6), the fish treated with 4.87 ppm of NaAsO₂ and fed with fish food mixed with 5g of leaf extract showed tubular necrosis,

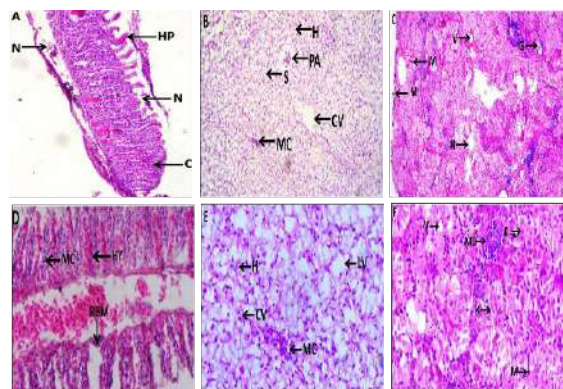


Fig 4: Plate 4 Group 3: Treated with 4.87 ppm of NaAsO₂ and fed with fish food mixed with 2.5g of leaf extract/kg of fish food.

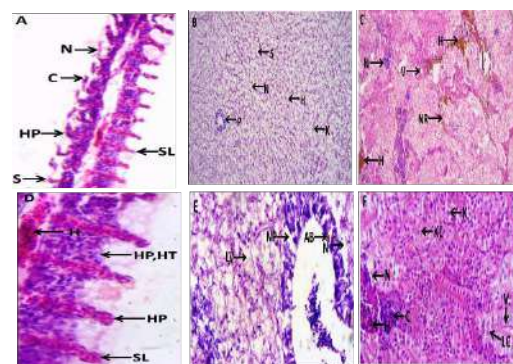


Fig 5: Plate 5 Group 4: Fed with fish food mixed with 5g of leaf extract/kg of fish food.

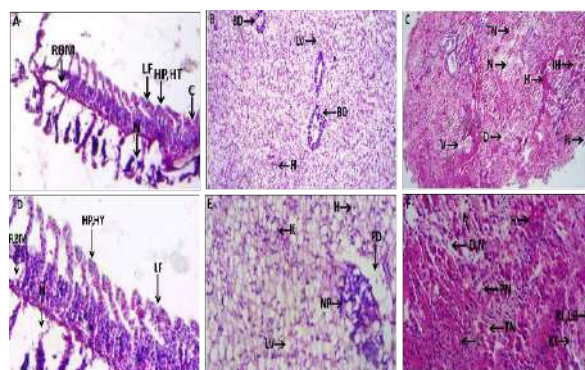


Fig 6: Plate 6 Group 5: Treated with 4.87 ppm of NaAsO₂ and fed with fish food mixed with 5 g of leaf extract/kg of fish food.

pyknotic nuclei, leucocytes, karyolysis, degeneration and necrosis, hemorrhage, intertubular hemorrhages, reduced lumen and loss of brush border in proximal convoluted tubules.

The control and various experimental groups are illustrated from plates 1 to 6 (Figs. 1 to 6). An increased level of damage is found in group 5 gill, liver, and kidney which is exposed to NaAsO_2 and fed with fish food mixed with 5g of *G. pentaphylla* leaf extract. This damage was higher when compared with fishes exposed to NaAsO_2 and fed with normal fish food (group 1). Tissue repairing activity is evident in group 3 gill, liver, and kidney that are exposed to NaAsO_2 and fed with fish food mixed with 2.5g of leaf extract/kg of fish food. 2.5 g of leaf extract with fish food has no effect on fish gill, liver, and kidney and it is shown in group 2. At the same time, 5g of leaf extract fed with fish food caused damage to fish gill, liver, and kidney but the intensity of damage is lesser than NaAsO_2 alone treated group.

DISCUSSION

The present study thus shows that NaAsO_2 is very toxic to fish even at sub-lethal and short-term exposure. It can seriously affect fish health by causing harmful changes in the structure of the gill, liver, and kidney and 2.5 g of leaf extract of *G. pentaphylla* can repair the damaged gill, liver, and kidney tissues to a certain extent.

Arsenic is an influential environmental contaminant that has been reported as one of the most alarming chemicals released into the aquatic ecosystem as a result of the geogenic and anthropogenic processes (Gonzalez et al. 2006). Fishes are very sensitive to changes in their environment and seem to be specifically vulnerable to arsenic toxicity (Hamilton & Buhl 1990), estimated LC_{50} values of arsenic in salmonids were found between 3 and 167 $\text{mg}\cdot\text{L}^{-1}$. The median lethal concentration (96 h; LC_{50}) of arsenic (NaAsO_2) was calculated as 28.22 ppm in a repeated semi-static test method by Ahmed et al. (2013). In the present investigation, the 96 h LC_{50} value of NaAsO_2 in *O. mossambicus* was found to be 48.790 ppm. This difference in acute toxicity might be due to the difference in species, size of the fish, and environmental conditions.

The gills are important organs for respiration, osmoregulation, acid-base balance, and nitrogenous waste excretion (Heath 1987). After exposure to metals, an excessive amount of mucus was observed over the gills. Stress caused by variations in the environmental conditions induces the proliferation of mucus cells and increased mucous secretion (Fernandes et al. 2007). The histopathological changes in the gill such as edema, epithelial necrosis, the fusion of secondary lamellae, hemorrhage at filaments, hypertrophy of epithelial cells, and sloughing off of epithelial surface are

the major effects reported in gills from the fish exposed to various types of pollutants (Mallatt 1985). Fishes exposed to nanometals, gills respond through the generation of edema with the lifting of gill lamellar epithelium by binding to Na^+/K^+ -ATPase, which results in osmotic imbalance and inhibits the entry of toxins (Al-Bairuty et al. 2013, Pane et al. 2004, Fanta et al. 2003, Stagg & Shuttleworth 1982). In the present study, the gill showed histological changes such as hemorrhage, curling of secondary lamellae, desquamation, necrosis, and hyperplasia of epithelial cells in *O. mossambicus* exposed to NaAsO_2 . These changes correlate with the above results.

The liver is the organ most associated with processes of detoxification and biotransformation, and due to its function, position, and blood supply, it is one of the organs most affected by contaminants in the water. The liver tissue of *O. mossambicus* showed focal lymphocytic and macrophage infiltration, congestion, vacuolization and shrinkage of hepatocytes, dilation of sinusoids, cloudy swelling, vacuolar degeneration, focal necrosis, and nuclear hypertrophy (Ahmed et al. 2013).

Vacuolation of hepatocytes has been shown as a common response to exposure of fish to a variety of different pollutants (Meyers & Hendricks 1985). In the present study, after the exposure to NaAsO_2 , the liver showed fatty infiltration, apoptosis, pigment, central vein, pyknotic nuclei, mild congestion, an abundance of Kupffer cell, leucocyte infiltration, and degenerated hepatocytes. These changes were similar to the previous results.

Next, the kidney is one of the major organs that express toxic effects. The kidney of the fish receives the largest proportion of postbranchial blood, and therefore renal lesions might be expected to be good indicators of environmental pollution (Ortiz et al. 2003). The exposure of fish to toxic agents such as pesticides and heavy metals induces histological alterations in several components of the trunk kidney (Kendall 1975, Kirubakaran & Joy 1988, Velmurugan et al. 2007). Similar to our observations, Gupta et al. (2016) displayed degeneration of renal tubules, a few necrotic cells in the hematopoietic tissue, and the presence of sinusoidal space in the Cu NPs treated *C. carpio*. They have also reported an increase in the space in between glomerulus and Bowman's capsule at higher dosage of NPs. In another study, alterations in Bowman's space, degeneration of renal tubule, vacuolation, and necrosis of hematopoietic tissue were reported by Kaya et al. (2016) in the kidney of *O. niloticus* after ZnO NPs exposure. In the present study epithelial lifting, necrosis, vacuole formation, degeneration and necrosis of cells, hemorrhage, and lymphocytic infiltration were observed in the trunk kidney tissues of fish exposed to 4.87 ppm of NaAsO_2 . The same changes were seen in the above results too.

G. pentaphylla (Gin Berry) is a plant possessing various medicinal properties. It is believed to have wound-healing properties. A study of hepatoprotective activity of *G. pentaphylla* in Swiss albino mice against paracetamol-induced toxicity reported that there was a decrease in total protein after administration of ethanolic extracts of *G. pentaphylla* (Nayak et al. 2010). Another study revealed the effect of various fractions of *G. pentaphylla* (Retz.) DC leaves on the cell cycle and apoptosis of breast cancer cells viz. MCF-7 and MDA-MB-231 (Shoja et al. 2015). In the present study, fish gill, liver, and kidney exposed to NaAsO₂ and fed with fish food treated with 2.5 g of leaf extract of *G. pentaphylla* have tissue repairing activity and 5g of the same leaf extract have toxic effects on fish. From the above results, it is evident that *G. pentaphylla* leaf extract has tissue repairing activity against arsenic exposed toxicity.

The histological changes in the current study were observed in the gill, liver, and kidney of *O. mossambicus*. It was indicative that the fishes were responding differently to the different quantities of *G. pentaphylla* leaf extract. The pathological changes were induced in the gill, liver, and kidney, but the extent of damage varies depending upon the dose of *G. pentaphylla*. Overall, this information confirms that histopathological alterations can be repaired to a certain extent by an appropriate quantity of *G. pentaphylla*. The result of this study had proven that 2.5g of leaf extract of *G. pentaphylla* alone caused no more damages in fish gill, liver, and kidney. But 5g of the same leaf extract caused damage to tissues of all organs. When 2.5g of leaf extract is fed with 4.87 ppm of NaAsO₂ exposed fish, it shows tissue repairing activity. 5g of leaf extract to the same amount of NaAsO₂ exposed fish caused severe damage than NaAsO₂ alone exposed fish. Hence, it shows that 2.5 g of leaf extract is ideal for tissue repairing activity for *O. mossambicus* exposed to NaAsO₂. An increased amount of this leaf extract alone can cause damage to tissues and if it is with NaAsO₂ it can cause severe damages to the tissues. The results of the present study suggest that treatment with leaf extract of *G. pentaphylla* has tissue repairing activity in *O. mossambicus* gill, liver, and kidney at a dose of 2.5g of leaf extract/kg of fish food after exposed to NaAsO₂. At the same time increase in the dose of this leaf extract to 5g, the NaAsO₂ exposed *O. mossambicus* gill, liver and kidney had toxic effects and caused severe damages to the fish tissues. Hence it is evident that 2.5g of leaf extract is ideal for tissue repairing in *O. mossambicus* after being exposed to NaAsO₂.

REFERENCES

- Ahmed, K., Habibullah, M., Elora, P., Mosammat, S.A. and Mohammad, S. K. 2013. Arsenic induced toxicity and histopathological changes in gill and liver tissue of freshwater fish, tilapia (*Oreochromis mossambicus*). *Experim. Toxicol. Pathol.*, 65(6): 903-909.
- Ahmed, K.K.M., Rana A.C. and Dixit V.K. 2005. *Calotropis* species (Asclepiadaceae): A comprehensive review. *Pharmacogn. Mag.*, 16: 48-52.
- Al-Bairuty, G.A., Shaw, B.J., Handy, R.D. and Henry, T.B. 2013. Histopathological effects of waterborne copper nanoparticles and copper sulfate on the organs of rainbow trout (*Oncorhynchus mykiss*). *Aquat. Toxicol.*, 126: 104-115.
- Argal, A. and Pathak, A.K. 2005. Antidiarrhoeal activity of *Calotropis gigantea* flowers. *Indian J. Nat. Prod.*, 21: 42-44.
- BibhaKumari, V., Amit, K.S., Jawaid, A.K., Ghosh, A., Hanping, W. and Gudrun, D. 2016. Toxicology of arsenic in fish and aquatic systems. *Environ. Chem. Lett.*, 15: 43-64.
- Chitme, H.R., Ghobadi, R., Chandra, M. and Kaushik, S. 2004. Studies on the anti-diarrhoeal activity of *Calotropis gigantea* R. Br. in experimental animals. *J. Pharm. Sci.*, 7: 70-75.
- Cragg, G.M. and Newman, D.J. 2002. In: Iwu M.M. and Wootton, J.C. (Eds.) *Drugs from Nature: Past Achievements, Future Prospects*. *Ethnomedicine and Drug Discovery*. Elsevier Science, Amsterdam, pp. 23-37.
- Domingo, J.L. 1995. Prevention by chelating agents of metal-induced developmental toxicity. *Reprod. Toxicol.*, 9: 105-113.
- Fanta, E., Rios, F.S., Romão, S., Vianna, A.C.C. and Freiberger S. 2003. Histopathology of the fish *Corydoras paleatus* contaminated with sublethal levels of organophosphorus in water and food. *Ecotoxicol. Environ. Safety*, 54: 119-130.
- Fernandes, C.A., Fontáfnhas-Fernandes, F. and Peixoto, M.A. 2007. Bioaccumulation of heavy metals in *Liza saliens* from the Esmeriz-Paramos coastal lagoon, Portugal. *Ecotoxicol. Environ. Safety*, 66(3): 426-431.
- Finney, D.J. 1952. Statistical method in a biological assay. *Statistical method in a biological assay*. Charles Griffin and Co. Ltd, UK, pp. 236-252.
- Gonzalez, H.O., Roring, J.A., Baldwin, W.S. and Bain, L.J. 2006. Physiological changes and differential gene expression in mummichogs (*Fundulus heteroclitus*) exposed to arsenic. *Aquat. Toxicol.*, 77(1): 43-52.
- Gupta, Y.R., Sellegounder, D., Kannan, M., Deepa, S., Senthilkumaran, B. and Basavaraju, Y. 2016. Effect of copper nanoparticles exposure in the physiology of the common carp (*Cyprinus carpio*): Biochemical, histological, and proteomic approaches. *Aquacult. Fish.*, 1: 15-23.
- Hamilton, S.J. and Buhl, K.J. 1990. Safety assessment of selected inorganic elements to fry Chinook salmon (*Oncorhynchus tshawytscha*). *Ecotoxicol. Environ. Safety*, 20(3): 307-324.
- Heath, A.G. 1987. *Water pollution and fish physiology*. CRC Press, Boca Raton, Florida. 245
- Kaya, H., Aydın, F., Gürkan, M., Yılmaz, S., Ates, M., Demir, V. and Arslan, Z. 2016. A comparative toxicity study between small and large size zinc oxide nanoparticles in tilapia (*Oreochromis niloticus*): Organ pathologies, osmoregulatory responses, and immunological parameters. *Chemosphere*, 144: 571-582.
- Kendall, M.W. 1975. Acute effect of methyl mercury toxicity in channel catfish kidney. *Bull. Environ. Contam. Toxicol.*, 13(5): 570-575.
- Kirubagarán, R. and Joy, K.P. 1988. Toxic effects of three mercurial compounds on survival, and histology of the kidney of the catfish, *Clarias batrachus*. *Ecotoxicol. Environ. Safety*, 15: 172-279.
- Klaassen, C.D. 1996. Heavy metals and heavy metal. *The Pharmacol. Basis Therap.*, 9: 1592-1614.
- Mallatt, J. 1985. Fish gill structural changes induced by toxicants and other irritants: A statistical review. *Can. J. Fish. Aquat.*, 42: 630-648.
- McIntyre, O. and Linton, T.K. 2011. Arsenic. *Fish Physiol.*, 31: 297-349.
- Meyers, T.R. and Hendricks, J.D. 1985. Histopathology. In: Rand, G.M. and Petrocelli, S.R. (eds), *Fundamentals of aquatic toxicology*, Hemisphere Publishing Corp, New York, pp. 283-331.
- Mohammed, R., Rowan, J., Azad, A.K., Syeda, S., Mahbubur, R., Anita, R.C., Rahima, B., Zubaida, K., Mohammad, S.H., Afsana, K. and Emdadullah, M. 2010. A randomized survey of medicinal plants used

- by folk medicinal practitioners in six districts of Bangladesh to treat rheumatoid arthritis. *Adv. Nat. Appl. Sci.*, 4: 124-127.
- Nayak, S.S., Jain, R. and Sahoo, A.K. 2010. Hepatoprotective activity of *Glycosmis pentaphylla* against paracetamol-induced hepatotoxicity in Swiss albino mice. *Pharm. Biol.*, 49(2): 111-117.
- Ortiz, J.B., De Canales, M.L.G. and Sarasquete, C. 2003. Histopathological changes induced by lindane (-HCH) in various organs of fishes. *Sci. Mar.*, 67(1): 53-61.
- Oudhia, M., Gungordu, A., Kucukbay, F.Z. and Guler, R.E. 2006. Monitoring the effects of water pollution on *Cyprinus carpio* in Karakaya dam Lake Turkey. *Ecotoxicology*, 15(2): 157-169.
- Pane, E.F., Haque, A. and Wood, C.M. 2004. Mechanistic analysis of acute, Ni-induced respiratory toxicity in the rainbow trout (*Oncorhynchus mykiss*): An exclusively branchial phenomenon. *Aquat. Toxicol.*, 30: 11-24.
- Ratnaik, R.N. 2003. Acute and chronic arsenic toxicity. *Postgrad. Med. J.*, 79(933): 391-396.
- Shoja, M.H., Neetinkumar, D.R., Pawan, G., Nayak, K.K., Srinivasan, R.C. and Mallikarjuna, R. 2015. *Glycosmis pentaphylla* (Retz.) DC arrests the cell cycle and induces apoptosis via caspase-3/7 activation in breast cancer cells. *J. Ethnopharmacol.*, 168: 50-60.
- Sivarajan, V.V. and Balachandran, I. 1994. *Ayurvedic Drugs and Their Plant Sources*. Oxford and IBH Publishing, London, UK, pp. 527-544.
- Stagg, R.M. and Shuttleworth, T.J. 1982. The effects of copper on ionic regulation by the gills of the seawater-adapted flounder (*Platichthys flesus* L.). *J. Comp. Physiol.*, 149: 83-90.
- Velmurugan, B., Selvanayagam, M., Cengiz, E.I. and Unlu, E. 2007. The effects of fenvalerate on different tissues of freshwater fish, *Cirrhinus mrigala*. *J. Environ. Sci. Health B*, 42(2): 157-163.



Preparation, Characterization and Application of Sulphuric Acid-Treated Soursop (*Annona muricata* L.) Seeds Powder in the Adsorption of Cu(II) Ions

Megat Ahmad Kamal Megat Hanafiah*, Nurul Amira Abu Bakar*, Waheeba A. Al-Amrani**, Shariff Ibrahim***†, Nik Ahmad Nizam Nik Malek**** and Ali H. Jawad***

*Faculty of Applied Sciences, Universiti Teknologi MARA, 26400, Jengka, Pahang, Malaysia

**Department of Chemistry, Faculty of Science, Ibb University, Ibb, Yemen

***Faculty of Applied Sciences, Universiti Teknologi MARA, 40450, Shah Alam, Selangor, Malaysia

****Department of Biosciences, Faculty of Science, Universiti Teknologi Malaysia, 81310, Skudai, Johor, Malaysia

†Corresponding author: Shariff Ibrahim; sha88@uitm.edu.my

Nat. Env. & Poll. Tech.
Website: www.neptjournal.com

Received: 12-02-2021

Revised: 25-05-2021

Accepted: 07-06-2021

Key Words:

Adsorption
Annona muricata
Copper
Isotherm
Kinetics

ABSTRACT

This work presented the adsorption of Cu(II) ions using agriculture waste coming from soursop (*Annona muricata* L.) seeds. The chemical treatment performed on *Annona muricata* L. seeds was carried out using 1.0 M H₂SO₄ solutions. The Fourier-transform infrared (FTIR) spectrophotometer, scanning electron microscope coupled with energy dispersive X-ray (SEM-EDX), pH of point-zero-charge (pH_{PZC}), and pH_{slurry} analyses were done to characterize the surface properties of the adsorbent. Experimental conditions such as contact time, adsorbent dosage, pH, and initial Cu(II) ion concentrations, all of which could affect Cu(II) ions adsorption, were studied. The adsorption kinetics was successfully described by the pseudo-second-order model. The Langmuir and Freundlich models were applied to interpret the Cu(II) ions' adsorption at equilibrium. The isotherm data fitted well with the Freundlich model and the maximum adsorption capacity was 187.83 mg.g⁻¹ based on the Langmuir model.

INTRODUCTION

The discharge of heavy metal ions into water bodies from different industrial effluents, such as metal plating, petrochemicals, batteries, chemicals, paints, and pesticide production has caused serious global environmental issues (Zafar et al. 2020). Heavy metal ions can enter the food chain, accumulate in the aquatic ecological system, and cause harmful effects on humans, plants, animals, and the environment (Afroze & Sen 2018). Copper (Cu) at trace level is essential to human life. In tiny quantities, the metal is crucial in maintaining the health of an individual. In contrast, prolonged exposure to surplus Cu(II) ions causes serious illnesses to humans, such as kidney and liver damage, headaches, increased heart rate, and schizophrenia (Al Zabadi et al. 2018). The World Health Organization (WHO) and Environmental Protection Agency (EPA) have set the maximum allowable concentrations of 1.3 and 2.0 mg.L⁻¹, respectively for Cu(II) ions in drinking water (Zafar et al. 2020). Therefore, it is crucial to remove Cu(II) ions from industrial effluents to avoid environmental catastrophe.

Numerous techniques have already been implemented to reduce Cu(II) ions concentration in aqueous solutions,

including chemical precipitation, coagulation, adsorption, electrolysis, ultrafiltration, ion exchange, reverse osmosis, and advanced oxidation. Adsorption in particular is much preferred due to the high and fast removal efficiency, relatively low cost, and design simplicity (Karimi et al. 2019). Synthetic materials such as polymers have been developed as adsorbents for heavy metals removal. However, prolonged and extensive use of synthetic adsorbents will lead to secondary pollutants in the form of by-products (Wang et al. 2020). Therefore, the use of natural adsorbents derived from renewable biomaterials with a lower risk to the environment has gained more attention (Li et al. 2007, Wang et al. 2020).

Annona muricata L. fruit or soursop has many functional groups such as -OH (hydroxyl), -NH₂ (amino), -COOH (carboxylic acid), C-O-C (ether), and aromatic rings (Sawant & Dongre 2014, Anaya Esparza & Montalvo-González 2020), which play a dynamic role in the metal binding mechanisms. These functional groups originate from chemical components such as lignin, cellulose, hemicellulose, fatty acids, lipids, sugars, and proteins (Menzes et al. 2019). Untreated and chemically treated *A. muricata* L. seeds have been used as an adsorbent to remove pollutants, such as Tartrazine dye (Fauzia et al. 2015), Rhodamine B dye (Cairdir et al. 2015),

and heavy metal ions (Oboh & Aluyor 2008, Kurniawan et al. 2014) from their aqueous solutions.

Oboh & Aluyor (2008) studied the adsorption of four heavy metal ions using untreated *A. muricata* L. seeds powder under batch mode. The removal efficiencies were 77.6, 68.5, 56.4, and 40.6% for Cu(II), Ni(II), Zn(II), and Pb(II) ions, respectively. Kurniawan et al. (2014) performed the removal of Pb(II) and Cu(II) ions using HNO₃-treated *A. muricata* L. seeds powder. The results showed that the maximum adsorption capacities for Pb(II) and Cu(II) ions were 5.58 and 4.16 mg.g⁻¹, respectively. Fauzia et al. (2015) reported a maximum adsorption capacity of 23.63 mg.g⁻¹ for Tartrazine dye using HCl-treated *A. muricata* L. seeds powder. Another study done by Cairdir et al. (2015) found the maximum adsorption capacity of 53.37 mg.g⁻¹ for Rhodamine B using HCl-treated *A. muricata* L. seeds powder. However, it could be noticed that the untreated, HCl and HNO₃-treated *A. muricata* L. seeds did not show a high adsorption capacity towards heavy metal ions and dyes. Therefore, there is a need to search for another acid treatment method that enhances the adsorption performance of *A. muricata* L. seeds.

In this work, the applicability of *A. muricata* L. seeds powder treated with 1.0 M sulphuric acid solution as an adsorbent to remove Cu(II) ions from aqueous solutions has been investigated. Characterization of the surface of *A. muricata* L. seeds powder using the Fourier-transform infrared (FTIR) spectrophotometer, scanning electron microscope coupled with energy dispersive X-ray (SEM-EDX), pH of point-zero-charge (pH_{PZC}) and pH_{slurry} were performed. Furthermore, the physiochemical parameters such as contact time, pH, adsorbent dosage, and the initial Cu(II) concentration were studied. The rate of adsorption and determination of maximum adsorption capacity of *A. muricata* L. seeds powder was determined using kinetics and isotherm models, respectively.

MATERIALS AND METHODS

A. muricata L. fruits were bought from an orchard in Temerloh, Malaysia. The fruits were cut and the black seeds were collected. The seeds were rinsed thoroughly with deionized water several times before being dried in an oven (Electro-thermal Blast Drying Oven, China) at 90°C overnight. After drying, the seeds were crushed using a mechanical crusher into a powdered form. To remove the fat, a pre-treatment was done by mixing 20 g of the powder with 200 mL of hexane (ratio of 1:10 (w/v) seeds powder to hexane) for 16 h at 28°C. The hexane-treated powder was filtered and dried at 80°C for 3 h and was abbreviated as AMSP. The preparation of treated AMSP using sulphuric acid (98% w/w; Loba Chemie, India) was performed to enhance the adsorption properties

of AMSP. The dried AMSP was mixed with 100 mL (1.0 M H₂SO₄) for 2 h, washed thoroughly with deionized water until the final pH reached near 7. Finally, the powder was dried at 80°C overnight and was labeled SA-AMSP.

Characterization

The functional groups, surface properties and elemental composition of the AMSP and SA-AMSP, and the Cu(II) ions-loaded SA-AMSP were inspected using a Fourier-transform infrared (FTIR) spectrophotometer (PerkinElmer, Spectrum 100, USA) and a scanning electron microscope (SEM, Carl Zeiss SMT, Germany) coupled with energy dispersive X-ray (EDX, Oxford Instrument, UK) spectrometer. The pH_{slurry} was determined by mixing 0.10 g of SA-AMSP with 50 mL of distilled water. The mixture was left for 24 h at 29°C. The mixture was filtered using a Whatman filter paper (No. 42), and the final pH in the supernatant was measured using a pH meter. The pH_{PZC} determination of SA-AMSP was performed as follows: firstly, a series of 50 mL (0.01 M) NaCl solutions at different initial pH (pH_i) of 2 to 10 were prepared in 100 mL conical flasks. Then, 0.10 g of SA-AMSP was added to the NaCl solutions, and the mixture was stirred using a magnetic stirrer for 24 h. The mixture was filtered using a Whatman filter paper (No. 42), and the final pH of the solution (pH_f) was recorded. The plot of pH_i-pH_f versus pH_i was constructed, and the curve that intercepted the pH_i axis represented the pH_{PZC} value of SA-AMSP.

Batch Adsorption Process

Batch adsorption experiments were performed in stoppered conical flasks, stirred using a magnetic stirrer (120 rpm) at 302 K for 120 min, and the volume of Cu(II) ions was kept at 50 mL. A stock solution of Cu(II) concentration (1000 mg.L⁻¹) was prepared by dissolving the measured amount of copper nitrate salt, Cu(NO₃)₂.3H₂O (Merck, Germany) in deionized water. Then, the stock solution was diluted to prepare the required Cu(II) concentrations. The pH varied from 2 to 6, and the SA-AMSP dosage changed from 0.02 to 0.10 g depending on the effects of pH and adsorbent dosage to adsorb 20 mg.L⁻¹ of Cu(II) ions, respectively. Drops of 0.1 M NaOH and 0.1 M HCl solutions were added to adjust the pH of the solutions using a pH meter (EUTECH Instruments, USA). Two different concentrations of 10 and 20 mg.L⁻¹ were used in the kinetics study. The Cu(II) concentrations varied from 10 to 60 mg.L⁻¹ in the isotherm study at pH 6. The mixture was filtered using a Whatman filter paper (No. 42) and the residual concentration of Cu(II) ions was measured using an atomic absorption spectrophotometer (AAS, PerkinElmer, PinAAcle 900T model, USA). All adsorption experiments were done in duplicates, and the results were

presented as the average. The removal of Cu(II) ions was calculated using the following equation:

$$\% \text{ Removal} = \frac{C_o - C_e}{C_o} \times 100 \quad \dots(1)$$

where, C_o and C_e represent the Cu(II) concentration before and after adsorption ($\text{mg}\cdot\text{L}^{-1}$), respectively. The amount of Cu(II) ions adsorbed on SA-AMSP at equilibrium was calculated using the following equation:

$$q_e = \frac{V(C_o - C_e)}{m} \quad \dots(2)$$

where V is the volume of adsorbate (L), q_e is the amount of Cu(II) ions adsorbed ($\text{mg}\cdot\text{g}^{-1}$) at equilibrium and m is the weight of SA-AMSP (g). The non-linear trial-and-error methods were performed using the Solver add-in (Microsoft Excel) to calculate the parameters of adsorption kinetics and isotherm models. The chi-square (χ^2) test expressed in Eq. 3 and the regression coefficient (R^2 , Eq. 4) were used to compare the best fit of the kinetics and isotherm models:

$$\chi^2 = \sum \frac{(q_e^{\text{exp}} - q_e^{\text{cal}})^2}{q_e^{\text{cal}}} \quad \dots(3)$$

$$R^2 = 1 - \frac{\sum (q_e^{\text{exp}} - q_e^{\text{cal}})^2}{\sum (q_e^{\text{exp}} - q_e^{\text{mean}})^2} = \frac{\sum (q_e^{\text{exp}} - q_e^{\text{cal}})^2}{\sum (q_e^{\text{cal}} - q_e^{\text{mean}})^2 + \sum (q_e^{\text{cal}} - q_e^{\text{exp}})^2} \quad \dots(4)$$

Where, q_e^{exp} and q_e^{cal} are the amount of Cu(II) ions adsorbed ($\text{mg}\cdot\text{g}^{-1}$) at equilibrium determined from Eq. 2 and the model after using the Solver add-in, respectively; and q_e^{mean} ($\text{mg}\cdot\text{g}^{-1}$) is the mean of q_e^{exp} values.

RESULTS AND DISCUSSION

Characterization

Fig. 1A shows *A. muricata* L. seeds while Figs. 1B and 1C show the powder of AMSP and SA-AMSP, respectively. SA-AMSP had a darker color compared to AMSP. The FTIR spectra of AMSP, SA-AMSP, and Cu(II)-loaded SA-AMSP are shown in Fig. 2. The FTIR spectrum of AMSP displayed a number of characteristic bands at 2500 to 3600 cm^{-1} , 3286 cm^{-1} , 3008 cm^{-1} , 2923 cm^{-1} , 1744 cm^{-1} , 1639 cm^{-1} , 1460 cm^{-1} , 1020 cm^{-1} , and 722 cm^{-1} , representing the -COOH group, -OH and -NH groups, =C-H in aromatic rings, asymmetric -CH₂ groups, COO⁻ groups, -C=N groups, C=C stretching, C-O-C, and C-H bending (out of plane) of aromatic rings, respectively. The FTIR spectrum of raw AMSP also revealed the abundance of carboxyl, hydroxyl, amino and aromatic groups. The same observations were reported using other

adsorbents (Fauzia et al. 2015, Hanafiah et al. 2018). Meanwhile, the SA-AMSP spectrum showed several shifts in the wavenumbers or reduction and increment of the intensity of the peaks. The spectrum of Cu(II)-loaded SA-AMSP displayed almost the same characteristic bands of SA-AMSP. However, the percentage transmittance of some functional at 1744 and 1021 cm^{-1} had decreased in the Cu(II)-loaded

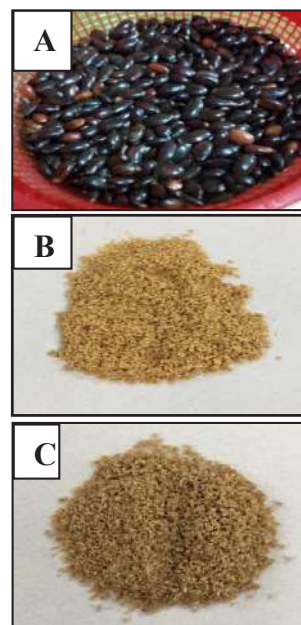


Fig. 1: (A) Raw *A. muricata* L. seeds, (B) *A. muricata* L. seed powder washed with hexane (AMSP), and (C) Sulphuric acid-treated *A. muricata* L. seed powder (SA-AMSP).

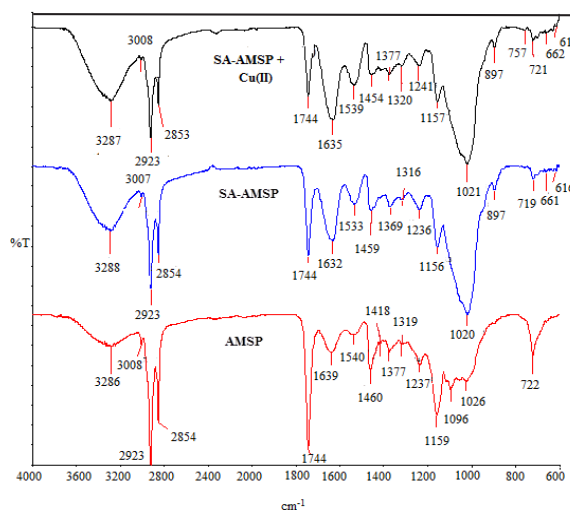


Fig. 2: FTIR spectra of raw AMSP, SA-AMSP (before Cu(II) adsorption), and Cu(II)-loaded SA-AMSP.

SA-AMSP. We have observed shifts in wavenumber from 1632 to 1635 cm^{-1} , 1533 to 1539 cm^{-1} , and 1459 to 1454 cm^{-1} . Based on this observation, it can be concluded that the $-\text{COO}^-$, $-\text{OH}$, $-\text{NH}$ and aromatic rings were the active adsorption sites and that Cu(II) ions adsorption could occur possibly through the ionic attraction and weak electrostatic attraction.

The SEM and EDX images of AMSP, SA-AMSP, and Cu(II)-loaded SA-AMSP are shown in Fig. 3 (A to F). Fig. 3A shows that the AMSP has an irregular surface, and it lacks porous structure and contains essential metal ions (Mg^{2+} , Na^+ and K^+) on its surface (Fig. 3B). After the acid treatment, there was no obvious difference in the surface structure between SA-AMSP (Fig. 3C) and AMSP. However, the essential metal ions were no longer detected by the EDX due to the dissolution of these ions in the acid (Fig. 3D).

The presence of Cu(II) ions on SA-AMSP was confirmed by the SEM-EDX images as shown in Fig. 3 (E and F). The $\text{pH}_{\text{slurry}}$ of SA-AMSP was 5.46. The acidic nature of SA-AMSP was due to the carboxylic acid groups as confirmed by the FTIR spectrum. The pH_{PZC} plot is shown in Fig. 4, with a value of 4.50. At $\text{pH} > \text{pH}_{\text{PZC}}$, the SA-AMSP surface would have a more negative charge, consequently favoring the adsorption of Cu(II) ions.

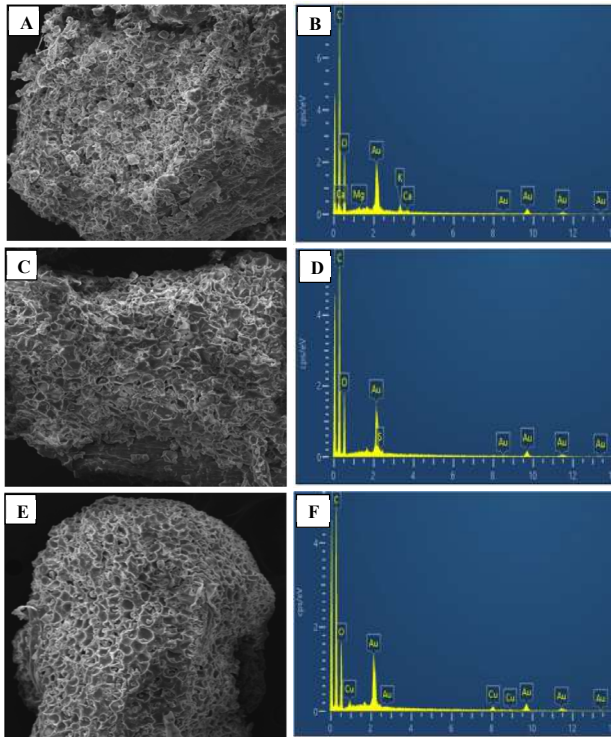


Fig. 3: SEM images (200x magnification) and EDX images of AMSP (A, B), SA-AMSP (C, D) and Cu(II)-loaded SA-AMSP (E, F); respectively.

Batch Adsorption Process

Effects of pH and SA-AMSP dosage: The effects of pH on Cu(II) uptake are shown in Fig. 5. The amount of Cu(II) adsorbed on SA-AMSP increased with increasing pH of the solution from 2 to 6. At pH 2, the q_e value was very low due to the strong electrostatic repulsion between the protonated functional groups in SA-AMSP and Cu(II) ions. However, at $\text{pH} > 2$, the deprotonated functional groups such as carboxyl in SA-AMSP increased gradually, and they could readily adsorb Cu(II) ions. Therefore, the subsequent adsorption experiments were conducted at pH 6.

Fig. 6 shows the effects of SA-AMSP dosage on the adsorption of Cu(II) ions. The amount of Cu(II) adsorbed onto the SA-AMSP decreased with increasing SA-AMSP dosage. It may be attributed to the overlapping or aggregation of the adsorption sites at higher adsorbent dosages, consequently reducing the exposed surface area for adsorption of adsorbates (Anbalagan et al. 2016, Mansur et al. 2020). Thus, 0.02 g of SA-AMSP was chosen for the subsequent kinetics and isotherm experiments.

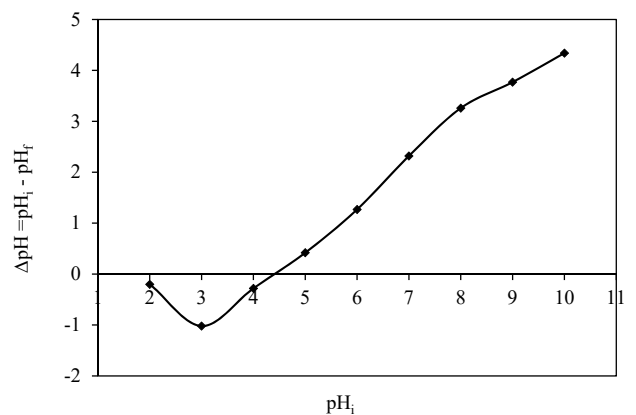


Fig. 4: The pH_{PZC} plot for SA-AMSP.

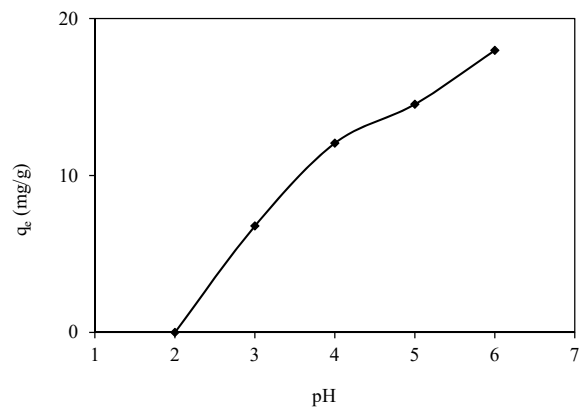


Fig. 5: Effect of solution pH on Cu(II) ions adsorption.

Adsorption kinetics: The changes in the amount of Cu(II) adsorbed on SA-AMSP as a function of time at two different initial concentrations of Cu(II) ions (10 and 20 mg.L⁻¹) are shown in Fig. 7. The plots showed three succeeding stages during the adsorption process, including (i) initial rapid adsorption process (0 to 5 min) where up to 70 and 86% of Cu(II) ions were adsorbed onto SA-AMPSP for 10 and 20 mg.L⁻¹, respectively, due to the high availability of the active adsorption sites; (ii) slow adsorption process (5 to 20 min) where only 13% and 10% of Cu (II) ions were adsorbed onto SA-AMPSP for 10 and 20 mg.L⁻¹, respectively, because of the stiff competition among Cu(II) ions for the remaining active adsorption sites; and (iii) dynamic equilibrium adsorption process (20 to 120 min) where only a small change in the amount of Cu(II) ions adsorbed was observed as the active adsorption sites were fully saturated. Besides that, the amount of Cu(II) ions adsorbed increased with increasing initial Cu(II) concentration. This could be due to the higher driving force at higher Cu(II) ions concentrations, making them capable of overcoming the mass transfer resistance between the adsorbent and liquid phase (Hanafiah et al. 2018).

The adsorption data of Figure 7 were analyzed using the non-linear and linear kinetics models to further investigate the rate of Cu(II) ions adsorption. The non-linear pseudo-first-order (PFO) and pseudo-second-order (PSO) models were given by Eqs. (5) and (6) (Ho & McKay 1998), respectively.

$$q_t = q_e (1 - e^{-k_1 t}) \quad \dots(5)$$

$$q_t = \frac{q_e^2 k_2 t}{(1 + k_2 q_e t)} \quad \dots(6)$$

The linear PFO and PSO kinetic equations were presented by eqs. (7) and (8), respectively:

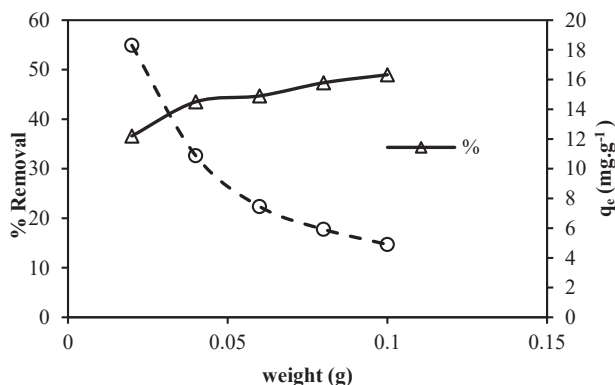


Fig. 6: Effect of SA-AMSP dosage on Cu(II) ions adsorption.

$$\log(q_e - q_t) = \log q_e - \frac{k_1}{2.303} t \quad \dots(7)$$

$$\frac{t}{q_t} = \frac{1}{k_2 q_e^2} + \frac{1}{q_e} t \quad \dots(8)$$

where q_e and q_t refer to the amount of Cu(II) ions adsorbed at equilibrium (mg.g⁻¹) and at the time, t , respectively. The k_1 and k_2 represent the overall rate constants of PFO (min⁻¹) and PSO (g.mg.min⁻¹) models. The kinetic parameters obtained from the non-linear and linear equations as well as the R^2 and χ^2 values are reported in Table 1. For the PFO model, the calculated values of q_e did not match the experimental ones while the values of R^2 were lower and the values of χ^2 were higher compared with the PSO model. This indicated the non-validity of the PFO model to explain the kinetics behavior of the adsorption process. A satisfactory agreement was obtained between the calculated and experimental values of q_e with the values of R^2 being close to unity. The χ^2 values were much lower, confirming the validity of the PSO to the adsorption process.

Isotherm studies: The adsorption capacity at the equilibrium state (q_e , mg.g⁻¹) for SA-AMSP was plotted against the equilibrium concentration of Cu(II) ions (C_e , mg.L⁻¹) as shown in Figure 8. The equilibrium adsorption capacity increased with the increase in the initial Cu(II) ions concentration possibly due to the increased rate of mass transfer of adsorbates on the adsorbent (Anbalagan et al. 2016). The adsorption isotherm data obtained in Figure 8 were analyzed using the non-linear

Table 1: Kinetic parameters of Cu(II) ions adsorption on SA-AMSP.

Models	Parameters	10 mg.L ⁻¹	20 mg.L ⁻¹	
Pseudo-first order	q_e^{exp} (mg.g ⁻¹)	12.80	22.22	
	q_e^{cal} (mg.g ⁻¹)	12.17	20.88	
	k_1 (min ⁻¹)	0.390	0.495	
	R^2	0.749	0.348	
	χ^2	0.062	0.206	
	Pseudo-second order	q_e^{cal} (mg.g ⁻¹)	1.36	2.59
k_1 (min ⁻¹)		0.004	0.008	
R^2		0.373	0.679	
Non-linear		q_e^{cal} (mg.g ⁻¹)	12.51	21.36
		k_2 (g.mg.min ⁻¹)	0.086	0.073
		R^2	0.922	0.626
Linear	χ^2	0.019	0.117	
	q_e^{cal} (mg.g ⁻¹)	12.74	22.27	
	k_2 (g.mg.min ⁻¹)	0.050	0.022	
	R^2	0.999	0.998	

Langmuir (Langmuir 1918) (Eq. 9) and Freundlich models (Freundlich 1906) (Eq. 10).

$$q_e = \frac{Q_{\max} K_L C_e}{1 + K_L C_e} \quad \dots(9)$$

$$q_e = K_F C_e^{1/n} \quad \dots(10)$$

where Q_{\max} is the theoretical maximum adsorption capacity (mg.g^{-1}), K_L is the Langmuir isotherm constant related to the strength of adsorbent-adsorbate interaction (L.mg^{-1}), K_F and n are the Freundlich constants related to the adsorption capacity and intensity, respectively. The values of the Langmuir and Freundlich constants were calculated from the non-linear regression for each model (Table 2).

Fig. 8 shows that the experimental data of the adsorption of the Cu(II) ions on SA-AMSP had a better fit to the Freundlich model than the Langmuir model. Furthermore, the Freundlich model's strong representation of the experimental data was supported by higher R^2 and lower χ^2 values, both of which are measures of goodness of fit. This indicated the non-homogeneity of active sites on the surface of the SA-AMSP adsorbent. The adsorption capacity of SA-AMSP calculated from the Langmuir model was 187.83 mg.g^{-1} , which recorded a higher capacity compared with the other adsorbents reported in the literature (Table 3). Therefore, SA-AMSP has an excellent potential application to treat wastewater containing Cu(II) ions.

CONCLUSION

Sulphuric acid-treated *A. muricata* L seeds powder (SA-AMSP) showed an excellent ability to remove Cu(II) ions from aqueous solutions using the batch mode adsorption technique. Based on the FTIR spectrum of SA-AMSP, the detected functional groups such as carbonyl (C=O), hydroxyl

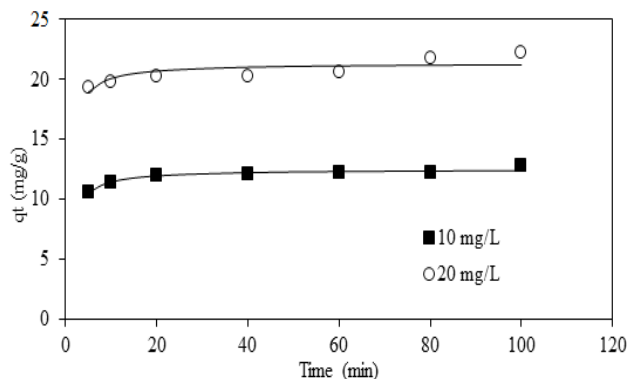


Fig. 7: Effects of initial concentration and contact time on Cu(II) ions adsorption.

(-OH), the carboxylic acid (-COOH), amino (-NH₂), ether (C-O-C), and aromatic groups acted as the active sites for the Cu(II) ions. The attachment of Cu(II) ions on SA-AMSP was confirmed by the EDX images. The maximum adsorption capacity was found to be 187.8 mg.g^{-1} , suggesting that the SA-AMSP could be a low-cost and environmentally friendly adsorbent for treating Cu(II)-containing wastewaters.

REFERENCES

- Afroze, S. and Sen, T.K. 2018. A Review on heavy metal ions and dye adsorption from water by agricultural solid waste adsorbents. *Water Air Soil Pollut.*, 229: 225.
- Al Zabadi, H., Sayeh, G. and Jodeh, S. 2018. Environmental exposure assessment of cadmium, lead, copper, and zinc in different Palestinian canned foods. *Agric. Food Sec.*, 7: 50.
- Anaya Esparza, L.M. and Montalvo-González, E. 2020. Bioactive compounds of soursop (*Annona muricata* L.) fruit. In: Murthy, H. and Bapat, V. (eds.), *Bioactive Compounds in Underutilized Fruits and Nuts*. Reference Series in Phytochemistry. Springer, Cham, pp. 1-13.

Table 2: Langmuir and Freundlich parameters for Cu(II) ions adsorption onto SA-AMSP at 302 K.

Isotherm models	
Non-linear Langmuir model	
Q_{\max} (mg.g^{-1})	187.8
K_L (L.mg^{-1})	0.010
R^2	0.997
χ^2	0.234
Non-linear Freundlich model	
K_F (L.mg^{-1})	2.570
N	0.820
R^2	0.999
χ^2	0.038

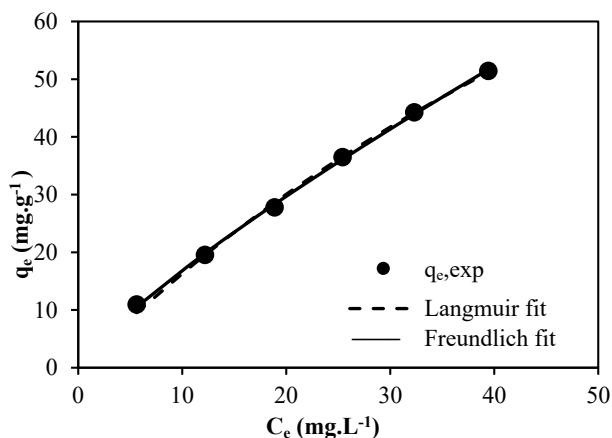


Fig. 8: Langmuir and Freundlich isotherm plots for Cu(II) ions adsorption onto SA-AMSP.

Table 3: Maximum adsorption capacities of Cu(II) ions by different adsorbents.

Adsorbent	Q_{max} (mg.g ⁻¹)	pH	Temperature (K)	Equilibrium time	References
H ₂ SO ₄ -treated <i>A. muricata</i> L. seed powder	187.83	6.0	302	40	Present study
Bentonite supported nanoscale zero-valent iron	52.63	4.0	298	50	Zhang and Qiu (2019)
NaOH-treated- rice husk	48.84	NA	280	30	Zafar et al. (2020)
Na ⁺ -treated Pisha Sandstone	21.37	5.0	303	60	Wang et al. (2020)
Pisha Sandstone	19.49	5.0	303	60	Wang et al. (2020)
NaOH-treated rubber leaf powder	14.97	4.0	300	60	Wan Ngah and Hanafiah (2008)
Sulphuric acid-treated peanut husk	10.15	4.0	298	60	Li et al. (2007)
Sawdust	6.58	4.0	298	60	Li et al. (2007)
Montmorillonite-biochar composite	6.92	4.0	303	30	Cai et al. (2019)
HNO ₃ -treated <i>A. muricata</i> L. seed powder	5.54	4.0	NA	60	Kurniawan et al. (2014)

NA: Not available

- Anbalagan, K., Kumar, P.S. and Karthikeyan, R. 2016. Adsorption of toxic Cr(VI) ions from aqueous solution by sulphuric acid-modified *Strychnos potatorum* seeds in batch and column studies. *Desal. Water Treat.*, 57(27): 12585-12607.
- Cai, Y., Du, Y., Wang, Y., Song, J., Liu, B., Zhang, C. and Qiu, M. 2019. Adsorption of copper ions in aqueous solution by montmorillonite-biochar composite. *Nat. Environ. Pollut. Technol.*, 18(4): 1201-1209.
- Cairdir, Z., Furqani, F., Zein, R. and Munaf, E. 2015. Utilization of *Annona muricata* L. seeds as potential adsorbents for the removal of rhodamine B from aqueous solution. *J. Chem. Pharm. Res.*, 7(4): 879-888.
- Fauzia, S., Furqani, F., Zein R. and Munaf, E. 2015. Adsorption and reaction kinetics of tartrazine by using *Annona muricata* L seeds. *J. Chem. Pharm. Res.*, 7(1): 573-582.
- Freundlich, H.M.F. 1906. About the in solutions. *J. Phys. Chem.*, 57: 385-470.
- Hanafiah, M.A.K.M., Mohd Jamaludin, S.Z., Khalid, K. and Ibrahim, S. 2018. Methylene blue adsorption on Aloe vera rind powder: Kinetics, isotherm, and mechanisms. *Nat. Environ. Pollut. Technol.*, 17(14): 1055-1064.
- Ho, Y.S. and McKay, G. 1998. Comparison of chemisorption kinetic models applied to pollutant removal on various sorbents. *Process Saf. Environ. Prot.*, 76: 332-340.
- Karimi, S., Yarak, M.T. and Karri, R.R. 2019. A comprehensive review of the adsorption mechanisms and factors influencing the adsorption process from the perspective of bioethanol dehydration. *Renew. Sust. Energ. Rev.*, 107: 535-553.
- Kurniawan M.I., Abdullah, Z., Rahmadani A., Zein R. and Munaf, E. 2014. Isotherm and kinetic modeling of Pb(II) and Cu(II) uptake by *Annona muricata* L. seeds. *Asian J. Chem.*, 26(12): 3588-3594.
- Langmuir, I. 1918. The adsorption of gases on plane surfaces of glass, mica, and platinum. *J. Am. Chem. Soc.*, 40: 1361-1403
- Li, Q., Zai, J., Zhang, W., Wang, M. and Zhou, J. 2007. Kinetic studies of adsorption of Pb(II), Cr(III), and Cu(II) from aqueous solution by sawdust and modified peanut husk. *J. Hazard Mater.*, 141: 163-167.
- Mansur, N.F., Hanafiah, M.A.K.M. and Ismail, M. 2020. Pb(II) adsorption onto urea treated *Leucaena leucocephala* leaf powder: Characterization, kinetics, and isotherm studies. *Nat. Environ. Pollut. Technol.*, 19(11): 311-318.
- Menzes, E.G.T., Oliviera, E.R., Carvalho, G.R., Guimaraes, I.C., and Queiroz, F. 2019. Assessment of chemical, nutritional and bioactive properties of *Annona crassiflora* and *Annona muricata* wastes. *Food Sci. Technol.*, 39(2): 662-672.
- Oboh, O.I. and Aluyor, E.O. 2008. The removal of heavy metal ions from aqueous solutions using soursop seeds as biosorbent. *Afr. J. Biotechnol.*, 7(24): 4508-4511.
- Sawant, T.P. and Dongre, R.S. 2014. Bio-chemical compositional analysis of *Annona muricata*: A miracle fruit's review. *Int. J. Univers. Pharm. Bio Sci.*, 3(2): 82-104.
- Wan Ngah, W.S. and Hanafiah, M.A.K.M. 2008. Biosorption of copper ions from dilute aqueous solutions on base treated rubber (*Hevea brasiliensis*) leaves powder: kinetics, isotherm, and biosorption mechanisms. *J. Environ. Sci.*, 20: 1168-1176.
- Wang, X., Cui, Y., Peng, Q., Fan, C., Zhang, Z. and Zhang, X. 2020. Removal of Cd(II) and Cu(II) from aqueous solution by Na⁺-Modified Pisha Sandstone. *J. Chem.*, 28: 579.
- Zafar, S., Khan, M.I., Lashari, M.H., Khraisheh, M., Almomani, F., Mirza, M.L., and Khalid, N. 2020. Removal of copper ions from aqueous solution using NaOH-treated rice husk. *Emerg. Mater.*, 3: 857-870.
- Zhang, J. and Qiu, M. 2019. Adsorption kinetics and isotherms of copper ion in aqueous solution by bentonite supported nanoscale zero-valent iron. *Nat. Environ. Pollut. Technol.*, 18(1): 269-274.



Preparation of Copolymer of 2-Methacryloyloxyethyl dimethyl-3-sulfonic Acid Propylammonium Hydroxide and 3-(Methacryloyloxy) Propyltrimethoxysilane and Its Dye Adsorption Properties

Fenfeng Xi*, Liping Liang*, Weishou Tan*, Yanyan Dong*, Linshuang Yu*, Huiting Ma*, Gaosheng Yue****† and Xu Meng*(**)(***) †

*College of Life Science, College of Textile and Garment, Shaoxing University, Shaoxing, China

**Key Laboratory of Clean Dyeing and Finishing Technology of Zhejiang Province, Shaoxing University, Shaoxing, China

***Zhejiang Sub-center of National Carbon Fiber Engineering Technology Research Center, Shaoxing, China

****Zhejiang Transchem Chemical Co. Ltd., Hangzhou, 311215, China

†Corresponding author. Gaosheng Yue; yuegaosheng2012@163.com, Xu Meng; mengqiaoshen@163.com

Nat. Env. & Poll. Tech.
Website: www.neptjournal.com

Received: 26-02-2021

Revised: 25-04-2021

Accepted: 01-05-2021

Key Words:

Dyeing wastewater
Treatment
Adsorption
Dyes
Polymer gel

ABSTRACT

While printing and dyeing bring us huge economic benefits, it also brings us huge challenges. Printing and dyeing will produce a large amount of wastewater, and the treatment of printing and dyeing wastewater has always been a concern. This work uses 2-methacryloyloxyethyl dimethyl-3-sulfonic acid propyl ammonium hydroxide, 3-(methacryloyloxy) propyl trimethoxysilane, and N, N'-methylene bispropylene as raw materials, and a photoinitiator is used to initiate polymerization under an ultraviolet lamp to prepare a copolymer gel. Taking the aqueous solution containing soap yellow as simulated dye wastewater, the adsorption performance of the prepared polymer for dyes was investigated. An ultraviolet spectrophotometer was used to investigate the effects of adsorption time, initial dye concentration, and polymer dosage on the adsorption performance. The performance test results show that the prepared polymer has high adsorption and removal efficiency for dyes containing soap yellow simulation, and has a potential application value.

INTRODUCTION

While printing and dyeing bring us huge economic benefits, it also brings us huge challenges (Ajmal et al. 2014). The printing and dyeing process of textile factories in traditional industries is a major discharger of industrial sewage (Liu et al. 2019). Most of the pollutants in the sewage come from various dyes, slurries, surfactants, auxiliaries, acids, and alkalis in the textile manufacturing process (Khan & Lo 2016). Most of these additives are toxic and harmful, with complex impurities, diverse ingredients, and obvious differences in water quality, threatening the ecological environment and human health, and they are very difficult to deal with industrial pollution (Mittal et al. 2016).

For many years, people have been committed to the treatment of dye wastewater, and many methods have been discussed around how to quickly, effectively, scientifically, and environmentally solve the problem of dye wastewater. Treatment methods include coagulation precipitation method (Chethana et al. 2016, Dotto et al. 2019), membrane separation technology (Şen et al. 2018, Hosseini et al. 2018),

ultrasonic oxidation method (Zia et al. 2019, Wang et al. 2019), photocatalytic oxidation method (Stock et al. 2000), micro electrolysis method (Han et al. 2016), biological treatment method (Paz et al. 2017) and adsorption method (Yagub et al. 2014), etc. Each of these methods has certain shortcomings, such as complicated procedures, a high proportion of chemical costs, complex technology, and a large number of impurities after treatment (Monier et al. 2010, Varaprasad et al. 2017). And with the development of chemical fibers and the increasing requirements for finishing after printing and dyeing, a large number of refractory organics such as pulp, new dyes, and chemical auxiliaries enter the textile printing and dyeing wastewater, posing a serious challenge to the traditional wastewater treatment process. Therefore, the development of new materials for dye treatment has become a research hotspot.

At present, people have conducted a lot of research on new materials for dye treatment, and have developed adsorbents with different properties and uses. Mittal et al. (Mittal et al. 2021) focused on the preparation of xanthan gum-based novel hydrogel nanocomposites via chemical crosslinking

with graphene oxide for highly efficient adsorption of crystal violet dye from contaminated wastewater. With unique structure and properties, the composite is a great candidate for cationic dyes removal from wastewater. Vigneshwaran et al. (Vigneshwaran et al. 2021) successfully fabricated sulfur tethered adsorbent of Tapioca peel (S@TP) biochar and utilized it for the removal of organic dyes such as Malachite Green (MG) and Rhodamine B (RhB) from water. The newly fabricated bio-mass could be visualized as a capable adsorbent for the water/wastewater treatment process since the S@TP matrix possesses high removal and reusable efficiency towards dye molecules. Hydrogel has the characteristics of high separation efficiency and high selectivity in adsorption, and it is an adsorption method with good application prospects (Chaudhary et al. 2021, Binaeian et al. 2020, Marrakchi et al. 2020). The research results provide a feasible method for the separation of soluble dyes from dye waste liquid, and also provide a new idea for industrial wastewater purification.

In the work, 2-methacryloxyethyl dimethyl-3-sulfonic acid propylammonium hydroxide, 3-(methacryloxy) propyltrimethoxysilane, and N, N'-methylene bis acrylamide cross-linking agent are used as raw material, and a photoinitiator is used to initiate polymerization under ultraviolet light to prepare a copolymer gel. Fig. 1 shows the schematic diagram of the preparation of copolymer gel. Use scanning electron microscope, Fourier transforms infrared spectrometer, thermogravimetric analyzer, and other instruments to characterize the surface morphology and chemical composition of the product. Taking the aqueous solution containing soap yellow as simulated dye wastewater, the adsorption performance of the prepared polymer for dyes was investigated. An ultraviolet spectrophotometer was used to investigate the effects of adsorption time, initial dye concentration, and polymer dosage on the adsorption performance. The performance test results show that the prepared polymer has high adsorption and removal efficiency for dyes containing soap yellow simulation, and has a potential application value.

MATERIALS AND METHODS

Materials

2-methacryloxyethyl dimethyl-3-sulfonic acid propyl ammonium hydroxide, 3-(methacryloxy) propyl trimethoxysilane, and N, N'-methylene bispropylene were procured from Aladdin Industrial Inc., Shanghai, China.

Preparation of Copolymer Gel

Add 0.5 g of 2-methacryloxyethyl dimethyl-3-sulfonic acid propylammonium hydroxide, 0.05 g of N, N'-methylenebisacrylamide, and 0.05 g of 3-(Methacryloxy) propyltrimethoxysilane, dissolved in 30 mL of distilled water, irradiated under UV light for about 2 h. A colloidal gel solid can be obtained, which is then dried in a freeze dryer to obtain the final product.

Characterization

After spraying a gold film with an ion sputtering instrument, the microstructure of the samples was characterized by an SNE-15000X scanning electron microscope (SEC, Korea). The composition of the polymer was analyzed by the Fourier transform infrared spectrometer (FTIR, Japan IRPrestige-21) with a wavelength range of 500-4000 cm^{-1} . The thermal stability was demonstrated via the thermogravimetric/differential thermal comprehensive analyzer (TG, Japan TG/DTA6300), which heated from 25°C to 700°C with a heating rate of 10°C.min⁻¹ in an air atmosphere. The UV absorption of the dye was tested by a UV spectrophotometer (UV2600, Japan).

Effect of Adsorption Time on Dye Adsorption Performance

The polymer was used to adsorb 5 mg.L⁻¹ soap yellow dye solution, and the UV-visible spectrophotometer was used to perform adsorption on the solution after 10 min, 20 min, 30

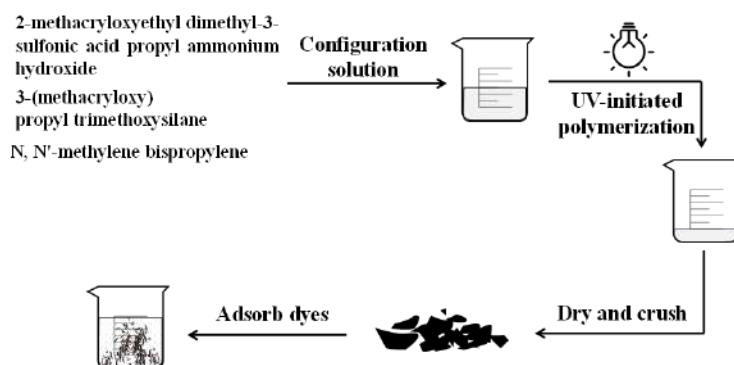


Fig. 1: Schematic diagram of the preparation of copolymer gel.

min, 40 min, 50 min, 60 min, 120 min, 240 min, 480 min, etc. The purpose of this experiment is to see how adsorption duration affects dye adsorption performance.

Effect of Initial Dye Concentration on Adsorption Performance

The aqueous solution containing soap yellow dye was used as simulated dye wastewater, and the initial concentrations were 0.4, 1.2, 5.0, and 10.0 mg.L⁻¹ dye respectively. The effect of the initial concentration of dye on the adsorption performance was investigated.

Impact of Polymer Dosage on Adsorption Performance

An aqueous solution containing 5 mg.L⁻¹ of soap yellow dye was used as simulated dye wastewater. Under the condition of immersion for the same time, the effect of polymer dosage on adsorption performance was investigated.

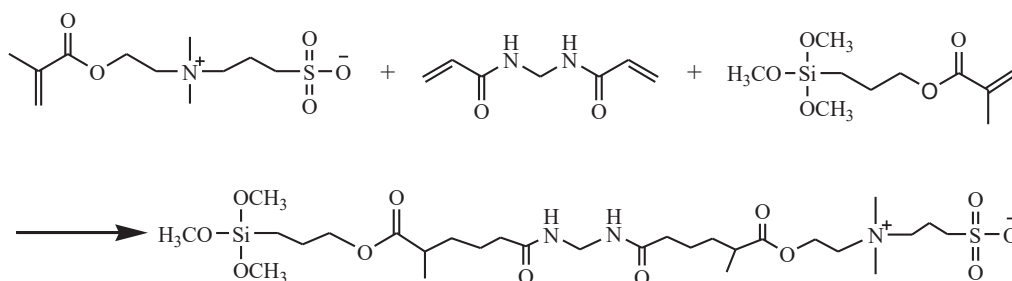
RESULTS AND DISCUSSION

FTIR Spectrum Analysis

The infrared spectrum of the prepared polymer product is shown in Fig. 2. The absorption peak at 615 cm⁻¹ in the spectrum may be due to the out-of-plane bending vibration of C-H. The absorption peak near 1196 cm⁻¹ is presumably caused by the vibration of the C-C framework or the stretching vibration of C-O. The absorption peak at 1713 cm⁻¹ may be the vibration of C=O, and the absorption peak at 2961 cm⁻¹ should be the contraction vibration of -CH₂. From the experimental results, there are a variety of functional groups on the polymerized hydrogel. The existence of these functional groups makes the adsorption performance more excellent and has a better effect on the adsorption of dyes in dye wastewater.

Surface Morphology Analysis of Synthetic Polymers

The surface morphology is characterized by a scanning



Scheme 1 polymerization equation of copolymer gel.

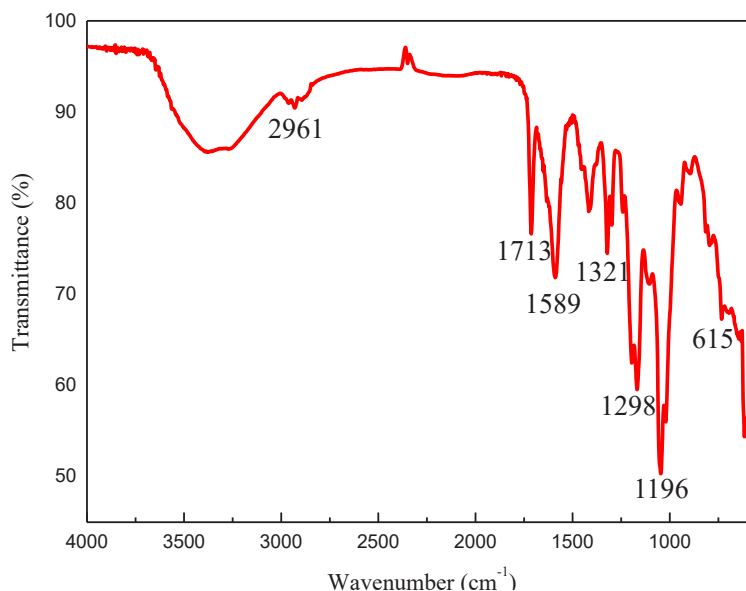


Fig. 2: FTIR spectrum of synthetic polymer.

electron microscope, which can directly observe the fine structure of the material surface. To prevent changes in the structure and pore morphology of the gel, the polymerized gel is freeze-dried, and the water in the gel is directly sublimated to avoid the decomposition of the gel and the destruction of the gel structure. Generally, the adsorption phenomenon occurs on the surface of the adsorbent or inside the pores of the fibers. The physical structure of the adsorbent, such as the pore size and specific surface area, has a greater influence on the adsorption. Fig. 3 is an electron micrograph of synthetic polymer. The results show that the appearance of the polymer particles with pores is rough. The prepared polymer has a uniform spatial structure and a relatively large specific surface area, which greatly improves its adsorption performance. These pores can increase the contact area with the dye and can more effectively improve the adsorption performance of the product.

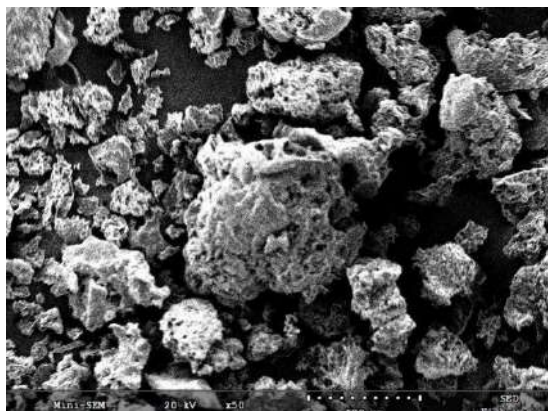


Fig. 3: Surface topography of synthetic polymer.

Thermogravimetric Analysis

When investigating the thermal stability of the polymer, the initial temperature is set to 40°C, the final temperature is 600°C, and the selected gas is air. Fig. 4 shows the thermogravimetric analysis of the synthetic polymer. It can be seen from the results that the mass loss rate of the gel particles is relatively low at 40-120 °C. The mass change is relatively stable between 120°C and 270°C, and the loss rate is relatively small; while the mass of the polymer over 280°C begins to increase. The range is reduced, and the material is decomposed in a large amount. When the temperature reaches 360°C -600°C, the material mass loss efficiency is small and tends to be flat. It can be seen from the results that the synthesized polymer has good thermal stability before 280°C.

Effect of Adsorption Time on Dye Adsorption Performance

Configure a 1.2 mg.L⁻¹ soap yellow dye solution, measure 5 mL of the dye solution, and a polymer dosage of 0.015 g to study the effect of different adsorption times on the dye adsorption performance. The time gradient is set to 10 min, 20 min, 30 min, 40 min, 50 min, 60 min, 120 min, 240 min, 480 min, the results are shown in Fig. 5. The results showed that the adsorption capacity of the synthetic polymer to the soap yellow dye increased with time. In a relatively short period of time, the increase in the amount of adsorption is larger and the adsorption efficiency is fast; with the increase of time, the increase in the amount of adsorption gradually tends to be flat and the adsorption rate becomes slower. This is mainly due to the attraction between the synthetic polymer and the dye molecule so that the anionic dye is adsorbed on the polymer at a faster speed. As the adsorption sites on the synthetic polymer gradually bind to the dye molecules, the

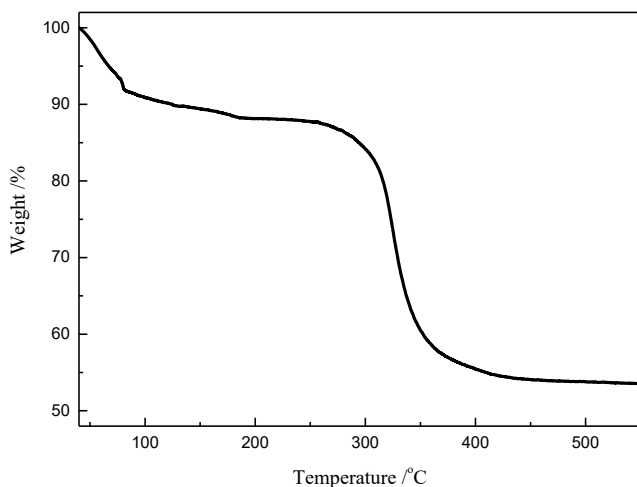


Fig. 4: Thermogravimetric analysis diagram of synthetic polymer.

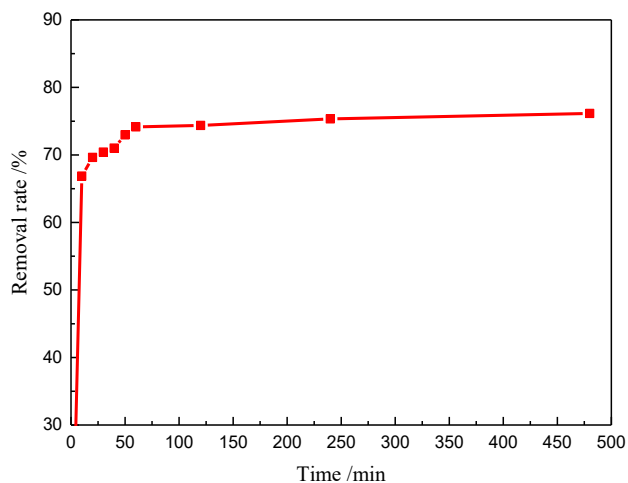


Fig. 5: The effect of adsorption time on dye adsorption performance.

adsorption sites are reduced, the driving force of adsorption is weakened, and the subsequent adsorption rate is reduced. It shows that the adsorption speed of the prepared polymer is faster, and the utility can be realized in a shorter time.

Effect of Initial Dye Concentration on Adsorption Performance

Weigh 0.015 g of the polymer as the adsorbent, add it to the dye solution with an initial concentration of 0.4, 1.2, 5.0, 10.0 mg.L⁻¹, respectively. The amount of dye solution is 5 mL, and the adsorption time is 10 min. The effect of initial dye concentration on adsorption performance is shown in Fig. 6. The results show that under the conditions of different initial dye concentrations, as the dye concentration increases, the driving force continues to increase, the chance of the polymer contacting dye molecules increases, and more dye molecules can be adsorbed on the polymer, which increases the adsorption capacity. However, with the further increase of the dye concentration, the absorption rate of the polymer to the dye decreases. This is because the adsorption sites on the polymer are already occupied by the dye molecules, and the adsorption capacity decreases. Among them, the dye adsorption quantity is calculated by the formula.

$$Q_t = (C_0 - C_t)V/M$$

Among them, C_0 is the concentration of initial dye, mg.L⁻¹. C_t is the concentration of dye in solution at time t , mg.L⁻¹. V is the volume of dye solution, L. M is the mass of modified synthetic adsorbent, g. The adsorption capacity of the adsorbent for dye at $Q_t - t$ time, mg.g⁻¹.

Impact of Polymer Dosage on Adsorption Performance

A 1.2 mg.L⁻¹ soap yellow dye solution was prepared, and 5

mL of the dye solution was measured. The polymer dosages were 5, 10, 15, 20, and 25 mg, respectively. The effect of the polymer dosage on the adsorption performance was studied. The results are as follows shown in Fig. 7. The adsorption rate of dyes gradually increased with the increase of polymer dosage. When the dosage of the polymer is less than 15 mg, the adsorption rate of the dye increases rapidly. When the dosage of the polymer is greater than 15 mg, the increase in the absorption rate of the dye is smaller. This is because increasing the dosage of the polymer can increase the available adsorption sites, thereby increasing the dye adsorption rate. However, when the dosage of the polymer exceeds 15 mg, the dye in the solution is adsorbed and removed by the polymer, and the excess adsorption sites are not used, which makes the adsorption rate decrease.

CONCLUSION

This work uses 2-methacryloxyethyl-dimethyl-3-sulfonic acid propylammonium hydroxide, 3-(methacryloxy)propyltrimethoxysilane, and N, N'-methylene bis acrylamide crosslinking agent as the raw material, and the copolymer gel is prepared by a photoinitiator under ultraviolet light to initiate polymerization. Use scanning electron microscope, Fourier transforms infrared spectrometer, thermogravimetric analyzer, and other instruments to characterize the surface morphology and chemical composition of the product. It can be seen from the SEM image that the polymer has a uniform spatial structure and a relatively large specific surface area, so the prepared polymer has excellent adsorption performance and can quickly and effectively absorb the dye in the dyeing solution. An ultraviolet spectrophotometer was used to investigate the effects of adsorption time, initial dye concentration, and polymer dosage on the adsorption

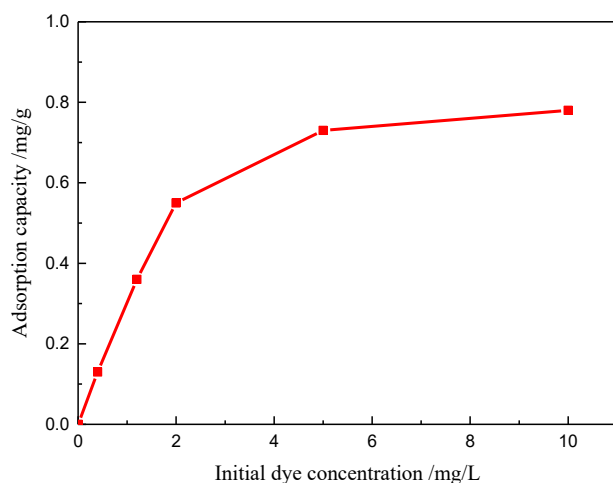


Fig. 6: The effect of initial dye concentration on adsorption performance.

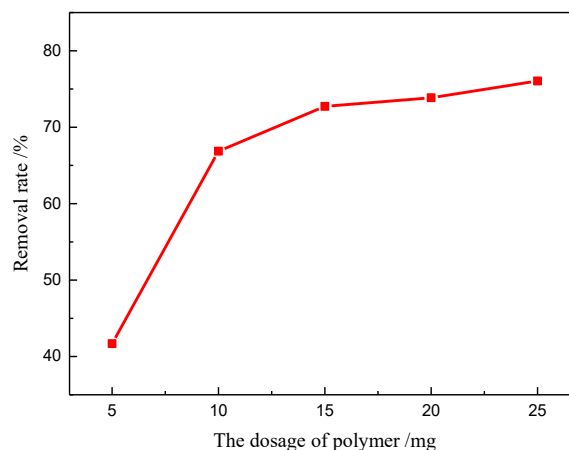


Fig. 7: The effect of polymer dosage on adsorption performance.

performance. The results show that the prepared polymer has a higher adsorption removal rate and a faster adsorption rate for dyes containing soap yellow simulation, and has a potential application value.

ACKNOWLEDGEMENT

The authors gratefully acknowledge the financial support of the International Science and Technology Cooperation Project of Shaoxing University (Grant No. 2019LGGH1004).

REFERENCES

- Ajmal, A., Majeed, I., Malik, R.N., Idriss, H. and Nadeem, M.A. 2014. Principles and mechanisms of photocatalytic dye degradation on TiO₂ based photocatalysts: a comparative overview. *RSC Adv.*, 4: 37003-37026.
- Binaeian, E., Babaei Zadvarzi, S. and Yuan, D. 2020. Anionic dye uptake via composite using chitosan-polyacrylamide hydrogel as matrix containing TiO₂ nanoparticles; comprehensive adsorption studies. *Int. J. Biol. Macromol.*, 162: 150-162.
- Chaudhary, J., Thakur, S., Mamba, G., Prateek, Gupta, R.K. and Thakur, V.K. 2021. The hydrogel of gelatin in the presence of graphite for the adsorption of dye: Towards the concept for water purification. *J. Environ. Chem. Eng.*, 9: 104762.
- Chethana, M., Sorokhaibam, L.G., Bhandari, V.M., Raja, S. and Ranade, V.V. 2016. Green approach to dye wastewater treatment using bio-coagulants. *ACS Sust. Chem. Eng.*, 4: 2495-2507.
- Dotto, J., Fagundes-Klen, M.R., Veit, M.T., Palácio, S.M. and Bergamasco, R. 2019. Performance of different coagulants in the coagulation/flocculation process of textile wastewater. *J. Cleaner Prod.*, 208: 656-665.
- Han, Y., Li, H., Liu, M., Sang, Y., Liang, C. and Chen, J. 2016. Purification treatment of dyes wastewater with a novel micro-electrolysis reactor. *Sep. Purif. Technol.*, 170: 241-247.
- Hosseini, S.A., Vossoughi, M., Mahmoodi, N.M. and Sadrzadeh, M. 2018. Efficient dye removal from aqueous solution by high-performance electrospun nanofibrous membranes through incorporation of SiO₂ nanoparticles. *J. Cleaner Prod.*, 183: 1197-1206.
- Khan, M. and Lo, I.M.C. 2016. A holistic review of hydrogel applications in the adsorptive removal of aqueous pollutants: Recent progress, challenges, and perspectives. *Water Res.*, 106: 259-271.
- Liu, H., Yu, D., Sun, T., Du, H., Jiang, W., Muhammad, Y. and Huang, L. 2019. Fabrication of surface alkalized g-C₃N₄ and TiO₂ composite for the synergistic adsorption-photocatalytic degradation of methylene blue. *Appl. Surf. Sci.*, 473: 855-863.
- Marrakchi, F., Hameed, B.H. and Hummadi, E.H. 2020. Mesoporous bio-hybrid epichlorohydrin crosslinked chitosan/carbon-clay adsorbent for effective cationic and anionic dyes adsorption. *Int. J. Biol. Macromol.*, 163: 1079-1086.
- Mittal, H., Al Alili, A., Morajkar, P.P. and Alhassan, S.M. 2021. Graphene oxide crosslinked hydrogel nanocomposites of xanthan gum for the adsorption of crystal violet dye. *J. Mol. Liq.*, 323: 115034.
- Mittal, H., Maity, A. and Ray, S.S. 2016. Gum karaya based hydrogel nanocomposites for the effective removal of cationic dyes from aqueous solutions. *Appl. Surf. Sci.*, 364: 917-930.
- Monier, M., Ayad, D.M., Wei, Y. and Sarhan, A. 2010. Adsorption of Cu(II), Co(II), and Ni(II) ions by modified magnetic chitosan chelating resin. *J. Hazard. Mater.*, 177: 962-970.
- Paz, A., Carballo, J., Pérez, M.J. and Domínguez, J.M. 2017. Biological treatment of model dyes and textile wastewaters. *Chemosphere*, 181: 168-177.
- Sen, F., Demirba, Ö., Çalıklı, M.H., Aygün, A., Alma, M.H. and Nas, M.S. 2018. The dye removal from aqueous solution using polymer composite films. *Appl. Water Sci.*, 8: 206.
- Stock, N., Peller, J., Vinodgopal, K. and Kamat, P. 2000. Combinative sonolysis and photocatalysis for textile dye degradation. *Environ. Sci. Technol.*, 34: 114
- Varaprasad, K., Jayaramudu, T. and Sadiku, E.R. 2017. Removal of dye by carboxymethyl cellulose, acrylamide, and graphene oxide via a free radical polymerization process. *Carbohydr. Polym.*, 164: 186-194.
- Vigneshwaran, S., Sirajudheen, P., Karthikeyan, P. and Meenakshi, S. 2021. Fabrication of sulfur-doped biochar derived from tapioca peel waste with superior adsorption performance for the removal of Malachite green and Rhodamine B dyes. *Surf. Interfaces*, 23: 100920.
- Wang, J., Wang, Z., Vieira, C.L.Z., Wolfson, J.M., Pingtian, G. and Huang, S. 2019. Review on the treatment of organic pollutants in water by ultrasonic technology. *Ultrasonics Sonochemistry*, 55: 273-278.
- Yagub, M.T., Sen, T.K., Afroze, S. and Ang, H.M. 2014. Dye and its removal from aqueous solution by adsorption: A review. *Advances in Colloid and Interface Science*, 209: 172-184.
- Zia, J., Ajeer, M. and Riaz, U. 2019. Visible-light driven photocatalytic degradation of bisphenol-A using ultrasonically synthesized polypyrrole/K-birnessite nanohybrids: Experimental and DFT studies. *Journal of environmental sciences (China)*, 79: 161-173.



Noise Levels in Urban and Rural Settlements of Bhubaneswar: A Case Study

G. Ayush*, A. J. Elizabeth*, V. V. Patil*† and M. Herlekar**

*School of Sustainability, XIM University, Bhubaneswar, Harirajpur-752 050, Odisha, India

**Department of Environmental Science, The Institute of Science, Dr. Homi Bhabha State University, Mumbai-400 032, Maharashtra, India

†Corresponding author: V. V. Patil; vikrant@xim.edu.in

Nat. Env. & Poll. Tech.
Website: www.neptjournal.com

Received: 10-06-2021
Revised: 29-06-2021
Accepted: 14-07-2021

Key Words:

Noise
Health
GIS
Urban and rural settlements

ABSTRACT

Noise is an underestimated threat that can cause several short- and long-term health problems. It is increasingly becoming a potential hazard to health, physically and psychologically, and affects the general well-being of an individual. The objective of the current study was to examine noise levels at ten different locations in the city of Bhubaneswar, Odisha State, India based on the land use pattern in urban and rural setup. The paper focuses on deploying geospatial techniques using ArcGIS desktop to perform better sampling and further interpolate the statistical data using the Kriging technique to generate a surface representing the distribution of noise levels in various areas. In addition, a health impact survey enabled us to understand the perspectives of the people in and around the monitoring location where health issues like stress, headache, hypertension, and sleeping disorders emerged as some of the most common issues faced. Noise levels were in the range of 43.0 to 74.5 (A) Leq. in rural areas and 61 to 96.5 dB (A) Leq in urban areas. In the current study, noise levels in rural and urban areas exceeded the recommended noise limits as per The Noise Pollution (Regulation and Control) Rules, 2000.

INTRODUCTION

Sound occurs due to changes in air pressure inside the ear canal that cause our inner ears to vibrate and produces the auditory sensations which our brain interprets as sound. Noise pollution is any unwanted or disturbing sound that harms the health and well-being of humans and wildlife (Jain et al. 2015). This type of interference often causes discomfort in residents, which sometimes ends up being hazardous. The effects of noise are seldom catastrophic and are often only transitory, but adverse effects can be cumulative with prolonged or repeated exposure and can significantly impair the quality of life (Capetown, n.d.).

Noise is an undervalued danger causing a lot of short- and long-term health problems (WHO n.da). Noise exposure among vulnerable groups, such as children, is an area of major concern (Jamir et al. 2014, Khatik et al. 2019). Excessive noise interferes with people's daily activities at work, school, home, and leisure time. It can disturb sleep, cause cardiovascular and psychophysiological effects, reduce performance, and provoke annoyance responses and social behavior changes (WHO n.db). Since there are direct links between noise and health, identifying sources of loud noise will assist the administration to abate high noise problematic areas, thus becoming compliant with city and other noise criteria and ordinances as defined by CPCB (2010).

Several studies in the recent past indicate that noise levels have crossed the set limits in India. 27 sites were monitored for noise level around a sensitive zone for 24 hours (Khairwal et al. 2016). It included various categories viz. outdoor, indoor, road, and residential areas. The noise level ranged from 45 dB to as high as 120 dB exceeding the prescribed daytime standard for the sensitive zone. Further, a pan India study was conducted at 35 locations between 2011 and 2014 (Garg et al. 2017). These 35 locations were distributed among commercial zone (14 locations), Industrial (5 locations), residential (7 Locations), and the silence zone (9 Locations). This study was constructive in ascertaining the magnitude of annual average ambient noise levels, noise abatement action plans, and the formulation of revised ambient noise standards in Indian scenarios. Further noise levels were measured at 227 sites of Malda, West Bengal, India, covering major roads, some important nodes, railway stations, bus stops, rail crossing, commercial area, and residential area (Das et al. 2019). The recorded noise levels varied between 25dB to 83 dB. The study concluded that noise annoyance is sensitive to age, sex, economic folks, and facing the window to the road. Out of the total study area, 9.94% area has emerged as the most vulnerable area to noise exposition.

Bhubaneswar's foremost challenges include rapid unplanned development, especially construction, increasing pollution from vehicles and commercial establishments,

road dust and other fugitive emissions, and significantly higher noise levels (Bisht 2021). In India, though noise levels are measured at the community level, limited studies have been published on the health effects of noise levels (Jamir et al. 2014). With this background, the research focuses on monitoring noise levels in rural and urban settlements of Bhubaneswar city. The data is further analyzed statistically and geographically to generate noise pollution maps. Noise mapping is one of the new methods to assess noise levels, and it helps plan to control noise pollution effects (Olayinka 2013). Several studies have warranted the importance of GIS-based noise mapping to make informed decisions related to its management. GIS can be beneficial in identifying the noise intensity, building density, and spatial layouts of the buildings (Yuan et al. 2019)

In India, along with air pollution, increasing sound levels is also a public health concern. Despite high noise levels, many people are not aware that it is hazardous to their health. Therefore, a survey was carried out to understand health risk perception among residents due to noise pollution. The way people perceive health impacts will help in mitigating noise levels.

MATERIALS AND METHODS

Study Area

A total of 10 sampling areas were identified for data collection, with five of them constituting rural fabric and five areas representing urban fabric. The five rural areas were villages chosen within a proximity of 5 km. from XIM University, New Campus. Jamukoli and Niranjapur are villages in Khordha District, whereas Kakudia, Bahelipada, and Harirajpur are in the Puri district (Fig. 1a). All five villages have agricultural operations throughout the year. Probable sources of noise pollution in and around rural areas include brick factories, mining and laterite stone cutting, sand mining, poultry, and movement of vehicles. Occasionally festive and private celebrations also contribute to the noise levels.

The five urban areas were identified in the urban fabric by determining different land use patterns, namely - commercial, residential, kerbside, mixed and institutional (Fig. 1b). Subsequently, for each location, six spatially spread points were identified for data collection, allowing for mapping a representative model. Palashpalli is a residential area close to the Biju Patnaik airport; Jagmara is an institutional area close to Khandagiri, a tourist place. Nuasahi is also a kerbside area close to National Highway 5. Mancheswar represents an industrial area with small and medium scale industries, automobile service stations. Fig. 1a and 1b further depict the sampling locations in rural and urban areas.

Noise Monitoring Equipment and Measurement Frequency

The Phoenix Professional Sound Level Meter SM-10 was used for data collection. The instrument, once powered by 3 AAA batteries, provides a lifespan of 50 hours. It uses a ½ inch electret condenser microphone that converts sound pressure levels to electrical signals, displaying them in decibels on a four-digit LCD module. The equivalent noise level (Leq) was calculated by estimating the average noise levels collected from a sampling location 4 times at an interval of 4 minutes. The monitoring at each location was carried out twice during the first and second rounds of sampling.

Data Collection for the Spatial Distribution of Noise Levels

The latitude and longitude readings on the sampling as described above were collected using a GPS device, the 'Garmin eTrex® 20x.'. The sampling was performed for ten days over two months during 2020 (February-March).

The 60 sampling locations (10 sampling locations monitored at six different points each) formed a baseline

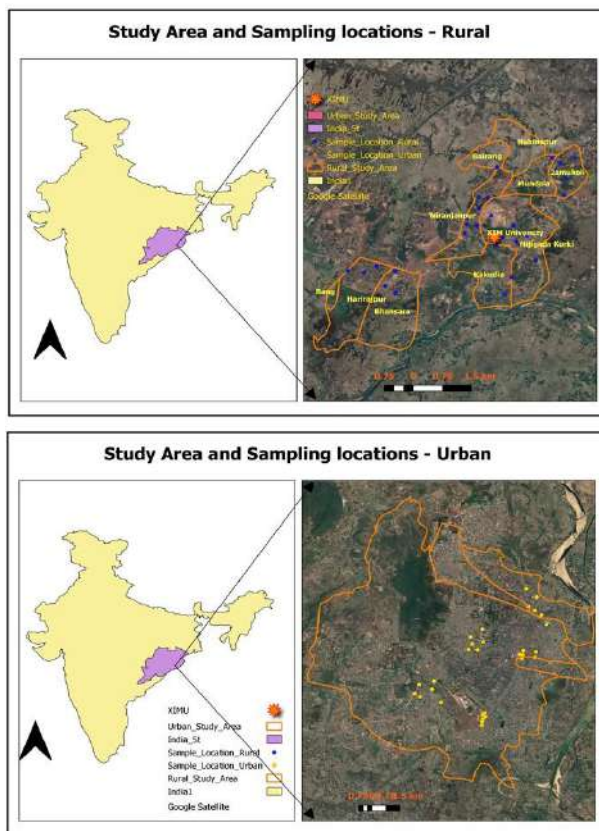


Fig. 1: Study area and sampling locations a) Rural area, b) Urban area.

survey and were further analyzed using the Spatial Analyst extension of ArcGIS desktop. Kriging model was used to prepare a prediction output of noise levels. The prediction was further verified by generating a prediction error raster. The prediction error raster proved very useful in identifying the areas with maximum prediction errors, and thus a new set of 60 sample points were created for the second round of sampling. A remarkable reduction in prediction error was observed after the second round of sampling.

Health Survey and Data Analysis

A ground survey was also conducted to study the impact of noise levels on health. The nature of the survey was to collect door-to-door information based on five survey questions. The survey data was collected from the ground using a verbal interview. A total of 101 respondents were interviewed over eight days. An effort was made to collect data from at least ten responses from each study area using both the methods i.e., google form and personal interviews. The respondents were people of different ages and sex and were involved in different occupations. A questionnaire prepared by the Indic Society for Education and Development (INSEED), available in the public domain, was used to carry out a health survey (<http://www.inseed.org/>).

The data collected through the survey was analyzed using Microsoft Excel 2016. For spatial data analysis of noise levels, ArcGIS version 10.3 was used.

RESULTS AND DISCUSSION

This section presents the interpretations based on the descriptive statistical analysis of noise level data, spatial analysis using ArcGIS, and health surveys.

Noise Levels At Rural Locations

The Leq noise levels, calculated from average noise levels at five rural locations during the 1st and 2nd rounds of sampling, are discussed in this section.

Sampling Round 1

During this sampling period, the highest Leq noise level

was observed at Harirajpur (61.2 ± 4.2). The reason for high noise levels at the Harirajpur location may be due to school, commercial activities, and stone mining activities carried out here.

For the Jamukoli region, the noise levels ranged between 52.1 dB to 61 dB. The average noise level observed during this sampling round was 55.6 ± 4.0 dB. The lowest noise levels were reported at the Niranjapur site (50.6 ± 5.5 dB). At this site, the noise level varied between 46.4 dB to 58.2 dB. These noise levels are lower than those reported recently (Pal & Mandal 2021), near a stone mining and crushing area in the Dwarka river basin of Eastern India. The noise levels reported in their study were more than 85 dB from 6 am to 4 pm. The noise level ranged between 50.3 dB to 59.6 dB and 49.2 dB to 61.8 dB at Kakudia and Bahelipada sites. According to a study carried out at Shirdi in Maharashtra (Kankal & Gaikwad 2011), the noise levels at the corner of the temple were observed to be in the higher range and found to be varying between 64.9 to 73.6 dB. The respective average values at these two sites were 55.9 ± 4.1 dB and 52.5 ± 4.9 dB. The slightly higher noise levels at Kakudia can be attributed to sources like poultry farms, red-brick factories, cement factories, and sand mining activities. The descriptive statistics of noise levels reported during this sampling round is presented in Table 1.

Sampling Round 2

Unlike in the case of the first sampling round, during this sampling period, the highest Leq noise level was reported at the Kakudia site (61.6 ± 9.0 dB). This probably can be attributed to increased activity at this location during the monitoring period.

The next highest average Leq values were reported at Niranjapur (57.1 ± 12.9 dB). Here, the noise levels ranged between 44.2 dB to 70.9 dB. At Jamukoli, Leq noise values varied from 46.4 dB to 66.2 dB with an average value of 55.6 ± 6.8 dB. The noise levels at Bahelipada were in the range of 44.3 dB to 72.7 dB with an average value of 54.3 ± 12.2 dB. Lastly, the lowest average noise levels of 53.0 ± 10.2 dB were reported at the Harirajpur site. The noise levels at this site varied from 43.4 dB to 67.3 dB. This site showed

Table 1: Noise levels reported at rural locations during sampling round 1.

Location	Jamukoli	Niranjapur	Kakudia	Bahelipada	Harirajpur
Minimum	52.1	46.4	50.3	49.2	56.7
Maximum	61	58.2	59.6	61.8	66.3
Average	55.6	50.6	55.9	52.5	61.2
Standard deviation (\pm)	4.0	5.5	4.1	4.9	4.2
Count	6	6	6	6	6

Note: All the values except count are expressed in dB.

the highest avg value in the first round. The descriptive statistics of noise levels reported during sampling round 2 is presented in Table 2.

Noise Levels at Urban Locations

The Leq noise levels, calculated from average noise levels at 5 urban locations, representing different land-use patterns during the 1st and 2nd rounds of sampling, are discussed in this section.

Sampling Round 1

During this sampling period, the highest Leq noise level was observed at Mancheswar (81.3 ± 6.6). The reason for high noise levels at this location maybe because it represents the industrial area with small and medium scale industries and automobile service stations etc. The noise levels varied between 69 dB to 87 dB. In a study carried out in the two industrial areas of Kolhapur city in Maharashtra, India (Mangalekar et al. 2012), slightly lower noise levels were reported during the study period. The Leq noise levels were found to be varying between 70.3 dB to 79.3 dB.

The next highest average Leq noise level of 79.6 ± 14.8 dB was reported at the Jagmara location. The high noise levels at this location can be attributed to the continuous movement of tourists and their tourist vehicles visiting this place. The noise level ranged between 60.6 dB to 98.6 dB at this location. Nuasahi site had an average Leq noise level of 74.2 dB which can be justified because it is a kerbside area near National Highway 5, which is characterized by a con-

tinuous movement of vehicles. The minimum and maximum noise levels reported at this site were 62.9 dB and 87.7 dB, respectively. Satyanagar site, representing the commercial and residential area, recorded an average Leq level of 70.8 dB. In one of the studies (Hunashal & Patil 2012) a commercial cum residential area in the city of Kolhapur in the state of Maharashtra recorded Leq noise levels of 64.47 dB. The minimum and maximum noise levels reported at this site are 63.4 dB and 80.2 dB, respectively. Amongst all the urban sites, the lowest average Leq noise levels of 68.9 ± 5.7 dB were reported at Palashpalli. These results can be justified by the fact that this is a residential site. This site's noise levels varied at this site from 61.9 dB to 79.2 dB, which also might be attributed to its proximity to Biju Patnaik airport. The descriptive statistics of noise levels reported during sampling round 1 is presented in Table 3.

Sampling Round 2

As observed in the case of rural locations, the highest average Leq values were observed at different locations than observed in the first round of sampling in urban locations. During this sampling round, the highest average Leq noise levels (75.2 ± 10.2 dB) were reported at the Satya Nagar site. At this site, the noise levels varied between 58.4 dB to 87.2 dB.

The next highest average Leq noise levels were reported at Mancheswar (69.6 ± 13.9 dB), being an industrial site. The minimum and maximum noise levels were reported to be varying between 45.5 dB to 88 dB at this site. Palashpalli site had average Leq noise levels of 68.8 ± 12.3 dB. The

Table 2: Noise levels reported at rural locations during sampling round 2.

Location	Jamukoli	Niranjanpur	Kakudia	Bahelipada	Harirajpur
Minimum	46.4	44.2	44.1	44.3	43.4
Maximum	66.2	70.9	70.2	72.7	67.3
Average	55.6	57.1	61.6	54.3	53.0
Standard deviation (\pm)	6.8	12.9	9.0	12.2	10.2
Count	6	6	6	6	6

Note: All the values except count are expressed in dB.

Table 3: Noise levels reported at urban locations during sampling round 1.

Location	Palashpalli	Jagmara	Satya Nagar	Nuasahi	Macheswar
Minimum	61.9	60.6	63.4	62.9	69
Maximum	79.2	98.6	80.2	87.7	87
Average	68.9	79.6	70.8	74.2	81.3
Standard deviation (\pm)	5.7	14.8	6.2	8.2	6.6
Count	6	6	6	6	6

Note: All the values except count are expressed in dB.

maximum and minimum noise levels reported at this site were 50.6 dB and 84.2 dB, respectively. At the Jagmara site, the average Leq noise level of 68.6 ± 12.6 dB was reported. The minimum noise level at this site was estimated to be 46.7 dB, while the maximum noise level was 85 dB. The least average Leq noise level of 65.1 ± 13.8 dB was recorded at the Nuasahi site. The minimum and maximum noise levels varied between 44.9 dB and 83 dB, respectively. The descriptive statistics of noise levels reported during sampling round 2 is presented in Table 4.

Spatial Analysis of Noise Levels

The data collected was spatially analyzed using ArcGIS desktops spatial analyst extension. Since the noise data was collected from different locations on land, it also qualifies that the data points were sampled from a continuous phenomenon in space. Kriging was used to generate a prediction model and a continuous raster. Continuous rasters are represented in Fig. 2a, 3a for rural areas and Fig. 4a, 5a for urban areas. The continuous prediction surface is useful for making educated

judgments, such as identifying regions where noise decibel levels are beyond the restrictions. Certain places have lower noise decibel levels as a result of land use patterns or other geographical factors.

However, this can stand true only when the predictions are accurate, and hence to check the prediction accuracy, prediction error maps were generated using the same set of data as shown in Fig. 2b for rural areas and Fig. 4b for urban areas. These rasters depicted in Figs. 2b and 4b, show high prediction errors in certain areas. High prediction errors correspond to significant gaps/differences between actual values and the value generated by kriging.

In a rural setup, the prediction errors were higher on the boundaries of the study area, i.e. north and south. These areas were ignored in the first round of sampling as they were either part of agricultural fields or abandoned stone quarries (Fig. 1a). Also, as seen in Fig. 1a, the sampling locations are not equally distributed across the study area, causing higher prediction errors in the areas where sampling was not carried out. It is observed that the RMS value is more than one at

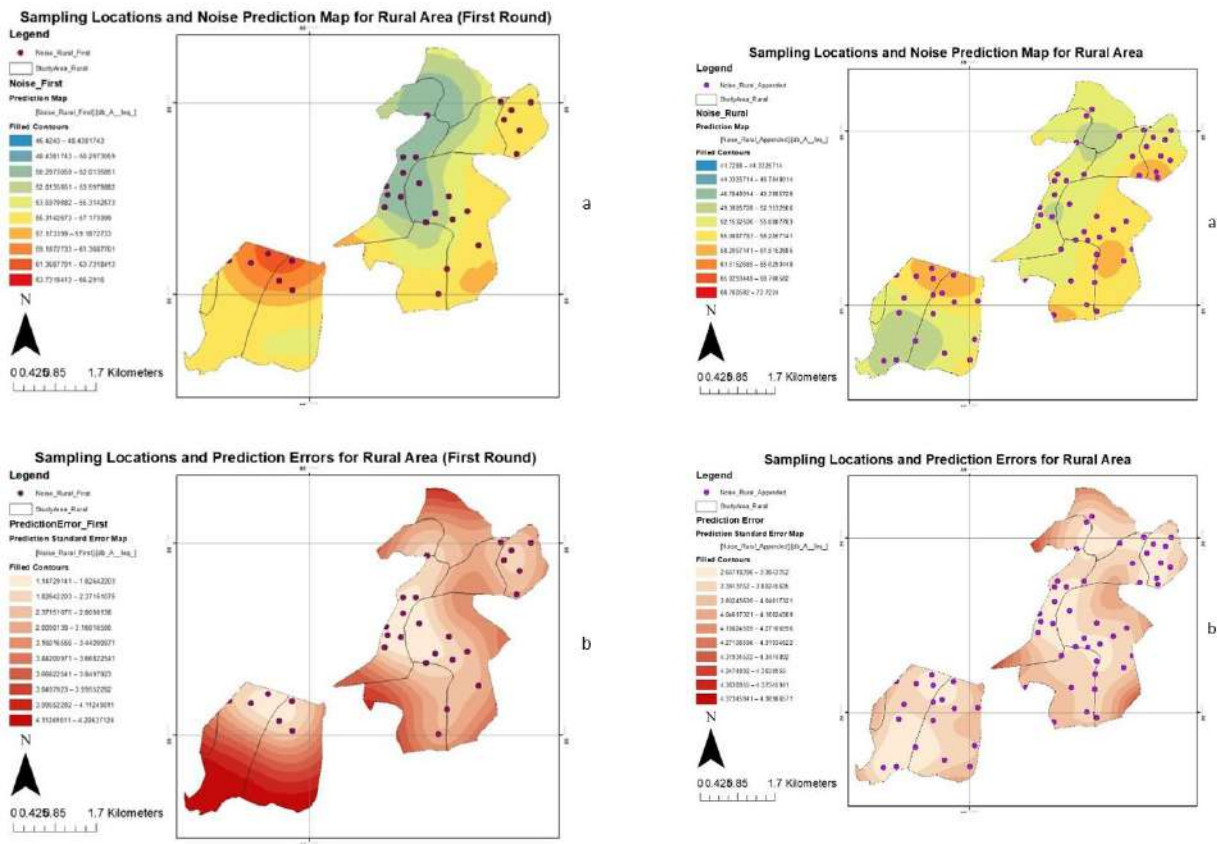


Fig. 2: Raster represents Noise levels in dB and prediction errors. a) Sampling locations and Noise level raster in Rural area, b) The prediction errors after Kriging applied on the sampling locations for rural areas.

Fig. 3: Raster representing Noise levels in dB and prediction errors after the second round of sampling. a) Sampling locations and Noise level raster in Rural area, b) The prediction errors after Kriging applied on the sampling locations for rural areas.

Table 4: Noise levels reported at urban locations during sampling round 2.

Location	Palashpalli	Jagmara	Satya Nagar	Nuasahi	Mancheswar
Minimum	50.6	46.7	58.4	44.9	45.5
Maximum	84.2	85.0	87.2	83.0	88
Average	68.8	68.6	75.2	65.1	69.6
Standard deviation (\pm)	12.3	12.6	10.2	13.8	13.9
Count	6	6	6	6	6

Note: All the values except count are expressed in dB.

all locations in the study area and goes up to 4.4 in some areas.

Thus, the second round of sampling in and beyond our study areas improvise the prediction accuracy on the fringes. The data from the first and second rounds of sampling is further appended, forming 62 locations to predict the noise levels in the rural area (Fig. 3a). The areas which bear an orange tone are those which see active transportation. Similarly, the areas represented by darker shades of green are open space/farmland. Xavier City Campus is represented as XUB on the map. Due to a larger population density, the noise levels are also high in the area. Noise levels at the rural

locations were under-regulated limits. Almost all the areas in the rural study area show error in the range of 2.6 to 4.1 (Fig. 3b). Towards the edges of the study area, the error becomes significantly higher owing to a lack of representation.

However, in an urban area, the reason for high prediction errors was different. From Fig. 4b, it is seen that the sampling locations in the urban areas were clustered, resulting in better predictions near to the cluster and higher prediction errors farther from the cluster, especially in the northern region of the urban area. The northern area was initially not considered as the land use was dominated mainly by forest area (Fig. 1b). It is observed that the RMS value is more than one at all

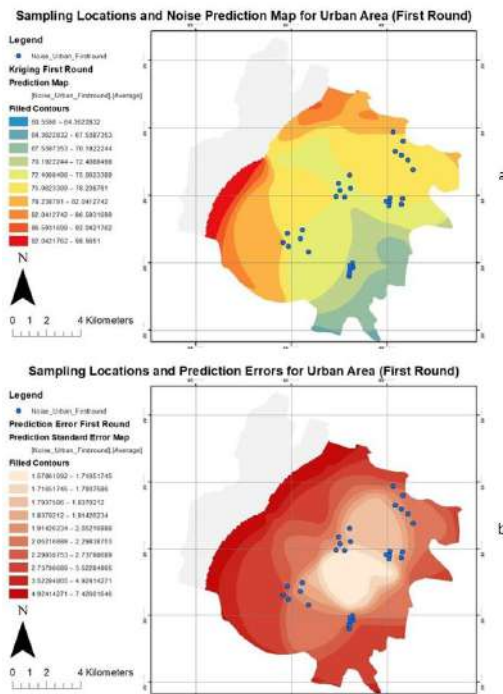


Fig. 4: Raster representing Noise levels in dB and prediction errors. a) Sampling locations and Noise level raster in the urban area, b) The prediction errors after Kriging applied on the sampling locations for urban areas.

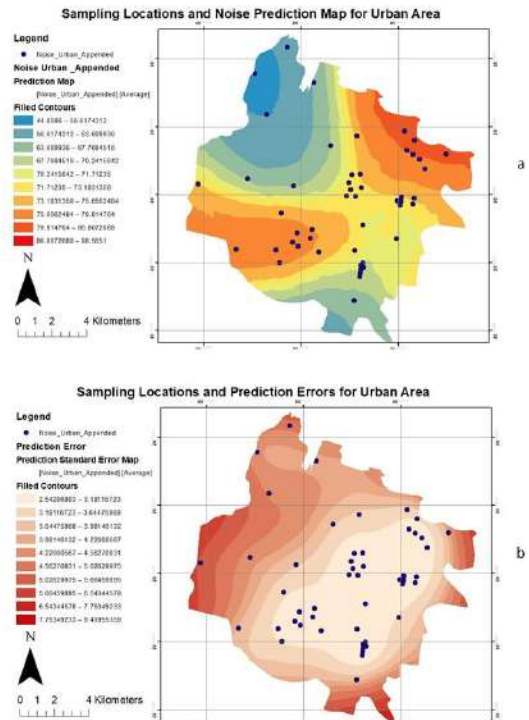


Fig. 5: Raster representing Noise levels in dB and prediction errors after the second round of sampling. a) Sampling locations and Noise level raster in the urban area, b) The prediction errors after Kriging applied on the sampling locations for urban areas.

locations in the study area and goes as high as 7.4 towards the edges of the study area. It indicated the need for an increase in the sample points. Sampling data from the first and second rounds were appended together to get a prediction map and a prediction error map.

The prediction error model (Fig. 5b) shows a relatively low range of error (2.5 to 3.2) in the study area that is within the core city limit. The five localities identified within the city limit have higher predictability. This proves that attenuation of the 1st and 2nd rounds of samplings has led to better probability mapping and the map thus obtained has low errors. There can be two reasons for no substantial improvement in the prediction errors. The first is that the sample points in the first round of sampling were clustered, and hence appending them with the second-round sample dataset will not significantly improve the prediction accuracy. The second reason is that the study area is too large to be represented by 60 points. Hence, larger areas are recommended to create a fishnet overlay on the study area and use the centroid of the individual cells of the fishnet as the sampling locations.

As seen in the data records, Jagmara and Mancheswar Industrial Estate have the highest levels of sound pollution and are marked so in the prediction map. The city's center is defined by residential and mixed-use land patterns, with noise levels averaging 70 decibels. This is higher than the minimum requirements for industrial land use. Thus, using geo-statistics in this research not only provided an optimal prediction surface (prediction map) but it delivered a measure of confidence of how likely that prediction will be accurate (prediction error map).

Health Survey Findings

The survey findings revealed that 36.6% of respondents were unaware of the regulations about noise levels, as shown in Fig. 6a, while 13.9% of the respondents had merely heard of it from somewhere. This highlights a lack of awareness among the citizens. A probable reason is the higher rates of illiteracy in the village population (50% of the villagers being villagers). Only 26% of the respondents were aware of such rules and regulations. More surprisingly, 45.5% of the respondents were not aware that noise pollution is a punishable offense (Fig. 6b).

Of the total respondents, only 36.8% of respondents said that noise pollution was an issue. More interestingly, 63.2% of respondents said that they had no issue with noise pollution or were accustomed to the noise levels. The field data on noise levels showed that the sound levels in the city were much higher than the acceptable levels, irrespective of which these respondents did not find the levels to be polluting. This throws light that noise has become an inescapable part of

modern life even though it causes nuisance and excessive noise has a negative physical and psychological impact on us. As shown in Fig. 6c, the people in the study area are habituated to the higher levels of noise in their surroundings. 42% of respondents said that transportation does contribute to high sound levels, and they felt that these sound levels were not a problem for them. Adding to that, 17% said that transportation does not cause harmful noise levels. 41% said that transportation causes noise pollution. The findings in the present study corroborated with the study conducted in Jharsuguda, Orissa found that people were unaware of the noise pollution effects though they experienced noise-induced symptoms such as headache, bad temper, hearing problem, loss of concentration, and sleep disturbance (Patel et al. 2006). The study by Hakzah et al. (2020) shows that

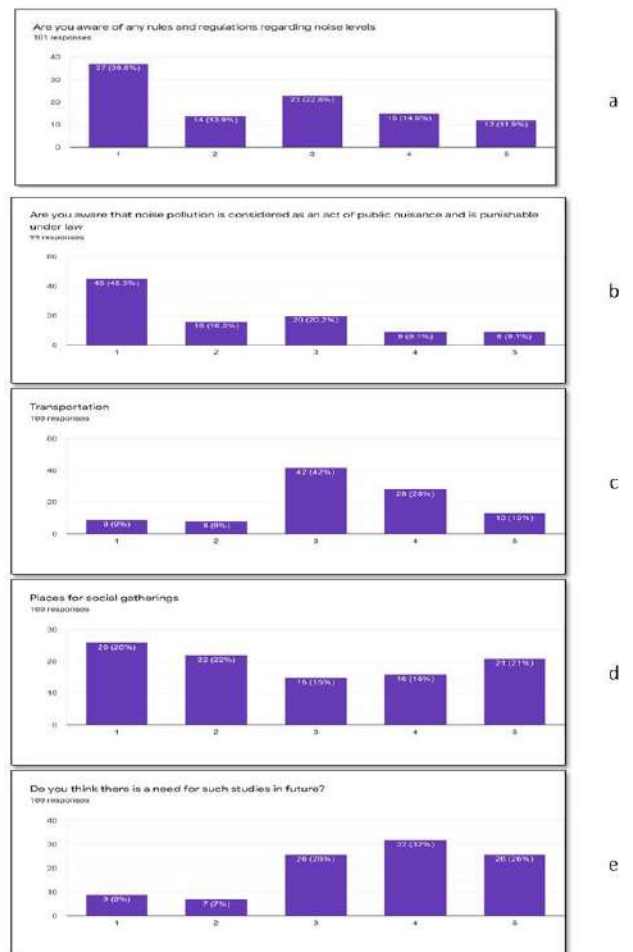


Fig. 6: Health Survey Response related to noise pollution a) Awareness of rules and regulations, b) Awareness of Noise pollution as a punishable offense, c) Perception of respondents related to noise pollution and transportation, d) Perception of respondents related to social gatherings as a source, e) Need for studies related to noise pollution in future.

the impact of noise on public health by traffic on people who live around the road is a psychological disorder (80%), physiological disorder (35.7%), and the highest is a communication disorder (84.3%).

India has a significant number of middle-class people, and with the increasing affordability of vehicles and loan schemes with manageable monthly installments, every household has a vehicle. As we go higher in the income groups, people prefer to have a personal vehicle for each household. This increases pollution levels and leads to vehicle congestion on the roads, meaning that people need to spend more time on the road. It directly affects the annoyance level/capacity of individuals traveling and leads to honking on congested roads and speeding on open roads.

During the survey, it was noticed that even the rural areas had seen a sharp increase in the number of vehicles and that almost every household in the village owns a two-wheeler. This has led to noise pollution within the cramped earthen roads of the village, and the number of accidents has also increased- something that was rarely experienced inside the villages even five years ago.

Our Indian culture is full of festivities. Every season is a festive season, and every occasion provides a reason to celebrate. Such celebrations involve the social gathering of people. Over the years, light and sound have become a symbol of expression and happening. So, these gatherings often consist of large music systems, which cause a significant amount of noise. As seen in Fig. 6d, a significant 37% of people agreed that social gatherings are a definite source of noise pollution. At the same time, 15% said that they were habituated to these high levels.

An exception to this is that due to the nature of the occasion, such high levels of noise are not considered annoying or polluting in nature. However, it does cause significant damage to humans and their surroundings. As per the study by Xu et al. (2020) living noise pollution which comes from entertainment activities, commercial activities, and other activities in people's daily life is considered most serious as it has the closest relationship with the acoustic environment of urban areas.

The following observations have been made while carrying out the survey:

- i. Older adults experienced elevated heart rates when attending such events.
- ii. If the magnitude of the noise is considered, social gatherings pollute more than transportation at any given time. However, it has more widespread acceptance.
- iii. Any social gathering that uses a high-power speaker system

needs to be permitted by authorities. The majority of respondents interviewed were not aware of this.

- iv. In villages, people had complained that noise generated from these speaker systems damages their walls, and there have been cases where walls had collapsed when a procession that used speaker systems passed through their narrow roads.

Since noise levels are significantly high in the study areas, it is essential to establish the health effects on the people. In the present study, 27.7% of respondents agreed that changes in noise levels affected their sleep. At the same time, 12.9% of respondents said that they were accustomed to these noise levels.

Though noise levels may not physically harm, the degree of annoyance related to it can decrease comfort levels. Almost 21.8% of people agreed that noise levels lead to stress. Medical studies have established the link between stress and increased blood pressure, cardiovascular diseases, and the potential risk of stroke (Esler 2017). Many respondents in the current study also said that driving in traffic causes stress due to the constant honking and running of engines. Moreover, traffic congestion itself is a stressful site. As seen in Fig. 6e, 58% of people said that there was a need for studies on noise pollution in the future. This result highlights the essence of the survey and the need for the research.

CONCLUSION

This study focused on collecting noise level data from study areas located in both urban and rural setups. The recorded noise levels were much beyond the regulated limits in the Urban areas. In the rural areas, noise levels were lower yet were still beyond prescribed limits. The data thus collected suggested possible violation of The Noise Pollution (Regulation and Control) Rules, 2000. On spatially analyzing the data using ArcGIS, possible trends were seen in the variation of noise levels throughout the geography of the study area. The data was used to prepare a prediction model, which can be used to determine the noise levels at any given place within the study area. The purpose of the model thus created is to aid in developmental activities. The effort was also made to conduct a health survey to study the effect of this noise exposure. The study highlighted the lack of awareness regarding noise rules as applicable by law. The findings suggested a significant level of annoyance generated by the noise. The majority of the respondents said that the noise in their area was not tolerable and that further studies need to be conducted pertaining to this issue. This study like any other has its limitations. During the study, noise levels were recorded only during the daytime (6 a.m. to 10 p.m.) because

of which the possibility of a 24-hour study was ruled out. The data was collected from specific locations and a maximum of 60 points was considered for data recording. It increased the spatial distance between the points and thus increased the error in the prediction map generated. Also, the time frame for data collection was limited to February and March. There was however uniqueness to the study as previously no such research has been believed to be completed for the area of concern.

To manage noise levels, a monitoring network needs to be established and increase green spaces as their ecosystem services are noise reduction (Dwevedi et al. 2018). Some of the additional measures that can be adopted to minimize noise levels are building noise barriers around highways, no honking awareness plans, responsible behavior in playing TV, radio, and musical instruments during festive celebrations. The overall aim is to improve the environmental quality and make the place more livable.

ACKNOWLEDGMENTS

The authors are thankful to the residents of Bhubaneswar and those of the neighboring villages of XIM University for providing us with their valuable inputs on noise pollution and health effects.

REFERENCES

- Bisht, D.S. Smart cities: Testing ground for sensor-based instruments. 2020. Retrieved from <https://www.downtoearth.org.in/blogger/digvijay-singh-bisht-90299> (Accessed on May 15, 2021).
- Capetown, G. n.d. What Is Noise? Retrieved from <https://www.capetown.gov.za/City-Connect/Report/Report-noise-pollution> (Accessed on May 15, 2021).
- CPCB. 2010. The Noise Pollution (Regulation And Control) Rules, 2000. http://cpcbenvi.nic.in/noisepollution/noise_rules_2000.pdf
- Das, P., Talukdar, S., Ziaul, S., Das, S. and Pal, S. 2019. Noise mapping and assessing vulnerability in meso level urban environment of Eastern India. *Sust. Cities Soc.*, 46: 101416. <https://doi.org/10.1016/j.scs.2019.01.001>
- Dwevedi, R., Krishna, V. and Kumar, A. 2018. Environment and big data: Role in smart cities of India. *Resources*, 7(4): 1–10. <https://doi.org/10.3390/resources7040064>
- Esler, M. 2017. Mental stress and human cardiovascular disease. *Neurosci. Biobehav. Rev.*, 74: 269–276. <https://doi.org/10.1016/j.neubiorev.2016.10.011>
- Garg, N., Sinha, A.K., Dahiya, M., Gandhi, V., Bhardwaj, R.M. and Akolkar, A.B. 2017. Evaluation and analysis of environmental noise pollution in seven major cities of India. *Arch. Acoust.*, 42(2): 175–188. <https://doi.org/10.1515/aaa-2017-0020>
- Hakzah, P.A.I., Nasir, N. and Hamzah, S. 2020. The effect of traffic noise on public health. *Enferm. Clinica*, 30: 249–253. <https://doi.org/10.1016/j.enfcli.2020.06.057>
- Hunashal, R.B. and Patil, Y.B. 2012. Assessment of noise pollution indices in the city of Kolhapur, India. *Procedia - Soc. Behav. Sci.*, 37, 448–457. <https://doi.org/10.1016/j.sbspro.2012.03.310>
- Jain, R.K., Cui, Z. and Domen, J.K. 2015. *Environmental Impact of Mining and Mineral Processing: Management, Monitoring, and Auditing Strategies*. Elsevier Inc, The Netherlands. <https://doi.org/10.1016/C2014-0-05174-X>
- Jamir, L., Nongkynrih, B. and Gupta, S.K. 2014. Community noise pollution in urban India: Need for public health action. *Indian J. Community Med.*, 39(1): 8-12. <https://doi.org/10.4103/0970-0218.126342>
- Kankal, S.B. and Gaikwad, R.W. 2011. Studies on noise and air quality monitoring at Shirdi(Maharashtra), India. *Adv. Appl. Sci. Res.*, 1(2): 63-75.
- Khaiwal, R., Singh, T., Tripathy, J.P., Mor, S., Munjal, S., Patro, B. and Panda, N. 2016. Assessment of noise pollution in and around a sensitive zone in North India and its non-auditory impacts. *Sci. Total Environ.*, 566-567: 981-987. <https://doi.org/10.1016/j.scitotenv.2016.05.070>
- Khatik, V.A., Intarak, R. and Foto, T.G. 2019. Development and mapping of noise risk zones in neighbourhoods along Saensaep Canal: revealing the public health burden of water transport in Bangkok. *Nat. Env. Poll. Tech.*, 18(2): 645-650.
- Mangalekar, S.B., Jadhav, A.S. and Raut, P.D. 2012. Study of noise pollution in Kolhapur City, Maharashtra, India. *Online*, 2(1): 65-69.
- Olayinka, O.S. 2013. Effective noise control measures and sustainable development in Nigeria. *World J. Environ. Eng.*, 1(1): 5-15. <https://doi.org/10.12691/wjee-1-1-2>
- Pal, S. and Mandal, I. 2021. Noise vulnerability of stone mining and crushing in Dwarka river basin of Eastern India. *Environ. Develop. Sustain.*, 12: 1-22. <https://doi.org/10.1007/s10668-021-01233-2>
- Patel, R., Tiwari, T.N. and Patel, T. 2006. Noise pollution in residential areas of Jharsuguda Town, Orissa (India) and its impact. *J. Environ. Sci. Eng.*, 48(3): 209-212. <https://pubmed.ncbi.nlm.nih.gov/17915786/>
- WHO. n.da. Noise - Data and statistics. Retrieved May 15, 2021, from <https://www.euro.who.int/en/health-topics/environment-and-health/noise/noise>
- WHO. n.db. Noise - Data and statistics. Retrieved May 15, 2021, from <https://www.euro.who.int/en/health-topics/environment-and-health/noise/data-and-statistics>
- Xu, C., Yiwen, Z., Cheng, B., Li, L. and Zhang, M. 2020. Study on environmental Kuznets Curve for noise pollution: A case of 111 Chinese cities. *Sust. Cities Soc.*, 63, 102493. <https://doi.org/10.1016/j.scs.2020.102493>
- Yuan, M., Yin, C., Sun, Y. and Chen, W. 2019. Examining the associations between the urban built environment and noise pollution in high-density high-rise urban areas: A case study in Wuhan, China. *Sust Cities Soc.*, 50, 101678. <https://doi.org/10.1016/j.scs.2019.101678>



The Effect of *Moringa oleifera* as a Primary Treatment in Urban Wastewater in Martínez De La Torre, Veracruz

M.A. López-Ramírez†*, C. Argüelles-López**, M.R. Aguilar-Rodríguez*, J. Barragán-Díaz***, O.P. Castellanos-Onorio**** and F. Lango-Reynoso*****

*Department of Environmental Engineering, Tecnológico Nacional de México/Instituto Tecnológico Superior de Martínez de la Torre, Ignacio de La Llave 182, Centro, 93600, Martínez de la Torre, Veracruz, México

**Department of Business Management's Engineering, Tecnológico Nacional de México/Instituto Tecnológico Superior de Martínez de la Torre, Ignacio de La Llave 182, Centro, 93600, Martínez de la Torre, Veracruz, México

***Department of Industrial Maintenance, Engineering Universidad Tecnológica de Gutiérrez Zamora, Prolongación Dr., Miguel Patiño s/n, Centro, 93556 Gutiérrez Zamora, Veracruz, México

****Department of Chemical-Biochemical Engineering, Tecnológico Nacional de México/Instituto Tecnológico de Veracruz, Calzada Miguel Ángel de Quevedo 2779, Formando Hogar, 91897, Veracruz, Veracruz, México

*****Department of Postgraduate and Research, Tecnológico Nacional de México/Instituto Tecnológico de Boca de Río, Carretera Veracruz-Córdoba Km.12, 94290. Boca del Río, Veracruz, México

†Corresponding author: M.A. López-Ramírez; malopez@tecmartinez.edu.mx

Nat. Env. & Poll. Tech.
Website: www.neptjournal.com

Received: 16-04-2021

Revised: 14-05-2021

Accepted: 08-06-2021

Key Words:

Moringa oleifera

Coagulant

Primary treatment

Urban wastewater

ABSTRACT

Wastewater treatment is a priority, as most of this is discharged into rivers, lakes, seas, and soil. Since there is no treatment facility in Martínez de la Torre, Veracruz, these fluids are released straight into the Filobobos River without treatment. Hence, the *Moringa oleifera* seed was evaluated as a primary treatment. In this study using wastewater from a direct discharge, pH, turbidity, total suspended solids, and conductivity were determined as control measures. In the jar test, the treatments were carried out using different amounts of coagulant salts (aluminum and iron sulfate) and moringa powder; starting the agitation at 120 rpm for 5 minutes and immediately it was reduced to 60 rpm in 10 minutes with a rest time of 1 hour. After that, the quality parameters were analyzed. The moringa coagulant achieved an average maximum reduction of 71.84 per cent and 89.36 per cent in turbidity and Total Suspended Solids, respectively, which was higher than the salts used. Furthermore, its application had no effect on pH and conductivity parameters, and the coagulant based on *Moringa oleifera* as a primary treatment agent, since these qualities do not alter and post-treatment is not required, as in the case with salts.

INTRODUCTION

Water is the most significant resource in this study and our daily lives, and its availability is decreasing as a result of physical, chemical, and/or biological contamination, which degrades quality and has an impact on health, social, technical, and economic development.

Currently, research into better processes and the elimination of contaminants that impair water quality is of the utmost importance; one of these processes is the improvement in coagulation, using natural agents which can reduce the process and the cost of operation.

As a result, the need to detoxify effluents is becoming increasingly essential, necessitating the search for innovative solutions based on research into various water treatment methods that enable improved quality and adequate

protection of water resources. Table 1 shows typical pollutants in wastewater.

The advantages of using natural methods for the treatment of domestic wastewater are: the implementation of relatively simple technology, low operating and investment costs, low energy consumption, the treatment process can be adapted quickly, achieving a high level of performance after the start of operations, and high nutrient removal (Rozkosný et al. 2014) since they possess a complex chemical structure, which generally consists of various types of polysaccharides and proteins. Some of them have coagulating or flocculating qualities, and in many places, the natives use them scientifically to purify murky water with excellent results (Vásquez 1994). Among the group of known substances that possess these binding properties are some organic compounds of plant origin, which can be obtained from the stem or seeds

Table 1: Contaminants in water.

Class	Examples
Suspended solids	Rubbish, water erosion, powder, and colloids.
Organic matter	Organic chemicals and organic residues like lees or sediment.
Dissolved ionics	Heavy metals, nitrates, carbonates, chlorates.
Microorganisms	Pathogens, viruses, and parasites
Gases	Methane, carbon monoxide, carbon dioxide, and sulfide
Other	Micro plastic, medicines, and colorants

of a huge variety of plants such as beans, corn, *Moringa oleifera*, among others (Norde 2011).

MATERIALS AND METHODS

Twelve urban residual water samplings were made from a direct discharge located in the eastern coordinates: 703 632.2, North: 2 219 480.1 Zone: 14 hemispheres: North; As can be observed in Fig. 1, the discharge of residual water is continuous during February and May, as the dry season in Martínez de la Torre is anticipated during these months. Each sample was tested for pH, conductivity, turbidity, Biochemical Oxygen Demand in Five Days (BOD₅), Total Suspended Solids (TSS), Fats and Oils, Fecal and Total Coliforms, Total Nitrogen, and Ammoniacal Nitrogen, following the Techniques outlined in the Standard Methods (APHA-AWWA-WPCF 1998).

Because the residual water in the jar test had sediment particles, the dose of coagulants 300, 600, and 900 mg.L⁻¹ in a multiple agitation equipment for 5 min at a revolution of 120 rpm and then 10 min at 60 rpm in the jar test, leaving to stand and settle for one hour to obtain coagulation and a better reading of data. Since documented data such as those of Solís-Silvan et al. (2012) show that chemical coagulants such as iron sulfate and aluminum sulfate have an ideal floc formation range of 6.0-8.0, the pH was used without dampening the water for this operation.



Fig. 1: Wastewater discharge point.

To determine the optimal doses of the coagulation-flocculation process, 3 doses were tested for each coagulant (300, 600, and 900 mg) evaluated in triplicate. In jar testing, tests were conducted on leftover water that had been exposed to the coagulation process. The turbidity removal, measured in NTU, was used to evaluate the results. The results were compared with the different coagulants to determine the most effective one. In addition, parameters such as pH and conductivity were monitored.

The reduction of Turbidity was determined by the HACH 2100AN team performing 27 tests: 9 using *Moringa oleifera* powder in the coagulation process, 9 using industrial grade aluminum sulfate, and 9 with reactive grade iron sulfate heptahydrate; with doses of 300, 600, and 900 mg.L⁻¹ of each coagulant.

The results of the optimal dose were subjected to an analysis of a statistical mean test with a confidence level of 95%, and the same statistical method was performed for the conductivity and hydrogen potential parameters.

RESULTS AND DISCUSSION

Results

Table 2 shows the findings of the residual water characterization, and Table 4 lists the treatments that were performed to find the best coagulant doses. The clearance efficiencies

Table 2: Characterization of the wastewater generated in Martínez de la Torre, Veracruz.

Parameter	Unit	Average	Minimum	Maximum
pH	pH Units	7.77	7.65	7.9
Conductivity	mS.cm ⁻¹	638.67	636.00	642.00
Turbidity	NTU	25.00	36.70	16.90
BOD ₅	mg.L ⁻¹	56.60	54.50	58.00
TSS	mg.L ⁻¹	49.70	20.00	112.00
Fats and oils	mg.L ⁻¹	13.31	13.10	13.45
Nitrogen Total	mg.L ⁻¹	10.89	10.72	11.00
Ammoniacal Nitrogen	mg.L ⁻¹	9.76	9.67	9.85
Fecal Coliforms	NMP.100mL ⁻¹	4 600.00	4 600.00	4600.00
Total Coliforms	NMP.100mL ⁻¹	24 000.00	24 000	24 000.00

Source: Author

of turbidity and TSS obtained to estimate the appropriate coagulant dose are shown in Table 5.

DISCUSSION

As can be seen from the characteristics of the wastewater obtained and compared to Metcalf and Eddy, Inc. (1998) classification, wastewater is classified as gross domestic water of weak concentration; however, as shown in Table 3, wastewater has three parameters that override national and international Mexican standards.

According to the findings, the United States Environmental Protection Agency (1998) recommends that the turbidity of residual water at the exit of the clarification processes (coagulation-flocculation) be less than 1 NTU because filtration processes can cause pressure elevation and inadequate treatment; and the American Water Works Association (2001) recommends 1 NTU as the average value and 5 NTU as the maximum allowable value for clarified water. On the other hand, the European Union (1998) established 2 and 1 NTU, respectively, and the World Health Organization (WHO) suggests that the median turbidity of treated water is ideally less than 0.1 UNT for effective disinfection, although the WHO does not determine an admissible value of turbidity based on health criteria (WHO 2006, Montoya et al. 2011).

However, water turbidity can be considered as a parameter both in supply sources and in distribution processes and systems (Burlingame et al. 1998, Lusardi & Consonery 1999, Letterman & Viswanathan 2004), since it is a fast and inexpensive interpretation to interpret water quality (Burlingame et al. 1998).

Furthermore, turbidity is associated with the potential microbiological risk in water for human consumption.

In the case of coliforms, the microorganisms that make up this group, *Escherichia*, *Enterobacter*, *Klebsiella*, *Serratia*, *Edwardsiella*, and *Citrobacter*, live as independent saprophytes or as intestinal bacteria; fecal coliforms (*Escherichia*) are of intestinal origin (Canosa 1995), and their presence in water

Table 3: National and international maximum allowable limits.

Parameter	Unit	Average amount	MAL 1	MAL 2
Turbidity	NTU	25.00	-	2
Fecal Coli-forms	NMP.100mL ⁻¹	4 600.00	1 000	1 000
Total Coli-forms	NMP.100mL ⁻¹	24 000.00	-	1 000

*MAL: Maximum Allowable Limit; **MAL 1: Maximum Allowable Limit NOM-001-SEMARNAT-1996; ***MAL 2: Maximum Allowable Limit Environmental Protection Agency 1998

indicates recent bacterial contamination and is an indicator of water body degradation and it was recommended by the United States Environmental Protection Agency (1998) and is based on studies that showed that they have a direct relationship with diseases associated with swimming in marine and freshwater environments (Arcos-Pulido et al. 2005).

The reduction of TSS and turbidity have a close relationship, as seen in Fig. 2. In Fig. 3 you can see that the TSS is present homogeneously in the samples. TSS is responsible for the gray color of domestic water, and when these waters are treated, the solids agglomerate and degrade because of gravity.

Similarly, Henckens et al. (2002) found that turbidity is a metric that is affected by a variety of factors, the most important of which are the properties of the suspended particles in the water, such as form, color, size, and organic and inorganic matter ratio (BOD/COD).

Studies such as those by Tomanovic & Maksimovic (1996) and Henckens et al. (2002), show that there is a good correlation between TSS and turbidity in water bodies, while Bertrand-Krajewski (2004) discovered a linear relationship

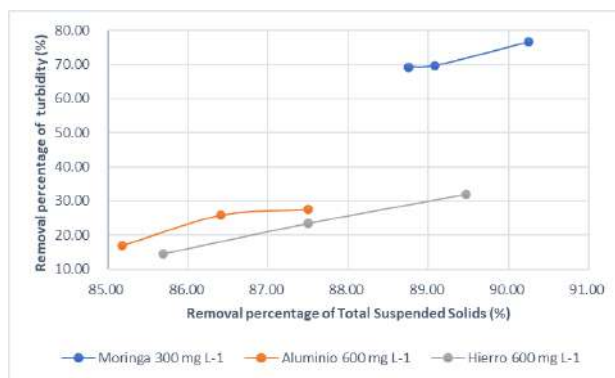


Fig. 2: Optimal per centages of pollutant removal.



Fig. 3: Homogenization of domestic wastewater from Martínez de la Torre, Veracruz.

between these parameters by analyzing unit networks in dry weather conditions and concluded that turbidity is a good indicator of TSS in wastewater, which we can confirm in Fig. 2 because increasing the percentage of turbidity removal is directly proportional to the reduction of TTS.

A 95 per cent mean analysis test was used to determine the significant differences (Fig. 4). It can be seen that the chemical coagulants (Industrial Aluminum Sulfate and Iron Sulfate Heptahydrate reactive grade) both had the same percentage of turbidity removal statistically at a concentration of 600 mg.L⁻¹, whereas the use of *Moringa oleifera* at a concentration of 300 mg.L⁻¹ has a different statistical percentage than this, being this the concentration used.

Subsequently, the removal percentage of TTS was observed by the same statistical method at 95% as shown in Fig. 5. The concentrations of chemical coagulants at 600 mg.L⁻¹ and *Moringa oleifera* at 300 mg.L⁻¹ show statistically the same efficiencies, in addition to being the most efficient

with removal averages of 86.36%, 87.55%, and 89.36% respectively.

The effects of the coagulants were analyzed using surface tests to see how they affected the pH and conductivity of the samples before and after the coagulation-flocculation treatments proposed by chemical salts and *Moringa oleifera* powder. Fig. 6 shows that the turbidity removal and TSS percentages corresponding to *Moringa oleifera* powder show positive pH differences, whereas the results of the coagula-

Table 4: Treatments to determine the optimal concentration values per coagulant.

Treatment	pH	Coagulant [mg]			Sample [1000 mL]
<i>Moringa oleifera</i>	7.0	300	600	900	1 000
Aluminum sulfate	7.0	300	600	900	1 000
Iron sulfate	7.0	300	600	900	1 000

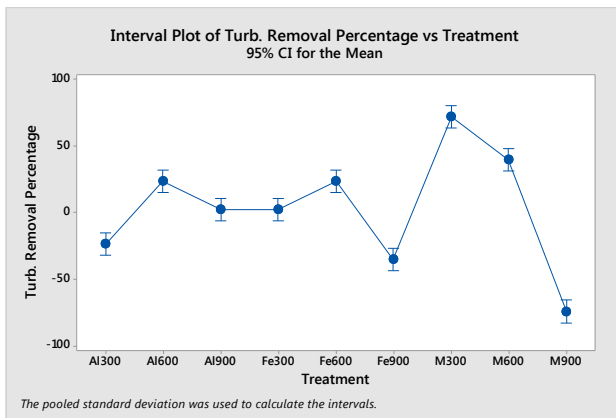


Fig. 4: Mean test with a 95% confidence level for the determination of the optimal dose vs. turbidity.

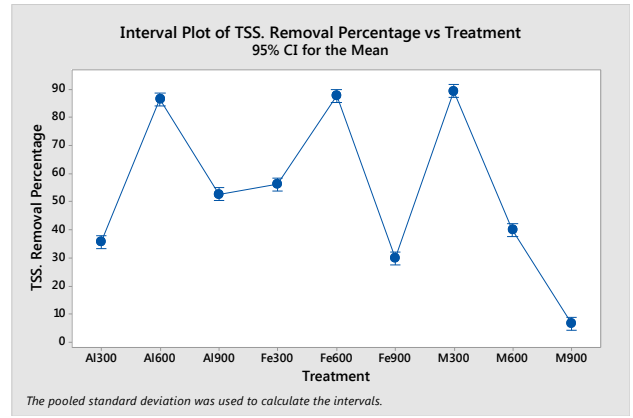


Fig. 5: Mean test with a 95% confidence level for the determination of the optimal dose vs TSS.

Table 5: Per centage of removal of turbidity and total suspended solids.

Treatment	Concentration	Turbidity removal per centage			TSS removal rate		
<i>Moringa oleifera</i>	300	69.23	69.60	76.68	88.75	89.08	90.25
	600	28.79	31.43	58.70	38.75	40.14	41.11
	900	-74.79	-73.85	-73.3	6.54	6.66	6.80
Aluminum sulfate	300	-25.75	-24.74	-20.54	33.93	36.36	36.93
	600	17.03	25.82	27.52	85.18	86.41	87.50
	900	2.02	2.50	2.56	50.00	50.72	57.25
Iron sulphate	300	1.87	1.89	3.79	54.27	56.25	57.89
	600	14.53	23.44	31.90	85.69	87.50	89.47
	900	-38.18	-36.75	-29.88	28.15	30.71	30.89

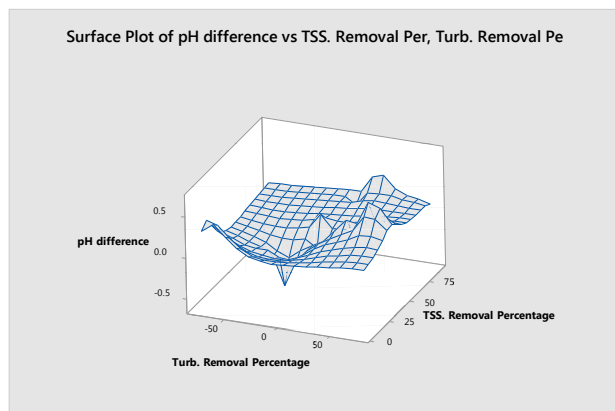


Fig. 6: Test of surfaces applied at pH and removal of contaminants after treatment.

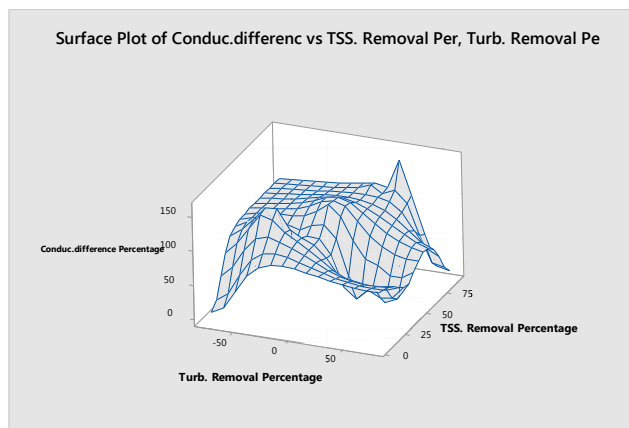


Fig. 7: Surface test applied to the percentage of difference in conductivity and removal of contaminants after treatment.

tion tests with aluminum and iron show negative peaks, due to the pretreatment with aluminum.

Fig. 7 shows that chemical salts tend to increase the conductivity of treated wastewater due to the presence of metal ions. Sandoval & Laines (2013) compared the coagulation efficiency of three types of solutions obtained from *Moringa oleifera* seeds and aluminum sulphate, finding that moringa treatments did not change the chemical properties of the treated water, which is confirmed in said work, since the said solute did not change the properties of conductivity and pH during experimentation, whereas aluminum sulphate, as a chemical salt with metal ions, tends to acidify the water.

CONCLUSION

For the treatment of wastewater from the sewage system in Martínez de la Torre, Veracruz, moringa seed powder is effective as a flocculant and natural coagulant. The appropriate dose of moringa powder for urban wastewater from Martínez de la Torre, Veracruz is 300 mg.L^{-1} . Because it did not present free sulfate ions in the medium after the decantation period, the optimal dose of *Moringa oleifera* obtained the maximum percentage of turbidity degradation (71.84 per cent) in 15 minutes of stirring and 1 hour of rest. The decrease in Total Suspended Solids from the moringa coagulant was statistically similar to that obtained by aluminum and iron salts.

Moringa oleifera seed powder does not produce changes in control parameters such as pH and conductivity, whereas aluminum and ferric salts in this experiment reported 42% and 56% due to the presence of metal ions in the wastewater.

The use of *Moringa oleifera* powder is a natural, efficient, and easy to use as an alternative. This type of unconventional treatment will be able to recover the water used within the metropolitan area of Martínez de la Torre and improve the

quality of the water of the Filobobos river, in addition, to contributing to the reduction of sludge.

ACKNOWLEDGEMENTS

We are grateful to the Tecnológico Nacional de México/Instituto Tecnológico Superior de Martínez de la Torre and the Tecnológico Nacional de México, in addition to the teachers Edwin Daniel Méndez Cruz, Leonides Sánchez Mota and the students Rigo Adalberto Ruiz Alberto and Ana Cristina Sandría, for their support and dedication in taking samples.

REFERENCES

- Arcos-Pulido, M.P., Ávila de Navia, S.L., Estupiñan-Torres, S.M. and Gómez-Prietp, A.C. 2005. Microbiological indicators of contamination of water sources. Nova-Sci. Pub., 3(4): 69-79.
- APHA-AWWA-WPCF 1998. Standards Methods For the Examination of Water and Wastewater. 20th Edition, USA.
- American Water Works Association 2001. Self-Assessment for Treatment Plant Optimization. International Edition, Denver.
- Bertrand-Krajewski, J.L. 2004. TSS concentration in sewers was estimated from turbidity measurements by means of linear regression accounting for uncertainties in both variables. Water Sci. Technol., 50(11): 81-88
- Burlingame, G.A., Pickel, M.I.J. and Roman, J.T. 1998. Practical application of turbidity monitoring. J. AWWA, 90(8): 57-69.
- Canosa, A. 1995. Bacteriological Indicators of Eutrophication in the Chuza, Neusa, and Tominé Reservoirs, and the Chingaza Lagoon. Bogota Colombia. The Jorge Tadeo Lozano University of Bogotá Foundation, Center for Scientific Research.
- European Union. 1998. Council Directive 98/83/EC. Relating to the quality of water intended for human consumption.
- Henckens, G.J.R., Veldkamp, R.G. and Schuit, T.D. 2002. On monitoring of turbidity in sewers. American Society of Civil Engineers, Proceedings of the Ninth International Conference on Urban Drainage, Portland, 8-13 September.
- Letterman, R.D., Johnson, C.E. and Viswanathan, S. 2004. Low-level turbidity measurements: A comparison of instruments. J. AWWA, 96(8): 125-137.

- Lusardi, P.J.Y. and Consonery, P.J. 1999. Factors affecting filtered water turbidity. *J. AWWA*, 91(12): 28-40.
- Metcalf and Eddy, Inc. 1998. *Wastewater Engineering. Treatment, Discharge, and Reuse*. McGraw Hill Publisher, Mexico.
- Montoya, C., Loaiza, D., Torres, P., Hernán-Cruz, C.Y. and Escobar, J.C. 2011. Effect of the increase in the turbidity of raw water on the efficiency of conventional purification processes. *J. Sch. Eng. Antioquia*, 16: 137-148.
- Norde, W. 2011. *Colloids and Interfaces in Life Sciences and Bionanotechnology*. 2nd Edition, CRC Press, Boca Raton, FL.
- Rozkosný, M., Kriska, M., Sálek, J., Bodík, I. and Istenic, D. 2014. Natural Technologies of Wastewater Treatment. *Global Water Partnership, Central and Eastern Europe*, p. 138.
- Tomanovic, A. and Maksimovic, C. 1996. Improved modeling of suspended solids discharges from asphalt surface during the storm event. *Water Science and Technology*, 33(4-5): 363-369.
- Sandoval, M. and Laines, J. 2013. *Moringa oleifera* is an alternative to replacing metallic coagulants in surface water treatment. *Eng. FI-UADY Acad. Rev.*, 17(2): 93-10.
- Solís-Silvan, R., Laines-Canepa, L.C. and Hernández-Barajas, J.R. 2012. Mixtures with coagulating potential to clarify surface water. *Rev. Inv. Cont. Amb.*, 28(3): 229-236
- The United States Environmental Protection Agency. 1998. Optimizing water treatment plant performance using the composite correction program. EPA/625/6-91/027. USEPA, Washington, D.C.
- Vásquez, O. 1994. Extraction of Natural Coagulants from Nopal and Application in Clarification of Surface Water [Thesis]. Universidad Autónoma de Nuevo León, Monterrey, México, pp. 28-57.
- World Health Organization (WHO). 2006. *Guidelines for Drinking Water Quality*. Third Edition. Volume 1. WHO, Geneva, Switzerland.



Florida's Aquifer Vulnerability to Nitrate Contamination: A GIS Model

M. Jamuna*†, M. Gandhimathi*, J. Abdul Bari** and T. Niveditha***

*Department of Civil Engineering, Kumaraguru College of Technology, Coimbatore, India

**Department of Civil Engineering, K.S. Rangasamy College of Technology, Tiruchengode, India

***Department of Environmental Engineering, Florida University, USA

†Corresponding author: M. Jamuna; jamuna.m.ce@kct.ac.in

Nat. Env. & Poll. Tech.
Website: www.neptjournal.com

Received: 17-04-2021

Revised: 12-05-2021

Accepted: 25-05-2021

Key Words:

Groundwater
Nitrogen contamination
GIS techniques
Kriging interpolation
DRASTIC model
Thematic map

ABSTRACT

Groundwater is a crucial natural resource in the state of Florida. since it supports to environmental, social, and economic aspects of the country. Groundwater will not be contaminated easily but it is difficult to restore once it is contaminated. Since its extensive usage in agricultural activities in the state of Florida, groundwater has degraded in recent years, resulting in many direct and indirect impacts, particularly nitrogen content in the form of nitrates using Geographical Information System (GIS) technology, the researchers investigated the effects of groundwater on Nitrogen (NO₃) content in the study area by creating a spatial distribution of NO₃ contamination, which was then analyzed using GIS, Kriging Interpolation, and the DRASTIC model to determine the susceptibility of groundwater to NO₃ contamination. The final result depicts the model's performance as vulnerability groups, which are based on natural breaks showing places that are more susceptible to nitrogen pollution. The map highlighted that the south zone of Florida was more vulnerable to nitrogen contamination, necessitating more careful wastewater disposal system planning.

INTRODUCTION

The importance of water in human life and culture cannot be overstated. Both groundwater and surface water play important roles in economic, social, health, recreational, and cultural activities, as well as in environmental and ecosystem preservation (Abdul Bari et al. 2015, Tirkey et al. 2013, Anornu et al. 2012). Although water covers 70 per cent of the Earth, groundwater accounts for just 0.6 per cent of all usable water; however, that 0.6 per cent accounts for 98 per cent of all freshwater available for human use. Water found in soil and rock pore spaces underneath the Earth's crust, as well as in the cracks of rock formations, is known as groundwater, while water found above the ground is known as surface water. Because of rapid population growth, surface water volume and quality are dwindling, leaving groundwater as the most reliable source of water in terms of quality. The most critical water resource on the planet is groundwater (Abdul Bari & Jamuna 2020). It is the sole source of water for drinking, agriculture, and industrial uses in many arid and semi-arid areas around the world (Tesoriero et al. 1998). Residential, municipal, commercial, manufacturing, and agricultural activities can all affect groundwater quality, particularly when it comes to fertilizer overuse and unsanitary conditions (Tesoriero et al. 1998). Fertilizers contain nitrogen compounds which increase the productivity of crops. The

increasing demand for nitrogen disposal regulation in recent years prompted the selection of this topic for research. The problem of nitrate leaching in the surface and groundwater has been studied in recent years. Excess Nitrogen has harmed nearly 4,800 water bodies in the United States (U.S. EPA 2012). Septic systems are recognized as one of the major sources of Nitrogen pollution. The rising nutrient content in treated sewage is posing a threat to the ecosystem by causing many environmental issues such as eutrophication (example: summer algal blooms). The high level of NO₃ in the water affects the health of human beings and causes methemoglobinemia called Blue Baby Syndrome, Birth Malformation, and other issues. Nitrate concentrations in drinking water exceeding 10 milligrams per liter (10 mg.L⁻¹) can be dangerous if consumed, according to US Environmental Protection Agency (EPA) guidelines (EPA 2009). Several studies have used different approaches to determine the susceptibility of groundwater to nitrate pollution and other contaminants. These techniques can be classified as follows: Overlay and Index Methods, Process-Based Methods, and Statistical Methods (Tesoriero et al. 1998, Thirumalaivasan & Venugopal 2003), out of which the DRASTIC model, which comes under the Overlay and Index group, is one of the most commonly used groundwater vulnerability mapping methods. DRASTIC is an acronym that stands for Depth to water, net Recharge, Aquifer media, Soil media, Topography,

Impact of the vadose zone, and hydraulic Conductivity (Aller et al. 1987). The purpose of this study is to explore nitrogen's existence and transportation to find and recognize areas in Florida that are more vulnerable to pollution. The ultimate goal of this research work is to use GIS-based modeling to create a model that can identify areas that are most susceptible to nitrogen pollution.

STUDY AREA

The state of Florida was chosen because of its exceptional hydrogeological features. The most striking conclusion that historical research conveys about Florida and its ecosystems is that in any one area there have been immense changes (Webb 1990).

Florida is a living example of S.D. Webb's terms. It incorporates hydrogeological history (from shallow waterfronts to aquifers), climatic conditions, geography, and environmental forces in a specific way. These characteristics have resulted in Florida being a vast repository of landscape, plant population, and species diversity, which supports significant ecological, taxonomic, and genetic diversity. Because of these distinguishing characteristics, spatial differences in Florida's groundwater are susceptible to nitrogen contamination from onsite wastewater treatment facilities. Exposure to oceanic waters has a major impact on the state's climatic conditions. This is particularly apparent when it comes to temperature and rainfall. The temperature is warm, the rain is heavy, and the humidity is high. With an average daily temperature of 70.7°F (21.5°C), Florida is the warmest state in the United States. In July, average high temperatures range from 90°F (32.2°C) to 95°F (35°C), while average low temperatures in January range from 40°F (4.4°C) to 45°F (7.2°C) in the northern part of the state and 60°F (15.6°C) to 65°F (18.3°C) in the southern part. The great majority of the state is located within a region with annual rainfall ranging from 48 to 57 inches. The average annual rainfall for the entire state is about 54 inches. Rainfall occurs in irregular patterns during the year.

MATERIALS AND METHODS

The main aim of this project is to create a thematic map for Florida that portrays the areas most susceptible to nitrogen pollution. Using the Soil Data Viewer method in ArcGIS, this can be achieved spatially. When used independently of ArcGIS, this tool allows users to create soil-based thematic maps or generate a tabular report. Soil Data Viewer could be used to access soil properties and interpretations after shielding them from the soil database's complexity. The methodology used for this investigation is shown in Fig. 1 (United States Department of Agriculture 2015).

Method of Research Focused on GIS

Since the 1980s, GIS has been successfully used to determine the susceptibility of groundwater to pollution (Al-Adamat et al. 2003, Vias et al. 2005, Baalousha 2006, Jamrah et al. 2007, Sener et al. 2009, Massone et al. 2010). For groundwater analyses, several recent studies have used interpolation approaches, the most popular of which are Inverse Distance Weighting (IDW) and kriging. In situations where there is little or no groundwater monitoring data, researchers have used a different approach, in which a vulnerability model is first established using site-specific geological data, and then field-tested using either current or specially acquired groundwater data (Margat 1968). Since then, several vulnerability mapping methods have appeared, including CMLS (Nofziger & Hornsby 1986, 1987), DRASTIC (Aller et al. 1987), GOD (Foster 1987), LEACHM (Wagenet & Hutson 1989), AVI (Van Stempvoort et al. 1993), and SINTACS (Van Stempvoort et al. 1993, Ersoy & Gultekin 2013).

DRASTIC Model

Several studies have used the DRASTIC model to determine groundwater and aquifer risk in different parts of the world. The model generates regional maps that demarcate areas of low, moderate, and high vulnerability, which could be followed up with additional site-specific analysis. The use of the DRASTIC index model to evaluate the study area's groundwater vulnerability has been meticulously investigated. The application procedure was given in Table 1.

The DRASTIC index is calculated using Equation

$$\text{DRASTIC index} = DrDw + RrRw + ArAw + SrSw + TrTw + IrIw + CrCw$$

Where D, R, A, S, T, I, and C are the seven parameters



Fig. 1: Methodology.

described subscript r is the corresponding rating of the parameter, and subscript w is the corresponding weights of the parameters.

Where,

Dr = Ratings to the depth to the water table

Dw = Weight assigned to the depth to the water table

Rr = Ratings for ranges of aquifer recharge

Rw = Weight for aquifer recharge

Ar = Ratings assigned to aquifer media

Aw = Weight assigned to aquifer media

Sr = Ratings for soil media

Sw = Weight for soil media

Tr = Ratings for topography

Tw = Weight assigned to topography

Ir = Ratings assigned to vadose zone

Iw = Weight assigned to vadose zone

Cr = Ratings for rates of hydraulic conductivity

Cw = Weight given to hydraulic conductivity

A Geographic Information System (GIS) was also used in the DRASTIC model to visualize the areas of Florida

that are most vulnerable to nitrogen contamination (Arthur et al. 2007). The most limitation of this approach is that all seven parameters are rated on a specific scale in some order, preventing continuous data from being considered. Fig. 2 Shows the DRASTIC vulnerability map.

FAVA Model

Florida's Department of Environmental Protection created a descendant model, the Florida Aquifer Vulnerability Assessment (FAVA). FAVA employs the Weight of Evidence (WOE) model to make predictions based on nitrate concentrations in wells and other spatial data, which are then shown as vulnerability maps.

The FAVA model made use of training points, which are places where prior likelihood and spatial data results are known. The training points in this case were wells with total dissolved nitrogen samples that were less than the median value. The data is weighted and evidential maps are built based on areas that have a strong resemblance to the training point areas. Several of these maps are combined in GIS to make response maps which are used to generate

Table 1: The pollution potential conditioning factors (PPCFs) ratings and their weights (Chen et al. 2009).

Criteria	Ranges	Pollution Potentiality for groundwater vulnerability	Weight Assigned
Depth to water (D)	0.34 – 1.58	High	5
	1.86 - 2.14	Medium	4
	2.14 – 2.53	Low	3
Recharge Rate (R)	228.68 – 243.33	Low	1
	243.33- 256.56	Medium	2
	256.56 – 278.77	High	5
Aquifer Media (A)	250 - 305Ω	Medium	3
	367 - 445Ω	Low	2
	445 - 600Ω	High	5
Soil Media (S)	Igneous Rocks	Low	2
	Sedimentary Rocks	Medium	3
	Low Humic Gley soil developed in the valley and flood plain	High	5
Topography (T)	0 – 2.57	High	4
	8.77-15.54	Medium	3
	15.54-25.83	Low	2
Impact of Vadose Zone(I)	388 - 511Ω	High	5
	511 - 793 Ω	Medium	3
	793- 1464 Ω	Low	2
Hydraulic conductivity (C)	0.0018- 0.0034	Low	2
	0.0034-0.0069	Medium	3
	0.00127-0.0270	High	5

the probability map displaying aquifer vulnerability to nitrogen.

The main change that would be implemented in this model is that it includes details considering human sources of contamination from OWTS and also it considers the areas other than SAS (Surficial Aquifer System) region.

The maps of the DRASTIC (Fig. 2) and FAVA (Fig. 3) model show that the SAS region of Florida has not been considered in the study. The contaminant removal equation also involves parameters including reaction rates and retardation factors. This method would assess Nitrogen risk for the entire state of Florida by looking at contaminant fate and transport processes for nitrate.

Fate and Transport Equation

The advection-dispersion equation in N-calc (McCray et al. 2005) was used to calculate nitrogen removal in the vadose region. It's simplified by ignoring dispersion's effects and assuming steady-state conditions.

The elementary equation for contaminant removal is an exponential decay function,

$$C(z)=C_0 \exp\left(\frac{-RK_r}{V_z} Z\right)$$

Where,

C(z) is the ultimate measuring point (i.e.) the amount of Nitrogen concentration left in the water table

C₀ is the initial concentration of ammonium or nitrate (mg.L⁻¹)

R is retardation factor

K_r is the first-order reaction rate

V_z is the vertical water velocity (cm.day⁻¹)

Z is the soil depth (cm)

This can be used to calculate the concentration of

ammonium and nitrate as a function of the removal processes.

- The initial concentration, C₀ can be obtained from the source of contamination, OWTS (Onsite Wastewater Treatment Systems)
- The retardation factor, R is got from various soil properties like distribution coefficient, bulk density, soil moisture content.

$$R=1+\frac{K_d}{\theta} \rho$$

Where,

K_d is the distribution coefficient (L.kg⁻¹)

θ is the soil moisture content (%)

ρ is the bulk density of the soil (g.cm⁻³)

- K_r is the first-order reaction rate, that can be attained from the cumulative frequency diagram (CFD) of reaction rates (McCray et al. 2005)
- Depth of water table is obtained from Web soil survey by USDA.

The model input parameters that are included in this model are

- The initial concentration of ammonium or nitrate
- Distribution coefficient
- Soil moisture content
- Bulk density of the soil
- First-order reaction rate
- Depth to the water table

The Initial Concentration of Ammonium or Nitrate

The primary source of nitrogen disposal is onsite wastewater treatment facilities (Fig. 4). The Florida Department of Health maintains a list of OWTS locations in the state. The

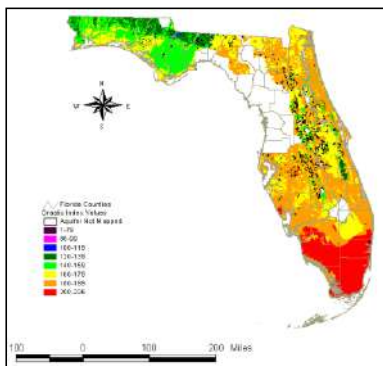


Fig. 2: DRASTIC vulnerability map for the Surficial Aquifer System.

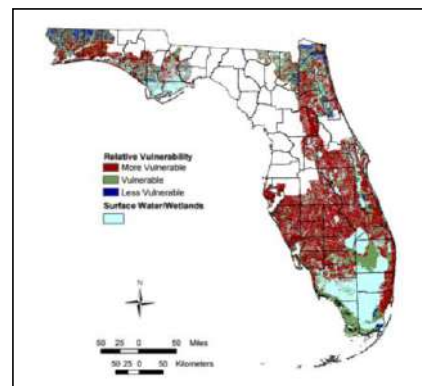


Fig. 3: Florida Aquifer Vulnerability Assessment (FAVA) response theme.

nitrogen content in the effluent disposed of is 60 mg.L⁻¹, which is the median concentration.

Depth to the Water Table

- The depth to groundwater for the Model was collected from the National Water Information System of the United States Geological Survey (NWIS). The NWIS database provides information on active good networks, as well as statistics on groundwater levels. The GA tool in ArcMap was then used to construct a continuous projected depth water table surface (using ordinary kriging interpolation), which was then translated into a raster file for further analysis. The map was categorized into ranges identified by the DRASTIC Model after the IDW (1-10, with 1 representing minimal impact to vulnerability and 10 representing maximum impact). The lower the ranking score, the deeper the groundwater. The depth to water map is given in Fig. 5. Depth to the water table is one of the major factors affecting contaminant transformation.
- The term (z/v_z) from the equation is taken as Depth to the water table.
- This is also obtained using the Soil Development Tool, which gives the annual minimum water table depth in centimeters. The water table depth ranged from 0 to 201 cm throughout the area of Florida.



Fig. 4: The point locations of OWTS.

Retardation Factor

The retardation factor, R is got from

$$R = 1 + \frac{K_d}{\theta} \rho$$

A new field showing the K_d value based on clay content is generated.

Soil moisture content and bulk density are obtained from USDA soil literature (Table 2) based on soil texture. Soil texture data is also available from the Soil Development Tool and two new fields are added as soil moisture content and bulk density. The soil moisture content is assumed to be porosity. The values of bulk density and porosity are obtained from Table 3 and are added manually to the new fields based on the soil texture. With these obtained values, a new field is created with all the factors substituted and hence Retardation Factor is obtained (Fig. 6). The Retardation Factor value ranges from 1.17 to 5.30. A symbology map showing the variation is generated as shown.

RESULTS AND DISCUSSION

The various layers were generated based on the above section using the databases listed in data sources and the Soil data viewer tool. The soil texture thematic map was created as shown in Fig. 7.

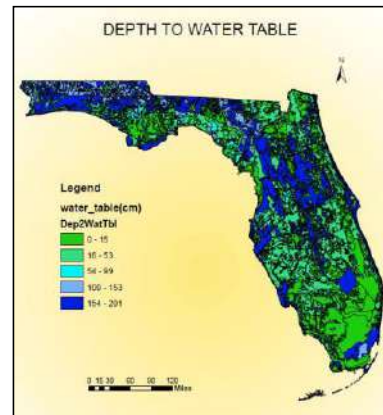


Fig. 5: Depth to water table for the State of Florida.

Table 2: Data sources of parameter values and spatial data used in the study.

Name	Source	Description
Web Soil Survey Geographic database	U.S. Department of Agriculture (USDA)	Soil data
Wastewater inventory database	Florida Department of Health	Florida Water Management Inventory
Porosity	Rawls et al. 1982	Porosity values for USDA soil textures

As a result, 18 soil layers were formed, one of which was a variable field into which the sample mean values were fed. The Retardation factor map was created after the parameters for the Retardation factor were obtained. The range of retardation factors corresponded to the theoretical range for Florida. It was in the range of 1.16 to 5.3. (no unit). After the individual layers, the final map depicting the remaining Nitrate concentration is produced which is shown in Fig. 8

The residual nitrate concentration varied between less than 1 mg.L⁻¹ and 60 mg.L⁻¹. The higher concentration zones are caused by shallow depth to aquifer values and/or low Kr concentrations, which prevent complete ammonium to nitrate conversion. From Fig. 5, it is evident that most of the area is prone to contamination owing to the fact that the annual Depth to the water table in Florida is generally shallow, ranging from 0 cm to 201 cm with about 25% of the area ≤5cm. In addition, the more susceptible areas of

Florida share the same limestone layers and wetlands found in the southern part of the state. The areas within the gravel and sand aquifer are also less vulnerable.

CONCLUSION

The map’s findings show that the most vulnerable areas have a shallow depth to water table measurements, as can be seen on the depth to water table map (Fig. 5) and the remaining nitrate content map (Fig. 8). This would improve wastewater laws to a greater degree. If the appropriate equation and parameters are available, the same modeling technique can be established for any contaminant in any given field.

REFERENCES

Abdul Bari, J., Vennila, G. and Shanmugaraja, T.M. 2015. Physico-chemical characteristics of groundwater of Bhavani block, Erode District, Tamilnadu, India Rasayan J. of Chem., 8(2): 198 -202.
 Abdul Bari, J. and Jamuna, M. 2020. Assessment of hydrogeochemistry and evaluation of groundwater quality feasibility zones in Bhavani Taluk, Tamilnadu, India. Int. J. of Adv. Sci. Tech., 29(7): 8323-8333.

Table 3: Porosity classified by soil texture. (Rawls et al. 1982)

USDA Soil Texture	Sample Size	Total Porosity/Saturation Θ_s [cm ³ .cm ⁻³]
Sand	762	0.437
Loamy sand	338	0.437
Sandy loam	666	0.453
Loam	383	0.463
Silt loam	1206	0.501
Sandy clay loam	498	0.398
Clay loam	366	0.464
Silty clay loam	689	0.471
Sandy clay	45	0.430
Silty clay	127	0.479
Clay	291	0.475

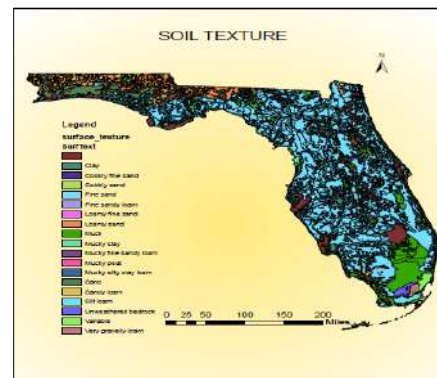


Fig. 7: Soil texture layer for the state of Florida.

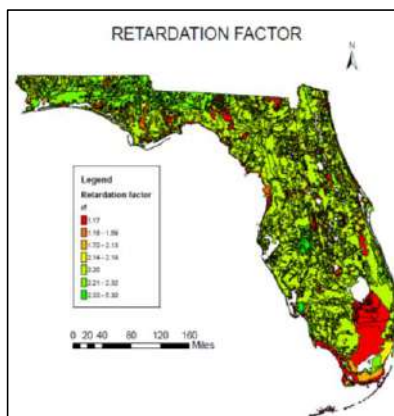


Fig. 6: Retardation Factor layer for the state of Florida.

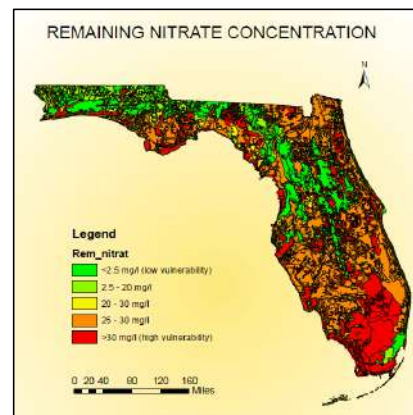


Fig. 8: Florida nitrogen vulnerability map.

- Al-Adamat, R., Ian, L.F. and Serwan, M.J. B. 2003. Groundwater vulnerability and risk mapping for the basaltic aquifer of the Azraq Basin of Jordan using GIS, Remote Sensing, and DRASTIC. *Appl. Geog.*, 23(4): 303-324.
- Aller, L., Todd, B., Jay, H.L. and Richard, J.P. 1987. DRASTIC: A Standardized System for Evaluating Ground Water Pollution Potential Using Hydrogeologic Settings. EPA/600/2-85/018, US Environmental Protection Agency, Robert S. Kerr Environmental Research Laboratory, Office of Research and Development.
- Anornu, G.K., Kabo-bah, A.T. and Anim-Gyampo, M. 2012. Evaluation of groundwater vulnerability in the Densu River basin of Ghana. *Amer. J. of Human Ecol.*, 1(3): 79-86.
- Arthur, J. D., Wood, H. A. R., Baker, A. E., Cichon, J. R. and Raines, G. L. 2007. Development and implementation of a Bayesian based aquifer vulnerability assessment in Florida, *Natural Resources Research*, 16: 93-107.
- Baalousha, H. 2006. Vulnerability assessment for the Gaza Strip, Palestine using DRASTIC. *Environ. Geol.*, 50: 405-414.
- Chen, Y., Khan, S. and Paydar, Z. 20010. To retire or expand? A fuzzy GIS-based spatial multi-criteria evaluation framework for irrigated agriculture. *Irrig. Drain.*, 59(2): 174-188.
- Ersoy, A.F. and Gultekin, F. 2013. DRASTIC-based methodology for assessing groundwater vulnerability in the Gumushacikoy and Merzifon Basin (Amasya, Turkey). *Earth Sci. Res. J.*, 17(1): 33-40.
- EPA 2009. National Primary Drinking Water Regulations, U.S. Environmental Protection Agency Report 816-F-09-004.
- Foster, S. 1987. *Fundamental Concepts in Aquifer Vulnerability, Pollution Risk and Protection Strategy.* The Netherlands Vulnerability of Soil and Groundwater to Pollutants The Hague. Noordwijk Aan Zee: Netherlands Organization for Applied Scientific Research., pp. 69-86.
- Jamrah, A., Al-Futaisi, A. and Rajmohan, N. 2008. Assessment of groundwater vulnerability in the coastal region of Oman using DRASTIC index method in GIS environment. *Environ. Monit. Assess.*, 147: 125-138.
- McCray, J.E., S.L Kirkland., R.L. Siegrist, and G.D. Thyne 2005. Model Parameters for Simulating Fate and Transport of On-Site Wastewater Nutrients. *Ground Water*, 43(4): 628-639.
- Massone, H., Mauricio, Q.L. and Daniel, M. 2010. Enhanced groundwater vulnerability assessment in geological homogeneous areas: A case study from the Argentine Pampas. *Hydrogeol. J.*, 23: 371-379.
- Margat, J. 1968. *Groundwater Vulnerability to Contamination.* Doc, Orleans, France: 68 SGC 198 HYD, BRGM.
- Nofziger, D.L. and Hornsby, A.G. 1986. A microcomputer-based management tool for chemical movement in the soil. *Appl. Agric. Res.*, 1: 50-56.
- Nofziger, D. L. and Hornsby, A.G. 1987. *CMLS: Chemical Movement through Layered Soils Model Users Manual.* Gainesville, FL: University of Florida.
- Rawls, W. J., D. L. Brakensiek, and K. E. Saxton. 1982. Estimation of soil water properties. *Trans. ASAE* 25(5): 1316-1320
- Sener, E., Sehnaz, S. and Aysen, D. 2009. Assessment of aquifer vulnerability based on GIS and DRASTIC methods: A Case Study of the Senirkent-Uluborlu Basin (Isparta, Turkey). *Hydrogeology Journal* 2023-2035.
- Tirkey, P., Gorai, A.K. and Iqbal, J. 2013. AHPGIS-based DRASTIC model for groundwater vulnerability to pollution assessment: A case study of Hazaribag district, Jharkhand, India. *International Journal of Environmental Protection.*, 3(9): 20-24.
- Tesoriero, A.J., Inkpen, E.L. and Voss, F.D. 1998. Assessing Groundwater Vulnerability Using Logistic Regression. In *Proceedings for the Source Water Assessment and Protection 98 Conference*, Dallas, TX (Vol. 157165).
- Thirumalaivasan, D.K. and Venugopal, M.K. 2003. AHP-DRASTIC: Software for specific aquifer vulnerability assessment using DRASTIC model and GIS, *Environmental Modelling & Software*, 18: 645-656
- U.S. Department of Agriculture, Natural Resources Conservation Service (USDA, NRCS). 2015.
- U.S. EPA, 2012. <http://water.epa.gov/drink/contaminants/basicinformation/nitrate.cfm>
- Vias, J.M., Andreo, B., Perles, M.J. and Carrasco, F. 2005. A comparative study of four schemes for groundwater vulnerability mapping in a diffuse flow carbonate aquifer under Mediterranean climatic conditions. *Environ. Geol.*, 586-595.
- Van Stempvoort, D., Lee, E. and Leonard, W. 1993. *Aquifer Vulnerability Index (AVI): A GIS Compatible Method for Groundwater Vulnerability Mapping.* Canadian Water Resources Journal, 25-37.
- Wagenet, J.R., and Hutson, J.L. 1989. *LEACHM: A Model for Simulating the Leaching and Chemistry of Solutes in the Plant Root Zone.* Water Resources Institute, New York.
- Webb, S.D. 1990. Historical biogeography. In R. L. Myers and J. J. Ewel (eds). *Ecosystems of Florida*, University of Central Florida Press, Orlando, Florida, pp. 70-102.



Use of Remote Sensing and GIS Techniques in Identification of Landslide Vulnerable Zones of Shastri River Basin Along the West Coast of Ratnagiri District, Maharashtra

S. B. Joshi *† and D. D. Kulkarni**

*Department of Geology, Walchand College of Arts & Science, Solapur, Maharashtra, India

**Department of Geology, School of Earth Sciences, P.A.H. Solapur University, Maharashtra, India

†Corresponding author: S. B. Joshi; sanjaybj65@rediffmail.com

Nat. Env. & Poll. Tech.
Website: www.neptjournal.com

Received: 08-06-2021

Revised: 09-07-2021

Accepted: 14-07-2021

Key Words:

Natural hazards
Remote sensing
DEM
GIS
Landslide

ABSTRACT

The atmosphere, hydrosphere, and lithosphere are subjected to different processes, leading to natural hazards like weathering, erosion, floods, cyclones, landslides, earthquakes, tectonic movements, etc. Environmental degradation is a serious aspect of the recent past, mainly due to natural and manmade interactions. The pressure for infrastructure development due to rapid urbanization has led to the expansion of construction activities. It has catapulted the frequency of landslides to dramatic proportions in recent decades, especially along western ghats. The West Coast of India (WCI) has attracted the attention of Geo-scientists due to its neo-tectonic setup, continuing seismic activities, sea-level changes, and also due to environmental degradation. It is followed that very limited attempts have been made related to the land sliding along the west coast tract of Maharashtra. The present investigations are emphasized mainly to locate the landslide vulnerable zones of Shastri River Basin (SRB), Ratnagiri district of Maharashtra by using remote sensing data, GIS techniques along field studies. The area lies within a triple junction of Koyana-Kurduwadi Lineament (KKL), West Coast Fault (WCF), and Panvel Flexure (PF). Based on the integration of data from various thematic maps viz. lithology, lineaments, slope, geomorphology, land use-land cover along with inventory map, Landslide Vulnerable Map (LVM) of the SRB has been prepared. It follows that about 29% area of the SRB forms a highly vulnerable zone for land sliding. These zones are mainly confined to steep slopes, wasteland, highly weathered basalts, and deep valleys and in the vicinity of lineaments.

INTRODUCTION

Land degradation is one of the serious environmental problems, causing due to the demand for natural resources by the growing population for food, fodder, fuelwood, and intensive industrial as well as anthropogenic activities. The key problems of land degradation are desertification, deforestation, soil erosion, waterlogging, salination, economic pressure, and poverty. Due to natural and manmade interactions, the atmosphere, hydrosphere, and lithosphere are subjected to different processes, leading to natural hazards. Natural hazards and disasters continue to have an increasing impact on humans around the world. However, studies show that this impact is heavily tilted towards developing countries like India, which might be due to the increasing population. Amongst all the natural disasters, landslides severely damage infrastructure, cause a loss of life and properties, and impact the daily life of people living in the affected regions (Juang et al. 2019). The pressure for infrastructure development due to rapid urbanization has led to the expansion of construction activities. It has accelerated the frequency of landslides to dramatic proportions

in recent decades, especially in hilly terrains.

The studies carried out by many scholars have indicated that the various geosystems viz. lithology, lineaments, geomorphology, slope, land use/land cover, etc. occurring in different combinations, assign differing landslide vulnerability grades (Nagarajan et al. 1998, Guzzetti et al. 2012, Meena et al. 2019, Prakash et al. 2020, Edison & Ganpati 2020). Ramakrishnan et al. (2002) prepared thematic layers in a GIS platform using aerial photos and orthophotos. Heavy rainfall is a critical factor in triggering landslides as it generates a rapid increase in pore pressure in the vadose zone and groundwater flow in the saturated area (Jiu et al. 2005). Various geological structures along with lineaments and lithology play a vital role in triggering landslides (Greenbaum et al. 1995). The susceptibility of the slopes for landslides can also be influenced by land-use and landcover changes caused due to natural or manmade activities (Diaz et al. 2005). According to Van Westen et al. (2006), the soil also acts as one of the most sensitive parameters of land sliding.

The pre- and post-disaster landslide studies have been carried out by many governments and semi-government agencies, academic institutions viz. GSI, CBRI, CRRI, NRSA, WIHG, DTRL, Govind Ballabh Pant Institute of Himalayan Environment, IIT-Roorkee, etc. These organizations have carried work mostly related to landslide-prone regions of the parts of the Himalayas, Uttarakhand, and most of the North-Eastern parts of India. However, very limited attempts have been made with respect to land sliding along Western escarpments of India, especially the west coast of Maharashtra. Therefore, the present studies have been envisaged to locate the landslide-prone zones present within the Shastri River Basin (SRB), Ratnagiri district of Maharashtra. The SRB lies within a triple junction of Koyana- Kurduwadi Lineament (KKL), West Coast Fault (WCF), and Panvel Flexure (PF). It forms a part of one of the seismically active regions of the Indian continent (Valdiya 2011), characterized by sloping topography, presence of shear zones, accelerating rain-splash erosion, sheet erosion as well as gully erosion.

OBJECTIVES

The main objectives of the present study of SRB are to

- Investigate the causative factors of landslides.
- Prepare various thematic maps of these factors viz. slope, geology, lineament, geomorphology, land use/land cover, etc.
- Prepare a map of the landslide vulnerable zones of SRB.

STUDY AREA

The area lies along the West Coast of Maharashtra (India) (lat.16°57'N; long.73°15'E and lat. 17°30'N; long. 73°50' E) (Figs. 1 and 2). Shastri is a seventh-ordered river having a length of about 72 km. It flows from NE to SW direction following major trends of the lineaments and covers an area of about 2098 km² (SOI topographic sheet Nos. 47 G/3, G/4,



Fig. 1: Location map of the area (Shastri River Basin).

G/7, G/8, G/11, G/12, and 47 H/9). The SRB forms a part of the western periphery of the Deccan Trap province of India. It represents the presence of basaltic lava flows of Cretaceous to Eocene age (Mitchell & Cox 1988), exposed along river valleys, valley sides, and near shore. Most of these are capped by laterites of the Pleistocene age. The drainage pattern is dendritic to sub-dendritic, with trellis and sub-parallel at some places controlled by lineaments.

MATERIALS AND METHODS

Present investigations have been carried through the following stages (Fig. 3).

Pre-field studies: These include the review of literature related to landslides, collection of data from topographic sheets, and remote sensing data

Field studies: These include identification of landslides in the field; a collection of their coordinates using GPS, a collection of attributes and training data (GCP) for supervised classification of remote sensing data, and identification of various types of anthropogenic activities in the study region. The GPS data is also collected for the ground truth,



Fig. 2: Map of the SRB (Google Image).

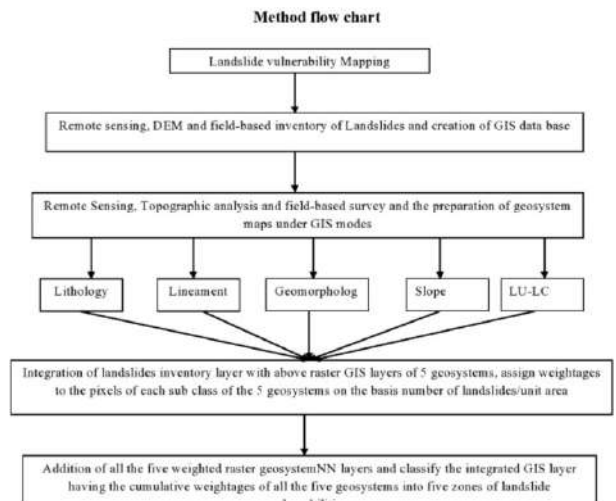


Fig. 3: Method flow chart.

Table 1: Distribution and the morphology of the existing landslides in SRB.

Location No.	L. S. – 1	L. S. – 2	L. S. – 3	L. S. – 4	L. S. – 5	L. S. – 6	L. S. – 7	L. S. – 8
Location	Bhatgaon	Bhatgaon	Near Ukshi village	Close to Konkan Railway line	Karjuve Bridge	Near Bhatgaon village	Near Bhatgaon village	Near Bhuiwadi village
Road Status	Bhatgaon-Abloli Road	Bhatgaon-Abloli Road	Jaigarh-Ukshi Road	Phungus-Sangmeshwar Road	Phungus-Sangmeshwar Road	Bhatgaon-Asore Road	Bhatgaon-Asore Road	Narsinge-Bhuiwadi Road
Lat. And Long.	17°18'20", 73°21'33"	17°17'54", 73°21'45"	17°06'35", 73°26'30"	17°09'55", 73°29'29"	17°11'15", 73°28'22"	17°12'26", 73°25'00"	17°11'46", 73°25'10"	17°12'40", 73°24'00"
Altitude	220 m	120 m	210 m	100 m	100 m	140 m	180 m	200 m
Nature of Slope	Naturally Moderately Steep	Naturally Moderately Steep	Naturally Moderate Top cut Slope	Naturally Moderate Top cut Slope	Natural Top cut Slope	Naturally Moderate Top Cut Slope	Naturally Top cut Slope (Hill Side)	Naturally Steep Top Cut Slope
Strike Dir. of Hill	NNW-SSE	NNW-SSE	N-S	NNE-SSW	NNE-SSW	NNW-SSE	N-S	N-S
Rock Type	Highly altered Deccan Basalt	Lateritic rock mass	Highly Jointed Deccan Basalt	Lateritic soil	Highly altered Laterite	Highly weathered, porphyritic Basalt	Highly weathered Lateritic Soil	Weathered Basalt
Soil Type	Fine Yellowish to Brown, 3 m thick	Dark Brown, 1 m thick	Light yellow thin < 0.5 m	Deep red, Depth couldn't ascertain	Dark brown Lateritic Soil, upto 4 m thick	Brown, thin < 0.5 m	Brown, thin 2-5 m	Brown, 4-5 m thick
Type of L. S.	Debris Slide	Minor Slump	Rock Fall	Soil slump	Soil Slump	Rock Slide	Soil Slump	Soil Slump
L. S. Dimensions	Ht. of Crown ≈ 10 m, Width ≈ 4 m	Ht. of Crown ≈ 3.5 m, Width ≈ 7 m	Ht. of Crown ≈ 2-4 m, Width ≈ 60 m	Ht. of Crown ≈ 2.5 m, Width ≈ 70 m	Ht. of Crown ≈ 4 m, Width ≈ 52 m	Ht. of Crown ≈ 6 m, Width ≈ 85 m	Ht. of Crown ≈ 3 m, Width ≈ 40 m	Ht. of Crown ≈ 4 m, Width ≈ 25 m

Location No.	L. S. – 9	L. S. – 10	L. S. – 11	L. S. – 13	L. S. – 14	L. S. – 15
Location	Near Bhuiwadi village	Near Bhuiwadi village	Near Dhamnase village	Near Kondye village	Near Chavanwadi village	Near Nayari village (Hilltop)
Road Status	Chaphe – Agarnaral - Bhuiwadi Road	Khalgaon – Bhuiwadi Road	Ratnagiri - Ganpatipule Road	Close to Sangmeshwar - Ratnagiri Road	Devrukh – Sangmeshwar Road	Nayari – Sangmeshwar Road
Lat. and Long.	17°13'14", 73°20'15"	17°12'48", 73°23'21"	17°07'55", 73°19'31"	17°10'11", 73°27'35"	17°07'04", 73°32'32"	17°12'55", 73°39'11"
Altitude	200 m	180 m	160 m	200 m	200 m	300 m
Nature of Slope	Naturally Small cut Slope	Natural Moderate Top Cut Slope	Natural Top cut Slope (Hillside)	Naturally Moderate cut Slope	Natural Moderately cut Slope (Hillside)	Natural Steep Slope
Strike Dir. Of Hill	N-S	NE-SW	NW-SE	N-S	NNE-SSW	N-S
Rock Type	Deccan Basalt with 3 sets of joints	Soil with Colluvial Material	Lateritic Blocks	Laterite, Jointed Basalt at Base	Laterite	Poorly jointed Basalt
Soil Type	Dark Brown, 1.5 m thick	Lateritic Red, 4-5 m thick	Lateritic Red Soil	Red Lateritic, 3 m Thick	Red, 5 m thick	Yellow, Murum, < 0.5 m thick
Type of L. S.	Rock Fall	Debris Fall	Soil Creep	Debris Slide	Moderate Soil Slump	Debris Fall, Cracks to ground
L. S. Dimensions	Ht. of Crown ≈ 3.5 m, Width ≈ 25 m	Ht. of Crown ≈ 9 m, Width ≈ 15 m	Ht. of Crown ≈ 3-4 m, Width ≈ 9 m	Ht. of Crown ≈ 5 m, Width ≈ 50 m	Ht. of Crown ≈ 8 m, Width ≈ 60 m	Ht. of Crown ≈ 10 m, Width ≈ 25 m

validation, and accuracy assessment of multispectral and elevation data.

Post-field studies: Post-field study was carried out after preparing thematic maps for validation and accuracy assessment of LVZ using techniques such as Geo-referencing of maps and images; digitization of topographic maps; supervised classification of remote sensing data; generation of Digital Elevation Model (DEM); preparation of various thematic maps viz. slope, geological, lineament, land use/landcover, etc. and preparation of final Landslide Vulnerable Zone (LVZ) map of SRB using ArcGIS techniques.

Data Used

For the comprehensive study and to achieve more accurate results, following types of data have been used.

- Topographic sheets of 1:50000 scale to create GIS-based vector layers
- IRS-R2 LISS III remote sensing data for temporal and spatial changes and also to prepare various thematic maps in raster format
- Digital Elevated Model (DEM) (Fig. 4)
- Rainfall data from GSDA, Ratnagiri, Govt. of Maharashtra
- IDRISI 3 software for image raster analysis and Arc GIS software for vector analysis.

Attempts have been made to generate a landslide vulnerability map for the study area using a GIS-based geosystem response model.

Location and Characters of Existing Landslides

In the first step, distribution and the morphology of the existing landslides observed during the field inventories with GPS and data have been presented in (Table 1). The preliminary inventory map has been prepared (Fig. 5).

Generation of GIS Databases on Geosystem Parameters

Then vector GIS databases showing the features (in the form of polygons) were generated for various geological parameters viz. lithology, lineaments, geomorphology, slope, land use /land cover, etc. which only dominantly assign the landslide vulnerability grades to the area. These five vector GIS layers were converted into raster layers using ArcGIS (Figs. 6, 7, 8, 9 and 10). Over these five raster GIS layers, the landslide distribution map (Fig. 5) was independently overlaid using Arc GIS software. Based on the number of landslides falling in each subclass of the five geosystem layers, landslides per unit area (weightage) were worked out. This was obtained by dividing the number of landslides falling in each subclass by the total number of pixels of the corresponding subclass. Thus, the weightages were assigned to each subclass or the polygon class of all the five geosystem GIS layers. The data is given in respective tables. The weightage was also assigned to road frequencies. These weighted raster GIS layers were then added using the raster calculator menu of Arc GIS software and thus the final integrated GIS layer was generated with each pixel having the cumulative weightage of all the GIS geosystem layers. Finally, based on the dynamic range of the weightages of the

Table 2: Landslide vulnerability weightages of various classes of lithology (SRB).

Sr. No.	Lithology	No. of Landslides (LS)	Area or No. of Pixel (A)	(LS /A)	LV weightage (LS/A) × 1000
1	Laterite	15	12070	0.0012428	1.24
2	Alluvium	0	169	0	0
3	Purandargadh weathered basalt	10	6773	0.0014765	1.48
4	Diveghat	9	16221	0.0005548	0.55
5	Shastri River	5	1882	0.0026567	2.66

Table 3: Landslide vulnerability weightages of various classes of lineaments (SRB).

Sr. No.	Lineament Buffer	No. of Landslides (LS)	Area or No. of Pixel (A)	(LS /A)	LV weightage (LS/A) × 1000
1	400	23	11555	0.0019905	1.99
2	800	10	10671	0.0009371	0.94
3	1200	4	7696	0.0005198	0.52
4	1600	1	4765	0.0002099	0.21
5	2000	0	3051	0	0

Table 4: Landslide vulnerability weightages of various classes of geomorphology (SRB).

Sr. No.	Geomorphology	No. of Landslides (LS)	Area or No. of Pixel (A)	(LS /A)	LV weightage (LS/A) × 1000
1	Deep Valley	14	658663	0.000021	0.0212
2	Shallow Valley	4	400006	0.000009	0.0099
3	Plain	1	150126	0.000006	0.0066
4	Slope	12	43833	0.000274	0.2737
5	Ridges	8	766442	0.000010	0.0104

Table 5: Landslide vulnerability weightages of various classes of slope (SRB).

Sr. No.	Slope	No. of Landslides (LS)	Area or No. of Pixel (A)	(LS /A)	LV weightage (LS/A) × 1000
1	Gentle (0°-5°)	1	686389	0.00000	0.0014
2	Moderate (6°-10°)	4	596648	0.00001	0.0067
3	Steep (11°-20°)	33	709059	0.00005	0.0465
4	Very Steep (21°-35°)	1	29376	0.00003	0.0340
5	Precipitous (>35°)	0	4553	0.00000	0

final integrated GIS layer, the study area (SRB) was classified into 5 Landslide vulnerable zones viz. very high, high, moderate, low, and very low (Fig. 11). Details of various steps are discussed in the following paragraphs.

Lithology: SRB is predominantly covered by Deccan Basalts. It has undergone different degrees of weathering. The area has been studied by using tonal difference, drainage density, vegetal coverage from the satellite data and subsequently followed by the field checks. Litho-logically the area is classified into different categories viz. highly weathered, weathered, moderately weathered, poorly weathered, and un-weathered. The zones covered by these classes were digitized into five polygon classes using the screen digitization technique by Arc-GIS. The GIS layer was generated by

the conversion of vector to raster form for the lithological studies (Fig. 6).

Lineament density: Based on the tonal, textural, topographical, drainage, and vegetation linearities and curvi-linearities, the fracture-controlled lineaments were observed in IRS- R2 LISS III raw, FCC data, and DEM data. It was mapped and checked in the fields. The buffering technique was adapted to understand the influence of lineaments. For this purpose, five buffer zone classes were marked viz. 400 m, 800 m, 1200 m, 1600 m, and 2000 m. The GIS database in the form of a raster layer was generated using these five classes with the help of ARC-GIS (Fig. 7).

Geomorphology: For geomorphic studies, the IRS R2 LISS-III data were subjected to various image processing

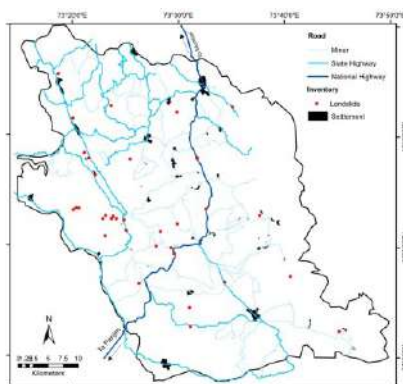


Fig. 5: Landslide inventory and road map of SRB.

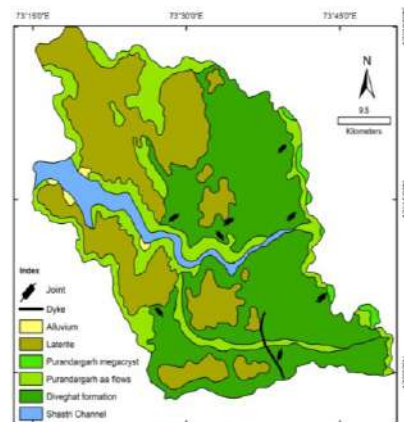


Fig. 6: Lithological map of SRB.

Table 6: Landslide vulnerability weightages of various classes of LULC (SRB).

Sr. No.	LULC	No. of Landslides (LS)	Area or No. of Pixel (A)	(LS / A)	LV weightage (LS/A) × 1000
1	Grassy land	23	117890	0.0001951	0.1951
2	Water	0	24393	0	0
3	Barren (Laterite)	6	431900	0.0001389	0.0139
4	Forest	9	528741	0.0001722	0.0170
5	Agriculture	1	475596	0.0002103	0.0021

Table 7: Landslide vulnerability weightages of various classes of roads (SRB).

Sr. No.	Distance	No. of Landslides (LS)	Area or No. of Pixel (A)	(LS / A)	LV weightage (LS/A) × 1000
1	50	7	1854	0.00377562	3.7756
2	100	4	1731	0.002310803	2.3108
3	150	1	1656	0.000603865	0.6039
4	200	1	1586	0.000630517	0.6305
5	250	8	1546	0.005174644	5.1746

techniques, like contrast stretching, false-color composites, color composites of principal component images, etc. Various geomorphic features considered for the landslide studies viz. deep valleys, plains, ridges, shallow valleys and slopes, etc. along with vegetation were interpreted and vectorized as individual polygon classes. The GIS database was generated by the conversion of the data into the raster layer (Fig. 8).

Slope: To understand the landslide vulnerability zones, the slopes were classified into five categories viz. precipitous ($> 35^{\circ}$), very steep ($35^{\circ} - 21^{\circ}$), steep ($11^{\circ} - 20^{\circ}$), moderate ($6^{\circ} - 10^{\circ}$), and gentle ($0^{\circ} - 5^{\circ}$) (Wentworth, C. K., 1930). The vector GIS layer was generated for these zones showing five polygon classes of slopes and then converted into a raster layer (Fig. 9).

Land use/Land cover: This parameter provides varying

degrees of protection and vulnerability to landslides. The natural vegetation and the thick forests anchor the soils and protect the slopes from slope failures, while, the plantations, settlements, highly developed areas with a network of roads, increase the probability of the occurrence of landslides. For this study, the digitally processed IRS R2 LISS –III data were used. The features viz. water bodies, agriculture, forests, built-up, and wasteland were interpreted. They were digitized and a vector GIS layer was generated showing all the features as different polygon classes (Fig. 10).

Assigning Landslide Vulnerability Weightages to Geosystem Parameters

Generation of raster GIS layers is followed by the assignment

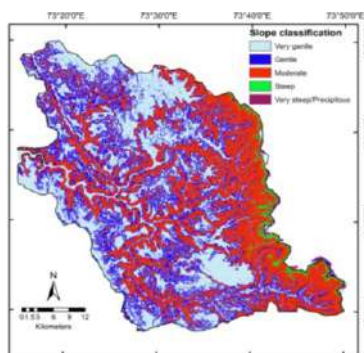


Fig. 9: Slope map of SRB.

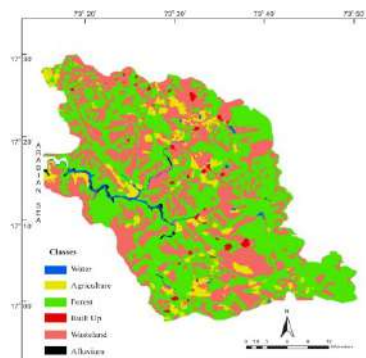


Fig. 10: Land use/Landcover Map of SRB.

Table 8: Distribution of landslide vulnerable zones (SRB).

Sr. No.	Class	Area or No. of Pixel (A)	Percentage of Area
1	Very High	12212	28.20
2	High	422	0.98
3	Moderate	10274	23.73
4	Low	11331	26.17
5	Very Low	9058	20.92

of the landslide vulnerability weightages to each feature class of all the five geosystem layers, based on the number of landslides per unit area. These are raster layers and hence the polygon classes are referred to as the feature classes. The same procedure is done by overlaying the GIS layer of landslides inventory map (Fig. 5) over the above five raster GIS layers of different geosystems individually. It is followed by the counting of the total number of landslides falling in the individual feature class of these five raster layers. It includes counting the total number of pixels in each feature class. The number of landslides (LS) has been divided by the data so obtained, falling in each feature class with the total number of pixels (A) covered by the corresponding feature class. In this step, we assign “weights” to the normalized inputs by multiplying each of them by a value by 1000 and the landslide vulnerability weightages (LVW) assigned to each

feature class. (Table 2 – Lithology, Table 3 – Lineaments, Table 4– Geomorphology, Table 5– Slope, Table 6 - LULC and Table 7 - road frequencies).

GIS Integration and Landslide Vulnerability

After assigning the Landslide Vulnerable Weightages (LVW) to the 5 rasterized geosystem layers’ feature classes, they were all merged using Raster Calculator. The LVW value of each pixel of the weighted raster layers of all Geo systems and roadways (Fig. 5) was then added and matched, and the final integrated GIS layer representing different landslide vulnerable zones (LVZ) was generated (Fig. 11). In all 43297 pixels, such an integrated GIS output has completely collected LV weightages. Five LVZs have been found based on the LVZ map and data (Table 8), including very high, high, moderate, low, and very low.

CONCLUSION

The map showing LVZ was prepared by superimposing the landslide inventory layer over the final integrated GIS layer on landslide vulnerability. From the above investigations, it can be concluded that

About 29% area of the Shastri River Basin (SRB) forms a highly vulnerable zone for land sliding.

These zones are mainly confined to steep slopes (11°-20°), grassy-land, highly weathered basalts (Purandargarh and Diveghat formation) (Figs. 12 and 13), and deep valleys, and in the vicinity of lineaments (400 m).

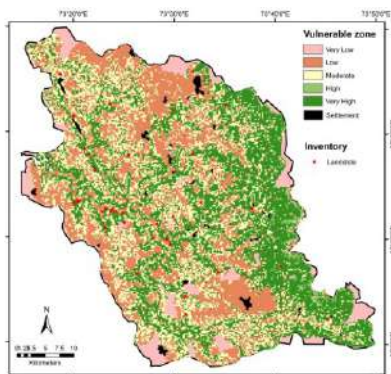


Fig. 11: Landslide vulnerable zone map of SRB.



Fig. 12: Rockfall near Bhatgaon – (17°16’ N, 73° 24’ E).



Fig. 13: Debris Slide near Asore (17°18’ N, 73°22’ E).

Results so obtained were validated in the field using GPS.

ACKNOWLEDGMENT

Dr. S. B. Joshi is thankful to Dr. S. V. Koti, Principal, Walchand College of Arts and Science, Solapur for extending help during present work and encouragement.

REFERENCES

- Diaz, S., Fargione, J., Chapin, F.S. and Tilman, D. 2005. Biodiversity loss threatens human well-being, *PLoS Biol.*, 4: 1300-1305.
- Edison, T. and Ganapathy, P. 2020. Evaluation of landslide hazard and its impacts on the hilly environment of the Nilgiris District - a geospatial approach. *Geoenviron. Disasters*, 7(3): 139. <https://doi.org/10.1186/s40677-019-0139-3>
- Greenbaum, D., Tutton, M., Bowker, M., Browne, T., Bulekha, J., Grealley, K., Kuna, G., McDonald, A., Marsh, S., O'Connor, E. and Tragheim, D. 1995. Rapid methods of landslide mapping: Papua New Guinea case study. *British Geol. Sur.*, Keyworth, Nottingham, UK, Tech. Report WC/95/27, p. 121
- Guzzetti, F., Mondini, A.C., Cardinali, M., Fiorucci, F., Santangelo, M. and Chang, K.T. 2012. Landslide inventory maps: new tools for an old problem. *Earth Sci. Rev.*, 112: 42-66. <https://doi.org/10.1016/j.earscirev.2012.02.001>
- Jiu, J.J., Xu-Sheng, W. and Subhas, N. 2005. Confined groundwater zone and slope instability in weathered igneous rocks in Hong Kong. *Eng. Geol.*, 80: 71-92
- Juang, C.S., Stanley, T.A. and Kirschbaum, D.B. 2019. Using citizen science to expand the global map of landslides: introducing the cooperative open online landslide repository (COOLR). *PLoS One*, 14: e0218657
- Meena, S.R., Ghorbanzadeh, O. and Hölbling, D. 2019. Comparison of Event-Based landslide inventories: A case study from Gorkha earthquake 2015, Nepal. Paper presented at the European Space Agency's 2019 Living Planet Symposium, Milan, Italy, 13-17 May 2019, European Space Agency, Paris, France, pp. 1-18.
- Mitchell, C. and Cox, K.G. 1988. A geological sketch map of southern part of the Deccan province. *Memoir of Geol. Soc. India*, 10: 27-33
- Nagarajan, R., Mukharji, A., Roy, A. and Khaire, M.V. 1998. Temporal remote sensing data and GIS application in landslide hazard zonation of part of Western Ghat, India. *Int. J. Remote Sens.*, 19(4): 573-585
- Prakash, N., Manconi, A. and Loew, S. 2020. Mapping landslides on EO data: performance of deep learning models vs. traditional machine learning models. *Remote Sens.*, 18: 1937-1950
- Ramakrishnan, S.S., Sanjeevi Kumar V., Zaffar Sadiq, M.G.S.M., Arulraj, M. and Venugopal, K. 2002. Landslide disaster management and planning: A GIS-based approach. *Indian Cartog.*, 05: 192-195
- Valdiya, K.S. 2011. Some geodynamic hot spots in India require urgent comprehensive studies. *Curr. Sci.*, 100 (10): 1490-1499
- Van Westen, T.W.J. Van, A. and Soeters, R. 2006. Landslide hazard and risk zonation: Why is it so difficult? *Bull. Eng. Geo. Env.*, 65(2): 167-184
- Wentworth, C.K. 1930. A simplified method of determining the average slope of land surfaces *Am. J. Sci.*, 21: 184-194



Mechanism and Chemical Stability of U(VI) Removal by Magnetic Fe₃O₄@Biochar Composites

Erhui Zhao*, Anjie Wang*, Luoia Huang**, Chengguang Chen** and Muqing Qiu*†

*School of Life Science, Shaoxing University, Shaoxing, 312000, P. R. China

**School of Architectural Engineering, Shaoxing University Yuanpei College, Shaoxing, 312000, P. R. China

†Corresponding author: Muqing Qiu; qiumuqing@126.com

Nat. Env. & Poll. Tech.
Website: www.neptjournal.com

Received: 16-04-2021

Revised: 13-05-2021

Accepted: 08-06-2021

Key Words:

Magnetic Fe₃O₄@Biochar
U(VI)
Chemical stability
Radioactive wastewater

ABSTRACT

Biochar is typically made via pyrolysis of organic materials under anoxic conditions, due to its high surface area and significant negative charge. It also has the ability to minimize the mass or volume of waste items. As a result, biochar is frequently used in the remediation of environmental contamination. To overcome the shortcoming of biochar in the application, the magnetic Fe₃O₄@Biochar from walnut shells were prepared. The magnetic Fe₃O₄@Biochar from walnut shells is used to study the adsorption of U(VI) in the solution. SEM, XRD, and FT-IR are used to determine the properties of magnetic Fe₃O₄@Biochar. The results revealed that magnetic Fe₃O₄@Biochar has a fragmented and irregular form. On the surface of magnetic Fe₃O₄@Biochar, several functional groups can aid in the adsorption of pollutants. The adsorption capacity of U(VI) by magnetic Fe₃O₄@Biochar is influenced by the contact time and initial concentration of U(VI). For the adsorption of U(VI) in solution by magnetic Fe₃O₄@Biochar, the pseudo-first-order kinetic equation and the Langmuir isotherm equation can be fitted. The adsorption of the process is chemical adsorption and monolayer adsorption. The chemical stability of magnetic Fe₃O₄@Biochar is very well.

INTRODUCTION

Uranium is a heavy metal element with radioactivity and high toxicity, which poses a great threat to the ecological environment and human health (Dong et al. 2017, Qiu et al. 2021). During the various stages of nuclear power plants and nuclear accidents, a certain amount of uranium-containing radioactive wastewater will be generated (Vogel et al. 2010, Qiu et al. 2018, Hu et al. 2021). Therefore, the uranium-containing radioactive wastewater must be treated. Physical or physical-chemical approaches are used in the majority of traditional radioactive wastewater treatment procedures. Chemical precipitation, evaporation, ion exchange, and membrane separation are commonly used to treat low and medium concentrations of radioactive wastewater (Bhat et al. 2008, Qiu & Huang 2017, Hao et al. 2021, Liu et al. 2021).

In most circumstances, traditional radioactive wastewater treatment methods have a high removal efficiency. However, several issues remain, such as high chemical consumption, high energy consumption, rapid corrosion and scaling, and secondary pollution (Febrianto et al. 2009, Das 2012, Wang et al. 2021). The adsorption method has gradually attracted people's attention due to its characteristics of high efficiency, energy saving, environmental protection, and recyclability.

Because of the high surface area and considerable negative charge, biochar is ordinarily fabricated by the pyrolysis

of organic materials under anoxic conditions (Zhang et al. 2013, Li et al. 2019, Dai et al. 2021). Moreover, it can also reduce the mass or volume of waste materials (Han et al. 2016, Yao et al. 2021). Therefore, biochar is applied to the remediation of environmental pollution widely (Qiu and Huang 2017, Jang et al. 2018, Mohanty et al. 2018, Wang et al. 2020). The spectrum of raw materials available to identify affordable biochar resources has been expanding in recent years (Sun et al. 2015, Dutta & Nath 2018, Li et al. 2019). Agricultural by-products and industrial waste, such as peanut shells, straws, walnut shells, and so on, are available in addition to standard high-quality wood and wood chips (Xu et al. 2014, Chang et al. 2017, Wang et al. 2018). The annual output of walnuts in China is more than 200,000 tons, and its shell and outer peel are almost discarded as waste. A large number of walnut shells were burned, causing great waste of resources and air pollution. Therefore, biochar is applied to the remediation of environmental pollution widely, such as heavy metals, organic pollution, and inorganic pollution (Chen et al. 2021). Biochar, on the other hand, is difficult to recycle in the application. As a result, magnetic biochar may be readily recycled, reused, and costs can be lowered.

Therefore, in this study, walnut shells are used as raw materials to prepare biochar. The main objectives are: 1) the magnetic Fe₃O₄@Biochar is synthesized; 2) the characteristics of magnetic Fe₃O₄@Biochar are discussed in

detail according to the results of SEM, EDS, XRD, and FT-IR; 3) the adsorption experiments are also carried out; 4) the adsorption mechanism is elaborated according to adsorption kinetics and adsorption isotherm. This study is of great significance for new sources of biochar raw materials. It provides a new way for the resource utilization of crop wastes.

MATERIALS AND METHODS

Materials

Walnut shells are obtained from a farm in the City of Linan, Zhejiang Province, P.R. China. Biochar was prepared using walnut shells. The walnut shells were washed three times with water and dried at 378 K to a consistent weight. Then they were pulverized and passed through a 20 meshes sieve. At a temperature of 523 K, 10 g of walnut shell is pyrolyzed for 2 h in a nitrogen atmosphere. It was pulverized through 100 meshes after cooling to room temperature. Then, the biochar from walnut shells is obtained.

1 g of biochar was added to 250 mL Erlenmeyer flask. Then, we added 100 mL of 1 mol.L⁻¹ Fe³⁺ and stirred for 30 min under ultrasonic conditions. Finally, we added 100 mL of 3 mol.L⁻¹ NaOH solution and stirred for 60 min under ultrasonic conditions. They were washed with DMF until the supernatant was clear. Then, they were dried under vacuum at 80° for 12 h. The magnetic Fe₃O₄@Biochar was obtained for adsorption experiments.

Adsorption Experiment

Adsorption tests were carried out in a set of 250 mL Erlenmeyer flasks containing magnetic Fe₃O₄@Biochar and 100 mL U(VI), with initial concentrations in an aqueous solution. The flasks were shaken at 303 K and 150 rpm at a steady temperature. After that, the samples were filtered, and the residual U(V) concentration was determined.

Analytical Methods

The concentration of U(VI) ion in solution was measured with a UV-1600 spectrophotometer. The adsorption capacity of U(VI) and removal rate of U(VI) were calculated as follows:

$$q_e = \frac{(C_0 - C_e) \times V}{m} \quad \dots(1)$$

$$R = \frac{C_e}{C_0} \times 100\% \quad \dots(2)$$

Where, C_0 and C_e (mg.L⁻¹) are the initial and equilibrium concentrations of U(VI) in solution respectively. q_s (mg.g⁻¹) is the adsorption amount per unit mass of the biochar at adsorption equilibrium. V (mL) is the volume of solution, m (g) is the mass of the biochar. R (%) is the removal rate of U(VI) ions in an aqueous solution.

SEM (Ultra 55), X-ray diffraction (Ulitma IV), and Fourier transform infrared spectroscopy spectra (Nicolet 5700) were used to study the physicochemical features of the magnetic Fe₃O₄@Biochar made from walnut shells.

RESULTS AND DISCUSSION

The Characteristic of the Magnetic Fe₃O₄@Biochar from Walnut Shells

Fig.1 (A and B) shows the SEM images of biochar and the magnetic Fe₃O₄@Biochar. It suggests that the shape of biochar and the magnetic Fe₃O₄@Biochar are fragmented and irregular. They have no pore structure. The irregular structure is an advantage for the adsorption of U(VI) ions in the solution. Additionally, as shown from Fig. 1B, a lot of small particles can be observed on the surface of magnetic Fe₃O₄@Biochar. It indicates that Fe₃O₄ nanoparticles are loaded successfully. This result can be verified by the EDS (Fig. 2). As shown from Fig. 2A and 2B, the elements of C, O, K and Mg appeared on the surface of biochar. After

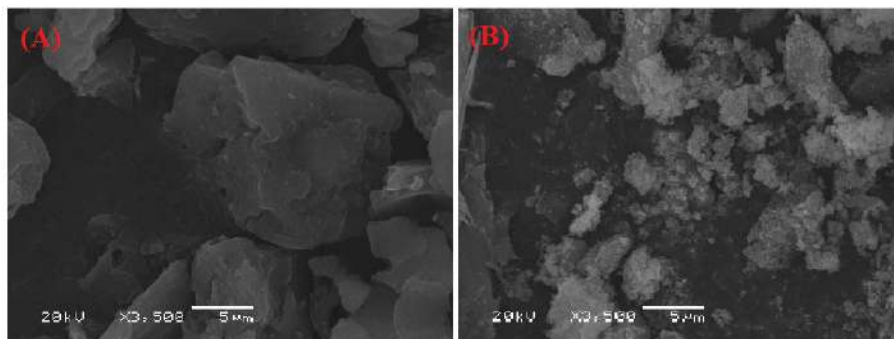


Fig.1: SEM image of biochar (A) and the magnetic Fe₃O₄@Biochar (B).

preparation, the element of Fe can be determined on the surface of the magnetic Fe₃O₄@Biochar.

The possible function groups of the magnetic Fe₃O₄@Biochar are observed by FT-IR (Fig. 3A). There are seven peaks on the magnetic Fe₃O₄@Biochar. They are 3358, 2332, 1608, 1377, 1059, 569 and 405 cm⁻¹, respectively. They are assigned as -O-H, -C≡C-, -C=C-, -C-H, -C-C, and -C-H, respectively. It suggests that there are a large number of functional groups on the surface of the magnetic Fe₃O₄@Biochar, which can facilitate the adsorption of pollutants. The results of the XRD pattern are shown in Fig. 3B. The characteristic peak of the magnetic Fe₃O₄@Biochar can be observed. It is 21.35°. This result corresponds to previous studies.

Adsorption Experiment

Adsorption experiments are conducted in a set of 250 mL Erlenmeyer flasks. First, the effect of contact time on adsorption capacity is tested. Experimental conditions are followings: C₀ = 60 mg.L⁻¹, pH = 4.31, Temperature 308 K, rotating speed = 150 rpm, dosage of the magnetic Fe₃O₄@Biochar is 0.4 g. The results of the experiment are shown in Fig. 4A and 4B.

At the first stage of adsorption, the adsorption rate increases quickly. It may be the reason that there are a large number of adsorption sites on the surface of the magnetic

Fe₃O₄@Biochar. Therefore, the adsorption rate increases very quickly. After 30 min, as the contact time increases, the adsorption rate increases slowly. It may be the reason that the adsorption sites on the surface of the magnetic Fe₃O₄@Biochar begin to decrease. As the adsorption time continues to increase, adsorption gradually reaches adsorption equilibrium. The influence of initial solution concentration U(VI) on adsorption capacity is then tested. Experimental conditions are followings: contact time 360 min, pH = 4.31, Temperature 308 K, rotating speed = 150 rpm, the dosage of the magnetic Fe₃O₄@Biochar is 0.1 g. The results of the experiment are shown in Fig. 4B. As the adsorption time increases, the adsorption capacity gradually decreases. When the initial concentration of U(VI) in solution is 100 mg.L⁻¹, the adsorption capacity of U(VI) by the magnetic Fe₃O₄@Biochar reaches 4.71 mg.g⁻¹.

Adsorption Kinetics

To describe the adsorption kinetic of U(VI) in solution by the magnetic Fe₃O₄@Biochar, pseudo-first-order kinetic equation and pseudo-second-order kinetic equation are used in this study. Their equations are as follows (Mellah et al. 2006, Troyer et al. 2016):

$$q_t = q_e(1 - e^{-K_1 t}) \quad \dots(3)$$

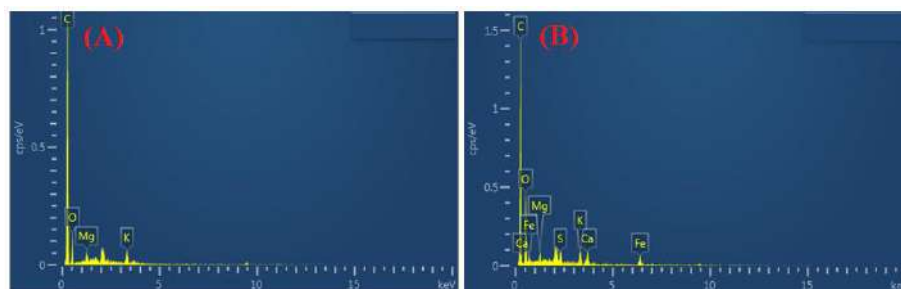


Fig. 2: EDS of biochar (A) and the magnetic Fe₃O₄@Biochar (B).

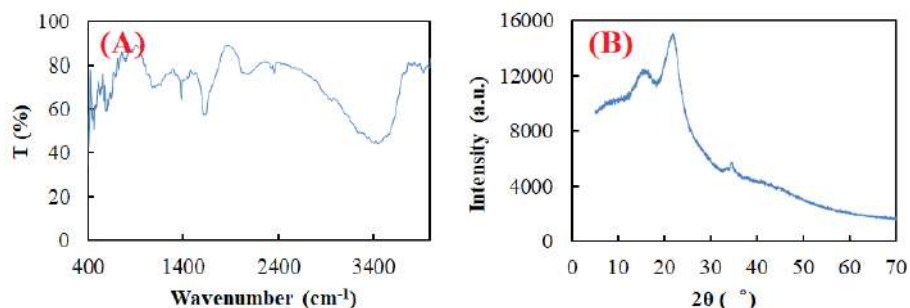


Fig. 3: FT-IR spectra (A) and XRD pattern (B) of the magnetic Fe₃O₄@Biochar.

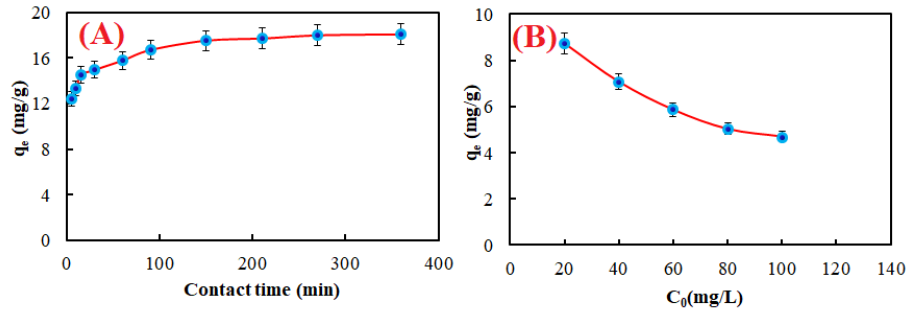


Fig. 4: Effect of contact time (A) and initial concentration of U(VI) (B) on adsorption capacity by the magnetic Fe₃O₄@Biochar.

$$\frac{t}{q_t} = \frac{1}{K_2 q_e^2} + \frac{t}{q_e} \quad \dots(4)$$

$$\lg q_e = \lg K_F + \frac{1}{n} \lg c_e \quad \dots(6)$$

Where q_t (mg.g⁻¹) and q_s (mg.g⁻¹) are adsorption capacity of U(VI) in solution by the magnetic Fe₃O₄@Biochar at adsorption time t and adsorption equilibrium respectively. K_1 (min⁻¹) and K_2 (min⁻¹) are the adsorption rate constants.

The adsorption kinetic equation of U(VI) ion by the magnetic Fe₃O₄@Biochar from walnut shells is shown in Fig. 5A and 5B. As shown in Fig. 5A and 5B, it can be concluded that the adsorption process can be ascribed with a pseudo-second-order kinetic equation ($R^2 = 0.9997$). It indicates that the adsorption process of U(VI) in solution by the magnetic Fe₃O₄@Biochar is chemical adsorption. Chemical adsorption is the most common form of adsorption.

Adsorption Isotherms

To describe the adsorption isotherm of U(VI) ion by the magnetic Fe₃O₄@Biochar, Langmuir isotherm equation and Freundlich isotherm equation are applied in this study. Their equations are follows (Freundlich 1906, Langmuir 1918):

$$\frac{c_e}{q_e} = \frac{c_e}{q_{max} K_L q_{max}} \quad \dots(5)$$

Where q_e (mg.g⁻¹) is the adsorption capacity of U(VI) in solution by the magnetic Fe₃O₄@Biochar at adsorption equilibrium. q_{max} (mg.g⁻¹) is the maximum adsorption capacity of the adsorbent under specific adsorption conditions. K_L (L.mg⁻¹) and K_F (L.mg⁻¹) are the adsorption rate constants. C_S (mg.L⁻¹) is equilibrium concentrations of U(VI) in solution.

The adsorption isotherm of U(VI) ion by the magnetic Fe₃O₄@Biochar from walnut shells is shown in Fig. 6. According to the value of R^2 , it can be suggested that Langmuir isotherm is more suitable for the adsorption of U(VI) ions in solution by the magnetic Fe₃O₄@Biochar. The adsorption process is the adsorption of the monolayer.

Stability of Adsorption U(VI) Ions in Aqueous Solution

100 mL of 0.1 mol.L⁻¹ NaOH and 100 mL of 0.01 mol.L⁻¹ HCl were used to rinse the magnetic Fe₃O₄@Biochar. Then it's washed again with distilled water for 5 min. The magnetic Fe₃O₄@Biochar prepared in this way is used as adsorbents in recycling experiments. The repeated reusability of the magnetic Fe₃O₄@Biochar is displayed in Fig.7. It shows that the removal rate of U(VI) decreases from 65.56% to 49.14% during five adsorption and desorption experiments.

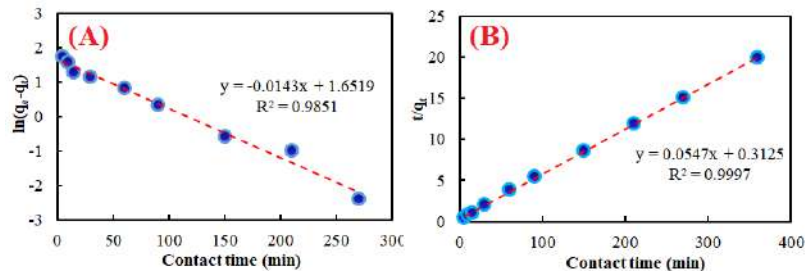


Fig. 5: Adsorption kinetic equation of U(VI) ion by the magnetic Fe₃O₄@Biochar from walnut shell (pseudo-first-order kinetic (A) and pseudo-second-order kinetic (B)).

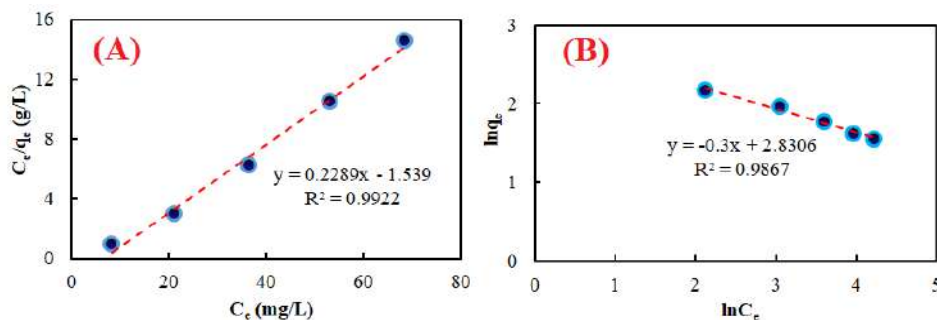


Fig. 6: Adsorption isotherm of U(VI) ion by the magnetic Fe₃O₄@Biochar from walnut shell [Langmuir isotherm (A) and Freundlich isotherm (B)].

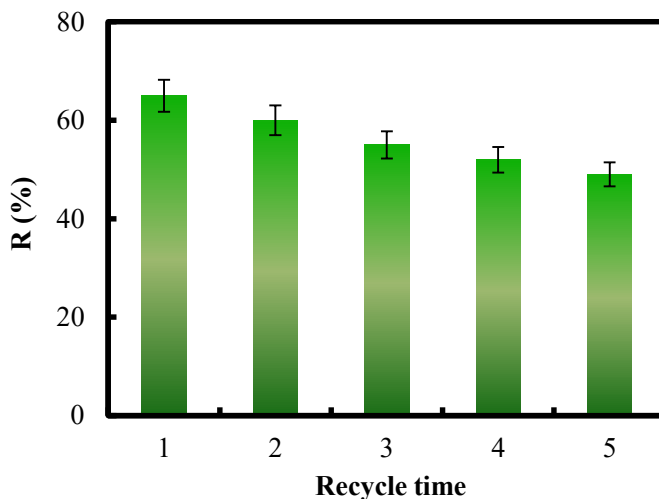


Fig. 7: The repeated reusability of the magnetic Fe₃O₄@Biochar for removal U(VI) ions in solution.

The chemical stability of the magnetic Fe₃O₄@Biochar is good.

CONCLUSION

Biochar is obtained from walnut shells according to the method of pyrolyzed. Additionally, the magnetic Fe₃O₄@Biochar is synthesized. The adsorption of U(VI) ions in solution by the magnetic Fe₃O₄@Biochar is tested. The shape of the magnetic Fe₃O₄@Biochar is fragmented and irregular. There are a large number of functional groups on the surface of the magnetic Fe₃O₄@Biochar, which can facilitate the adsorption of pollutants. The pseudo-first-order kinetic equation and the Langmuir isotherm equation can be fitted for the adsorption of U(VI) in solution by the magnetic Fe₃O₄@Biochar. The maximum adsorption capacity can reach 4.37 mg.g⁻¹. The adsorption of the process is chemical adsorption and monolayer adsorption. The chemical stability of the magnetic Fe₃O₄@Biochar is very well.

ACKNOWLEDGEMENTS

This study was financially supported by the project of science and technology plan in Zhejiang Province (LGF20C030001 and LGF21C030001). The authors are very grateful for their support.

REFERENCES

- Bhat, S.V., Melo, J.S., Chaugule, B.B. and Souza, S.F.D. 2008. Biosorption characteristics of uranium (VI) from aqueous medium onto *Catenella repens*, a red alga. *J. Hazard. Mater.*, 158: 628-635.
- Chang, K., Li, X., Liao, Q., Hu, B., Hu, J., Sheng, G., Linghu, W., Huang, Y., Asiri, A.M. and Alamry, K.A. 2017. Molecular insights into the role of fulvic acid in cobalt sorption onto graphene oxide and reduced graphene oxide. *Chem. Eng. J.*, 327: 320-327.
- Chen, G., Wang, H., Han, L., Yang, N., Hu, B., Qiu, M. and Zhong, X. 2021. Highly efficient removal of U(VI) by novel biochar supported with FeS nanoparticles and chitosan composites. *J. Mol. Liq.*, 327: 114807.
- Dai, J., Xu, R.L., Li, W.Y., Yang, Y., Xiao, Y., Mao, H., Qiu, M.Q., Wang, H., Yang, N.C. and Han, L. 2021. Effect of pyrolysis temperature on

- adsorption characteristics of biochar derived from corn straw. *Nature Environ. Poll. Technol.*, 20: 291-296.
- Das, N. 2012. Remediation of radionuclide pollutants through biosorption-an overview. *Clean Soil Air Water*, 40: 16-23.
- Dong, L., Yang, J., Mou, Y., Sheng, G., Wang, L., Linghu, W., Asiri, A.M. and Alamry, K.A. 2017. Effect of various environmental factors on the adsorption of U(VI) onto biochar derived from rice straw. *J. Radioanal. Nucl. Chem.*, 314: 377-386.
- Dutta, D.P. and Nath, S. 2018. Low-cost synthesis of SiO₂/C nanocomposite from corn cobs and its adsorption of uranium(VI), chromium(VI), and cationic dyes from wastewater. *J. Mol. Liq.*, 269: 140-151.
- Febrianto, J., Kosasih, A.N., Sunarso, J., Ju, Y.H., Indraswati, N. and Ismadji, S. 2009. Equilibrium and kinetic studies in adsorption of heavy metals using biosorbent: a summary of recent studies. *J. Hazard. Mater.*, 162: 616-645.
- Freundlich, H. 1906. Over the adsorption in solution. *Z. Phys. Chem.*, 57: 385-470.
- Jang, J., Mirana, W., Divine, S.D., Nawaz, M., Shahzad, A., Woo, S.H. and Lee, D.S. 2018. Rice straw-based biochar beads for the removal of radioactive strontium from aqueous solution. *Sci. Total Environ.*, 615: 698-707.
- Han, Y., Cao, X., Ouyang, X., Sohi, S.P. and Chen J. 2016. Adsorption kinetics of magnetic biochar derived from peanut hull on the removal of Cr(VI) from aqueous solution: effects of production conditions and particle size. *Chemosphere*, 145: 336-341.
- Hao, M.J., Qiu, M.Q., Yang, H., Hu, B.W. and Wang, X.X. 2021. Recent advances on preparation and environmental applications of MOF-derived carbons in catalysis. *Sci. Total Environ.*, 760: 143333.
- Hu, B.W., Wang, H.F., Liu, R.R. and Qiu M.Q. 2021. Highly efficient U(VI) capture by amidoxime/carbon nitride composites: Evidence of EXAFS and modeling. *Chemosphere*, 274: 129743.
- Langmuir, I. 1918. The adsorption of gases on plane surfaces of glass, mica, and platinum. *J. Am. Chem. Soc.*, 40: 1361-1403.
- Li, M.X., Liu, H.B., Chen, T.H., Dong, C. and Sun Y.B. 2019. Synthesis of magnetic biochar composites for enhanced uranium(VI) adsorption. *Sci. Total Environ.*, 651: 1020-1028.
- Li, N., Yin, M.L., Tsang, D.C.W., Yang, S.T., Liu, J., Li, X., Song, G. and Wang, J. 2019. Mechanisms of U(VI) removal by biochar derived from *Ficus microcarpa* aerial root: A comparison between raw and modified biochar. *Sci. Total Environ.*, 697: 134115-134124.
- Liu, X.L., Pang, H.W., Liu, X.W., Li, Q., Zhang, N., Mao, L., Qiu, M.Q., Hu, B.W., Yang, H. and Wang, X.K. 2021. Orderly porous covalent organic framework-based materials: superior adsorbents for pollutants removal from aqueous solutions. *The Innovations*, 2: 100076.
- Mellah, A., Chegrouche, S. and Barkat, M. 2006. The removal of uranium(VI) from aqueous solutions onto activated carbon: kinetic and thermodynamic investigations. *J. Colloid Interfaces Sci.* 296: 434-441.
- Mohanty, S.K., Valenca, R., Berger, A., Yu, I.K.M., Xiong, X., Saunders, T. and Tsang, D.C.W. 2018. Plenty of room for carbon on the ground: Potential applications of biochar for stormwater treatment. *Sci. Total Environ.*, 625: 1644-1658.
- Qiu, M.Q. and Huang, P. 2017. Kinetic and thermodynamic studies on the adsorption of zinc ions from aqueous solution by the blast furnace slag. *Nature Environ. Poll. Technol.*, 16: 639-642.
- Qiu, M.Q., Wang, M., Zhao, Q.Z., Hu, B.W. and Zhu, Y.L. 2018. XANES and EXAFS investigation of uranium incorporation on nZVI in the presence of phosphate. *Chemosphere*, 201: 764-771.
- Qiu, M.Q., Liu, Z.X., Wang, S.Q. and Hu, B.W. 2021. The photocatalytic reduction of U(VI) into U(IV) by ZIF-8/g-C₃N₄ composites at visible light. *Environ. Res.*, 196: 110349.
- Sun, Y., Yang, S., Chen, Y., Ding, C., Cheng, W. and Wang, X. 2015. Adsorption and desorption of U(VI) on functionalized graphene oxides: a combined experimental and theoretical study. *Environ. Sci. Technol.*, 49: 4255-4262.
- Troyer, L.D., Maillot, F., Wang, Z., Wang, Z., Mehta, V.S., Giammar, D.E. and Catalano, J.G. 2016. Effect of phosphate on U(VI) sorption to montmorillonite: Ternary complexation and precipitation barriers. *Geochim. Cosmochim. Acta.*, 175: 86-99.
- Vogel, M., Günther, A., Rossberg, A., Li, B., Bernhard, G. and Raff, J. 2010. Biosorption of U(VI) by the green algae *Chlorlla vulgaris* in dependence of pH value and cell activity. *Sci. Total Environ.*, 409: 384-395.
- Wang, H., Yang, N.C. and Qiu, M.Q. 2020. Adsorption of Cr(VI) from aqueous solution by biochar-clay derived from clay and peanut shell. *J. Inor Mater.*, 35: 301-308.
- Wang, H.F., Zhang, Q.Q., Qiu, M.Q. and Hu, B.W. 2021. Synthesis and application of perovskite-based photocatalysts in environmental remediation: A review. *J. Mol. Liq.*, 334: 116029.
- Wang, L., Yu, K., Li, J.S., Tsang, D.C.W., Poon, C.S., Yoo, J.C., Baek, K., Ding, S., Hou, D. and Dai, J.G. 2018. Low-carbon and low-alkalinity stabilization/solidification of high-Pb contaminated soil. *Chem. Eng. J.*, 351: 418-427.
- Xu, D., Zhao, Y., Sun, K., Gao, B., Wang, Z., Jin, J., Zhang, Z., Wang, S., Yan, Y. and Liu, X. 2014. Cadmium adsorption on plant-and manure-derived biochar and biochar amended sandy soils: Impact of bulk and surface properties. *Chemosphere*, 111: 320-326.
- Yao, L., Yang, H., Chen, Z.S., Qiu, M.Q., Hu, B.W. and Wang, X.X. 2021. Bismuth oxychloride-based materials for the removal of organic pollutants in wastewater. *Chemosphere*, 273: 128576.
- Zhang, M., Gao, B., Varnosfaderani, S., Hebard, A., Yao, Y. and Inyang, M. 2013. Preparation and characterization of novel magnetic biochar for arsenic removal. *Bioresour. Technol.*, 130: 457-462.



Analysis of Agricultural Non-point Source Pollution in Henan Province (China) from the Perspective of Time and Space

Aping Chang[†], Hua Qiong and Zheng Binguo

School of Economics, Zhengzhou University of Aeronautics, Zhengzhou 450046, PR China

[†]Corresponding author: Aping Chang; guobinzheng@126.com

Nat. Env. & Poll. Tech.
Website: www.neptjournal.com

Received: 08-03-2021

Revised: 21-04-2021

Accepted: 03-05-2021

Key Words:

Agricultural Non-point source
Pollution
Analysis
Chemical fertilizer

ABSTRACT

Henan is China's most populous agricultural province. Wheat, cotton, oil crops, and other farming and animal husbandry industries rank first in China in terms of output value. The agricultural sector has grown significantly, and rural populations' living standards have greatly improved. The effects of rural urbanization can be seen all over the place. However, the rural economy's rapid growth has resulted in a slew of environmental contamination issues. Chemical fertilizer emissions of chemical oxygen demand (COD) and total nitrogen (TN) have been decreasing for a long time in Henan Province, whereas total phosphorus (TP) emissions are increasing. The usage load of pesticides went high in Zhoukou, Nanyang, Shangqiu, Xinyang, Xinxiang, and Zhumadian. The application of agricultural film was relatively common in Nanyang, Zhoukou, Anyang, Xinyang, Zhumadian, Kaifeng, and Shangqiu. Wheat, corn, and oil-bearing crop stalks are the main sources of crop solid waste in Henan Province, and the solid waste generated by these three crops accounted for 93.96% of the province's total amount. In Zhumadian, Zhoukou, Nanyang, and Shangqiu, there was a lot of crop stalk trash.

INTRODUCTION

Henan Province is a major agricultural province and a major food province in China (Zhang & Shou 2021). The output value of wheat, cotton, oil crops, and other cultivation and animal husbandry industries are among the best in the country. In recent years, the rural economy of Henan has developed rapidly. Some regions have achieved their goal of prosperity. Rural dwellers' living standards have substantially improved, and rural urbanization can be seen everywhere (Yuan et al. 2018, Yan et al. 2021). However, the rural economy's rapid growth has resulted in a slew of environmental contamination issues (Zhang et al. 2020, Zhou et al. 2020), which are mainly manifested in the pollution caused by the large-scale use of pesticides and fertilizers (Zheng et al. 2020, Liu et al. 2017, Gu et al. 2015) and the improper use of crop straws and other solid wastes in agricultural production (Li et al. 2016, Qiu et al. 2016, Zhang et al. 2016).

The key concerns of agricultural non-point source pollution in rural areas of Henan Province are analyzed and studied based on the third agricultural census data and the statistical yearbook of Henan Province over the years. The findings of the study have significant practical implications for the long-term development of rural areas in emerging countries.

MATERIALS AND METHODS

To estimate the agricultural non-point source pollution loads

in Henan Province, the agricultural input and output database was established; the database includes the prefecture-level city of Henan Province annual data of the pure consumption of nitrogen, phosphate, and compound fertilizers; the application of pesticide; and the consumption of agricultural film from 2010 to 2019. In addition, the agriculture acreage for the prefecture-level city of Henan Province was included.

RESULTS AND DISCUSSION

Consumption of chemical fertilizers: Fertilization in fields releases large amounts of nitrogen and phosphorus compounds into soil and water, causing soil and water pollution (Xue et al. 2020). According to the national pollution census in 2010, the total nitrogen (TN) and total phosphorus (TP) loads from agricultural non-point sources (AGNPS) accounted respectively for 57.2% and 67.4% of the total emissions in China (Xue et al. 2020). Agricultural chemical fertilizers mainly include nitrogen fertilizer, phosphate fertilizer, potash fertilizer, and compound fertilizer in China. From 2009 to 2019, the trends of scalar fertilization and fertilization in Henan Province are shown in Fig.1.

From 2009 to 2015, the scalar amount of chemical fertilizer application in Henan increased year by year. It was 6,282,700 tons in 2009, but increased to 7,160,900 tons in 2015. From 2016 to 2019, the scalar amount decreased year by year and reduced to 6,667,200 tons in 2019. The amount of fertilizer application was also determined in this work

since the scalar amount of chemical fertilizer application is related to the area of cultivated land, which changed in Henan over the study period. The findings revealed that the fertilizer application pattern in Henan has been steady from 2009 to 2019. From Fig. 2, we can know the fertilizer application load increased year by year from 2009 to 2015. It was $767.42 \text{ kg}\cdot\text{ha}^{-1}$ in 2009 and increased to $883.42 \text{ kg}\cdot\text{ha}^{-1}$ in 2015. It began to decline in 2019 and fell to $818.64 \text{ kg}\cdot\text{ha}^{-1}$ in 2019. Based on the two indicators, since 2016, the amount of fertilizer input to agricultural land in Henan Province has decreased year by year in terms of both total amount and unit intensity indicators.

As for the spatial distribution of agricultural fertilizer application in Henan, the average scalar amount of agricultural fertilizer application in 18 local cities in 2019 was 370,401 tons, and the cities with higher scalar amount levels were Zhoukou (860678 tons), Shangqiu (778648 tons), Nanyang (762346tons), Zhumadian (733984tons), Xinxiang (519743tons), Xinyang (448822tons), and Anyang (432097tons), These seven cities accounted for 68% of the

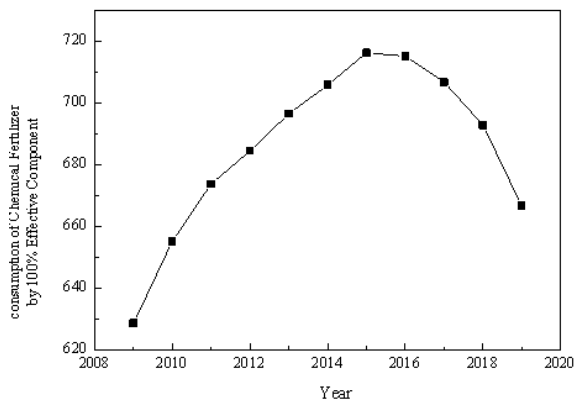


Fig. 1: Consumption of chemical fertilizer by 100% effective component.

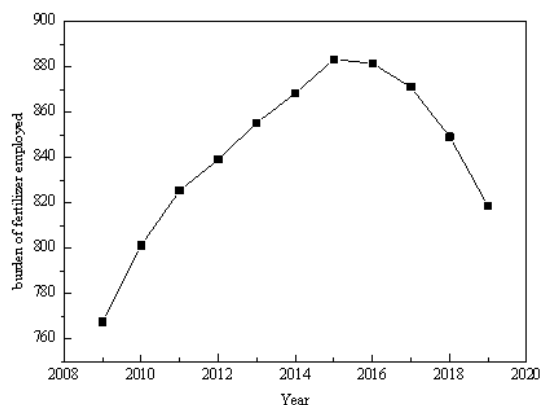


Fig. 2: Load of fertilizer employed.

whole agricultural fertilizer scalar amount in Henan. To eliminate the impact of different cultivated land areas on the conversion of agricultural fertilizers, we calculated the fertilizer usage load of 18 local cities in 2019. The results showed that in 2019 the average level of fertilizer usage in 18 local cities was $819.54 \text{ kg}\cdot\text{ha}^{-1}$ and the cities with a higher amount than the average were Xinxiang ($1096.69 \text{ kg}\cdot\text{ha}^{-1}$), Shangqiu ($1093.58 \text{ kg}\cdot\text{ha}^{-1}$), Pingdingshan ($1061.52 \text{ kg}\cdot\text{ha}^{-1}$), Anyang ($1059.25 \text{ kg}\cdot\text{ha}^{-1}$), Puyang ($1037.08 \text{ kg}\cdot\text{ha}^{-1}$), Zhoukou ($1003.00 \text{ kg}\cdot\text{ha}^{-1}$), Jiaozuo ($992.45 \text{ kg}\cdot\text{ha}^{-1}$) and Luohe ($908.85 \text{ kg}\cdot\text{ha}^{-1}$). The city with the highest amount was Xinxiang which reached $1096.69 \text{ kg}\cdot\text{ha}^{-1}$ and the lowest one was Sanmenxia with $485.68 \text{ kg}\cdot\text{ha}^{-1}$. Chemical fertilizer application on agricultural land was extremely diverse depending on the spatial distribution in terms of total volume and intensity.

Chemical fertilizer pollution: The nitrogen fertilizer pollution load in Henan Province was calculated using the following equation, $L(n) = M(n) \times \text{ROC}(n)$, Where, $L(n)$ is the nitrogen fertilizer pollution load ($\text{kg}\cdot\text{ha}^{-1}$), $M(n)$ is net nitrogenous fertilizer consumption ($\text{kg}\cdot\text{ha}^{-1}$), $\text{ROC}(n)$ is run-off coefficient of nitrogen fertilizer pollution (Zhang et al. 2020). The phosphorus fertilizer pollution load in Henan Province was calculated using the following equation, $L(p) = M(p) \times \text{ROC}(p) \times 43.33$, Where, $L(p)$ is the phosphorus fertilizer pollution load ($\text{kg}\cdot\text{ha}^{-1}$), $M(p)$ is net phosphorus fertilizer consumption ($\text{kg}\cdot\text{ha}^{-1}$), $\text{ROC}(p)$ is the loss coefficient of phosphorus fertilizer pollution (Zhang et al. 2020).

The pollution loads of nitrogen fertilizer and phosphate fertilizer were calculated in 18 local cities in Henan in 2019. The 8 cities with higher nitrogen fertilizer pollution load than the average were Zhoukou, Nanyang, Xinyang, Shangqiu, Xinxiang, Zhumadian, Anyang, and Kaifeng in the order from high to low, accounting for 74.55%. Meanwhile, the 7 cities where the phosphate fertilizer pollution load exceeded the average were Zhoukou, Nanyang, Shangqiu, Zhumadian, Xinyang, Xinxiang and Kaifeng, accounting for 72.08%.

The CODTN emissions generated by fertilizer application in Henan Province are decreasing, whereas the TP emissions are growing, according to the analysis. Fertilizer TN emissions account for around 37% of agricultural source TN emissions. Fertilizer TP emissions account for roughly 36% of agricultural source TP emissions. CODTN and TP emissions are high in Puyang, Anyang, Shangqiu, Xuchang, Kaifeng, and other northeast Henan plain areas, but emissions are low in the southern hilly mountain area, Xinyang, and Nanyang. This phenomenon may be caused by the following aspects: first, the cultivated land resources and population density of southern hilly and mountainous areas are smaller than a plain area; second, the surface water resources of southern hilly and mountainous area are rich, the threat to

local water resources caused by farmland fertilizer source pollution is small. Nanyang, Shangqiu, Xinyang, Zhoukou, and Kaifeng account for almost 60% of the total quantity of agriculture pollution emissions in Henan Province.

Consumption of pesticides and their environmental effects:

Pesticides play an important role in increasing productivity, reducing crop loss, controlling disease vectors, ensuring the provision of adequate healthy food, and reducing the labor, fuel, and machinery needed for crop protection activities. China consumes around 43% of global pesticides on less than 9% of global cropland. The average intensity of pesticide use per unit of cropland in China is 13.1 kg per hectare, versus 3.7 kg per hectare in Asia, and 2.6 kg per hectare worldwide (Zhu & Wang 2021). While agricultural pesticides are an important tool in agriculture and other industries, their widespread use poses a significant environmental threat due to their toxic effects and bioaccumulation tendencies in non-target organisms (Sahin & Karpuzcu 2020). Pesticides are frequently linked to risks to soil health, ecosystem function, and human safety (Yang et al. 2021). China is the largest agricultural country in the world (Kuang et al. 2020), and the average amount of pesticides used per hectare is about 1.5 to 4 times as much as the world average. Pesticides can go into surface water through surface runoff, soil erosion, spray drift, drainage, and leaching. Henan Province is one of the regions with the highest population density, developed agriculture, and the fastest growth in national economic output and per capita income in China. The main pesticides used in agricultural production in Henan Province are dichlorvos, trichlorfon, omethoate, parathion, parathion methyl, methamidophos, and other organophosphates and carbamate mushrooms such as carbaryl, as well as packs pyrethroids such as fenvalerate and cypermethrin. The utilization rate of pesticides sprayed on crops is about 20% ~30%, and the other 70% ~80% are lost to non-target crops, soil, or waters. The residual pesticides in the soil environment of Henan Province mainly include atrazine, pentachlorophenol, malathion, DDT and glyphosate.

Figs. 3 and 4 show that the amount of pesticide applied in Henan Province increased from 121,400 to 130,100 tonnes from 2009 to 2013, then declined from 129,900 to 107,200 tonnes from 2014 to 2019. From the viewpoint of the intensity index of pesticide application per cultivated land unit, it increased yearly in 2009-2014, from 14.82 kg.ha⁻¹ to 15.99 kg.ha⁻¹, and decreased year by year from 2015 to 2019, from 15.88 kg.ha⁻¹ to 13.17 kg.ha⁻¹. The results showed that pesticide application in Henan has begun to drop and stabilize in recent years, both in terms of total amount and intensity index, and agricultural production consumption has decreased.

From the spatial distribution of pesticide usage in Henan, the average usage in 18 provincial cities in 2019 was 5,957 tons. Cities with amounts higher than average were Zhoukou (18192), Nanyang (14620), Shangqiu (11476), Xinyang (10371), Xinxiang (8309), and Zhumadian (7613), accounting for 65.82%. In 2019, the average pesticide usage per unit cultivated area in 18 cities was 12.60 tons/1000 hectares. The above-average cities were Zhoukou (21.20), Jiaozuo (18.83), Xinxiang (17.53) and Shangqiu (16.12), Sanmenxia (14.13), Nanyang (13.87), and Anyang (13.81).

Consumption of agricultural mulch film and its environmental effects:

Agricultural mulch film is widely used in agriculture for improving agricultural production (Li et al. 2021, 2020), but it is also the main pollution source of agricultural non-point source pollution in Henan Province. Agricultural mulch film is a synthetic polymer compound material, which will stay in the soil for a long time if it is not cleaned or picked up in agricultural production. In recent decades, with the expansion of global mulch film consumption, the use of agricultural mulch film has also increased

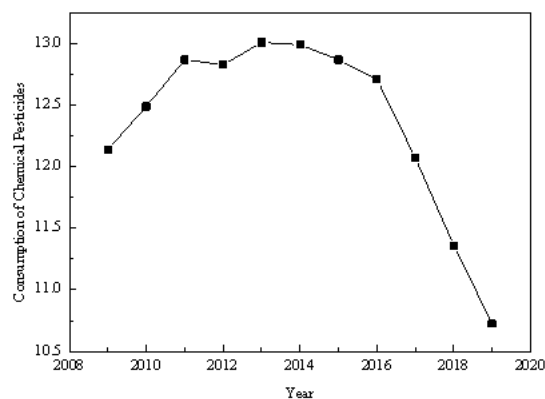


Fig. 3: Consumption of chemical pesticides.

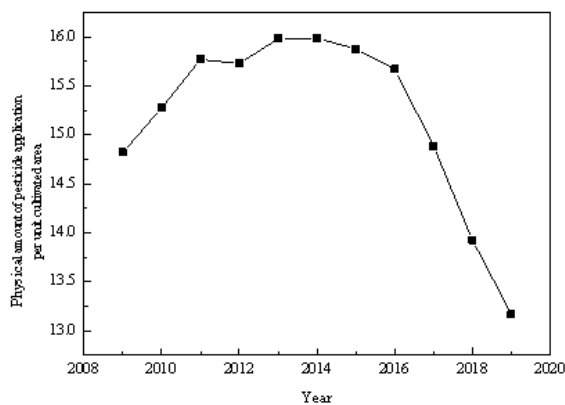


Fig. 4: Physical amount of pesticide application per unit cultivated area.

yearly in China. Debris is likely to remain in the soil due to the thin mulch film's fragility. The mulch is primarily made of polyvinyl chloride, which is difficult to decompose and recycle (Liu et al. 2019). The remaining mulch film in the soil degrades the soil structure and alters the normal movement and distribution of water and nutrients (Liu et al. 2019). Currently, the agricultural mulch film generally used in Henan Province is an ultra-thin film with a thickness of less than 0.008 mm, which has poor ductility, wear resistance, and a short period of use. After being fragmented, it will remain in the soil and extremely difficult to clean.

There is little variation in the average dosage of agricultural mulch film for different crops, and the average dosage of agricultural mulch film for tobacco and watermelon is 45 kg.hm⁻², the average dosage of agricultural mulch film for peanuts is 33.75 kg.hm⁻², and the average dosage of agricultural mulch film for garlic is 37.5 kg.hm⁻². The total residue of agricultural mulch film in the cultivated soil is 8.19~17.60 kg.hm⁻² in Henan Province, with an average of 0.10 kg.hm⁻². The residual membrane bigger than 100 cm² is overwhelming, accounting for 71.9% on average, 20~100 m² accounting for 19.2%; 2~20 cm² being 7.3%, and debris less than 2 cm² being only 1.6%. The residual mulch film in the soil has a large molecular mass and stable performance and, it can stay in the soil and cannot decompose under natural conditions for a long time. The residual mulch film poses a great threat to the soil environment, agricultural production, ecological environment, livestock, and human health, especially to soil and crop growth and development.

Fig. 5 shows the amount of agricultural mulch film used in Henan Province from 2009 to 2016. It can be seen that the usage continues to rise, with the minimum usage of 141,400 tons and maximum usage of 163,100 tons in 2013. From 2017 to 2019, agricultural mulch film usage was declining year by year. From 157,300 tons it fell to 150,800 tons and tended to be stabilized. As to the plastic film usage, during 2019 in the 18 local cities, Nanyang (16.78), Zhoukou (12.83), Anyang (12.05), Xinyang (9.26), Zhumadian (8.35), Kaifeng (8.32), and Shangqiu (8.02) accounted for respectively more than 8% of the total agricultural mulch film usage. These 7 cities accounted for 75.61% in total.

The Yield of agricultural straw and its environmental effects: Agricultural straw is an important byproduct of agricultural systems. With the continuous and active support of Chinese authority to modern agriculture, China's grain acreage and production are gradually increasing, and the amount of crops straw is also increasing yearly. Agricultural straws' functions can be broadly split into three categories: The first is that straw can be utilized as a source of nourishment and as a feed and fertilizer (Wang et al. 2021, Zhang et al. 2021).

The second is energy, which can be employed in an industrial project because of its biomass (Yang et al. 2021). Straw can be utilized as a raw material for technical reasons as the third function (Rojas et al. 2019). China offers some policies and financial supports for the comprehensive use of straw (Zou et al. 2020). However, due to various restrictions, 60% of straw resource processing is effectively used as fertilizers, feed, and raw materials, while 40% of the processing is still not used effectively or even discarded at will, which may cause environmental pollution.

Open burning is a prevalent phenomenon during harvest seasons in certain areas of Indoor burning for energy has been regarded to cause health difficulties, particularly lung cancer as well as cardiovascular and respiratory disorders, in Henan Province, generating significant air pollution (Sun et al. 2020). The main characteristic of grain cultivation in Henan Province is numerous in crop variety with large quantities, but at the same time, it faces the big problem of straw processing. The total amount of crop stalk resources in Henan Province can be estimated based on the amount of crop production, and the estimation method is as follows,

$S = \sum_{j=1}^k s_j d_j$, where S is the number of straw resources, s_j is the yield of a certain crop, and d_j is the grass and valley of a certain crop, as shown in Table 1. The estimation of straw production in Henan Province in 2019 is shown in Table 2.

From the calculated proportion of straw stalk in the above table, the main sources of crop straw in Henan are wheat, corn, and oilseeds, which produce 93.96% of the total straw. We estimated the straw stalk output ratio from the production of major crops in each city in 2019. According to the findings, the cities with the highest ratios were Zhumadian (13.48%), Zhoukou (13.17%), Nanyang (12.22%), and Shangqiu (10.87%), accounting for 49.74 per cent of the total. The rate of exploitation of straw resources is low (less than 60%), while the possibility of resource utilization is great.

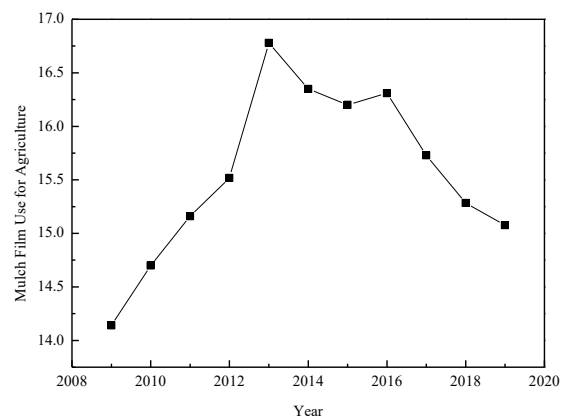


Fig. 5: The amount of agriculture mulch film.

Table 1: Grain-straw ratio.

grain-straw ratio			
paddy	1.0	wheat	1.4
beans	1.5	cotton	3.0
bast fiber crop	1.0	oilcrops	2.0
		corn	2.0
		potato	0.5
		carbohydrate crop	0.1

Table 2: Henan Province’s straw production in 2019 (×10⁷ kg).

	Paddy	Wheat	Corn	Beans	Cotton	Potato	Hemp	Oil	Carbohydrate
Yield	512.50	3741.77	2247.37	102.00	2.71	64.50	1.94	645.45	11.93
Straw	512.50	5238.48	4494.74	153.00	8.13	32.25	1.94	1290.90	1.19
Percentage	4.37	44.65	38.31	1.30	0.07	0.27	0.02	11.00	0.01

CONCLUSION

In the last decades, agricultural non-point source pollution is attracting more and more attention in Henan Province, China, due to the rapid development of agriculture there. This study analyses the agricultural non-point source pollution from 2008 to 2019. The total phosphorus loads showed an increasing trend; The chemical oxygen demand, total nitrogen, and total phosphorus pollution loads showed a decreasing trend. The pesticide use load of Zhoukou, Nanyang, Shangqiu, Xinyang, Xinxiang, and Zhumadian cities were higher in Henan; the plastic film use intensity of Nanyang, Zhoukou, Anyang, Xinyang, Zhumadian, Kaifeng, and Shangqiu was higher; the crop waste discharge amount of Zhumadian, Zhoukou, Nanyang and Shangqiu cities were higher. Due to the development of national policies and agricultural technology, in addition to total phosphorus pollution, the farmland non-point source pollution load is decreasing in Henan Province year by year.

ACKNOWLEDGMENTS

This research was financed by Henan Province Science and Technology Attack Plan Project (Grant No. 212102310069, 212102300964) and the Third Agricultural Census in Henan Province (Grant No.SNP031).

REFERENCES

Gu, B.J., Ju, X.T., Chang, J., Ge, Y. and Vitousek, P.M. 2015. Integrated reactive nitrogen budgets and future trends in China. *Proc. Natl. Acad. Sci. U.S.A.*, 112: 8792-8797.

Kuang, L.H., Hou, Y.Z., Huang, F.Q., Guo, Aidi, W.J., Sun, H.J., Shen, L.G., Lin, H.J. and Hong H.C. 2020. Pesticides in human milk collected from Jinhua, China: Levels, influencing factors and health risk assessment. *Ecotoxicol. Environ. Saf.*, 205:111331.

Li, C., Sun, M.X., Xu, X.B. and Zhang, L.X. 2021. Characteristics and influencing factors of mulch film used for pollution control in China: Microcosmic evidence from smallholder farmers. *Resour. Conserv. Recycl.*, 164: 105222.

Li, X., Chen, M., Le, H.P., Wang, F., Guo, Z., Iinuma, Y., Chen, J. and Herrmann, H. 2016. The atmospheric outflow of PM2.5 saccharides from megacity Shanghai to the East China Sea: Impact of biological and biomass burning sources. *Atmos. Environ.*, 143: 1-14.

Li, Y.Q., Zhao, C.X., Yan, C.R., Mao, L.L., Liu, Q., and He, W.Q. 2020. Effects of agricultural plastic film residues on transportation and distribution of water and nitrate in the soil. *Chemosphere*, 242:125131.

Liu, E., He, W. and Yan C. 2014. ‘White revolution’ to ‘white pollution’-Agricultural plastic film mulch in China. *Environ. Res. Lett.*, 9(9): 091001.

Liu, Y.L., Li, Y. and Zhang, Y.R. 2017. Effect of long-term application of NPK fertilizer on maize yield and yellow soil nutrients sustainability in Guizhou, China. *J. Appl. Ecol.*, 28 (11): 3581.

Qiu, X.H., Duan, L., Chai F.H., Wang S.X., Yu Q. and Wang S.L. 2016. Deriving high-resolution emission inventory of open biomass burning in China based on satellite observations. *Environ. Sci. Technol.*, 50:11779-11786.

Rojas, C., Cea, M., Iriarte, A., Valdés, G., Navia, R. and Cádenas, R.J.P. 2019. Thermal insulation materials based on agricultural residual wheat straw and corn husk biomass, for application in sustainable buildings. *Sustain. Mater. Technol.*, 20: 00102.

Sahin, C. and Karpuzcu M. E. 2020. Mitigation of organophosphate pesticide pollution in agricultural watersheds. *Sci. Total Environ.*, 710: 136261.

Sun, M.X., Xu, X.B., Wang, C.D., Bai, Y.L., Fu, C., Zhang, L.X., Fu, R. and Wang Y.T. 2020. Environmental burdens of the comprehensive utilization of straw: wheat straw utilization from a life-cycle perspective. *J. Clean. Prod.*, 259: 120720.

Wang, W.S., Yang, S.Q., Zhang, A.P. and Yang Z.L. 2021. Synthesis of a slow-release fertilizer composite derived from waste straw that improves water retention and agricultural yield. *Sci. Total Environ.*, 768: 144978.

Xue, L.H., Hou, P.F., Zhang, Z.Y., Shen, M.X., Liu, F.X. and Yang L.Z. 2020. Application of systematic strategy for agricultural non-point source pollution control in Yangtze River basin, China. *Agric. Ecosyst. Environ.*, 304: 107148.

Yan, B.J., Yan, J.J., Li, Y.X., Qin, Y.F. and Yang L.J. 2021. Spatial distribution of biogas potential, utilization ratio, and development potential of biogas from agricultural waste in China. *J. Clean. Prod.*, 292: 126077.

Yang, Z.P., Li, X.Y., Wang, Y., Chang, J.Z. and Liu X.R. 2021. Trace element contamination in urban topsoil in China during 2000–2009 and 2010–2019: Pollution assessment and spatiotemporal analysis. *Sci. Total Environ.*, 758: 143647

Yuan, J.J., Lu, Y.L., Ferrier, R.C., Liu, Z.Y., Su, H.Q., Meng, J., Song, S. and Jenkins A. 2018. Urbanization, rural development, and environmental health in China. *Environ. Dev.*, 28: 101-110.

Zhang, H.Y., Hobbie, E.A., Feng, P.Y., Zhou, Z.X., Niu, L.A., Duan, W.K., Hao, J.M. and Hu, K.L. 2021. Responses of soil organic carbon and crop yield to 33-year mineral fertilizer and straw additions under different tillage systems. *Soil Till. Res.*, 209: 104943.

- Zhang, J.J. and Shou, Y.J. 2021. Research on the construction of agricultural meteorological disaster prevention service system in Henan Province under the rural revitalization strategy. *Agric. Biotechnol.*, 10(1): 79-82.
- Zhang, J.K., Cheng, M.T., Ji, D.S., Liu, Z.R., Hu, B., Sun, Y. and Wang, Y.S. 2016. Characterization of submicron particles during biomass burning and coal combustion periods in Beijing. *Sci. Total Environ.*, 562: 812-821.
- Zhang, Y.N., Long, H.L., Li, Y.R., Tu, S.S. and Jiang, T.H. 2020. Non-point source pollution in response to rural transformation development: A comprehensive analysis of China's traditional farming area. *J. Rural Stud.*, 83: 165-176.
- Zheng, W.L., Luo, B.L. and Hu, X.Y. 2020. The determinants of farmers' fertilizers and pesticide use behavior in China: An explanation based on label effect. *J. Clean. Prod.*, 272(1): 123054.
- Zhou, W. and Wang R.M. 2021. Impact of farm size on the intensity of pesticide use: Evidence from China. *Sci. Total Environ.*, 753: 141696.
- Zou, L.L., Liu, Y.S., Wang, Y.S. and Hu X.D. 2020. Assessment and analysis of agricultural non-point source pollution loads in China: 1978-2017. *J. Environ. Manage.*, 263: 110400.



Development and Fabrication of A Portable Shredding Machine for Rapid Composting of Organic Waste

Resmi G.*† and Vinod V.**

*Department of Civil Engineering, N.S.S. College of Engineering, Palakkad, Kerala, India

**Department of Mechanical Engineering, N.S.S. College of Engineering, Palakkad, Kerala, India

†Corresponding author: Resmi G.; resmivinod@gmail.com

Nat. Env. & Poll. Tech.
Website: www.neptjournal.com

Received: 03-06-2021

Revised: 26-06-2021

Accepted: 12-07-2021

Key Words:

Organic waste

Shredder

Accelerated composting

Composting parameters

ABSTRACT

Solid waste management is found to be a matter of great concern all over the world. As the population grows, the volume of food waste also increases. Vegetable waste discarded from markets, waste discarded from slaughterhouses, and food waste left out after large social gatherings are becoming unmanageable heaps of organic waste. Composting is an effective process that can be used for the biodegradation of solid waste. Researchers have studied the influence of many parameters to accelerate the composting process such as adjusting the C/N ratio, pH, temperature, and moisture content. Reducing the size of larger pieces into small particles is found to accelerate the microbial activity and hence composting. This paper discusses the development and fabrication of a shredding machine used for cutting large volumes of vegetable waste. As per the studies conducted, the shredding machine can cut down 360 kg of vegetable waste into shredded waste within one hour. The quantity of petrol required for operating the engine for one hour was observed as one liter. Hence the fabricated shredding machine is found as cost-effective. The portable unit can be taken to various locations where solid organic waste has to be shredded and hence there is no need to transport waste which is a cumbersome task that consumes more energy.

INTRODUCTION

As the world populations grow there occurs increased demand for food as well as various consumable items. The rate of production of waste also gets increased as a result of this. Almost all parts of the world are struggling to manage the huge heaps of garbage dumps generated by this. It is stated by National Environmental Engineering Research Institute (NEERI) that the per capita generation of municipal solid waste in large cities of India is around 0.5kg per day. Many vegetable markets, slaughterhouses, etc. generate large quantities of organic waste. In many places, unscientific and crude methods are used for the disposal of this waste. If proper treatment is not provided, these wastes start emitting a bad odor. Among the various solid waste management techniques used, such as landfilling, incineration, pyrolysis, etc. composting is found to be the best-suited method for managing biodegradable solid waste (Argun et al. 2017). It is an environmentally safe method as the mature compost can be used as a bio-fertilizer.

Aerobic composting leads to mature compost when all factors affecting composting are properly monitored (Jain et al. 2019). But one of the major problems is the requirement of the long time needed for the formation of compost. Many

researchers have studied various parameters of composting and they have found that pH, temperature, C/N ratio of waste, and moisture content are some of the most important factors influencing the nature of compost. (Ameen et al. 2016, Sundberg & Jonsson 2016, Nikaju et al. 2018). It is reported that the addition of inoculum with microbial culture will accelerate the composting activities (Pan et al. 2012, Payel & Rounak 2017). Some of the researchers have also observed that reduction of the size of waste has a good influence on microbial decomposition (Tanugur 2009, Jain et al. 2019). Cutting or chopping of organic waste is therefore highly needed for compost acceleration (Pavankumar et al. 2018). As manual cutting is a time-consuming process it was decided to develop a shredding machine that satisfies our requirements. Some researchers have studied the performance of agricultural waste shredder machines for reducing the size of organic waste such as coconut leaves (Sanjay Kumar & Hemanth Kumar 2015). The existing system of machines used for composting depend on manual labor for its operation and it is a time-consuming process (Katiar et al. 2019). As an improvement over this, a machine connected with an engine and a gearbox was designed. Many researchers have emphasized the importance of shredding matter for active decomposition but the cost to buy a shredder is not afforda-

ble for the tail end users. Hence a shredding machine that can be manufactured in a cost-effective manner is designed. The machine is working with petrol and the wheel assembly provided helps the users to take to various destinations such as market areas or dumping yards where waste accumulation is taking place. In every integrated municipal solid waste management (MSWM) facility, composting is given special importance as it is well suited for the decomposition of organic waste. In the case of the success story of Indore Municipal Corporation (IMC), India small composting units were deployed in integrated MSWM (Prashant et al. 2021).

MATERIALS AND METHODS

The research work mainly concentrated on the development of various parts and the fabrication of a shredding machine suitable for cutting down huge organic waste. Also, composting studies are done using two methods 1. Raw vegetables cut manually and 2. Vegetables shredded with the shredding machine. In each case, the vegetables were collected from the local market and aerobic composting was carried out under laboratory conditions. Analysis of variation in temperature, pH, and moisture content in the composting samples was carried out to observe the time needed for mature compost formation.

Shredding Machine

The shredding machine comprises of main parts like 1.5 HP petrol engine, gearbox, two sets of shredder blades (primary and secondary), hopper for putting the biowaste, a tray for collecting the shredded organic matter (Table 1).

The following figures show the graphical representation of the machine. 3D view of the machine (Fig. 1) gives an idea about the overall shape of the machine.

Fig. 2 shows the position of the engine connected to the gearbox through a chain pulley. The gearbox is connected to the primary and secondary blades through a chain drive. The hopper for feeding the vegetable waste to the primary

blades and the collection of shredded waste in the discharge tray is also shown in the side view.

The top view of the machine is given in Fig. 3. The primary shredder blades which are visible through the hopper are shown in the figure.

Based on the developed design and 3 D views the machine was fabricated and the pictures of the shredding machine are shown in the following figures (Figs. 4, 5).

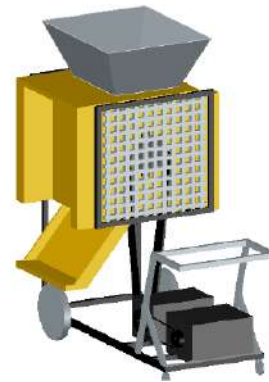


Fig. 1: 3D view of the machine (Graphical representation).

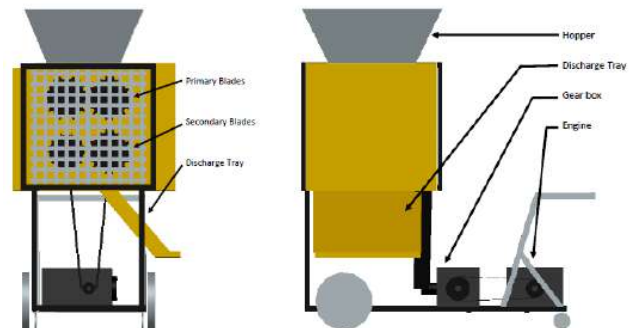


Fig. 2: Side views of the machine (Graphical representation).

Table 1: Specifications of the machine.

Sl No.	Item Name	Specifications
1	Engine	Fuel Type- Petrol, 4 Stroke, 3.5BH-P@3600Rpm
2	Gear Box	Ratio 1:40, Load Capacity-2 Ton
3	Shredding Blades-Primary	Dimensions 472 mm x262mm
4	Shredding Blades-Secondary	Dimensions 360mm x262mm

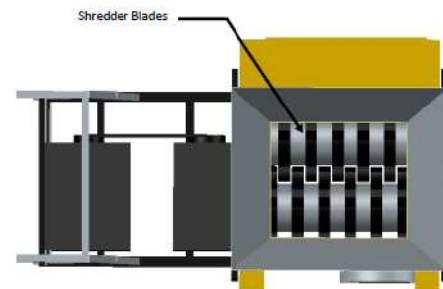


Fig. 3: Top view of the machine (Graphical representation).

A 4 stroke petrol engine with 3.5 BHP is used to power the machine with a gearbox having a gear ratio of 1:40. It provides ample torque for taking the load for shredding the matter. The shredding blades are made of steel with specialized contours to shred the organic waste into reduced size. The machine has two sets of shredding blades. One primary blade set consists of two specially set steel contour rollers with spacers in such a way that the materials which are placed in the hopper will be directed to it. The primary rollers are aligned with more center to center spacing compared to the set of secondary rollers. The vegetable waste to be shredded is kept in the hopper and when passed through the primary hopper it will be shredded into pieces. It will be again fed into the secondary rollers to shred into still smaller particles.

The secondary sets of rollers with special contours have very little spacing so that the waste particles after passing through these rollers will be crushed to the reduced form. The powdered vegetable waste will be coming out through the discharge tray kept at the bottom. The side panels of the machine are made using SS steel sheets to avoid corrosion. The gear wheels for the primary and secondary blades are protected using the metallic mesh so that effective heat transfer is made during its working. Maintenance operations can be effectively done with this arrangement.

The entire machine is fixed in four castor wheels so that it can be transported from one place to another very easily. The entire size of the machine is 2m (Length) × 1m (Width) × 1.6m (Height). Thus it is very compact and portable.

Bio Bin Formation

Aerobic composting was carried out in specially designed buckets. The bins had holes all around so that aerobic conditions could be maintained inside (Fig. 6). Daily mixing and turning of waste were done to ensure aeration. Layers in the bins were formed with vegetables, printed paper, dry leaves, and coir pith added with microbial inoculum. The

proportion was so adjusted that the resulting C/N ratio was less than 30:1. The C/N ratio values of all ingredients were calculated separately and the ratio of the sample was obtained as 26:1. Comparison of accelerated composting was made between vegetables cut manually (Fig. 7) and that shredded using the machine (Fig. 8) based on the parameters like pH, temperature, and moisture content.



Fig. 5: Rear view of the shredding machine.



Fig. 6: Bins with openings all around.



Fig. 4: Side view of the shredding machine.



Fig. 7: Vegetables cut manually.

Composting

Raw vegetables collected from the market were used for the study. Mainly Potato, cucumber, onion, Tomato, Orange, and Banana were taken for the initial trials. First of all, the vegetables were cut into small pieces manually. Then the layers of cut vegetables were sprayed with inoculum based on coir pith. Specially designed bins with holes all around and with meshed lids were used for aerobic composting. The physical characteristics, pH, temperature, and moisture content were monitored at regular intervals. Two sets of treatments were done. One was with manually cut vegetables of size 10-30mm (Sample 1). In the second treatment, the sets of experiments were repeated with shredded vegetables (Sample 2). The comparison of the influencing parameters till 90 days or up to the compost maturity was done.

Testing of Parameters

Physical parameters influencing the composting were monitored continuously in the bio bin. The temperature of the compost was observed daily using a digital thermometer. The temperature in the top, middle and bottom portions of the bio bin were observed and an average value was taken for reporting. For measuring pH, the method described by Annacarol et al. (2019) was used. For this 10 gm of compost was taken from the compost bin and put into a 250 mL beaker having 90 mL distilled water in it. The mixture was stirred well and allowed to settle. the pH of the supernatant was tested using a digital pH meter.

RESULTS AND DISCUSSION

Performance Evaluation of Shredding Machine

During initial testing, the time taken for shredding 15kgs of vegetable waste was around 2.5 minutes. The vegetables were

passed through the hopper twice to pass through the primary and secondary blades for better shredding into smaller particles. Even though cutting down of organic matter helped accelerate the composting; the formation of fine powder is not advisable. While particle size reduction is favorable for biological activities, minimizing the size to fine powder form leads to slumping and compaction of the material (Zhang et al. 2019). The presence of slightly larger particles ensures bigger void spaces and better oxygen access. The shredding was repeated twice for making the waste into a mass with crushed form as well as medium-sized pieces. It is observed that if the machine is effectively loaded the machine is capable of converting around 360 kg of vegetable waste into a fine mix in one hour. The fuel consumption for the operation of the machine was measured at around 1 liter for one hour. Thus at the expense of one liter of petrol, vegetable waste of any type around 360 kgs can be converted into small particles so that it can be effectively converted into bio compost.

The main advantage of the machine fabricated is that it is light in weight, portable, and very compact. Since this machine is running on petrol fitted with the gearbox to take uploads and portable it can be used for continuous running applications like composting units. This can also be a livelihood for different neighborhood groups such as Kudumbashree units (Kudumbashree Mission is the Kerala State Government's instrument for poverty eradication under the Local Self-Government Department) to earn money for making compost and converting it into manure.

Studies on Compost Maturity

Compost maturity and stabilization were monitored through parameters such as pH, Moisture level, and physical characteristics of compost. The vegetables which were shredded manually and with the help of a shredding machine were



Fig. 8: Vegetable waste shredded using the machine (Left- first trial, Right- Second trial)

taken and filled in separate bins. The productivity of the shredding machine is very high compared to manual shredding. It was observed that the quantity of vegetable waste that can be processed by the machine is around 20 times more compared to manual cutting by a single individual and it also takes only nearly one-tenth of the time for its processing the entire mass into smaller particles.

Physical characteristics of the compost were noted and the bin having maximum bacterial activity and shorter compost duration was noted down. The physical nature of compost like color, temperature, smell, and moisture content was observed directly. The physical changes in compost were observed every day.

Observation on the 5th day showed no remarkable change in color or heat formation in the bin carrying the vegetables cut manually (Sample 1). There was little variation in some of the physical characteristics in the compost bin containing the shredded waste (Sample 2). A slight foul smell combined with medium moisture content was noted by the 10th day in Sample 1. The pH variation, heat change, and change in moisture content were monitored continuously. The readings are represented in the following graphs. For sample 1 there were remarkable changes observed from the second week onwards. But sample 2 took three weeks to start with changes in physical characteristics.

Variation in Temperature

Temperature indicates the microbial activity taking place in the bin during the composting process. It is one of the key factors influencing the degradation process (Jain et al. 2019). A few days after starting, the temperature in the compost samples showed an increasing tendency. This increase was steady in sample 1 and it was rapid in sample 2. The rapid increase of temperature in sample 2 to the thermophilic range may be due to the higher microbial activity on the substrate.

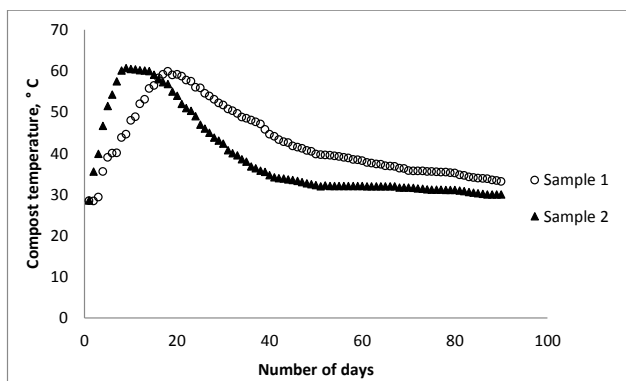


Fig. 9: Variation in temperature during composting.

The following graph (Fig. 9) shows the changes observed in both cases.

As per the study, it could be observed that the bio bin containing vegetables cut in the shredding machine and bulking agents with inoculum i.e. sample 2 have reached the thermophilic stage very rapidly. The maximum temperature was observed on the 9th day and it was around 60.7°C. In the case of sample 1 maximum temperature was observed on the 18th day and it was 59.9°C. In the case of sample 2, composting continued in thermophilic and mesophilic stages for one month, and then it started showing stability. After 45 days stable temperature was observed for sample 2. While in the case of manual shredding of vegetables this phenomenon was not observed. The thermophilic and mesophilic stages lasted for 50 days duration. It is reported that temperature between 30 and 55°C enhance microbial activity (De Bertoldi et al. 1983) Nearly stable condition was noticed from 80 days onwards. During the observation continued for 90 days, the temperature in the compost bin did not reach ambient temperature. It could be understood that the shredding of waste to small pieces using the shredding machine is highly effective in accelerating the composting process. Fig. 10 shows the compost obtained using shredded waste after two weeks.

Variation in Moisture Content

Moisture content in the compost bin is a factor that significantly influences the process of composting. If vegetables alone are taken it may lead to large moisture content and it may lead to the development of anaerobic conditions. Hence dry leaves and paper were added to the samples. Also, the coir pith-based inoculum was highly effective in absorbing moisture and maintaining aerobic conditions in the bin. Even though moisture was developed during the decomposition it was getting absorbed by the other accelerators and bulking agents added. Initial moisture content in the vegetables was as high as 84%. Due to the mixing with bulking agents, the initial moisture content in the compost bin was observed as 68%. Reduced moisture content shows increased microbial



Fig. 10: Compost formation after 18th day.

activity (Ameen et al. 2016). This may be due to the presence of the anaerobic condition in sample 1 where more moisture is present in the waste. The waste contained in the bin by manual cutting of vegetables showed a reduction in moisture content on a gradual basis (Sample 1). There was a rapid reduction of moisture content in the shredded waste sample (Sample 2). The figure below shows the reduction occurred in moisture content during composting process (Fig. 11). It shows that the shredding of waste is accelerating the absorption of moisture and leachate generated in the bin.

This is due to the reason that as the waste is shredded into smaller particles its surface area is increased and this improves the amount of heat transfer and thus the moisture is removed at a faster pace compared to manual shedding. It can be observed from the graph that within 10 days the sample 2 shows a reduction in moisture content of 10% and sample 1 takes nearly 30 days to reach the same moisture content. Thus a significant improvement in moisture reduction is observed due to shredding.

Variation in pH

Continuous monitoring of pH was carried out using a digital pH meter. The variation in pH indicated the progress of biological activities going on inside the bio bin during the composting process. In the present study, there was an increase in pH during the initial phase of composting. Compared to sample 1 the variation was rapidly occurring in sample 2 (Fig. 12). This may be due to the higher activity of microorganisms when the particles are very small in size. It is reported by many investigators that bacterial culture will take part in decomposition and as a result ammonium will be formed. At a later stage, there is a chance for reduced pH when Carbon dioxide and organic acid production starts (Zakarya et al. 2018). In the current experimental investigation pH in the compost bin was always in a range of 6.8 to 7.9. In the case of maximum and minimum pH, there was no significant variation between manually cut organic matter and those shredded using the machine. But pH increased to 7.9 by the end of 5 days in shredded waste. It shows that

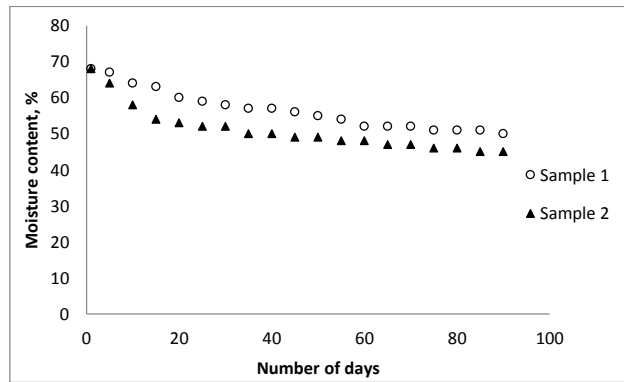


Fig. 11: Variation in moisture content during the composting process.

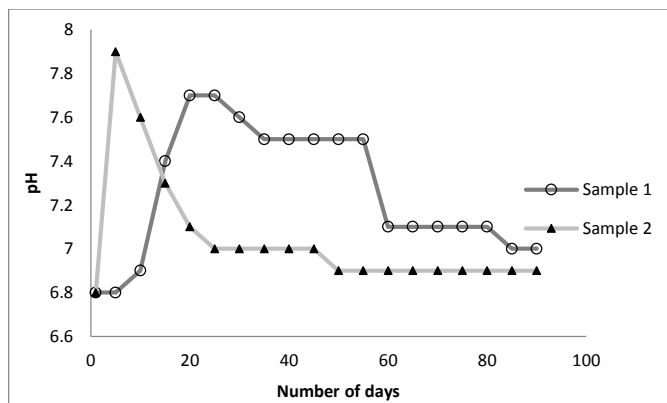


Fig. 12: Variation in pH during the composting process.

organic matter powdered using the machine is acted upon by the micro-organisms without delay. The gradual change in pH was observed in sample 1. The value of pH reached to neutral condition by 25 days in sample 2 and it took nearly 85 days in the case of sample 1. Studies in composting have shown that starting with a fairly neutral pH will ensure high levels of microorganisms for efficient decomposition and the pH should be around neutral conditions for obtaining stable compost (Risse & Faucette 2009).

CONCLUSION

A portable shredding machine was fabricated for cutting down organic waste and composting carried out. The benefit of shredding is that as the waste particles are properly shredded, the surface area of the waste materials will be increased so that they can be effectively degraded by microorganisms. As a result, the efficiency of composting is increased and productivity is improved. Neutral pH condition was reached within 25 days for shredded waste. Thermophilic conditions occurred rapidly and mesophilic decomposition started after two weeks duration. After one month of decomposition, moisture content was within the range of 50% to 40% which was ideal for good compost. Composting done by vegetables cut manually has taken nearly 80 days to reach stable conditions. Thus with the help of shredding machines within lesser time, more waste can be converted into manure. This portable unit can be utilized in restaurants, auditoriums, housing colonies, markets, etc. The panchayats can even use this portable machine as a mobile unit with the help of Kudumbashree units to operate in various housing colonies at least once a week to convert the collected waste from houses and turn it into powder. Hence the need for the collection and transportation of vegetable waste can be avoided. Composting plays a vital role in environmental regulations because the discarded organic waste can be converted into value-added product/manure at the source itself. As landfill space is reducing day by day and the fee for transport of waste is getting increased there is wider scope for accelerated composting. It can be concluded that with the help of a shredding machine effective waste management can be achieved in a highly economical and sustainable manner.

ACKNOWLEDGMENT

The authors gratefully acknowledge the financial assistance provided by APJ Abdul Kalam Technological University, Centre for Engineering Research and Development (CERD)

as Research Seed Money (RSM) for carrying out the experimental investigations at N.S.S. College of Engineering Palakkad, Kerala, India.

REFERENCES

- Ameen, A., Ahmad, A., Munir, N. and Raza, S. 2016. Physical and chemical analysis of compost to check its maturity and stability. *Eur. J. Pharm. Med. Res.*, 3(5): 84-87.
- Anncarol, W.K., Ezekiel, M.N. and Maingi J.M. 2019. Assessment of physic-chemical changes during composting rice straw with chicken and donkey manure. *Int. J. Recycl. Org. Waste Agric.*, 8 (1): S65-S72.
- Argun, Y., Karacali, A., Calisir, U. and Kilinc, N. 2017. Composting is a waste management method. *J. Int. Environ. Appl. Sci.*, 12(3): 244-255
- Jain, M.S., Daga, M. and Kalamdhad, A.S. 2019. Variation in the key indicators during composting of municipal solid organic wastes. *Sustain. Environ. Res.*, 29(9): doi.org/10.1186/s42834-019-0012-9.
- Katiar, A., Gaur A., Shrivastava, A., Khan, M.A., Sing, N.P., Saini, R. and Kaur, G. 2019. Design and construction of a shredding machine for recycling and management of organic waste. *Int. J. Sci. Res. Dev.*, 3(4): 707-712.
- De Bertoldi, G., Vallini, M. and Pera, A. 1983. The biology of composting: A review. *Waste Manage. Res.*, 1(2): 157-176.
- Nikaju, J., Borkar, V., Pise, A. and Pawar, S. S. 2018. Organic waste compost machine, International Conference on Emanations in Modern Engineering Science & Management (ICEMESM-2018), 23-24 March 2018, Nagpur Maharashtra, India, IJET, India, pp. 1-5
- Pan, I., Dam, B. and Sen, S.K. 2012. Composting of common organic wastes using microbial inoculants. *Biotech*, 2: 127-134 <https://doi.org/10.1007/s13205-011-0033-5>.
- Pavankumar, S.B., Sachin, K.R., Shankar, R., Thyagaraja, B. and Madhusudhan, T. 2018. Design and fabrication of organic waste shredding machine. *Int. J. Engg. Sci. Invent.*, 7(6): 26-31.
- Payel, S. and Rounak, C. 2017. Bioconversion of organic solid wastes into biofortified compost using a microbial consortium. *Int. J. Recycl. Org. Waste Agricult.*, 6: 321-334.
- Prashant, S., Sharma, P.K., Pandey, S. and Chintala V. 2021. Unsegregated municipal solid waste in India: Current scenario, challenges, and ways forward. *Nature Environ. Pollut. Technol.*, 20(2): 851-863.
- Risse, M. and Faucette, B. 2009. Food waste composting: Institutional and Industrial Applications What Is Compost? *Univ. Georg.*, 1189: 1-8.
- Sanjay Kumar, I.M. and Hemanth Kumar, T. R. 2015. Design and development of agricultural waste shredder machine. *Int. J. Innov. Sci. Engg. Technol.*, 2(10): 164-172.
- Sundberg, C. and Jonsson, H. 2016. Higher pH and faster decomposition in bio-waste composting by increased aeration. *Waste Manage.*, 28(3): 518-526.
- Tanugur, I. 2009. Aerobic composting of broiler waste with different amendments. M.Sc. thesis. Institute of Science and Technology, Istanbul Technical University, Istanbul Turkey.
- Zakarya, I.A., Khalib, S.N.B. and Ramzi, N.M. 2018. Effect of pH, temperature, and moisture content during composting of rice straw burning at different temperatures with food waste and effective microorganisms. *E3S Web of Conf.*, 34: 02019. <https://doi.org/10.1051/e3sconf/20183402019>
- Zhang, Y., Kusch-Brandt, S., Gu, S. and Heaven, S. 2019. Particle size distribution in municipal solid waste pre-treated for bioprocessing. *Resources*, 8(166): 1-24. doi:10.3390/resources8040166



Application of Analytical Hierarchy Process (AHP) for Assessment of Collection and Transportation of Solid Waste: An Empirical Study

Gnanasekaran Sasikumar*†, A. Sivasangari** and N.Venkatachalam***

*Department of Mechanical Engineering, GMR Institute of Technology, Srikakulam-532 127, Andhra Pradesh, India

**Department of Electronics and Communication Engineering, GMR Institute of Technology, Srikakulam-532 127, Andhra Pradesh, India

***Department of Mechanical Engineering, Excel Engineering College, Komarapalayam-637303, Tamilnadu, India.

†Corresponding author: Gnanasekaran Sasikumar; sasikumar.g@gmrit.edu.in

Nat. Env. & Poll. Tech.
Website: www.neptjournal.com

Received: 08-06-2021

Revised: 06-07-2021

Accepted: 13-07-2021

Key Words:

Urban local bodies
Analytical hierarchy process
Solid waste management
Consistency ratio

ABSTRACT

Cities and Urban Local Bodies (CULB) are considered to be the engines of economic growth and any significant improvement in their operational efficiency will lead to a positive impact on the economy. The major portion of expenditure on Solid waste management (SWM) of CULBs is spent on waste collection and transportation activities. To enhance the efficiency of SWM, it is essential to collect and transport solid waste in a scientific manner. As a result, systematic solid waste collection and transportation will effectively resolve and improve SWM concerns. In this paper, Analytical Hierarchy Process (AHP) method is adopted to appraise various alternatives of solid waste collection and transportation methods of municipal solid waste in Visakhapatnam city, India. The additive normalization method is applied for calculating the criteria weights. The fairness of judgment is checked by the consistency ratio. To calculate AHP accurately and fast, a decision support system was built. The findings of the study will be beneficial in evaluating existing solid waste collection and transportation processes to improve the operational efficiency of managing SWM.

INTRODUCTION

Waste is generated from various sources such as households, markets, industries, hotels and restaurants, institutions, and other organizations. Waste can exist in solid, liquid, and air forms. According to India's 2011 census, urban India contributed 63 per cent of the country's GDP, with that figure expected to rise to over 75 per cent by 2030. The country's strong GDP development is being hampered by the waste crisis, with waste generation expected to reach 165 million tonnes by 2030. The challenges of proper collection and transportation play a vital role in making our cities clean and smarter. Apart from the quantity of waste generated, proper waste collection, sorting, and transportation must be carried out in a methodical manner. The existing collection, waste separation, and transportation CULBs techniques are not designed to handle solid wastes efficiently. As a result, in order to meet the public's requests and clean up the city, a resilient, robust, scientific, and people-centric SWM method is required. Such scientific SWM procedures will allow for more efficient resource management and improved usage. Solid waste management is a difficult operation that necessitates a lot of attention from the public and the institutions involved (Chouhan & Reddy 1996, Mazumdar 1994).

PAST STUDIES

Poor practices of solid waste management will lead to major financial, environmental pollution, and health problems to society (Hazra et al. 2017). Due to the decentralization of funds, the evaluation of municipal budgets requires a lot of attention. The municipal budgets of five significant Indian cities were analyzed to see how much money could be spent on SWM (Sekhar & Bidarkar 1999). Multi-Criteria Decision Making (MCDM) techniques such as the Simple additive weighting method and TOPSIS were applied to study and relate the SWM methods (Jovanovic et al. 2016). The selection of suitable solid waste collection systems with a major focus on improving waste recovery rate was dealt and the use of environmental impact data was reported (Ulukan & Kop 2009). A combined model based on the weighted linear combination method and AHP is applied for evaluating the fitness of the landfill site for MSW (Mazaher Moeinaddini 2010). A novel Stratified Best-Worst method was implemented for identifying a suitable waste disposal technology selection in Iran (Torkayesh et al. 2021).

Geographical Information System and TOPSIS technique were used to identify alternative solid waste landfill sites among six areas in Turkey (Yildirim et al. 2018). A

review of MCDM applications in Municipal SWM including methodology, type of wastes, priority methods, calculation of consistency ratio was discussed elaborately (Goulart Coelho LM et al. 2017). An MCDM model was developed using ELECTRE III to identify the best location for waste treatment plants to handle e-wastes in Greece (Ch. Achillas et al. 2010).

Based on the literature review, it is found that evaluation of solid waste collection and transportation method falls that under MCDM includes the following issues:

- Conflicting criteria and their objectives with respect to the problem
- Nature of criteria and sub-criteria
- Alternatives with different merits and demerits

Hence, the above issues are solved using the AHP method as it is considered to be the best method to address the above problems.

EXISTING PRACTICES OF SOLID WASTE MANAGEMENT IN VISAKHAPATNAM

Visakhapatnam is positioned in the northeastern part of the state of Andhra Pradesh, India which has a population of 2,175,000 as of 2020. The city is located 170–15 'and 180–32' in the north latitude and 180–54 and 830–30 'east latitude. Many reputable industrial settings are located in and around Visakhapatnam, resulting in a higher volume of waste generation. The city is managed by the Greater Visakhapatnam Municipal Corporation (GVMC).

Collection and Transportation of Waste in GVMC

The collection, transportation, and disposal of solid waste are carried out by the Public Health Department of GVMC. The GVMC follows 3 levels of waste collection systems such as (Kameswar Rao 2019):

- i. Door-to-door waste collection (primary collection system): The separated waste at the domestic level is collected and conveyed by Push Carts and Tri-Cycle to transfer centers.
- ii. Waste collection from households by dumper and RCC bins (secondary collection).
- iii. Shipping of waste to landfill sites (third level).

The main compositions of solid waste produced in Visakhapatnam are organic waste. The city generates 1100 MT of waste per day out of which domestic waste accounts for 450 tons.day-1 and commercial, drain silt, and others will be 550-600 tons.day-1.

Solid trash collection and transportation take place in two shifts. During the first shift, workers collect and transfer

waste to open collection stations using six container wheelbarrows, push cars, or tricycles. This waste is transported to transfer facilities using dumper placers, tippers, and tractors. The waste from the transfer station is then collected and transported to the disposal site by 20 tonners and open trucks.

ANALYTIC HIERARCHY PROCESS MODEL DEVELOPMENT

The AHP is one of the Multiple Criteria Decision Making (MCDM) techniques for evaluating alternatives which was introduced by Saaty (1980). In AHP, quantitative and qualitative performances of alternatives are evaluated through a simple hierarchy structure and application of numerical scale (Lee et al. 2001). This AHP model involves subsequent steps:

- Step 1:** Identifying the criteria for the MCDM problem
Step 2: Constructing decision structure by dividing the problem into different levels consisting of criteria and alternatives
Step 3: Developing pairwise comparison matrix 'A' using equation 1:

$$A=[a_{ij}] = \begin{matrix} & \begin{matrix} C_1 & C_2 & \dots & C_n \end{matrix} \\ \begin{matrix} C_1 \\ C_2 \\ \vdots \\ C_n \end{matrix} & \begin{bmatrix} 1 & a_{12} & \dots & a_{1n} \\ 1/a_{12} & 1 & \dots & a_{2n} \\ \vdots & \vdots & \ddots & \vdots \\ 1/a_{1n} & 1/a_{2n} & \dots & 1 \end{bmatrix} \end{matrix} \dots(1)$$

where $a_{ij}=1$ and $a_{ji}=1/a_{ij}$, $i, j = 1, 2, \dots, n$
 C_1, \dots, C_n signifies criteria involved in the problem, while a_{ij} shows decision on criteria $C_i C_j$.

The comparative importance of two elements is valued by 1, 3, 5, 7, and 9, where 1 means "equally important", 3 indicates "slightly more important", 5 shows "significantly more important", 7 signifies "strongly more important", and 9 means "extremely more important" (Saaty 2000).

Step 4: By normalizing the column, adding each row element, and dividing the total by the number of elements in the row, the weight of the pairwise comparison matrix may be calculated.

Step 5: Checking the consistency of each comparison matrix to ascertain the consistency of expert judgment by computing the consistency index (CI) and consistency ratio (CR) by equations 2 & 3:

$$CI = \frac{(\lambda_{max}-n)}{(n-1)} \dots(2)$$

$$CR = CI/RI \dots(3)$$

where n and λ_{max} denotes the size of matrix and Eigenvalue. The judgment consistency is tested by CR which is obtained by dividing CI with Random index (RI) from Table 1. The CR is satisfactory if it is below 0.10 (Saaty 1980).

APPLICATION OF ANALYTIC HIERARCHY PROCESS MODEL FOR SOLID WASTE MANAGEMENT

The AHP method is used for assessing the SWM practices particularly for solid waste collection and transportation at GVMC and the following steps are involved in the case study:

Defining Qualitative and Quantitative Criteria

Constructing a hierarchy structure for AHP based SWM with 4 main criteria (Technical, Environmental, Economic, and Socio-cultural) and 12 sub-criteria (Collection method, Collection frequency, Regulatory norms, air quality, energy savings, energy awareness, capital cost, operating cost, maintenance cost, public participation, planning, monitoring and control, public health and hygiene)

saving, Environmental awareness, capital cost, operation cost maintenance cost, participation of public, planning, monitoring & control of operations and public health and hygiene) and 4 alternatives (Door to Door collection of waste using wheelbarrow (CT-1), Door to Door collection using rickshaw and tri-cycle (CT-2), collection by compact truck (CT-3) (from collection point to landfill) and collection by trucks and tippers (CT-4) (from households). Fig. 1 shows the hierarchical structure developed for selecting the best alternative of solid waste collection and transportation.

Establishing the Pairwise Comparison Matrix for Criteria and Sub-Criteria

The comparative importance of criteria are evaluated by six experts and the scores were totaled by the geometric mean method. The criteria weights are computed using the Additive Normalization Method as described in section 4. The pairwise comparison matrix of criteria and sub-criteria are presented in Table 2 and Table 3 respectively. Table 4 shows

Table 1: RI values based on matrix size.

n	1	2	3	4	5	6	7	8	9	10
RI	0	0	0.58	0.9	1.12	1.24	1.32	1.41	1.45	1.49

Table 2: Pair-wise comparison matrix of criteria.

Criteria	Technical	Environmental	Economical	Socio-cultural	Weights
Technical	1	5	5	5	0.4942
Environmental	0.2	1	5	5	0.2822
Economical	0.2	0.2	1	5	0.1515
Socio-cultural	0.2	0.2	0.2	1	0.072

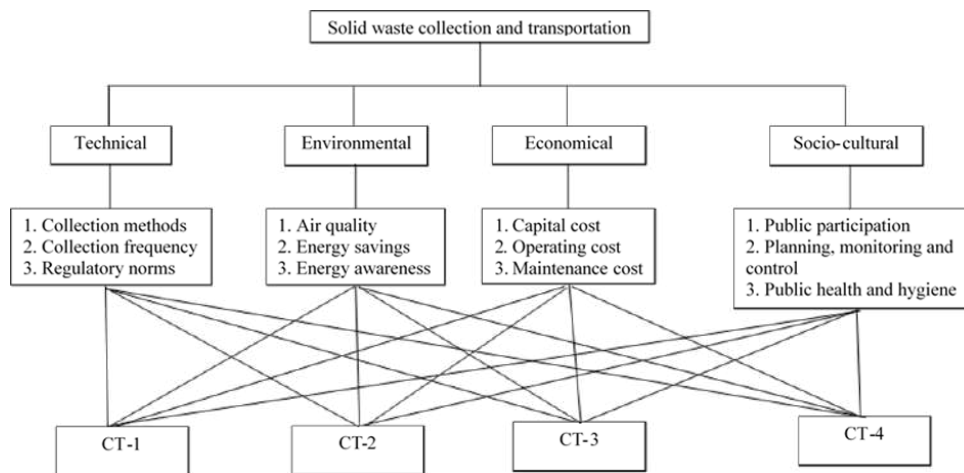


Fig. 1: Hierarchical structure for selecting the best alternative of solid waste collection and transportation.

Table 3: Pair-wise comparison matrix of sub-criteria (relating to technical).

Sub-criteria	Collection method	Collection frequency	Regulation	Weights
Collection method	1	7	5	0.6845
Collection frequency	0.142	1	5	0.2274
Regulation	0.2	0.2	1	0.0879

Table 4: Pair-wise comparison matrix of alternatives relating to collection method.

Alternatives	CT-1	CT-2	CT-3	CT-4	Weights
CT-1	1	0.33	0.1428	0.2	0.0567
CT-2	3	1	0.2	0.33	0.1218
CT-3	7	5	1	3	0.5579
CT-4	5	3	0.33	1	0.2633

the pair-wise comparison matrix of alternatives in regard to the collection method.

Computing the Final Weight of Each Sub-Criterion

The final weight of each sub-criterion is calculated and depicted in Table 5.

Arriving AHP Performance Scores and Ranking for each Alternative

The scores are computed by adding the product weight of the alternatives with the corresponding sub-criteria weight. The final scores of alternatives are computed and depicted in Table 6.

From Table 6, it is found that final AHP score is 29.21%, 18.92%, 33.89% and 17.89% for alternative 1, 2, 3 and 4 respectively. Since alternative 3 has the highest score (33.89%)

than other options, it will be ranked as the best choice while considering all criteria and sub-criteria. To simplify the calculations involved in the proposed model, a decision support system was developed using EXCEL. This DSS will help the decision-makers to get the solutions quickly and accurately.

CONCLUSION

Due to population growth, industrialization, and urbanization solid waste management has become a significant issue worldwide. Unproductive waste collection methods have an impact on the public health and aesthetics of towns and cities. In this study, the existing practice of solid waste collection and transportation methods adopted in GVMC is explained. It is found that waste collection and transportation is the major problem in implementing effective SWM. To evaluate the collection and transportation of solid wastes, an

Table 5: Computation of final weight of sub-criteria.

Criteria	Weight of criteria	Sub-criteria	Weight of Sub-criteria	Total of weight of Sub-criteria
Technical	0.4942	Collection method	0.6845	0.3382
		Collection frequency	0.2274	0.1124
		Regulation	0.0879	0.0434
Environmental	0.2822	Air quality	0.6582	0.1857
		Energy saving	0.2806	0.0792
		Energy awareness	0.061	0.0172
Economical	0.1515	Capital cost	0.663	0.1004
		Operating cost	0.2558	0.0388
		Maintenance cost	0.0811	0.0122
Socio-cultural	0.072	Participation of public	0.7288	0.0524
		Planning, monitoring, and control	0.2161	0.0155
		Public health and hygiene	0.0549	0.0039

Table 6: Computation of final scores of alternatives.

Sub-criteria	CT-1	CT-2	CT-3	CT-4
Collection method	0.338*0.056	0.338*0.122	0.338*0.558	0.338*0.263
Collection frequency	0.112*0.623	0.112*0.216	0.112*0.105	0.112*0.054
Regulation	0.043*0.05	0.043*0.283	0.043*0.345	0.043*0.32
Air quality	0.186*0.548	0.186*0.255	0.186*0.144	0.186*0.051
Energy saving	0.079*0.574	0.079*0.276	0.079*0.114	0.079*0.035
Energy awareness	0.017*0.596	0.017*0.241	0.017*0.124	0.017*0.07
Capital cost	0.100*0.042	0.100*0.114	0.100*0.49	0.100*0.343
Operating cost	0.038*0.049	0.038*0.098	0.038*0.515	0.038*0.336
Maintenance cost	0.012*0.042	0.012*0.141	0.012*0.473	0.012*0.342
Participation of public	0.052*0.505	0.052*0.325	0.052*0.109	0.052*0.06
Planning, monitoring and control	0.015*0.613	0.015*0.208	0.015*0.128	0.015*0.05
Public health and hygiene	0.004*0.158	0.004*0.190	0.004*0.45	0.004*0.20
Total weight	0.2921	0.1892	0.3389	0.1789

Analytic hierarchy process is applied and it is found to be an effective tool for evaluating the suitable collection and transportation alternatives in GVMC.

The decision hierarchy for this problem is constructed by considering 4 criteria, 12 sub-criteria, and four alternative methods of collection and transportation. Out of the 4 criteria identified, technical factors of collection and transportation is considered to be more important as it has more weight than the other three. It is evident that alternative 3, collection by compact truck is having the highest overall AHP score (33.90%) than the other three alternatives. By considering all criteria and sub-criteria, it can be found that alternative 3 is ranked as the best alternative for solid waste collection and transportation in GVMC.

The benefits of the proposed AHP model are listed below:

- (i) Scores of the criteria are computed to show the comparative significance of all criteria and sub-criteria.
- (ii) The consistency of pairwise comparisons is checked through the consistency ratio
- (iii) The alternative selection by AHP matches with the actual scenario

Limitations of the Proposed Model

The proposed model is based on the existing practices of GVMC for evaluating the suitable collection and transportation alternatives of solid waste using AHP. The criteria and alternatives chosen in this model are restricted to the case study conditions.

Other MCDM methods, combined with various ranking methodologies, should be considered for enhancing the solid

waste collection and transportation evaluation process. Other parameters that will have an impact on the selection problem should be included in addition to the criteria presented in this case study. The research can be expanded to include other SWM applications, such as determining the best landfill location and SWM equipment.

ACKNOWLEDGEMENT

The authors are grateful to their management for allowing them to do this research and thankful to the anonymous referees for their valuable suggestions to enhance the features of the content.

REFERENCES

Achillas, C.H., Vlachokostas, C.H., Moussiopoulos, N. and Baniyas, G. 2010. Decision support system for the optimal location of electrical and electronic waste treatment plants: A case study in Greece. *Waste Management*, 30 (5): 870-879.

Chouhan B.M and Reddy B.K. 1996. Bio-energy scenario in India. *IREDA News*. 7(1): 20-27.

Goulart Coelho, L.M., Lange, L.C. and Coelho, H.M. 2017. Multi-criteria decision making to support waste management: A critical review of current practices and methods. *Waste Manag. Res.*, 35(1): 3-28.

Greater Visakhapatnam Municipal Corporation, www.gvmc.gov.in.

Hazra, T., Maitra, B. and Goel, S. 2017. Development and application of a multi-criteria decision making (MCDM) tool for solid waste management: Kolkata as a case study. *Adv. Solid Hazard. Waste Manag.*, 3: 275-300 https://doi.org/10.1007/978-3-319-57076-1_14.

Jovanovic, S., Savic, S., Jovicic N, Boskovic, G. and Djordjevic, Z. 2016. Using multi-criteria decision making for selection of the optimal strategy for municipal solid waste management. *Waste Manag. Res.*, 34(9): 884-895.

Kameswar Rao, S. 2019. Municipal solid waste management in Visakhapatnam city, India. *Int. J. Eng. Adv. Technol.*, 8(6): 3604-3607.

- Lee, W.B., Lau, H., Liu, Z.Z. and Tam, S. 2001. Fuzzy analytic hierarchy process approach in modular product design. *Expert Sys.*, 18: 32-42.
- Mazumdar, N.B. 1994. Municipal solid waste management the Indian perspectives, *Environment Monitor*, 12(2): 257-269.
- Moeinaddini, M., Lee Khorasani, N., Danehkar, A., Darvishsefat, A.A. and Zienalyan, M. 2010. Siting MSW landfill using weighted linear combination and analytical hierarchy process (AHP) methodology in GIS environment (case study: Karaj). *Waste Management*, 30(5): 912-920.
- Saaty, T.L. 1980. *The Analytic Hierarchy Process*. McGraw-Hill, New York (NY).
- Saaty, T.L. 2000. *Fundamentals of Decision Making and Priority Theory with AHP*. RWS Publications, Pitsburg.
- Sekhar, S. and Bidarkar, S. 1999. Municipal budgets in India: Comparison across five cities. *Econ. Pol. Weekly*, 34(20): 1202-1208.
- Torkayesh, A.E., Malmir, B. and Rajabi Asadabadi, M. 2021. Sustainable waste disposal technology selection: The stratified best-worst multi-criteria decision-making method. *Waste Manag.*, 122 (2): 100-112.
- Ulukan, H.Z. and Kop, Y. 2009. Multi-criteria decision making (MCDM) of solid waste collection methods using Life Cycle Assessment (LCA) outputs. *International Conference on Computers & Industrial Engineering*, 6-9 July 2009, University of Technology of Troyes, France, Piscataway, NJ IEEE, pp. 584-589. doi: 10.1109/ICCIE.2009.5223862.
- Yildirim, V., Memisoglu, T., Bediroglu, S. and Colak, H. E. 2018. Municipal solid waste landfill site selection using Multi-Criteria Decision Making and GIS: A case study of Bursa province. *J. Environ. Eng. Landscape Manag.*, 26(2): 107-119.



Effect of Surface Modification on the Characteristics of Sisal Fiber Reinforced Concrete Treated with Na_2CO_3

R. Abirami† and S. P. Sangeetha

Department of Civil Engineering, Aarupadai Veedu Institute of Technology, Vinayaka Missions Research Foundation, Chennai, T.N., India

†Corresponding author: R. Abirami; abirami.civil@avit.ac.in; abirajan26@gmail.com

Nat. Env. & Poll. Tech.
Website: www.neptjournal.com

Received: 09-06-2021

Revised: 02-07-2021

Accepted: 14-07-2021

Key Words:

Aspect ratio

Sisal fiber

Green technology

Material characteristics

Volume fraction

ABSTRACT

Concrete with fiber as a reinforcing material is one of the important fields of research that is gaining traction in this upcoming green technology revolution. By adding fibers to concrete, the tensile strength properties are vastly improved without compromising the strength characteristics, and cost fluctuation is minimal. This research is being carried out to improve the qualities of concrete that have been infused with chemically treated sisal fiber in varied ratios. The paper investigates and describes the effects of sisal fiber when it is chemically treated and infused with concrete, comparing it to ordinary concrete in strength tests. Water absorption, workability, and other material characteristics of Sisal fiber reinforced concrete with 0.5 per cent, 1 per cent, 1.5 per cent, and 2 per cent fiber replacing cement by volume fraction and a sisal fiber aspect ratio of 1:100 are compared to the traditional M30 concrete grade. After being treated with an alkaline solution, 0.5 per cent and 1 per cent sisal fiber reinforced concrete increased tensile and compressive strength, as well as the formation of calcium carbonate deposits on the fiber interfaces; this also contributes to the concrete's corrosion resistance and durability.

INTRODUCTION

Natural fibers are biodegradable and are extensively being used in new generation concrete technologies. For the past 20 years, this technology is being tested and developed. There is a conclusive result of all the experiments stating that adding natural fibers such as sisal, coir, hemp, Kenaf, pineapple fiber will be used as reinforcement and will provide better strength qualities (Jitendra et al. 2016). In addition, they also provide better insulation against electrical and thermal objects and have acoustic effects (Wei & Meyer 2014). Fibers in general are added to reduce the plastic shrinkage and drying shrinkage that occurs during formation. They can also reduce water draining in concretes by decreasing permeability (Silva et al. 2008). There are fibers that can improve the impact, shatter resistance, and abrasion of concrete. By adjusting the aspect ratio of the fiber, the tension strength of the material can be modified (Naresh et al. 2017). Sisal fiber is the object of interest in the following study conducted and tabulated in the paper. The characteristics of sisal fiber differ based on the manufacturing process, the age of the plant, the location, and other factors. Sisal fiber may be reinforced in a variety of ways because it is a surplus by-product from the agriculture sector and hence inexpensive, and it can be reused to avoid sending it to landfills. Sisal fiber is high in tension and low in density, hence many studies were conducted to understand

its effectiveness and its application in concrete structural material (Abirami et al. 2020). The value fluctuates between experimental specimens due to the heterogeneity in the size of naturally available sisal fibers. However, the evidence is conclusive and gives a one-sided result when it comes to the usage of sisal fibers in concrete. (Sabarish et al. 2017).

Moisture absorption is a significant concern in natural fiber. The natural fiber's water content causes poor bonding between the fiber and the matrix (Melkamu et al 2018). Typically, fiber treatment is used to address this problem. Researchers usually use two separate fiber treatment methods such as thermal treatment and chemical treatment. Chemical treatments include alkaline treatment, acidic treatment, and benzolization. Natural fiber composites may reduce strength and durability as a result of fiber weakening caused by the combination of alkaline attack and crystallization caused by the migration of hydrogen products to lumens and spaces (Okeola et al. 2018, Ozerkan et al. 2016).

The aspect ratio of the test specimen height (h) to diameter (d) ratio is essential for loading for the sake of confinement effects. When the strength of concrete of cubes and cylinders with identical aspect ratios is studied, the correction factor rises as the aspect ratio rises (Hamad 2017). A higher aspect ratio means less isolation when it comes to a single specimen. Assuming the amount of slope utilized is equal to 4,

a cylindrical sample having a specific aspect ratio of 2 will sustain less load than a cylindrical sample with a ratio of 1. Another component is fiber dispersion; less fiber dispersion results in a loose bundle with a lower aspect ratio and thus less reinforcing power than a single fiber. Furthermore, due to poor adhesion, the bundle itself may be weak. Any of the above factors minimize the composite's overall power (Sangeetha & Joanna 2014). Additionally, fiber bundles serve as stress transfer barriers, as a result, they have impaired properties. The presence of a powerful interface also influences the production of strength in a composite (Ghorpade & Sudarsanarao 2010).

Mwaikambo & Ansell (2006) had experimented with alkali-treated sisal fibers and examined the changes in internal structure and diameter, like cellulose material, micro-fibril angle, and crystallinity index. Alkalization was observed to affect the microstructure of sisal fibers, which had the same specific stiffness as steel. It's been found that alkali treatment is used to strengthen the crystalline quality of treated fibers, by altering the structure of sisal fiber to compete with the synthetic fibers.

The results of the treatment methods used in sisal fiber to make it corrosion resistant in alkaline concrete environments, as well as the toughness of the natural fiber being reinforced in the concrete in hostile situations, are described in this study.

Alkaline treatment is a technique for treating fiber with an alkaline solution, usually Na_2CO_3 or NaOH (Bjork & Carl 2002). The alkaline solution eliminates the active polar group of the fiber, removes moisture from the fiber, and improves the bonding between the fiber and matrix (Mithun et al. 2019).

MATERIALS AND METHODS

PPC cement that meets Indian standard IS 1489 (Part 2): 1991 is used in this present study. The characteristics of PPC cement were tested in the laboratory.

Manufactured sand is a rock that has been crushed to the proper grain size distribution (M- sand). The crushed materials are crushed in a specific rock crusher to obtain the necessary grain size, and the portion of the crushed materials is washed to extract fines. As fines aggregate, M-sand was used. As a result, the consistency and longevity of concrete have improved. The aggregate size passing through a 20 mm sieve was used as coarse aggregate for this work as per grading requirements.

Sodium Carbonate Solution

To soak the dry fiber, a Na_2CO_3 solution was used to take

advantage of sisal fiber's water absorption (Fig. 1). After ten days in a saturated solution, a considerable amount of sodium ions and carbonate ions will accumulate on the fiber surface. When fibers are added to a concrete mixture, the Ca^{2+} in the cement causes chemical reactions on the fiber surface.

Sisal Fiber

Agave sisilana is the botanical name for sisal fiber. The material is primarily used in the production of rope for use in the marine and construction industries. Because of its inexpensive cost, lightweight, tensile strength and elastic modulus, low health risk, widespread availability in several places, and environmental friendliness, sisal fiber promises to be a cement composite with adequate natural reinforcement. This fiber was chosen for the current study because it has a high strength relative to other fiber materials. As indicated in the pictures Fig. 2 & Fig. 3 every fiber is layered, with a thin primary wall (the initial layer generated during cell development) enclosing a secondary wall. The intermediate



Fig. 1: Sodium carbonate.

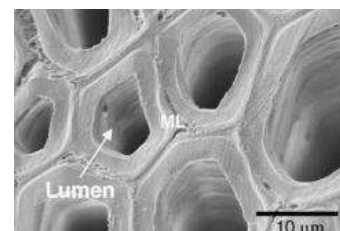


Fig. 2: Sisal fiber cell wall arrangement.

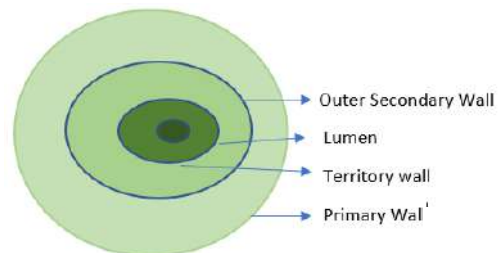


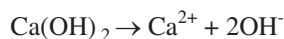
Fig. 3: Sisal fiber cell wall arrangement.

wall consists of three layers, the thickest of which influences the mechanical properties of the fiber. The intermediate layer consists of thin-walled wrapped cellular microfibrillar consisting of long-chain cellulose molecules. The microfibrillar angle is the angle formed by the fiber axis and the microfibrils. The cellulose angle's characteristic value varies from fiber to fiber. Because hemicelluloses and lignin in the center lamellae of fibers and celluloid particles have low corrosion resistance, they lose their capacity to strengthen the cement matrix later in its service life. To increase sisal fiber degradation resistance in alkaline environments alkaline solutions were used to partially extract lignin, cellulose, and hemicellulose as well as other residues from the surface of the fiber.

In this study, a dried and slightly processed sisal fiber with no knots or other impurities was employed. These fibers had a moisture content of 11.5%. Sisal fiber is made up of cellulose, hemicelluloses, lignin, and waxes. Sisal Fiber selected for this project contains cellulose (64%), hemicellulose (12.2%), lignin (10%), waxes (2%). Characteristic value and mechanical properties of sisal fiber are summarised in Table 1 and Fig. 4 represent fresh sisal fiber.

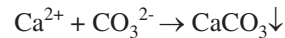
Casting of Specimens

Na₂CO₃ treatment: A Na₂CO₃ solution was used to soak the dry fiber, taking advantage of sisal fiber's water absorption. After several days of treatment in a Na₂CO₃ solution, the number of Na⁺ and CO₃²⁻ ions accumulated on the fiber's surface would rapidly increase. When fresh concrete is applied to the fiber surface, a chemical reaction occurs as a result of the Ca²⁺ in the cement. The following chemical reaction is the primary cause of concrete alkalinity:



To protect the inside of the fiber from the strong alkali solution formed during the cement hydration process, a coating of calcium carbonate sediments was created and

poured into pits and holes on the surface of the sisal fiber.



Concrete's alkalinity prevents ionization of the particles, allowing the outer layer to last for a long period of time. The alkaline pore solution successfully resists the dissolving of hemicellulose and lignin found in the intermediate lamellae of the fibers, as well as cellulose molecule hydrolysis.

Basic material studies were carried out on cement, fine aggregates, coarse aggregates, and fibers. The M30 grade concrete is designed utilizing the IS10262-2009 material test values for cement in M-Sand, coarse aggregate, and sisal fiber using norm IS10262-2009. To effectively increase their degradation resistance, sisal fibers are soaked in Na₂CO₃ solution for 10 days, with varying percentages of sodium carbonate treated sisal fibers, such as 0%, 0.50, 1.00, 1.50, and 2.0%, as shown in Figs. 5 and 6. Cubes and cylinders are cast for seven, fourteen, and twenty-eight days, respectively. Based on compressive and tensile strength, we will establish the optimal dosage of Na₂CO₃ to be treated with sisal fibers.

Mix Proportion

According to IS 10262-2009, the mix was formulated to have a characteristic compressive strength of 30N.mm⁻². Based on the mix design, the cement content was determined to be

Table 1: Physical property of sisal fiber.

Fiber Property	Results
Fiber Diameter, mm	0.3-05
Fiber Length, mm	35-40
Aspect Ratio	1 in 100
Density, g.cm ⁻³	1.33
Tensile Strength, N.mm ⁻²	400 -700 MPa
%age of Elongation	13.5%
Young Modulus	9.4-22



Fig. 4: Sisal fiber.

387 kg.m⁻³. In this analysis, the water-cement ratio was set at 0.42, and Gallium, Superplasticiser was used. Table 2 shows the specifics of the blend proportion and content quantity.

For both natural and sisal fiber reinforced concrete, cubes of 150mm × 150mm × 150mm, cylinders of 150mm diameter, and cylinders of 300mm height are cast at M30 grade concrete. Water curing is an important part of the cement concrete strength-building process. For the method

Table 2: Mix proportion.

Components	Quantity [kg.m ⁻³]
Cement	387
M-Sand	740
Coarse aggregate	1206
Water	162.3



Fig.5: Sisal fiber immersed in Na₂CO₃ solution.

depicted in Fig. 7, the concrete mix specimens were cured in the storage tank for 7, 14, and 28 days.

RESULTS AND DISCUSSION

The Impact of Sisal Fiber on Concrete Workability

In this project, the design technique was to keep all variables constant while adding sisal fibers in intervals of 0.5 per

Table 3: Percentage of reduction in slump and compaction factor.

Fiber %age	Slump	% Reduction in a slump	Compaction factor	% of Reduction in compaction factor
0%	95	0	0.94	0
0.5%	72	21.73	0.91	3.19
1%	65	31.57	0.87	7.44
1.5%	58	38.94	0.82	12.76
2% fiber	34	64.21	0.80	14.89



Fig. 6: After 10 days fiber immersed in Na₂CO₃.



Fig. 7: Casting and curing of specimens.

cent by weight of cement. Table 3 shows the slump test and compaction factor results, as well as the overall slump value and compaction factor values with each combination based on the proportion of sisal fiber applied.

The workability of fresh sisal fiber reinforced concrete decreased overall, as evidenced by decreases in a slump and compaction factor values as the per centage of sisal fibers in the mix grew, and with a constant w/c of 0.42 utilized in the mix design.

Moisture Content Test on Sisal Fiber Reinforced Concrete

The moisture content of concrete is an indirect way of analyzing the pore structure and durability efficiency in a corrosive setting. Fig. 8 shows the moisture content of sisal fiber reinforced concrete in this analysis. The results show that reinforcing concrete with sisal fibers significantly increases the moisture content of the concrete. By adding 0.5 per cent sisal fiber, concrete absorption increased by 1.3 per cent after 28 days. Furthermore, incremental additions of 0.5 per cent sisal fiber resulted in minor improvement until a total of 2 per cent sisal fiber was added to the mix, resulting in an 11.5 per cent increase in water absorption above normal concrete.

Compression Test

Concrete cubes measuring 150mmX150mmX150mm are cast to test the compressive power. Specimens are cured for 7, 14, and 28 days at room temperature. Ultimate load (N) is considered at the point at which the specimen fails, and the cross-section of the specimen is known. Table 4 summarises the compressive strength results.

Na₂CO₃ sisal fibers are mixed with concrete in percentages of 0 per cent, 0.5 per cent, 1 per cent, 1.5 per cent, and 2 per cent, then cured for 7, 14, and 28 days to determine the compressive strength of sisal fiber reinforced concrete. Table 4 is depicted in Fig. 9 as a visual representation of the data. According to the experimental results, increasing the fiber content in concrete increases the compressive strength by up to 1%, while increasing the fiber content further reduces the concrete's strength.

Split Tensile Test

Casted cylinders of 150mm diameter (D) and 300mm height (H) are used for these tests. These specimens are mounted horizontally in between the compression testing machine's plates, and the maximum load (P) at which the specimen fails

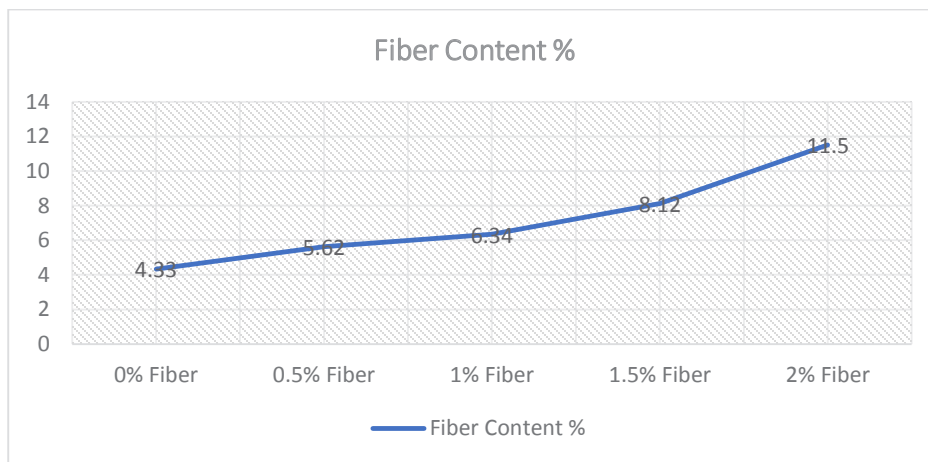


Fig. 8: Moisture content percentage of concrete.

Table 4: Compressive strength test.

S. No.	Fiber %age	Compressive strength N.mm ⁻²		
		7 days	14 days	28 days
1	0%	13.28	25.86	32.75
2	0.5%	14.78	28.07	34.15
3	1%	17.29	29.14	35.17
4	1.5%	16.26	28.64	33.10
5	2%	16.01	27.17	32.15

is reported, as well as the tensile strength values, which are tabulated in Table 5.

According to the test observations, the tensile strength of M30 grade concrete at the ages of 7, 14, and 28 days is represented in the above bar map. Fig. 10 depicts a graphical representation of the data in Table 5. The tensile strength of the concrete improves gradually until it reaches 1%, after which it tends to decrease as the fiber concentration increases.

CONCLUSION

Natural fibers are being reviewed as a potential substitute for synthetic fiber in the fiber/polymer composites materials industry. But in terms of environmental impact, cost of production, and biodegradability natural fibers have a huge advantage.

The effects of sodium carbonate processed sisal fibers on the characteristics of normal concrete, such as strength,

Table 5: Overall results of tensile strength values.

S. No.	Fiber %age	Tensile strength N.mm ⁻²		
		7 days	14 days	28 days
1	0%	2.03	2.56	2.78
2	0.5%	2.15	2.62	2.96
3	1%	2.24	2.74	3.12
4	1.5%	2.22	2.68	2.85
5	2%	2.12	2.52	2.74

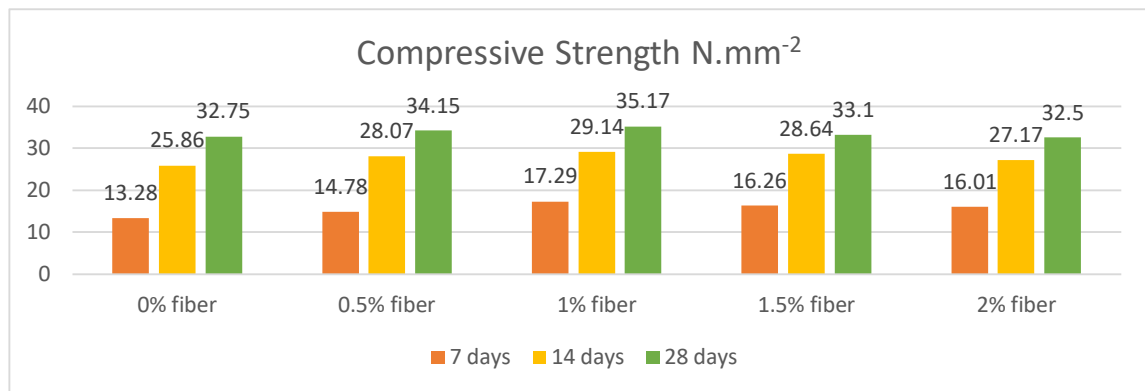


Fig. 9: The results of the compressive strength test.

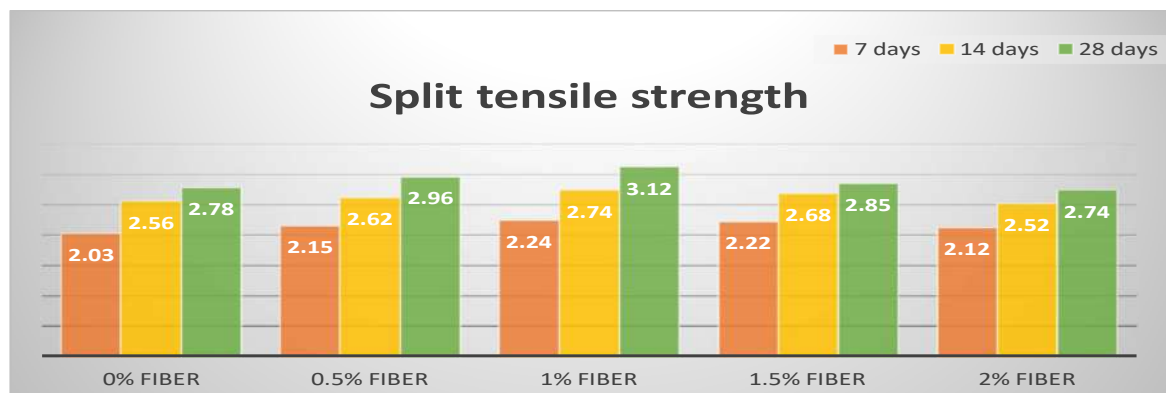


Fig. 10: The results of a tensile strength test.

were studied and tabulated using IS10262-2009 and varied per centages up to 2% for M30 grade concrete used for construction. Based on the findings, 1% sodium carbonate treatment of fibers added to concrete increases the concrete's compression strength by 3.5%.

The compressive and tensile strength of sisal fiber reinforced concrete will increase when 0.5 and 1% of fiber content are added. As 1.5 to 2% sisal fiber is added, the strength decreases. In addition to the increase in strength, it was discovered that this rise is due to the production of calcium carbonate deposits on the fiber interfaces as a result of being treated with an alkaline solution, which also improves the concrete's corrosion resistance and durability.

REFERENCES

- Abirami, R., Sangeetha, S.P., Nadeemshah, K., Yasirvaseem, P. and SuhailSad, K. 2020. Experimental behavior of sisal and kenaf fiber reinforced concrete. AIP Conf. Proc., 2271: 030023.
- Bjork, F. and Carl, A.E. 2002. Measurement of alkalinity in concrete by a simple procedure, to investigate the transport of alkaline material from the concrete slab to a self-leveling screed. Constr. Build. Mater., 16: 535-542.
- Ghorpade, V.G. and Sudarsanarao, H. 2010. Strength and permeability characteristics of fiber-reinforced recycled aggregate concrete with different fibers. Nat. Environ. Pollut. Technol., 9(1): 179-188.
- Hamad, A.J. 2017. Size and shape effect of specimen on the compressive strength of HPLWFC reinforced with glass fibers' J. King Saud. Univ. Eng. Sci., 29(4): 373-380.
- Jitendra, D., Kalwane, U. and Pallavi, P. 2016. Effect of fiber length and per centage of sisal on strength of concrete. Multidiscip. J. Res. Eng. Technol., 3(1): 923-932.
- Melkamu, A., Kahsay, M.B. and Tesfay, A.G. 2018. Mechanical and water-absorption properties of sisal fiber (Agave sisalana)-reinforced polyester composite. J. Nat Fibers., 14: 877-885.
- Mithun, K., Gowda, R.M. and Phulara, S.C. 2019. A study on structural characteristics of sisal fiber reinforced concrete. Int. J. Eng. Res., 8(06): 616-636.
- Mwaiambo, L.Y. and Ansell, M.P. 2006. Mechanical properties of alkali-treated plant fibers and their properties. J. Mater. Sci., 41: 2497-2508.
- Naresh, J., Nalin Pandian, T. and Priyavadhani, S. 2019. Study on the result of the implementation of sisal fiber in reinforced cement concrete. Int. Res. J. Eng. Technol., 06(04): 51-79.
- Okeola, A.A., Abuodha, S.O. and Mwero, J. 2018. The effect of specimen shape on the mechanical properties of sisal fiber-reinforced concrete. Open. Civ. Eng. J., 12(01): 368-382
- Ozerkan, N.G., Tokgoz, D.D.G., Kowita, O.S. and Antony, S.J. 2016. Assessment of microstructural and mechanical properties of hybrid fibrous self-consolidating concretes using ingredients of plastic waste. Nat. Environ. Pollut. Technol., 15(04): 1161-1168.
- Silva, F.A., Chawla, N. and Toledo Filho, R.D. 2008. Tensile behavior of high performance natural (sisal) fibers. Comp. Sci. Technol., 68(15): 3438-3443.
- Sabarish, K.V., Dhanasekar, K., Manikandan, R., Ancil, R., Venkat Raman, R. and Selva Surender, P. 2017. Strength and durability evaluation of sisal fiber reinforced concrete. Int. J. Civ. Eng., 8(9): 741-748.
- Sangeetha, S.P. and Joanna. P.S. 2014. Flexural behavior of reinforced concrete beams with partial replacement of GGBS. Am. J. Eng. Res., 03(01): 119-127.
- Wei, J. and Meyer, C. 2014. Improving degradation resistance of sisal fiber in concrete through fiber surface treatment. Appl. Surf. Sci., 289: 511-523.



Study of Water Quality Pollution Index, Land-Use and Socio-Economic Factors in Yingkou Irrigation District of China Based on Redundancy Analysis

Ji He*, Xiao-Ling Hou* and Wen-chuan Wang*†

*School of Water Conservancy, North China University of Water Resources and Electric Power, Zhengzhou City, Henan Province, 450045, PR China

†Corresponding author: Wen-chuan Wang; wwc_hs@126.com

Nat. Env. & Poll. Tech.

Website: www.neptjournal.com

Received: 11-02-2021

Revised: 21-03-2021

Accepted: 14-04-2021

Key Words:

Water quality

Irrigation district

Redundancy analysis

Land-use

Socio-economic factors

ABSTRACT

Water quality in irrigation areas is related to food security and many other national strategies. This study takes China's Yingkou Irrigation District as the research object and analyzes 4 water quality indicators, including $\text{NH}_4^+\text{-N}$, TP, DO and COD, from 2017 to 2019 at 3 water quality monitoring points set up in the irrigation area. Simultaneously, a comprehensive pollution index is introduced to evaluate the quality of returned water in the irrigation area. Using Redundancy Analysis (RDA), the correlation between water quality indicators and Land-use and socio-economic indicators are analyzed separately. The results show that the water quality of the Yingkou Irrigation District varies greatly within and between years, and the months with poor water quality are concentrated in autumn and winter. This is mainly related to the geographical location of the irrigation area and the drainage cycle of rice planting. The quality of receding water shows a positive correlation with the water area and a negative correlation with the unused land. The RDA analysis with socio-economic indicators shows that PD and IP are the ones that have a more significant impact on the quality of return water in irrigation areas. The prevention and control of industrial point source pollution, as well as the interception of non-point source pollution in water regions, should be the focus of water pollution prevention and control in irrigation areas.

INTRODUCTION

As the most populous country in the world, China's food security is related to social stability, economic development, and even national security. Irrigation areas are the primary food production areas, especially large-scale irrigation areas where rice is the main crop. Studying the water quality of its irrigation water, accurately evaluating water quality categories, and clarifying the response relationship between water quality and Land-use in irrigation areas are of vital importance for ensuring the country's food security.

The influence of agricultural non-point source pollution on the quality of the water environment has been increasingly significant in recent years. If it is released directly without treatment as one of the main output channels of farmland retreat, it would not only wastewater resources but also have an impact on the water quality of receiving water bodies. Yang et al. (2009) pointed out that the unreasonable application of farmland chemical fertilizers, pesticides, livestock and poultry breeding, and agricultural film residues all produced agricultural pollution to varying degrees, which entered the Yellow River along with runoff or drainage, resulting in deterioration of water quality. Xing et al. (2011) selected 3 typical agricultural irrigation drainage ditches to estimate the amount of non-point source pollutants entering the Yellow

River in the Ningxia irrigation area and pointed out that the main reason for the sharp increase in water mineralization in the Ningxia section of the Yellow River is the non-point source of agricultural irrigation. Point source pollution is primarily to blame for the increase in COD levels. Point and non-point source pollution both contribute to the rise in nitrogen pollution concentrations. Yang et al. (2015a) studied the Yinxin ditch and the fifth drainage ditch and found that there is a significant positive correlation between the pollution load of farmland in the two ditches and the amount of returned water.

At the same time, there are many methods for evaluating surface water quality (Wang et al. 2019, Zhou et al. 2016). There are mainly analytic hierarchy processes and fuzzy evaluation methods (Zhang 2019). Others include the gray evaluation method and the support vector machine classification method (Chen et al. 2013). Baghapour et al. (2013) used the pollution index approach to assess the water quality of an irrigation area in Canada. In comparison to other water quality evaluation methods, it can authentically and thoroughly depict water quality by taking into account the diversity of water quality indicators and combining them with water quality requirements through the weighted average procedure.

Many scholars have studied the relationship between Land-use types and farmland withdrawal from different perspectives. The intensity of the land use/cover type of the watershed and the different scales from the river bank also have an important impact on various water quality indicators in the water body (Wang et al. 2015). In addition, studies have shown that the social economy of the basin also has an individual impact on the quality of the water environment (Wang et al. 2018). Land-use types can reveal the status quo of regional socio-economic development to a certain extent (Yang 2004, Yang et al. 2015b), and affect the spatial changes of population settlement and mobility (Zhao et al. 2018). At the same time, social development, economic structure, population, and residents' lifestyles also affect the spatial changes of regional land-use types (Seto & Fragkias 2005, Yang 2015, Li et al. 2017b). This circular effect always affects the water environment quality of the basin in the process of social development (Wang et al. 2012, Zhao et al. 2013, Li et al. 2017a).

The Daliao River is the principal water source for the Yingkou Irrigation District in Liaoning Province, China, and two separate irrigation and drainage systems have been established within the irrigation area. The irrigation area adopts extensive irrigation methods, and the controlled irrigation area is large, the drainage and other facilities are low, and the field irrigation water utilization coefficient is low. There is a large amount of irrigation water in the irrigation area to replenish groundwater or drain into the trench by way of serious leakage. The excessive problem is more serious, which is not conducive to the rational use of water resources. As the retreating water enters the river, there are also farmland nutrients and agricultural chemicals, which not only affect the water quality of the river, but the retreat from the irrigation area will eventually enter the Daliao River, which will also have a certain impact on the water environment of the Daliao River. This study takes Yingkou Irrigation District as the research object, uses the comprehensive pollutant index method to evaluate the water quality, and analyzes the intra-year and inter-annual changes in water quality. Simultaneously, the link between Land-use and socio-economic parameters in the irrigation region and the quality of returned water was investigated using RDA analysis. It is planned to serve as a foundation for Land-use optimization and water pollution prevention and management in the Yingkou Irrigation District.

MATERIALS AND METHODS

Study Area

Yingkou Irrigation District is located at the southern end of the Central Plains of Liaoning, China, on the left bank of

the lowest reaches of the Daliao River. It involves Zhanqian, Laobian, and Dashiqiao City in Yingkou City, with a total land area of 91246 hectares (Fig. 1). The irrigation area is flat, with many river networks and depressions. The terrain is high in the northeast and low in the southwest, and the ground elevation is mostly between 2.0m and 6.0m.

The study area has a monsoon climate with cold and dry winters, windy and less rainy in spring, concentrated hot rainfall in summer, and long cool sunshine in autumn. The annual average temperature is 9.1°, the monthly average temperature is 27.1° in July, and the lowest in January is -15.0°. The average yearly precipitation is 650.5 mm. The precipitation is unevenly distributed throughout the year, and the main period (June to September) accounts for about 71.9% of the annual rainfall.

The western and southern parts of the study area developed into irrigation areas after long-term river alluvium and human activities. Most plots of topsoil salt are separated into extremely mild and moderate after decades of rice farming improvements, and there are fewer salinized soils above moderate. During the flood season, the groundwater level in the irrigation region is rather high, with a burial depth of 0.7-1.0 m and it being close to the surface.

Data Source

Landuse data: The Landsat satellite remote sensing image (spatial resolution 30 m) in September 2018 was used to cut out the study area corresponding to the Yingkou Irrigation Area and perform related pre-processing image enhancement in ArcGIS and ENVI software. Combining field surveys, Google Earth software, and image resolution characteristics, remote sensing images are interpreted and classified based on the Recognition software supervised classification method. The Land-use categorization system is based on the Chinese Academy of Sciences' land resources classification system, which covers six types of land use: forest land, grassland, agricultural land, construction land, water area, and unused land.

Water quality monitoring: The local environmental protection bureau set up water quality sampling points at the section of the main canal of the Laodong River into the Daliao River estuary. The location of the monitoring section is shown in Fig. 1. The water quality monitoring period is from January 2017 to December 2019. The monitoring frequency is once a month. The measured water quality indicators include NH_4^+ -N TP, DO, and COD.

Research Methods

Pollution index evaluation: The pollution index evaluation method is a relatively common method for evaluating river pollution levels at home and abroad. The evaluation

indicators involve various organic pollutants and inorganic pollutants, such as nitrogen, phosphorus, and COD. The water quality evaluation in this paper adopts the average pollution index method, which is:

$$PI = \frac{1}{n} \sum_{i=1}^n c_i / S_i$$

Where PI is the average pollution index, n is the number of pollution factors participating in the evaluation, i is the pollution factor, c_i is the measured content of the pollution factor i, and S_i is the standard evaluation value of the pollution factor i. Refer to the surface water environmental quality standard (GB 3838- 2002) and comprehensively determine the water quality standards of the water function zone where the river section is located. (Because the more extensive the dissolved oxygen value, the smaller the pollution, so this index adopts its reciprocal value).

RDA Analysis

Redundancy analysis (RDA) is a sorting method developed based on correspondence analysis. It is a restricted ranking. It can be found by comparing principal component analysis. Redundancy analysis is constrained principal component analysis, which combines correspondence analysis and multiple regression analysis. Each step of the calculation is a regression with environmental factors, also known as multiple direct gradient analysis.

In this study, the proportion of Land-use types and socio-economic parameters were used as environmental factors, and the above indicators were used to reflect the relationship between water quality parameters. The RDA analysis of this research is realized by CANOCO 5.0 software.

RESULTS AND DISCUSSION

Water Quality Change Trend

This study analyzed the four water quality indicators of NH_4^+-N , TP, DO, and COD monitored by three water quality monitoring stations in Yingkou Irrigation District from 2017 to 2019, as well as the calculated PI. The inter-annual analysis of each parameter is shown in Table 1, and the multi-year statistical data is shown in Fig. 2.

Through analysis, it can be seen that various indicators have changed significantly during the year. For NH_4^+-N , the maximum value appeared in February 2018, which was 26 $mg.L^{-1}$, and the minimum value appeared in June 2017, which was only 0.12 $mg.L^{-1}$. The main reason for this phenomenon may be that in February, the entire river in the study area was frozen, the fluidity of the water body was weak, and the dilution effect of the water body on the pollutants was not strong, which caused the appearance of the maximum value. In June, the study area was in the flood season. At this time, the water in the study area was abundant. At the same time, in terms of irrigation, the rice was in the growth period and the paddy field drainage was less during this period. The above reasons caused the lowest ammonia nitrogen concentration in the month.

For TP, the inter-annual and intra-annual changes are relatively small, the maximum occurs in April, at 0.83 $mg.L^{-1}$, and the minimum occurs in June, at 0.11 $mg.L^{-1}$. The main reason for the peak value in April maybe because the paddy

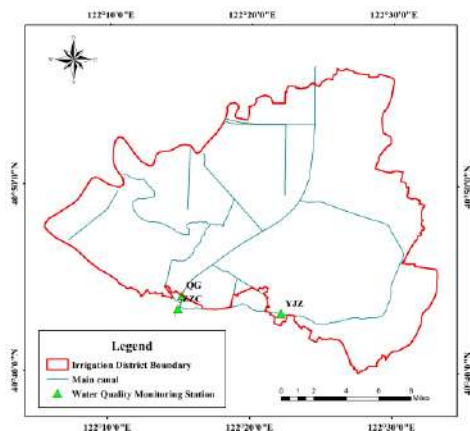


Fig.1: Geographic location of the study area.

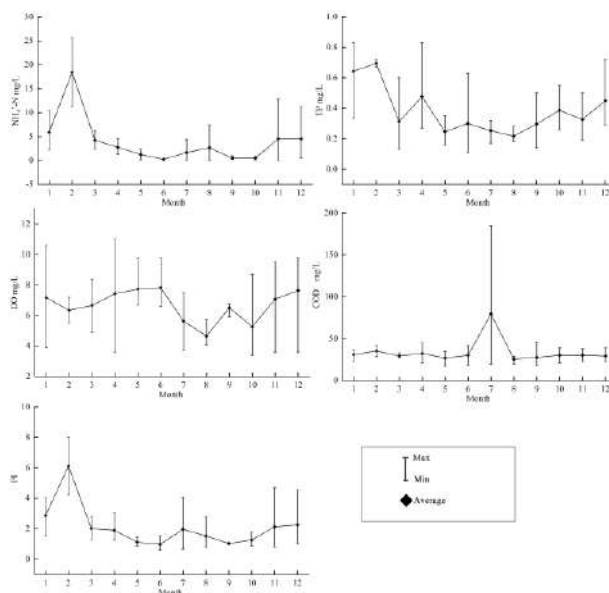


Fig. 2: Changes in water quality parameters during the year.

Table 1: Interannual statistical analysis of water quality parameters.

YEAR		NH ₄ ⁺ -N	TP	DO	COD	PI
2017	AVERAGE	5.74	0.51	5.10	45.36	2.90
	MIN	0.12	0.16	3.40	18.00	1.05
	MAX	13.00	0.83	7.00	185.00	4.70
	STDEV	4.77	0.23	1.46	44.70	1.39
2018	AVERAGE	3.80	0.35	7.48	32.08	1.97
	MIN	0.16	0.14	3.90	21.00	0.80
	MAX	25.60	0.83	9.80	46.00	8.00
	STDEV	7.14	0.23	2.14	7.28	2.04
2019	AVERAGE	0.79	0.26	7.52	23.73	1.00
	MIN	0.08	0.11	3.70	17.00	0.61
	MAX	2.40	0.35	11.00	33.00	1.50
	STDEV	0.85	0.09	2.38	6.05	0.28

field in the irrigation area just ended during this period. Phosphorus-containing pollutants adhered to the suspended solids such as silt and entered the river with the receding water from the farmland. Rise. The reason for the minimum value is the same as NH₄⁺-N.

The largest month of DO appearance is April 2019. The emergence of the maximum value is accompanied by the spring floods and the receding of farmland during the same period. The increase of surface runoff greatly increases the water volume in the river, and the water flow is sufficient, which significantly increases the dissolved oxygen content in the water body. The DO content was the lowest in October 2017. During this season, a certain degree of freezing has occurred in the rivers in the study area, the exchange between water and air has weakened, and the water has low oxygen content.

COD index time variability is large. The maximum value (185 mg.L⁻¹) is 10.9 times the minimum value (17 mg.L⁻¹).

The main reason for the large deviation of COD may be due to the different levels of pesticides applied in the irrigation areas at different times, which caused large differences in COD content. At the same time, due to the continuous accumulation of organic pollutants, some areas, especially downstream rivers, will be more affected by organic pollutants.

PI can comprehensively reflect the pollutant situation. As can be seen in Fig. 3, there is a big difference in PI during the year, with the largest average value occurring in February and the smallest value occurring in June. The freezing of rivers in February weakened the dilution of pollutants from external water sources, resulting in higher pollutant concentrations during this period. During the flood season in June, there was more precipitation and less drainage from the rice fields, which dilutes the concentration of pollutants and does not increase the number of new pollutants in the river. This is the main reason for the small pollutant index during this period.

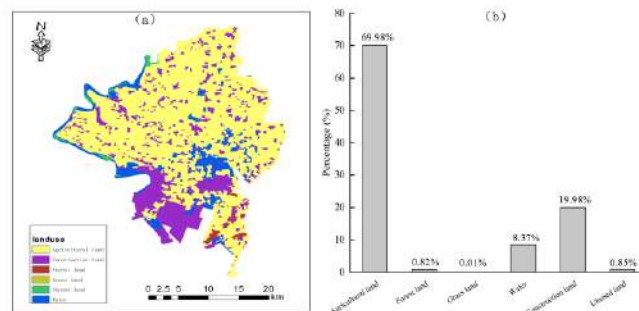


Fig. 3: The area proportion of different land-use types in Yingkou Irrigation Area

The Impact of Land-use on Water Quality

Land-use composition of yingkou irrigation district:

The spatial analysis software of ArcGIS 10.2 is used to superimpose analysis and calculation of the boundary and Land-use data of the irrigation area, and the distribution of each land-use type in the irrigation area is shown in Fig. 3.

It can be seen from the figure that the primary Land-use type in the irrigation area is agricultural land, accounting for 69.98%, followed by construction land (19.98%), and the remaining land is water area (8.37%) and unused land (0.85%), woodland (0.82%), and grassland has the smallest area. As the irrigation area is mainly planted with rice and corn, the area of agricultural land is the largest. The southern part of the irrigation area is currently mixed with major industrial and mining enterprises in the main urban area, so the construction land area is also relatively large. A large number of fish ponds and dense channels distributed in the irrigation area are the main reasons for the large water area.

Correlation analysis between the quality of returning water and land use: It can be seen from Fig. 4 that DO has a negative correlation with water surface area and a positive correlation with unused land. This may be mainly because the unused land in the irrigation area contains less organic matter, so there are fewer oxygen-consuming microorganisms, which makes the dissolved oxygen content in the water higher. The NH4-N, TP, COD, and PI indexes of Yingkou Irrigation District all show a positive correlation with water area and a negative correlation with unused land. This may be because the receding water in the Yingkou Irrigation District is the receding water of the rice fields. The receding water from the

fields entrained pollutants into the water body, thus showing a positive correlation with the water area.

The Impact of Socio-Economic Indicators on Water Quality

This study selects four indicators, including population density (PD), agricultural production value (AP), industrial production value (IP), and service industry production value (SIP) as social-economic factors, to evaluate the correlation between them and water quality indicators. It can be seen from Fig. 5 that, except for the dissolved oxygen index, other indicators, including the comprehensive pollution index, show a positive correlation with the GDP of the secondary industry. DO shows a positive correlation between PD and AP. The main reason may be that some industries in the Yingkou Irrigation District currently do not have sewage interception pipes, and the direct discharge of sewage has caused the degradation of water quality. In pollution prevention and control, attention should be paid to the impact of industrial point source pollution on water quality.

In addition to the above-mentioned impact analysis, attention should also be paid to controlling drainage in Yingkou Irrigation District. By controlling the drainage to regulate and control the return of water in the irrigation area, the field drainage and the output of pollutants can be effectively reduced (Skaggs et al. 1994, Wesstrom et al. 2001). As a water-deficient area, the Yingkou Irrigation District has huge potential for reuse. Therefore, in future research, we must consider the combination of project operation mode

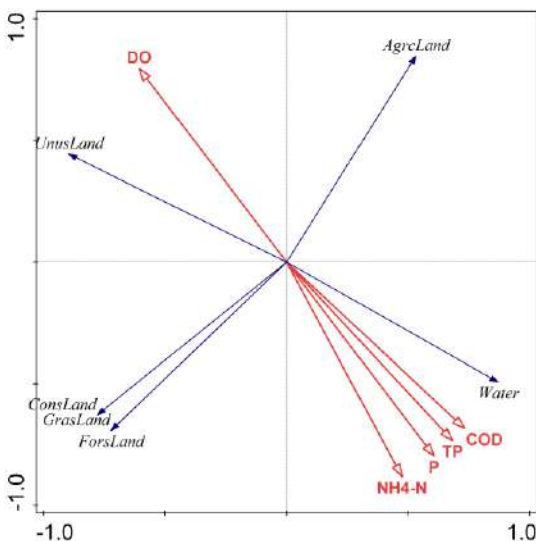


Fig. 4: Correlation between water quality indicators and Land-use types.

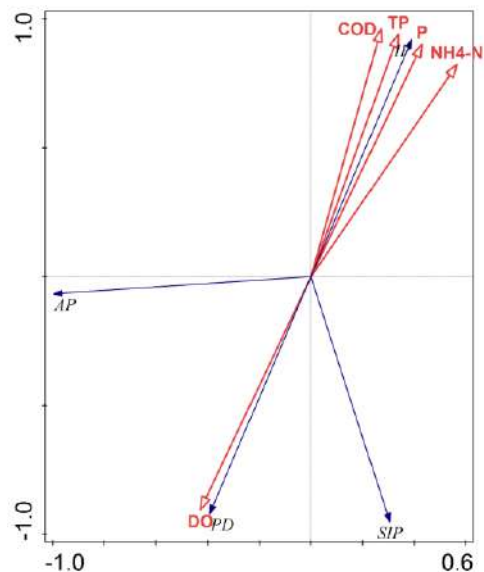


Fig. 5: Correlation between water quality indicators and socio-economic indicators.

and irrigation management measures to jointly promote the construction of the irrigation area.

CONCLUSIONS

This paper introduces the comprehensive pollution index and analyzes the time changes of the pollution index and the water quality index of Yingkou Irrigation District. At the same time, using the method of RDA analysis, the correlation between the quality of returning water and Land-use and socio-economic indicators are analyzed, and the main conclusions are as follows:

- (1) The pollutant indicators of the Yingkou Irrigation District show significant variability during and interannual. The extreme values of indicators are mainly concentrated in autumn and winter. The possible reason is that the particular geographical and meteorological conditions of the Yingkou Irrigation District have weakened water flow. Decrease and cause deterioration of water quality. The fall is mainly because the backwater from farmland was discharged into river water bodies during this period, which resulted in poor water quality during this period. Pollution prevention and control should pay enough attention to these two periods.
- (2) The ammonia nitrogen, total phosphorus, COD, and PI indexes of Yingkou Irrigation District all show a positive correlation with water area and a negative correlation with unused land. Water quality pollution indicators indicate a positive link with a water area as backwater from paddy fields increases. To limit the number of contaminants entering the river, measures such as planting buffer zones around the waterways can be explored.
- (3) The RDA analysis of water quality pollutant indicators and socio-economic indicators shows that pollutant indicators show a positive correlation with the secondary industry but show a negative correlation with population density and gross agricultural production. The next step is to strengthen industrial power pollution treatment and adopt measures such as interception and pipes to reduce the amount of pollution.

REFERENCES

Baghapour, M.A., Nasser, S. and Djahed, B. 2013. Evaluation of Shiraz wastewater treatment plant effluent quality for agricultural irrigation by Canadian Water Quality Index (CWQI). *Ir. J. Environ. Health Sci. Eng.*, 10: 1-9.

- Chen, X., Qiu, L. and Huang, Z. 2013. Application of least square support vector machine in water quality assessment of Taihu Lake Basin. *J. of Hydroecol.*, 34: 16-21.
- Li, L., Zhang, Y., Tang, C., Zheng, L., Meng, W., Lu, S. and Dun, Y. 2017a. Modeling of water quality response to land-use patterns in Taizi river basin based on partial least squares. *Environ. Sci.*, 38: 1376-1383.
- Li, S., Zhou, J. and Wang, J. 2017b. Spatio-temporal LUCC and driving force in Fuxian Lake watershed from 1974 to 2014. *Remote Sens. Land Resour.*, 29: 132-139.
- Seto, K.C. and Fragkias, M. 2005. Quantifying spatiotemporal patterns of urban land-use change in four cities of China with time series landscape metrics. *Landsc.Ecol.*, 20: 871-888.
- Skaggs, R.W., Brevé, M.A. and Gilliam, J. W. 1994. Hydrologic and water quality impacts of agricultural drainage*. *Crit. Rev. Environ. Sci. Technol.*, 24: 1-32.
- Wang, J., Ma, K., Zhang, Y. and Tang, R. 2012. Impacts of Land-use and socioeconomic activity on river water quality. *Acta Sci. Circum.*, 32: 57-65.
- Wang, P., Qi, S. and Chen, B. 2015. Influence of Land-use on river water quality in the Ganjiang basin. *Acta Ecol. Sin.*, 35: 4326-4337.
- Wang, Q., Wang, S.X., Fan, Z.P. and Li, F.Y. 2018. Impacts of Land-use and socioeconomic activity on spatial variation of water quality in the upper area of Dahuofang Reservoir [in chinese]. *Ecol.Sci.*, 37: 153-161.
- Wang, Z., Zhu, S., Liu, Y. and Wang, F. 2019. Comparative application of different water quality evaluation methods in the downstream section of Luanhe River. *Water Sav. Irrig.*, 290: 72-76+81.
- Westrom, I., Messing, I., Linner, H. and Lindstrom, J. 2001. Controlled drainage -- effects on drain outflow and water quality. *Agric. Water Manag.*, 47: 53.
- Xing, J., Qi, X., Huang, Z., Fan, X. and Zhu, D. 2011. The application of the grey clustering method for evaluating the subsiding water quality from cropland in the irrigation area of the Yellow River. *J. Irrig. Drain.*, 11: 74-77.
- Yang, G. 2004. Land-use and land cover change and regional economic development: The revelation of the change in cropland area in the Yangtze River Delta during the Past 50 years. *J. Geogr. Sci.*, A: 41-46.
- Yang, L., Wang, Ruan, S. and Guan, X. 2015a. Evolution of drain-based research of irrigation return flow pollution in Yinbei irrigation area. *Chin. J. Eco-Agric.*, 23: 1580-1587.
- Yang, R. 2015. Spatiotemporal change and driving forces of urban landscape pattern in Beijing. *Acta Ecol. Sin.*, 35: 4357-4366.
- Yang, R., Liu, Y. and Long, H. 2015b. The study on non-agricultural transformation co-evolution characteristics of "population-land-industry": A case study of the Bohai Rim in China. *Geogr. Res.*, 34: 475-486.
- Yang, S., Zhang, A., Yang, Z. and Yang, S. 2009. Agricultural non-point source pollution in Ningxia irrigation district and preliminary study of load estimation methods. *Sci. Agric. Sin.*, 42: 3947-3955.
- Zhang, X. 2019. Application of fuzzy comprehensive evaluation in comprehensive evaluation of water. *Environ. Qual. Sci. Technol. Eco. Guide*, 27: 124-124.
- Zhao, M., Liu, S. and Qi, W. 2018. Spatial identification and scale effects of floating population agglomerations at the community scale: A case study of Beijing. *Geogr. Res.*, 37: 1208-1222.
- Zhao, W., Lin, J., Wang, S., Liu, J., Chen, Z. and Kou, W. 2013. Influence of human activities on groundwater environment based on coefficient variation method environmental. *Science*, 34: 1277-1283.
- Zhou, M., Li, W. and Yi, L. 2016. Characteristics and comparison of four water quality evaluation methods. *Environ. Sci. Manag.*, 41: 173-177.



Poultry Wastes Effect on Water Qualities of Shallow Wells of Farms in Two Locations of Kwara State, Nigeria

O. M. Abioye*†, K. A. Adeniran** and T. Abadunmi***

*Department of Agricultural and Biosystems Engineering, Landmark University, PMB 1001, Omu Aran, Nigeria

**Department of Agricultural and Biosystems Engineering, University of Ilorin, PMB 1515, Ilorin, Nigeria

***Division of Agricultural Colleges, Ahmadu Bello University, Zaria, Nigeria

†Corresponding author: O. M. Abioye; abioye.oluwaseyi@lmu.edu.ng

Nat. Env. & Poll. Tech.

Website: www.neptjournal.com

Received: 05-08-2021

Revised: 15-10-2021

Accepted: 01-11-2021

Key Words:

Poultry wastes

Number of birds

Water quality indices

Water resources management

ABSTRACT

The study investigated poultry waste effect on water quality of shallow wells in Asa and Ilorin, south local government areas of Kwara State. The factors considered are the number of birds (N), years of existence of the farm (Y), and the distance between the shallow wells and the poultry dump sites (D). Physicochemical parameters of the water collected were analyzed. The data obtained were analyzed using SPSS Software (Version 16.0). For the number of birds, the result shows that the mean turbidity, Chemical Oxygen Demand COD, and fecal coliform were between 23.25 -101.92 NTU, 85.22-111.56 mg.L⁻¹, and 0.00-0.34 cfu.mL⁻¹ respectively. For the year of existence of the farm, the mean turbidity, phosphate, COD were between 14.10-56.6 NTU, 1.07-2.30 mg.mL⁻¹, 88.00-95.43 mg.mL⁻¹ respectively. The mean turbidity was found to be between 11.81 NTU and 58.85 NTU, phosphate 1.09-2.06 mg.mL⁻¹, COD 86.73-94.57 mg.mL⁻¹, and fecal coliform 0.00-0.24 cfu.mL⁻¹ for the distance between dumpsites and water source. The number of birds has a significant effect on turbidity, BOD, COD and fecal coliform at $p \leq 0.05$ compared to the measured control 400 m away from the dumpsites. As a result, there is evidence of pollution risks from poultry wastes. Proper treatment and the placement of farms far away from dumpsites will assist maintain the water's suitability and sustainability.

INTRODUCTION

The management of waste in large poultry facilities in rural and urban communities is crucial for the long-term expansion and sustainability of poultry production. It also ensures the protection of the environment, human health, and the quality of life of workers and people living close to the poultry facilities (Nahm & Nahm 2004). An increase in the demand for meat, eggs, and other poultry products has led to an increase in poultry production, which has caused an excessive generation of waste. The increase of poultry production and its spread across the country, as well as the potential environmental consequences, are major concerns. Poultry comprises broilers, layers, and turkeys that are grown using a combination of manure and bedding material (Collins 1996, Wilson et al. 1998, Zhao et al. 2008). Poultry waste includes a mixture of excreta, bedding material (e.g. wood shaving, straw), waste feed, dead birds, broken eggs, and detached feathers (Evers 1996, Weaver 1998, Kelleher et al. 2002). Poultry waste poses significant risks to the environment, including contamination of drinking waters, eutrophication, and odors due to poor management (Ezekoye et al. 2017). Water and living organisms are inseparable. Water is required for domestic and industrial purposes

and can be obtained from a variety of sources, including groundwater, surface water, rainfall, boreholes, and wells (Kushreshtha 1998). Poultry wastes in surface water have led to an increase in nutrients, solids, and metals which in turn lead to algae production, increased turbidity, reduction in light penetration, toxic metals bioaccumulation, and thus causing interruption of the ecosystem (Adewale et al. 2013). Furthermore, most surface water is dirtier, more turbid, and contains more sediment, necessitating greater and more careful purification processes. Pathogens can be introduced into drinking water as a result of poor management, posing a health risk (Koelkebeck et al. 1999, Manning et al. 2007). Both wells and borehole water are less contaminated when they are located far away from any potential sources of pollution, and when they are constructed with good well design and disinfection. (Akpoveta et al. 2011).

However, depending on water environment management and temperature gradients, there is a risk of pollutant introduction (Frederick 1990, Kushreshtha, 1998). Hand-dug wells are shallow wells with diameters ranging from 0.9 to 1.8 m and depths ranging from 4.5 to 10 m, depending on the point where groundwater is found (Orebiyi et al. 2010). Water pollution is a result of suspended solid particles, insoluble

liquid droplets (Plant et al. 2001). Groundwater gets polluted by land disposal of solid wastes, sewage disposal on land, and runoff (Jain et al. 1995). The destination and transit of nutrients and contaminants in variable saturated porous media are influenced by a multitude of interconnected physical, chemical, and biological processes (Jacques et al. 2008). Water quality can be degraded by contaminants contained in manure. Poultry wastes can contaminate water by leaching through the soil, runoff, and where wastes have been held for a long time due to poor waste management. Excessive discharge of these wastes can be caused by a large number of birds raised on the farm (Ezekoye et al. 2017). Large amounts of poultry waste are often a source of pollution in the environment. These are a serious threat, and the quality of surface and subsurface water has deteriorated as a result. The frequent discharge of untreated wastes at dumpsites without regard for the impact on nearby water bodies pollutes the ecosystem greatly. Since the sanitary state of drinking water varies considerably among farms, methods and strategies for identifying major contamination locations for the prevention of waterborne diseases must be found. Therefore, the aim of the study was to investigate the effect of poultry wastes on the water quality of shallow wells of selected farms in two local government areas (LGAs) of Kwara State, Nigeria. The outcomes of this study will be an effective tool for predicting the extent of water pollution on livestock farms and also serve as a guide for proper planning and designing of a farmstead.

MATERIALS AND METHODS

Description of the Study Area

The fields of research are Asa and Ilorin South Local Government Areas (LGAs) in Kwara State, Nigeria. Asa LGA is located on latitude $8^{\circ}00'1$ and $9^{\circ}10'1$ North of the Equator and longitude $2^{\circ}45'1$ and $4^{\circ}15'1$ East of the Greenwich meridian. It has its headquarters in Afon, and it is 27 km from Ilorin. It is about 1,525 sq.km and it stretches from the peri-urban

fringes of the city of Ilorin to Oyo State. The average annual rainfall is between 1,000 mm-1,500 mm and the highest rainfall is between June and early August (Ajibade 2006). It falls within the tropical hinterland with a wet and dry climate. Their major occupations are farming and trading. Ilorin South Local Government has its headquarters situated in Fufu, latitude $8^{\circ}24' N$ and $8^{\circ}36' N$ and longitude $4^{\circ}10' E$ and $4^{\circ}36' E$ (Jimoh 2003). The temperature of the area ranges between $33^{\circ}C$ and $35^{\circ}C$ from November to January and $34^{\circ}C$ - $37^{\circ}C$ from February to April. The average annual rainfall ranges from 990.3 mm to 1,318 mm (Ajibade & Ojelola 2004).

Water Collection Procedures, Quality and Data Analysis

Water samples from thirty (30) farms in the two LGAs were collected between June-August. The experimental layout was designed in a completely randomized experimental design (CRD) manner as shown in Table 1. The factors considered for each farm in the design of the experiment were the number of birds (N), year of existence (Y), the distance between dump sites and shallow wells (D), and hydraulic conductivity of soil (H). Three soil samples from each farm were also collected using a spiral soil auger (H-4250, 40 mm diameter cutting head, 600 mm long with a bayonet connector.) to a depth ranging from 0–40 cm and the average values were imputed into Soil Water Characteristics (SWC) software to estimate the hydraulic conductivity of the soil. The hydraulic conductivity of the soil was between 0.010–0.19 in/hr. The farms were denoted as $S_1, S_2, S_3, S_4 \dots S_{30}$ with combinations of factors (N, Y, D) Samples of water from shallow wells at a distance of 400 m far away from the farms were used as controls. All the samples were analyzed at the Laboratory of the Department of Chemistry, the University of Ilorin, Ilorin, Nigeria for the following quality: pH, turbidity, phosphate, nitrate, Dissolved Oxygen (DO), Biochemical Oxygen Demand (BOD), Chemical Oxygen Demand (COD) using AOAC (1990) standard and Fecal coliform using Most Prob-

Table 1: Experimental design and layout.

$S_{25}(N_{5000}Y_5$ $D_{250})$	$S_{23}(N_{5000}Y_{15}$ $D_{150})$	$S_{17}(N_{10000}Y_{15}$ $D_{236})$	$S_{11}(N_{10000}Y_7$ $D_{50})$	$S_9(N_{1000}Y_7$ $D_{31})$	$S_{27}(N_{1000}Y_5$ $D_{216})$
$S_8(N_{1000}Y_7$ $D_{19})$	$S_1(N_{1000}Y_{10}$ $D_{40})$	$S_4(N_{500}Y_5$ $D_{17})$	$S_7(N_{500}Y_5$ $D_{32})$	$S_{10}(N_{1000}Y_7$ $D_{36})$	$S_{22}(N_{500}Y_{15}$ $D_{180})$
$S_{30}(N_{2000}Y_7$ $D_{120})$	$S_3(N_{500}Y_5$ $D_{10})$	$S_5(N_{2000}Y_3$ $D_{11})$	$S_{16}(N_{10000}Y_{15}D_{120})$	$S_{21}(N_{5000}Y_{15}$ $D_{180})$	$S_{29}(N_{2000}Y_5$ $D_{100})$
$S_2(N_{1000}Y_{10}$ $D_{38})$	$S_6(N_{1000}Y_5$ $D_{30})$	$S_{12}(N_{500}Y_{15}$ $D_{62})$	$S_{26}(N_{5000}Y_5$ $D_{216})$	$S_{14}(N_{200}Y_4$ $D_{30})$	$S_{18}(N_{2000}Y_{15}$ $D_{218})$
$S_{13}(N_{200}Y_3$ $D_{38})$	$S_{20}(N_{10000}Y_{15}$ $D_{303})$	$S_{15}(N_{5000}Y_{20}$ $D_{360})$	$S_{28}(N_{5000}Y_{10}$ $D_{180})$	$S_{19}(N_{10,000}Y_{15}$ $D_{218})$	$S_{24}(N_{5000}Y_5$ $D_{250})$

S-farm; N-number of birds per farm; Y-year of the existence of farm; D-distance between dumpsites and shallow wells.

able Number (MPN) technique. The quality levels of these samples were tested and compared with the control sample. The data obtained from the research conducted was subjected to the statistical analysis of variance (ANOVA) and multiple comparisons of means with Duncan's New Multiple Range Test (DNMRT) using Statistical Package for Social Sciences (SPSS) (version 16.0.).

RESULTS AND DISCUSSION

Effect of Number of Birds (N) on Water Quality

Table 2, indicates the analysis of the water sample during the studies indicated no significant changes in pH, DO, nitrate, and phosphate. From the table, it could be seen that the turbidity of water becomes significantly higher with a higher number of birds (2000) but reduces when the number of birds increases to (5000) birds. High turbidity values are a result of poor covering of wells. Mishra et al. (2009) reported that the closeness of dumpsites to where runoff and leaching occur could be the possibility of the presence of suspended particles and other contaminants in water. Higher turbidity levels are a result of disease-causing microorganisms such as bacteria, viruses, parasites (EPA 2020). Comparing the turbidity with the control (0.426 NTU), the water is highly polluted. Kulabako et al. (2007) and Pritchard et al. (2007) concluded that rainfall causes turbidity levels in well to increase due to transportation of colloidal particles into the wells, as high turbidity inhibit treatment. Also, the BOD of the water decreases progressively as the number of birds increases up to 2000 birds and slightly increased. The mean higher value of 8.41 mg.L⁻¹ was observed at ≤500 birds. This could be attributed to a large number of wastes produced from the birds which are high in organic content thereby causing pollution. Comparing this with the control of (15.20 mg.L⁻¹), the BOD of the water is not polluted. The COD of the

water increased with a higher number of birds but becomes significantly higher with 2000 birds (111.56 mg.L⁻¹). This could be as a result of a high oxidizable organic pollutant from the birds that enter the water source. Comparing this with the control of 24.62 mg.L⁻¹, the wastes produced by birds have a pollution effect. Fecal coliform was found in water with a lower number of birds 500 or less and 100 birds respectively, 34.4 x 10⁻² cfu.mL⁻¹ with 1000 birds, this could be as a consequence of an increased number of birds. Fecal coliform is important in assessing the suitability of water and higher coliform indicates high contamination probably due to the presence of pathogens (Aderemi et al. 2013).

Effect of Year of Existence (Y) on Water Quality

Table 3 shows that the year of farm existence has a significant effect on turbidity, phosphate, DO, and BOD at p ≤ 0.05. From the Table, turbidity steadily increases from 5 years to 10 years at 44.6 NTU and 56.60 NTU respectively, (Nephelometric Turbidity Units) and later decreases as the year of the farm increases. The increase can be possibly due to the effects of run-off water which carries several compounds such as suspended solids (Rahmanian et al. 2015). Turbidity is caused due to the presence of particulate matter in water sources as a result of inadequate filtration (Harter 2003). Phosphate of water of ≤ 5 years increases progressively from 1.53 mg.L⁻¹ to 2.29 mg.L⁻¹ and decrease from year 15 but is not significantly different from others. Compared with the control of 0.68 mg.L⁻¹ it indicated that the water is polluted. This could be as a result of dumping the wastes for a longer period on the sites which then percolates down. According to Adeoye et al. (2012), phosphate can enter groundwater due to the percolation of animal wastes as groundwater contain minimal phosphate due to low solubility and retention of phosphate by soil during percolation. Adewale et al. (2013) also reported that phosphate sources which are anthropo-

Table 2: Effect of the number of birds (N) on water quality.

Water Quality	Number of Birds per Farm				
	≤500	1000	2000	5000	Control
pH	6.721 ^a	6.681 ^a	6.789 ^a	6.731 ^a	6.90
Turbidity (NTU)	23.252 ^a	38.132 ^b	101.924 ^c	39.721 ^b	0.426
Phosphate (mg.L ⁻¹)	1.632 ^a	1.839 ^a	2.180 ^b	1.411 ^a	0.68
Nitrate (mg.L ⁻¹)	1.874 ^a	1.942 ^a	2.303 ^b	2.173 ^b	28.42
DO (mg.L ⁻¹)	28.190 ^a	24.457 ^b	17.668 ^b	24.282 ^b	46.84
BOD (mg.L ⁻¹)	8.414 ^a	5.969 ^b	3.569 ^c	6.762 ^d	15.20
COD (mg.L ⁻¹)	92.750 ^a	90.231 ^a	111.556 ^b	85.222 ^d	24.62
Faecal coliform (cfu.mL ⁻¹)	0.028 ^a	0.344 ^b	0.000 ^c	0.000 ^c	0.001

Means with the same alphabet in the same row are not significantly different from each other.

genic and non-point may also be a source of pollution apart from poultry farm operation. Quan et al. (2011) reported that phosphate in groundwater aid microbial growth. DO of the water increased from 26.01 mg.L⁻¹ to 32.21 mg.L⁻¹. The higher value found in year 20 could be due to poor management practices of the farm. DO level indicates how well the water is aerated, as low level affects aquatic life (Singaraja et al. 2012). The lower concentration of (46.84 mg.L⁻¹) compared to the control indicates a level of organic pollution and is linked to bacterial activity, photosynthesis, land availability, and stratification (Vikal 2009). High DO could be ascribed to a high stream aeration flow rate at the time of collection and also due to pollution from poultry wastes (Ayoade et al. 2006). BOD of the water at 5 years or less was significantly higher from Table 4. It can be inferred that BOD increases progressively as the years of poultry increase from 15 years to 20 years respectively ranging between 7.28-8.97 mg.L⁻¹. This can be linked to the fact that the wells were unprotected and that the seasons varied. The percentage of biodegradable soil, organic matter is utilized to assess the organic strength of the water, according to Mocuba (2010). According to Lukubye & Andama (2017), high BOD can be caused by an increase in bacteria, which corresponds to increased microbial activity. Contamination is caused by the proximity of water sources to animal wastes, which easily reach the groundwater (Bello et al. 2013).

Effect of Distance Between Dumpsites and Shallow Wells (D) on Water Quality

Table 4 demonstrates that turbidity, DO, and BOD are all significant at p<0.05. The turbidity of the water was lower in locations farther away from the dumpsite than in places closer to the dumpsite. This observation was in agreement with Sangodoyin & Agbawhe (1991) who found that turbidity of water decreases as the distance between the dumpsite and the water source increases and that leachates affect pollutant

concentrations in shallow groundwater from a distance of 250 meters. High turbidity between 200 m and 400 m downstream poultry sampling points may be attributed to the dumping of poultry waste (Nduka et al. 2008). DO of the water progressively increases from distance 50 m to 200 m at 18.86-34.55 mg.L⁻¹. A higher value of DO was found in surrounding water in areas with higher distances of dumpsite to water sources. The highest value was found at a distance of 200 m. DO generally increases with higher distances of dumping sites from water sources. A somewhat high value of DO, according to Lukubye & Andama (2017), could be attributed to the well's slightly low temperature, which may or may not be related to the presence of photosynthetic activities that can reduce carbon dioxide. The water's BOD increased from 4.89 mg.L⁻¹ at 500 m to 8.59 mg.L⁻¹ at 500 m. The water is less polluted when compared to the control of 15.20 mg.L⁻¹. This is because the wells were protected, as well as seasonal variations. Contamination is caused by the proximity of water sources to animal wastes, which easily reach the groundwater (Bello et al. 2013).

Summary of Considered Factors

Table 5. shows the result of ANOVA of the effect of the number of birds per farm, the year of the existence of the farm, the distance between dumpsites and shallow wells, on the pH, turbidity, phosphate, nitrate, DO, BOD, COD, and fecal coliform of water from shallow wells of poultry farms from Asa and Ilorin South LGAs of Kwara state, Nigeria. From the table, the number of birds per farm, year of the existence of the farm have a significant effect on turbidity, BOD, COD, and fecal coliform. The year of the existence of the farm and the distance between dumpsite and shallow wells all had a significant effect on turbidity, phosphate, DO, and BOD at p ≤ 0.05. The interpretation of the observation is that those factors that had significant effects on respective water quality should be given proper attention. This could

Table 3: Effect of the year of existence (Y) on water quality.

Water Quality	Years of operation of the farm				Control
	≤5	10	15	20	
pH	6.760 ^a	6.733 ^a	6.649 ^a	6.707 ^a	6.90
Turbidity (NTU)	44.611 ^a	56.601 ^b	32.536 ^c	14.100 ^d	0.43
Phosphate (mg.L ⁻¹)	1.530 ^a	2.294 ^b	1.516 ^a	1.067 ^a	0.68
Nitrate (mg.L ⁻¹)	1.835 ^a	2.123 ^a	2.106 ^a	1.330 ^a	28.42
DO (mg.L ⁻¹)	26.011 ^a	17.388 ^b	30.079 ^c	32.207 ^d	46.84
BOD (mg.L ⁻¹)	8.130 ^a	4.335 ^b	7.277 ^a	8.977 ^c	15.20
COD (mg.L ⁻¹)	88.069 ^a	95.433 ^a	93.233 ^a	88.000 ^a	24.62
Faecal coliform (cfu.mL ⁻¹)	0.042 ^a	0.249 ^a	0.153 ^a	0.000 ^a	0.001

Means with the same alphabet are not significantly different from each other at p ≤ 0.05

Table 4: Effect of distance between dumpsites and shallow wells (D) on water quality.

Water Quality	Distance from Source of Water				Control
	≤50m	100m	200m	>200m	
pH	6.747 ^a	6.746 ^a	6.638 ^a	6.634 ^a	6.90
Turbidity (NTU)	55.209 ^a	58.847 ^a	21.837 ^b	11.808 ^c	0.43
Phosphate (mg.L ⁻¹)	2.062 ^a	2.014 ^a	1.370 ^b	1.091 ^b	0.68
Nitrate (mg.L ⁻¹)	2.087 ^a	2.329 ^a	2.105 ^a	1.559 ^a	28.42
DO (mg.L ⁻¹)	18.864 ^a	20.423 ^a	34.551 ^b	32.706 ^b	46.84
BOD (mg.L ⁻¹)	4.899 ^a	5.693 ^b	8.078 ^c	8.591 ^c	15.20
COD (mg.L ⁻¹)	94.569 ^a	95.958 ^b	96.125 ^a	86.733 ^a	24.62
Faecal coliform (cfu.mL ⁻¹)	0.244 ^a	0.000 ^b	0.050 ^b	0.227 ^a	0.001

Means with the same alphabet are not significantly different from each other at $P \leq 0.05$

Table 5: Result of ANOVA of effect of independent variables on water quality.

Water Quality	Number of Birds (N)	Years of Operation of Farm (Y)	Distance between Dumpsite and Water Source (D)	Control
pH	0.200	0.118	0.259	6.90
Turbidity (NTU)	0.000*	0.004*	0.000*	0.43
Phosphate (mg.L ⁻¹)	0.290	0.011*	0.072	0.68
Nitrate (mg.L ⁻¹)	0.260	0.241	0.217	28.42
DO (mg.L ⁻¹)	0.430	0.017*	0.006*	46.84
BOD (mg.L ⁻¹)	0.030*	0.000*	0.021*	15.20
COD (mg.L ⁻¹)	0.010*	0.435	0.656	24.62
Faecal coliform (cfu.mL ⁻¹)	0.000*	0.304	0.58	0.001

*Significant at $P \leq 0.05$

cause positive or negative effects on those water quality. The effect can either be an increase or decrease in the respective values of the aforementioned water quality.

CONCLUSION AND RECOMMENDATIONS

This study revealed the quality of water for poultry management can be affected by the number of birds, years of existence of the farm, the relative distance between the dumpsite of the farm, and the location of the water source. The water from shallow wells located within the farm site was of poor quality and below the recommended standard compared with the control; an indication that it is not fit for consumption. There is an urgent need for improved water resource management for continued suitability and sustainability. Shallow wells should be lined and sited upstream of the poultry dumpsite, water purification procedure is important in poultry farm site and further analysis work for proper testing of the sampled wells should be carried out.

REFERENCES

- Adeoye, P.A., Hasfalina, C.M., Mohammed, A.S., Thamer, A.M. and Akinbile, C.O. 2012. Poultry waste effect on shallow groundwater quality in selected farms in Minna, North-Central Nigeria. Proceedings of International Conference on Agricultural and Food Engineering for life. University of Putra, Malaysia: 554-565.
- Aderemi, P.A., Adeolu, A.R. and Ibrahim, H.M. 2013. Appraisal of rural water supply: A case study of Kwara State, North Central Nigeria. Int. J. Basic Appl. Sci., 1(4): 816-826.
- Adewale, M.T., Toyin, A., Iheoma, A. and Michael, T.A. 2013. Evaluating the environmental impact of poultry farming on stream water quality: A study from Abeokuta, Nigeria. Environ. Quality Manag., 22(4): 79-93.
- Ajibade, L.T. and Ojelola, A. O. 2004. Effects of automobile mechanics on soils in Ilorin. Geo- Stud. Forum: Int. J. Environ. Policy Issues, 2(1): 18-27.
- Ajibade, L.T. 2006. A preliminary assessment of the comparative study of indigenous and scientific methods of land evaluation in Asa L.G.A., Kwara State. Geo-Stud. Forum, 3(1 and 2): 1-8.
- Akpoveta, O.V., Okoh, B. E. and Osakwe, S. A. 2011. Quality assessment of borehole water used in the vicinities of Benin, Edo State, Agbor, Delta State of Nigeria. Curr. Res. Chem., 3: 62-69.
- Association of Official Analytical Chemists (AOAC). 1990. Official method of analysis 15th Edition, Arlington, Virginia.

- Ayoade, A.A., Fagade, S. O. and Adebisi, A.A. 2006. Dynamics of limnological features of two man-made lakes in relation to fish production. *Afr. J. Biotechnol.*, 5: 1013-1021.
- Bello, O.O., Osho, A., Bankole, S.A. and Bello, T.K. 2013. Bacteriological and physicochemical analysis of borehole and well sources in Ijebu-ode, Southwestern Nigeria. *Int. J. Pharma Bio Sci.*, 8: 18-25.
- Collins, E. 1996. Poultry litter management and carcass disposal. *Virginia Tech. Pub.*, 44: 442-053.
- EPA. 2020. Groundwater and drinking water: National primary drinking water regulation. Available online: <https://www.epa.gov/ground-water-and-drinking-water/national-primary-drinking-water-regulations> (accessed on 18 May 2020).
- Evers, G.W. 1998. The economic value of poultry litter as fertilizer for east Texas pastures. 20th Edition. Texas A & M University, Texas.
- Ezekoye, C.C., Amakoromo, E.R. and Ibiene, A.A. 2017. Laboratory-based bioremediation of hydrocarbon polluted mangrove swamp soil in the Niger Delta using poultry wastes. *Microbiol. Res. J. Int.*, 19(2) 1-14.
- Frederick, W.P. 1990. *Water Quality and Treatment: A Handbook on Community Water Supply*. 4th Edition. R.R. Donnelly, U.S.A. pp.1,80-89,100,134,195.
- Harter, T. 2003. *Groundwater Quality and Groundwater Pollution*. FWQP Reference Sheet11.2, ANR Publication 8084, University of California.
- Jacques, D., Simunek, J., Mallants, D. and Th. Van Genuchten, M. 2008. Modeling coupled water flows, solute transport, and geochemical reactions affecting heavy metal migration in a podzol soil. *Geoderma*, 145(3-4): 449- 461.
- Jain, C.K., Bhatia, K.K.S. and Vijay, T. 1995. *Groundwater Quality Monitoring and Evaluation in and Around Kakinada, Andhra Pradesh*. Technical Report, CS (AR) 172, National Institute of Hydrology, Roorkee.
- Jimoh, H.I. 2003. The erosion tolerance range of land use surface: Implication on land resource use and management techniques in Ilorin, Nigeria. *Int. J. Environ. Stud.*, 60(5): 445-452.
- Kelleher, B.P., Leahy, J.J., Henihan, A.M., O'Dwyer, T.F., Sutton, D. and Leahy, M.J. 2002. Advances in poultry litter disposal technology. *Bioresour. Technol.*, 83: 27-36.
- Koelkebeck, K.M., McKee, J.S., Harrison, P.C. and Parsons, C.M. 1999. Performance of laying hens provided water from two sources. *J. Appl. Poultry Res.*, 8: 374-379.
- Kulabako, N.R., Nalubega, M. and Thunvik, R. 2007. Study of the Impact of land use and hydrological settings on the shallow groundwater quality in a peri-urban area of Kampala, Uganda. *Science of the Total Environment*, 381(1-3): 180-199. Doi: 10.1016/j.scitotenv.2007.03.035.
- Kushreshtha, S.I.N. 1998. A global outlook for water resources to the year 2012. *Water Resour. Manag.*, 12 (1): 1-18.
- Lukubye, B. and Andama, M. 2017. Physicochemical quality of selected drinking water sources in Mbarara Municipality, Uganda. *J. Water Resour. Protect.*, 9: 707-722. <https://doi.org/10.4236/jwarp.2017.97047>.
- Manning, L., Chadd, S.A. and Baines, R.N. 2007. Key health and welfare indicators for broiler production. *World Poultry Sci. J.*, 63: 46-62.
- Mishra, D., Mudgal, M., Khan, M.A., Padmakaran, P. and Chakradhar, B. 2009. Assessment of groundwater quality of the Bhavnagar region (Gujarat). *J. Sci. Ind. Res.*, 68: 964-966.
- Mocuba, J. 2010. Dissolved oxygen and biochemical oxygen demand in the waters close to the quelimane sewage discharge. Thesis, University of Bergen, Bergen.
- Nahm, K.H. and Nahm, B.A. 2004. *Poultry Production and Waste Management*, Republic of Korea Yu Han Publishing ISBN 89-7722-623-6.
- Nduka, J. K., Orish, E.O. and Linus, O.E. 2008. Some physicochemical parameters of potable water supply in Warri, Niger Delta areas of Nigeria. *Sci. Res. Essay*, 3(11): 547-551.
- Orebiyi, E.O., Awomeso, J.A., Idowu, O.A., Martins, O., Oguntoke, O. and Taiwo, A.M. 2010. Assessment of pollution hazards of shallow well water in Abeokuta and environs, Southwest, Nigeria. *Am. J. Environ. Sci.*, 6(1): 50-56.
- Plant, J.S., David, S. Barry, F. and Lorraire, W. 2001. Environmental geochemistry at the global scale. *J. Sci. Direct*, 16: 1291-1308.
- Pritchard, M., Nkandawire, T. and O'Neill, J.G. 2007. Biological, Chemical and physical drinking water quality from shallow wells in Malawi: Case Study of Blantyre, Churadzulu and Mulanje. *Phys. Chem. Earth*, 32, 1167.
- Quan, J., Wang, L., Zhan, H. and Chen, Z. 2011. Urban land use effects on groundwater phosphate distribution in a shallow aquifer, Nanfei river basin, china. *Hydrogeol. J.*, doi:10.1007/S10040-001-0770-X.
- Rahmanian, N., Ali, S.H.B., Homayoonfard, M., Ali, N.J., Rehan, M., Sadef, Y. and Nizami, A.S. 2015. Analysis of physicochemical parameters to evaluate the drinking water quality in the State of Perak, Malaysia. *J. Chem.*, 2015: 716125.
- Sangodoyin, A.Y. and Agbawhe, O.M. 1991. Environmental study on surface and groundwater pollutants from abattoir effluents. *Bioresour. Tech.*, 41(1992): 193-200.
- Sibbsen, E. and Sharpley, A.N. 1997. Setting and justifying upper critical limits phosphorus in soils. CAB International, New York, pp. 151-176.
- Singaraja, C., Chidambaram, S., Prasanna, M.V., Paramaguru, P., Johnsonbabu, G., Thivya, C. and Thilagavathi, R. 2012. A Study on the Behaviour of the Dissolved Oxygen in the Shallow Coastal wells of Cuddalore District Tamilnadu, India. *Water Qual. Expo. Health*, 4: 1-16.
- Vikal, P. 2009. Multivariate analysis of drinking water quality parameters of lake Pichhola in Udaipur, India. *Biol. Forum: Int. J.*, 1(2): 97-102.
- Weaver, T. 1998. Managing poultry manure reduces runoff: Poultry production and product safety research. University of Arkansas, Fayetteville, AR.
- Wilson, A. 1998. *Wilson's Practical Meat Inspection*. Blackwell Science Ltd., Malden M.A.
- Zhao, Z., Knowlton, K.F. and Love, N.G. 2008. Hormones in waste from concentrated animal feeding operations. In D.S. Aga (ed). *Fate and Transport of Pharmaceuticals in the Environment and Water Treatment System*. CRC Press, Boca Raton, FL, pp. 291-239.



Pollution Characteristics of Surface Sediments in Luhun Drinking Water Reservoir in the Middle China

Zizhen Zhou*†, Yu Xu* and Zhen Dai*

*School of Energy and Environment, Zhongyuan University of Technology, Zhengzhou, 450007, P. R. China

†Corresponding author: Zizhen Zhou; 6623@zut.edu.cn

Nat. Env. & Poll. Tech.
Website: www.neptjournal.com

Received: 19-03-2021

Revised: 19-04-2021

Accepted: 05-05-2021

Key Words:

Reservoir
Sediment
Nitrogen
Phosphorus
Metals

ABSTRACT

The pollution status of surface sediments in the Luhun drinking water reservoir in the central of China was analyzed and evaluated, and three sampling points were selected for this study. The results showed that the organic matter content of the Luhun reservoir was as high as 5.2%, which was at a high level. The analysis of nitrogen, phosphorus, and their components showed that the total nitrogen (TN) and total phosphorus (TP) pollution in Luhun reservoir was in the medium pollution level, among which the ion-exchange state of nitrogen component and the strong-alkali extraction state of phosphorus component accounted for a relatively high risk of release into the overlying water. The results showed that the bioavailability index of Pb and Cr was as high as 0.73 and 0.62, which was of big pollution risk. Generally speaking, the sediment of Luhun reservoir had a high risk of pollution to the overlying water. The results of this study can provide a theoretical basis for urban safe water supply and provide support for water quality improvement.

INTRODUCTION

In recent years, with the aggravation of groundwater pollution, the water quantity is not enough to meet the needs of urban development. So more and more reservoirs gradually have become the drinking water source of big cities (Zhou et al. 2017a, Zhang et al. 2017, Tang et al. 2014), for example, Xi'an, Beijing, and Shenzhen. However, as a semi-natural water body, the water exchange capacity of the reservoir is weak, so the hydraulic retention time is long, and the artificial pollution intensifies, which leads to the gradual decline of water quality of the reservoir (Gu et al. 2020, Zhang et al. 2017, Li et al. 2015, Guo et al. 2018). Some researchers pointed out that sediment was the source of pollutants in reservoir water, and its pollution degree directly affected the water quality of overlying water. Heavy metals, nitrogen, phosphorus, and organic matter are the main pollutants in sediments, and heavy metals have attracted more and more researchers' attention due to their ecological toxicity (Zhou et al. 2020, Huang et al. 2021, Gao et al. 2020).

Studies on heavy metals in sediment majorly focus on Mn, Cr, Al, and Pb. These metal elements are also the compounds with the highest concentration in sediment, which have a significant impact on the safety of water supplies. For deep water source reservoirs, the water at the bottom of the reservoir has entered an anaerobic state (due to the dual oxygen consumption of the water body and sediment, the dissolved oxygen concentration of the bottom water body

is less than 2 mg.L^{-1} , even 0 mg.L^{-1}). At this time, metal elements, nitrogen, phosphorus, and other pollutants in the sediment easily change into a reduction state, and then enter the overlying water body, causing water pollution (Wang et al. 2019a, Zackary et al. 2016, Dadi et al. 2016). The metal elements in sediment are complex. According to different extraction methods, the metal elements in sediment are generally divided into five components, F1, F2, F3, F4, and F5 (Zhou et al. 2017b). The metal contamination level in sediment may be analyzed using quantitative statistics based on the percentage of different components, and then the threat to safe water supply can be assessed.

The central drinking water reservoir (Luhun reservoir) was taken as the research object, and three representative monitoring points, S1, S2, and S3 (Fig. 1) were selected for analyzing the different contents of sediment components, especially heavy metal elements, and evaluating the pollution status by using safety evaluation method. This study can provide a scientific basis for water quality protection and guarantee of the reservoir, and provide a theory for water quality improvement of reservoir support.

MATERIALS AND METHODS

Sampling Sites and Sampling Methods

Luhun reservoir is 67 km away from Luoyang City, and the control basin area is 3492 m^3 , accounting for 57.9% of the

basin area. The annual average runoff at the dam site is 1.025 billion cubic meters (1951-1968), with an annual average flow of $32.5 \text{ m}^3 \cdot \text{s}^{-1}$.

The annual average sediment transport is about 3 million tons, the average sediment content is $3.2 \text{ kg} \cdot \text{m}^{-3}$, and the sediment concentration is more than 90% in flood season from July to October, and there is clear river bottom during the non-flood period. The peak discharge of the 1000 year return period is $12400 \text{ m}^3 \cdot \text{s}^{-1}$, the peak discharge of the 10000 year return period is $17100 \text{ m}^3 \cdot \text{s}^{-1}$, and the flood peak discharge of dam protection (20% of the flood peak plus 20% of the flood peak in the 10000 year return period) is $20520 \text{ m}^3 \cdot \text{s}^{-1}$.

In this study, three representative sampling points were selected, namely, the tail of the reservoir, the middle of the reservoir, and the area in front of the dam. The basic distribution was shown in Fig. 1.

Methods for Determination of Chemical Indicators of Sediments

The surface 5 mm sediment samples of each sampling point were collected by Peterson grab sampler, and the mud was taken 3 times at each sampling point and mixed as the sediment samples at this point. The samples were transported back to the laboratory, were grounded and sieved after freeze-drying, and stored in sealed bags for standby.

Pb, Cr, Al, and Mn in sediment were determined by the Tessier extraction method (Deng et al. 2016, Dubravka et al. 2014). The loss of fire technique was used to assess the amount of organic matter (OC) in sediment. The potassium persulfate technique was used to detect TN in sediment, whereas the SMT method for phosphorus separation in freshwater sediment was developed under the auspices of

the European Standard Test Committee (Zhou et al. 2020), and the extraction and determination of nitrogen and phosphorus components were determined according to relevant literature reports (Kwak et al. 2018, Jin et al. 2013). The metal elements were extracted by Tessier continuous extraction method, which mainly included the following five forms: exchangeable state (F1), carbon binding state (F2), iron-manganese oxide binding state (F3), organic compound state (F4), and residue state (F5). The sediment samples were first digested with an $\text{HCl-HNO}_3\text{-HF-HClO}_4$ mixture, and then gradually extracted. The metal concentration of the extract was determined by ICP-MS.

RESULTS AND DISCUSSION

Analysis of Physicochemical Composition of Sediments

The branches, gravel, small stones, and other substances in the collected sediment samples were removed, and then the sediment was freeze-dried, grounded, and mixed for determination. The test results were shown in Table 1. In the three monitoring points, silt was the main component of sediment, accounting for 85.7% on average. Clay was the second most abundant element in the sediments of the S1, S2, and S3 monitoring stations, accounting for 10.1 percent, 9.8 percent, and 6.5 percent, respectively. Gravel, with an average content of 5.8 percent, was the least sediment component, owing to the low fluidity of the water body in the area in front of the dam and the deposition of big particles in the area at the reservoir's tail.

The water content of sediment was the ratio of the weight of moisture in the wet sample to the total weight of sediment, which indirectly reflected the level of dissolved oxygen in sediment (Li & Zhang 2019). As shown in Table 1, the average water content of sediment in the Luhun reservoir was 79.7%. The higher water content of sediment indicated that the sediment texture in front of the Luhun reservoir dam was very loose, and it was easy to resuspend under disturbance. The loss of ignition of sediments reflected the organic matter composition in sediments. The average loss on ignition of sediments in Luhun reservoir was 5.2%, which was higher than that of the same type of reservoirs in China



Fig. 1: Distribution of sampling points in LH water source reservoir.

Table 1: Physicochemical composition of surface sediment in LH reservoir.

Component	S1	S2	S3
silt [%]	83.6	84.4	88.1
Clay [%]	10.1	9.8	6.5
gravel [%]	6.3	5.8	5.4
Moisture content [%]	80.1	82.4	76.5
Loss on ignition [%]	4.8	5.2	5.5

(Zhu et al. 2004, Zhang et al. 2019b, 2019c, Yu et al. 2019), indicating that the organic matter pollution of sediments in front of Luhun reservoir dam was serious. The redox and microbiological conditions at the sediment-water interface, for example, vary, and the contaminants in the sediment are easily released into the overlying water, resulting in contamination of the overlying water (Ma et al. 2015).

Analysis of Nitrogen and Phosphorus in Sediments

The nitrogen and phosphorus components in the surface sediment of the Luhun reservoir were measured. The results are shown in Fig. 2. The total nitrogen concentration of surface sediment was between 1.21-1.58 mg.g⁻¹ and the total nitrogen pollution degree of Luhun reservoir sediment was in the middle level compared with the same type reservoir (Wang et al. 2019b, Fang et al. 2019, Li 2019, Wen et al. 2019). The proportion of ion-exchange nitrogen in the total nitrogen component was significant, accounting for 37.2 percent at the S1 sampling point and 45.6 percent at the S3 sample point. The ion-exchange nitrogen had a relatively easy transformation form in all nitrogen components. The increased ion-exchange nitrogen in the sediments of the Luhun reservoir implies that nitrogen components in the sediments were easily transferred to the overlying water. Strong alkali-exchange nitrogen was second to ion-exchange nitrogen in terms of percentage, accounting for 23.8 percent on average.

Among the four phosphorus components, the strong base extracted phosphorus was more likely to migrate and transform than other forms. The ratio of concentration to total phosphorus concentration was called the bioavailability of phosphorus, which can be used to evaluate the risk of phosphorus pollution. The average concentration of total phosphorus in the surface sediment of Luhun reservoir was 1.06 mg.g⁻¹, and the proportion of four phosphorus

components was not significant. The concentration of P extracted from strong alkali was 0.257 mg.g⁻¹, 0.304 mg.g⁻¹ and 0.312 mg.g⁻¹ respectively, which accounted for 22.4%, 28.9% and 28.7% respectively in each sampling point. The bioavailability of phosphorus in the sediment of sample locations S2 and S3 was found to be greater than that of sampling point S1.

Generally speaking, the average content of total nitrogen in the surface sediment of Luhun reservoir is 1.39 mg.g⁻¹, with a larger proportion of ion exchangeable nitrogen in the components, posing a significant danger of migration and transformation. The average content of total phosphorus in sediment was 1.06 mg.g⁻¹, and the average proportion of strong alkali extracted phosphorus in its components was 26.7%, indicating that the bioavailability index of phosphorus is 26.7%, which had a high risk of migration and transformation.

Analysis of Heavy Metals in Sediments

Surface sediments from three sample stations in the Luhun reservoir were continually extracted and examined for the four metals Pb, Cr, Al, and Mn. The results are shown in Fig. 3. The average concentrations of the four metals in sediments were 15.0 mg.kg⁻¹, 13.4 mg.kg⁻¹, 982.3 mg.kg⁻¹ and 1132 mg.kg⁻¹ respectively. Among the five components, F1 is exchangeable. When the redox conditions, microbial conditions, and water disturbance of the overlying water change, it is easy to transfer and transform at the mud water interface, which causes water quality pollution in the overlying water. The exchangeable metal concentration reflects the risk of pollution to water.

The bioavailability factor (BF) $BF = C_{bio}/total$, where C_{bio} is the sum of F1, F2, F3, and F4 components, and C_{Total} is the total metal concentration (Frémion et al.2016, Aleksandra et al. 2013). It can be seen that the bioavailability

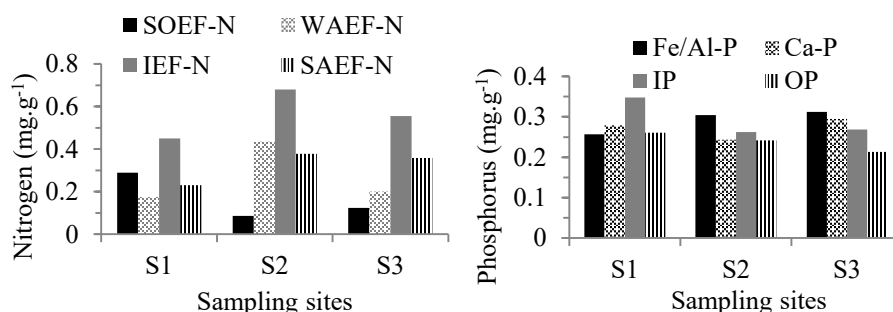


Fig. 2: Components of nitrogen and phosphorus in the sediments of 3 sampling points of LH reservoir (SOEF-N: strongly oxidized extracted nitrogen, WAEF-N: weakly acid exchangeable nitrogen, IEF-N: ion exchangeable nitrogen, SAEF-N: strongly alkali exchangeable nitrogen; Fe/ Al-P: strongly alkali extracted phosphorus, Ca-P: strongly acid extracted phosphorus, IP: inorganic phosphorus, OP: organic phosphorus).

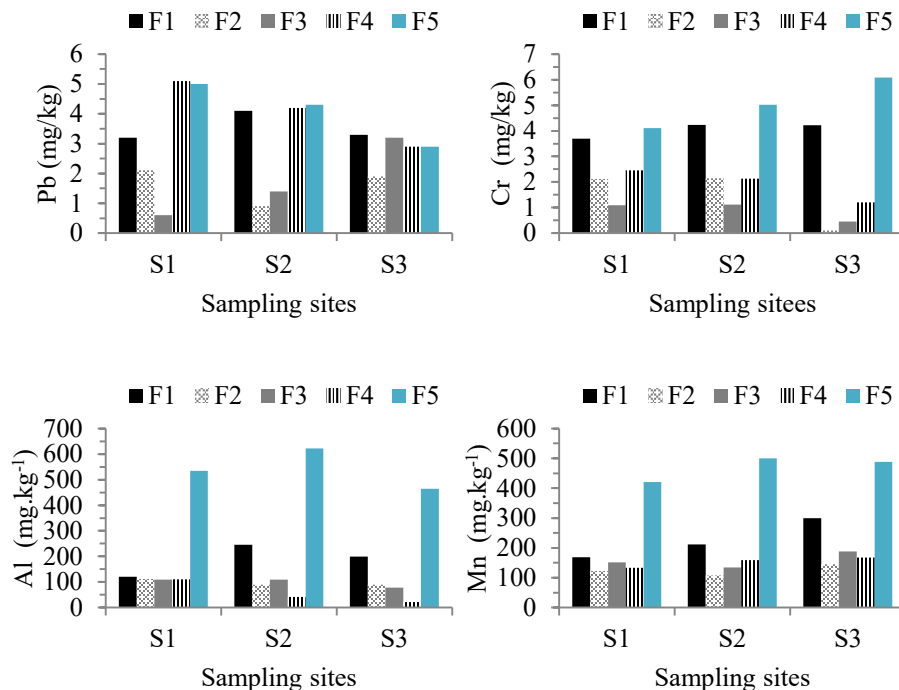


Fig. 3: Pb, Cr, Al, and Mn components in sediments of 3 sampling points in LH reservoir.

index of Pb in the surface sediments of the Luhun reservoir was 0.69, 0.71, and 0.79 respectively, and the BF average value of Pb was 0.73. BF of Pb indicated that Pb migration and transformation ability in sediment was strong, and there was a high pollution risk. The bioavailability index of Cr at three sampling points was 0.69, 0.66, and 0.50 respectively, and the BF average value of Cr was 0.62. BF of Cr indicated that Cr migration and transformation ability in sediment was stronger than Pb, but there was still a high risk of pollution. The bioavailability index of Al at three sampling points was 0.46, 0.44, and 0.45 respectively, and the BF average of Al was 0.45. BF of Al showed that the migration and transformation ability of Al in sediment was lower than that of Pb and Cr, and the pollution risk was low. The bioavailability index of Mn at three sampling points was 0.58, 0.55, and 0.62 respectively, and the BF average value of Mn was 0.58. BF of Mn indicated that Mn migration and transformation capacity in sediment was lower than Pb and Cr, and pollution risk was low.

According to the above analysis, compared with other similar reservoirs in China (Jiang & Zeng 2019, Zhu 2019, Zhang et al. 2019a), Pb, Cr, Al, and Mn concentrations in Luhun reservoir sediment were basically at the middle level; through the analysis of bioavailability index, it was found that the migration and transformation capacity of Pb and

Cr in the sediments of Luhun reservoir was strong and the pollution risk was high.

CONCLUSION

- (1) The results showed that the average loss on ignition was 5.2%, which indicated that the pollution of organic matter in the reservoir sediments was serious, and the pollution in the area in front of the dam was the most serious.
- (2) The average concentration of total nitrogen in the surface sediments of Luhun reservoir was 1.39 mg.g⁻¹, in which the most active ion-exchange nitrogen accounted for 45.6%, the average concentration of total phosphorus was 1.06 mg.g⁻¹, and the strong alkali-extracted phosphorus accounted for 26.7%, indicating that the change of redox conditions and microbial conditions at the sediment-water interface was easy to cause nitrogen and phosphorus pollution in the overlying water.
- (3) The overall amounts of Pb, Cr, Al, and Mn in the Luhun reservoir's surface sediments were comparable to those found in similar reservoirs in China. The bioavailability index of Pb and Cr was high, and there was a higher risk of water pollution of Pb and Cr.

ACKNOWLEDGEMENT

This research was funded by Key Scientific Research Projects of Higher Education Institutions in Henan Province (20A560023), Independent Innovation Application Research Project of Zhongyuan University of Technology (K2020YY012), Science and Technology Guidance Project of China Textile Industry Federation (2018040), Young Backbone Teachers Grant Scheme of Zhongyuan University of Technology.

REFERENCES

- Aleksandra, B.G., Ewa, R., Krzysztof, M.K. and Zamo J.C. 2013. Distribution, unavailability, and fractionation of metallic elements in allotment garden soils using the BCR sequential extraction procedure. *Pol. J. Environ. Stud.*, 22 (4): 1013-1021.
- Dadi, T., Friese, K. and Wendt-Potthoff, K. 2016. Benthic dissolved organic carbon fluxes in a drinking water reservoir. *Limnol. Oceanogr.*, 61(2): 445-459.
- Deng, X.X., Mi, Y.H., Li, Q.W., Duan, H.P., Du, L.J., He, L.Z., Yin, B.L. and Chen, L. 2016. Comparative study on extraction of Pb and Cd from paddy soil by improved BCR method and Tessier method. *Acta Agric. Jiangxi*, 28(09): 64-68.
- Dubravka, V., Zivorad, V. and Srbljub, S. 2014. The impact of the Danube Iron Gate Dam on heavy metal storage and sediment flux within the reservoir. *Catena*, 113: 18-23.
- Fang, J.Q., Qi, C., Zhang, X.H., Han, R.M., Huang, H.X., Wang, Z.S. and Wang, G.X. 2019. Distribution characteristics of carbon, nitrogen, and phosphorus and pollution assessment in sediments of Zhushan Bay, Taihu Lake. *Environ. Sci.*, 40(12): 5367-5374.
- Frémion, F., Courtin-Nomade, A., Bordas, F., Lenain, J., Jugé, P., Kestens, T. and Mouriera, B. 2016. Impact of sediments resuspension on metal solubilization and water quality during recurrent reservoir sluicing management. *Sci. Tot. Environ.*, 562: 201-215.
- Gao, J.C., Tang, Q., Long, Y., Zhang, X.B. and He, X.B. 2020. Heavy metal sources and ecological risk assessment in Changshou Lake reservoir sediments. *Yangtze River*, 51(04): 20-25.
- Gu, M., Zhao, L., Chen, Q. and Zhao, Z.J. 2020. Heavy metal pollution and ecological risk assessment of soil in Miyun reservoir. *Environ. Pollut. Control*, 42(11): 1398-1404+1442.
- Guo, Y., Chen, D., Wang, M., Yang, C., Wang, Z. K. and Zhao, Y. Z. 2018. Distribution characteristics and potential ecological risk assessment of heavy metals in sediments of Aha Reservoir. *J. Hydroecol.*, 39(04): 24-30.
- Huang, D.J., Xue, R.K., Li, K., Xu, M., Li, Y.C., Sun, W.B. and Huang, T.L. 2021. Characteristics and evaluation of sediment pollution in a reservoir in northwest China. *J. Xi'an Univer. Arch. Technol. (Nat. Sci. Ed.)*, 53(01): 103-108.
- Jiang, W.Y. and Zeng, Z.X. 2019. Distribution of heavy metals in sediments of Yuqiao Reservoir and its relationship with benthic fauna. *J. Hydroecol.*, 40(05): 32-39.
- Jin, X.D., He, Y.L., Kirumba, G., Hassan, Y. and Li, J.B. 2013. Phosphorus fractions and phosphate sorption-release characteristics of the sediment in the Yangtze River estuary reservoir. *Ecol. Eng.*, 55: 62-66.
- Kwak, D.H., Jeon, Y.T. and Hur, Y.D. 2018. Phosphorus fractionation and release characteristics of sediment in the Saemangeum Reservoir for seasonal change. *Int. J. Sediment Res.*, 33(03): 250-261.
- Li, M.M. 2019. Effects of Phosphorus Forms on Water Nutrition in the Sediment Of Lakes in Jiangxi Province. East China Jiaotong University, Nanchang, Jiangxi, China.
- Li, Q. and Zhang, X.H. 2019. Application of BP neural network model based on genetic algorithm in predicting the burning loss of Marine sediments. *Metall. Anal.*, 39(04): 25-30.
- Li, Y.C., Yang, L. and Zhu, Q.D. 2015. Analysis of pollution sources and ecological restoration in Chongqing reservoir type drinking water source area. *South-to-North Water Transf. Water Sci. Technol.*, 13(05): 867-870+882.
- Ma, W.X., Huang, T.L. and Li, X. 2015. Study of the application of the water-lifting aerators to improve the water quality of a stratified, eutrophicated reservoir. *Ecol. Eng.*, 83: 281-290.
- Tang, X.Q., Wu, M., Dai, X.C. and Chai, P. H. 2014. Phosphorus storage dynamics and adsorption characteristics for sediment from a drinking water source reservoir and its relation with sediment compositions. *Ecol. Eng.*, 64: 276-284.
- Wang, H., Jiao, Z.H., Liu, C.Y., Sun, L.N., Luo, Q., Wu, H. and Wang, X.X. 2019a. Study on the content and form of phosphorus in the surface sediments of Liaohe River in Liaoning section. *J. Ecol. Environ.*, 28(12): 2409-2415.
- Wang, Y.Y., Li, L.P., Ji, D.B., Fang, H.T., Zhu, X. S., Zhang, Q.W., Huo, J. and He, J.Y. 2019b. Spatial and temporal distribution characteristics and retention effect of nutrients in Xiangjiaba Reservoir. *Environ. Sci.*, 40(08): 3530-3538.
- Wen, S.L., Wu, T., Yang, J., Li, X., Gong, W.Q. and Zhong, J.C. 2019. Characteristics and exchange fluxes of nitrogen and phosphorus at the sediment-water interface in Daheiting Reservoir in winter. *China Environ. Sci.*, 39(03): 1217-1225.
- Yu, K., Zhang, K., Sun, Q.Y., Wu, J.L. and Sun, L.L. 2019. Evaluation of surface sediment pollution in Dongpu reservoir and inflow river. *J. Ecol. Eng.*, 28(10): 2045-2052.
- Zackary, W., Munger, C.C., Care, Y., Alexandra, B., Gerling, H., Kathleen, D., Doubek, J.P. 2016. Effectiveness of hypolimnetic oxygenation for preventing the accumulation of Fe and Mn in a drinking water reservoir. *Water Res.*, 106: 1-14.
- Zhang, J.Y., Yu, J.S., Li, Z. J., Zhang, Y.W. and Liu, Y. 2017. Short-term distribution of chlorophyll-a concentration in summer at Guanting Reservoir. *South-to-North Water Transf. Water Sci. Technol.*, 15(02): 95-100+115.
- Zhang, J., Wang, Y.S., Guo, X.Y., Zhu, J.G. and Deng, J.C. 2019a. Distribution and pollution assessment of nutrients in the surface sediments of a macrophyte-dominated zone in Lake Taihu. *Environ. Sci.*, 40(10): 4497-4504.
- Zhang, Q., Feng, M.Q. and Hao, X.Y. 2019b. Pollution characteristics and ecological risk assessment of heavy metals in sediments of Zhangze reservoir. *Environ. Eng.*, 37(01): 11-17.
- Zhang, X.J., Lu, J.P., Zhang, S.W., Ma, T.L. and Zhang, Z.H. 2019c. Characteristics and source analysis of organic matter in surface sediments of Dahekou Reservoir. *J. Agro-Environ. Sci.*, 38(12): 2835-2843.
- Zhou, Z.Z., Huang, T.L., Gong, W.J., Li, Y., Zhao, F.W., Liu, Y., Zhao, F.W., Zhou, S.L. and Dou, Y.Y. 2020. Field research on nitrogen removal performance of aerobic denitrifiers in source water reservoir by mixing aeration. *Nat. Environ. Pollut. Technol.*, 19(1): 133-140.
- Zhou, Z.Z., Huang, T.L., Li, Y., Long, S.H. and Zhou, S.L. 2017a. Water quality improvement and sediment control of water source reservoir by lifting aerator. *China Environ. Sci.*, 37(01): 210-217.
- Zhou, Z.Z., Huang, T.L., Li, Y., Ma, W.X., Zhou, S.L. and Long, S.H. 2017b. Sediment pollution characteristics and in situ control in a deep drinking water reservoir. *J. Environ. Sci.*, 52(02): 223-231.
- Zhu, G.W., Qin, B.Q., Gao, G., Zhang, L. and Luo, L.C. 2004. Effect of burning on the loss of burning and determination of iron and phosphorus in sediments. *Chinese J. Anal. Lab.*, (09): 72-76.
- Zhu, L. 2019. Study on the Migration and Enrichment Effect of Heavy Metals in Reservoir Sediments. The Dalian University of Technology, China, Liaoning, Dalian.



Exploring the Spatial Pattern of Damage Caused by Typhoon Meranti on the Urban Green Space on Xiamen Island

Huifen Luo*(**)[†] and Junlin Wu***

*College of Geographical Sciences, Shanxi Normal University, Taiyuan 030000, China

**Department of Geography, Modern College of Humanities and Science of Shanxi Normal University, Linfen 041000, China

***Shanxi Huaye Survey Engineering Technology Co. Ltd., No. 3 Bureau, China Metallurgical Geology Bureau, Taiyuan 030002, China

[†]Corresponding author: Huifen Luo; luohuif@foxmail.com

Nat. Env. & Poll. Tech.
Website: www.neptjournal.com

Received: 18-12-2021
Revised: 25-02-2021
Accepted: 04-03-2021

Key Words:

Spatial pattern
NDVI
Getis-Ord Gi*
Typhoon Meranti
Xiamen island

ABSTRACT

Typhoons are the main cause of disturbances in the natural environment of coastal cities. Typhoons often damage the urban green space (UGS) of coastal cities, and the spatial pattern of such damages provides important information for disaster recovery. For acquiring such information, remote sensing technology offers a fast and effective means. This study investigated the spatial pattern of typhoon damage to UGS using Sentinel-2 data. To this end, the damage caused by Typhoon Meranti to the UGS of Xiamen Island (including Gulangyu Island) in 2016 was taken as a case study. The results showed that the overall area without vegetation coverage increased by 1159.7 ha. Areas with high vegetation coverage experienced less damage than areas with low vegetation coverage. A coldspot map of damage clusters was generated, and the map showed that severely damaged green areas were distributed in a striped pattern, indicating serious damage to road greening. In terms of direction, east-west roads experienced a higher degree of damage than north-south roads. The determined spatial pattern of the damage caused by Typhoon Meranti on the UGS of Xiamen Island provides a basis for the post-disaster restoration of the landscape of Xiamen Island.

INTRODUCTION

Typhoon disasters are natural disasters caused by tropical cyclones (Lee et al. 2008, Rossi et al. 2013). Particularly in coastal cities, typhoons are the main cause of disturbances to the natural environment. Accordingly, the monitoring of typhoon damage to the natural environment has received extensive attention from scholars. In this regard, research has been conducted considering various aspects, such as the carbon cycle, forest management, and post-disaster recovery process (Lee et al. 2008, Wang et al. 2010, Zhang et al. 2013).

On making landfall, typhoons often damage the urban green space (UGS) of coastal cities. Therefore, the rapid detection of changes in UGS is of great significance for post-disaster reconstruction and garden planning. Compared with field surveys, remote sensing technology is more effective for evaluating the extent and distribution of damage after natural disasters, because it can provide the overall situation of the damage before and after the disaster. Optical remote sensing data is used in the analysis of environmental damage caused by typhoons, focusing on changes in vegetation and land use (Wang et al. 2010, Zhang et al. 2013). The degree of

damage to vegetation can be quantitatively evaluated using remote sensing and geospatial analysis methods.

Coastal areas in China are affected by tropical cyclones from the western Pacific and the South China Sea. In 2016, Typhoon Meranti attacked Xiamen Island. In this study, the damage caused by Typhoon Meranti to the UGS of Xiamen was quantitatively analyzed using remote sensing and geospatial analysis methods, and the spatial pattern of the damage was characterized using remote sensing image data. The findings provide deeper insight into the mechanism of typhoon damage, which would serve as a basis for the restoration of the UGS after the disaster.

MATERIALS AND METHODS

Study area and Typhoon Meranti

Xiamen is located in the eastern part of Fujian province, China, on the southeastern edge of the East Asian continent, facing the western Pacific and the South China Sea to the west. Due to its special geographical location and climatic conditions, Xiamen is often hit and affected by typhoons.

The wind is usually strong when typhoons make landfall or impact, which often triggers heavy rainfall, posing serious threats to life and property as well as to economic and social development. In this research, the entire Xiamen Island (including Gulangyu) was taken as the study area. Fig. 1 shows the location of the study area. The Typhoon of Meranti track information is from the Water Resources Department of Zhejiang Province (<http://typhoon.zjwater.gov.cn/>). The main road is downloaded from Geofabrik GmbH (<https://download.geofabrik.de/>).

Typhoon Meranti was one of the strongest storms in the global seas in 2016, and it was also the strongest typhoon that landed in southern Fujian since 1949. It landed on the coast of Xiang'an district at 3:05 am on September 15, 2016, with a maximum wind force of 15 ($52 \text{ m}\cdot\text{s}^{-1}$) near the center (<http://typhoon.zjwater.gov.cn/>). Typhoon Meranti uprooted a large number of trees in Xiamen and damaged green areas, houses, and crops, resulting in a direct economic loss of 10.2 billion Yuan, 28 deaths, 49 injured people, and 18 missing people (Wang & Xu 2018, Wu et al. 2020).

Materials

The 1C level data of two scenes before and after the typhoon were obtained by using Sentinel-2 in the Copernicus Plan of the European Space Agency (ESA) on November 26, 2015, and October 31, 2016 (<https://scihub.copernicus.eu/dhus/#/home>). In this study, the whole Xiamen Island (including Gulangyu) without cloud cover was taken as the target.

Methodology

Atmospheric correction: Before change detection, Sentinel-2A 1C level data were converted to Sentinel-2A 2A level data, i.e., converting Top of Atmosphere (TOA) reflectance

data to Bottom of Atmosphere (BOA) reflectance images. In the experiment, the Sen2Cor (V. 2. 8.0.) module provided by ESA was used to realize atmospheric correction (Main-Knorn et al. 2017). The core algorithm of this module was libRadtran, which is used for calculating radiative transfer in Earth's atmosphere (Mayer & Kylling 2005).

Normalized difference vegetation index: Vegetation indices are used to describe the large-scale distribution and changes in vegetation over a specific area. The normalized difference vegetation index (NDVI) is a commonly used vegetation index, obtained from remote sensing measurements of electromagnetic energy in the red and infrared spectral regions (Ashcroft et al. 1990, Defries & Townshend 1994). NDVI uses the difference in leaf absorption in the red and near-infrared (NIR) bands. Such measurements are feasible because green vegetation absorbs and reflects more visible red and infrared wavelength radiation. Most spectral vegetation indices are based on some combination of the ratio between the red bands, where chlorophyll absorbs a large amount of incident light and NIR wavelengths, and the latter corresponds to the area of maximum reflectivity of incident radiation, such as healthy green leaves (attributable to their internal mesophyll structure). The advantage of NDVI is that it is seldom affected by the angle of the sun and sunlight, and hence it provides relatively reliable information on the dynamics of vegetation cover. Considering these advantages, we used NDVI to identify and investigate the spatial distribution of green cover in this study. NDVI is the normalized ratio of the NIR and Red bands,

$$\text{NDVI} = (\rho_{\text{NIR}} - \rho_{\text{Red}}) / (\rho_{\text{NIR}} + \rho_{\text{Red}}) \quad \dots(1)$$

where the NIR and Red bands correspond to the surface reflectance values of Band8 and Band4 of Sentinel-2A data. The NDVI calculated using this formula ranges from -1.0

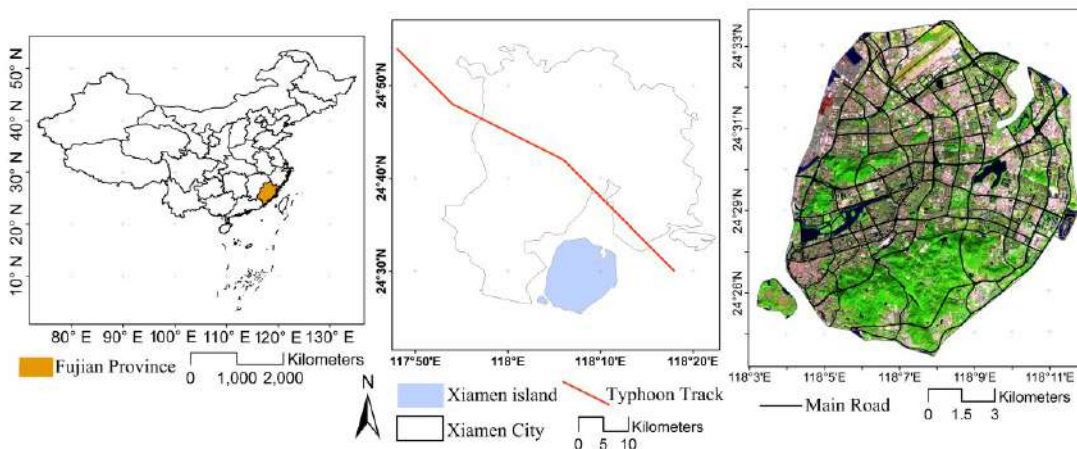


Fig. 1: Location map of the study area and typhoon path map.

to +1.0, with high positive values indicating dense and/or healthy vegetation.

Getis-Ord G_i^* of differenced normalized difference vegetation index: Differenced vegetation indices are the most commonly used indices for vegetation change detection. Differenced indices can be used to analyze surface change characteristics before and after typhoons in a quick, simple and quantitative manner. To quantitatively analyze the damage caused by Typhoon Meranti to the UGS of Xiamen Island, the difference between the NDVI of the study area before and after the typhoon was calculated to obtain the dNDVI, i.e., the NDVI value of the post-typhoon image minus that of the pre-typhoon image.

Hotspot analysis was used to calculate Getis-Ord G_i^* statistics on the elements of the data, to determine locations of high or low clustering in space (Barrell & Grant 2013, Getis & Ord 1992, Patel et al. 1995, Peeters et al. 2015). As a spatial event, the impact of typhoons on UGS has spatial autocorrelation. With the hotspot analysis, dNDVI was used to determine areas with concentrated vegetation cover, which can reflect the spatial pattern of damage to UGS. The Getis-Ord G_i^* formula for calculation is as follows:

$$G_i^* = \left(\sum_{j=1}^n w_{i,j} x_j - \bar{X} \sum_{j=1}^n w_{i,j} \right) / \left(S * \sqrt{ \left[n \sum_{j=1}^n w_{i,j}^2 - \left(\sum_{j=1}^n w_{i,j} \right)^2 \right] / (n - 1) } \right) \dots(2)$$

$$\bar{X} = \sum_{j=1}^n x_j / n \dots(3)$$

$$S = \sqrt{ \sum_{j=1}^n x_j^2 / n - (\bar{X})^2 } \dots(4)$$

Where x_j is the value of dNDVI, w_{ij} is the Spatial Weigh between i and j , n is the count of the whole image. Statistically significant samples were determined by calculating the Z score based on Getis-Ord G_i^* statistics (<https://www.esri.com/en-us/arcgis/products/arcgis-pro/resources>).

RESULTS AND DISCUSSION

Statistical Analysis of NDVI

Fig. 2 (a) and (b) show spatial distribution maps of the NDVI of Xiamen Island before and after the typhoon. Fig. 2(c) shows the change ratio of vegetation at each level of NDVI before and after the typhoon. The post-typhoon image was taken half a month after the typhoon landed, and grass or crops might have been artificially restored during this period. The average NDVI of all pixels (except the water) of Xiamen Island before the typhoon was 0.3088, and that after the typhoon was 0.2814, reflecting a decrease by 0.0276. The most obvious feature of abrupt canopy detected through optical remote sensing was the loss of leaves, which was directly related to the decrease of NDVI. Although the overall change of NDVI was not large, NDVI tended to be saturated under a high leaf area index, and hence relatively small changes may reflect larger changes on the ground from satellite remote sensing images (Carlson & Ripley 1997).

The area without any vegetation cover (NDVI <0.05) increased by 1159.7 ha according to statistics. Compared with the area before the typhoon, the area without any vegetation cover increased by 17.55-25.67% with a range of 46.28%, accounting for 8.12% of the entire study area. In terms of decreased NDVI, areas with low vegetation coverage showed the largest decrease with a value of 507.6

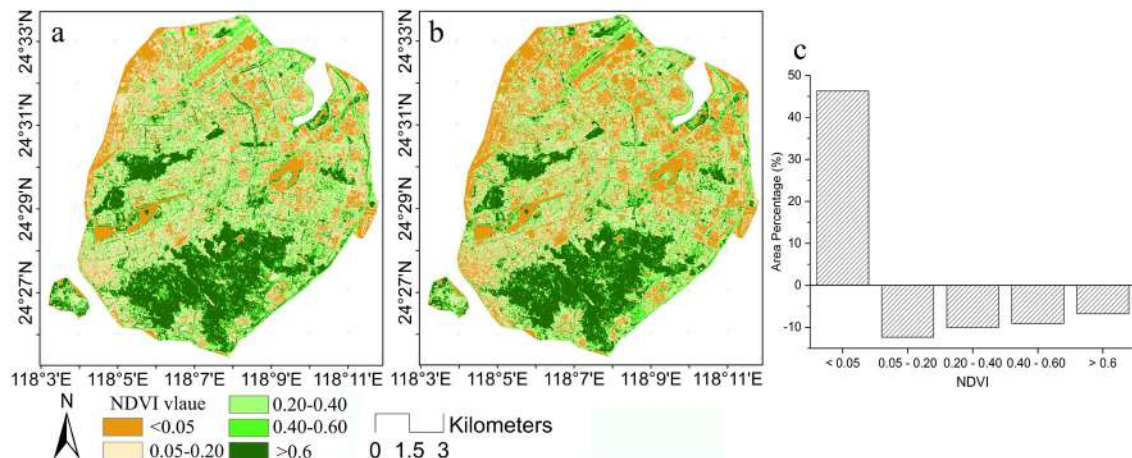


Fig. 2: NDVI (a) before and (b) after Typhoon Meranti; (c) change ratio of vegetation.

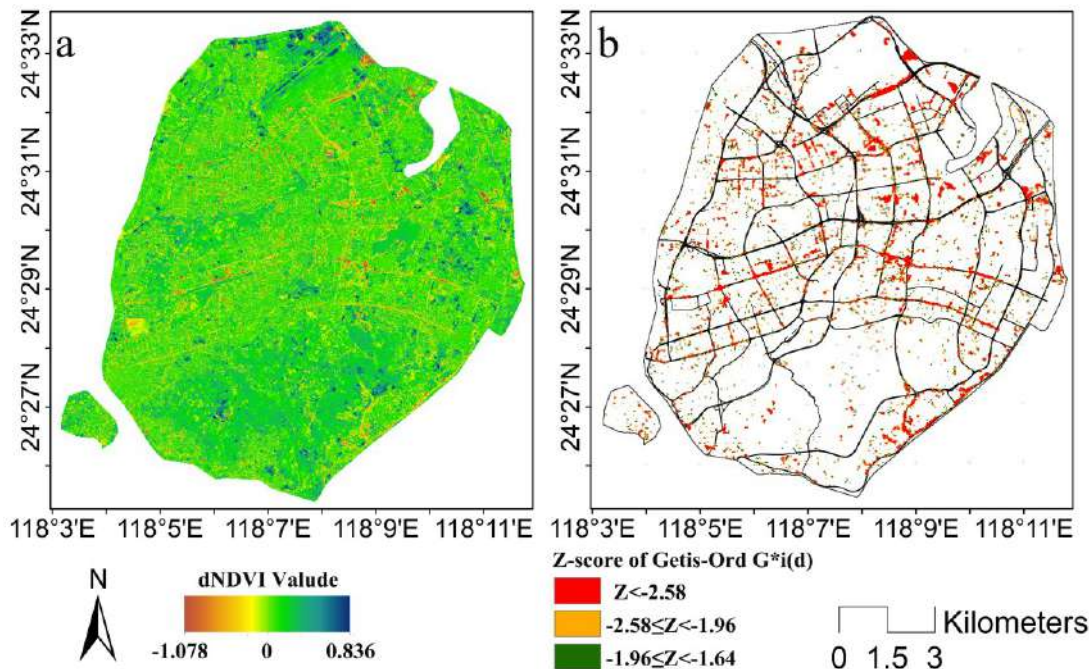


Fig. 3: (a) dNDVI (NDVI-pre subtracting NDVI-post); (b) the coldspots of reduced dNDVI.

ha. Areas with medium, high, and extremely high vegetation coverage decreased by 272.8 ha, 173.3 ha, and 206.0 ha, respectively. From the change ratio of the areas, the rate of change gradually decreased from low vegetation coverage to extremely high vegetation coverage, indicating that areas with low vegetation coverage were seriously affected by typhoons. Areas with high and extremely high vegetation coverage in Xiamen Island mainly include Xiamen Botanic Garden, Dongpingshan Park, and Xianyue Park in the south, Huawei Mountain and Bay Park in the west, the Convention and Exhibition Center and Wuyuan Wetland Park in the east, as well as the Gulangyu Island and some other small parks. Areas with low vegetation coverage area and medium vegetation coverage were mainly community green areas, sidewalk green areas, and small park vegetation. The above data showed areas with high vegetation coverage experienced a lower degree of damage than areas with low vegetation coverage. This result is consistent with the analysis results of Wang & Xu (2018).

Spatial Aggregation Analysis of dNDVI

Fig. 3 (a) shows the difference between the NDVI of the study area before and after the typhoon. dNDVI indicates the change rate of the decrease. As observed, NDVI mainly increased in areas near airports, large parks, and some residential communities, reflecting human intervention to

increase UGS. Areas with UGS decrease were consistent with the above NDVI analysis, mainly concentrated in streets and residential communities. Fig. 3(b) shows the coldspot map obtained by analyzing dNDVI data using the hotspot analysis function of ArcGIS software, revealing areas where damages to UGS were concentrated. According to the coldspot map, the damage to UGS in Xiamen Island was distributed in a striped pattern. In other words, heavily affected areas were concentrated along streets (street greening). This might be because the same street planting, tree species, as well as planting methods, such as the level of tree pit depth and tree crown trimming, were usually adopted in urban road vegetation.

Streets with significantly damaged UGS were mainly located in the central and northern parts of the island: Lianqian East Road, Luling Road, and Hubin North Road in the middle, and Fangzhong Road and Fangzhong North Road in the north. These roads have a common characteristic in that they all run east-west. Overall, damaged green areas were rarely concentrated along the north-south roads. The UGS of the southeast section of Huandao East Road showed prominent concentrated damage. However, the sidewalk green space on Xianyue Road, which is the main road running parallel to Hubin North Road with a distance of about 800 m, was not significantly damaged. The distance of Xianyue Road to the typhoon path was farther than that of the southeast

section of Huandao East Road, but the southeast section of Huandao East Road did not show concentrated vegetation damage. We also observed prominent concentrated damage to the green space at the crossroads. The degree of typhoon damage to UGS was related to not only the distance of the road from the typhoon path and wind direction, but also the type of trees and the size of the tree canopy, depth of root system, planting space, and plant conditions.

CONCLUSION

This study investigated the spatial pattern of the damage caused by Typhoon Meranti to the UGS of Xiamen Island, mainly using vegetation index and hotspot analysis. The vegetation index showed that the typhoon seriously damaged the vegetation of Xiamen Island and increased the area without vegetation by 1159.7 ha. Using the coldspot map generated through hotspot analysis, the distribution of areas with concentrated UGS damage could be rapidly determined. The precise spatial aggregation of areas in Xiamen Island affected by Typhoon Meranti could be obtained through the hotspot analysis. From the overall perspective of the spatial pattern, areas with severely damaged UGS were distributed in strips, indicating that road greening was seriously damaged. In terms of direction, areas with severely damaged UGS were more concentrated along east-west roads than along north-south roads. The distribution of severe damage to UGS was not centralized in large parks and other places in high vegetation areas. The determined spatial pattern of the damage caused by Typhoon Meranti to the UGS of Xiamen Island provides a spatial planning basis for urban construction and garden planning of coastal cities similar to Xiamen Island.

ACKNOWLEDGMENTS

This research was financially supported by Scientific and Technological Innovation Programs of Higher Education Institutions in Shanxi, China (Grant No. 2020L0751).

REFERENCES

- Ashcroftj, P.M., Cattj, J.A., Curran, P.J., Mundenj, J. and Webster, R. 1990. The relation between reflected radiation and yield on the broad back winter wheat experiment. *Int. J. Remote Sens.*, 11(10): 1821-1836.
- Barrell, J. and Grant, J. 2013. Detecting hot and cold spots in a seagrass landscape using local indicators of spatial association. *Landsc. Ecol.*, 28(10): 2005-2018.
- Carlson, T.N. and Ripley, D.A. 1997. On the relation between NDVI, fractional vegetation cover, and leaf area index. *Remote Sens. Environ.*, 62(3): 241-252.
- Defries, R.S. and Townshend, J.R. 1994. NDVI-derived land cover classifications at a global scale. *Int. J. Remote Sens.*, 15(17): 3567-3586.
- Getis, A. and Ord, J.K. 1992. The analysis of spatial association by use of distance statistics. *Geogr. Anal.*, 24(3): 189-206.
- Lee, M.F., Lin, T.C., Vadeboncoeur, M.A. and Hwong, J.L. 2008. Remote sensing assessment of forest damage in relation to the 1996 strong typhoon Herb at Lienhuachi experimental forest, Taiwan. *Forest Ecol. Manag.*, 255(8-9): 3297-3306.
- Main-Knorn, M., Pflug, B., Louis, J., Debaecker, V., Müller-Wilm, U. and Gascon, F. 2017. Sen2Cor for Sentinel-2, 3: 111
- Mayer, B. and Kylling, A. 2005. Technical note: The libRadtran software package for radiative transfer calculations - description and examples of use. *Atmos. Chem. Phys.*, 5(7): 1855-1877.
- Patel, K.A., Davis, S.D., Johnson, R. and Esther, C.R. 1995. Local spatial autocorrelation statistics: Distributional issues and an application. *Geogr. Anal.*, 27(4): A3288-A3288.
- Peeters, A., Zude, M., Käthner, J., Ünlü, M., Kanber, R. and Hetzroni, A. 2015. Getis-Ord's hot- and cold-spot statistics as a basis for multivariate spatial clustering of orchard tree data. *Comp. Electr. Agric.*, 6: 5-15.
- Rossi, E., Rogan, J. and Schneider, L. 2013. Mapping forest damage in northern Nicaragua after Hurricane Felix (2007) using MODIS enhanced vegetation index data. *GISci. Remote Sens.*, 50(4): 385-399.
- Wang, M. and Xu, H. 2018. Remote sensing-based assessment of vegetation damage by a strong typhoon (Meranti) in Xiamen Island, China. *Nat. Haz.*, 93(3): 1231-1249.
- Wang, W., Qu, J.J., Hao, X., Liu, Y. and Stanturf, J.A. 2010. Post-hurricane forest damage assessment using satellite remote sensing. *Agric. Forest Meteorol.*, 150(1): 122-132.
- Wu, K.S., He, Y., Chen, Q.J. and Zheng, Y.M. 2020. Analysis of the damage and recovery of typhoon disaster based on UAV orthograph. *Microelectron. Reliab.*, 107(2019): 113337.
- Zhang, X., Wang, Y., Jiang, H. and Wang, X. 2013. Remote-sensing assessment of forest damage by Typhoon Saomai and its related factors at the landscape scale. *Int. J. Remote Sens.*, 34(21): 7874-7886.



Evolution of Technologies for Cadmium Remediation and Detoxification

Sneh Lata* and Sukhminderjit Kaur*†

*University Institute of Biotechnology, Chandigarh University, Gharuan, India

†Corresponding author: Sukhminderjit Kaur: sukhminderjit.uibt@cumail.in

Nat. Env. & Poll. Tech.
Website: www.neptjournal.com

Received: 18-06-2021

Revised: 10-08-2021

Accepted: 20-08-2021

Key Words:

Cadmium remediation

Vitrification

Phytoremediation

Nanocomposites

Iron nanoparticles

ABSTRACT

Heavy metal pollution is one of the most serious global environmental concerns. As a result, the current research includes an overview of technologies that are being developed for remediating or eliminating such contaminants from the environment, such as physical and chemical approaches, as well as their ineffectiveness. A wide range of minute species was discovered for their potential to tolerate, resist, accumulate and absorb heavy metals. But they all are naturally occurring species and need optimal conditions as well as a longer duration to grow. Thus, there is a need for more reliable, efficient, and productive techniques to address the issue. The use of nanoparticles for remediation has paved the way for more research in this subject and the development of useful technology to cope with problems. The evolution of technologies for heavy metal remediation, particularly cadmium, is discussed in this article because it is one of the most hazardous heavy metals that necessitates immediate attention.

INTRODUCTION

The expeditious urbanization and industrialization undoubtedly led to exceptional growth but also has directly affected the environment. As a result, the contamination and degradation of the whole ecosystem have become a major problem and a threat to all life forms especially to human beings (EPA 1990). The research in this field has also gained its speed, particularly in the area of risk associated with heavy metal dispersal in the food chain and their remedies. Heavy metals can be derived from multiple sources, including industrial effluents and mining sectors. As a result, researchers have developed a keen interest in recovering heavy metals from effluents and soil. Cadmium is used in many industries. Uses of cadmium are shown in Fig. 1.

Many clean-up techniques were proposed and practiced by many researchers which mainly include reverse osmosis and active sludge treatments. But these techniques also have many disadvantages like reduction in biodiversity and inhibitory effects on plant growth (Chaudhury et al. 1999). Researchers have a lot of options when it comes to using microorganisms to change or convert heavy metal toxins into a less harmful state. Bioremediation has a few drawbacks, the most significant of which is the presence of toxic microbial metabolites that might interfere with the entire remediation process, resulting in heavy metal non-degradation. However, as compared to alternative physical and chemical processes, this technology is a better option in terms of environmental friendliness and economic effectiveness.

HEAVY METALS SOURCES IN THE ENVIRONMENT

Natural and Anthropogenic Sources

Heavy metals have their origins in rocks. Heavy metals were absorbed into rocks as a result of physical damage caused by bad weather. They are found in soils as metal sulfides in combination with copper and iron sulfides. Similarly, cadmium is mostly created as a by-product of the zinc refining process, as it is with the zinc ore sphalerite. As a result, cadmium is found in water, soil, and the air. Heavy metals make their way into sewage and reservoirs from the surface of the soil.

There are many human-induced sources of heavy metals which mainly include: sewage sludge, paper industries, pesticides, batteries, tanneries, fertilizer industries, wastewater irrigation. Cadmium is mainly present in phosphate fertilizers. The use of phosphate fertilizers in fields led to contamination of water and soil with cadmium which ultimately takes Cd into the food chain. The sources of cadmium are shown in Fig. 2.

Human Cadmium Exposure and Its Toxicity

Prolonged exposure to cadmium through water, food, and soil is very toxic which leads to cancer. Humans are exposed to cadmium mainly through ingestion or inhalation. High cadmium levels can be measured in different body parts like hair, nails, urine, saliva, and blood. The major sources of cadmium toxicity are contaminated food, beverages,

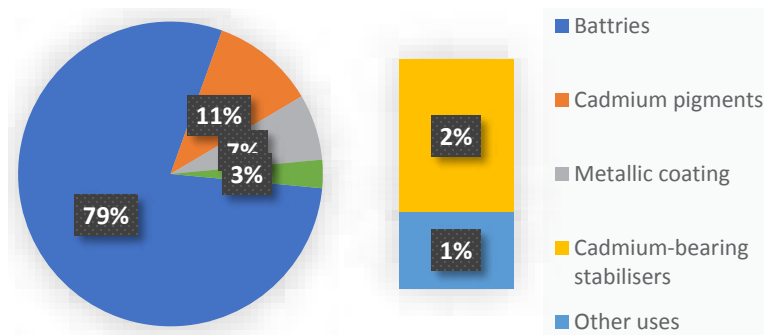


Fig. 1: Cadmium uses in industries (Sharma et al. 2015).

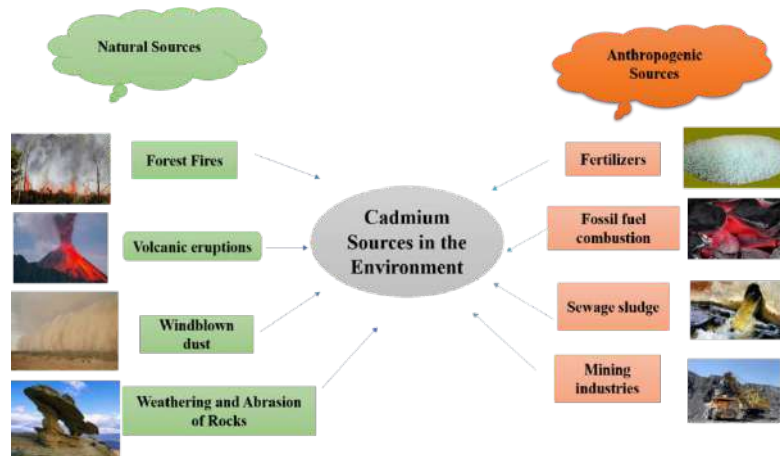


Fig. 2: Natural and anthropogenic sources of cadmium (Thornton 1992).

cigarette smoking (Friberg 1983), and welding purposes. The cadmium can be detoxified with the help of EDTA and other chelates. Antidotes with nanoparticles are required for patients with cadmium toxicity. Cadmium exposure to humans is depicted in Fig. 3.

The toxic nature of cadmium imposes harmful effects on human health. It mainly targets the kidney, bones, and reproduction system. Toxicity and health effects are depicted in Fig.4.

Technologies for Remediation and Detoxification

Physical Methods of Heavy Metal Remediation

This technique of remediation mainly involves the following methods:

Soil isolation: The onsite remediation of heavy metals is accomplished by soil isolation. It essentially entails the separation of polluted and uncontaminated soil. However, this technique is not comprehensive; several other engineering processes are needed. This technique restricts the other contaminants in a specified area. This method is used only when

other methods are not economically feasible. Subsurface barriers are used in this technique to limit surface water and groundwater flow and to extract contaminated water from the soil. These barriers are used to keep uncontaminated water from flowing into contaminated water (Dawson 1996). Examples of subsurface barriers are grout curtains, sheet piles, and slurry walls. The barriers can be employed surrounding the contaminated site, downstream or upstream. To prevent the infiltration of contaminated water, these barriers are used in combination with the capping system to maintain the continuity of isolation of contaminated soil. Clay can be used underneath the contaminated soil.

Soil replacement: Before 1984, the soil replacement off-site removal method was commonly used for the removal of various contaminants from soil. In this method, the contaminated soil is replaced from the uncontaminated soil. This technique enhances soil efficiency by diluting the concentration of heavy metals. It can be done in two ways- 1. Soil spading 2. Importing new soil to the site. In spading technique, the soil is dug thoroughly and heavy metals are spread there. But in the 2nd method, the new clean soil is imported to the

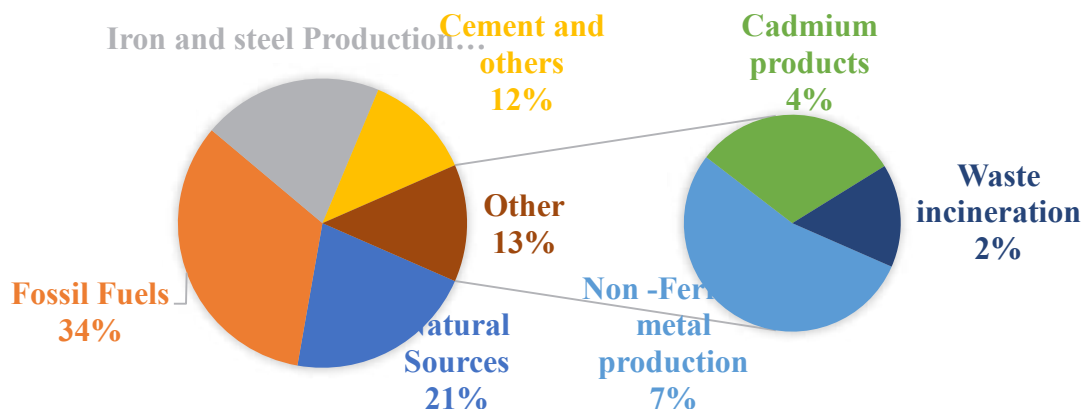


Fig. 3: Human cadmium exposure (Jaishankar et al. 2014).

contaminated site. The purpose of both methods was simply to dilute the concentration of heavy metal at the contaminated site. The main disadvantage of the soil replacement method is high labor work. But it is appropriate and efficient for removing contaminants from the soil in a small area.

Electrokinetic remediation: This remediation method involves the pouring of contaminated soil into the electrolytic tank and then applying an electric field gradient of suitable intensity. The principle behind this process is electro-migration and electrophoresis. A suitable electrolyte is required to efficiently remove the contaminated soil. The efficiency also depends upon the metal to be remediated. Ethylenediamine disuccinate (EDDS) was used to decontaminate cadmium and lead (Suzuki et al. 2014). This method is very easy to install and perform which makes it economical in nature. Also, it does not change the basic nature of the soil. The maintenance of soil pH is the limiting factor as pH cannot be easily maintained.

Vitrification: To restrict the mobility of heavy metals, a vitreous material can be produced inside the soil by applying

high temperatures (Mallampati et al. 2015). This technique is easy to apply than other classical and physical remediation techniques. Both organic and inorganic contaminants can be remediated with the help of this technique. Vitrification is conducted in two different means, in-situ and ex-situ. In the in-situ technique, the electric current is provided by using an array of electrodes inside the soil. Also, in-situ is more favorable as compared to ex-situ due to its less energy requirements and low cost. Ex-situ technique involves many stages like excavation, mixing, pretreatment, melting, feeding, and casting of the melted product (Dellisanti et al. 2009). The efficiency of the technique can be enhanced by mixing additives. This technique is mainly suitable for pollution of large scale.

Chemical Methods of Heavy Metal Remediation

This technique of remediation uses reagents and chemicals to remediate heavy metals. It mainly involves the following methods:

Soil washing: In this technique, the heavy metals are leached out of the soil by using chemicals and reagents. Chelators

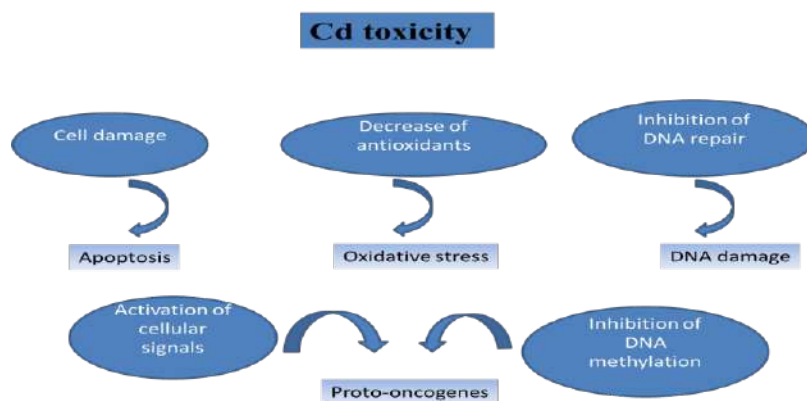


Fig. 4: Cadmium toxicity in human beings (Rafati et al.2017).

like EDTA are added to immobilize toxic elements in a less bioavailable form. During this technique, the contaminated part of the soil is dug out and then treated with the appropriate extractants. The choice of extractant depends upon the soil and the heavy metal to be extracted out. Both soil and extractant are then mixed thoroughly. Furthermore, the soil is transferred to the liquid phase through techniques like precipitation, absorption or chelation, etc. Soil washing is a widely used method of remediation of heavy metals due to its quality of completely removing the toxins and speedy performance. A huge number of reagents and chemicals are used such as EDTA, organic acids, cyclodextrins, and surfactants. Coal ash and EDTA have become popular materials for the extraction of heavy metals. The soil wash method was developed for cadmium-contaminated paddy fields (Kimura et al. 2007).

Immobilization techniques: It involves confining heavy metals in soil by using immobilizing agents. Many methods have been employed for the immobilization process such as adsorption, precipitation, and complexation. Organic and inorganic agents can be used for immobilizing heavy metals in contaminated soil. It mainly includes clay, zeolites, minerals, cement, etc. Heavy metals can be immobilized on solid particles to reduce their availability in soil. Organic agents and organic amendments are widely used which mainly includes biosolids and animal manures. Negative effects of biosolid application in the soil were reported (Cele et al. 2016). However, there are positive effects too as it is the best adsorbent for heavy metal stabilization in the soil (Venegas et al. 2015). Remediation methods are shown in Fig. 5.

Biological Methods of Heavy Metal Remediation

Biological methods mainly include approaches like bioremediation which uses living microorganisms as well as plants to remove pollutants heavy metals from the environment. Bioremediation itself has two approaches namely in-situ and ex-situ. In-situ is the removal of heavy metals on the contaminated site and ex-situ is treating them somewhere else. Both the approaches are being summarized in Table 1.

Table 1: Approaches of bioremediation.

Technology	Benefits	Limitations
In-situ	Cost-effective Treats both water and soil Can easily deal with dissolved and sorbed pollutants Minimal site disruption	Long treatment time Difficulty in the monitoring process Toxicity
Ex-situ	Low cost Can be done on-site pH can be controlled	Space requirements Limited groundwater depth (90-300 cm) Mass transfer problems

Many microorganisms and plants are reported to date for effective removal of cadmium from contaminated sites. A few recent studies have been mentioned below in Table 2.

Nanomaterials for Heavy Metal Remediation

Out of these methods, the biological method of wastewater treatment is widely accepted as they use efficient microorganisms but they are often slow and expensive. As a result, there is a pressing need for practical methods for long-term water management to achieve water security. Nanotechnology's progress has been noted recently, and its potential for removing pollutants from wastewater has been demonstrated. Nanotechnology uses nanoparticles with a size of a few nanometers to treat groundwater, surface water, drinking water, and industrial effluents, providing a new way to eliminate toxins from wastewater and lessen its impact on people. For the removal of heavy metals, various nanomaterials have been developed to date. A few of their types are presented in Fig. 6.

The attractive features of nanomaterials are high heavy metal removal rates, also they are cost-effective and easy to regenerate. With this context, a few newer nanotechnologies are discussed below

Carbon-based nano adsorbents: The main process by which the removal of heavy metals is achieved is adsorption. Carbon nanotubes are the most popular carbonaceous nanomaterials because of their high adsorption rates, mechanical strength, and chemical resistivity (Lee et al. 2012). The hydrophobicity of CNT graphite surfaces causes them to aggregate. The presence of grooves and interstitial spaces in the aggregates capture the organic molecules of wastewater through covalent bonding, hydrogen bonding, and electrostatic interactions (Rao et al. 2007). Due to electrostatic interactions and chemical bonding between surface functional groups, large metals or organic molecules adsorb onto the

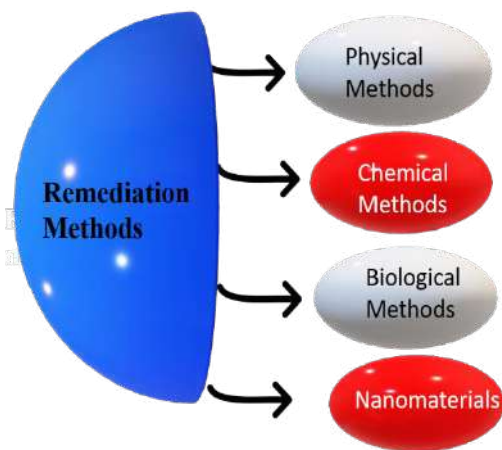


Fig. 5: Remediation methods



Fig. 6: Types of nanoparticles.

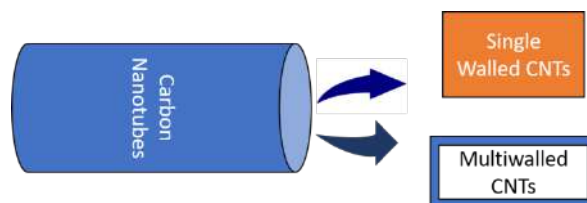


Fig. 7: Types of carbon nanotubes.

pores and become stuck on CNTs (Zhang et al. 2010). CNTs are of two types as depicted in Fig. 7 given below:

a. Single-walled carbon nanotubes (SWCNT): SWCNTs are constructed using a hollow tube having one atom thick wall made of a single layer of graphene, called one-dimensional carbon nanomaterials. 1-D SWCNT has a unique structure with porosity and high surface area. Many successful studies are being conducted by using SWCNTs for wastewater treatment. Adsorption of cadmium, copper, lead, and mercury was investigated using SWCNTs-COOH, SWCNTs-OH, and SWCNTs-NH₂ and it was observed that SWCNTs-COOH was having high adsorption capacity (150-230%) as that of others stated earlier (Anitha et al. 2015). SWCNTs nanocomposite designed with polysulfone showed 94% removal of

extremely toxic heavy metals i.e., lead (Gupta et al. 2015). Thus, the above studies revealed that carbon nanotubes are promising tools for the removal of heavy metals from contaminated wastewater.

b. Multiwall carbon nanotubes (MWCNTs): MWCNTs have multiple layers of graphene. Numerous nanocomposites of MWCNTs were designed to remove heavy metals. Heavy metals such as As, Cr, Pb, Ni, and Cu were successfully conducted by using MWCNTs-Fe₂O₃, MWCNTs-MnO₂-Fe₂O₃, MWCNTs-Al₂O₃, MWCNTs-ZrO₂, and MWCNTs-Fe₃O₄ nanocomposites (Yang et al. 2009). MWCNTs which were oxidized with acid (Chemically) were studied for sorption of lead, cadmium, and chromium (Moosa et al. 2015). Plasma oxidized MWCNTs are known for having more sorption efficiency than chemically oxidized as they have more oxygenated functional groups (Li et al. 2009). Additionally, plasma-oxidized nanotubes are recyclable and reusable.

Metal oxide-based nano adsorbents: Metal oxide adsorbents are capable and efficient enough to remove heavy metals from wastewater. The nanometal oxides (NMOs)

Table 2: Recently studied microorganisms and plants for remediation.

Bacterial Strains	Targeted heavy metals	References
<i>Cupriavidus necator</i>	Cadmium, Copper, and Zinc	Vicentin et al. (2018)
<i>Pseudomonas sp.</i> Al-Dhabi-126	Cadmium	Al-Dhabi et al. (2019).
<i>B. cereus</i> A2 and <i>P. aeruginosa</i> PS	Cadmium and lead	Makki et al. (2019)
<i>Bacillus sp.</i>	Cadmium and lead	Heidari and Panico (2020)
<i>Cupriavidus sp.</i>	Cadmium	Minari et al. (2020)
<i>Bacillus sp.</i> TZ5	Cadmium	Ma et al. (2020)
<i>Lactobacillus plantarum</i> MF042018	Cadmium and Lead	Ameen et al. (2020)
Plants	Targeted heavy metals	References
<i>Acacia nilotica</i>	Cadmium	Shabir et al. (2018)
<i>Atriplex lentiformis</i>	Cadmium	Eissa and Abeer (2018)
<i>Boehmeria nivea</i>	Cadmium	Pan et al. (2019)
<i>Noccaea caerulea</i>	Cadmium and Zinc	Kozhevnikova et al. (2020)
<i>Sedum alfredii</i>	Cadmium	Wu et al. (2020)
<i>Youngia japonica</i>	Cadmium	Yu et al. (2020)

which are commonly used are iron oxides, aluminum oxides, cerium oxides, titanium oxides, etc. as depicted in Fig. 8. Their shape and size play an important role in making them suitable nano adsorbents for heavy metals. Many methods are being employed to control their shape and make them highly stable (Cushing et al. 2004). The high adsorption ability of NMOs is due to the reaction of oxygen molecules of metal oxides with heavy metals.

There are numerous findings narrating the importance and extreme use of metal oxides for removing heavy metals. Few are depicted in Table 3.

Magnetic nanomaterials: Magnetic nanoparticles offer a faster and more economical approach for heavy metal removal from wastewater. They mainly comprise two components namely magnetic material (Iron, Cobalt) and a chemical component with the ability to remove metals. Super magnetic particles are magnetic particles with a smaller size that are highly effective for wastewater treatment. The nanoparticles' magnetic property allows them to easily separate the adsorbents and reuse them in the system. Structural components are depicted in Fig. 9.

Among all magnetic nanoparticles studied to date, Fe_3O_4 magnetic nanoparticles were widely used and modified for cadmium removal from wastewater. Few findings are mentioned in Table 4.

Polymer-based nanocomposites: Polymer-based composites offer a reliable approach for the removal of heavy metals because of internal environment-friendly and decomposable features. They present superior physical, chemical, mechanical properties, pore size distribution, rigidity, compatibility as well as regeneration (Mahmoodi et al. 2013). Polyaniline-based nano adsorbents and their derivatives have recently acquired popularity. As shown in Fig. 10, polymeric adsorbents can be divided into carbohydrate and synthetic

polymers. Carbohydrate polymers include starch, cellulose, dextran, alginate, and other carbohydrates that are used to remove heavy metals from wastewater.

These polymers have functional groups like hydroxyl, amine, amide, and carboxyl which helps in removing heavy metals. Alginate offers the highest adsorption capacity due to carboxyl functional groups (Zare et al. 2018). However, the absorption ability of functional groups can be enhanced by using monomers such as carboxylic and amino groups which bind to polymeric matrices and help in targeting the contaminants (Mahmoodi et al. 2013). Numerous synthetic polymers have been used for wastewater treatment such as poly (styrene-alt-maleic anhydride) and poly (N-vinyl capro-

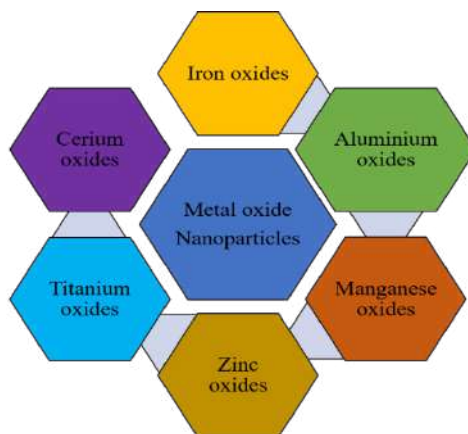


Fig. 8: Types of metal oxide nanoparticles.

Table 3: Metal oxides for the removal of heavy metals.

Metal Oxide Nanoparticles	Targeted heavy metals	References
Aluminum Oxides	Cd (II) ions	Afkhami et al. (2010)
TiO ₂ nanoparticles	Cd (II) ions	Engates and Shipley (2011)
Iron oxide	Cd (II) ions	Al-Saad et al. (2012)
Zinc oxide (ZnO) nanoparticles	Cd (II) ions	Sheela et al. (2012)
Manganese dioxide (MnO ₂)	Cd (II) ions	Luo et al. (2013)
Copper oxide particles	Cd (II), Pb (II)	Taman et al. (2015)
Copper oxide nanoparticles	Cd (II), Ni ions	Hassan et al. (2017)

Table 4: Recently synthesized magnetic nanoparticles for heavy metal removal.

Magnetic Nanoparticles	Targeted heavy metals	References
Aminopropyltriethoxy-silane Coated Fe ₃ O ₄ nanoparticles (MNP)	Cd ⁽²⁺⁾ , Pb ⁽²⁺⁾	Chen et al. (2016)
Superparamagnetic Iron Oxide	Cadmium	Goher et al. (2017)
Magnetite Fe ₃ O ₄ nanoparticles	Cr (VI)	Rivera et al. (2019)
Fe ₃ O ₄ magnetic nanoparticles	Zinc, Cadmium and Lead	El-Dib et al. (2020)
Silica coated Fe ₃ O ₄ -MNPs	Sr ²⁺	Salwa et al. (2020)
Magnetic zeolite nanocomposite	Cd (II), Zn (II)	Shubair et al. (2019)
Magnetic Fe ₃ O ₄ @SiO ₂ -ethylenediamine tetra acetic acid	Pb (II), Cu (II)	Gong and Tang (2020)
Fe ₃ O ₄ @SiO ₂ Nanoparticles	Cu ²⁺ Ions	Irfai et al. (2020)

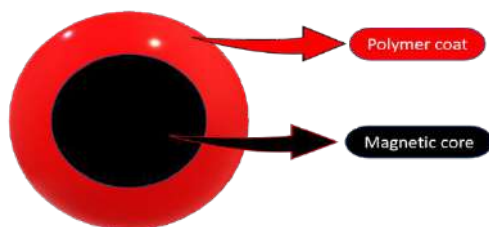


Fig. 9: Components of magnetic nanoparticles.

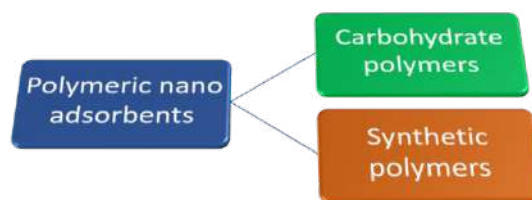


Fig. 10: Types of polymeric adsorbents.

lactam-co-maleic acid) (Azarudeen et al. 2015, El-Aassar et al. 2016). Synthetic polymers have two main constituents namely polymer matrix and chelating groups. The PACA polymer is widely used as it has maximum adsorption capacity. The carbohydrate and synthetic polymers used to remove heavy metals are depicted in Table 5.

Zero valent nanoparticles: Zero valent ions are recently being used to remove heavy metals due to their enhanced reactivity and small size. The ordinate usage of zero-valent nanoparticles has increased owing to its high specific surface area (Galdames et al. 2020). The reaction of ZVI nanoparticles with heavy metals was investigated by looking at several parameters such as pH, dose, and the heavy metal's initial concentration (Chen et al. 2008). The potential adsorption of Pb⁽²⁺⁾, Cu⁽²⁺⁾, and Zn⁽²⁺⁾ ions was examined using nanoscale zerovalent iron beads made from polyvinyl alcohol and guar gum (Zhang et al. 2019). Zero-Valent iron nanoparticles are extensively used for the decontamination of wastewater. It is reported to have a core-shell in the structure that contains oxidized iron (Phenrat et al. 2015)

Nano zero-valent iron nanoparticles were proved to be effective in lead removal (Ahmed et al. 2017). Nano dis-

Table 5: Carbohydrate and synthetic polymers used for removal of heavy metals.

Carbohydrate based polymers	Targeted metals	References
Alginate	Fe, Ag	Lu et al. (2015)
Starch	As, Pb	Cheng and Ou (2016)
Cellulose	Cd, Pb	Wang et al. (2013)
Synthetic polymers	Targeted metals	References
Polyethylene terephthalate, polyethylene, and polystyrene	Pb	Alsewailem and Al-Dzhilil (2016)
β -cyclodextrin polymers	Pb (II), Ni (II)	Yu et al. (2018)
Metal ion-imprinted polymers	Ni ⁽²⁺⁾ or Co ⁽²⁺⁾	Işıkver and Baylav (2018)
PVA with multiwalled carbon nanotubes	Pb	Zulfiqar et al. (2020)

persed powders of zero-valent iron were synthesized and effectively used for the removal of Cu (II), Cd (II), Co (II), Zn (II), Cr (VI) (Kholodko et al. 2021). The removal of cesium was also achieved by using nanoparticles-zeolite composites (Eljamal et al. 2019). Zero-valent iron nanoparticles were also reported to have the potential to remove Cd (II) and Pb (II) ions (Danila et al. 2018). Zero-Valent iron nano adsorbents are employed to remove and remediate a wide variety of heavy metals as depicted in Fig. 11

Besides iron nanoparticles, zero-valent silver nano adsorbents were synthesized and studied for their application in the decontamination of wastewater by removing Hg²⁺ ions (Sundarajan et al. 2013). Effective removal of cadmium was achieved by zero-valent silver nanoparticles which were synthesized using *Benjamina* leaves extract (Al-Qahtani 2017) and observed that the rate of removal increased with the dosage of bio adsorbent.

CONCLUSION

The escalated urbanization and industrialization led to the massive generation of effluents with toxic pollutants such as cadmium in them. Thus, it is at utmost priority to remove contaminants and achieve water security too. In this regard, the use of nanomaterials is highly recommended owing to its numerous benefits not only to detoxify the wastewater but it is eco-friendly and cost-effective also. Many researchers are



Fig. 11: Applications of zero-valent iron nano adsorbents.

keen to develop creative, effective, and innovative approaches to deal with the problem and attain sustainability, such as the application of the green synthesis concept. The unique features of nano adsorbents have added a new dimension to wastewater treatment, however further industrial and pilot-scale research is needed to evaluate the total efficiency of nanomaterials for cadmium removal.

ACKNOWLEDGMENT

The authors are grateful to the University Institute of Biotechnology, Chandigarh University, Gharuan for providing a platform for study and valuable guidance.

REFERENCES

- Al-Dhabi N.A., Esmail G.A., Mohammed Ghilan A.K. and Valan Arasu M. 2019. Optimizing the management of cadmium bioremediation capacity of metal-resistant *Pseudomonas sp.* strain Al-Dhabi-126 isolated from the industrial city of Saudi Arabian environment. *Int. J. Environ. Res. Public Health*, 16(23): 4788. <https://doi.org/10.3390/ijerph16234788>
- Ameen, F.A., Hamdan, A.M. and El-Naggar, M.Y. 2020. Assessment of the heavy metal bioremediation efficiency of the novel marine lactic acid bacterium, *Lactobacillus plantarum* MF042018. *Sci. Rep.*, 10(1): 111-121.
- Anitha, K., Namsani, S. and Singh, J.K. 2015. Removal of heavy metal ions using a functionalized single-walled carbon nanotube: a molecular dynamics study. *J. Phys. Chem. A.*, 119(30): 8349-8358. <https://doi.org/10.1021/acs.jpca.5b03352>
- Afkhami, A., Tehrani, M.S. and Bagheri, H. 2010. Simultaneous removal of heavy metal ions in wastewater samples using nano-alumina modified with 2,4-dinitrophenylhydrazine. *J. Hazard. Mater.*, 181(1-3): 836-844.
- Al-Saad, K.A., Amr, M.A., Hadi, D.T., Arar, R.S., AL-Sulaiti, M.M., Abdulmalik, T.A., Alsahamary, N.M. and Kwak, J.C. 2012. Iron oxide nanoparticles: applicability for heavy metal removal from contaminated water. *Arab. J. Nucl. Sci. A.*, 45(2): 335-346.
- Azarudeen, R.S., Riswan Ahamed, M.A., Thirumarimurugan, M., Prabu, N. and Jeyakumar, D. 2015. Synthetic functionalized terpolymeric resin for the removal of hazardous metal ions: synthesis, characterization, and batch separation analysis. *Poly. Adv. Technol.*, 27(2): 235-244. <https://doi.org/10.1002/pat.3626>.
- Alsewailem, F.D. and Al-Dzhlil, S.A. 2016. Synthetic polymers and their blends for removing lead from aqueous solutions. *J. Water. Chem. Technol.*, 38: 89-95. <https://doi.org/10.3103/S1063455X16020053>
- Ahmed, M.A., Bishay, S.T., Ahmed, F.M. and El-Dek, S.I. 2017. Effective Pb²⁺ removal from water using nanozerovalent iron stored 10 months. *Appl. Nanosci.*, 7(7): 407-416. <https://doi.org/10.1007/s13204-017-0581-z>
- Al-Qahtani, K.M. 2017. Cadmium removal from aqueous solution by green synthesis zero-valent silver nanoparticles with *Benjamina* leaves extract. *Egypt. J. Aquat. Res.*, 43(4): 269-274. <https://doi.org/10.1016/j.ejar.2017.10.003>
- Chaudhury, T.M., Hill, L., Khan, A.G. and Kuek, C. 1999. Colonization of Iron and Zinc Contamination Dumped Filter Cake Waste By Microbes, Plants, and Associated Mycorrhizae. In: Ming, M.H., Wong, J.W.C. and Baker, A.J. (eds.), *Remediation and Management of Degraded Lands*, CRS Press, Boca Raton, Florida, USA, pp. 275-283.
- Cele, E.N. and Maboeta, M. 2016. A greenhouse trial to investigate the ameliorative properties of biosolids and plants on physicochemical conditions of iron ore tailings: Implications for an iron ore mine site remediation. *J. Environ. Manag.*, 165: 167-174. <https://doi.org/10.1016/j.jenvman.2015.09.029>
- Cushing, B.L., Kolesnichenko, V.L. and O'Connor, C.J. 2004. Recent advances in the liquid-phase syntheses of inorganic nanoparticles. *Chem. Rev.*, 104(9): 3893-3946. <https://doi.org/10.1021/cr030027b>
- Chen, D., Awut, T., Liu, B., Ma, Y., Wang, T. and Nurulla, I. 2016. Functionalized magnetic Fe₃O₄ nanoparticles for removal of heavy metal ions from aqueous solutions. *E-Polymers*, 16(4): 313-322. <https://doi.org/10.1515/epoly-2016-0043>
- Cheng, R. and Ou, S. 2016. *Textbook of Polymer Science: Research Advances, Practical Applications, and Educational Aspects: Application of Modified Starches in Wastewater Treatment*. 1st edition. Formatex Research Center, Badajoz, Spain.
- Chen, S.Y., Chen, W.H. and Shih, C.J. 2008. Heavy metal removal from wastewater using zero-valent iron nanoparticles. *Water Sci. Technol.*, 58(10): 1947-1954. <https://doi.org/10.2166/wst.2008.556>
- Dawson, J. 1996. Barrier containment technologies for environmental remediation applications. *J. Hazard. Mater.*, 51(1-3): 256.
- Dellisanti, F., Rossi, P.L. and Valdrè, G. 2009. In-field remediation of tons of heavy metal-rich waste by Joule heating vitrification. *Int. J. Miner. Process.*, 93(3-4): 239-245.
- Danila, V., Vasarevicius, S. and Valskys, V. 2018. Batch removal of Cd(II), Cu(II), Ni(II), and Pb(II) ions using stabilized zero-valent iron nanoparticles. *Energy Procedia*, 147: 214-219. <https://doi.org/10.1016/j.egypro.2018.07.062>
- Environmental Protection Agency (EPA). 1990. Office of emergency and remedial response: EPA/540/2-89/054. *Remediation J.*, 1(1): 108-109.
- Eissa, M.A. and Abeed, A.H.A. 2018. Growth and biochemical changes in quail bush (*Atriplex lentiformis* (Torr.) S.Wats) under Cd stress. *Environ. Sci. Pollut. Res.*, 26(1): 628-635. <https://doi.org/10.1007/s11356-018-3627-1>
- Engates, K.E. and Shipley, H.J. 2011. Adsorption of Pb, Cd, Cu, Zn, and Ni to titanium dioxide nanoparticles: effect of particle size, solid concentration, and exhaustion. *Environ. Sci. Pollut. Res. Int.*, 18(3): 386-395.
- El-Dib, F. I., Mohamed, D. E., El-Shamy, O. A. A. and Mishrif, M. R. 2020. Study the adsorption properties of magnetite nanoparticles in the presence of different synthesized surfactants for heavy metal ions removal. *Egypt. J. Pet.*, 29(1): 1-7. <https://doi.org/10.1016/j.ejpe.2019.08.004>
- El-Aassar, M.R., El-Kady, M.F., Hassan, H.S. and Al-Deyab, S.S. 2016. Synthesis and characterization of surface-modified electrospun poly (acrylonitrile-co-styrene) nanofibers for dye decolorization. *J. Taiwan Inst. Chem. Eng.*, 58:274-282. <https://doi.org/10.1016/j.jtice.2015.05.042>
- Eljamal, O., Shubair, T., Tahara, A., Sugihara, Y. and Matsunaga, N. 2019. Iron-based nanoparticles-zeolite composites for the removal of cesium from aqueous solutions. *J. Mol. Liq.*, 277: 613-623. <https://doi.org/10.1016/j.molliq.2018.12.115>
- Friberg, L. 1983. Cadmium. *Annu. Rev. Pub. Health.*, 4(1): 367-367.
- Gupta, S., Bhatiya, D. and Murthy, C. N. 2015. Metal removal studies by the composite membrane of polysulfone and functionalized single-walled carbon nanotubes. *Separation. Sci. Technol.*, 50(3): 421-429. <https://doi.org/10.1080/01496395.2014.973516>
- Goher, M.E.S., Emara, M.M., Abdo, M.H., Refaat Mah, N.M., Abdel-Sata, A.M. and El-Shamy, A.S. 2017. Cadmium removal from aqueous solution using superparamagnetic iron oxide nanosorbents on amberlite IR 120 H support. *J. Appl. Sci.*, 17(6): 296-305. <https://doi.org/10.3923/jas.2017.296.305>
- Gong, T. and Tang, Y. 2020. Preparation of multifunctional nanocomposites Fe₃O₄@SiO₂-EDTA and its adsorption of heavy metal ions in water solution. *Water Sci. Technol.*, 81(1): 170-177. <https://doi.org/10.2166/wst.2020.099>
- Galdames, A., Ruiz-Rubio, L., Orueta, M., Sánchez-Arzalluz, M. and Vilas-Vilela, J.L. 2020. Zero-valent iron nanoparticles for soil and groundwater remediation. *Int. J. Environ. Res. Pub. Health*, 17(16): 817. <https://doi.org/10.3390/ijerph17165817>

- Heidari, P. and Panico, A. 2020. Sorption mechanism and optimization study for the bioremediation of pb(ii) and Cd(II) contamination by two novel isolated strains Q3 and Q5 of *Bacillus sp.* Int. J. Environ. Res. Public Health, 17(11): 4059. <https://doi.org/10.3390/ijerph17114059>
- Hassan, K., Jarullah, A.A. and Saadi, S. 2017. Adsorbent for removal of Cd (II) and Ni (II) ions from a binary system. Int. J. Appl. Environ. Sci., 12(11): 1841-1861.
- Irfai, R.A., Roto, R. and Aprilita, N.H. 2020. Preparation of Fe₃O₄@SiO₂ nanoparticles for adsorption of waste containing Cu²⁺ ions. Key Eng. Mater., 840: 43-47. <https://doi.org/10.4028/www.scientific.net/kem.840.43>
- I ikver, Y. and Baylav, S. 2018. Synthesis and characterization of metal ion-imprinted polymers. Bull. Mater. Sci., 41: 49. <https://doi.org/10.1007/s12034-018-1578-2>
- Jaishankar, M., Tseten, T., Anbalagan, N., Mathew, B.B. and Beeregowda, K.N. 2014. Toxicity, mechanism, and health effects of some heavy metals. Interdiscip. Toxicol., 7(2): 60-72. <https://doi.org/10.2478/intox-2014-0009>
- Kimura, T., Takase, K. and Tanaka, S. 2007. The concentration of copper and a copper-EDTA complex at the pH junction formed in soil by an electrokinetic remediation process. J. Hazard. Mater., 143(3): 668-672.
- Kozhevnikova, A.D., Seregin, I.V., Aarts, M.G.M. and Schat, H. 2020. Intra-specific variation in zinc, cadmium, and nickel hypertolerance and hyperaccumulation capacities in *Noccaea caerulea*. Plant Soil, 452(1-2): 479-498. <https://doi.org/10.1007/s11104-020-04572-7>
- Kholodko, Y.M., Bondarieva, A.I., Tobilko, V.Y., Kovalchuk, I.A. and Komilovych, B.Y. 2021. Removal of Cu(II), Cd(II), Co(II), Zn(II), Cr(VI) from wastewater by stabilized nanoscale zero-valent iron. KPI Sci. News, 1. <https://doi.org/10.20535/kpissn.2021.1.217279>
- Lee, Z.H., Lee, K.T., Bhatia, S. and Mohamed, A. R. 2012. Post-combustion carbon dioxide capture: Evolution towards utilization of nanomaterials. Renew. Sustain. Energy Rev., 16(5): 2599-2609. <https://doi.org/10.1016/j.rser.2012.01.077>
- Li, H., Ha, C.S. and Kim, I. 2009. Fabrication of Carbon Nanotube/SiO₂ and Carbon Nanotube/SiO₂/Ag Nanoparticles Hybrids by Using Plasma Treatment. Nanoscale Res. Lett., 4(11): 1384-1388. <https://doi.org/10.1007/s11671-009-9409-4>
- Luo, C., Wei, R., Guo, D., Zhang, S. and Yan, S. 2013. Adsorption behavior of MnO₂ functionalized multi-walled carbon nanotubes for the removal of cadmium from aqueous solutions. Chem. Eng. J., 225: 406-415. <https://doi.org/10.1016/j.cej.2013.03.128>
- Lu, T., Xiang, T., Huang, X.L., Li, C., Zhao, W.F., Zhang, Q. and Zhao, C.S. 2015. Post-crosslinking towards stimuli-responsive sodium alginate beads for the removal of dye and heavy metals. Carbohydr. Polym., 133: 587-595. <https://doi.org/10.1016/j.carbpol.2015.07.048>
- Mallampati, S.R., Mitoma, Y., Okuda, T., Simion, C. and Lee, B.K. 2015. Dynamic immobilization of simulated radionuclide 133 Cs in soil by thermal treatment/vitrification with nano metallic Ca/CaO composites. J. Environ. Radioact., 139: 118-124.
- Makki, R., El-Hamshary, O. and Almarhabi, Z. 2019. Isolation and molecular identification of bacterial strains to study biofilm formation and heavy metals resistance in Saudi Arabia. J. Pure Appl. Microbiol., 13(1): 45-56.
- Minari, G.D., Saran, L.M., Lima Constancio, M.T., Correia da Silva, R., Rosalen, D.L., José de Melo, W. and Carareto Alves, L.M. 2020. Bioremediation potential of new cadmium, chromium, and nickel-resistant bacteria isolated from tropical agricultural soil. Ecotoxicol. Environ. Saf., 204: 111038.
- Ma, H., Wei, M., Wang, Z., Hou, S., Li, X. and Xu, H. 2020. Bioremediation of cadmium polluted soil using novel cadmium immobilizing plant growth promotion strain *Bacillus sp.* TZ5 loaded on biochar. J. Hazard. Mater., 388:122065. <https://doi.org/10.1016/j.jhazmat.2020.122065>
- Moosa, A.A., Ridha, A.M. and Abdulla, I.N. 2015. Chromium ions removal from wastewater using carbon nanotubes. Int. J. Innov. Res. Sci. Eng. Technol., 4(2): 8.
- Mahmoodi, N.M., Najafi, F. and Neshat, A. 2013. Poly (amidoamine-co-acrylic acid) copolymer: Synthesis, characterization, and dye removal ability. Ind. Crops Prod., 42: 119-125. <https://doi.org/10.1016/j.indcrop.2012.05.025>
- Pan, P., Lei, M., Qiao, P., Zhou, G., Wan, X. and Chen, T. 2019. Potential of indigenous plant species for phytoremediation of metal(loid)-contaminated soil in the Baoshan mining area, China. Environ. Sci. Pollut. Res., 26(23): 23583-23592. <https://doi.org/10.1007/s11356-019-05655-4>
- Phenrat, T., Thongboot, T. and Lowry, G. V. 2015. Electromagnetic induction of zerovalent iron (Zvi) powder and nanoscale zerovalent iron (NZVI) particles enhance dechlorination of trichloroethylene in contaminated groundwater and soil: proof of concept. Environ. Sci. Technol., 50(2): 872-880. <https://doi.org/10.1021/acs.est.5b04485>
- Rafati, R.M., Kazemi, S. and Moghadamnia, A.A. 2017. Cadmium toxicity and treatment: An update. Casp. J. Intern. Med., 8(3): 135-145.
- Rao, G., Lu, C. and Su, F. 2007. Sorption of divalent metal ions from aqueous solution by carbon nanotubes: A review. Sep. Purif. Technol., 58(1): 224-231. <https://doi.org/10.1016/j.seppur.2006.12.006>
- Rivera, F.L., Palomares, F.J., Herrasti, P. and Mazario, E. 2019. Improvement in heavy metal removal from wastewater using an external magnetic inductor. Nanomaterials, 9(11): 1508. <https://doi.org/10.3390/nano9111508>
- Sharma, H., Neetu, R. and Blessy, M. 2015. The characteristics, toxicity, and effects of cadmium. Int. J. Nanotech. Nanosci., 3: 1-9.
- Suzuki, T., Niinae, M., Koga, T., Akita, T., Ohta, M. and Choso, T. 2014. EDDS-enhanced electrokinetic remediation of heavy metal-contaminated clay soils under neutral pH conditions. Colloid Surf. A-Physicochem. Eng. Asp., 440: 145-150. <https://doi.org/10.1016/j.colsurfa.2012.09.050>
- Shabir, R., Abbas, G., Saqib, M., Shahid, M., Shah, G.M., Akram, M., Ni-azi, N.K., Naeem, M.A., Hussain, M. and Ashraf, F. 2018. Cadmium tolerance and phytoremediation potential of acacia (*Acacia nilotica L.*) under salinity stress. Int. J. Phytoremed., 20(7): 739-746. <https://doi.org/10.1080/15226514.2017.1413339>
- Sheela, T., Nayaka, Y.A., Viswanatha, R., Basavanna, S. and Venkatesha, T. G. 2012. Kinetics and thermodynamics studies on the adsorption of Zn(II), Cd(II), and Hg(II) from aqueous solution using zinc oxide nanoparticles. Powder Technol., 217: 163-170. <https://doi.org/10.1016/j.powtec.2011.10.023>
- Salwa, A.A., Karima, M.Z. and Ezzat, M.S. 2020. Facile synthesis of silica-coated magnetic nanoparticles via green microwave-solventless technique for purification of water from toxic heavy metals. Int. J. Nanop. Nanotech., 6(1). <https://doi.org/10.35840/2631-5084/5536>
- Shubair, T., Eljamal, O., Tahara, A., Sugihara, Y. and Matsunaga, N. 2019. Preparation of new magnetic zeolite nanocomposites for removal of strontium from polluted waters. J. Mol. Liq., 288: 111026. <https://doi.org/10.1016/j.molliq.2019.111026>
- Sundarajan, S., Sameem, S.M., Sudharsan, S. and Sayeekannan. R. 2013. Synthesis, characterization, and application of zero-valent silver nano adsorbents. Int. J. Innov. Res. Sci. Eng. Technol., 2(12):8023-8037.
- Thornton, I.1992. Sources and pathways of cadmium in the environment. IARC Sci. Pub., (118): 149-162.
- Taman, R., Ossman, M., Mansour, M.S. and Farag, H. 2015. Metal oxide nanoparticles as an adsorbent for removal of heavy metals. J. Adv. Chem. Eng., 5: 3 DOI:10.4172/2090-4568.1000125
- Venegas, A., Rigol, A. and Vidal, M. 2015. Viability of organic wastes and biochars as amendments for the remediation of heavy metal-contaminated soils. Chemosphere., 119: 190-198.
- Vicentin, R.P., Santos, J.V., Labory, C.R.G., Costa, A.M. Moreira, F.M. and Alves, E. 2018. Tolerance to and accumulation of cadmium, copper, and zinc by *Cupriavidus necator*. Rev. Bras. Ciênc. Solo., 42(10): 337. <https://doi.org/10.1590/18069657rbc20170080>
- Wu, Y., Ma, L., Zhang, X., Topalovi, O., Liu, Q., Feng, Y. and Yang, X. 2020. A hyperaccumulator plant *Sedum alfredii* recruits Cd/Zn-tolerant

- but not Pb-tolerant endosphere bacterial communities from its rhizospheric soil. *Plant Soil.*, 455(1-2): 257-270. <https://doi.org/10.1007/s11104-020-04684-0>
- Wang, L. and Li, J. 2013. Adsorption of C.I. Reactive Red 228 dye from aqueous solution by modified cellulose from flax shive: Kinetics, equilibrium, and thermodynamics. *Ind. Crops Prod.*, 42: 153-158. <https://doi.org/10.1016/j.indcrop.2012.05.031>
- Yu, B., Peng, Y., Xu, J., Qin, D., Gao, T., Zhu, H., Zuo, S., Song, H. and Dong, J. 2020. Phytoremediation potential of *Youngia japonica* (L.) DC: A newly discovered cadmium hyperaccumulator. *Environ. Sci. Pollut. Res.*, 28(5): 6044-6057. <https://doi.org/10.1007/s11356-020-10853-6>
- Yang, S., Li, J., Shao, D., Hu, J. and Wang, X. 2009. Adsorption of Ni(II) on oxidized multi-walled carbon nanotubes: Effect of contact time, pH, foreign ions, and PAA. *J. Hazard. Mater.*, 166(1): 109-116. <https://doi.org/10.1016/j.jhazmat.2008.11.003>
- Yu, T., Xue, Z., Zhao, X., Chen, W. and Mu, T. 2018. Green synthesis of porous -cyclodextrin polymer for rapid and efficient removal of organic pollutants and heavy metal ions from water. *New J. Chem.*, 42(19): 16154-16161. <https://doi.org/10.1039/c8nj03438a>
- Zhang, L.L., Xiong, Z. and Zhao, X.S. 2010. Pillaring chemically exfoliated graphene oxide with carbon nanotubes for photocatalytic degradation of dyes under visible light irradiation. *ACS Nano.*, 4(11): 7030-7036. <https://doi.org/10.1021/nn102308r>
- Zare, E.N., Motahari, A. and Sillanpää, M. 2018. Nanoadsorbents based on conducting polymer nanocomposites with main focus on polyaniline and its derivatives for removal of heavy metal ions/dyes: A review. *Environ. Res.*, 162: 173-195. <https://doi.org/10.1016/j.envres.2017.12.025>
- Zulfiqar, M., Lee, S.Y., Mafize, A.A., Kahar, N.A.M.A., Johari, K. and Rabat, N.E. 2020. Efficient removal of pb(ii) from aqueous solutions by using oil palm bio-waste/MWCNTS reinforced PVA hydrogel composites: kinetic, isotherm, and thermodynamic modeling. *Polymers*, 12(2): 430. <https://doi.org/10.3390/polym12020430>
- Zhang, X., Yan, L., Liu, J., Zhang, Z. and Tan, C. 2019. Removal of different kinds of heavy metals by novel PPG-nZVI beads and their application in simulated stormwater infiltration facility. *Appl. Sci.*, 9(20): 4213. <https://doi.org/10.3390/app9204213>



Life Time Cancer Risk Evaluation Due to Inhalation of Radon Gas in Dwellings of Al-Diwaniyah Governorate, Iraq

M. Sh. Aswood*[†], Sh. F. Alhous** and S. A. Abdulridha*

*Department of Physics, College of Education, University of Al-Qadisiyah, Diwaniyah-Iraq

**Department of physics, College of Education for Girls, University of Kufa, Najaf, Iraq

[†]Corresponding author: M. Sh. Aswood: murtadhababylon@gmail.com; murtadha.alnafiey@qu.edu.iq

Nat. Env. & Poll. Tech.
Website: www.neptjournal.com

Received: 10-05-2021

Revised: 09-06-2021

Accepted: 15-07-2021

Key Words:

Inhalation of radon gas
Annual effective dose
Cancer risks
CR-39 alpha detector

ABSTRACT

Radon is a radioactive natural gas that tends to concentrate in indoor homes and has major health consequences, the most serious of which is the ability to cause lung cancer. This research involves measuring indoor radon concentrations in different types of homes (non-smokers and smokers) in Al-Diwaniyah, Iraq, as well as assessing radon concentrations in cigarette samples acquired from Iraqi markets. nuclear track detectors were used to measure radiological parameters to determine annual effective dose levels and the associated cancer risk (CR-39). The average indoor radon concentrations, annual effective dose, and increased cancer risk attributable to the inhalation of indoor radon were $22.93 \pm 3.67 \text{ Bq.m}^{-3}$, $0.58 \pm 0.08 \text{ mSv.y}^{-1}$ and $2.2 \times 10^{-3} \pm 0.35$ respectively, for non-smokers home. For smokers' home, these parameters were $29.77 \pm 5.24 \text{ Bq.m}^{-3}$, $0.75 \pm 0.12 \text{ mSv.y}^{-1}$, and $2.89 \times 10^{-3} \pm 0.50$, respectively. The value of radon gas in cigarette samples ranged from 24.16 ± 2.55 to $33.91 \pm 5.13 \text{ Bq.m}^{-3}$. The obtained results have been compared with limits recommended by International Commission on Radiological Protection (ICRP) and found to be within allowed limits.

INTRODUCTION

Humans are exposed to large levels of internal and external radiation on a daily basis without even realizing it. Radiation exposure is defined as the introduction of radionuclides into the human body through the consumption of contaminated water and food, inhalation of contaminated air, or contact with contaminated soil and air (Aswood et al. 2019, Salih et al. 2019, Al-Gharabi & Al-Hamzawi 2020). According to the National Council on Radiation Protection (NCRP) and the United Nations Scientific Committee on the Effects of Atomic Radiation (UNSCEAR), natural radiation in the environment is the major source of radiation exposure. One of these radiation sources is radon, a colorless, odorless gas with high toxicity and three naturally occurring isotopes: ^{222}Rn , ^{219}Rn , and ^{220}Rn . Radon-222 occurs naturally in minute quantities as an intermediate step in the normal radioactive decay chains through which thorium and uranium slowly decay into lead and various other short-lived radioactive elements. Radon itself is the immediate decay product of radium (Ra). Its most stable isotope, ^{222}Rn , has a half-life of only 3.8 days, making it one of the rarest elements. Hence, radon represents the most harmful and important natural isotopes of the radioactive element, making it one of the rarest elements (Okeji & Agwu 2012). Radon undergoes radioactive decay when it releases ionizing radiation and forms "daughter" elements, known as decay products. It is

the release of radiation from this decay process that leads to exposure and health risks from radon. During the decay process, radon normally decays to short-lived nuclides called radon daughters, producing harmful particles, including alpha particles, as well as beta and gamma rays. Once these particles enter the body and destroy most of the living cells passing through them. Because radon can enter the human body through ingestion or inhalation, the absorbed dosage of radon into the body will increase, and because people spend so much time in their homes, their exposure to internal radon will be higher. As a result, there will be more illnesses related to environmental exposures due to indoor radon exposure (Sharma & Virk 2001). Also, because of the dangers of the radioactive gas radon in homes. The International Agency for Research on Cancer classed it as a carcinogen, malignant, and high-risk substance (IARC 1988). Even though there are three distinctive isotopes of radon produced in the natural decay series, the most important one is ^{222}Rn ($T_{1/2} = 3.82 \text{ d}$), which is a progeny of ^{226}Ra . Radon decays by alpha particle emission, while also generating gamma rays with very low probability (<0.08%). Together with its mainly short-lived daughters, radon's contribution to the world annual dose from background radiation is on the level of 1.2 mSv, representing roughly 50% of the overall dose (UNSCEAR 1988)

Many researchers have studied radon and its impact on human health through thorough investigations of indoor

exposure rates, annual effective dose, and residents' lifetime cancer risk (Aswood et al. 2020, Warner et al. 1996, Al-Hamzawi et al. 2019). The goal of this study is to determine the indoor radon concentration and annual effective inhalation in the homes tested in Al-Diwaniyah, Iraq's southern governorate. As a result, using the effective approach of CR-39 solid state alpha track detectors with decay emitters, determine the lifetime cancer risk of residents.

MATERIALS AND METHODS

Collection and Preparation of Samples

The present work was to determine the cancer risk and estimate the annual effective dose due to inhalation of indoor radon through measuring the indoor radon levels in the dwellings of Al-Qadisiyah, Iraq. This study included 60 subjects (20 non-smokers dwellings and 20 smokers' dwellings, in addition to 20 cigarette samples collected from Iraqi

markets), Table 1 includes the collected data and information on locations, codes, types of cigarettes, and other data. The CR-39 nuclear track detector was primarily employed in this study, with a thickness of around 500 m (Tasl Company, UK). The detectors were carefully cut into little pieces with dimensions of (1.51.5) cm² so that they could be used immediately. The storage in this study covers non-smokers' and smokers' houses, which was accomplished by exposing nuclear reagents to the indoor air openly to detect radon concentrations in the residences and determine the health risks associated with them. CR-39 was cultivated on the walls of Al-Diwaniyah governorate houses, at a distance of 150 cm from the ground, with a double-sided tape, and specific codes were placed on it, taking into consideration the date of cultivating (Obed et al. 2018). The closed tube technique (Poly Vinyl Chloride) PVC-tube was used to store the cigarette samples for analysis. It was developed with length, thickness, and diameter measurements of 10.5 cm,

Table1: Database dwellings (non-smokers and smokers) and cigarettes samples in this study.

Studied Samples	Location	Code and number of samples
Non- smokers' dwellings	Al- Karama	N ₀₁ -N ₀₄
	Al-Wehda	N ₀₅ -N ₀₈
	Al-Jazayir	N ₀₉ -N ₁₂
	Al- Euruba	N ₁₃ -N ₁₆
	Al- Jumhuri	N ₁₇ -N ₂₀
Total		20
Smokers' dwellings	Al- Karama	S ₀₁ -S ₀₄
	Al-Wehda	S ₀₅ -S ₀₇
	Al-Jazayir	S ₀₈ -S ₁₃
	Al- Euruba	S ₁₄ -S ₁₇
	Al- Jumhuri	S ₁₈ -S ₂₀
Total		20
Cigarettes	Type of cigarettes	
	KENT SILVER	C ₀₁ -C ₀₂
	OSCAR	C ₀₃ -C ₀₄
	SUMER	C ₀₅ -C ₀₆
	PINE	C ₀₇ -C ₀₈
	ASPEN	C ₀₉ -C ₁₀
	BON	C ₁₁ -C ₁₂
	MAC	C ₁₃ -C ₁₄
	MIAMI	C ₁₅ -C ₁₆
	MASTER	C ₁₇ -C ₁₈
ESSE BLACK	C ₁₉ -C ₂₀	
Total		20

2 mm, and 2.1 cm, respectively, to ensure that only radon reaches the CR-39 detector and no other gases (Salih et al 2019). The cigarette samples were dried in an electric oven for 15 minutes at 150°C. The samples were then pulverized and sieved many times with a hand mill (mortar) to generate a homogeneous dry powder. After that, 10 gm of sample powder was placed in the bottom of the tube, a CR-39 detector was installed by adhesive tape at the bottom of the tube cover, and the forms were stored as a whole from March 24, 2020, to June 22, 2020; this is equivalent to 90 days to ensure the radionuclides in the samples reach equilibrium state (Fig. 1a, b). After 90 days, all detectors and samples of cigarettes were collected from the homes for process etching of the CR-39 detectors using NaOH etching solution in a water bath to reveal the latent tracks on the CR-39 arising from the radon indoor decay process. At 70°C for 8 h, a 6.25 mol.L⁻¹ of this solution was used (Fig. 1c). Then, the pathways of the alpha particles (latent tracks) that emerge on the surface of the CR-39 detectors are traced using an optical microscope with a magnification of 400X and a divided lens with a known area (Fig. 1d, e). The equation below is used to measure the density of latent tracks (Showard & Aswood 2020)

$$\rho\left(\frac{tr}{cm^2}\right) = \frac{\text{Average number of total tracks (N)}}{\text{(Area of view field (A))}} \quad \dots (1)$$

CALCULATIONS

After the density of the tracks was calculated, the concentrations of indoor radon in dwellings of (non-smokers and smokers) were calculated, thus the radiation doses and lifetime cancer risk due to inhalation of radon can be determined, and from the same equation, we can calculate radon concentration for cigarettes samples. Therefore, the equation used to measure radon concentration (C_{Rn}) is given by the following relationship (Aswood et al. 2018):

$$C_{Rn}\left(\frac{Bq}{m^3}\right) = \frac{\rho}{k \times t} \quad \dots (2)$$

k: calibration factor which equals to 0.212 (tr.cm⁻²)/ d. (Bq.m⁻³);

t: exposure time (90 d).

The formula used to measure the annual effective dose (AED) is (Obed et al. 2018):

$$AED\left(\frac{mSv}{y}\right) = C_{Rn} \times F \times O \times T \times DCF \quad \dots (3)$$

C_{Rn} : radon concentration Bq.m⁻³;

F: equilibrium factor (0.4);

O: occupancy factor (0.8);

T: indoor occupancy time in a year (8760 h.y⁻¹);

DCF: dose conversion factor (9.0×10⁻⁶ mSv.h⁻¹. (Bq.m⁻³)). Based upon calculated values of (AED), excess lifetime cancer risk (ELCR) is calculated using the following equation (Obed et al. 2018):

$$ELCR = AED\left(\frac{mSv}{y}\right) \times DL(y) \times RF\left(\frac{1}{Sv}\right) \quad \dots (4)$$

DL: life expectancy (70 y);

RF: risk factor (0.055 1.Sv⁻¹)

RESULTS AND DISCUSSION

Table 2 summarizes indoor radon concentrations in non-smokers' and smokers' homes, as well as radon concentrations in cigarettes samples, in the Al-Diwaniyah governorate. The highest value of indoor radon concentration in non-smokers' households was 26.33 4.31 Bq.m⁻³ (N₀₁ sample) and the lowest value was 16.75 1.08 Bq.m⁻³ (N₁₀ sample). These were found in Al-Karama and Al-Jazayir

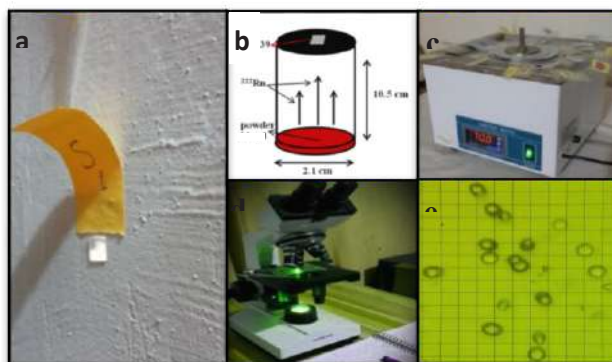


Fig. 1: The storage of detectors in dwellings and cigarettes samples(a, b), water bath with the detectors(c), optical microscope (d), the tracks of radon on the detectors under a microscope (e).

localities respectively. Also, the highest and lowest values of indoor radon concentration for smokers' homes were $32.94 \pm 5.33 \text{ Bq.m}^{-3}$ (S_{07} sample) and $25.22 \pm 4.66 \text{ Bq.m}^{-3}$ (S_{04} sample), found in Al-Wehda and Al- Karama areas, respectively. For cigarettes samples, the radon concentration varied from $22.88 \pm 3.54 \text{ Bq.m}^{-3}$ (C_{18}) sample to $33.91 \pm 5.13 \text{ Bq.m}^{-3}$ in the (C_{08}) sample. The average value of indoor radon gas in non-smokers' and smokers' homes are 22.93 ± 3.67 and $29.77 \pm 5.24 \text{ Bq.m}^{-3}$, respectively. While the average value of radon levels in cigarette samples is $29.34 \pm 4.42 \text{ Bq.m}^{-3}$.

Table 3 shows the annual effective dose (AED) and excess lifetime cancer risk (ELCR) associated with radon inhalation in non-smokers' and smokers' homes. The average (AED) in non-smokers' and smokers' homes were $0.58 \pm 0.08 \text{ mSv.y}^{-1}$ and $0.75 \pm 0.12 \text{ mSv.y}^{-1}$, respectively. The average values of ELCR in non-smokers' and smokers' homes were 2.23 ± 0.35 and 2.89 ± 0.50 , respectively. These results show that the radon concentrations in non-smokers' homes are lower than the concentrations in smokers' homes and cigarettes samples due to many reasons, including the ventilation factor, air extractor, design and modernity of construction, etc.

Therefore, it was found that smoking had a clear effect on increasing radon concentrations.

Table 4 shows a comparison of the current study's indoor radon concentration (C_{Rn}) and annual effective dose (AED) with those of previous studies in different locations. Except for Babylon in Iraq, and Japan, the current indoor radon levels are lower than all the values of previous studies. The indoor radon concentration range is well under the EPA's permitted limit (148 Bq.m^{-3}) (EPA 2003). Table 4 shows that the current values of annual effective dose (AED) in non-smokers' homes are lower than those of previous studies, with the exception of Baghdad and Babylon in Iraq and Japan. However, the annual effective dosage range is within the ICRP permissible limit (3mSv.y^{-1}) (ICRP 1993). Fig. 2 provides a comparison of the average values of ELCR of non-smokers' homes in the current study with the results of previous studies. Except for Baghdad, Iraq, the results in this study are less than all the results of the previous studies. The extra lifetime cancer risk range, on the other hand, is less than the EPA's permitted levels (EPA 2003). In general, an estimate of the excess lifetime cancer risks due to inhalation radon was obtained

Table 2: Radon gas concentrations (Bq.m^{-3}) in studied samples.

Non-smokers' dwellings		Smokers' dwellings		Cigarettes samples	
SC	Indoor radon	SC	Indoor radon	SC	Radon content
N_{01}	26.33 ± 4.31	S_{01}	32.11 ± 4.62	C_{01}	32.33 ± 5.02
N_{02}	24.18 ± 3.29	S_{02}	30.24 ± 5.50	C_{02}	31.22 ± 5.61
N_{03}	20.47 ± 4.85	S_{03}	28.46 ± 5.03	C_{03}	27.91 ± 5.92
N_{04}	20.75 ± 5.11	S_{04}	25.22 ± 4.66	C_{04}	26.11 ± 2.02
N_{05}	24.89 ± 2.13	S_{05}	31.17 ± 5.99	C_{05}	31.87 ± 5.11
N_{06}	23.72 ± 2.62	S_{06}	27.09 ± 2.19	C_{06}	30.01 ± 5.83
N_{07}	24.42 ± 5.08	S_{07}	32.94 ± 5.33	C_{07}	$33.73.16 \pm$
N_{08}	26.30 ± 4.51	S_{08}	32.41 ± 5.81	C_{08}	33.91 ± 5.13
N_{09}	25.59 ± 3.06	S_{09}	32.16 ± 5.60	C_{09}	24.19 ± 4.01
N_{10}	16.75 ± 1.08	S_{10}	27.25 ± 4.19	C_{10}	23.92 ± 3.43
N_{11}	22.82 ± 4.03	S_{11}	29.19 ± 6.33	C_{11}	25.33 ± 1.44
N_{12}	20.24 ± 5.05	S_{12}	28.01 ± 5.43	C_{12}	24.16 ± 2.55
N_{13}	24.91 ± 4.02	S_{13}	27.31 ± 1.44	C_{13}	33.03 ± 5.65
N_{14}	23.28 ± 3.12	S_{14}	31.11 ± 6.54	C_{14}	31.39 ± 2.55
N_{15}	21.17 ± 5.17	S_{15}	29.32 ± 4.65	C_{15}	32.56 ± 5.98
N_{16}	22.82 ± 2.19	S_{16}	31.17 ± 4.55	C_{16}	31.04 ± 7.44
N_{17}	20.24 ± 2.31	S_{17}	29.68 ± 5.98	C_{17}	24.89 ± 3.17
N_{18}	23.68 ± 3.81	S_{18}	28.77 ± 7.44	C_{18}	22.88 ± 3.54
N_{19}	22.56 ± 3.61	S_{19}	32.35 ± 6.43	C_{19}	33.49 ± 5.19
N_{20}	23.52 ± 4.18	S_{20}	29.52 ± 7.13	C_{20}	32.76 ± 6.12
Mean \pm S.D	22.93 ± 3.67		29.77 ± 5.24		29.34 ± 4.42

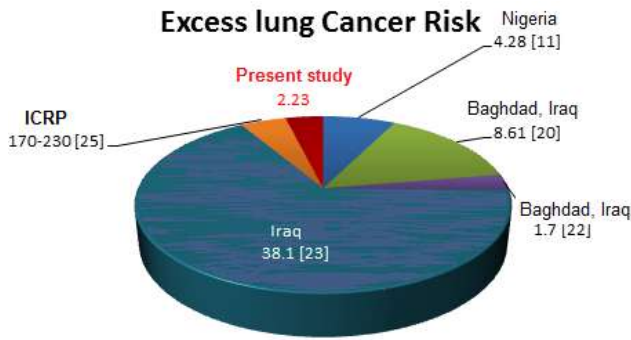


Fig. 2: A comparison between average excess lifetime cancer risk (ELCR) in non-smokers dwellings in the present study with previous studies.

inside the dwellings of Al-Diwaniyah, Iraq, in spite of Fig. 3 showed that the high the indoor radon values, the annual effective dose and the excess lifetime cancer risk in the dwellings of smokers compared to non-smokers, but the results showed that all these values were within the internationally allowable limits. Finally, the findings showed that higher radon concentrations in cigarettes samples were associated

with higher radon concentrations in smokers' houses. As a result, there is an elevated risk of cancer throughout one's lifetime (ELCR). The ratio of non-smokers' calculated values to smokers' calculated values was 0.77 percent.

CONCLUSION

The findings show that non-smokers' indoor radon concentrations (CRn), annual effective dose (AED), and excess lifetime cancer risk (ELCR) are all lower than smokers' homes. However, high values in some dwellings could be owing to building materials and types, or insufficient ventilation and air extractors, among other things. Furthermore, a positive relationship exists between the increase in indoor radon concentrations in smokers' homes and the increase in radon concentrations in cigarette samples. As a result, the annual excess lifetime cancer risk (ELCR) in smokers' homes will increase. The current study shows that the measured levels of radon gas in Al-Diwaniyah, Iraq, are within the global permitted limit, indicating that these havens are moderately protected. The intake of natural indoor radon gas in homes poses no significant risk to people.

Table 3: Annual effective dose (AED) and excess lifetime cancer risk (ELCR) from indoor radon of non-smokers and smokers' dwellings.

Non-smokers' dwellings			Smokers' dwellings		
SC	AED in (mSv.y ⁻¹)	ELCR×10 ⁻³	SC	AED in (mSv.y ⁻¹)	ELCR×10 ⁻³
N ₀₁	0.66±0.10	2.56±0.41	S ₀₁	0.81±0.11	3.12±0.44
N ₀₂	0.61±0.08	2.35±0.31	S ₀₂	0.76±0.13	2.94±0.53
N ₀₃	0.52±0.12	1.99±0.47	S ₀₃	0.72±0.12	2.76±0.48
N ₀₄	0.52±0.12	2.02±0.49	S ₀₄	0.64±0.11	2.45±0.45
N ₀₅	0.63±0.05	2.42±0.20	S ₀₅	0.79±0.15	3.03±0.58
N ₀₆	0.6±0.06	2.3±0.25	S ₀₆	0.68±0.05	2.63±0.21
N ₀₇	0.62±0.12	2.37±0.49	S ₀₇	0.83±0.13	3.20±0.51
N ₀₈	0.65±0.11	2.55±0.43	S ₀₈	0.81±0.14	3.15±0.56
N ₀₉	0.65±0.07	2.49±0.29	S ₀₉	0.81±0.14	3.12±0.54
N ₁₀	0.42±0.02	1.63±0.10	S ₁₀	0.69±0.10	2.65±0.40
N ₁₁	0.58±0.10	2.22±0.39	S ₁₁	0.74±0.15	2.84±0.61
N ₁₂	0.51±0.12	1.97±0.49	S ₁₂	0.71±0.13	2.72±0.52
N ₁₃	0.63±0.10	2.42±0.39	S ₁₃	0.69±0.03	2.65±0.13
N ₁₄	0.59±0.07	2.26±0.30	S ₁₄	0.78±0.16	3.02±0.63
N ₁₅	0.53±0.13	2.06±0.50	S ₁₅	0.74±0.11	2.85±0.45
N ₁₆	0.58±0.05	2.22±0.21	S ₁₆	0.79±0.11	3.03±0.44
N ₁₇	0.51±0.05	1.97±0.22	S ₁₇	0.75±0.15	2.88±0.58
N ₁₈	0.60±0.09	2.30±0.37	S ₁₈	0.73±0.18	2.79±0.72
N ₁₉	0.57±0.09	2.19±0.35	S ₁₉	0.82±0.16	3.14±0.62
N ₂₀	0.59±0.10	2.28±0.40	S ₂₀	0.74±0.17	2.87±0.69
Ave.	0.58±0.08	2.23±0.35		0.75±0.12	2.89±0.50

Table 4: A comparison between average indoor radon concentration (C_{Rn}) and annual effective dose (AED) in non-smokers homes in the present study with previous studies.

No.	C_{Rn} (Bq.m ⁻³)	AED (mSv.y ⁻¹)	Country	References
1	4.18	0.11	Babylon, Iraq	Obaed & Aswood (2020)
2	176.15	1.114	Ibadan, Oyo State, Nigeria	Obed et al. (2018)
3	25.52	0.64	Pirayiri- Palakkad, India	Ramsiya et al. (2013)
4	-	3	ICRP	ICRP (1993)
5	148	-	EPA	EPA (2003)
6	45.487	0.478	Bagdad, Iraq	Al-Alawy and Fadhil (2016)
7	143.77	-	Kurdistan, Iraq	Ismail and Jaafar (2010)
8	6.1	0.45	Japan	et al. (2003)
9	27.83	0.70	Al-Diwaniyah, Iraq	Present study

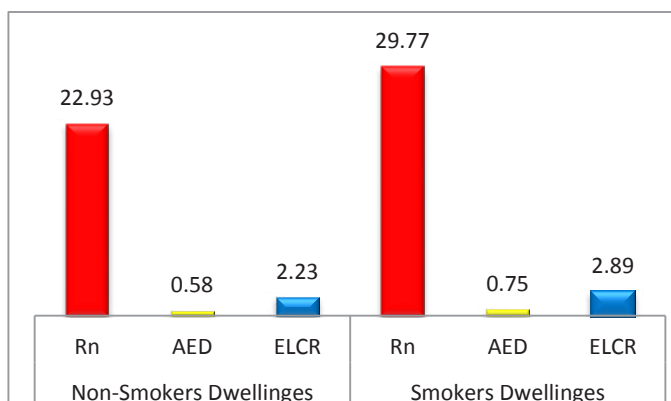


Fig. 3: Average values for indoor radon concentration (Bq.m⁻³), annual effective dose (mSv.y⁻¹), and excess lifetime cancer risk of non-smokers and smokers' dwellings.

ACKNOWLEDGEMENTS

The authors acknowledge, with gratitude, the assistance received from the Department of Physics, University of Al-Qadisiyah-Iraq. They would also like to extend their heartfelt appreciation to the dwellings that participated in the survey and their assistance to complete and succeed this research work.

REFERENCES

- Al-Alawy, I.T. and Fadhil, H.R. 2016. Measurements of radon concentrations and dose assessments in chemistry department /Science College/ Al-Mustansiriyah University, Baghdad-Iraq. *Int. J. Sci. Res. Sci. Technol.*, 2(4): 72-82.
- Al-Gharabi, M. and Al-Hamzawi, A. 2020. Measurement of radon concentrations and surface exhalation rates using CR-39 detector in soil samples of Al-Diwaniyah Governorate, Iraq. *Iran. J. Med. Phys.*, 17(4): 220-224.
- Al-Hamzawi, A.A., Tawfiq, N.F., Aswood, M.S. and Najim, F.A. 2019. Determination of radon concentrations near mobile towers in selected cities of Babylon governorate, Iraq. *J. Phys. Conf. Ser.*, 1234(1): 012026- 012032.
- Aswood, M.S., Abojassim, A.A. and Al Musawi, M.S.A. 2019. Natural radioactivity measurements of frozen red meat samples consumed in Iraq. *Radiat. Detect. Technol. Methods*, 3(4): 1-4.
- Aswood, M.S., Al Musawi, M.S.A., Mahdi, N.K. and Showard, A.F. 2020. Evaluation of committed effective dose of radon gas in drinking water in Al-Qadisiyah province, Iraq. *Tche Quimica J.*, 17 (36): 1-12.
- Aswood, M.S., Jaafar, M.S. and Salih, N.F. 2018. Determination of radon and heavy metals in soil samples from Seberang Perai, Malaysia. *Pollut. Res.*, 37(3): 646-651.
- Environmental Protection Agency (EPA). 2003. Assessment of Risks from Radon in Homes. Office of Radiation and Indoor Air United States. Environmental Protection Agency, Washington, DC.
- International Agency for Research on Cancer (IARC). 1988. Monographs on the Evaluation of Carcinogenic Risks to Humans. IARC, Lyon, France.
- International Commission on Radiological Protection (ICRP). 1993. Against Radon-222 at Home and Work. ICRP, Stockholm, Sweden.
- Ismail, A.H. and Jaafar, M.S. 2010. Indoor radon concentration and its health risks in selected locations in Iraqi Kurdistan using CR-39 NTDS. In 2010 4th International Conference on Bioinformatics and Biomedical Engineering, IEEE, 18-20 Chengdu, China, IEEE, pp. 1-8
- Obaed, H.K. and Aswood, M.S. 2020. Estimated of U, Rn, and Po concentrations in smokers blood samples collected from Babylon, Iraq. *IOP Conf. Ser. Mater. Sci. Eng.*, 928 (7): 072043- 072055.
- Obed, R.I., Oyelade, E A. and Lateef, H.T. 2018. Indoor radon levels in some selected nurseries and primary schools in Ibadan, Oyo State, Nigeria. *J. Radiat. Res. Appl. Sci.*, 11(4): 379-382.

- Oikawa, S., Kanno, N., Sanada, T., Ohashi, N., Uesugi, M., Sato, K., Abukawa, J. and Higuchi, H. 2003. A nationwide survey of outdoor radon concentration in Japan. *J. Environ. Radioact.*, 65(2): 203-213.
- Okeji, M.C. and Agwu, K.K. 2012. Assessment of indoor radon concentration in phosphate fertilizer warehouses in Nigeria. *Radiat. Phys. Chem.*, 81(3): 253-255.
- Ramsiya, M., Joseph, A. and Jojo, P.J. 2017. Estimation of indoor radon and thoron in dwellings of Palakkad, Kerala, India using solid-state nuclear track detectors. *J. Radiat. Res. Appl. Sci.*, 10(3): 269-272.
- Salih, N.F., Aswood, M.S. and Hamzawi, A.A. 2019. Effect of porosity on evaluation of radon concentration in soil samples collected from Sulaymanya governorate, Iraq. *J. Phys. Conf. Ser.*, 1234(1): 012024- 012035.
- Sharma, N. and Virk, H.S. 2001. Exhalation rate study of radon/thoron in some building materials. *Radiat. Measure.*, 34(1-6): 467-469.
- Showard, A.F. and Aswood, M.S. 2020. Effect of gender and occupations on uranium concentration in human blood and soil samples collected from Babylon, Iraq. *Pol. J. Med. Phys. Eng.*, 26(3): 143-148.
- Warner, K.E., Mendez, D. and Courant, P.N. 1996. Toward a more realistic appraisal of the lung cancer risk from radon: The effects of residential mobility. *Am. J. Public Health*, 86(9): 1222-1227.
- The United Nations Scientific Committee on the Effects of Atomic Radiation (UNSCEAR). 1988. Report 1988: Sources, Effects, and Risks of Ionizing Radiation. New York, UNSCEAR.



Low-Cost Calibration MOS Gas Sensor for Measuring SO₂ Pollutants in Ambient Air

R. Purbakawaca*†, A.S. Yuwono**, I.D.M. Subrata* and H. Alatas***

*Department of Mechanical and Biosystems Engineering, IPB University, Bogor, 16680, Indonesia

**Department of Civil and Environmental Engineering, IPB University, Bogor, 16680, Indonesia

***Department of Physics, IPB University, Bogor, 16680, Indonesia

†Corresponding author: R. Purbakawaca; purbakawaca09rady@apps.ipb.ac.id

Nat. Env. & Poll. Tech.
Website: www.neptjournal.com

Received: 09-05-2021

Revised: 30-06-2021

Accepted: 15-07-2021

Key Words:

SO₂ gas sensor
Gas sensor calibration
Low-cost gas calibration
Voltage response MOS
Raw signal MOS

ABSTRACT

Air pollution has evolved into a global issue that necessitates immediate and accurate pollution control. The usage of the Metal Oxide Semiconductor (MOS) sensor as a monitoring system for air pollution levels is one possible answer to this challenge. The MQ-136 sensor is calibrated using standard SO₂ (0, 5, 10, 20, 30, 40, 50, 60, 70) ppm as the test gas in this study. To collect the sensor output signal, a variety of equipment was created, including a gas test box, a voltage divider, and follower circuit, and a gas flow control unit operated by a microcontroller. The test gas can be pumped into the test box at a constant rate of 1.0 L.min⁻¹ by the apparatus. To evaluate a significant difference ($\alpha = 0.05$), an analysis of variance was performed on the response signal generated by a series of sensors due to the concentration of the test gas. To examine the correlation between the sensor response signal and the test gas concentration treatment, as well as the sensor performance, linear regression analysis was used. The ANOVA results demonstrate no significant differences amongst the sensors, indicating that they all follow the same routine. Furthermore, ANOVA analysis reveals that the sensors respond differently at each level of SO₂ concentration. According to linear regression, the relationship between gas concentration and sensor-1, sensor-2, and sensor-3 output signals is reflected by coefficients of determination of 0.94, 0.91, and 0.93, respectively.

INTRODUCTION

Air pollution has become a global problem given the risk it poses to human health and the environment. Air pollution is increasing as a result of rapid urbanization, industrialization, population, and economic growth (Rumana et al. 2014). Air pollution has been found to have harmful consequences on human health and the environment in recent studies. Air pollution, for example, has a social and economic impact on crop yields in developing countries (Ahmed 2015).

Measurement of SO₂ is an important component of air pollution control initiatives. Fossil fuels, refining and combustion, non-ferrous smelting, iron ore smelting, pulp, and paper mills, transportation sources, and steel mills all contribute about 99 per cent of sulfur dioxide to the environment (Riordan & Adeeb 2004). These pollutants, when emitted in high quantities into the ambient air, can cause health problems such as pulmonary, asthma, and other respiratory illnesses.

Many countries have set guidelines for determining the level of pollution and its consequences, recognizing the hazards of air pollution. Government legislation and national

norms influence air pollution levels in Indonesia. The threshold values for air pollutant levels, as well as the methods and equipment for measuring the level of pollutants in the air, are all defined by these laws. The traditional approach is used because it is accurate and selective to the observed parameters, but it has significant maintenance costs and takes a long time to analyze.

Designing a low-cost air pollutant meter that takes advantage of the potential of a solid-state gas sensor is one viable approach to complement existing methods. Solid-state gas sensors, particularly those based on MOS, have become the industry standard in various household, commercial, and industrial gas sensor systems in recent decades (Liu et al. 2012). The MOS gas sensor is connected to an instrumentation system and a network to monitor pollution levels in real-time (Arroyo et al. 2019). Although MOS gas sensors have been used to assess pollutant levels in the ambient air, the gas detection technique is complicated.

MOS gas sensors have benefits over other types of sensors, according to Korotcenkov (2007), especially in terms of sensitivity, stability, price, and reaction time. However, to assure accuracy, evaluation, and validation of gas sensor

performance, MOS gas sensors must be calibrated (Adithyan et al. 2016). When using MOS sensors as a low-cost air quality monitoring system, several factors must be considered, including producing, transferring, and combining data from numerous sensors, as well as reviewing accuracy and predictions (Snyder et al. 2013). The calibration of gas sensors, on the other hand, is neither cheap nor simple.

The calibration of the MQ-136 sensor with standard gas using the apparatus used in this investigation is presented in this publication. In addition, to learn more about sensor performance, ANOVA and linear analysis were used in this study.

MATERIAL AND METHODS

Experimental Setup

To get the sensor output, a series of equipment was created in this study, including a gas test box, voltage divider, follower circuit, and gas flow control unit operated by a microcontroller, as shown in Fig. 1. As shown in Fig. 2, all these components are combined to form an experimental setup for gas sensor calibration.

The test box is a container for holding the test gas and contains a series of gas sensors installed with a fully functional gas flow system. The test box is made of acrylic material with a bending technique to minimize gas leakage. The test box is in the form of a cube with a volume of free space of 1000 cm³, as shown in Fig. 3. The test box consists of two

parts: the top in the form of a lid and the bottom as a gas storage container. The lid is equipped with a rubber seal, a mount for attaching the gas sensor circuit board, and a seven-pin female connector. The gas container is equipped with a 12VDC fan which functions to homogenize the standard gas in the container, and a pneumatic fitting is installed for the gas line.

The MOS gas sensor used is a low-cost sensor manufactured by Hanwei Electronics Co., Ltd, the MQ-136 variant of three sensors. The MQ-136 sensor was chosen because it has a high sensitivity to H₂S gas and can detect other gases containing sulfur (Zhengzhou 2015). However, more detailed and complete information about these sensors is minimal, especially regarding sensor calibration for SO₂ gas. As a result, the sensor will be tested with SO₂ gas in this study to see how accurate the response signal is to the gas concentration level.

As seen in Fig. 4, the standard circuit on the MQ series sensor consists of two parts, namely the heating circuit (R_H) and the signal output circuit (R_S). When the sensor is activated, the heating component will light up and cause the sensing material to activate so that the electrons on the sensing component's surface move freely. Electrons will react with oxygen in the air around the material, thereby increasing the sensing material's resistance R_S (Barsan et al. 2012). However, when the target gas appears, the oxygen molecules will react with the target gas, which causes the R_S to decrease with the target gas content in the air. When R_S

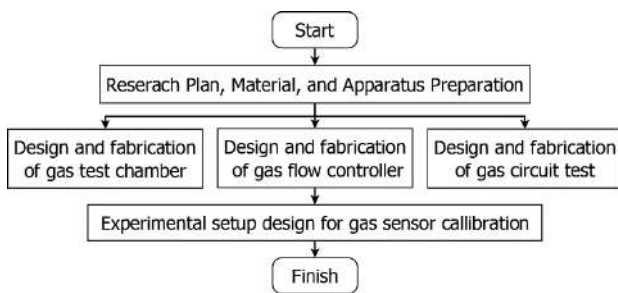


Fig. 1: Design of gas sensor calibration equipment

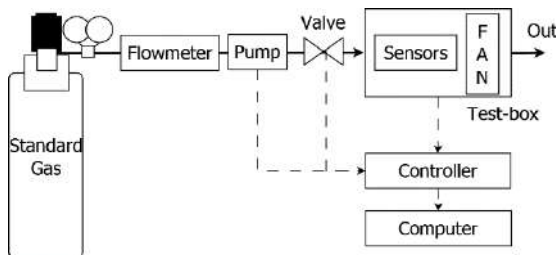


Fig. 2: Experimental setup for low-cost gas sensor calibration.

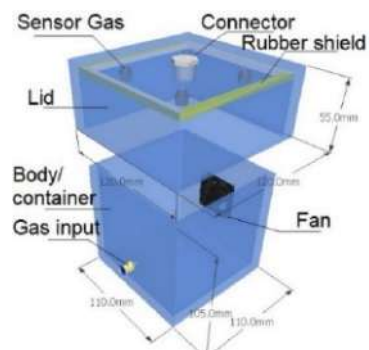


Fig. 3: Design of test box with 5 mm thickness acrylic material.

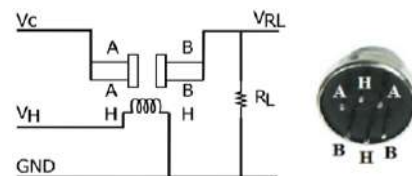


Fig. 4: Illustration of primary test circuit MQ sensor (Zhengzhou 2015).

is combined serially with constant resistance R_L , an electric current is applied due to the potential difference V_C , and there will be a voltage variation V_{RL} due to changes in target gas levels in the air. The relationship between R_S and R_L is described in equation 1.

$$R_S = R_L \left(\frac{V_C}{V_{RL}} - 1 \right) \quad \dots(1)$$

where V_{RL} is the sensing output (V_O) from the sensor in volt.

The primary test circuit for the MQ sensor above becomes a reference in making the sensor PCB. The suitability of the sensor leads and symbol in Fig. 4 and Fig. 5 is as follows:

- a. Pin A is lead numbers 1 and 3, pin B is lead numbers 4 and 6, and pin H is lead numbers 2 and 5.
- b. R_L is equivalent to the combination of resistance of R_2 and R_3 or R_5 and R_6 or R_8 and R_9 .
- c. V_C and V_H represented by V_{CC} .

The gas sensor array system is designed to detect the test gas in the test box. The PCB is designed to mount three sensors at once. $R_2, R_5,$ and R_8 are variable resistors value of 100 kOhm. $R_3, R_6,$ and R_9 have the same resistance value of 1 kOhm. $R_1, R_4,$ and R_7 are used to build a voltage divider with R_H . The MQ sensor manual states that the R_L can be determined as 10 kOhm \pm 5%. As shown in Fig. 5, the resistances $R_2, R_5,$ and R_8 are 9 kOhm. So, equation 1 can be rewritten into equation 2.

$$R_S = R_L \frac{(V_{CC} - V_O)}{V_O} \quad \dots(2)$$

where R_L is the load resistor equivalent $R_2 + R_3$ in kOhm. V_{CC} is applied at 5V.

According to Tian et al. (2005), the MOS sensor output signal, as illustrated in Fig. 6, possesses characteristics with a significant enough gain. Therefore, V_O is observed only

by connecting the sensor to the Atmega 328 via a voltage follower circuit as a buffer between the sensor output and the A / D channel. V_O is converted into a digital signal via a 10-bit resolution ADC channel.

In this paper, a Moving Average Filter (MAF) is selected as a general denoising method equivalent to low pass filtering (Bassey et al. 2014). MAF works by averaging several points within a specified data point range from the input signal to produce each output signal point described by equation 3.

$$y[k] = \frac{1}{N} \sum_{n=0}^{N-1} x[k+n] \quad \dots(3)$$

where y is the output signal, N is the number of points of data before the output signal.

This research can obtain the variation in the target concentration level by flowing the standard gas into the test box for a particular duration. This gas flow must be kept constant at 1.0 L.min⁻¹ to reach the desired gas concentration. Therefore, the gas standard in the tube is not directly flowed into the test box but through a flow controller in the form of a 12 VDC 5 L.min⁻¹ vacuum pump, a Wiebrock 3 KPa 1.5 NL.min⁻¹ flowmeter, and a 12 VDC solenoid valve is shown in Fig. 7. The gas flow duration setting is based on a logical button combination. In Table 1, the gas flow duration in code letters will be mapped based on the desired gas concentration in the test box.

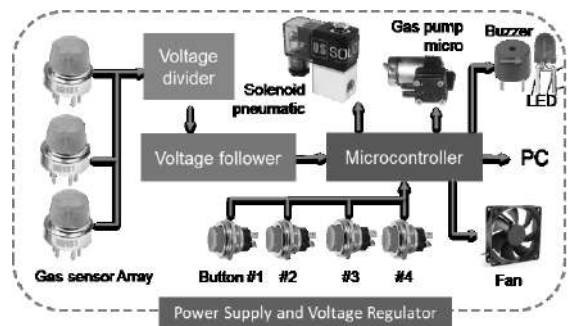


Fig. 7: Electrical schematic of low-cost gas sensor calibration.

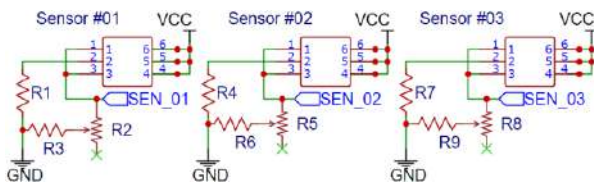


Fig. 5: PCB design for the primary test circuit of the MQ sensor.

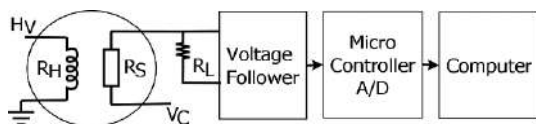


Fig. 6: Interface circuit diagram of MOS gas sensor (Tian et al. 2005).

Table 1: Logical combination of the button to select a flow duration.

Button				Combination	
B#1	B#2	B#3	B#4	Decimal	Duration
0	0	0	0	0	A
0	0	0	1	1	B
0	0	1	0	2	C
0	0	1	1	3	D
0	1	0	0	4	E
0	1	0	1	5	F
0	1	1	0	6	G
0	1	1	1	7	H
1	0	0	0	8	I

The flow control performance test is conducted to determine the stability of the gas flow. The test was carried out by opening and closing the gas flow rate for 10 repetitions using a flow controller with 100 seconds to flow the gas and 20 seconds to monitor the gas flow. Stability is indicated by the difference in the actual gas flow value on the flowmeter against the target value represented in the Mean Absolute Percentage Error (MAPE) as in equation 4. The same test is also carried out without a flow controller for comparison.

$$MAPE = \frac{1}{N} \sum_{i=1}^N \left| \frac{A_i - F_i}{A_i} \right| \quad \dots(4)$$

where A_i and F_i are the actual and forecast value at data point- i . N is the number of data (Kim & Kim 2016).

Gas Concentration Level

To determine the relationship of the sensor response signal to the treatment of the test gas concentration, Air Liquide standard SO₂ gas is used with a concentration of 100 ppm with an accuracy of 99.0%. The gas concentration in the test box is calculated based on the dilution of the gas as in equation 5. In this study, the range of initial SO₂ gas concentrations is shown in Table 2.

$$C_1 \times V_1 = C_2 \times V_2 \quad \dots(5)$$

where C_1 is the initial concentration of SO₂ gas, V_1 is the initial volume of SO₂ gas, C_2 is the final concentration SO₂ gas, and V_2 is the final volume SO₂ gas in the test box.

Data Acquisition

Before collecting calibration data, the MQ-136 goes through a preheating phase. The purpose of this step is to determine the nature of the sensor output signal in the target gas condition of 0 ppm in normal settings, as well as the sensor output

Table 2: Dilution of SO₂ gas level in normal condition (25°C).

No	Standard SO ₂ (ppm)	Flow rate (NL.min ⁻¹)	Duration time (ms)	Volume target of SO ₂ (mL)	Level of SO ₂ (ppm)
1	100	1.0	0	0	0
2	100	1.0	3000	50	5
3	100	1.0	6000	100	10
4	100	1.0	12000	200	20
5	100	1.0	18000	300	30
6	100	1.0	24000	400	40
7	100	1.0	30000	500	50
8	100	1.0	36000	600	60
9	100	1.0	42000	700	70

range and sensor performance similarity. Furthermore, before the initial stage of calibration, the sensor will be turned on for 1 minute at 1-second intervals to establish the sensor’s baseline by exposing it to clean air. The data is then subjected to baseline differential modification, as described in equation 7.

$$X_j(t) = V_j(t) - Av_j \quad \dots(7)$$

where $X_j(t)$ is the corrected raw data value of the sensor- j at time- t , $V_j(t)$ is raw data value of the sensor sensor- j at time- t , and Av_j is mean baseline value of 1 minute.

All stages of the calibration are shown in Fig. 8. First, the test box is cleaned of residue or other contaminant gases by turning on the fan for 5 min, then the lid is closed and stabilizes for 3 min. Next, select the combination to select the gas flow duration and start recording sensor response before gas flows into the test case for 60 seconds. Gas starts flowing by first activating the flow controller. Simultaneously, the fan is turned on for 60 seconds to distribute the gas in the test box evenly. Recording continues for 240 seconds to determine the sensor response after gas flow. Finally, the lid is opened, and the reading is continued for 240 seconds. Repeat all of the above steps three times for the same concentration level and another concentration level. Experiments were carried out in the laboratory by maintaining a temperature of 25 ± 1 °C and relative humidity of 50 ± 5 %.

Analysis of Variance and Linear Regression

Analysis of Variance (ANOVA) is a statistical method

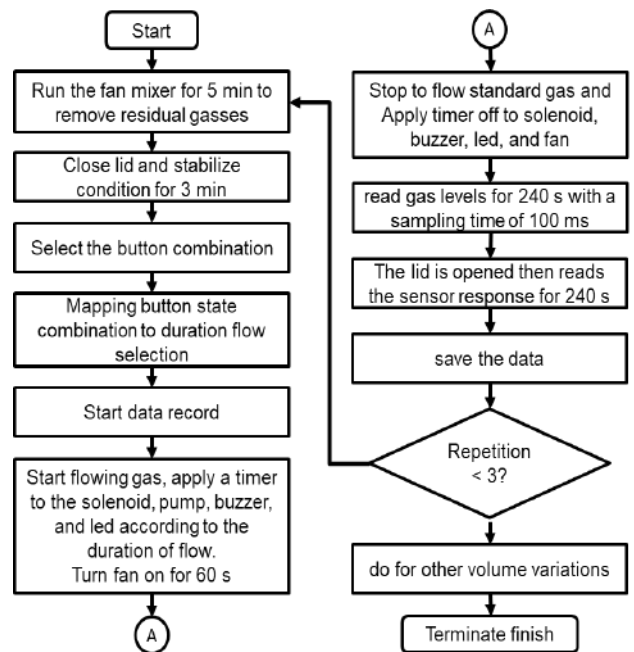


Fig. 8: Workflow of gas sensor calibration.

Table 3: Comparison of the performance stability of flow controller and direct flowing gas.

No	Actual gas flow (f _a)		Target gas flow (f _t) (L.min ⁻¹)	Error value	
	(L.min ⁻¹)			(%)	
	Flow controller	Direct flowing		Flow controller	Direct flowing
1	1.0	1.0	1.0	0.0	0.0
2	1.1	1.0	1.0	10.0	0.0
3	1.0	1.0	1.0	0.0	0.0
4	1.0	0.9	1.0	0.0	10.0
5	1.0	0.9	1.0	0.0	10.0
6	1.0	0.9	1.0	0.0	10.0
7	1.1	0.8	1.0	10.0	20.0
8	1.0	0.8	1.0	0.0	20.0
9	1.1	0.6	1.0	10.0	40.0
10	1.0	0.6	1.0	0.0	40.0
MAPE				3.0	15.0

commonly used in experimental research. The experimental design was applied using Microsoft Excel software by considering two factors, namely the exposure of the test gas to the sensor gas and the sensor sensitivity, which was calculated from the sensor’s response to variations in the concentration of the test gas. ANOVA analysis is used to analyze whether there are differences in the performance of the three sensors from the same sensor variant tested simultaneously and in iteration.

Analysis of Linear Regression

In general, regression analysis is used to determine the relationship between two or more variables (Rawlings et al. 1998). In this study, the gas sensor output signal was chosen as the dependent variable and the variation of the test gas concentration as a predictor variable. The value of the dependent variable can be estimated using the mathematical model defined in equation 8.

$$Y_i = \beta_0 + \beta_1 X_i + \varepsilon_i \quad \dots(8)$$

Where Y_i shows the concentration of the test gas, X_i is the sensor output signal. β₀ and β₁ are constants. ε_i is a random variable that includes all other factors.

RESULT AND DISCUSSION

Equipment Calibration Performance

The results of standard gas flow rate testing using and without a gas flow controller are shown in Table 3. Comparing the actual data (f_a) with the target gas flow (f_t) using and without a flow controller can determine the MAPE value. The MAPE

value system is equipped with a 3.0 % flow controller. Meanwhile, the system direct flowing gas was 15.0 %. Comparing the MAPE values shows that the test gas flow rate using the flow control design is more stable than directly passing the gas into the test box.

Preheating of Gas Sensor

The sensor first goes through a preheating process to achieve chemical equilibrium. The MQ-136 sensor used in this study is still in a new condition, but it is unknown how long it has been in storage since production. Therefore, preheating is essential to avoid instability in the reading of the sensor output signal. In this study, the preheating process was carried out at a test gas concentration level of 0 ppm for 30 hours with an interval of 3 seconds and using a 30 point MAF. MAF with 30 points was chosen because it considers the filter’s ability to reduce noise and limited memory Atmega 328.

Fig. 9 shows that the sensor response signal fluctuates and then stabilizes after 24 hours. According to the MQ-136 sensor datasheet, this may be due to the long sensor storage

Table 4: Comparison of the maximum, minimum, average, standard deviation and range values of the three MQ-136 sensors.

Parameter	Sensor-1	Sensor-2	Sensor-3
Mean	876.42	880.06	888.86
Standard Deviation	17.78	29.22	29.88
Range	78.15	139.03	139.03
Minimum	826.05	825.15	834.93
Maximum	904.20	964.18	973.96

time, and the sensor needs time to reach chemical equilibrium through the preheating process. In addition, the fluctuating sensor response can also be caused by changes in temperature and humidity during the preheating process, which affects the basic resistance, sensitivity, and reactivity (Samad et al. 2020). The statistical analysis of the three sensors resulting from the preheating process is presented in Table 4. This shows the similarity of the response signal behavior of the three MQ-136 sensors. In addition, the standard deviation indicates that the data is different from the mean value of each sensor.

Raw Signal Output

The testing of the three MQ-136 sensors was carried out simultaneously at each test gas concentration level of 0, 5, 10, 20, 30,40, 50, 60, and 70 ppm. Sensor testing at each concentration level was repeated three times. Raw data from the sensor output signal for each iteration is digitally processed with the 5-point MAF algorithm on the microcontroller.

Overall, the time taken to test the sensor was 600 seconds. After the sensor is put into the test box, in the time range 0-60 seconds (t_{0-60}), the output signal reads in the condition that SO₂ gas has not flowed into the test box, as shown in Fig. 10. This signal shows the baseline condition of the sensor in the range of 0-60 seconds (baseline t_{0-60}) before the test gas is applied. Fig. 11 indicates that the baseline t_{0-60} values

for the three sensors are pretty flat and tend to be the same in each iteration.

The results of the calculation of the mean t_{0-60} for each sensor are presented in Fig. 12. With a rise in the measured SO₂ concentration, the baseline value of the average t_{0-60} increases. The sensor response that does not completely recover after recording a given concentration level can cause this increase in the baseline t_{0-60} . In other words, there is still residual test gas on the sensor surface, resulting in a high sensor response value when detecting different concentration levels. In addition, because the gap between repetitions was only 5 minutes, the baseline reading result of t_{0-60} was higher than before, as shown in Fig. 11.

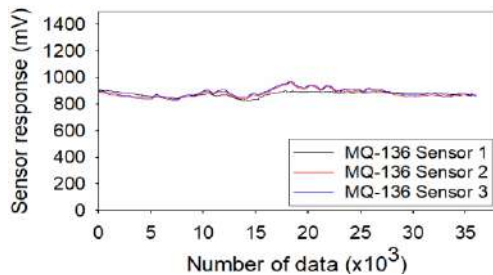


Fig. 9: The baseline value of the MQ-136 sensor is under normal conditions.

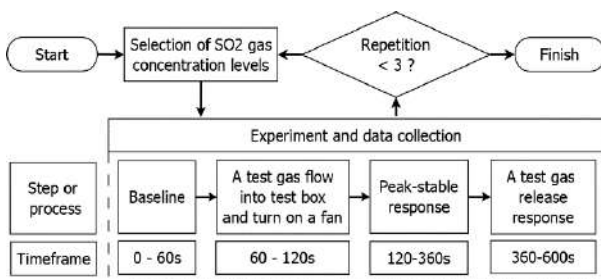


Fig. 10: The baseline value of the MQ-136 sensor is under normal conditions.

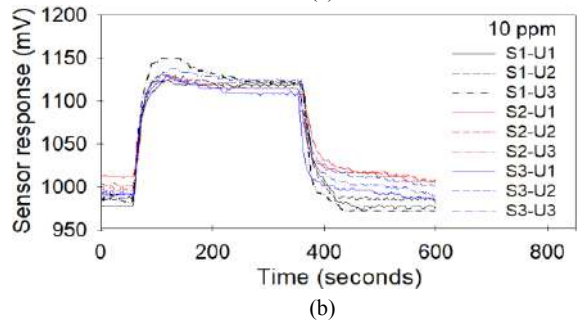
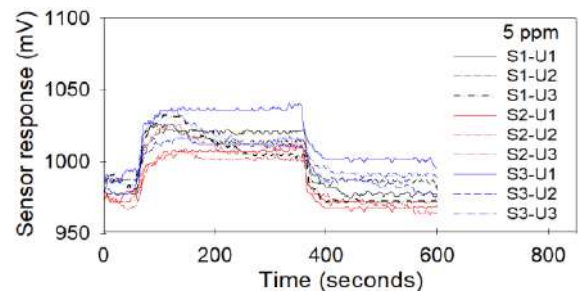


Fig. 11: Raw signal response of sensor MQ-136 for each repetition of each level concentration SO₂ gas in normal condition.

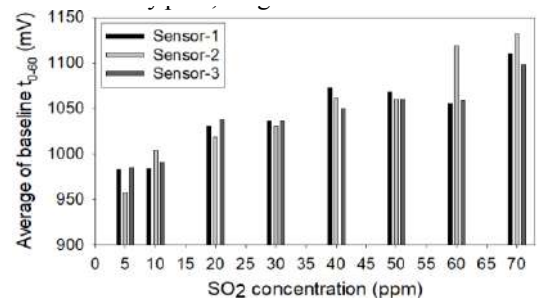


Fig. 12: The average baseline t_{0-60} value of the MQ-136 for each repetition of each level concentration SO₂ gas.

SO₂ gas is pumped into the test box for 60 seconds, depending on the desired concentration level. The fan is then switched on for 60 seconds to ensure that the gas is evenly spread throughout the box. The response signal rises at the same time until it reaches a steady peak value. The considerable concentration of the test gas influences the sensor's ability to reach a consistent peak time. The longer the output signal from the MQ-136 sensor reaches a steady peak, the greater the concentration value, as illustrated in Fig. 13.

Sensor Response Correction

By using the differential approach, the raw output signal for each sensor is averaged and then corrected by the mean baseline value. As a result, equation 7 corrects the sensor response signal to give it a new range, as shown in Fig. 14, in which each average baseline value subtracts all raw signals from each repetition at each concentration. This is done to account for any variations or changes in sensor response readings and to make comparing sensor output values at different test gas concentration levels easier.

Analysis of Variance

Table 5 shows the mean peak stable signal values at 200-350 second intervals ($t_{200-350}$) of the corrected data. The time

range $t_{200-350}$ was chosen because almost all of the sensor output signals are stable or flat in that period. The results of data analysis using ANOVA with a significant difference ($\alpha = 0.05$) using Microsoft Excel are presented in Table 7.

Based on Table 6, the term "sample" refers to the MQ-136 sensor group, while the "column" refers to the SO₂ concentration treatment. The sample obtained p -value > 0.05 and $F < F_{crit}$, so it can be said that there is no significant difference in the response signal generated between sensors. In contrast, the column obtained p -value < 0.05 and $F > F_{crit}$, so it can conclude that the concentration of SO₂ gas treatment affects the signal output generated by the sensor.

Tukey's yardstick method was used to determine whether there is a significant difference between the sensor's output signal at each SO₂ concentration treatment. To create the comparison matrix displayed in Table 8, this method compares the average response signal at each concentration level (AMS). The equation for Tukey's yardstick value will be return ω of 77.41. This value is added to the sensor's AMS so that the range value (AMS + ω) is formed (Table 7). At a concentration of 5 ppm, the range value is 77.41+32.40=109.81. If the AMS value at a concentration of 10 ppm is greater than the range value, the sensor output value at a concentration of 5 ppm-10 ppm is significantly

Table 5: Peak-stable value sensor response in millivolt.

Sensor	Repetition	The concentration of SO ₂ gas (ppm)							
		5	10	20	30	40	50	60	70
Sensor-1	1	43.06	140.23	221.54	324.79	426.95	542.21	572.77	562.10
	2	26.65	134.12	200.01	283.03	348.33	519.89	527.80	537.60
	3	20.99	137.20	182.28	264.33	354.21	491.29	559.46	497.16
Sensor-2	1	31.94	97.64	221.00	308.64	400.22	506.80	510.44	540.28
	2	27.85	117.29	208.00	294.77	360.84	503.81	452.82	500.02
	3	33.19	112.39	203.51	276.71	351.68	482.65	479.16	507.25
Sensor-3	1	46.62	117.19	230.77	301.21	449.25	507.04	557.14	537.79
	2	32.67	122.18	192.83	285.64	409.72	504.21	496.89	507.73
	3	28.96	136.83	174.52	267.02	395.63	472.82	514.43	471.84

Table 6: Results of the ANOVA for each sensor for each iteration at each concentration level of SO₂ ($\alpha = 0.05$).

Source of Variation	SS	df	MS	F	P-value	F crit
Sample	3201.86	2	1600.93	3.02	0.0584	3.1907
Columns	2274017.98	7	324859.71	612.03	1.15E-44	2.2074
Interaction	12376.00	14	884.00	1.67	0.096	1.9037
Within	25477.95	48	530.79			
Total	2315073.79	71				

different. This process is continued for a concentration of 10-20 ppm, 20-30 ppm, and so on.

Analysis of Linear Regression

In Table 8, the value “1”, shows the significant difference between the average sensor output signal at a certain concentration level and the average value of the output signal at a certain concentration level. Meanwhile, the value “0” indicates the opposite meaning. For example, the ratio of the average response of a sensor signal at a concentration level of 50-60 ppm, 60-70 ppm, and 50-70 ppm are “0”. This means that the signal in the concentration treatment is not significantly different. Thus it can be concluded that the sensor can only read SO₂ gas concentrations below 50 ppm.

CONCLUSION

Table 7: The mean and standard deviation of ANOVA for each sensor for each replication at each level of SO₂ concentration.

SO ₂ (ppm)	Sensor-1		Sensor-2		Sensor-3		Average of the mean (AMS*)
	Mean	SD	Mean	SD	Mean	SD	
5	30.2	11.5	30.1	2.8	36.1	9.3	32.4
10	137.1	3.1	109.1	10.2	125.4	10.2	123.9
20	191.2	19.6	210.7	9.2	199.4	28.7	200.4
30	290.7	31.0	293.4	16.0	284.6	17.1	289.6
40	376.5	43.8	370.9	25.8	418.2	27.8	388.5
50	517.8	25.5	497.8	13.2	494.7	19.0	503.4
60	553.3	23.1	480.8	28.9	522.8	31.0	519.0
70	532.3	32.8	515.9	21.5	505.8	33.0	518.0

*AMS (Average of mean response signal at each concentration level)

Table 8: Matrix compares the total value of the average response signal with the range values calculated by Tukey’s yardstick.

SO ₂ concentration (ppm)	5	10	20	30	40	50	60	70
5	0	1	1	1	1	1	1	1
10		0	1	1	1	1	1	1
20			0	1	1	1	1	1
30				0	1	1	1	1
40					0	1	1	1
50						0	0	0
60							0	0
70								0

The calibration findings reveal that the sensor output signal and the SO₂ concentration treatment have a link. The coefficients of determination for sensor-1, sensor-2, and sensor-3 are 0.94, 0.91, and 0.93, respectively (Fig. 15). The MQ-136

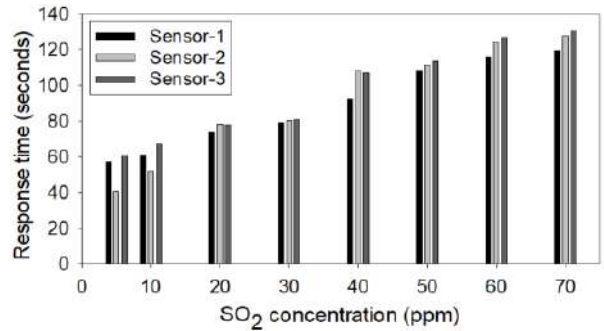


Fig.13: The average response time of the MQ-136 for each repetition of each level concentration SO₂ gas.

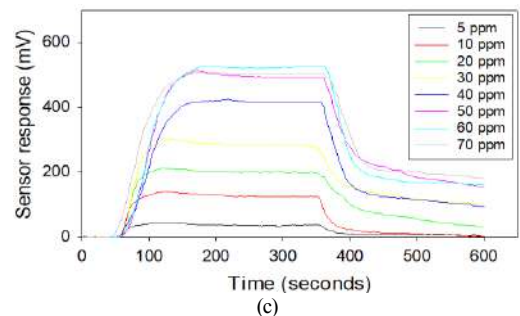
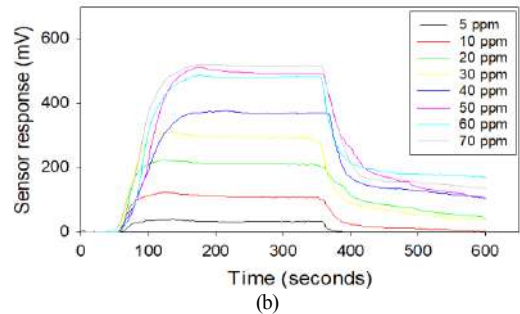
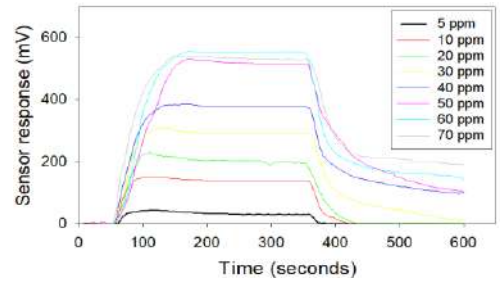


Fig. 14: Sensor response correction of each sensor MQ-136, sensor-1 (a), sensor-2 (b), and sensor-3 (c).

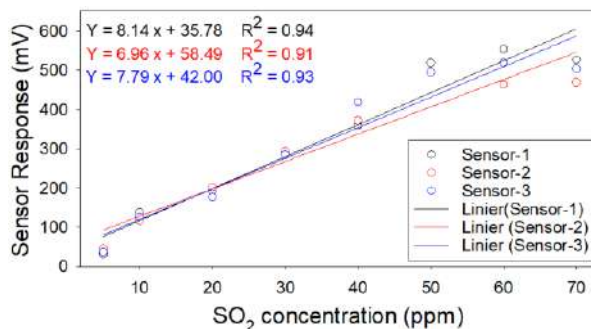


Fig. 15: The coefficient of determination of the effect of SO₂ gas concentration on the sensor response signal.

sensor utilized in this investigation, however, has an optimal reading range in the SO₂ concentration range of 5 to 50 ppm, according to the ANOVA analysis results. Furthermore, the calibration findings reveal that the three MQ-136 sensors perform similarly. This is based on an ANOVA analysis that found no significant differences between the sensors.

ACKNOWLEDGMENTS

This research was supported by the Unilab Perdana Laboratory in a collaborative program with IPB University.

REFERENCES

- Adithyan, R., Mohammed, A., Naseer, F.M., Ganesh, G., Nema, T., Sharma, P. and Mishra, V. 2016. Auto-Calibration of MOS gas sensor based on goodness of fit algorithm. *Int. J. Adv. Sci. Eng. Technol.*, 4(2): 98-101.
- Ahmed, S. 2015. Air pollution and its impact on agricultural crops in developing countries: A review. *J. Anim. Plant Sci.*, 25(3): 297-302.
- Arroyo, P., Herrero, J.L., Suárez, J.I. and Lozano, J. 2019. Wireless sensor network combined with cloud computing for air quality monitoring. *Sensors (Switzerland)*, 19(3): 691. doi:10.3390/s19030691
- Barsan, N., Weimar, U. and Chemistry T. 2012. Fundamentals of metal oxide gas sensors. *Int. Meet. Chem. Sensors*, 51: 618-621. doi:10.5162/IMCS2012/7.3.3
- Bassey, E., Whalley, J. and Sallis P. 2014. An evaluation of smoothing filters for gas sensor signal cleaning. *Int. Conf. Adv. Commun. Comput.*, 21(1): 19-23.
- Rawlings, J.O., Pantula, S.G. and Dickey, D.A. 1998. *Applied Regression Analysis: A Research Tool*. Springer, New York
- Kim, S. and Kim, H. 2016. A new metric of absolute percentage error for intermittent demand forecasts. *Int. J. Forecast.*, 32(3): 669-679. doi:10.1016/j.ijforecast.2015.12.003
- Korotcenkov, G. 2007. Metal oxides for solid-state gas sensors: What determines our choice? *Mater. Sci. Eng. B Solid-State Mater. Adv. Technol.*, 139(1): 1-23. doi: 10.1016/j.mseb.2007.01.044
- Liu, X., Cheng, S., Liu, H., Hu, S., Zhang, D. and Ning, H. 2012. A survey on gas sensing technology. *Sensors (Switzerland)*, 12(7): 9635-9665. doi:10.3390/s120709635
- Riordan, D. and Adeb, F. 2004. Air quality monitoring for sulfur dioxide in metropolitan Adelaide. *Environ. Prot. Auth.*, 7: 27 https://www.epa.sa.gov.au/files/477254_so2_repo
- Rumana, H.S., Sharma, R.C., Beniwal, V. and Sharma, A.K. 2014. A retrospective approach to assess human health risks associated with growing air pollution in the urbanized area of Thar Desert, Western Rajasthan, India. *J. Environ. Health Sci. Eng.*, 12: 23. doi.org/10.1186/2052-336X-12-23
- Samad, A., Nuñez, D.R.O., Castillo, G.C.S., Laquai, B. and Vogt, U. 2020. Effect of relative humidity and air temperature on the results obtained from low-cost gas sensors for ambient air quality measurements. *Sensors (Switzerland)*, 20(18): 1-29. doi:10.3390/s20185175
- Snyder, E.G., Watkins, T.H., Solomon, P.A., Thoma, E.D., Williams, R.W., Hagler, G.S.W., Shelow, D., Hindin, D.A., Kilaru, V.J. and Preuss, P.W. 2013. The changing paradigm of air pollution monitoring. *Environ. Sci. Technol.*, 47(20): 11369-11377. doi:10.1021/es4022602
- Tian, F., Yang, S.X. and Dong, K. 2005. Circuit and noise analysis of odorant gas sensors in an E-nose. *Sensors*, 5(1-2): 85-96. doi:10.3390/s5010085
- Zhengzhou, W.E.T. 2015. *Manual for Hydrogen Sulfide Gas Sensor Model MQ136 version 1.4*. Springer, New York



Rapid Extraction of Yam Peel Total Flavonoids in A Cholinium-Based Magnetic Ionic Liquid Aqueous Biphasic System

Y. Wang[†], F.W. Wang, M.F. Jia, L.N. Huang, Y.Q. He and S.Q. Dong

College of Life and Health Sciences, Anhui Science and Technology University, Fengyang 233100, China

[†]Corresponding author: Y. Wang; yanwang0129@126.com

Nat. Env. & Poll. Tech.
Website: www.neptjournal.com

Received: 14-05-2021

Revised: 20-06-2021

Accepted: 15-07-2021

Key Words:

Magnetic ionic liquid
Aqueous biphasic system
Flavonoids
Yam peel

ABSTRACT

In this study, for the first time, a magnetic ionic liquid-based aqueous biphasic system (MIL-ABS) was developed to extract total flavonoids from crude extracts of yam (*Dioscorea alata* L.) peel. The effect of various conditions on the separation behavior was systematically examined and optimized. A relatively high extraction efficiency (96.4%) and partition coefficient ($K = 33.2$) for total flavonoids could be achieved. MI-ABS not only has the advantage of being able to extract quickly in the absence of an organic solvent, but it also responds to a simple external magnetic field. This work has the potential to be a useful reference for practical enrichment or separation of active ingredients.

INTRODUCTION

Yam is one of the major food crops cultivated in many tropical and subtropical countries (Hu et al. 2018, Yeh et al. 2013). As a potential functional food, it has been widely used to promote therapeutic benefits (Xue et al. 2019, Zhou et al. 2018). Modern pharmacological researchers have revealed that yam is effective in promoting immunity (Liu et al. 2009), anti-oxidation (Zhang et al. 2018), anti-inflammation (Chen et al. 2017a), and protecting the heart function (Chen et al. 2017b). Based on previous studies, various active components, including polysaccharide, steroidal sapogenin, allantoin, polyphenol, flavonoids, and protein have been reported in yam (Hsu et al. 2011, Huang et al. 2007, Zhang et al. 2018). Flavonoids are the principal antioxidative component of yam, and they have been shown to have potential benefits on biological activities and human health. Although yam flavonoids have received a lot of attention, there have been few studies on yam peel flavonoids. As a result, given the potential value of yam peel as a waste, the extraction technology for flavonoids in yam peel needs to be researched further. In addition, the crude ethanol-water extract contains a significant amount of non-flavonoids. This factor surely adds to the difficulties of flavonoid separation post-processing. Polysaccharide, protein, and vitamin have been identified as co-existing components with similar solubility and polarity to the target flavonoids. Although polyamide resin (Liu et al. 2017), adsorption (Zhang et al. 2020), high-performance

liquid chromatography (HPLC) (Yeh et al. 2013), and two-dimensional reversed-phase liquid chromatography (2D-RPLC/RPLC) (Cai et al. 2020) have already been used to solve the separation post-processing problem, there is scope for exploring new methods for selective extraction and enrichment of flavonoids.

The aqueous biphasic system (ABS) is now one of the most promising technologies for separating bioactive compounds. It is a promising alternative to traditional organic solvent extraction methods because of its short time consumption, mild operating conditions, low cost, ease of scale-up, and relative environmental friendliness (He et al. 2018, Nie et al. 2018, Ren et al. 2018). ABS is also used to separate a variety of bioactive chemicals such as dyes (Penido et al. 2019), antibiotics (Mokhtarani et al. 2008), proteins (Gu & Glatz 2007), and so on. Gutowski et al. (2003) were the first to show that an ionic liquid (IL) may generate ABS in the presence of K_3PO_4 in 2003. In the years since, IL-based ABS has been used for a variety of purposes, including the enrichment of bioactive substances. The high designability of IL due to the variation in different cations and anions is the most appealing feature of IL-based ABS (Dimitrijevic et al. 2020). Thus, IL can be effectively designed with a desired affinity and polarity for a specific application.

Up to now, IL-based ABS has been successfully employed for the effective separation/extraction of many bioactive compounds and drugs (Belchior et al. 2020, Li et

al. 2010, Neves et al. 2016, Nie et al. 2018, Ren et al. 2018, Requejo et al. 2019). However, due to the small density difference, IL-based ABS still suffer from inefficient phase separation (Yao & Yao 2017). As a result, the centrifugation step is often used in common IL-based ABS to aid phase separation. Magnetic ionic liquid (MIL) has recently emerged as a new research focus in the separation/extraction fields (Trujillo-Rodriguez et al. 2017, Wang et al. 2014, Zhou et al. 2017). And the related aqueous biphasic system (MIL-ABS) is stimulating interest. Yao and Yao (2017) employed a MIL-ABS system based on guanidinium ionic liquid to detect trace amounts of chloramphenicol in a water sample. The results revealed a considerable enrichment effect, and chloramphenicol recovery was likewise satisfactory in the real water sample. Nie et al. (2018) developed the MIL-ABS for the extraction of berberine hydrochloride in *Rhizoma coptidis* using cholinium-based MIL. This research found that using a simple external magnetic field to separate the phases eliminates the need for centrifugation, making this technique more time-efficient and simple.

For the first time, an ABS method based on cholinium in extraction for flavonoids from crude extracts of yam (*Dioscorea alata* L.) peel was established based on the above. As a result, when the phenomena of aqueous biphasic system emerged, the extraction equilibrium was nearly realized. To aid phase separation, an external magnetic field was used. The single factor experiment was used to systematically adjust parameters, and an acceptable recovery efficiency was attained under optimal conditions. In summary, the findings of this study provided an alternative method for investigating the flavonoids separation procedure.

MATERIALS AND METHODS

Reagents and Materials

All reagents were of analytical pure grade. 4-Hydroxy-TEMPO (4-OH-TEMPO, >98%) and was purchased from Adama-beta Co. Ltd (Shanghai, China). N,N-dimethylethanolamine, chlorosulfonic acid, 1-bromopropane, 1-bromobutane, 1-bromopentane, and 1-bromohexane were supplied by Aladdin Reagent Co. Ltd (Shanghai, China). The standard of rutin selected as a standard compound for determining the total flavonoids content was provided by Macklin Biochemical Co., Ltd (Shanghai, China). Crude extracts of yam peel were self-made, which was obtained by the extraction of yam peel powder with 50% ethanol according to a previous study with minor modifications (Hsu et al. 2011). And the other reagents/salts were all bought from Macklin Biochemical Co., Ltd (Shanghai, China).

Synthesis of Cholinium-based Magnetic Ionic Liquids

The cholinium-based magnetic ionic liquids (MILs) were synthesized according to the procedure of previously reported literature with a minor modification (Nie et al. 2017). Briefly, two intermediates were prepared first. They were the alkyl-(2-hydroxyethyl)-dimethylammonium bromide ($[N_{11n}2OH]Br$, $n = 3, 4, 5, 6$) and sodium 4-sulfonatoxy-2,2,6,6-tetramethyl piperidine-1-yloxy ($[TEMPO-OSO_3]Na$), respectively. $[N_{11n}2OH]Br$ was synthesized as follows. First, N,N-dimethylethanolamine (0.2 mol) was dissolved in 30 mL ethanol, and then *n*-alkyl bromide (0.22 mol) was slowly added into the solution. The mixture system was refluxed under continuous stirring for 24 h. After the reaction, most ethanol solvents were removed under a vacuum. And the product was recrystallized in diethyl ether for purification and then dried at 50°C. In addition, the synthesis of $[TEMPO-OSO_3]Na$ was conducted as follows. 4-Hydroxy-TEMPO (0.05 mol) was dissolved in dichloromethane at 0-5°C, and then an equal molar of chlorosulfonic acid was added dropwise within 1 h. The above mixture was reacted under continuous stirring for 4 h at room temperature. After the reaction, the mixture was filtered and washed with dichloromethane 3 times, then dried under vacuum at 50°C. Subsequently, the obtained solid suffered a simple neutralization with NaOH aqueous solution to prepare the $[TEMPO-OSO_3]Na$ intermediate. Finally, the cholinium-based MILs $[N_{11n}2OH][TEMPO-OSO_3]$ ($n = 3, 4, 5, 6$) were prepared by the metathesis reaction between $[TEMPO-OSO_3]Na$ and $[N_{11n}2OH]Br$ in ethanol. The mixture was reacted at 50°C for 24 h followed by filtration. The obtained product was washed with acetone until no precipitation and dried under vacuum at 50°C. The final products were dark-reddish viscous liquids. The MILs were characterized by FT-IR spectra.

Extraction of Flavonoids with MIL-ABS

A certain volume of crude extracts of yam peel was transferred into a 5 mL sample vial, and a specific amount of MIL was successively dissolved in this solution. Afterward, inorganic salt was added and dissolved in the solution to form MIL-ABS at a constant temperature. After thorough extraction, a NdFeB magnet was employed to assist phase separation. Parameters, including the type of MILs, salts, each mass fraction of MIL + salt + crude extracts, extraction temperature, and time were systematically optimized to obtain higher extraction efficiency (E , %) and partition coefficient (K), which could be calculated according to Eqs. (1) and (2).

$$E(\%) = \frac{C_o \times V_o - C_b \times V_b}{C_o \times V_o} \times 100\% \quad \dots(1)$$

$$K = C_t/C_b \quad \dots(2)$$

where C_o ($\text{mg}\cdot\text{mL}^{-1}$) and V_o (mL) represents the initial concentration of total flavonoids in crude extracts and initial volume, respectively. C_b ($\text{mg}\cdot\text{mL}^{-1}$) and V_b (mL) are the concentration of total flavonoids in the bottom (b) phase and volume of the bottom phase, respectively. By subtracting the residual amount in the water-phase from the total amount before extraction, the amount of extracted flavonoids in the MIL phase was estimated.

RESULTS AND DISCUSSION

FT-IR Spectra

Fig.1 exhibits the FT-IR spectra of synthesized MILs. Herein, $[\text{N}_{11620\text{H}}][\text{TEMPO-OSO}_3]$ is taken as an example to analyze the infrared spectrum. The peak above 3000 cm^{-1} is related to the stretching vibration of the hydroxyl group in the cation structure of MIL. Peaks between 2800 cm^{-1} and 3000 cm^{-1} are attributed to C-H stretching. The band 1660 cm^{-1} may be assigned to the skeleton vibration of the anion structure. 1483 cm^{-1} corresponds to C-H asymmetric in-plane bending vibration. The absorption band at 1386 cm^{-1} is mainly assigned to the symmetric in-plane bending vibration of the C-H bond in the gem-dimethyl of the anion (Nie et al. 2017). The band at 1264 cm^{-1} is assigned to the stretching vibration absorption of the C-N bond. In addition, 1095 cm^{-1} corresponds to the stretching vibration of N-O in the anionic structure. The peak at 972 cm^{-1} belongs to the asymmetric stretching vibration of O-S-O in the anion.

Effect of Different MILs

The extraction and partition performance of target compounds can be influenced by the composition of the two phases

in the ABS. According to earlier studies, MIL's extraction behavior is mostly determined by its dissolving capacity for the target compound and the cluster characteristics generated by MIL. Thus, the effect of MILs $[\text{N}_{11n20\text{H}}][\text{TEMPO-OSO}_3]$ ($n=3, 4, 5, 6$) on the extraction efficiency (E) and partition coefficient (K) was tested. The condition of 10 wt% IL + 40wt% K_3PO_4 + 2 mL crude extracts was selected and the comparison result was presented in Fig. 2. According to the result, it can be observed that the level of both E and K are simultaneously increased with the prolongation of the alkyl chain. The trend is consistent with the previous report, which mentioned that the capability of MILs phase-separation can improve when the length of the alkyl chain becomes longer (Nie et al. 2018). The hydrophobicity can be reinforced with the carbon chain of MILs getting longer. Thus, the interaction between MIL and flavonoids can be determined by the hydrophobic effect and van der Waals's interaction (Mumcu & Seyhan Bozkurt 2019).

Effect of Weight Percent of MIL

The effect of MIL amount on extraction performance of total flavonoids was tested. Different weight percent of MIL $[\text{N}_{11620\text{H}}][\text{TEMPO-OSO}_3]$ with 2 mL crude extracts and 40wt% K_3PO_4 were investigated (see Fig. 3). It is obvious that a higher MIL amount leads to higher extraction efficiency and partition coefficient until the extraction system becomes saturated. It is well known that the larger amount of MIL was added, the more MIL-phase volume, which suggested that more flavonoids were transmitted into the MIL-rich phase. However, an excessive amount of MIL makes no contribution to the improvement of partition coefficient. This is maybe owing to the increasing volume of the top phase. Thus, 12 wt% MIL shows the optimal effect for extracting the target compound.

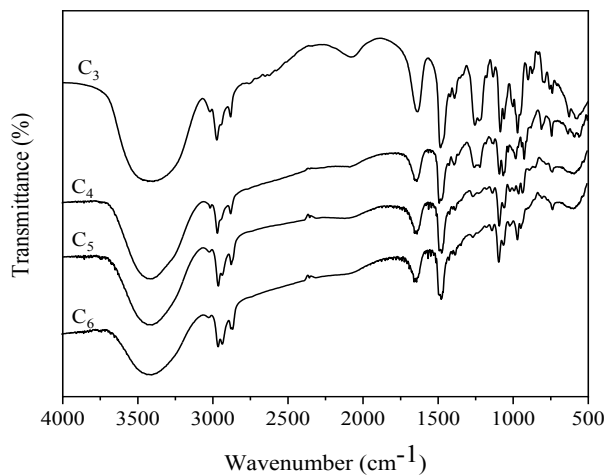


Fig. 1: FT-IR spectra of MILs.

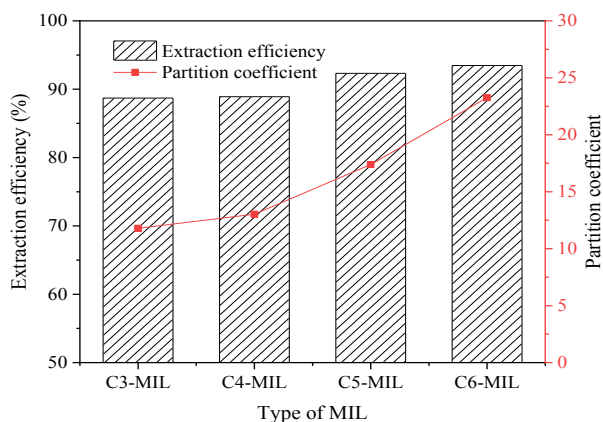


Fig. 2: The effect of different MILs on extraction efficiency and partition coefficient of total flavonoids.

Effect of Weight Percent of K_3PO_4

The weight percent of K_3PO_4 can also play an important role in the system. The weight percent of MIL $[N_{116}2OH]$ [TEMPO- OSO_3] was maintained at 12 wt% in the following tests, and the explored results were displayed in Fig. 4. It was observed that both the extraction efficiency and partition coefficient increase first, and then decrease with the addition of K_3PO_4 growing from 20 wt% to 40 wt%. The increasing amount of K_3PO_4 boosts the formation of two phases. Flavonoids provide a stronger salting-out effect, which is followed by flavonoids being transferred to the MIL-rich phase. Thus, at a concentration of 35 wt% K_3PO_4 , the maximum extraction efficiency and partition coefficient were achieved. Nonetheless, when its concentration is beyond 35% wt%, the values of E and K decline with the further addition of K_3PO_4 . Therefore, 35 wt% of K_3PO_4 was selected for further experiments.

Effect of Extraction Temperature

The result of the influence of temperature on extraction and partition performance of target compounds in MIL-ABS was shown in Fig. 5. Obviously, the extraction efficiency decreases slightly with a temperature range of 20°C to 50°C. This may be attributed to the viscosity of MIL reduced with the advanced temperature. The result will bring about the reduced mass transfer resistance of the target compound in the top and the bottom phases, resulting in a slight shrink in the extraction efficiency. As such, to predigest the operation, the room temperature was selected for the experiments.

Effects of Extraction Time

To explore the effect of extraction time on the extraction and partition performance, various durations (10-50 min) were

tested and presented in Fig. 6. Clearly, 10 min is enough to extract the target compound. Continuously increasing the extraction time results in a slight decrease in extraction efficiency, but not a significant change. Total flavonoids have a relatively low extraction time. This occurrence could be explained by MIL's high affinity for the target flavonoids. As a result, 10 min was sufficient for complete flavonoid enrichment with a high extraction efficiency and partition coefficient.

CONCLUSION

The MIL-ABS, which was made up of four MILs, was used to design the extraction procedure of total flavonoids from the crude extract of yam peel. $[N_{11n}2OH]$ [TEMPO- OSO_3] ($n=3, 4, 5, 6$). It was shown that the MIL $[N_{116}2OH]$ [TEMPO- OSO_3] exhibited a stronger ability for ABS phase formation. Under the optimal extraction condition, the extraction efficiency of total flavonoids is above 96%, which means the method is a relatively effective approach. This research has the potential to provide a useful reference for the enrichment or separation of natural products from complex samples in the real world. The MIL-ABS process could benefit from simplification of magnetic ionic liquid preparation and recycling to be applied at large scales.

ACKNOWLEDGEMENTS

This work was supported by the Projects of Anhui Science and Technology University for Talent Introduction (No. SKYJ201601) and the University Natural Science Research Project of Anhui Province (No. KJ2021A0884). The work also acknowledges the support from the National College Student Innovation Training Program (No. 201910879076, No. 202010879005).

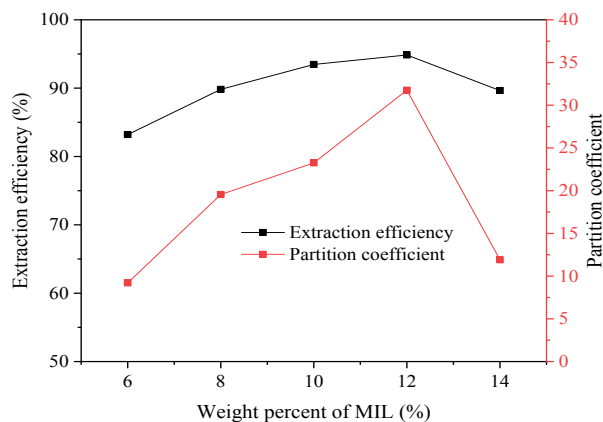


Fig. 3: The effect of weight percent of MIL on extraction efficiency and partition coefficient of total flavonoids.

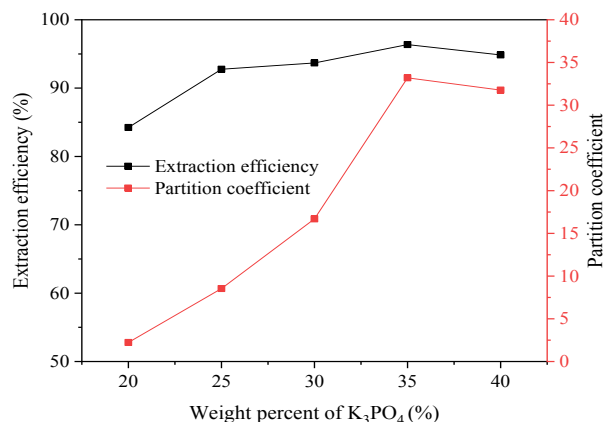


Fig. 4: The effect of weight percent of salt on extraction efficiency and partition coefficient of total flavonoids.

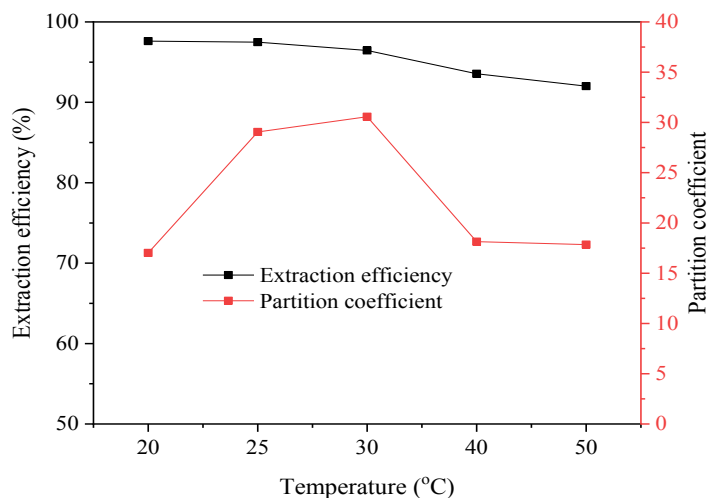


Fig. 5: The effect of extraction temperature on extraction efficiency and partition coefficient of total flavonoids.

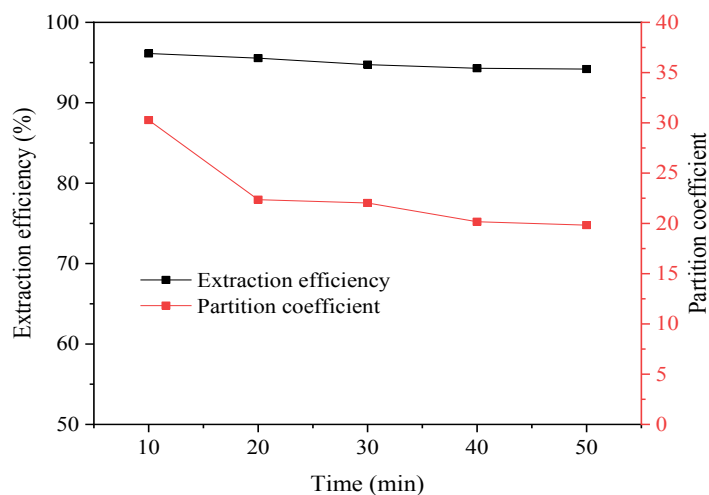


Fig. 6: The effect of extraction time on extraction efficiency and partition coefficient of total flavonoids.

REFERENCES

- Belchior, D.C.V., Quental, M.V., Pereira, M.M., Mendonça, C.M.N., Duarte, I.F. and Freire, M.G. 2020. Performance of tetraalkylammonium-based ionic liquids as constituents of aqueous biphasic systems in the extraction of ovalbumin and lysozyme. *Sep. Purif. Technol.*, 11: 233.
- Cai, R., Sun, Y., Guo, X., Wan, H., Xu, Q. and Wang, S. 2020. Separation and identification of polyphenol compounds in propolis using offline 2D-RPLC/RPLC coupled with Q-TOF-mass spectrometry. *J. Apicult. Res.*, 5: 1-11.
- Chen, C.T., Wang, Z.H., Hsu, C.C., Lin, H.H. and Chen, J. H. 2017a. Taiwanese and Japanese yam (*Dioscorea* spp.) extracts attenuate doxorubicin-induced cardiotoxicity in mice. *J. Food Drug Anal.*, 25(4): 872-880.
- Chen, T., Hu, S., Zhang, H., Guan, Q., Yang, Y. and Wang, X. 2017b. Anti-inflammatory effects of *Dioscorea alata* L. anthocyanins in a TNBS-induced colitis model. *Food Funct.*, 8(2): 659-669.
- Dimitrijevic, A., Tavares, A.P.M., Jocic, A., Maric, S., Trtic-Petrovic, T., Gadzuric, S. and Freire, M.O.G. 2020. Aqueous biphasic systems comprising copolymers and cholinium-based salts or ionic liquids: Insights on the mechanisms responsible for their creation. *Sep. Purif. Technol.*, 16: 248.
- Gu, Z. and Glatz, C.E. 2007. Aqueous two-phase extraction for protein recovery from corn extracts. *J. Chromatogr. B*, 845(1): 38-50.
- Gutowski, K.E., Broker, G.A., Willauer, H.D., Huddleston, J.G., Swatoski, R.P., Holbrey, J.D. and Rogers, R.D. 2003. Controlling the aqueous miscibility of ionic liquids: aqueous biphasic systems of water-miscible ionic liquids and water-structuring salts for recycling, metathesis, and separations. *J. Am. Chem. Soc.*, 125: 6632-6633.
- He, A., Dong, B., Feng, X. and Yao, S. 2018. Extraction of bioactive ginseng saponins using aqueous two-phase systems of ionic liquids and salts. *Sep. Purif. Technol.*, 196: 270-280.
- Hsu, C.K., Yeh, J.Y. and Wei, J.H. 2011. Protective effects of the crude extracts from yam (*Dioscorea alata*) peel on tert-butyl hydroperoxide-induced oxidative stress in mouse liver cells. *Food Chem.*, 126(2): 429-434.

- Hu, G.J., Zhao, Y., Gao, Q., Wang, X.W., Zhang, J.W., Peng, X., Tanokura, M. and Xue, Y.L. 2018. Functional properties of Chinese yam (*Dioscorea opposita* Thunb. cv. Baiyu) soluble protein. *J. Food Sci. Technol.*, 55(1): 381-388.
- Huang, C.C., Chiang, P.Y., Chen, Y.Y. and Wang, C.C.R. 2007. Chemical compositions and enzyme activity changes occur in yam (*Dioscorea alata* L.) tubers during growth. *LWT - Food Sci. Technol.*, 40(9): 1498-1506.
- Li, Z., Pei, Y., Wang, H., Fan, J. and Wang, J. 2010. Ionic liquid-based aqueous two-phase systems and their applications in green separation processes. *TrAC Trend. Anal. Chem.*, 29(11): 1336-1346.
- Liu, G., Zhuang, L., Song, D., Lu, C. and Xu, X. 2017. Isolation, purification, and identification of the main phenolic compounds from leaves of celery (*Apium graveolens* L. var. dulce Mill./Pers.). *J. Sep. Sci.*, 40(2): 472-479.
- Liu, Y.W., Liu, J.C., Huang, C.Y., Wang, C.K., Shang, H.F. and Hou, W.C. 2009. Effects of oral administration of yam tuber storage protein, dioscorin, to BALB/c mice for 21-Days on immune responses. *J. Agric. Food Chem.*, 57: 9274-9279.
- Mokhtarani, B., Karimzadeh, R., Amini, M.H. and Manesh, S.D. 2008. Partitioning of ciprofloxacin in an aqueous two-phase system of poly(ethylene glycol) and sodium sulfate. *Biochem. Eng. J.*, 38(2): 241-247.
- Mumcu, T. and Seyhan Bozkurt, S. 2019. Aqueous two-phase extraction technique based on magnetic ionic liquid-nonionic surfactant for phenolic acids in grape, apple, pear, and banana. *Turk. J. Chem.*, 43(6): 1672-1685.
- Neves, C., Shahriari, S., Lemus, J., Pereira, J.F.B., Freire, M.G. and Coutinho, J.A.P. 2016. Aqueous biphasic systems composed of ionic liquids and polypropylene glycol: insights into their liquid-liquid demixing mechanisms. *Phys. Chem. Chem. Phys.*, 18(30): 20571-20582.
- Nie, L.R., Song, H., Yohannes, A., Liang, S. and Yao, S. 2018. Extraction in a cholinium-based magnetic ionic liquid aqueous two-phase system for the determination of berberine hydrochloride in *Rhizoma coptidis*. *Rsc. Adv.*, 8(44): 25201-25209.
- Nie, L.R., Yao, S., Dong, B., Li, X.L. and Song, H. 2017. Synthesis, characterization, and physical properties of novel cholinium-based organic magnetic ionic liquids. *J. Mol. Liq.*, 240, 152-161.
- Penido, J.A., Mageste, A.B., Martins, P.L. and Ferreira, G.M.D. 2019. Surfactant is a selective modulator in the partitioning of dyes in aqueous two-phase systems: A strategy for separation. *J. Mol. Liq.*, 293.
- Ren, J., Li, Z., Liu, J., Pei, Y., Wang, H. and Wang, J. 2018. Choline derivative ionic liquids-based aqueous two-phase systems: Phase diagrams and partition of purine alkaloids. *J. Chem. Thermodyn.*, 118: 51-57.
- Requejo, P.F., Gómez, E. and Macedo, E.A. 2019. Partitioning of DNP-amino acids in new biodegradable choline amino acid/ionic liquid-based aqueous two-phase systems. *J. Chem. Eng. Data*, 64: 4733-4740.
- Trujillo-Rodriguez, M.J., Pino, V. and Anderson, J.L. 2017. Magnetic ionic liquids as extraction solvents in vacuum headspace single-drop microextraction. *Talanta*, 172: 86-94.
- Wang, Y., Sun, Y., Xu, B., Li, X., Jin, R., Zhang, H. and Song, D. 2014. Magnetic ionic liquid-based dispersive liquid-liquid microextraction for the determination of triazine herbicides in vegetable oils by liquid chromatography. *J. Chromatogr. A*, 1373: 9-16.
- Xue, H.Y., Li, J.R., Liu, Y.G., Gao, Q., Wang, X.W., Zhang, J.W., Tanokura, M. and Xue, Y.L. 2019. Optimization of the ultrafiltration-assisted extraction of Chinese yam polysaccharide using response surface methodology and its biological activity. *Int. J. Biol. Macromol.*, 121: 1186-1193.
- Yao, T. and Yao, S. 2017. The magnetic ionic liquid aqueous two-phase system coupled with high-performance liquid chromatography: A rapid approach for determination of chloramphenicol in a water environment. *J. Chromatogr. A*, 1481: 12-22.
- Yeh, Y.H., Hsieh, Y.L. and Lee, Y.T. 2013. Effects of yam peel extract against carbon tetrachloride-induced hepatotoxicity in rats. *J. Agric. Food Chem.*, 61(30): 7387-7396.
- Zhang, J., Tian, H., Zhan, P., Du, F., Zong, A. and Xu, T. 2018. Isolation and identification of phenolic compounds in Chinese purple yam and evaluation of the antioxidant activity. *LWT-Food Sci. Technol.*, 96: 161-165.
- Zhang, K., Wang, Q., Zhou, Y., Gao, J., Li, C. and Jiang, X. 2020. A low-cost crosslinked polystyrene derived from environmental wastes for adsorption of phenolic compounds from aqueous solution. *J. Mol. Liq.*, 314.
- Zhou, N., Zeng, M.N., Li, K., Yang, Y.Y., Bai, Z.Y., Zheng, X.K. and Feng, W.S. 2018. An integrated metabolomic strategy for the characterization of the effects of Chinese yam and its three active components on septic cardiomyopathy. *Food Funct.*, 9(9): 4989-4997.
- Zhou, S.Y., Song, N.Z., Lv, X.J. and Jia, Q. 2017. Magnetic dual task-specific polymeric ionic liquid nanoparticles for preconcentration and determination of gold, palladium, and platinum prior to their quantitation by graphite furnace AAS. *Microchim. Acta*, 184(9): 3497-3504.



Green Synthesis Of Bimetallic Iron/Copper Nanoparticles Using Ficus Leaves Extract For Removing Orange G(OG) Dye From Aqueous Medium

Mohammed A. Atiya*, Ahmed K. Hassan**† and Imad M. Luaibi*

*Al-Khwarizmi College of Engineering, University of Baghdad, Baghdad, Iraq

**Environment and Water Directorate, Ministry of Science and Technology, Baghdad, Iraq

†Corresponding author: Ahmed K. Hassan; emad.iq84@gmail.com

Nat. Env. & Poll. Tech.
Website: www.neptjournal.com

Received: 22-04-2021

Revised: 24-06-2021

Accepted: 14-07-2021

Key Words:

Ficus leaves

Green synthesis

Bimetallic nanoparticles

Orange G dye

ABSTRACT

This study shows that it is possible to fabricate and characterize green bimetallic nanoparticles using eco-friendly reduction and a capping agent, which is then used for removing the orange G dye (OG) from an aqueous solution. Characterization techniques such as scanning electron microscopy (SEM), Energy Dispersive Spectroscopy (EDAX), X-Ray diffraction (XRD), and Brunauer-Emmett-Teller (BET) were applied on the resultant bimetallic nanoparticles to ensure the size, and surface area of particles nanoparticles. The results found that the removal efficiency of OG depends on the G-Fe/Cu-NPs concentration (0.5-2.0 g.L⁻¹), initial pH (2-9), OG concentration (10-50 mg.L⁻¹), and temperature (30-50 °C). The batch experiments showed that 54% of 10 mg.L⁻¹ of OG was removed within the optimum dose, pH, and temperature which were 1 g.L⁻¹, 7 and 30 °C respectively. The results of kinetic adsorption models and mechanisms indicate that OG uptake on G-Fe/Cu-NPs follows the pseudo-second-order kinetic model, physisorption, and exothermic process with (-22.9 kJ.mol⁻¹) activation energy. Adsorption isotherm investigated with models of Freundlich, Langmuir, Temkin, and Dubinin, in addition, the parameters of thermodynamic such as ΔG° , ΔH° , and ΔS° were -0.462 kJ.mol⁻¹, -35.88 kJ.mol⁻¹, and 0.116 kJ.mol.K⁻¹ respectively, this indicated spontaneous, exothermic and favorable adsorption.

INTRODUCTION

Different wastes are generated by a variety of industries and discharged into water effluents, thereby affecting the aesthetic and quality of water and causing a serious problem by decreasing the amount of pure and clean water available in our world (Tara et al. 2019). Among these wastes are organic pollutants, especially, dyes which cause a bad effect on the environment and humans (Ismail et al. 2019).

A coloring process, which is widely employed in consumer products such as paper, plastics, textiles, cosmetics, and leather, is one of the most common industrial processes that discharge pollutants into the aqueous medium. Although dye types differ by industry, azo dyes account for more than half of all dyes used worldwide due to their versatility and chemical durability. However, discharging azo dyes into aquatic media hinders algae and other aquatic plants from absorbing sunlight and performing photosynthesis. Moreover, most azo dyes are carcinogenic in nature, toxic, and non-biodegradable, so it causes negative effects on people's health and the aquatic ecosystem (Homaeigohar 2020).

Adsorption, oxidative-reductive degradation, membrane separation, chemical coagulation, precipitation, and electro-coagulation are some of the materials and procedures that

have been utilized to clean up dye-polluted water (Atiya et al. 2020). The adsorption process, however, stands out among these approaches because of its capacity to remove organic contaminants (Campos et al. 2019).

Diverse adsorbents have been used for removing contaminants of wastewater, recently, nanotechnologies have proven to be very important in the removal of environmental pollutants, particularly, in the field of aqueous pollution. It deals with the synthesizing of tiny particles in the range of 1-100 nm which are labeled as nanoparticles (NPS). These molecules show unique properties such as small size, shape, large surface area, etc. that provide nanoparticles with better catalytic function, strong surface activity, and simple interaction with another particle (Pavithran et al. 2020).

Different techniques are used to synthesize nanomaterials such as physical technique that includes milling, vacuum sputtering, and thermal decomposition. Moreover, the chemical technique uses borohydride (NaBH₄) as a reduction agent. These two techniques may need a piece of sophisticated equipment, difficult conditions to control during the experiment, long procedures, and toxic capping agents. As a result, the biological method is a promising technique for overcoming these issues while achieving a safe and suitable procedure for synthesizing nanoparticles,

as well as treatment technology based on plant extract and microorganisms, which has been used as a substitute for physical and chemical techniques (Ma et al. 2020).

Due to its cost feasibility and ease of synthesis, biological synthesis utilizing plant leaf extract is a very promising technique. Plant leaves contain a considerable number of both capping and reducing agents, such as flavonoids, polyphenols, and other reducing components, which can reduce salts to zero-valent and avoid agglomeration. An abundance of plants that are free of compounds with negative side effects, non-toxic, high-efficiency, and low-cost have been certified for use in manufacturing green nanoparticles for wastewater treatment (Abd El-Aziz et al. 2020).

The ficus tree is one of the most abundant evergreens in several Asian countries and the United States. It belongs to the Moraceae family and can grow up to 30 meters in its normal habitat (Al-Qahtani 2017). Ficus contains numerous bioactive compounds such as phenolic, flavonoids, and tannins. These components are critical to the creation of ficus-zero valent iron nanoparticles (F-Fe⁰) because they do not have negative or toxic side effects. They are also biodegradable, environmentally safe, and can act as capping and reducing agents.

Although iron nanoparticles (Fe-NPs) have become widely used as a promising metal in treatment processes for the removal of various environmental contaminants, however, the reactivity of (Fe-NPs) may be impacted by the development of an oxide layer around particle surfaces. To prevent this reaction, bimetal is used to protect nanoparticles from oxidizing by adding a second catalyst such as Cu, Pt, Pd, Ni to the (Fe-NPs). The mutual effect of two metals improves the properties of nanoparticles over the use of just one metal (monometallic); therefore, bimetallic nanoparticles have become of great interest to researchers. Due to the economically and safely uses of copper compared to Pd and Ni, it has been used for coating the catalyst to enhance the rate of decolorization. (Dhruval et al. 2020, Gopal et al. 2020).

This study aims to prepare different ratios of iron/copper nanoparticles using the extract from the ficus plant, then, these ratios are evaluated for selecting the effective ratio of removing orange G dye (OG) which is an example of an azo dye. Thereafter, the effective ratio is used with complete batch experiments to investigate the effects of all required experimental conditions on the OG removal.

MATERIALS AND METHODS

Chemical and Reagents

The purity of all chemicals utilized was high (99.9 %), ficus leaves were collected from the University of Baghdad at Main Campus nearest Al-Khwarizmi College, Baghdad, Iraq. The

OG was purchased from Central Drug House (BDH), and Table 1 shows the properties of this dye. FeSO₄·7H₂O was purchased from BDH, CuSO₄·5H₂O was purchased from Fluka, and anhydrous ethanol was purchased from Carlo Erba. The change of pH was adjusted using 1.0 M H₂SO₄ and 1.0 M NaOH solutions.

Adsorbent Preparation

The G-Fe/Cu-NPs were made using the same processes as in the previous work (AbdelAziz et al. 2019), with the following changes.

Step 1: Fresh ficus leaves were washed several times using tap water and then washed with distilled water to eliminate any impurities or dust, followed by drying in an oven at 60 °C. Additionally, they were cut using mortar and pestle into small pieces with sifting using a 2.5 mm sieve.

Step 2: The ficus leaf extract was made with 150 mL deionized water and 20 g of ficus leaf pieces, which were then boiled for 20 minutes at 70°C and then filtered to remove suspended ficus particles using filter paper. Finally, the filtrate is chilled at 4°C until it is utilized as a reducing and capping agent.

Step 3: A solution of Fe (II) and Cu (II) mixed with the ratios varying as specified for this experiment was prepared. In this study, the Fe to Cu ratio of 1:1, 3:1, and 5:1 (w/w) was chosen to determine the amount of Cu that

Table 1: Characteristics of OG.

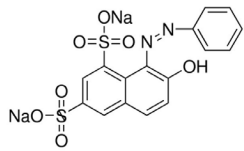
Properties of OG	
Molecular structure	
Molecular formula	C ₁₆ H ₁₀ N ₂ Na ₂ O ₇ S ₂
Molecular weight (g.mole ⁻¹)	452.37
Bulk density (kg.m ⁻³)	430
Solubility in water	Soluble in water
λ _{max} (nm)	478

Table 2: The ratio between iron and copper.

Fe:Cu ratio (w:w)	Fe (g)	Cu (g)	FeSO ₄ ·7H ₂ O (g)	CuSO ₄ ·5H ₂ O (g)
1:1	0.3	0.3	1.4935	1.1357
3:1	0.3	0.1	1.4935	0.7
5:1	0.3	0.06	1.4935	0.3929

will optimize the reactivity of the nanoparticles. The Fe: Cu ratio is made solely by measuring the weight of the two metals as shown in Table 2 below:

According to the selected ratio, $\text{FeSO}_4 \cdot 7\text{H}_2\text{O}$ and $\text{CuSO}_4 \cdot 5\text{H}_2\text{O}$ salts were dissolved in 100 mL of deionized water. After the salts had completely dissolved, the impurities were removed using a filter paper filtration procedure. 100 mL of extract from step 2 was added dropwise to the 100 mL Fe (II)/Cu (II) mixture to develop the synthesis of G-Fe/Cu-NPs. The color of the mixture changed gradually from yellow to brown to black when many drops of ficus extract were added, suggesting that the metals equivalents were reduced to zero-valent and the production of G-Fe/Cu-NPs was completed. To speed up the decrease, the remaining ficus extract is added. In addition, the mixture is continually mixed for 15 minutes. The black precipitate of G-Fe/Cu-NPs nanoparticles was separated by vacuum filtration using filter paper and then washed several times with distilled water before being rinsed with 100% ethanol. The washing and rinsing processes are crucial in the synthesis because they prevent nanoparticles from oxidizing too quickly. The G-Fe/Cu-NPs were then dried at room temperature overnight before being ground to a fine powder with a mortar and pestle.

Characterization of G-Fe/Cu-NPs

To prove the chemical classification, structure, size, and surface area of nanoparticles, different techniques are used. The SEM model was used to determine the shape, topography, and average size of these nanoparticles. The EDAX approach is a confirmatory procedure that ensures each particle's identification and chemical classification. In addition, the crystallinity of the materials is examined using the XRD technique. According to the primary choices, the XRD system can precisely analyze the crystalline state of nanoparticles. Finally, the BET approach determines the specific surface area, average pore size radius, average porosity radius, and nanoparticle pore volume.

Analytical Methods

Before starting the experiments, a calibration curve for standard OG solution was done to find the maximum wavelength of dye and the equation that joined the absorbance with concentration. Thus, the maximum wavelength of OG was found to be 478 nm as shown in Fig. 1.

The ratio between the adsorbate amounts (mg) per adsorbent (g) can be defined as the adsorption capacity at equilibrium q_e and can be estimated by the following formula:

$$q_e = \frac{C_o - C_e}{W} \times V \quad \dots(1)$$

Where the C_o is the initial concentrations and C_e is the equilibrium concentrations of adsorbate (in mg.L^{-1}), V is the volume of working solution, and W is the amount of adsorbent (g).

According to the below formula the removal efficiency (RE) was calculated:

$$RE \% = \frac{C_o - C_t}{C_o} \times 100 \quad \dots(2)$$

Where C_t is the OG concentration at time t .

Batch Adsorption Experiments

After selecting the best ratio of Fe to Cu, characterization of nanoparticles for this ratio would be performed, and batch adsorption experiments would be carried out to evaluate the OG removal efficiency. The working solution of 50 mg.L^{-1} of OG was prepared followed by adjusting pH before adding G-Fe/Cu-NPs. Some operating parameters were changed such as

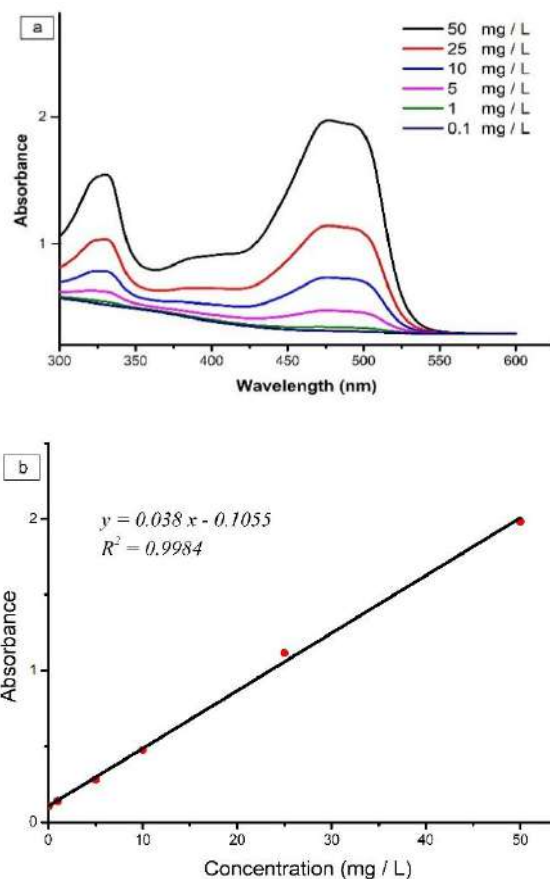


Fig. 1: UV-Vis analysis for various concentrations of OG solutions (a) Absorption and (b) Calibration plot.

G-Fe/Cu-NPs dosage ranged (0.5 – 2 g), pH ranging from (2 - 9), the range of initial OG concentrations were (10-50 mg.L⁻¹), contact time interval up to 120 min, the temperature ranged from (30 - 50 °C), and agitation rate from (100-600 rpm). A particular amount of G-Fe/Cu-NPs was added to the OG solution and stirred using a magnetic hot plate. The temperature remained constant, and each parameter's value was tuned separately. 10 ml samples were obtained at regular intervals during each run and evaluated by UV-Vis after filtering the sample with a 0.22 µm membrane filter.

RESULTS AND DISCUSSION

Formation and Characterization of G-Fe/Cu-NPs

The change in color of the solution from yellow to brown to black indicates that the reduction process took place and that G-Fe/Cu-NPs were formed, as well as the difference in pH before and after the reduction process, with the pH of the ficus extract being 5.42 and the pH of the mixture after reduction being 3.24. As a result, the pH of the solution drops along the reduction route, moving into the more acidic range.

The G-Fe/Cu-NPs have already been characterized, and the 3:1 Fe to Cu ratio has greater removal effectiveness than the 1:1 and 5:1 ratio.

Synthesized G Fe/Cu NPs were porous and formed as semi-spherical with diameters ranging from 32 to 59 nm, as seen in SEM images in Fig. 2. The porous and hollow nanoparticles aid in the elimination of OG. Furthermore, the size fluctuation of G-Fe/Cu-NPs is owing to agglomeration caused by the magnetic nature of the NPs, as well as variations in the local concentration of the ficus extract, which is responsible for the reduction of metal ions.

The EDAX spectrum of nanoparticles presented in

Fig. 3 contains further information about the synthesis of G-Fe/Cu-NPs, where the place of atomic distribution on the surface and chemical composition of G-Fe/Cu-NPs was demonstrated by the intense peaks of Fe, Cu, C, and O, 5.51 wt%, 3.33 wt%, 48.67 wt%, and 42.49 wt%, respectively. The finding of adjoint elements such as C and O signals resulted mainly from the ficus extracts that contain organic compounds C and O molecules which play a major role in the reduction and stabilizing process of G-Fe/Cu-NPs (Abd El-Aziz et al. 2020).

Fig. 4 shows the XRD curve of produced nanoparticles, which lacks any strong peaks, showing that there is no crystal structure in this case, despite a wide range of diffraction peaks (from 20o-25o). The amorphous nature of the bimetallic G-Fe/Cu-NPs generated by the green technique is demonstrated by the above result (Wang et al. 2018).

Table 3 shows the results of G-Fe/Cu-NPs surface area obtained by the BET technique. In this analysis, the pore size for G-Fe/Cu-NPs was 8.828 nm which can be classified as mesopore according to the classification of the IUPAC that categorized the pore size as macropore (50 > nm), mesopore (2 to 50 nm), super-micropore (0.7 to 2 nm) and ultra-micropore (0.7 < nm). Thus, as the catalytic performance is highly dependent on accessible pore channels due to their benefits for the diffusion of material, these size of pores provide more stability by acting as a shielding agent to prevent the harsh reaction conditions of the nanoparticles active sites (Elahimehr et al. 2020).

Best Ratio of Fe to Cu with Highest Removal Efficiency

The experiments for the three ratios are carried out, and the results show that the 3:1 ratio of Fe to Cu has the highest level of removal efficiency than the 1:1 and 5:1 ratio. As demon-

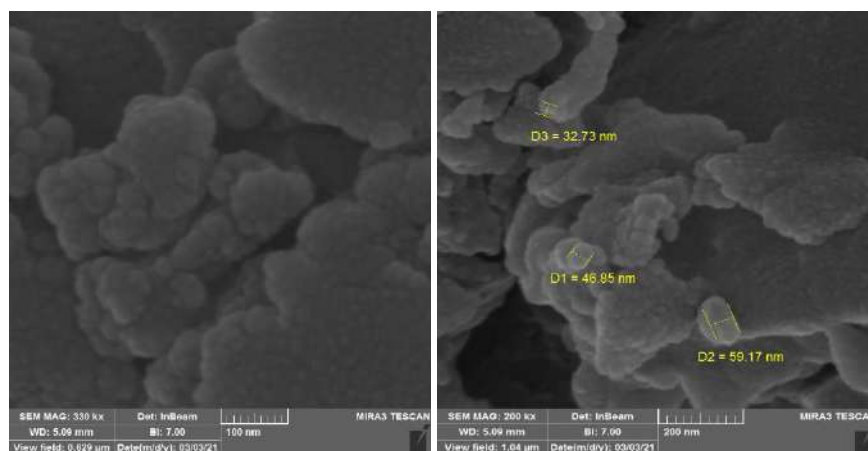


Fig. 2: SEM images of G-Fe/Cu-NPs.

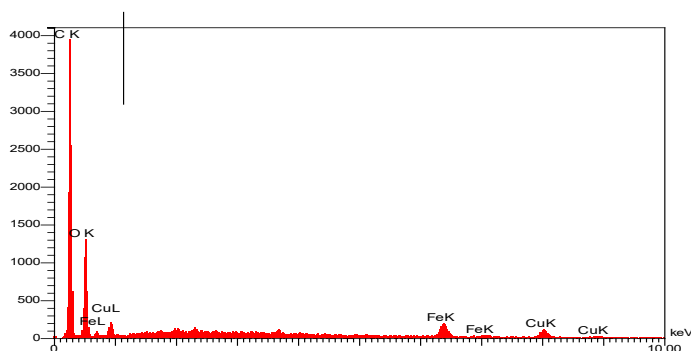


Fig. 3: EDX of prepared G-Fe/Cu-NPs sample.

strated in the results for three ratios in Fig. 5, a substantial increase in OG degradation was observed in the first 20 minutes due to the availability of active sites on the adsorbent surface that absorbed a high quantity of dye, but the rate of degradation slowed as unoccupied sites became saturated.

Effect of the Amount of G-Fe/Cu-NPs Dose

The impact of G-Fe/Cu-NPs dose on the degradation of OG was investigated. The dosage of nanoparticles was changed in the range 0.5-2.0 g.L⁻¹ by keeping the rest of the operating conditions constant (Fig. 6). The removal rate of OG were 10, 15, 19, 20, and 21 % for doses 0.5, 0.75, 1.0, 1.5, and 2.0 g.L⁻¹ respectively at 120 min period time. The removal effectiveness of OG improved as the number of G Fe/Cu-NPs was increased, owing to the availability of more vacant adsorption sites as the overall surface area of the adsorbate increased. Also, because of the repulsive forces that exist between the dyed surface and the adsorbate, the removal of OG increased dramatically at the start of contact time and then increased at a slow rate after reaching equilibrium, because it would be difficult to adsorbed OG ions by the remaining active sites (Mahmoud et al. 2019). However, as improving the removal of OG with more concentrated G-Fe/Cu-NPs, 1.0 g.L⁻¹ was chosen to be the optimum dose for

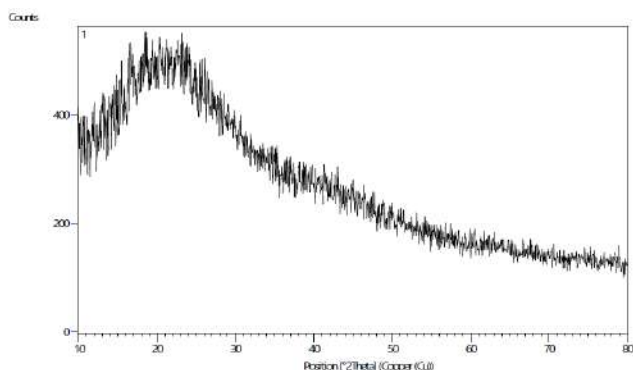


Fig. 4: XRD of prepared G-Fe/Cu-NPs sample.

G-Fe/Cu-NPs among doses 1.5 and 2.0 g/L, due to nearest removal efficiency and because 1.0 g.L⁻¹ is cost-effective.

Effect of Initial pH

The surface of the adsorbent charge and the solubility qualities of adsorbate are organized by how acidic, neutral, or basic the working solution is, and this has a big impact on dye removal. Fig. 7 shows the OG removal efficiency at various pH 2, 3, 4, 5, 7, and 9 along with 120 min, whereas the other parameters were kept constant. The OG removal efficiencies were 12, 15, 19, 22, 24, and 20 respectively. The adsorption capacity of OG increases with acidic pH (2-6) until it reaches a maximum for G-Fe/Cu-NPs adsorbent at neutral pH7, after which it decreases as pH7 is exceeded. The dissociation of surface functional groups on G-Fe/Cu-NPs is the cause of this pH effect. As a result, pH7 is the best pH for removing OG.

Effect of Initial Concentration

Because the degradation rate is a function of the dye's starting concentration, it's an important metric to consider for successful adsorption. The initial concentration acts as a driving force, allowing dye ions to transfer between the liquid and solid phases despite their resistance. As a result, many OG concentrations of 10, 20, 30, 40, and 50 mg.L⁻¹ were tested to see how they affected the removal efficiency. The removal rates were 54%, 48%, 38%, 32%, and 24% respectively, under the other operation conditions. The degradation of OG declines with increasing dye concentrations, as shown in Fig. 8, indicating that unoccupied sites are available with

Table 3: The BET parameters for G-Fe/Cu-NPs.

Parameter	Value
BET (m ² .g ⁻¹)	3.243
Pore size (nm)	8.828
Pore volume (cm ³ .g ⁻¹)	0.016

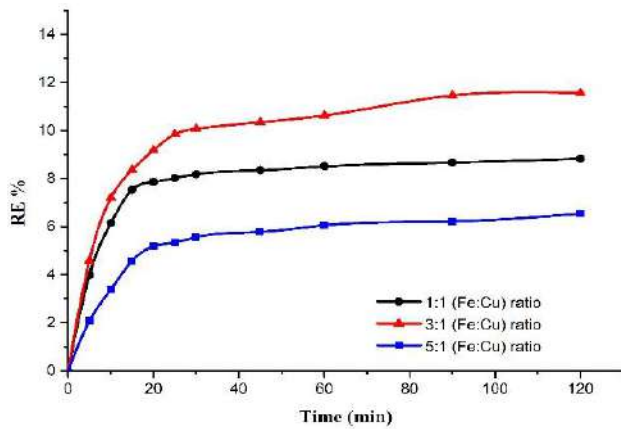


Fig. 5: The OG Removal for the ratios of Fe to Cu (1:1, 3:1, and 5:1) at G-Fe/Cu-NPs dose, pH, initial concentration, temperature, agitation speed, and time were 0.5 g.L⁻¹, 4, 50 mg.L⁻¹, 25 °C, 150 rpm, and 120 min.

low OG concentrations, resulting in more dye ions moving toward these vacant sites of the nanoparticles. With increasing concentrations of OG, the adsorbent's available active sites decrease, resulting in a lower OG removal percentage.

Effect of Temperature

By keeping all the other operation conditions constant, the experiments with various temperatures of 30, 40, and 50 °C were carried out to examine the removal of OG with two initial concentrations of 10 and 50 mg.L⁻¹, as shown in Fig. 9. The removal percentages with 10 mg.L⁻¹ of initial dye

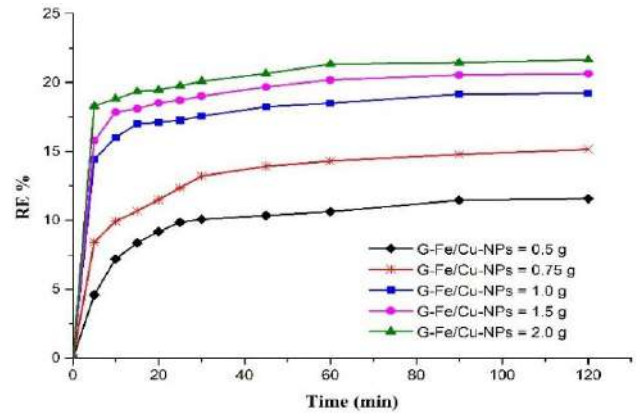


Fig. 6: Effect of the amount of G-Fe/Cu-NPs at initial OG concentration, pH, temperature, and agitation rate were 50 mg.L⁻¹, 4, 30 °C, and 150 rpm.

concentration for the studied above temperatures were 54%, 47%, and 33% respectively, whereas the removal percentages for 50 mg.L⁻¹ of initial concentration were 23%, 21%, and 10% respectively. It can be noted that the removal rate efficiency decreased with increasing the temperature from 30°C to 50°C, which means the adsorption of OG on G-Fe/Cu-NPs is exothermic in nature. The reason for decreasing removal efficiency with increasing temperature is probably due to the weakness of the adsorptive powers between the molecules of the adsorbed phases and also between the OG molecules and G-Fe/Cu-NPs active sites.

Table 4: Kinetic equations.

Model	Equation	Parameters
Pseudo-first order	$\log(q_e - q_t) = \log q_e - \frac{k_1 t}{2.303}$	q_t : adsorption capacities at time t (mg.g ⁻¹). k_1 : pseudo-first-order rate constant (min ⁻¹).
Pseudo-second-order	$\frac{t}{q_t} = \frac{1}{k_2 q_e^2} + \frac{t}{q_e}$	k_2 : pseudo-second order constant (g.[mg. min] ⁻¹)
Elovich	$q_t = \frac{1}{\beta} \ln(\alpha\beta) + \frac{1}{\beta} \ln(t)$	α : initial adsorption rate constant (mg.[g. min] ⁻¹) β : desorption rate constant (g.mg ⁻¹)

Table 5: The kinetic parameters for the adsorption of OG onto G-Fe/Cu-NPs at various initial dye concentrations.

OG (mg.L ⁻¹)	Pseudo-first order		Pseudo-second order		Elovich – Model		
	k ₁	R ²	k ₂	R ²	A	β	R ²
10	0.634	0.83	0.061	0.999	3.085	0.981	0.862
20	0.945	0.73	0.05	0.999	7.428	0.526	0.804
30	1.522	0.833	0.024	0.998	5.947	0.415	0.864
40	1.566	0.84	0.023	0.998	7.876	0.412	0.849
50	1.565	0.812	0.023	0.998	6.192	0.41	0.866

Effect of Agitation Intensity

The effect of agitation was investigated at speeds of 100, 150, 250, 400, and 600 rpm to see how much OG was removed at each of these rates. The batch adsorption studies were carried out at 1.0 g, 7, 10 mg.L⁻¹, and 30°C, with the dose of G-Fe/Cu-NPs, pH, and initial OG concentration set at 1.0 g, 7, 10 mg.L⁻¹, and 30°C, respectively. The results showed that mixing rates had no significant effect on OG degradation percentages. The phenomena can be shown by the controlling of adsorption rate, which was either by diffusion of film or pore, where at lower mixing speeds, the fluid film around the particle is thick and the rate-limiting step is perhaps diffusion of film. At greater mixing speeds, pore diffusion may be the rate-limiting stage since film diffusion has reached its maximum value. The fact that the resistance of the boundary layer is extremely tiny and the mobility of the process is highly regulated by the experimental conditions explains why varied agitation speeds are ineffective in this case. Alternatively, the ions of OG are diffused from the solution to the surface of G-Fe/Cu-NPs and subsequently into the pores easily and quickly.

Adsorption Kinetics

The pseudo-first-order, pseudo-second-order, and Elovich models were used to estimate the adsorption data in the kinetic investigation (Ma et al. 2020)

To investigate the above kinetics, Table 4 shows the kinetic equations were used:

The value of constant rate k_1 can be found from the slope of the graph between $\log(q_e - q_t)$ and time (t) as shown in Fig. 11-a. On the other hand, the values of k_2 and q_e for pseudo-second-order can be obtained from the slope and

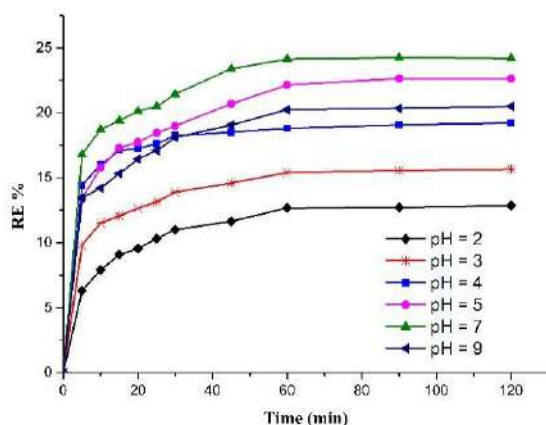


Fig. 7: Effect of initial pH at G-Fe/Cu-NPs dose, initial OG concentration, temperature, and agitation speed were 1 g.L⁻¹, 50 mg.L⁻¹ OG, 30 °C, and 150 rpm.

intercept of the plot between t/q_t versus t which is depicted in Fig. 11-b. It can be seen from Table 5 that the regression coefficient R^2 for pseudo-second-order is higher than R^2 for pseudo-first-order, which indicates that the pseudo-second-order kinetic model is the best fit model for OG kinetic adsorption by G-Fe/Cu-NPs.

The Elovich model is connected to the chemisorption kinetics of a solution onto the solid surface of adsorbents, as well as the activation energy and extent of surface coverage for chemisorption (Olivia et al. 2021). The values of Elovich coefficients α and β can be attained from the slope and intercept between q_t and $\ln(t)$ as presented in Fig. 11-c. It can be seen from Table 6 that the values of α and β are influenced by varying the initial concentration of OG, thus, as the initial OG concentration increased from 10-50 mg.L⁻¹ the value of β decreased, and no significant variation with α . Also, the results illustrated that the rate of adsorption α is higher than desorption constant β , which indicated the viability of adsorption. Further, the value of the regression coefficient R^2 of the Elovich model was already low which referred to a poor fit for this model.

In conclusion from Table 5, it can be observed that the pseudo-second-order model was most suitable to represent the G-Fe/Cu-NPs system kinetics.

Adsorption Isotherm

The adsorption isotherm is commonly used to determine adsorbates and adsorbents' maximal sorption capacity. The Langmuir, Temkin, Freundlich, and Dubinin isotherm models are used to examine the interaction between G-Fe/Cu-NPs (the adsorbent) and OG (the adsorbed dye), and the formulae for these expressions are shown in Table 6.

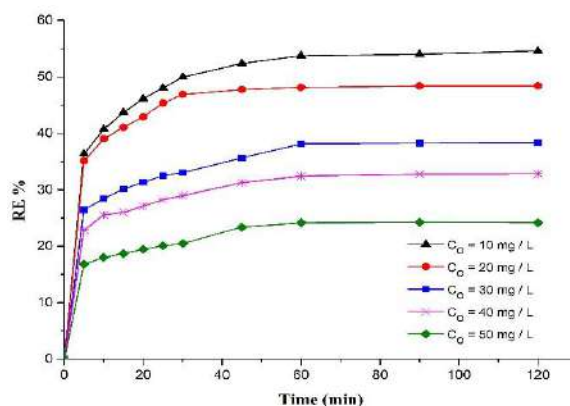


Fig. 8: Effect of initial OG concentration at a dosage of G-Fe/Cu-NPs, pH, temperature, time, and agitation rate were 1 g.L⁻¹, 7, 30°C, 120 min, and 150 rpm.

The Langmuir parameters of q_{max} and K_L can be calculated from the slope and intercept of plot $1/q_e$ versus $1/C_e$. Furthermore, the separation factor R_L is a dimensionless constant which represents a good indicator of the Langmuir isotherm, this expression can be obtained by the equation:

$$R_L = \frac{1}{1 + K_L C_o} \quad \dots(3)$$

Where R_L values was used to describe whether the adsorption is favorable when $R_L < 1$, linear when $R_L = 1$, unfavorable when $R_L > 1$, or irreversible when $R_L = 0$ (Al-Qahtani 2017).

Furthermore, the $1/n$ and K_F parameters of Freundlich isotherm can be found from the slope and intercept of graph $\log C_e$ versus $\log K_F$. In addition, the values of $1/n$ can verify if the isotherm is favorable when $0 < 1/n < 1$, unfavorable when $1/n > 1$ or irreversible when $1/n = 0$. The adsorption isotherm parameters are listed in Table 7, and Fig. 12 shows the isotherm models.

The data of isotherms in Table 7 indicated the Langmuir model has a good regression coefficient ($R^2=0.969$) and the values of R_L are ranged ($0 < R_L < 1$). These two parameters revealed a high degree of contact between the adsorbent and the adsorbate, as well as a favorable isotherm. Another indicator from the Freundlich isotherm is the value of the Freundlich constant K_F , which indicates increased adsorption capacity because its value is substantial (2.43); also, the value

of $1/n$ is between 0 and 1, indicating a favorable isotherm. The maximum binding heat of sorption B_T obtained from Temkin isotherm was a positive number ($0.263 \text{ kJ.mol}^{-1}$) and this refers to an exothermic adsorption process. The good regression coefficient R^2 obtained from Dubinin isotherm is higher also ($R^2 = 0.986$) which refers to the strong interaction between the reactive group of OG and the adsorbent G-Fe/Cu-NPs, further, the E value was ($0.395 \text{ kJ.mol}^{-1}$) which indicated to the type of adsorption, this value referred to physisorption (Maguana et al. 2020). Finally, the Langmuir and Dubinin isotherms are the best fitting models for the adsorption of OG on the G-Fe/Cu-NPs.

Adsorption Thermodynamic

The OG adsorption onto bimetallic G-Fe/Cu-NPs was investigated at various temperatures (303, 313, and 323 K) to determine the adsorption spontaneity, adsorption nature, and adsorbent applicability. These properties of adsorption can be found from the thermodynamic parameters of standard Gibbs free energy (ΔG°), standard enthalpy (ΔH°), and standard entropy (ΔS°) of the adsorption which derived by the following equations (Edet & Ifelebuegu 2020).

$$\Delta G^\circ = \Delta H^\circ - T \Delta S^\circ \quad \dots(4)$$

$$\Delta G^\circ = -RT \ln K_C \quad \dots(5)$$

$$K_C = \frac{q_e}{C_e} \quad \dots(6)$$

Table 6: Isotherm equations.

Model	Equation	Parameters
Langmuir	$\frac{1}{q_e} = \frac{1}{q_{max} \cdot K_L} \left(\frac{1}{C_e} \right) + \frac{1}{q_{max}}$	q_{max} : saturation adsorption of Langmuir (mg.L^{-1}). K_L : equilibrium constant of Langmuir (L.mg^{-1})
Freundlich	$\log q_e = \left(\frac{1}{n} \right) \log C_e + \log K_F$	K_F : the Freundlich adsorption constants. $1/n$: factor of heterogeneity
Temkin	$q_e = B_T \ln C_e + B_T \ln K_T$ $B_T = \frac{RT}{b_T}$	K_T : factor of the maximum binding energy (L.g^{-1}) B_T : maximum binding heat of sorption (KJ.mol^{-1}). R : ideal gas constant ($0.008314 \text{ kJ.mol}^{-1}.\text{K}^{-1}$). T : absolute temperature (K).
Dubinin	$nq_e = \ln q_m - \beta \varepsilon^2$ $\varepsilon = RT \ln \left(1 + \frac{1}{C_e} \right)$ $E = \frac{1}{\sqrt{(2\beta)}}$	q_m : the theoretical saturation capacity β : Dubinin constant ($\text{mol}^2.\text{kJ}^{-2}$) ε : Dubinin isotherm constant E : adsorption energy (kJ.mol^{-1}).

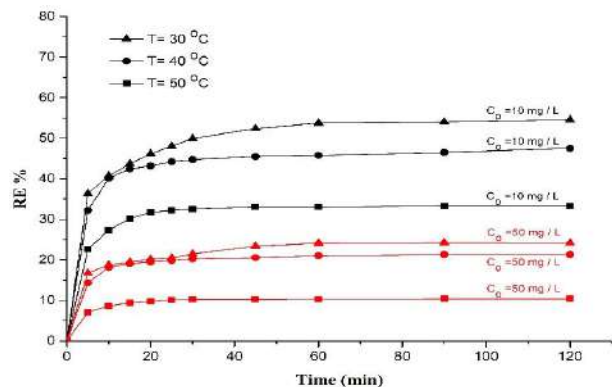


Fig. 9: Effect of temperature for 10 and 50 mg/L OG concentration, and at a dosage of G-Fe/Cu-NPs, pH, time, and agitation rate were 1 g.L⁻¹, 7, 120 min, and 150 rpm.

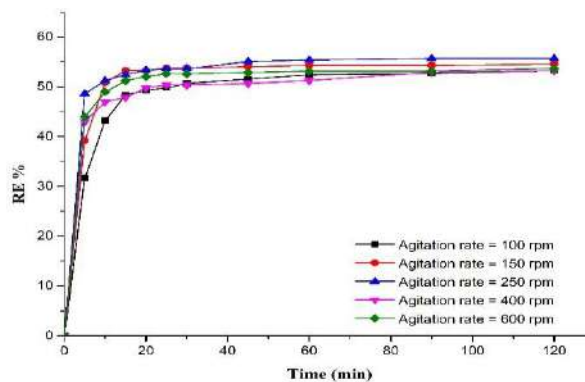


Fig. 10: Effect of agitation rate.

Where K_C is the distribution constant (L.g⁻¹). Hence, ΔS° and ΔH° can be obtained from the intercept and slope of graph ΔG° versus Temperature (K) as depicted in Fig. 13a.

Furthermore, the activation energy can be obtained from the Arrhenius equation shown below

$$\ln k_{obs} = \ln A - \frac{E_a}{RT} \quad \dots(7)$$

$$\ln\left(\frac{C_t}{C_o}\right) = -k_{obs} t \quad \dots(8)$$

Where k_{obs} is the rate constant (min⁻¹), E_a is the activation energy (kJ.mol⁻¹), and A is the Arrhenius constant (J.mol⁻¹.K⁻¹). E_a represents the slope of the plot between $\ln(k_{obs})$ versus $1/T$ as shown in Fig. 13b.

The thermodynamic parameters of OG adsorption onto G-Fe/Cu-NPs are illustrated in Table 8.

The Gibbs free energy ΔG° had a negative value at the optimum temperature studied (Table 8), thus confirming the spontaneity adsorption nature. On the other hand, the value of ΔG° (-0.462 kJ/mol) was between 0 kJ.mol⁻¹ and -20 kJ.mol⁻¹ which suggests a physisorption process (Romdhane et al. 2020). The negative value obtained for ΔH° (-35.884 kJ.mol⁻¹) indicated that adsorption of OG onto G-Fe/Cu-NPs was an exothermic process of the adsorption process at the solid-solution interface and a suitable affinity of OG ions towards nanoparticles. The result of (ΔS°) was positive (0.116 kJ.mol⁻¹.K⁻¹), indicating increased random interference of the adsorption process at the solid-liquid interface and an appropriate affinity of OG ions for nanoparticles (Edet & Ifelebuegu 2020).

Table 7: The isotherm parameters for the adsorption of OG onto G-Fe/Cu-NPs at various initial concentrations of OG.

Langmuir			Freundlich				Temkin			Dubinin			
q_{max}	K_L	R^2	R_L	K_F	$1/n$	R^2	K_T	B_T	R^2	q_m	β	E	R^2
17.03	0.105	0.969	0.281	2.43	0.385	0.862	1	0.263	0.858	12.299	3.205	0.395	0.986

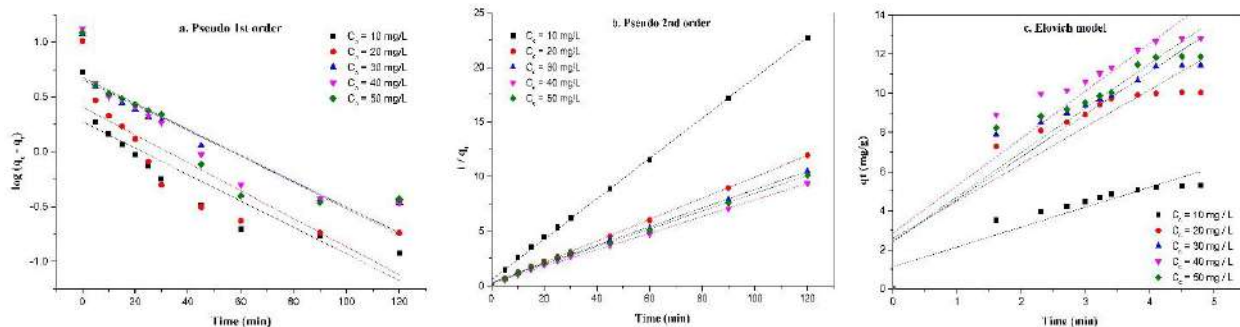


Fig. 11: Kinetic models at a different initial concentration of OG adsorption.

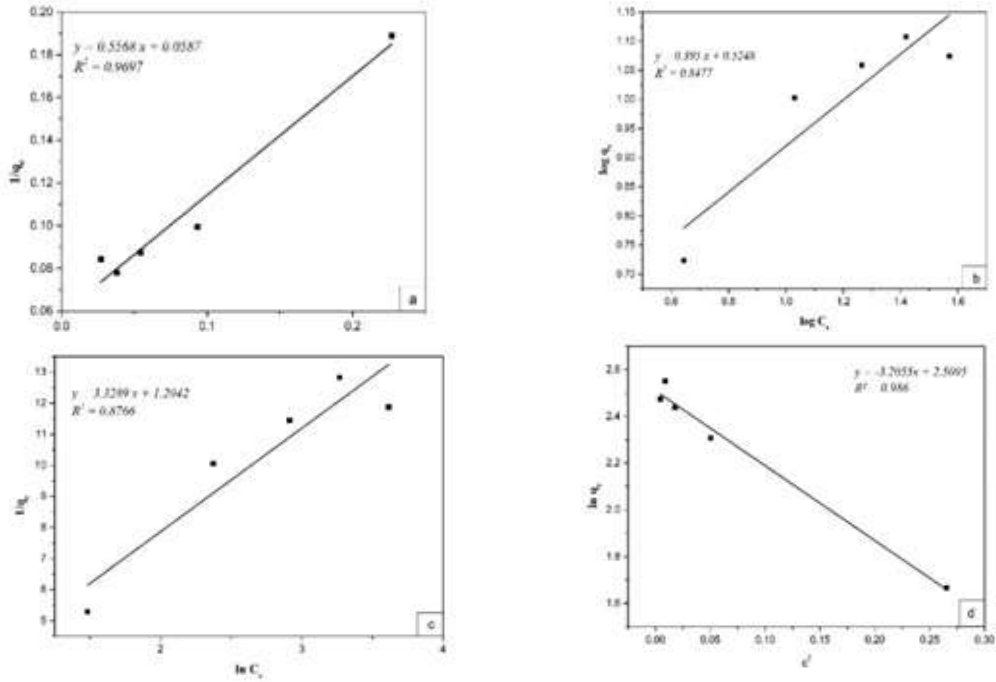


Fig. 12: Isotherm models plots (a) Langmuir, (b) Freundlich, (C) Temkin, and (d) Dubinin isotherm.

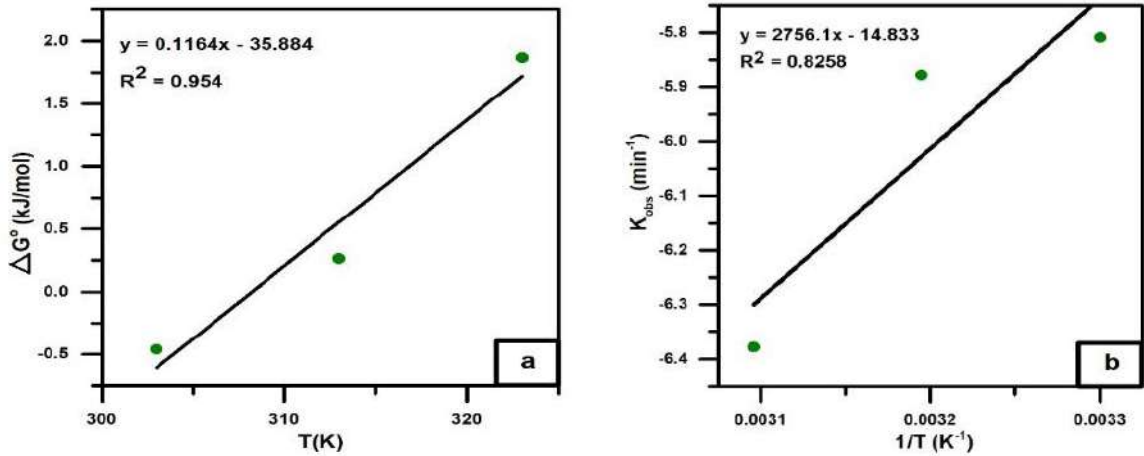


Fig. 13: Thermodynamic parameters.

CONCLUSIONS

The effectiveness of the produced nanoparticles in relation to orange G dye adsorption in a batch system was tested in this work, which investigated a green preparation of bimetallic nanoparticles utilizing cost-effective material. Because of its availability and low cost, ficus extract has been demonstrated to be a viable material for capping and reducing agents. This study looked at the biosynthesis of bimetallic iron/copper

Table 8: Thermodynamic parameters.

Parameter	Value
ΔG° (kJ.mol ⁻¹)	-0.462
ΔH° (kJ.mol ⁻¹)	-35.884
ΔS° (kJ.mol.K ⁻¹)	0.116
E_a (kJ.mol ⁻¹)	-22.91
A	3.615×10^{-7}

nanoparticles with various ratios, and the optimal ratio of Fe to Cu for removing orange G dye was 3:1. However, this ratio was characterized using SEM, EDAX, XRD, and BET. Specifically, the semi-spherical and porous morphology of G-Fe/Cu-NPs was found with the diameter ranges from 32-59 nm and the surface area was $3.243 \text{ m}^2 \cdot \text{g}^{-1}$. In addition, the EDAX confirmed the bimetallic nature of nanoparticles by confirming the presence of iron and copper in the analyzed sample, while the amorphous of nanoparticles was confirmed by the XRD analysis. Then, using a comprehensive batch procedure, the adsorbent was tuned for all essential parameters. As a result, the G-Fe/Cu-NPs have a beneficial effect when used as adsorbents to remove OG, with batch trials yielding a final OG removal effectiveness of (54%) at the optimum conditions. It is found that the best values of the adsorption parameters such as G-Fe/Cu-NPs dose, pH, initial OG concentration, and temperature were $1 \text{ g} \cdot \text{L}^{-1}$, 7, $10 \text{ mg} \cdot \text{L}^{-1}$, and 30 respectively along with 120 min contact time, while the agitation speed showed no significant effect upon the degradation rate of OG.

The kinetic study exhibited that the removal of OG by G-Fe/Cu-NPs fit the pseudo-second-order kinetic model. Furthermore, the intra-particle diffusion of the adsorption mechanism demonstrated that the diffusion of OG inside the pore of G Fe/Cu-NPs is the rate-limiting step. Furthermore, the Langmuir and Dubinin isotherms were shown to be the most fitting models for the adsorption of OG on G Fe/Cu NPs. Furthermore, the Temkin model's binding heat of sorption was positive, indicating an exothermic adsorption process, and the adsorption energy showed physisorption adsorption. Finally, the adsorption thermodynamic parameters revealed the nature of spontaneity adsorption, physisorption, exothermic process, and random interference of the adsorption process, which increased at the solid-solution interface and a reasonable affinity of OG ions towards nanoparticles.

REFERENCES

- Atiya, M., Ridha, M.J. and Saheb, M. 2020. Removal of aniline blue from textile wastewater using electrocoagulation with the application of the response surface approach. *Iraqi J. Sci.*, 61: 114 doi: 10.24996/ijs.2020.61.11.4.
- Abd El-Aziz, H.M., Farag, R.S. and Abdel-Gawad, S.A. 2020. Removal of contaminant metformin from water by using Ficus Benjamina zero-valent iron/copper nanoparticles. *Nanotechnol. Environ. Eng.*, 5(3): 1-9. doi: 10.1007/s41204-020-00086-w.
- Abdel-Aziz, H.M., Farag, R.S. and Abdel-Gawad, S.A. 2019. Carbamazepine removal from aqueous solution by green synthesis. *Int. J. Environ. Res.*, 19: 220. doi: 10.1007/s41742-019-00220-w.
- Al-Qahtani, K.M. 2017. Cadmium removal from aqueous solution by green synthesis zero-valent silver nanoparticles with Benjamina leaves extract. *J. Aquat. Res.*, 43(4): 269-274. doi: 10.1016/j.ejar.2017.10.003.
- Campos, S., Salazar, R., Arancibia-Miranda, N., Rubio, M.A., Aranda, M., García, A., Sepúlveda, P. and Espinoza, L.C. 2019. Nafcillin degradation by heterogeneous electro-Fenton process using Fe, Cu and Fe/Cu nanoparticles. *Chemosphere*, 12: 813. doi: 10.1016/j.chemosphere.2020.125813.
- Dhruval, S.R., Pai, N., Dhanwant, S.S., Hussein, B., Nayak, S., Rao, C.V., Kumar, A. and Janakaraj, M. 2020. Rapid synthesis of antimicrobial Fe/Cu alloy nanoparticles using waste silkworm cocoon extracts for cement mortar applications. *Adv. Nat. Sc.: Nanosci. Nanotechnol.*, 11(2): 25006. doi: 10.1088/2043-6254/ab8790.
- Edet, U.A. and Ifelebuegu, A.O. 2020. Kinetics, isotherms, and thermodynamic modeling of the adsorption of phosphates from model wastewater using recycled brick waste. *Processes*, 8(6): 665. doi: 10.3390/pr8060665.
- Elahimehr, Z., Nemati, F. and Elhampour, A. 2020. Synthesis of a magnetic-based yolk-shell nano-reactor: A new class of monofunctional catalyst by Cu0-nanoparticles and its application as a highly effective and green catalyst for A3 coupling reaction effective and green catalyst for the A3 coupling reaction. *Arab. J. Chem.*, 11: 211. doi: 10.1016/j.arabj.2018.11.011.
- Gopal, G., Sankar, H., Natarajan, C. and Mukherjee, A. 2020. Tetracycline removal using green synthesized bimetallic nZVI-Cu and bentonite supported green nZVI-Cu nanocomposite: A comparative study. *J. Environ. Manag.*, 254: 109812. doi: 10.1016/j.jenvman.2019.109812.
- Homaieghar, S. 2020. The nanosized dye adsorbents for water treatment. *Nanomaterials*, 10(2): 295. doi: 10.3390/nano10020295.
- Ismail, M., Khan, M., Khan, M.A. and Asiri, A.M. 2019. Pollution, toxicity, and carcinogenicity of organic dyes and their catalytic bio-remediation. *Curr. Pharma. Design*, 25(34): 3645-3663. <https://doi.org/10.2174/1381612825666191021142026>
- Ma, P., Liu, Q., Liu, P., Li, H., Han, H., Liu, L. and Zou, W. 2020. Green synthesis of Fe/Cu oxides composite particles stabilized by pine needle extract and investigation of their adsorption activity for norfloxacin and ofloxacin. *J. Dispers. Sci. Technol.*, doi: 10.1080/01932691.2020.1764367.
- Maguana, Y., El, N., Elhadiri, M.B. and Chikri, R. 2020. Activated carbon for dyes removal: Modeling and understanding the adsorption process. *J. Chem.*, 15: 683. doi: 10.1155/2020/2096834.
- Mahmoud, A.S., Ismail, A., Mostafa, M.K., Mahmoud, M.S., Ali, W. and Shawky, A.M. 2019. Isotherm and kinetic studies for heptachlor removal from aqueous solution using Fe/ Cu nanoparticles, artificial intelligence, and regression analysis. *Sep. Sci. Technol.*, 55(4): 684-696. doi: 10.1080/01496395.2019.1574832.
- Olivia, E.N., Adimchinobi, E.S. and Uzoma, O.T. 2021. Equilibrium and kinetic studies of liquid-phase adsorption of methylene blue onto phosphoric acid modified Bambara nutshell. *Acta Chem. Malay.*, 16: 222. doi: 10.2478/acmy-2021-0007.
- Pavithran, S., Pappuswamy, M., Annadurai, Y., Arumugam, V.A. and Periyaswamy, T. 2020. Green synthesis of copper nanoparticles: Characterization and their application. *J. Appl. Life Sci. Int.*, 23: 172. doi: 10.9734/JALSI/2020/v23i730172.
- Romdhane, D.F., Satlaoui, Y., Nasraoui, R., Charef, A. and Azouzi, R. 2020. Adsorption, modeling, thermodynamic, and kinetic studies of methyl red removal from textile-polluted water using natural and purified organic matter-rich clays as low-cost adsorbent Dalila. *J. Chem.*, 20: 617.
- Tara, N., Siddiqui, S.I., Rathi, G., Chaudhry, S.A., Inamuddin, R. and Asiri, A.M. 2019. Nano-engineered adsorbent for the removal of dyes from water. *Rev. Curr. Anal. Chem.*, 16(1): 14-40. doi: 10.2174/1573411015666190117124344.
- Wang, X., Jiang, C., Hou, B., Wang, Y., Hao, C. and Wu, J. 2018. Carbon composite lignin-based adsorbents for the adsorption of dyes. *Chemosphere*, 4: 183. doi: 10.1016/j.chemosphere.2018.04.183.



Properties and Distribution of Seed Banks in a Black Locust (*Robinia pseudoacacia*) Plantation in Central China

K.Q. Zhang*, X.C. Yang**, Z. Shen***, L.Y. Ma*†, J. Duan* and Y. Li*

*Key Laboratory for Silviculture and Conservation, Ministry of Education, Beijing Forestry University, Beijing 100083, P.R. China

**Department of Biology, Xinzhou Teachers University, Xinzhou 034000, P.R. China

***College of Forestry, Jiangxi Agricultural University, Nanchang 330045, P.R. China

†Corresponding author: L. Y. Ma; maluyi@bjfu.edu.cn

Nat. Env. & Poll. Tech.
Website: www.neptjournal.com

Received: 23-01-2021

Revised: 01-03-2021

Accepted: 12-04-2021

Key Words:

Germination
Multigenerational plantation
Robinia pseudoacacia
Seed bank
Spatial pattern

ABSTRACT

We aimed to compare the properties of seed banks in different types of *Robinia pseudoacacia* stands and different substratum layers. We established four Black locust plots (each 50 × 50 m) that included two second-generation stands and two third-generation stands. Spatial coordinates, diameter at breast height, and the heights of all trees were measured in the four plots. In each plot, we set a total of 259 points using the regular grid design method. At these points, we sampled the seed banks in the litter and soil (0-5 cm) layers. The coordinates of the 259 points were recorded. After the samples had been collected and screened, a germination trial was performed using the collected seeds from the different layers and stands. We used variogram and kriging interpolation geostatistical methods to analyze the distribution of the seed banks. A kernel density estimation map was generated to examine the relationship between the seed bank and trees in each stand. The results showed that seed bank density was high in the four stands (4005-7325 seeds.m⁻²), and was higher in the third-generation stands (6085 and 7325 seeds.m⁻²) than in the second-generation stands (4005 and 5659 seeds.m⁻²). The seed bank density in the litter layer (3225 seeds.m⁻²) exceeded that in the soil layer (2164 seeds.m⁻²). The spatial pattern of the seed banks varied among different stands and was positively correlated with the distribution of trees in each stand. Furthermore, we found that spatial autocorrelation in the seed banks occurred at a variety of scales. Seeds in the litter layer were significantly more active than those in the soil layer; the germination rate varied from 6.67% to 28.89%. The findings of this study suggest that the *Robinia pseudoacacia* plantation in the Luoning area may exhibit potential for regeneration from seeds, and this will be the focus of our future studies.

INTRODUCTION

Seed banks provide important information on vegetation composition and dynamics, and they play critical roles in forest regeneration (Bigwood & Inouye 1988, Hille Ris Lambers et al. 2005, Skowronek et al. 2014), and are thought to represent potential plant communities within ecosystems (Hu et al. 2013). Both biotic and abiotic environmental factors affect the size, distribution, and species composition of seed banks in forests and other ecosystems. The total seed density within a seed bank is mainly influenced by stand age in natural forests (Bossuyt et al. 2002). When tree species are pollinated by insects, such as the honeybee, seed bank size is influenced by the extent of apicultural practice (Masaka et al. 2010). Investigations have shown that seeds in the bank are concentrated in the leaf litter, humus, and shallow soil depths (0–2 cm). The highest seed bank species richness is typically found in the 0–10-cm soil depth layer (Du et al. 2007, Cseresnyés & Csontos 2012, Hu et al. 2013, Douh et al. 2018).

Most of the studies about seed banks have focused on natural and mixed forests. However, seed banks are also important in the development and regeneration of pure artificial forests, especially in degraded multi-generation stands, but the compositional characteristics and spatial patterns of seed banks in such forests have rarely been studied directly. Black locust (*Robinia pseudoacacia*) is a native tree of North America. And the species was introduced to Luoning (Henan Province, China) from North Korea and planted widely in local hilly locations (Zhang et al. 2019). Natural regeneration in this area depends on root sucker production and stump sprouting after clear-cutting for timber production. However, stand growth has declined due to excessive asexual reproduction following several generations of rotation. Masaka et al. (2010) found that the density of black locust seeds in banks varied from 6.4 to 13757seeds.m⁻² depending on honeybee pollination effectiveness and the basal area of the stands.

The characteristics of seed banks and seed germination need to be further studied in black locust plantations. To determine the spatial distribution of seed banks, large and small quadrat samples were collected for improved resolution and precision in predicting spatial patterns (Bigwood & Inouye 1988). Geostatistics is a suite of tools used to analyze regional variables based on variograms and kriging interpolation. We used kernel density estimation to analyze the spatial patterns in stands to assess the relationship between the seed banks and the aboveground trees in a black locust plantation. Our objective was to investigate (1) the density of the seed banks in the soil and litter layers, (2) the spatial patterns of the seed banks, (3) the relationship between each seed bank and the aboveground tree stand, and (4) seed germination capacity.

MATERIALS AND METHODS

Site Description and Experimental Design

The study area was located in Henan Province in central China. The site we chose is part of a government-owned forest farm. The climate is a warm temperate continental monsoon climate with an average annual temperature of 13.7°C (min. -21°C and max. 42°C), and the flora of this area belongs to the Chinese–Japanese plant sub-region of the Pan-Arctic plant region (Zhang et al. 2019). We selected four

experimental sites (Fig. 1) containing *R. pseudoacacia* stands in May 2017. The sites included two second-generation stands and two third-generation stands, which experienced once and twice clear-cutting respectively. For convenience, we used the abbreviations II-25, II-30, III-10, and III-17 as codes for the different stands. Codes II-25 and II-30 refer to second-generation stands that had been first clear cut 25 and 30 years previously, respectively. Codes III-10 and III-17 refer to third-generation stands, clear cut a second time 10 and 17 years previously, respectively.

A 50 × 50 m plot was established at each study site to investigate forest growth and seed bank properties. Basic information on the four plots is listed in Table 1. And 259 sampling points were selected at different scales in each plot (Fig. 2a) using a regular grid design procedure. At each sampling point, we set a 10 × 10 cm quadrat in which surface litter was collected. We collected a soil sample from the center of each of these quadrants. Cylindrical soil samples (5 cm radius, 5 cm depth) were collected using a soil ring knife (Fig. 2b). We then counted the number of seeds in the litter layer at each sampling position. The soil samples were sieved to separate the soil and seeds. Eight types of seed banks were categorized according to three factors: stand generation, stand age, and seed bank substratum (litter or soil), i.e., II-25-L, II-25-S, II-30-L, II-30-S, III-10-L, III-10-S, III-17-L, II-17-S.

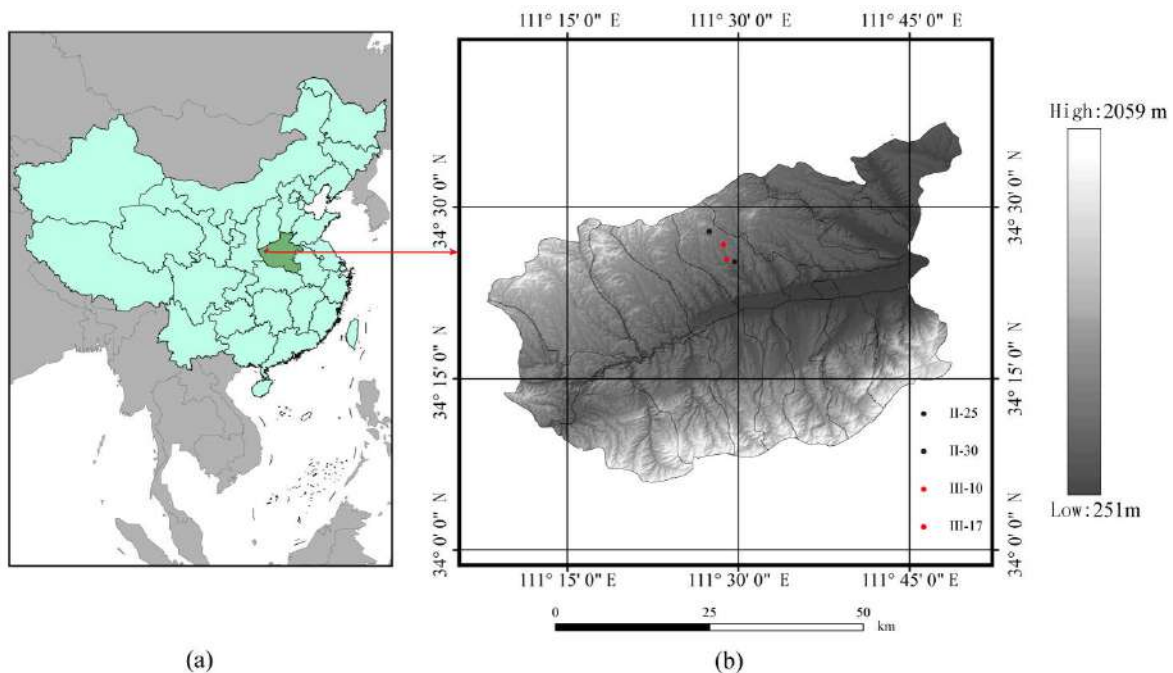


Fig. 1: (a) Location of the study area in China. (b) The distribution of the four plots (colored circles) overlain on a topographic map of the study area.

Table 1: Summary data for the four study plots.

Plot no.	Frequency of clear cutting	Age of stand (years)	Density of stand – [stems.ha ⁻¹]	Average DBH [cm]	Average height [m]	Tending after tree felling	Apicultural utilization	Slope aspect
II-25	1	25	1660	12.57 ± 4.47	9.83 ± 2.56	Yes	Yes	N-E
II-30	1	30	1224	14.00 ± 4.96	10.43 ± 2.64	Yes	Yes	E
III-10	2	10	5976	5.19 ± 1.64	6.85 ± 1.46	No	Yes	Flat
III-17	2	17	4056	6.84 ± 1.94	7.52 ± 2.38	No	Yes	W

Note: DBH, tree diameter at breast height

Germination Tests

We performed germination tests in the laboratory without physical or chemical interference to determine the germinability of Black locust seeds from different substrata and different stand types under natural conditions. Seeds of each seed bank type in each sample were mixed. We then randomly selected three replicates of 30 seeds from the litter and soil layers in each plot. In total, we selected 720 seeds from eight seed bank types for the germination experiment. The seeds were rinsed with distilled water before sowing. We sowed seeds in 24 flat nursery trays containing a mixture of nutritional soil and perlite in a 3:1 ratio. Trays were held at room temperature (20-25°C). Water was supplied daily for 30 days. The numbers of germinated seeds were counted daily at each census.

Data Analysis

Spatial Dependencies of the Soil Seed Banks

We chose geostatistical analysis, which is the best-known tool for assessing spatial autocorrelation (Matheron 1963, Wang 1999), to better understand the spatial characteristics of the seed banks of Black locust in an artificial pure forest, semivariograms to assess random and structural elements in soil seed bank distribution. The procedure defines the variance of an increment [$Z_{x+h} - Z_x$] over distance h and is expressed as follows:

$$\gamma(h) = \frac{1}{2N(h)} \sum_{i=1}^{N(h)} (Z_{x+h} - Z_x)^2 \quad \dots(1)$$

where h is the lag distance, $\gamma(h)$ is the semivariance at lag distance h , $N(h)$ is the number of sample pairs at lag distance

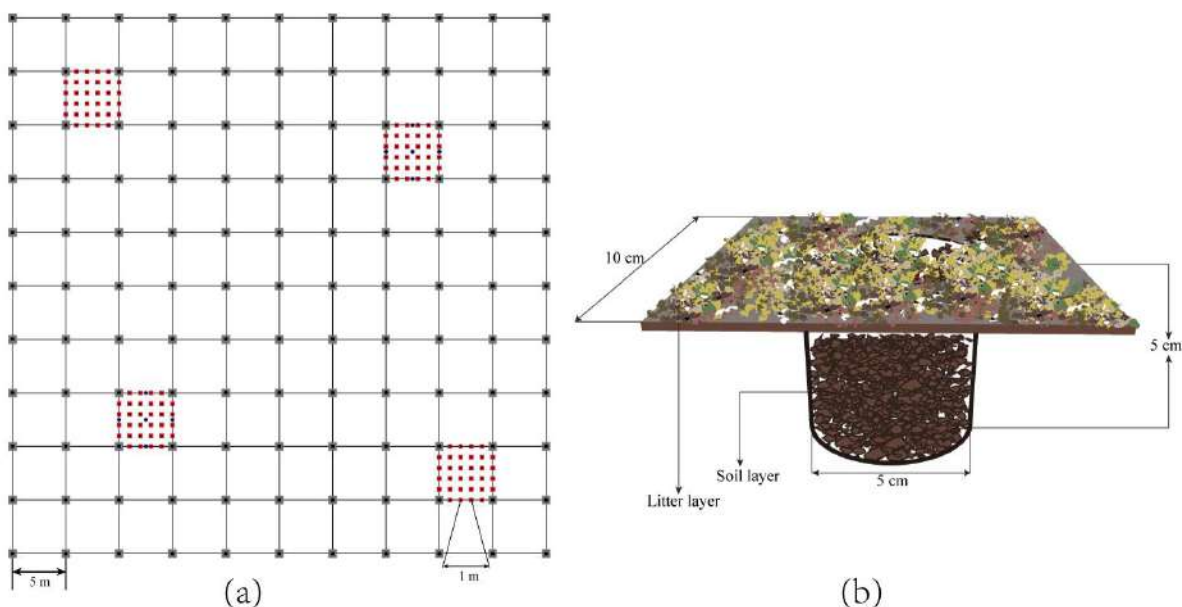


Fig. 2: (a) Distribution of 259 seed bank sampling points in each 50 × 50 m plot. (b) Schematic diagram of the litter- and soil-layer sampling at each point.

h , and Z_x and Z_{x+h} are the measured and observed values at point x and point $x+h$, respectively. A theoretical model can be used to fit the semivariance at different lag distances. This model will generate three characteristic parameters: nugget (C_0), sill ($C_0 + C$), and range (a), as shown in Fig. 3 for the spherical model.

The fractal dimension D is the slope of a log-log semivariogram plot (Orey 1970, Mandelbrot 1977, Burrough 1983) and reflects the complexity of information in a system (Ma & Zu 2000). We calculated fractal dimensions for the distributions of eight types of seed banks (according to generation, age, and substratum type). Semivariograms and fractal dimensions were calculated using GS+ software (Version 9.0, Gamma Design Software, Plainwell, MI, USA).

Kriging and Kernel Density Analysis

Kriging estimation is a procedure for “optimally predicting” points in space based on observations taken at known nearby locations (Cressie 1990). It offers an effective way of estimating a regionalized variable. Kriging was established by structural analysis of our semivariograms. The value of a point to be estimated is defined as follows:

$$Z_v^\#(x) = \sum_{i=1}^n \lambda_i Z(x_i) \quad \dots(2)$$

where λ_i is the weight coefficient of each point i around point v , and $Z(x_i)$ is the observed or measured value at the point i , and in this equation, $\sum_{i=1}^n \lambda_i = 1$.

To test the spatial relationship between the seed banks and stands, we used kernel density estimation to assess the spatial pattern of the stands. And we tested radii of 1, 2, 3, 4, and 5 m and the default search radius for each stand. We

selected 4 m as the most appropriate search radius in our study. Re-sampling was performed with bilinear interpolation after kernel density analysis to better display the density graph. Pixel sizes were set to 0.2×0.2 m in both kriging and kernel density analysis. We performed cell statistics and cell correlation analysis to examine the relationship between kriging and kernel estimation. All the analyses in this section were conducted using ArcMap 10.2 software (ESRI 2013).

Germination Analysis

Seeds were grouped into eight different categories (generation/age/substratum type). We assessed the influence on seed germination rate of (1) different stand ages, (2) the litter vs. soil layer, (3) different generations, and (4) seed bank category. The mean germination rate was subjected to multiple-comparisons tests or Student’s t-test ($p \leq 0.05$). We also analyzed the germination trend through the 30-day experimental period. All analyses were performed with the “multicomp” (Hothorn et al. 2008) and “ggplot2” (Hadley 2016, Team 2013) packages in R version 3.3.1 software.

RESULTS AND DISCUSSION

Results

Basic Characteristics of the Seed Banks

The density of seed bank (DSB) varied from 1762 to 4722 seeds.m⁻²; the maximum DSB occurred in the litter layer of the 17-year-old stand (III-17-L), and the minimum DSB occurred in the litter layer of the 30-year-old stand (II-30-L). The average variable coefficient of DSB in the second-generation stands (52.89%) was a little larger than that in the third-generation stands (50.32%) (Table 2). The DSBs in third-generation stands tended to be larger than those in second-generation stands (Fig. 4a). The DSB in the litter

Table 2: Statistical parameters for seed bank density (DSB) according to different generations, ages, and substratum types.

Type	n	Mean Density [seeds.m ⁻²]	Median Density [seeds.m ⁻²]	SD	CV [%]
II-25-L	259	3162	2800	2094	66.22
II-25-S	259	2497	2546	1284	51.42
II-30-L	259	1762	1700	764	43.35
II-30-S	259	2243	2037	1135	50.60
III-10-L	259	4267	3700	2533	59.36
III-10-S	259	1818	1527	925	50.88
III-17-L	259	4722	4700	2335	49.44
III-17-S	259	2603	2546	1091	41.91

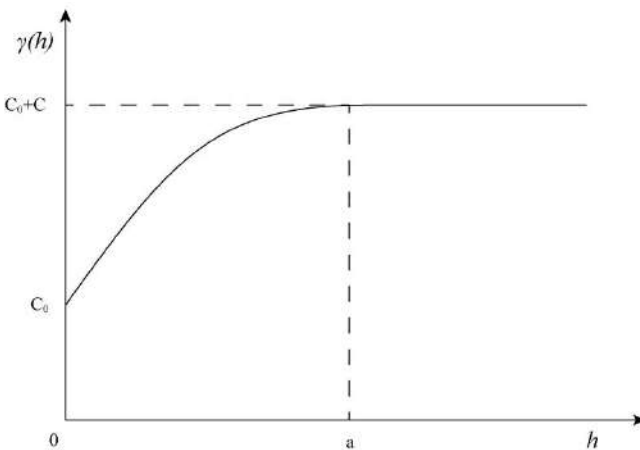


Fig. 3: The theoretical spherical semivariogram model. (h), semivariance at lag distance h ; $C_0 + C$, the sill parameter; C_0 , the nugget parameter; h , lag distance; a , range.

layer was larger than that in the soil layer (Fig. 4b), but not significantly so.

Spatial Autocorrelation in the Seed Banks

Most of the best-fitting variogram models were spherical models, though the exponential model fit well to II-25-L and II-25-S, and the Gaussian model fit well to II-30-L. Only the DSB variogram for stand II-25 had different model fits for the soil and litter layers. The spherical model provided the best fit for all DSB variograms for the third-generation stands (Fig. 5).

Variograms provided a measure of spatial variation in DSB with distance. Table 3 presents an overview of models and parameters for DSB variograms for each stand/layer type. All data were converted to normal distributions using square-root or log transformations, except the data for II-25-S and III-17-S. The range of spatial autocorrelation for the seed banks was 5.83–22.33 m. Spatial autocorrelation tended to be smaller in the soil layer than in the litter layer, except in stand II-25. The variance caused by spatial autocorrelation (defined as $C/[C+C_0]$) ranged from 50% for II-25-L to 75.8% for II-30-L. The spatial dependencies for all seed bank types (generation/age/substratum type) were $\geq 50\%$. The values of R^2 reflected a good fit (Table 3). The fractal dimension of the spatial pattern of DSB for all seed bank types was between 1.838 and 1.941, and the fractal dimension in the soil layer was a little larger than that in the litter layer, except in stand II-25. Overall, the fractal dimension (close to 2) revealed the complex spatial pattern of DSB (Table 3).

Spatial Relationship between Tree Stands and Seed Banks

Kernel density estimation of the stands and kriging interpolation in the DSB analysis showed that positive spatial relationships between the DSB and stand stem density existed

in all eight seed bank types (generation/age/substratum type) (Table 4). The maximum correlation coefficient (0.567) occurred in type III-17-L; the minimum value (0.432) occurred in type II-25-L. Spatial patterns of DSB in the litter and soil layers exhibited similar distribution trends (Fig. 6). DSB exhibited a decreasing trend with increasing stand age (Table 4). The kriging map showed that the DSB spatial pattern exhibited obvious patch characteristics, reflecting the

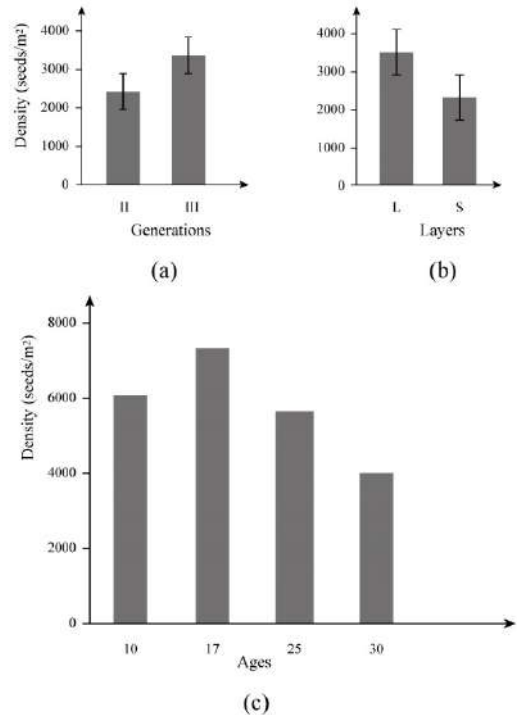


Fig. 4: Density of the seed bank (DSB) in second- and third-generation tree stands (a), different substratum types (b), and under trees of different ages (years) (c). II and III, generations 2 and 3, respectively; L, litter layer; S, soil layer.

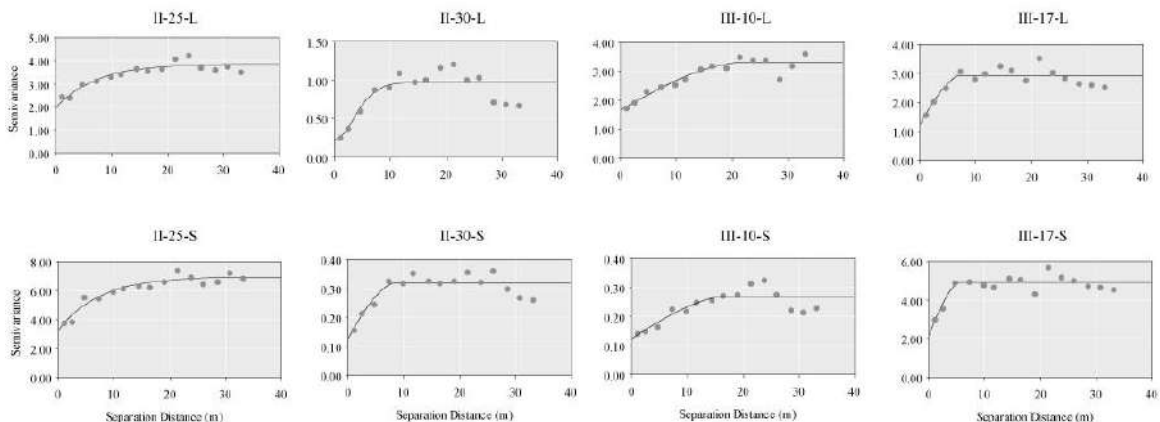


Fig. 5: DSB variograms for eight stand/layer types.

Table 3: Seed bank density (DSB) variogram parameters for each stand/layer type.

Type	Isotropic model	R ²	Still	Nugget	Range	C/C ₀ +C	Fractal dimension	Transformation
II-25-L	Exponential	0.849	3.837	1.918	19.92	50.00%	1.927 ± 0.236	Square-root transformation
II-25-S	Exponential	0.909	6.932	3.210	21.54	53.70%	1.907 ± 0.177	None
II-30-L	Gaussian	0.698	0.960	0.232	8.97	75.80%	1.838 ± 0.427	Square-root transformation
II-30-S	Spherical	0.754	0.321	0.126	8.83	60.80%	1.917 ± 0.466	Square-root transformation
III-10-L	Spherical	0.876	3.291	1.645	22.33	50.01%	1.899 ± 0.192	Square-root transformation
III-10-S	Spherical	0.703	0.268	0.122	17.33	54.50%	1.900 ± 0.382	Log transformation
III-17-L	Spherical	0.716	2.935	1.238	7.71	57.80%	1.930 ± 0.510	Square-root transformation
III-17-S	Spherical	0.763	4.913	2.149	5.83	56.25%	1.941 ± 0.469	None

Notes: Nugget and Still are characteristic parameters generated by the theoretical model fitting of the semivariance at different lag distances. C/C₀+C is the proportion of variation caused by spatial autocorrelation

heterogeneity of DSB. Patches of high value in the kriging map became larger with increases in high values of patches in the kernel density map for each stand generation. In summary, density and spatial distribution in the seed banks were positively influenced by tree distributions in stands within the *R. pseudoacacia* forest.

Germination Pattern During the Experimental Period

The trial showed that only a small proportion (<28.9%) of the seeds germinated during the study period. In the II-30-S

sample, only 6.67% ($\pm 2.72\%$) of the seeds germinated. In the t-tests and analysis of variance, there were no significant differences ($p > 0.05$) between second- and third-generation stands, and the rates did not differ significantly among stand ages. The germination rate of seeds from the third-generation stands was a little higher than that from the second-generation stands, but negligibly so (Fig. 7a). Germination rates were significantly different between the litter and soil layers ($t = 6.66$, $p < 0.01$); only 10% ($\pm 3.33\%$) of the seeds from the soil layer germinated (Fig. 7c). The germination rate of

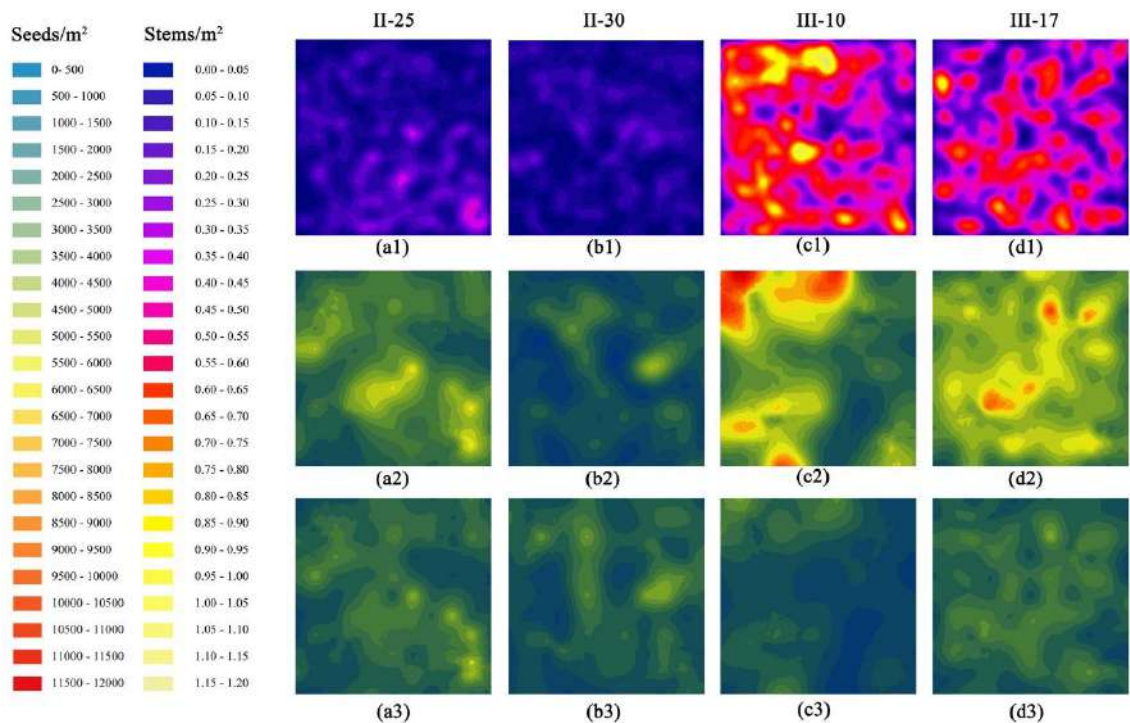


Fig. 6: Stand kernel density and kriging interpolation map of DSB. (a1), (b1), (c1) Kernel estimation map; (a2), (b2), (c2) kriging map of the seed bank in the litter layer; (a3), (b3), (c3) kriging map of the seed bank in the soil layer.

seeds differed significantly between the soil and litter layers in three stands, but not in stand III-10 (Fig. 7d). All seeds stopped germinating 19 days after sowing during the study period. Seeds from the litter layer began to germinate after 4 days, and the number of germinated seeds increased through 16 days. Germination occurred later in seeds from the soil layer and stopped after 19 days. The average number of days with germinating seeds for the litter layer (10 ± 1.87 days) exceeded the number of germination days for the soil layer (8.75 ± 3.56 days) (Fig. 8).

Discussion

Characteristics of the Seed Banks

The seed production of black locusts varies from year to year, and a good seed crop is generated approximately every 1–2 years after first flowering (Jastrzębowski et al. 2017). The DSB in stand III-17-L exceeded those in other stands, although the DSB in stand III-10-L was only slightly lower (Fig. 4). This DSB inequality among stands may be related to stand density, stand age, or seed production by mother trees. Stand development was shown to be an important factor influencing black locust DSB in Japan; stand biomass and apicultural activity can also be dominant determining

factors for the seed bank, rather than stand age (Masaka et al. 2010). The DSBs in four of our stand types were relatively high (4005–7325 seeds.m⁻²), far exceeding values in one previous report on DSB in forest soil (Silvertown & Charlesworth 2009). During the black locust flowering season, many beekeepers gather honey in the forests in our study area. This has a positive influence on seed production. Our seed bank sampling was conducted in May of 2017 because a large proportion of seed pods continue falling until April of the following year (Cierjacks et al. 2013), which may explain the DSB difference between the litter and soil layers.

Seed Bank Distribution

The spatial distribution of the seed bank is a function of dispersal processes related to the mother plants (Shaukat & Siddiqui 2004), as we demonstrated in our findings on the spatial relationship between the seed bank and stand (Table 4). The C/(C₀ + C) parameter in the variograms (Figs. 3, 5) represents the strength of spatial autocorrelation in the regional variable (Wang 1999). All structural variance ratios were >50%, indicating that the distribution of seeds in black locust stands depended more on biological processes than on random effects. We found strong autocorrelation in seed distribution at scales <9 m in the 25-year-old stand, which

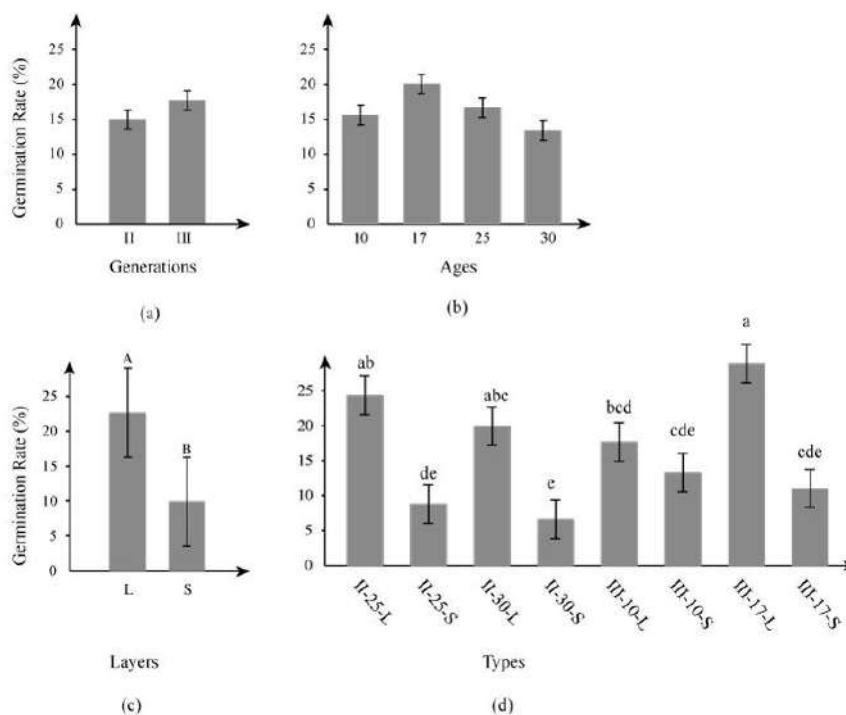


Fig. 7: Germination rates by tree generation (a), tree age (b), substratum type (litter vs. soil) (c), and seed bank type (generation/age/substratum type) (d). Each seed bank type was coded as follows: II and III, second and third generations, respectively; 10, 17, 25, and 30, stand ages in years; L and S, litter and soil, respectively. Different uppercase letters (A and B) in (c) indicate significant differences between layers (t-test, p < 0.01). Different lowercase letters in (d) identify significant pairwise differences between means (p < 0.05, Tukey's test).

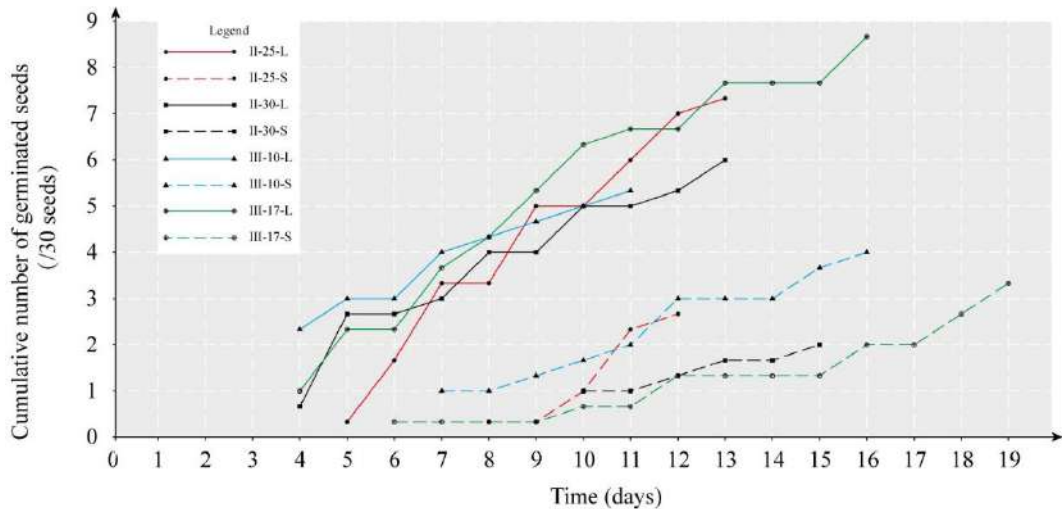


Fig. 8: Germination dynamics of seeds over 30 days in eight seed bank types (generation/age/substratum type).

was sparsely populated with trees. The sparseness of trees caused small patches in the kernel estimation (Fig. 6); consequently, the seeds were most aggregated at small scales.

Different models that fit variograms are representative of different types of spatial patterns in the field of geostatistics (Yavitt et al. 2009). Most of our variograms fitted well to spherical models, indicating the presence of distinct patches with high or low DSB, especially in the third-generation stands. We found a variety of best model fits for our variograms, suggesting that there is variation in the processes underlying the spatial patterns of seed banks.

Seed Germination According to Tree Generation, Tree Age and Substratum Type

The germination rate of black locust in nature is very low, as shown in many investigations (Masaka & Yamada 2009, Giuliani et al. 2015, Jastrz bowski et al. 2017) because the hard impermeable seed coat (Nicolescu et al. 2020), and no germinating seeds were found in the field during the season we surveyed. The germination rate of seeds from the litter layer significantly exceeded that of seeds from the soil layer (0-5 cm depth) (Fig. 7). Seeds from the litter also germinated earlier than seeds from soil (Fig. 8); hence, seeds in the litter layer were more active, suggesting that there may be varying degrees of seed dormancy in different layers of the black locust seed bank. Furthermore, seeds from our litter samples might have fallen in 2017, because we found that many seeds were still in the pods after collection.

Management Implications for Black Locust Plantations

The seed bank represents the regeneration potential of a forest

(Skowronek et al. 2014). The bank plays a major role in the restoration of degraded forest reserves and in maintaining ecosystem health (Taiwo et al. 2018). Seed germination under natural conditions is limited but can be improved greatly by scarification of the hard coat (Jastrz ebowski et al. 2017). Furthermore, root suckers and stump shoots play important roles in the survival and spread of black locust stands (Carl et al. 2019). From a long-term forest management perspective, seedlings produced from seeds are healthier than new growth from root suckers, and root suckers produced far from the mother tree are healthier than stump shoots. An abundant seed bank provides great potential for sexual regeneration. We suggest that the frequencies of seedlings should be increased

Table 4: Statistics from kernel density estimation and kriging interpolation.

Kernel density or kriging map	Mean value of the pixel	SD	Correlation coefficient with stand
II-25 stand (A1)	0.158	0.073	–
II-25-L (A2)	3117.410	861.130	0.432
II-25-S (A3)	2493.640	570.340	0.496
II-30 stand (B1)	0.116	0.057	–
II-30-L (B2)	1697.090	652.680	0.512
II-30-S (B3)	2156.410	595.800	0.490
III-10 stand (C1)	0.4890	0.184	–
III-10-L (C2)	4110.740	1808.070	0.501
III-10-S (C3)	1751.790	604.210	0.497
III-17 stand (D1)	0.386	0.140	–
III-17-L (D2)	4561.310	926.300	0.567
III-17-S (D3)	2502.549	494.380	0.524

during tending and cutting. This will be an important focus in our future investigations.

CONCLUSION

The seed bank in forest soil and litter layers is essential and important for regeneration, but there are few specific studies on seed banks in artificial pure forests of Black locusts. Our study focused mainly on seed germination, and the properties and distribution of seed banks in four black locusts stand types in central China, and this study set out to explore the seed bank patterns and germination potential of multi-generation Black locust plantation. We found that seeds were abundant in the litter and soil layers, the DSBs (density of seed banks) in the third-generation stands exceeded those in the second-generation stands. What's more, we found spatial dependence at different scales in different types of seed banks and the large spatial structure ratio in the variograms indicated that the seed bank pattern was strongly influenced by autocorrelation. By fitting different semi-variance models, the results of this study suggest that spherical, exponential, and Gaussian models fit well to different variograms for the eight seed bank types (stratified by generation/age/substratum type). The germination rate varied with the substrate, the results have shown that seeds in the litter layer were more active than those in the soil layer. Based on these findings, our future investigations will consider the potential role of the seed bank in the regeneration of black locust plantations; we intend to create gaps in the forest and use artificial seed scarification to break dormancy, thereby increasing the proportion of seedlings in black locust forests.

ACKNOWLEDGMENT

This study was funded by the National Key R&D Program of China (2017YFD0600503), the National Science Foundation of China (31570677), and the International S&T Cooperation Program of China (2014DFA31140).

REFERENCES

- Bigwood, D.W. and Inouye, D. W. 1988. Spatial pattern analysis of seed banks: an improved method and optimized sampling. *Ecology*, 69(2): 497-507.
- Bossuyt, B., Heyn, M. and Hermy, M. 2002. Seed bank and vegetation composition of forest stands of varying age in central Belgium: consequences for regeneration of ancient forest vegetation. *Plant Ecol.*, 162(1): 33-48.
- Burrough, P.A. 1983. Multiscale sources of spatial variation in soil. I. The application of fractal concepts to nested levels of soil variation. *J. Soil Sci.*, 34(3): 577-597.
- Carl, C. , Lehmann, J.R. , Landgraf, D. and Pretzsch, H. 2019. *Robinia pseudoacacia* L. in short rotation coppice: Seed and stump shoot reproduction as well as UAS-based spreading analysis. *Forests*, 10(3): 235.
- Cierjacks, A., Kowarik, I., Joshi, J., Hempel, S., Ristow, M., von der Lippe, M. and Weber, E. 2013. Biological flora of the British Isles: *Robinia pseudoacacia*. *J. Ecol.*, 101(6): 1623-1640.
- Cressie, N. 1990. The origins of kriging. *Math.Geol.*, 22(3): 239-252.
- Cseresnyés, I. and Csontos, P. 2012. Soil seed bank of the invasive *Robinia pseudoacacia* in planted *Pinus nigra* stands. *Acta Botan. Croat.*, 71(2): 249-260.
- Douh, C., Daïnou, K., Loumeto, J.J., Moutsambote, J., Fayolle, A. , Tosso, F., Forni, E., Gourlet-Fleury, S. and Doucet, J. 2018. Soil seed bank characteristics in two central African forest types and implications for forest restoration. *Forest Ecol. Manag.*, 409: 766-776.
- Du, X., Guo, Q., Gao, X. and Ma, K. 2007. Seed rain, soil seed bank, seed loss, and regeneration of *Castanopsis fargesii* (*Fagaceae*) in a subtropical evergreen broad-leaved forest. *Forest Ecol. Manag.*, 238(1-3): 212-219.
- ESRI. 2013. ArcGIS 10.2 for desktop.
- Giuliani, C., Lazzaro, L., Lippi, M.M., Calamassi, R. and Foggi, B. 2015. Temperature-related effects on the germination capacity of black locust (*Robinia pseudoacacia* L., Fabaceae) seeds. *Folia Geobotanica*, 50(3): 275-282.
- Hadley, W. 2016. Ggplot2: Elegant Graphics for Data Analysis. Springer, New York.
- Hille Ris Lambers, J., Clark, J.S. and Lavine, M. 2005. Implications of seed banking for recruitment of southern Appalachian woody species. *Ecology*, 86(1): 85-95.
- Hothorn, T., Bretz, F. and Westfall, P. 2008. Simultaneous inference in general parametric models. *Biom. J.: J. Math. Methods Biosci.*, 50(3): 346-363.
- Hu, Z., Yang, Y., Leng, P., Dou, D., Zhang, B. and Hou, B. 2013. Characteristics of the soil seed bank in plantation forest in the rocky mountain region of Beijing, China. *J. Forest Res.*, 24(1): 91-97.
- Jastrzębowski, S., Ukalska, J., Kantorowicz, W., Klisz, M., Wojda, T. and Sułkowska, M. 2017. Effects of thermal-time artificial scarification on the germination dynamics of black locust (*Robinia pseudoacacia* L.) seeds. *European Journal of Forest Research*, 136(3): 471-479.
- Ma, K.M. and Zu, Y.G. 2000. Fractal model of vegetation pattern: The fractal properties of vegetation pattern. *Chinese Journal of Plant Ecology*, 24(1): 111.
- Mandelbrot, B.B. 1977. *Fractals: Form, Chance, and Dimension*. W. H. Freeman and Company, New York
- Masaka, K. and Yamada, K. 2009. Variation in germination character of *Robinia pseudoacacia* L.(Leguminosae) seeds at individual tree level. *Journal of Forest Research*, 14(3): 167-177.
- Masaka, K., Yamada, K., Koyama, Y., Sato, H., Kon, H. and Torita, H. 2010. Changes in the size of the soil seed bank in *Robinia pseudoacacia* L.(Leguminosae), an exotic tall tree species in Japan: Impacts of stand growth and apicultural utilization. *Forest Ecol.Manag.*, 260(5): 780-786.
- Matheron, G. 1963. Principles of geostatistics. *Econ.Geol.*, 58(8): 1246-1266.
- Niculescu, V., Rédei, K. , Mason, W.L. , Vor, T., Pöetzelberger, E., Bastien, J., Brus, R., Ben a , T., Dodan, M. and Cvjetkovic, B. 2020. Ecology, growth, and management of black locust (*Robinia pseudoacacia* L.), a non-native species integrated into European forests. *J. Forest. Res.*, 31(4): 1081-1101.
- Orey, S. 1970. Gaussian sample functions and the Hausdorff dimension of level crossings. *Zeitschrift für Wahrscheinlichkeitstheorie und verwandte Gebiete.*, 15(3): 249-256.
- Shaukat, S.S. and Siddiqui, I.A. 2004. Spatial pattern analysis of seeds of an arable soil seed bank and its relationship with above-ground vegetation in an arid region. *Journal of Arid Environments*, 57(3): 311-327.
- Silvertown, J. and Charlesworth, D. *Introduction to Plant Population Biology*. John Wiley and Sons, CA.
- Skowronek, S., Terwei, A., Zerbe, S., Mölder, I., Annighöfer, P., Kawaletz,

- H., Ammer, C. and Heilmeyer, H. 2014. Regeneration potential of floodplain forests under the influence of nonnative tree species: Soil seed bank analysis in Northern Italy. *Restor. Ecol.*, 22(1): 22-30.
- Taiwo, D.M., Oyelowo, O.J., Ogedengbe, T.C. and Woghiren, A.I. 2018. The role of the soil seed bank in forest regeneration. *Asian J. Res. Agric. Forest.*, 1-10.
- Team, R.C. 2013. R: A language and environment for statistical computing. Available from <http://www.r-project.org/>
- Wang, Z.Q. 1999. *Geostatistics and its Application in Ecology*. Science Press, Beijing.
- Yavitt, J.B., Harms, K.E., Garcia, M.N., Wright, S.J., He, F. and Mirabello, M.J. 2009. Spatial heterogeneity of soil chemical properties in a lowland tropical moist forest, Panama. *Soil Res.*, 47(7): 674-687.
- Zhang, K., Shen, Z., Yang, X., Ma, L., Duan, J. and Li, Y. 2019. Spatial patterns in different stages of regeneration after clear-cutting of a black locust forest in Central China. *Forests*, 10(12): 1066.



Insight into Effects of Initial Moisture Content on the Heat-Up of Sewage Sludge Composting During Mesophilic Phase

Yu Li*, Yuran Su**, Bin Hu* and Chuang Ma*†

*Zhengzhou University of Light Industry, Zhengzhou, Henan province, China

**Qiushi Honors College, Tianjing University, Tianjing, China

†Corresponding author: Chuang Ma; 115409085@qq.com

Nat. Env. & Poll. Tech.
Website: www.neptjournal.com

Received: 16-04-2021

Revised: 02-06-2021

Accepted: 06-06-2021

Key Words:

Moisture content
Sewage sludge
Composting
Mesophilic phase

ABSTRACT

The effects of initial moisture content (55%, 60% and 65%) on the heat-up of sewage sludge (SS) composting during the mesophilic phase were investigated. Monitoring results showed that low moisture content (55%) increased the heating rate, high initial moisture content (60% and 65%) significantly improved the activities of cellulase and peroxidase during the mesophilic phase. Furthermore, although high moisture content improved the diversity of bacteria during composting, there were no significant differences in the microbial structure during the process of succession. So, rather than inhibiting the activity of the bacterial population, the negative effect of high moisture content (60 and 65 per cent) on composting temperature heat up was attributable to the difficulty of heating produced by the specific heat capacity of water. The correlation index between initial moisture content and microorganisms was relatively low, while the temperature was the largest environmental factor affecting the bacterial community. This conclusion provided a hint to make an association between initial moisture content and composting temperature-rising stage..

INTRODUCTION

Sewage sludge (SS) is a by-product of municipal wastewater treatment plants, and the production of municipal SS is steadily growing as sewage treatment expands (Ma et al. 2019). Composting is one of the most widely used biological treatment processes to achieve biodegradation and stabilization of organic matter in sludge while reducing the negative impact of organic matter in sludge (Zhou et al. 2018). The initial qualities of the material, such as moisture content (MC), bulking agents, organic matter content (OM), bulk density, C/N ratio, pH value, and process-related elements, such as aeration mode and flow rates, all have an impact on the process' performance (Zhou et al. 2014). Initial MC has attracted wide attention due to water's ability to dissolve organic matter, participate in microbial metabolism, evaporate away heat and regulate composting temperature. Appropriate MC is the basis of biological decomposition, too high MC can lead to anaerobic conditions, while persistent anaerobic incomplete decomposition can produce odor and phytotoxicity.

As the driving force in the composting process, microbes play a vital role in the degradation of organic matter. Unlike agricultural composting, which aims to produce organic fertilizer, the primary goal of SS composting is to dewater, deodorize, and reduce the volume and mass of the SS (Zhou et al. 2017). As a result, the higher the sludge mixing ratio

in the composting mixture and the larger the SS treatment capacity of each composting tank in actual production, the higher the initial moisture content of the sludge composting process. At the same time, a higher SS mixing ratio can effectively reduce the proportion of excipients and operation costs (Zhou et al. 2018). As a result, it is widely anticipated that the initial MC of the compost mixture would be increased as much as possible to improve treatment efficiency and lower the cost of composting operations in composting facilities (Zhou et al. 2014, Zhou 2017).

Water not only provides a carrier for soluble nutrients needed by composting microorganisms but also provides a medium for chemical and biological reactions during composting (Hamoda 1998). In the composting environment, MC below 40% or above 65% also limits the growth of microorganisms. At the same time, existing references and experience demonstrate that a high MC (65%) can have negative consequences such as a lower heating rate and thermophilic phase duration. As a result, the proportion of sludge mixtures in actual sludge composting projects is often increased in summer, and the compost has a relatively high MC. The proportion of sludge mixtures is lowered in the winter, as is the MC of the compost.

During composting, bio-heat is crucial for temperature-rising, and it is produced via the microbial degradation

of the compounds (e.g., complex carbon, cellulose, hemicelluloses, and proteins) in the material. As a result, the temperature may be used to not only represent microbial metabolism but also to screen bacteria for OM transformation (Ma et al. 2019).

Generally speaking, microbial activity produces heat and promotes the heating of the pile, air blast, and water evaporation cause heat loss (Cai et al. 2016). Insufficient microbial heat generation or a high specific heat capacity of water are the two explanations for the difficulties of heating the pile with a high initial MC at the same ventilation rate (Cai et al. 2016). However, the causes of MC on composting heat up, whether high specific heat capacity of water or diverse microbiological activity cause different heat up effects, are not yet obvious in principle, and even more so in practice.

As a result, it's intriguing and crucial to investigate beginning MC during the temperature-rising stage of SS composting. Gaining a better understanding of the succession of microbial communities and initial MC will considerably improve composting efficiency.

MATERIALS AND METHODS

Composting Materials

Dewatered SS was collected from Wulongkou municipal wastewater treatment plant (Zhengzhou, China). Sawdust was pinewood particles (particle size 1-2 mm). Sewage sludge and sawdust were homogenized to obtain a mixture at a ratio of 3:1 (w/w, fresh weight) as the main raw materials. To alter the initial MC of composting, three distinct piles were set up with a varying dosage of water: piles A, B, and C were added with water at a dosage of 0, 10, and 30 kg, respectively. The physicochemical properties of the experimental materials are given in Table 1.

Composting Process

Composting was conducted in three separate but identical reactors for 30 days. The reactors had a height of 120 cm, an inner diameter of 60 cm, and an effective volume of 280 L. They were made from polyethylene and covered with a

3 cm thick rubber board for thermal insulation. On the top of each reactor was a removable lid with a small hole (2 cm in diameter), and at the bottom of the reactor were uniformly distributed holes (1 cm in diameter). Temperature sensors were embedded in a metal bar and placed at heights of 20, 40, and 60 cm, with the temperature probe recording and storing temperature data once every minute.

Physicochemical Analysis

During the mesophilic phase (temperature-rising stage), triplicate samples were obtained from each pile at a depth of approximately 50cm on days 0, 1, 2, 3, 5, 7, and 10 and stored at -4°C until analysis (Fig.1).

The MC of raw materials was determined by drying the samples at 105°C for 24 h. The volatile solid (VS) content was determined by measuring the loss of dry-solid mass after ignition at 550°C in a muffle furnace for 24 h. Using a combination pH meter, the pH was measured at a ratio of 1:5 after 30 minutes of shaking equilibration. Phenol disulfonic acid colorimetry is used to detect nitrate-nitrogen concentration. The activities of two microbial enzymes (cellulase and peroxidase) were determined at each sampling time. The activities of peroxidase and cellulase activity were measured according to the method of Ghose (1987).

Microbial DNA was collected from each pile on days 2, 5, and 10 during the mesophilic phase using a FastDNA soil rotation kit (MPBIO, USA) according to the trend of temperature change to determine bacterial diversity during the composting process. The concentration of the final DNA was measured using a NanoDrop 2000 UV-vis spectrophotometer (Thermo Scientific, Wilmington, USA). Primer 338F was used to amplify the V3-V4 hypervariable sections of the bacterial 16S rRNA gene (ACTCCTACGGGAGGCAGCAG).

Statistical Analysis

The average values and standard deviations of the data were calculated using Microsoft Excel software (Version 2016, USA) and figures were generated using OriginPro (Version 9.4, USA). The least significant differences (LSD) among the mean values during composting were calculated at a

Table 1: Physicochemical properties of the raw materials.

	Moisture content [%]	pH	Total organic carbon [%]	Total nitrogen [%]	Weight [kg]	Bulk density [g·cm ⁻³]
Sewage sludge	75.21	8.12	28.11	2.05	-	-
Sawdust	2.12	5.55	52.82	0.41	-	-
Pile A	56.75	8.74	49.32	1.32	120.00	428.57
Pile B	60.07	8.63	48.66	1.50	130.00	464.29
Pile C	65.40	8.60	48.97	1.49	150.00	535.71

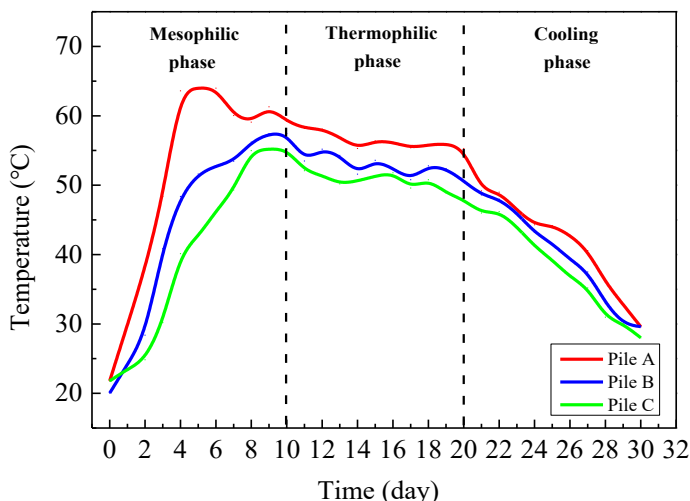


Fig. 1: Temperature of the material in the three composting piles throughout the composting process.

confidence level of $p < 0.05$ using SPSS software (Version 24.0, USA).

The degradation rates of VS were calculated as follows:

$$\text{Degradation Rate} = \frac{(A_i \times C_0 - A_0 \times C_i)}{(A_i \times C_0)} \times 100\%$$

where A_0 is the ash content of the original material of compost, A_i is the ash content of the compost on the day i , C_0 is the VS content of the original material of the compost, and C_i is the VS content of the compost on the day i .

RESULTS AND DISCUSSION

Dynamic of Physicochemical Parameters

Temperature changes: Initial MC has the greatest impact on temperature, which is widely considered as one of the most important parameters in the composting process (Zhou 2017, Ma et al. 2019). According to the change of temperature in the composting process, we divide composting processes into three phases, the rising temperature stage (0-10 days), the thermophilic stage (11-20 days), the cooling phase (20-30 days). Three piles reached the highest temperatures of 64.05°C, 57.44°C, and 56.21°C on day 5, day 10, and day 10, respectively (Fig. 1). Among them, Pile A had the highest heating rate, and Pile C had the lowest heating rate. Different initial MC causes significant changes in heating effects, which could be because water has a higher specific heat capacity than other composts (Cai et al. 2016). Heat transfer from water results in a slower heating rate and a longer composting cycle. The high MC may also cause anaerobic conditions as a result of water plugging, which will inhibit and terminate the composting process (Tiquia et

al. 1996). As a result, high-throughput sequencing analysis for microbial succession during the composting process is required to better understand the effects of early MC on the mesophilic phase of SS composting, particularly insight into the microorganisms' water response mechanism during SS composting.

Changes in moisture content: Water not only provides a carrier for soluble nutrients needed by composting microorganisms but also provides a medium for chemical and biological reactions in composting (Hamoda 1998). And MC affects microbial activity, as well as the physical structure, in the composting process, and thus has a central influence on the biodegradation of organic materials (Makan et al. 2013). As shown in Fig. 2a, the MC of the three piles showed a gradual decline. On day 10, the MC of Pile A, Pile B, and Pile C decreased from 55.49%, 60.30% and 65.06% to 50.98%, 56.61% and 62.25%, respectively, down 4.51%, 3.69% and 2.81%, respectively. Because the loss of water is primarily the consequence of water evaporation, which is directly related to composting temperature and ventilation pore, Pile A's rapid heating and high temperature resulted in the biggest decrease in MC. The greater the evaporation of water with constant ventilation and ventilation pores, the higher the temperature (Cai et al. 2016, Ma et al. 2019).

Changes in volatile solids: VS is an important energy source for microbes (Jain et al. 2015). As shown in Fig. 2b, the VS of the three piles of treatments showed a gradual decline. The VS of Pile A, Pile B, and Pile C decreased from the initial 83.83%, 82.97%, and 82.20% to 74.31%, 76.11%, and 78.31% during the mesophilic phase, respectively. The VS degradation rates of the three piles were 11.3%, 8.2%, and 4.7%, respectively. Among them, the degradation rate

of VS in Pile A was the highest, while that in Pile C was the lowest. This may be due to the premature dehydration of the compost due to the low MC in the composting process, which made the heap physically stable, but biologically unstable (Makan et al. 2013).

Changes in pH: The pH strongly affects microbial activity during composting and the degradation process can be enhanced by pH control (Gajalakshmi & Abbasi 2008). As shown in Fig. 2c, the changing trend of pH in the three piles was similar, showing a trend of first decreasing and then rising. The pH of Pile A, Pile B, and Pile C decreased from the initial 8.64, 8.63, and 8.60 to 8.5, 8.54, and 8.57 on day 3, and then gradually increased to 8.79, 8.75, and 8.67 on day 10. There was no significant difference in pH among the three piles during 0 to 2 days, but the pH in Pile C during 3 to 10 days was significantly lower than that in Pile A and Pile B. This may be due to the partial anaerobic reaction of high moisture content in Pile C, which results in low pH.

Changes in NO_3^- -N: The changing trend of NO_3^- -N content in the three treatments was similar (Fig. 2d). NO_3^- -N in Pile A, Pile B, and Pile C increased gradually from initial 0.83 $\text{g}\cdot\text{kg}^{-1}$, 0.86 $\text{g}\cdot\text{kg}^{-1}$ and 0.82 $\text{g}\cdot\text{kg}^{-1}$ to 2.5 $\text{g}\cdot\text{kg}^{-1}$, 2.6

$\text{g}\cdot\text{kg}^{-1}$ and 1.4 $\text{g}\cdot\text{kg}^{-1}$ during mesophilic phase, respectively. There was no significant increase in NO_3^- -N content in the three piles during the mesophilic phase. However, until the thermophilic phase and the cooling phase of composting, the NO_3^- -N in Pile A and Pile B began to rise rapidly, while the NO_3^- -N in Pile C increased relatively slowly. This is due to the rapid degradation of organic matter into NH_4^+ -N during the mesophilic phase, and the transformation of NH_4^+ -N to NO_3^- -N during the thermophilic phase and cooling phase (Gajalakshmi & Abbasi 2008). However, due to the high MC in Pile C, the local anaerobic reactions in the bioreactor lead to the low NO_3^- -N content (Makan et al. 2013).

Activities of peroxidase: Peroxidase is the most intensively studied extracellular enzyme of white-rot fungi, which can oxidize the lignin polymer (Wu et al. 2017). As shown in Fig. 2e, the changing trend of peroxidase was different among the three piles. The content of peroxidase in Pile A increased first and then decreased. The maximum content of peroxidase was 136.74 $\mu\text{mol}(\text{h}\cdot\text{g})^{-1}$, which appeared on day 5. However, Pile B and Pile C decreased first and then increased, from 141.6 $\mu\text{mol}(\text{h}\cdot\text{g})^{-1}$ and 205 $\mu\text{mol}(\text{h}\cdot\text{g})^{-1}$ on day 0 to 126.16 $\mu\text{mol}(\text{h}\cdot\text{g})^{-1}$ and 126.75 $\mu\text{mol}(\text{h}\cdot\text{g})^{-1}$

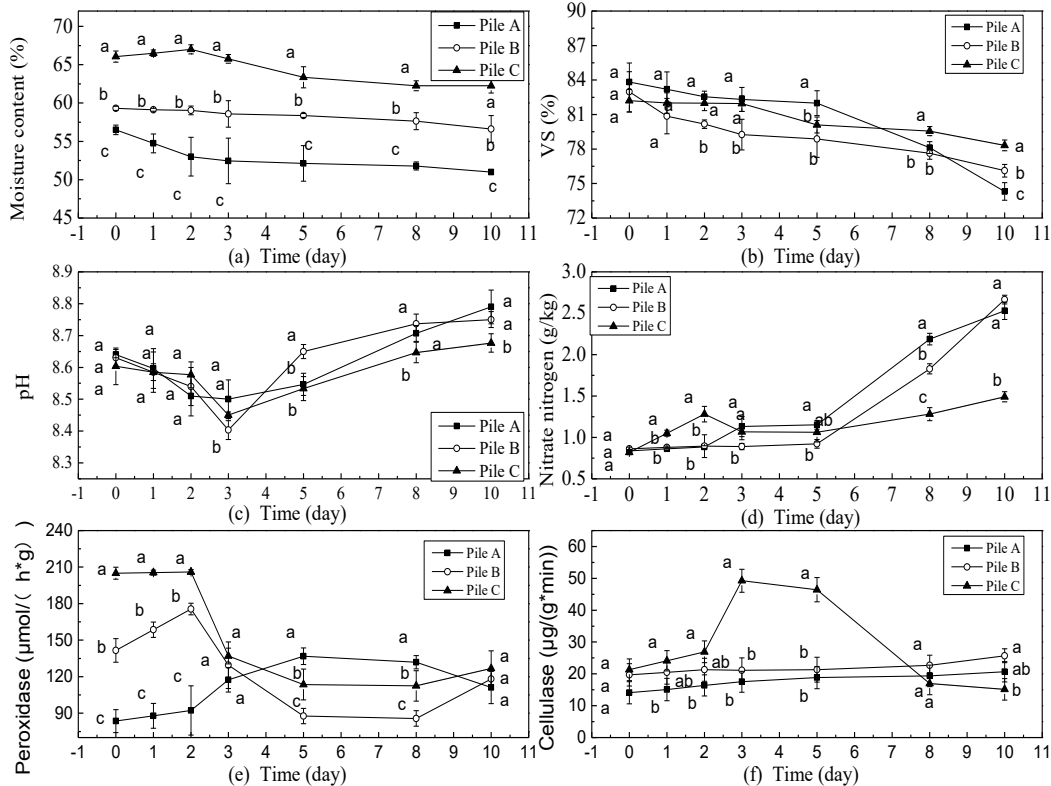


Fig. 2: Moisture content, VS, pH values, NO_3^- -N content, peroxidase content, and cellulase content of three composting piles during the mesophilic phase. Note: Significance (*) is considered at $P < 0.05$.

on day 10, respectively. The content of peroxidase in Pile B and Pile C was significantly higher than that in Pile A during the first three days, but the content of peroxidase in Pile A was significantly higher than that in Pile B and Pile C during day 5 to day 8. It may be deduced that high MC promotes the rise of peroxidase activity in the early stages of the mesophilic phase, which may help the compost biodegrade (Hu et al. 2019).

Activity of cellulase: The types of cellulolytic microorganisms present in the mixture influence cellulase activity, which catalyzes the hydrolysis of cellulose to D-glucose (Castaldi et al. 2008). The three heaps' cellulase change trajectories were substantially different (Fig. 2f). The cellulase content in Pile A and Pile B increased gradually, reaching the maximum on day 10, respectively. The cellulase content in Pile C increased first and then decreased, reaching its maximum on day 3. This may be due to the fact that high MC can increase the solubility of cellulase substrate, and stimulate the production of cellulase enzymes.

Evolution of Bacterial Community

Effects of moisture content on bacterial diversity: The coverage index was commonly used to describe the depth of sequencing, which presented results that accurately reflect the depth of sequencing samples (Li et al. 2015). During composting, the excellent coverage index of all samples was greater than 0.98 (Table 2), indicating that the sequencing data was appropriate. The ace index was used to measure the diversity of bacterial communities, with a higher value indicating greater diversity (Liu et al. 2017). The Shannon index was chosen to reflect the degree of bacterial community diversity, and the greater Shannon index indicated the higher diversity of the bacterial community (Huang et al. 2013, Liu et al. 2017). On day 2, the Shannon index of Pile B was significantly higher than that of Pile A and Pile C. On day 5, the Shannon index of Pile A was the lowest, while that of Pile C was the highest, and that of Pile B was in the middle. On day 10, the Shannon index of Pile B was significantly higher than that of Pile A and Pile C, and the Shannon index of Pile A was the lowest. According to the trends of the Shannon index in the three piles (Table 2), the results showed that the

microbial diversity was the lowest when the initial moisture content was 55% and the highest when the initial moisture content was 60%, which was most conducive to bacterial reproduction and degradation of organic matter.

Effects of moisture content on bacterial community structure: The dynamic of bacterial community at the genus level is shown in Fig.3. On day 2, *Pseudomonas*, *Acinetobacter*, and *Candidatus_Microthrix* were the dominant bacteria in the three piles. Pile C (26.0%) had the highest proportion of *Pseudomonas* and Pile B (11.4%) had the lowest proportion of *Pseudomonas*. *Pseudomonas* is correlated with organic acids synthesis and with a concomitant drop in pH (Kiymaci et al. 2018). Pile C (19.5%) had the highest percentage of *Acinetobacter* while Pile B (10.9%) had the lowest percentage of *Acinetobacter*. *Acinetobacter* not only plays an important role in the rapid degradation of OM in compost but also relates to the metabolism of carbon and nitrogen. Pile B (11.5%) had the highest proportion of *Candidatus_Microthrix* and Pile A (8.1%) had the lowest proportion of *Candidatus_Microthrix*. The genus *Candidatus_Microthrix* was related to lipid metabolism by using long-chain fatty acids as a carbon and energy source (Levantesi et al. 2010). On day 5, *Planifilum*, *Bacillus*, and *Candidatus_Microthrix* were the dominant bacteria in the three piles. *Planifilum*, a thermophilic genus within Thermoactinomycetaceae (Yu et al. 2018), accounted for the highest proportion (23.3%) in Pile A and the lowest proportion (0%) in Pile C, the reason is that the temperature of Pile B and Pile C was relatively low on day 5 (Fig. 1). *Bacillus* accounted for the highest proportion (17.7%) in Pile A and the lowest proportion (0.5%) in Pile C. *Bacillus* can degrade protein and starch, was known as competent cellulose-degrading bacteria. *Candidatus_Microthrix* accounted for the highest proportion (13.5%) in Pile C and the lowest proportion (2.4%) in Pile A. On day 10, *Planifilum*, *Candidatus_Microthrix*, and *Thermobifida* were the dominant bacteria in the three piles. *Planifilum* accounted for the highest proportion (22.4%) in Pile A and the lowest proportion (0%) in Pile C. *Thermobifida* has been stated to be effective on cellulose and hemicellulose degradation while secreting hemicellulases and cellulases (Zhang et al. 2015). *Candidatus_Microthrix* accounted for the highest proportion

Table 2: Bacterial alpha diversity index.

Time	OTUs			Shannon			Simpson			Ace			Coverage		
	Pile A	Pile B	Pile C	Pile A	Pile B	Pile C	Pile A	Pile B	Pile C	Pile A	Pile B	Pile C	Pile A	Pile B	Pile C
DAY 2	722	749	719	4.30	4.40	4.10	0.039	0.036	0.050	885.5	942.7	924.2	0.9902	0.9912	0.9901
DAY 5	580	794	858	3.98	4.50	4.68	0.058	0.035	0.032	976.0	1012.3	1093.9	0.9904	0.9895	0.9884
DAY 10	607	766	890	4.11	4.79	4.60	0.055	0.021	0.032	985.6	961.1	1138.4	0.9905	0.9907	0.9878

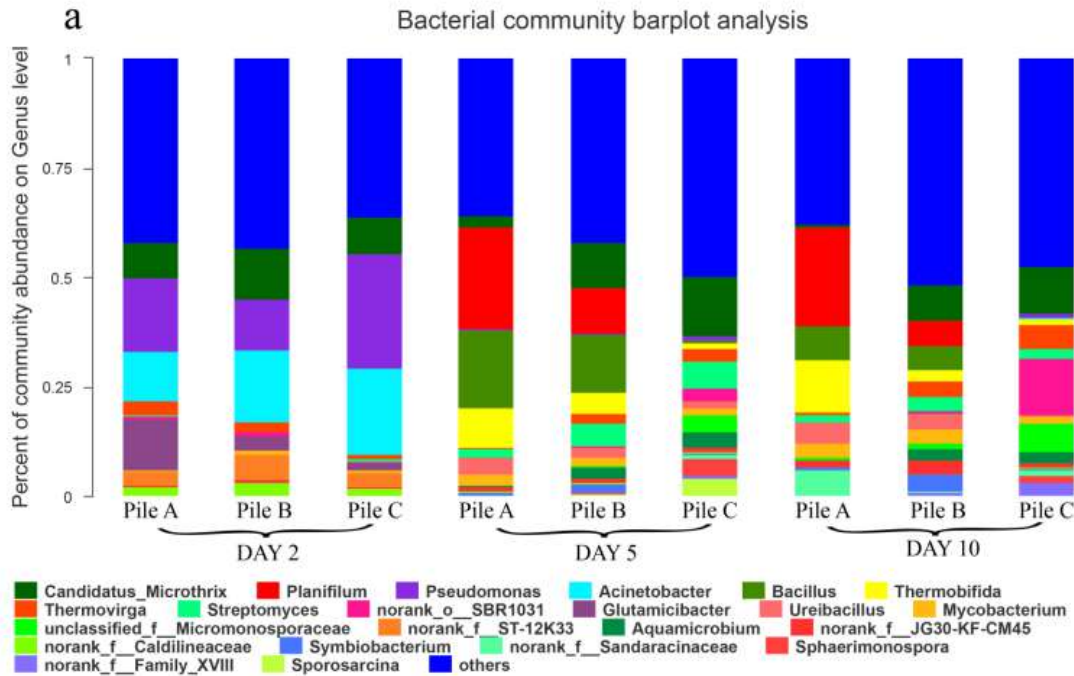


Fig. 3: Distribution of bacterial community compositions at the different composting times.

(10.7%) in Pile C and the lowest proportion (0.6%) in Pile A. *Thermobifida* accounted for the highest proportion (12.0%) in Pile A and the lowest proportion (1.2%) in Pile C.

CONCLUSIONS

The initial MC influenced the heat up during sewage sludge composting; a larger MC reduced the heating rate and the duration of the thermophilic phase. High initial MC considerably increased the activities of cellulase and peroxidase during the composting mesophilic phase. The high MC could slow down the heating process because water has a higher specific heat capacity than microbial activity, which produces insufficient heat. The impact of varied initial MC on microorganisms is primarily to alter the fraction of dominant strains rather than the species of dominant strains.

ACKNOWLEDGEMENTS

This research was financially supported by the Henan Province Key R&D and promotion projects (Grant No. 212102310063).

REFERENCES

Cai, L., Chen, T.B., Gao, D. and Yu, J. 2016. Bacterial communities and their association with the bio-drying of sewage sludge. *Water Res.*, 90: 44-51.

- Castaldi, P., Garau, G. and Melis, P. 2008. Maturity assessment of compost from municipal solid waste through the study of enzyme activities and water-soluble fractions. *Waste Manag.*, 28(3): 534-540.
- Gajalakshmi, S. and Abbasi, S.A. 2008. Solid waste management by composting: State of the art. *Crit. Rev. Environ. Sci. Technol.*, 38(5): 311-400.
- Ghose, T.K. 1987. Measurement of cellulase activities. *Pure Appl. Chem.*, 59(2): 257-268.
- Hamoda, M.F., Abu Qdais, H.A. and Newham, J. 1998. Evaluation of municipal solid waste composting kinetics. *Resour. Conserv. & Recycl.*, 23: 209-223.
- Hu, T., Wang, X., Zhen, L., Gu, J., Zhang, K., Wang, Q., Ma, J., Peng, H., Lei, L. and Zhao, W. 2019. Effects of inoculating with the lignocellulose-degrading consortium on cellulose-degrading genes and fungal community during co-composting of the spent mushroom substrate with swine manure. *Bioresour. Technol.*, 291.
- Huang, K., Li, F., Wei, Y., Chen, X. and Fu, X. 2013. Changes of bacterial and fungal community compositions during vermicomposting of vegetable wastes by *Eisenia foetida*. *Bioresour. Technol.*, 150: 235-241.
- Kiyimaci, M.E., Altanlar, N., Gumustas, M., Ozkan, S.A. and Akin, A. 2018. Quorum sensing signals and related virulence inhibition of *Pseudomonas aeruginosa* by a potential probiotic strain's organic acid. *Microb. Pathog.*, 121: 190-197.
- Levantesi, C., Rossetti, S., Thelen, K., Kragelund, C., Krooneman, J., Eikeboom, D., Nielsen, P.H. and Tandoi, V. 2006. Phylogeny, physiology, and distribution of '*Candidatus Microthrix calida*', a new Microthrix species isolated from industrial activated sludge wastewater treatment plants. *Environ. Microbiol.*, 8(9): 1552-1563.
- Jain, S., Jain, S., Wolf, I.T., Lee, J. and Tong, Y.W. 2015. A comprehensive review on operating parameters and different pretreatment methodologies for anaerobic digestion of municipal solid waste. *Renew. Sust. Energy Rev.*, 52: 142-154.

- Li, R., Wang, Q., Zhang, Z., Zhang, G., Li, Z., Wang, L. and Zheng, J. 2015. Nutrient transformation during aerobic composting of pig manure with biochar prepared at different temperatures. *Environ. Technol.*, 36(7): 815-826.
- Liu, N., Zhou, J., Han, L., Ma, S., Sun, X. and Huang, G. 2017. Role and multi-scale characterization of bamboo biochar during poultry manure aerobic composting. *Bioresour. Technol.*, 241: 190-199.
- Ma, C., Hu, B., Wei, M., Zhao, J. and Zhang, H. 2019. Influence of matured compost inoculation on sewage sludge composting: enzyme activity, bacterial and fungal community succession. *Bioresour. Technol.*, 20: 13-26.
- Makan, A., Assobhei, O. and Mountadar, M. 2013. Effect of initial moisture content on the in-vessel composting under air pressure of organic fraction of municipal solid waste in Morocco. *Iran. J. Environ. Health Sci. Eng.*, 10: 54.
- Tiquia, S.M., Tam, N.F.Y. and Hodgkiss, I.J. 1996. Microbial activities during composting of spent pig-manure sawdust litter at different moisture contents. *Bioresour. Technol.*, 55(3): 201-206.
- Wu, J., He, S., Liang, Y., Li, G., Li, S., Chen, S., Nadeem, F. and Hu, J. 2017. Effect of phosphate additive on the nitrogen transformation during pig manure composting. *Environ. Sci. Pollut. Res.*, 24(21): 17760-17768.
- Yu, Z., Tang, J., Liao, H., Liu, X., Zhou, P., Chen, Z., Rensing, C. and Zhou, S. 2018. The distinctive microbial community improves composting efficiency in a full-scale hyperthermophilic composting plant. *Bioresour. Technol.*, 265: 146-154.
- Zhou, H., Shen, Y., Meng, H., Gao, D. and Chen, T. 2018. Effect of air temperature and aeration strategy on water removal during sewage sludge composting. *Dry. Technol.*, 36: 1474-1480.
- Zhang, L., Ma, H., Zhang, H., Xun, L., Chen, G. and Wang, L. 2015. *Thermomyces lanuginosus* is the dominant fungus in maize straw composts. *Bioresour. Technol.*, 197: 266-275.
- Zhou, H.B., Ma, C., Gao, D., Chen, T.B., Zheng, G.D., Chen, J. and Pan, T.H. 2014. Application of a recyclable plastic bulking agent for sewage sludge composting. *Bioresour. Technol.*, 152: 329-336.
- Zhou, J. M. 2017. The effect of different C/N ratios on the composting of pig manure and edible fungus residue with rice bran. *Comp. Sci. Util.*, 25(2): 120-129.



The Effects of Disturbance on the Release of Nitrogen and Phosphorus from Sediment in Rural Ditches

Silin Yang^{*(**)}, Pengrui Du^{*}, Yungen Liu^{*(**)}†, Yan Wang^{*(**)}, Rong Ma^{*(**)} and Yunhui Gong^{*}

^{*}Faculty of Ecology and Environment, Southwest Forestry University, Kunming, 650224, China

^{**}Center for Water Science and Engineering, Southwest Forestry University, Kunming, 650224, China

†Corresponding author: Yungen Liu; henryliu1008@163.com

Nat. Env. & Poll. Tech.
Website: www.neptjournal.com

Received: 18-04-2021

Revised: 24-05-2021

Accepted: 08-06-2021

Key Words:

Nitrogen
Phosphorus
Sediment
Rural ditches

ABSTRACT

Reduced nitrogen (N) and phosphorus (P) released from sediments in rural areas pose a significant challenge to residential sewage treatment and management. Under different disturbance velocities, simulation experiments were undertaken to investigate the effect of disturbance on the release of N and P from rural ditch sediments into the water at the water-sediment interface. No significant difference in the release characteristics of N and P was found among different disturbance velocities. The release fluxes of TN and $\text{NH}_4^+\text{-N}$ in the non-disturbance water body were significantly higher than in the disturbance water body, which suggests that increasing water flow influences the release of TN and $\text{NH}_4^+\text{-N}$ from sediment into the water. The release fluxes of TP and $\text{PO}_4^{3-}\text{-P}$ were significantly lower in non-disturbance than the disturbance water body, which suggested that disturbance increased the release of TP and $\text{PO}_4^{3-}\text{-P}$ in sediments. For both disturbance and non-disturbance conditions, TN and $\text{NH}_4^+\text{-N}$ in the sediment were rapidly released into the water body at 0-10 days, and TP and $\text{PO}_4^{3-}\text{-P}$ steadily rose in the disturbance water body until stabilizing after 20 days. TN, $\text{NH}_4^+\text{-N}$, TP, and $\text{PO}_4^{3-}\text{-P}$ concentrations all had a negative correlation with DO, and the correlations between TN and $\text{NH}_4^+\text{-N}$ were substantial. The percentages of a certain N or P speciation fraction in sediments did not alter between disturbance and non-disturbance conditions, implying that disturbance had no effect on N or P speciation.

INTRODUCTION

The cycle of nitrogen (N) and phosphorus (P) in nature is of critical importance because they are essential nutrient elements in the ecosystem. However, excessive N and P can cause serious ecological problems. Due to the extensive application of fertilizers (Howarth 2004) and discharge of domestic water, a large amount of N and P is released into natural water (Isermann 1990, Zhu et al. 2018), leading to the eutrophication of rivers and lakes. Sediment plays an important role in regulating the nutrient content in the water body environment (Meade 1982, Span et al. 1990).

Numerous studies have shown that the absorption and desorption of N and P in the water-sediment interface are affected by multiple factors, such as temperature, pH, the concentration of organic matter, and hydraulic disturbance (Rzepecki 2010, Zhang et al. 2012). Therefore, nutrient release characteristics in river and lake sediment have received extensive attention (Rozan et al. 2002), and various simulation experiments under controlled conditions have been developed to elucidate the mechanism underlying nutrient release (Geng et al. 2020, Luo & Lu 2020, Wang et al. 2008, Yiping et al. 2004). Previous studies, on the other

hand, have focused on sediments in rivers and lakes, with less attention paid to sediment in rural areas due to the difficulty of home sewage treatment and management caused by scattering. Because of the population disparity, sediments in rural ditches are affected by water flow, and the effects of disturbance on nitrogen and phosphorus release in rural sediment are unknown.

In this study, disturbed simulation experiments were used to explore the release characteristics of N and P in the water-sediment interface and their effect on the different disturbance velocities of N and P concentrations of rural ditch sediment into the water. This study provides fundamental information for sewage management and environmental protection in rural areas.

MATERIALS AND METHODS

Sediment Collection and Preparation

Trial sediment samples were collected from a rural ditch in Xiaokanglang Village, Kunming City, Yunnan Province, China. Approximately 112 kg of sediments were collected at a depth of 0-3 cm. The sample was returned to the laboratory to

determine the N and P release characteristics of the sediment. Sediment particle size (PS), N, and P background contents are listed in Table 1. According to Canadian environmental quality guidelines (CEQGs), total nitrogen (TN, 6.15 g.kg⁻¹) and total phosphorus (TP, 5.91 g.kg⁻¹) in sediments exceeded the threshold effect concentrations (TN, 2 g.kg⁻¹; TP, 4.8 g.kg⁻¹) for toxic biological effects, which indicated that N and P have potential ecological risks, and their potential ecological risk assessment is needed for extended discussion.

Batch Disturbance Experiments

The collected ditch sediments were placed into five pre-designed and manufactured rectangle polyvinyl chloride sinks (sink 1) with a width and height of 16 cm to a length of 1000 cm (Fig. 1). Approximately 7.5 kg of the sediments were mixed to an average depth of 3 cm and then allowed to stand for 24 h. Distilled water (15 L) was introduced into each water sink 2, covered with a water pump, and the water flow velocities were adjusted to 5, 15, 30, and 60 L.h⁻¹ using a float flowmeter. Water was then circularly injected into sink 1 from sink 2 by a water pump (Risheng, RS-468B). At the setting times, approximately 20 mL of the water samples were collected from the water body in sink 2, and 1.5 g of sediment samples were collected from surface sediment in sink 1. The samples were collected at five-day intervals until day 30. Distilled water was added to the original scale of sink 2 after the water sample was collected. Moreover, 15L of distilled water was added to water sink 1 in a non-disturbance experiment. 20 mL of water samples and 1.5 g of sediment samples were taken from sink 1.

The water samples were immediately filtered, and the pH, dissolved oxygen (DO), oxidation-reduction potential (Eh), and electric conductivity (EC) in the water were determined (HACH-HQ40d). Total nitrogen (TN), total phosphorus (TP),

and orthophosphorus (PO₄³⁻-P) in the water were determined by potassium persulfate oxidation-UV spectrophotometry, and ammonia (NH₄⁺-N) was determined by Nessler's reagent spectrophotometry (Wang & Wu 2016). Each sample was evaluated three times, and the results are presented as average values. The nitrogen in all the sediment samples was fractionated as ion-exchanged form nitrogen (IEF-N), weak acid extractable form nitrogen (WAEF-N), strong alkaline extractable form nitrogen (SAEF-N), and strong oxidant extractable form nitrogen (SOEF-N), and phosphorus was fractionated as labile phosphorus (Labile-P), reducible soluble phosphorus (RSP), iron- and aluminum-bound phosphorus (Fe/Al-P), and calcium-bound phosphorus (Ca-P), according to the sequential extraction method (Wang & Wu 2016).

The release flux (R) of nitrogen and phosphorus in sediments was calculated using the following equation:

$$R = [V(C_n - C_0) + \sum_{j=1}^n V_j(C_{j-1} - C_a)] / At \quad \dots(1)$$

where R(mg.m⁻².d⁻¹) is the release flux, V(L) is the water volume, C₀, C_n, and C_{j-1} (mg.L⁻¹) are the concentrations of nutrients in the water body in the starting sampling, the nth and j-1th sampling, C_a (mg.L⁻¹) is the nutrient concentration of the added water sample, V_j (L) is the sampling volume, A is the water-sediment contact interface (m²), and t is release time (d).

Statistical Analysis

The statistical differences in pH, DO, Eh, EC, TN, and TP contents between disturbance and non-disturbance water from each collection time were determined using the paired *t*-test, with statistical significance defined as $p \leq 0.05$. The association between nutritional species concentrations and pH, DO, Eh, and EC content was investigated using bivariate

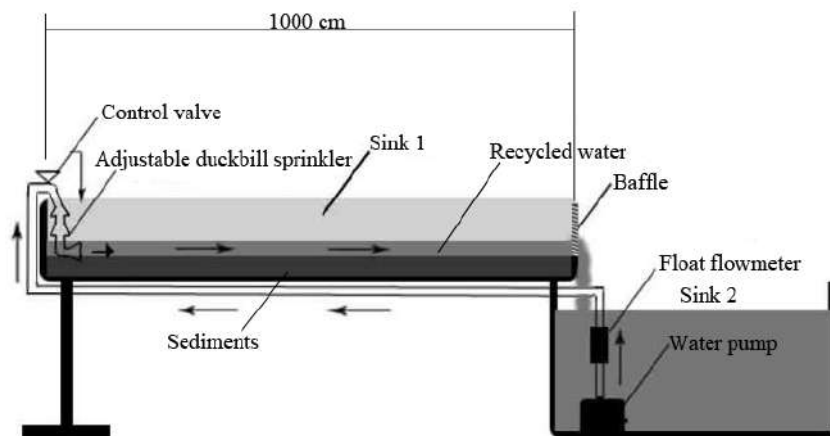


Fig. 1: Simulation device for the release experiment.

Table 1: Basic properties of the sediment.

PS (μm)			Nitrogen contents (g.kg^{-1})					Phosphorus contents (g.kg^{-1})				
<2	2~20	20~2000	TN	IEF-N	WAEF-N	SAEF-N	SOEF-N	TP	Labile-P	RSP	Fe/Al-P	Ca-P
0.0%	72.5%	27.5%	6.15	0.78	1.14	0.30	3.34	5.91	0.59	0.57	0.92	3.12

IEF-N: ion-exchanged form nitrogen; WAEF-N: weak acid extractable form nitrogen; SAEF-N: strong alkaline extractable form nitrogen; SOEF-N: strong oxidant extractable form nitrogen;

Labile-P: labile phosphorus; RSP: reducible soluble phosphorus;

Fe/Al-P: iron and aluminum-bound phosphorus; Ca-P: calcium-bound phosphorus

correlation in a two-tailed test, with statistical significance defined as $p \leq 0.05$. SPSS22.0 software was used for all statistical analyses.

RESULTS AND DISCUSSION

pH, DO, Eh and EC

The overall pH, DO, Eh, and EC contents of disturbance and non-disturbance water bodies are summarized in Table 2. The pH, DO, Eh, and EC values of non-disturbance water were 8.53, 3.86 (g.kg^{-1}), 97.51 (mV), and 707.14 ($\mu\text{s.cm}^{-1}$), respectively. The paired *t*-test showed no remarkable differences in the pH, Eh, and EC between disturbance and non-disturbance water ($p > 0.05$). DO contents were significantly higher in disturbance water than non-disturbance water ($p < 0.05$), and their contents slightly increased with disturbance velocity (0-60 L.h^{-1}). Due to the increased surface of water interaction with air, this finding demonstrated that disturbance could enhance DO levels in contrast to non-disturbance. For the same disturbance velocity owing to oxygen in the water for consumption by microorganisms, DO contents steadily dropped with time (0-10 days), and DO contents stabilized after 10 days (Beutel 2006).

Release Characteristics of N in Disturbance and Non-Disturbance Water bodies

The release dynamics of TN and $\text{NH}_4^+\text{-N}$ in the sediments from water bodies with different disturbance velocities are shown in Fig. 2. The concentrations of TN and $\text{NH}_4^+\text{-N}$ in

disturbance and non-disturbance water bodies gradually increased and then gradually decreased and stabilized. The maximum concentrations of TN and $\text{NH}_4^+\text{-N}$ in the disturbance water body were all observed at day 10, and the maximum concentrations of TN and $\text{NH}_4^+\text{-N}$ in the non-disturbance water body were found at day 20. Similar results have been reported in which TN and $\text{NO}_3^-\text{-N}$ in the sediment pore water were generally released into the water body during the first 10 days (Chen et al. 2020). In the early stage (0-10 days) of the experiment, there was a concentration difference between TN and $\text{NH}_4^+\text{-N}$ at the water-sediment interface, resulting in a quick release of $\text{NH}_4^+\text{-N}$, $\text{NO}_3^-\text{-N}$, and inorganic salt nitrogen in the sediment into the water body and, thus, a rapid increase in the TN and $\text{NH}_4^+\text{-N}$ concentrations in the water body (Zhu et al. 2018). It has been shown that the oxygen content in the water is sufficient, the aerobic microorganisms grow rapidly, and the organic matter released from the sediment is quickly decomposed to NH_3 (Beutel 2006).

From days 0 to 10, there were no noticeable differences in TN, $\text{NH}_4^+\text{-N}$ concentrations between disturbance and non-disturbance water bodies, however, from days 10 to 30, the non-disturbance water body had greater TN, $\text{NH}_4^+\text{-N}$ concentrations than the disturbance water body. This result indicated that disturbance of the water body did not increase the release of TN and $\text{NH}_4^+\text{-N}$ from bottom sediments into the water body, which might be related to nitrogen adsorption by suspended particulate matter in the water body caused by disturbance. This phenomenon was found in the water-sed-

Table 2: The pH, DO, Eh and EC values and the concentrations of N and P in disturbance and non-disturbance water samples.

DV (L.h^{-1})	pH (H_2O)	DO (g.kg^{-1})	Eh (mV)	EC ($\mu\text{s.cm}^{-1}$)	Nutrients concentration (g.kg^{-1})			
					TN	$\text{NH}_4^+\text{-N}$	TP	$\text{PO}_4^{3-}\text{-P}$
0	8.53±0.19	3.86±2.70	97.51±66.15	707.14±240.27	18.23±9.02	13.48±6.87	0.40±0.20	0.03±0.02
5	8.61±0.08	6.36±1.18	98.17±42.46	696.95±182.22	9.10±6.51	6.25±6.48	0.88±0.48	0.30±0.19
15	8.63±0.12	6.54±1.32	98.00±51.82	701.81±182.88	7.30±5.49	4.67±5.00	0.93±0.46	0.33±0.20
30	8.70±0.15	6.71±1.27	100.25±53.71	696.29±192.16	5.75±4.37	4.62±4.85	0.87±0.43	0.31±0.18
60	8.64±0.23	6.99±1.04	100.69±57.37	631.38±146.42	8.43±7.24	5.83±6.29	0.77±0.39	0.26±0.18

DV: Disturbance velocity (L.h^{-1}); 0: non-disturbance water; 5-60: disturbance water.

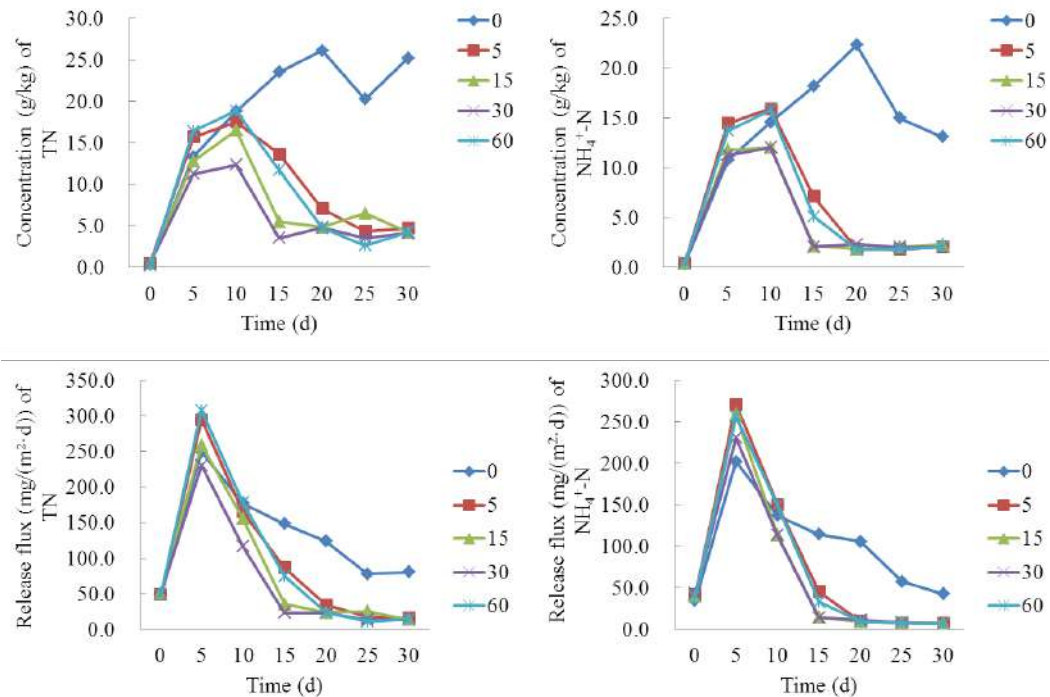


Fig. 2: Release concentrations and fluxes of TN and $\text{NH}_4^+\text{-N}$ in disturbance and non-disturbance water bodies. The 0 represents the concentrations in the non-disturbance water body; the 5-60 represent concentrations in the disturbance water body.

iment interface from Poyang and Dongting Lake, where influences of variable disturbance velocity on ammonium nitrogen and nitrate nitrogen concentrations of the overlying water in the sediment-water interface were not obvious (Ni et al. 2020, Tong et al. 2016).

The release fluxes of TN and $\text{NH}_4^+\text{-N}$ in different disturbance and non-disturbance water bodies are listed in Fig. 2. For disturbance and non-disturbance conditions, the release fluxes of TN and $\text{NH}_4^+\text{-N}$ reached the highest levels at 5 days and subsequently, gradually declined. The highest TN release fluxes of 0, 5, 15, 30, and 60 $\text{L}\cdot\text{h}^{-1}$ were 249.91, 295.23, 259.19, 230.69, and 307.84 $\text{mg}\cdot(\text{m}^2\cdot\text{d})^{-1}$, and the highest $\text{NH}_4^+\text{-N}$ release fluxes of 0, 5, 15, 30, and 60 $\text{L}\cdot\text{h}^{-1}$ were 202.12, 271.06, 259.18, 230.68, and 256.81 $\text{mg}\cdot(\text{m}^2\cdot\text{d})^{-1}$, respectively. The release fluxes of TN, $\text{NH}_4^+\text{-N}$ were higher in the non-disturbance than the disturbance water body after 10 days. This result revealed an effect of increasing water flow on TN and $\text{NH}_4^+\text{-N}$ release from sediment into water that was not obvious. The release flux of nitrogen was related to nitrogen morphological characteristics, physical and chemical properties of the sediment, microbial activities, and external environmental factors (Domagalski et al. 2007). The same trend was found for release fluxes of TN and $\text{NH}_4^+\text{-N}$ for different disturbance velocities.

Release Characteristics of P in Disturbance and Non-Disturbance Water bodies

The concentrations of TP and $\text{PO}_4^{3-}\text{-P}$ gradually increased in the disturbance water body and then basically stabilized after 20 days (Fig. 3). The concentrations of TP gradually increased in the non-disturbance water body, and the $\text{PO}_4^{3-}\text{-P}$ concentrations were relatively stable. The concentrations of TP and $\text{PO}_4^{3-}\text{-P}$ were higher in the disturbance than in the non-disturbance water body. The TP concentrations increased with time in non-disturbance sediments. The above results indicated that the disturbance increased TP and $\text{PO}_4^{3-}\text{-P}$ in the water body sediments. Previous studies have reported that increases in the disturbance velocity can enhance the disturbance intensity in sediments, causing an increase in the suspended solid concentration, total phosphorus concentration in the overlying water, and release ability of phosphorus to overlying water from enhanced sediments (Tong et al. 2017). These observations could be explained by the release of absorbed phosphorous by the particles into the water body through sediment re-suspension at the sediment-water interface before the release reached equilibrium.

The release fluxes of $\text{PO}_4^{3-}\text{-P}$ reached the highest level in the disturbance water body at 10 days, after which it gradually declined. The highest $\text{PO}_4^{3-}\text{-P}$ release fluxes of 0,

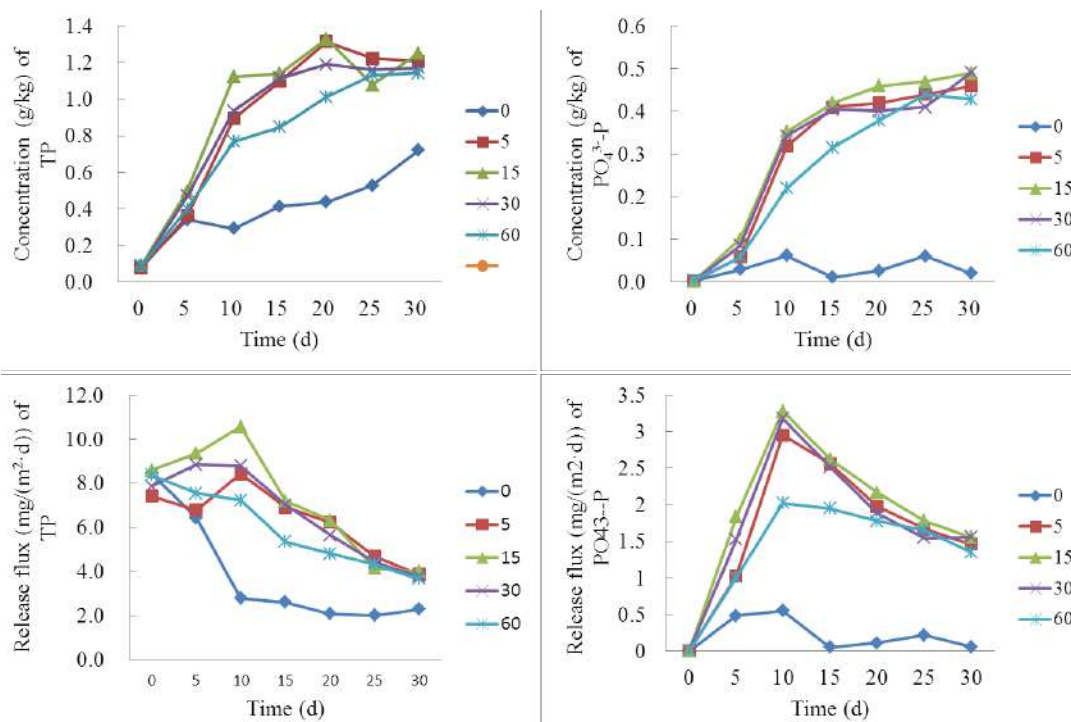


Fig. 3: Release concentrations and fluxes of TP and $\text{PO}_4^{3-}\text{-P}$ in the disturbance and non-disturbance water bodies. The 0 represents concentrations in the non-disturbance water body; the 5-60 represents concentrations in the disturbance water body.

5, 15, 30, and 60 $\text{L}\cdot\text{h}^{-1}$ were 0.55, 2.96, 3.28, 3.18, and 2.03 $\text{mg}\cdot(\text{m}^2\cdot\text{d})^{-1}$, respectively. The release fluxes of TP, $\text{PO}_4^{3-}\text{-P}$ were higher in the disturbance than the non-disturbance water body, suggesting that the disturbance increased the release of TP and $\text{PO}_4^{3-}\text{-P}$ in sediments.

Effect of Disturbance on the Release and Speciation of N and P in Sediments

In this study, the correlation between TN, $\text{NH}_4^+\text{-N}$, TP and $\text{PO}_4^{3-}\text{-P}$ concentrations and DO, Eh, pH, and EC contents was analyzed. The results showed that the concentrations of TN, $\text{NH}_4^+\text{-N}$, TP, and $\text{PO}_4^{3-}\text{-P}$ were negatively correlated with DO (Table 3), and the correlations of TN, $\text{NH}_4^+\text{-N}$, with DO were significant. These findings indicated that nitrogen and phosphorus release from sediment into the water body was

affected by DO. Previous studies have shown that nitrogen and phosphorus release in the water-sediment interface is influenced by many factors, such as temperature, pH, DO, the concentration of organic matter, and the oxygen state at the water-sediment interface, which is strongly correlated with the nitrogen and phosphorus transport and release rate (Beutel et al. 2008, Ding et al. 2016). Aerobic conditions can inhibit the release of nutrients from sediments to overlying water (Nausch et al. 2009, Wang et al. 2016). Improving the DO concentration at the water-sediment interface is an important tactic to control the release of sedimentary nutrients in a lake (Wang et al. 2020).

There were significant correlations between the different disturbance water bodies for TN and $\text{NH}_4^+\text{-N}$, while no significant correlation was found between disturbance and

Table 3: Correlation between TN, $\text{NH}_4^+\text{-N}$, TP, and $\text{PO}_4^{3-}\text{-P}$ with pH, DO, Eh and EC.

Nutrients	pH	DO	Eh	EC
TN	-0.044	-0.621**	-0.512**	0.401*
$\text{NH}_4^+\text{-N}$	0.012	-0.453**	-0.394*	0.258
TP	0.483**	-0.327	-0.716**	0.734**
$\text{PO}_4^{3-}\text{-P}$	0.497**	-0.130	-0.562**	0.582**

* Significance at the 0.05 probability level.

** Significance at the 0.01 probability level.

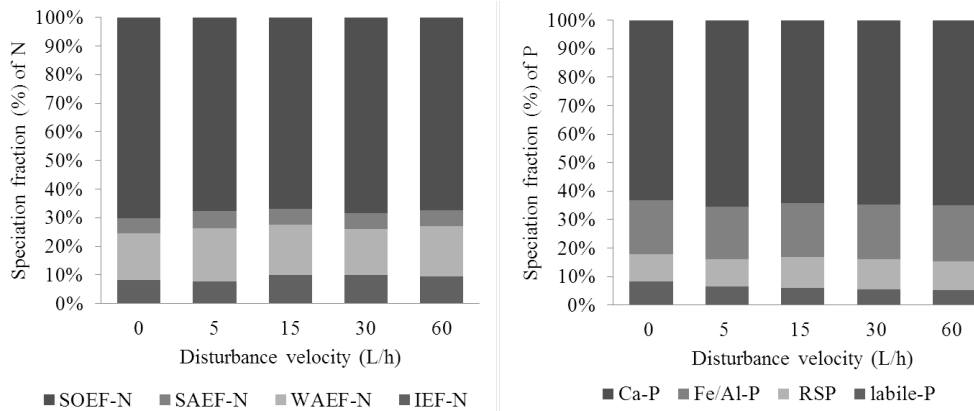


Fig. 4: Speciation distribution of N and P in sediments.

non-disturbance water bodies, which indicated that the nitrogen release process from sediments to the water body was the same in the disturbance body. The contribution of ammonia nitrogen released from the sediment to total nitrogen was the largest among all nitrogen components (Chen et al. 2015). Studies have reported that the nitrogen forms released from interstitial to overlying water are mainly $\text{NH}_4^+\text{-N}$, followed by $\text{NO}_3^-\text{-N}$, and most of this nitrogen released from sediments is due to the degradation of organic matter (Markou et al. 2007).

The speciation fractions of N and P in sediments expressed as percentages to their total concentrations are shown in Fig. 4. The distribution patterns of the percentages for N or P nutrient speciation fractions were similar in disturbance and non-disturbance sediments. The percentage of SOEF-N was greater than 60% of their total concentrations in both disturbance and non-disturbance sediments, and the percentage of IEF-N was less than 10% of their total concentrations. Regarding phosphorus in disturbance and non-disturbance sediments, Ca-P accounted for more than 50% of the total concentration, and Labile-P was less than 10%. This result is consistent with the speciation fractions of N and P in sediment from Dianchi Lake (Li et al. 2012). The SOEF-N was primarily made up of organic nitrogen, and its content was primarily linked to organic matter, making it a minor contributor to lake eutrophication. In the transferable nitrogen fractions, this component was the hardest to release. It might, however, be converted to a bio-available pool through nitrogen mineralization, making it a possible nitrogen source. The IEF-N was easily released into the water as an ion-exchangeable form, which is critical for N cycling. Therefore, IEF-N release and migration cannot be ignored. The Ca-P was considered a relatively stable fraction of sedimentary P and contributed to a permanent burial of P in sediments, and it was generally regarded as autogenetic with little relevance to the eutrophic status (Kaiserli et al. 2002).

The percentages for a certain speciation fraction of nitrogen or phosphorus were not remarkably different between disturbance and non-disturbance sediments, suggesting an unobvious influence of disturbance on N or P speciation.

CONCLUSION

The dynamic release process of N and P in the different disturbance and non-disturbance water bodies and their effect on water quality were studied through simulation experiments. The release characteristics of N and P at different disturbance velocities were the same, and the release fluxes of TN, $\text{NH}_4^+\text{-N}$ were higher in the non-disturbance than the disturbance water body. The release fluxes of TP and $\text{PO}_4^{3-}\text{-P}$ were lower in the non-disturbance than the disturbance water body, which indicated that the disturbance increased the release of TP and $\text{PO}_4^{3-}\text{-P}$ in sediments. The TN and $\text{NH}_4^+\text{-N}$ in the sediment were released into the water body rapidly in the early 0-10 days for disturbance and non-disturbance water bodies, and the TP and $\text{PO}_4^{3-}\text{-P}$ gradually increased in the disturbance water body and then stabilized after 20 days. The concentrations of TN, $\text{NH}_4^+\text{-N}$, TP, and $\text{PO}_4^{3-}\text{-P}$ were negatively correlated with DO, and the correlations of TN, $\text{NH}_4^+\text{-N}$ with DO were significant. The percentages of a certain speciation fraction of N or P were not different between disturbance and non-disturbance sediments. This study suggested that P release in disturbance sediment for rural ditches should not be overlooked, and its release and migration should be monitored with great concern for the environmental protection of rural regions.

ACKNOWLEDGEMENTS

We thank Chao Zhang (Faculty of Forestry, Southwest Forestry University, Kunming, 650224, China) for his kind help in the experiments. This work was financially supported by the National Natural Science Foundation of China

(41761098, 21767027) and the Basic Research Foundation of Yunnan Province of China (202001AT070117).

REFERENCES

- Beutel, M. 2006. Inhibition of ammonia release from anoxic profundal sediments in lakes using hypolimnetic oxidation. *Ecol. Eng.*, 28: 271-279.
- Beutel, M.W., Leonard, T.M., Dent, S. R. and Moore, B.C. 2008. Effects of aerobic and anaerobic conditions on P, N, Fe, Mn, and Hg accumulation in waters overlaying profundal sediments of an oligo-mesotrophic lake. *Water Res.*, 42: 1953-1962.
- Chen, H., Zhuo, Q.F., Xu, Z.C., Wang, J.S. and Guo, Q.W. 2015. Nitrogen release performance of sediments in drainage pipeline. *Environ. Sci.*, 36: 2918.
- Chen, Q., Wang, Q., Li, Z., Zhang, M. and Sun, M. 2020. Release characteristics of inorganic nitrogen in different water layers and its impact on overlying water from Liaohe River, China. *Ecotoxicology*, 41: 1138.
- Ding, S., Wang, Y., Wang, D., Li, Y.Y., Gong, M. and Zhang, C. 2016. In situ, high-resolution evidence for iron-coupled mobilization of phosphorus in sediments. *Sci. Rep.*, 6: 24341.
- Domagalski, J., Lin, C., Luo, Y., Kang, J., Wang, S., Brown, L.R. and Munn, M.D. 2007. Eutrophication study at the Panjiakou-Daheiting Reservoir system, northern Hebei Province, People's Republic of China: Chlorophyll-a model and sources of phosphorus and nitrogen. *Agric. Water Manag.*, 94: 43-53.
- Geng, X., Li, D., Xu, C. and Sun, P. 2020. Using sediment resuspension to immobilize sedimentary phosphorus. *Environ. Sci. Pollut. Res.*, 16: 541
- Howarth, R.W. 2004. Human acceleration of the nitrogen cycle: drivers, consequences, and steps toward solutions. *Water Sci. Technol.*, 49: 7.
- Isermann, K. 1990. Share of agriculture in nitrogen and phosphorus emissions into the surface waters of Western Europe against the background of their eutrophication. *Nut. Cycl. Agroecosys.*, 26: 253-269.
- Kaiserli, A., Voutsas, D. and Samara, C. 2002. Phosphorus fractionation in lake sediments-lakes Volvi and Koronia N Greece. *Chemosphere*, 46:47-55.
- Li, H., Wang, Y., Shi, L.Q., Mi, J. and Pan, X.J. 2012. Distribution and fractions of phosphorus and nitrogen in surface sediments from Dianchi Lake, China. *Int. J. Environ. Res.*, 6: 195-208.
- Luo, W. and Lu, J. 2020. Inhibition of in situ coating of sediment ceramsite on sediment nutrient release of eutrophic lakes. *Environ. Geochem. Health*, 13: 114
- Markou, D.A., Sylaios, G.K., Tsihrintzis, V.A., Gikas, G.D. and Haralambidou, K. 2007. Water quality of Vistonis Lagoon, Northern Greece: Seasonal variation and impact of bottom sediments. *Desalination*, 210: 83-97.
- Meade, R.H. 1982. Sources, sinks, and storage of river sediment in the Atlantic drainage of the United States. *J. Geol.*, 90: 235-252.
- Nausch, M., Nausch, G., Lass, H.U., Mohrholz, V., Nagel, K., Siegel, H. and Wasmund, N. 2009. Phosphorus input by upwelling in the eastern Gotland Basin (Baltic Sea) in summer and its effects on filamentous cyanobacteria. *Estuar. Coast. Shelf Sci.*, 83: 434-442.
- Ni, Z., Wang, S., Wu, Y., Liu, X. and Liu, Z. 2020. Influence of exposure time on phosphorus composition and bioavailability in wetland sediments from Poyang lake, since the operation of the Three Gorges Dam. *Environ. Pollut.*, 263: 114591.
- Rozaan, T., Taillefert, M., Trouwborst, R., Glazer, B., Ma, S., Herszage, J., Valdes, L. and Luther, G. 2002. Iron-sulfur-phosphorus cycling in the sediments of a shallow coastal bay: Implications for sediment nutrient release and benthic macroalgal blooms. *Limnol. Oceanogr.*, 47: 1346-1354.
- Rzepecki, M. 2010. The dynamics of phosphorus in lacustrine sediments: Contents and fractions in relation to lake trophic state and chemical composition of bottom deposits. *Pol. J. Ecol.*, 58: 409-427.
- Span, D., Arbouille, D., Howa, H. and Vernet, J.P. 1990. Variation of nutrient stocks in the superficial sediments of Lake Geneva from 1978 to 1988. *Hydrobiologia*, 207: 161-166.
- Tong, Y., Liang, T., Wang, L. and Tian, S. 2016. Characteristics of nitrogen release from Lake Dongting sediments under variable water level and velocity in the two-way annular flume. *J. Lake Sci.*, 28: 59-67.
- Tong, Y., Liang, T., Wang, L. and Tian, S. 2017. Simulation on phosphorus release characteristics of Poyang Lake sediments under variable water levels and velocities. *J. Geogr. Sci.*, 27: 697-710.
- Wang, P., Song, J., Guo, Z. and Li, X. 2008. The release behavior of inorganic nitrogen and phosphorus in sediment during the disturbance. *Chinese J. Oceanol. Limnol.*, 54: 1104.
- Wang, J., Chen, J., Ding, S., Guo, J., Dallimore, C., Dai, Z. and Haiquan, Y. 2016. Effects of seasonal hypoxia on the release of phosphorus from sediments in a deep-water ecosystem: A case study in Hongfeng Reservoir, Southwest China. *Environ. Pollut.*, 87: 219.
- Wang, J., Chen, J., Yu, P., Yang, X., Zhang, L., Geng, Z. and He, K. 2020. Oxygenation and synchronous control of nitrogen and phosphorus release at the sediment-water interface using oxygen nano-bubble modified material. *Sci. Tot. Environ.*, 725: 138258.
- Wang, S. and Wu, Z. 2016. *The Basic Theory of P-process at Sediment/Water Interface (SWI) in Lake*. Springer, Singapore.
- Yiping, L., Yong, P., Jun, L.U., Gang, Z. and Lili, F. 2004. On the relation between the release rate of TN, TP from sediment, and water velocity. *J. Lake Sci.*, 16: 318-324.
- Zhang, L., Yin, J., Jiang, Y. and Wang, H. 2012. Relationship between the hydrological conditions and the distribution of vegetation communities within the Poyang Lake National Nature Reserve, China. *Ecol. Inform.*, 11:n65-75.
- Zhu, Y., Tang, W., Jin, X. and Shan, B. 2018. Using biochar capping to reduce nitrogen release from sediments in eutrophic lakes. *Sci. Tot. Environ.*, 646: 93-104.



PM_{2.5} Concentration Prediction Based on Pollutant Pattern Recognition Using PCA-clustering Method and CS Algorithm Optimized SVR

Wei Liu*, Fuji Chen*† and Yihui Chen*

*School of Economics & Management, Fuzhou University, Fuzhou 350116, PR China

†Corresponding author: Fuji Chen; chenfuji@fzu.edu.cn

Nat. Env. & Poll. Tech.
Website: www.neptjournal.com

Received: 17-04-2021

Revised: 27-06-2021

Accepted: 14-07-2021

Key Words:

PM_{2.5} concentrations
PCA-clustering
Cuckoo search algorithm
SVR

ABSTRACT

Environmental issues, particularly air pollution, are a matter of concern for people all around the world. PM_{2.5} levels that are too high harm people's physical and mental health. For government air pollution control, more accurate PM_{2.5} concentration predictions are critical. In this paper, we explored the relationship between pollutants (PM₁₀, SO₂, NO₂, O₃, CO) and meteorological factors (atmospheric pressure, relative humidity, air temperature, wind speed, wind direction, cumulative precipitation) that affect the generation and transmission of PM_{2.5}. To better predict the concentration of PM_{2.5}, we innovatively combined principal component analysis (PCA) and clustering methods to extract pollutant variables and patterns as important PM_{2.5} concentration predictors of different models such as support vector regression (SVR), multivariate nonlinear regression (MNR), and artificial neural network (ANN). Compared to MNR and ANN models, SVR presented better prediction accuracy. Moreover, cuckoo search (CS), cross-validation (CV), and particle swarm optimization (PSO) algorithms were used to further optimize the parameters in the process of SVR. And to evaluate the above PM_{2.5} concentration prediction results, we introduced several evaluating indicators including root mean squared error (RMSE), mean absolute error (MAE), mean absolute percentage error (MAPE), and person correlation coefficient (R) between predicted and measured values. The obtained results confirmed that when the pollutant data was divided into three patterns, the best prediction accuracy was achieved by the CS-SVR model.

INTRODUCTION

Particulate matter (PM) in the atmosphere has gotten a lot of attention in recent decades because it has a big impact on human health. PM_{2.5} is made up of harmful chemicals such as heavy metals and carcinogenic organic compounds with aerodynamic diameters less than 2.5μm. It can easily and deeply penetrate the human lungs to cause serious health issues (Thomaidis et al. 2003, Yuan et al. 2019, Badaloni et al. 2017). High PM_{2.5} level exposure is correlated to the increase in respiratory and cardiovascular diseases (Ostro et al. 1999, Biancofiore et al. 2017) and population mortality (Di et al. 2017, Liang et al. 2018). It has also been proven that prenatal exposure to PM_{2.5} can decrease corpus callosum volume and affect children's neuropsychological development (Mortamais et al. 2019, Suades-González et al. 2015).

International environmental organizations and countries all over the world pay great attention to the negative effects of PM_{2.5}. According to the WHO guideline and China's current situation, in 2012 the Ministry of Ecology and Environment (MEE) published Chinese ambient air quality standards, in which the daily and annual average PM_{2.5} limits were set as 75 and 35 μg.m⁻³ (State Bureau of Environment Protection

2012). In Beijing, for example, days with air quality surpassing the MEE limit accounted for 43.5% of the total, which is higher than days with other pollutants such as O₃, PM₁₀, and NO₂ (Beijing Municipal Ecology and Environment Bureau 2019, 2018). PM_{2.5} concentration predictions that are more accurate help not only people in planning their daily activities but also government regulation.

PM_{2.5} concentration is influenced by a number of factors, the most important of which are pollutant emission factors and meteorological conditions. The former takes part in the chemical process of PM_{2.5} formations, and the latter influences the dissipation of PM_{2.5} (Liang et al. 2015, Wang et al. 2015). With the development of statistical methods, data mining, and artificial intelligence technology, researchers hope to use more simple and effective methods to predict the PM_{2.5} concentrations. Many efforts have been committed to the data algorithm and optimization. Marsha and Larkin (2019) used a multiple linear regression scheme to forecast daily PM_{2.5} concentrations using the previous day's PM_{2.5} measurements as well as fire and smoke-related variables from satellite observations. Sun et al. (2013) used hidden Markov models to forecast daily average PM_{2.5} concentrations for the next 24 hours. Liu and Sun (2019) used the

supplementary ensemble empirical modal decomposition algorithm, in which the random forest was applied to the decomposition sequence, to effectively reflect the trend of PM_{2.5} concentration.

In recent years, more effective data mining methods like artificial neural networks and support vector machines have also been successfully implemented in air pollution forecasting. Artificial neural networks, principal component analysis, and k-means clustering technology were combined by Franceschi et al. (2018) to forecast the PM₁₀ and PM_{2.5} concentrations in Bogotá, Colombia. A hybrid model based on principal component analysis (PCA) and cuckoo search algorithm (CS) optimized least square support vector machine (LSSVM) method was developed by Sun and Sun (2016) to predict PM_{2.5} concentrations. Gan et al. (2018) proposed a new method based on the secondary-decomposition-ensemble learning paradigm to forecast hourly PM_{2.5} concentration, in which the least square support vector was used to model all reconstructed components independently. These findings show that the support vector machine method is very effective at predicting PM_{2.5} concentrations.

In this work, we introduced the PCA-clustering method to CS algorithm optimized SVR for the prediction of PM_{2.5} concentrations in Beijing. In the beginning, we investigated the correlation between pollutant factors, meteorological factors, and PM_{2.5} concentrations, and extracted the pollutant variables and patterns using the PCA-clustering method to assist prediction. Then, contrastive studies on parameters optimization algorithms for SVR have been carried out, including cross-validation (CV), particle swarm optimization (PSO), and cuckoo searching (CS) algorithms, to achieve better prediction efficiency. Evaluation metrics such as RMSE, MAE, MAPE, and R were introduced as part of the process. Finally, to further verify the effectiveness of our

method, other predictive models like multivariate nonlinear regression (MNR) and artificial neural network (ANN) were also tested. The obtained results indicated that The PCA-clustering approach with SVR optimized by CS algorithm produced the best prediction accuracy.

MATERIALS AND METHODS

Sites and Data

Yizhuang station in Beijing has the most advanced meteorological observation equipment in China, enabling it to provide the most accurate data. Therefore, we model and simulate the PM_{2.5} predictions with the pollutant data and meteorological data from the Yizhuang observation station as shown in Fig. 1.

The pollutant factors include PM₁₀, SO₂, NO₂, O₃, CO which were collected from Beijing Municipal Environmental Monitoring Center, and the meteorological factors include atmospheric pressure (P), relative humidity (RH), air temperature (T), wind speed (WS), wind direction (WD), 20-20 hours' cumulative precipitation (CP) which were collected from the National Meteorological Information Center. The details of the original data are shown in Table 1. The 24 h average of the pollutant factors was calculated for the purpose of PM_{2.5} concentration prediction. Fig. 2 shows the PM_{2.5} concentration and temperature of Yizhuang station from October 14, 2014, to December 31, 2017. When some variables' data was missing for several days in a row, the associated dates data was removed, and the sporadic missing data was imputed using the EM imputation method.

As shown in Fig. 2, the trends of PM_{2.5} concentration and temperature are opposite. Low PM_{2.5} values were observed in the warm period from April to September, while high PM_{2.5} values were observed in the cold days from October



Fig. 1: The geography of Yizhuang pollutant and meteorological monitoring Station (39.795N, 116.506 E).

Table 1: Original pollutant and meteorological variables.

Pollutant Variables	Frequency	Pollutant Variables	Frequency
PM2.5	hourly	atmospheric pressure (P)	24 h average
PM10	hourly	relative humidity (RH)	24 h average
SO ₂	hourly	air temperature (T)	24 h average
NO ₂	hourly	wind speed (WS)	Max wind speed
O ₃	hourly	wind speed (WD)	Max wind direction
CO	hourly	cumulative precipitation (CP)	20-20 h

to March next year, some of which were even more than 500µg/m³. Considering that high-level PM2.5 concentration has a great impact on people’s lives, we use the atmospheric environment data of cold days to establish a prediction model for PM2.5 concentration.

Methods

PCA-clustering method to extract pollutant variables and pollutant patterns: The principal component analysis (PCA) algorithm has been widely applied for reducing the dimension of the data set on the premise of retaining the main variance. A new set of variables can be achieved by PCA transforming which are called principal components (PCs). To simplify the structure of the dataset, only the first few PCs with large variance are usually chosen to reflect the information of the original variables in the real research process. In most cases, a cumulative variance contribution rate of more than 85% for the first several major components is appropriate. For the purpose of this study, PCA was combined with the correlation coefficient between PM2.5 concentration and related covariates to find the primary influencing factors. Moreover, k-meaning clustering was further introduced to extract pollutant patterns.

Support vector machine regression model: Support vector machine (SVM), originally developed by Vapnik in the 1990s (Vapnik 1995, 1998), is one of the most robust and accurate data mining algorithms, mainly including support vector machine classification (SVC) and support vector machine regression (SVR). It is very flexible to solve all kinds of nonlinear classification regression problems (Wu & Kumar 2013). In this paper, SVR has been used to build the PM2.5 concentration prediction model for satisfying results.

In the SVR model, the training data is set as

{ (x_i, y_i) | i = 1, 2, ..., n }, where x_i ∈ Rⁿ is the input variable and y_i is the corresponding dependent variable. To learn a g(x) close to y, the SVR linear regression model can be as follows:

$$g(x) = w^T \cdot x_i + b \quad \dots(1)$$

where w, b are the pending parameters. To obtain larger intervals and smaller amounts of noise data, relaxation variables

ξ_i and ξ̂_i are further introduced, and the SVR regression problem can be expressed as follows:

$$\min \frac{1}{2} \|\omega\|^2 + C \sum_{i=1}^n (\xi_i + \hat{\xi}_i) \quad \dots(2)$$

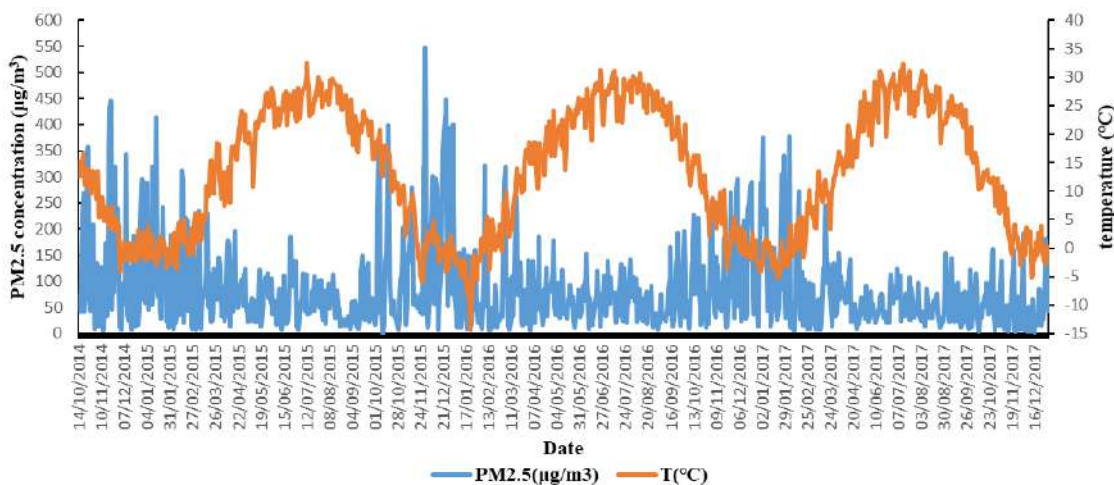


Fig. 2: The PM2.5 concentration and temperature of Yizhuang from October 14, 2014, to December 31, 2017.

$$\begin{aligned} \text{s.t } & \mathbf{g}(x_i) - y_i \leq \epsilon + \xi_i, \\ & y_i - \mathbf{g}(x_i) \leq \epsilon + \hat{\xi}_i, \end{aligned}$$

$$\xi_i \geq 0, \hat{\xi}_i \geq 0, i = 1, 2, \dots, n.$$

where parameter C is the penalty factor to solve the optimization problem, where $\alpha_i, \mu_i \in R$ are Lagrange multiplier.

Meanwhile, $\alpha, \hat{\alpha}, \mu, \hat{\mu} \in R$ are introduced to build the Lagrange function as follows:

$$\begin{aligned} L(\omega, \mathbf{b}, \alpha, \hat{\alpha}, \xi, \hat{\xi}, \mu, \hat{\mu}) &= \frac{1}{2} \|\omega\|^2 + C \\ & \sum_{i=1}^n (\xi_i + \hat{\xi}_i) - \sum_{i=1}^n \mu_i \xi_i - \sum_{i=1}^n \hat{\mu}_i \hat{\xi}_i + \\ & \sum_{i=1}^n \alpha_i (\mathbf{g}(x_i) - y_i - \epsilon - \xi_i) + \sum_{i=1}^n \\ & \hat{\alpha}_i (y_i - \mathbf{g}(x_i) - \epsilon - \hat{\xi}_i) \end{aligned} \quad \dots(3)$$

In Eq. (3), by fixing $\alpha, \hat{\alpha}, \mu, \hat{\mu}$, calculating derivation of $\omega, \mathbf{b}, \xi, \hat{\xi}$ and setting the results as 0, the following Eqs. are obtained:

$$\begin{aligned} \omega &= \sum_{i=1}^n (\hat{\alpha}_i - \alpha_i) x_i, \quad \dots(4) \\ 0 &= \sum_{i=1}^n (\hat{\alpha}_i - \alpha_i), \\ C &= \alpha_i + \mu_i, \\ C &= \hat{\alpha}_i + \hat{\mu}_i. \end{aligned}$$

Putting the four Eqs. (4) into Eq. (3), and adding Karush-Kuhn-Tucker conditions to the obtained duality problem, Eq. (5) is achieved as follows:

$$\begin{aligned} \max \sum_{i=1}^n y_i (\hat{\alpha}_i - \alpha_i) - \epsilon (\hat{\alpha}_i + \alpha_i) - \frac{1}{2} \sum_{i=1}^n \\ \sum_{j=1}^n (\hat{\alpha}_i - \alpha_i) (\hat{\alpha}_j - \alpha_j) \langle x_i, x_j \rangle \end{aligned} \quad \dots(5)$$

$$\text{s.t } \sum_{i=1}^n (\hat{\alpha}_i - \alpha_i) = 0,$$

$$0 \leq \alpha_i, \hat{\alpha}_i \leq C.$$

$$\text{KKT: } \alpha_i (\mathbf{g}(x_i) - y_i - \epsilon - \xi_i) = 0,$$

$$\hat{\alpha}_i (y_i - \mathbf{g}(x_i) - \epsilon - \hat{\xi}_i) = 0,$$

$$\alpha_i \hat{\alpha}_i = 0, \xi_i \hat{\xi}_i = 0$$

$$(C - \alpha_i) \xi_i = 0, (C - \hat{\alpha}_i) \hat{\xi}_i = 0.$$

To efficiently solve the above optimization problem, the SMO algorithm is used. After determining the optimal Lagrange multiplier, the values of ω and b can be obtained. Accordingly, the final SVM regression modal can be defined as follows:

$$\begin{aligned} \mathbf{g}(x) &= \sum_{i=1}^n (\hat{\alpha}_i - \alpha_i) \langle \Phi(x_i), \Phi(x) \rangle + b \\ &= \sum_{i=1}^n (\hat{\alpha}_i - \alpha_i) k(x_i, x) + b \end{aligned} \quad \dots(6)$$

where $\Phi(x)$ is the nonlinear mapping function that maps the data into a linear feature space with a higher dimension. The kernel function $k(x_i, x)$ satisfying Mercer's condition can be used instead of the mapping function to solve the complex dimensions and computing problems. In this paper, the radial basis function is used as the kernel function (Eq. (7)):

$$k(x_i, x) = \exp\left(-\frac{|x - x_i|^2}{2\sigma^2}\right) \quad \dots(7)$$

where σ^2 is the width of the kernel parameter.

SVR Optimized by the Cuckoo Search Algorithm

In the SVR nonlinear prediction model with radial basis function as kernel function, the penalty C and the width σ^2 are the parameters. In this paper, the cuckoo search (CS) algorithm is introduced to optimize these two parameters to improve the efficiency and accuracy of prediction.

Yang & Deb (2009) presented the Cuckoo search natural heuristic method, which mimics cuckoo brood parasitism behavior. The algorithm can be enhanced by Levy flight rather than a simple isotropic random walk. The CS algorithm combines global search and local search which are controlled by discovery probability (P_d). This makes it possible to explore the search space more efficiently in the global scope, achieving global optimum with a higher probability. Although the PSO algorithm may converge to local optimization prematurely, it is not necessarily the global optimal solution. While CS can usually converge to global optimization.

In the D dimensional space, the population of the nest is n, $X_{Nestpop} = [X_1, X_2, \dots, X_n]^T$, and each nest is the solution to the problem. In each nest, there is a D dimension vector $\{X_i = [X_{i1}, X_{i2}, \dots, X_{iD}]^T | i = 1, 2, \dots, n\}$.

After the nest population is formed randomly, CS updates the individual through two paths:

i) the cuckoo uses Levy flight-based Eq (8) to find the nest and lay an egg.

$$X_{t+1} = X_t + \alpha S = X_t + \alpha \otimes Levy(\beta) \quad \dots(8)$$

$$Levy(\beta) \sim \mu = t^{-\beta}, 1 \leq \beta \leq 3 \quad \dots(9)$$

In combined Eq. (8) and Eq. (9), S is the random step size obeying Levy distribution.

$$S = \frac{U}{|V|^{\frac{1}{\beta}}}, (U \sim N(0, \sigma^2), V \sim N(0, 1)) \quad \dots(10)$$

$$\sigma = \left\{ \frac{\Gamma(1+\beta) * \sin(\frac{\pi\beta}{2})}{\beta * \Gamma(\frac{1+\beta}{2}) * 2^{\frac{\beta-1}{2}}} \right\}^{\frac{1}{\beta}} \quad \dots(11)$$

where α is the scaling factor of step size, which is to 0.01, and β is set to 1.5.

ii) the host uses random walk to rebuild its nest after finding the alien egg with the probability of P_a (Eq. (12)).

$$X_{t+1} = X_t + \gamma \otimes Heaviside(P_a - \epsilon) \otimes (X_i - X_j) \quad \dots(12)$$

where $P_a = 0.25$ is recommended. γ, ϵ are random numbers subject to a uniform distribution. $Heaviside(P_a - \epsilon)$ is the Heaviside step function. When $P_a > \epsilon$, $Heaviside(P_a - \epsilon) = 1$, when $P_a < \epsilon$ $Heaviside(P_a - \epsilon) = 0$, when $P_a = \epsilon$ $Heaviside(P_a - \epsilon) = 0.5$ X_i, X_j are any other nests.

The flow chart of SVR prediction optimized by the CS algorithm (CS-SVR) is shown in Fig. 3.

Evaluation index for prediction results: To investigate the accuracy of different PM2.5 concentration prediction models, four evaluation indexes are applied, including person correlation coefficient (R), root mean squared error (RMSE), mean absolute error (MAE), and mean absolute percentage

error (MAPE). R can release the relevance between the observed value and the predicted value (Eq. (12)). Mean squared error (MSE) is the expected value of the square of the difference between the predicted value and the observed value. Correspondingly, RMSE is the square root of MSE which is more intuitive in order of magnitude (Eq. (13)). And the smaller the RMSE value, the better the accuracy of the prediction model. MAE represents the mean of the absolute error between the predicted value and the observed value, which can better reflect the actual predicted error (Eq. (14)). MAPE is used to better evaluate different models with the same set of data (Eq. (15)).

$$R = \frac{cov(observed, predicted)}{\sigma_{observed} \sigma_{predicted}} \quad \dots(12)$$

$$RMSE = \sqrt{\frac{1}{N} \sum_{t=1}^N (observed_t - predicted_t)^2} \quad \dots(13)$$

$$MAE = \frac{1}{N} \sum_{t=1}^N |observed_t - predicted_t| \quad \dots(14)$$

$$MAPE = \frac{1}{N} \sum_{t=1}^N \left| \frac{observed_t - predicted_t}{observed_t} \right| \times 100\% \quad \dots(15)$$

RESULTS AND DISCUSSION

The Results of Extracting Pollutant Variables for Pattern Calculation

The atmospheric environment affecting PM2.5 concentration consists of pollutant factors and meteorological factors. We

Table 2: Correlation coefficient (R) between the PM2.5 concentration and 6 pollutant variables, 5 meteorological variables.

	PM2.5	PM10	SO ₂	NO ₂	O ₃	CO	P	RH	T	WS	WD	CP
PM2.5	1	-	-	-	-	-	-	-	-	-	-	-
PM10	.913**	1	-	-	-	-	-	-	-	-	-	-
SO ₂	.575**	.541**	1	-	-	-	-	-	-	-	-	-
NO ₂	.785**	.745**	.574**	1	-	-	-	-	-	-	-	-
O ₃	-.296**	-.245**	-.373**	-.523**	1	-	-	-	-	-	-	-
CO	.832**	.755**	.574**	.782**	-.434**	1	-	-	-	-	-	-
P	.086**	.040	.324**	.226**	-.671**	.233**	1	-	-	-	-	-
RH	.406**	.279**	-.126**	.262**	-.049	.374**	-.271**	1	-	-	-	-
T	-.245**	-.202**	-.486**	-.351**	.758**	-.381**	-.880**	.269**	1	-	-	-
WS	-.362**	-.300**	-.251**	-.515**	.286**	-.376**	-.049	-.379**	.057	1	-	-
WD	.275**	.241**	.159**	.275**	-.038	.276**	-.081**	.353**	.077**	-.264**	1	-
CP	.009	.004	-.072*	-.004	.070*	.021	-.125**	.128**	.136**	.006	.067*	1

Note: **p-value ≤ 0.01, *p-value ≤ 0.05

Table 3: The total variance explained of 6 pollutant variables and 6 meteorological variables.

Component	Initial Eigenvalues			Extraction Sums of Squared Loadings		
	Total	% of Variance	Cumulative %	Total	% of Variance	Cumulative %
1	4.847	40.388	40.388	4.847	40.388	40.388
2	2.517	20.975	61.362	2.517	20.975	61.362
3	1.105	9.212	70.574	1.105	9.212	70.574

Table 4: The rotated component matrix of pollutant variables of the 12 variables calculation, indicating their interpretive competence to each principal component.

pollutant variables and meteorological variables	Component		
	1	2	3
PM2.5	0.929	-0.050	0.223
PM10	0.928	0.015	0.116
SO ₂	0.728	-0.321	-0.189
NO ₂	0.799	-0.304	0.291
O ₃	-0.232	0.863	-0.159
CO	0.831	-0.249	0.265

examined their relationship with PM2.5 concentrations. The correlation coefficient (R) between the 11 variables (from 14th October 2014 to 31st December 2017) and PM2.5 concentrations is shown in Table 2. The R values between pollutant factors and PM2.5 concentrations are mostly higher than 0.5, but the R values in the meteorological parts are between 0.1 and 0.4. These results indicate that pollutant factors have a greater impact on the PM2.5 concentrations. Therefore, we decided to extract pollutant patterns to improve the prediction accuracy. The PCA-clustering method was employed for extracting needed variables.

In the beginning, all the 12 atmospheric environment variables including 6 pollutant components (PM2.5, PM10, SO₂, NO₂, O₃, CO) and 6 meteorology factors (P, RH, T, WS, WD, CP) were examined by PCA methods, and the results are shown in Tables 3 and 4. In our previous work, we have confirmed that relative humidity (RH), temperature (T), and wind speed (WS) have a more significant impact on the concentration level of PM2.5 (Liu et al. 2019). As a result,

the PCA method was used to construct an examination using nine variables (PM2.5, PM10, SO₂, NO₂, O₃, CO, RH, T, and WS) (Tables 5 and 6). As shown in Table 3 and Fig. 4, the first three principal components can explain the degree of data variation as 70.57%, with the first one accounting for 40.39%. However, for the 9 variables calculation, the first three principal components can explain 82.017%, and the first one accounts for 51.321% (Table 5 and Fig. 4). Therefore, 3 meteorological variables (RH, T, WS) will be introduced for predicting PM2.5 concentrations in the next part.

The rotated component matrix in Table 4 shows the interpretive competency of pollutant variables to each primary component in the 12 variables (6 pollutant and 6 meteorology variables) computation. PM2.5, PM10, SO₂, NO₂, and CO all strongly explain the first principal component, however, O₃ is shifted to the second principal component. The same pattern may be seen in the findings of the 9 variable calculation (6 pollutant and 3 meteorology variables) and the results as shown in Table 6. PM10, SO₂, NO₂, and CO are used in the

Table 5: The total variance explained of 6 pollutant variables and 3 meteorological variables.

Component	Initial Eigenvalues			Extraction Sums of Squared Loadings		
	Total	% of Variance	Cumulative %	total	% of Variance	Cumulative %
1	4.619	51.321	51.321	4.619	51.321	51.321
2	1.749	19.429	70.750	1.749	19.429	70.750
3	1.014	11.267	82.017	1.014	11.267	82.017

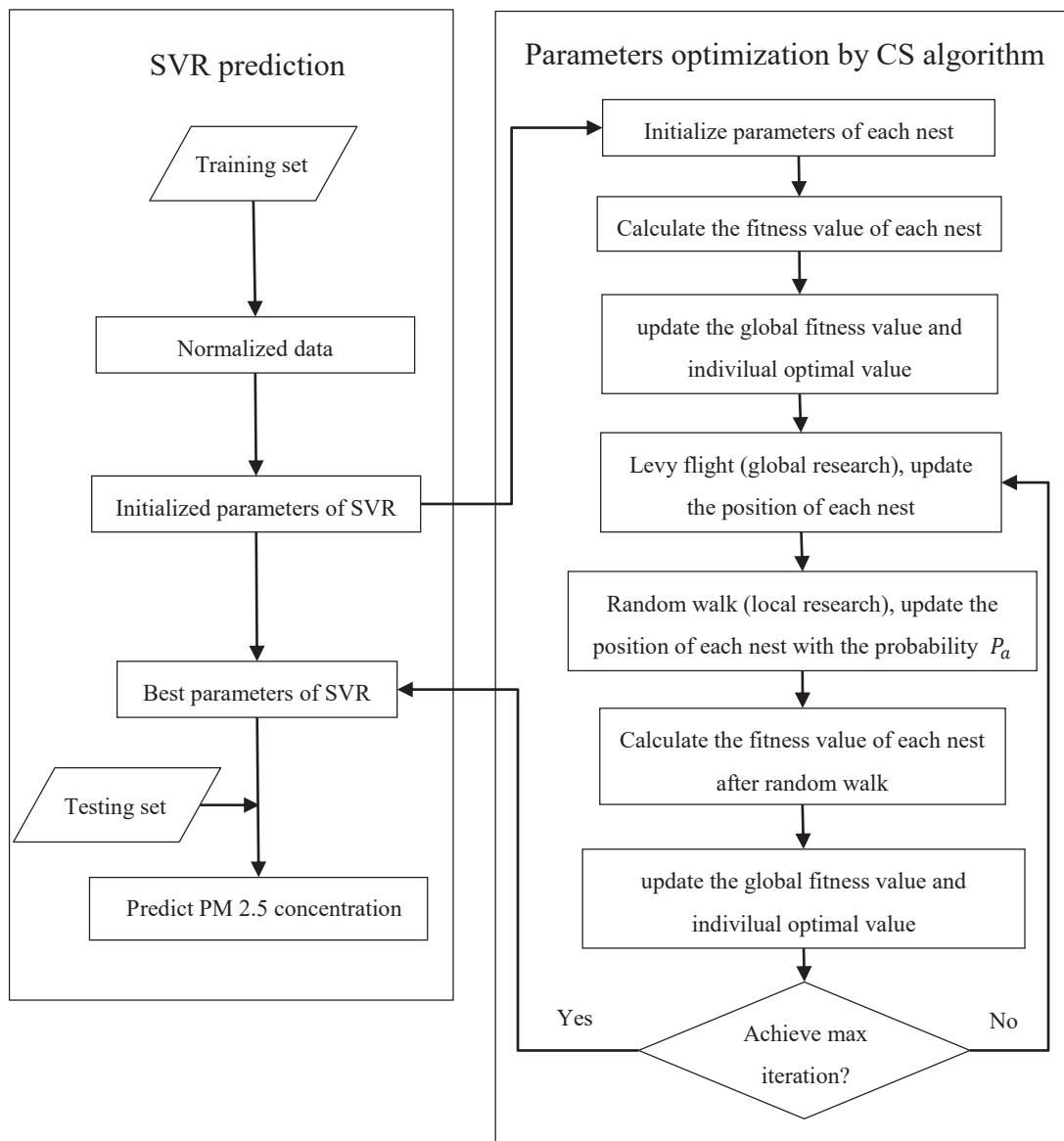


Fig. 3: The flow chart of CS algorithm optimized SVR prediction (CS-SVR).

extraction of pollutant patterns, which will be generated using the clustering approach and used as a key input factor for the subsequent prediction model, based on the study above.

The Results of PM_{2.5} Concentration Prediction by CS-SVR Model

All cold day data from October to the following March 2014-2017 was used as a training set, while the data from November and December 2017 was used as a testing set for PM_{2.5} concentration prediction. The population of the nest

is set to 20 in the CS optimization procedure. The discovery probability $P_a = 0.25$ is recommended. Penalty C and the width σ^2 as parameters to be optimized are set to [0.01, 100]. In the optimization process, 100 iterations have been carried out.

First, three prediction models including CS-SVR, multivariate nonlinear regression (MNR), and artificial neural network (ANN) have been studied using 11 variables. As shown in Fig. 5, the absolute value of relative errors of CS-SVR is much better than those of MNR and ANN. The

prediction accuracy of different models was further compared using four evaluation indexes such as R, MAE, RMSE, and MAPE (Table 7). The R values between the predicted and observed PM_{2.5} concentration by CS-SVR (0.9430) are higher than ANN (0.9342) and MNR (0.9326). Meanwhile, the MAE, RMSE, and MAPE indicators of CS-SVR decreased by 30.10%, 10.22%, 70.87% than MNR, and by 13.88%, 3.4451%, 51.48% than ANN, respectively. All of these findings indicate that the CS-SVR model outperforms

the MNR and ANN models in predicting PM_{2.5} concentrations. In addition, different optimization methods for SVR were also investigated (Table 7). All the four indexes (R, MAE, RMSE, and MAPE) of CS-SVR are better than those of CV-SVR and POS-SVR.

In addition, eight factors were used in the CS-SVR prediction model. CS-SVR still outperforms ANN and MNR in terms of prediction performance, as demonstrated in Fig. 6 and Table 8, despite the greater R-value and smaller MAE,

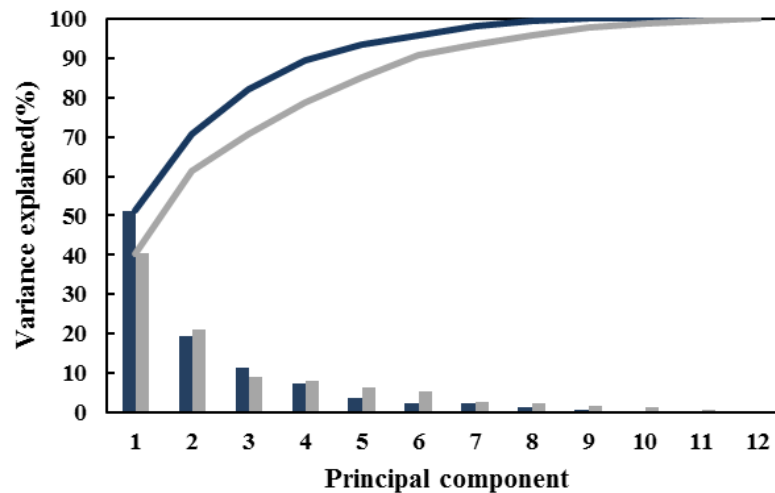


Fig. 4: The scree plots of 11 variables (gray) vs. 9 variables (black).

Table 6: The rotated component matrix of pollutant variables of the 9 variables calculation, indicating their interpretive competence to each principal component.

pollutant variables and meteorological variables	Component		
	1	2	3
PM _{2.5}	0.924	-0.067	0.271
PM ₁₀	0.927	-0.016	0.157
SO ₂	0.710	-0.407	-0.195
NO ₂	0.758	-0.363	0.342
O ₃	-0.166	0.896	-0.228
CO	0.817	-0.262	0.303

Table 7: The evaluation index results of CS-SVR, CV-SVR, POS-SVR, ANN, and MNR models using 11 pollutant and meteorological variables.

Models	Index			
	R	MAE	RMSE	MAPE
CS-SVR	0.9430	11.5785	18.2506	0.3141
CV-SVR	0.9341	13.2025	19.6715	0.5225
POS-SVR	0.9423	11.6407	18.7494	0.3158
ANN	0.9342	13.4451	18.9453	0.6480
MNR	0.9326	16.5625	20.3276	1.0794

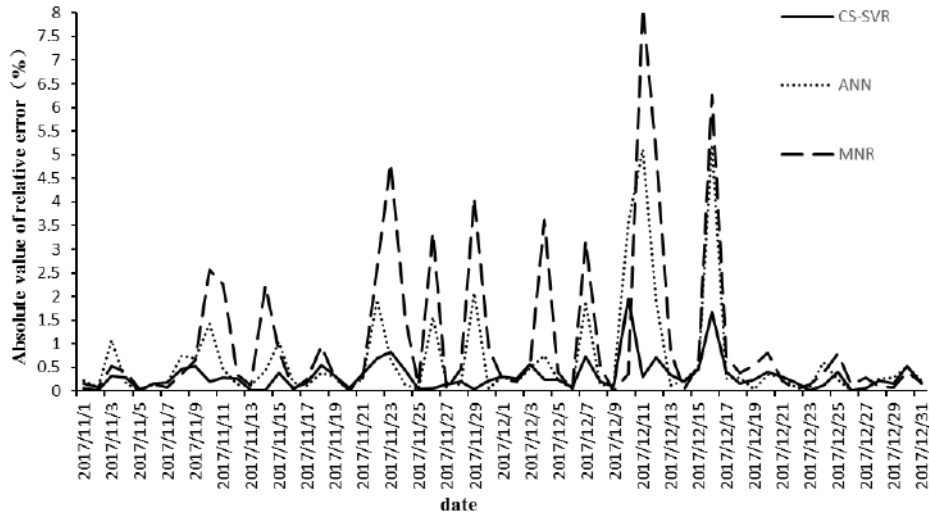


Fig. 5: The absolute value of the relative error of different prediction models using 11 pollutant and meteorological variables (PM10, SO₂, NO₂, O₃, CO and P, RH, T, WS, WD, CP).

RMSE, and MAPE indicators. Therefore, from the above two groups of comparative experiments, the prediction accuracy of the CS-SVR model is better than the other two models in terms of each index.

Interestingly, although using fewer variables, the 8 variables CS-SVR prediction shows acceptable prediction accuracy. However, the R-value of the 8 variables CS-SVR prediction is a little bit lower than the 11 variables one (0.9388 vs 0.9430). To further improve the prediction accuracy of the 8 variables CS-SVR model, we used the PCA-clustering method to extract the pollutant pattern as an additional variable for PM_{2.5} concentration prediction. The obtained

prediction results taking into account the pollutant pattern variable are shown in Table 9. It is quite clear that when the pollutant pattern variable is involved in the calculation, the prediction accuracy of all models improved. Especially, for the CS-SVR model, when the pollutant data was divided into three patterns ($k = 3$) by k-meaning clustering, the best prediction accuracy was achieved. The R-value increased to 0.9455, while the MAE, RMSE, and MAPE values decreased to 11.2523, 16.7114, and 0.3006, respectively, the lowest values of all models. As a result, the PCA-clustering extracted pollutant pattern-based CS-SVR model predicts PM_{2.5} concentrations the best.

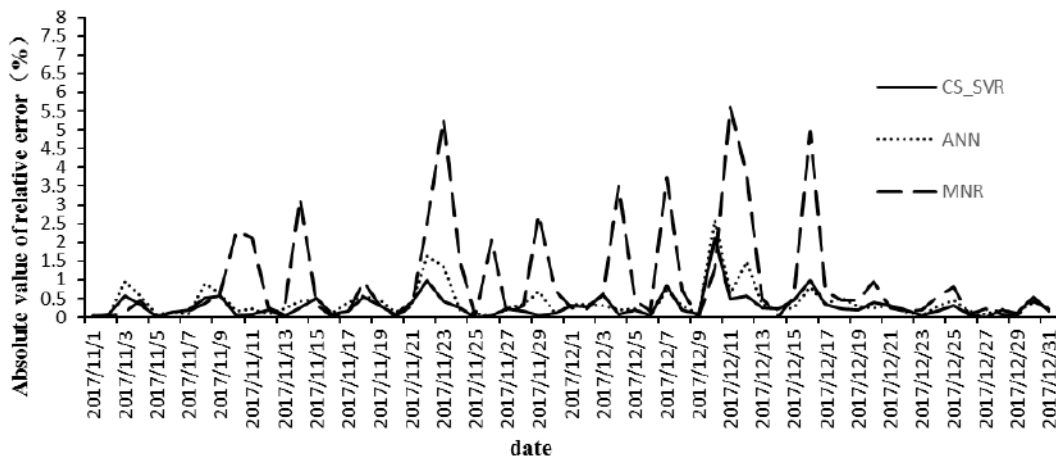


Fig. 6: The absolute value of the relative error of different prediction models using 8 pollutant and meteorological variables (PM10, SO₂, NO₂, O₃, CO and RH, T, WS).

Table 8: The evaluation index results of CS-SVR, ANN, and MNR models using 8 pollutant and meteorological variables.

Models	Index			
	R	MAE	RMSE	MAPE
CS-SVR	0.9388	11.4269	18.6665	0.3008
ANN	0.9316	12.7832	19.2167	0.4021
MNR	0.9367	15.7408	19.8749	0.9721

Table 9: The evaluation index results of CS-SVR, CV-SVR, PSO-SVR, ANN, and MNR models using 5 pollutant variables, 3 meteorological variables, and 1 pollutant pattern variable.

Models	k	Index			
		R	MAE	RMSE	MAPE
CS-SVR	1	0.9388	11.4269	18.6665	0.3008
	2	0.9378	12.0629	18.9555	0.3207
	3	0.9455	11.2523	16.7114	0.3006
	4	0.9453	11.6977	16.9446	0.422
	5	0.9392	11.6424	18.6715	0.316
CV-SVR	1	0.91158	13.6238	20.8764	0.6888
	2	0.9253	12.0441	19.0600	0.4241
	3	0.9292	11.8964	18.3937	0.5254
	4	0.9366	11.9500	17.6161	0.5364
	5	0.9295	12.5774	19.1370	0.5066
PSO-SVR	1	0.9338	11.7656	18.9985	0.3722
	2	0.9345	11.7015	18.8554	0.3350
	3	0.9424	11.7059	18.8421	0.3119
	4	0.9464	11.7066	18.4610	0.3328
	5	0.9377	11.9483	19.0073	0.3990
ANN	1	0.9316	12.7832	19.2167	0.4021
	2	0.9298	13.3388	20.0169	0.3789
	3	0.9455	11.6921	17.1260	0.3241
	4	0.9480	12.5176	17.7708	0.4623
	5	0.9397	11.97	18.0200	0.5673
MNR	1	0.9367	15.7408	19.8749	0.9721
	2	0.9388	15.2120	19.3763	0.8988
	3	0.9478	14.9337	18.8504	0.8527
	4	0.9471	15.0780	18.6994	0.8325
	5	0.9383	15.7837	19.8648	0.9405

k is the number of pollutant patterns

CONCLUSION

In this work, we applied principal component analysis (PCA)-clustering-based pollutant pattern recognition and CS algorithm optimized SVR for the PM_{2.5} concentration prediction. In comparison to a prediction based on all

meteorological factors, relative humidity, air temperature, and wind speed could be chosen to provide an acceptable prediction accuracy. To further improve the prediction results, a new variable (k) of pollutant pattern was extracted by the PCA-clustering method and added to the calculation. Support vector regression outperforms multivariate nonlinear

regression and artificial neural network models, as seen by indices like RMSE, MAE, MAPE, and R. Furthermore, the cuckoo search was used to further optimize the parameters in the SVR process, which resulted in a better prediction of PM_{2.5} concentration than cross-validation and particle swarm optimization algorithms. According to these comparative studies, the best PM_{2.5} concentration prediction accuracy could be obtained by the CS-SVR model with three pollutant patterns ($k = 3$). Pollutant and meteorological data from more observation stations will be introduced in the future to further prove the reliability of our prediction model and acquire higher prediction accuracy.

ACKNOWLEDGMENTS

Research reported in this publication was supported by the National Natural Science Foundation of China (71271056).

REFERENCES

- Badaloni, C., Cesaroni, G., Cerza, F., Davoli, M., Brunekreef, B. and Forastiere, F. 2017. Effects of long-term exposure to particulate matter and metal components on mortality in the Rome longitudinal study. *Environ. Int.*, 109: 146-154.
- Beijing Municipal Ecology and Environment Bureau. 2019. Beijing Ecology and Environment Statement 2018.
- Beijing Municipal Ecology and Environment Bureau. 2018. Beijing Ecology and Environment Statement 2017.
- Biancofiore, F., Busilacchio, M., Verdecchia, M., Tomassetti, B., Aruffo, E., Bianco, S., Tommaso, S.D., Colangeli, C., Rosatelli, G. and Carlo, P.D. 2017. Recursive neural network model for analysis and forecast of PM₁₀ and PM_{2.5}. *Atmos. Pollut. Res.*, 8: 652-659.
- Di, Q., Wang, Y., Zanobetti, A., Wang, Y., Koutrakis, P., Choirat, C., Dominici, F. and Schwartz, J.D. 2017. Air pollution and mortality in the medicare population. *N. Engl. J. Med.*, 376: 2513-2522.
- Franceschi, F., Cobo, M. and Figueredo, M. 2018. Discovering relationships and forecasting PM₁₀ and PM_{2.5} concentrations in Bogotá, Colombia, using Artificial Neural Networks, Principal Component Analysis, and k-means clustering. *Atmos. Pollut. Res.*, 9: 912-922.
- Gan, K., Sun, S., Wang, S. and Wei, Y. 2018. A secondary-decomposition-entsemble learning paradigm for forecasting PM_{2.5} concentrations. *Atmos. Pollut. Res.*, 9: 989-999.
- Liang, F., Xiao, Q., Gu, D., Xu, M., Tian, L., Guo, Q., Wu, Z., Pan, X. and Liu, Y. 2018. Satellite-based short- and long-term exposure to PM_{2.5}, and adult mortality in urban Beijing, China. *Environ. Pollut.*, 242: 492-499.
- Liang, X., Zou, T., Guo, B., Li, S., Zhang, H., Huang, H. and Chen, S.X. 2015. Assessing Beijing's PM_{2.5} pollution: severity, weather impact, APEC and winter heating. *Proc. R. Soc. A.*, 471: 20150257.
- Liu, D. and Sun, K. 2019. Short-term PM_{2.5} forecasting based on CEEMD-RF in five cities of China. *Environ. Sci. Pollut. Res.*, 26: 32790-32803.
- Liu, W., Guo, G., Chen, F. and Chen, Y. 2019. Meteorological pattern analysis assisted daily PM_{2.5} grades prediction using SVM optimized by PSO algorithm. *Atmos. Pollut. Res.*, 10: 1482-1491.
- Marsha, A. and Larkin, N.K. 2019. A statistical model for predicting PM_{2.5} for the western United States. *J. Air Waste Manag. Assoc.*, 69: 1215-1229.
- Mortamais, M., Pujol, J., Martínez-Vilavella, G., Fenoll, R., Reynes, C., Sabatier, R., Rivas, I., Forns, J., Vilor-Tejedor, N., Alemany, S., Cirach, M., Alvarez-Pedrerol, M., Nieuwenhuijsen and M., Sunyer, J. 2019. Effects of prenatal exposure to particulate matter air pollution on corpus callosum and behavioral problems in children. *Environ. Res.*, 178: 108734.
- Ostro, B., Chestnut, L., Vichit-Vadakan, N. and Laixuthai, A. 1999. The impact of particulate matter on daily mortality in Bangkok, Thailand. *J. Air & Waste Manag. Assoc.*, 49: 100-107.
- State Bureau of Environment Protection of China. 2012. Ambient air quality standards. (GB3095-2-12).
- Suades-González, E., Gascon, M., Guxens, M. and Sunyer, J. 2015. Air pollution and neuropsychological development: A review of the latest evidence. *Endocrinology*, 156: 3473-3482.
- Sun, W. and Sun, J. 2016. Daily PM_{2.5} concentration prediction based on principal component analysis and LSSVM optimized by the cuckoo search algorithm. *J. Environ. Manag.*, 188: 144-152.
- Sun, W., Zhang, H., Palazoglu, A., Singh, A., Zhang, W. and Liu, S. 2013. Prediction of 24-hour-average PM_{2.5} concentrations using a hidden Markov model with different emission distributions in Northern California. *Sci. Total. Environ.*, 443: 93-103.
- Thomaidis, N.S., Bakeas, E.B. and Siskos, P.A. 2003. Characterization of lead, cadmium, arsenic, and nickel in PM_{2.5} particles in the Athens atmosphere, Greece. *Chemosphere*. 52: 959-66.
- Vapnik, V. (ed.). 1995. *The Nature of Statistical Learning Theory*. Springer, New York.
- Vapnik, V. (ed.). 1998. *Statistical Learning Theory*. Springer, New York.
- Wang, L., Zhang, N., Liu, Z., Sun, Y., Ji D. and Wang, Y. 2015. The influence of climate factors, meteorological conditions, and boundary-layer structure on severe haze pollution in the Beijing-Tianjin-Hebei region during January 2013. *Adv. Meteorol.*, 2014: 1-14.
- Wu, X. and Kumar, V. (ed.) 2013. *The top ten algorithms in data mining*. CRC Press, Boca Raton, Florida, USA.
- Yang, X.S. and Deb, S., 2009. Cuckoo Search via Lévy Flights. *World Congress on Nature & Biologically Inspired Computing IEEE*, 9-11 December 2009, Coimbatore, India, IEEE, Piscataway, NJ, pp. 1-7.
- Yuan, Y., Wu, Y., Ge, X., Nie, D., Wang, M., Zhou, H. and Chen, M. 2019. In vitro toxicity evaluation of heavy metals in urban air particulate matter on human lung epithelial cells. *Sci. Total. Environ.*, 678: 301-308.



Influence of Dissolved Organic Carbon on the Adsorption and Desorption of Cadmium in Reclaimed Soil

Yonghong Zheng*, Zhiguo Zhang*†, Yongchun Chen*, Shikai An*, Lei Zhang***, Fangling Chen***, Chengnan Ma*** and Weiqing Cai***

*Huainan Mining (Group) Co. Ltd., Huainan 232001, China

**National Engineering Laboratory for Protection of Colliery Eco-environment, Huainan 232001, China

***School of Earth and Environment, Anhui University of Science and Technology, Huainan 232001, China

†Corresponding author: Zhiguo Zhang; zzgust@qq.com

Nat. Env. & Poll. Tech.
Website: www.neptjournal.com

Received: 20-05-2021

Revised: 07-07-2021

Accepted: 19-07-2021

Key Words:

Cadmium

Citric acid

Dissolved organic carbon

Humic acid

Reclaimed soil

ABSTRACT

Organic acids are widespread in the environment and play an important role in the adsorption, desorption, and migration of soil cadmium (Cd). Under the effect of humic acid (HA) and citric acid, the properties and mechanism of Cd adsorption and desorption in reclaimed soil from the Panyi Mine in the Huainan mining area were investigated (CA). The addition of HA and CA inhibited the adsorption and enhanced the desorption of Cd in reclaimed soil, with HA having a stronger effect than CA. As the concentration of added HA or CA increased, the adsorption capacity of Cd in the reclaimed soil gradually decreased, while the desorption capacity gradually increased. That is, the adsorption inhibition/desorption promotion effect was stronger for higher concentrations of organic acid. Cd adsorption and desorption could be described as a logarithmic function of organic acid concentration. The kinetic curves of Cd adsorption and desorption in reclaimed soil under the influence of organic acids show that both adsorption and desorption involved two stages: a fast reaction stage followed by a slow reaction stage.

INTRODUCTION

Coal mining has been going on in the Huainan mining area for over a century. Significant-scale coal mining has resulted in large amounts of solid waste and coal gangue, as well as land subsidence, with the subsidence area expanding. Since 2003, in the Huainan mining area, coal gangue filling and soil covering techniques have been employed to backfill subsided terrain with coal gangue to the original surface height, allowing the area to be reused (Bian 2001). However, reclamation activities have affected the soil quality in the mining area to a certain extent. The soil is easily compacted, has a low nutrient content and large volume, and is potentially contaminated by heavy metals. In particular, the content of the heavy metal cadmium (Cd) has exceeded the agricultural land filter value for soil pollution risk (Yao et al. 2010, Zhang et al. 2010, Zhao et al. 2020, He 2019, Jiang et al. 2020, Zhang et al. 2019, Li et al. 2008, Xie et al. 2020).

Dissolved organic carbon (DOC) refers to organic carbohydrates with relatively low molecular weights and simple structures. DOC can be dissolved in water and pass through a 0.45- μ m microporous membrane. DOC is the most active component of soil organic carbon and the main carrier of many trace organic and inorganic pollutants (Kalbitz et al.

2000, Yang et al. 2020, Li et al. 2003, Ye 2020, Wang et al. 2020, Liu 2019a, Huang et al. 2015). DOC reacts directly with metal ions in water, soil, and sediment through a series of reactions such as ion exchange, adsorption, complexation, chelation, flocculation, and precipitation, thereby affecting the adsorption and desorption behaviors of heavy metals in soil (Yang & Zeng 2007, Wang 2016, Li 2017). Therefore, changes in the content of DOC inevitably lead to changes in the contents of heavy metals in soil. Studies have shown that DOC in soil affects the adsorption and improves the mobility of heavy metals in the soil (Jagadamma et al. 2014). Mahara et al (2007) reported that low-molecular-weight DOC in soil strongly affects the migration and transformation of Cd in the environment. Zhang (2020) found a strong correlation between dissolved heavy metals in the natural environment and the concentration of DOC. Liu (2019b) reported that DOC easily adsorbs and binds Cd in the soil. Adding DOC to the soil can increase the content of soil-exchanged Cd, and correlation analysis revealed a significant positive correlation between soil-exchanged Cd and soil DOC.

Previous research on soil DOC in China and elsewhere mainly focuses on the distribution and composition of DOC in soil, vegetation coverage and soil fertilization, and the adsorption, desorption, complexation, dissociation, precipitation, and

dissolution of soil heavy metal ions in the presence of DOC. However, the basic chemical equilibria along with the corresponding mechanisms, laws, and kinetic processes associated with the interactions between soil DOC and heavy metals have received less research attention. In this study, reclaimed soil in the subsidence area of Panyi Mine was chosen as the research object. Humic acid (HA) with the largest content of soluble humus was selected as a representative DOC molecule. The citric acid (CA), a small-molecule organic acid, served as a control. These two organic acids were used to prepare DOC solutions with different concentrations, which were used to determine the effects of DOC on the characteristics and kinetics of Cd adsorption and desorption in reclaimed soil. The results provide fundamental data for evaluating the Cd pollution status of reclaimed soil along with a scientific method for risk assessment and prediction. The findings also provide guidance for the rational application of organic materials.

MATERIALS AND METHODS

Study Area

The Panyi Mine Reclamation Area is located approximately 1.0 km east of the Panyi Mine, Panji District, Huainan City. A coal gangue hill is located on the southern side of the reclamation area. The reclamation area is formed by filling and rolling coal gangue in the coal mining subsidence area. The coal gangue is covered by clay with a design thickness of 100 cm. Tree species including poplar, privet, metasequoia, cedar, and Sichuan juniper were planted in the subsidence area after treatment. This area lies in a warm temperate semi-humid continental monsoon climate zone. The average annual temperature is 15.3°C, the highest temperature occurs in July, and the lowest occurs in January. The average annual precipitation is 926 mm.

Sample Collection and Pretreatment

Three sampling lines were established in the Panyi Mine Reclamation Area. A sampling point was located every 5 m on each sampling line, resulting in a total of 60 sampling points. At each sampling point, a soil heavy metal sampler was used to collect 0–20 cm of reclaimed soil. Each sample had a mass of at least 1 kg. After removing impurities, the soil sample was crushed and spread flat on an air-dried soil dish to dry. The sample was sieved using the quarter method, ground with an agate mortar, passed through a 100-mesh nylon screen, packed in a Ziploc bag, and labeled for use. Its physico-chemical properties were shown in Table 1.

Experimental Methods

As mentioned above, HA was selected as a representative DOC molecule, and CA served as a control. These two

organic acids were used to prepare DOC solutions with different concentrations.

Adsorption of Cd in reclaimed soil under the influence of DOC: A reclaimed soil sample (1.000 g, passed through an 18-mesh screen) was weighed and placed in a 50-mL centrifuge tube. Twenty milliliters of Cd(NO₃)₂ solution with a Cd concentration of 0, 0.2, 0.4, 0.6, 0.8, 1, 1.5, 2, 2.5, 3, 4, 5, 8, 10, 15, 20, 25, 30, 35, 40, 45, 50, 55, 60, 65, 70, 75, or 80 mg.L⁻¹ was added to the centrifuge tube followed by the addition of 1 mL of HA or CA solution with a concentration of 10 mg.L⁻¹. The centrifuge tube was then capped, shaken at 200 r.min⁻¹ at a constant temperature of 25°C for 24 h, and then centrifuged at 4000 r.min⁻¹ for 20 min. Finally, the supernatant was filtered through a 0.45-μm filter membrane, and one drop of 1% nitric acid was added to the filtrate followed by shaking for Cd determination. The concentration of Cd was analyzed by AAS (PerkinElmer AA800). The Cd adsorption capacity (Q_a , in mg.kg⁻¹) was determined based on the difference between the concentrations of Cd before and after adsorption:

$$Q_a = \frac{C_0 - C \times V}{m}, \quad \dots(1)$$

where C_0 is the concentration of Cd in the initial solution (mg.L⁻¹); C is the concentration of Cd in the equilibrium solution at adsorption equilibrium (mg.L⁻¹); V is the initial volume of liquid added (mL), and m is the mass of the sample (g). A control experiment was simultaneously carried out with 60 mg.L⁻¹ HA and CA solution.

Desorption of Cd from reclaimed soil under the influence of DOC: The desorption experiment was carried out after the adsorption experiment was completed. The reclaimed soil after Cd adsorption was washed once with absolute ethanol to remove free Cd and placed at a constant temperature of 25°C for 1 h. Next, 20 mL of NaNO₃ solution (0.01 mol.L⁻¹) was added to the soil followed by covering and shaking at 200 r.min⁻¹ and 25°C for 24 h. The solution was then centrifuged at 4000 r.min⁻¹ for 20 min. Finally, the supernatant was filtered through a 0.45-μm filter membrane, and one drop of 1% nitric acid was added to the filtrate followed by shaking for Cd determination. The concentration of Cd was

Table 1: The physico-chemical properties of the soil.

Parameters	Values
PH	7.92±0.36
Organic matter (%)	1.06±1.08
Total N (%)	0.22±0.11
Available K (mg.kg ⁻¹)	127.28±16.26
Cd concentration (mg.kg ⁻¹)	0.80±0.22

analyzed by AAS (PerkinElmer AA800). The Cd desorption capacity (Q_d) was determined as

$$Q_d = \frac{c \times V}{m} \quad \dots(2)$$

The Cd desorption rate (W) was calculated as

$$W (\%) = \frac{Q_d}{Q_a} \times 100\% \quad \dots(3)$$

Data Analysis

The experimental data were statistically analyzed using SPSS 24.0 software. Plots were created using Origin8.0 software.

RESULTS AND DISCUSSION

Characteristics and Mechanism of Isothermal Cd Adsorption Under the Influence of HA and CA

As shown in Fig. 1, the two organic acids had different effects on Cd adsorption. As the concentration of Cd in the equilibrium solution increased, the adsorption capacity of reclaimed soil for Cd gradually increased. When the Cd concentration was low ($0.2\text{--}10 \text{ mg.L}^{-1}$), the amount of adsorbed Cd was

similar in the presence and absence of HA and CA. Thus, under low Cd concentrations, HA and CA had little effect on the ability of reclaimed soil to adsorb Cd. In contrast, when the Cd concentration was $15\text{--}80 \text{ mg.L}^{-1}$, the presence of HA and CA significantly reduced the adsorption of Cd by the reclaimed soil, and the amount of adsorbed Cd decreased as the concentration of added Cd increased. Thus, the addition of HA and CA significantly inhibited the adsorption of Cd by reclaimed soil. HA had a stronger inhibitory effect than CA, and the high organic acid concentration (60 mg.L^{-1}) produced a stronger effect than the low concentration (10 mg.L^{-1}). Different DOC components have been demonstrated to affect the migration of organic and inorganic contaminants in the soil in studies (Li et al. 2003, Zsolnay 1996, Gao et al. 2011, Lei et al. 2015, Bhattacharya & Osburn 2020). HA and CA contain a variety of active groups. In particular, HA contains abundant benzene rings, carboxyl groups, alcoholic hydroxyl groups, phenolic hydroxyl groups, and amino groups, which can undergo exchange, adsorption, and chelation reactions with heavy metals (Ma et al. 2020, Shan et al. 2015, Xu et al. 2008, Huang 2020). These sites compete with recovered soil for Cd adsorption, limiting the soil's ability to adsorb

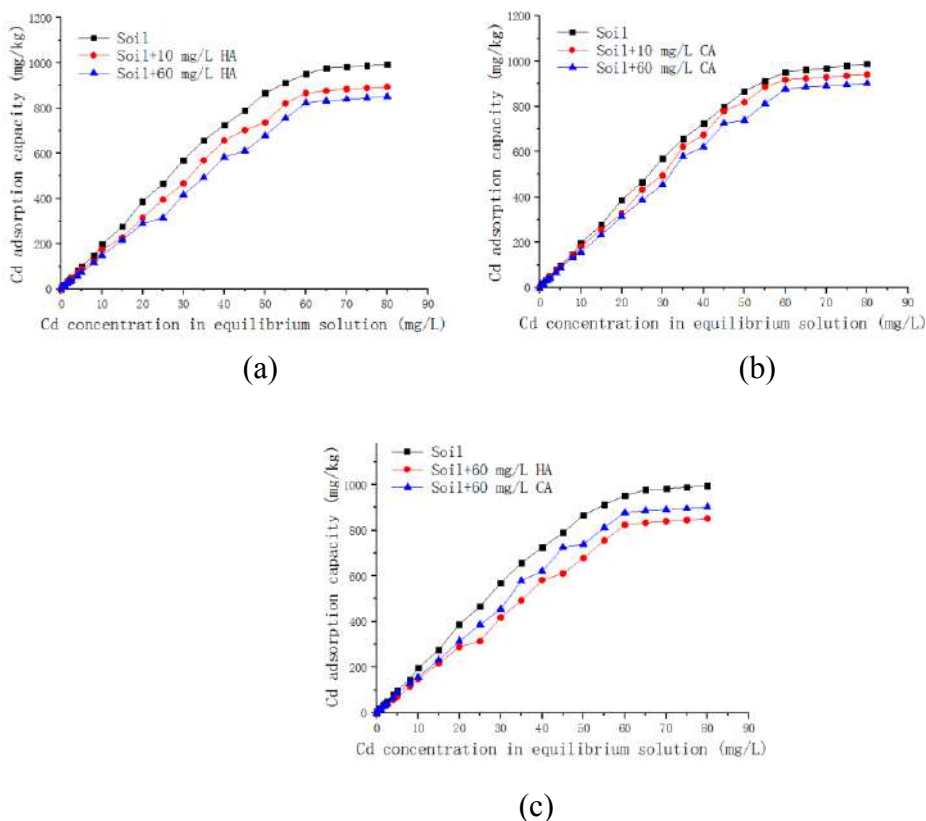


Fig. 1: Cd adsorption capacity vs. Cd concentration in solution in the presence and absence of HA and CA (60 mg.L^{-1}).

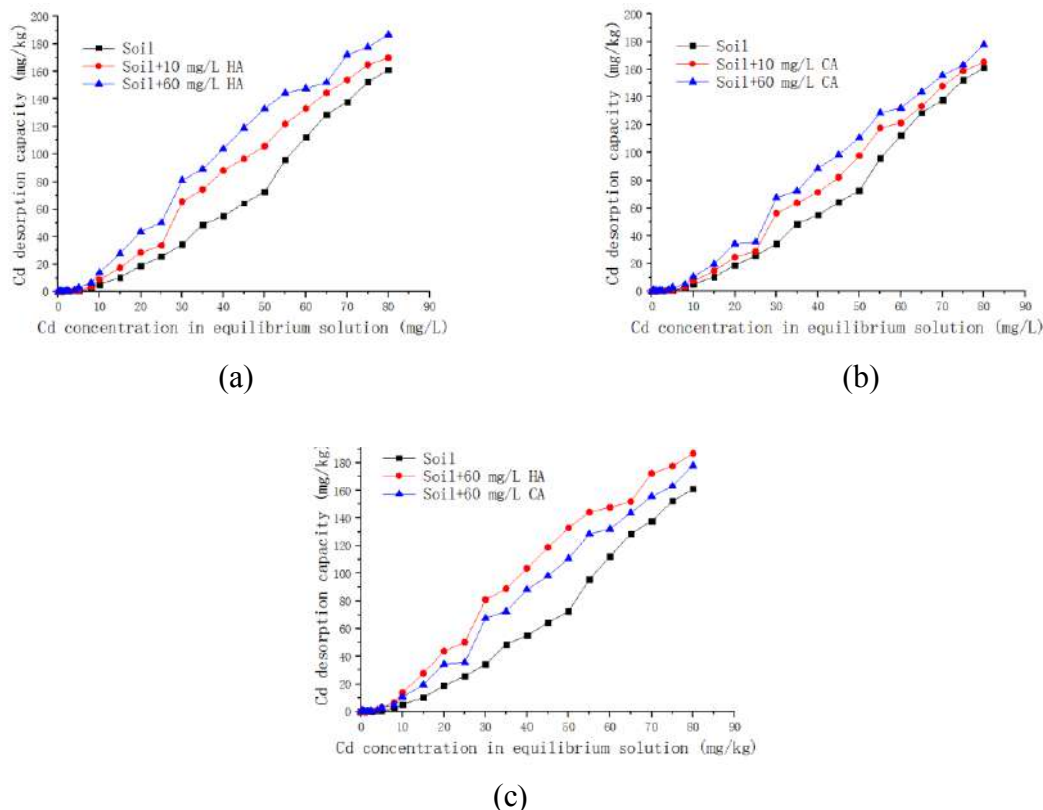


Fig. 2: Cd desorption capacity vs. Cd concentration in solution in the presence and absence of HA and CA (60 mg.L⁻¹).

Cd. The ionization of H⁺ in the oxygen-containing functional groups of HA and CA lowers the pH of the reclaimed soil solution, altering metal solubility and lowering the soil's Cd adsorption capacity (Li et al. 2018, Yang 2018, Yan 2019, Jagadamma et al. 2014). In addition, HA, which is rich in anionic groups such as phenolic, hydroxyl, and carboxyl groups, precedes Cd to occupy the soil seat sites through soil surface adsorption (He et al. 2020, Izosimova et al. 2020), thereby reducing the Cd adsorption capacity of reclaimed soil. This is consistent with previous results indicating that DOC has a significant inhibitory effect on Cd adsorption in soil (Chen & Chen 2002).

Characteristics and Mechanism of Isothermal Cd Desorption Under the Influence of HA and CA

As shown in Fig. 2, the ability of the two organic acids to desorb Cd was quite different. As the concentration of Cd in the equilibrium solution increased, the Cd desorption capacity of reclaimed soil gradually increased. When the Cd concentration was low (0.2–10 mg.L⁻¹), the amounts of desorbed Cd were similar in the presence and absence of HA and CA. Thus, under low Cd concentrations, HA and CA

had little effect on the ability of reclaimed soil to desorb Cd. When the Cd concentration was 15–80 mg.L⁻¹, the presence of HA or CA significantly increased the desorption of Cd in the reclaimed soil, and the amount of desorbed Cd increased as the concentration of added Cd increased. Due to the different physical and chemical properties of reclaimed soils, HA and CA had different effects on desorption capacity. HA had a stronger enhancement effect on Cd desorption, and high organic acid concentration (60 mg.L⁻¹) produced a larger effect than the low concentration (10 mg.L⁻¹).

As shown in Fig. 3, the desorption rate of Cd from reclaimed soil increased upon the addition of HA or CA. The Cd desorption rate of reclaimed soil increased on average by 5.71% and 3.21% upon the addition of high (60 mg.L⁻¹) and low (10 mg.L⁻¹) concentrations of HA, respectively. The Cd desorption rate increased by 3.48% and 1.94% in the presence of high and low concentrations of CA, respectively. The adsorption process of Cd is dominated by chemical bonding and electrostatic attraction. The activation energy required for adsorption is low, and the adsorption affinity is high. The desorption process of Cd is an ion exchange process. Organic ligands contained in organic acids can form soluble

organometallic complexes with Cd, thereby reducing the adsorption of Cd in reclaimed soil. In addition, the protons in HA and CA can activate Cd in reclaimed soil and promote its desorption (Xu et al. 2015).

Kinetics and Mechanism of Cd Adsorption and Desorption Under the Influence of HA and CA

As shown in Fig. 4, compared to the normal reclaimed soil, Cd adsorption was significantly reduced in the soil containing HA or CA. Under the influence of HA, Cd adsorption was reduced by 17.06%–18.80% (average = 18.18%). In the presence of CA, Cd adsorption in the reclaimed soil decreased by 12.58%–15.34% (average = 13.66%). Thus, HA reduced Cd adsorption in the reclaimed soil more obviously than CA. These results show that HA and CA changed the migration behavior of Cd in the reclaimed soil by affecting its adsorption.

The adsorption of Cd in reclaimed soil containing HA or CA followed the same pattern as it did in the absence of organic acids. Adsorption took place in two stages: a quick adsorption stage lasting 0–0.5 hours and a slower adsorption stage lasting 1–12 hours. The adsorption capacity of Cd in reclaimed soil increased substantially during the

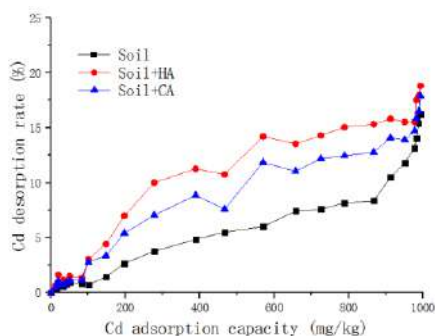


Fig. 3: Cd desorption rate vs. Cd adsorption capacity for reclaimed soil in the presence and absence of HA and CA.

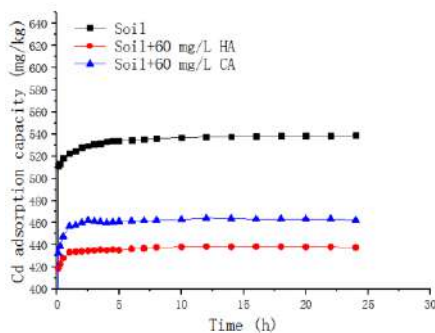


Fig. 4: Kinetic curves of Cd adsorption in reclaimed soil in the absence and presence of CA and HA.

fast absorption stage. Under the influence of HA, the Cd adsorption rate was 71.36%, corresponding to reductions of 15.04% compared to the normal reclaimed soil, respectively. In the presence of CA, the Cd adsorption rate was 72.15%, representing reductions of 11.80% compared to the normal reclaimed soil, respectively. In the slow reaction stage from 1–12 h, the amount of adsorbed Cd continued to increase, but the rate of increase was slower compared to in the fast reaction stage. Compared to in the normal reclaimed soil, the Cd adsorption capacity increased more slowly in the presence of HA or CA, and adsorption equilibrium was reached after 12 h. These results further demonstrate that HA and CA can inhibit the adsorption of Cd in reclaimed soil.

As shown in Fig. 5, under the influence of HA or CA, the Cd desorption capacity in reclaimed soil first decreased and then increased over time, revealing two desorption stages: a fast reaction stage from 0–2 h from the beginning of the experiment and a slow reaction stage from 2.5–12 h. In the first 2 h, desorption capacity decreased rapidly, reaching the lowest value at 2 h. In the subsequent slow reaction stage, the desorption capacity increased slowly, reaching equilibrium after approximately 12 h. Both HA and CA significantly increased the desorption capacity of Cd in reclaimed soil; HA increased the Cd desorption capacity by 28.51%–72.98% (average = 50.29%), while the effect of CA was weaker (increase in desorption capacity of 9.56%–42.67% with an average increase of 26.34%). These results demonstrate that HA and CA can alter the migration activity of Cd in reclaimed soil by affecting the desorption of Cd.

Adsorption and Desorption Characteristics and Mechanism of Cd in the Presence of Different Concentrations of HA and CA

As shown in Fig. 6, the two organic acids had different effects on the adsorption of Cd in the reclaimed soil, with HA having a stronger effect than CA. Within the range of organic acid concentrations examined in this study (0–80 mg.L⁻¹), the

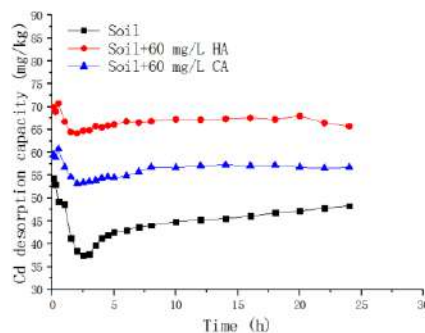


Fig. 5: Kinetic curves of Cd desorption from reclaimed soil in the presence and absence of CA and HA.

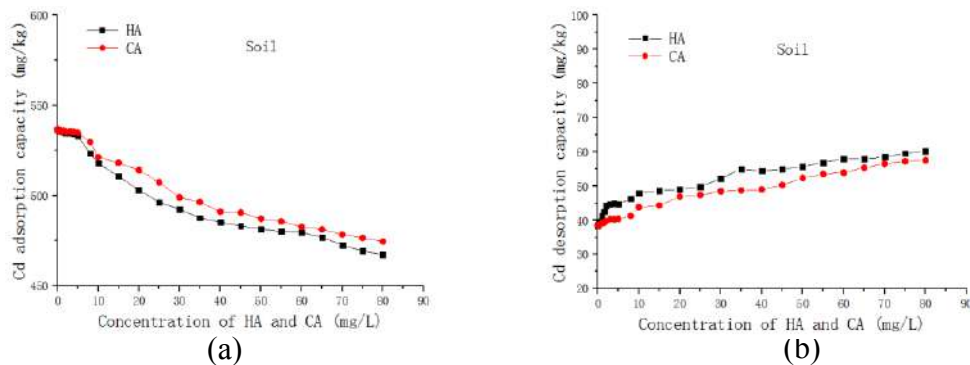


Fig. 6: Plots of Cd adsorption capacity (left) and desorption capacity (right) vs. HA and CA concentration.

adsorption capacity of Cd in the reclaimed soil gradually decreased with increasing HA or CA concentration. In the HA system, the adsorption rate of Cd in the reclaimed soil was reduced from the initial value of 95.02% to 80.60%; in the CA system, the adsorption rate of Cd decreased to 82.39%. The reclaimed soil was weakly alkaline (pH = 7.91). Since alkaline soil contains more clay minerals than acidic soil, the adsorption capacity for Cd in alkaline soil is relatively high. The addition of organic acids results in the complexation between organic ligands and Cd. The negative charge in the soil solution repels the negative charge on the soil surface (Wang 2012). In this case, the addition of organic acid reduced the adsorption capacity of Cd, and as the concentration of added organic acid increased, the adsorption capacity gradually decreased.

The two organic acids had different effects on the desorption of Cd in the reclaimed soil, with HA having a stronger effect than CA. As the concentration of organic acid increased within the tested range (0–80 mg.L⁻¹), the amount of desorbed Cd in the reclaimed soil gradually increased; that is, the organic acids promoted Cd desorption in the reclaimed soil. In the HA system, the desorption rate of Cd from the reclaimed soil increased from the initial value of 7.18% to 12.87%; in the CA system, the desorption rate increased to 12.12%.

Regression analysis revealed that the relationship between the concentration of organic acid (Y) and the Cd adsorption or desorption capacity (X) in reclaimed soil was best described by the logarithmic function $Y = a \ln X + b$, where a and b reflect the differences in the behaviors of HA and CA. The specific functions for Cd adsorption and desorption are shown in Table 2 and Table 3, respectively.

The established logarithmic function $Y = a \ln X + b$ is suitable for describing Cd adsorption and desorption in reclaimed soil under the influence of organic acids in the study area. The adsorption and desorption of Cd in reclaimed soil in the presence of varied organic acid concentrations can be calculated by varying the values of a and b .

CONCLUSION

The effects of organic acids on Cd adsorption and desorption in reclaimed soil are complicated. In this study, the addition of two representative organic acids, HA and CA, inhibited the adsorption of Cd in reclaimed soil, with HA having a stronger inhibitory effect than CA. Furthermore, both HA and CA increased Cd desorption in reclaimed soil, with HA being more effective than CA.

Table 2: Logarithmic regression equations for the relationship between HA and CA concentration (Y) and adsorption capacity (X).

Organic acid	Sample	Equation	R^2	n
HA	Soil	$Y = -28.3 \ln X + 610.26$	0.9943	27
CA	Soil	$Y = -25.141 \ln X + 607.59$	0.9937	27

Table 2: Logarithmic regression equations for the relationship between HA and CA concentration (Y) and adsorption capacity (X).

Organic acid	Sample	Equation	R^2	n
HA	Soil	$Y = -28.3 \ln X + 610.26$	0.9943	27
CA	Soil	$Y = -25.141 \ln X + 607.59$	0.9937	27

Table 3: Logarithmic regression equations for the relationship between HA and CA concentration (Y) and desorption capacity (X).

Organic acid	Sample	Equation	R^2	n
HA	Soil	$Y = 5.5037\ln X + 34.855$	0.9532	27
CA	Soil	$Y = 5.6876\ln X + 30.544$	0.9536	27

The adsorption and desorption kinetics of Cd in reclaimed soil could be divided into two stages: an initial fast reaction stage followed by a slow reaction stage. For Cd adsorption, the adsorption capacity of reclaimed soil increased rapidly during the fast reaction stage from 0–0.5 h. During the slow reaction stage from 1–12 h, the Cd adsorption capacity continued to increase but at a slower rate. The adsorption equilibrium was reached after 12 h. The adsorption rates of Cd in reclaimed soil were 15.04% and 11.80% lower in the presence of HA (60 mg.L⁻¹) and CA (60 mg.L⁻¹) than in the absence of organic acids, respectively.

For Cd desorption, the desorption capacity decreased rapidly in the fast reaction stage from 0–2 h. In the slow reaction stage from 2.5–12 h, the desorption capacity increased slowly with time and reached equilibrium after 12 h. In the presence of HA (60 mg.L⁻¹) and CA (60 mg.L⁻¹), the Cd desorption rate in reclaimed soil was 50.29% and 26.34% higher than in the absence of organic acids, respectively.

The relationship between the adsorption or desorption capacity of Cd and the concentration of organic acid was best described by the logarithmic function $Y = a\ln X + b$.

ACKNOWLEDGMENTS

This research was supported by the Natural Science Research Project of the University in Anhui Province (No. KJ2018A0072), the National Natural Science Foundation of China (No. 51904014), and the Postdoctoral Foundation of Anhui Province (No. 2019B337). The authors appreciate the constructive comments from the anonymous reviewer

REFERENCES

- Bhattacharya, R. and Osburn, C.L. 2020. Chromophoric dissolved organic matter composition and load from a coastal river system under variable flow regimes. *J. Sci. Total Environ.*, 760: 143414.
- Bian, Z. 2001. Research on the Succession Law and Regulation of Interface Elements of Land Reclamation in the Mining Area. Higher Education Press, Beijing.
- Chen, T.B. and Chen, Z.J. 2002. Cadmium adsorption in the soil is influenced by dissolved organic matter derived from rice straw sediment. *Chin. J. Appl. Ecol.*, 2: 156-159.
- Gao, T., Zhang, H. and Zhou, J. 2011. The influence of dissolved organic matter on the environmental behavior of heavy metals in soil. *J. Ecol. Environ.*, 20: 652-658.
- He, J., Lu, W. and Zhang, N. 2020. Research progress in the application of humic acid in the remediation of heavy metal contaminated soil. *Humic Acid*, 02: 38-55.
- He, L. 2019. Research on chemical remediation technology of heavy metal contaminated soil in the mining area. *J. Henan Univ. Sci. Technol.*, 11: 134-136.
- Huang, J. 2020. The Effect of Exogenous Organic Acids on the Migration of Cd in the Soil-Rice System. Dissertation, Central South University of Forestry and Technology, Hunan, China.
- Huang, Q., Wu, J. and Chen, J. 2015. Research progress in soil adsorption of soluble organic carbon. *J. Soil*, 47: 446-452.
- Izosimova, Y., Tolpeshta I. and Gurova, I. 2020. Sorption of Cu²⁺ Ions by bentonite modified with Al Keggin cations and humic acid in solutions with pH 4.5. *J. Minerals*, 12: 1121.
- Jagadamma, S., Mayes, M.A. and Zinn, Y.L. 2014. Sorption of organic carbon compounds to the fine fraction of surface and subsurface soils. *J. Geoderma.*, 213: 79-86.
- Jiang, B., Zhang, B. and Wang, X. 2020. Soil heavy metal pollution and potential risk assessment in Fushun West Open-pit Mine. *J. Northeastern Univ. Nat. Sci. Edn.*, 41: 568-574.
- Kalbitz, K., Solinger, S. and Park, J.H. 2000. Controls on the dynamics of dissolved organic matter in soils: A review. *J. Soil Sci.*, 165: 277-304.
- Lei, H., Pan, H. and Han, Y. 2015. Spectroscopic study on the influence of dissolved organic matter on pesticide residues and distribution in soil. *J. Spectro. Spectral. Anal.*, 35: 1926-1932.
- Li, H., Yan, S. and Cui, L. 2008. Evaluation of soil heavy metal pollution in Huainan Xinji mining area. *J. Min. Saf. Environ. Protect.*, 35: 36-37.
- Li, J., Zhang, J. and Li, Y. 2018. Analysis of the influence of dissolved organic matter on soil heavy metal activity. *J. South Agric.*, 12: 62-64.
- Li, S., Yu, Y. and He, S. 2003. The relationship between dissolved organic carbon and soil factors in southern forest soils. *J. Zhejiang Forest. College*, 20: 119-123.
- Li, W. 2017. The Structure Composition and Environmental Effects of Dissolved Humus in Lake Taihu. Dissertation, East China Normal University, China.
- Liu, C. 2019a. Sources and impact mechanisms of eroded soil organic carbon in the hilly area of the Loess Plateau. Dissertation, Hunan University, Hunan, China.
- Liu, G. 2019b. The Effect of Organic Materials on the Dissolved Organic Matter of Purple Soil and the Accumulation of Cadmium in Rice. Dissertation, Southwest University, Chongqing, China.
- Ma Y., Xie, G. and Liu, Z. 2020. On the repair principle of humic acid and food safety. *Food Saf. Guide*, 16: 55-57.
- Mahara, Y., Kubota, T. and Wakayama, R. 2007. Effects of molecular weight of natural organic matter on cadmium mobility in soil environments and its carbon isotope characteristics. *J. Sci Total Environ.*, 387: 220-227.
- Shan, R., Huang, Z. and Ke, C. 2015. The leaching effect of humic acid on soil heavy metal cadmium and the mechanism of adsorption and desorption. *Humic Acid*, 1:12-17.
- Wang, C., Xue, L. and Dong, Y. 2020. Soil organic carbon fractions, C-cycling hydrolytic enzymes, and microbial carbon metabolism in Chinese fir plantations. *J. Sci. Total Environ.*, 758: 143695.
- Wang, J. 2012. Study on the Adsorption-Desorption Characteristics of Heavy Metal Cadmium in Typical Farmland Soils in My Country. Dissertation, Northwest Sci-Tech University of Agriculture and Forestry, Shaanxi, China.
- Wang, Q. 2016. Research on the Influence of Freeze-Thaw and Snow-Melt Processes on Dissolved Organic Matter in Soil. Dissertation, Liaoning University, China.

- Xie, C., Qin, Y. and Chao, L. 2020. Applied research on the numerical simulation of Cu and Cd transport laws in a metal mining area. *AIP Adv.*, 10: 2158-3226.
- Xu, R., Li, X. and Sun, L. 2015. The leaching kinetic characteristics and removal mechanism of Pb and Cd in soil by organic acids. *J. Saf. Environ.*, 15: 261-266.
- Xu, Y., Wu, P. and Dang, Z. 2008. Experimental study on the adsorption of heavy metal ions by montmorillonite /humic acid complex. *J. Impur. Rock Mineral.*, 27: 221-226.
- Yan, A. 2019. Study on the Adsorption Characteristics and Mechanism of Soil Humic Substances on Heavy Metals. Dissertation, Jilin Agricultural University, Jilin, China.
- Yang, J. and Zeng, X. 2007. The chemical behavior of water-soluble organic matter in soil and its impact on the environment. *Chin. J. Eco-Agric.*, 615: 206-211.
- Yang, L., Zhang, J. and Yang, G.P. 2020. Mixing behavior, biological and photolytic degradation of dissolved organic matter in the East China Sea and the Yellow Sea. *J. Sci. Total Environ.*, 762: 143164.
- Yang, Y. 2018. Study on the Effects of Two Organic Acids on the Adsorption-Desorption Characteristics of Zn²⁺ and Cd²⁺ in Tea Garden Soil Aggregates. Dissertation, Sichuan Agricultural University.
- Yao, D., Meng, J. and Zhang, Z. 2010. Heavy metal pollution and potential ecological risk in reclaimed soils in Huainan mining area. *J. Coal Sci. Eng.*, 16: 316-319.
- Ye, J. 2020. The Composition and Structure Characteristics of Soil Dissolved Organic Matter and its Effect on Cadmium Phytotoxicity. Dissertation, Wuhan University of Science and Technology, Wuhan, China.
- Zhang, B., Mi, W. and Xiao, Y. 2019. The current status of soil heavy metal pollution in coal mining areas and an overview of its evaluation method. *J. Proceed. Chin. Soc. Environ. Sci.*, 1541: 2946-2951.
- Zhang, S. 2020. The Characteristics of Dissolved Organic Matter in the Black and Smelly River and Its Correlation with Heavy Metals. Dissertation, Northwest Normal University, Gansu, China.
- Zhang, Z., Yao, D. and Zheng, Y. 2010. Research on soil heavy metal pollution remediation potential of six composite plants in coal mine subsidence reclamation area. *J. Chin. Coal Soc.*, 35: 1742-1747.
- Zhao, Y., Zhang, T. and Tian, Z. 2020. Research progress in phytoremediation technology of heavy metal contaminated soil around the mining area. *J. Urban Geol.*, 15: 22-33.
- Zsolnay, A. 1996. Dissolved Humus in Soil Waters. In: Piccolo A., (ed). *Humic Substances in Terrestrial Ecosystems*. Elsevier, Amsterdam, pp. 171-223.



Application of KOH-ethanol Solution in Separation of Waste Photovoltaic Panels

Jiyang Cai†

International Department, Shanghai World Foreign Language Middle School, Shanghai 200233, China

†Corresponding author: Jiyang Cai; yabgql180@163.com

Nat. Env. & Poll. Tech.

Website: www.neptjournal.com

Received: 03-06-2021

Revised: 29-06-2021

Accepted: 25-07-2021

Key Words:

Photovoltaic panels
KOH-ethanol solution
Recycling
EVA film

ABSTRACT

With the continuous development of photovoltaic panel technology in recent years, the frequency of replacement has accelerated, which has led to the continuous increase of waste photovoltaic panels. Developing the separation technology of waste photovoltaic panels can effectively solve the problems of resource shortage and environmental pollution. According to the sticking mechanism of EVA film, this paper proposes a KOH-ethanol solution to degrade EVA film and recover silicon from waste photovoltaic panels. In this paper, the key factors affecting the separation of photovoltaic panels are studied through experiments indicating that compared with NaOH-ethanol solution, KOH-ethanol solution has better separation efficiency. Sample after crushing treatment has higher separation efficiency, the best temperature for sample separation is 200 degrees Celsius, and the best sample area is 1×1 square centimeter, the optimal concentration of the solution is 0.20 mol/L, and the optimal reaction time is 3.0 hours.

INTRODUCTION

As the global population continues to increase, our demand for new energy will increase, and the resulting environmental pollution problems will become more prominent. Research and analysis point out that in the next 60 years, the existing fossil fuels on the earth will be at risk of being depleted (Li et al. 2018). The CO₂, SO_x, NO_x and other pollutants generated in the process of fossil resource consumption will cause acid rain and greenhouse effect, which will seriously pollute water, soil and air. At the same time, the reserves of fossil resources are relatively limited, and the difficulty and cost of mining continue to increase. Therefore, in terms of energy supply, it is necessary to follow the path of sustainable development and vigorously develop new types of high-efficiency, clean and renewable energy sources, which has become a common consensus of all countries in the world. With the continuous advancement of current technology, people have begun to regard solar energy as an important part of new energy, and develop a variety of new technologies to replace fossil fuels. As an emerging renewable energy, solar energy has the following advantages: (1) Energy can be used for a long time; (2) Abundant reserves; (3) High safety; (4) Low cost; (5) Clean energy has relatively small impact on the environment. Therefore, solar energy has always been considered to have broad development prospects (Yan et al. 2012).

The life span of photovoltaic panels is 25-30 years (Ma et al. 2021). Due to the long service life, waste photovoltaic panels have been ignored by humans. However, according to

related reports, photovoltaic panels have been installed from the earliest 80s to 90s, and in recent years there have been photovoltaic panels that have reached their lifespan (Aflaki et al. 2021). In addition, due to the replacement of photovoltaic technology, the reduction of photoelectric conversion rate, the damage of photovoltaic equipment, the aging of photovoltaic modules, etc., the growth of waste photovoltaic panels has been further accelerated and has attracted widespread attention (Paiano 2015). According to statistics, the global photovoltaic waste volume reached 43,500 to 25 million tons in 2016. It is estimated that the world will reach 1.7-8 million tons in 2030, and the global photovoltaic waste will reach 0.6-78 million tons in 2050. Among them, there will be about 500 tons of waste photovoltaic panels in China in 2020. It is estimated that China will reach 20 million tons in 2050, which is equivalent to 2000 times the weight of the Eiffel Tower. Based on the above data analysis, there will be a large number of waste photovoltaic panels in the world that need to be processed in the future (Hu 2008, Farrell et al. 2019, Tian et al. 2021, Maranghi et al. 2019).

In order to cope with the substantial growth of photovoltaic cell waste in the future, it is of great significance to study the multi-component high-efficiency separation technology of photovoltaic panels.

Due to the large reserves of silicon and easy exploitation, silicon-based photovoltaic panels account for 90% of the entire photovoltaic market. The remaining 10% photovoltaic panels mainly include copper, indium, gallium, selenium,

amorphous silicon and cadmium telluride (Stephanie et al. 2016, Xu et al. 2018, Azeumo et al. 2019). Therefore, this research focuses on the recycling of silicon-based photovoltaic panels.

Traditional silicon-based photovoltaic panels are single-layer glass crystalline silicon solar panels (single-glass photovoltaic cells). Single-glass photovoltaic cells mainly include toughened glass, polyethylene-vinyl acetate copolymer (EVA) film, silicon-based solar cells, polyvinyl fluoride composite (TPT) backplanes, metal electrodes, aluminum frames, and connectors. Among them, the aluminum frame plays the role of protecting the solar panels and fixing connections, and can be directly recycled by mechanical or manual removal. Photovoltaic panels are generally placed outdoors for a long time. In order to protect photovoltaic panels from external moisture and external forces, tempered glass and TPT backplanes play a role in protecting silicon-based solar cells. At present, the most widely used adhesive for photovoltaic panels is EVA adhesive film, which has the advantage of low cost, good performance, and stable chemical properties. The main component of the TPT backsheet is a polyvinyl fluoride composite film, which consists of two parts, namely ethylene phthalate and polyvinyl fluoride. Its function is to seal, insulate, waterproof, and resist aging. The connector is to protect the normal operation of the entire power generation system.

In traditional chemical separation, organic chemical swelling agents (such as toluene and trichloroethylene) are used to dissolve the EVA film in the photovoltaic panel to achieve complete separation of photovoltaic cells. However, organic chemical swelling agents usually have greater volatility and toxicity which does not meet the green, environmental, and sustainable recycling goals.

In this paper, based on the sticking mechanism of EVA film, the structure of EVA and the characteristics of the interface of each component are destroyed by chemical reagents, and a new chemical reagent KOH-ethanol is developed to realize the separation of the components of photovoltaic cells. This chemical reagent has the characteristics of low toxicity and recyclability, and has the characteristics of low energy consumption compared with the high-temperature heat treatment separation method. Therefore, using this method of recycling, photovoltaic panels can effectively protect the environment and carry out secondary use of resources.

This work carried out a detailed experimental study on the separation mechanism of KOH-ethanol on photovoltaic panel modules, focusing on the influence of size, alkali type, experimental temperature, KOH concentration and the solid-liquid ratio of the material on the separation rate of photovoltaic panels.

BASIC THEORY

As an adhesive, EVA is the most commonly used material for bonding the components of photovoltaic panels and protecting photovoltaic panels from external moisture and mechanical damage. It is generally believed that the most important step in the recycling process of photovoltaic panels is the removal of EVA. Therefore, this article focuses on the adhesion theory of EVA.

Since EVA is a weakly polar substance, it has weak adhesion to glass and TP backplanes. Generally, a coupling agent is added to increase the viscosity during the EVA cross-linking process. The commonly used coupling agent is a silane coupling agent, the chemical formula of is SiRX_3 . Its R is an organophilic group, which can chemically react with EVA, such as amino, vinyl, epoxy, methacryloxy and so on. X is an inorganic group, which can react chemically with the surface of an inorganic substance, such as an alkoxy group. The adhesion mechanism of EVA and photovoltaic panels are shown in Fig. 1.

Through the analysis of the adhesion theory, the adhesion of each component of the photovoltaic panel is mainly connected by chemical bonds. The different components are bonded together through the action of chemical bonds. EVA forms a gel with a three-dimensional network structure during the cross-linking process, and the coupling agent plays a role in enhancing the adhesion of EVA.

In the process of separating the components of the photovoltaic panel, it is first necessary to ensure that the chemical test reagent can effectively penetrate the middle layer of the photovoltaic panel and can immediately react with the EVA film. For example, the use of high-frequency vibration in ultrasonic radiation technology can effectively promote the diffusion process of chemical reagents in the middle layer of the photovoltaic panel, and at the same time can effectively accelerate the dissolution rate of EVA. In addition, the use of alkaline solution such as NaOH or KOH can also promote the reaction between it and the anti-reflective coating, thereby separating other layers including aluminum and silicon.

MATERIALS AND METHODS

Experimental Materials and Reagents

Experimental raw materials: Waste silicon-based photovoltaic panels and crushed materials.

The main reagents of the experiment: KOH, NaOH, absolute ethanol, deionized water (conductivity $<0.1 \mu\text{S}/\text{cm}$, derived from CM-230 deionized water).

Laboratory Equipment

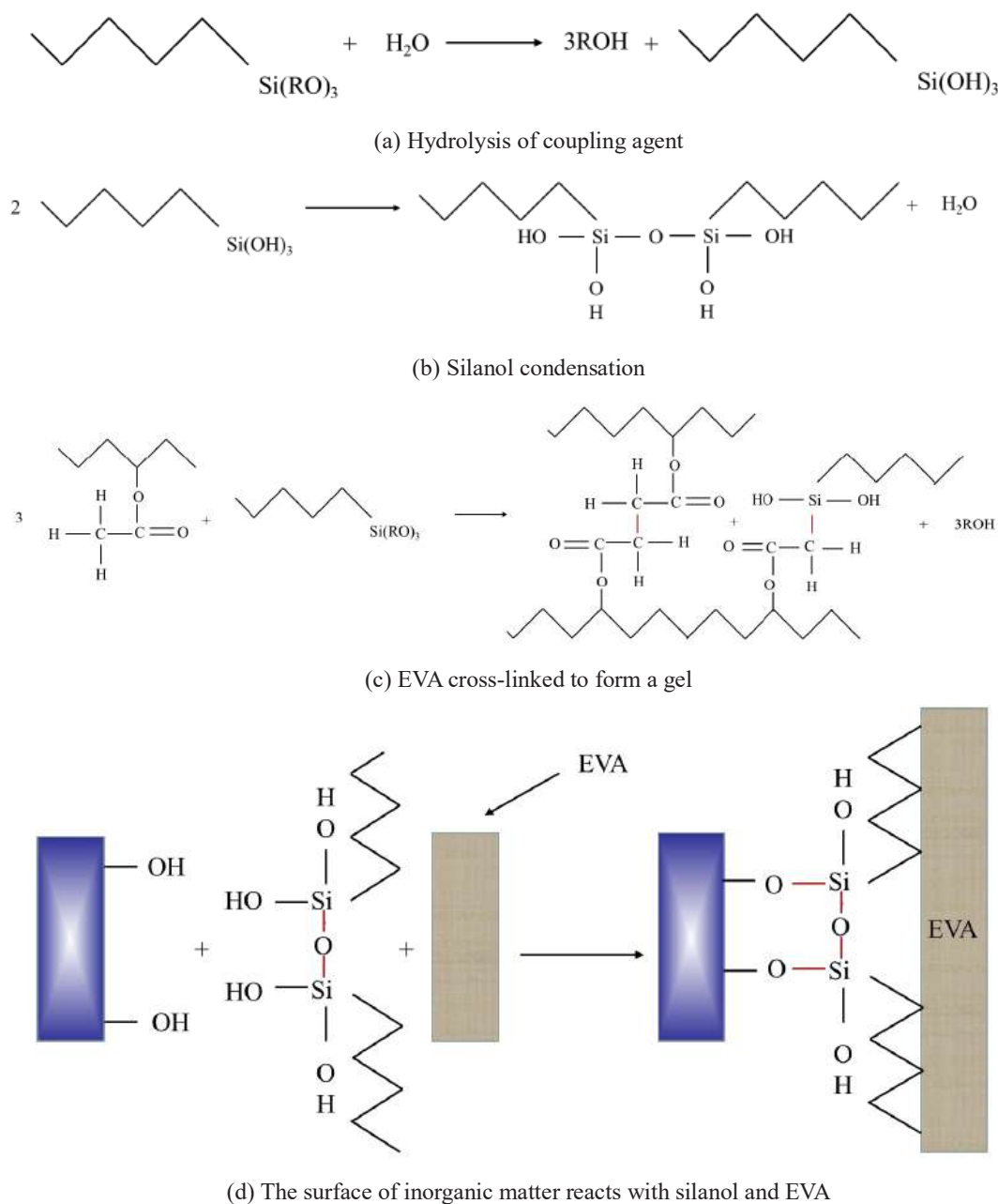


Fig. 1: The adhesion mechanism of EVA and photovoltaic panels.

Main experimental equipment: As shown in Fig. 2, using KSS-1350° type muffle, the temperature of the reactor is controlled by a programmable temperature controller with an accuracy of $\pm 2^\circ$. DF-1015 type heat-collecting magnetic heating stirrer.

Other equipment: SHB-III type circulating water multi-purpose vacuum pump. One PG-2D metallographic polishing

machine. One ZK-1BS electric heating vacuum drying oven. Hydrothermal reactor, 1 condensation recovery device. BS-224S electronic balance, precision 0.0001 g.

Analysis Test Method

The weighing method is used to calculate the separation rate of photovoltaic panels by weighing the mass before



Fig. 2: Picture of Muffle furnace

and after the separation with an electronic balance (Formula 1).

$$\text{Separation ratio (\%)} = \left(1 - \frac{G_b}{G_a}\right) \times 100 \quad \dots(1)$$

In the above formula, G_a represents the total mass of photovoltaic panels, and G_b represents the mass of unseparated photovoltaic panels.

Since silicon-based cells have cathodes and anodes, an oxide layer will be generated on the surface of the silicon wafers during the process of separating photovoltaic panels using high-temperature heat treatment or alkali-ethanol solvents. In order to study the influence characteristics of wafer recovery rate under different separation methods, after the photovoltaic panels are completely separated by different treatment methods, the recovery rate of the silicon wafers was computed using the Formula 2.

$$W_{q1} (\%) = \left(1 - \frac{W_{b1}}{W_{a1}}\right) \times 100 \quad \dots(2)$$

In the above formula, the recovery rate of the silicon wafer is represented by W_{q1} , the thickness of the oxide layer is represented by W_{b1} , and the thickness of the silicon

wafer is represented by W_{a1} . There is a close relationship between the degree of oxidation of the silicon wafer and its recovery rate.

1) Detection of the Oxidation Degree of the Surface

Experimental test method: X-ray photoelectron spectrometer was used to measure the valence state of the silicon wafer surface.

2) Scanning Electron Microscope Analysis (SEM)

Experimental test method: The morphology of the silicon-based cell was obtained by the JSM-7800 scanning electron microscope detecting high temperature heat treatment, KOH ethanol and NaOH-ethanol separation. The thickness of EVA film before and after the KOH-ethanol treatment was measured.

3) Measurement of Silicon Oxide Layer Thickness

Experimental test method: The wavelength or intensity of the characteristic X-rays generated by an energy spectrometer (EDS) was measured, so as to quantitatively analyze the oxide layer thickness of silicon wafers by measuring the wavelength of silicon and oxygen in the measurement area.

4) Contact Angle Measurement

Experimental test method: Use DSA100 contact angle measuring instrument, and high-speed camera to record the wetting process of water and ethanol droplets on the glass respectively; intercept the image at the time when the drop is stable, take the picture; and use the five-point method to automatically fit the circle to calculate contact angle.

5) Roughness Measurement

Experimental test method: The Nano GT-K optical profiler provided by the German Bruker Company was used. The roughness of the glass obtained by high-temperature heat treatment, KOH ethanol and NaOH-ethanol separation was carried out respectively.

6) Fourier Infrared Test and Analysis (FTIR)

Experimental test method: The original swelling agent, the post-reaction swelling agent, and the EVA film before and after swelling were analyzed by T-27 Fourier infrared spectroscopy provided by the German Bruker Company. The infrared spectrum was recorded in the transmission mode, and the recording range was between $7.0E+02$ and $4.0E+03 \text{ cm}^{-1}$. The manual sampling method was used to sample the EVA film of the photovoltaic panel, and the ATR attenuated total reflection was used. The method scans the film sample. In the process of preparing the solution sample, the ethanol

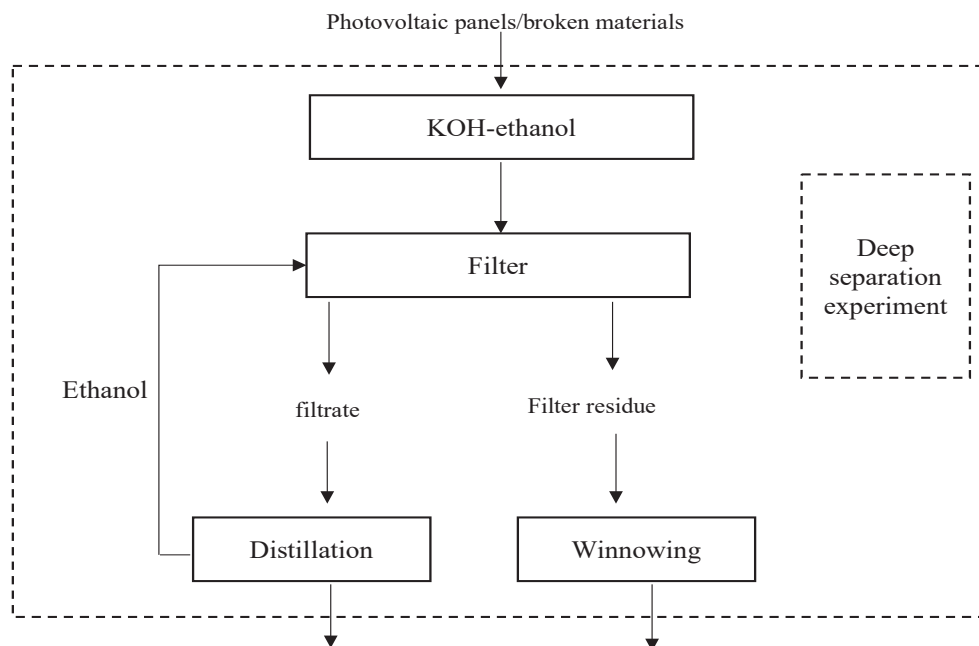


Fig. 3: Flow chart of deep separation of photovoltaic panels by chemical method.

in the solution was removed through the evaporation process, thereby reducing its influence on the measurement results.

Experimental Steps

The experimental steps are shown in Fig. 3.

- (1) Cut the waste photovoltaic panels into 1×1 , 2×2 and 3×3 cm^2 and mechanically crush the pretreated materials.
- (2) The photovoltaic panel was crushed into fragments, and at the same time, 200 mL of alkali-ethanol solution was used to soak, and the solution was heated in a muffle furnace to control the reaction temperature.
- (3) After the reaction, the solution was suction filtered, the filter residue was thoroughly washed and dried at 130°C for 12 h. Winnowing was used to obtain silicon wafers and glass.
- (4) The filtrate was distilled, the remaining KOH crystallizes out, and the ethanol solution was recycled.

RESULTS AND DISCUSSION

Study on the Variation of Separation Rate in Different Alkali Types

In order to study the relationship between the separation rate of photovoltaic panels and the KOH-ethanol or NaOH-ethanol solution, and to determine the effect of different alkali types on the separation rate, experimental methods were used to carry out the research. The experimental temperature was 200 degrees Celsius, the alkali concentration was 0.21

mol/L, and the area of the photovoltaic panel was 1×1 cm^2 . As shown in Fig. 4, the separation speed in KOH-ethanol was higher than that in NaOH-ethanol solution. The former requires 3.1 hours to complete the separation, while the latter requires 4.1 hours to complete the separation. The conclusions of this research show that the separation rate of photovoltaic panels in KOH-ethanol increases faster than that of NaOH-ethanol. Therefore, due to its better separation effect, the subsequent experiments used KOH-ethanol solution as the reaction reagent.

Photovoltaic Panel Size and Effect of Temperature on Separation Rate

This paper studies the effect of photovoltaic panel size on its

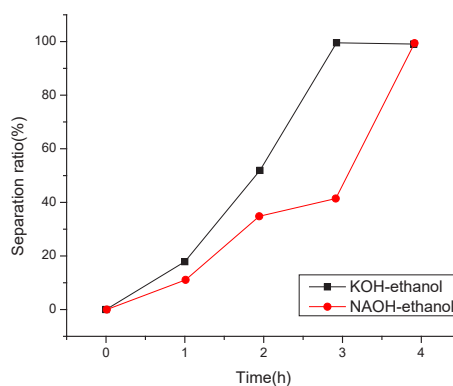


Fig. 4: Variation curve of separation rate in different solutions.

separation rate. The research conclusion shows that when the size of the photovoltaic panel is 1×1 square centimeter, the separation rate increases rapidly, and the entire separation can be completed within 3 hours. However, when the size is 2×2 square centimeters, the entire separation process cannot be completed within 3 hours. When the size is 3×3 square centimeters, the separation rate is very slow. At 3 hours, the separation rate is only 65%. Therefore, a photovoltaic panel of 1×1 square centimeter can obtain the highest separation rate.

This paper studied the effect of using KOH-ethanol solution for the separation of waste photovoltaic panels when the temperature is between 160-200°C, the solution concentration of KOH is 0.2 mol/L KOH, the solid-to-liquid ratio is 55 g/L, and the size of the photovoltaic panel is 1×1 square centimeter. The research conclusion shows that at 160°C, 43% of the photovoltaic panels can be separated in 6 hours, the separation rate shows an increasing trend between 1-3 hours. At 180°C, 75% of the photovoltaic panels can be separated in 6 hours. At 200°C, it only takes 3 hours to complete the separation of the entire photovoltaic panel. Therefore, considering the separation effect of photovoltaic panels, the optimal reaction temperature and reaction time can be set at 200°C and 3 h.

The Effect of Alkali Concentration on Separation Rate

During the study, the concentration of the KOH solution was 0.10-0.30 mol/L, the temperature of the experiment was 200 degrees Celsius, and the duration of the experiment was 2.51 h. The solid-to-liquid ratio in the solution is 54 g/L, and the area of the sample is 1×1 square centimeters. As shown in Fig. 5, the separation rate increases with the increase of the solution concentration. During the process of increasing the solution concentration from 0.10 to 0.20 mol/L, the increase in the separation rate is larger, and at 0.2-0.3 mol/L. In the

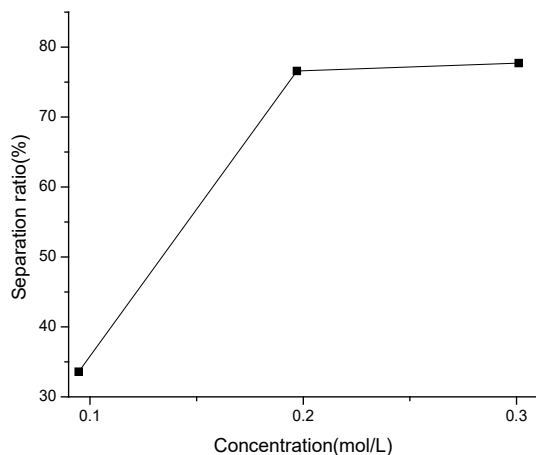


Fig. 5: Change curve of solution concentration and separation rate.

solution concentration range of, the increase in separation rate does not change significantly, so the optimal solution concentration value is 0.2 mol/L.

Mechanical Crushing Strengthens Chemical Separation

In order to explore the impact of mechanical crushing pretreatment on the separation of waste photovoltaic panels, the experiments were carried out in KOH-ethanol solution with unbroken photovoltaic cells and crushed materials of one size. The area of the sample is 1×1 square centimeter, the experimental temperature is 200 degrees Celsius, the solution concentration is 0.20 mol/L, and the solution concentration is 55.0 g/L. As shown in Fig. 6, the separation rate of photovoltaic cells is closely related to the degree of fragmentation. After the sample is broken, the separation rate reaches 58.0%. When the reaction reaches 2 h, the separation rate is 58%. However, when the raw material is a photovoltaic panel that has not been mechanically broken, even if the reaction time is 2 h, the separation rate is only 42%. In order to achieve complete separation of photovoltaic panels, the reaction time needs to be extended to 3 h. Therefore, according to the above experiments, the mechanical crushing treatment greatly shortens the separation time of photovoltaic panels and improves the recycling efficiency.

The Influence of Different Media on the Separation Rate

In order to study the influence of different media on the separation of photovoltaic panels, after the mechanical crushing pretreatment, KOH-water solution and KOH-ethanol solution were used for experiments. The experimental temperature is 200 degrees Celsius, the solution concentration is 0.20 mol/L, and the solid content is 55.0 g/L. The results are shown in Fig. 7. It can be seen that the KOH-ethanol solution system is better than the KOH-water system. Using KOH-ethanol solution, the photovoltaic panels can be completely separated

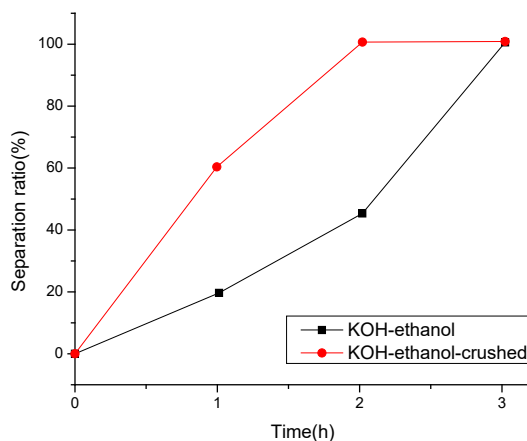


Fig. 6: Change curve of separation rate of crushed sample.

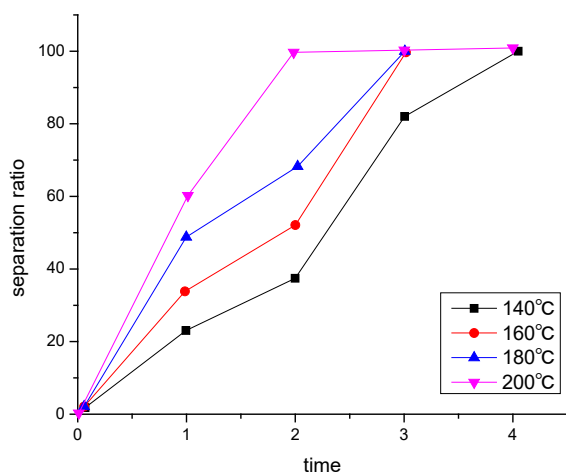


Fig. 7: Variation curve of separation rate under different media.

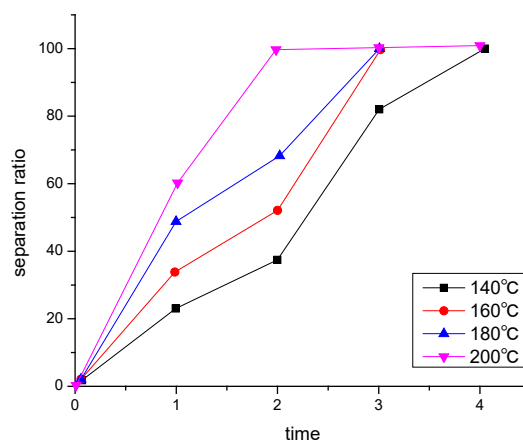


Fig. 8: Variation curve of separation rate of broken samples at different temperatures.

after only 2 hours of reaction. When using the KOH-water system to react from 1 h to 2 h, the separation rate of photovoltaic panels increased from 8% to 22%. Although the reaction time was increased to 3 hours, the separation rate of photovoltaic panels was only 38%. Therefore, the follow-up experiment uses the KOH-ethanol system to separate photovoltaic panels.

Effect of Reaction Temperature on Separation Rate After Mechanical Crushing

In order to discuss the influence of the reaction temperature on the separation of photovoltaic panels, the experimental temperature was separately discussed (140-200°C) for 2 h. The concentration of the solution is 0.20 mol/L, and the solid-to-liquid ratio in the solution is 55.0 g/L. As shown in Fig. 8, when the reaction temperature rose from 140°C to 200°C, it was found that the separation rate of photovoltaic panels increased significantly. When the reaction temperature is 140°C, the separation rate increases slowly compared with other experimental temperatures. When the reaction temperature increases to 160°C, it takes 4 h for the photovoltaic panels to completely separate. When the reaction temperature is 180°C and the reaction is carried out for 2 hours, the separation rate of the photovoltaic panels is 63%, and the complete separation requires 3 hours of reaction. However, when the reaction temperature is 200°C, the separation rate of the photovoltaic panels increases rapidly, and the complete separation only takes 2 h. Therefore, the subsequent experiment uses 200°C, and the reaction temperature time is 2 h.

Medium Circulation

The use of KOH-ethanol solution to separate photovoltaic panels requires a large amount of ethanol solution. Therefore, from the perspective of green, environmentally friendly and sustainable recycling, it is necessary to consider the

recycling and utilization of waste liquid. In the experiment, the separated solution was distilled for 0.5 h at a reaction temperature of 130°C. The distilled solution was analyzed by FT-IR, and the solution recovered has the same structure as the original solution. Therefore, the waste liquid can be recycled and reused by distillation.

CONCLUSION

This paper has developed an environmentally friendly, efficient, and closed-loop recycling process. Compared with NaOH-ethanol solution, KOH-ethanol solution has better separation efficiency. The sample after crushing treatment has higher separation efficiency. The best temperature for sample separation is 200 degrees Celsius, and the best sample area is 1×1 square centimeter, the optimal concentration of the solution is 0.20 mol/L, and the optimal reaction time is 3.0 hours. Compared with water, ethanol is more suitable as a solvent for separation of photovoltaic panels. Ethanol solvent can make sample components enter the inner layer of photovoltaic panels faster, thereby effectively separating specific components in the sample. The research results of this article have broad application prospects in engineering projects.

REFERENCES

- Aflaki, S., Basher, S.A. and Masini, A. 2021. Technology-push, demand-pull and endogenous drivers of innovation in the renewable energy industry. *Clean Technol. Envir.*, 23: 1563-1580.
- Azeumo, M.F., Germana, C., Ippolito, N.M., Franco, M., Luigi, P. and Settimo, S. 2019. Photovoltaic module recycling, a physical and a chemical recovery process. *Sol. Energ. Mat. Sol. C.*, 193: 314-319.
- Farrell, C., Osman, A.I., Zhang, X.L., Murphy, A., Doherty, R., Morgan, K., Rooney, D.W., Harrison, J., Coulter, R. and Shen, D.K. 2019. Assessment of the energy recovery potential of waste Photovoltaic (PV) modules. *Sci. Rep.-UK*, 9(1): 5267-5280.

- Hu, X.J. 2008. Overview of the development of solar photovoltaic power generation industry. *Anhui Electric Power Science and Technology Information*, 4: 29-32.
- Li, J.Y., Cai, M., Wu, X.W. and Tan, Y. 2018. Research on the recycling and reuse of polycrystalline silicon solar cells. *J. Inorg. Mater.*, 33(9): 68-73.
- Ma, L., Ge, H., Wang, L. and Wang, L.Z. 2021. Optimization of passive solar design and integration of building integrated photovoltaic/thermal (BIPV/T) system in northern housing. *Build. Simul.-China*, 14: 1467-1486.
- Maranghi, S., Parisi, M. L., Basosi, R. and Sinicropi, A. 2019. Environmental profile of the manufacturing process of perovskite photovoltaics: Harmonization of life cycle assessment studies. *Energies*, 12: 3746.
- Paiano, A. 2015. Photovoltaic waste assessment in Italy. *Renew. Sust. Energ. Rev.*, 41(Jan.): 99-112.
- Stephanie, W., Andreas, W. and Garvin, H. 2016. End-of-Life Management: Solar Photovoltaic Panels. UAE: International Renewable Energy Agency (IRENA).
- Tian, X., Stranks, S.D. and You, F., 2021. Life cycle assessment of recycling strategies for perovskite photovoltaic modules. *Nature Sustainability*, 4(9): 821-829.
- Xu, Y., Li, J.H., Tan, Q.Y., Peters, A.L. and Yang C.R. 2018. Global status of recycling waste solar panels: A review. *Waste Manage.*, 75: 450-458.
- Yan, Y.F., Zhang, Z.E., Zhang, L. and Dai, C.L. 2012. Application and utilization technology of solar energy. *Acta Energiæ Solaris Sinica*, 33(Suppl.): 47-56.

... Continued from inner front cover

- The text of the manuscript should run into **Abstract, Introduction, Materials & Methods, Results, Discussion, Acknowledgement** (if any) and **References** or other suitable headings in case of reviews and theoretically oriented papers. However, short communication can be submitted in running with **Abstract and References**. The references should be in full with the title of the paper.
- The figures should preferably be made on a computer with high resolution and should be capable of withstanding a reasonable reduction with the legends provided separately outside the figures. Photographs may be black and white or colour.
- Tables should be typed separately bearing a short title, preferably in vertical form. They should be of a size, which could easily be accommodated in the page of the Journal.
- References in the text should be cited by the authors' surname and year. In case of more than one reference of the same author in the same year, add suffix a,b,c,.... to the year. For example: (Thomas 1969, Mass 1973a, 1973b, Madony et al. 1990, Abasi & Soni 1991).

List of References

The references cited in the text should be arranged alphabetically by authors' surname in the following manner: (Note: The titles of the papers should be in running 'sentence case', while the titles of the books, reports, theses, journals, etc. should be in 'title case' with all words starting with CAPITAL letter.)

- Dutta, A. and Chaudhury, M. 1991. Removal of arsenic from groundwater by lime softening with powdered coal additive. *J. Water Supply Res. Techno. Aqua.*, 40(1) : 25-29.
- Hammer, D.A. (ed.) 1989. *Constructed Wetlands for Wastewater Treatment-Municipal, Industrial and Agricultural*. Lewis Publishers Inc., pp. 831.
- Haynes, R. J. 1986. Surface mining and wetland reclamation. In: Harper, J. and Plass, B. (eds.) *New Horizons for Mined Land Reclamation*. Proceedings of a National Meeting of the American Society for Surface Reclamation, Princeton, W.V.

Submission of Papers

- The paper can be submitted by e-mail as an attachment in a single WORD file at **contact@neptjournal.com**
- The paper can also be submitted online in a single WORD file through the **online submission portal** of journal's website: **www.neptjournal.com**

Attention

1. Any change in the authors' affiliation may please be notified at the earliest.
2. Please make all the correspondence by e-mail, and authors should always quote the manuscript number.

Note: In order to speed up the publication, authors are requested to correct the galley proof immediately after receipt. The galley proof must be checked with utmost care, as publishers owe no responsibility for mistakes. The papers will be put on priority for publication only after receiving the processing and publication charges.

Nature Environment and Pollution Technology

(Abbreviation: Nat. Env. Poll. Tech.)

(An International Quarterly Scientific Journal)

Published by



Technoscience Publications

A-504, Bliss Avenue, Opp. SKP Campus
Balewadi, Pune-411 045, Maharashtra, India

In association with

Technoscience Knowledge Communications

Mira Road, Mumbai, India

For further details of the Journal, please visit the website. All the papers published on a particular subject/topic or by any particular author in the journal can be searched and accessed by typing a keyword or name of the author in the 'Search' option on the Home page of the website. All the papers containing that keyword or author will be shown on the home page from where they can be directly downloaded.

www.neptjournal.com

©**Technoscience Publications:** The consent is hereby given that the copies of the articles published in this Journal can be made only for purely personal or internal use. The consent does not include copying for general distribution or sale of reprints.

Published for Proprietor, Printer and Publisher: Mrs. T. P. Goel, A-504, Bliss Avenue, Balewadi, Pune, Maharashtra, India; Editors: Dr. P. K. Goel (Chief Editor) and Prof. K. P. Sharma